



ERCOFTAC SERIES

Direct and Large-Eddy Simulation V

Edited by Rainer Friedrich,
Bernard J. Geurts and Olivier Métais



Springer Science+Business Media, B.V.

DIRECT AND LARGE-EDDY SIMULATION V

ERCRAFT SERIES

VOLUME 9

Series Editors

R.V.A. Oliemans, *Chairman ERCRAFT,*
Delft University of Technology, Delft, The Netherlands

W. Rodi, *Deputy Chairman ERCRAFT,*
Universität Karlsruhe, Karlsruhe, Germany

Aims and Scope of the Series

ERCRAFT (European Research Community on Flow, Turbulence and Combustion) was founded as an international association with scientific objectives in 1988. ERCRAFT strongly promotes joint efforts of European research institutes and industries that are active in the field of flow, turbulence and combustion, in order to enhance the exchange of technical and scientific information on fundamental and applied research and design. Each year, ERCRAFT organizes several meetings in the form of workshops, conferences and summerschools, where ERCRAFT members and other researchers meet and exchange information.

The ERCRAFT Series will publish the proceedings of ERCRAFT meetings, which cover all aspects of fluid mechanics. The series will comprise proceedings of conferences and workshops, and of textbooks presenting the material taught at summerschools.

The series covers the entire domain of fluid mechanics, which includes physical modelling, computational fluid dynamics including grid generation and turbulence modelling, measuring-techniques, flow visualization as applied to industrial flows, aerodynamics, combustion, geophysical and environmental flows, hydraulics, multi-phase flows, non-Newtonian flows, astrophysical flows, laminar, turbulent and transitional flows.

The titles published in this series are listed at the end of this volume.

Direct and Large-Eddy Simulation V

*Proceedings of the fifth international ERCOFTAC Workshop
on direct and large-eddy simulation,
held at the Munich University of Technology, August 27–29, 2003*

Edited by

RAINER FRIEDRICH

*Technische Universität München,
München, Germany*

BERNARD J. GEURTS

*University of Twente,
Enschede, The Netherlands*

and

OLIVIER MÉTAIS

*ENSHMG/INPG,
St Martin d'Hères, France*



Springer Science+Business Media, B.V.

A C.I.P. Catalogue record for this book is available from the Library of Congress.

ISBN 978-90-481-6575-9 ISBN 978-1-4020-2313-2 (eBook)
DOI 10.1007/978-1-4020-2313-2

Printed on acid-free paper

All Rights Reserved
© 2004 Springer Science+Business Media Dordrecht
Originally published by Kluwer Academic Publishers in 1988
Softcover reprint of the hardcover 1st edition

No part of this work may be reproduced, stored in a retrieval system, or transmitted in any form or by any means, electronic, mechanical, photocopying, microfilming, recording or otherwise, without written permission from the Publisher, with the exception of any material supplied specifically for the purpose of being entered and executed on a computer system, for exclusive use by the purchaser of the work.

Contents

Preface	xi
Part 1 ISSUES IN LES MODELING AND NUMERICS	
1.1 SUBGRID MODELING	3
Invited lecture: Nonlinear regularization for large-eddy simulation <i>Bernard J. Geurts, Darryl D. Holm</i>	5
Implicit and subgrid-scale modeling by adaptive local deconvolution <i>N. A. Adams</i>	15
Selective filtering versus eddy viscosity for subgrid modeling in LES <i>Christophe Bogey and Christophe Bailly</i>	23
High resolution DNS of a shear-free mixing layer and LES <i>O. Debligny, B. Knaepen, D. Desmidt, D. Carati</i>	31
A nonlinear interactions approximation model for LES <i>M.U.Haliloglu and R.Akhavan</i>	39
Two level simulation of high-Re turbulent flows <i>Konstantin Kemenov and Suresh Menon</i>	49
Analysis of relaxation regularization as subgrid-scale model for LES <i>S.B. Müller, N.A. Adams and L. Kleiser</i>	57
Relaxation-term models for LES of transitional/turbulent flows <i>P. Schlatter, S. Stolz & L. Kleiser</i>	65
Kolmogorov equation for LES and its use for subgrid modeling <i>L. Shao, J.P. Bertoglio, G.X. Cui, H.B. Zhou and Z.S. Zhang</i>	73
High-pass filtered eddy viscosity models for LES <i>S. Stolz, P. Schlatter, D. Meyer & L. Kleiser</i>	81

A synthesis of similarity and eddy-viscosity models <i>Roel Verstappen</i>	89
1.2 WALL MODELS FOR LES AND RELATED ISSUES	97
Development of wall models for LES based on NSE <i>Markus Abel, Dragan Stojković and Michael Breuer</i>	99
POD of the autonomous near-wall region in a minimal channel flow <i>D. Desmidts, O. Debliquy, B. Knaepen, D. Carati</i>	109
On the difficulties in resolving the viscous sublayer <i>Franz Durst and Kamen N. Beronov</i>	117
A priori tests of models for the mean and fluctuating wall shear stress <i>H.-J. Kaltenbach</i>	125
1.3 NUMERICAL TECHNIQUES AND ERROR ESTIMATION	133
Invited lecture: Symmetry-preserving discretization for DNS <i>R.W.C.P. Verstappen, M.T. Dröge and A.E.P. Veldman</i>	135
Three-dimensional adaptive wavelet method for fluid–structure interaction <i>N.K.-R. Kevlahan, O.V. Vasilyev, D. Goldstein and A. Jay</i>	147
Dynamics of commutator-errors in LES with non-uniform filter-width <i>Fedderik van der Bos, Bernard J. Geurts</i>	155
Identification of global error behavior in LES using a database approach <i>Johan Meyers, Bernard J. Geurts and Martine Baelmans</i>	163
Part 2 LAMINAR-TURBULENT TRANSITION	
2.1 INCOMPRESSIBLE FLOWS	173
Invited lecture: DNS of streak breakdown in boundary layers <i>Luca Brandt and Dan S. Henningson</i>	175
Numerical simulation of transition to turbulence in MHD channel flow <i>D.S. Krasnov, E. Zienicke, A. Thess, O. Zikanov, T. Boeck</i>	197
DNS of transitional and turbulent rotor-stator cavity flows <i>Eric Serre, Patrick Bontoux and Brian Launder</i>	205

<i>Contents</i>	vii
DNS of a laminar separation bubble affected by free-stream disturbances <i>Jan Wissink and Wolfgang Rodi</i>	213
2.2 COMPRESSIBLE FLOWS	221
DNS of transonic flow about a supercritical airfoil <i>Igor Klutchnikov and Josef Ballmann</i>	223
DNS and LES of the transition process in a laminar separation bubble <i>Olaf Marxen and Ulrich Rist</i>	231
Crossflow vortices near the attachment line of a swept airfoil at $M = 8$ <i>Jörn Sesterhenn and Rainer Friedrich</i>	241
Part 3 TURBULENT FLOWS INVOLVING COMPLEX PHYSICAL PHENOMENA	
3.1 MULTIPHASE AND NON-NEWTONIAN FLOWS	251
LES of small-scale ocean turbulence coupled with buoyant plumes <i>B. Chen, Y. Song, M. Nishio, M. Akai, Lars Golmen</i>	253
LES of turbulent bubble formation and break-up based on interface tracking <i>Petar Liovic, Djamel Lakehal and Jong-Leng Liow</i>	261
LES of a particle-laden turbulent channel flow <i>A.W. Vreman, B.J. Geurts, N.G. Deen and J.A.M. Kuipers</i>	271
Analogy between SGS model and constitutive equations for viscoelastic fluids <i>Kiyosi Horiuti</i>	279
Turbulent channel flow of a suspension of fibrous particles <i>Michael Manhart and Rainer Friedrich</i>	287
3.2 ACTIVE AND PASSIVE SCALARS	297
LES of a stably stratified flow over longitudinally ridged walls <i>V. Armenio, L. Falcomer, G. F. Carnevale</i>	299
LES of conjugate heat-transfer using thermal wall-functions <i>Alexandre Chatelain, Frédéric Ducros and Olivier Métais</i>	307
Modeling of a passive scalar in a turbulent pipe flow using DNS <i>J. de Hoogh, M.P.B. Veenman and J.G.M. Kuerten</i>	315

LES and extreme value theory <i>Zhengdong Xie, Peter R. Voke, Paul Hayden and Alan G. Robins</i>	323
3.3 NONPREMIXED AND PREMIXED TURBULENT COMBUSTION	333
Invited lecture: Simulation of three-dimensional turbulent flames <i>Dominique Thevenin</i>	335
Large-eddy simulation of a gas turbine combustion chamber <i>Christophe Duwig, Laszlo Fuchs</i>	343
Modeling of pollutant formation near lean blow-out in gas turbine engines <i>G. Eggenpieler and S. Menon</i>	351
Direct numerical simulation of turbulent non-premixed flames <i>Renan Hilbert and Dominique Thévenin</i>	359
Transient inflow-data for LES <i>A. Kempf, M. Klein, J. Janicka</i>	367
Enhancement of mixing and combustion in buoyant non-circular plumes <i>K. H. Luo</i>	375
3.4 COMPRESSIBLE TURBULENCE	385
Invited lecture: DNS of an oblique shock wave impinging upon a turbulent boundary layer <i>Qinling Li and Gary N. Coleman</i>	387
Large-eddy simulations of compressible mixing layers <i>C. Le Ribault</i>	397
On the turbulence structure in compressible turbulent isothermal channel flow <i>S. Sarkar, H. Foyi and R. Friedrich</i>	405
3.5 NOISE GENERATION AND RADIATION	413
Invited lecture: Noise radiation from high-speed jets: some insights from numerical simulations <i>Sanjiva K. Lele</i>	415
Flow patterns and sound generation in low speed cavities <i>E. J. Avital and R. E. Musafir</i>	431

<i>Contents</i>	ix
Direct numerical simulation of the acoustic field of a turbulent offset jet <i>Bendiks Jan Boersma</i>	439
 Part 4 TURBULENT FLOWS IN COMPLEX GEOMETRIES AND IN TECHNICAL APPLICATIONS	
4.1 LES-RANS COUPLING AND DETACHED EDDY SIMULATION	449
Invited lecture: Merging LES and RANS strategies: zonal or seamless coupling? <i>K. Hanjalić and M. Hadžiabdić, L. Temmerman and M. Leschziner</i>	451
Invited lecture: Detached-eddy simulation: current status and perspectives <i>Kyle D. Squires</i>	465
Detached-eddy simulation over a reference Ahmed car model <i>S. Kapadia, S. Roy, M. Vallero, K. Wurtzler and J. Forsythe</i>	481
LES and DES for broadband noise prediction in complex geometries <i>Massimiliano Ciardi and William N. Dawes</i>	489
4.2 EFFECTS OF WALL PERMEABILITY, ROUGHNESS AND PRESSURE-GRADIENT	499
Turbulent channel flow over a permeable wall <i>Wim-Paul Breugem & Bendiks-Jan Boersma</i>	501
Budgets of Reynolds stress in a rough wall channel flow <i>S. Leonardi, E. Mostarda, P. Orlandi, R.A. Antonia</i>	509
Effect of application/removal of adverse pressure gradient to wall layers <i>Christopher P. Yorke and Gary N. Coleman</i>	517
4.3 FLOWS INVOLVING STREAMLINE CURVATURE AND SWIRL	525
LES of turbulent flow in curved and S-shape ducts <i>Cécile Münch, Jérôme Hébrard and Olivier Métais</i>	527
LES of a flow with multiple streamwise curvatures <i>A. Silva Lopes, U. Piomelli and J.M.L.M. Palma</i>	537
Comparison of SGS models in swirling co-annular jets <i>Robert Zoltan Szasz, Johan Revstedt and Laszlo Fuchs</i>	545

4.4 FLOW CONTROL AND FLUID-STRUCTURE INTERACTION	555
LES of controlled turbulent flow over a rounded step <i>Jens Neumann and Hans Wengle</i>	557
Application of DNS and LES to prediction of tube flow-induced vibrations <i>Elisabeth Longatte, Zaky Bendjeddou, Mhamed Souli</i>	565
DNS of the flow around a cylinder using an immersed boundary method <i>E.R.A. Coyajee & B.J. Boersma</i>	573
Immersed boundary method for DNS in complex geometry <i>Philippe Parnaudeau, Eric Lamballais, Dominique Heitz, Jorge H. Silvestrini</i>	581
4.5 AERODYNAMIC AND TURBOMACHINERY FLOWS	591
Invited lecture: Perspectives of LES in turbomachinery design <i>Peter Flohr and Carlos Härtel</i>	593
Large-eddy simulation of a jet in a crossflow <i>Xuyao GUO, Matthias MEINKE and Wolfgang SCHRÖDER</i>	603
Separated flow past an airfoil at high angle of attack: LES predictions <i>Nikola Jovičić and Michael Breuer</i>	611
LES of cylinder wake T106 turbine blade interaction <i>M. Opiela, M. Meinke and W. Schröder</i>	619
LES of wake-blade interference in a low-pressure turbine <i>B. Raverdy, I. Mary, P. Sagaut, J.M. Roux</i>	627
LES of passing wakes influencing transition on turbine blades <i>S. Sarkar, Peter R Voke</i>	635
LES of flow in a low pressure turbine cascade with oncoming wakes <i>Jan Wissink, Wolfgang Rodi, Vittorio Michelassi</i>	643

Preface

The fifth ERCOFTAC workshop 'Direct and Large-Eddy Simulation-5' (DLES-5) was held at the Munich University of Technology, August 27-29, 2003. It is part of a series of workshops that originated at the University of Surrey in 1994 with the intention to provide a forum for presentation and discussion of recent developments in the field of direct and large-eddy simulation. Over the years the DLES-series has grown into a major international venue focussed on all aspects of DNS and LES, but also on hybrid methods like RANS/LES coupling and detached-eddy simulation designed to provide reliable answers to technical flow problems at reasonable computational cost.

DLES-5 was attended by 111 delegates from 15 countries. Its three-day programme covered ten invited lectures and 63 original contributions partially presented in parallel sessions. The workshop was financially supported by the following companies, institutions and organizations: ANSYS Germany GmbH, AUDI AG, BMW Group, ERCOFTAC, FORTVER (Bavarian Research Association on Combustion), JM BURGERS CENTRE for Fluid Dynamics. Their help is gratefully acknowledged.

The present Proceedings contain the written versions of nine invited lectures and fifty-nine selected and reviewed contributions which are organized in four parts:

- 1 Issues in LES modelling and numerics
- 2 Laminar-turbulent transition
- 3 Turbulent flows involving complex physical phenomena
- 4 Turbulent flows in complex geometries and in technical applications.

Part 1 combines three important topics, namely 'Subgrid modelling', 'Wall models for LES and related issues' and 'Numerical techniques and error estimation'. In their invited paper *B.J. Geurts and D.D. Holm* propose a nonlinear regularization formulation of the nonlinear convective Navier-Stokes fluxes which leads to new subgrid scale models with strongly improved accuracy of predictions compared to dynamic SGS models. *N.A. Adams* describes a new

approach to construct implicit SGS models based on adaptive local deconvolution. These models use the truncation error of the numerical discretization to handle the energy transfer at the cutoff wavenumber. Here, the discretization is adjusted to obtain an optimized implicit SGS model. The contributions by the team of *L. Kleiser* cover three aspects of improved SGS modelling. *Stolz et al.* discuss high-pass filtering employed to the resolved quantities prior to computing the eddy-viscosity and strain rate. It allows for good predictions of transitional and turbulent flows. SGS models based on relaxation regularization are investigated and applied to incompressible transitional and turbulent channel flow by *Schlatter et al.* They also examine the connection between aliasing errors and SGS modelling. Finally, *S.B. Muller et al.* connect the eddy-viscosity concept employed in the EDQNM theory with the relaxation term concept in the ADM formulation and assess the model properties for forced isotropic turbulence. *M.U. Haliloglu and R. Akhavan* propose a nonlinear interactions approximation model that uses graded filters and deconvolution to parameterize local interactions across the LES cutoff and an eddy viscosity term to treat the distant interactions. An unconventional SGS modelling approach is that of *L. Shao et al.* making use of the Kolmogorov equation for the resolved velocity field to derive new SGS models. *C. Bogey and C. Bailly* contrast the effect of explicit filtering of the resolved field variables with that of a dynamic Smagorinsky eddy-viscosity model in the LES of a high Reynolds number subsonic jet. *O. Debliquy et al.* perform a high resolution DNS of a shear-free mixing layer and LES with various isotropic SGS models to show that the main features of the flow are properly reproduced with these models. *R.W.C.P. Verstappen* comes up with a proposition to stabilize similarity SGS models by projecting them onto an eddy-viscosity model. This results in a self-calibrating eddy-viscosity and leads to surprisingly good predictions of high-Re channel flow. An alternative to LES for high-Re flows is suggested by *K. Kemenov and S. Menon*. It consists in decomposing the velocity vector into large-scale and small-scale components. A coupled system of equations has to be solved where the small scale equations are modelled without referring to eddy-viscosity assumptions.

Powerful wall models (section 1.2) are needed to make LES a tool to predict high Reynolds number wall-bounded flows reliably. A thorough understanding of the structure and dynamics of near-wall turbulence obviously is a useful prerequisite of modelling. To this end the work of *D. Desmidts et al.* decouples the wall layer from the outer layer and constructs an empirical eigenfunction basis (determined by POD) on which the low-dimensional dynamics of the near-wall flow is projected. *F. Durst and K.N. Beronov* investigate intermittency effects in the viscous sublayer of wall-bounded turbulence and errors arising primarily in the vertical velocity component in direct numerical simulations which unfortunately increase with higher resolution and affect 2nd and

4th order statistical moments. *M. Abel et al.* apply nonlinear stochastic estimation to derive generalizations of known algebraic wall models which are expected to provide improved predictions of separated flows. *K.-J. Kaltenbach* develops and validates models for the prediction of the fluctuating wall-shear stresses in separating and reattaching flows.

Besides modelling unresolved scales modern numerical techniques and error estimation play a viable role in these Proceedings (section 1.3). The invited paper of *R.W.C.P. Verstappen et al.* is a nice example of possible improvements in numerical accuracy of DNS results when discrete differential operators are used which possess the same conservation and dissipation properties as the continuous operators. The strategy is also generalized to flow problems with arbitrarily-shaped solid boundaries. *N.K.R. Kevlahan et al.* are the first to present a three-dimensional adaptive wavelet collocation method and to apply it to the flow past a sphere. This method may have the potential to reduce the overall computational effort based on uniform grids from a Re^3 - to a Re -proportionality. The paper by *F.v.d. Bos and B.J. Geurts* discusses effects of non-uniform filters in LES leading to commutator-errors and proposes to model these errors based on a material derivative of the filter-width and dimensional arguments. Using a database of DNS/LES of isotropic turbulence *J. Meyers et al.* investigate the global error of LES performed with eddy-viscosity SGS models as function of LES parameters and develop 'near-optimal refinement strategies' for practical LES.

Part 2 is dedicated to laminar-turbulent transition phenomena. In their invited paper *L. Brandt and D. Henningson* present direct simulation results of bypass transition in incompressible Blasius boundary layers. They focus on the breakdown of streamwise streaks by two different mechanisms, namely by nonlinear saturation of optimal perturbations in the case of steady, spanwise periodic basic flow and by free-stream turbulence. Both mechanisms lead to almost identical structures. *D.S. Krasnov et al.* investigate the process of instability and transition to turbulence in Hartmann flow and observe within a critical Reynolds number range of 350 to 400 that the streak breakdown scenario (coupled with realistic perturbation amplitudes) describes the transition process to turbulence in MHD flow successfully. A flow that involves laminar, transitional and turbulent regimes is that between a stationary and a rotating disc appearing in computer disc-drives. *E. Serre et al.* investigate this flow with a pseudo-spectral method and provide a useful database for SGS and statistical modelling. *J. Wissink and W. Rodi* present results of a series of DNS of laminar separation bubbles affected by different levels of free-stream disturbances. Separation occurs on a flat plate induced by an adverse streamwise pressure gradient. Free-stream perturbations trigger transition in the free shear layer surrounding the separation bubble and can even lead to its disappearance. A similar situation is encountered in flow over turbine blades. Hence, this ide-

alized situation serves to better understand the flow over turbine blades subject to periodically oncoming wakes. Among the three contributions dealing with transition in compressible flow, the one by *I. Klutchnikov and J. Ballmann* investigates the transonic flow about a supercritical airfoil at a Reynolds number based on chord-length of $Re_c = 2.14 \cdot 10^6$. A λ -shock develops on the upper side of the airfoil causing the boundary layer to separate and the free shear layer to generate vortices. The shock-boundary layer interaction process turns out to be highly unsteady. *O. Marxen and U. Rist* perform a DNS of laminar-turbulent transition in a separation bubble induced by strong local adverse pressure gradients and use this as a reference case to analyse an LES technique closely related to the ADM method. The unstable flow in the vicinity of the swept leading edge of a parabolic profile in supersonic flow is studied by *J. Sesterhenn and R. Friedrich* with special emphasis to understand the response of the boundary layer to random perturbations in the stagnation region. Both leading-edge and cross-flow instabilities are observed with the latter clearly dominating.

Turbulent flows involving complex physical phenomena are treated in part 3 starting with multiphase and Non-Newtonian flows. In section 3.1. *B. Chen et al.* combine an LES technique with two-fluid theory to simulate small-scale ocean turbulence coupled with buoyant plumes. Buoyant droplets are treated as a quasi-fluid in an Eulerian framework. *P. Liovic et al.* use LES and a VOF-based interface tracking technique in their contribution to predict bubble rise, fragmentation and coalescence phenomena which result from air venting into a water pool through a downcomer pipe. In their LES of particle-laden turbulent vertical channel flow *A.W. Vreman et al.* address the importance of taking into account particle collisions which leads to full four-way coupled models for detailed simulation. In the first of the two remaining papers on Non-Newtonian fluid flow, *K. Horiuti* highlights the analogy between the lowest-order approximation of the Bardina SGS stress and the conformation stress tensor of Oldroyd-A- and B-fluids used to predict flow of dilute polymer solutions. Its impact on the formation of turbulence structures in isotropic turbulence is worked out. *M. Manhart and R. Friedrich* use DNS to investigate the effect of drag reduction in turbulent channel flow by dilute suspensions of small fibrous particles in a Newtonian solvent. The constitutive equation for a single fibre incorporates the strain and rotation rates of the solvent fluid and Brownian motion. It is solved using a Monte Carlo method.

Effects of active and passive scalars are discussed in four papers in section 3.2. LES of turbulent flow in a stably-stratified open channel with longitudinal ridges along the bottom wall performed by *V. Armenio et al.* aims at answering the question how large-scale secondary motions which in neutrally stable situations contribute to vertical fluid transport are affected by stable stratification. LES of conjugate heat transfer, a topic of considerable industrial interest,

is investigated by A. Chatelain *et al.* using a wall function approach in order to reduce the computational effort. It is pointed out that standard approaches can lead to biased predictions and that more sophisticated solution strategies are needed. *J. de Hoogh et al.* perform DNS of passive scalar transport in fully developed turbulent pipe flow in order to test diffusion theory based on a Fokker-Planck equation for the PDF of the scalar concentration. A theory that is of great value in predicting the occurrence of rare events of scalar transport from LES or experimental data, is EVT (Extreme Value Theory). It is successfully used by *Z. Xie et al.* in predicting concentration fluctuations of passive plumes in a turbulent boundary layer over a rough wall using LES.

There are six papers dealing with nonpremixed and premixed turbulent combustion. The invited paper by D. Thevenin demonstrates that DNS of 3D turbulent methane/air flames is nowadays feasible even for low-temperature kinetics by prolongating the Intrinsic Low-Dimensional Manifold in combustion space using the laminar premixed flame structure. In a companion paper *R. Hilbert and D. Thevenin* use 2D DNS and detailed chemistry to describe the effect of differential diffusion on combustion of hydrogen in air in a turbulent non-premixed flame. The results show a strong impact of differential diffusion on the local flame structure. The contribution by *K.H. Luo* discusses 3D DNS results of mixing and combustion of buoyant reacting flows from rectangular, square and round sources. A one-step global reaction is simulated. Buoyancy effects result from the dynamics described by the full compressible Navier-Stokes equations without invoking the Boussinesq approximation. The data are used to construct two new SGS models for radiative heat transfer. The importance of generating suitable inflow conditions for LES of non-premixed flames is stressed by *A. Kempf et al.* A grid independent approach is presented and applied to jet flames. Two more papers are related to LES of combustion in gas turbines. *C. Duwig and L. Fuchs* investigate the influence of the subgrid flame thickness on a swirl stabilized flame using a premixed flamelet formulation in the LES framework. A parameter is defined which expresses the relative importance of the turbulent filtered flame speed and its thickness in comparison to the effective diffusivity. Its influence on the flame brush turns out to be significant. *G. Eggenspieler and S. Menon* report on LES of turbulent premixed combustion in a gas turbine engine close to lean blow out, a regime where classical flamelet assumption breaks down. A subgrid combustion model based on the linear-eddy mixing model is used along with transport models to predict pollutant (CO and NO) formation. The inclusion of unburned hydrocarbons turns out to be important in the CO emission prediction.

Traditionally, the compressible turbulence community is small. Three papers are included in section 3.4. The invited paper by *Q. Li and G.N. Coleman* is an investigation of oblique shock wave / turbulent boundary layer interaction by DNS at Mach 2. A new efficient technique of generating inflow conditions

for compressible wall-bounded turbulence is presented and applied. The impinging shock induces significant intrinsic compressibility effects forming a challenge for turbulence modellers. *C. Le Ribault* discusses LES results of spatially developing mixing layers obtained for two different dynamic SGS models. Convective Mach number effects are shown and compared with those obtained from experiment and DNS of Pantano and Sarkar (2002). The paper by *S. Sarkar et al.* provides scaling laws and conclusive explanations for the change in turbulence structure due to compressibility in fully developed channel flow along isothermal cooled walls.

The last topic in section 3.5 involving complex physics is noise generation by turbulent flow and its radiation into the far-field. In his invited paper *S.K. Lele* covers a broad range of aspects related to noise emanating from high-speed jets. Starting with features of such jets and their relationship to the radiated noise, analysed by DNS, the paper discusses the mechanism responsible for the generation of strong screech noise and implications of a new analytical model of shock-cell noise generation. *B.J. Boersma* uses DNS to study the flow and acoustic field of a subsonic round turbulent jet spreading parallel to a flat wall. He finds that a solid wall enhances the acoustic emission and also the angle under which the sound is emitted, a result which is in agreement with real life situations. *E.J. Avital and R.E. Musafir* couple incompressible LES with the Lighthill-Curle acoustic analogy in order to investigate flow patterns and sound generation in open cavities with different shape. Elliptic cavities turn out to produce lower dipole noise than box configurations.

Turbulent flows appearing in complex geometries and in technical applications form the topic of the fourth and last part. It includes prediction methods which deviate from the classical DNS/LES path, namely hybrid methods like LES/RANS coupling and detached-eddy simulation techniques. They are dealt with in section 4.1. The invited paper by *K. Hanjalic et al.* discusses issues related to zonal and seamless combinations of LES and URANS, designed for high Reynolds number flows. These promising methods are tested in fully developed turbulent channel flow on coarse grids. The invited paper by *K.D. Squires* provides an overview of the current status of detached-eddy simulation and its perspectives. This technique designed to predict massively separated flows avoids the Reynolds number limitations that plague LES and provides results the accuracy of which is typically superior to that of steady or unsteady RANS methods. Computations of flow around a fighter aircraft (F-15E) highlight the strengths of the DES method. The paper by *S. Kapadia et al.* presents, like most of the DES applications, DES results based on the Spalart-Allmaras model. The Ahmed reference car model with 25° and 35° slant angles is investigated using an unstructured grid method. Since the flow over the base slant in the experiments is attached at 25° and separated at 35° , its accurate prediction forms a challenge for statistical models, because

the boundary layer separation has to be predicted accurately. The paper by *M. Ciardi and W.N. Dawes* focusses on implementing four SGS models into an unstructured Navier-Stokes solver, tailored to broadband noise analysis in turbomachinery. It also addresses the problem of limiting the commutative error by using an implicit filter. Preliminary 2D tests of the ERCOFTAC square cylinder case are performed.

Section 4.2 deals with turbulence modification due to permeable, rough and non-stationary walls. *W.P. Bréugem and B.J. Boersma* pursue an interesting approach to compute turbulent flow over a permeable wall. They perform a volume averaging of the Navier-Stokes equations within the porous layer which leads to transport equations for a sort of pore-averaged velocity incorporating dispersion and drag terms and needs closure, similar to the filtered equations used in LES. Results show that wall permeability increases the friction factor and enhances turbulent mixing. Turbulent channel flow with a smooth and a rough wall, generated with the help of circular cylinders and square bars is investigated by *S. Leonardi et al.* using DNS. The roughness elements are treated with the immersed boundary technique of Fadlun et al. (2000). Budgets of the four Reynolds stress components are analyzed in order to clarify the mechanisms by which these components are enhanced on the rough wall side. *C.P. Yorke and G.N. Coleman* apply an ingenious method to generate and remove adverse pressure gradients (APG) in DNS of turbulent channel flow with periodic boundary conditions. They reproduce, e.g., the irrotational plane strain found in an APG boundary layer by streamwise compression of the flow domain and wall normal divergence. The work aims at better understanding the dominant mechanisms controlling APG boundary layers and improving turbulence models.

Flows involving streamline curvature and swirl are the subject of section 4.3. The paper of *C. Münch et al.* presents large-eddy simulations of turbulent weakly compressible flow in a curved and S-shaped duct of square cross section using the selective structure function model. The simulations mimic the transport of heat in cooling channels of heat exchangers and reveal the enhancing and inhibiting effect of concave and convex wall curvature on the heat flux. Effects of multiple streamline curvature in a duct are predicted by *A. Silva Lopes et al.* using LES and a Lagrangian-dynamic eddy-viscosity SGS model. Zones of flow transition from convex to concave curvature and vice versa are of special concern since they produce major changes in the turbulence structure and lead to instantaneous separation with time-dependent recirculation bubbles. *R.Z. Szasz et al.* perform LES of momentum and passive scalar transport in swirling co-annular jets with various SGS models in order to reveal their influence on the flow field and mixing characteristics.

Control of turbulent flow and interaction of turbulent flow with elastic structures are the themes of two papers in section 4.4. Two more papers discuss im-

mersed boundary methods that are very well suited for fluid structure interaction simulations. *J. Neumann and H. Wengle* perform LES of a controlled turbulent flow over a rounded backstep. The incoming turbulent boundary layer is either passively controlled by a surface-mounted fence or actively by blowing/suction. The impact of the specific control mechanism, the position of the control device and the amplitude as well as frequency of the forcing (in the active case) are thoroughly investigated. The paper by *E. Longatte et al.* provides an overview of the use of DNS and LES techniques to the prediction of flow-induced vibrations in tube-bundles. Near-wall fluid forces acting on the tubes are estimated, e.g., in terms of spectral density obtained from LES in the case of weak coupling. Modal spectral calculations are carried out to compute the tube dynamic response. The fully coupled problem is treated as well. The immersed boundary method described by *E.R.A. Coyajee and B.J. Boersma* represents complex geometries on a regular Cartesian grid and enables highly efficient flow calculations based on second-order central finite differences. It is tested in a DNS of flow around a circular cylinder. The technique presented by *P. Parnaudeau et al.* combines a direct forcing method with high-order compact schemes in order to represent solid walls of arbitrary shape. Results of flow around circular cylinders demonstrate improvements achieved with this new approach.

Flows of practical relevance appearing in aerodynamic and turbomachinery applications are at the heart of section 4.5. The invited paper by *P. Flohr and C. Hartel* contributes a case study for LES in turbomachinery flows, analyzing the flow and mixing pattern in a swirl-stabilized gas turbine burner. By demonstrating the fact that such flows can only be properly predicted with unsteady simulations, this paper underlines the potential of LES in gas turbine combustors. The highly complex flow phenomenon of a round jet in a turbulent crossflow at high local Reynolds numbers, is predicted and analyzed in detail by *X. Guo et al.* using LES. The separated flow past an airfoil at high angle of attack and confined between two parallel walls to provide well-defined upper and lower boundary conditions is studied by *N. Jovicic and M. Breuer* using LES. Due to a laminar separation bubble on the upper side of the profile, subsequent transition to turbulence and turbulent separation in the rear part, this flow forms a challenge for LES. *M. Opiela et al.* apply LES to predict the effect of an upstream wake on the flow around a low-pressure turbine blade. A sliding interface technique is used to ensure flux conservation in the numerical scheme between the rotor and stator sides. The comparison with time-averaged experimental data for various Reynolds and Mach numbers shows good agreement. The same flow configuration is investigated also by *B. Raverdy et al.* using well-resolved LES and a sliding interface technique. Only the lowest Reynolds number case is analyzed, but with two different SGS models showing good agreement with experimental data. A slightly different approach to

predict the effect of cylinder wakes on a turbine blade has been used in an LES by *S. Sarkar and P. Voke*. Here, the cylinder wake is generated in a precursor simulation and the flow data are interpolated onto the grid of the inlet plane to the turbine cascade. Flow data are collected and phase-averaged over 8 wake passing cycles in order to provide insight into the underlying physical mechanisms. Finally, *J. Wissink et al.* present large-eddy simulations of flow in a modern highly loaded turbine cascade affected by impinging wakes which result from cylinders upstream. For weak wakes and low wake-frequency a natural transition scenario is found in the simulation on the blade suction side, while strong wakes and high wake-frequencies give evidence of a by-pass transition scenario.

The organizers take this opportunity to thank all the scientists who, through their valuable contributions, made DLES-5 a real success. They also express their hope that the material contained in these Proceedings will inspire future developments. Finally, they wish to express their appreciation to the responsible persons of Kluwer Academic Publishers for producing this volume in a short time.

Rainer Friedrich, Bernard Geurts, Olivier Métais
München, November 2003

ISSUES IN LES MODELING AND NUMERICS

1.1 SUBGRID MODELING

NONLINEAR REGULARIZATION FOR LARGE-EDDY SIMULATION

Bernard J. Geurts

Mathematical Sciences, J.M. Burgers Center, University of Twente, P.O. Box 217, 7500 AE Enschede, The Netherlands

Darryl D. Holm

*Theoretical Division, Los Alamos National Laboratory, Los Alamos, NM 87545, USA
and*

Mathematics Department, Imperial College London, SW7 2AZ, London UK

Abstract We review the spatial filtering approach to large-eddy simulation and describe the intuitive dissipation and similarity requirements, commonly imposed on models for the turbulent stress. Then we present direct regularization of the nonlinear convective flux which provides a systematic framework for *deriving* the implied subgrid model. This approach allows one to incorporate several rigorous mathematical properties of solutions to the Navier-Stokes system into the modeled large-eddy formulation. Regularization maintains the central transport structure of the governing equations. We illustrate the approach with Leray regularization and the Lagrangian averaged Navier-Stokes- α model. The new subgrid models are applied to turbulent mixing. These models display a strongly improved accuracy of predictions compared to dynamic subgrid models, as well as robustness at high Reynolds number.

Keywords: Regularization, turbulence, large-eddy simulation, Kelvin theorem

1. Introduction

Modern strategies for the computation of turbulent flow are aimed at reducing the dynamical complexity of the Navier-Stokes solutions, while reliably retaining their primary flow phenomena. In large-eddy simulation (LES) a balance of these two requirements is approached through subgrid modeling, designed to compensate for a coarsened numerical description. LES coarsening is achieved by spatial filtering $L : u_i \rightarrow \bar{u}_i$ where \bar{u}_i (resp. u_i) denotes the filtered (resp. unfiltered) component of the velocity field in the x_i direction. Spatial filtering selects the physical detail that will be retained in the LES solution; moreover, it gives rise to the central closure problem in LES.

Clearly, the adopted spatial filter L defines all aspects of the flow smoothing. Among others, L should identify the subgrid model. However, subgrid models for LES have traditionally been obtained through physical or mathematical reasoning that may be only loosely connected to a specified filter L . For example, traditional subgrid modeling approaches are primarily based on dissipation and similarity considerations (e.g., Geurts, 2003).

In contrast to this traditional LES modeling, the regularization approach is based on an explicit alteration of the convective nonlinearity and the introduction of a filter and its (formal) inverse: (L, L^{-1}) . In this setting the adopted regularization principle specifies both the implied subgrid model and the interpretation of its LES predictions in terms of reference DNS results. This modeling strategy has a number of benefits. For example, it addresses directly the filtered nonlinear convective contributions instead of ‘manually’ adding smoothing through eddy-viscosity. Moreover, it requires no ‘external’ *ad hoc* parameters. Proper regularization principles make the modeled system of equations to adhere to certain fundamental properties of the Navier-Stokes equations in a transparent way, maintaining, e.g., symmetries, transformation properties, Kelvin’s circulation theorem, Karman-Howarth theorem, etc. Finally, the implied model is quite simple to implement, with the major technical complication arising from the construction of an accurate inverse operator L^{-1} .

The organization of this paper is as follows. In section 2 we review the filtering approach to large-eddy simulation and discuss traditional subgrid modeling based on dissipation and similarity considerations. Then we consider the benefits of direct regularization of the convective fluxes in section 3. The corresponding subgrid models are tested in turbulent mixing and compared to dynamic subgrid models in section 4. Concluding remarks are in section 5.

2. Filtering for large-eddy simulation

In this section we shall briefly review the spatial filtering formulation for large-eddy simulation. Moreover, we will sketch the central intuitive features of dissipation and similarity that are often ascribed to turbulent stress models. We also discuss the dynamic procedure used to optimize parameters in a subgrid model in accordance with the local, instantaneous flow.

Filtering the Navier-Stokes equations requires a spatial filter, L . For convenience we consider a convolution filter in one spatial dimension:

$$\bar{u} = L(u) = \int G_{\Delta}(x - \xi)u(\xi) d\xi = G_{\Delta} * u \quad (1)$$

with normalized filter-kernel G_{Δ} characterized by a width Δ . For incompressible fluids, the application of the filter L leads to:

$$\partial_j \bar{u}_j = 0 \quad ; \quad \partial_t \bar{u}_i + \partial_j (\bar{u}_j \bar{u}_i) + \partial_i \bar{p} - \frac{1}{Re} \partial_{jj} \bar{u}_i = -\partial_j (\bar{u}_i \bar{u}_j - \bar{u}_j \bar{u}_i) \quad (2)$$

Here ∂_t (resp. ∂_j) denotes partial differentiation with respect to time t (resp. spatial coordinate x_j). The component of velocity in the x_j direction is \bar{u}_j and \bar{p} is the filtered pressure. In this formulation of the ‘LES-template’ we recognize the application of the ‘Navier-Stokes operator’ to the filtered solution $\{\bar{u}_j, \bar{p}\}$ on the left-hand side. On the right-hand side the turbulent stress tensor $\tau_{ij} = \overline{u_i u_j} - \bar{u}_i \bar{u}_j$ appears. This tensor can not be evaluated from the filtered solution alone and hence a closure problem arises. One of the central aims in the development of successful large-eddy simulations is the effective capturing of the dynamical relevance of τ_{ij} in terms of model tensors that can be evaluated using the filtered solution.

In the absence of a comprehensive theory of turbulence, empirical knowledge about modeling τ_{ij} is essential, but it is rather incomplete. Commonly, LES subgrid models are proposed on the basis of their presumed dissipative nature, or in view of the similarity of τ_{ij} in an inertial range (Meneveau, Katz, 2000). As further guidance in the construction of suitable models, one may attempt to incorporate constraints associated with rigorous properties of the modeling problem such as realizability conditions (Vreman *et al.*, 1994), algebraic identities (M Germano, 1992) or approximate inversion of the filter (Geurts, 1997, Kuerten *et al.*, 1999; Stolz, Adams, 1999). While realizability conditions may impose bounds on certain model parameters, the incorporation of algebraic identities such as Germano’s identity has led to a successful class of so called ‘dynamic’ subgrid models.

Dissipation of turbulent kinetic energy is parameterized in eddy-viscosity models. The earliest of these was Smagorinsky’s model (Smagorinsky, 1963):

$$\tau_{ij} \rightarrow m_{ij}^S = -(C_S \Delta)^2 |S| S_{ij} \quad (3)$$

where C_S denotes Smagorinsky’s constant, Δ is the grid scale, $S_{ij} = \partial_i \bar{u}_j + \partial_j \bar{u}_i$ is the rate of strain tensor and $|S|^2 = S_{ij} S_{ij}$ is its magnitude. The similarity aspects of the closure problem were first parameterized by the Bardina model (Bardina *et al.*, 1984):

$$\tau_{ij} \rightarrow m_{ij}^B = \overline{\bar{u}_i \bar{u}_j} - \bar{u}_i \bar{u}_j \quad (4)$$

Thus, the Bardina model applies the definition of τ_{ij} to the filtered velocity.

These subgrid models separately describe important intuitive features of the turbulent stresses. However, these models are well known to be seriously flawed in their own ways. The Smagorinsky model displays low levels of correlation with τ_{ij} and often leads to excessive dissipation, especially near solid walls and in laminar flows with large gradients. This may even hinder a modeled flow from going through a complete transition to turbulence. The similarity model of Bardina is known to display high correlation, but it fails to provide effective dissipation of energy and it may give rise to unrealistically high levels of small scale fluctuations in the solution. For these

reasons, so-called ‘mixed’ models have been proposed which combine similarity with eddy-viscosity models. As an example, a basic mixed model is $\tau_{ij} \rightarrow m_{ij}^M = m_{ij}^B - C_d \Delta^2 |S| S_{ij}$ in which C_d denotes the ‘dynamic’ eddy coefficient. The central problem that now arises is how the dynamic coefficient should be specified in accordance with the evolving flow. A well-known and elegant way to achieve this without unduly introducing ad hoc parameters is based on Germano’s identity (M Germano, 1992).

In dynamic models the eddy-viscosity is intended to reflect local instantaneous turbulence levels. One starts from Germano’s identity: $T_{ij} - \widehat{\tau}_{ij} = R_{ij}$, where $T_{ij} = \widehat{\overline{u_i u_j}} - \widehat{\overline{u_i}} \widehat{\overline{u_j}}$ and $R_{ij} = \overline{(\widehat{u_i} \widehat{u_j})} - \widehat{\overline{u_i}} \widehat{\overline{u_j}}$. Here, in addition to the basic LES-filter $(\overline{\cdot})$ of width $\overline{\Delta}$, a so-called ‘test’-filter $(\widehat{\cdot})$ of width $\widehat{\Delta}$ is introduced. The only external parameter to be specified is the ratio of filter widths, which is commonly assigned as $\widehat{\Delta}/\overline{\Delta} = 2$.

The implementation for obtaining optimal model parameters starts by assuming a mixed model $m_{ij} = a_{ij}(\overline{\mathbf{u}}) + cb_{ij}(\overline{\mathbf{u}})$ for τ_{ij} and $M_{ij} = A_{ij} + cB_{ij}$ for T_{ij} where $A_{ij} = a_{ij}(\widehat{\overline{\mathbf{u}}})$, $B_{ij} = b_{ij}(\widehat{\overline{\mathbf{u}}})$. Here a_{ij} and b_{ij} express assumed basic models. Insertion in Germano’s identity yields $\mathcal{A}_{ij} + c\mathcal{B}_{ij} = R_{ij}$ where $\mathcal{A}_{ij} = A_{ij} + \widehat{a_{ij}}$, $\mathcal{B}_{ij} = B_{ij} + \widehat{b_{ij}}$ and we used the approximation $\widehat{cb_{ij}} \approx c\widehat{b_{ij}}$. In a least squares optimization we can solve the local coefficient as (Lilly, 1992)

$$c = \frac{\langle (R_{ij} - \mathcal{A}_{ij}) \mathcal{B}_{ij} \rangle}{\langle \mathcal{B}_{ij} \mathcal{B}_{ij} \rangle} \quad (5)$$

where we assumed $\langle c f g \rangle \approx c \langle f g \rangle$. The additional averaging operator $\langle f \rangle$ is usually defined in terms of an integration over homogeneous directions of the flow-domain (Ghosal, 1999). In complex flow-domains, averaging over homogeneous directions may no longer be possible or sufficient to smoothen fluctuations in c . Taking an average over t may provide a workable solution. In order to prevent numerical instability caused by negative values of the eddy-viscosity, the dynamic coefficient is also artificially set to zero where (5) returns negative values. This is referred to as ‘clipping’.

Dynamic models have become popular in LES but they suffer from some important drawbacks. The dynamic procedure is quite expensive and the implementation contains a number of ad hoc features or inaccurate assumptions. Moreover, the achieved accuracy remains quite limited due to shortcomings in the assumed base models. Since the dynamic approach does not contain ad hoc parameters, there is no chance of improving the predictions by ‘tinkering’ with parameters. Finally, an extension to flows involving complex physics and/or developing in complex domains is difficult since no rigorous systematic framework exists for this purpose.

For these reasons, an alternative modeling approach is summoned and we turn to the recently proposed regularization modeling (Geurts, Holm, 2003).

Regularization *does* provide a systematic mathematical framework for *deriving* a subgrid model. This is in sharp contrast with traditional subgrid modeling in which the desired smoothing of a turbulent flow is achieved only indirectly through the introduction of an eddy-viscosity. However, introducing diffusion by eddy-viscosity does not do justice to the intricacies of turbulent transport phenomena; it can at best perhaps characterize effective statistical properties of the kinetic energy dynamics.

Applying a specific filter in a regularization of Navier-Stokes equations allows one to obtain systematically the implied subgrid closure and to incorporate rigorous mathematical properties and energy balances from first principles into the modeled equations. The central question then becomes, “Which physical principles lead to successful regularization for turbulent flow?” We turn to this in the next section and discuss the formal similarities between the regularization approach and the large-eddy formulation.

3. Derivation of implied subgrid models: connection to large-eddy simulation

In this section we consider two regularization principles and derive the associated subgrid models in case the basic filter L has an inverse L^{-1} (Geurts, Holm, 2003). We consider Leray regularization (Leray, 1934) and the Lagrangian averaged Navier-Stokes- α (LANS- α) approach (Foias *et al.*, 2001).

A mathematically rigorous modeling approach for large-eddy simulation can be obtained by combining a ‘regularization principle’ with an explicit filter and its inversion on the given mesh (Geurts, Holm, 2003). Historically, the first example of a smoothed flow description in this category is the Leray regularization (Leray, 1934). Although this regularization was introduced for entirely different reasons, we may reinterpret the Leray proposal in terms of its implied subgrid-model. This provides the connection with large-eddy simulation.

In Leray regularization one alters the convective fluxes into $\bar{u}_j \partial_j u_i$, i.e., the solution \mathbf{u} is convected with a smoothed velocity $\bar{\mathbf{u}}$. Consequently, the nonlinear effects are reduced by an amount governed by the smoothing properties of the filter operation, L . The governing Leray equations are (Leray, 1934)

$$\partial_j \bar{u}_j = 0 \quad ; \quad \partial_t u_i + \bar{u}_j \partial_j u_i + \partial_i p - \frac{1}{Re} \partial_{jj} u_i = 0 \quad (6)$$

For proper filters, Leray solutions possess global existence and uniqueness. That is, they possess proper smoothness and boundedness, whose demonstration depends on the energy balance for $\int |\mathbf{u}|^2 d^3x$. Based on the Leray equations (6) we may eliminate \mathbf{u} by assuming $\bar{\mathbf{u}} = L(\mathbf{u})$ and $\mathbf{u} = L^{-1}(\bar{\mathbf{u}})$. For convolution filters one may derive after some manipulation

$$\partial_t \bar{u}_i + \partial_j (\bar{u}_j \bar{u}_i) + \partial_i \bar{p} - \frac{1}{Re} \partial_{jj} \bar{u}_i = -\partial_j \left(m_{ij}^L \right) \quad (7)$$

The implied asymmetric, filtered similarity-type Leray model m_{ij}^L is:

$$m_{ij}^L = L\left(\overline{u_j} L^{-1}(\overline{u_i})\right) - \overline{u_j} \overline{u_i} = \overline{\overline{u_j} u_i} - \overline{u_j} \overline{u_i} \quad (8)$$

Simulations based on this model remain stable at arbitrarily high Reynolds numbers (Geurts, Holm, 2003). In (8) the reconstructed solution u_i is found from any formal or approximate inversion L^{-1} . For this purpose one may use a number of methods, e.g., polynomial inversion (Geurts, 1997), geometric series expansions (Stolz, Adams, 1999) or exact numerical inversion of Simpson top-hat filtering (Kuersten *et al.*, 1999).

A regularization principle which additionally possesses correct circulation properties may be obtained by starting from the following Kelvin theorem:

$$\frac{d}{dt} \oint_{\Gamma(\mathbf{u})} u_j dx_j - \frac{1}{Re} \oint_{\Gamma(\mathbf{u})} \partial_{kk} u_j dx_j = 0 \quad (9)$$

where $\Gamma(\mathbf{u})$ is a closed fluid loop moving with the Eulerian velocity \mathbf{u} . The derivation of the Navier-Stokes equations from (9) was used to inspire a guiding regularization principle for Navier-Stokes turbulence (Foiás *et al.*, 2001). In fact, the basic regularization principle was originally derived by applying Taylor's hypothesis of frozen-in turbulence in a Lagrangian averaging framework (Holm, 1999). In this framework, the fluid loop is considered to move with the smoothed 'transport' velocity $\overline{\mathbf{u}}$, although the circulation velocity is still the unsmoothed velocity, \mathbf{u} . That is, in (9) we replace $\Gamma(\mathbf{u})$ by $\Gamma(\overline{\mathbf{u}})$. From this filtered Kelvin principle, we may obtain the Euler-Poincaré equations governing the smoothed solenoidal fluid dynamics, with $\partial_i \overline{u_i} = 0$ and

$$\partial_t u_j + \overline{u_k} \partial_k u_j + u_k \partial_j \overline{u_k} + \partial_j p - \partial_j \left(\frac{1}{2} \overline{u_k} u_k \right) - \frac{1}{Re} \partial_{kk} u_j = 0 \quad (10)$$

For the specific Helmholtz operator $u_i = (1 - \alpha^2 \partial_{jj}) \overline{u_i} = \text{He}_\alpha(\overline{u_i})$ we recover the LANS- α equations (Foiás *et al.*, 2001). The LANS- α model derives its name from the length-scale parameter $\alpha \approx \Delta/5$ (Geurts, Holm, 2002). Comparison with the Leray regularization principle in (6) reveals two additional terms in (10). These terms guarantee the regularized flow to be consistent with the modified Kelvin circulation theorem with $\Gamma(\mathbf{u}) \rightarrow \Gamma(\overline{\mathbf{u}})$. For LANS- α the analytical properties of the regularized solution are based on the energy balance for $\int \mathbf{u} \cdot L(\mathbf{u}) d^3x$.

The Kelvin-filtered equation (10) can also be rewritten in the form of the LES template. The extra terms that arise in (10) in order to maintain the Kelvin circulation theorem also yield additional terms in the implied subgrid model:

$$\begin{aligned} \partial_t \overline{u_i} &+ \partial_j (\overline{u_j} \overline{u_i}) + \partial_i \overline{p} - \frac{1}{Re} \partial_{jj} \overline{u_i} \\ &= -\partial_j \left(\overline{\overline{u_j} u_i} - \overline{u_j} \overline{u_i} \right) - \frac{1}{2} \left(\overline{u_j \partial_i \overline{u_j}} - \overline{u_j} \partial_i \overline{u_j} \right) \end{aligned} \quad (11)$$

We observe that the Leray model (8) reappears as part of the LANS- α model. The additional second term on the right hand side takes care of recovering the Kelvin circulation theorem for the smoothed solution. This formulation is given in terms of a general filter L and its inverse. After some further rewriting it may be shown that this model can be formulated fully in conservative form, i.e., a tensor m_{ij}^α can be found such that the right hand side of (11) can be written as $-\partial_j m_{ij}^\alpha$.

The subgrid scale model presented in (11) can be specified further when a particular class of filters is considered. For the case in which the Helmholtz operator He_α is used, the following parameterization for the turbulent stress tensor is obtained:

$$m_{ij}^\alpha = \alpha^2 \text{He}_\alpha^{-1} \left(\partial_k \bar{u}_i \partial_k \bar{u}_j + \partial_k \bar{u}_i \partial_j \bar{u}_k - \partial_i \bar{u}_k \partial_j \bar{u}_k \right) \quad (12)$$

This formulation recovers the LANS- α model reviewed in (Foias *et al.*, 2001) and studied numerically in (Geurts, Holm, 2002). The subgrid model m_{ij}^α has three distinct contributions. The first term on the right-hand side is the *Helmholtz-filtered* tensor-diffusivity model. The second term combined with the first term, corresponds to Leray regularization using Helmholtz inversion as filter. The third term completes the LANS- α model and maintains Kelvin's circulation theorem. In (12) an inversion of the Helmholtz operator He_α is required which implies application of the 'exponential' filter (M. Germano, 1986). However, since the Taylor expansion of the exponential filter is identical at quadratic order to that of the top-hat or the Gaussian filters, one may approximate He_α^{-1} , e.g., by an application of the explicit top-hat filter, for reasons of computational efficiency.

Although the regularized turbulence equations (11) and the 'subgrid stress' (12) are formally similar to LES turbulence equations, they arose from different principles. In fact the LANS- α formulation arose by combining Lagrangian averaging with Taylor's hypothesis of frozen-in turbulent fluctuations (Holm, 1999). The literature underlying this derivation will not be discussed here. Instead, we emphasize that, through the combination of an explicit filter and its inversion, the regularization principle allows a systematic derivation of the implied subgrid-model. This resolves the closure problem consistent with the adopted filter. Even though the LANS- α formulation may be interpreted *a posteriori* in terms of an implied subgrid-model, the regularization equations were not obtained by applying the LES filtering method. We emphasize that this approach to modeling turbulence from the viewpoint of mathematical regularization is an *alternative* to LES, whose results may be related to the filtering approach to LES, but they are not derivable from it.

4. Regularization modeling of turbulent mixing

In this section we present some simulation results obtained with the Leray, LANS- α and dynamic eddy-viscosity model. We consider flow in a temporal mixing layer (Vreman, *et al.*, 1997) at a moderate Reynolds number $Re = 50$ based on the upper stream velocity and half the initial vorticity thickness. The flow displays a rapid mixing transition to small scale turbulence. The large-eddy simulations of this flow adopted a second order accurate finite volume spatial discretization, combined with explicit Runge-Kutta time-stepping. We consider LES on a number of grids with 32^3 , 64^3 and 96^3 cells while keeping $\Delta = \ell/16$. Here, ℓ denotes the length of the side of the cubical computational domain that was used. In this way we can separately influence the numerical errors in the description and assess the quality of the (approximately) grid-independent simulation (Geurts, Froehlich, 2002).

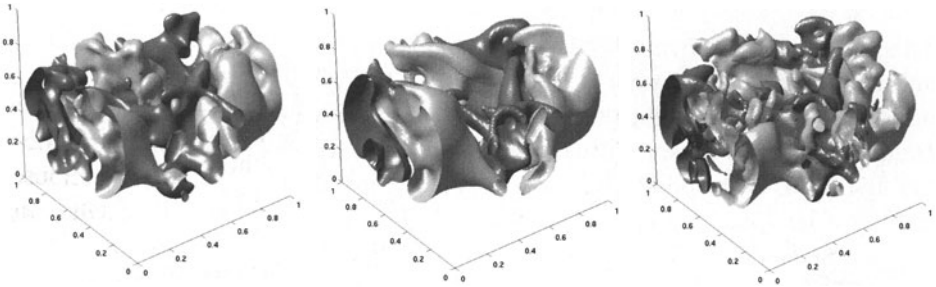


Figure 1. Snapshots of the vertical velocity in the turbulent regime at $t = 80$; light (dark) surface corresponds to $u_2 = 0.3$ ($u_2 = -0.3$). From left to right: filtered DNS at 192^3 , Leray prediction and LANS- α using $\Delta = \ell/16$ and a resolution of 96^3 .

A first introductory test of the subgrid models is obtained by studying structures in instantaneous solutions. As a typical illustration of the mixing layer, the filtered DNS prediction of the vertical velocity, and the corresponding Leray and LANS- α results are shown in the turbulent regime in Fig. 1. We approximately eliminated the spatial discretization effects by using $\Delta = \ell/16$ and a resolution of 96^3 . This allows us to separately assess the quality of the subgrid models in predicting the physical aspects of the flow, without the interference of discretization errors. Even at the instantaneous solution level, both the Leray and LANS- α models capture the ‘character’ of the filtered solution. While the Leray prediction appears to provide a slight under-prediction of the influence of the small scales, the LANS- α result appears to correspond more closely with the filtered DNS findings, restoring some of the small scale variability. These instantaneous predictions are both much better than those obtained with the dynamic eddy-viscosity model which turn out to be too smooth.

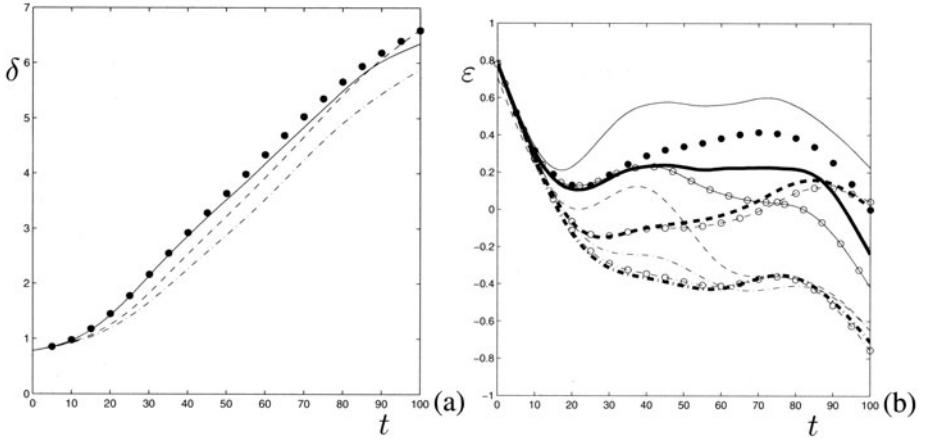


Figure 2. Momentum thickness δ for $\Delta = \ell/16$ and three LES models: LANS- α (solid), Leray (dashed) and dynamic model (dash-dotted), compared with filtered DNS (solid circles). In (a) the approximately grid-independent prediction at 96^3 is shown; in (b) convergence toward the grid-independent solution is illustrated with $\varepsilon(t) = \delta_{LES}(t) - \delta_{DNS}(t^*)(t/t^*)$ for $t^* = 100$: 32^3 : no markers, 64^3 : open circles and 96^3 : thick lines.

The evolution of a crucial mean-flow property such as the momentum thickness is shown in Fig. 2. First, we concentrated on the grid-independent predictions obtained at 96^3 . We observe a strong improvement of the predictions using Leray or LANS- α compared to the dynamic model predictions. The LANS- α results agree almost perfectly with the filtered DNS results. In Fig. 2(b) we consider the convergence of the predictions as a function of spatial resolution. We observe that the dynamic model results are less accurate but numerically captured well already at 32^3 while the Leray predictions require 64^3 cells in order to attain their full potential. The results of the LANS- α model are slightly more sensitive and show near grid-independence at 96^3 .

5. Concluding remarks

In this paper we reviewed the filtering approach to large-eddy simulation and proposed an alternative ‘regularization’ formulation to obtain accurate and robust descriptions of the smoothed turbulence dynamics. Proper regularization principles imply that the smoothed description has a unique, strong solution and the modeled system of equations possesses an attractor of finite dimension. This contributes to the ‘computability’ of the solution and illustrates that one may incorporate from first principles, various rigorous mathematical properties of (filtered) Navier-Stokes solutions into the modeled LES system.

The ‘mixed’ formulation of regularized flow descriptions in terms of the filtered as well as the unfiltered solution can be turned into one involving the

filtered solution alone, by incorporating the (formal, approximate) inverse L^{-1} of the filter L . The implied subgrid model can directly be derived from the adopted regularization principle, which renders the modeling processes not only theoretically transparent and mathematically sound, but, as illustrated for turbulent mixing flow, leads also to accurate and robust subgrid models, which compare well against popular dynamic modeling.

References

- Bardina, J., Ferziger, J.H., Reynolds, W.C.: 1984. Improved turbulence models based on LES of homogeneous incompressible turbulent flows. Department of Mechanical Engineering. *Report No. TF-19*, Stanford.
- Foias, C., Holm, D.D., Titi, E.S.: 2001. The Navier-Stokes-alpha model of fluid turbulence. *Physica D*, **152**, 505.
- Germano, M.: 1986. Differential filters for the large-eddy numerical simulation of turbulent flows. *Phys. of Fluids*, **29**, 1755.
- Germano, M.: 1992. Turbulence: the filtering approach. *J. Fluid Mech.*, **238**, 325.
- Geurts, B.J.: 1997. Inverse modeling for large-eddy simulation. *Phys. of Fluids*, **9**, 3585.
- Geurts, B.J., Froehlich, J.: 2002. A framework for predicting accuracy limitations in large-eddy simulation. *Phys. of fluids*, **14**, L41.
- Geurts, B.J., Holm, D.D.: 2002. Alpha-modeling strategy for LES of turbulent mixing. *Turbulent Flow Computation*. Eds: D. Drikakis, B.J. Geurts. Fluid mechanics and its applications 66, Kluwer Academic Publishers, 237.
- Geurts, B.J., Holm, D.D.: 2003. Regularization modeling for large-eddy simulation. *Phys. of Fluids*, **15**, L13.
- Geurts, B.J.: 2003. Elements of direct and large-eddy simulation. *Edwards Publishing, Inc.*
- Ghosal, S.: 1999. Mathematical and physical constraints on large-eddy simulation of turbulence. *AIAA J.*, **37**, 425.
- Holm, D.D.: 1999. Fluctuation effects on 3D Lagrangian mean and Eulerian mean fluid motion. *Physica D*, **133**, 215.
- Kuerten, J.G.M., Geurts, B.J., Vreman, A.W., Germano, M.: 1999. Dynamic inverse modeling and its testing in large-eddy simulations of the mixing layer. *Phys. of Fluids*, **11**, 3778.
- Leray, J.: 1934. Sur les mouvements d'un fluide visqueux remplissant l'espace. *Acta Mathematica*, **63**, 193.
- Lilly, D.K.: 1992. A proposed modification of the Germano subgrid-scale closure method. *Phys. of Fluids A*, **4**, 633.
- Meneveau, C., Katz, J.: 2000. Scale-invariance and turbulence models for large-eddy simulation. *Annu. Rev. Fluid Mech.*, **32**, 1.
- Smagorinsky, J.: 1963. General circulation experiments with the primitive equations. *Mon. Weather Rev.*, **91**, 99.
- Stolz, S., Adams, N.A.: 1999. An approximate deconvolution procedure for large-eddy simulation. *Phys. of Fluids*, **11**, 1699.
- Vreman, A.W., Geurts, B.J., Kuerten, J.G.M.: 1994. Realizability conditions for the turbulent stress tensor in large eddy simulation. *J. Fluid Mech.*, **278**, 351.
- Vreman, A.W., Geurts, B.J., Kuerten, J.G.M.: 1997. Large-eddy simulation of the turbulent mixing layer. *J. Fluid Mech.*, **339**, 357.

IMPLICIT SUBGRID-SCALE MODELING BY ADAPTIVE LOCAL DECONVOLUTION

N. A. Adams

*Institut für Strömungsmechanik,
Technische Universität Dresden,
D-01062, Dresden, Germany*

Nikolaus.Adams@ism.mw.tu-dresden.de

Abstract In this article we describe a new approach for the construction of implicit subgrid-scale models for Large-Eddy Simulation based on adaptive local deconvolution. An approximation of the unfiltered solution is obtained from a quasilinear combination of local interpolation polynomials. The effective subgrid-scale model can be determined by a modified differential equation analysis. Model parameters are found by evolutionary optimization. Computational results for the stochastically forced Burgers equation show that the proposed model gives significantly better results than other implicit subgrid-scale models.

Keywords: large-eddy simulation, subgrid-scale modeling, deconvolution, finite-volume method

1. Introduction

The original intention of subgrid-scale modeling was to stabilize under-resolved flow simulations under the constraint that correct results on the resolved scales are obtained (Smagorinsky, 1963; Schumann, 1975). The filtering approach (Leonard, 1974) to Large-Eddy Simulation (LES) provides the mathematical framework for physical modeling and sparked the development of a wide range of explicit subgrid-scale (SGS) models, for a summary see, e.g., Sagaut, 2000. It also was found that good results with explicit SGS models can be obtained only with numerical discretizations which have good wave-resolution properties or with sufficient subfilter-scale resolution (Ghosal, 1996, Stolz et al., 2001, Geurts and Fröhlich, 2002).

The idea of implicit SGS modeling has been introduced by Boris et al., 1992. In this approach the truncation error of the numerical discretization functions as SGS model and no explicit computation of model terms is necessary. The solution of the discretized transport equations is an exact solution of the modified differential equation which gives the means for a nonlinear

analysis of implicit SGS models (Fureby et al., 1997; Adams, 2001; Margolin and Rider, 2002). In this paper we construct a discretization from an approximate local deconvolution of the filtered solution. The deconvolution adapts locally to the smoothness properties of the solution and contains a SGS model implicitly. Here we restrict ourselves to one spatial dimension.

For a given generic nonlinear transport equation with solution v the corresponding truncated and filtered equation for the grid function v_N is given by

$$\partial_t v_N + \partial_x F(v_N) = \mathcal{E}_{SGS}. \quad (1)$$

\mathcal{E}_{SGS} is the subgrid-scale contribution which arises due to nonlinearity of $F(v)$. A semi-discretization of the filtered, fully resolved ($\mathcal{E}_{SGS} = 0$) eq. (1) is given by

$$\partial_t \bar{u}_N + G * \partial_x F_N(\bar{u}_N) = 0, \quad (2)$$

where $\bar{u}_N \doteq u_N$ results from an approximate inversion of the filtering $\bar{u}_N = G * u_N$. This equation can be written as transport equation for \bar{u}_N

$$\partial_t \bar{u}_N + G * \partial_x F(u_N) = \mathcal{E}_N, \quad (3)$$

where $\mathcal{E}_N = G * \partial_x F(u_N) - G * \partial_x F_N(\bar{u}_N)$ is the truncation error. A comparison between eq. (1) and eq. (3) shows that if \mathcal{E}_N approximates \mathcal{E}_{SGS} in some sense the discretization contains an implicit subgrid-scale model. An explicit expression for \mathcal{E}_N can be obtained by performing a modified differential equation analysis of eq. (3), as explained in section 3.3.

2. Approximate deconvolution

The use of a top-hat filter allows for a primitive-function reconstruction (Harten et al., 1987) as deconvolution operation. From the filtered solution sampled at the cell centers $\{x_j\}_{j=0}^{N-1}$ for a cell of width h_j

$$\bar{u}_j = \frac{1}{h_j} \int_{x_{j-1/2}}^{x_{j+1/2}} u(x') dx' \quad (4)$$

an approximation for the unfiltered solution at the left and right faces of each cell j has to be reconstructed, $u_{j-1/2}^+$ and $u_{j+1/2}^-$. For this purpose a set of Newton polynomials of order $k-1$ with $k = 1, \dots, K$ is used, for each k with shift $r = 0, \dots, k-1$ of the left-most stencil point. The stencil ranges from $j-r$ to $j-r+k-1$ which we express by (k, r) . Right-face interpolants at $x_{j+1/2}$ and left-face interpolants at $x_{j-1/2}$ are obtained from

$$p_{k,r}^-(x_{j+1/2}) = \sum_{l=0}^{k-1} c_{r,l}^{(k)}(j) \bar{u}_{j-r+l}, \quad p_{k,r}^+(x_{j-1/2}) = \sum_{l=0}^{k-1} c_{r-1,l}^{(k)}(j) \bar{u}_{j-r+l}. \quad (5)$$

For each k these expressions represent the information contained in admissible polynomials, interpolating u at $x_{j\pm 1/2}$. The construction of the discrete deconvolution operator $c_{r,l}^{(k)}(j)$ follows Shu and Osher, 1988,

$$c_{r,l}^{(k)}(j) = h_{j-r+l} \sum_{\mu=l+1}^k \frac{\sum_{p=0}^k \prod_{\substack{\nu=0 \\ \nu \neq \mu, p}}^k x_{j+1/2} - x_{j-r+\nu-1/2}}{\prod_{\substack{\nu=0 \\ \nu \neq \mu}}^k x_{j-r+\mu-1/2} - x_{j-r+\nu-1/2}}. \quad (6)$$

The index range of $c_{r,l}^{(k)}(j)$ is $r = 0, \dots, k-1$ and $l = 0, \dots, k-1$ for each $k = 1, \dots, K$. Quasi-linear combinations of (5) under the restriction that a sum of all weights $\omega_{k,r}^{\pm}(j)$ over k and r is unity result in the following approximants for the deconvolved cell-face solutions

$$u_{j\pm 1/2}^{\mp} = \sum_{k=1}^K \sum_{r=0}^{k-1} \omega_{k,r}^{\mp}(j) p_{k,r}^{\mp}(x_{j\pm 1/2}). \quad (7)$$

Finally, a numerical flux function needs to be chosen. We propose a formulation which resembles the Lax-Friedrichs flux function

$$F_N(x_{j+1/2}) = F\left(\frac{u_{j+1/2}^- + u_{j+1/2}^+}{2}\right) - \sigma_{j+1/2} \left(u_{j+1/2}^+ - u_{j+1/2}^-\right), \quad (8)$$

where $\sigma_{j+1/2}$ can be any shift-invariant functional of \bar{u}_N .

3. Modified-differential-equation analysis

The modified-differential equation analysis (MDEA) is performed here for the semi-discretization only. Discretization of time integration is not considered. This is consistent with the spatially filtered interpretation of the LES equations, the time step being sufficiently small for the spatial truncation error to be dominant. For the numerical experiments with the forced Burgers equation, section 3.5, an explicit third-order accurate Runge-Kutta time integration (Shu, 1988) is used. For larger time-step sizes MDEA needs to be extended to the full discretization.

For performing the MDEA we use the fact that the discrete unfiltered solution u_N in a neighborhood of x_j can be represented by local approximation polynomials of degree up to $K-1$

$$\bar{u}_N(x) \doteq \sum_{\mu=0}^{K-1} \partial_x^{\mu} u_N(x_j) M^{(\mu)}(x - x_j), \quad (9)$$

where $M^{(\mu)}(x - x_j)$ is the μ -th moment of the filter kernel G with Taylor-series factors included. This equation can be inverted by taking the first $K - 1$ derivatives of \bar{u}_N and solving for u_N and its first $K - 1$ derivatives (Harten et al., 1987; Geurts, 1997). Note that this procedure implies a regularization of the inverse filter operation. $\tilde{u}_N \doteq u_N$ is obtained in terms of the first $K - 1$ derivatives of \bar{u}_N which can be inserted into eq. (2). For SGS modeling only the convective term of eq. (1) is relevant, so that we will show results of MDEA for this term only. Also, MDEA is performed for equidistant meshes with $h_j = h$. The exact expression for the Burgers equation with $2\partial_x F(u_N) = \partial u_N^2 / \partial x$ is

$$G * \partial_x F(u_N) = \bar{u}_N \partial_x \bar{u}_N + \frac{1}{12} \partial_x \bar{u}_N \partial_x^2 \bar{u}_N - \frac{1}{720} \partial_x \bar{u}_N \partial_x^4 \bar{u}_N h^4 + \dots, \quad (10)$$

where derivatives are to be taken at x_j .

On the example of Burgers equation we show as an illustration of MDEA for finite K that by proper choice of parameters in the adaptive local deconvolution of \bar{u}_N , eq. (7), and in the numerical flux function eq. (8) the Smagorinsky model can be obtained implicitly up to leading order $\mathcal{O}(h^2)$. A simple MAPLE¹ exercise shows that for $\omega_{1,0}^+ = 1$, $\omega_{1,0}^- = 1$, $\omega_{2,1}^+ = 1/3$, $\omega_{2,1}^- = -1/3$, $\omega_{2,0}^+ = -1/3$, $\omega_{2,0}^- = 1/3$, and $\sigma_{j+1/2} = 2C_S |u_{j+1} - u_j|$ the truncation error is

$$\mathcal{E}_N = 2C_S h^2 |\partial_x \bar{u}_N| \partial_x^2 \bar{u}_N + \frac{1}{30} h^4 \partial_x \bar{u}_N \partial_x^4 \bar{u}_N - \frac{1}{6} h^4 C_S |\partial_x \bar{u}_N| \partial_x^4 \bar{u}_N + \dots. \quad (11)$$

4. Implicit SGS model

For the proposed model we will use local approximation polynomials up to order $K - 1 = 3$. In order to ensure that the leading term of \mathcal{E}_N is $\mathcal{O}(h^2)$ we set $\omega_{1,0}^\pm = 1/(K - 1)$. The remaining weights are defined in analogy to the WENO approach (Liu et al., 1994) as

$$\omega_{k,r}^\pm = \alpha_{k,r}^\pm \left((K - 1) \sum_{\mu=0}^{k-1} \alpha_{k,\mu}^\pm \right)^{-1}, \quad \beta_{k,r} = \sum_{\mu=-r}^{k-r-2} |\bar{u}_{j+\mu+1} - \bar{u}_{j+\mu}|, \quad (12)$$

where $\alpha_{k,r}^\pm = \gamma_{k,r}^\pm (\varepsilon + \beta_{k,r})^{-2}$. ε is a small number to prevent singularity and the smoothness measure is $\beta_{k,r}$ which weighs the contributions of each stencil (k, r) to the approximation $u_{j+1/2}^\pm$ given by eq. (7).

¹Maple 7, Waterloo Maple Inc., 2001

In eq. (8) we set $\sigma_{j+1/2} = |\bar{u}_{j+1} - \bar{u}_j|$. Eq. (12) contains free parameters $\gamma_{k,r}^- = \gamma_{k,k-1-r}^+$. These parameters determine the implicit SGS model. We estimate these parameters by evolutionary optimization. A computer code for this purpose was provided by P. Koumoutsakos of the Institute of Computational Sciences at ETH Zurich, Switzerland. Within the present one-dimensional model development the appropriate underlying eq. (1) is Burgers equation. For a resemblance of Navier-Stokes dynamics a stochastic forcing is added which generates a stationary state with an energy spectrum $\hat{E}(\xi) \sim \xi^{-5/3}$. The formulation is detailed in section 3.5. We found that a suitable definition of the cost function is based on the slope of a linear regression $\ln \hat{E}(\xi) \doteq a + b \ln \xi$ within the inertial range. The cost function is then defined as $f_\chi = |b - 5/3|$. It is computed by integrating the forced Burgers equation in time, performing time averaging and ensemble averaging since a moderate dependency of the cost function on the initial random seed was found. Initial parameter guesses for optimization are the values which deliver interpolation order $\mathcal{O}(h^{2k-1})$ for each k .

The following set of parameters is identified: $\gamma_{2,0}^+ = 0.9629$, $\gamma_{2,1}^+ = 0.0016$, $\gamma_{3,0}^+ = 0.5790$, $\gamma_{3,1}^+ = 0.0105$, $\gamma_{3,2}^+ = 0.0015$. For these parameters we find the following expression for the truncation error

$$\begin{aligned} \mathcal{E}_N = & (0.0553 \bar{u}_N \partial_x^3 \bar{u}_N + 0.0275 \partial_x \bar{u}_N \partial_x^2 \bar{u}_N) h^2 \\ & + \left(-0.0505 \frac{|\partial_x \bar{u}_N|}{\partial_x \bar{u}_N} \partial_x^2 \bar{u}_N \partial_x^3 \bar{u}_N - 0.0591 \partial_x \bar{u}_N \partial_x^4 \bar{u}_N \right. \\ & \quad - 0.0006 \frac{(\partial_x^2 \bar{u}_N)^2}{(\partial_x \bar{u}_N)^2} \bar{u}_N \partial_x^3 \bar{u}_N + 0.0013 \partial_x^2 \bar{u} \partial_x^3 \bar{u} \\ & \quad + 0.0041 \frac{\partial_x^2 \bar{u}_N}{\partial_x \bar{u}_N} \bar{u}_N \partial_x^4 \bar{u}_N + 0.0238 |\partial_x \bar{u}_N| \partial_x^4 \bar{u}_N \\ & \quad \left. - 0.0011 \frac{(\partial_x^2 \bar{u}_N)^3}{|\partial_x \bar{u}_N|} - 0.0006 \frac{(\partial_x^2 \bar{u}_N)^3}{\partial_x \bar{u}_N} \right) h^4 + \dots \end{aligned}$$

5. Results for forced Burgers equation

A relevant one-dimensional model for Navier-Stokes turbulence is a properly forced Burgers equation. Here we employ a stochastic force as suggested by Chekhlov and Yakhot, 1995,

$$\frac{\partial u}{\partial t} + u \frac{\partial u}{\partial x} = \nu \frac{\partial^2 u}{\partial x^2} + f(x, t). \quad (13)$$

The solution u is 2π -periodic. As Reynolds number we choose $1/\nu = 10^5$. For the forcing defined below we obtain a dissipation scale of order $\eta \simeq 10^{-3}$. The random force $f(x, t)$ is defined in wavenumber space as $\hat{f}(\xi) = A e^{i\phi}/|\xi|$,

where $-\pi \leq \phi \leq \pi$ is randomly chosen for every wavenumber and at every time step. After an initial transient a stationary state is reached which exhibits an $\hat{E}(\xi) \sim \xi^{-5/3}$ inertial range. The time-step size τ is determined by a Courant-Friedrichs-Lewy criterion with $CFL = 0.5$. Time integration is performed with a TVD Runge-Kutta scheme of Shu, 1988. It is found that neither a reduction of the time-step size nor a different Runge-Kutta time integration scheme has a significant effect on the results.

In figure 1 we show our main results. Eq. c(13) has been integrated up to $t = 500$. Statistics were gathered after a short initial transient. First, we note that the prediction by the implicit Smagorinsky model as given at the end of section 3.3 agrees for the inertial-range well with that of an explicit Smagorinsky model computed with a spectral discretization. Discrepancies at small wavenumbers are caused by the different discretization schemes and different random seeds. Improved results are observed with a 3rd-order WENO scheme which represents the use of a standard shock-capturing scheme for implicit SGS modeling. With the optimized model a significantly better agreement with the theoretical $\xi^{-5/3}$ spectrum is achieved.

6. Conclusions

We have shown that, based on adaptive local deconvolution, subgrid-scale model and discretization of a conservation law can be merged. The discretization can be adjusted systematically in order to obtain a desired implicit SGS model up to a certain order in terms of grid spacing, or to find an optimized implicit model, provided that turbulent statistics for the considered case are available. The extension of the approach to the three-dimensional Navier-Stokes equations is subject of ongoing work.

Acknowledgment

The presented research is supported by the German Research Council (Deutsche Forschungsgemeinschaft - DFG). P. Koumoutsakos of ETH Zurich provided the evolutionary optimization algorithm. S. Hickel (TU Dresden) helped proof-reading the article.

References

- Adams, N. A. (2001). The role of deconvolution and numerical discretization in subgrid-scale modeling. In *Direct and Large-Eddy Simulation IV*.
- Boris, J. P., Grinstein, F. F., Oran, E. S., and Kolbe, R. L. (1992). New insights into large eddy simulation. In *Fluid Dynamics Research*, volume 10, pages 199–228. North Holland.
- Chekhlov, A. and Yakhot, V. (1995). Kolmogorov turbulence in a random-force driven Burgers equation: anomalous scaling and probability density function. *Phys. Rev. E*, 52:5681–5684.

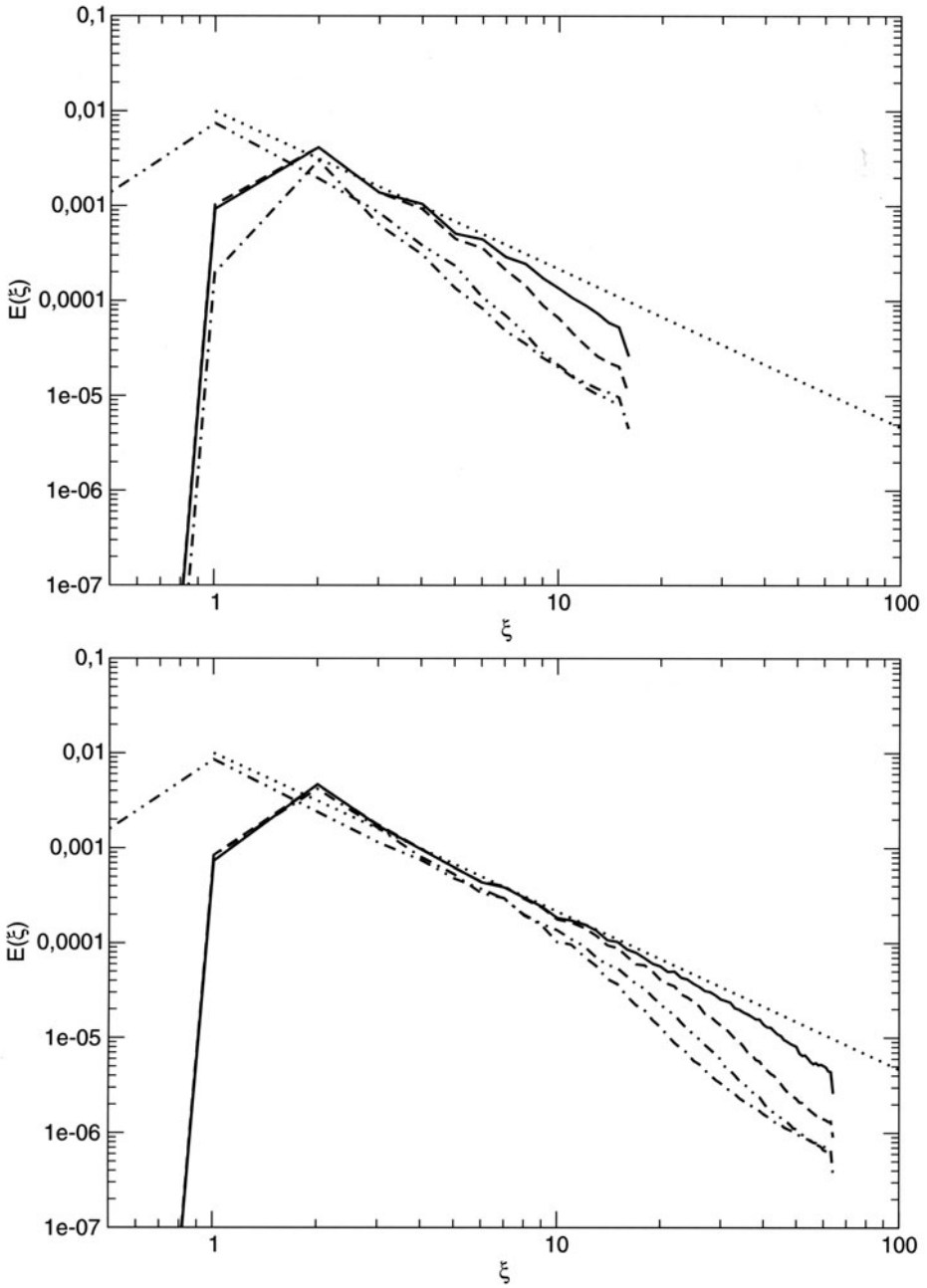


Figure 1. Averaged energy spectra $\hat{E}(\xi)$, ———optimal formulation, ----3rd-order WENO discretization, -·-·-implicit Smagorinsky model, —·—·—explicit Smagorinsky model with spectral discretization, ····· line $\sim \xi^{-5/3}$. Upper figure for $N = 32$ grid points, lower figure for $N = 128$ grid points.

- Fureby, C., Tabor, G., Weller, H. G., and Gosman, A. D. (1997). A comparative study of subgrid scale models in homogeneous isotropic turbulence. *Phys. Fluids*, 9:1416–1429.
- Geurts, B. (1997). Inverse modeling for large-eddy simulation. *Phys. Fluids*, 9:3585–3587.
- Geurts, B. and Fröhlich, J. (2002). A framework for prediction accuracy limitations in large-eddy simulation. *Phys. Fluids*, 14:L41–L44.
- Ghosal, S. (1996). An analysis of numerical errors in large-eddy simulations of turbulence. *J. Comput. Phys.*, 125:187–206.
- Harten, A., Engquist, B., Osher, S., and Chakravarthy, S. (1987). Uniformly high order essentially non-oscillatory schemes, III. *J. Comp. Phys.*, 71:231–275.
- Leonard, A. (1974). Energy cascade in large eddy simulations of turbulent fluid flows. *Adv. Geophys.*, 18A:237–248.
- Liu, X.-D., Osher, S., and Chan, T. (1994). Weighted essentially non-oscillatory schemes. *J. Comp. Phys.*, 115:200–212.
- Margolin, L. G. and Rider, W. J. (2002). A rationale for implicit turbulence modeling. *Int. J. Numer. Meth. Fluids*, 39:821–841.
- Sagaut, P. (2000). *Large-Eddy Simulation for Incompressible Flows*. Springer.
- Schumann, U. (1975). Subgrid scale model for finite-difference simulations of turbulence in plane channels and annuli. *J. Comput. Phys.*, 18:376–404.
- Shu, C.-W. (1988). Total-variation-diminishing time discretizations. *SIAM J. Sci. Stat. Comput.*, 9(6):1073–1084.
- Shu, C.-W. and Osher, S. (1988). Efficient implementation of essentially non-oscillatory shock-capturing schemes. *J. Comput. Phys.*, 77:439–471.
- Smagorinsky, J. (1963). General circulation experiments with the primitive equations. *Mon. Weath. Rev.*, 93:99–164.
- Stolz, S., Adams, N. A., and Kleiser, L. (2001). The approximate deconvolution model for compressible flows: decaying turbulence and shock-turbulent-boundary-layer interaction. In Friedrich, R., editor, *Large-Eddy simulation of complex transitional and turbulent flows*. Kluwer.

SELECTIVE FILTERING VERSUS EDDY VISCOSITY FOR SUBGRID MODELLING IN THE LES OF A SUBSONIC JET

Christophe Bogey¹ and Christophe Bailly²

¹*Laboratoire de Mécanique des Fluides et d'Acoustique
Ecole Centrale de Lyon, UMR CNRS 5509
69134 Ecully, France*

christophe.bogey@ec-lyon.fr

<http://acoustique.ec-lyon.fr>

²*Same address*

christophe.bailly@ec-lyon.fr

Abstract This paper reports LES of a high Reynolds number subsonic jet performed using an explicit filtering alone or in combination with the dynamic Smagorinsky eddy-viscosity model. The results of the two LES are compared and the way the energy is dissipated by the filtering or by the eddy-viscosity model is investigated from the energy balance.

Keywords: Large Eddy Simulation, subgrid modelling, selective filtering, high-order schemes, eddy viscosity, jet

1. Introduction

In Large Eddy Simulation, for flows at sufficiently high Reynolds number, the fine turbulent scales affected by viscous diffusion are not resolved. An artificial damping is therefore required to dissipate the turbulent kinetic energy. The classical approach consists in using eddy-viscosity models [1], developed from physical considerations to represent the subgrid stress tensor, the most famous one being the Smagorinsky model [2] recently improved by dynamical formulations [3]. However, the use of an eddy viscosity in LES raises questions still to be discussed. For instance, since an eddy viscosity has the same functional form as the molecular viscosity, it is difficult to define the effective Reynolds number of the simulated flows [4]. Moreover, an eddy viscosity might dissipate the turbulent energy through a wide range of scales up to larger ones which should be dissipation-free at high Reynolds number.

Alternatives to the eddy-viscosity approach have therefore been proposed using numerical dissipation for modelling the effects of the subgrid scales. In the so-called Implicit LES (ILES), dissipation is provided implicitly by the numerical scheme [5], and no additional subgrid-scale model is implemented. One difficulty of this approach concerns the dissipation of the low-order schemes used, which might be too strong as shown for instance for the shock-capturing schemes [6]. To closely control the dissipation, it then appears more appropriate to use low-dissipative numerical schemes, while applying explicitly a compact/selective filter to the flow variables with the aim of removing only the higher wave numbers located near the grid cutoff wave number. Note that this approach was recently successfully applied to isotropic turbulence, channel flows and jets [7],[8, 9].

The present paper reports LES of a Mach number $M = 0.9$ circular jet at a high Reynolds number $Re_D = 4 \times 10^5$. The LES have been performed using explicitly a selective filtering, alone or in combination with the dynamic Smagorinsky eddy-viscosity model [9], [10], [11]. The motivation is to show the effects of these two kinds of subgrid modelling, filtering and eddy viscosity, on the turbulent flow features, and also to evaluate the relative role of these two artificial dissipations in the energy balance. This can be done since the numerical solver used displays spectral-like accuracy providing negligible dispersion and dissipation on the resolved scales. The selective filtering was indeed designed to eliminate grid-to-grid oscillations without affecting significantly the scales discretized by more than four grid points [9, 12]. It is thus useful to distinguish two cutoff wave numbers in the present LES: the grid cutoff wave number for two points per wavelength at $k_c^g = \pi/\Delta x$ (Δx is the mesh grid size) and the filtering cutoff wave number at $k_c^f = \pi/(2\Delta x)$. The resolved, the filtered and the subgrid scales can then be defined as shown in Figure 1.

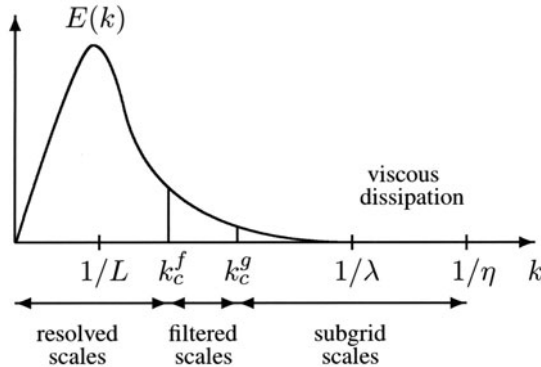


Figure 1. Schematic representation of the spectrum of turbulent kinetic energy with the wave numbers associated to the integral, Taylor and Kolmogorov scales, L , λ and η , and with the filtering and grid cut-off wave numbers, k_c^f and k_c^g .

2. Jet simulations

The present jet simulations have been initially performed to obtain directly the radiated sound field using LES, with the aim of investigating the noise sources as done in a preliminary simulation of a jet at moderate Reynolds number [13]. In the present work, the jet has a Mach number of $M = 0.9$ and a higher Reynolds number of $Re_D = 4 \times 10^5$. Its inflow shear layer is forced with random velocity disturbances to seed the turbulence. The jet flow and noise features are compared systematically with experimental data in [9] where all the simulation parameters can be found by the reader. The influence of the inflow forcing is also studied in detail in [10].

The objective is then to investigate the effects of the subgrid modelling on the jet [11]. First, simulations have been carried out using an explicit filtering alone for subgrid modelling. By applying the filtering differently in two simulations, every two and three iterations respectively, the results are found not to be appreciably modified. This can be easily understood from Figure 1: owing to the high selectivity of the filter, the resolved scales which contain most of the kinetic energy are developing independently from the filtering procedure. Simulations have been then performed using also the Dynamic Smagorinsky eddy-viscosity Model (DSM) [3]. They show that the use of a subgrid scale kinetic energy in the DSM has a negligible influence on the turbulence results. They also provide results with significant discrepancies with respect to those obtained using the filtering alone. The major ones are given in what follows.

The vorticity fields obtained from the simulations referred to as LESsf and LESdsm, using the filtering alone or with the DSM respectively, are presented in Figure 2. The jet developments appear similar with for instance the same potential core length. However the turbulent flow field seems to display more fine scales in LESsf than in LESdsm.

To illustrate more quantitatively the effects of the DSM on the turbulent jet development, the centerline profile of the axial turbulence intensity is presented in Figure 3(a). In both LES the self-similarity plateau where $u'_{rms}/u_c \simeq 0.25$ is not reached as expected [14], but the increase is much faster in LESdsm than in LESsf. Since the jets appear to become self-similar more rapidly at low than at high Reynolds numbers, this could indicate that the effective Reynolds number of the simulated flow is artificially decreased in LESdsm by the use of the eddy viscosity.

Moreover the structures of the turbulence obtained from the two simulations are quite different as shown by the velocity spectra of Figure 3(b). On the one hand, the magnitude of the higher wave numbers is reduced in LESdsm, with an eddy viscosity which visibly damps wave numbers located well below the filtering cutoff wave number. On the other hand, the magnitude of the large scales is enhanced in LESdsm, in agreement with the larger turbulence

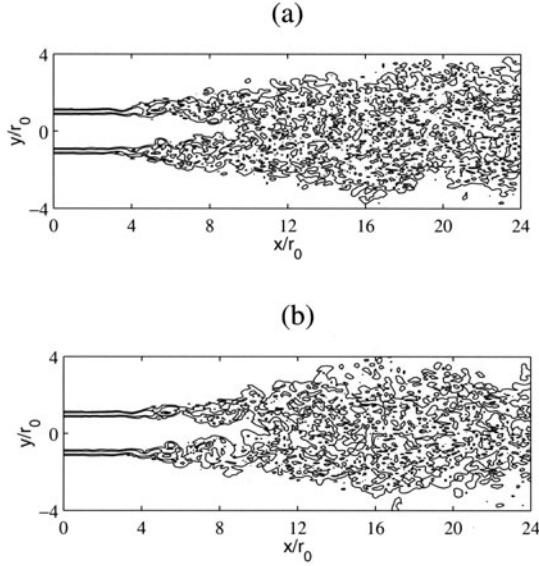


Figure 2. View in the plane $z = 0$ of the two vorticity-norm contours associated with the magnitudes of 3.2×10^4 and $9.6 \times 10^4 \text{ s}^{-1}$, obtained from LESsf (a) and LESdsm (b).

intensity observed in Figure 3(a). In the same way note that the integral length scales are also larger in LESdsm than in LESsf as reported in [11]. These results show that the large-scale features of the jet computed by LES depend significantly on the way the energy is dissipated, by filtering or by the eddy-viscosity model.

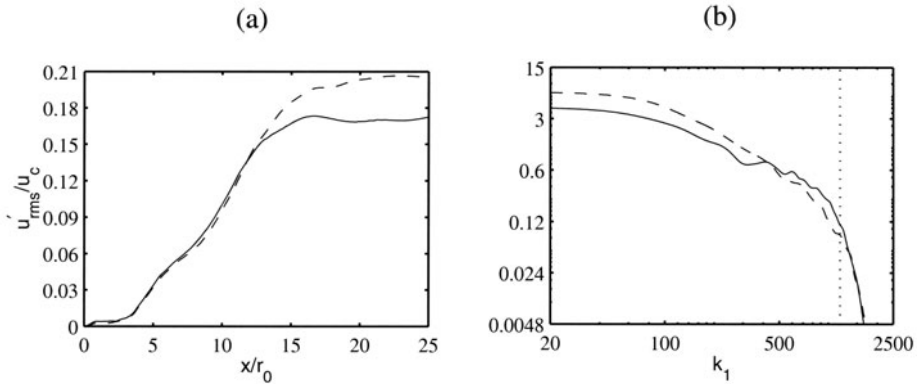


Figure 3. Flow features obtained from LESsf (solid lines) and LESdsm (dashed lines): (a) centerline profiles of the turbulence intensity u'_{rms}/u_c (u' is the axial fluctuating velocity, u_c the centerline velocity); and (b) one-dimensional spectrum $E_u^{(1)}(k_1)$ of the u' velocity for $x = 20r_0$ and $r = 0$, as a function of the axial wave number k_1 . The dotted line represents the filtering cut-off wave number $k_c^f = \pi/(2\Delta x)$.

3. Energy balance and dissipation

The budget of the turbulent kinetic energy is calculated in order to determine the relative contributions of the explicit filtering and of the molecular and eddy viscosities to the energy dissipation. This study on the dissipation mechanisms involved in the different LES is feasible thanks to the low-dissipative feature of the time-integration algorithm. The maximum numerical dissipation, obtained for the higher angular frequency resolved by the optimized Runge-Kutta algorithm, is indeed only of 3×10^{-5} per iteration.

The equation for the kinetic energy budget is derived from the filtered Navier-Stokes equations given in [9]. It writes

$$\begin{aligned}
 0 = & \underbrace{-\frac{\partial}{\partial x_j} \langle \rho \rangle k [u_j] - \langle \bar{\rho} u'_i u'_j \rangle \frac{\partial [u_i]}{\partial x_j}}_A - \underbrace{\left\langle \tilde{\tau}_{ij} \frac{\partial u'_i}{\partial x_j} \right\rangle}_B - \underbrace{\left\langle \mathcal{T}_{ij} \frac{\partial u'_i}{\partial x_j} \right\rangle}_C \\
 & - \underbrace{\frac{1}{2} \frac{\partial}{\partial x_j} \langle \bar{\rho} u'_j u'_i u'_i \rangle}_D - \underbrace{\frac{\partial}{\partial x_i} \langle p' u'_i \rangle}_E + \underbrace{\frac{\partial}{\partial x_j} \langle u'_i \tilde{\tau}_{ij} \rangle}_F + \underbrace{\frac{\partial}{\partial x_j} \langle u'_i \mathcal{T}_{ij} \rangle}_G \\
 & - \underbrace{\langle u'_i \rangle \frac{\partial \langle p \rangle}{\partial x_i}}_H - \underbrace{\left\langle p' \frac{\partial u'_i}{\partial x_i} \right\rangle}_I
 \end{aligned} \tag{1}$$

where the turbulent kinetic energy is defined by $\langle \bar{\rho} \rangle k = \langle \bar{\rho} u_i'^2 / 2 \rangle$. Density, velocity and pressure are represented by ρ , u_i and p , the turbulent and subgrid stress tensors by τ_{ij} and $\mathcal{T}_{ij} = \bar{\rho} \tilde{u}_i \tilde{u}_j - \bar{\rho} \overline{u_i u_j}$. The tilde and overbar indicate Favre and Reynolds grid-filtered quantities, and the prime fluctuating quantities. Statistical averaging is denoted by $\langle \cdot \rangle$, and $[u_i] = \langle \bar{\rho} \tilde{u}_i \rangle / \langle \bar{\rho} \rangle$. The main terms in (1) are referred to as (A) to (F), and correspond to meanflow advection (A), to production (B), to viscous dissipation (C), to subgrid dissipation (D), to turbulent diffusion (E) and to the pressure-velocity term (F).

To quantify the dissipation due to the explicit filtering, observe that the filtering is equivalent to a second-order explicit integration over the simulation time step Δt of the following term

$$D_{sf}(f_i) = -\frac{\sigma_d}{\Delta t} \sum_{j=-n}^n d_{i+j} (f_{i+j} - \langle f_{i+j} \rangle) \tag{2}$$

in the mass and momentum conservation equations, with $f = \bar{\rho}$ and $f = \bar{\rho} \tilde{u}_i$, respectively (d_j : coefficients of the filter, $0 \leq \sigma_d \leq 1$ is arbitrary). Two terms are thus added in the energy equation which becomes

$$(1) + \underbrace{\langle u'_i D_{sf}(\bar{\rho} \tilde{u}_i) \rangle}_G - \langle u'_i \tilde{u}_i D_{sf}(\bar{\rho}) \rangle \tag{3}$$

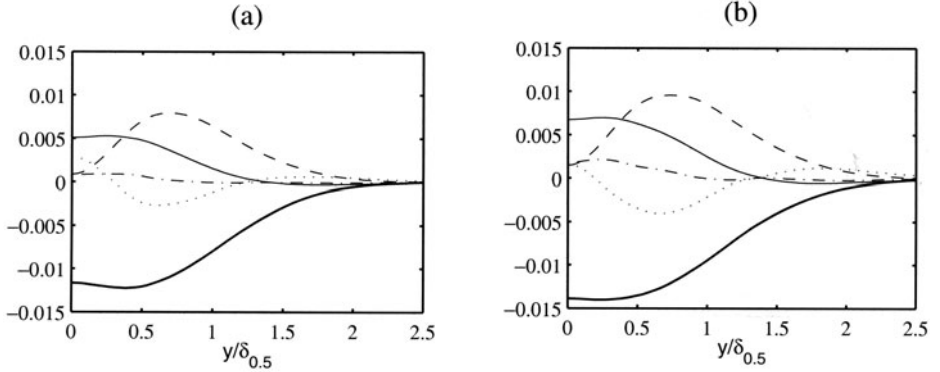


Figure 4. Kinetic energy budget at $x = 20r_0$ from LESsf (a) and LESdsm (b). The curves are normalized by $\rho_c u_c^3 \delta_{0.5}$ (ρ_c and u_c : centerline mean density and axial velocity, $\delta_{0.5}$: jet half-width): advection (thin solid lines), production (dashed lines), total dissipation (thick solid lines), turbulent diffusion (dotted lines), and pressure diffusion (dashdot lines).

where the dissipation due to the filtering is mainly given by (G).

The kinetic energy budget across the jet at $x = 20r_0$ is shown in Figure 4 for the two simulations LESsf and LESdsm. The total dissipation, *i.e.* the sum of the three terms (C)+(D)+(G), is represented here. The different curves display similar shapes in LESsf and LESdsm, and agree also fairly well with the corresponding experimental curves [15, 16]. The slight discrepancy in amplitude is certainly due to the location of the study section which is far from the self-similarity region where the measurements are done. We can also note that the low magnitude of the pressure-velocity term is rather in agreement with [15] where it was neglected, than with [16] where it was found to be of the order of the advection term on the centerline.

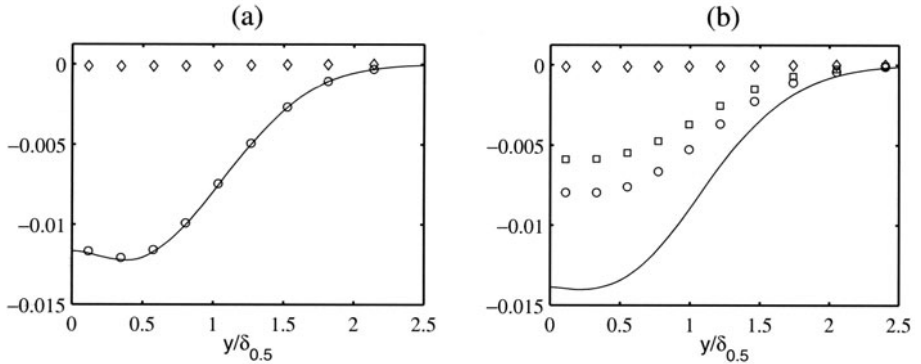


Figure 5. Dissipation at $x = 20r_0$ from LESsf (a) and LESdsm (b). The curves are normalized by $\rho_c u_c^3 \delta_{0.5}$: total dissipation (solid lines), dissipation due to molecular viscosity (diamond), eddy viscosity (square), and selective filtering (o).

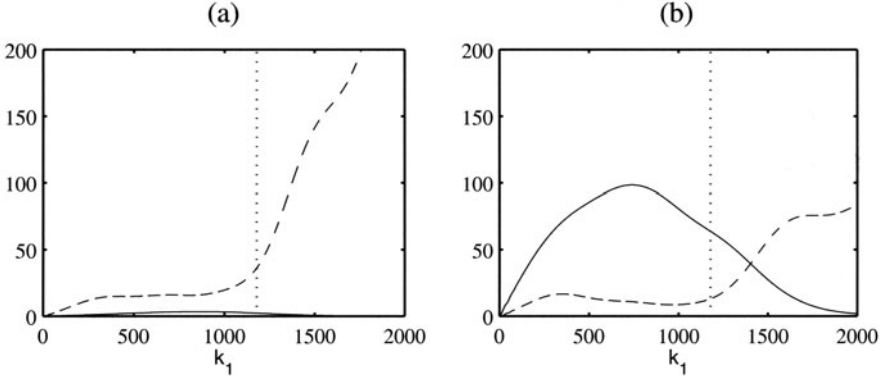


Figure 6. Dissipation curves obtained from LESsf (a) and LESdsm (b) for $x = 20r_0$ and $r = 0$, given by $(\nu + \nu_t)k_1^2 E_{u'}^{(1)}(k_1)$ (solid lines) and by $D_{sf}(k_1 \Delta x) E_{u'}^{(1)}(k_1)$ (dashed lines), as a function of the axial wave number k_1 , in m.s^{-3} ($D_{sf}(k_1 \Delta x)$ is the transfer function of (2) in the wave number space). The dotted line represents the filtering cutoff wave number $k_c^f = 2k_c^g$ where the grid cutoff wave number is $k_c^g = \pi/\Delta x = 2357\text{m}^{-1}$.

The different contributions to the total dissipation are shown in Figure 5 for LESsf and LESdsm. In both simulations, the effects of the molecular viscosity are negligible as expected owing to the flow high Reynolds number. In LESsf the dissipation is thus due to the filtering alone, whereas in LESdsm the turbulent energy is found to be dissipated both by the filtering and by the eddy viscosity, in comparable proportions.

To characterize the scales affected by the dissipation mechanisms, the one-dimensional spectra of the u' -velocity at $x = 20r_0$ and $r = 0$ are now multiplied by their respective transfer functions. The corresponding curves are presented in Figure 6 for the two simulations. They illustrate clearly that the explicit filtering and the eddy viscosity dissipate energy through different turbulence scales: the filtering through the scales referred to as filtered in Figure 1 located beyond the filter cutoff wave number, the viscosity mainly through the so-called resolved scales. This may be a major deficiency of eddy-viscosity models, especially at high Reynolds number where the dissipation on the large scales must be negligible.

4. Conclusion

In the present work, the influence of the modelling used to dissipate the turbulent energy instead of the subgrid scales in LES is shown for a high Reynolds number jet. The ways the energy is dissipated by selective filtering and by eddy-viscosity models are found to basically differ. In the latter case indeed, all the turbulent scales are significantly affected, which is likely to bias the turbulence development, and also to artificially decrease the effective Reynolds

number of the simulated flows. Considering this, the use of selective filtering alone may appear one appropriate way to compute by LES the physics of turbulent flows at high Reynolds number.

References

- [1] Lesieur, M., and Métais, O. (1996). "New trends in large-eddy simulations of turbulence," *Annu. Rev. Fluid Mech.*, **28**, 45-82.
- [2] Smagorinsky, J.S. (1963). "General circulation experiments with the primitive equations: I. the basic experiment," *Mon. Weath. Rev.*, **91**, 99-163.
- [3] Moin, P., Squires, K., Cabot, W., and Lee, S. (1991). "A dynamic subgrid-scale model for compressible turbulence and scalar transport," *Phys. Fluids A*, **3**(11), 2746-2757.
- [4] Domaradzki, J.A., and Yee, P.P. (2000). "The subgrid-scale estimation model for high Reynolds number turbulence," *Phys. Fluids*, **12**(1), 193-196.
- [5] Grinstein, F.F., and Fureby, C. (2002). "Recent progress on MILES for high Reynolds number flows," *J. Fluids Eng.*, **124**, 848-861.
- [6] Garnier, E., Mossi, M., Sagaut, P., Comte, P., and Deville, M. (1999). "On the use of shock-capturing schemes for large-eddy simulation," *J. Comput. Phys.*, **153**, 273-311.
- [7] Visbal, M.R., and Rizzetta, D.P. (2002). "Large-Eddy Simulation on curvilinear grids using compact differencing and filtering schemes," *J. Fluids Eng.*, **124**, 836-847. See also AIAA Paper 2003-4098.
- [8] Mathew, J., Lechner, R., Foysi, H., Sesterhenn, J., Friedrich, R. (2003). "An explicit filtering method for large eddy simulation of compressible flows," *Phys. Fluids*, **15**(8), 2279-2289.
- [9] Bogey, C., and Bailly, C. (2002). "Direct computation of the sound radiated by a high Reynolds number, subsonic round jet," *CEAS Workshop From CFD to CAA*, Athens, Greece.
- [10] Bogey, C., and Bailly, C. (2003). "LES of a high Reynolds, high subsonic jet : effects of the inflow conditions on flow and noise," *9th AIAA/CEAS Conference*, AIAA Paper 2003-3170.
- [11] Bogey, C., and Bailly, C. (2003). "LES of a high Reynolds, high subsonic jet : effects of the subgrid modellings on flow and noise," *16th AIAA CFD Conference*, AIAA Paper 2003-3557.
- [12] Bogey, C., and Bailly, C. (2004). "A family of low dispersive and low dissipative explicit schemes for flow and noise computations," accepted in *J. Comput. Phys.* See also AIAA Paper 2002-2509.
- [13] Bogey, C., Bailly, C., and Juvé, D. (2003). "Noise investigation of a high subsonic, moderate Reynolds number jet using a compressible LES," *Theoret. Comput. Fluid Dynamics*, **16**(4), 273-297.
- [14] Wgnanski, I., and Fiedler, H. (1969). "Some measurements in the self-preserving jet," *J. Fluid Mech.*, **38**(3), 577-612.
- [15] Panchapakesan, N.R., and Lumley, J.L. (1993). "Turbulence measurements in axisymmetric jets of air and helium. Part I. Air jet," *J. Fluid Mech.*, **246**, 197-223.
- [16] Hussein, H.J., Capp, S.P., and George, W.K. (1994). "Velocity measurements in a high-Reynolds-number, momentum-conserving, axisymmetric, turbulent jet," *J. Fluid Mech.*, **258**, 31-75.

HIGH RESOLUTION DNS OF A SHEAR-FREE MIXING LAYER AND LES

O. Debligny¹, B. Knaepen², D. Desmidts¹, D. Carati¹

¹*Université Libre de Bruxelles, Statistical and Plasma Physics,
Bld du Triomphe, Campus Plaine - CP 231, B-1050 Bruxelles, Belgium.*

²*Center for Turbulence Research, Stanford University/NASA Ames Research Center,
488 Escondido, Building 500/500A, Stanford University, 94305-3035.*

odeblign@ulb.ac.be, bknaepen@stanford.edu, ddesmidt@ulb.ac.be, dcarati@ulb.ac.be

Abstract Results from a high resolution ($512 \times 1024 \times 512$) DNS of a shear-free mixing layer are investigated. The mixing layer consists of the transition between two regions of homogeneous turbulence characterized by different turbulent intensities and energy spectra. The simulation has been initialised in order to reproduce the conditions of laboratory investigations of the same flow and an extensive comparison between the DNS and the experimental results is proposed. Also, the possibility to reproduce the main features of this flow using LES is explored.

Keywords: Mixing layer, inhomogeneous flow

1. Introduction

The shear-free mixing layer represents one of the simplest inhomogeneous flows. It consists of two distinct homogeneous regions of different turbulent kinetic energy interacting through a layer of rapid transition. The layer is said to be shear-free since the two homogeneous regions have no relative velocity. This configuration is an interesting test case in which the influence of inhomogeneity on the turbulence properties can be studied in detail without having to deal with the influence of solid boundary.

Both experimental and numerical studies of this problem have already been performed in the past. The most extensive and well-documented experiment is due to Veeravalli and Warhaft, 1989. It is used here as the main benchmark. In this experimental setup, the flow was obtained by forcing a flow through a grid with two different meshes. From the numerical point of view, DNS with a resolution of 128^3 have been done by Briggs et al., 1996. These authors

also targeted the Veeravali & Warhaft experiment. When properly nondimensionalized, they were able to reproduce satisfactorily the turbulence statistics of the flow. However, they couldn't reach the microscale Reynolds number of the experiment.

The scope of this study is twofold. First, with today's computers, DNS reaching the experimental Reynolds number could be performed so that results achieved by Briggs et al. could be complemented. Secondly, a LES of the shear-free mixing layer was also processed. In that context, the behaviour of traditional LES models in the presence of an inhomogeneity could be tested without having to deal with complex numerical issues. Indeed, the mixing layer can be computed with a spectral code (fully de-aliased) for which the accuracy of the modelling is largely decoupled from the numerics.

In this paper, a brief introduction devoted to the initial condition is followed by an extensive comparison between experimental and DNS results. The DNS approach is also used to characterize the inhomogeneity and the anisotropy of the mixing layer by computing quantities like the Reynolds tensor, the skewness, the kurtosis and the Shebalin angles. Finally, a comparison between DNS data and LES predictions is also presented.

2. Initial condition

As mentioned before, the shear-free mixing layer can be studied using a three dimensional spectral code. Indeed, periodicity can be enforced by considering a second mixing layer which performs the "reverse" transition compared to the first one. This also has the advantage that results gathered from both mixing layers can be averaged to improve the statistics. Obviously, for long enough times, the two mixing regions would interact. The simulations presented here have been stopped before this interaction is observed. This is not very restrictive since the typical time scale characterizing the increase of the mixing layers is much longer than the typical decaying time of the homogeneous regions.

Initializing isotropic turbulence with a prescribed energy spectrum and preserving incompressibility is a standard procedure (Rogallo, 1981). The details of the procedure used for initializing the mixing layer can be found in Knaepen et al., 2003. In practice, the amplitudes of the velocity modes $u_i(k_x, y, k_z)$ transformed by FFT in the direction of the inhomogeneity, chosen here to be y are prescribed. For values of y inside the homogeneous layers, these amplitudes basically correspond to isotropic turbulence with spectra chosen to reproduce the main properties like energy, dissipation, Reynolds number and integral scale of the two homogeneous layers reported by Veeravali & Warhaft for the experiments with the 3:1 perforated plate. Incompressibility is enforced

using an iterative procedure that allows simultaneously to satisfy continuity and to match the desired spectra.

The computational domain is a rectangular box of size $l_x = 2\pi$, $l_y = 4\pi$ and $l_z = 2\pi$ with periodic boundary conditions. The 4π -length is chosen along the inhomogeneity direction in order to ensure the existence of sufficiently large homogeneous layers. The kinematic viscosity ν is set to $6 \cdot 10^{-3}$ and the microscale Reynolds numbers in each homogeneous regions are respectively 70 and 30. The DNS is performed using $512 \times 1024 \times 512$ modes.

3. DNS results

3.1 Moments profiles

All statistics extracted from the DNS will be averaged over the direction of homogeneity (x and z). This averaging operation is denoted by the overbar $\overline{\cdot}$. In order to compare to the Veeravalli and Warhaft (1989) experiment, the results have been normalized using the same conventions. Time is normalized using the initial eddy-turnover time. The curves are centred around the inflection point y^* of the variance curves and normalized by the half-width $l_{1/2}$ (see Veeravalli and Warhaft (1989) for details). In Figure 1(a), (b) and (c), we present respectively the variance, the skewness and the kurtosis of the velocity component v at three different times. The skewness and kurtosis are defined as,

$$S_v = \frac{\overline{v^3}}{(\overline{v^2})^{\frac{3}{2}}}, \quad K_v = \frac{\overline{v^4}}{(\overline{v^2})^2}. \quad (1)$$

The variance has been divided by its (average) value reached in the high energy region, $\overline{v_H^2}$. First, we observe for the three profiles that the comparison with the experiment is satisfying. For homogeneous and isotropic turbulence, measures of the skewness and the kurtosis show that they are very close to those calculated for a Gaussian signal, i.e., $S = 0$ and $K = 3$. However, both curves show deviations from those values in the location of the mixing layer and indicate that the deviations occur on the low energy side. This supports the idea that these deviations result from the more likely penetration of intermittent structures from the high-energy region to the low-energy region.

3.2 Kinetic energy

Fig 2(a) represents the profile of the kinetic energy $E(y) = \overline{|u_i(\mathbf{x})|^2}/2$ at three different times in the simulation. In order to explore which mechanisms are responsible for the evolution of the energy, we have considered the balance equation obtained by multiplying the Navier-Stokes equation by the velocity

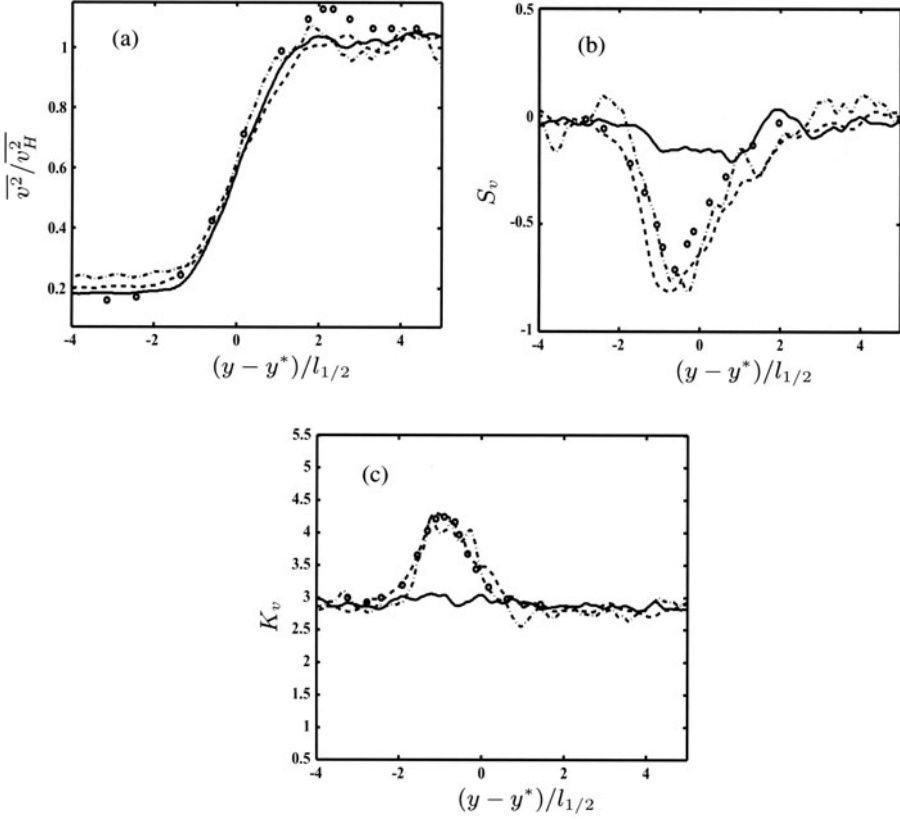


Figure 1. Variance (a), skewness (b) and kurtosis (c) profiles of the velocity component v at three different times; — : $t^* = 0$; --- : $t^* = 0.56$; - · - : $t^* = 1.51$; \circ : experimental data from Veeravalli and Warhaft, 1989.

and averaged over the xz -plane:

$$\partial_t E(y) = -\partial_y \Phi(y) - \varepsilon(y). \quad (2)$$

Two type of terms are responsible for the evolution of the energy $E(y)$. The first one is a flux term that does not affect the total energy but modifies its spatial distribution in y . It can be decomposed into three contributions: a convective flux $\Phi^c(y) = \overline{|u_i|^2 u_y}/2$, a pressure flux $\Phi^p(y) = \overline{p u_y}$ and a viscous flux $\Phi^\nu(y) = \overline{2\nu S_{iy} u_i}$, which is the smallest contribution to the total flux. The second term is due to the viscous dissipation. In Fig. 2(b), the contributions due to these two terms of this equation are shown. One can observe that the flux has no mean in the homogeneous parts while in the mixing layer it has a negative contribution. As a result, it almost cancels the effect of the dissipation and tends to maintain a higher energy in that region.

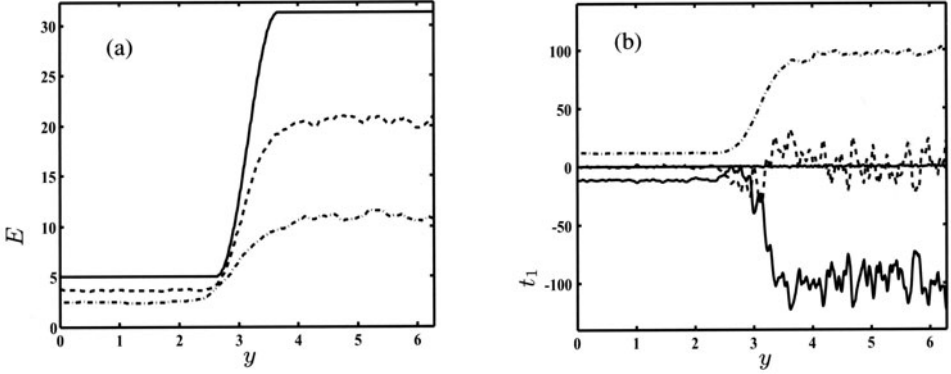


Figure 2. Profile of $E(y)$ at three different time; — : $t^* = 0$; --- : $t^* = 0.56$; ··· : $t^* = 1.51$. Profile of the different contributions to the evolution of $E(y)$ (right) at $t^* = 0.56$. ··· : $\varepsilon(y)$; — : $\partial_t E(y)$; --- : $\partial_y \Phi(y)$. The sum of these three terms must be zero to numerical accuracy, as shown by the dotted line.

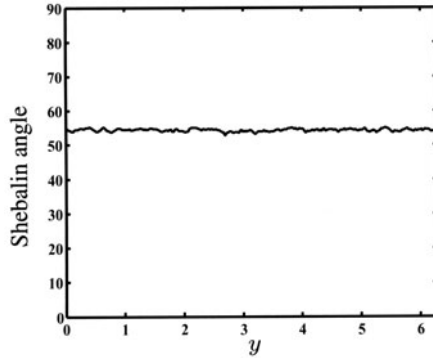


Figure 3. Profile of the Shebalin angle at $t^* = 0.56$.

3.3 Anisotropy

In the study of Briggs et al., 1996, it was noted that the shear-free mixing layer was not strongly anisotropic. We decided to explore in more detail this property for the higher Reynolds number considered here. This property is very important in the context of LES since isotropy of the small scales is usually assumed in most LES models. To that end, we have recorded the Shebalin angle (Shebalin et al., 1983) defined as:

$$\tan^2 \theta = 2 \frac{G_{xx} + G_{xy} + G_{xz}}{G_{yx} + G_{yy} + G_{yz}}, \quad (3)$$

where G_{ij} is the average square value of the velocity gradient components:

$$G_{ij} = \overline{(\partial_i u_j)^2} \quad (\text{no summation}). \quad (4)$$

According to the theory of isotropic turbulence (Batchelor, 1953), the following relation should hold for all $i \neq j$:

$$G_{ii} = \frac{1}{2} G_{ij} \quad (\text{no summation}). \quad (5)$$

and, based on this, $\theta = \arctan \sqrt{2} \approx 54^\circ$. This is indeed the case as presented on Fig. 3, not only for the homogeneous layers but also for the mixing layers. This tends to support the idea that isotropic LES models are well adapted for flows with rather strong inhomogeneities in the energy distribution.

4. LES

Within the framework of LES, a filter kernel is applied to the Navier-Stokes equations in order to obtain a set of equations for the resolved quantities. Here, because our code is spectral, we adopt the sharp fourier cut-off for the filtering operator, denoted here $\widetilde{\cdot}$. The filtered equations thus read:

$$\partial_t \widetilde{u}_i = -\partial_j (\widetilde{u_i u_j}) + \nu \nabla^2 \widetilde{u}_i - \partial_i \widetilde{p} - \partial_j \widetilde{\tau}_{ij}. \quad (6)$$

The unknown subgrid-scale stress (SGS) tensor $\widetilde{\tau}_{ij} = \widetilde{u_i u_j} - \widetilde{u_i} \widetilde{u_j}$ accounts for the effects of the small scales on the large scales and cannot be computed directly from the resolved quantities. Therefore, in order to close the equation (6), $\widetilde{\tau}_{ij}$ needs to be modelled. In this work, the model proposed in Wong and Lilly, 1994 is used. It is defined by :

$$\widetilde{\tau}_{ij} - \frac{1}{3} \widetilde{\tau}_{kk} \delta_{ij} = -2C \widetilde{\Delta}^{\frac{4}{3}} \widetilde{S}_{ij} \quad (7)$$

where $\widetilde{S}_{ij} = (\partial_i \widetilde{u_j} + \partial_j \widetilde{u_i})/2$ is the resolved strain tensor and $\widetilde{\Delta}$ is the LES filter width. The dimensional parameter C is evaluated by introducing a second (coarser) filter $\widehat{\cdot}$ (the test filter) and using the dynamic procedure (Germano et al., 1991). Since the dynamic procedure was developed initially for the case of the homogeneous isotropic turbulence, only minor changes have to be done while dealing with inhomogeneous flow. Indeed, here it can be assumed that C is a function of the direction of inhomogeneity $C = C(y)$. It can be obtained by averaging only in the $x - z$ directions, considered as homogeneous:

$$C(y) = \frac{1}{2(\widetilde{\Delta}^{4/3} - \widehat{\Delta}^{4/3})} \frac{\langle \widehat{L}_{ij} \widehat{S}_{ij} \rangle_{xz}}{\langle \widehat{S}_{ij} \widehat{S}_{ij} \rangle_{xz}} \quad (8)$$

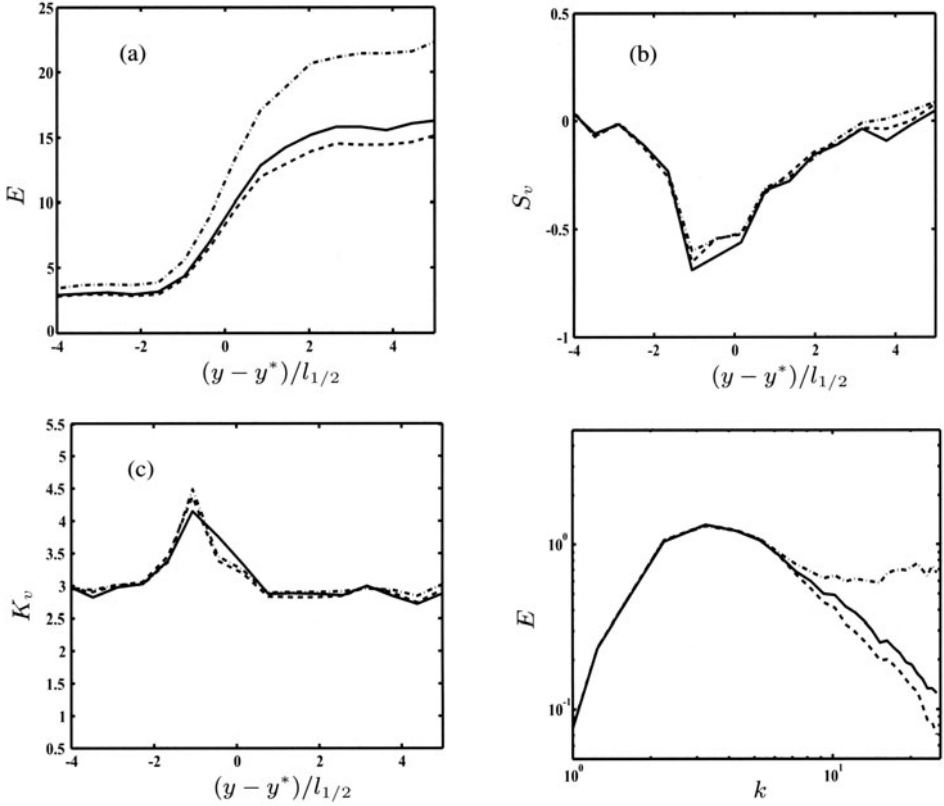


Figure 4. Energy (a), skewness (b) and kurtosis (c) profiles. Energy spectrum (d). All curves computed at $t^* = 0.56$. — : filtered DNS; --- : LES; ··· : no model.

where $\widehat{L}_{ij} = \widehat{\tilde{u}_i \tilde{u}_j} - \widehat{\tilde{u}_i} \widehat{\tilde{u}_j}$ is the Leonard tensor. The free parameter $\tilde{\Delta}/\widehat{\Delta}$ is set to be 2. It should be noticed that we have made use of the following relation: $\widehat{\cdots} = \widehat{\cdots}$, valid for cut-off filters. The LES initial condition was obtained by filtering the DNS field at time t_0 down to $32 \times 64 \times 32$ modes. In order to emphasize the importance of the model, a run without any model (referred to as the no-model) has been performed also. Finally, we have plotted for comparison the results obtained for the filtered DNS.

Fig. 4(a), (b), (c) shows the profiles of the resolved energy, the skewness and the kurtosis respectively. For the energy diagnostic, the LES run shows clearly a better agreement with the DNS than the no-model while both perform well for the skewness and kurtosis profiles. Surprising at first, this is to be expected since the intermittency is attributed to large-scale structures penetrating the low energy region from the high energy region. A more sensitive measurement of the effect of the model is the energy spectrum. It is shown on Fig. 4(d). The

expected piling up of the energy in the high wave vector modes is observed for the no-model while the simulation performed with the SGS model is capable of reproducing well the filtered DNS. Results obtained at later time show similar behaviors.

5. Conclusion

We have presented the results obtained for a high resolution DNS and have shown that most of the aspects of the experimental database of Veeravali & Warhaft (1989) could be reproduced. In particular the skewness and kurtosis show a good agreement despite the fact that they cannot be prescribed by the initialization procedure. It is also observed that, in the absence of shear, no significant anisotropy is observed in the flow. Finally, the comparisons between the predictions of LES and DNS show very good agreement, supporting the idea that isotropic models can reasonably be used for inhomogeneous flows.

References

- Batchelor, G. K. (1953). *The theory of homogeneous turbulence*. Cambridge University Press.
- Briggs, D. A., Ferziger, J. H., Koseff, J. R., and Monismith, S. G. (1996). Entrainment in a shear-free turbulent mixing layer. *J. Fluid Mech.*, 310:215–241.
- Germano, M., Piomelli, U., Moin, P., and Cabot, W. (1991). A dynamic subgrid-scale eddy-viscosity model. *Phys. Fluids A*, 3(7):1760–1765.
- Knaepen, B., Debliquy, O., and Carati, D. (2003). Dns and les of a shear-free mixing layer. *CTR Manuscript 182*.
- Rogallo, R. (1981). Numerical experiments in homogeneous turbulence. NASA technical Memorandum 81315, NASA, Ames Research Center.
- Shebalin, J., Matthaeus, W., and Montgomery, D. (1983). Anisotropy in mhd turbulence due to a mean magnetic field. *J. Plasma Physics*, 29:525–547.
- Veeravalli, S. and Warhaft, Z. (1989). The shearless turbulence mixing layer. *J. Fluid Mech.*, 207:191–229.
- Wong, V. and Lilly, D. (1994). A comparison of two subgrid closure methods for turbulent thermal convection. *Phys. Fluids*, 6:1016–1023.

A NONLINEAR INTERACTIONS APPROXIMATION MODEL FOR LES

M. U. HALILOGLU AND R. AKHAVAN*

Department of Mechanical Engineering

University of Michigan, Ann Arbor, MI 48109-2125, USA

* corresponding author. E-mail: raa@umich.edu

Abstract A new approach to LES modelling based on direct approximation of the non-linear terms in the filtered Navier-Stokes equations is presented. The proposed Nonlinear Interactions Approximation (NIA) model uses graded filters and deconvolution to parameterize the local interactions across the LES cutoff and an eddy viscosity term to parameterize the distant interactions. A dynamic procedure is used to determine the unknown eddy viscosity coefficient, rendering the model free of adjustable parameters. The proposed NIA model has been applied to LES of turbulent channel flow at $Re_\tau \approx 210$ and $Re_\tau \approx 570$. The results show that NIA significantly improves the prediction of turbulent flows compared to standard existing models such as the dynamic Smagorinsky or the dynamic mixed models.

Keywords: Large eddy simulation, subgrid scale modelling, explicit filtering, deconvolution, turbulent channel flow.

1. Introduction

In LES the flow variables are separated into large-scales and subgrid-scales by applying a low-pass spatial filter to the Navier-Stokes and continuity equations to damp out the fluctuations with a characteristic scale smaller than a given value Δ . This filtering operation introduces an unknown term $\overline{u_i u_j}$ in the Navier-Stokes equations which needs to be modelled. The traditional approach to modelling this term is to rewrite $\overline{u_i u_j} = \overline{u_i} \overline{u_j} + \tau_{ij}$ and to model the subgrid-scale (SGS) stress tensor, τ_{ij} . Existing SGS models can be broadly classified into five categories: eddy viscosity models [24, 22],[20],[8, 18] similarity and tensor diffusivity models [2, 31],[29], [14],[6, 15], generalized similarity and deconvolution models [23, 7],[26, 10], hyperviscosity models [5, 3], and spectral eddy viscosity models [13, 17],[5]. See [16] and [19] for comprehensive reviews.

The detailed interactions between the resolved and subgrid scales of motion can be modelled analytically in inertial range turbulence based on classical two-point closures such as TFM [13] and EDQNM [17, 5]. The effect of the subgrid scales on the resolved scales is captured in a k -dependent spectral eddy viscosity $\nu(k|\bar{k})$, representing the effective eddy viscosity acting on a resolved scale k due to nonlinear interactions with subgrid scales with $k > \bar{k}$ [13]. The spectral eddy viscosity is found to have a dual character [13, 1]. For $k/\bar{k} \ll 1$, the spectral eddy viscosity is k -independent and always positive. This portion of the spectral eddy viscosity represents a forward drain of energy from the resolved scales to disparate subgrid scales and can be well represented by an eddy viscosity model in the physical space. For a spectral cutoff filter, these interactions account for 25% of the total transfer across \bar{k} . For $k/\bar{k} \sim 1$, the above eddy viscosity mechanism is still at work, accounting for an additional 25% of the transfer across \bar{k} in the case of a spectral cutoff filter. However, there is now an additional mechanism arising from mutual shearing of resolved and subgrid vortical structures of scale comparable to $\bar{\Delta}$. These interactions give rise to both a forward transfer of energy from the resolved to subgrid scales, as well as a backscatter of energy from the subgrid to resolved scales. These ‘local’ (in wavenumber space) interactions can not be properly represented by an eddy viscosity model in the physical space. However, they contribute a significant portion of the total transfer (50% in the case of a spectral cutoff filter) and their accurate modelling is critical to the success of LES. Until recently it has not been clear how to incorporate these k -dependent features of the spectral eddy viscosity into physical-space SGS models. The structure function model [20] was proposed as a representation of the low wavenumber ($k \rightarrow 0$) asymptote of the spectral eddy viscosity in the physical space; hyperviscosity models [5, 3] have been proposed to mimic the cusps in the net spectral eddy viscosity observed with spectral cutoff filters near \bar{k} ; while similarity, generalized similarity, and deconvolution models can be viewed as attempts to model the ‘local’ interactions across the LES cutoff [1].

In this study we present an alternative modelling approach for LES based on direct approximation of the nonlinear terms, $\overline{u_i u_j}$, instead of the SGS stress, τ_{ij} . The proposed model, which we call the Nonlinear Interactions Approximation (NIA) model, is derived from the physical space representation of the spectral eddy viscosity which was suggested in [1]. Section 2 describes the NIA model and its implementation in LES. In section 3, the model performance is evaluated by LES of turbulent channel flow at $Re_\tau \approx 210$ and $Re_\tau \approx 570$. Section 4 provides a summary and conclusions.

2. The nonlinear interactions approximation model and its implementation in LES

In Akhavan et al. [1], a detailed analysis of the subgrid-scale interactions in a numerically simulated turbulent jet was performed in both the spectral-space and physical-space representations. Based on this analysis, a formulation of the spectral eddy viscosity in terms of a physical space SGS model was proposed. It was shown that the low wavenumber asymptote of the spectral eddy viscosity can be represented by a Smagorinsky term in the physical space, while the local interactions near the cutoff can be represented in terms of the dynamics of the scales near the cutoff. This suggests a parameterization of τ_{ij} as

$$\tau_{ij}^* \equiv (\overline{u_i u_j} - \overline{u_i} \overline{u_j})^* = (\tilde{u}_i \tilde{u}_j - \tilde{u}_i \tilde{u}_j)^* - 2C\overline{\Delta}^2 |\overline{S}| \overline{S}_{ij}, \quad (1)$$

where the $*$ superscript denotes the deviatoric part of the stress tensor, \overline{u}_i is the large-scale velocity field, \overline{S}_{ij} is the large-scale rate of strain tensor, $\overline{\Delta}$ is the characteristic width of the LES filter, and \tilde{u}_i represents the velocity field truncated (using a spectral cutoff filter) to a scale \tilde{k} where $1.25 \leq \tilde{k}/\overline{k} \leq 2$. While a value of $\tilde{k}/\overline{k} \approx 2$ ensures that all the ‘local’ interactions are captured in the first term on the r.h.s. of Eq. (1), it was shown in [1] that even for $\tilde{k}/\overline{k} \approx 1.25$ the bulk of the ‘local’ interactions are well represented. When the LES filter applied at \overline{k} is sharp (spectral cutoff), recovering \tilde{u}_i from \overline{u}_i is not an easy task and one has to either resort to approximations of the form suggested in [1] or perform nested computations as suggested for example in [7] or [4]. However, if the LES filter at \overline{k} is graded, \tilde{u}_i can be easily recovered from \overline{u}_i by inverse filtering or deconvolution because the resolved and subgrid scales have some overlap. In this case, to within the accuracy of the numerical discretization, one can assume $\overline{u_i u_j} \approx \tilde{u}_i \tilde{u}_j$. Equation (1) then reduces to a parameterization for the nonlinear terms in the filtered Navier-Stokes equations instead of the SGS stress term, given by

$$\overline{u_i u_j} = \tilde{u}_i \tilde{u}_j - 2C\overline{\Delta}^2 |\overline{S}| \overline{S}_{ij} + \frac{\delta_{ij}}{3} (\overline{u_k u_k} - \tilde{u}_k \tilde{u}_k). \quad (2)$$

This model, which we call the Nonlinear Interaction Approximation (NIA) model, is the subject of the present study. With NIA, the governing equations for LES of incompressible flow can be written as

$$\frac{\partial \overline{u}_i}{\partial t} + \frac{\partial}{\partial x_j} (\tilde{u}_i \tilde{u}_j) = -\frac{\partial \overline{p}}{\partial x_i} + \frac{1}{Re} \frac{\partial^2 \overline{u}_i}{\partial x_j \partial x_j} - \frac{\partial \psi_{ij}}{\partial x_j}, \quad (3)$$

$$\frac{\partial \overline{u}_i}{\partial x} = 0, \quad (4)$$

where $\psi_{ij} = -2C\overline{\Delta}^2 |\overline{S}| \overline{S}_{ij}$, and the isotropic term $\frac{\delta_{ij}}{3} (\overline{u_k u_k} - \tilde{u}_k \tilde{u}_k)$ is absorbed into pressure. The unknown coefficient C is found using the dynamic

procedure suggested by Germano [8] and Lilly [18]. To do this, an auxiliary graded filter is introduced at scale $\tilde{\Delta} = 2\bar{\Delta}$ and the nonlinear interactions at this scale are expressed as

$$\widetilde{\overline{u_i u_j}} = \widetilde{\hat{u}_i \hat{u}_j} - 2C \tilde{\Delta}^2 |\tilde{S}| \tilde{S}_{ij} + \frac{\delta_{ij}}{3} (\widetilde{\overline{u_k u_k}} - \widetilde{\hat{u}_k \hat{u}_k}), \quad (5)$$

where $\hat{\cdot}$ denotes a spectral cutoff filter. Combining Eqs. (5) and (2) gives C as

$$C = \frac{1}{2} \frac{H_{ij} M_{ij}}{M_{kl} M_{kl}}, \quad (6)$$

where $M_{ij} = (\bar{\Delta}^2 |\tilde{S}| \tilde{S}_{ij} - \tilde{\Delta}^2 |\tilde{S}| \tilde{S}_{ij})$ and $H_{ij} = (\widetilde{\overline{\hat{u}_i \hat{u}_j}} - \widetilde{\hat{u}_i \hat{u}_j})$. Note that, unlike DSM, no averaging is required in time or in space in the expression for C in Eq. (6). This makes NIA an inherently local model suitable for applications in complex geometry and non-equilibrium flows.

We solve Eqs. (3) and (4) for a turbulent channel flow using standard pseudospectral methods employing Fourier series in the homogeneous (x and y) directions and Chebyshev polynomials in the wall-normal (z) direction [1]. The simulations are de-aliased using the 2/3 rule. Filtering is applied only in the homogeneous (x and y) directions. The characteristic filter widths $\bar{\Delta}$ and $\tilde{\Delta}$ are defined as $\bar{\Delta} = (\bar{\Delta}_x \bar{\Delta}_y \Delta_z)^{1/3}$ and $\tilde{\Delta} = (\tilde{\Delta}_x \tilde{\Delta}_y \Delta_z)^{1/3}$, where Δ_z denotes the grid size in the z -direction. The graded LES and test filters are applied at $\bar{\Delta}_i = 2\Delta_i$ and $\tilde{\Delta} = 4\Delta_i$, respectively, where Δ_i denotes the grid size in the i th direction. The spectral cutoff filters at \check{k}_i and \hat{k}_i are applied at $\check{k}_i = 4/3(\pi/\bar{\Delta}_i) = 2/3k_{i,m}$ and $\hat{k}_i = 2(\pi/\tilde{\Delta}_i) = 1/2k_{i,m}$, respectively, where $k_{i,m}$ denotes the maximum wavenumber used in the simulations in the i th direction. For the graded filter, we use a discrete symmetric three-point box filter evaluated using the trapezoidal rule. With a uniform grid, this filter can be defined in each dimension as

$$\bar{u}_j = \sum_{l=-K_j}^{K_j} w_l^j u_{j+l}, \quad (7)$$

where w_l^j are the weights. In the Fourier space, this filter can be represented by the kernel [27]

$$\bar{G}(k_i) = \sum_{l=-K_j}^{K_j} w_l^j e^{-i\Delta_i k_i l}, \quad (8)$$

where Δ_i is the grid spacing and k_i is the wavenumber in the direction in which the filter is applied. The inverse of this filter kernel in the spectral space is used

Table 1. Computational parameters used in the simulations and predicted C_f values

Case	Resolution	Re_τ	L_x/h	L_y/h	$\overline{\Delta}_x^+$	$\overline{\Delta}_y^+$	$\Delta_{z_{max}}^+$	$C_f \times 10^3$
DNS	$64 \times 128 \times 129$	210	$8\pi/5$	$8\pi/5$	24.7	12.4	5.2	7.922
NIA	$16 \times 64 \times 65$	210	$8\pi/5$	$8\pi/5$	131.9	33.0	10.3	7.964
DMM	$16 \times 64 \times 65$	210	$8\pi/5$	$8\pi/5$	98.9	24.7	10.3	7.254
DSM	$16 \times 64 \times 65$	210	$8\pi/5$	$8\pi/5$	98.9	24.7	10.3	7.638
NIA(L)	$8 \times 32 \times 33$	210	$8\pi/5$	$8\pi/5$	263.9	66.0	20.58	6.920
DNS	$256 \times 256 \times 257$	570	$5\pi/3$	$5\pi/9$	17.5	5.8	7.0	5.671
NIA	$64 \times 64 \times 65$	570	$5\pi/3$	$5\pi/9$	93.3	31.1	27.9	5.699
DMM	$64 \times 64 \times 65$	570	$5\pi/3$	$5\pi/9$	69.9	23.3	27.9	5.770
DSM	$64 \times 64 \times 65$	570	$5\pi/3$	$5\pi/9$	69.9	23.3	27.9	5.343
NIA(L)	$32 \times 32 \times 65$	570	$5\pi/3$	$5\pi/9$	186.5	62.2	27.9	5.332

to construct the velocity field \tilde{u}_i up to $2/3k_{i,m}$, from which \hat{u}_i is also calculated. Since deconvolution is performed only up to $2/3k_{i,m}$, the singularities of the filter are avoided. As an alternative to the above exact deconvolution procedure, one can use approximate deconvolution as suggested for example by [9] or [25].

3. Results

The performance of NIA is evaluated in LES of incompressible turbulent channel flow at $Re_\tau = u_\tau h/\nu \approx 210$ and $Re_\tau \approx 570$, where u_τ is the wall-friction velocity and h denotes the channel half-width. The results are compared to DNS, available experimental data [30, 12], LES with no model, and LES using two popular SGS models, namely, the Dynamic Smagorinsky Model (DSM) [8, 18] and the Dynamic Mixed Model (DMM) [31]. The computational parameters used in these simulations and the predicted skin friction coefficients, C_f , are summarized in Table 1. To demonstrate that NIA remains robust at marginal LES resolutions, simulations are also reported with NIA at half the resolution of the original LES. The simulations with DSM and DMM were performed with filter widths of $\overline{\Delta}_i = 1.5\Delta_i$, instead of $\overline{\Delta}_i = 2\Delta_i$ used with NIA. This is done in order to employ the full computational resolution with these models. Furthermore, since DSM is known to perform poorly with graded filters [21], spectral cutoff filters were used with DSM instead of box filters. Simulations performed using DSM and DMM with the same filters as those used with NIA (i.e., box filters at $\overline{\Delta}_i = 2\Delta_i$) gave much poorer results. As such, the reported results for DSM and DMM represent the best possible performance of these models at the given resolution of the computations.

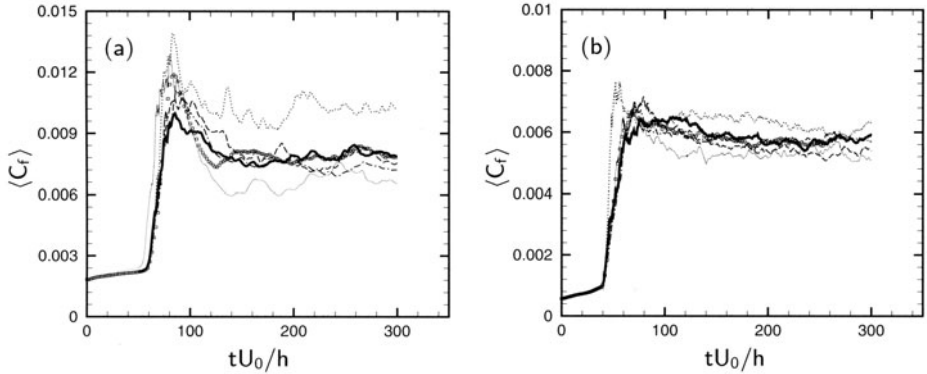


Figure 1. Evolution of the skin friction coefficient for (a) $Re_\tau \approx 210$, and (b) $Re_\tau \approx 570$. \square , DNS; thick solid lines, NIA; $-\cdot-$, DMM; $- -$, DSM; $---$, NIA(L); \cdots , no model.

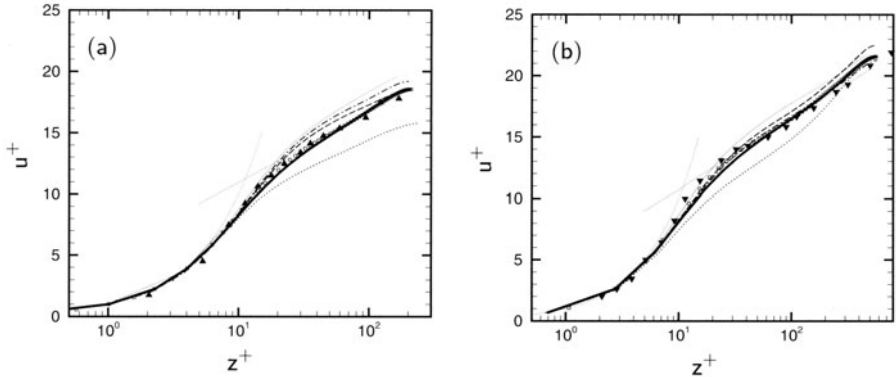


Figure 2. Mean velocity profile normalized by the friction velocity at (a) $Re_\tau \approx 210$, and (b) $Re_\tau \approx 570$. \square , DNS; thick solid lines, NIA; $-\cdot-$, DMM; $- -$, DSM; $---$, NIA(L); \cdots , no model; \blacktriangle , experiments at $Re_\tau \approx 170$ [30]; \blacktriangledown , experiments at $Re_\tau \approx 640$ [12].

All the simulations were started from laminar flow on which a combination of two- and three-dimensional least stable eigenmodes of the Orr-Sommerfeld equation were superimposed. A constant flow rate was imposed in the channel during the course of the simulations. Fig. 1 shows the time history of the skin friction coefficient, $C_f = 2\tau_w/\rho U_{bulk}^2$, as a function of tU_0/h , where $U_0 = 3/2U_{bulk}$ denotes the centerline velocity in the initial laminar channel. The flow undergoes transition between $60 < tU_0/h < 120$ and equilibrates to a stationary turbulent state after $tU_0/h \sim 200$. In the fully-developed turbulent state, NIA predicts a skin friction coefficient within 0.5% of the DNS results at both Reynolds numbers. In contrast, DSM and DMM incur errors of up to 6% and 8.5% in the prediction of C_f , respectively, as shown in Table 1. Even at marginal LES resolutions, NIA remains robust and predicts C_f values within 13% and 6% of DNS at Re_τ of 210 and 570, respectively.

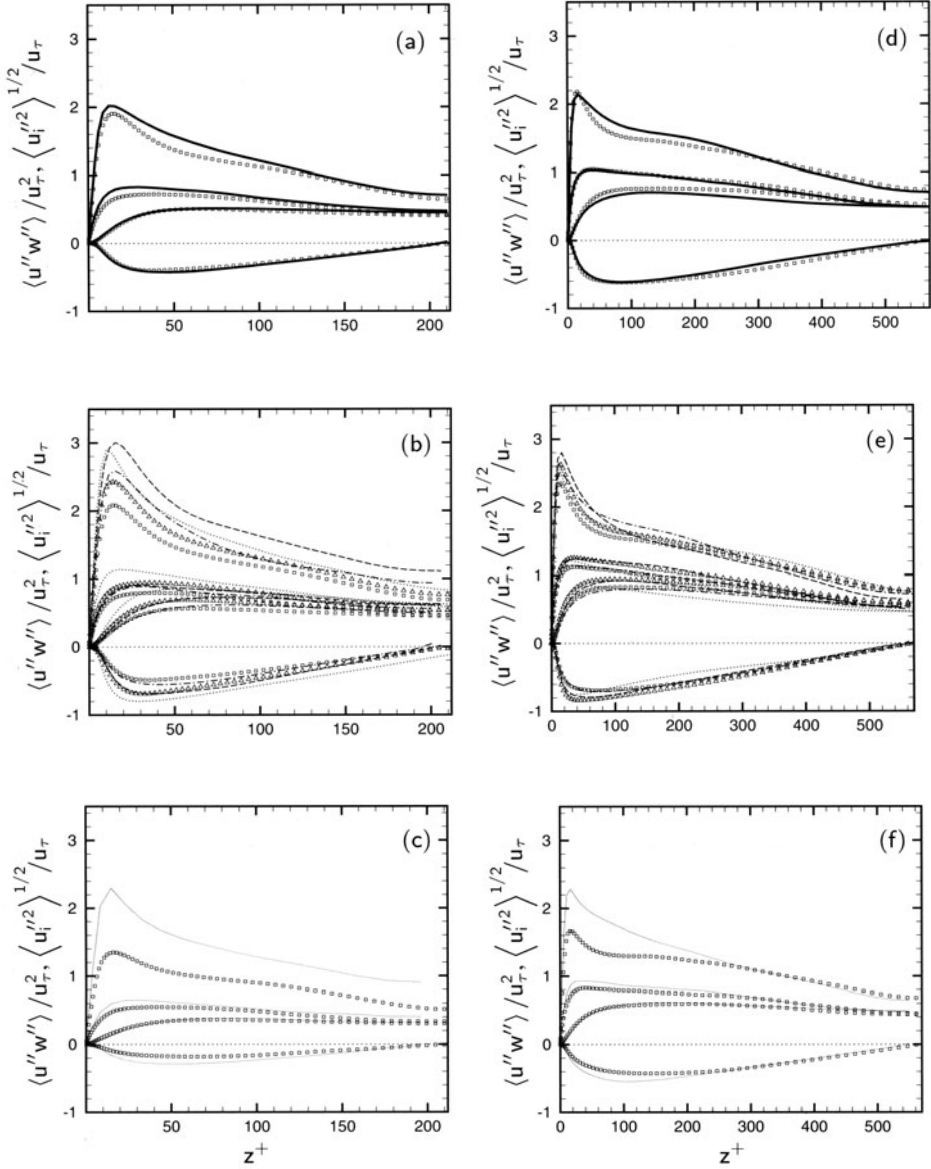


Figure 3. Resolved r.m.s. velocity fluctuations and Reynolds stresses at (a-c) $Re_\tau \approx 210$, (d-f) $Re_\tau \approx 570$. \square , DNS filtered using box filter at the resolution of (a,d) NIA, (b,e) DMM or (c,f) NIA(L); Δ , DNS filtered using spectral cut-off filter at resolution of DSM; thick solid lines, NIA; $-\cdot-$, DMM; $---$, DSM; $—$, NIA(L); \cdots , no model.

The mean velocity profiles predicted by these models are shown in Fig. 2. NIA predicts a mean velocity profile in good agreement with DNS, the avail-

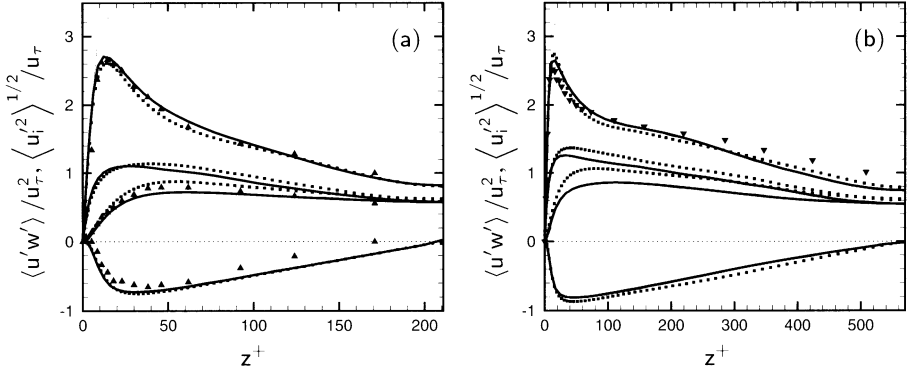


Figure 4. Full (resolved plus subgrid) r.m.s. velocity fluctuations and Reynolds stresses at (a) $Re_\tau \approx 210$, and (b) $Re_\tau \approx 570$. ■, DNS; thick solid lines, NIA; —, NIA(L); ▲, experiments at $Re_\tau \approx 170$ [30]; ▼, experiments at $Re_\tau \approx 640$ [12].

able experimental data [30, 12], and the law of the wall at both Reynolds numbers. Even at marginal LES resolutions, the model remains robust and predicts a logarithmic layer with the correct slope at both Reynolds numbers. However, due to the under-prediction of the wall-shear stress at marginal resolutions, the non-dimensional velocities are somewhat overpredicted here. In contrast, DSM fails to predict a logarithmic layer with the correct slope at both Reynolds numbers even at high LES resolutions. DMM performs better, but its predictions are not as good as those obtained with NIA at comparable LES resolutions.

The resolved root-mean-square velocity fluctuations and Reynolds stresses predicted by these models are compared to filtered DNS results in Fig. 3. NIA (Figs. 3a, 3d) predicts r.m.s. velocity fluctuations in good agreement with filtered DNS at both Reynolds numbers. At $Re_\tau \approx 210$, the peak of the streamwise r.m.s. velocity fluctuations is overpredicted by 6% compared to filtered DNS. However, this is significantly improved compared to DSM and DMM (Figs. 3b, 3e), which overpredict the peak of the r.m.s. streamwise velocity fluctuations by nearly 25% compared to their respective filtered DNS results at $Re_\tau \approx 210$.

With NIA, one can also predict the magnitude of the full (resolved plus subgrid) r.m.s. velocity fluctuations and Reynolds stresses. These quantities are computed using $\langle u'_i u'_j \rangle \approx \langle u''_i u''_j \rangle + \langle \tau_{ij} \rangle$ [28], where u'_i denotes the full (resolved plus subgrid) velocity fluctuations, u''_i denotes the resolved velocity fluctuations, $\tau_{ij} = \overline{u_i u_j} - \overline{u_i} \overline{u_j}$ with $\overline{u_i u_j}$ given by Eq. (2), and we have assumed the term $\frac{\delta_{ij}}{3} (\overline{u_k u_k} - \overline{u_k} \overline{u_k})$ to be negligible. The results are shown in Fig. 4. NIA predicts full r.m.s. velocity fluctuations and Reynolds stresses in good overall agreement with DNS and available experimental data

at both Reynolds numbers. The slight under-prediction of the full r.m.s. velocity fluctuations arises from the use of the Smagorinsky model for the ‘distant interactions’. Since the kinetic energy can not be properly recovered from an eddy-viscosity model, the only contribution to the subgrid kinetic energy here comes from the ‘local interactions’. As a result, the subgrid (and full) turbulence intensities are somewhat underpredicted.

4. Summary

A new approach to LES modelling is presented based on direct approximation of the nonlinear terms in the filtered Navier-Stokes equations. The proposed model, which we call the Nonlinear Interactions Approximation (NIA) model, uses graded filters and deconvolution to parameterize the ‘local interactions’ across the LES cutoff, and a Smagorinsky eddy viscosity term to parameterize the ‘distant interactions’. A dynamic procedure is used to determine the unknown eddy viscosity coefficient, rendering the model free of adjustable parameters. The proposed NIA model has been applied to LES of turbulent channel flow at $Re_\tau \approx 210$ and $Re_\tau \approx 570$. The results show good agreement with DNS and available experimental data, and are significantly improved compared to existing models such as DSM and DMM. The improvements in NIA arise from its more accurate modelling of the ‘local interactions’ across the LES cutoff. The inclusion of the ‘local interactions’ term in NIA results in a dynamic model coefficient C which on average is about 60% of that associated with DMM and 25% of that associated with DSM with box filters (DSM with spectral cutoff filters has a substantially lower C than DSM with box filters). Proper accounting of the local-interactions in NIA also results in a much narrower distribution of the dynamic model coefficient compared to DSM. This eliminates the need for any averaging of the dynamic model coefficient in time or space, making NIA an inherently localized model suitable for applications in complex and non-equilibrium flows.

Acknowledgments

This work was supported in part by DARPA Award#MDA972-01-1-0015. The computations were performed on resources provided through NRAC Award MCA02N025.

References

- [1] Akhavan, R., Ansari, A., Kang, S. and Mangiavacchi, N. (2000) *J. Fluid Mech.* **408**, 83–120.
- [2] Bardina, J., Ferziger, J.H. and Reynolds, W.C. (1983) *Technical Report No. TF-19*, Department of Mechanical Engineering, Stanford University, Stanford, CA.
- [3] Borue, V. and Orszag, S.A. (1995) *Phys. Rev. E*, **51**(2), R856–R859.

- [4] Bouchon, F. and Dubois T. (2001) in *Direct and Large-Eddy Simulation IV*, edited by B. J. Geurts, R. Friedrich and O. Metais (Kluwer, 2001), pp. 97–104.
- [5] Chollet, J.P. and Lesieur, M. (1981) *J. Atmos. Sci.* **38**, 2647–2757.
- [6] Clark, R.A., Ferziger, J.H. and Reynolds, W.C. (1979) *J. Fluid Mech.* **91** 1–16.
- [7] Domaradzki, J.A., Loh, K.C. and Yee, P.P. (2001) in *Direct and Large-Eddy Simulation IV*, edited by B. J. Geurts, R. Friedrich and O. Metais, pp. 45–54.
- [8] Germano, M., Piomelli, U., Moin, P. and Cabot, W.H. (1991) *Phys. Fluids A* **3**, 1760–1765.
- [9] Geurts, B.J. (1997) *Phys. Fluids* **9**(12), 3585–3587.
- [10] Geurts, B.J. and Holm, D.D. (2003) *Phys. Fluids* **15**(1), L13–L16.
- [11] Ghosal, S. (1996) *J. Comput. Phys.* **125**, 187–206.
- [12] Hussain, A.K.M.F., Reynolds, W.C. (1975) *J. Fluids Eng.* **97**(4), 568–580.
- [13] Kraichnan, R.H. (1976) *J. Atmos. Sci.* **33**, 1521–1536.
- [14] Leonard, A. (1974) *Adv. Geophys.* **18A**, 237–248.
- [15] Leonard, A. and Winckelmans, G. (1999) in *Direct and Large-Eddy Simulation III*, edited by P. Voke, N. D. Sandham and L. Kleiser, pp. 147–162.
- [16] Lesieur, M. and Metais, O. (1996) *Annu. Rev. Fluid Mech.* **28**, 45–82.
- [17] Leslie, D.C. and Quarini, G.L. (1979) *J. Fluid Mech.* **91**, 65–91.
- [18] Lilly, D.K. (1992) *Phys. Fluids A* **4** 633–635.
- [19] Meneveau, C. and Katz, J. (2000) *Annu. Rev. Fluid Mech.* **32** 1–32.
- [20] Metais, O. and Lesieur, M. (1992) *J. Fluid Mech.* **23**, 157–194.
- [21] Piomelli, U., Moin, P., and Ferziger, J.H. (1988) *Phys. Fluids* **31**(7), 1884–1891.
- [22] Schumann, U. (1975) *J. Comput. Phys.* **18**, 376–404.
- [23] Shah, K.B. and Ferziger, J.H. (1995) *CTR Annual Research Briefs*, pp. 73–90.
- [24] Smagorinsky, J. (1963) *Mon. Weather Rev.* **91**, 99–164.
- [25] Stolz, S. and Adams, N.A. (1999) *Phys. Fluids* **11**(7), 1699–1701.
- [26] Stolz, S., Adams, N.A. and Kleiser, L. (2001) *Phys. Fluids* **13**, 997–1015.
- [27] Vasilyev, O.V., Lund, T.S. and Moin, P. (1998) *J. Comput. Phys.* **146**, 82–104.
- [28] Voelkl, T. and Pullin, D.I. (2000) *Phys. Fluids* **12**(7), 1810–1825.
- [29] Vreman B., Geurts, B. and Kuerten, H. (1994) *Phys. Fluids* **6**(12), 4057–4059.
- [30] Wei, T. and Willmarth, W.W. (1989) *J. Fluid Mech.* **204**, 57–95.
- [31] Zang, Y., Street, R.L. and Koseff, J.R. (1993) *Phys. Fluids A* **5** 3186–3196.

TWO LEVEL SIMULATION OF HIGH-RE TURBULENT FLOWS

Konstantin Kemenov and Suresh Menon

*School of Aerospace Engineering, Georgia Institute of Technology,
Atlanta, Georgia 30332-0150*

suresh.menon@ae.gatech.edu

Abstract A new approach, two level simulation (TLS), has been developed based on the decomposition of velocity into large-scale and small-scale components. A coupled system of equations that is not based on an eddy-viscosity type of assumption has been implemented to simulate high-Re temporal mixing layer and channel flow. The small-scale equations are modeled on a family of three one-dimensional, orthogonal lines that are embedded inside the three-dimensional large-scale grid. Results suggest that the baseline TLS approach can capture high-Re flows in both free shear and wall-bounded layers using very coarse grids.

Keywords: Turbulent flows, small scales, large eddy simulation, subgrid scale modeling

1. Introduction

Direct numerical simulation (DNS) of high Reynolds (Re) number wall-bounded flows is computationally very expensive because of the resolution requirement in the near-wall region. Even with the advent of massively parallel supercomputers, DNS is still limited to low Re number flows ($Re_\tau = 590$, Moser et al., 1999). Recently, large eddy simulation (LES) has become a viable method to study high-Re complex flows. However, past LES of high-Re wall-bounded flows have not proven successful in capturing the near-wall dynamics, which is dominated by quasi-streamwise vortices, unless DNS like resolution is employed near the wall. This has led to methods in which only the outer layer is computed while the near-wall region is modeled. Many near-wall subgrid models have been proposed (Piomelli and Balaras, 2002), but so far such models have shown a relatively limited success. A fundamental limitation is that most models employ empirical arguments about small-scale isotropy and requires the introduction of arbitrary model parameters. However, the near-wall region is strongly anisotropic and to resolve it near-DNS resolution has been required. This resolution need is prohibitive for high-Re flows

and thus, new methods are needed that are not dependent on DNS resolution near the wall.

The present approach, called two level simulation (TLS), departs significantly from LES and is similar to several alternative approaches (referred loosely here as “decomposition” approaches) that have emerged in literature recently. In contrast to LES, where decomposition is introduced through spatial filtering and the major effort is concentrated on SGS modeling, in “decomposition” approaches considerable attention is devoted to modeling of small-scale velocity itself. This usually involves a derivation of the governing equation for small-scale velocity with its subsequent simplification based on some physical arguments (Foias et al., 1988; Laval et al., 2000). In TLS, the small-scale velocity field is explicitly reconstructed by solving approximate small-scale equations on a family of 1D grid lines embedded inside the 3D resolved grid. The 3D small-scale velocity field constructed from these 1D lines serves as a closure for the 3D large-scale equations. The reduction in dimensionality for the small-scale equations allows the coupled TLS approach to be computationally feasible (on massively parallel machines). In this paper, the mathematical formulation of the TLS approach is highlighted and its application to simulation of high-Re temporal mixing layers and channel flow is discussed.

2. Mathematical Formulation

We split the velocity and pressure fields into large-scale (LS, superscript L) and small-scale (SS, superscript S) components:

$$u_i(\bar{x}, t) = u_i^L(\bar{x}, t) + u_i^S(\bar{x}, t), \quad p(\bar{x}, t) = p^L(\bar{x}, t) + p^S(\bar{x}, t) \quad (1)$$

and substitute into the incompressible Navier-Stokes equations to obtain the baseline TLS equations:

$$\frac{\partial}{\partial t}(u_i^L + u_i^S) + \frac{\partial}{\partial x_j}(u_i^L + u_i^S)(u_j^L + u_j^S) = -\frac{\partial}{\partial x_i}(p^L + p^S) + \nu \frac{\partial^2}{\partial x_j^2}(u_i^L + u_i^S) \quad (2)$$

$$\frac{\partial}{\partial x_i}(u_i^L + u_i^S) = 0 \quad (3)$$

If the SS fields (u_i^S, p^S) are known, the LS fields (u_i^L, p^L) can be determined by integrating Eqs. (2, 3). The LS velocity represents not only the filtered quantity with respect to some spatial filter (as in LES) but also any LS velocity that can be defined based on its values at LS grid points. Once a LS quantity is defined any small-scale quantity is defined based on decomposition similar to Eq. (1). Rearranging Eq. (2) results in the coupled LS and SS equations:

$$\frac{\partial u_i^L}{\partial t} + \frac{\partial}{\partial x_j}(u_i^L + u_i^S)(u_j^L + u_j^S) = -\frac{\partial p^L}{\partial x_i} + \nu \frac{\partial^2 u_i^L}{\partial x_j^2} + F_i^S(u_i^S, p^S) \quad (4)$$

$$\frac{\partial u_i^S}{\partial t} + \frac{\partial}{\partial x_j} (u_i^L + u_i^S)(u_j^L + u_j^S) = -\frac{\partial p^S}{\partial x_i} + \nu \frac{\partial^2 u_i^S}{\partial x_j^2} + F_i^L(u_i^L, p^L) \quad (5)$$

The LS and SS velocities affect each other through the forcing terms F_i^S, F_i^L :

$$F_i^L(u_i^L, p^L) = -\frac{\partial u_i^L}{\partial t} - \frac{\partial p^L}{\partial x_i} + \nu \frac{\partial^2 u_i^L}{\partial x_j^2} \quad (6)$$

$$F_i^S(u_i^S, p^S) = -\frac{\partial u_i^S}{\partial t} - \frac{\partial p^S}{\partial x_i} + \nu \frac{\partial^2 u_i^S}{\partial x_j^2} \quad (7)$$

Note that all forms of the TLS Eqs. (2, 4-5) are different forms of the full Navier-Stokes equations written for different unknown velocities, and most importantly, they do not involve any type of LES spatial filtering. Thus, the TLS formulation is inherently free from problems associated with filtering such as commutativity between filtering and differentiation, which is an issue in LES formalism near boundaries and on non-uniform grids (Ghosal, 1999).

A numerical simulation of the TLS equations is quite challenging and will require computational effort similar to that for a DNS. Therefore, although Eq. (4) is solved in 3D domain, Eq. (5) is simplified while retaining the underlying picture of multi-scale interaction. Since the SS field evolves on a much faster time scale than the LS field we introduce two time coordinates such that:

$$u_i(\bar{x}, t) = u_i(\bar{x}, t^L; t^S) = u_i^L(\bar{x}, t^L) + u_i^S(\bar{x}, t^L; t^S). \quad (8)$$

Here, we assume that u_i^L does not depend on the SS time coordinate t^S , and is set to a constant in the t^S time scale. Thus, the time derivative in Eq. (5) is assumed to be with respect to t^S and all LS quantities in Eq. (5) depend only on the spatial coordinates.

To model the SS field in a 3D domain Ω , we consider a family of three 1D lines embedded in Ω (Fig. 1). Generally, the lines can be arbitrarily positioned in space, even in random fashion, and do not have to be straight. Here, we consider a Cartesian and orthogonal (for simplicity) system of three lines $\{l_1, l_2, l_3\}$ that are parallel to the corresponding LS coordinates x_i and model the SS field on these lines such that: $u_i^S(\bar{x}, t^L; t^S) \rightarrow u_{i,l_j}^S(l_j, t^L; t^S)$, $l_j \in \Omega$. The simplified set of 1D equations obtained from Eq. (5) requires closure for SS velocity gradients with respect to directions orthogonal to the lines. We make one assumption that:

$$\frac{\partial u_i^S}{\partial l_1} = \frac{\partial u_i^S}{\partial l_2} = \frac{\partial u_i^S}{\partial l_3} \quad (9)$$

and obtain the 1D small-scale equations:

$$\frac{\partial u_{ij}^S}{\partial t} + NL(u_{ij}^S, u_{ij}^L, l_j) = 3\nu \frac{\partial^2 u_{ij}^S}{\partial l_j^2} - \frac{\partial p_j^S}{\partial l_j} + F_{ij}^L(u_{ij}^L, p_j^L, l_j) \quad (10)$$

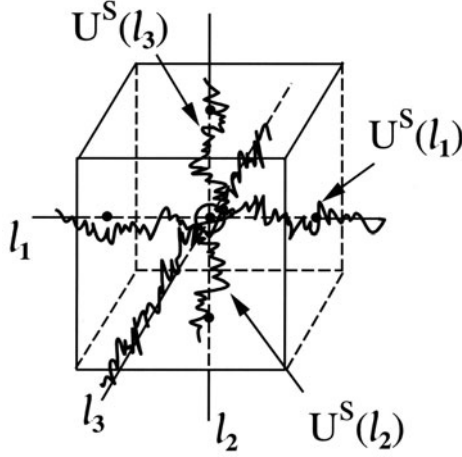


Figure 1. The small-scale 1D line arrangement within a 3D large-scale grid in the TLS model. One component of the SS velocity is shown on each line schematically.

$$\frac{\partial}{\partial l_j}(u_{1j}^S + u_{2j}^S + u_{3j}^S) = 0 \quad (11)$$

Here, the following notation is used: $u_{ij}^S(l_j, t^S) \equiv \{u_i^S(\bar{x}, t^S) \mid \bar{x} \in l_j\}$ represents the i -th component of the small-scale velocity belonging to the j -th type of line. The small and large scales are coupled through the non-linear convective term NL which subsumes all terms of the small-scale equation except diffusion, pressure gradient, non-stationary and the large-scale forcing terms F_{ij}^L . For example, the 1D equation for $u^S \equiv u_{1,l_1}^S$ along l_1 -line is:

$$\begin{aligned} \frac{\partial u^S}{\partial t} + \frac{\partial}{\partial l_1} \left[uu + u^S(v+w) + u^L(v^S + w^S) \right] + u^S \left[\frac{\partial v^L}{\partial y} - \frac{\partial v^L}{\partial x} + \frac{\partial w^L}{\partial z} - \frac{\partial w^L}{\partial x} \right] + \\ v^S \left[\frac{\partial u^L}{\partial y} - \frac{\partial u^L}{\partial x} \right] + w^S \left[\frac{\partial u^L}{\partial z} - \frac{\partial u^L}{\partial x} \right] + \frac{\partial u^L v^L}{\partial y} + \frac{\partial u^L w^L}{\partial z} = 3\nu \frac{\partial^2 u^S}{\partial l_1^2} - \frac{\partial p^S}{\partial l_1} + F^L, \end{aligned} \quad (12)$$

where $u = u^L + u^S = u_{1,l_1}^L + u_{1,l_1}^S$, $p^S = p_{l_1}^S$, $F^L = F_{1,l_1}^L$, and so on.

3. Results and Discussion

In the numerical implementation, four steps are involved: (i) at the n -th time step t_n^L , interpolate u_i^L and p^L onto each of the 1D lines, such that: $u_i^L(\bar{x}, t_n^L) \rightarrow u_{ij}^L(l_j)$, $p^L(\bar{x}, t_n^L) \rightarrow p_j^L(l_j)$; (ii) solve Eqs. (10, 11) on each line with corresponding boundary condition to obtain $u_{ij}^S(l_j, t^S; t_n^L)$; (iii) obtain the SS velocity on the LS grid u_i^S by averaging $u_{ij}^S(l_j, t^S)$ over the three

lines intersecting at the LS grid point: $\left[u_i^S(\bar{x}, t_n^L) \right]_L \leftarrow u_{ij}^S(l_j, t^S; t_n^L)$; (iv) advance the LS velocity $u_i^L(\bar{x}, t_n^L)$ to time $t_{n+1}^L = t_n^L + \Delta t^L$ by solving Eq. (4). Here, Δt^L is the time step for evolving the LS field. In step (ii), u_{ij}^S evolves from an initial zero state at a time step Δt^S for a number of time steps $N = O(\Delta t^S / \Delta t^L)$ before it is spatially averaged over all three 1D lines within each LS 3D cell to obtain u_i^S . This averaged u_i^S is considered the LS part of the SS velocity that is evolving at the slow time t^L on the LS grid. In step (iv), the LS field (Eq. 4) is forced by the LS part of the SS field in each cell. Further details on the implementation of TLS model can be found elsewhere (Kemenov and Menon, 2003).

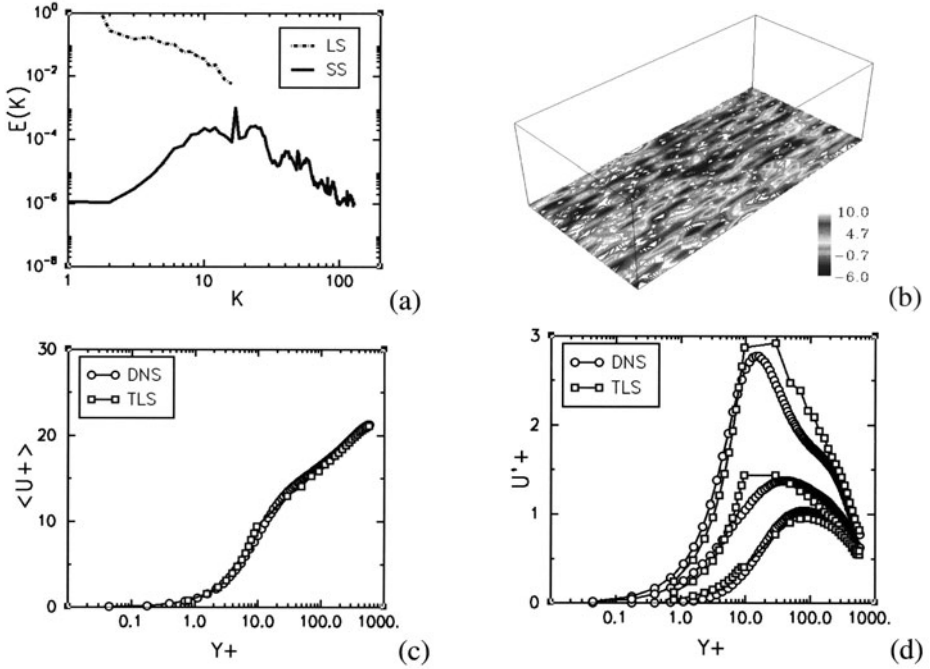


Figure 2. TLS prediction of channel flow compared to DNS (Moser et al., 1999). (a) LS and SS averaged energy spectra over streamwise lines in near-wall plane; (b) near-wall (LS+SS) streamwise velocity fluctuation contours at $y^+ = 9.5$; (c) mean streamwise velocity $\langle u^+ \rangle$ and (d) rms velocities $u_i'^+$ (in descending order: streamwise, spanwise, wall-normal).

TLS of channel flow has been conducted using a second-order accurate staggered grid technique using a third-order, low storage Runge-Kutta scheme for temporal discretization. A $Re_\tau=590$ turbulent channel flow is simulated using a $32 \times 40 \times 32$ LS grid with no stretching in the streamwise and the spanwise directions and only a nominal stretching in the wall-normal direc-

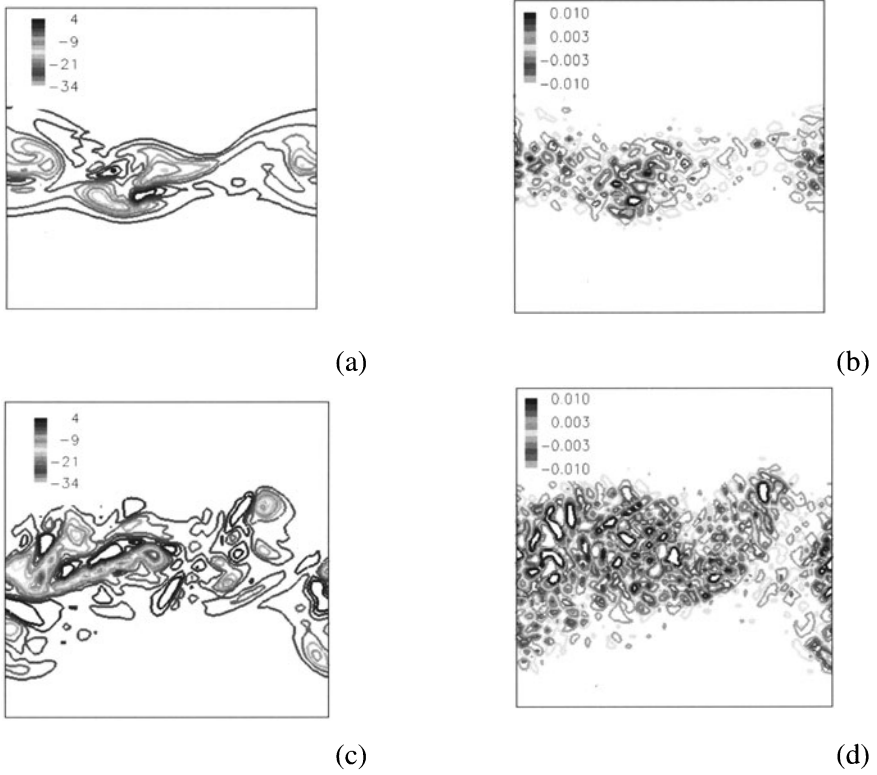


Figure 3. LS (a, c) and SS (b, d) spanwise vorticity contours at $T = 40$ and 75 .

tion ($\Delta y_{min}^+ = 19$). This near-wall resolution is very coarse even for LES (the DNS resolution is $384 \times 257 \times 384$). The near-wall turbulent field is not expected to be captured completely in the LS field and the burden of the accurate reconstruction of the total turbulent field is on the SS model. A uniform grid of 8 SS cells per LS cell is used in the periodic directions and a variable grid of 12 (near the wall) to 4 (in the centerline region) is used in the wall-normal direction.

Typical results are summarized in Figs. 2(a-d). It can be seen that the TLS approach recovers both LS and SS spectra (Fig. 2a). The near-wall velocity contours (Fig. 2b) show the characteristic high-speed streaks observed in past DNS and LES studies. The comparison between the DNS and TLS mean streamwise velocity and rms fluctuations (Figs. 2c, d) show that the present approach can capture the near-field turbulence reasonably well. Analysis of the results suggest that the non-linear interactions between the LS and SS fields in the RS equation (Eq. 4) provide an adequate 3D forcing effect on the LS

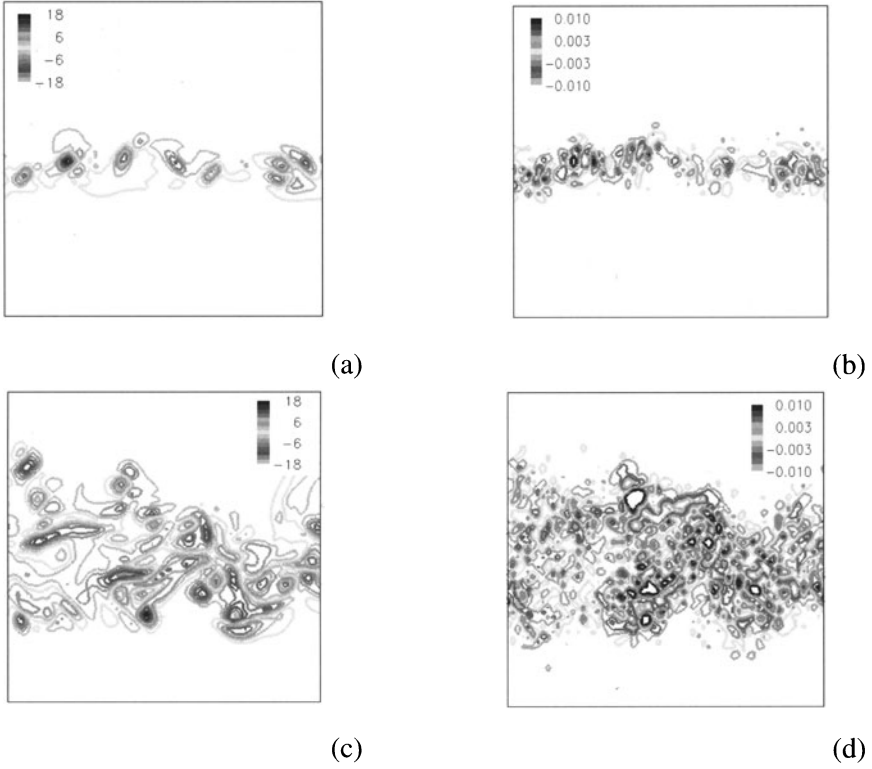


Figure 4. LS (a,c) and SS (b,d) streamwise vorticity contours at $T = 40$ and 75 .

field. More detailed analysis is underway to determine how the TLS method recovers the near-wall anisotropy using the SS model developed here.

Temporal mixing layers are also simulated primarily with the goal of evaluating the performance of TLS away from the wall and also in regions where 2D coherent modes dominate (where SS field should be negligible). The TLS used for the channel case is used here without any modification. A uniform resolution of the 64^3 LS grid is employed (with 4 SS cells per LS cell) to discretize a 4π cubic domain and Re_δ number is 200 (based on the initial vorticity thickness and the half of the maximum difference of the initial velocity across the layer). The hyperbolic tangent mean velocity profile with the superimposed 3D random fluctuations of high intensity is employed as an initial condition.

The contours of the LS and SS spanwise and streamwise vorticity at the non-dimensional times $T = 40$ and $T = 75$ are given in Figs. 3 (a-c), 4 (a-c). The occurrence of positive LS spanwise vorticity regions (Fig. 3d) indicates the presence of the vortex-stretching mechanism responsible for transition to 3D turbulence. It is also seen that the SS vorticity field is almost three order of

magnitude smaller than LS vorticity since the most of energy is concentrated in LS structures. Nevertheless the SS field is still created in regions with high LS velocity gradients which indicates the TLS ability to capture the physically correct SS vorticity pattern.

4. Conclusion

A new TLS approach, as an alternative to LES, has been developed based on the decomposition of velocity into large and small-scale components. A coupled system of the large and small-scale equation, that is not based on an eddy-viscosity type of assumptions and requires no adjustable parameters, has been derived and implemented to simulate two very different turbulent flows: channel flow with $Re_\tau = 590$ and temporal mixing layer with $Re_\delta = 200$. Results suggest that the TLS approach has the potential for capturing turbulent flow behavior at high-Re numbers using very coarse grids. The more detailed comparison of temporal mixing layer results with benchmark LES results (Vreman et al., 1997) is currently underway. Further study is still needed to understand all the nuances of the TLS approach. Issues related to optimal large-scale grid resolution and different flow geometries are currently being addressed.

Acknowledgments

This work is supported by the Office of Naval Research. Computational time has been provided at DOD HPCC at Maui, HI and NAVOCEANO, AL.

References

- Foias, C., Manley, O., and Temam, R. (1988). Modeling on the interaction of small and large eddies in two-dimensional turbulent flows. *Mathematical Modeling and Numerical Analysis*, 22:93–114.
- Ghosal, S. (1999). Mathematical and physical constraints on large eddy simulation of turbulence. *AIAA Journal*, 37:425–433.
- Kemenov, K. and Menon, S. (2003). Two level simulation of high- Re number non-homogeneous turbulent flows. *AIAA paper 2003-0084*.
- Laval, J.P., Dubrulle, B., and Nazarenko, S. (2000). Dynamical modeling of sub-grid scales in 2D turbulence. *Physica D*, 142:231–253.
- Moser, R.D., Kim, J., and Mansour, N.N. (1999). Direct numerical simulation of turbulent channel flow up to $Re_\tau = 590$. *Physics of Fluids*, 11:943–945.
- Piomelli, U. and Balaras, E. (2002). Wall layer models for large eddy simulation. *Annual Review of Fluid Mechanics*, 34:349–374.
- Vreman, B., Geurts, B., and Kuerten, H. (1997). Large-eddy simulation of the turbulent mixing layers. *Journal of Fluid Mechanics*, 339:357–390.

ANALYSIS OF RELAXATION REGULARIZATION AS SUBGRID-SCALE MODEL FOR LARGE-EDDY SIMULATION

S.B. Müller¹, N.A. Adams² and L. Kleiser¹

¹ *Institute of Fluid Dynamics, ETH Zürich, CH-8092 Zürich, Switzerland*
se@ifd.mavt.ethz.ch, kleiser@ifd.mavt.ethz.ch

² *Institute of Fluid Mechanics, Technical University of Dresden, D-01062 Dresden, Germany*
Nikolaus.Adams@ism.mw.tu-dresden.de

Abstract We connect the eddy-viscosity concept employed in the eddy-damped quasi-normal Markovian (EDQNM) theory of turbulence with the relaxation-term concept which is being used with great success in the approximate deconvolution model (ADM) for large-eddy simulation. We present a representation of the eddy viscosity ν_e in terms of a relaxation-term formulation with optimized filter kernel. Subgrid-scale modeling properties of the relaxation regularization are assessed for forced isotropic turbulence at high Reynolds number. We also propose a new formulation of the relaxation regularization where the inverse relaxation time scale is derived from theory.

Keywords: Large-eddy simulation, isotropic turbulence

1. Introduction

The spectral eddy-viscosity approach (Kraichnan, 1976, Chollet and Lesieur, 1981) is a widely used approach to large-eddy simulation in spectral computations and is based on a wavenumber dependent eddy viscosity that has been derived from analytical theory of turbulence. In this contribution, the relation between a relaxation regularization as used in ADM (Stolz et al., 2001) and the spectral eddy-viscosity concept is investigated. We derive filter-based representations of spectral eddy-viscosity dissipation for application to the incompressible Navier-Stokes equations.

2. Relaxation regularization and spectral eddy viscosity

When studying the relation between relaxation regularization and commonly used subgrid-scale models, several questions arise immediately: What are the

effects of the relaxation regularization when added to the system of filtered equations? Why does this type of dissipation prove to be successful in numerous simulations? In order to answer these questions, it is useful to shortly review existing subgrid-scale model formulations. An important modeling approach in large-eddy simulation is the eddy-viscosity concept where the global drain of energy from large (resolved) to small (unresolved) scales is modeled by a simple eddy viscosity, invoking the fact that the unclosed terms arising in the filtered Navier-Stokes equations represent stresses (stresses are naturally related to the strain rate tensor by a molecular viscosity, at least in constitutive material laws for Newtonian fluids).

Refinements of this modeling concept resulted in numerous models: (i) models that take into consideration that the eddy viscosity acts differently on different scales of motion, yielding wavenumber-dependent eddy-viscosity approximations derived from analytical theories of turbulence; (ii) models that dismiss simplifying assumptions such as subgrid equilibrium where it is assumed that changes in the resolved scales are immediately detected by the subgrid field: additional transport equations for the subgrid-scale kinetic energy are employed and the usefulness of these models is shown in a number of test cases, e.g. Menon et al., 1996; (iii) models that explicitly distinguish between transfer from large scales to small scales and backward transfer from small to large scales (so-called *backscatter*); the latter transfer terms are modeled by incorporation of stochastic random forcings, e.g. Chasnov, 1991: in case of homogeneous isotropic turbulence certain turbulence statistics can be improved; (iv) extensive work has also been spent on the development of physical-space formulations with adequate determination of time-dependent model constants varying locally in space, see e.g. the dynamic procedure for the Smagorinsky model (Germano et al., 1991); (v) recent developments aim at vanishing the eddy viscosity dissipation at lower wavenumbers and allowing it to act only at higher wavenumbers, see e.g. the models of Hughes et al., 2001, Stolz et al., 2003.

On the other hand, increasing publications report success using implicit large-eddy simulations where the features of particular numerical methods are used to construct implicit subgrid-scale models, e.g. Grinstein and Fureby, 2002.

In the present contribution, we focus on the spectral eddy-viscosity model for comparison with relaxation regularization since the spectral model was constructed to exhibit desirable properties like accounting for the correct effective energy transfer from large to small scales in isotropic turbulence. Furthermore, it was successfully used as a research tool in various fundamental investigations concerning isotropic turbulence and the inertial subrange.

In order to compare the relaxation regularization with the theoretical eddy viscosity, we define the relaxation term of ADM (see Stolz et al., 2001) in

spectral space as the right-hand side of the Fourier-transformed incompressible Navier-Stokes equations

$$\left[\frac{\partial}{\partial t} + \nu k^2 \right] \hat{\mathbf{u}}(\mathbf{k}, t) + \hat{\mathbf{N}}(\mathbf{k}, t) = -\chi(t) \left(1 - \hat{Q}_N(\mathbf{k}) \hat{G}(\mathbf{k}) \right) \hat{\mathbf{u}}(\mathbf{k}, t), \quad (1)$$

where $\hat{\mathbf{u}}(\mathbf{k}, t)$ denotes the Fourier-transformed filtered solution. $\hat{\mathbf{N}}(\mathbf{k}, t)$ represents the resolved-scale nonlinear term. For a definition of this term in spectral space see Pope, 2000 (p. 606). It is important to notice that in this contribution this term is not treated by approximate deconvolution operations, unlike in the ADM formulation. \hat{G} is the primary filter kernel, and \hat{Q}_N is the kernel of the approximate deconvolution operator defined as

$$\hat{Q}_N = \sum_{\nu=0}^N \left(1 - \hat{G} \right)^\nu, \quad (2)$$

e.g. Stolz et al., 2001, where N is the deconvolution order. The parameter χ is the relaxation parameter that determines the total amount of dissipation by relaxation regularization. The specific amount of dissipation at a certain (resolved) wave length is controlled by the form of \hat{G} . We refer to the product $\hat{G}_2 := \hat{Q}_N \hat{G}$ as secondary filter kernel. The relaxation term (1) can be related to a spectral vanishing viscosity mechanism since the combination of, e.g. Q_5 with G , essentially represents a relaxation regularization being inactive at low wavenumbers but acting strongly at wavenumbers near the numerical cutoff (see also figure 1 (a)).

We next consider the formulation for the spectral eddy-viscosity model. This model is typically defined as

$$\left[\frac{\partial}{\partial t} + (\nu_e + \nu) k^2 \right] \hat{\mathbf{u}} = \hat{\mathbf{N}}(\mathbf{k}, t), \quad (3)$$

where the effective subgrid-scale dissipation (at different scales of motion) is represented by a wavenumber-dependent spectral eddy viscosity

$$\nu_e(k|k_c, t) = \nu_e^+(k|k_c) \cdot \sqrt{\frac{E(k_c, t)}{k_c}} \quad (4)$$

with a non-dimensional eddy viscosity written as

$$\nu_e^+(k|k_c) = C_K^{-3/2} \left[0.441 + 15.2 \exp \left(-3.03 \cdot \frac{k_c}{k} \right) \right], \quad 0 < k \leq k_c, \quad (5)$$

(Chollet, 1983), where C_K is the Kolmogorov constant, k_c the numerical cutoff wavenumber and $E(k_c, t)$ is the spectral energy density at k_c as function of

time. Eq. (5) arises from EDQNM theory, a well-known analytical framework to investigate eddy-viscosity concepts (Chollet, 1983).

In our investigations, motivated by ADM (Stolz et al., 2001 and references therein) we replace the spectral eddy-viscosity dissipation

$$-\nu_e(k|k_c, t)k^2\hat{\mathbf{u}} \quad (6)$$

by a relaxation regularization using a filter \hat{G}_2 such that $\chi(t)(1 - \hat{G}_2) \approx \nu_e(k|k_c, t)k^2$ or,

$$\frac{1 - \hat{G}_2}{k^2} \approx \frac{\nu_e^+(k|k_c)}{\chi^+}, \quad \chi^+ := \nu_e^+(k_c|k_c)k_c^2. \quad (7)$$

How we adapt the filter kernel \hat{G}_2 is documented in the next section.

3. Optimizing filter definitions

In this section, we detail procedures to obtain filters which approximate the spectral eddy viscosity with sufficient accuracy. For simplicity we begin by trying to fit explicit discrete filters.

Explicit Filters. For a solution being available on a set of discrete grid points, explicit symmetric filter definitions can be implemented in physical space by

$$\bar{f}_i = a f_i + \frac{b}{2} (f_{i+1} + f_{i-1}) + \frac{c}{2} (f_{i+2} + f_{i-2}) + \frac{d}{2} (f_{i+3} + f_{i-3}) + \dots \quad (8)$$

Given such an approximation, the task consists of finding coefficients a, b, c, d, \dots such that the transfer function of (8) has characteristics corresponding to spectral eddy-viscosity dissipation. The transfer function of (8) can be easily derived and has the general form (e.g. Lele, 1992)

$$\hat{G}_2(\omega) = a + b \cos(\omega) + c \cos(2\omega) + d \cos(3\omega) + \dots, \quad \omega \equiv \pi \frac{k}{k_c}. \quad (9)$$

A Taylor series expansion of (9) yields

$$\hat{G}_2(\omega) = \sum_{m=0}^{\infty} \frac{1}{(2m)!} \hat{G}_2^{(2m)}(0) \omega^{2m}. \quad (10)$$

Matching the Taylor series coefficients from this expansion with the coefficients of a polynomial representing the EDQNM working fit (5) reduces the number of free parameters in the transfer function (9). The expression (5) emphasizes that the constant part of the normalized eddy viscosity (commonly called *plateau*) is the only remaining asymptotic value as $k \rightarrow 0$ and does only

depend on the Kolmogorov constant C_K . The remaining free parameters of the filter transfer function can be determined by minimizing the integral

$$J = \int \left[\nu_e^+(\omega k_c/\pi|k_c)/\nu_e^+(k_c|k_c) - (1 - \hat{G}_2(\omega, a, b, c, \dots))/(\omega/\pi)^2 \right]^2 d\omega. \quad (11)$$

We require $(1 - \hat{G}_2(\omega, a, b, c, \dots))/(\omega/\pi)^2$ to match $\nu_e^+(\omega k_c/\pi|k_c)/\nu_e^+(k_c|k_c)$ in a fairly wide wavenumber range, $\omega \leq 9/10\pi$. The upper bound was chosen because the slope of the transfer function (9) vanishes in the neighborhood of k_c and the spectral eddy-viscosity dissipation can not be represented accurately in this wavenumber range. Equality constraints arising from the comparison of Taylor series expansions were incorporated prior to optimization and serve to match the spectral eddy viscosity for low ω .

Compact filters. Apart from the common filters employed in LES such as Gaussian, top-hat or spectral filter, Padé filters have gained increased popularity in recent years. We employed also this type of filter definition to construct a 'filter'-representation of the theoretical eddy-viscosity dissipation. The classical form of implicit symmetric Padé-filters (Lele, 1992) is given by the equation

$$\beta \bar{f}_{i+2} + \alpha \bar{f}_{i+1} + \bar{f}_i + \alpha \bar{f}_{i-1} + \beta \bar{f}_{i-2} = a + \frac{b}{2}(f_{i+1} + f_{i-1}) + \frac{c}{2}(f_{i+2} + f_{i-2}) + \frac{d}{2}(f_{i+3} + f_{i-3}). \quad (12)$$

The transfer function corresponding to equation (12) is

$$\hat{G}_2(\omega) = \frac{a + b \cos \omega + c \cos 2\omega + d \cos 3\omega}{1 + 2\alpha \cos \omega + 2\beta \cos 2\omega}. \quad (13)$$

The difference of this filter definition compared to its explicit counterpart is that the width of the stencil required to achieve characteristics corresponding to spectral eddy-viscosity dissipation is much smaller. The definition (13) is symmetric with respect to $\omega = 0$, as was also the case for the explicit filter transfer function (8). Again we compare the Taylor-series expansion of the filter kernel (12) with the corresponding coefficients of the spectral eddy-viscosity polynomial (resulting in equality constraints) and perform a nonlinear minimization to find optimally adjusted parameters. The optimization was accomplished using a $(\mu/\mu_I, \lambda)$ -Covariance-Matrix-Adaptation Evolution Strategy (Hansen and Ostermeier, 1997).

4. The relaxation parameter

In our investigations, the parameter χ could be easily determined in spectral space by $\chi := \chi^+ \sqrt{E(k_c, t)/k_c}$. However, this definition is not suitable

for physical-space applications. To obtain a physical-space estimate, we conceptually followed the derivation of the structure function model (Métais and Lesieur, 1992) and obtained

$$\chi(\mathbf{x}, \Delta x, t) \approx 1.826648 \cdot C_K^{-3/2} \frac{1}{\Delta x} \sqrt{\overline{F}_2(\mathbf{x}, \Delta x, t)} \quad (14)$$

where

$$\overline{F}_2(\mathbf{x}, \Delta x, t) = \langle ||\overline{\mathbf{u}}(\mathbf{x}, t) - \overline{\mathbf{u}}(\mathbf{x} + \mathbf{r}, t)||^2 \rangle_{||\mathbf{r}||=\Delta x} \quad (15)$$

represents the local second-order velocity structure function. In case of a regular cubic grid, one can estimate this local structure function at each point by averaging over the six closest surrounding points. Comparisons of simulations using the spectral estimate $\chi := \chi^+ \sqrt{E(k_c, t)/k_c}$ and simulations using (14), (15) did not show major differences in the turbulence statistics of forced as well as decaying isotropic turbulence and are therefore not documented here. Modifications of (14), (15) are investigated in Schlatter et al., 2003.

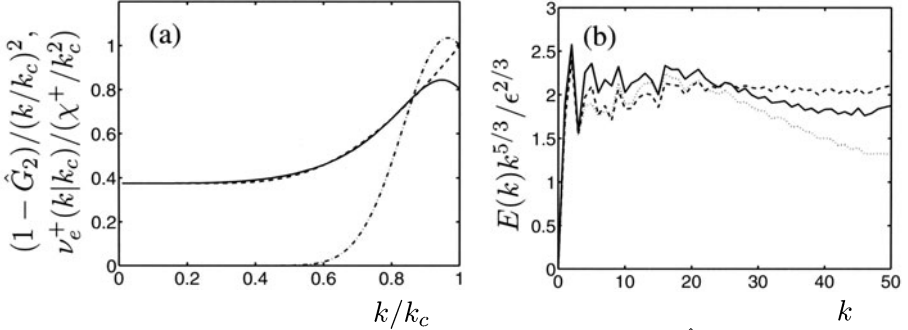


Figure 1. (a) Solid line: Inverse optimized filter transfer function $1 - \hat{G}_2$ divided by wavenumber ratio $(k/k_c)^2$ for an optimized Padé-filter. Dashed line: $\nu_e^+(k/k_c)/(\chi^+/k_c^2)$. Dashed-dotted line: $(1 - \hat{Q}_5 \hat{G})$ divided by wavenumber ratio $(k/k_c)^2$ with $\hat{G}(\omega) = 5/8 + 1/2 \cos \omega - 1/8 \cos 2\omega$. (b) Compensated three-dimensional energy density spectra of LES. Solid line: relaxation-term formulation using $C_K = 1.62$, dashed line: spectral model (5) with $C_K = 2.1$, dotted line: spectral model (5) with $C_K = 1.62$.

5. Results

Several explicit and compact filter definitions were analyzed. In case of explicit filters, a comparatively satisfactory fit was achieved for a stencil width of 15 points. For smaller number of points (i.e. smaller width of the stencil), it was possible to adapt the plateau behavior of spectral eddy viscosity but the cusp could not be represented really well. In case of the compact filter, very good approximations had been obtained for a filter with a stencil width of five points on both the explicit and implicit side. A representative filter transfer function is plotted in figure 1 (a) (solid line).

Simulation results using this compact filter and the spectral estimate of χ for isotropic turbulence with forcing (to achieve a stationary state, see Müller et

al., 2002) were obtained with a Fourier pseudospectral code with full dealiasing and a resolution of 120 grid points in each coordinate direction. The non-dimensional kinematic viscosity was $\nu = 1/400000$ in all simulations resulting in $\text{Re}_\lambda \approx 4900$. It has been observed previously that spectral large-eddy simulations exhibit a dependence of the spectral statistics on the choice of the Kolmogorov constant C_K in (5), e.g. Alvelius and Johansson, 2000. This is confirmed in our spectral eddy-viscosity simulations, see figure 1 (b). We observe a wavy shape in the compensated 3-D energy spectra for $C_K = 1.62$ and a more elongated inertial range for $C_K = 2.1$. The local deviation of \hat{G}_2 from ν^+ near the cutoff (see figure 1 (a)) appears to have the same effect as increasing the value of the Kolmogorov constant in the spectral eddy-viscosity simulations using (5). Results are closer to the spectral model with $C_K = 2.1$ than with $C_K = 1.62$.

6. Conclusions

Relaxation regularization as a method to dissipate small-scale energy in LES of turbulent flows has been investigated with the emphasis on its relation to the well-established concept of spectral eddy viscosity. It has been shown that by devising a suitable secondary filter G_2 it is possible to represent a wavenumber-dependent eddy viscosity by a relaxation term employing G_2 . The relaxation parameter is given in spectral as well as real-space formulation. The theoretical considerations were confirmed by low-resolution (120^3) numerical simulations of forced isotropic turbulence at high Reynolds number ($\text{Re}_\lambda \approx 4900$). We conclude that it is well possible to represent subgrid-scale dissipation based on analytical theory of turbulence by a relaxation term.

Although relaxation in the ADM formulation does reflect qualitative features of theoretical eddy viscosities, it does not reproduce the quantitative details of subgrid-scale dissipation as predicted by the EDQNM approximation. However, one should keep in mind that in ADM in addition to the use of relaxation, modeling of the nonlinear term by filtered products of approximately deconvolved quantities is included. The specific shape of a spectral eddy-viscosity appears to be less important if one is primarily interested in the correct global dissipation. The corresponding filter could also be constructed to satisfy properties different from fitting the plateau and cusp behavior. The success of ADM (or high-pass filtered Smagorinsky-type models, e.g. Stolz et al., 2003, or implicit LES modeling, e.g. Grinstein and Fureby, 2002) in a variety of flows at moderate Reynolds numbers gives rise to the question how important the precise form of the energy dissipation term really is for obtaining good simulation results. This point has not yet been fully explored but it appears to be important for reliable LES of realistic engineering flows.

Acknowledgments

The authors wish to thank Dr. S. Stolz and R. von Kaenel for useful discussions. Computations were performed at the Swiss Center for Scientific Computing Manno.

References

- Alvelius, K. and Johansson, A. V. (2000). LES computations and comparison with Kolmogorov theory for two-point pressure-velocity correlations and structure functions for globally anisotropic turbulence. *J. Fluid Mech.*, 403:23–36.
- Chasnov, J. R. (1991). Simulation of the Kolmogorov inertial subrange using an improved subgrid model. *Phys. Fluids A*, 3(1):188–200.
- Chollet, J. P. (1983). Two-point closure used for a sub-grid scale model in large eddy simulations. In Bradbury, L., Durst, F., Launder, B., Schmidt, F., and Whitelaw, J., editors, *Turbulent Shear Flows 4*, pages 62–72. Springer.
- Chollet, J. P. and Lesieur, M. (1981). Parameterization of small scales of three-dimensional isotropic turbulence utilizing spectral closures. *J. Atmos. Sci.*, 38:2747–2757.
- Germano, M., Piomelli, U., Moin, P., and Cabot, W. H. (1991). A dynamic subgrid-scale eddy viscosity model. *Phys. Fluids*, A3:1760–1765.
- Grinstein, E. E. and Fureby, C. (2002). Recent progress on MILES for high Reynolds number flow. *Journal of Fluids Engineering*, 124(4):848–861.
- Hansen, N. and Ostermeier, A. (1997). Convergence properties of evolution strategies with the derandomized covariance matrix adaptation: The $(\mu/\mu_I, \lambda)$ -ES. In *EUFIT'97, 5th European Congress on Intelligent Techniques and Soft Computing*, pages 649–654. ELITE Foundation (European Laboratory for Intelligent Techniques Engineering).
- Hughes, T. J. R., Oberai, A. A., and Mazzei, L. (2001). Large eddy simulation of turbulent channel flow by the variational multiscale method. *Phys. Fluids*, 13(6):1784–1799.
- Kraichnan, R. H. (1976). Eddy viscosity in two and three dimensions. *J. Atmos. Sci.*, 33:1521–1536.
- Lele, S. K. (1992). Compact finite difference schemes with spectral-like resolution. *J. Comput. Phys.*, 103:16–42.
- Menon, S., Yeung, P.-K., and Kim, W. W. (1996). Effect of subgrid models on the computed interscale energy transfer in isotropic turbulence. *Comput. Fluids*, 25:186–180.
- Métais, O. and Lesieur, M. (1992). Spectral large-eddy simulation of isotropic and stably stratified turbulence. *J. Fluid Mech.*, 239:157–194.
- Müller, S. B., Adams, N. A., Stolz, S., and Kleiser, L. (2002). Analysis of LES with the approximate deconvolution model for forced and decaying isotropic turbulence. In Castro, I. P., Hancock, P. E., and Thomas, T. G., editors, *Advances in Turbulence IX*, pages 591–594. CIMNE.
- Pope, S. B. (2000). *Turbulent Flows*. Cambridge University Press, Cambridge, UK.
- Schlatter, P., Stolz, S., and Kleiser, L. (2003). Relaxation-term models for LES of turbulent and transitional wall-bounded flows. In *DLES-5 Proceedings*.
- Stolz, S., Adams, N. A., and Kleiser, L. (2001). The approximate deconvolution model for LES of compressible flows and its application to shock-turbulent-boundary-layer interaction. *Phys. Fluids*, 13(6):2985–3001.
- Stolz, S., Schlatter, P., Meyer, D., and Kleiser, L. (2003). High-pass filtered eddy-viscosity models for LES. In *DLES-5 Proceedings*.

RELAXATION-TERM MODELS FOR LES OF TRANSITIONAL/TURBULENT FLOWS AND THE EFFECT OF ALIASING ERRORS

P. Schlatter, S. Stolz & L. Kleiser

Institute of Fluid Dynamics, ETH Zürich, CH-8092 Zürich, Switzerland

schlatter@ifd.mavt.ethz.ch, stolz@ifd.mavt.ethz.ch, kleiser@ifd.mavt.ethz.ch

Abstract Subgrid-scale (SGS) models based on relaxation regularization are investigated for incompressible transitional and turbulent channel flow using a spectral method. The main focus is on a simple model formalism which can be used on very coarse LES grids. During the initial phase of transition, the models remain inactive as long as the flow is still well resolved on the coarse LES grid. During the late stages of transition and the following fully-turbulent phase the models provide necessary SGS dissipation. The connection of aliasing errors and SGS modelling is examined. Of particular importance is that SGS models based on relaxation regularization reduce the effects of aliasing errors, allowing to perform numerical simulations even without dealiasing and thus lowering the computational time significantly. Furthermore, the performance of the models is evaluated for different dynamic and non-dynamic model coefficients all showing good agreement with fully-resolved DNS.

Keywords: Large-eddy simulation, transition, turbulent channel, SGS models, relaxation term, aliasing errors, dealiasing

1. Introduction

The use of large-eddy simulations (LES) to predict transitional and turbulent flows is appealing as they promise to provide accurate results at greatly reduced computational cost in comparison with fully-resolved direct numerical simulations (DNS). Numerical simulations always introduce modeling and discretization errors due to truncation of the physical domain and the discrete representation of the solution and its derivatives. Moreover, aliasing errors due to misrepresentation of high-frequency components which cannot be resolved on the computational grid are present if no special treatment of aliasing errors is employed. As in large-eddy simulations the computational grid is much coarser than that of a corresponding DNS, the numerical errors are more severe (Chow and Moin, 2003). Numerical errors mainly contaminate the small-scale

content of the resolved solution which in a LES is the range of scales interacting with the non-resolved scales. In spectral simulations it is possible to minimize the derivative errors and eliminate the aliasing errors by employing the 3/2-rule with additional computational effort. On the other hand, most LES simulations of flows in complex geometries are performed with non-spectral discretization, usually finite-difference or finite-volume methods, where these numerical errors are inherently present. Although strategies for the reduction of errors with such methods exist, e.g. filtering method (Lele, 1992), increased filter-to-grid-ratio (Chow and Moin, 2003) and the skew-symmetric form (Kravchenko and Moin, 1997), they are not commonly employed. For this reason, it seems important to examine both the influence of dealiasing on the LES results and the usability of SGS models, i.e. the relaxation term, to minimize the effects of aliasing errors.

A SGS model suitable to simulate laminar-turbulent transition should be able to deal with laminar, various stages of transitional and turbulent flow states. The models should only be active, in an appropriate way, when non-linear interactions between the resolved and non-resolved scales become important. Due to the possible intermittent character of transitional flows (e.g. spatial simulations, bypass transition), spatial averaging of any model coefficients over the integration domain should be avoided. Furthermore, for the sake of generality, a fully three-dimensional formulation of the model is required. A particularly troublesome problem for SGS models is to avoid any singularity when dealing with laminar flows (e.g. a singularity in the midplane of laminar channel flow for the dynamic Smagorinsky model).

There are substantial differences between laminar, transitional and turbulent flows in many respects. In laminar and transitional flows, initially, there is no fully-developed energy cascade. Furthermore, the flow development is often governed by slow growth and subtly complex interactions between large-scale flow structures and various instability modes that can affect the physical changeover from the laminar to the turbulent state and must thus be resolved or modeled reliably.

There are many reports on LES subgrid-scale models for turbulent wall-bounded flows (see e.g. Lesieur and Métais, 1996). Only recently, transitional flows have been simulated with LES, mainly using SGS models based on the Smagorinsky (1963) model. It is well known that Smagorinsky's model in its original form is too dissipative and usually relaminarizes transitional flows. Therefore, several refined and alternative SGS models for transitional flows have been proposed, most prominently the dynamic model which computes its model coefficient during the simulation (Germano et al., 1991; Lilly, 1992). This class of models has been successfully used in a variety of flow configurations.

Recently, the approximate deconvolution model (ADM), which has been applied before to turbulent flows such as incompressible channel flow (Stolz et al., 2001a) and compressible boundary layer flow (Stolz et al., 2001b), has been adapted successfully to transitional channel flow (Schlatter et al., 2003). It was found that for ADM with deconvolution applied for the computation of the nonlinear terms a certain minimum resolution in the wall-normal direction has to be maintained. It was shown further that an ADM-type SGS model without deconvolution yielded very appealing results for incompressible channel flows at even lower resolution. Based on those findings, models based on an ADM-type relaxation term formulation are analyzed further in this contribution and validated with results of direct numerical simulations. Comparisons to the ADM and the dynamic Smagorinsky model are given and the effects of aliasing errors are examined.

2. SGS model and numerical method

As SGS model a relaxation term similar to that of ADM (Stolz et al., 2001a) is employed and added to the right-hand side of the Navier-Stokes equations,

$$\frac{\partial \bar{u}_i}{\partial t} + \frac{\partial \bar{u}_j \bar{u}_i}{\partial x_j} + \frac{\partial \bar{p}}{\partial x_i} - \frac{1}{Re} \frac{\partial^2 \bar{u}_i}{\partial x_j \partial x_j} = -\chi \cdot H_N * \bar{u}_i, \quad (1)$$

where \bar{u}_i and \bar{p} are the grid-filtered velocity and pressure, respectively. The modeled equations are solved together with the incompressibility constraint $\frac{\partial \bar{u}_i}{\partial x_i} = 0$. H_N is a high-pass filter which is defined in physical space on an implicit 5-point stencil (see also Stolz et al., 2003). The formulation of the filters in physical space allows greater flexibility, e.g. extension to non-spectral numerics such as finite differences. Spectral filtering has been tested yielding similar results. For equidistant grids the filters are given equivalently in Fourier space as

$$\hat{H}_N(\omega) = [1 - \hat{G}(\omega)]^{N+1} \quad (2)$$

with the implicit filter

$$\hat{G}(\omega) = \frac{\hat{G}_{ex}(\omega)}{1 + K[\hat{G}_{ex}(\omega) - 1]}, \quad K = \frac{2\hat{G}_{ex}(\omega_c) - 1}{\hat{G}_{ex}(\omega_c) - 1}, \quad (3)$$

and the explicit filter \hat{G}_{ex}

$$\hat{G}_{ex}(\omega) = 0.625 + 0.5 \cos \omega - 0.125 \cos 2\omega. \quad (4)$$

Filters employed for non-equidistant grids are described in Stolz et al., 2001a. For the present results, $N = 5$ and the cutoff wavenumber $\omega_c = 2\pi/3$ is used. Note that \hat{H}_N is equivalent to the high-pass filter used in ADM (Stolz et al., 2001a), $\hat{H}_N(\omega) = [1 - \hat{G}(\omega)]^{N+1} = 1 - \hat{Q}_N(\omega)\hat{G}(\omega)$ with $\hat{Q}_N(\omega) =$

$\sum_{\nu=0}^N [1 - \hat{G}(\omega)]^\nu \approx \hat{G}^{-1}(\omega)$ being the transfer function of the approximate deconvolution filter.

High-pass filtered quantities $H_N * \bar{u}_i$ with $N \geq 0$ are vanishing for low-order polynomials which represent laminar (channel) or smooth flows and also, approximately, in the viscous sublayer of turbulent flows (see also Stolz et al., 2003). Herewith, model contributions of the relaxation term vanish in such flow regions.

An important feature of the present SGS model (1)-(4) is the determination of the model coefficient χ . In a previous investigation (Schlatter et al., 2003) the above model was used with the dynamic procedure $\chi = \chi_{\text{dyn}}$ of Stolz et al., 2001b. In the present contribution, additional tests have been performed with simplified definitions of χ , e.g. $\chi = (U_b/h)C_1 = \text{const.}$, $\chi = C_2 \|\nabla \bar{\mathbf{u}}\|$ and $\chi = C_3 \|\nabla(H_N * \bar{\mathbf{u}})\|$ with the bulk velocity U_b and the channel half-width h . The term $\|\nabla(H_N * \bar{\mathbf{u}})\|$ is closely related to $\sqrt{F_2(H_N * \bar{\mathbf{u}})}/\Delta$ where F_2 denotes the second-order velocity structure function and Δ the grid spacing (Lesieur and Métais, 1996). The structure function is easier to evaluate in physical space. A similar approach was also studied in Müller et al., 2003 for isotropic homogeneous turbulence. In principle, the constants C_i can be derived from energy considerations similar to Ducros et al., 1996 for homogeneous isotropic flow. No additional artificial bounds (clippings) or filter operations need to be applied.

The SGS model has been implemented in a spectral Fourier-Chebyshev code (Gilbert and Kleiser, 1990) with periodic boundary conditions in the wall-parallel and no-slip conditions in the wall-normal direction. The 3/2-rule in all three spatial directions is used to prevent aliasing errors, unless mentioned otherwise.

3. Results

Two different incompressible flow situations are considered: Subcritical temporal K-type transition with the Reynolds number based on bulk velocity and channel half-width $Re_b = 3333$ ($Re_\tau \approx 210$ in fully developed turbulence) and fully turbulent channel flow with $Re_\tau \approx 180$ ($Re_b = 2800$, Moser et al., 1999). The transition simulations used the same parameters and initial conditions as Gilbert and Kleiser, 1990 and were performed for the DNS using up to $160^2 \times 161$ grid points while for the LES a deliberately chosen coarse resolution of $32^2 \times 33$ points is used (see Schlatter et al., 2003 for a discussion). The same LES resolution was also used for the turbulent case with $Re_b = 2800$. At this resolution, a computation without any model is significantly underresolved (except for the laminar case) in all three spatial directions.

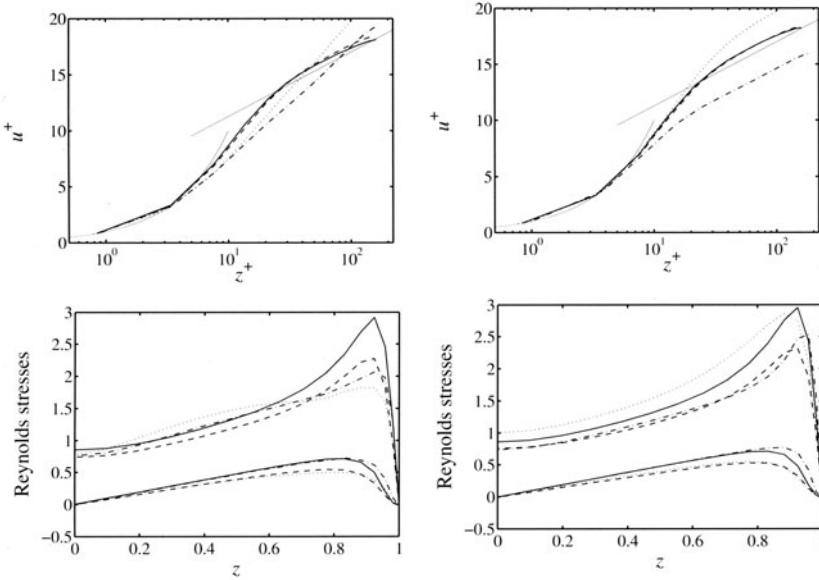


Figure 1. Turbulent statistics for $Re_b = 2800$. Left column: calculations without dealiasing. Right column: calculations using 3/2-rule for dealiasing. Top row: Mean velocity profile in wall units. Bottom row: Reynolds stresses $(\overline{u'_1 u'_1})^{1/2}/u_\tau$ and $\overline{u'_1 u'_3}/u_\tau^2$: — $\chi = \chi_{\text{dyn}}$, --- ADM (with deconvolution, Stolz et al., 2001a), - · - DNS $32^2 \times 33$, ····· dynamic Smagorinsky model.

Figure 1 shows different calculations of turbulent channel flow, both with aliasing errors and with full dealiasing. It can be seen that for the simulations involving a relaxation term of the form (1) the lack of dealiasing does not worsen the results. On the other hand, the calculations using the dynamic Smagorinsky model and the no-model calculations are much worse without the dealiasing procedure. It should be noted that the computational effort without dealiasing is reduced by at least a factor of two for the present spectral code. Moreover, proper dealiasing can usually only be performed with spectral numerics (Chow and Moin, 2003). However, as shown here, the effects of aliasing errors can be reduced significantly by using a relaxation term. An interesting observation is that with the dynamic estimation χ_{dyn} is automatically increased if no dealiasing is employed.

Furthermore, the different variants of determining the relaxation parameter χ have been investigated for transitional and fully turbulent channel flow with $Re_b = 3333$. In figure 2, statistical quantities of the fully turbulent simulations with and without dealiasing are depicted. It is evident that the coarse-grid DNS deviates significantly from the fine-grid DNS. However, all LES results agree better with the fully resolved DNS data concerning the law of the wall and the turbulent fluctuations. The simulations without dealiasing depicted on the left

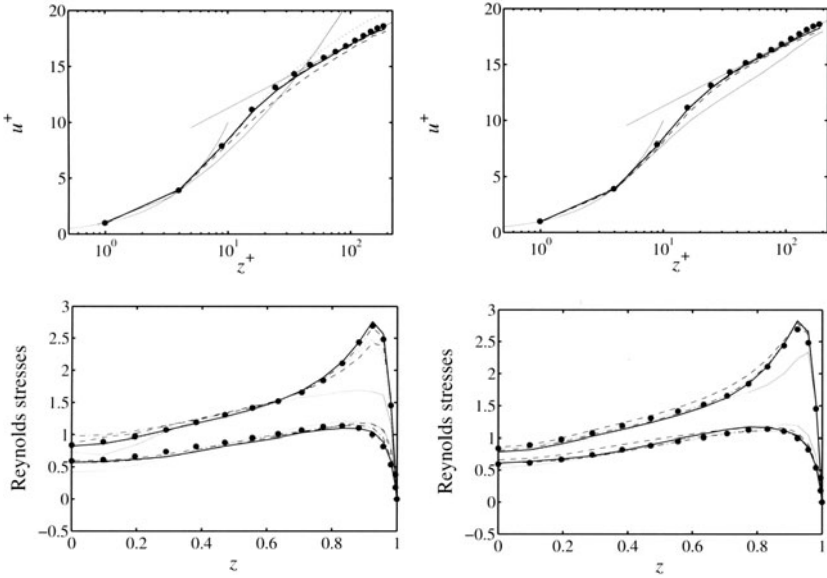


Figure 2. Turbulent statistics for $Re_b = 3333$. *Left column*: calculations without dealiasing. *Right column*: calculations using 3/2-rule for dealiasing. *Top row*: Mean velocity profile in wall units. *Bottom row*: Reynolds stresses $(\overline{u'_1 u'_1})^{1/2}/u_\tau$ and $(\overline{u'_2 u'_2})^{1/2}/u_\tau$: — $\chi = \chi_{\text{dyn}}$, - - - $\chi = (U_b/h)C_1 = \text{const.}$, - · - $\chi = C_2 \|\nabla \mathbf{u}\|$, · · · $\chi = C_3 \|\nabla H * \mathbf{u}\|$, — DNS $32^2 \times 33$, ● grid-filtered DNS $128^2 \times 129$

confirm the above-mentioned findings and show that it is possible to even use a constant χ to reduce the effects of aliasing errors significantly.

It is interesting to note that the results of the three LES are similar, although different formulations of the model coefficient χ were used. It can therefore be concluded that for fully turbulent channel flow the specific form of χ is less important as long as an appropriate amount of energy is dissipated and, additionally, effects of aliasing errors are reduced.

The evolution of the shape factor H_{12} and the wall friction Re_τ during the transitional phase is shown in figure 3. The underresolved DNS shows premature transition compared to the fully resolved DNS for the dealiasied simulation whereas it completely fails in the presence of aliasing errors ($H_{12} \approx 1.8$ after transition). Generally, the effects of aliasing errors lead to slightly earlier transition for the LES; nevertheless, all LES with the relaxation term as model produce acceptable results for transition, i.e. showing correct onset of transition and the well-known overshoot of Re_τ of approximately 15%. However, the inclusion of high-pass filtering in the model coefficient, e.g. χ , seems to lead to more accurate results (see also Stolz et al., 2003). On the other hand, assuming constant $\chi = (U_b/h)C_1$ gives very appealing results, only slightly less accurate than the dynamic determination $\chi = \chi_{\text{dyn}}$.

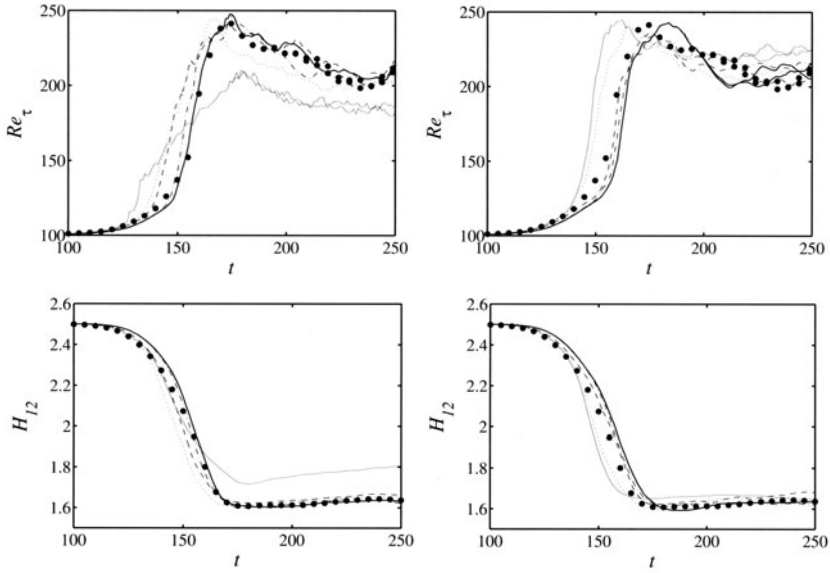


Figure 3. Time evolution of the shape factor H_{12} and the Reynolds number Re_τ based on the skin friction for simulations of K-type transition. *Left column:* calculations without dealiasing. *Right column:* calculations using 3/2-rule for dealiasing. Line captions see figure 2. Multiple values indicate lower/upper channel wall.

4. Conclusions

SGS models based on high-pass filtered relaxation regularization have been investigated in incompressible transitional and fully turbulent channel flow using a deliberately coarse grid. The SGS model is easy to implement and does need only a small computational overhead. The appropriate definition of the relaxation term has the effect that model contributions vanish during the initial stage of transition and, approximately, in the viscous sublayer of wall turbulence. The relaxation term models are also quite insensitive to the exact determination of the model coefficient χ and its absolute value, see also Stolz et al., 2001a.

Numerical tests confirmed that these models are insensitive to a proper correction of aliasing errors as opposed to DNS calculations and classical LES models such as the dynamic Smagorinsky model. This property is very important for numerical schemes where proper dealiasing is not straight-forward or impossible; for spectral simulations additional computational effort can be saved. In other words, the relaxation term SGS models can be employed to reduce the effects of aliasing errors inherently present in flow computations using other than spectral schemes.

Acknowledgements

This work has been supported by the Swiss National Science Foundation (SNF) and the Swiss Center for Scientific Computing (CSCS). Calculations have been performed at CSCS.

References

- Chow, F. K. and Moin, P. (2003). A further study of numerical errors in large-eddy simulations. *J. Comput. Phys.*, 184:366–380.
- Ducros, F., Comte, P., and Lesieur, M. (1996). Large-eddy simulation of transition to turbulence in a boundary layer developing spatially over a flat plate. *J. Fluid Mech.*, 326:1–36.
- Germano, M., Piomelli, U., Moin, P., and Cabot, W. H. (1991). A dynamic subgrid-scale eddy viscosity model. *Phys. Fluids*, 3(7):1760–1765.
- Gilbert, N. and Kleiser, L. (1990). Near-wall phenomena in transition to turbulence. In Kline, S. J. and Afgan, N. H., editors, *Near-Wall Turbulence - 1988 Zoran Zarić Memorial Conference*, pages 7–27. Hemisphere.
- Kravchenko, A. G. and Moin, P. (1997). On the effect of numerical errors in large eddy simulations of turbulent flows. *J. Comput. Phys.*, 131:310–322.
- Lele, S. K. (1992). Compact finite difference schemes with spectral-like resolution. *J. Comput. Phys.*, 103:16–42.
- Lesieur, M. and Métais, O. (1996). New trends in Large-Eddy simulations of turbulence. *Annu. Rev. Fluid Mech.*, 28:45–82.
- Lilly, D. K. (1992). A proposed modification of the Germano subgrid-scale closure method. *Phys. Fluids*, A 4(3):633–635.
- Moser, R. D., Kim, J., and Mansour, N. N. (1999). Direct numerical simulation of turbulent channel flow up to $Re_\tau = 590$. *Phys. Fluids*, 11(4):943–945.
- Müller, S. B., Adams, N. A., and Kleiser, L. (2003). Analysis of relaxation regularization as subgrid-scale model for large-eddy simulation. In *DLES-5 Proceedings*.
- Schlatter, P., Stolz, S., and Kleiser, L. (2003). LES of transitional flows using approximate deconvolution. In Kasagi, N., Eaton, J. K., Friedrich, R., Humphrey, J. A. C., Leschziner, M. A., and Miyauchi, T., editors, *Turbulence and Shear Flow Phenomena 3*, pages 923–928.
- Stolz, S., Adams, N. A., and Kleiser, L. (2001a). An approximate deconvolution model for large-eddy simulation with application to incompressible wall-bounded flows. *Phys. Fluids*, 13(4):997–1015.
- Stolz, S., Adams, N. A., and Kleiser, L. (2001b). The approximate deconvolution model for large-eddy simulations of compressible flows and its application to shock-turbulent-boundary-layer interaction. *Phys. Fluids*, 13(10):2985–3001.
- Stolz, S., Schlatter, P., Meyer, D., and Kleiser, L. (2003). High-pass filtered eddy-viscosity models for LES. In *DLES-5 Proceedings*.

KOLMOGOROV EQUATION FOR LES AND ITS USE FOR SUBGRID MODELING

L. Shao, J.P. Bertoglio

LMFA UMR CNRS 5509 Ecole Centrale de Lyon, France

shao@mecaflu.ec-lyon.fr

G.X. Cui, H.B. Zhou and Z.S. Zhang

Department of engineering mechanics, Tsinghua University, China

demzsz@tsinghua.edu.cn

Abstract The present study uses the Kolmogorov equation for large eddy simulation (KE-LES, see C. Meneveau [1]) for the purpose of subgrid modeling. We will show that when a scale-similarity hypothesis is injected, suitable subgrid models can be obtained. The resulting subgrid models have no "model coefficient". A dynamic method for the evaluation of the coefficient in existing subgrid models is also obtained. The new models are successfully tested and compared to the Métais-Lesieur model [2] in decaying and forced homogeneous isotropic turbulence. The coefficient evaluation method is applied with success to the Smagorinsky model [3].

Keywords: LES, Kolmogorov Equation, scale-similarity, dynamic subgrid modeling

1. Introduction

The Kolmogorov equation for the filtered velocity field can be written as:

$$-\frac{4}{5}\epsilon_f r = \overline{D}_{LLL} - 6G_{LLL} \quad (1)$$

In this expression, \overline{D}_{LLL} is the third order longitudinal velocity correlation of the filtered field:

$$\overline{D}_{LLL}(r) = \langle [\overline{u}(x+r) - \overline{u}(x)]^3 \rangle; \quad (2)$$

G_{LLL} is the longitudinal velocity-stress correlation tensor:

$$G_{LLL}(r) = \langle \overline{u}_1(x)\tau_{11}(x+r) \rangle; \quad (3)$$

and ϵ_f is the subgrid dissipation:

$$\epsilon_f = - \langle \tau_{ij} \bar{S}_{ij} \rangle \quad (4)$$

where \bar{S}_{ij} is the resolved scale strain rate. As the Kolmogorov equation for the real fluid, the KELES can be interpreted as an energy balance for the resolved scales.

Although the KELES is a "closed" equation in the sense of classic statistical modeling, it does not constitute a stand alone necessary and sufficient condition for subgrid modeling. The KELES is a direct consequence of the large eddy simulation equation. During an A Priori test where the real fluid (experimental or DNS data) is available, the KELES could give good results for model testing or recasting, see Meneveau 1994. In an A Posteriori LES, the Kolmogorov equation is not unique as it would be for a real fluid. Each subgrid model will provide a modeled LES equation that must satisfy a subgrid-model-Kolmogorov equation. The subgrid-model-KELES only reflects the energy balance obtained by the input subgrid model if no other physical condition has been supplied. In the context of a LES, the KELES is similar to the Germano identity [4]. When the dynamic procedure of Germano is employed in subgrid modeling, a scale similarity condition is implicitly assumed. Similarly, if we want to use the Kolmogorov equation for large eddy simulation to derive a practically useful subgrid model, we need a physical condition which can correctly represent the action of the velocity-stress correlation. This is the aim of the present paper.

2. Subgrid modeling with the Kolmogorov equation for LES

From extensive numerical experiments (see [6]), eddy viscosity type subgrid models are able to reproduce subgrid dissipation and, qualitatively, the velocity-stress correlation according to Meneveau [1]. We therefore limit our investigation to the viscosity type subgrid model.

2.1 Scale-similarity condition for G_{LLL}

Scale similarity [7] is a good candidate for physical interpretation of the real subgrid stresses mechanism. Numerous works support the scale-similarity type of subgrid models, for an extensive review, see Meneveau 2000 [5]. We now introduce a scale-similarity hypothesis on the velocity-stress correlation:

$$G_{LLL}(r) \propto r^p \quad (5)$$

There is a particular issue of the above relationship in the case of constant eddy viscosity subgrid model. It is exact. Indeed, G_{LLL} is:

$$\begin{aligned} G_{LLL} &= 2\nu_t < \bar{u}_1(x_1) \bar{s}_{11}(x_1 + r_1) > \\ &= -2\nu_t \bar{R}_{LL,r_1} \\ &= \nu_t \bar{D}_{LL,r_1} \end{aligned} \quad (6)$$

Comma separated indices denote derivatives. Extending the Kolmogorov 2/3 power law of a real fluid to \bar{D}_{LL} , we have: $p = 2/3 - 1 = -1/3$. Now the KELES and the scale-similarity condition can be assembled in a simple relationship:

$$\frac{0.8\epsilon_f r_1 + \bar{D}_{LLL}(r_1)}{0.8\epsilon_f r_2 + \bar{D}_{LLL}(r_2)} = \left(\frac{r_1}{r_2}\right)^{-1/3} \quad (7)$$

No subgrid term is explicitly present in the above equation. ϵ_f is the large scale energy time derivative. It is a scale-similar, G_{LLL} independent KELES. In the next section, the subgrid model evaluated with equation 7 will be refereed as *multi-scale model*; when the KELES with 2/3 power law is used at one separation distance, so-evaluated models are referred to as *1-scale model*.

2.2 1-scale subgrid model

Constant eddy viscosity. For a given filter and for homogeneous isotropic turbulence, consider a constant eddy viscosity subgrid model. We have:

$$\tau_{ij} = -2\nu_t \bar{S}_{ij}, \quad \epsilon_f = 2\nu_t < \bar{S}_{ij} \bar{S}_{ij} > \quad (8)$$

Replacing the above two expressions in equation 1, we get:

$$\nu_t = \frac{5S_k \bar{D}_{LL}^{1/2} r}{-8 \frac{< \bar{S}_{ij} \bar{S}_{ij} > r^2}{\bar{D}_{LL}} - 20 \frac{r \bar{D}_{LL,r}}{\bar{D}_{LL}}} \quad (9)$$

where S_k is the skewness of the longitudinal velocity increment for the filtered velocity: $S_k = \bar{D}_{LLL} / \bar{D}_{LL}^{3/2}$. Imposing the Kolmogorov scaling on $\bar{D}_{LL}, r = \frac{2}{3} \bar{D}_{LL} / r$, we obtain the following expression:

$$\nu_t = \frac{-S_k}{1.6 \frac{r^2 < \bar{S}_{ij} \bar{S}_{ij} >}{\bar{D}_{LL}} - 4} \bar{D}_{LL}^{1/2} r \quad (10)$$

The first term of the denominator of the above equation can be simplified. Isotropy implies: $< \bar{S}_{ij} \bar{S}_{ij} > = \frac{15}{2} < \bar{u}_{1,1}^2 >$. For r of the same order of the filter size Δ and for $\frac{r}{L} \ll 1$, where L is the integral length scale, $< \bar{u}_{1,1}^2 >$ can be approximated by $< \bar{u}_{1,1}^2 > \approx \frac{\bar{D}_{LL}}{r^2}$. Although this approximation would

not be appropriate for the full velocity field, it is acceptable for the resolved velocity scales as the smallest scale in a LES is of order Δ . We obtain an "asymptotic" expression for ν_t :

$$\nu_t = -\frac{S_k}{8} \overline{D}_{LL}^{1/2} r \quad (11)$$

The skewness is a spectral measure of the rate between the energy cascade and the viscous dissipation. Therefore the inter-scale energy transfer information is included in the present subgrid viscosity. Note that the well known Métais-Lesieur subgrid model

$$\nu_{t_{ml}} = 0.063 \overline{D}_{LL} (\Delta)^{1/2} \Delta \quad (12)$$

is a particular form of the simplified form of equation 11. If one takes the separation distance r to be equal to the filter size Δ and a value of -0.5 for S_k , one obtains the Métais-Lesieur model.

Non-constant Smagorinsky eddy viscosity. We address the possibility to use the Kolmogorov equation for LES in the case of a non constant eddy viscosity subgrid model. A local strain rate subgrid eddy viscosity is considered. In this case, it is interesting to link the Smagorinsky constant to the velocity derivative skewness. To do so we suppose the following form of G_{LLL} :

$$G_{LLL} = \alpha < \nu_t > \overline{D}_{LL,r} \quad (13)$$

in which α is a proportion coefficient, supposed to be a constant. The value of α can be determined using the knowledge of LES of homogeneous isotropic turbulence. ϵ_f is:

$$\epsilon_f = - < \tau_{ij} \overline{S}_{ij} > = 2(C_s \Delta)^2 < \overline{S}^{3/2} > \quad (14)$$

In the case of a fully developed homogeneous isotropic turbulence, the value of the Smagorinsky coefficient is about 0.18 in a LES with spectral method, see Bertoglio [8]. Using the value of the skewness S_k from the previous section, -0.5 , the value of α is nearly 2.0. Therefore for the general case, the Smagorinsky coefficient could be approximated by the following expression:

$$C_S \approx \frac{\sqrt{-S'_k}}{3.5} \quad (15)$$

in which S'_k is the skewness of the longitudinal velocity derivative.

2.3 Multi-scale subgrid model

Now we apply the multi-scale KELES 7 for 2 different separation distances. Expressing ϵ_f as $- < \tau_{ij} \overline{S}_{ij} >$, we get the following solution for constant

eddy viscosity:

$$\nu_t = \frac{\overline{D}_{LLL}(r_1) - (\frac{r_1}{r_2})^{1/3} \overline{D}_{LLL}(r_2)}{-0.8 < \overline{S}^2 > (1 - (\frac{r_1}{r_2})^{4/3}) r_1} \quad (16)$$

For the Smagorinsky model with local strain rate, an expression for C_s is:

$$(C_s \Delta)^2 = \frac{\overline{D}_{LLL}(r_1) - (\frac{r_1}{r_2})^{1/3} \overline{D}_{LLL}(r_2)}{-0.8 < \overline{S}^{3/2} > (1 - (\frac{r_1}{r_2})^{4/3}) r_1} \quad (17)$$

It is easy to generalize this method for 3 scales, for example, by assuming:

$$\frac{G_{LLL}(r_1)}{G_{LLL}(r_2)} (\frac{r_1}{r_2})^{-1/3} = \frac{G_{LLL}(r_2)}{G_{LLL}(r_3)} (\frac{r_2}{r_3})^{-1/3} \quad (18)$$

In this method, multi-scale spectral information can be easily input via the number of separation distance r_i . We expect also to generalize this approach to subgrid model having two or more coefficients, for example, a mixed model. However, no attempt has been done.

3. Numerical applications: LES of decaying and forced homogeneous isotropic turbulence with new models

Two cases of homogeneous isotropic turbulence are computed. One corresponds to the decay at moderate Reynolds number, the case of the Comte-Bellot and Corrsin experiment [9]. The other simulates a statistically stationary turbulence at high Reynolds number. A deterministic or a Langevin equation forcing method are indifferently used. The initial field is generated using the method of Rogallo [10] with randomly distributed velocity phases. The numerical scheme is the classic pseudo-spectral method. The Métais-Lesieur model is used for comparison. Due to the particular spectral cut-off filter in this numerical method, the resulting "cusp" effect is accounted for by a correction from Chollet [11].

3.1 1-point and 2-point statistics

Figure 1 shows the ratio between the value 1-scale constant ν_t and that of Métais-Lesieur, obtained during two 32^3 LES: one with 1-scale constant ν_t and the other with the Métais-Lesieur model. Both oscillate around 1. In figure 2, time averaged spectra using 1-scale constant ν_t obtained on 32^3 , 64^3 and 128^3 grids are plotted. $-5/3$ inertial behavior can be clearly observed for all spectra. The above simulations correspond to the forced turbulence. 1-scale Smagorinsky constant is checked in decaying low Reynolds isotropic turbulence against the coefficient obtained with the Germano [4] dynamic procedure. Figure 3 show the time evolution C_s obtained using both methods. Agreement is good.

2-scale evaluated Smagorinsky model coefficient is shown in figure 4 in case of forced turbulence. The value of three C_s are very close. Figure 6 shows spectra of the decaying turbulence, obtained with both the Métais-Lesieur model and the 1-scale constant ν_t , in comparison with experiment. Both subgrid models give satisfactory results.

3.2 Model sensitivity to the power law exponent n of \overline{D}_{LL}

The influence of the exponent of the input power law for \overline{D}_{LL} is checked by comparing the so obtained spectrum slope. Recall that this exponent is one of the key parameters of multi-scale model. The value of input n are, $1/9$, $2/3$ and 1 . According to a simple β -model, the corresponding spectrum slope would be expected to be $-10/9$, $-5/3$ and -2 . Results are shown in figure 7 (2-scale constant ν_t) and figure 8 (2-scale evaluated Smagorinsky coefficient). It seems that the input power law, is almost recovered on the output spectral slopes.

4. Concluding remark

The Kolmogorov equation for large scale velocity is used for subgrid modeling. We introduced a scale similarity condition on the two-point velocity-stress correlation term in the KELES : $-1/3$ power law. The resulting KELES is a "scale-similar Kolmogorov equation for LES". Success in LES of homogeneous turbulence demonstrate A Posteriori, that this scale-similarity hypothesis can correctly reproduce the real cross velocity-stress correlation mechanism. Subgrid modeling using this scale-similar KELES is studied with an eddy viscosity type subgrid model.

Particular solution for constant subgrid eddy viscosity ν_t is found. A class of multi-scale subgrid models is deduced. Resulting subgrid eddy viscosity are closely linked the inter-scale energy exchange via the velocity increment skewness or the third order structure function. New models are successfully used in LES of decaying and forced isotropic turbulence. A multi-scale method for dynamically evaluating the Smagorinsky coefficient is also derived. When used in LES, the resulting Smagorinsky fluid has a good initial range spectral slope. The results are in excellent agreement with those obtained with the Germano dynamical model in decaying isotropic turbulence. Since the new subgrid models are derived with the Kolmogorov equation, it is expected that they can be easily extended to weakly inhomogeneous flow, ie., turbulent shear flow. When new models are applied to the turbulent channel flow, preliminary results compare very well to those obtained with the Germano dynamic procedure applied to the Smagorinsky model.

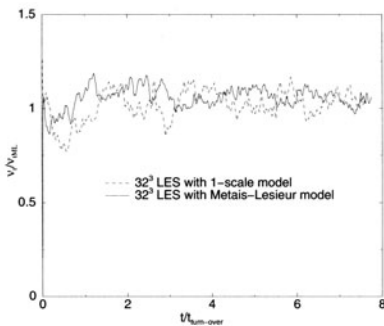


Figure 1. Comparison of $\nu_t/\nu_{t,1}$ in forced turbulence, 32^3 LES run with Métais-Lesieur and 1-scale constant ν_t .

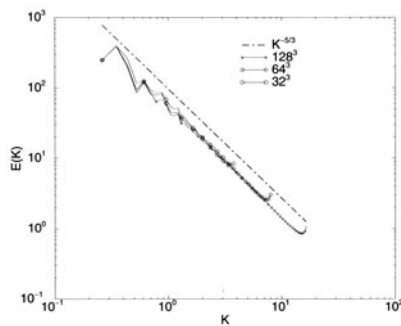


Figure 2. Comparison of spectra with different grid resolution. 1-scale constant ν_t .

Acknowledgments

The authors would like to thank Prof. G.N. Gence for helpful discussion. This work was partly supported by the Sino-French Laboratory LIAMA.

References

- [1] C. Meneveau, 1994, "Statistics of turbulence subgrid-scale stresses: Necessary condition and experimental tests", *Phys. Fluids*, **6** (2), 815-833.
- [2] O. Métais and M. Lesieur, 1992, "Spectral large-eddy simulation of isotropic and stably stratified turbulence," *J. Fluid Mech.*, **239**, 157-194.
- [3] J. Smagorinsky, 1963, "General circulation experiments with the primitive equations. I. The basic experiment," *Mon. Weather Rev.*, **91**.
- [4] M. Germano, 1992, "Turbulence: the filtering approach," *J. Fluid Mech.*, **23**.
- [5] C. Meneveau and J. Katz, 2000, "Scale-invariance and turbulence model for large eddy simulation", *Ann. Rev. Fluid Mech.*, **32**, 1-33.
- [6] M. Lesieur, 1997, *Turbulence in Fluids* Kluwer Academic Publishers
- [7] S. Liu, C. Meneveau, J. Katz, 1994, "On the properties of similarity subgrid-scales as deduced from measurements in turbulent jet", *J. Fluid Mech.*, **275**, 83-119.
- [8] J.P. Bertoglio, 1986, *Thèse d'Etat*.
- [9] Comte-Bellot and Corrsin, 1966, "The use of contraction to improve the isotropy of grid generated turbulence," *J. Fluid Mech.*, **25**.
- [10] R.S. Rogallo, 1981, "Numerical experiments in homogeneous turbulence," *NASA Report*, **81315**.
- [11] Chollet, J.P., 1983, "Statistical closure to derive a sub-grid-scale modeling for large eddy simulations of three dimensional turbulence", Tech. note TN 206, NECTAR.

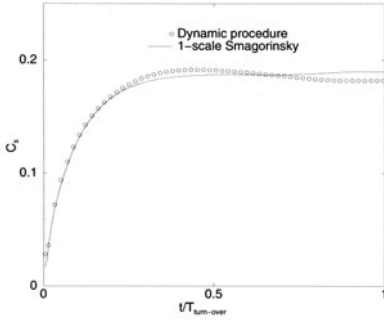


Figure 3. Time evolution of C_s of Germano dynamical model and of 1-scale Smagorinsky model in decaying turbulence, 64^3 LES run.

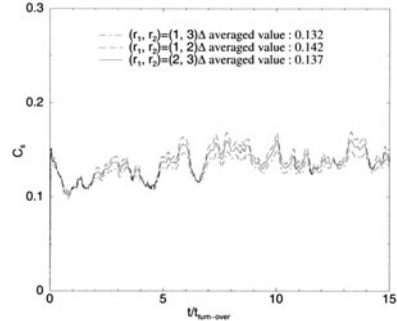


Figure 4. 2 scale Smagorinsky model coefficient evaluated with different r_1/r_2 in force turbulence. 32^3 LES run.

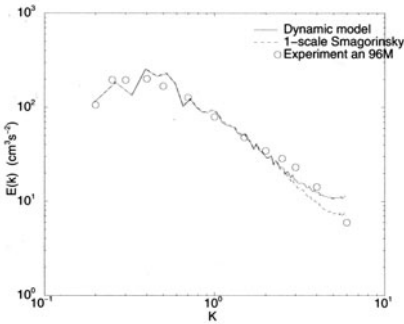


Figure 5. Comparison of spectrum in decaying turbulence. 1-scale Smagorinsky and Germano dynamic Smagorinsky model. 64^3 LES.

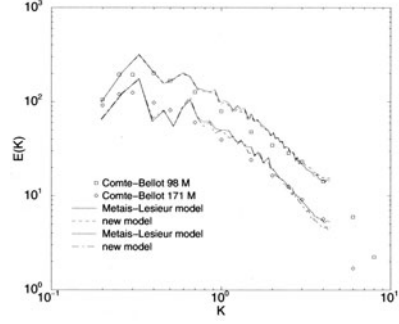


Figure 6. Comparison of spectrum in decaying turbulence. 1-scale constant ν_t and Métais-Lesieur model. 48^3 LES.

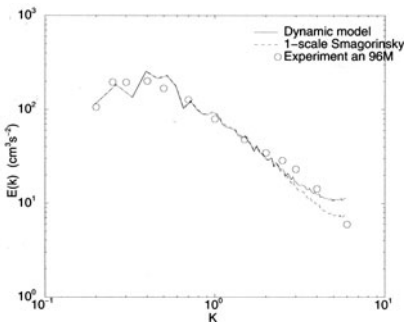


Figure 7. Model sensitivity to the input exponent in forced turbulence. 2-scale constant ν_t case. 32^3 LES run. Spectra are shifted for visibility

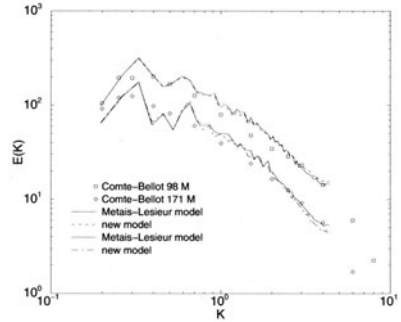


Figure 8. Model sensitivity to the input exponent in forced turbulence. 2-scale Smagorinsky model case. 32^3 LES run. Spectra are shifted for visibility

HIGH-PASS FILTERED EDDY-VISCOSITY MODELS FOR LES

S. Stolz, P. Schlatter, D. Meyer & L. Kleiser

Institute of Fluid Dynamics, ETH Zürich, CH-8092 Zürich, Switzerland

stolz / schlatter / meyer / kleiser@ifd.mavt.ethz.ch

Abstract In this contribution we propose high-pass filtering suitable for high-pass filtered (HPF) eddy-viscosity models, e.g. the Smagorinsky or (filtered) structure-function model, and investigate their influence on the results of large-eddy simulations of laminar, transitional and turbulent flows. High-pass filtering employed to the computational quantities prior to computation of the eddy-viscosity and/or strainrate in the subgrid-scale model allows for a good prediction of transitional and turbulent flows without using any ad-hoc adaptation. Of particular importance is that the sensitivity of the results to the model coefficient is considerably reduced compared with non-HPF models. Furthermore, the proposed high-pass filters enable the computation of the structure function in the filtered or HPF structure-function model in all spatial directions even for inhomogeneous flows, removing the arbitrariness of special treatment of selected (e.g. wall-normal) directions.

Keywords: LES, subgrid-scale modeling, high-pass filtered models, transition, turbulence, Smagorinsky model, structure-function model, eddy-viscosity.

1. Introduction

Eddy-viscosity models such as the Smagorinsky model (1963) or structure-function (SF) model (Métais and Lesieur, 1992) are the most often employed subgrid-scale (SGS) models for large-eddy simulations (LES). Variants of these models with fixed coefficients require special treatment of the viscous sublayer of wall-bounded turbulent flows or laminar flow regions. Ad-hoc measures frequently used are the van-Driest damping function for the model coefficient in the near wall region or intermittency functions for transitional flows (Piomelli et al., 1990). However, such methods are designed for special flow situations only. Ideally, the SGS model used for LES should be defined locally and fully three-dimensional, i.e. without special treatment of selected spatial directions, and it should not require ad-hoc adaption to the specific flow configuration.

In general, the dynamic Smagorinsky model (Germano et al., 1991; Lilly, 1992) is defined locally and adapts itself automatically to different flow situations, e.g. laminar, transitional, and turbulent flows. However, it does not necessarily predict a vanishing value of the model coefficient for laminar flows as it should, not even for the incompressible laminar channel flow. Due to a vanishing strain rate, it is singular in the midplane of a laminar channel. Averaging in homogeneous directions is usually employed for turbulent flows in order to minimize the occurrence of singularities in the dynamic coefficient computation, which is not possible for non-homogeneous flow directions. Furthermore, with averaging over homogeneous directions, the dynamic model forfeits its local definition.

In this contribution, we consider a different approach for SGS modeling suitable for laminar, transitional and turbulent flows without ad-hoc adaption by analyzing high-pass filtered (HPF) eddy-viscosity models. The concept of HPF models and the relation to the variational multiscale method was proposed very recently, independently from our work, by Vreman, 2003. However, different from the method discussed herein, filtering is performed by Vreman using a real-space top-hat filter, which in general does not avoid unphysical non-vanishing model contributions in laminar flow regions and the viscous sublayer of near-wall turbulence. Furthermore, the filtered subgrid-scale models introduced by Sagaut et al., 2000 can be recovered by our modeling strategy. Additionally, we propose high-pass filters for the filtered structure-function model (FSF, Ducros et al., 1996) which allow for the use of a three-dimensional formulation of the FSF even for non-homogeneous flows.

From a physical point of view, the HPF models take into account only the most important interactions between the non-resolved subgrid scales and the resolved scales, which take place between the smallest resolved scales and the largest subgrid scales, while the interactions between large-scale flow and the subgrid scales are negligible (Domaradzki et al., 1994; Vreman, 2003).

2. High-pass filtered eddy-viscosity models

For a correct prediction of laminar flows or the viscous (sometimes called “laminar”) sublayer of turbulent flows, the results should generally not be affected by the subgrid-scale model. This is obviously not true for fixed-coefficient eddy-viscosity models for the SGS stresses, $\tau_{ij} = \bar{u}_i \bar{u}_j - \bar{u}_i u_j$, e.g. the Smagorinsky model (SM)

$$\tau_{ij} - \frac{\delta_{ij}}{3} \tau_{kk} \approx m_{ij} = 2(C_S \Delta)^2 |S(\bar{\mathbf{u}})| \cdot S_{ij}(\bar{\mathbf{u}}) = \nu_{t,SM} S_{ij}(\bar{\mathbf{u}}), \quad (1)$$

with $S_{ij}(\bar{\mathbf{u}}) = \frac{1}{2} \left(\frac{\partial \bar{u}_i}{\partial x_j} + \frac{\partial \bar{u}_j}{\partial x_i} \right)$ and $|S(\bar{\mathbf{u}})| = \sqrt{2S_{ij}(\bar{\mathbf{u}})S_{ij}(\bar{\mathbf{u}})}$ or the structure-function (SF) model given by

$$m_{ij} = C_{SF} C_k^{-3/2} \Delta \sqrt{F_2(\bar{\mathbf{u}}, \mathbf{x}, \Delta \mathbf{x})} S_{ij}(\bar{\mathbf{u}}) = \nu_{t,SF} S_{ij}(\bar{\mathbf{u}}), \quad (2)$$

with F_2 being the (three-dimensional) structure function which is computed from $\bar{\mathbf{u}}$ at the 6 neighboring points (Lesieur and Métais, 1996),

$$F_2(\bar{\mathbf{u}}, \mathbf{x}, \Delta \mathbf{x}) = \frac{1}{6} \sum_{i=1}^3 \left\{ |\bar{\mathbf{u}}(\mathbf{x}) - \bar{\mathbf{u}}(\mathbf{x} - \Delta x_i \mathbf{e}_i)|^2 + |\bar{\mathbf{u}}(\mathbf{x}) - \bar{\mathbf{u}}(\mathbf{x} + \Delta x_i \mathbf{e}_i)|^2 \right\} \left(\frac{\Delta}{\Delta x_i} \right)^{\frac{2}{3}} \quad (3)$$

and $\Delta = (\Delta x_1 \Delta x_2 \Delta x_3)^{1/3}$ and C_k the Kolmogorov constant.

Vanishing model contributions (in laminar flows or the viscous sublayer of turbulent flows) can be achieved by a vanishing turbulent eddy viscosity ν_t or a vanishing strain rate S_{ij} . The dynamic Smagorinsky model (Germano et al., 1991; Lilly, 1992) and the filtered structure-function model (FSF, Ducros et al., 1996) attempt to give a vanishing turbulent eddy viscosity, which however, is not necessarily vanishing truly for both SGS models in their three-dimensional formulation used for inhomogeneous flows. For the FSF, high-pass filtering as described below can be employed in order to obtain a vanishing coefficient.

The HPF eddy-viscosity models can feature both a vanishing turbulent eddy viscosity and a vanishing strain rate. These models employ high-pass filtered quantities $H_N * \bar{\mathbf{u}}$ instead of $\bar{\mathbf{u}}$ for the computation of the turbulent eddy viscosity and/or strain rate. The HPF Smagorinsky model is then given by

$$m_{ij} = 2(C_{S,\omega_c}^{HPF} \Delta)^2 |S(H_{N_\nu} * \bar{\mathbf{u}})| \cdot S_{ij}(H_{N_S} * \bar{\mathbf{u}}), \quad (4)$$

and the HPF structure-function model by

$$m_{ij} = C_{SF,\omega_c}^{HPF} C_k^{-3/2} \Delta \sqrt{F_2(H_{N_\nu} * \bar{\mathbf{u}}, \mathbf{x}, \Delta \mathbf{x})} \cdot S_{ij}(H_{N_S} * \bar{\mathbf{u}}). \quad (5)$$

With suitable filters, high-pass filtered quantities are vanishing for smooth velocity profiles (e.g. low-order polynomials) and the corresponding SGS model contributions are evanescent. High-pass filtering is performed by subtracting low-pass filtered quantities from the unfiltered ones. Three-dimensional low-pass filters are derived from one-dimensional ones by dimensional splitting, resulting in a tensor-product of one-dimensional operators. A detailed description of the construction of the low-pass filter G used herein can be found in Stolz et al., 2001. The high-pass filtered quantity is then given by

$$H_N * \bar{\mathbf{u}} = (I - Q_N * G) * \bar{\mathbf{u}} = (I - G)^{N+1} * \bar{\mathbf{u}} = \mathcal{O}(\Delta^{r(N+1)}) \quad (6)$$

with $Q_N = \sum_{\nu=0}^N (I - G)^\nu$ (Stolz and Adams, 1999), r being the order of the low-pass filter G . For arbitrary grids $r = 3$, however, for equidistant grids odd-numbered moments are vanishing and r increases to 4 (Stolz et al., 2001). $H_0 * \bar{\mathbf{u}}$ is vanishing if $\bar{\mathbf{u}}$ is a polynomial of up to degree $(r(N+1) - 1)$. The cut-off wavenumber ω_c , defined arbitrarily by $|\hat{H}_N(\omega_c)| = 1/2$, of the (implicit) filter can easily be adjusted. Except for the filter shape, the cutoff wavenumber

ω_c is the only additional parameter entering the model. However, results obtained with the HPF Smagorinsky model and different cutoff wavenumbers ω_c indicate that for the HPF Smagorinsky model the influence of ω_c on the LES results in the range $[\pi/3, 3\pi/4]$ can be corrected approximately by setting

$$C_{S,\omega_c}^{HPF} \approx \frac{\pi}{\pi - \omega_c} \cdot C_0, \quad (7)$$

where the recommended value for C_0 is $0.1/3$, e.g. $C_{S,\omega_c}^{HPF} = 0.1$ for $\omega_c = 2\pi/3$.

3. Incompressible channel flow

For computation of incompressible channel flow the HPF eddy-viscosity models have been implemented into the spectral DNS code of Gilbert and Kleiser, 1990. As a first test case the turbulent channel flow with a Reynolds number based on the bulk velocity and the channel half width h of $Re_b = u_b h / \nu = 2800$ ($Re_\tau = u_\tau h / \nu \approx 180$ based on the friction velocity) is considered. For the corresponding DNS the same parameters were used as in Moser et al., 1999, i.e. $128^2 \times 129$ grid points in the computational domain of the size $L_1 \times L_2 \times L_3 = 4\pi h \times 4\pi h / 3 \times 2h$. For all LES computations presented here, a resolution of $32^2 \times 33$ points is used, which is to be considered rather coarse especially in the wall-normal direction x_3 .

The sensitivity to the parameter C_0 of the HPF Smagorinsky model is investigated in Fig. 1(a). As high-pass filter prior to the computation of the strain rate S_{ij} and the norm $|S|$ we employed $H_0 = 1 - G$ with cutoff wavenumber $\omega_c = 2\pi/3$, i.e. the filter parameters $N_\nu = N_S = 0$. In Fig. 1(a) the mean velocity profile is depicted for three different model coefficients, $C_0 = 0.05/3$, $C_0 = 0.1/3$, and $C_0 = 0.15/3$. It should be noted that C_0^2 enters the model. For all cases we compare LES data with grid-filtered DNS data. For comparison also LES without any SGS-model ("noSGS") and data obtained with the dynamic Smagorinsky model (test-filtering employed in all three directions) are shown. The results for the HPF Smagorinsky model are much less sensitive to the model coefficient than the classical Smagorinsky model (not shown here). The law of the wall is predicted best for $C_0 = 0.1/3$ with the HPF model. For the deliberately chosen coarse grid, the dynamic Smagorinsky model predicts a too low friction velocity and overpredicts the normal streamwise Reynolds stresses and underpredicts other Reynolds stresses. For the HPF Smagorinsky model all Reynolds stresses are in good agreement with the DNS data and vary only slightly when changing the model coefficient from 0.05 to 0.15.

Furthermore, the effect of different high-pass filters has been investigated. LES with the HPF Smagorinsky model have been performed the $3^{rd}/4^{th}$ order (non-equidistant/equidistant grids) high-pass filter H_0 , the $18^{th}/24^{th}$ order filter H_5 and with a second-order Padé filter. Fig. 1(b) depicts the mean-flow profile and the Reynolds stresses for the different high-pass filters with a fixed cutoff

wavenumber $\omega_c = 2\pi/3$. It is apparent that the choice of the parameter N and thus the order of the high-pass filter $H_N = 1 - Q_N * G$ has only a negligible effect on the results. However, the use of the 2^{nd} order Padé filter does not result in a vanishing high-pass filtered quantity even for a linear profile on non-equidistant grids and results for the near-wall behavior of the flow deteriorate compared to those obtained with the high-pass filters H_N based on the filters proposed in Stolz et al., 2001 (see also the close-up of the near-wall velocity profile in Fig. 1(b)).

Furthermore, we compare results obtained with the FSF model with results of the HPF structure-function model (HPF-SF). For both models, prior to the computation of the structure function F_2 the high-pass filter H_0 with $\omega_c = 2\pi/3$ is used, $N_\nu = 0$. In contrast to the FSF, where no high-pass filtering is employed before the computation of the strain rate S_{ij} , for the HPF-SF the strain rate is computed from high-pass filtered velocities, $N_S = 0$. Different from Ducros et al., 1996 who computed the structure function from high-pass filtered quantities in the homogeneous wall-parallel directions only, in this work the computation of the structure function and the high-pass filtering is performed in all three spatial directions.

Fig. 1(c) shows the mean velocity profile and the Reynolds stresses for the FSF and the HPF-SF with $C_{SF, \omega_c}^{HPF} = 0.05$ and $C_k = 1.4$. Although a still better agreement might be obtained by further adjusting the coefficient, in both cases the error of the predicted Re_τ is within 3.5% of the DNS value. The FSF well predicts the mean-flow profile, however, the Reynolds stresses show some deviation from the grid-filtered DNS data. Better results for both mean-flow and Reynolds stresses are obtained with the HPF-SF, see Fig. 1(c). The prediction of the near-wall flow behavior obtained with the HPF-SF is better than the prediction with the FSF, which is due to a vanishing (high-pass filtered) strain rate for the statistically averaged near-wall flow. It can be shown further that the HPF-SF is slightly less sensitive to the choice of the model coefficient.

Next, we turn to the computation of K-type transition in channel flow. As initial field the laminar (parabolic) profile with superimposed disturbances was chosen as in the fully resolved DNS of Gilbert and Kleiser, 1990. The Reynolds number is $Re_b = 3333$. Fig. 2 shows the temporal evolution of the Re_τ and the centerline Reynolds number Re_{CL} for (a) Smagorinsky-type and (b) structure-function models. For all LES $32^2 \times 33$ grid points were used. Although our fine-grid DNS with up to $160^2 \times 161$ grid points shows slightly later transition than both the no-model simulation and the HPF Smagorinsky model LES, the simulations show comparable onset of transition and initial growth, see Fig. 2(a). Furthermore, the skin friction peak value with the well-known overshoot of Re_τ of about 15% (Gilbert and Kleiser, 1990) is visible for the no-model simulation and the LES using the HPF Smagorinsky model with H_0 . The HPF Smagorinsky using the 2^{nd} order Padé filter overpredicts the peak in the fric-

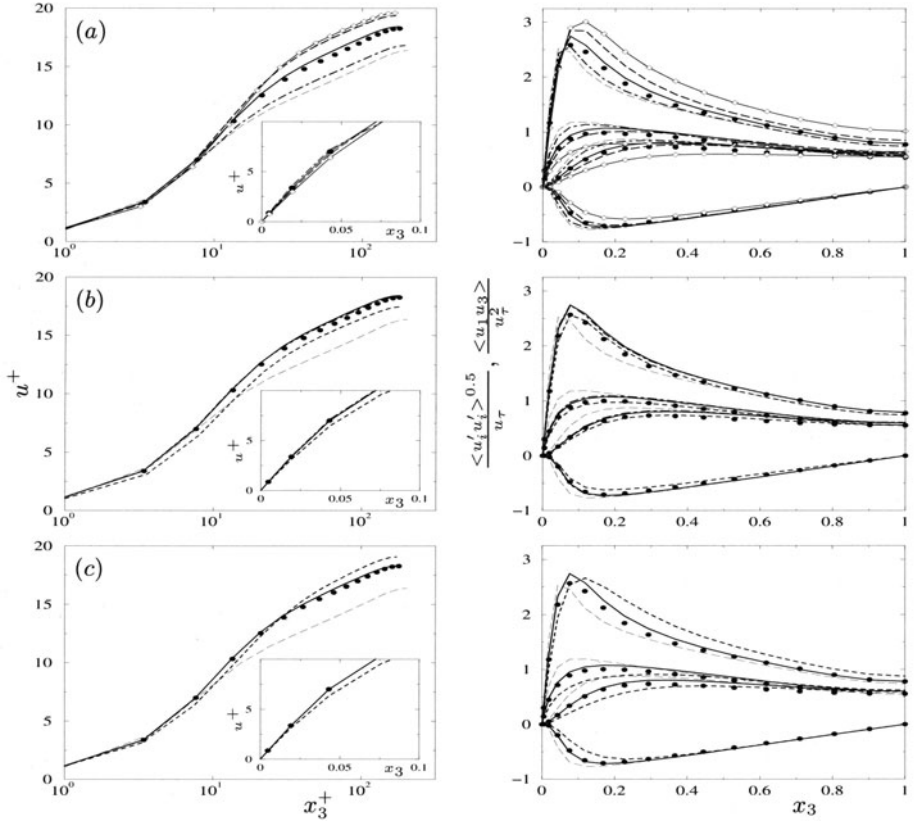


Figure 1. Results of LES for turbulent channel flow. Left column: mean velocity profiles; right column Reynolds stresses. (a) HPF Smagorinsky model with different model coefficients: \cdots — $C_0 = 0.05/3$, — — $C_0 = 0.1/3$, and --- — $C_0 = 0.15/3$; (b) HPF Smagorinsky model with $C_0 = 0.1/3$ and different high-pass filters ($\omega_c = 2\pi/3$): — — H_0 , --- — H_5 (results coincides with those for H_0), and --- — 2^{nd} order filter; (c) — —HPF structure-function (HPF-SF) model and --- —filtered structure-function model (FSF) model both with $C_{SF,\omega_c}^{HPF} = 0.05$; also shown \bullet DNS data, \diamond —dynamic Smagorinsky, and --- —noSGS.

tion velocity by about 8%. Although not apparent on first sight from Fig. 2, the statistical average of Re_τ for the turbulent phase for the no-model simulation and the HPF Smagorinsky model with the 2^{nd} order Padé filter shows too large values for the wall friction, see also Fig. 1(b). The time evolution of Re_τ for the classical Smagorinsky model clearly shows that the model fails to predict transition as the base flow is changed nonphysically by model contributions. For the same value of the model coefficient, however, the classical Smagorinsky model gives a good prediction of turbulence when turbulent initial data are used. The dynamic Smagorinsky model predicts transition at a correct position, however, it fails to reproduce the peak in the skin-friction. For the turbulent phase the dynamic Smagorinsky model turns out to be too dissipative. Considering the time evolution of Re_τ for the FSF, see Fig. 2(b), the FSF pre-

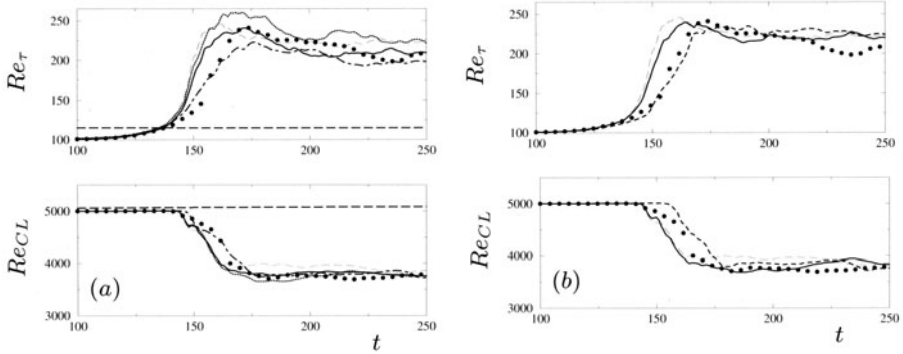


Figure 2. Time evolution of Re_τ and Re_{CL} during the transitional phase; (a) ---- classical Smagorinsky with $C_S = 0.1$, — HPF Smagorinsky model using H_0 and HPF Smagorinsky model using 2^{nd} order filter with $C_0 = 0.1/3$, — · — dynamic Smagorinsky model; (b) — HPF structure-function model (HPF-SF) and ---- filtered structure-function (FSF) both with $C_{SF} = 0.05$; also shown ---- noSGS, and • DNS data.

dicts the onset of transition very well but fails to predict the peak in Re_τ . For the centerline velocity a slightly too late onset of transition is observed. Similar to the HPF-Smagorinsky model, the HPF-SF predicts the transition slightly too early, however, the results show a correct overshoot in Re_τ and a correct prediction of the turbulent phase, see also Fig. 1(c).

4. Conclusions

We have proposed a high-pass filtering approach suitable for constructing high-pass filtered (HPF) eddy-viscosity models. High-pass filtering is employed to the computational quantities before computing the eddy-viscosity and/or strainrate of the subgrid-scale model, e.g. Smagorinsky or (filtered) structure-function model.

The high-pass filters are constructed such that laminar flow and the viscous sublayer of wall turbulence are not affected by the model as the model contributions are vanishing. This is of primary interest for LES of transitional flows as for a correct prediction of transition the models have to be able to deal with at least the two limits of laminar and turbulent flow. The sensitivity of the results on the cutoff wavenumber of the high-pass filter has been investigated and an empirical correction which eliminates this dependency for a wide range of cutoff wavenumbers has been proposed. The high-pass filters and HPF models are formulated entirely in real space which allows for an implementation in codes using among other finite-difference or spectral numerical schemes.

For the filtered structure-function model the proposed high-pass filters enable the computation of the structure function in all spatial directions even for inhomogeneous flows, thus removing the arbitrariness of special treatment of selected directions, e.g. the wall-normal direction.

The performance of the HPF Smagorinsky and HPF structure-function model

have been examined for laminar, transitional and turbulent channel flow obtaining good results for all configurations without using any ad-hoc adaptation. Of particular importance is that the HPF models also feature a better prediction of turbulent flows as their sensitivity to the model coefficient is reduced and, e.g., no wall-damping functions are needed. Unlike the dynamic Smagorinsky model, the HPF models are formulated locally and no averaging over homogeneous directions is needed. For this reason the model is suitable also for non-homogeneous flows.

Acknowledgments

P. Schlatter was supported by the Swiss National Science Foundation and the Swiss Center of Scientific Computing (CSCS). Calculations have been performed at CSCS.

References

- Domaradzki, J. A., Liu, W., Härtel, C., and Kleiser, L. (1994). Energy-transfer in numerically simulated wall-bounded turbulent flows. *Phys. Fluids*, 6:1583–1599.
- Ducros, F., Comte, P., and Lesieur, M. (1996). Large-eddy simulation of transition to turbulence in a boundary layer developing spatially over a flat plate. *J. Fluid Mech.*, 326:1–36.
- Germano, M., Piomelli, U., Moin, P., and Cabot, W. H. (1991). A dynamic subgrid-scale eddy viscosity model. *Phys. Fluids A*, 3:1760–1765.
- Gilbert, N. and Kleiser, L. (1990). Near-wall phenomena in transition to turbulence. In Kline, S. J. and Afgan, N. H., editors, *Near Wall Turbulence*, pages 7–27. Hemisphere.
- Lesieur, M. and Métais, O. (1996). New trends in large-eddy simulations of turbulence. *Annu. Rev. Fluid Mech.*, 28:45–82.
- Lilly, D. (1992). A proposed modification of the Germano subgrid-scale closure model. *Phys. Fluids A*, 4:633–635.
- Métais, O. and Lesieur, M. (1992). Spectral large-eddy simulations of isotropic and stably-stratified turbulence. *J. Fluid Mech.*, 239:157–194.
- Moser, R. D., Kim, J., and Mansour, N. N. (1999). Direct numerical simulation of turbulent channel flow up to $Re_\tau = 590$. *Phys. Fluids*, 11(4):943–945.
- Piomelli, U., Zang, T. A., Speziale, C. G., and Hussaini, M. Y. (1990). On the large-eddy simulation of transitional wall-bounded flows. *Phys. Fluids A*, 2(2):257–265.
- Sagaut, P., Comte, P., and Ducros, F. (2000). Filtered subgrid-scale models. *Phys. Fluids*, 12:233–236.
- Smagorinsky, J. (1963). General circulation experiments with the primitive equations. *Mon. Weath. Rev.*, 93:99–164.
- Stolz, S. and Adams, N. A. (1999). An approximate deconvolution procedure for large-eddy simulation. *Phys. Fluids*, 11:1699–1701.
- Stolz, S., Adams, N. A., and Kleiser, L. (2001). An approximate deconvolution model for large-eddy simulation with application to incompressible wall-bounded flows. *Phys. Fluids*, 13:997–1015.
- Vreman, A. W. (2003). The filtering analog of the variational multiscale method in large-eddy simulation. *Phys. Fluids*, 15:L61–L64.

A SYNTHESIS OF SIMILARITY AND EDDY-VISCOSITY MODELS

Roel Verstappen

Research Institute of Mathematics and Computer Science

University of Groningen, P.O.Box 800, 9700 AV Groningen, The Netherlands.

verstappen@math.rug.nl

Abstract In large-eddy simulation, a low-pass spatial filter is usually applied to the Navier-Stokes equations. The resulting commutator of the filter and the nonlinear term is usually modelled by an eddy-viscosity model, by a similarity model or by a mix thereof. Similarity models possess the proper mathematical structure; particularly, they satisfy all fundamental properties of a commutator. Additionally, they correlate well with the real commutator. Yet, their leading term has directions of negative diffusion. We propose to stabilize similarity models by projecting them onto an eddy-viscosity model. The projection eliminates the dynamically unstable part and results in a self-calibrating eddy-viscosity. The numerical algorithm used to solve the governing equations preserves the skew-symmetry of the nonlinear term, and is therefore well-suited to test the proposed model. The model is successfully tested for turbulent channel flow (at $Re_\tau = 1025$ and $Re_\tau = 2520$).

Keywords: Large-eddy simulation, turbulence modelling, subgrid models.

1. Introduction to eddy-viscosity and similarity models

Most turbulent flows can not be computed directly from the (incompressible) Navier-Stokes equations, because they possess far too many dynamically significant scales of motions. Therefore, in large-eddy simulation (LES), a low-pass filter is usually applied to the equations. When the spatial filtering operator \mathcal{F} commutes with partial derivatives, the filtered equations are

$$\partial_t \bar{u} + \mathcal{N}\mathcal{S}(\bar{u}) + \nabla \bar{p} = -\nabla \cdot \tau(u) \quad \text{with} \quad \tau(u) = \mathcal{F}(uu^T) - \mathcal{F}(u)\mathcal{F}(u)^T, \quad (1)$$

where the left-hand side depends on the filtered velocity $\bar{u} = \mathcal{F}u$, whereas the right-hand side depends on the unfiltered velocity u via the commutator of the Navier-Stokes operator $\mathcal{N}\mathcal{S}(u) = \nabla \cdot (uu^T) - \nabla^2 u / Re$ and the filter. To close the filtered equations, the subfilter tensor τ has to be modelled in terms of the filtered velocity \bar{u} . Often this is done by means of an eddy-viscosity model, by a (scale) similarity model, or by a mix thereof.

Smagorinsky proposed an eddy-viscosity model of the form

$$-\tau(u) + \frac{1}{3} \text{trace}(\tau(u))\mathcal{I} \approx \nu(\nabla\bar{u} + \nabla\bar{u}^*), \quad (2)$$

in which the eddy-viscosity ν is taken proportional to the product of the square of the filter-length and $|\nabla\bar{u} + \nabla\bar{u}^*|$. Here, the isotropic part $\frac{1}{3} \text{trace}(\tau)\mathcal{I}$ need not be modelled, as it can be incorporated into the pressure. To obtain a better model, Germano (1992) replaced the constant of proportionality by a function of space and time, which is determined dynamically with the help of a fundamental property of a commutator. This dynamical procedure has the advantage of being self-calibrating and requires no *a priori* specification of the model constant. However, the resulting eddy-viscosity can take values for which the filtered equations are (locally) unstable. In such situations, one resorts to a clipping scheme that restricts ν , see *e.g.* Ghosal *et al.* (1995).

Similarity models are based upon an approximate defiltering procedure: $u \approx \tilde{u} = \tilde{\mathcal{F}}^{-1}\bar{u}$, where $\tilde{\mathcal{F}}^{-1}$ stands for an approximate inverse of \mathcal{F} . The commutator is modelled by substituting \tilde{u} for u ,

$$-\tau(u) + \frac{1}{3} \text{trace}(\tau(u))\mathcal{I} \approx -\tau(\tilde{u}) + \frac{1}{3} \text{trace}(\tau(\tilde{u}))\mathcal{I}. \quad (3)$$

Similarity models have the proper mathematical structure, meaning that the model (3) possesses all characteristic properties of a commutator. The error emanates from the defiltering. Bardina *et al.* (1984) were the first who applied a similarity model; they took simply $\tilde{u} = \bar{u}$. Stolz and Adams (1999) took the first (three or) five terms of a series expansion of \mathcal{F}^{-1} .

Carati *et al.* (1999) have shown that for all filters (that are C^∞ in wave space) the series expansion of $\tau(\tilde{u})$ starts with a generic term that is known under various names, among others nonlinear model, gradient model and tensor-diffusivity model and is basically due to Leonard (1974). Later (Leonard, 1997), he notes that the gradient model can be seen as a tensorial eddy-viscosity model with directions of positive as well as negative diffusion. The stability of this model has been analyzed with the help of the one-dimensional Burgers' equation by Vreman (1995). He showed that the gradient model gives rise to severe instabilities.

In the original form of Clark *et al.* (1979), the instability of the gradient model was overcome by combining the gradient model with (2). Bardina *et al.* (1984) used a mixed approach too. The basic idea underlying mixed models is that the similarity model takes into account the contributions of the defiltered, filtered velocity \tilde{u} only. Yet, in a discrete setting, defiltering can merely yield the leading part of the residual velocity $u - \bar{u}$, *i.e.* the part that most likely possesses the strongest dynamical interaction with the filtered velocity. To illustrate this, we consider a discretized filtered velocity in Fourier space. In Fourier space, the velocity is described by a limited number of modes. Inverting the discrete filter does not extend the number of Fourier-modes; the filtered and defiltered

discrete velocity have the same spectral support, which is too small to represent the unfiltered velocity u fully, see Zhou *et al.* (1989). Therefore, similarity models are expected to underestimate the dissipation at scales too small to be recovered by the defiltering procedure. Mixed models try to make up for the shortage of dissipation by adding dissipative terms.

In this paper, we propose to stabilize the similarity model (3) by projecting it onto a stable eddy-viscosity model. In other words, we do not add dissipative terms to stabilize (3) as is done in mixed modelling, but instead we propose to remove the dynamically unstable part. Before describing the stabilization technique in detail, we will discuss the filter and its approximate inverse first.

2. Filtering and defiltering

Filtering is usually done by means of an integral operator with a symmetrical convolution kernel. We apply the elliptic, differential filter (Germano 1986)

$$\bar{u} = \mathcal{F}u = u + \alpha^2 \nabla^2 u, \quad (4)$$

where α parametrizes the filter-length. The boundary conditions that supplement the Navier-Stokes equations are applied to the filter too. This filter is generic in the sense that any symmetric convolution filter can be approximated by the diffusive process (4), where the error in the approximation is of the order α^4 , see Carati *et al.* (1999). Additionally, Montgomery and Pouquet (2002) have shown that the (second-order accurate) approximate inverse of (4)

$$u \approx \tilde{u} = \tilde{\mathcal{F}}^{-1} \bar{u} = (1 - \alpha^2 \nabla^2) \bar{u}, \quad (5)$$

forms the essence of the recently proposed ‘alpha-model’; compare Eq. (5) to Eq. (8) in Montgomery and Pouquet’s paper.

3. A stabilized similarity/eddy-viscosity model

The commutator of the elliptic, differential filter (4) and the Navier-Stokes operator is given by the right-hand side of Eq. (1), where the subfilter stress τ depends upon the velocity-gradient:

$$\tau_{ij}(\nabla u) = 2\alpha^2 \nabla u_i \cdot \nabla u_j - \alpha^4 \nabla^2 u_i \nabla^2 u_j. \quad (6)$$

Now, when the unfiltered velocity u is replaced by the defiltered approximation \tilde{u} , $\tau_{ij}(\nabla u) \approx \tau_{ij}(\nabla \tilde{u})$, we are placed in a dilemma. The resulting scale similarity model possesses the correct mathematical structure; particularly, it satisfies all fundamental properties of a commutator. Additionally, the correlation between the approximation $\tau_{ij}(\nabla \tilde{u})$ and $\tau_{ij}(\nabla u)$ is generally strong, typically between 0.6 and 0.9. On the other hand, however, the leading term of $\tau_{ij}(\nabla \tilde{u})$ has directions of negative dissipation. To eliminate the dynamically

unstable part from $\tau_{ij}(\nabla \tilde{u})$, we propose to project $\tau_{ij}(\nabla \tilde{u})$ onto the eddy-viscosity model (2), where the projection is constrained by the requirement that the net dissipation must be positive everywhere:

$$\nu + \frac{1}{Re} > 0. \quad (7)$$

That is, the eddy-viscosity $\nu(x, t)$ is computed such that the best approximation of $-\tau(\nabla \tilde{u}) + \frac{1}{3}\text{trace}(\tau(\nabla \tilde{u}))\mathcal{I}$ is obtained in a least-squares sense,

$$\min \int e_{ij}e_{ij}dV, \quad (8)$$

where the integral extends over the entire flow domain, the residuals are $e_{ij} = -\tau_{ij}(\nabla \tilde{u}) + \frac{1}{3}\delta_{ij}\tau_{kk}(\nabla \tilde{u}) - \nu(\partial_j \bar{u}_i + \partial_i \bar{u}_j)$ and the minimum is computed (with respect to ν) subject to the stability constraint (7). The Euler-Lagrange equation for the constrained variational problem (7)-(8) can be solved analytically. The solution reads

$$\nu = \frac{(-\tau_{ij}(\nabla \tilde{u}) + \frac{1}{3}\delta_{ij}\tau_{kk}(\nabla \tilde{u}))(\partial_j \bar{u}_i + \partial_i \bar{u}_j)}{(\partial_n \bar{u}_m + \partial_m \bar{u}_n)^2}, \quad (9)$$

if the right-hand side is larger than $-1/Re$; and $\nu = -1/Re$ otherwise. In summary, the stabilized similarity/eddy-viscosity model is given by Eq. (2), where the eddy-viscosity is computed according to Eq. (9), in which \tilde{u} is taken as in Eq. (5) and τ as in Eq. (6).

Note that the variational problem (7)-(8) may be constrained further, for instance by restricting ν to functions independent of any homogeneous directions. A near-wall analysis of (9) shows that the eddy-viscosity behaves like $\nu \sim y^3$ near a no-slip wall $y = 0$. Consequently, the model (2)-(9) predicts the most relevant entries of τ (τ_{12} , e.g.) with the right near-wall behavior.

4. Symmetry-preserving discretization

To evaluate the performance of the model given by (2)-(9), the results from a LES that uses this model are compared with data from experiments in the next section. In such an *a posteriori* test modelling errors and discretization errors are mixed together. This mix of errors is inherent in LES. Consequently, the discretization of the governing equations is a very important point when dealing with *a posteriori* performance tests for LES-models. Since the dissipation of the large-eddies should not be caused by the discretization of the nonlinear (convective) term in the Navier-Stokes equations, but by the viscous term and the subfilter model, we apply the recently developed symmetry-preserving discretization scheme (Verstappen and Veldman 2003), which convects the total energy of the large-eddies without numerical dissipation.

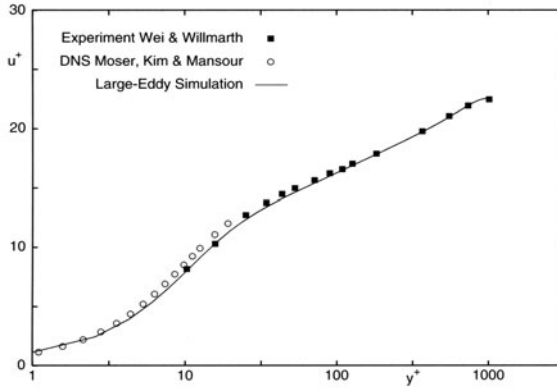


Figure 1. Comparison of the mean streamwise velocity u^+ as function of y^+ at $Re_\tau = 1025$.

5. Results for turbulent channel flow - an a posteriori test

As a first step in application of the proposed model, it is tested for a turbulent channel flow by comparing the results of large-eddy simulations with those of the water/wind tunnel experiments performed by Wei and Willmarth (1989) and Comte-Bellot (1963). Based on the channel half-width and the bulk mean velocity the Reynolds numbers are 20,200 and 57,000, respectively. In terms of the wall-shear velocity the Reynolds numbers become 1025 and 2520. Since making good near-wall measurements is extremely difficult, we will also make a comparison with a direct numerical simulation (DNS) by Moser *et al.* (1999). Because this DNS has been done at $Re_\tau = 590$, the comparison with DNS is to be restricted to the direct vicinity of the wall (where Reynolds-number effects can be properly scaled). As usual, the flow is assumed to be periodic in the stream- and spanwise direction. The computational grid consists of 128 streamwise points, 64 spanwise points and 300 points between the channel walls. All LES-results are approximately defiltered by means of Eq. (5) in order to compare them directly with the available experimental data. Details of the computational procedure are discussed elsewhere (Verstappen and Veldman 2003); here we focus on the principal results.

$Re_\tau = 1025$. We attempt to simulate the experiment by Wei and Willmarth (1989), which was carried out at $Re_\tau = 1025$. The profile of the mean velocity is shown in Fig. 1. Overall good agreement between the computation and the experiment is observed. Near the wall, where no experimental data is available, the present result collapses with that of the DNS by Moser *et al.* (1999). The skin friction coefficient 0.00518 and the centre-line velocity 1.131 are in excellent agreement with the data (0.0051 and 1.13, resp.) compiled by Dean (1978). Comparison of the fluctuating velocities with reference data shows good agreement too, see Fig. 2.

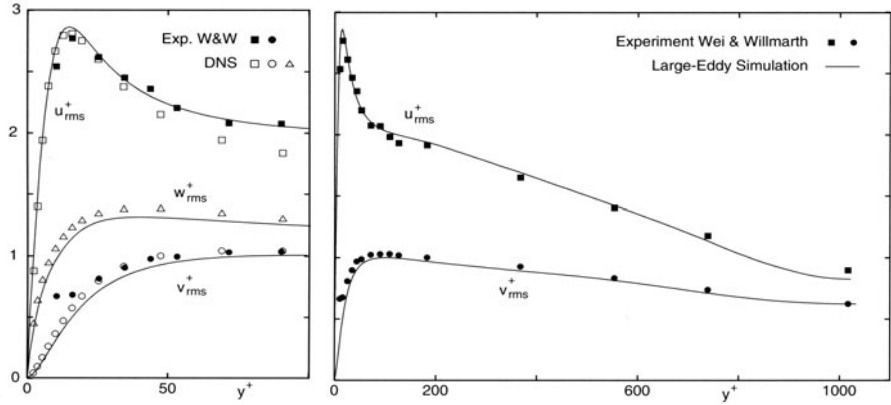


Figure 2. Comparison of the root-mean-square of the fluctuating velocity at $Re_\tau = 1025$. The solid markers correspond to the experimental data of Wei and Willmarth (1989); the lines represent the present results. The left-hand side displays a near-wall zoom. Here, the open markers depict the results of the DNS by Moser *et al.* (1999), which has been performed at $Re_\tau = 590$. Note that for $y^+ > 30$ the comparison with the fluctuating streamwise velocity of the DNS does not hold due to Reynolds-number effects, see also Fig. 4.

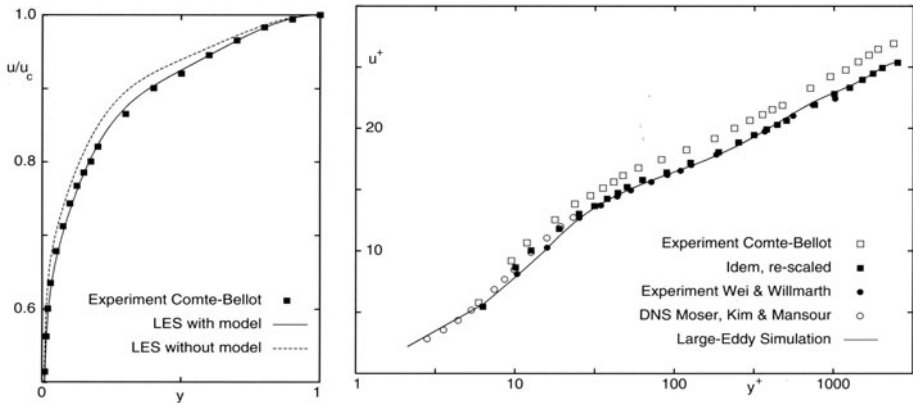


Figure 3. Comparison of the mean streamwise velocity at $Re_\tau = 2520$. In the left-hand side the velocity is normalized by the centre-line velocity. Here, the mid of the channel is located at $y = 1$. The squares depict the experimental data of Comte-Bellot (1963); the line represents the (approximately) defiltered LES-results; the dashed line is obtained without model/filter. The right-hand side figure shows u^+ as function of y^+ . The open squares correspond to the original experimental data of Comte-Bellot (1963); the solid squares represent rescaled data, see text.

$Re_\tau = 2520$. The least to be expected from a LES is a good prediction of the mean flow. As can be seen in Fig. 3 (left) the present LES satisfies that minimal requirement: without any models the prediction of the mean flow worsens significantly. With model, the agreement with the data from the experiment by Comte-Bellot (1963) is good. Yet, the wall-shear velocities differ. Comte-Bellot deduced the wall-shear velocity from measurements of the lon-

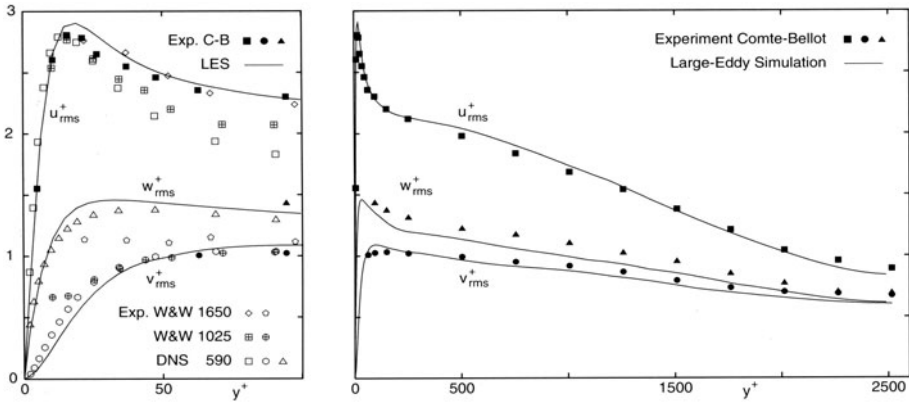


Figure 4. Comparison of the root-mean-square of the fluctuating velocity at $Re_\tau = 2520$. Note: the results by Comte-Bellot are rescaled, like in Fig. 3. Near the wall (at the left-hand side) two experiments by Wei and Willmarth are shown, namely at $Re_\tau = 1650$ and $Re_\tau = 1025$. The DNS by Moser *et al.* (1999) has been performed at $Re_\tau = 590$.

gitudinal pressure gradient. She found $u_\tau = 0.0416$. We have $u_\tau = 0.0442$, which is in good agreement with Dean's result $u_\tau = 0.0445$. Consequently, when the mean velocity is normalized by the wall-shear velocity the profiles do not correspond, see Fig. 3 (right). Therefore, we have rescaled the mean-velocity profile reported by Comte-Bellot (1963) with the help of our u_τ . After this rescaling the result of Comte-Bellot shows an excellent agreement with the data obtained by Wei and Willmarth (1989) for $y^+ > 30$ and with the DNS by Moser *et al.* (1999) for $y^+ < 30$. Fig. 3 shows also that the present result agrees well with the rescaled data of Comte-Bellot.

In Fig. 4, the turbulent intensities measured by Comte-Bellot (1963) are rescaled as before. The agreement with the LES is good, except for the spanwise fluctuations, which agree fairly: the spanwise turbulence intensity of Comte-Bellot is consistently higher than that of the LES. Near the wall there also exists a good agreement between the streamwise intensity measured by Wei and Willmarth at $Re_\tau = 1650$ and the present result. For $y^+ > 30$ the comparison with the fluctuating streamwise velocity obtained at lower Reynolds numbers does not hold due to Reynolds-number effects. In summary, good agreement with previously reported experimental results is observed.

Concluding remarks. We have shown how a synthesis of a scale similarity and an eddy-viscosity model can be used to approximate the subfilter tensor in large-eddy simulations of turbulence. The resulting stabilized similarity/eddy-viscosity model (2)-(9) has been successfully applied to compute a turbulent channel flow at $Re_\tau = 1025$ and $Re_\tau = 2520$. Given the inherent difficulty of turbulence modelling, more thorough investigations and comparisons need be carried out to clarify the pros and cons of the synthesis discussed here.

Acknowledgements

The author wishes to thank Prof.Dr. Genevieve Comte-Bellot for sending a copy of her Ph.D.-thesis, which, forty years after publication, formed a rich source of flow data.

References

- Bardina, J., Ferziger, J.H., & Reynolds, W.C. (1984). Improved turbulence models based on LES of homogeneous incompressible turbulent flows. Report TF-19, Stanford.
- Carati, D., Winckelmans, G.S. & Jeanmart, H. (1999). Exact expansions for filtered-scales modelling with a wide class of LES filters. In *Direct and Large-Eddy Simulation III* (ed. Voke *et al.*), pp. 213–224, Kluwer.
- Clark, R.A., Ferziger J.H. & Reynolds, W.C. (1979). Evaluation of subgrid-scale models using an accurately simulated turbulent flow. *J. Fluid Mech.* 91:1–16.
- Comte-Bellot, G. (1963). Turbulent flow between two parallel walls. PhD thesis, University of Grenoble, Grenoble, France.
- Dean, R.B. (1978). Reynolds number dependence of skin friction and other bulk flow variables in two-dimensional rectangular duct flow. *J. Fluids Engng.* 100:215–223.
- Germano, M. (1986). Differential filters for the large eddy numerical simulation of turbulent flows. *Phys. Fluids* 29(6):1755–1758.
- Germano, M. (1992). Turbulence: the filtering approach. *J. Fluid Mech.* 238:325–336.
- Ghosal, S., Lund, T.S., Moin, P. & Akselvoll, K. (1995). A dynamic localization model for large-eddy simulation of turbulent flows. *J. Fluid Mech.* 286:229–255.
- Holm, D.D., Marsden, J.E. & Ratiu, T.S. (1998). The Euler-Poincaré equations and semidirect products with applications to continuum theories. *Adv. Math.* 137:1.
- Leonard, A. (1974). Energy cascade in large-eddy simulations of turbulent fluid flows. *Adv. Geophys. A* 18:237–248.
- Leonard, A. (1997). Large-eddy simulation of chaotic convection and beyond. 35th Aerospace Sciences Meeting & Exhibit, Reno, NV, *AIAA Paper* 97-0204.
- Montgomery, D.C. & Pouquet, A. (2002). An alternative interpretation for the Holm “alpha model”. *Phys. Fluids* 14(9):3365–3366.
- Moser, R.D., Kim, J. & Mansour, N.N. (1999). Direct numerical simulation of turbulent channel flow up to $Re_\tau = 590$. *Phys. Fluids* 11:943–945.
- Smagorinsky, J. (1963). General circulation experiments with the primitive equations. I: The basic experiment. *Month. Weath. Rev.* 91(3):99–165.
- Stolz, S. & Adams, N.A. (1999). An approximate deconvolution procedure for large-eddy simulation. *Phys. Fluids* 11(7):1699–1701.
- Verstappen, R.W.C.P. & Veldman, A.E.P. (2003). Symmetry-preserving discretization of turbulent flow. *J. Comp. Phys.* 187:343–368.
- Vreman, B. (1995). Direct and large-eddy simulation of the compressible turbulent mixing layer. PhD thesis, University of Twente, Enschede, The Netherlands.
- Wei, T. & Willmart, W.W. (1989). Reynolds number effects on the structure of a turbulent channel flow. *J. Fluid Mech.* 204:57–95.
- Zhou, Y., Hossain, M. & Vahala, G. (1989). A critical look at the use of filters in large eddy simulation. *Phys. Lett. A* 139(7):330–332.

1.2 WALL MODELS FOR LES AND RELATED ISSUES

DEVELOPMENT OF WALL MODELS FOR LARGE-EDDY SIMULATION BASED ON NONLINEAR STOCHASTIC ESTIMATION

Markus Abel¹, Dragan Stojković² and Michael Breuer²

¹*Institute of Physics, University of Potsdam, D-14415 Potsdam, Germany*

²*Institute of Fluid Mechanics, University of Erlangen-Nürnberg, D-91058 Erlangen, Germany*

Abstract We present results on a priori estimation of LES wall models by nonlinear stochastic estimation (NLSE). The results are given in form of nonparametric, generalized additive models. First results on a posteriori LES are shown. The analyzed data are taken from a DNS of plane channel flow. The applied method allows for quantitative identification of important model terms and reveals physical mechanisms of the near-wall region. Investigated models are generalizations of known algebraic models. With usual linear methods the resulting functions cannot be found. Additional terms like the wall-normal velocity component and the streamwise pressure gradient are included in the wall model. We find that different terms become important in different regions near the wall.

Keywords: Wall modeling, nonlinear data analysis, generalized additive models

1. Introduction

Even though LES has been discussed as one of the most promising tools for turbulence simulations, one of its shortcomings is not yet overcome: the existence of walls in a system yields the requirement to either fully resolve the wall region or to derive a good approximation of the dynamics in form of a model bridging the region between the wall and the first grid point. The first is easily done, but numerically expensive with computational cost $\propto Re^{2.4}$ (see review of Piomelli and Balaras, 2002). For the second, some models exist, but none is satisfactory. Our aim is to find better wall models using approach of nonparametric data analysis.

2. Wall Models for LES

In LES, the subgrid scale contributions appearing in the filtered (incompressible) Navier-Stokes equations have to be modeled. The credibility of LES

results strongly depends on the model for the subgrid scale stress tensor τ_{ij} (Moin, 2002). We focus on wall models where the flow is intrinsically inhomogeneous and anisotropic. In the following we briefly describe the models which have been used in our analysis, others can be treated in a similar way. In the notation x denotes the streamwise, y the wall-normal, and z the spanwise coordinates, and t the time. In the approach of Schumann (1975), the wall shear stresses and the velocity components in the first off-the-wall cell have been specified directly. The resulting system of model equations reads:

$$\tau_{w,xy} = \langle \tau_w \rangle / \langle \bar{u}(Y) \rangle \bar{u} , \quad \tau_{w,yy} = 0 , \quad \tau_{w,zy} = Re^{-1} \bar{w} / Y , \quad (1)$$

where $\tau_{w,ij}$ depends on (x, z, t) and the filtered streamwise and spanwise velocity components, \bar{u} and \bar{w} , are functions of (x, Y, z, t) with Y the distance of the wall-nearest grid point to the wall. Brackets, $\langle \cdot \rangle$, denote spatio-temporal averaging. At the wall, \bar{v} is set to zero. This model contains no adjustable parameters, but a slope which varies with $\langle \tau_w \rangle / \langle \bar{u}(Y) \rangle$. If we take the mean of $\bar{u}(Y)$ and of τ_w as given and work with normalized variables $(\tau_{w,xy}(x, z, t) / \langle \tau_w \rangle)$ and $\bar{u}(x, Y, z, t) / \langle \bar{u}(Y) \rangle$ the slope is fixed to unity.

In the following non-dimensional quantities are used:

$$\frac{\tau_w}{\partial_x p / (\rho \langle \bar{u}(Y) \rangle^2 / \delta_{Ch})} \mapsto \tau_w / \langle \tau_w \rangle , \quad u \mapsto \bar{u} / \langle \bar{u}(Y) \rangle , \quad v \mapsto \bar{v} / \langle \bar{u}(Y) \rangle , \quad \partial_x p \mapsto \partial_x p / (\rho \langle \bar{u}(Y) \rangle^2 / \delta_{Ch}) .$$

Many modifications and extensions of Schumann's model have been proposed, see the refs. in Piomelli and Balaras (2002). We focus on algebraic models as in Piomelli et al. (1989) ("Piomelli's model"). To consider inclined structures near the wall, these authors shifted the streamwise location, x , such that \bar{u} , \bar{v} , \bar{w} depend on $(x + \delta, Y, z)$.

The procedure applied in the following is: take a "standard" model such as Piomelli's and generalize it by using nonparametric functions instead of linear dependences, as in Eq. (1). The generalized Piomelli model then reads

$$\tau_{w,xy} = f_{u,P}(u) + \epsilon , \quad \tau_{w,yy} = 0 , \quad \tau_{w,zy} = f_{w,P}(w) + \epsilon , \quad (2)$$

where τ_w depends on (x, z, t) and \bar{u} , \bar{w} on $(x + \delta, Y, z, t)$ and ϵ denotes the model error. The generalized Schumann model is included by setting $\delta = 0$. Additional dependence on v is included in the "ejection model":

$$\tau_{w,xy} = f_{u,e}(u(\vec{r}, t)) + f_{v,e}(v(\vec{r}, t)) + \epsilon . \quad (3)$$

Dependence on $\partial_x p$ yields the "gradient model":

$$\tau_{w,xy} = f_{u,g}(u(\vec{r}, t)) + f_{v,g}(v(\vec{r}, t)) + f_{g,g}(\partial_x p(\vec{r}, t)) + \epsilon . \quad (4)$$

Below, we show that our analysis allows for the identification of important (and unimportant) modeling terms. The addition of terms is understood as a tentative input to the analysis.

In the next section, we briefly explain the main ideas of stochastic estimation and show how to treat generalized additive models (GAM) of the type (2)-(4), which are generically nonparametric and nonlinear. We omit most technical details (see Abel et al., 2003) explaining the basic principles.

3. Nonparametric Stochastic Estimation

The simplest model equation is of the type (2). The basic idea of stochastic estimation is to take data from DNS or measurements and apply a least-square minimization procedure (Adrian et al., 1989; Langford and Moser, 1999): $E[\epsilon^2] = E\left[\left(\tau_w(\vec{r}, t) - \hat{f}_u(u(\vec{r}, t))\right)^2\right] = \min$. Here, \hat{f} is the optimal estimate for f_u . If $f_u(u)$ is linear one can use standard linear regression, consequently the procedure has been called **Linear Stochastic Estimation**, LSE (Adrian et al., 1989; Nichoud et al., 2001).

If the function f_u is *a priori* unknown one guesses a nonparametric, possibly nonlinear function. Now the minimization is achieved by nonparametric regression (Hastie and Tibshirani, 1990). The procedure works using the conditional expectation value operator $E(\tau_w|u)$ (Adrian et al., 1989); we obtain for \hat{f}_u :

$$\hat{f}_u(u) = E(\tau_w|u) = \int P(\tau'_w|u) \tau'_w d\tau'_w, \quad (5)$$

where $P(\tau'_w|u)$ denotes the conditional probability. Equivalently, one can maximize the correlation, C (Honerkamp, 1994). This will be used as criterion below. The range of C goes from minus one (anti-correlation) over zero (complete decorrelation) to one (correlation). Mean values are subtracted, the variances are divided out. Effects of nonlinearities are then more directly seen.

If additive models of the type (4) are considered, the estimation procedure is slightly more complicated and of iterative nature, since the problem is intrinsically nonlinear (Abel et al., 2003; Hastie and Tibshirani, 1990). To obtain a criterion of the importance of a single term, say $f_{u,g}$ in Eq. (4), one calculates $\tau_{w,xy} - f_{v,g} - f_{g,g}$ to isolate $f_{u,g}$ to the rhs of an equation and further computes

$$C[f_{u,g}, (\tau_{w,xy} - f_{v,g} - f_{g,g})]. \quad (6)$$

This is used extensively below. In the following, the hat for estimated quantities and the dependence on the parameters space and time is omitted.

4. Results

4.1 DNS Data

We use instantaneous data from DNS by the second-order, finite-volume code *LESOC* (Breuer, 1998). Because the plane channel flow is one of the “stan-

standard” test cases for wall-bounded flows, we considered this simple setup in order to compare our results with the literature.

To investigate Reynolds number effects, data are generated for $Re = 2800$ and $Re = 4000$. The channel geometry is $L_x/\delta_{Ch} = 2\pi$, $L_y/\delta_{Ch} = 2$ and $L_z/\delta_{Ch} = \pi$. The flow is driven by a pressure gradient in streamwise direction, adjusted during simulation to guarantee a fixed mass flux. In streamwise and spanwise directions boundary conditions are periodic; at the walls no-slip and impermeability conditions are applied. The number of grid points is $n_x = 120$, $n_y = 168$, and $n_z = 112$ for $Re = 2800$ and $n_x = 150$, $n_y = 214$, and $n_z = 120$ for $Re = 4000$. In both cases the dimensionless time step is set to $\Delta t = 0.0025$.

For the analysis a sub-domain of $\Delta x^+ \simeq 1000$, $\Delta y^+ \simeq 80$ and $\Delta z^+ \simeq 100$ is used. The complete data sets of all instantaneous quantities are stored for the subsequent analysis. We assembled data over 25 eddy-turnover times, $T_{turn} = L_y/U_b = 2$, with sampling at $T_{turn}/8$.

We compare LSE with NLSE results and check differences for the two Reynolds numbers. Below, we will illustrate our results on specific examples. Mean values such as $\langle \tau_w \rangle$ and $\langle \bar{u} \rangle$ are obtained from the DNS data in order to separate effects coming from different sources. Such quantities are part of the LES itself, determined on-the-fly by averaging the corresponding unsteady values.

4.2 A Priori Analysis

The model equations for the wall shear stress include two components treated separately. The results for the most important one, $\tau_{w,xy}$, will be explained in detail, the $\tau_{w,zy}$ component is treated briefly. We will first analyze Schumann’s model (1), then step to Piomelli’s model (2) and present the ejection (3) and gradient model (4) at the end. Results for LSE are presented for Schumann’s model only, the other models behave similarly. For comparison, we plot the correlation C against the normalized y coordinate, y^+ . To save space, we show mostly results for $Re = 4000$ and comment on the results for $Re = 2800$, if necessary.

Schumann’s Model. Schumann’s model for the xy component of τ_w reads $\tau_{w,xy} = \alpha + \beta u + \epsilon$ with $\alpha = 0$ and $\beta = 1$. This case will be referred to as (S1). Allowing for a variable slope $\beta(Y)$ and variable $\alpha(Y)$ yields two linear generalizations, (S2) and (S3), respectively. The nonparametric model (S4) reads $\tau_{w,xy} = f_{u,S}(u) + \epsilon$. For comparison of the linear models, it is convenient to use the modeling error $D_\epsilon = \|\epsilon\|$. This is plotted in Fig. 1a, and the corresponding correlation is plotted in Fig. 1b. The main findings are: for $y^+ \lesssim 20$ the error increases similarly for all models. For $y^+ > 20$, the error of the original model (S1, circles) increases further linearly. For (S2)-

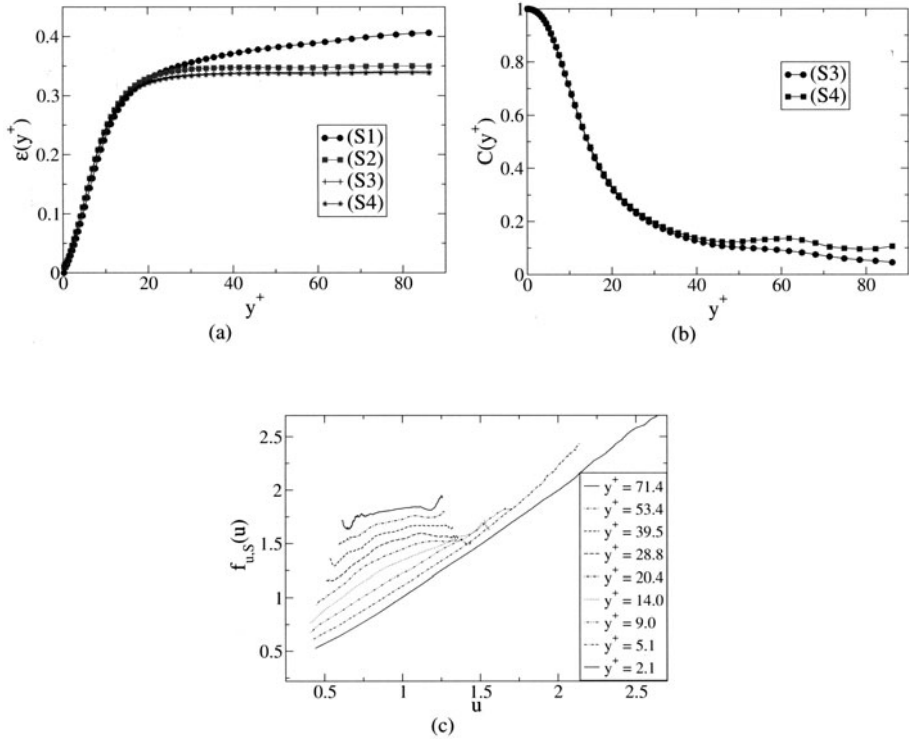


Figure 1. Error estimates (a) and correlations (b) for LSE and NLSE variants of Schumann's model, and (c) a plot of the optimal functions for several values of y^+ (an offset is added to separate the curves).

(S4) the curves settle at values between 0.333 and 0.342. Now, one might be tempted to conclude that a linear model suffices and nonlinear modeling should be discarded.

However, the nonparametric function $f_{u,S}$ shows nonlinearities, see Fig. 1c, where y^+ increases from bottom to top. For small y^+ the function is basically linear, for larger distances curvature occurs, indicating nonlinear behavior. For very large distances, correlation between the wall and the velocity field is lost and $f_{u,S} \simeq \text{const.}$ Qualitatively, there is no difference between $Re = 2800$ and 4000.

Piomelli's Model. The nonparametric Piomelli model is given by Eq. (2). The regression now has to find the optimal function *and* the optimal delay δ . This is achieved by running the regression for the possible values of δ and identify the maximum correlation among those. In Fig. 2 one recognizes that

the correlation is higher than for Schumann's model. The delay increases approximately linearly. Additionally, a brief comparison of $Re = 2800$ and $Re = 4000$ is given. Except for $20 \lesssim y^+ \lesssim 50$ the curves coincide. For the delay δ , saturation is reached earlier for $Re = 2800$. The resulting optimal functions resemble a lot the results for $f_{u,v}$ and $f_{u,g}$ and we refer to the discussion below.

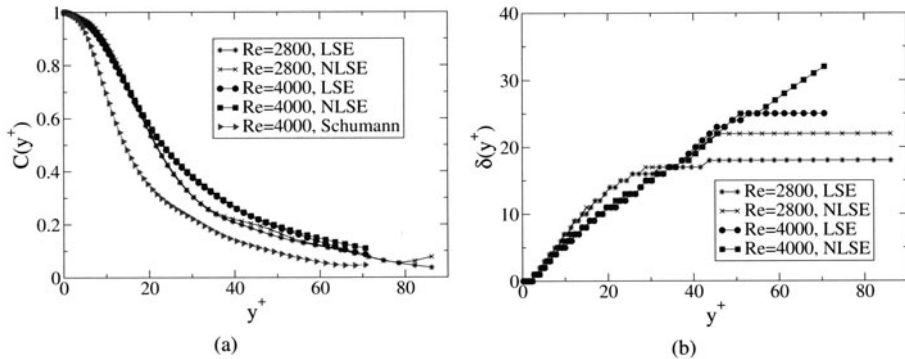


Figure 2. a) Correlation function for Piomelli's model; b) corresponding optimal delay. One observes a difference between $Re = 2800$ and $Re = 4000$ for $20 < y^+ < 50$. LSE and NLSE yield almost the same results.

Ejection and Gradient Model. The corresponding models are given by eqs. (3) and (4). Due to the additional terms we show $C_0 = C(\tau_w, f_u + f_v)$, $C_1 = C(f_u, \tau_w - f_v)$, $C_2 = C(f_v, \tau_w - f_u)$, and $C_3 = C(fg, \tau_w - f_u - f_v)$ for ejection and gradient model, respectively (see Eq. (6)). These correlations are plotted in Fig. 3a and b, respectively. The additional wall normal velocity function $f_{v,e/g}$ is unimportant close to the wall, gains importance until a maximum at $y^+ \simeq 18$ to become unimportant again for larger distances. This is confirmed by the gradient model, where one finds additionally and surprisingly an important contribution of the pressure gradient close to the wall. The inlets show the space delay (Fig. 3a) and a magnification of the region $y^+ < 10$ (Fig. 3b). In the latter case a raise of the correlation and thus better modeling occurs visibly. A plot of the optimal functions for the gradient model provides further insight.

For f_u (Fig. 4a) one observes close to the wall linear behavior, farther away curves are convex, for large distance a constant is found. This holds for the models (2)-(4). During this process the slope decreases constantly, indicating the progressing decorrelation of the wall shear stress and the velocity. For f_v (Fig. 4b) one finds a function which decreases roughly linearly for

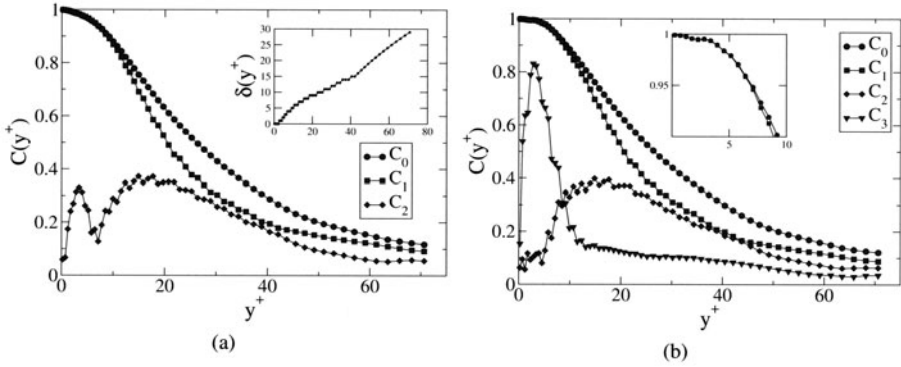


Figure 3. Correlations for ejection (a) and gradient (b) model correlation. The insets show the optimal delay (a) and a magnification for $y^+ < 10$ (b). The main part of the correlation, C_0 , is due to the streamwise velocity component in f_u (C_1). In some range $20 < y^+ < 50$ the modeling error is lowered by the wall-normal velocity component. For the gradient model, close to the wall the pressure gradient is highly correlated.

$v < v_c \simeq -0.032$ and is constant for $v > v_c$. Consequently, sweeps are more important for the dynamics of the near-wall flow and the model's name is misleading. A linear regression is unable to find these details. With increasing y^+ decorrelation sets in again and the function tends to a constant. The function of the streamwise pressure gradient (Fig. 4c) is only important in a range $y^+ < 10$. In this case as well, a highly nonlinear optimal function is found, antisymmetric about zero. One can expect that this function and related ones become important in the case of separation.

A short discussion of the results concerning $\tau_{w,zy}$: one does not find a contribution of \bar{v} , \bar{u} , or $\bar{\partial_z p}$, rather the spanwise velocity \bar{w} is the only important one. The function is antisymmetric and a fit yields approximately a polynomial of 5th order. We did not go into more detail yet and delay deeper investigations for a case study with filtering.

A Posteriori Analysis: First Results. For use in LES predictions we fit the nonparametric functions for the gradient model piecewise with analytical functions. The first tests were done with the first grid point at $y^+ = 5.8$, using the same x and z resolution as for DNS and the Smagorinsky model. Results for $\langle u(Y) \rangle$, $u_{rms}(Y)$, $v_{rms}(Y)$, and $w_{rms}(Y)$ are displayed in Fig. 5a, b, and c, respectively. The average streamwise velocity agrees better with the DNS prediction than Schumann's model in the log layer, only the first point is slightly overpredicted (Fig. 5a). For u_{rms} , we find a good coincidence with DNS and fully resolved LES in the bulk region and close to the wall; in between underprediction of the peak value is observed (Fig. 5b). The reason for these effects

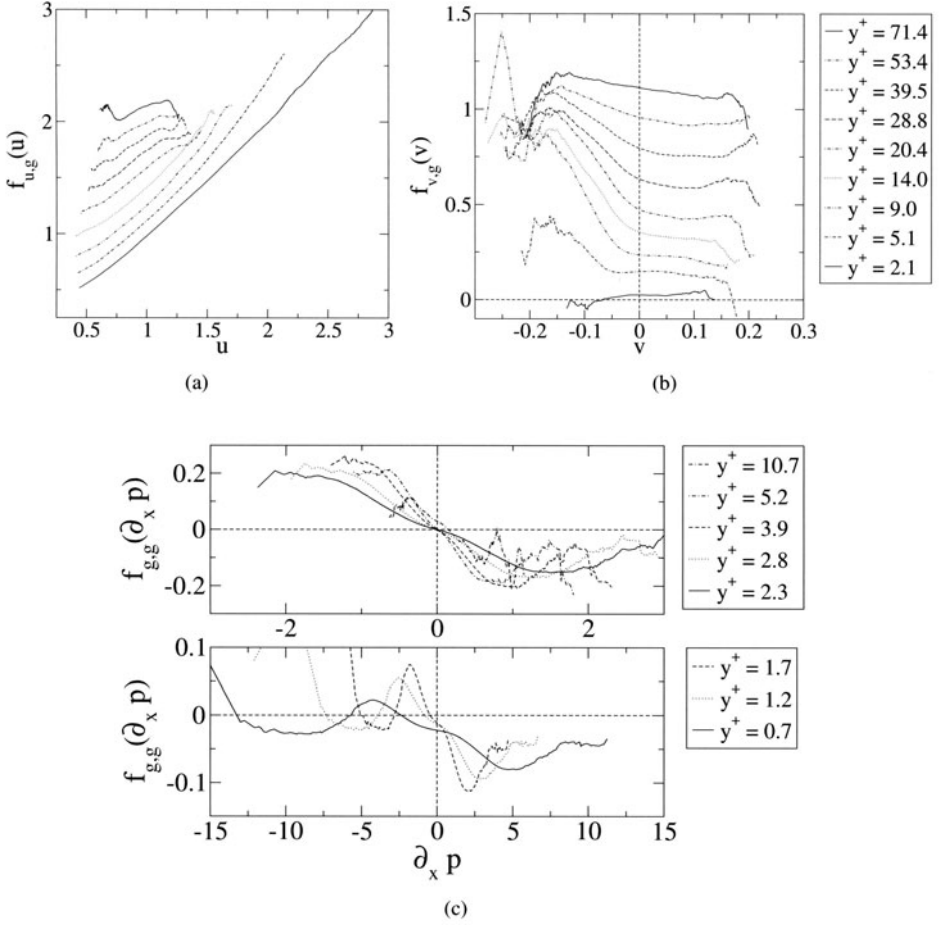


Figure 4. Optimal functions for the gradient model: (a) $f_{u,g}$ (b) $f_{v,g}$, and (c) $f_{g,g}$ ($Re=4000$).

is an underestimation of the velocity gradient $\partial \bar{u} / \partial y$ by the gradient model in the LES prediction leading to a reduced turbulence production in this near-wall region. For v_{rms} and w_{rms} (Fig. 5c), our results are substantially better than for the corresponding Schumann model in the whole channel region.

5. Conclusions

A priori analysis with NLSE yields clearly higher correlations for nonlinear and nonparametric modeling. For the implementation of models, one is, however, faced with the problem to find the correct asymptotics of generalized

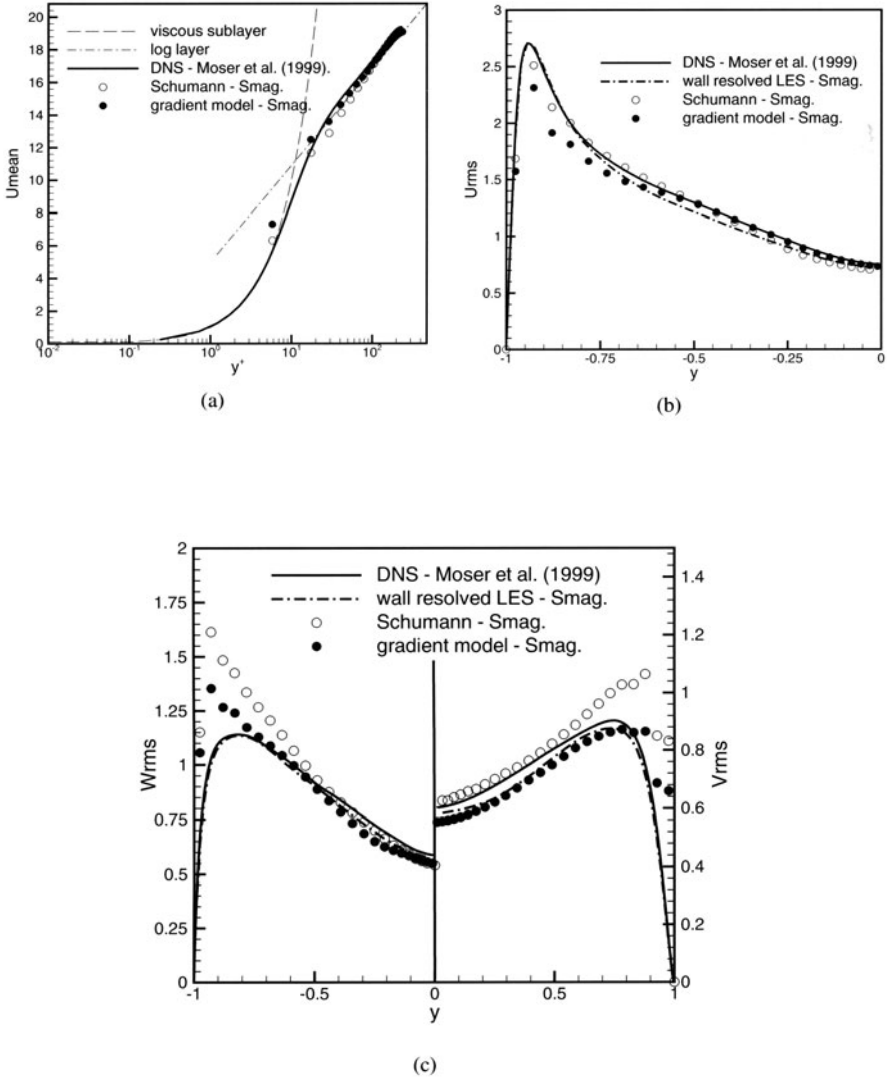


Figure 5. First results on a posteriori LES for $\langle u(Y) \rangle$ (a), $u_{rms}(Y)$ (b), $v_{rms}(Y)$, and $w_{rms}(Y)$ (c), DNS data by Moser et al. (1999).

functions. The first results of implementations let us hope that for more detailed investigations, including correct filtering and possibly larger data sets, better results are obtained. We think, that the true strength of the method will be the more correct modeling of wall dynamics in separated flows.

Acknowledgments

This work is supported by the *Deutsche Forschungsgemeinschaft* under contract numbers BR 1847/3 and PI 220/7.

References

- Abel, M., Stojković, D., and Breuer, M. (2003). Nonlinear stochastic estimation of wall functions for LES. submitted to *Phys. Fluids*.
- Adrian, R. J., Jones, B. G., Chung, M. K., Hassan, Y., Nithianandan, C. K., and Tung, A. (1989). Approximation of turbulent conditional averages by stochastic estimation. *Phys. Fluids A*, 1:992.
- Breuer, M. (1998). Large eddy simulation of the sub-critical flow past a circular cylinder: Numerical and modeling aspects. *Int. J. for Numerical Methods in Fluids*, 28:1281–1302.
- Hastie, T.J. and Tibshirani, R.J. (1990). *Generalized Additive Models*. Chapman Hall, London.
- Honerkamp, J. (1994). *Stochastic dynamical systems*. VCH, New York.
- Moser, R.D., Kim, J., Mansour, N.N. (1999) Direct numerical simulation of turbulent channel flow up to $Re_\tau=590$. *Phys. of Fluids A*, 11(4):943–945
- Langford, J. and Moser, R. D. (1999). Optimal LES formulations for isotropic turbulence. *J. Fluid Mech.*, 398:321–346.
- Moin, P. (2002). Advances in large eddy simulation methodology for complex flows. *Int. J. Heat Fluid Flow*, 23:710–720.
- Nichoud, F., Baggett, J. S., Moin, P., and Cabot, W. (2001). Large eddy simulation wall-modeling based on suboptimal control theory and linear stochastic estimation. *Phys. Fluids*, 13(10):2968–2984.
- Piomelli, U. and Balaras, E. (2002). Wall-layer models for large eddy simulations. *Annu. Rev. of Fluid Mech.*, 34:349–374.

POD OF THE AUTONOMOUS NEAR-WALL REGION IN A MINIMAL CHANNEL FLOW

D. Desmidts¹, O. Debligny¹, B. Knaepen², D. Carati¹

¹*Université Libre de Bruxelles, Statistical and Plasma Physics,
Bld du Triomphe, Campus Plaine - CP 231, B-1050 Bruxelles, Belgium.*

²*Center for Turbulence Research, Stanford University/NASA Ames Research Center,
488 Escondido, Building 500/500A, Stanford University, 94305-3035.*

d-desmidt@ulb.ac.be, odeblign@ulb.ac.be, bknaepen@stanford.edu, dcarati@ulb.ac.be

Abstract We propose to examine the structure and the dynamics of the empirical eigenfunctions of the autonomous near-wall region in a turbulent minimal channel flow. This simplified and artificial situation consists of a severe restriction of the interactions between the outer flow and the structures of the viscous and buffer layers so that it is possible to maintain turbulence in the near-wall region without any input from the outer flow. This is achieved in a DNS of a pressure-gradient driven turbulent channel flow for a minimal flow unit by damping artificially fluctuations in the outer flow while the near-wall region survives indefinitely. The use of empirical eigenfunctions (determined by the Karhunen-Loève procedure or Proper Orthogonal Decomposition) reveals being an adequate tool for analysing the low-dimensional dynamics of the flow.

Keywords: Coherent structures, near-wall turbulence, POD

1. INTRODUCTION

Wall bounded turbulence and, in particular, the coherent structures in the near-wall region has been discussed extensively in the literature (see for instance Panton [1]). The fundamental physics of wall bounded turbulence is conveniently studied through channel flow, i.e., flow between two parallel plates and driven by a uniform pressure gradient. The simplicity of the channel flow geometry allows for DNS at low and moderate Reynolds numbers which provide an abundance of accurate flow data.

The investigation of the mechanisms that produce wall bounded turbulence can be helped by the identification of these coherent patterns. For instance,

the knowledge of the organised structures is often considered as a major prerequisite for efficient control of near-wall turbulence. In the last few decades, transport mechanism of wall turbulence has been examined in detail. It has been found that the dominant structures of the near-wall region are the stream-wise velocity streaks and the quasi-streamwise vortices. Coherent structures in the near-wall region are observed to burst, transferring energy from the large to the small scales and producing turbulent fluctuations. The bursting process is responsible for the production of most of the turbulent kinetic energy in turbulent boundary layer.

For a long time, the description of coherent structures has been limited to a statistical level in experimental and DNS study of turbulence. Jiménez & Moin [2] introduced the minimal flow unit as a tool for studying near-wall turbulent flow. Minimal flow unit corresponds to the smallest such computational box in which turbulence may be sustained. Accordingly, reduced dynamical models based on this approach have been formulated to examine the dynamically elementary processes of turbulent generation in the near-wall region. It was found that turbulence is sustained not by a random process but by a quasi-cyclic process passing quiescent and activated periods in turn. This so-called self-sustaining process (SSP) seems to reproduce most of the features of near-wall turbulence (see Waleffe [3]).

More recently, traveling-wave solutions (TWS) in minimal channel flow were identified by Waleffe [4] and Toh & Itano [5], suggesting a dynamical reformulation of the bursting process, that is, turbulent generation in the near-wall region. Jimenez & Pinelli [6] showed, by means of numerical experiments which mask the influence of the outer flow, that this generation cycle is autonomous, in the sense that it can run by itself without any input from the exterior. Moreover, the autonomous region is able to run on a single copy of the fundamental TWS solution in a minimal channel.

In the present work, the unbiased statistical analysis method, Proper Orthogonal Decomposition (POD) (see Lumley [7]) is applied to a set of datafields extracted from a DNS of a minimal autonomous-wall turbulent channel flow in order to investigate the spatiotemporal properties of the velocity field and to extract information on coherent structures in the autonomous near-wall region. Characteristic structures are computed in terms of POD eigenfunctions which can be used to derive reduced dynamical models for the autonomous near-wall region.

2. NUMERICAL METHODS AND RESULTS

2.1 Minimal channel flow simulation

We consider in this work turbulence in a minimal channel flow, i.e. the narrowest channel for fixed length in which turbulence is maintained on both walls.

The numerical method used in the present study is the same as that of Jiménez & Pinelli [6]. A pseudo-spectral method with Fourier series is employed in the streamwise (x) and spanwise (z) directions, while a Chebyshev polynomial expansion is used in the normal direction (y). A third-order Runge-Kutta scheme and a second-order Crank-Nicholson scheme are used for the discretization of the nonlinear terms and the viscous terms, respectively.

The Reynolds number $Re_\tau = u_\tau h/\nu$ is fixed to 180 and the flow rate is kept constant. Hereafter, u , v , and w denote the velocity components in the x -, y -, and z -directions respectively. Superscript $(+)$ represents quantities non-dimensionalized with the friction velocity $u_\tau = \sqrt{\nu \partial U / \partial y}$ and the kinematical viscosity ν . Here, U denotes the mean velocity. In the case of the autonomous wall region simulation, the right-hand sides of the evolution equations are multiplied at each time step by a damping filter

$$\begin{aligned} F(y) &= 1 & \text{if } y \leq \delta_1 \\ F(y) &= F_0 < 1 & \text{if } y \geq \delta_2. \end{aligned}$$

with the two limits connected smoothly by a cubic spline. In all of our experiments $\delta_2 = 1.5 \delta_1$. The value $F_0 = 0.95$ produces a very effective damping of vorticity fluctuations until midway between δ_1 and δ_2 . For our simulations, we chose $\delta_1^+ = 80$. These values have been chosen in accordance with Jimenez & Pinelli's [6] results. Other values and alternative damping techniques will be explored in further studies.

2.2 Turbulence statistics

Unfiltered channel. Using the methods defined here above, we have simulated turbulence in a minimal channel for a $32 \times 65 \times 32$ grid under a constant mass flux condition for a time of approximately $30 h/u_\tau$ or $t^+ = 4000$. At this Reynolds number and box size, we find fully developed turbulent activity on both walls. At a lower bulk Reynolds number or box size, Jiménez & Moin [2] find turbulent activity on only one wall, which switches in an intermittent fashion from one wall to the other. We note that the turbulent activity on one wall tended to dominate over the other through some portions of the simulation, but this effect did not cause a noticeable asymmetry in the mean velocity profile (Fig 1a) or any other statistics that we examined.

Filtered channel. In the case of the filtered channel, the volumetric flux is adjusted so that its Reynolds number would have been equal to the $Re_\tau = 180$ of the undamped minimal channel. Because there are no Reynolds stresses in the region in which the filter is active, the mean velocity profile is there parabolic (Fig 1a), sequestering much of the total mass flux, and the flow stabilizes, after a long transient, to a relatively low final Reynolds number closer

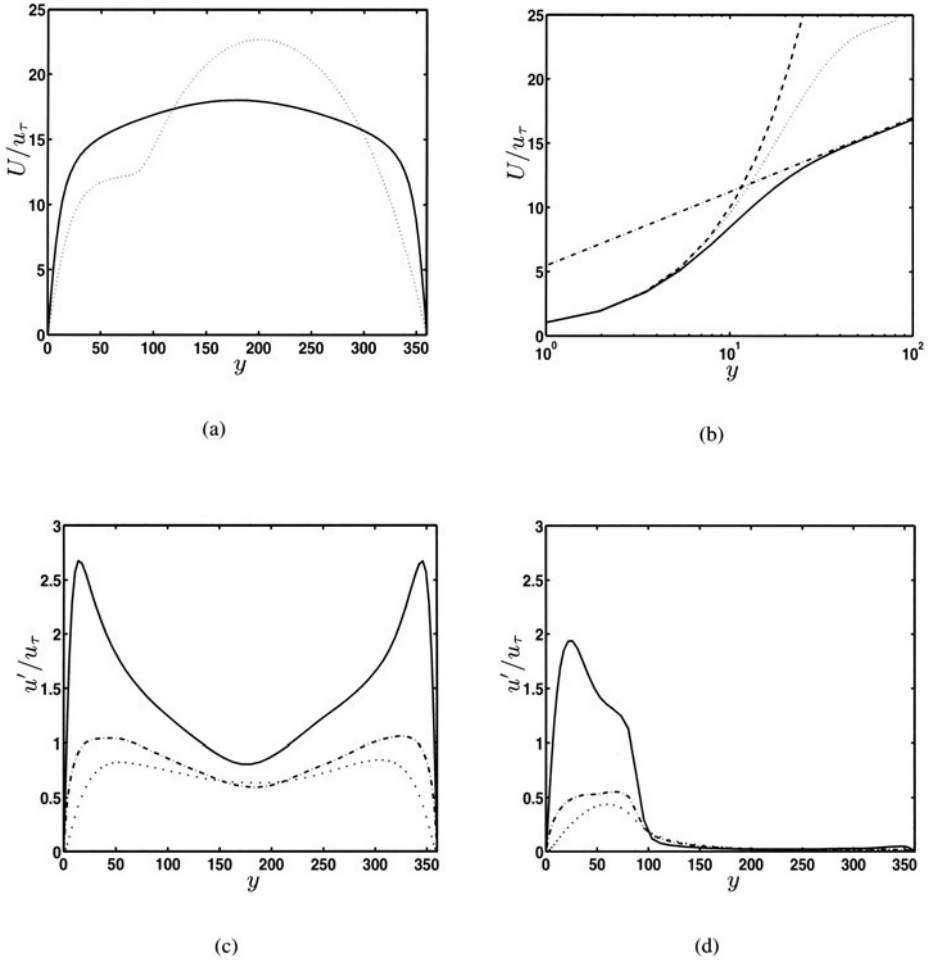


Figure 1. (a) Mean streamwise velocity. Solid line: unfiltered channel, dotted line: filtered channel. (b) Same as (a) in logarithmic scale. Dashed line: $U/u_\tau = y^+$, dashdotted line: $U/u_\tau = 2.5 \log y^+ + 5.5$. (c) RMS velocity fluctuations, unfiltered case. Solid line: u'^{rms}/u_τ , dashdotted line: v'^{rms}/u_τ , small dotted line: w'^{rms}/u_τ . (d) Same as (c) for the filtered case

to $Re_\tau = 120$. Since no turbulent flow extends to the far wall, the relevant turbulent Reynolds number is the one based on the filter height of the damping function $\delta_1^+ = u_\tau \delta_1 / \nu$. The Reynolds number based on the filter height is $Re_\tau = 100$ and all the fluctuations are effectively damped above $y^+ = 80$. We observe that the value of the bulk Reynolds number corresponding to the $Re_\tau = 180$ calculation falls clearly in the fully developed range where a log-layer of universal character is observed in the velocity profile results shown in 1(b). For the filtered case, the mean velocity profile in Figure 1(a) shows a plateau which can be interpreted as an abortive logarithmic layer.

2.3 Karhunen-Loève eigenfunctions

We use the Karhunen-Loève procedure to produce an optimal basis set which best represents the turbulent activity of the minimal channel flow. The ideas stem from Lumley's [7] suggestion of decomposing the flow into a sum of eigenfunctions ϕ_i of the two-point correlation tensor. In homogeneous directions, POD eigenmodes are simply Fourier modes. In the wall-normal direction and in Fourier space, the eigenfunctions ϕ^n associated with the eigenvalue λ^n are solutions of

$$\int \langle \hat{u}_{\mathbf{k}}^i(y) \hat{u}_{\mathbf{k}}^{*j}(y') \rangle \phi_{\mathbf{k}}^{nj}(y') dy' = \lambda_{\mathbf{k}}^n \phi_{\mathbf{k}}^{ni}(y), \quad (1)$$

where $\hat{u}_{\mathbf{k}}^i(y, t)$ and $\langle \hat{u}_{\mathbf{k}}^i(y, t) \hat{u}_{\mathbf{k}}^{*j}(y', t) \rangle$ represent the Fourier transform in the homogeneous directions of respectively the velocity field and the spatial autocorrelation tensor at zero time lag $R_{ij}(x - x', y, z - z')$ and $\langle \rangle$ denotes an ensemble average. Let $\mathbf{k} = (k_1, k_3)$. The velocity field is then decomposed as follows :

$$\hat{u}_{k_1, k_3}^i(y, t) = \sum_{k_1, k_3, n} a_{k_1, k_3}^n(t) \phi_{k_1, k_3}^{ni}(y). \quad (2)$$

We chose to normalize the eigenfunction such that

$$\int_{domain} \phi_{k_1, k_3}^{ni}(y) \phi_{k_1, k_3}^{*nj}(y) dy = 1 \quad (3)$$

so that, by definition (2) of the eigenfunction,

$$\langle a_{k_1, k_3}^n(t) a_{k_1, k_3}^{*n}(t) \rangle = \lambda_{k_1, k_3}^n. \quad (4)$$

represents the energy in each KL mode. Consequently, the eigenfunctions can be sorted according to their contribution to the turbulent kinetic energy.

2.4 Energy spectra

In this paragraph we solve equation (1). Our procedure is very similar to Moin & Moser's [8] who applied the POD to the simulation of a fully developed

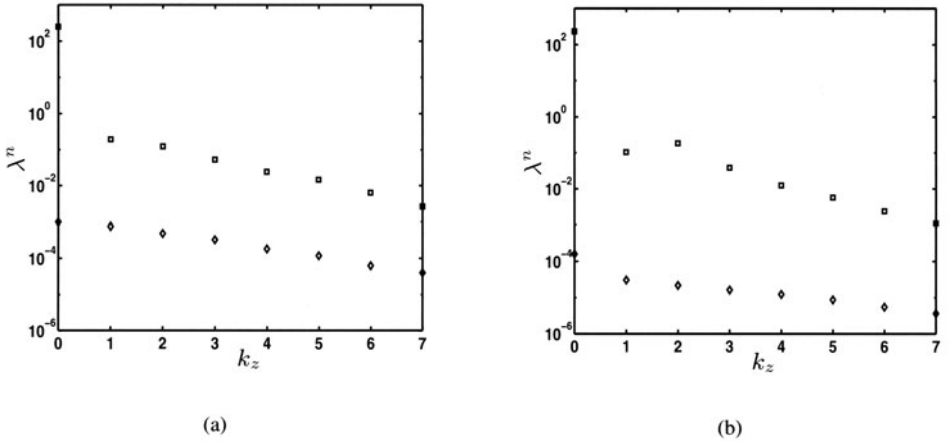


Figure 2. Energy spectra for the first two eigenmodes $n = 1, 2$ for $k_x = 0$. (a) Unfiltered channel. (b) Filtered channel

turbulent channel flow. To compute the kernel, i.e the Fourier transform of the autocorrelation tensor, we used an ensemble average over velocity fields taken at sufficiently large time intervals to be uncorrelated. The database consists of 3000 time samples for the first case, and 4000 time samples for the second case. Figure 2 displays the energy spectra for the first two eigenmodes $n = 1, 2$ at $k_x = 0$ for both cases. We did not subtract the mean flow prior to the Karhunen-Loève expansion. Hence a strong first eigenfunction appears in the mode $k_x = 0, k_z = 0$. Another conclusion that can be drawn from these results is that the effect of the filter is to reduce strongly the contribution from modes $n > 1$. This result supports the expectation that the autonomous wall-region has less structural complexity making the fundamental turbulent mechanisms easier to identify. We also note that the eigenvalue spectrum for $n = 1$ is not very much affected by the filter, except that the mode $k_x = 0, k_z = 2$ now corresponds to a peak. This might be due to the fact that pairs of streamwise rolls are less perturbed in the autonomous case.

2.5 Eigenfunctions

In Figure 3, we show the y -dependence of the first eigenfunctions for $k_x = 0, k_z = 0, n = 1$ which corresponds nearly to the mean profile (Fig. 3a and 3b), and for $k_x = 0, k_z = 2, n = 1$ (Fig. 3c and d). We have chosen to present this particular mode since it is the most energetic one for $k_x = 0$ in the filtered case.

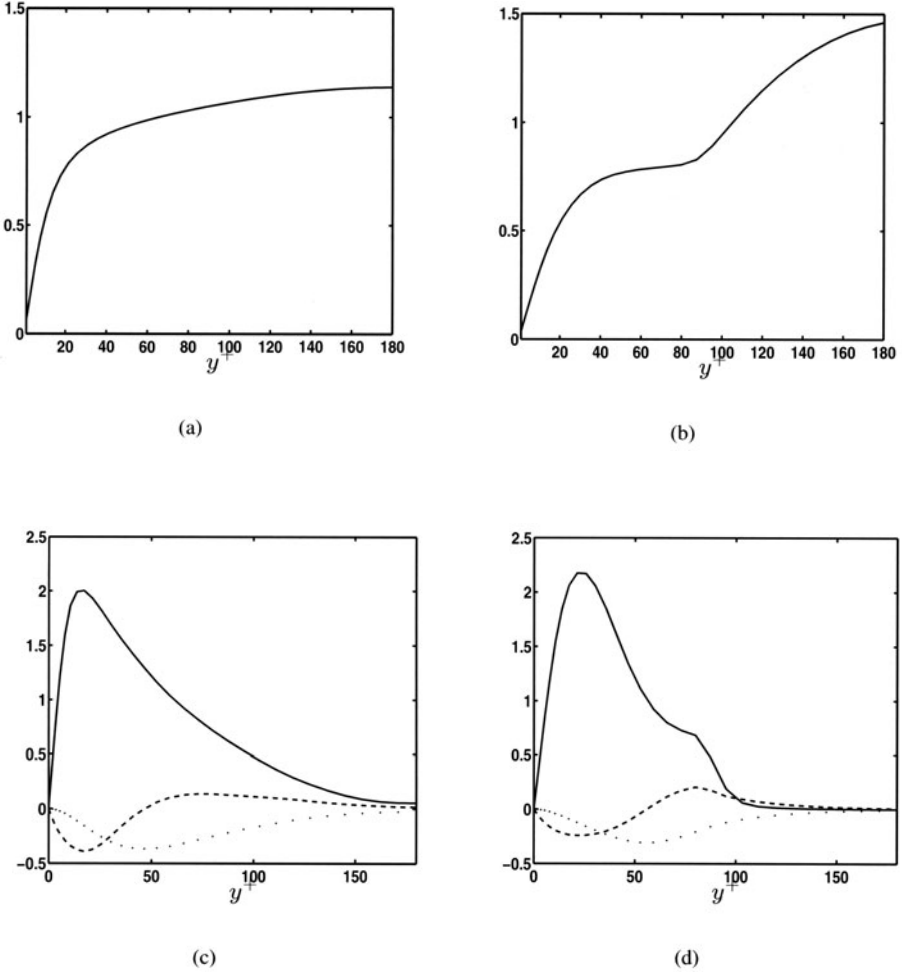


Figure 3. Spatial structure of the first eigenfunctions. (a) Unfiltered minimal channel. Solid line: $\phi_{k_x=0, k_z=0, n=1}^1$. The $\phi_{k_x=0, k_z=0, n=1}^2$ and $\phi_{k_x=0, k_z=0, n=1}^3$ modes are identically zero. (b) Same as (a) for the filtered case. (c) Unfiltered minimal channel. Solid line: $\phi_{k_x=0, k_z=2, n=1}^1$, dashed dotted line: $\phi_{k_x=0, k_z=2, n=1}^2$, small dotted line: $\phi_{k_x=0, k_z=2, n=1}^3$. (d) Same as (c) for the filtered case.

We note for this latter the appearance of a kink in the streamwise component of the eigenfunction ϕ_1 just above $y^+ = 80$, which corresponds to the filter height δ_1 . This kink is an artifact of the damping mask and is due to the reconnection of the vortex lines after they are truncated by the damping. A less pronounced but still significant kink in the vertical component, ϕ_2 , is also evident in Figure

3(b), consistent with the form of the *rms* intensity of the vertical velocity component shown in Figure 1. The most significant feature to observe for this latter is that, close to the wall, the most energetic empirical eigenfunctions are almost unaffected by the filtering, showing that they correspond to a part of dynamics that is not influenced by the outer region.

3. CONCLUSIONS

The Proper Orthogonal Decomposition has been performed for the classical and autonomous near-wall region in a minimal channel. Differences between the two flows have been described and quantified. For the filter height chosen ($\delta_1^+ = 80$), most kinematical features of the empirical eigenfunction are almost the same than in the unfiltered case although some discrepancies appear in the eigenvalue spectrum. This work will be continued in order to explore the possibility of using a filter that decouples even better the inner and outer region in order to construct a suitable empirical eigenfunction basis on which to project the low-dimensional dynamics of the autonomous wall region.

References

- Panton, R. L. (1997). Self-sustaining mechanisms of wall turbulence. *Computational Mechanics Publications*.
- Jiménez, J. & P. Moin, P. (1991). The minimal flow unit in near-wall turbulence. *J. Fluid Mech.*,225:213-240.
- Waleffe, F. (1997). On a self-sustaining process in shear flows. *Phys. Fluids.*,9:883-900.
- Toh, S. & Itano, T. (1999). Low-dimensional dynamics embedded in a plane Poiseuille flow turbulence. Traveling-wave solution is a saddle point? *Preprint physics/9905012*.
- Waleffe, F. (1998). Three-dimensional coherent states in plane shear flows. *Phys. Rev. Letters.*,81:4140-4143.
- Jiménez, J. & Pinelli, A. (1999). The autonomous cycle of near wall turbulence. *J. Fluid Mech.*,389:335-359.
- Lumley, J.L. (1971). Stochastic tools in turbulence. *Academic Press, New York*.
- Moin, P. & Moser, R. (1989). Characteristics-eddy decomposition of turbulence in a channel. *J. Fluid Mech.*,200:471-509.

ON THE DIFFICULTIES IN RESOLVING THE VISCOUS SUBLAYER IN WALL-BOUNDED TURBULENCE

Franz Durst and Kamen N. Beronov

*Institute of Fluid Mechanics, University Erlangen–Nuremberg
Cauerstr. 4, D-91058 Erlangen, Germany*

durst@lstm.uni-erlangen.de

Abstract Comparison of one-point statistics of turbulent velocities in the near-wall region $y^+ < 10$ from DNS of turbulent plane channel flows with corresponding data from experiments on wall-bounded turbulence show that DNS data are plagued by an overprediction of turbulent intensity and intermittency. This is the result of a spurious non-analyticity of logarithmic type, which arises from the violation by numerical approximations of a fine cancellation of high-order terms in y^+ in the equation for the wall-normal velocity component v . The arising non-analytic additive error propagates into all hydrodynamic fields, but affects most strongly v which vanishes at the wall faster than the other velocity components. Its normalized moments like the flatness factor F_v are dominated by the error, with dramatic effects. For example, overprediction of F_v is larger in DNS with higher resolution. This paradoxical observation is explained by a simple model accounting for the high intermittency and for the log-errors of v near the wall.

Keywords: wall-bounded turbulence, DNS, non-analyticity, velocity flatness factor

1. Introduction

Turbulence near smooth walls depends strongly on distance from the wall. In the viscous sublayer, the one closest to the wall, viscous diffusion and dissipation dominate the momentum and energy balance. It is often referred to as “laminar layer,” a misnomer because turbulence is actually generated at the wall and most of the basic turbulence statistics, when adequately normalized, have their extrema in it. The turbulence structure in that layer has a crucial influence on the transport processes in wall-bounded turbulence.

Numerical and experimental approaches play complementary roles in the investigation of wall-bounded turbulence and there are sufficiently wide parameter ranges over which quantitative comparisons are meaningful. A particular comparison in Section 2 focuses on the near-wall region $y^+ < 10$, highlight-

ing cases in which very good agreement between direct numerical simulation (DNS) and experiments is expected, but the qualitative behavior of numerical data is instead conspicuous and consistently different from that of experimental data. Inspection shows that this is related to a logarithmic non-analyticity of DNS velocity data in the viscous sublayer. This can either reflect a genuine phenomenon, or more probably, a systematic type of numerical error rooted in some peculiarity of the underlying dynamics.

To clarify the source of non-analyticity, a mathematical analysis of the incompressible Navier–Stokes equations is undertaken in Section 3. It shows that the commonly assumed scaling of turbulent velocities with vanishing distance y from the wall must be slightly modified, in order to obtain a consistent system of equations for the lowest-order terms in y . The corresponding equations for the wall-normal velocity v and the pressure are formally linear, inhomogeneous, with a singular left-hand-side operator. The v -equation contains a singular right-hand-side term, which cannot vanish identically in a typical simulation. But the solution of the whole Navier–Stokes system can only be analytic at the wall if it vanishes exactly. This term leads to $y^2 \log(y)$ errors in v which propagate into all other hydrodynamic fields, but are able to dominate only the v component. Feed-back into the v -equation generates $y^2 \log(y)^n$ errors in v for integer $n > 1$.

To demonstrate how these log-errors contaminate DNS turbulence statistics, a simple model for the computed flatness factor profiles $F_v(y)$ is proposed in Section 4. It accounts both for the strong intermittency of v in the viscous sublayer and for the spurious $\log(y)^n$ terms dominating v at leading order in y . The model predicts trends found in all DNS databases: One is the $F_v \sim \log(y)$ growth throughout the viscous sublayer, except for a saturation very close to the wall, $y^+ \ll 1$. Another is the paradoxical observation that DNS with higher spatial resolution produce a larger overprediction of F_v near the wall.

2. Numerical vs. Laboratory Experiments

With growing Reynolds number Re , the absolute dimensions of the viscous sublayer become extremely small, which makes that region difficult to measure experimentally. Nevertheless, state-of-the-art measurements using laser-Doppler anemometry (LDA) are able to resolve instantaneous velocity components at distances from the wall as small as $y^+ = 1$. Capturing the instantaneous flow structure, as a means towards understanding the detailed mechanisms of turbulence regeneration near the wall, is easier using spatially and temporally resolved DNS data. The main limitation of DNS is that they can only resolve flows at relatively low Re . Nevertheless, they have penetrated the range of turbulent Re and allowed meaningful investigation of the near-wall region, where approximate Re -independence with growing Re sets in at lower Re as com-

pared to regions farther off the wall. Because of their sufficient resolution, and of the well-documented dominance of viscous forces in the innermost layer of wall-bounded turbulence, a good quality of the DNS data and the establishment of a clear picture of the turbulence structure in that region are assumed. It is shown here that in a sense this is not true.

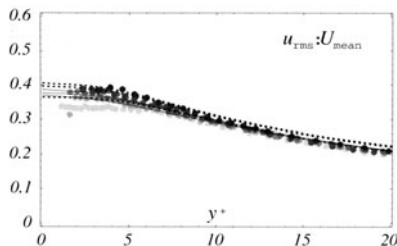


Figure 1. Streamwise turbulent r.m.s. velocity normalized by local mean velocity; lines: DNS with $130 \leq Re_\tau \leq 587$ (cf. Figure 2 for references); circles: LDA measurements (Fischer *et al.*, 2001) at $118 \leq Re_\tau \leq 350$

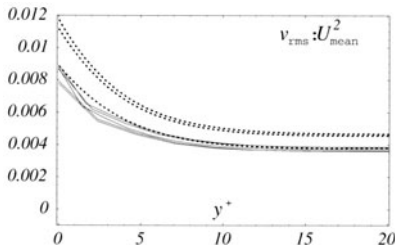


Figure 3. Wall-normal r.m.s. velocity intensity normalized by $U^+(y^+)^2$ where $U^+(y^+)$ is the local mean velocity in wall units. Data and lines as in Figure 2. A scaling $v \sim y^2$ would require convergence to a constant as $y \rightarrow 0$.

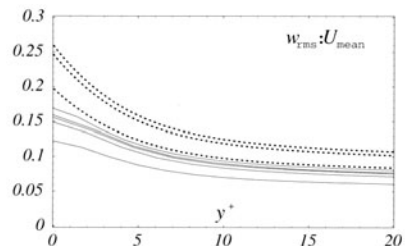


Figure 2. Spanwise r.m.s. velocity normalized by local mean flow; solid lines: $106 \leq Re_\tau \leq 180$ lattice Boltzmann DNS (Lammers *et al.*, 2002); dashed: $178 \leq Re_\tau \leq 587$ pseudospectral (Moser, Kim & Mansour, 1999).

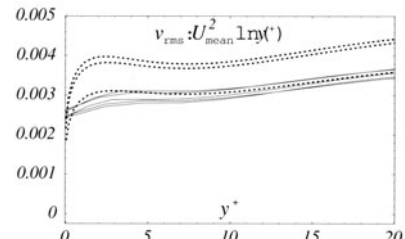


Figure 4. Same as Figure 3 but normalized by $U^+(y^+)^2 \ln(U^+(y^+))$ (here $\ln(\cdot)$ is the natural logarithm). A plateau in the viscous sublayer implies $v \sim y^2 \ln(y)$. Normalizations by $U^+(y^+)^{2+\alpha}$ (small $\alpha > 0$) give no plateau.

The problem of high turbulent velocity intensities. The first kind of one-point statistics, for which a comparison between numerical estimates and laboratory measurements was carried out, is the intensity of turbulent velocity fluctuations. This is done separately for each of the three velocity components; their intensity is the square root of the corresponding diagonal entry in the Reynolds stress tensor. The underlying averaging procedures are the usual ones: time averaging at a fixed location in the flow for LDA measurements and time + spatial averaging (parallel to the channel walls) in DNS. Two DNS databases are compared, obtained by completely different, but well-resolved DNS: a standard Chebyshev–pseudospectral code (Moser, Kim & Mansour, 1999) and a lattice Boltzmann code (Lammers *et al.*, 2002) using the “incompressible” D3Q19 lattice model. The intensities are shown in Figures 1–3 normalized not by a constant characteristic velocity scale (such as the friction velocity u_τ) but using the local mean flow velocity $U(y)$. Since $U^+(y^+) \approx y^+$

in the viscous sublayer, the normalizations correspond to the scalings $u \propto y$, $v \propto y^2$, and $w \propto y$, commonly assumed in the literature. Data lines appear horizontal wherever the data comply with the expected scaling.

First, the very good agreement between DNS and LDA data on the intensity of streamwise fluctuating velocity seen in Fig.1 will be noted. This includes the saturating trend towards increase, with growing Re , of the ratio $\lim_{y \rightarrow 0} u(y)/U(y)$. It may be added here that u is the least intermittent and the dominant in amplitude among the three turbulent velocity components.

Second, the expected nearly horizontal section of plotted data is found for all three components, but in different regions: closest to the wall, inside the viscous sublayer for u , but only outside the viscous sublayer for v (Fig.3) and w (Fig.2). Leading-order y -expansion coefficients which can be deduced from the horizontal sections appear to be consistent: their ratios can be related, using incompressibility, to the aspect ratios of typical intense turbulent structures in the viscous sublayer. Snapshots of normalized turbulent intensities (figures omitted) allow fairly robust estimates of such aspect ratios and show that they remain effectively unchanged throughout the viscous sublayer. The horizontal lines are thus expected to continue all the way to wall in Figs. 2 and 3 and the cusps seen in those graphs must be spurious numerical effects.

Third, the overshoots in DNS data for the v and w intensities reflect a non-analyticity of the underlying numerical solution. As shown for v in Fig.4, this non-analyticity is of logarithmic rather than of power-law type.

The problem of high flatness of wall-normal velocity. An uncertainty about the near-wall behavior of F_v , the flatness factor or kurtosis of the wall-normal turbulent velocity component v , remains an open topic for discussion in the turbulence research community. The reason is that DNS data lead to surprisingly high predicted F_v values, which are not supported by conclusive experimental data. On the other hand, laboratory measurements in the viscous sublayer, where these high values are predicted, is difficult. Systematic investigations require the comparison of independent and well-resolved DNS, preferably by different methods, and measurements by high-precision laboratory methods, such as up-to-date LDA. Profiles of $F_v(y^+)$ obtained by such numerical and laboratory experiments are compared in Fig.5.

Despite the excellent agreement for $y^+ > 12$, a clear qualitative discrepancy is found for $y^+ < 8$. Both kinds of profiles show a growth trend as y^+ falls below $y^+ \approx 20$. But experimental profiles remain bounded, approximately by $F_v \leq 10$, and eventually reverse their trend to decrease at the wall is further approached. Numerical data, on the other hand, exhibit no boundedness and reversal. It appears from Fig. 5 that DNS predictions of $F_v(y)$ grow like $\log(y)$ as y^+ decreases from 7 to 2; this overlaps with the range of logarithmic growth identifiable from Figs. 3 and 4. The rate of growth depends not only on the

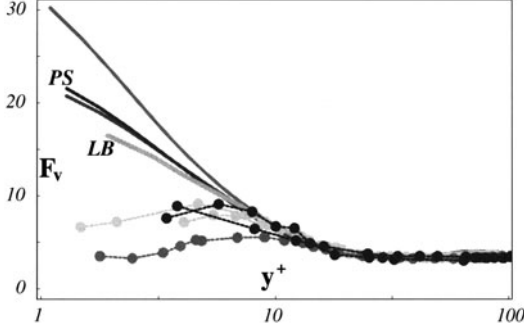


Figure 5. Comparison of flatness factor profiles $F_v(y^+)$ near the wall. Symbols and dashed lines show LDA laboratory measurements; solid lines: numerical data. Laboratory measurements are all from LDA and cover turbulent channel, pipe, and free boundary layer flows, at $180 \leq Re_\tau \leq 830$. DNS at $Re_\tau = 180$ predict substantially different F_v at $y^+ \leq 3$: predictions by a pseudospectral (PS) code lie higher than those by a lattice Boltzmann (LB) code.

Reynolds number, but also on the numerical method and resolution, so the observed effect is clearly a numerical artifact. Assuming that for a given grid step the pseudospectral method has higher precision than the lattice Boltzmann method, higher precision appears to lead to larger F_v overprediction. This surprising trend is further confirmed in Fig. 6 by comparing $F_v(u)$ predictions obtained at two different resolutions by running the same pseudospectral code with all other run parameters being the same.

3. Near-Wall Scaling of Turbulent Velocities

Arguments in the literature concerning the scaling of velocities near the wall rest on the implicit assumption of valid Taylor series at $y = 0$. It is tacitly assumed that, in addition, any well-resolved numerical solution will also be analytic at $y = 0$, with Taylor expansion terms scaling in agreement with the physical solution. These assumptions are not trivial.

Corresponding terms in the Taylor series of individual flow components must balance each other at all orders $O(y^n)$ and in all equations — the three scalar momentum equations, solenoidality as the continuity equation, and a resulting Poisson equation for the pressure. On the basis of observations, it is taken for granted that the mean flow velocity U as well as the streamwise turbulent velocity u scale $\sim y$. This and $u/U \approx \text{const.}$ hold only inside the viscous sublayer (Fig. 1a). It is convenient to factor out the leading-order scaling in y of all four basic fields and consider the resulting $O(1)$ “shape functions”

$$u = y \tilde{u}, \quad v = y^{a+1} \tilde{v}, \quad w = y \tilde{w}, \quad p = y^q \tilde{p}, \quad a, q \geq 0. \quad (1)$$

In wall units, the viscosity $\nu^+ = 1$ and the Navier–Stokes equations read

$$x\text{-momentum:} \quad D_t \tilde{u} = -y^{q-1} \partial_x \tilde{p} + (\partial_y^2 + (2/y) \partial_y - y^a \tilde{v}) \tilde{u}, \quad (2)$$

$$z\text{-momentum:} \quad D_t \tilde{w} = -y^{q-1} \partial_z \tilde{p} + (\partial_y^2 + (2/y) \partial_y - y^a \tilde{v}) \tilde{w}, \quad (3)$$

$$y\text{-momentum:} \quad D_t \tilde{v} = -y^{q-1-a} (q/y + \partial_y) \tilde{p} + \partial_y^2 \tilde{v} \\ + (a+1) (a/y^2 + (2/y) \partial_y - y^a \tilde{v}) \tilde{v}, \quad (4)$$

$$\text{continuity:} \quad 0 = \partial_x \tilde{u} + \partial_z \tilde{w} + y^{a-1} ((a+1) + y \partial_y) \tilde{v}, \quad (5)$$

where $D_t = \partial_t - (\partial_x^2 + \partial_z^2) + y(\tilde{u} \partial_x + y^a \tilde{v} \partial_y + \tilde{w} \partial_z)$. From (5), $a \geq 1$.

The problem with standard scaling. There is no singularity on the right side in (3) if $\partial\tilde{w}/\partial y = 0$ at the wall. But the term $a(a+1)y^{-2}\tilde{v}$ in (3) cannot be eliminated, because $a \geq 1$. The only possible balance for this singular term can be (one of) the two pressure terms in (3). There are two choices for the pressure scaling: If $q = 0$, then only $y^{-a}\partial_y\tilde{p}$ remains; otherwise, $qy^{q-a-1}\tilde{p}$ is the more singular term. The option $q = 0$ leads to the standard scaling found e.g. in (Moser, Kim & Mansour, 1988). It balances possible $O(y^{-1})$ singularities in (2) and (3). But as already mentioned, there are no such singularities if $\partial\tilde{u}/\partial y = \partial\tilde{w}/\partial y = 0$ at the wall. The shape functions are assumed regular, e.g. $\tilde{u}(\mathbf{x}) = \tilde{u}_0(x, z) + y\tilde{u}_1(x, z) + y^2\tilde{u}_2(x, z) + \dots$. The lowest orders in y of the above dynamical equations yield the following relations between Taylor coefficients: $\tilde{u}_1 = \partial_x\tilde{p}_0/2$ (x -momentum), $\tilde{w}_1 = \partial_z\tilde{p}_0/2$ (z -momentum), $\tilde{v}_0 = \tilde{p}_1/2$ and $\tilde{v}_1 = \tilde{p}_2/3$ (y -momentum), $\tilde{v}_0 = (\partial_x\tilde{u}_0 + \partial_z\tilde{w}_0)/2$ (continuity), $\tilde{p}_2 = -(\partial_x^2 + \partial_z^2)\tilde{p}_0/2$ and $\tilde{p}_3 = -(\partial_x^2 + \partial_z^2)\tilde{p}_1/6$ (pressure). These equations are rules to compute the fields appearing on the left-hand sides. The system includes no prescription for the fields \tilde{u}_0 , \tilde{w}_0 , \tilde{p}_0 and \tilde{p}_1 as functions of x, z, t . Three differential equations or boundary data are therefore missing.

Alternative scaling and its implications. The system of equations obtained under the assumption that $q = 0$ is underdetermined. A well-defined system, in which every scalar field is determined at leading order by its own partial differential equation, can be obtained assuming that $q = 1$. This balances both the $O(y^{-2})$ and $O(y^{-1})$ terms in (3) and yields for (3) and the pressure equation

$$(\partial_y^2 + (2/y)\partial_y)\tilde{v} + (\partial_x^2 + \partial_z^2)\tilde{v} = ((2/y)\partial_y + 1/y^2)(\tilde{p} - 2\tilde{v}) - \partial_t\tilde{v} \quad (6)$$

$$(\partial_y^2 + (2/y)\partial_y)\tilde{p} + (\partial_x^2 + \partial_z^2)\tilde{p} = 0 \quad (7)$$

at leading order. The most singular terms in (6) are collected in the expression $y^{-2}(\tilde{p} - 2\tilde{v})$. Their singularities must cancel out: $2\tilde{v} - \tilde{p} = 2y^2\tilde{r}$ where $\tilde{r}(y) = \tilde{r}_0 + y\tilde{r}_1 + \dots$ is regular at the wall. Eliminating \tilde{r} ,

$$\tilde{p} = 2\tilde{v} - (y^2/8)\partial_t\tilde{v} + O(y^3). \quad (8)$$

The numerically most sensitive hydrodynamic variable is \tilde{v} : First, \tilde{v} tends to zero faster than all other three variables as $y \rightarrow 0$ and has negligible magnitude at the numerical grid's y -level closest to the wall. Second, the regularity of the \tilde{v} -solution depends on an exact cancellation involving $y^2\tilde{r} = O(y^4)$. Third, this cancellation takes place only if the pressure scales as assumed whereas in production codes it is $O(1)$ due to *ad hoc* treatment of the pressure boundary condition. Fourth, time discretization algorithms will in general not respect this cancellation. Any of the Navier–Stokes solvers now in use is thus expected to introduce errors destroying the cancellation of singularities on the right in (6). Concerning DNS with periodicity conditions in the x - and z -directions, it is appropriate to Fourier-transform (6) and (7). Let $f(y)$ be the amplitude of any Fourier mode $\hat{v}(t, \mathbf{k}, y)$ of \tilde{v} , and $r(y)$ the amplitude of the corresponding

Fourier transform of the right-hand side of (6), which then yields

$$f''(y) + (2/y) f'(y) - k^2 f(y) = r(y) \quad (9)$$

at leading order in y , where $k = \|k\|$ is the wavenumber. The error initially occurring in $(\tilde{p} - 2\tilde{v})$ is $O(1)$, corresponding to $r \sim y^2$. For $r = \ln(y)^n / y^2$ with $n \geq 0$ integer and $\ln(y)$ the natural logarithm of y , (9) has analytic solutions:

$$\begin{aligned} r(y) = 1/y^2 &\rightarrow f(y) = \eta_0(k, y) \ln(y), \\ r(y) = \ln(y)/y^2 &\rightarrow f(y) = \eta_1(k, y) \ln(y)^2/2, \end{aligned}$$

and so on, where $\lim_{y \rightarrow 0} \eta_n(k, y) = O(1)$ is a function “slower” than $\log(y)$. For $k = 0$ in particular, $\eta_0 = 1$ and $\eta_1 = 1 + 2/\log(1/y)$. For $k \neq 0$ but $n = 0$, $2ky f(y) = (e^{ky} \text{Ei}(-ky) - e^{-ky} \text{Ei}(ky))$, where $\text{Ei}(y) = -\int_{-y}^{\infty} \zeta^{-1} e^{-\zeta} d\zeta$. As soon as an analytic ($n = 0$) error in $(\tilde{p} - 2\tilde{v})$ is introduced by any slightest numerical imprecision, it generates a nonanalytic ($n = 1$) error in \tilde{v} . This error propagates into the pressure and the other velocity components. It feeds back into \tilde{v} over the continuum equation and gives a $\sim \ln(y)$ error in $(\tilde{p} - 2\tilde{v})$. By the same kind of feed-back, a hierarchy of $\ln(y)^n$ error terms is generated; it affects all velocity components but dominates the correct solution only for \tilde{v} .

4. Modeling of log-error-dominated flatness profiles

The very strong intermittency of near-wall turbulence has been repeatedly noted (Xu *et.al.*, 1996). It appears concentrated in localized “spots” sweeping along the wall much faster than the local mean flow and creating short but intensive turbulent events that dominate all turbulence statistics. We have found that the spatial structure of these spots in terms of \tilde{u} , \tilde{v} , and \tilde{w} is nearly vertical throughout the viscous sublayer and that velocity intermittency is most strongly pronounced in the v -component. Combining these observations with the conclusion above — that close to the wall numerical errors in the v equation introduce spurious terms of magnitude $\log(y)^n$ relative to the physically correct, analytic solution for v — a qualitative model of the influence of the spurious terms on the numerically predicted $F_v(y)$ can be constructed. The $O(\log(y)^n)$ errors dominate the \tilde{v} -component locally, including the intermittent spots, and thus its one-point centered moments. Since those spots are well separated, their contributions to those moments can be approximated for a rough estimate as independent. Since errors with higher n need time to develop from errors with lower n , individual spots will be dominated by errors with different n , depending on their age. All data in a range $y^+ \gg 1$ where they are reliable suggest $\lim_{y \rightarrow \infty} F_v(y) = 3$, compatible with the nearly Gaussian velocity statistics of homogeneous turbulence there. With this constraint and truncated to $n \leq 4$ terms, our contaminated flatness profile $F_v^e(y)$ model is

$$F_v^e = \frac{3a_0 (a_0 + (a_1\xi)^4 + (a_2\xi)^8 + (a_3\xi)^{12} + (a_4\xi)^{16})}{(a_0 + (a_1\xi)^2 + (a_2\xi)^4 + (a_3\xi)^6 + (a_4\xi)^8)^2} \Big|_{\xi=\log_{10}(y^+/y_\infty)} \quad (10)$$

Smaller $|a_1/a_0|$ indicates a better precision of the numerical solution.

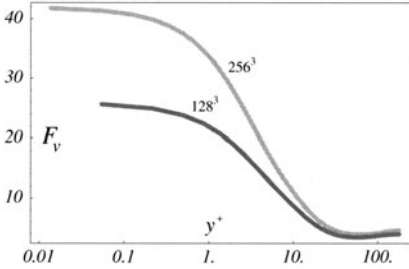


Figure 6. Effect of grid resolution in Chebyshev–pseudospectral DNS of plane channel flow at $Re_\tau = 180$: with all other parameters fixed, 2 times increased grid resolution increases the $F_v(y=0)$ prediction $\sim \sqrt{2}$ times.

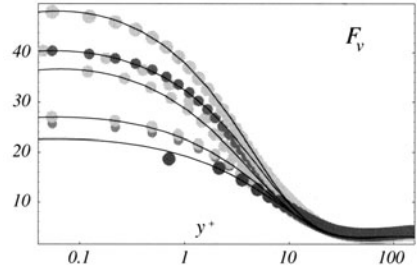


Figure 7. Fits to different DNS data sets (circles) for F_v , using the proposed (10) model form (lines) of $\log(y^+)$ –error dominated $F_v(y^+)$ predictions in the viscous sublayer ($\log_{10}(y^+) < 1$).

Figure 7 shows nearly optimal fits by (10) to DNS data by different numerical methods and codes. The corresponding parameters are quite consistent: $3.0 \leq a_1 \leq 3.2$, $1.73 \leq a_2 \leq 1.84$, $0.45 \leq a_3 \leq 0.50$, $0.49 \leq a_4 \leq 0.52$, $2.04 \leq \log_{10} y_\infty \leq 2.08$, except for $9.5 \leq a_0 \leq 22$. Fits without a_3 or a_4 were unsuccessful at $y^+ < 1$. Higher n 's brought no further improvement. The model suggests that F_v^e is limited in growth as $y \rightarrow 0$. It explains qualitatively the paradoxical observation (Fig. 6) that better precision (larger a_0 for fixed other a_n 's) leads to spurious higher levels of F_v^e at $y^+ \leq 10$.

References

- N.N. Mansour, R. Moser and J. Kim (1988) “Reynolds–stress and dissipation–rate budgets in a turbulent channel flow,” *J. Fluid Mech.* **194** 15–44.
- F. Durst and J. Jovanović (1995) “Investigations of Reynolds–averaged turbulence quantities,” *Proc. R. Soc. Lond. A* **451** 105–20.
- C. Xu, Z. Zhang, J.M.J. d.Tonnder, F.T.M. Nieuwstadt (1996) “Origin of high kurtosis levels in the viscous sublayer. Direct numerical simulation and experiment,” *Phys. Fluids* **8** 1938–44.
- R. Moser, J. Kim, N.N. Mansour (1999) “Direct numerical simulation of turbulent channel flow up to $Re_\tau=590$,” *Phys. Fluids* **11** 943–5, www.tam.uiuc.edu/faculty/moser/channel/
- M. Fischer, J. Jovanović, F. Durst (2001) “Reynolds number effects in the near–wall region of turbulent channel flows,” *Phys. Fluids* **13**(6) 1755–67.
- P. Lammers, K.N. Beronov, G. Brenner, F. Durst (2002) “Direct simulation with the lattice Boltzmann code BEST of developed turbulence in channel flows,” in *High Performance Computing in Science and Engineering, Munich 2002*, S. Wagner, W. Hanke, A. Bode, F. Durst (eds.), Springer.

A PRIORI TESTS OF MODELS FOR THE MEAN AND FOR THE FLUCTUATING WALL SHEAR STRESS IN FLOWS WITH SEPARATION

H.-J. Kaltenbach

Hermann-Föttinger Institut für Strömungsmechanik

Technische Universität Berlin, Sekretariat HF 1

Straße des 17. Juni 135, D-10631 Berlin, Germany

kaltenbach@pi.tu-berlin.de

Abstract Databases from LES of flow over a backward-facing step and flow inside an asymmetric diffuser are used in order to develop and to validate near-wall models for the prediction of the wall shear stress in a separating and reattaching flow.

Keywords: wall model for LES, separated flow, near-wall layer

1. Background and outline of the study

The resolution of all relevant spatial scales in the vicinity of walls is so expensive in LES that high Reynolds number calculations have to use wall models instead of enforcing the no-slip condition at solid walls. Wall modeling in separated and reattaching flows has to consider the fundamental differences which exist compared to an attached flow where the near-wall layer is in approximate equilibrium. The mean flow and the turbulent fluctuations are largely decoupled in the near-wall layer beneath a reverse flow region since turbulence is not a result of local production but rather supplied by turbulence diffusion or pressure-velocity interactions [13, 9]. As a consequence, eddy-viscosity type modeling as in the two-layer approach used in [1] and [2] is not appropriate in this situation. Furthermore, a Schumann-Grötzbach type wall model [4]

$$\tau_{12}(x, z, t) = \frac{\bar{\tau}_w(x)}{\bar{U}(x, y_m)} u(x, y_m, z, t) = \beta_{SG} u(x, y_m, z, t) \quad , \quad (1)$$

in which the coefficient β_{SG} is backed out from a similarity law, can not be used, since $\bar{U}(y_m) = 0$ implies that the mean and the fluctuating part of the wall shear stress vanish simultaneously. Rather, the mean $\bar{\tau}_w$ and the fluctuating parts τ'_{12} and τ'_{23} of the wall shear stress should be modeled separately

as, for example, in the ‘ejection model’ of [12] or in the ‘drag law’ proposed in [5].

Three new near-wall models for the prediction of the *mean* wall shear stress inside and downstream of reverse flow regions are described in [7]. The predictive capability of these models was explored by comparison with results from DNS and LES of flows with reverse-flow regions, both for fixed and non-fixed separation lines. In sections 3 and 4, the key steps of the derivation are briefly sketched. An additional data base for flow inside a diffuser is then used in order to further validate the models. In section 5 a new model for the *fluctuating* part of the wall-shear stress is proposed and validated.

2. Method

A database from the numerical simulation of flow over a backward-facing step at $Re_H = U_\infty H/\nu = 5000$ is used to examine the near-wall region both inside and downstream of a region with strong reverse flow. With a prediction of the mean reattachment length $x_R = 6.2 H$ the results from the well-resolved LES [7] employing $N_x \times N_y \times N_z = 314 \times 136 \times 48$ cells in a hybrid finite difference/spectral approach are in excellent agreement with available experimental and DNS results [9] for this configuration.

Profiles of mean velocity and Reynolds stresses are shown in Fig. 1. They serve as basis for the model development. In the region $-3.5 \leq (x - x_R)/H \leq 6$ mean velocity profiles $\bar{U}(x, y)$ exhibit an approximately constant slope at off-wall distances $0.1H \leq y_{ref} \leq 0.2H$. The decoupling of mean flow and turbulence becomes evident from the profiles of horizontal normal stresses $\overline{u'u'}$ and $\overline{w'w'}$ which are unaffected by the mean flow being reversed or nearly zero. The data base from a wall-resolving LES of flow through a planar, asymmetric diffuser [8] serves as another test case employing typical features of an internal flow with smooth-surface separation.

3. Modeling the mean wall shear stress

The mean streamwise momentum balance can be written in the form

$$0 = -\frac{1}{\rho} \frac{\partial \bar{p}}{\partial x} + \nu \frac{\partial^2 \bar{U}}{\partial y^2} - \frac{1}{\rho} \frac{\partial \bar{\tau}_t}{\partial y} + r \quad (2)$$

where $r = \nu \partial^2 \bar{U} / \partial x^2$ denotes the ‘residual’ and where the ‘total shear stress’

$$\frac{\bar{\tau}_t}{\rho} \equiv \int_0^y \left(\frac{\partial \bar{U}^2}{\partial x} + \frac{\partial \overline{u'u'}}{\partial x} \right) dy + \overline{u'v'} + \bar{U} \bar{V} \quad (3)$$

has been introduced. Fig. 1 shows that the Reynolds shear stress $\overline{\rho u'v'}$ contributes the largest share to $\bar{\tau}_t$ near the wall. In the near-wall region under a

separation bubble the near-wall momentum balance often has a fairly simple structure: the pressure gradient is balanced by the sum of the viscous term $\nu \partial^2 \bar{U} / \partial y^2$ and the derivative $\partial \bar{\tau}_t / \partial y$.

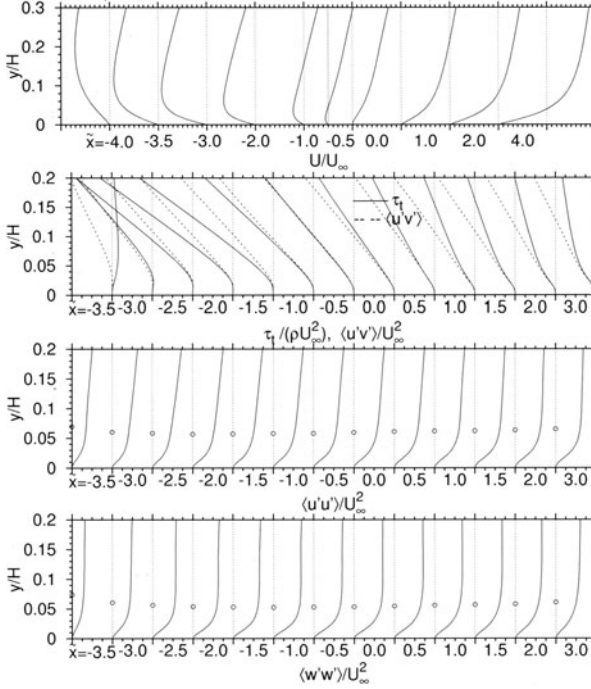


Figure 1. Profiles of mean streamwise velocity \bar{U}/U_∞ , total shear stress $\bar{\tau}_t/(\rho U_\infty^2)$ together with Reynolds shear stress $\overline{u'v'}/U_\infty^2$, and normal stresses $\overline{u'u'}/U_\infty^2$ and $\overline{w'w'}/U_\infty^2$ from the near-wall region behind a backward-facing step at $Re_H = 5000$. The streamwise position $\bar{x} \equiv (x - x_R)/H$ is given beneath the horizontal axis. The ticmark spacing along the horizontal axis is 0.02 (for \bar{U}), 0.0005 (for $\bar{\tau}_t$), and 0.005 (for variances). Circles mark the ‘edge location’ y_e of the viscosity-affected layer corresponding to $10(\nu/u_{\tau_{12}}^{rms})$ and $10(\nu/u_{\tau_{32}}^{rms})$ (details are given in Section 5).

The vanishing of the viscous term marks the edge of the near-wall layer. Outside of this layer, mean velocity profiles are approximately linear in y and the slope of the stress profiles $\bar{\tau}_t(y)$ becomes equal to the mean pressure gradient. It is useful to split $\bar{\tau}_t$ into a linear part τ_{lin} and the deviation τ'

$$-\bar{\tau}_t \equiv \tau_{lin} + \tau' \quad , \quad \text{where} \quad \frac{\tau_{lin}}{\rho} \equiv U_0^2 \left(\frac{y}{L_0} - 1 \right) \quad . \quad (4)$$

From the slope and intercept of τ_{lin} we obtain the characteristic scales U_0 and L_0 which are coupled through the relation $U_0^2/L_0 \approx \rho^{-1} \partial \bar{p} / \partial x$. Integration of the momentum balance (2) from the wall ($y = 0$) to y_{ref} using (4) yields

$$\frac{\bar{\tau}_w}{\rho} = - \underbrace{\int_0^{y_{ref}} \frac{1}{\rho} \frac{\partial \bar{p}}{\partial x} dy + \frac{U_0^2}{L_0} y - U_0^2 + \frac{\tau'(y_{ref})}{\rho}}_{\varepsilon_1} + \nu \left. \frac{\partial \bar{U}}{\partial y} \right|_{y_{ref}} + \underbrace{\int_0^{y_{ref}} r dy}_{\varepsilon_2} \quad . \quad (5)$$

From (2) follows that ε_1 vanishes exactly if $\partial \bar{U} / \partial y = \text{const.}$, if $\partial \bar{p} / \partial x \neq f(y)$, and if $r = 0$. As in most boundary layers $\partial^2 \bar{U} / \partial x^2 \ll \partial^2 \bar{U} / \partial y^2$ and therefore r and subsequently ε_2 can be neglected. Thus, for an off-wall location y_{ref} outside of the near-wall layer where $\tau' \approx 0$ holds, eq. 5 reduces to

$\bar{\tau}_w \approx \rho(\nu \partial \bar{U} / \partial y|_{y_{ref}} - U_0^2)$. In case of $\bar{\tau}_t \approx \rho \overline{u'v'}$ the intercept U_0^2 can be obtained from $\overline{u'v'}(y_{ref})$ at an off-wall position together with the pressure gradient $\partial \bar{p} / \partial x$, resulting in a parameter-free model for $\bar{\tau}_w$, see [7].

However, since accurate determination of $\overline{u'v'}$ at a position y_{ref} close to the wall might be difficult in practical situations [2] it is desirable to find a near-wall parametrization which does not require second moments from the flow interior. Such a model has been developed in [7] on basis of the observation that profiles of the total shear stress $\bar{\tau}_t$ approximately collapse if normalized by ρU_0^2 and plotted against y / L_0 . A key quantity in the new model is the definition of a virtual slip velocity U_w representing the intercept of the straight-line fit

$$U_{ref} \equiv y \cdot \left. \frac{\partial \bar{U}}{\partial y} \right|_{y_{ref}} + U_w \quad (6)$$

to the mean velocity profile outside of the viscosity-affected near-wall region. U_w can be obtained from extrapolation to the wall as sketched in Fig. 2.

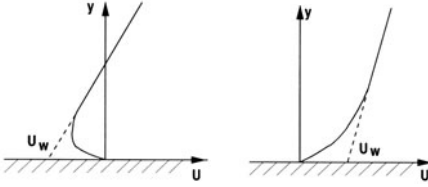


Figure 2. Sketch of near-wall profiles inside and downstream of a reversed flow region together with a linear extrapolation to the wall which defines the velocity scale U_w .

The resulting model for the mean wall-shear stress reads

$$\frac{\bar{\tau}_w}{\rho} \approx \nu \left. \frac{\partial \bar{U}}{\partial y} \right|_{y_{ref}} - \zeta \left[-\frac{\nu U_w}{\rho} \left. \frac{\partial \bar{p}}{\partial x} \right|_{y_{ref}} \right]^{0.5} \quad (7)$$

Its application range is restricted to the (rear) part of reverse flow regions where an adverse pressure $\partial \bar{p} / \partial x > 0$ exists and where (by definition) $U_w < 0$. This model requires as input the mean values of the pressure gradient, of the velocity, and its slope at a suitable off-wall location. In principle, these values can be obtained in a LES as running time averages. The model parameter ζ has been backed out from the data base using (7) with $y_{ref} \approx 0.15H$. Fig. 3a shows that $\zeta \approx 1.3$ remains almost constant in the region $-3 \leq (x - x_R) / H \leq -0.3$ where c_f experiences a drastic change in magnitude.

4. Defect scaling of the near-wall velocity profile

A more general model can be devised on basis of the observation that near-wall velocity profiles approximately collapse if plotted in the *defect* formulation

$$\frac{U_{def}}{U_w} = \frac{U_{ref} - \bar{U}}{U_w} \quad (8)$$

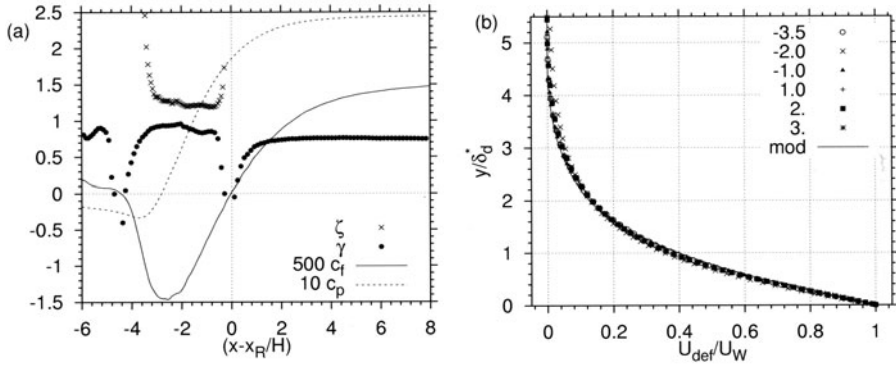


Figure 3. (a) Model coefficients ζ and γ as function of $(x - x_R)/H$. For better orientation, curves of friction and pressure coefficients c_f and c_p have been included. (b) Near-wall profiles in defect scaling at locations $(x - x_R)/H$ indicated in the legend.

as function of the normalized wall distance y/δ_d^* . Here, U_{ref} denotes the linear fit (6) to the mean flow. The length scale $\delta_d^* = \int (U_{def}/U_w) dy$ is a measure of the area under the defect profile. Unlike the edge position of the viscosity-affected layer used in [6], the ‘defect displacement’ thickness δ_d^* is unambiguously defined in regions with forward flow. Fig. 3b shows that the defect scaling (8) yields approximate collapse of near-wall profiles from both *upstream* and *downstream* of the mean reattachment location. This scaling is more general than Devenport’s modification [3] of Simpson’s proposal for a universal backflow profile since it is not restricted to the reverse flow region. Figures 4a,b indicate that the defect scaling is also appropriate in the near-wall region of the diffuser flow, although the profile shape differs slightly from the one found for the backstep. This might either indicate a Reynolds number dependence or be due to the coarse wall-normal grid spacing used in [8]. If the defect profiles have a universal functional dependence on y/δ_d^* , the corresponding wall shear stress model reads

$$\frac{\bar{\tau}_w}{\rho} = \nu \left(\frac{\partial \bar{U}}{\partial y} \Big|_{y_{ref}} + \gamma \frac{U_w}{\delta_d^*} \right) \quad (9)$$

which has a single model parameter γ . Fig. 3a shows the values of γ backed out from the simulation of flow over a backward-facing step. Downstream of reattachment $\gamma \approx 0.8$ appears to be a good choice whereas a slightly higher value is appropriate in the reverse flow region. Clearly, this model is ill-conditioned near locations where $\bar{\tau}_w \approx 0$ but these regions cause little problems in practice since there the drag law reduces to the equivalent of the no-slip condition.

The models (7) and (9) have been further tested using experimental data for flow over a backstep at $Re_H = 35000$, DNS data bases for smooth-surface separation from [11] and [10], and LES data [8] from a diffuser. For the latter

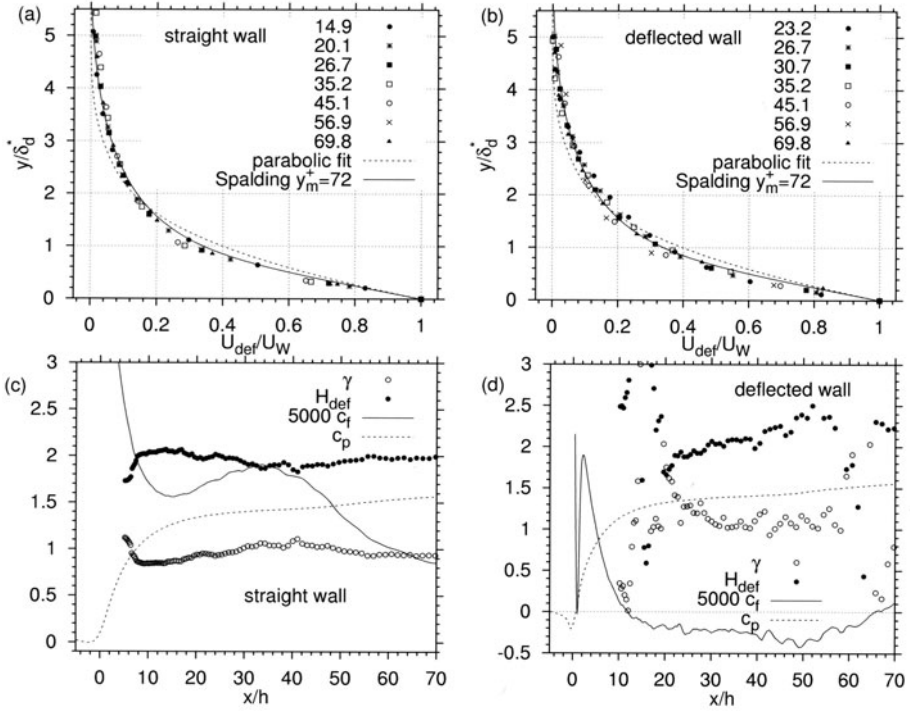


Figure 4. Model validation in the near-wall region of the flow in an asymmetric diffuser along the straight (a,c) and along the deflected (b,d) wall. (a,b) Defect profiles at different locations x/h ($2h$ corresponds to the height of the inlet duct) together with two different approximations explained in [7]. (c,d) Coefficient γ of the drag law (9), shape factor H_{def} (for definition, see [7]) of the defect profiles and curves of friction and pressure coefficients c_f and c_p .

case, Figures 4c,d show that $\gamma \approx 1$ would result in a reasonable prediction of $\bar{\tau}_w$ along both diffuser walls. Fig. 5 summarizes the model prediction based on eq. (9) which can be reformulated in terms of the drag law

$$c_{f,w} \equiv \frac{\bar{\tau}_w}{0.5\rho U_w^2} = \frac{2}{Re_w} \left[\gamma + \frac{\partial \bar{U}/\partial y|_{y_{ref}}}{U_w/\delta_d^*} \right] . \quad (10)$$

Fig. 5 shows that over a wide range of flow conditions the drag law can be approximated by $c_{f,w} \approx 1.8Re_w^{-1}$ – implying $\gamma \approx 0.9$ – which is consistent with eq. (10) if the second term in the bracket is much smaller than γ . Indeed, it has been confirmed from the data bases for the backstep and the diffuser that the magnitude of the second term remains below 0.1 over most parts of the regions considered.

5. A model for the fluctuating part of the wall shear stress

Formulation of a ‘drag law’ for the fluctuating components τ'_{12} and τ'_{32} requires the definition of a suitable length scale. Instead of deriving this length

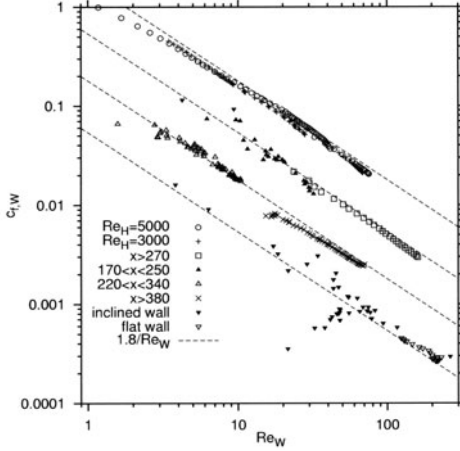


Figure 5. Drag law (10) in the form $c_f = |\bar{\tau}_w|/(0.5\rho U_w^2)$ versus $Re_w = U_w \delta_d^*/\nu$ for backward facing step flow at two Reynolds numbers (upper curve), for the separating boundary layer of [11] (second from top, scaled by 0.3), for the separation bubble of [10] (third from top, scaled by 0.1), and for the asymmetric diffuser of [8] (lowest curve, scaled by 0.03). Straight lines correspond to $c_{f,w} = 1.8Re_w^{-1}$. The list of symbols is organised in the following way: the first two entries refer to the backstep, entries 3-4 and 5-6 describe different ranges of the smooth-surface separation bubbles, and entries 7-8 correspond to the diffuser walls.

scale from mean velocity profiles as in [5] we propose to use the profiles of rms-values of velocity fluctuations as basis for the formulation of a model for the magnitude of wall-stress fluctuations. Figures 1 and 6a,b show that the viscous influence on the rms profiles extends to a wall distance which corresponds roughly to $y_e \approx 10\Delta_{i2}^*$ where the length scale $\Delta_{i2}^* \equiv \nu/u_{\tau_{i2}}^{rms}$ is defined on basis of the rms value of the $i2$ -component of the fluctuating wall stress. Furthermore, the rms profiles reach approximately an universal dependence on y^* if the velocity scale $u_{\tau_{i2}}^{rms}$ based on the fluctuating part of the wall-shear stress is used for normalization. Assuming that τ'_{i2} is in phase with the corresponding velocity fluctuation u'_i in a certain wall distance we arrive at the model

$$\frac{\tau'_{i2}(x, z, t)}{\rho} = \frac{u_i(x, y_e, z, t) - \bar{U}_i(x, y_e)}{u_{i,rms}(x, y_e)} (u_{\tau_{i2}}^{rms})^2. \quad (11)$$

For $y^* > 1$ the shape of the rms profiles might be approximated as

$$u_{i,rms}(y^*)/u_{\tau_{i2}}^{rms} = c_0 + c_1 \tanh((y^* + c_2) \cdot c_3), \quad (12)$$

from which $u_{\tau_{i2}}^{rms}$ can be backed out iteratively for a given $u_{i,rms}(y_e)$ at the off-wall location y_e . Fig. 6c shows the outcome of this procedure where y_e was fixed at $0.08H$ for all x -locations. The parameters of the assumed shape (12) were chosen as $c_0 = -1, c_1 = 4.2, c_2 = 2.1, c_3 = 0.17$. An excellent prediction is achieved for the spanwise component $u_{\tau_{32}}^{rms}$ whereas up to 20% modeling error is found for the component $u_{\tau_{12}}^{rms}$. This is consistent with Figures 6a,b which show larger scatter in the profiles for u_{rms} than for w_{rms} . For the shallow separation bubble of Manhart & Friedrich [10] $u_{\tau_{12}}^{rms}$ is predicted within 10% error if (12) is used with the coefficients $c_0 = -1, c_1 = 5.0, c_2 = 0.13, c_3 = -2.4$ and if u_{rms} is ‘measured’ at $y_e = 0.148\delta^*$ where δ^* corresponds to the displacement thickness of the incoming boundary layer.

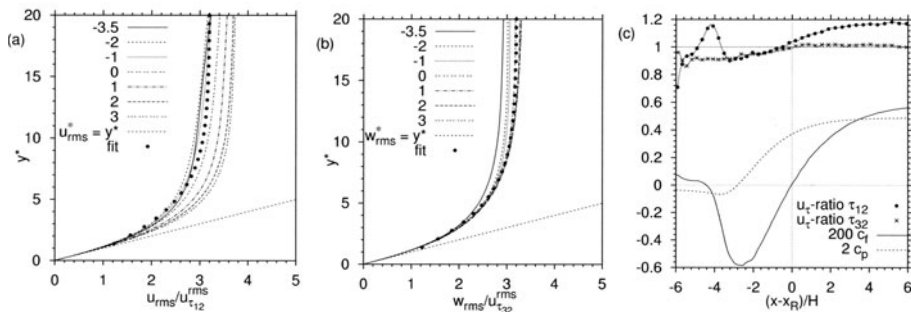


Figure 6. Normalized profiles of rms values of velocity fluctuations $u_{rms}/u_{\tau_{32}}^{rms}$ (a) and $w_{rms}/u_{\tau_{32}}^{rms}$ (b) versus $y^* \equiv y u_{\tau_{12}}^{rms}/\nu$ at different streamwise positions $(x - x_R)/H$ indicated in the legend. Dots denote the assumed profile (12). (c) Ratio of predicted and true rms value of wall shear stress fluctuations $u_{\tau_{12}}^{rms}|_{mod}/u_{\tau_{12}}^{rms}|_{true}$ as function of $(x - x_R)/H$. For better orientation c_f and c_p have been included.

References

- [1] Balaras, E., C. Benocci, and U. Piomelli: 1996, 'Two-layer approximate boundary conditions for large-eddy simulation'. *AIAA J.* **34**, 1111–1119.
- [2] Cabot, W. and P. Moin: 2000, 'Approximate wall boundary conditions in the large-eddy simulation of high Reynolds number flow'. *Flow, Turbul. Combust.* **63**, 269–291.
- [3] Devenport, W. J. and E. P. Sutton: 1991, 'Near-wall behavior of separated and reattaching flows'. *AIAA J.* **29**(1), 25–31.
- [4] Grötzbach, G.: 1987, 'Direct numerical and large-eddy simulation of turbulent channel flows'. In: *Encyclopedia of Fluid Mechanics*. Houston, pp. 1337–1391.
- [5] Hancock, P. E. and J. R. Hardman: 2000, 'Scaling of the near-wall layer beneath a three-dimensional turbulent separation bubble'. In: C. Dopazo (ed.): *Advances in Turbulence VIII*. Gran Capitan s/n, 08034 Barcelona, Spain, pp. 419–422.
- [6] Hardman, J. R. and P. E. Hancock: 2000, 'The near-wall layer beneath a moderately converging three-dimensional turbulent separated and reattaching flow'. *Eur. J. Mech. B - Fluids* **19**, 653–672.
- [7] Kaltenbach, H.-J.: 2003, 'A priori testing of wall models for separated flows'. *Phys. Fluids* **15**(10), 3048–3064.
- [8] Kaltenbach, H.-J., M. Fatica, R. Mittal, T. Lund, and P. Moin: 1999, 'Study of flow in a planar asymmetric diffuser using large eddy simulation'. *J. Fluid Mech.* **390**, 151–185.
- [9] Le, H., P. Moin, and J. Kim: 1997, 'Direct numerical simulation of turbulent flow over a backward-facing step'. *J. Fluid Mech.* **330**, 349–374.
- [10] Manhart, M. and R. Friedrich: 2002, 'DNS of a turbulent boundary layer with separation'. *Int. J. for Heat and Fluid Flow* **23**(5), 572–581.
- [11] Na, Y. and P. Moin: 1998, 'Direct numerical simulation of a separated turbulent boundary layer'. *J. Fluid Mech.* **374**, 379–405.
- [12] Piomelli, U., J. Ferziger, P. Moin, and J. Kim: 1989, 'New approximate boundary conditions for large eddy simulations of wall-bounded flows'. *Phys. Fluids A* **1**, 1061–1068.
- [13] Simpson, R. L., Y.-T. Chew, and B. G. Shivaprasad: 1981, 'The structure of a separating turbulent boundary layer. Part 2. Higher order turbulence results.'. *J. Fluid Mech.* **113**, 53–73.

1.3 NUMERICAL TECHNIQUES AND ERROR ESTIMATION

SYMMETRY-PRESERVING DISCRETIZATION FOR DNS

R.W.C.P. Verstappen, M.T. Dröge and A.E.P. Veldman

Research Institute of Mathematics and Computer Science

University of Groningen, P.O.Box 800, 9700 AV Groningen, The Netherlands.

verstappen@math.rug.nl, marc@math.rug.nl, veldman@math.rug.nl

Abstract This paper describes a numerical method for solving the (incompressible) Navier-Stokes equations that is based on the idea that the motivation for discretizing differential operators should be to mimic their fundamental conservation and dissipation properties. Therefore, the symmetry of the underlying differential operators is preserved. The resulting discretization is stable on any grid. Its accuracy is tested for a turbulent channel flow at $Re_\tau = 180$ by comparing the results to those of physical experiments and previous numerical studies. The method is generalized to compute flows in domains with arbitrarily-shaped boundaries, where the boundary is represented using the Cartesian grid approach. To that end, a novel cut-cell discretization has been developed. The boundary treatment is successfully tested for flow around a circular cylinder.

Keywords: Finite-volume discretization; conservation; stability; Navier-Stokes equations; turbulence; channel flow; Cartesian grid method; flow past circular cylinder.

1. Introduction

This paper describes a numerical method for solving the unsteady, incompressible Navier-Stokes equations in which the spatial difference operators inherit the symmetry of the underlying differential operators. The approach is motivated by the idea that the discrete convective and diffusive operators should possess the fundamental conservation and dissipation properties of the continuous convective and diffusive operators. To illustrate the need to preserve symmetry, we consider the linear convection equation

$$\partial_t u + \partial_x u = 0. \quad (1)$$

The spatial discretization problem reads: given three values of u , say $u_{i-1} = u(x_{i-1})$, $u_i = u(x_i)$ and $u_{i+1} = u(x_{i+1})$ with $x_{i-1} < x_i < x_{i+1}$, find an

approximation of $\partial_x u$ in x_i . Traditionally, the approximation is constructed to minimize the local truncation error, which results in

$$\partial_x u(x_i) \approx \frac{r_i u_{i+1} - (r_i - r_i^{-1})u_i - r_i^{-1}u_{i-1}}{x_{i+1} - x_{i-1}}, \quad (2)$$

where the grid stretching is given by $r_i = (x_i - x_{i-1})/(x_{i+1} - x_i)$. We see immediately that this approach leads to a coefficient matrix with nonzero diagonal entries for nonuniform grids ($r_i \neq 1$). Hence, if the local truncation error is minimized, the skew symmetry of the underlying differential operator ∂_x is lost on nonuniform grids. This forms our main motivation to consider

$$\partial_x u(x_i) \approx \frac{u_{i+1} - u_{i-1}}{x_{i+1} - x_{i-1}}, \quad (3)$$

instead of (2). Perhaps (3) seems not so accurate at first sight. Yet, Manteufel and White [1] have proven that (3) yields second-order accurate solutions on nonuniform meshes! To analyze the conservation and stability properties of (2) and (3), we write the spatial discretization of (1) in a finite-volume fashion,

$$\Omega \frac{d\mathbf{u}_h}{dt} + \mathbf{C}\mathbf{u}_h = \mathbf{0}, \quad (4)$$

where the semi-discrete velocities u_i constitute the vector \mathbf{u}_h , the diagonal matrix Ω is built of the control volumes $\frac{1}{2}(x_{i+1} - x_{i-1})$ and \mathbf{C} contains the coefficients of the discretization. The energy $\|\mathbf{u}_h\|^2 = \mathbf{u}_h^* \Omega \mathbf{u}_h$ of any solution of the dynamical system (4) is conserved if and only if the right hand-side of

$$\frac{d}{dt} \|\mathbf{u}_h\|^2 = \frac{d}{dt} (\mathbf{u}_h^* \Omega \mathbf{u}_h) \stackrel{(4)}{=} -\mathbf{u}_h^* (\mathbf{C} + \mathbf{C}^*) \mathbf{u}_h$$

is zero. This conservation property holds (for any \mathbf{u}_h) if and only if the coefficient matrix \mathbf{C} is skew symmetric. The discretization given by (3) satisfies that condition, whereas (2) violates it. Hence, the skew-symmetric discretization (3) is conservative as well as stable on any grid.

The example given by (1)-(4) illustrates the importance of the skew symmetry of the discrete convective operator \mathbf{C} . With this example in mind, we have developed a symmetry-preserving discretization method for solving the incompressible Navier-Stokes equations. Applied to these equations, we get

$$\Omega \frac{d\mathbf{u}_h}{dt} + \mathbf{C}(\mathbf{u}_h)\mathbf{u}_h + \mathbf{D}\mathbf{u}_h - \mathbf{M}^* \mathbf{p}_h = \mathbf{0} \quad \mathbf{M}\mathbf{u}_h = \mathbf{0}, \quad (5)$$

where p_h denotes the discrete pressure, Ω is a (positive-definite) diagonal matrix representing the sizes of the control volumes and M is the coefficient matrix of the discretization of the integral form of the law of conservation of mass. Here, the symmetries are preserved, that is the convective coefficient matrix $C(u_h)$ is skew symmetric like the convective operator $(u \cdot \nabla)$,

$$C(u_h) + C(u_h)^* = 0, \quad (6)$$

and the discrete diffusive operator D is symmetric, positive definite like $-\nabla^2$.

The evolution of the energy of any solution of (5) is then governed by

$$\begin{aligned} \frac{d}{dt}(u_h^* \Omega u_h) &\stackrel{(5)}{=} -u_h^*(C(u_h) + C(u_h)^*)u_h - u_h^*(D + D^*)u_h \\ &\stackrel{(6)}{=} -u_h^*(D + D^*)u_h, \end{aligned}$$

where the right-hand side is negative for all $u_h \neq 0$ since D is a symmetric, positive-definite matrix. This implies that the semi-discrete system (5) is stable, *i.e.* a solution of (5) can be obtained on any grid.

Note that the discrete pressure term in (5) does not contribute to the evolution of the discrete energy because the gradient matrix in (5) is taken equal to minus the transpose of the discrete divergence. Indeed, then we have: $(-M^* p_h)^* u_h = -p_h^* M u_h = 0$. In addition, we need not specify numerical boundary conditions for the pressure, because the discrete pressure gradient gets the boundary conditions from the discrete divergence.

So in conclusion, the rate of change of the discrete energy is not influenced by convective transport if and only if the discrete convective operator satisfies (6). Then, the energy decreases in time if the diffusive operator D is positive definite. Recently, conservation properties are also pursued by other researchers, cf. [2]-[4].

The paper is organized as follows. The symmetry-preserving discretization method is outlined in Sect. 2 and tested for turbulent channel flow in Sect. 3. In Sect. 4, the approach is generalized to a Cartesian grid method, which is evaluated for flow around a circular cylinder in Sect. 5.

2. Symmetry-preserving discretization

In the introductory section, we saw that conservation properties and stability are directly related to the symmetry of the discrete operator. In this section, the symmetry-preserving discretization is worked out in detail on a staggered grid (in two spatial dimensions to limit the length of the presentation).

Convective discretization. To prepare for the skew-symmetric discretization of the convective derivative, we recall the transport theorem: for any function f , we have

$$\frac{d}{dt} \int_{\Omega} f dV = \int_{\Omega} \frac{\partial f}{\partial t} dV + \int_{\partial\Omega} f \mathbf{u} \cdot \mathbf{n} dS, \quad (7)$$

where Ω is an arbitrary part of the fluid (at time t). The unit vector \mathbf{n} denotes the outward normal on the surface $\partial\Omega$ of Ω . The function f can have several meanings depending on what is transported. Taking f equal to the mass density gives the law of conservation of mass. For an incompressible fluid, it states that the net mass flux through the faces of any grid cell $[x_{i-1}, x_i] \times [y_{j-1}, y_j]$ is zero,

$$\bar{u}_{i,j} + \bar{v}_{i,j} - \bar{u}_{i-1,j} - \bar{v}_{i,j-1} = 0, \quad (8)$$

where the mass fluxes through the faces are defined by

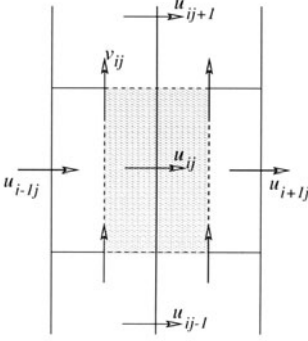
$$\bar{u}_{i,j} = \int_{y_{j-1}}^{y_j} u(x_i, y, t) dy \quad \text{and} \quad \bar{v}_{i,j} = \int_{x_{i-1}}^{x_i} v(x, y_j, t) dx. \quad (9)$$

The combination (8)-(9) does not yet contain a discretization error, since the integrals in (9) are exact. We postpone their discretization for a moment. The transport of momentum of a region Ω in an incompressible fluid is obtained if f in Eq. (7) is replaced by the momentum. As mass and momentum are transported at equal velocity, we will use the (9) for the transport velocity. Thus, the momentum flux through a surface S is approximated by

$$\int_S \mathbf{u} \mathbf{u} \cdot \mathbf{n} dS \approx u_S \int_S \mathbf{u} \cdot \mathbf{n} dS,$$

where u_S denotes a characteristic value of u at the surface S . At this stage, the integral in the right-hand side (that is the mass flux through S) is not approximated. The transport of momentum through the faces of the control volume $\Omega_{i,j}^u = [x_{i-1/2}, x_{i+1/2}] \times [y_{j-1}, y_j]$ for $u_{i,j}$ becomes approximately

$$\begin{aligned} |\Omega_{i,j}^u| \frac{du_{i,j}}{dt} &+ u_{i+1/2,j} \bar{u}_{i+1/2,j} + u_{i,j+1/2} \bar{v}_{i+1/2,j} \\ &- u_{i-1/2,j} \bar{u}_{i-1/2,j} - u_{i,j-1/2} \bar{v}_{i+1/2,j-1}. \end{aligned} \quad (10)$$



The figure alongside shows the control volume for $u_{i,j}$. The first term in (10) represents the discretization of the volume integral in the right-hand side of (7); the other terms form the approximation of the surface integral in (7) with $f = u$. The non-integer indices in (10) refer to the faces of the control cell for $u_{i,j}$. For example, $u_{i-1/2,j}$ stands for a characteristic u -velocity at the interface of $\Omega_{i-1,j}^u$ and $\Omega_{i,j}^u$ and $\bar{v}_{i+1/2,j}$ denotes the (exact) mass flux through the common boundary of the control volumes for $u_{i,j}$ and $u_{i,j+1}$, etc.

The velocity at a control face is approximated by the average of the velocity at both sides of it:

$$u_{i+1/2,j} = \frac{1}{2}(u_{i+1,j} + u_{i,j}) \quad \text{and} \quad u_{i,j+1/2} = \frac{1}{2}(u_{i,j+1} + u_{i,j}). \quad (11)$$

In addition to the set of equations for the u -component of the velocity $\mathbf{u} = (u, v)$, there is an analogous set for the v -component. We conceive the combination (10)-(11) as an expression for the velocities, where the mass fluxes form the coefficients. In matrix-vector notation, we can write (10)-(11), together with an analogous set for the v -component, as

$$\Omega \frac{d\mathbf{u}_h}{dt} + \mathbf{C}(\bar{\mathbf{u}})\mathbf{u}_h,$$

where the coefficient matrix $\mathbf{C}(\bar{\mathbf{u}})$ depends on the mass fluxes through the control faces. Note that we make liberal use of its name: so far \mathbf{C} was viewed as a function of \mathbf{u}_h , whereas \mathbf{C} is a function of exact mass fluxes here.

In the introductory section, we saw that (for $\mathbf{D} = \mathbf{0}$) the spatial discretization (5) conserves the energy $\mathbf{u}_h^* \Omega \mathbf{u}_h$ if and only if the convective coefficient matrix $\mathbf{C}(\bar{\mathbf{u}})$ is skew symmetric. The matrix $\mathbf{C}(\bar{\mathbf{u}}) - \text{diag}(\mathbf{C}(\bar{\mathbf{u}}))$ is skew symmetric if and only if the weights in the interpolation of u (and v) to the control faces are constant, as in Eq. (11). Therefore we use (11) also on nonuniform grids. To make $\mathbf{C}(\bar{\mathbf{u}})$ skew symmetric, the interpolation rule for \bar{u} and \bar{v} is determined by the requirement that the diagonal of $\mathbf{C}(\bar{\mathbf{u}})$ has to be zero. By substituting the interpolation (11) into (10) we obtain the diagonal coefficient

$$\frac{1}{2} (\bar{u}_{i+1/2,j} + \bar{v}_{i+1/2,j} - \bar{u}_{i-1/2,j} - \bar{v}_{i+1/2,j-1}).$$

This expression is zero if the mass is conserved in the grid cells and the mass fluxes in (10) are interpolated to the control faces with weights one half:

$$\bar{u}_{i+1/2,j} = \frac{1}{2}(\bar{u}_{i+1,j} + \bar{u}_{i,j}) \quad \text{and} \quad \bar{v}_{i+1/2,j} = \frac{1}{2}(\bar{v}_{i+1,j} + \bar{v}_{i,j}). \quad (12)$$

The discrete divergence and gradient. Obviously, the mass flux \bar{u} needs to be expressed in terms of the discrete velocity vector \mathbf{u}_h to close the discretization. The coefficient matrix becomes a function of the discrete velocity then: $C(\mathbf{u}_h) = C(\bar{\mathbf{u}}(\mathbf{u}_h))$. The matrix $C(\mathbf{u}_h)$ is skew symmetric for any relation between $\bar{\mathbf{u}}$ and \mathbf{u}_h . We take $\bar{u}_{i,j} = (y_j - y_{j-1})u_{i,j}$ and $\bar{v}_{i,j} = (x_i - x_{i-1})v_{i,j}$. Substituting these approximations into Eq. (8) yields the discrete continuity constraint, which confines the discrete velocity to $\mathbf{M}\mathbf{u}_h = \mathbf{0}$.

The discrete gradient matrix, describing the integration of the pressure gradient over the control volumes Ω , is given by $-\mathbf{M}^*$. Consequently, the pressure term in Eq. (5) does not contribute to the evolution of the discrete energy. To make the velocity field divergence-free, the pressure is computed from a Poisson equation, where the discrete Laplacian $-\mathbf{M}\Omega^{-1}\mathbf{M}^*$ is symmetric and negative definite.

Diffusive discretization. The method for discretizing the Laplacian in the Poisson equation for the pressure is also applied to discretize diffusion. In short, the diffusive operator is viewed as the product of a divergence and gradient. The divergence is discretized and the discrete gradient becomes the transpose of the discrete divergence (multiplied by a diagonal scaling). Unfortunately, we can not re-use the approximation $\mathbf{M}\Omega^{-1}\mathbf{M}^*$, since, due to staggering of the grid, the control volumes for u and v differ from the grid cells on which coefficient matrix \mathbf{M} is based. Therefore, we have to introduce the matrices \mathbf{M}_u and \mathbf{M}_v . They stand for the discrete integration of the divergence over the control volumes for u and v , respectively. Thus, the discrete diffusive operator in (5) becomes symmetric, positive definite:

$$\mathbf{D} = \frac{1}{Re} \text{diag} \left(\mathbf{M}_u \Omega_u^{-1} \mathbf{M}_u^*, \mathbf{M}_v \Omega_v^{-1} \mathbf{M}_v^* \right). \quad (13)$$

Higher-order, symmetry-preserving discretizations. To turn the symmetry-preserving discretization into a higher-order discretization, the leading term(s) in the discretization error may be removed by means of a Richardson extrapolation. For details, the reader is referred to [5].

3. Turbulent channel flow

The symmetry-preserving discretization is tested for turbulent channel flow. The Reynolds number is set equal to $Re_\tau = 180$ (based on the channel half-width and the wall-shear velocity). The computational domain is confined to a

channel unit of dimension $4\pi \times 2 \times 2\pi$. The computational grid consists of 64 streamwise points, 32 spanwise points and N_y wall-normal points.

Fig. 1 shows a comparison of the mean and root-mean-square velocity as ob-

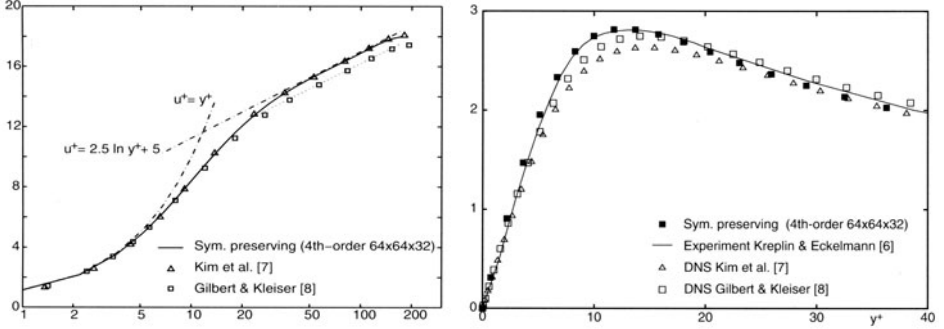


Figure 1. Comparison of the mean (left-hand) and root-mean-square (right-hand) velocity.

tained from our fourth-order symmetry-preserving simulation ($N_y = 64$) with those of other direct numerical simulations. Here it may be stressed that the grids used by the DNS's that we compare with have about 16 times more grid points than our grid has.

To investigate the convergence of the fourth-order method upon grid refinement, we have monitored the skin friction coefficient C_f for $N_y = 48, 56, 64, 96$ and 128. The convergence study shows that the skin friction coefficient is (approximately) given by $C_f = 0.00836 - 0.000004(y_1^+)^4$, where y_1^+ denotes the first (counted from the wall) grid line. The extrapolated value at $y_1^+ = 0$ lies in between the C_f 's reported in [7] (0.00818) and [9] (0.00844).

As the symmetry-preserving discretization is stable, a solution can be obtained on any grid and the main question becomes: how accurate is the method, or stated otherwise, how coarse may the grid be? To address this question, simulations have been performed on coarse grids. The results for the fluctuating streamwise velocity are shown in Fig. 2. The coarsest grid, with only $N_y = 16$ points, is coarser than most of the grids used to perform a large-eddy simulation (LES) of this flow. Nevertheless, the $N_y = 16$ solution is not that far off the solution on finer grids, in the near wall region. Further away from the wall, the turbulent fluctuations predicted on the coarse grids ($N_y \leq 32$) become too high compared to the fine grid solutions, as is shown in Fig. 2 (left). Perhaps, the solution with $N_y = 24$ forms an excellent starting point for evaluating the performance of LES-models in an *a posteriori* way.

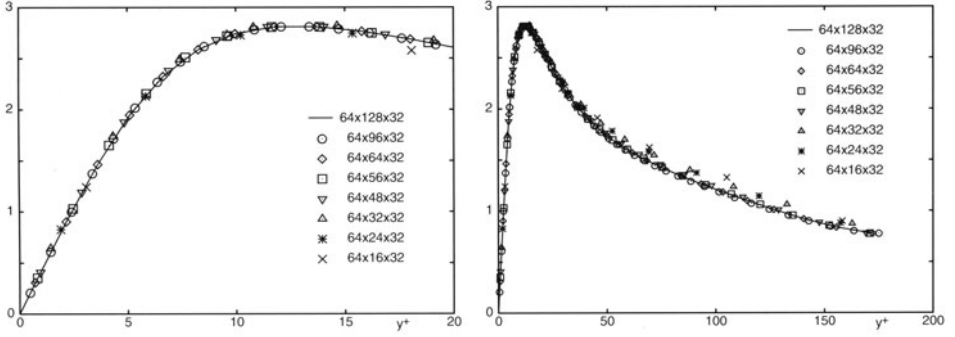


Figure 2. Root-mean-square of the streamwise velocity fluctuations at various (coarse) grids.

4. Symmetry-preserving Cartesian grid method

In this section, the symmetry-preserving discretization method is generalized to domains with arbitrarily-shaped boundaries, where the boundary is represented using the Cartesian grid approach cf. [10]–[12].

To start, we will explain our choice of the control volumes. The part of the grid cell $[x_{i-1}, x_i] \times [y_{j-1}, y_j]$ that is open to fluid flow is denoted by $F_{i,j}$. The discrete velocity $(u_{i,j}, v_{i,j})$ is staggered. The control volume for $u_{i,j}$ takes up the right half of $F_{i,j}$ and the left half of $F_{i+1,j}$. Here, we cut $F_{i,j}$ into two equal halves, by viewing $F_{i,j}$ as if it is built out of (an infinite number of) horizontal line-segments that run from x_{i-1} to x_i if the line-segment is uncut by a boundary, and from the boundary to either x_{i-1} or x_i (depending on which end lies in the fluid) if it is cut. Each line-segment is bisected and the half nearest to the grid line $x = x_i$ is taken, see Fig. 3. For an incompressible

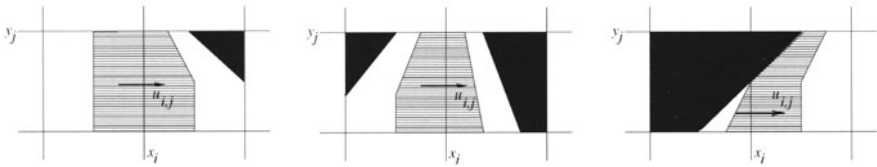


Figure 3. Control volumes for $u_{i,j}$. The parts that are not open to flow are colored black.

fluid, Eq. (8) holds again with

$$\bar{u}_{i,j} = \int_{y_{j-1}}^{y_j} u(x_i, y, t) \delta(x_i, y) dy, \quad \bar{v}_{i,j} = \int_{x_{i-1}}^{x_i} v(x, y_j, t) \delta(x, y_j) dx, \quad (14)$$

where the fluid domain is indicated by the function $\delta(x, y)$, which equals one inside the fluid and zero outside. The transport of momentum through the faces of a control volume for $u_{i,j}$ is again approximated according to (10), with \bar{u}

replaced by \bar{u}_n , because the mass flux through (part of) the interface between the control volumes for $u_{i,j}$ and $u_{i\pm 1,j}$ need not be aligned with u , see also Fig. 4 (left). As before, the matrix $\mathbf{C}(\bar{\mathbf{u}}) - \text{diag}(\mathbf{C}(\bar{\mathbf{u}}))$ is skew symmetric if and only if Eq. (11) is applied. Then, the diagonal of $\mathbf{C}(\bar{\mathbf{u}})$ vanishes if and only if the mass flux is interpolated by

$$\bar{u}_{ni+1/2,j} = \frac{1}{2}(\bar{u}_{i+1,j} + \bar{u}_{i,j}) \quad \text{and} \quad \bar{v}_{i+1/2,j} = \frac{1}{2}(\bar{v}_{i+1,j} + \bar{v}_{i,j}), \quad (15)$$

i.e. as in (12) with \bar{u} replaced by \bar{u}_n . The interpolation of $\bar{u}_{ni+1/2,j}$ is illustrated in Fig. 4 (left). The mass flux $\bar{u}_{ni+1/2,j}$ through the right-hand face of the control volume for $u_{i,j}$ is written as the average of the mass flux at both sides: $\bar{u}_{ni+1/2,j} = \frac{1}{2}(\bar{u}_{\text{left}} + \bar{u}_{\text{right}})$, where we take the flux through the face $x = x_i$ for the left-hand side, $\bar{u}_{\text{left}} = \bar{u}_{i,j}$. The right-hand contribution is approximated by the sum of the mass flux through the hypotenuse of the triangle that is not open to the flow and the mass flux through the open part of the face $x = x_{i+1}$: $\bar{u}_{\text{right}} = 0 + \bar{u}_{i+1,j}$. The flux $\bar{v}_{i+1/2,j}$ consists of two parts, one ($\frac{1}{2}\bar{v}_{i,j}$) results from the left-hand part of the cell face, the other one ($\frac{1}{2}\bar{v}_{i+1,j}$) stems from the right-half of the face, see Fig. 4 (right).

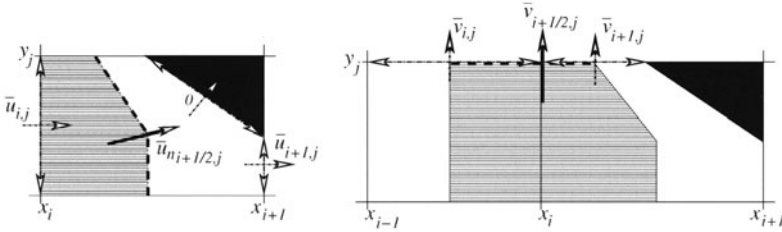


Figure 4. Interpolation of the mass flux $\bar{u}_{ni+1/2,j}$ (left-hand) and $\bar{v}_{i+1/2,j}$ (right-hand). Here, the black triangle is not open to flow. The dashed line represents the cell face.

The mass fluxes in Eq. (14) are related to the discrete velocity by means of:

$\bar{u}_{i,j} = u_{i,j} \int_{y_{j-1}}^{y_j} \delta(x_i, y) dy$ and $\bar{v}_{i,j} = v_{i,j} \int_{x_{i-1}}^{x_i} \delta(x, y_j) dx$. Substituting these approximations into (8) gives the discrete continuity constraint, $\mathbf{M} \mathbf{u}_h = \mathbf{0}$. The diffusive operator is discretized as in Eq. (13), where the matrices \mathbf{M}_u , \mathbf{M}_v , $\mathbf{\Omega}_u$ and $\mathbf{\Omega}_v$ are now based upon the open parts of the control volumes.

5. Flow over a circular cylinder

The symmetry-preserving, Cartesian grid method is applied to compute the unsteady flow around a circular cylinder at $Re = 100$, where the Reynolds number is based upon the diameter of the cylinder and the free stream velocity.

This flow has served as a test case for various numerical approaches. In this section, we will compare our results with those of Kravchenko *et al.* [13] and Persillon and Braza [14]. Kravchenko *et al.* [13] considered the flow past a circular cylinder to evaluate their Galerkin B-spline method. Persillon and Braza [14] studied the test case by means of a second-order, curvilinear, finite-volume method. Experimental data can be found in [15]-[16] and the references therein.

To confine the flow domain, fictitious boundaries are necessary (sufficiently) far away from the cylinder. We take the inflow boundary at four diameters upstream from the cylinder. The lateral boundaries are taken 8 diameters apart. The outflow is located at 10 diameters past the cylinder. Computations have been performed on two grids, a coarse grid consisting of 120×100 points (in the streamwise and lateral direction, respectively) and a finer grid with 240×200 points.

The bulk quantities as obtained from the fine- and coarse-grid simulations agree up to three digits. Table 1 shows a comparison of the fine-grid bulk quantities with those of the references mentioned above. The good agreement with the other numerical simulation techniques as well as with the physical experiments confirms the correct behavior of the present approach and shows that the symmetry-preserving Cartesian grid method forms a good alternative to boundary-fitted structured and boundary-fitted unstructured methods.

	St	$C_{D,p}$	$C_{D,f}$	mean C_D	max C_L	θ_{sep}
Present	0.165	0.93	0.31	1.24	0.30	117
Ref. [13]	0.164	0.97	0.34	1.31*	0.314	117.4
Ref. [14]	0.165			1.253	0.38	113.5
Exp. [15]		1.0	0.3	1.3		
Exp. [16]	0.164-0.165			1.24-1.26		122

Table 1. Comparison with other simulations and experiments. When given, the drag coefficient is written as the sum of the pressure drag and the viscous drag. Note: Ref. [13] gives the max C_D . In our case, max C_D is 0.02 higher than mean C_D .

Fig. 5 displays the pressure distribution at the surface of the cylinder as obtained with the symmetry-preserving Cartesian grid method. On both the coarse and the fine grid the numerical result is in good agreement with an experimentally determined pressure distribution.

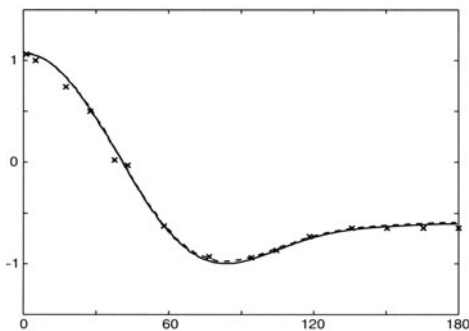


Figure 5 Pressure distribution at the surface of the cylinder, as function of the angle. The experimental data (depicted by the symbols) is taken from [16]. The continuous line corresponds to the fine-grid simulation, the dashed line represents the coarse-grid solution.

References

- [1] T.A. Manteufel and A.B. White, Jr. (1986). The numerical solution of second-order boundary value problems on nonuniform meshes, *Math. of Comp.* **47**, 511–535.
- [2] Y. Morinishi, T.S. Lund, O.V. Vasilyev and P. Moin (1998). Fully conservative higher order finite difference schemes for incompressible flow, *J. Comp. Phys.* **143**, 90–124.
- [3] O.V. Vasilyev (2000). High order finite difference schemes on non-uniform meshes with good conservation properties. *J. Comp. Phys.* **157**, 746–761.
- [4] F. Ducros, F. Laporte, T. Soulères, V. Guinot, P. Moinat and B. Caruelle (2000). High-order fluxes for conservative skew-symmetric-like schemes in structured meshes: application to compressible flows. *J. Comp. Phys.* **161**, 114–139.
- [5] R.W.C.P. Verstappen and A.E.P. Veldman (2003). Symmetry-preserving discretization of turbulent flow, *J. Comp. Phys.* **187**, 343–368.
- [6] H.P. Kreplin and H. Eckelmann (1979). Behavior of the three fluctuating velocity components in the wall region of a turbulent channel flow, *Phys. Fluids* **22**, 1233–1239.
- [7] J. Kim, P. Moin and R. Moser (1987). Turbulence statistics in fully developed channel flow at low Reynolds number, *J. Fluid Mech.* **177**, 133–166.
- [8] N. Gilbert and L. Kleiser (1991). Turbulence model testing with the aid of direct numerical simulation results, in *Proc. Turb. Shear Flows* 8, Paper 26-1.
- [9] R.B. Dean (1978). Reynolds number dependence of skin friction and other bulk flow variables in two-dimensional rectangular duct flow, *J. Fluids Engng.* **100**, 215–223.
- [10] J. Purvis and J. Burkhalter (1979). Prediction of critical Mach number store configurations, *AIAA J.* **17**, 1170–1177.
- [11] T. Ye, R. Mittal, H.S. Udaykumar and W. Shyy (1999). An accurate Cartesian grid method for viscous incompressible flow with complex boundaries, *J. Comp. Phys.* **156**, 209–240.
- [12] D. Calhoun and R.J. LeVeque (2000). A Cartesian grid finite volume method for the advection-diffusion equation in irregular geometries, *J. Comp. Phys.* **157**, 143–180.
- [13] A.G. Kravchenko, P. Moin and K. Shariff (1999). B-Spline method and zonal grids for simulations of complex turbulent flows, *J. Comp. Phys.* **151**, 757–789.
- [14] H. Persillon and M. Braza (1998). Physical analysis of the transition to turbulence in the wake of a circular cylinder by three-dimensional Navier-Stokes simulation, *J. Fluid Mech.* **365**, 23–88.

- [15] R.D. Henderson (1995). Details of the drag curve near the onset of vortex shedding, *Phys. Fluids* **7**, 2102–2104.
- [16] M.M. Zdravkovich (1997). *Flow around circular cylinders. Vol 1: Fundamentals*, Oxford University Press.

A THREE-DIMENSIONAL ADAPTIVE WAVELET METHOD FOR FLUID-STRUCTURE INTERACTION

N.K.-R. Kevlahan¹, O.V. Vasilyev², D. Goldstein² and A. Jay^{1,3}

kevlahan@mcmaster.ca

¹*Department of Mathematics & Statistics, McMaster University*

Hamilton, ON, Canada

²*Mechanical & Aerospace Engineering, University of Colorado at Boulder, Boulder, CO, USA*

³*École MatMéca, Université de Bordeaux I, Talence, France*

Abstract An adaptive wavelet collocation method for three-dimensional fluid–structure interaction at large Reynolds numbers is presented. This approach is shown to give accurate results with a reduced number of computational elements. The method is applied to two-dimensional flow past moving and fixed cylinders at $Re = 10^2$ and $Re = 10^4$, and to three-dimensional flow past a sphere at $Re = 500$. This is the first three-dimensional calculation of a flow past an obstacle using a dynamically adapted wavelet based approach.

Keywords: Turbulence, fluid–structure interaction, wavelets, penalization

1. Introduction

One of the most important applied problems in fluid dynamics is calculating moderate to high Reynolds number flow around solid obstacles of arbitrary shape. This problem arises in aerodynamics (e.g. turbulent flow over the wings and fuselage of airplanes), in off-shore drilling (e.g. water flow around riser tubes transporting oil from the sea bed to the surface), and in the wind engineering of buildings. In each case the primary difficulty arises from the need to calculate turbulent or transitional flow with boundary conditions on complicated domains. In addition, it may be important to allow for the obstacle to move or deform in response to the applied fluid forces (this motion in turn affects the flow).

In this paper we combine two mathematical approaches to calculate turbulent flow in complex domains. The first technique, the adaptive wavelet method, tackles the problem of efficiently resolving a high Reynolds number flow in complicated geometries (where grid resolution should depend both on time

and location). The second technique, Brinkman penalization, addresses the problem of efficiently implementing solid boundaries of arbitrary complexity. Adaptive wavelet methods have been developed recently to solve the Navier–Stokes equations at moderate Reynolds numbers (e.g. [8][12], [13],[5],[11]). Adaptive wavelet methods are appropriate for turbulence since wavelets (which are localized in both space and scale) adapt the numerical resolution naturally to the intermittent structure of turbulence at small scales. The wavelet method thus allows turbulent flows to be calculated with a greatly reduced number of modes and a well-controlled error. Furthermore, the computational cost is $O(\mathcal{N})$ (where \mathcal{N} is the total number of wavelets actually used), which does not depend directly on the dimensionality of the problem. In this work we employ a wavelet collocation method using second generation wavelets [10]. This approach allows the order of the method to be varied easily (we generally use a 6th-order method). Another advantage of the wavelet collocation approach is that it is equally easy to implement in two or three dimensions. Indeed, the same code is used to do both two-dimensional and three-dimensional simulations presented here.

Parallel to the development of efficient wavelet codes for turbulence, we have been investigating the use of the Brinkman equation to simulate the presence of arbitrarily complex solid boundaries ([6]). This technique allows boundary conditions to be enforced to a specified precision, without changing the numerical method (or grid) used to solve the equations. The main advantage of this method, compared to other penalization methods, is that the error can be estimated rigorously in terms of the penalization parameter. It can also be shown that the solution of the penalized equations converges to the exact solution in the limit as the penalization parameter tends to zero. Because this volume penalization is very simple and cheap to calculate, it is well-suited to moving obstacles. The adaptive wavelet method then allows the computational grid to follow the moving obstacle, without the need for accelerating reference frames, or large areas of very fine grids.

The combination of the above two methods is applied here to the two- and three-dimensional Navier–Stokes equations. We have also developed a multi-level elliptic solver, based on the adapted multiscale wavelet grid, to solve the Poisson problem for the pressure at each timestep. Note that we do not use a subgrid-scale model: we resolve fully all significant length-scales. Thus, the wavelet grid follows the natural intermittency of the flow.

In §20.2 and §20.3 we briefly sketch the penalization and numerical methods. Some results for two- and three-dimensional flow past obstacles for Reynolds numbers up to 10^4 are shown in §20.4, and in §20.5 we make some concluding comments. Note that this is the first time a dynamically adaptive wavelet method has been implemented for the three-dimensional Navier–Stokes equations with obstacles.

2. Brinkman penalization for complex geometries

Incompressible fluid flow is described by the Navier–Stokes equations:

$$\frac{\partial \mathbf{u}}{\partial t} + (\mathbf{u} + \mathbf{U}) \cdot \nabla \mathbf{u} + \nabla P = \nu \Delta \mathbf{u}, \quad (1)$$

$$\nabla \cdot \mathbf{u} = 0, \quad (2)$$

where \mathbf{U} is an imposed mean flow. We consider here the case where the fluid occupies the complement in Re^3 of a set of N obstacles O_i , $i = 1, \dots, N$. The problem is solved on a rectangular computational domain $\Omega = [L_{11}, L_{21}] \times [L_{12}, L_{22}] \times [L_{13}, L_{23}]$ containing all obstacles. To these equations are added appropriate external (inflow, outflow and side) boundary conditions.

On the surface of the obstacles the velocity must satisfy the no-slip condition,

$$\mathbf{u} + \mathbf{U} = \mathbf{U}_o \text{ on } \partial O_i, \forall i, \quad (3)$$

where \mathbf{U}_o is the velocity of the obstacle. Imposing these boundary conditions explicitly is difficult and computationally expensive when the obstacles have complicated shapes, move, or deform. To model the effect of the no-slip boundary conditions on the obstacles O_i without explicitly imposing (3) we replace (1-3) by the following set of L^2 -penalized equations ([2])

$$\begin{aligned} \frac{\partial \mathbf{u}_\eta}{\partial t} + (\mathbf{u}_\eta + \mathbf{U}) \cdot \nabla \mathbf{u}_\eta + \nabla P_\eta &= \nu \Delta \mathbf{u}_\eta \\ &\quad - \frac{1}{\eta} \chi(\mathbf{x}, t) (\mathbf{u}_\eta + \mathbf{U} - \mathbf{U}_o), \end{aligned} \quad (4)$$

$$\nabla \cdot \mathbf{u}_\eta = 0, \quad (5)$$

Note that equations (4-5) are valid in the entire domain Ω : the last term on the right hand side of (4) is a volume penalization of the flow inside the obstacle. Here $0 < \eta \ll 1$ is a penalization coefficient and χ is the characteristic (or mask) function defining the obstacle geometry:

$$\chi(\mathbf{x}, t) = \begin{cases} 1, & \text{if } \mathbf{x} \in O_i; \\ 0, & \text{otherwise.} \end{cases} \quad (6)$$

Angot ([1]) proved that the solution of the penalized equations (4-5) converges to that of the Navier–Stokes equations (1-2) with the correct boundary conditions (3) as $\eta \rightarrow 0$. For finite η the error in the boundary conditions is $O(\eta^{1/2})$. In general, the obstacles may be fixed, or allowed to move (or even deform). We consider here the case where there is a single obstacle that is either fixed or moves like a harmonic oscillator forced by the fluid. We therefore couple the penalized Navier–Stokes equations (4–5) to a harmonic oscillator equation for the motion of the obstacle's centre of mass \mathbf{x}_o ,

$$m \frac{d^2 \mathbf{x}_o}{dt^2} + b \frac{d \mathbf{x}_o}{dt} + k \mathbf{x}_o = \mathbf{F}(t), \quad (7)$$

where m is obstacle's mass, b is the mechanical damping, k is its natural frequency, and $\mathbf{F}(t)$ is the fluid force. Since $\mathbf{F}(t)$ is given by

$$\mathbf{F}_i(t) = \mathbf{F}_i(\mathbf{u}(t)) = \frac{1}{\eta} \int_{O_i} (\mathbf{u} + \mathbf{U} - \mathbf{U}_o) d\mathbf{x}. \quad (8)$$

the obstacle and fluid motions are fully and explicitly coupled.

The penalization error is found to be approximately $O(\eta)$ in practice, and we have found that a value of $\eta = 10^{-4}$ gives good results, in particular the drag and lift forces are accurate to within less than one percent.

3. Numerical method

We use an adaptive wavelet collocation method ([12],[13],[11]) to dynamically adapt the grid to the solution, and to interpolate on the adapted grid. Derivatives are then calculated on the adapted grid using high-order finite differences (usually 6th-order). The grid is adapted at each time step by nonlinear wavelet filtering: only those points whose associated wavelet coefficients are greater than a threshold ϵ are retained. The solution may then be interpolated onto the adapted grid with an L^∞ error of $O(\epsilon)$. Since the wavelet transform has $O(\mathcal{N})$ complexity (where \mathcal{N} is the number of points in the adapted grid), the method is computationally efficient and scales well to large problems.

To allow for the change in the solution over one time step, nearest neighbours in position and scale are added to the adapted grid. Adding nearest neighbours in position corresponds to a CFL criterion of one. As the scales are dyadic, adding nearest neighbours in scale means allowing for the creation of scales twice as small and twice as large via the quadratic nonlinearity of the Navier–Stokes equations.

Because the wavelet basis is not divergence free, we employ the usual split-step method to make the velocity of the first half-step \mathbf{u}^* divergence free. This Leray projection involves solving a Poisson equation for the pressure P ,

$$\nabla \cdot \nabla P = \frac{1}{\Delta t} \nabla \cdot \mathbf{u}_*. \quad (9)$$

Equation (9) is solved using a standard multilevel technique with V-cycles ([3]). In our case, however, the grids on each level are provided by the adaptive wavelet multiresolution, which produces a natural adaptive method for the Poisson equation. Wavelets are also used to interpolate between levels. This is the first time a wavelet multilevel solver has been developed, and it is described fully in a companion publication ([14]). Note that since it is based on the wavelet transform, the elliptic solver also has complexity $O(\mathcal{N})$.

Finally, we use a stiffly-stable 2nd-order time integration scheme that is semi-implicit for the advective term, and implicit for the penalization and diffusion terms.

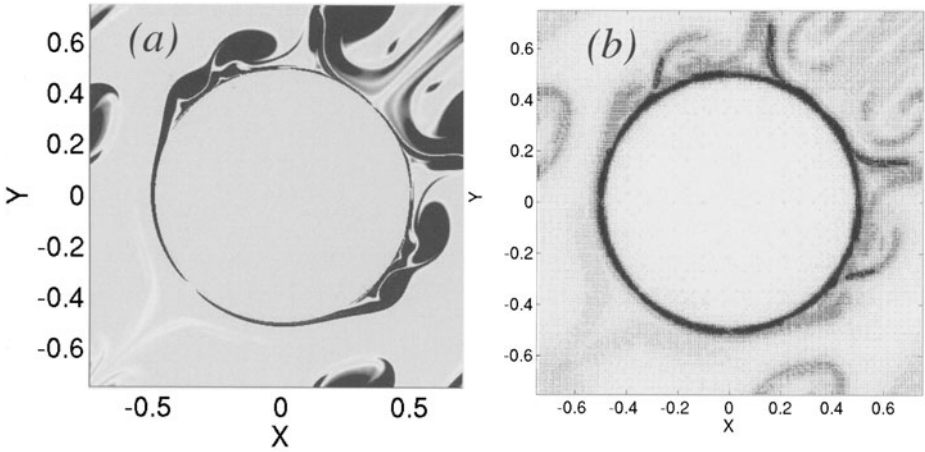


Figure 1. Two-dimensional periodic cylinder array at $Re = 10^4$, $t = 3.5$. (a) Vorticity. (b) Adapted grid.

4. Results

In this section we briefly present the results of some two- and three-dimensional calculations. They have been selected to illustrate the effectiveness of the dynamically adapted grid, and the flexibility of the method. The results presented below used a tolerance of $\epsilon = 10^{-4}$ for grid adaptivity, and the time step is chosen to maintain a CFL criterion of one. This value of ϵ corresponds to an L_∞ tolerance of 10^{-4} , and was found to be the largest value to give quantitatively accurate results. Note that this nonlinear wavelet filtering is not equivalent to the linear large-scale filtering done in LES: in wavelet filtering both large and small scales are retained. We have shown ([4]) that wavelet filtering retains the coherent vortices, and the neglected part of the flow is noise (i.e. dynamically unimportant).

The first example demonstrates the ability of the adaptive wavelet method to adapt the grid to fine-scale vortical structure. This result is interesting since although we actually solve the velocity form of the fluid equations, the grid points are distributed like the vortices of a (grid-free) vortex method. Figure 1 shows the vorticity and adapted grid for two-dimensional flow through a tightly packed periodic array of cylinders at $Re = 10^4$. Note that very few points are required inside the obstacle, and the grid refines and coarsens as needed in order to resolve the vorticity. Only 66 862 points out of a maximum of 896^2 are used, which corresponds to a compression ratio of 12.

In the second example we plot the drag, lift and amplitude of a two-dimensional cylinder moving in response to fluid forces at $Re = 10^2$. The oscillation amplitude $A = 0.42$, lift amplitude $C_L = 0.81$ and Strouhal frequency $St =$

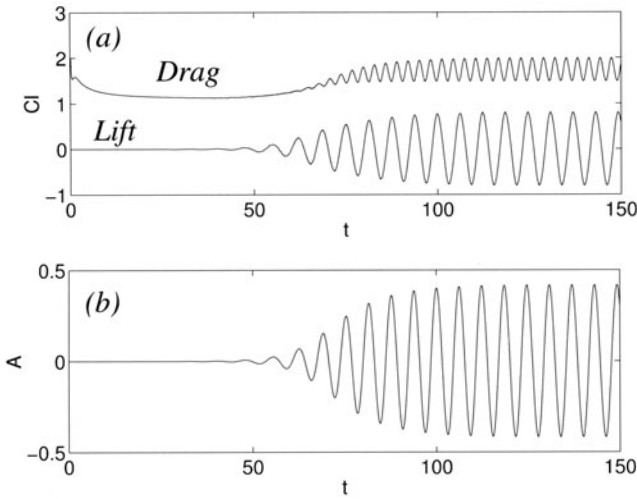


Figure 2. (a) Lift and drag for a moving cylinder at $Re = 100$. Note that the average drag during the shedding phase is $C_D = 1.74$, lift amplitude is $C_L = 0.81$, and the Strouhal number is $St = 0.189$. (b) Cylinder displacement as a function of time (amplitude $A = 0.42$).

0.189 are reasonably close to Shiels *et al.*'s ([9]) vortex method values of $A = 0.57$, $C_L = 0.83$, $St = 0.194$.

The final example is flow through a periodic array of spheres at $Re = 500$. This is a fully three-dimensional calculation, and shows the ability of the method to efficiently solve the three-dimensional Navier–Stokes equations with obstacles. Figure 3 shows an isosurface of the vorticity magnitude, and the computational grid at $t = 3.8$. Note that the flow is still at an early stage, so no instabilities have developed. The maximum resolution is 144^3 , but only 258 000, or 11.6%, of the points are active. This example shows the importance of using a dynamically adaptive method in three-dimensional calculations.

5. Conclusions

In this paper we have presented a new method for calculating three-dimensional flows at moderate to high Reynolds numbers with obstacles of arbitrary shape. The method uses an adaptive wavelet collocation method to dynamically adapt the grid to the flow, and as the basis of a multilevel solver for the associated Poisson equation for pressure.

We showed results for two-dimensional flow past a moving cylinder at $Re = 10^2$ and a fixed cylinder at $Re = 10^4$, and three-dimensional flow past a sphere at $Re = 500$. This is the first three-dimensional calculation of flow past an obstacle using a dynamically adapted grid.

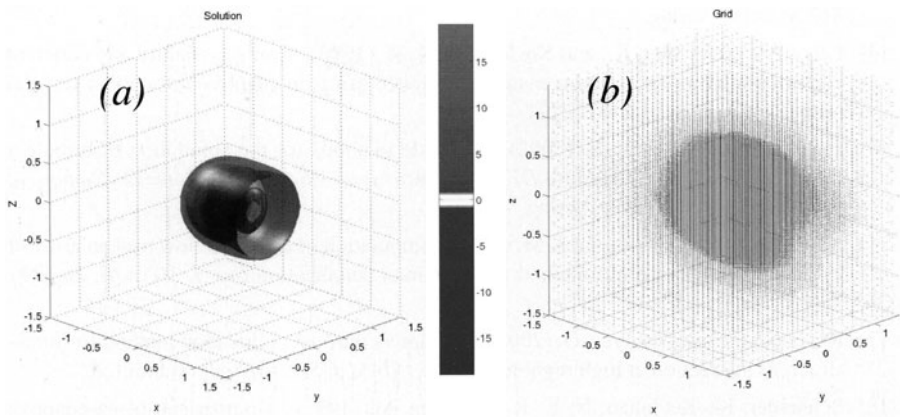


Figure 3. Flow past a sphere at $Re = 500$, $t = 3.4$ (looking upstream). (a) Isosurface of vorticity magnitude. (b) Computational grid. Note that the maximum resolution is much lower than in figure 1 (which means there is less detail in the grid), and we are showing the projection of a three-dimensional array of points (which means the centre of the sphere appears filled).

Further three-dimensional test cases will be investigated in future work. In particular, we would like to determine if the number of active grid points is proportional to the Taylor scale ($\lambda = Re^{-1/2}$), as is the case in two dimensions ([7]). If this is true, the overall computational complexity would scale like Re which is much better than the classical estimate of Re^3 based on a uniform grid.

Acknowledgments

The authors wish to thank P. Angot, P. Fabrie, K. Schneider, J.-M. Ghidaglia, and C.H.K. Williamson for their help and advice. N. Kevlahan would like to thank NSERC for financial support, and SHARCNET for computational facilities. Partial support for O. V. Vasilyev and D. E. Goldstein was provided by the National Science Foundation under grants No. EAR-0242591 and ACI-0242457 and National Aeronautics and Space Administration under grant No. NAG-1-02116.

References

- [1] Angot, P. (1999). Analysis of singular perturbations on the brinkman problem for fictitious domain models of viscous flows. *Mathematical Methods in the Applied Science*, 22:1395–1412.
- [2] Angot, P., Bruneau, C.-H., and Fabrie, P. (1999). A penalization method to take into account obstacles in viscous flows. *Numerische Mathematik*, 81:497–520.
- [3] Brandt, A. (1982). Guide to multigrid development. In Hackbusch, W. and Trottenberg, U., editors, *Multigrid methods*, volume 960 of *Lecture Notes in Mathematics*, pages 220–

312.Springer-Verlag.

- [4] Farge, M., Schneider, K., and Kevlahan, N. K.-R. (1999). Non-gaussianity and coherent vortex simulation for two-dimensional turbulence using an adaptive orthogonal wavelet basis.*Phys.Fluids*, 11:2187–2201.
- [5] Griebel, M. and Koster, K. (2002). Multiscale methods for the simulation of turbulent flows. In Hirschel, E.H., editor,*DFG/CNRS Workshop, Nice, 2001, Notes on Numerical Fluid Mechanics*. Vieweg-Verlag.
- [6] Kevlahan, N. and Ghidaglia, J.-M. (2001). Computation of turbulent flow past an array of cylinders using a spectral method with brinkman penalization.*Eur. J. Mech./B*, 20:333–350.
- [7] Kevlahan, N. and Vasilyev, O. (2003). An adaptive wavelet collocation method for fluid–structure interaction at high reynolds numbers. *SIAM J. Sci. Comput.* Submitted.
- [8] Schneider, K., Kevlahan, N. K.-R., and Farge, M. (1997). Comparison of an adaptive wavelet method and nonlinearly filtered pseudo-spectral methods for two-dimensional turbulence.*Theoret. Comput. Fluid Dynamics*, 9:191–206.
- [9] Shiels, D., Leonard, A., and Roshko, A. (2001). Flow-induced vibration of a circular cylinder at limiting structural parameters.*J. Fluids Structures*, 15:3–21.
- [10] Sweldens, W. (1998). The lifting scheme: A construction of second generation wavelets.*SIAM J. Math. Anal.*, 29(2):511–546.
- [11] Vasilyev, O. V. (2003). Solving multi-dimensional evolution problems with localized structures using second generation wavelets.*Int. J. Comp. Fluid Dyn.*, Special issue on high-resolution methods in Computational Fluid Dynamics, 17(2):151–168.
- [12] Vasilyev, O. V. and Bowman, C. (2000). Second generation wavelet collocation method for the solution of partial differential equations.*J. Comput. Phys.*, 165:660–693.
- [13] Vasilyev, O. V. and Kevlahan, N. K.-R. (2002). Hybrid wavelet collocation-brinkman penalization method for complex geometry flows.*Int. J. Num. Meth. Fluids.*, 30:531–538.
- [14] Vasilyev, O. V. and Kevlahan, N. K.-R. (2003). An adaptive multilevel wavelet collocation method for elliptic problems. In preparation.

DYNAMICS OF COMMUTATOR-ERRORS IN LES WITH NON-UNIFORM FILTER-WIDTH

Fedderik van der Bos, Bernard J. Geurts

Department of Applied Mathematics, J.M. Burgers Center, University of Twente, P.O. Box 217, 7500 AE Enschede, The Netherlands

f.vanderbos@math.utwente.nl, b.j.geurts@math.utwente.nl

Abstract In large-eddy simulation only the large scales in a turbulent flow are calculated explicitly and the small scales are effectively removed by the application of a filter with filter-width Δ . For LES of flows in complex geometries it is generally assumed that a non-uniform filter-width $\Delta(\mathbf{x})$ is advantageous. Application of non-uniform filters introduces additional sub-grid scale terms, referred to as commutator-errors. The commutator-error corresponds to filter-width variations along a flow-path and expresses differences in the local capturing of small scale flow-features. Therefore, a high correlation is expected between the specific filter-width non-uniformities and the production/dissipation of kinetic energy. This is confirmed by novel *a priori* analysis of turbulent mixing. In particular, commutator-errors arising from symmetric or non-symmetric filters are shown to differ considerably in dynamic implications.

Keywords: Turbulence, large-eddy simulation, non-uniform filters, commutator-error

1. Introduction

The phenomenology of turbulent flow can be depicted by the presence of a wide range of flow-scales. Present-day computational resources do not allow the computation of all turbulent scales up to the Kolmogorov length-scale η . Therefore, various reduced simulation strategies for turbulent flow have been introduced of which large-eddy simulation (LES) is one of the most promising. In LES the small-scales are effectively removed from the simulation by the application of a low-pass filter with an associated filter-width $\Delta \gg \eta$. The spatial filtering allows computation with grid-spacing of the order Δ . While in general the filter-width is defined to be constant across the domain, in this paper the filter-width is assumed to be non-uniform, i.e., $\Delta(\mathbf{x})$. For the application of LES to flows in complex domains the use of such a non-uniform filter-width is considered advantageous. Also the use of skewed filters with non-symmetric kernels can become unavoidable, especially close to bounding

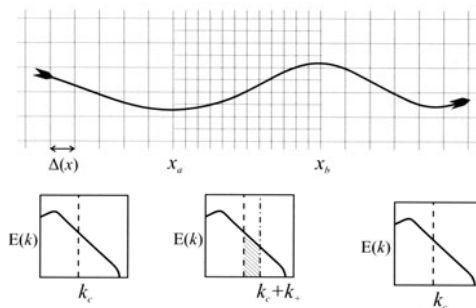


Figure 1. An illustration of a non-uniform filter-width. Commutator errors and the associated creation and destruction of scales will occur along the lines $x = x_a$ and $x = x_b$.

walls. Therefore, we consider extensions of convolution filters which allow for skewness and non-uniform filter-widths. As an example, an extension of the top-hat filter can be written as

$$\bar{u}(x) = L[u](x) = \int_{-\frac{1}{2}+a(x)}^{\frac{1}{2}+a(x)} u(x + \Delta(x)s) ds, \quad (1)$$

where a shift-function $-1/2 \leq a(x) \leq 1/2$ introduces skewness to the filter. The one-dimensional filter can be extended to three dimensions by consecutive application of one-dimensional filters, i.e., $\mathcal{L} = L_1 \circ L_2 \circ L_3$. Here, L_i has an associated filter-width $\Delta_i(\mathbf{x})$ and corresponds to filtering in the i -th direction. If a non-uniform filter is applied to the Navier-Stokes equations, different sub-grid scale terms (SGS-terms) show up. These SGS-terms incorporate the dynamical effects of the unresolved scales on the resolved scales and have to be modeled in order to close the filtered Navier-Stokes equations. Of all the SGS-terms the divergence of the SGS-stress $\tau_{ij} = \bar{u}_i \bar{u}_j - \bar{u}_i \bar{u}_j$ is the most important and has been extensively studied. However, with the introduction of a non-uniform filter-width $\Delta_i(\mathbf{x})$ a number of additional SGS-terms formally emerge. These additional SGS-terms are referred to as commutator-errors [1, 2] and are usually not considered in simulations up to now. For a field f we denote the flux due to the commutator-error by

$$C_j[f] = \overline{\partial_j f} - \partial_j \bar{f}, \quad (2)$$

where ∂_j is a short-hand notation for $\partial/\partial x_j$.

The dynamic effects of the commutator-error can be interpreted in a clear physical picture. In fact, the commutator-error can be associated with the apparent local creation and destruction of small-scale flow-features if the filter-width is decreased or increased along a flow-path respectively. This is illustrated in Figure 1. Consider a flow-path and assume that for $x < x_a$ all scales up to k_c are

resolved along this path, i.e., $\Delta(x) = \pi/k_c$ for $x < x_a$. If, for $x_a < x < x_b$ the filter-width is decreased to $\Delta(x) = \pi/(k_c + k_+)$, turbulent scales in the range $[k_c, k_c + k_+)$ become locally resolved if a flow-path passes x_a with $u > 0$. These scales contribute to the turbulent energy spectrum $E(k)$, because the dynamic wave-number range is extended from $[0, k_c)$ to $[0, k_c + k_+)$. Thus the local effect corresponding to a decrease of the filter-width should be an effective production of resolved kinetic energy. Similarly, the commutator-error should result in a decrease of resolved kinetic energy if the filter-width is increased along a flow-path as depicted at $x = x_b$ in Figure 1. This interpretation suggests to model the flux due to the commutator-error in terms of the material derivative of the filter-width variations. We will formalize this in the next section and in particular focus on the production and dissipation of kinetic energy.

The organization of this paper is as follows. In section 2 we introduce the commutator-error contribution to the evolution of the kinetic energy and propose a new explicit parameterization. In section 3 we describe the method of quantifying the commutator-errors and testing the new modeling. Results will be presented in section 4. Finally, in section 5 some concluding remarks are collected.

2. Commutator-error and kinetic energy dynamics

In this section we introduce the resolved turbulent kinetic energy equation and formalize the physical interpretation of the commutator-error to propose an explicit model for its contribution to the energy evolution.

In a domain $\Omega \subset \mathbb{R}^3$, the total dissipation-rate of resolved kinetic energy is defined as

$$\varepsilon = -\partial_t \left(\int_{\Omega} \frac{1}{2} \bar{u}_i \bar{u}_i d\mathbf{x} \right) = \varepsilon_p + \varepsilon_{\sigma} + \varepsilon_{\text{SGS}} + \varepsilon_{\text{CE}}, \quad (3)$$

with contributions from the pressure flux, the viscous stress tensor, the SGS-stress and the commutator-error respectively. The latter is defined as

$$\varepsilon_{\text{CE}} = \int_{\Omega} \bar{u}_i \mathcal{C}_j [u_i u_j] d\mathbf{x}, \quad (4)$$

where commutator-errors originating from the pressure and viscous fluxes have not been included. A contribution from the mean convective terms including a commutator error, $\int_{\Omega} \bar{u}_i \bar{u}_i \mathcal{C}_j [u_j] d\mathbf{x}$, has been shown to have only negligible influence on the results and has therefore been omitted in the analysis. From the total commutator error dissipation in (4) the local commutator-error dissipation rate density ψ is defined as $\psi = \bar{u}_i \mathcal{C}_j [u_i u_j]$.

The interpretation of the commutator-error given in the previous section suggests to parameterize ψ in terms of the material derivative of $\Delta_j(\mathbf{x})$ along a

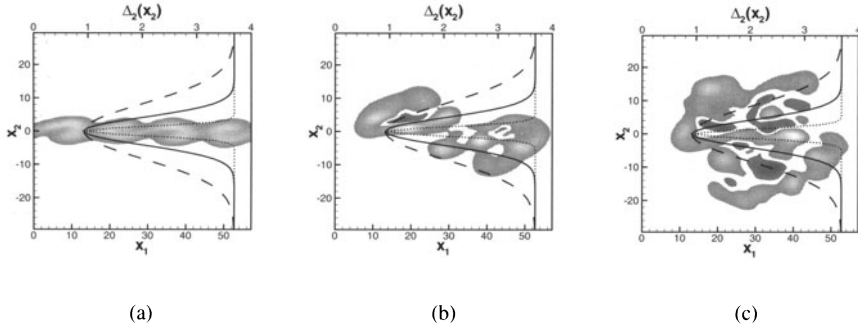


Figure 2. Contour plots of the spanwise vorticity of the developing mixing layer at a) $t = 20.0$, b) $t = 50.0$ and c) $t = 80.0$. Non-uniform filter-widths as defined in (6) with $\alpha = 3/4$ and $\beta = 5$ (dashed), $\beta = 10$ (solid) and $\beta = 30$ (dotted) are superimposed on these plots.

flow-path, i.e., $D_t \Delta_j = \partial_t \Delta_j + \bar{u}_k \partial_k \Delta_j = \bar{u}_k \partial_k \Delta_j$, where we assumed that Δ_j does not explicitly depend on time t . By defining ℓ and T as characteristic length and time-scales, one can readily verify that $D_t \Delta_j$ has dimension ℓT^{-1} , whereas the dimension of ψ is given by $(\ell T^{-1})^3 \ell^{-1}$. Accounting for the proper physical dimension the following parameterization for ψ is proposed

$$\psi \sim |\bar{\mathbf{u}}|^2 \Delta_j^{-1} \bar{u}_k \partial_k \Delta_j \equiv \xi, \quad (5)$$

where $|\bar{\mathbf{u}}|^2 = \bar{u}_i \bar{u}_i$ and ξ is introduced as a short-hand for the suggested parameterization of ψ . Expression (5) includes the material derivative of $\ln(\Delta_j)$ which is a measure of the relevance of the commutator-error relative to the turbulent stresses [3].

We will investigate the validity of the hypothesis in (5). Specifically, we consider an *a priori* analysis based on DNS-data of turbulent flow in a temporal mixing layer as depicted in Figure 2, following [4]. From the DNS-data the contributions to ε will be calculated for a variety of non-uniform filter-width distributions. The correlation between the local commutator-error dissipation rate density ψ and the right-hand side of (5) will be determined. Also, the probability distribution function (PDF) for these two quantities will be considered. The results will illustrate the large difference between commutator-errors arising from symmetric ($a = 0$ in (1)) or non-symmetric filters ($a \neq 0$).

3. A priori testing of commutator-error energy dynamics

We present the selected method and computational model for *a priori* testing of the commutator-error dissipation and its parameterization: $|\bar{\mathbf{u}}|^2 \Delta_j^{-1} \bar{u}_k \partial_k \Delta_j$. The actual test-results are collected in section 4.

We consider turbulent flow in a temporal mixing layer at Reynolds number $Re = 50$ in the incompressible limit. The governing equations are solved in a cubic geometry of side ℓ which is set equal to four times the wavelength of the most unstable mode according to linear stability theory. Periodic boundary conditions are imposed in the streamwise (x_1) and spanwise (x_3) direction, while in the normal (x_2) direction the boundaries are free-slip walls. We use a resolution of 192^3 grid-cells. The initial condition is formed by mean profiles corresponding to constant pressure, $u_1 = \tanh(x_2)$ for the streamwise velocity component and $u_2 = u_3 = 0$. Superimposed on the mean profile are two- and three-dimensional perturbation modes obtained from linear stability theory. We closely follow [4].

The filter-widths considered are constant in the x_1 and x_3 directions while in the x_2 direction we consider variations in the filter-width concentrated near the centerline. Specifically, we adopt

$$\Delta_1 = \Delta_3 = \Delta_r, \quad \Delta_2(x_2) = \Delta_r [1 - \alpha \exp(-(\beta x_2/\ell)^2)] \quad (6)$$

The reference filter-width Δ_r is taken equal to $\ell/16$. In the definition of the non-uniform filter-width $\Delta_2(x_2)$ the parameter α controls the ‘depth’ of the filter-width modulation, while β controls its width. The minimal filter-width Δ_{min} considered is $\Delta_r/4$ and corresponds to $\alpha = 3/4$. In Figure 2 different realizations of this non-uniform filter-widths have been superimposed on snapshots of the flow.

To test the kinetic energy modeling expressed in (5) we associate the stochastic variables Ψ and Ξ with ψ and ξ respectively. Since the filter is non-uniform only in the x_2 -direction, ξ reduces to $\xi = \bar{u}_i \bar{u}_i \Delta_2^{-1} \bar{u}_2 \Delta'_2$. In the following section we will focus on the correlation between Ψ and Ξ . Moreover, we determine the PDF $P(\xi, \psi)$ for these two variables.

The filtered quantities needed in the evaluations are obtained using the composite trapezoidal rule. In case end-points of the integration domain at $s = \pm \frac{1}{2} + a$ lie in between two data-points, a linear interpolation is used to approximate the values at the end-points. The derivatives are approximated using central finite differencing with grid-spacing $\Delta_r/4$.

β	time of DNS-field										
	0.0	10.0	20.0	30.0	40.0	50.0	60.0	70.0	80.0	90.0	100.0
5.0	0.20	0.27	0.39	0.51	0.54	0.58	0.61	0.55	0.50	0.52	0.56
10.0	0.49	0.53	0.60	0.61	0.58	0.60	0.58	0.51	0.53	0.57	0.64
30.0	0.77	0.75	0.67	0.62	0.63	0.60	0.56	0.48	0.55	0.61	0.64

Table 1. Correlation between $\xi = |\mathbf{u}|^2 \Delta_2^{-1} \Delta'_2 \bar{u}_2$ and $\psi = \bar{u}_i C_j [u_i u_j]$ as calculated from the DNS-fields at different moments in time over which different non-uniform filter-widths are applied (in all cases $\alpha = 3/4$).

4. Correlation and PDF of energy dynamics model

In this section we measure the quality of the commutator-error model (5) in terms of correlation and PDF, i.e., we treat the model testing from a statistical point of view.

In Table 1 the correlation between Ψ and Ξ is collected for different filter-width non-uniformities. Low correlation is observed in the initial stages in cases where the region of non-uniform filter-width is quite extended: $\beta = 5$ or $\beta = 10$. This can be explained noting that initially in large parts of the domain either $\Delta'_2 \approx 0$ or $\bar{u}_2 \approx 0$ (see Figure 2(a)). Once the flow has developed into the parts of the domain in which Δ'_2 is significant, a comparably high correlation is observed of about 0.6.

More details regarding the quality of the new model can be inferred from the PDF $P(\xi, \psi)$ between Ξ and Ψ . For the calculation of the PDF a binning procedure [5] has been used in terms of the quantities ξ^* and ψ^* defined by

$$\xi^* = \xi \langle \xi^2 \rangle^{-\frac{1}{2}} \quad \psi^* = \psi \langle \psi^2 \rangle^{-\frac{1}{2}} \quad (7)$$

In Figure 3 we observe that the PDF's are localized around the origin since either \bar{u}_2 or Δ'_2 is small in large parts of the domain. Moreover, we observe that contours of the PDF's are mainly located in the first and third quadrant which establishes our hypothesis formulated in (5).

These PDF's can be used to obtain one-dimensional conditional averages to further quantify the effectiveness of the model in (5). As an example, it is expected that 'events' in which $\Psi > 0$ will correspond closely with locations where $\xi > 0$ and vice versa. This relation can be illustrated by considering

$$\Psi^+(\xi) = \langle \Psi > 0 | \Xi = \xi \rangle \quad (8)$$

The function Ψ^+ denotes the expectation that the dissipation is positive given the value of ξ . By (5) it is expected that $\Psi^+(\xi) \rightarrow 1$ for $\xi > 0$ and $\Psi^+(\xi) \rightarrow 0$ for $\xi < 0$. In fact, there should be a sharp transition from $\Psi^+ \approx 0$ to $\Psi^+ \approx 1$ as ξ changes sign. Closely related is the conditional expectation of Ψ as a function of ξ

$$\mathcal{E}(\xi) = \langle \Psi^* | \Xi = \xi \rangle \quad (9)$$

Close correlation of ψ and ξ would imply an approximately linear dependence of \mathcal{E} as function of ξ .

In Figure 4 we plotted Ψ^+ and \mathcal{E} for the characteristic case $\alpha = 3/4$ and $\beta = 10$ at various stages in the development of the flow. In Figure 4(a) the expected behavior of Ψ^+ is indeed observed, including the sharp transition around $\xi^* = 0$. In Figure 4(b) an almost linear relation between \mathcal{E} and ξ is observed, which further establishes the quality of the new parameterization.

Finally, we turn to non-symmetric filters in the definition of the commutator-

errors. Remarkably, the local dissipation ψ is no longer as strongly related to ξ in these cases. This hints at a more complex contribution of ‘skewed commutator-errors’ to the kinetic energy dynamics. In Figure 5 the PDF $P(\xi, \psi)$ is shown for the cases $a = 1/4$ and $a = 1/2$ in (1). Almost no correlation is observed between ξ and ψ : the correlation coefficients drop to

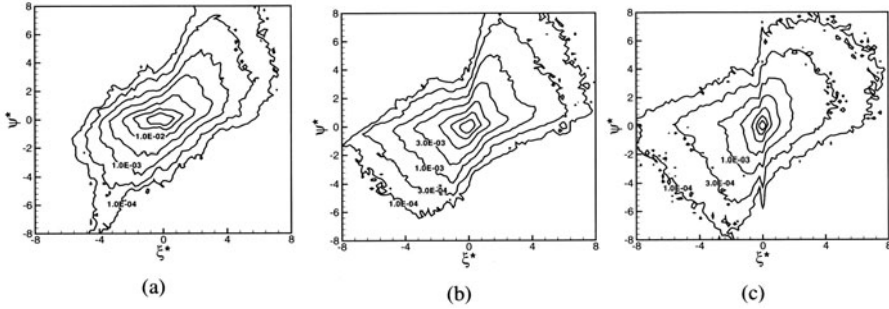


Figure 3. The PDF $P(\xi, \psi)$ for $t = 60$, $\alpha = 3/4$ and a) $\beta = 5$, b) $\beta = 10$ and c) $\beta = 30$.

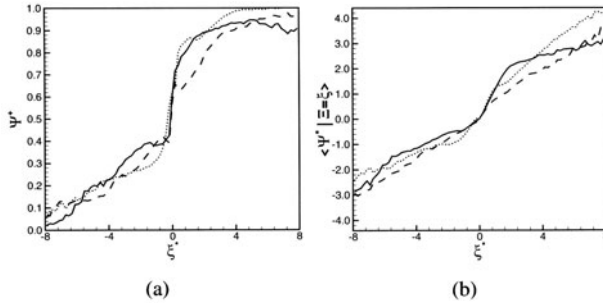


Figure 4. The stochastic variables a) $\Psi^+(\xi)$ and b) $\mathcal{E}(\xi)$ in case $\alpha = 3/4$, $\beta = 10$ and $t = 40$ (dotted), $t = 60$ (solid) and $t = 80$ (dashed).

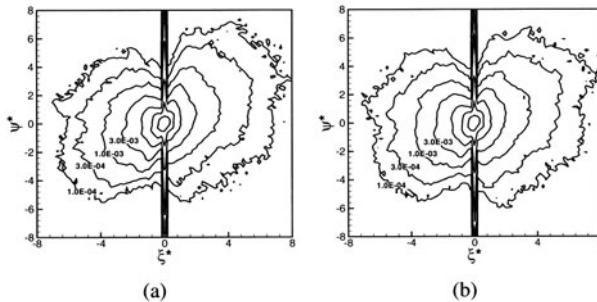


Figure 5. The PDF between ξ and ψ for $t = 60$, $\alpha = 3/4$ and $\beta = 10$ in case non-symmetric filters are applied, a) $a = 1/4$ and b) $a = 1/2$.

0.25 and 0.16 in these cases respectively. Moreover in Figure 5 the largest values of local commutator-error dissipation are found near $\xi^* \approx 0$ and can not be properly accounted for using (5).

A possible explanation for this difference can be inferred from Fourier analysis of the commutator-error. Additional dispersive effects are found in case non-symmetric filters are applied. Diffusive effects for the commutator-error have already been recognized in [1]. In our analysis, dispersion is seen to become relevant as well for skewed filters; the extension of (5) to these cases will be published elsewhere.

5. Concluding remarks

In this paper a new model for the kinetic energy dynamics of the commutator-error \mathcal{C}_j has been proposed, based on the material derivative of the filter-width and dimensional arguments. This is explicitly formulated in (5) and was validated *a priori* using DNS-data of turbulent mixing.

For filters characterized by a symmetric kernel, the model in (5) for the commutator-error was validated by focusing on correlation and PDF between the local dissipation and ξ . The model can also be formulated for \mathcal{C}_j in the momentum equations, which will become of interest when LES is applied to turbulent flows in complex geometries. A dynamic procedure can be developed to properly adapt the commutator-error model to the developing flow.

For complex flows in complicated domains the use of non-symmetric filters appears unavoidable, e.g., near solid boundaries. In case non-symmetric filters are used the correlation between the local dissipation and ξ is no longer as striking. This issue will be addressed in a separate paper.

References

- [1] S. Ghosal and P. Moin. The Basic Equation for the Large Eddy Simulation of Turbulent Flows in Complex Geometry. *Journal of Computational Physics*, 118:24–37, 1995.
- [2] S. Ghosal. Mathematical and Physical Constraints on Large-Eddy Simulation. *AIAA Journal*, 37(4):425–433, April 1999.
- [3] B.J. Geurts. How can we make Large Eddy Simulation to fulfill its promise? In R. Friedrich and W. Rodi, editors, *Advances in LES of complex flows*, pages 13–32. Kluwer Academic Publishers, Dordrecht, 2002.
- [4] B. Vreman, B. Geurts, and H. Kuerten. Large-eddy simulation of the turbulent mixing layer. *Journal of Fluid Mechanics*, 339:357, 1997.
- [5] F. van der Bos, B. Tao, C. Meneveau, and J. Katz. Effects of small-scale turbulent motions on the filtered velocity gradient tensor as deduced from holographic particle image velocimetry measurements. *Physics of Fluids*, 14(7), 2002.

IDENTIFICATION OF GLOBAL ERROR BEHAVIOR IN LES USING A DATABASE APPROACH

Johan Meyers¹, Bernard J. Geurts² and Martine Baelmans¹

¹*Department of Mechanical Engineering, Katholieke Universiteit Leuven, Celestijnenlaan 300 A, 3001 Leuven, Belgium*

johan.meyers@mech.kuleuven.ac.be, Martine.Baelmans@mech.kuleuven.ac.be

²*Mathematical Sciences, University of Twente, P.O. Box 217, 7500 AE Enschede, The Netherlands*

b.j.geurts@utwente.nl

Abstract A database of various LES and two reference DNS of homogeneous isotropic turbulence is constructed at $Re_\lambda = 50$ and 100. All LES are performed with Smagorinsky or dynamic Smagorinsky modeling. Using the database information, accuracy charts are constructed, which give a global view of the error as function of important LES parameters. Moreover, as a result, ‘optimal refinement strategies’ are identified for LES. Further, the dynamic model is shown to select its own refinement trajectory. The distance of this trajectory to the ‘optimal’ refinement path is a measure for the quality of the dynamic procedure.

Keywords: LES, errors, homogeneous isotropic turbulence, database analysis

1. Introduction

In recent LES history, a large variety of different subgrid scale models has been developed and tested. Although several of these models give good results in various specific simulations, the quality of actual LES predictions in general depends on a large number of additional factors that are part of the computational modeling of a flow. In fact, complications may arise from the specific flow geometry, from the flow regime, from the mesh and mesh-size and from the numerical method. These factors can simultaneously be quite important in view of the marginal resolution of many dynamically significant features of the

flow. This marginal resolution is imposed by practical restrictions arising from the computational capabilities of present-day computers.

Various studies on errors and error interaction in LES exist Geurts and Fröhlich, 2002; Geurts, 1999; Ghosal, 1996. However, a practical systematic framework in which the error-analysis can be interpreted is still lacking. In the present study, a database approach for such an error-analysis is introduced, where important parameters, such as the resolution, the filter-width to mesh-size ratio, the Reynolds number etc. are included.

The database information allows to obtain a global view on LES error behavior depending on model and numerical parameters. A concise representation is found in so called ‘accuracy charts’. A direct result is the determination of optimal working conditions for LES and more precisely ‘optimal refinement strategies’. These provide an excellent reference for the development of near optimal dynamic procedures.

First, in section 2, the general database methodology is presented. Subsequently, in section 3, a LES database is described for homogeneous isotropic turbulence involving the Smagorinsky model. Next, in section 4, global errors are presented in accuracy charts and optimal refinement strategies are determined. Finally, some concluding remarks are presented in section 5.

2. General methodology of error assessment

In a shorthand notation, the closed LES equations can be written as

$$\text{NS}_i(\bar{\mathbf{u}}, \bar{p}) = \frac{\partial}{\partial x_j} m_{ij}(\bar{\mathbf{u}}), \quad (1)$$

where NS is the Navier-Stokes operator, the spatial convolution filter is denoted by $\overline{(\cdot)}$ and $\{\bar{\mathbf{u}}, \bar{p}\}$ is the filtered solution with $\bar{\mathbf{u}} = [\bar{u}_1, \bar{u}_2, \bar{u}_3]$ the filtered velocity and \bar{p} the filtered pressure. Further, m_{ij} corresponds to the particular choice of subgrid scale model. The filtered solution obeys Navier-Stokes dynamics in which the subgrid-scale model is responsible for the smoothing of the turbulent flow field. Theoretically, the filter fully determines the closure problem for the subgrid scale stresses Geurts and Holm, 2003. However, in virtually all actual large-eddy simulations, the explicit role of the filter is limited to the inclusion of the filter width Δ in the model. Therefore, for each model, a detailed understanding of the LES behavior as function of Δ is imperative for good LES practice.

Next to the filter width, the grid spacing h of the computational grid is important. At constant filter width Δ , a decrease in h will reduce the discretization error and gradually give rise to a ‘grid-independent’ LES solution. After all, the continuous, *modeled* LES equations (i.e., eq. (1)) constitute a closed system of nonlinear partial differential equations with fixed, externally specified length-scale Δ . Clearly, grid-independent LES may require very high res-

olutions and may not be feasible (nor required) in many cases. To achieve a good approximation of the grid-independent solution, a subgrid resolution Δ/h of up to 6-8 might be required Geurts and Fröhlich, 2002. As such, ‘grid-independent’ LES should not be confused with a proposal to perform actual, practical LES in this way. Moreover, high subgrid resolution does not necessarily guarantee high overall accuracy Vreman et al., 1996; Meyers et al., 2003. By systematically varying Δ and the numerical resolution h , one may assess the complex interaction between numerical discretization effects and modeling effects.

To analyze the error behavior, let ϕ be a flow parameter of interest. The total error in ϕ , obtained from LES, with filter width Δ and grid spacing h is defined as

$$e_{total}(\Delta, h) = \phi_{DNS} - \phi_{LES}(\Delta, h) \quad (2)$$

Here, ϕ_{DNS} is obtained from the reference DNS solution. The total error e_{total} can be further decomposed into a contribution due to the discretization and the subgrid modeling Vreman et al., 1996. Hence, detailed error behavior can be quantified for any variable ϕ , where both ϕ and e can be functions of time and spatial location. Moreover, using an appropriate norm, a global relative error can be coupled to each separate LES run, e.g., using an L_2 -norm:

$$\delta_\phi = \frac{\|e_{total}\|^2}{\|\phi_{DNS}\|^2} = \frac{\int_{t_0}^{t_1} \int_{\Omega} e_{total}^2 d^3\mathbf{x} dt}{\int_{t_0}^{t_1} \int_{\Omega} \phi_{DNS}^2 d^3\mathbf{x} dt}. \quad (3)$$

This global error allows an efficient overview of LES error behavior as function of the numerical and the subgrid resolution. The error can be represented in so called ‘accuracy charts’ as will be demonstrated in section 4.

3. Outline of the DNS and LES reference runs

An extensive LES database was constructed for decaying homogeneous isotropic turbulence. For the LES, the numerical method consists of a 4th order discretization for the convective terms and a 2nd order discretization for the viscous terms together with a 2nd order Runge-Kutta scheme Vreman, 1995. First, we turn to LES employing the Smagorinsky model $m_{ij} = (C_s \Delta)^2 |S| S_{ij}$, where S_{ij} is the resolved strain tensor. The database contains a systematically ‘scanned’ region of different LES at various resolutions n^3 , with $16 \leq n \leq 128$ and effective subgrid resolutions $0 \leq C_s \Delta/h \leq 3/2$. In this section a short overview is presented of some simulation results.

The database consists of two reference DNS at two different Reynolds numbers, i.e., $Re_\lambda = 50$ and 100 on a 256^3 and 384^3 grid respectively, as well as a full set of different LES employing the Smagorinsky model. Furthermore, LES

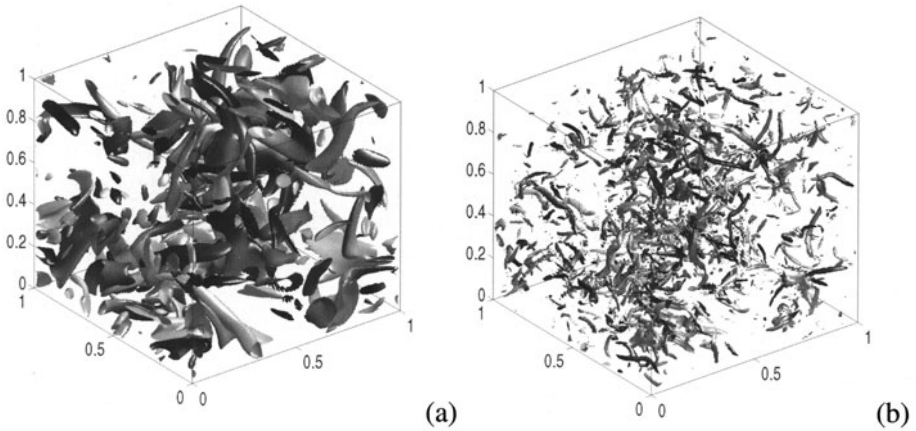


Figure 1. Snapshots of vorticity at $t=0.6$ (a) $Re_\lambda = 50$, (b) $Re_\lambda = 100$. Isolevels for (a) and (b) at $0.25|\omega|_{max}$

using a dynamic Smagorinsky model is employed at different resolutions Germano et al., 1991; Lilly, 1992. In contrast to the standard Smagorinsky model, where the effective filter width $C_s\Delta$ is a preset simulation coefficient, the dynamic eddy viscosity coefficient is adapted continuously using the Germano identity Germano, 1992.

In figure 1, the vortical structures for both DNS at $Re_\lambda = 50$ and 100 are visualized by plotting isosurfaces of the magnitude of the vorticity, i.e., $|\omega| = (\omega_i\omega_i)^{1/2}$ where ω_i is the i -th component of $\nabla \times \mathbf{u}$. These plots clearly illustrate the difference in complexity and required resolution for both Reynolds numbers.

The evolution of the turbulent kinetic energy is displayed in figure 2 for $Re_\lambda = 100$. Here, the unfiltered DNS reference is compared with LES results at a 48^3 resolution. A value of the effective filter width is selected ($C_s\Delta = 0.15h$) which is relatively close to the optimal (as obtained from the analysis in section 4). This is also compared to the ‘no model’ case ($C_s\Delta = 0$). Clearly, the $C_s\Delta = 0.15h$ case displays a good solution within the limitations of its numerical resolution. When the Smagorinsky constant is set to 0, a lack of energy dissipation is observed and the energy level starts to increase again at $t = 0.8$ (i.e., the numerical method used for the LES is not energy conserving). This clearly illustrates the relevance of the subgrid model at the 48^3 LES resolution.

4. Accuracy charts and optimal refinement strategies

In the present section, accuracy charts are presented, which reduce the extensive LES database information into a concise error overview. These charts,

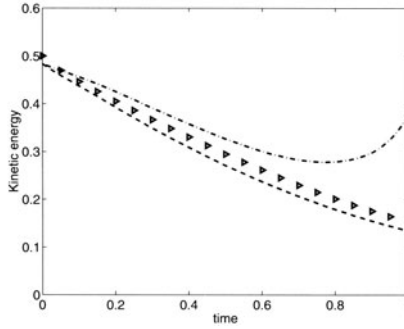


Figure 2. Evolution of the kinetic energy for $Re_\lambda = 100$. (\triangleright): DNS reference; (---): LES on 48^3 with $C_s \Delta/h = 0.15$; (-·-): LES on 48^3 without model.

which display error levels as a function of the LES resolution and the subgrid resolution, immediately allow to determine optimal working regions for the LES with respect to the subgrid model and the numerical method. This results in the specification of optimal refinement strategies.

A relative error is determined for each LES run in accordance with eq.(3). Figure 3 represents the accuracy charts based on the relative error in the kinetic energy δ_E for $Re_\lambda = 50$ and $Re_\lambda = 100$. In these plots, the classical refinement strategy towards DNS, i.e., reducing Δ at constant subgrid resolution Δ/h corresponds to refining the LES parallel to the horizontal axis. Grid refinement towards a grid independent LES, i.e., decreasing h at a constant filter width Δ corresponds to refining the grid along a line through the origin. Indeed, at constant Δ and decreasing h , the subgrid resolution $\Delta/h \sim n$. Further, contour levels of the relative error clearly outline unfavorable LES operating regions and more optimal regions. In this context, the optimal trajectory is defined as the curve through the minimal errors at each resolution.

Similarly, accuracy charts can be based on other flow quantities. For small scale properties, such as, e.g., the Taylor length scale, these accuracy charts may differ from those based on δ_E . As an example, with respect to the Taylor length scale, no-model LES is found to be favorable at all resolutions. However, by the very nature of large-eddy simulation one may put a larger emphasis on capturing flow quantities associated with the larger retained scales, such as the kinetic energy, compared to inertial range properties such as the Taylor length scale. This is particularly true in relation to the Smagorinsky model which is known to provide too much dissipation in the smaller retained scales and hence distorts the prediction of these quantities much more than occurs for the larger retained scales.

The identification of optimal strategies for the Smagorinsky model is useful for an optimal set-up of any Smagorinsky LES. In addition, the refinement trajec-

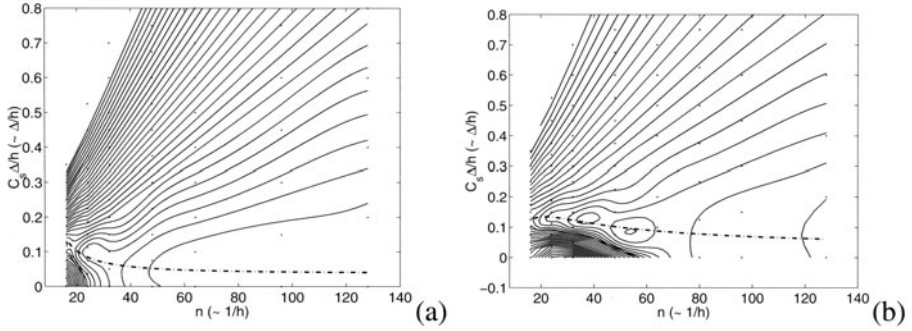


Figure 3. Optimal trajectory and accuracy chart based on δ_E [%]: (a) $Re_\lambda = 50$ and (b) $Re_\lambda = 100$. Optimal refinement trajectory: (—). Contour levels start at 1% (a) (2% (b)) at the lower right contour and increase in steps of 1% (2%). Bullets correspond to locations of individual LES runs.

tories can also be used as a point of reference for the dynamic procedure. In fact, the dynamic Smagorinsky model determines the effective subgrid resolution $C_s \Delta/h$ in a manner that is determined by the flow. In the present LES, the dynamic coefficient is found not to change drastically in time during a simulation. Hence, the dynamic procedure roughly corresponds to the automatic selection of an appropriate fixed coefficient.

Figure 4(a) represents the optimal lines for both Reynolds numbers compared to the dynamic refinement trajectories. Here, the implementation of the dynamic Smagorinsky model corresponds to the revised dynamic procedure Lilly, 1992. The test filter is a top-hat filter implemented with a trapezoidal rule. Clearly, the dynamic procedure overestimates the optimal ‘effective filterwidth’ $C_s \Delta/h$. However, it should be emphasized that the general tendency is similar. In figure 4(b), the errors along the optimal refinement trajectory as well as those along the dynamic model trajectory are displayed for both Reynolds numbers. The dynamic Smagorinsky coefficient resulting from this implementation of the dynamic procedure leads to a suboptimal refinement trajectory. The error related to the dynamic trajectory is roughly twice the minimal error on the ‘optimal refinement trajectory’.

Although results in figure 4 indicate that the dynamic procedure is sub-optimal, it clearly is able to follow the major trends observed in the database results without requiring external ad hoc interference with the model. The adaptation of the coefficient due to variations in the resolution as well as in the Reynolds number corresponds well to the observed variations along the optimal line. This clearly illustrates the strength of the dynamic procedure.

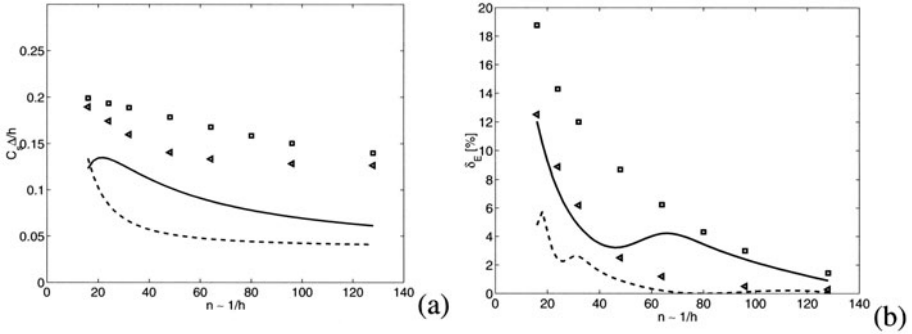


Figure 4. (a) Optimal refinement trajectory versus the refinement trajectory obtained from the dynamic procedure. (b) Errors along the optimal and dynamic refinement trajectories. (both) (—): ‘optimal’ for $Re_{\lambda} = 100$; (---): ‘optimal’ for $Re_{\lambda} = 50$; (□): dynamic for $Re_{\lambda} = 100$; (◁): dynamic for $Re_{\lambda} = 50$.

5. Concluding remarks

A general framework was presented to obtain an overview of the total error arising in practical LES. This leads to the representation of global error behavior in accuracy charts and the determination of optimal refinement trajectories. Results were presented for LES with the Smagorinsky model applied to decaying homogeneous turbulence at two different Reynolds numbers. The optimal refinement strategies obtained from the LES database with the Smagorinsky model formed a good point of reference for the evaluation of the dynamic Smagorinsky model.

The present methodology provides a framework to evaluate large-eddy simulation and allows for a systematic determination of the interaction between sub-grid scale modeling and numerical methods. As such, this framework can be used to support the development and testing of models and numerical methods. Moreover, the knowledge of optimal refinement strategies provides a standard for the development of ‘near-optimal’ dynamic procedures.

Acknowledgments

The authors Johan Meyers and Bernard J. Geurts gratefully acknowledge fruitful discussions with the members of the Turbulence working group Twente. All authors further acknowledge the financial support by FWO-Vlaanderen and support from NCF (National Computing Foundation) to make the extensive simulations possible.

References

- Germano, M. (1992). Turbulence: the filtering approach. *Journal of Fluid Mechanics*, 238:325–336.
- Germano, M., Piomelli, U., Moin, P., and Cabot, W. H. (1991). A dynamic subgrid-scale eddy viscosity model. *Physics of Fluids A*, 3(7).
- Geurts, B. J. (1999). Balancing errors in LES. In Voke, P. R. and Sandham, N. D., editors, *Direct and Large-Eddy Simulation III*, volume 7 of *Ercoftac Series*. Kluwer Academic Publishers.
- Geurts, B. J. and Fröhlich, J. (2002). A framework for predicting accuracy limitations in Large Eddy Simulations. *Physics of Fluids*, 14(6):L41–L44.
- Geurts, B. J. and Holm, D. D. (2003). Regularization modeling for large-eddy simulation. *Physics of Fluids*, 15(1):L13–L16.
- Ghosal, S. (1996). An analysis of numerical errors in large-eddy simulations of turbulence. *Journal of Computational Physics*, 125:187–206.
- Lilly, D. K. (1992). A proposed modification of the Germano subgrid-scale closure method. *Physics of Fluids A*, 4(3).
- Meyers, J., Geurts, B. J., and Baelmans, M. (2003). Database-analysis of errors in large-eddy simulation. *Physics of Fluids*, 15(9):2740–2755.
- Vreman, B. (1995). *Direct and Large-Eddy Simulation of the Compressible Turbulent Mixing Layer*. PhD thesis, Department of Applied Mathematics, University of Twente.
- Vreman, B., Geurts, B., and Kuerten, H. (1996). Comparison of numerical schemes in large-eddy simulations of the temporal mixing layer. *International Journal for Numerical Methods in Fluids*, 22:297–311.

LAMINAR-TURBULENT TRANSITION

2.1 INCOMPRESSIBLE FLOWS

DIRECT NUMERICAL SIMULATIONS OF STREAK BREAKDOWN IN BOUNDARY LAYERS

Luca Brandt and Dan S. Henningson

Department of Mechanics, Royal Institute of Technology (KTH), SE-10044 Stockholm, Sweden

Abstract Numerical simulations of bypass transition in Blasius boundary layers are presented. The breakdown of streamwise streaks is first considered in the case of the steady, spanwise periodic basic flows arising from the nonlinear saturation of optimal perturbations and then in the case of transition in boundary layers subject to free-stream turbulence. Similarity and differences with previous work are discussed.

1. Introduction

1.1 Transition in Blasius boundary layers

1.1.1 Natural transition. Historically, the first approach to transition was the analysis of the stability of a flow. Assuming a wave-like form of the velocity perturbation it reduces to an eigenvalue problem for exponentially growing or decaying disturbances. The first solutions for two-dimensional unstable waves in the Blasius boundary layer were presented by Tollmien, 1929 and Schlichting, 1933. The existence of such solutions (TS-waves) was experimentally shown to exist by Schubauer and Skramstad, 1947.

If an amplified Tollmien–Schlichting wave grows above an amplitude in u_{rms} of 1% of the free-stream velocity, the flow become susceptible to secondary instability. Klebanoff et al., 1962 observed that three-dimensional perturbations, which are present in any natural flow, were strongly amplified. This transition scenario was later denoted as K-type after Klebanoff but also fundamental since the frequency of the secondary, spanwise periodic, fluctuations is the same as the one of the TS-waves. In the nonlinear stages of the K-type scenario, rows of “ Λ -shaped” vortices, aligned in the streamwise directions, have been observed. An other scenario was also observed, first by Kachanov et al., 1977. This is denoted N-type after Novosibirsk, where the experiments were carried out or H-type after Herbert, who performed a theoretical analysis

of the secondary instability of TS-waves (Herbert, 1983). In this scenario, the frequency of the secondary instability mode is half the one of the TS-waves.

1.1.2 Bypass transition. In 1969 Morkovin coined the expression “bypass transition”, noting that “we can bypass the TS-mechanism altogether”. In fact, experiments reveal that many flows, including channel and boundary layer flows, may undergo transition for Reynolds numbers well below the critical ones from linear stability theory. An explanation for this was proposed by Ellingsen and Palm, 1975. They considered, in the inviscid case, an initial disturbance independent of the streamwise coordinate in a shear layer and showed that the streamwise velocity component may grow linearly in time, producing alternating low- and high-velocity *streaks*. Hultgren and Gustavsson, 1981 considered the temporal evolution of a three-dimensional disturbance in a boundary layer and found that in a viscous flow the initial growth is followed by a viscous decay (*transient growth*).

Landahl, 1975 proposed a physical explanation for this growth. A wall-normal displacement of a fluid element in a shear layer will cause a perturbation in the streamwise velocity, since the fluid particle will initially retain its horizontal momentum. An example is weak pairs of quasi streamwise counter rotating vortices are able to lift up fluid with low velocity from the wall and bring high speed fluid towards the wall forcing streamwise oriented *streaks* of high and low streamwise velocity. This mechanism is denoted *lift-up effect* and it is inherently a three-dimensional phenomenon.

From a mathematical point of view, it is now clear that since the linearised Navier–Stokes operator is non-normal for many flow cases (e.g. shear flows), a significant transient growth may occur before the subsequent exponential behaviour (see Schmid and Henningson, 2001). Such growth can exist for sub-critical values of the Reynolds number and it is the underlying mechanism in bypass transition phenomena. In particular, for the Blasius boundary layer, Andersson et al., 1999 and Luchini, 2000 used an optimisation technique to determine which disturbance present at the leading edge gives the largest disturbance in the boundary layer. This *optimal perturbation* was found to consist of a pair of steady streamwise counter-rotating vortices, which induce strong streamwise streaks.

An interesting application of bypass transition is boundary layers in the presence of free-stream turbulence. Inside the boundary layer the turbulence is highly damped, but low frequency oscillations, associated with long streaky structures, appear. The first experimental study of such disturbances is due to Klebanoff, 1971. Arnal and Juillen, 1978 also showed that for free-stream turbulence levels higher than 0.5–1%, the dominant disturbances inside the boundary layer are characterised by low frequencies and they are not TS-waves. Kendall, 1985 denoted these disturbances as Klebanoff modes. As

the streaks grow downstream, they break down into regions of intense randomised flow, turbulent *spots*. The leading edge of these spots travels at nearly the free-stream velocity, while the trailing edge at about half of the speed; thus a spot grows in size and merges with other spots until the flow is completely turbulent. Westin et al., 1994 presented detailed measurements of a laminar boundary layer subjected to free-stream turbulence and showed how different experiments with apparently similar conditions can disagree on the location and extent of transition. A recent review on the experimental studies of boundary-layer transition induced by free-stream turbulence can be found in Matsubara and Alfredsson, 2001, while the first numerical simulations are presented in Jacobs and Durbin, 2001.

2. Direct numerical simulations

2.1 Numerical method

The direct numerical simulations presented here have all been performed with the pseudo-spectral algorithm described in Lundbladh et al., 1999. The numerical code used solves the three-dimensional, time-dependent, incompressible Navier-Stokes equations. The algorithm uses Fourier representation in the streamwise and spanwise directions and Chebyshev polynomials in the wall-normal direction, together with a pseudo-spectral treatment of the non-linear terms. The time advancement used is a four-step low-storage third-order Runge–Kutta method for the nonlinear terms and a second-order Crank–Nicolson method for the linear terms. Aliasing errors from the evaluation of the nonlinear terms are removed by the $\frac{3}{2}$ -rule when the FFTs are calculated in the wall parallel plane. In order to set the free-stream boundary condition closer to the wall, a generalisation of the boundary condition used by Malik et al., 1985 is employed. It is an asymptotic condition applied in Fourier space with different coefficients for each wavenumber that exactly represents a potential flow solution decaying away from the wall.

To correctly account for the downstream boundary layer growth a spatial technique is necessary. This requirement is combined with the periodic boundary condition in the streamwise direction by the implementation of a “fringe region”, similar to that described by Bertolotti et al., 1992. In this region, at the downstream end of the computational box, the function $\lambda(x)$ in equation (1) is smoothly raised from zero and the flow is forced to a desired solution \mathbf{v} in the following manner,

$$\frac{\partial \mathbf{u}}{\partial t} = NS(\mathbf{u}) + \lambda(x)(\mathbf{v} - \mathbf{u}) + \mathbf{g}, \quad (1)$$

$$\nabla \cdot \mathbf{u} = 0, \quad (2)$$

where \mathbf{u} is the solution vector and $NS(\mathbf{u})$ the right hand side of the (unforced) momentum equations. Both \mathbf{g} , which is a disturbance forcing, and \mathbf{v} may depend on the three spatial coordinates and time. The forcing vector \mathbf{v} is smoothly changed from the laminar boundary layer profile at the beginning of the fringe region to the prescribed inflow velocity vector. This method damps disturbances flowing out of the physical region and smoothly transforms the flow to the desired inflow state, with a minimal upstream influence (see Nordström et al., 1999 for an investigation of the fringe region technique).

2.2 Disturbance generation

Using this numerical code, disturbances can be introduced in the laminar flow by including them in the flow field \mathbf{v} , thereby forcing them in the fringe region; by a body force \mathbf{g} , and by blowing and suction at the wall through non homogeneous boundary conditions. The first of these three methods is the most used in the simulations presented here. In fact, to study the instability and breakdown of steady, spanwise periodic streaks, the velocity fields \mathbf{v}_s and \mathbf{v}_d are added to the Blasius solution \mathbf{v}_0 to give a forcing vector of the form $\mathbf{v} = \mathbf{v}_0 + \mathbf{v}_s + \mathbf{v}_d e^{i\omega t}$. \mathbf{v}_s represents the steady streaks: the linear optimal ones computed by Andersson et al., 1999 are forced at the inflow. The time periodic disturbance \mathbf{v}_d is an instability mode riding on the streak which is used to simulate the full transition process of a steady streak in Brandt and Henningson, 2002.

To simulate a boundary layer under free-stream turbulence a more involved methodology has been implemented. Following Jacobs & Durbin (2001), a turbulent inflow is described as a superposition of modes of the continuous spectrum of the linearised Orr-Sommerfeld and Squire operators. These modes have also been added to the forcing vector \mathbf{v} and thus introduced in the fringe region. Isotropic grid turbulence can be reproduced by a sum of Fourier modes with random amplitudes (Rogallo, 1981); however in the presence of an inhomogeneous direction an alternative complete basis is required; in particular, in the present case, the new basis functions need to accommodate the wall. A natural choice is therefore the use of the modes of the continuous spectrum (Grosch and Salwen, 1978). A three-dimensional wave-vector $\kappa = (\alpha, \gamma, \beta)$ can be associated to each eigenfunction of the continuous spectrum: The streamwise and spanwise wave numbers α and β are defined by the normal mode expansion in the homogeneous directions of the underlying linear problem while the wall-normal wavelength is determined by the eigenvalue along the continuous spectrum. Invoking Taylor's hypothesis, the streamwise wavenumber α can be replaced by a frequency $\omega = \alpha U_\infty$ and the expansion may be written

$$u = \sum A_N \hat{u}_N(y) e^{(i\beta z + i\alpha x - i\omega t)},$$

where the real values of β and ω and the complex wavenumber α are selected according to the procedure described below. Note that the desired wall-normal wavenumber γ enters through the eigenfunction shape $\hat{u}_N(y)$ and it is defined by the eigenvalue α . In particular, the wave numbers pertaining to the modes used in the expansion are selected by defining in the wavenumber space (ω, γ, β) a number of spherical shells of radius $|\kappa|$. 40 points are then placed randomly but at equal intervals on the surface of these spheres. The amplitude $|A_N|$ is in fact the same for all modes on each shell and reproduces the following analytical expression for a typical energy spectrum of homogeneous isotropic turbulence

$$E(\kappa) = \frac{2}{3} \frac{a (\kappa L)^4}{(b + (\kappa L)^2)^{17/6}} L T u. \quad (3)$$

In the expression above, Tu is the turbulence intensity, L a characteristic integral length scale and a, b two normalisation constants. The methodology briefly introduced here is able to satisfactorily reproduce a boundary layer subject to free-stream turbulence as documented in Brandt et al., 2002b and Brandt, 2003.

3. Instability and breakdown of steady optimal streaks

3.1 Steady saturated streaks

The analysis performed here concerns the linear secondary stability of the streaks resulting from the nonlinear evolution of the spatial optimal perturbation in a Blasius boundary layer. The base flows under consideration are computed by solving the full Navier-Stokes equations (see Andersson et al., 2001). In particular, the complete velocity field representing the initial evolution of the steady, spanwise periodic, linear optimal perturbations calculated by Andersson et al., 1999, is forced in the fringe region as described in the previous section. To quantify the size of this primary disturbance at each streamwise position, an amplitude A is defined as

$$A(X) = \frac{1}{2} \left[\max_{y,z} \left(U(X, y, z) - U_B(X, y) \right) - \min_{y,z} \left(U(X, y, z) - U_B(X, y) \right) \right], \quad (4)$$

where $U_B(x, y)$ is the Blasius profile and $U(X, y, z)$ is the total streamwise velocity in the presence of streaks and they are made non dimensional with respect to the free-stream velocity U_∞ .

The downstream amplitude development is displayed in figure 1(a) for the set of upstream amplitudes considered. The abscissa X in the figure indicates

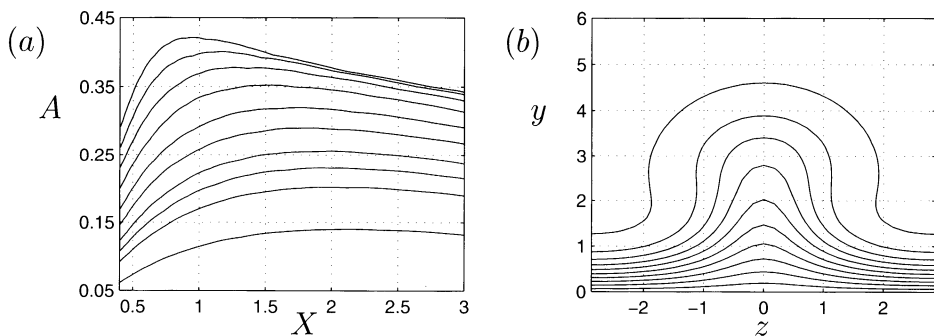


Figure 1. (a) Downstream development of the streak amplitude A versus streamwise coordinate X for different upstream amplitudes A_0 . (b) Streamwise velocity contour plot of the nonlinear base flow in a (y, z) cross-stream plane at $X = 2$, $A = 0.36$. The coordinates have been made non-dimensional using the local Blasius length scale δ . Maximum contour level 0.98, contour spacing 0.1.

the distance from the leading edge and it is divided by the reference length L , where $L = 1$ is the station at which the linear growth of the upstream streamwise vortices has been optimised (Andersson et al., 1999). The spanwise wavenumber $\beta = 0.45$ is the optimal one and it is scaled with respect to the local Blasius length $\delta = \sqrt{x\nu/U_\infty}$ at position $x = L$. In figure 1(b), a typical nonlinearly saturated streak is illustrated by its streamwise velocity contour plot in the cross-stream (y, z) plane. Regions of strong spanwise shear are formed on the sides of the low-speed region, which is also displaced further away from the wall during the saturation process.

3.2 Streak instability

If the amplitude of the streak grows to a sufficiently high value, instabilities can develop which may provoke early breakdown and transition to turbulence despite the predicted modal decay of the primary disturbance. A possible secondary instability is caused by inflectional profiles of the base flow velocity, a mechanism which does not rely on the presence of viscosity. This has been seen in Görtler vortices (Swearingen and Blackwelder, 1987, Park and Huerre, 1995; Bottaro and Klingmann, 1996) and in channel flow (Waleffe, 1995; Waleffe, 1997, Reddy et al., 1998, Elofsson et al., 1999).

The secondary instability of the steady, spanwise periodic streaks is studied under the assumptions that the basic flow will consist only of the parallel streamwise velocity U . This basic parallel flow is extracted at different streamwise stations X from the spatial numerical simulations presented in figure 1.

The equations governing the linear evolution of a perturbation velocity $\mathbf{u}(x, y, z, t) = (u, v, w)$, of corresponding pressure p , on the streak profile

$U(y, z)$ are obtained by substituting $U + \mathbf{u}$ into the Navier-Stokes equations and neglecting the quadratic terms in the perturbation. The marginal condition for streak instability is investigated here under the assumption of inviscid flow. If viscosity is neglected it is possible to find an uncoupled equation for the perturbation pressure (Henningson, 1987; Hall and Horseman, 1991)

$$\left(\frac{\partial}{\partial t} + U \frac{\partial}{\partial x}\right) \Delta p - 2U_y p_{xy} - 2U_z p_{xz} = 0. \quad (5)$$

This equation governs the linear stability of a parallel streak.

Since the flow is assumed parallel, solution can be sought in the form of streamwise waves. Further, due to the spanwise periodicity of the flow, Floquet theory can be applied (e.g. Nayfeh and Mook, 1979). As a consequence, for any flow quantity q , the instability modes of the basic flow U of spanwise wavelength $\lambda_z = 2\pi/\beta$ may be expressed in the form

$$p(x, y, z, t) = \tilde{p}(y, z) e^{i[\alpha x + \theta z - \omega t]}, \quad (6)$$

where \tilde{p} is spanwise periodic and it has the same periodicity λ_z of the basic flow. α , the streamwise wavenumber, and ω , the circular frequency, can assume complex values; θ is a real detuning parameter or Floquet exponent. Due to the spanwise symmetry of the basic streak profile $U(y, z)$ (see figure 1b), the modes can be divided into separate classes according to their odd or even symmetry. Further, it is sufficient to study values of the parameter θ between zero and π/λ_z , with $\theta = 0$ corresponding to a *fundamental* instability mode of spanwise wavelength λ_z and $\theta = \pi/\lambda_z$ corresponding to a *subharmonic* mode of wavelength twice that of the underlying streak. Symmetric and antisymmetric modes are called varicose and sinuous respectively, with reference to the visual appearance of the motion of the low-speed streak.

Since the flow has been assumed inviscid, a single control parameter, the streak amplitude A , is allowed to vary and the marginal condition for the instability reduces to a *neutral curve* in the (α, A) plane. The curves obtained are displayed in figure 2 for the fundamental and subharmonic sinuous symmetries. The dashed lines in the plots represent contour levels of positive growth rates. These results are obtained with the streak profiles extracted at $x = 2$ in figure 1(a), where the primary disturbance has saturated and, for the cases with lower initial energy, the streak amplitude achieves its maximum value. It is immediately observed that a streak amplitude of about 26% of the free-stream velocity is needed for an instability to occur. This critical value is much larger than the threshold amplitude for the secondary instability of Tollmien-Schlichting waves (1 – 2%) and roughly around the value of about 20% reported from the experimental study of Bakchinov et al., 1995. Similarly, in

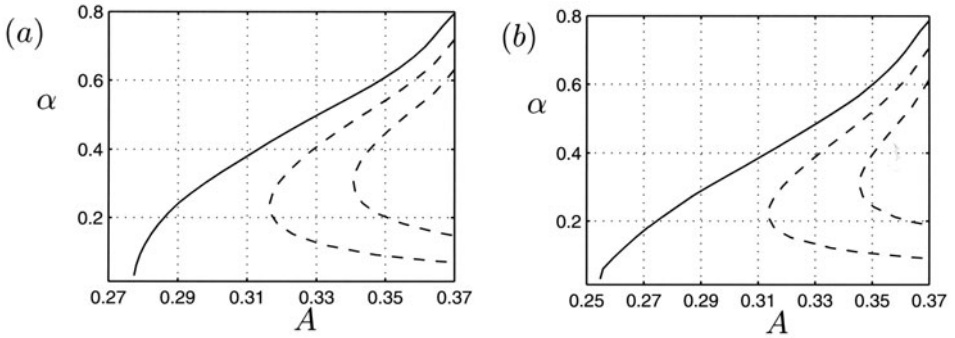


Figure 2. Neutral curves for streak instability in the (α, A) plane (solid line) for fundamental (a) and subharmonic (b) sinuous modes. The dashed lines represent contour levels of positive growth rates $\omega_i = 0.008$ and $\omega_i = 0.016$. The data have been made non-dimensional using the local Blasius length scale δ .

the case of plane Poiseuille flow, Elofsson et al. (1999) have shown that the threshold amplitude for streak breakdown is 35% of the centre line velocity. It can also be noticed from the figure that the subharmonic mode is unstable for lower amplitudes than the fundamental mode. When increasing the amplitude, not only do the growth rates increase but their maxima are also shifted towards larger values of the wavenumber α . For values of A larger than 0.3 the fundamental symmetry has slightly larger growth rates.

On the other hand, the varicose modes are unstable only for amplitudes larger than $A = 0.37$, with growth rates smaller than one fifth of the corresponding sinuous growth rates. From the results presented, it seems more likely that the transition of the considered steady optimal streaks is triggered by a sinuous instability, either of fundamental or subharmonic type. The common feature of the two scenarios is the spanwise oscillation of the low-speed streak.

3.3 Streak breakdown

The full transition scenario resulting from the fundamental sinuous instability is studied by forcing the saturated streaks and one of the instability modes of highest spatial growth rate as inflow perturbation in the fringe region of the numerical code.

First, the perturbation velocity fields obtained at each streamwise station are transformed in time and in the spanwise direction to Fourier space. To present the results, the notation (ω, β) is used, where ω and β are the frequency and spanwise wavenumber each normalised with the fundamental frequency and wavenumber of the secondary instability mode. In the present analysis we therefore consider the amplitude of the spanwise Fourier components of the periodic eigenfunction $\tilde{q}(y, z)$ and of its harmonics in time. The downstream

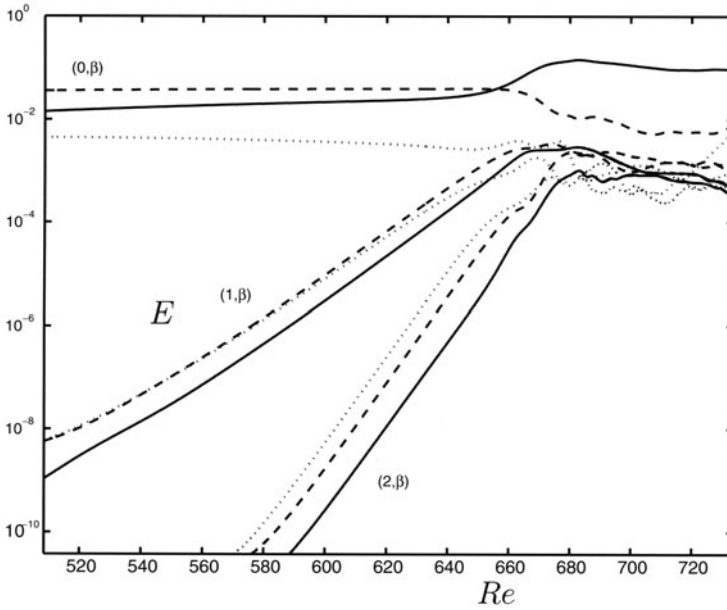


Figure 3. Energy in different Fourier modes (ω, β) versus the Reynolds number. Frequencies: zero (streaks), one (secondary instability), two (higher harmonic). —, $\beta = 0$; - - -, $\beta = 1$; \cdots , $\beta = 2$.

energy growth in some selected time and spanwise Fourier modes is displayed in figure 3. The zero-frequency mode, i.e. the streak, and the secondary instability ($\omega = 1$) are present at the beginning of the computation, while the higher harmonics ($\omega > 1$) are excited as the flow evolves downstream.

It can be seen in figure 3 that the energy content is of the same order for modes of different spanwise wave numbers but same frequency. This is due to the fact that the streak develops to a highly nonlinear stage before it becomes unstable to time-dependent disturbances. Therefore the harmonics in β are generated during the streak growth and they are responsible for the large spanwise shear of the flow. The instability of the streaks is characterised by modes localised in the spanwise direction so that a number of spanwise wave numbers is needed to correctly capture it. The growth in the different modes starts to saturate around position $Re = 650$ and soon the energy become of the same order for the different frequencies.

Vortical structures can be identified in the flow by plotting regions of low pressure, or, alternatively, regions where the second largest eigenvalue λ_2 of the Hessian of the pressure assumes negative values (Jeong et al., 1997). Both quantities enable to locate regions of strong rotational fluid motion. A top and side view of the flow structures characteristic of the late stages of the sinuous streak breakdown are shown in figure 4. The dark gray isosurfaces represent

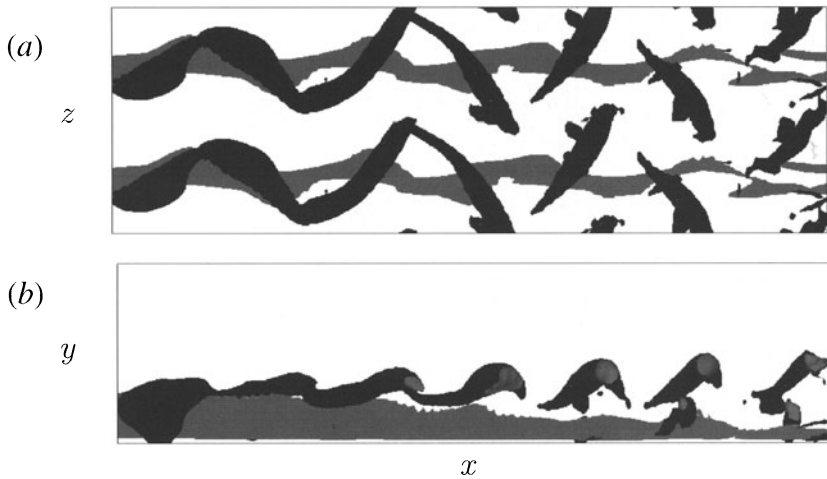


Figure 4. (a) Top and (b) side view of the structures at the late stages of transition. Lighter grey represents negative streamwise velocity perturbation and dark grey regions of low pressure. In (a) two spanwise streaks are displayed.

low-pressure regions while the low-speed streak is depicted with lighter grey. The main structures observed consist of quasi streamwise vortices located on the flanks of the low-speed streak, which is oscillating in the spanwise direction. Vortices of alternating sign are overlapping in the streamwise direction in a staggered pattern and they are symmetric counterparts, both inclined away from the wall and tilted in the downstream direction toward the middle of the undisturbed low-speed region. The strength and extent of these vortices and the spanwise motion of the low-speed streak increase downstream. It is also evident from the top view that the downstream end of the streamwise vortices, located in the outer part of the boundary layer, is tilted in the spanwise direction to form arch vortices.

It is interesting to note that the single streamwise vortex observed in figure 4 show similarities to the leg of the Λ -structures seen in transition initiated by TS-waves (e.g. Rist and Fasel, 1995; Bake et al., 2002) and in oblique transition (Berlin et al., 1999). In fact, in the latter scenarios, positive and negative streamwise vortices are also present on the side of the low-speed region but they are not staggered in the streamwise direction. Instead the left and right streamwise vortices join at the centre of the streak and form the typical Λ -structures. The different relative position of the streamwise vortices is found to depend on the symmetry of the streamwise vorticity of the secondary instability mode. In the present case, the vorticity disturbance is symmetric, while in oblique transition and TS-wave induced transition the streamwise vorticity is antisymmetric.

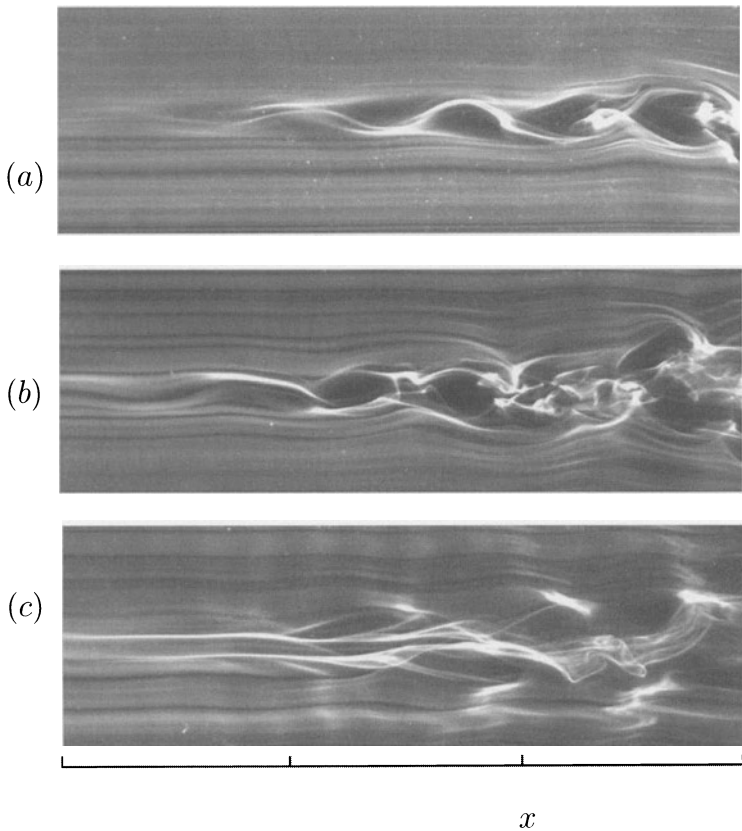


Figure 5. Visualisation of the development of the antisymmetric streak instability mode (60 Hz). Smoke is released at three different distances from the flat plate: (a), $y = 4$ mm; (b), $y = 3$ mm; (c), $y = 2$ mm. Figure 16 from Asai et al., 2002.

3.3.1 Comparison with other experimental and numerical results on streak breakdown. In order to study if and how the streak instability can operate as a dominant mechanism in transitional and turbulent flows, Asai et al., 2002 examined experimentally the instability characteristics and the resulting generation of coherent vortices for a single low-speed streak produced in a laminar boundary layer by setting a small piece of screen normal to the wall. Time-harmonic symmetric and antisymmetric modes are excited separately. A flow visualisation of the antisymmetric sinuous instability is reported here in figure 5. The three photographs show a top view of the flat plate, with smoke released from a wire stretched in the spanwise direction. It can be seen that the instability waves lead to the meandering of the low-speed streak. This results in the generation of a train of quasi-streamwise vortices with vorticity of alternate sign as in the numerical results (cf. figure 4).

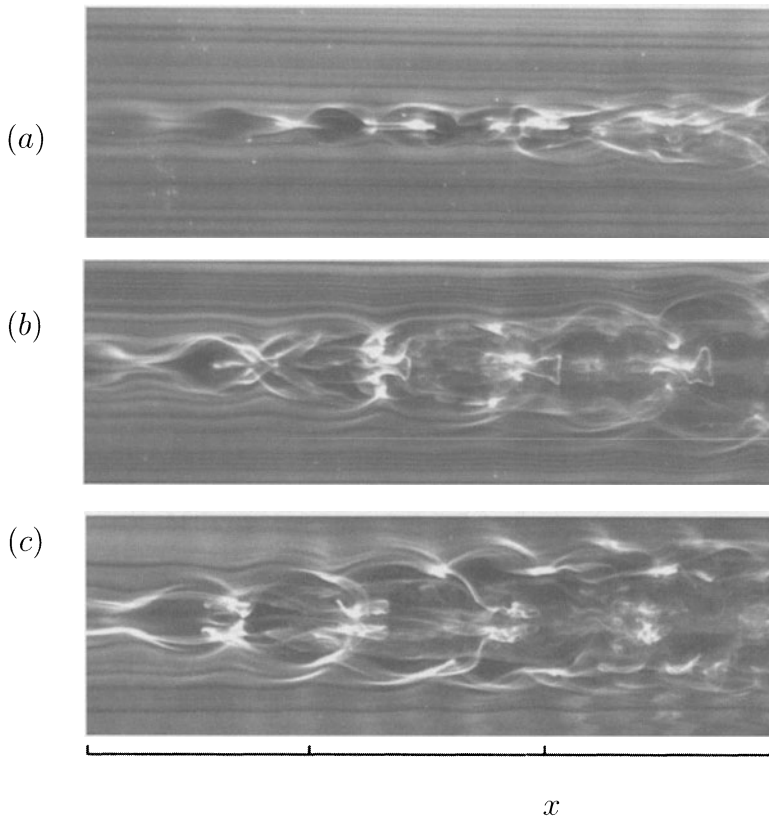


Figure 6. Visualisation of the development of the symmetric streak instability mode (110 Hz). Smoke is released at three different distances from the flat plate: (a), $y = 4$ mm; (c), $y = 3$ mm; (c), $y = 2$ mm. Figure 15 from Asai et al., 2002.

Asai et al., 2002 observed also that for a streak width larger than the spanwise shear-layer thickness, the low-speed streak becomes more unstable to symmetric (varicose) modes. It is clearly shown in the smoke visualisation in figure 6 that the growth of the symmetric mode leads to the formation of hairpin vortices with a pair of counter-rotating streamwise vortices.

4. Transition in boundary layers subjected to free-stream turbulence

Flow visualisations and analogies with transition in vortex-dominated flows led to believe that transition in boundary layers subjected to free-stream turbulence proceeds via the breakdown of the streaks induced inside the boundary layer. This motivated the studies presented in the first part of the review, where the streak transition is analysed in the simpler case of a steady spanwise-periodic

configuration. Here, simulations of a boundary layer subjected to free-stream turbulence are presented, where a synthetic turbulent inflow is generated by the procedure outlined earlier.

4.1 Receptivity

The occurrence of streamwise elongated structures in boundary layers subject to free-stream turbulence was first identified by Klebanoff, 1971 in terms of low-frequency oscillations in hot wire signals caused by slow spanwise motions of the streaks. However, the first theoretical explanations of this phenomenon were proposed about 25 years later. Bertolotti, 1997 has assumed as initial disturbances vortical modes, solutions of the linearised Navier-Stokes equations in the free stream, which are waves periodic in the spanwise direction and decaying in the streamwise. He has found receptivity to modes with zero streamwise wavenumber and has shown that the streak growth is connected to the theories of non-modal growth. Essentially the same linear mechanism for streak generation caused by the diffusion of a free-stream streamwise vortex into the boundary layer has been studied by Andersson et al., 1999 and Luchini, 2000 using the boundary layer approximation and by Wundrow and Goldstein, 2001 by means of asymptotic expansions. These studies assume the presence of the vortex at the leading edge show that the growth of the streak amplitude is proportional to the Reynolds number Re .

Besides these linear models, Berlin and Henningson, 1999 and Brandt et al., 2002a have proposed a nonlinear mechanism. Numerical simulations have in fact shown that oblique waves in the free stream can interact to generate streamwise vortices, which, in turn, induce streaks inside the boundary layer. The two mechanisms are compared by means of DNS to try to identify which of the two can be considered as the most relevant in cases with known free-stream perturbations. In order to do so different levels of free-stream turbulence intensity are considered and, moreover, the free-stream turbulence generation is manipulated in order to involve few or many modes with very low values of the frequency ω . In this way, we are able to control the amount of low-frequency perturbation part of the inflow turbulence. As shown by Hultgren and Gustavsson, 1981 among others, modes of the continuous spectra with very low values of α and ω do not feel the shear layer and they are therefore not zero inside the boundary layer.

The wall-normal maximum of the streamwise velocity perturbation induced inside the boundary layer is displayed in figure 7 versus the local Reynolds number for six cases considered. The results in figure 7(a) pertain to three different free-stream turbulence levels, $Tu = 4.7\%$, $Tu = 3\%$ and $Tu = 1.5\%$, with integral length scale $L = 7.5\delta_0^*$, where δ_0^* is the boundary-layer displacement thickness at the inlet of the computational domain ($Re_{\delta_0^*} = 300$). For all

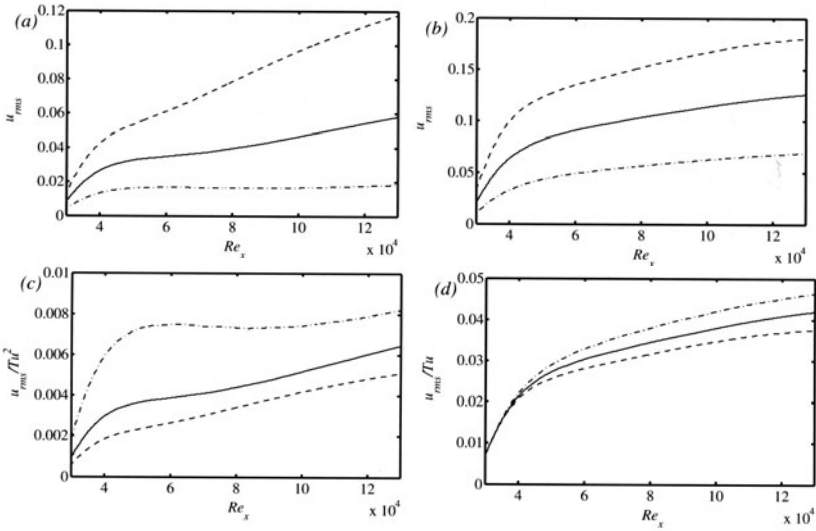


Figure 7. Streamwise evolution of the wall-normal maximum of u_{rms} for three levels of free-stream turbulence intensity: ---, $Tu = 4.7\%$; —, $Tu = 3\%$ and - · -, $Tu = 1.5\%$. The results in (a) pertain to the case of few low-frequency modes as part of the inflow perturbation spectrum, while the data in (b) to a free-stream turbulence spectrum rich with low-frequency modes. (c): The same rms -values as in (a) are scaled with the square of the free-stream turbulence intensity Tu . (d): The same rms -values as in (b) are scaled with the free-stream turbulence intensity Tu .

cases only few modes characterised by low frequency are introduced as part of the inflow perturbation spectrum. It is shown in figure 7(c) that by dividing the u_{rms} values in figure 7(a) with the square of the turbulence intensity Tu , the growth of the perturbation follows, after an initial phase, almost parallel lines. This is more evident in the case of largest intensities. Therefore the dominating receptivity mechanism is the nonlinear one (see Brandt, 2003 for more details). The results in figure 7(b) pertain to cases with the same free-stream turbulence levels and integral length scale, but this time the perturbation spectrum is characterised by many low-frequency modes, as shown by the high u_{rms} -values already at the inlet of the computational domain. In this case, the streaks formed in the boundary layer further downstream are stronger than before; the u_{rms} scales linearly with the perturbation intensity Tu (see figure 7d) and the receptivity mechanism responsible for the streak growth is the linear one. From the results in the figure it is possible to conclude that the linear mechanism is the most relevant if the free-stream turbulence contains significant low-frequency modes.

4.2 Effect of the integral length scales of the free-stream turbulence

Simulations have then been performed to follow the subsequent breakdown and transition to turbulence. Results are presented for three cases. In all of them the inlet of the computational box is at $Re_{\delta_0^*} = 300$ ($Re_{x_0} = 30000$) and the free-stream turbulence intensity is 4.7%. Different integral length scales of the inflow turbulence have been used, that is $L = 2.5 \delta_0^*$, $L = 5 \delta_0^*$ and $L = 7.5 \delta_0^*$ where L is related to the longitudinal two-point correlation as $L_{11} = 0.643L$.

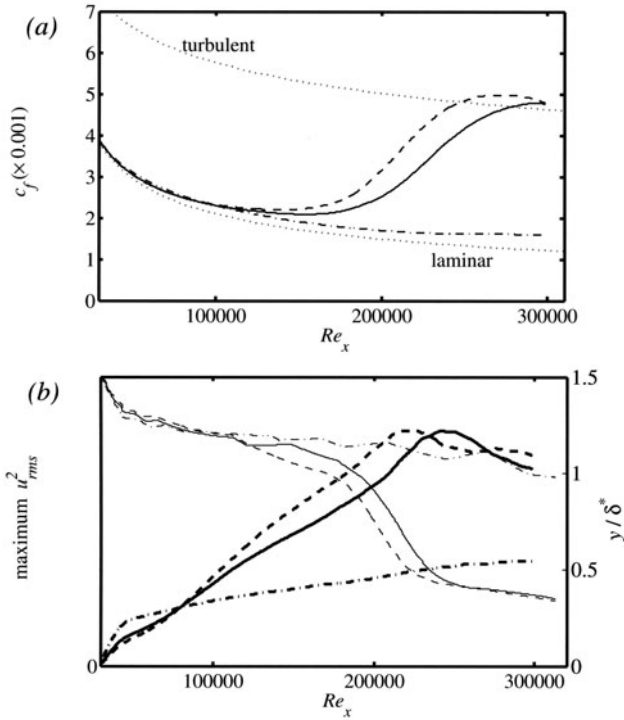


Figure 8. (a) Skin friction coefficient, (b) maximum u_{rms}^2 (thick lines) and its wall-normal position (thin lines), and (c); plotted for $L = 7.5\delta_0^*$ (dashed line), $L = 5\delta_0^*$ (solid line) and $L = 2.5\delta_0^*$ (dash-dotted line).

Some of the data obtained by averaging in time and in the spanwise direction are displayed in figure 8. The friction coefficient is shown in figure 8(a); also the values for a laminar and a turbulent boundary layer are displayed for comparison. For the case with the smallest integral length scale transition does not occur within the computational domain, while the transition location is at lower Re_x for $L = 7.5\delta_0^*$, in agreement with the experimental findings in Jonáš et al., 2000. In figure 8(b) the maximum u_{rms}^2 at each downstream

position is depicted to show the evolution of the streaks. In all cases the energy of the streaks is proportional to the distance from the leading edge, as observed in the experiments, and the growth is initially largest in the case of $L = 2.5 \delta_0^*$, indicating that the smallest scales penetrate easier into the boundary layer. However, this growth can not be sustained as in the other cases. In fact, the free-stream turbulence decays faster for smaller L and therefore it is less effective in continuously forcing the streaks along the plate. In figure 8(a) the wall-normal position of maximum u_{rms} is also shown. This is reported in units of δ^* , the local boundary-layer displacement thickness. The laminar streaks have a maximum at about $y = 1.3\delta^*$, while their turbulent counterparts are located much closer to the wall. In addition, the spanwise scales observed are in agreement with the experimental results in Matsubara and Alfredsson, 2001.

4.3 Turbulent spot generation

A snapshot of the flow is shown in figure 9 where the instantaneous streamwise and spanwise velocities are plotted in a plane parallel to the wall. The overall picture of the transition scenario can be deduced from the figure. Starting from the inlet position, the perturbation in the boundary layer appears mainly in the streamwise velocity component, in the form of elongated structures. Patches of irregular motion are seen to appear further downstream; these are more evident in the spanwise component. As they travel downstream, the spots become wider and longer. Note also that laminar streaks can be observed downstream of the spots. The turbulent region at the end of the domain is created by the enlargement and merging of the various spots and therefore the streamwise position at which the flow is turbulent varies with time; the turbulent flow is convected downstream and it would not be seen if new spots were not formed all the time.

The breakdown is analysed in detail by looking at the instantaneous three-dimensional flow configurations for a number of spots, tracing back in time the location of their formation. An important feature of the spot precursors, observed in all cases considered, is the presence of regions of positive and negative wall-normal and spanwise velocity arranged in a quasi-periodic array. Such quasi regular distribution of the cross-stream velocity components is responsible for the observed wavy motions of the streaks preceding the breakdown. Visual inspection of many velocity fields enabled to classify the type of breakdown occurring on the streaks by considering the spanwise symmetry of the wall-normal and spanwise velocities and their position relative to the underlying streak.

The flow structures at the incipient spot stage resemble very much those observed in previous study on the breakdown of steady symmetric streaks, both

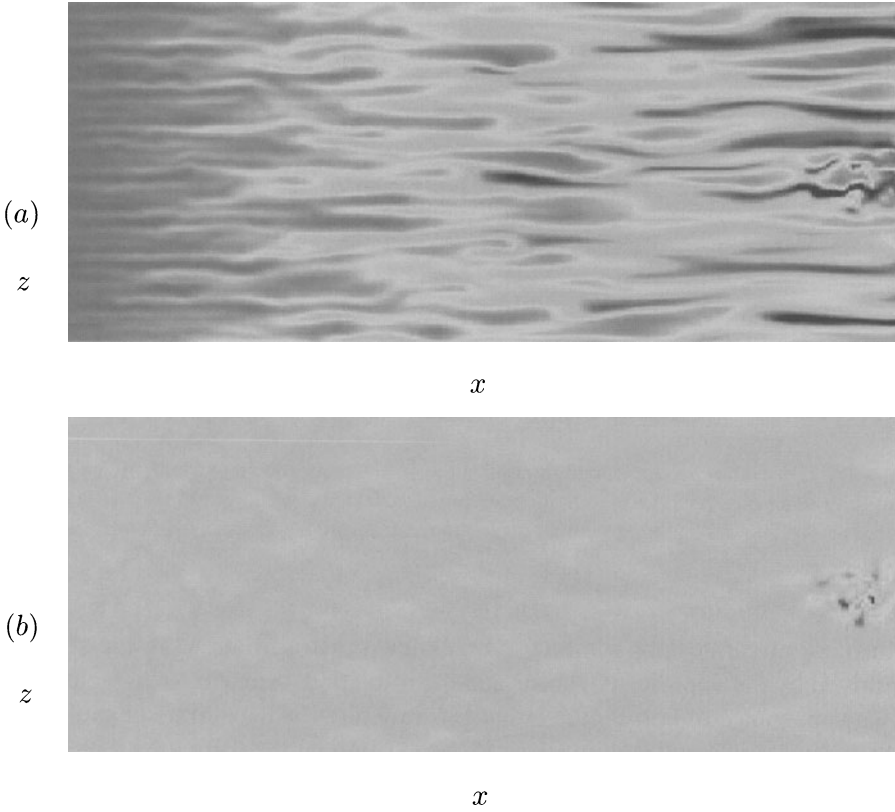


Figure 9. (a) Instantaneous streamwise velocity and (b) spanwise velocity (bottom figure) in a plane parallel to the wall at $y/\delta_0^* = 2$. The plots are not at the actual scale since the domain depicted is 900 units long and 90 units wide in terms of δ_0^* . The fringe region is not shown.

in the case of the scenario following a sinuous instability, see Brandt and Henningson, 2002, and in the case of a varicose scenario, see the experiments by Asai et al., 2002. The similarity with either of the two cases is observed in all spots under consideration.

In the case of the sinuous breakdown, a single low-speed streak undergoes spanwise antisymmetric oscillations, with strong high-frequency perturbation velocity located in the region of largest spanwise shear between the low- and high-speed streaks. An instantaneous flow configuration for this type of scenario is displayed in figure 10. The characteristic vortical structures, represented in dark gray by negative values of the eigenvalue λ_2 , consist of quasi-streamwise vortices located on the flanks of the low-speed streak (depicted here in gray colour). Vortices of alternating sign are overlapping in the streamwise direction in a staggered pattern, exactly as observed in figure 4 for the breakdown of a periodic array of steady streaks.

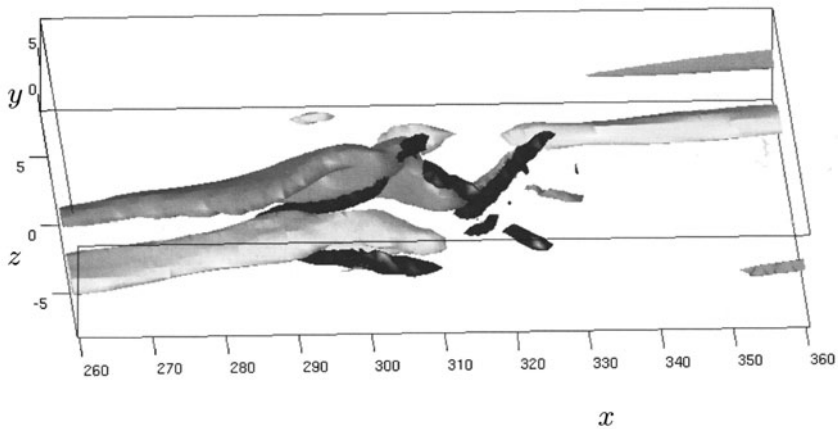


Figure 10. Instantaneous flow configuration at the sinuous breakdown of a streamwise streak. Light gray represents positive perturbation streamwise velocity, while gray indicates the low-speed streak. The dark gray structures are regions of negative λ_2 , used to identify vortical structures.

In the case of varicose or symmetric breakdown the oscillations of the streaks are driven by the wall-normal shear and the transition scenario is characterised by the appearance of horse-shoe or hairpin structures. An example of such vortical structures is displayed in figure 11. One can note the formation of hairpin vortices, with pairs of counter-rotating quasi-streamwise vortices joining in the middle of the streak, pointing alternatively upstream and downstream. The streaks generated by free-stream turbulence are obviously not symmetric and the perturbations riding on them are not symmetric either; however the velocity components of the high-frequency oscillations show almost the same pattern with respect to the mean shear of the streaks as in the model studies mentioned above. In particular, for the 'quasi-sinuuous' breakdown, it is observed that, for a significant number of spots considered, only streamwise vortices of same sign are clearly identified on one flank of the low-speed region. In these cases, in fact, the spanwise shear is sufficiently high only on one side of the low-speed streak. From the analysis of flow visualisations and animations, it is further noticed how the interaction between low- and high-speed streaks plays an important role for the formation of incipient spots. It can be seen in figure 11, for example, how the interaction of the low-speed streak with a fast-moving incoming region of high streamwise velocity is the triggering cause of the instability leading to the formation of the hairpin vortices. It is observed in experiments (Lundell and Alfredsson, 2003) that the streaks are tilted downstream so as the front part is located in the upper part of the boundary layer whereas the rear part is located closer to the wall. Such a structure is growing in the streamwise direction while convected downstream. As a con-

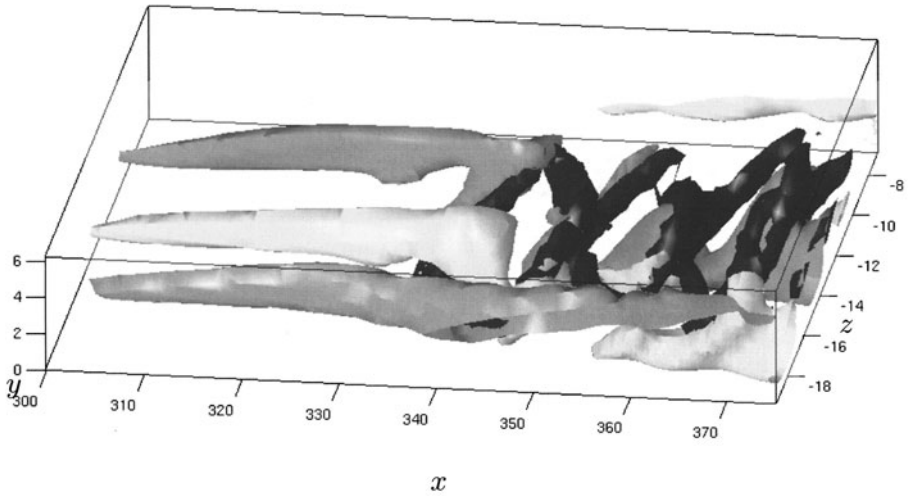


Figure 11. Instantaneous flow configuration at the varicose breakdown of a streamwise streak. Light gray represents positive perturbation streamwise velocity, while gray indicates the low-speed streak. The dark gray structures are regions of negative λ_2 , used to identify vortical structures.

sequence, highly inflectional wall-normal velocity profiles are induced by the high-speed region when reaching the tail of the low-speed region ahead, which thus becomes the site of a local instability. Similarly, the antisymmetric type of breakdown is induced whenever high-speed fluid is approaching a low-speed region on a side. In this case, an inflectional profile is forming in the spanwise direction (see figure 10). Note also that the streaks are not perfectly aligned in the streamwise direction but they slowly oscillates in the boundary layer.

It is finally important to note that the antisymmetric sinuous breakdown is found to be the most likely to occur; it is observed in 16 of the 28 spots considered. From the results presented one may conclude that the breakdown is related to local instabilities associated to the strong shear of the streaks; the fact that almost identical structures are observed in the case of transition induced by free-stream turbulence and in the previous model studies on streaks leads to believe that the relevant physics has correctly been captured by these studies on the breakdown of steady symmetric streaks.

Acknowledgments

This review is to a large degree based on the work presented in the Ph.D. thesis of Luca Brandt. The authors wish to acknowledge the collaboration with Philipp Schlatter, now at the Institute of Fluid Dynamics, ETH Zürich

References

- Andersson, P., Berggren, M., and Henningson, D. S. (1999). Optimal disturbances and bypass transition in boundary layers. *Phys. Fluids*, 11:134–150.
- Andersson, P., Brandt, L., Bottaro, A., and Henningson, D. S. (2001). On the breakdown of boundary layers streaks. *J. Fluid Mech.*, 428:29–60.
- Arnal, D. and Juillen, J. C. (1978). Contribution expérimentale à l'étude de la réceptivité d'une couche limite laminaire à la turbulence de l'écoulement général. Rapport Technique 1/5018, ONERA.
- Asai, M., Minagawa, M., and Nishioka, M. (2002). The instability and breakdown of a near-wall low-speed streak. *J. Fluid Mech.*, 455:289–314.
- Bakchinov, A. A., Grek, G. R., Klingmann, B. G. B., and Kozlov, V. V. (1995). Transition experiments in a boundary layer with embedded streamwise vortices. *Phys. Fluids*, 7:820–832.
- Bake, S., Meyer, D. G. W., and Rist, U. (2002). Turbulence mechanism in Klebanoff-transition: a quantitative comparison of experiment and direct numerical simulation. *J. Fluid Mech.*, (459):217–243.
- Berlin, S. and Henningson, D. S. (1999). A nonlinear mechanism for receptivity of free-stream disturbances. *Phys. Fluids*, 11(12):3749–3760.
- Berlin, S., Wiegel, M., and Henningson, D. S. (1999). Numerical and experimental investigations of oblique boundary layer transition. *J. Fluid Mech.*, 393:23–57.
- Bertolotti, F. P. (1997). Response of the Blasius boundary layer to free-stream vorticity. *Phys. Fluids*, 9(8):2286–2299.
- Bertolotti, F. P., Herbert, Th., and Spalart, P. R. (1992). Linear and nonlinear stability of the Blasius boundary layer. *J. Fluid Mech.*, 242:441–474.
- Bottaro, A. and Klingmann, B. G. B. (1996). On the linear breakdown of Görtler vortices. *Eur. J. Mech. B/Fluids*, 15:301–330.
- Brandt, L. (2003). *Numerical studies of bypass transition in the Blasius boundary layer*. PhD thesis, Royal Institute of Technology, Stockholm, Sweden.
- Brandt, L. and Henningson, D. S. (2002). Transition of streamwise streaks in zero-pressure-gradient boundary layers. *J. Fluid Mech.*, 472:229–262.
- Brandt, L., Henningson, D. S., and Ponziani, D. (2002a). Weakly non-linear analysis of boundary layer receptivity to free-stream disturbances. *Phys. Fluids*, 14(4):1426–1441.
- Brandt, L., Schlatter, P., and Henningson, D. S. (2002b). Numerical simulations of transition in a boundary layer under free-stream turbulence. In I. Castro, P. E. Hancock and Thomas, T. G., editors, *Advances in Turbulence IX, Proc. of the Ninth European Turbulence Conference*, pages 17–20. Springer.
- Ellingsen, T. and Palm, E. (1975). Stability of linear flow. *Phys. Fluids*, 18:487–488.
- Elofsson, P. A., Kawakami, M., and Alfredsson, P. H. (1999). Experiments on the stability of streamwise streaks in plane Poiseuille flow. *Phys. Fluids*, 11:915–930.
- Grosch, C. E. and Salwen, H. (1978). The continuous spectrum of the Orr-Sommerfeld equation. Part 1. The spectrum and the eigenfunctions. *J. Fluid Mech.*, 87:33–54.
- Hall, P. and Horseman, N. J. (1991). The linear inviscid secondary instability of longitudinal vortex structures in boundary-layers. *J. Fluid Mech.*, 232:357–375.
- Henningson, D. S. (1987). Stability of parallel inviscid shear flow with mean spanwise variation. Tech. Report FFA-TN 1987-57, Aeronautical Research Institute of Sweden, Bromma.
- Herbert, Th. (1983). Secondary instability of plane channel flow to subharmonic three-dimensional disturbances. *Phys. Fluids*, 26:871–874.

- Hultgren, L. S. and Gustavsson, L. H. (1981). Algebraic growth of disturbances in a laminar boundary layer. *Phys. Fluids*, 24(6):1000–1004.
- Jacobs, R. G. and Durbin, P. A. (2001). Simulations of bypass transition. *J. Fluid Mech.*, 428:185–212.
- Jeong, J., Hussain, F., Schoppa, W., and Kim, J. (1997). Coherent structures near the wall in a turbulent channel flow. *J. Fluid Mech.*, 332:185–214.
- Jonáš, P., Mazur, O., and Uruba, V. (2000). On the receptivity of the by-pass transition to the length scale of the outer stream turbulence. *Eur. J. Mech. B/Fluids*, 19:707–722.
- Kachanov, Y. S., Kozlov, V. V., and Levchenko, V. Y. (1977). Nonlinear development of a wave in a boundary layer. *Izv. Akad. Nauk SSSR Mekh. Zhid. Gaza*, 3:49–58. in Russian.
- Kendall, J. M. (1985). Experimental study of disturbances produced in a pre-transitional laminar boundary layer by weak free-stream turbulence. *AIAA Paper*, 85:1695.
- Klebanoff, P. S. (1971). Effect of free-stream turbulence on the laminar boundary layer. *Bull. Am. Phys. Soc.*, 10:1323.
- Klebanoff, P. S., Tidstrom, K. D., and Sargent, L. M. (1962). The three-dimensional nature of boundary layer instability. *J. Fluid Mech.*, 12:1–34.
- Landahl, M. T. (1975). Wave breakdown and turbulence. *SIAM J. Appl. Maths*, 28:735–756.
- Luchini, P. (2000). Reynolds-number independent instability of the boundary layer over a flat surface. Part 2: Optimal perturbations. *J. Fluid Mech.*, 404:289–309.
- Lundbladh, A., Berlin, S., Skote, M., Hildings, C., Choi, J., Kim, J., and Henningson, D. S. (1999). An efficient spectral method for simulation of incompressible flow over a flat plate. Technical Report KTH/MEK/TR-99/11-SE, KTH, Department of Mechanics, Stockholm.
- Lundell, F. and Alfredsson, P. H. (2003). Streamwise scaling of streaks in laminar boundary layers subjected to free-stream turbulence. *J. Fluid. Mech.* Submitted for publication.
- Malik, M. R., Zang, T. A., and Hussaini, M. Y. (1985). A spectral collocation method for the Navier-Stokes equations. *J. Comp. Phys.*, 61:64–88.
- Matsubara, M. and Alfredsson, P. H. (2001). Disturbance growth in boundary layers subjected to free stream turbulence. *J. Fluid. Mech.*, 430:149–168.
- Morkovin, M. V. (1969). The many faces of transition. In Wells, C. S., editor, *Viscous Drag Reduction*. Plenum Press.
- Nayfeh, A. H. and Mook, D. T. (1979). *Nonlinear oscillations*. Wiley-Interscience.
- Nordström, J., Nordin, N., and Henningson, D. S. (1999). The fringe region technique and the Fourier method used in the direct numerical simulation of spatially evolving viscous flows. *SIAM J. Sci. Comp.*, 20:1365–1393.
- Park, D. S. and Huerre, P. (1995). Primary and secondary instabilities of the asymptotic suction boundary layer on a curved plate. *J. Fluid Mech.*, 283:249–272.
- Reddy, S. C., Schmid, P. J., Baggett, J. S., and Henningson, D. S. (1998). On the stability of streamwise streaks and transition thresholds in plane channel flows. *J. Fluid Mech.*, 365:269–303.
- Rist, U. and Fasel, H. (1995). Direct numerical simulation of controlled transition in a flat-plate boundary layer. *J. Fluid Mech.*, 298:211–248.
- Rogallo, R. S. (1981). Numerical experiments in homogeneous turbulence. Technical Report Tech. Memo. 81315, NASA.
- Schlichting, H. (1933). Berechnung der anfängung kleiner störungen bei der plattenströmung. *ZAMM*, 13:171–174.
- Schmid, P. J. and Henningson, D. S. (2001). *Stability and Transition in Shear Flows*. Springer, New York.

- Schubauer, G. B. and Skramstad, H. F. (1947). Laminar boundary layer oscillations and the stability of laminar flow. *J. Aero. Sci.*, 14:69–78.
- Swearingen, J. D. and Blackwelder, R. F. (1987). The growth and breakdown of streamwise vortices in the presence of a wall. *J. Fluid Mech.*, 182:255–290.
- Tollmien, W. (1929). Über die entstehung der turbulenz. *Nachr. Ges. Wiss. Göttingen* 21-24,. English translation NACA TM 609, 1931.
- Waleffe, F. (1995). Hydrodynamic stability and turbulence: Beyond transients to a self-sustaining process. *Stud. Appl. Math.*, 95:319–343.
- Waleffe, F. (1997). On a self-sustaining process in shear flows. *Phys. Fluids*, 9:883–900.
- Westin, K. J. A., Boiko, A. V., Klingmann, B. G. B., Kozlov, V. V., and Alfredsson, P. H. (1994). Experiments in a boundary layer subject to free-stream turbulence. part i: Boundary layer structure and receptivity. *J. Fluid Mech.*, 281:193–218.
- Wundrow, D. W. and Goldstein, M. E. (2001). Effect on a laminar boundary layer of small-amplitude streamwise vorticity in the upstream flow. *J. Fluid Mech.*, 426:229–262.

NUMERICAL SIMULATION OF TRANSITION TO TURBULENCE IN MHD CHANNEL FLOW

D.S. Krasnov, E. Zienicke, A. Thess

Fakultät für Maschinenbau, Technische Universität Ilmenau, PF 100565, 98684 Ilmenau, Germany

thess@tu-ilmenau.de

O. Zikanov

Department of Mechanical Engineering, University of Michigan - Dearborn, Dearborn MI 48128-1491, USA

T. Boeck

Laboratoire de Modélisation en Mécanique, Université Pierre et Marie Curie, 8 rue du Capitaine Scott, 75015 Paris, France

Abstract Direct numerical simulation is applied to investigate instability and transition to turbulence in the flow of an electrically conducting incompressible fluid between two parallel unbounded insulating walls affected by a wall-normal magnetic field (the Hartmann flow). An explanation is based on the streak growth and breakdown mechanism described earlier for other shear flows. The mechanism is investigated using a two-step procedure that includes 2D optimal perturbations and the subsequent 3D instability of the modulated streaky flow. The calculations produce a critical range between 350 and 400 for the Hartmann thickness based Reynolds number that agrees with recent experimental investigations.

Keywords: Hartmann flow, transition in shear flow

Introduction

Several well known systems in fluid dynamics show a transition to turbulence that is not triggered by linear instability - as for example in Rayleigh-Bénard or the Taylor Couette systems - but appears long before the critical parameter for linear instability is reached. The most known examples are the plane Poiseuille flow with a critical Reynolds number of $Re_c = 5772$ and the pipe flow which never becomes unstable to infinitesimal perturbations. This kind of transition is typical for shear flows and characterized by the following features:

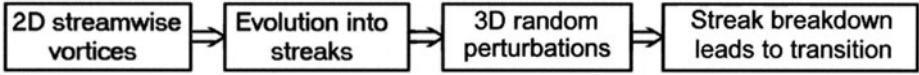


Figure 1. Transition to turbulence by the streak breakdown scenario.

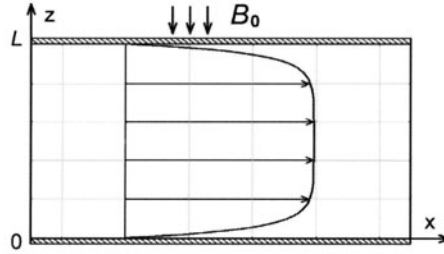


Figure 2. Hartmann flow between two parallel planes.

(i) The transition to turbulence has no sharp "critical" Reynolds number and (ii) initial perturbations of finite strength are necessary to excite the transition. In the last decade, some advances have been made towards a better theoretical understanding of this kind of transition (see Schmid & Henningson (2001)) for an overview). In spite of the absence of instability certain perturbations, called optimal disturbances can grow significantly before they decay again according to linear stability theory. Therefore perturbations can reach an energy that the nonlinearity of the Navier-Stokes equation comes into play and makes the disturbed flow unstable against infinitely small 3D-perturbations triggering the transition to turbulence. The optimal disturbances in our case are 2D streamwise vortices starting the transition scenario given in Figure 1.

We investigate the transition to turbulence in MHD channel flow (see Figure 2). The flow of an electrically conducting fluid is driven by a constant pressure gradient between two parallel non-conducting planes inside a uniform magnetic field normal to the walls. The laminar solution is the Hartmann flow, where the braking effect of the Lorentz force causes a flat profile in the middle of the channel and two Hartmann layers at the walls, in which the main velocity gradient is located. The thickness δ of the Hartmann layers is determined by the dimensionless Hartmann number: $\delta = L/Ha$, where L is the channel width and the Hartmann number is defined as $Ha = B_0 L \sqrt{\sigma/(\rho\nu)}$ (B_0 : magnetic field, σ : electric conductivity, ρ : density, ν : kinematic viscosity). The appropriate parameter to describe the stability of a single Hartmann layer is the Reynolds number $R = Re/Ha$ which is based on the thickness of the Hartmann layer as lengthscale. Linear stability analysis yields a critical Reynolds

number of $R_c = 48250$ (see Lingwood & Alboussière (1999) and further references therein), while experiments indicate a regime of $200 \leq R \leq 400$ for the transition to turbulence (e.g. Branover & Tsinober (1970), Moresco & Alboussière (2003)), which therefore happens at a Reynolds number orders of magnitudes below linear instability.

1. MHD-model and Spectral code

In the framework of this study we used the MHD approach which is based on the assumption that the magnetic Reynolds number is very small:

$$Re_m = UL/\eta \ll 1, \quad (1)$$

here $\eta = (\sigma\mu)^{-1}$ is the magnetic diffusivity, μ is magnetic permeability of free space and σ is the electric conductivity of the fluid. It can be shown that for small Re_m and small Prandtl number $Pr_m = Re_m/Re$ the so-called quasi-steady approximation can be applied (see e.g. Zikanov & Thess (1998) and references therein).

At first, the fluctuations \mathbf{b} of the magnetic field due to fluid motions are much smaller than the applied magnetic field. It is also assumed that \mathbf{b} and the electric current perturbations \mathbf{j} , induced by the movement of the electrically conducting fluid across the magnetic field lines, adjust instantaneously to the time-dependent velocity field. The Lorentz force, therefore, takes the form:

$$\mathbf{F} = \mathbf{j} \times (\mathbf{B}_0 + \mathbf{b}) \approx \mathbf{j} \times \mathbf{B}_0, \quad (2)$$

where \mathbf{j} is defined according to the Ohm's law

$$\mathbf{j} = \sigma [-\nabla\phi + \mathbf{v} \times (\mathbf{B}_0 + \mathbf{b})] \approx \sigma [-\nabla\phi + \mathbf{v} \times \mathbf{B}_0], \quad (3)$$

The solenoidal character of \mathbf{j} provides the Poisson equation for the electrostatic potential ϕ

$$\nabla^2\phi = \mathbf{B}_0 \cdot \boldsymbol{\omega} = B_0\omega_z, \quad (4)$$

where $\boldsymbol{\omega}$ is the flow vorticity.

We solve the incompressible Navier-Stokes equations with the additional Lorentz force term in a 3D rectangular domain with periodic boundary conditions in horizontal directions and no-slip conditions on upper and bottom walls (vertical direction). The flow solver implements a pseudo-spectral method using Fourier series in the horizontal and a Chebyshev polynomial expansion in the vertical directions. The algorithm of Fast Fourier Transformation is parallelized, inter-process communication is provided by the MPI library. The FFT algorithm utilizes two as a prime-factor to compute the Fourier series, so that we used two different resolutions, namely 64^3 or 128^3 collocation points, depending on the flow regime. For more details on the numerical method, discretization technique as well as validation procedures the interested reader is referred to Krasnov et al. (2003).

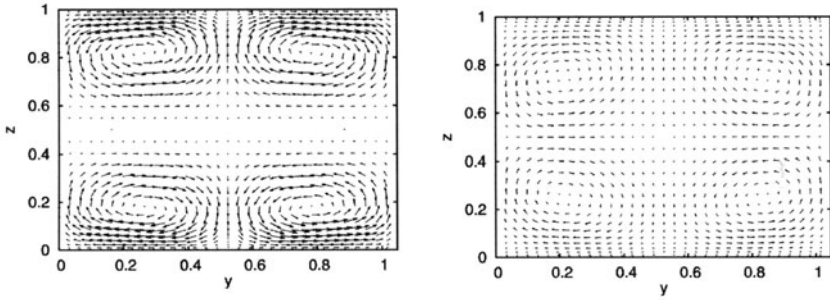


Figure 3. Evolution of 2D perturbations at $Re = 6000$, $Ha = 6$ ($R = 1000$); y- and z- components of the velocity field are shown for the initial state (left) and for the moment of maximum energy (right).

2. Application of the two-step mechanism for turbulence

We present numerical results indicating that the transition to turbulence in MHD-channel flow happens according to a two step mechanism as described above. We start with optimal disturbances in the form of two-dimensional streamwise vortices (see Figure 3, left plot) as were derived by Gerard-Varet (2002), and compute their two-dimensional evolution providing that streamwise dependence at this stage is suppressed in the code artificially. In the second step 3D-noise is added after the disturbance has evolved into streaks (Figure 3, right plot) and its energy has grown by a large factor. After that the simulation is continued solving full 3D Navier-Stokes equations to compute the time evolution.

Figure 4 demonstrates an example of the flow evolution at $Re = 6000$, $Ha = 6$ with stability loss followed by the transition to turbulence. The initial energy $E(0)$ of 2D-perturbations is equal to $5 \cdot 10^{-5}$, the transient process is initiated by 3D-random noise with the amplitude $E_{3D} = 1.5 \cdot 10^{-14}$, imposed at the moment $t_{opt} = 6 \cdot 10^{-3}$ when the energy of the 2D-perturbations has attained its maximum. The 3D-flow evolution is shown by the solid curve, the dashed curve accounts for the pure 2D-case. It is seen in figure 4 that the 3D-perturbations begin to grow significantly until the streak breakdown occurs, which is well recognized as an energy burst on the solid curve. The streamwise-independent component E_{2D} of the full 3D-field (dotted curve in figure 4) is also presented to give insight into how the kinetic energy of 2D-modulation decays in the process of streak breakdown.

To demonstrate the evolution into fully developed turbulence as a result of streak breakdown, we carried out a numerical experiment for parameter values of $Re = 4000$ and $Ha = 10$ (figure 5). Four typical stages of the flow evolution following the two-step scenario are presented by iso-surfaces of the

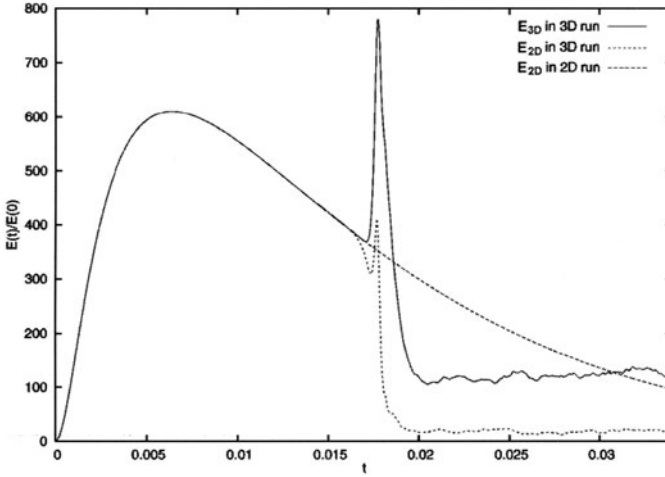


Figure 4. Transition to turbulence in MHD channel flow at $Re = 6000$, $Ha = 6$ ($R = 1000$). Temporal evolutions of the kinetic energy of 2D optimal disturbances (dashed line) and of fully 3D flow (solid line) including the decay of 2D modulation after the streak breakdown (dotted line). The transition is obtained by adding 3D random noise with amplitude $1.5 \cdot 10^{-14}$ at $t_{opt} = 6 \cdot 10^{-3}$.

streamwise vorticity component: the initial state (a), the maximum growth of the energy of streamwise streaks (b), streak breakdown phase (c) and fully-developed turbulence (d). The initial energy $E(0)$ of the 2D-streamwise vortices and the amplitude of 3D-noise, imposed at the moment t_{opt} , is 10^{-3} and $3 \cdot 10^{-6}$, respectively.

3. Search for the critical Reynolds number

Using the two-step mechanism we undertook an attempt to search for the critical R number and to compare the value obtained with the recent experimental result $R_c \approx 380$ of Moresco & Alboussière (2003). We carried out a simulation starting from $R = 200$ and increasing its value gradually while the Hartmann number was kept constant at $Ha = 10$. The initial energy $E(0)$ of the streamwise rolls and the initial amplitude E_{3D} of the random 3D-noise were varied up to 10^{-1} and 10^{-3} correspondingly.

We observed no transition at $R < 350$, in fact the simulations ended with relaminarization of the flow for $E_{3D} < 10^{-3}$ or numerical instability for stronger 3D perturbations. At $R > 400$ the transition occurred every time the amplitude of 2D perturbations was sufficient to form inflection points, so that a minimal level E_{3D} of 3D perturbations to trigger the instability could be easily found.

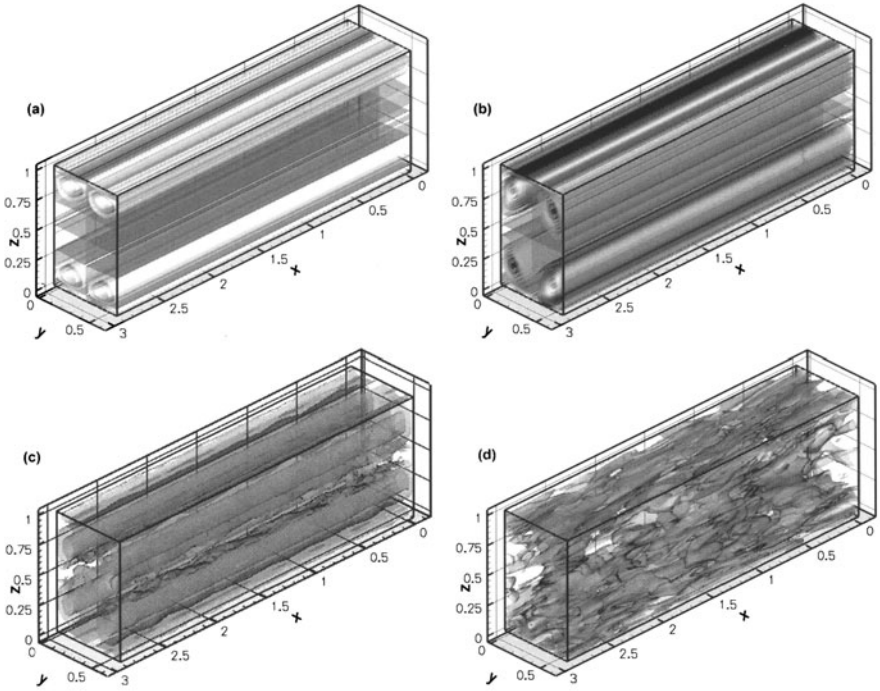


Figure 5. Iso-surfaces of the streamwise vorticity component at $Re = 4000$, $Ha = 10$ ($R = 400$) for four different phases of flow evolution: (a) initial state, (b) maximum growth of the energy of streamwise streaks at time t_{opt} , (c) streak breakdown $t = 4 \cdot t_{opt}$ and (d) fully-developed turbulence $t \gg t_{opt}$.

For the intermediate values $350 \leq R < 400$, where the transition was first detected, the modulated flow exposed more complicated behaviour. If the initial energy of 2D flow was below a certain level, no instability occurred at all, whereas a slight increase of $E(0)$ above this level made it possible to find the amplitude of 3D noise that triggers the transition. The difference between stable and unstable evolutions for the case with $(Re, Ha) = (3500, 10)$, $R = 350$ is demonstrated in figure 6, that shows the signals of the spanwise velocity component in the region of the inflection points. The initial energy $E(0)$ of the 2D modulation is $8 \cdot 10^{-3}$ and 10^{-2} (stable and unstable flows respectively), the initial amplitude of the random noise is $E_{3D}(t_{opt}) = 10^{-4}$ for both cases. The magnitude of the 2D perturbations for both "stable" and "unstable" modulated flow was strong enough to form well developed inflection points. In spite of the inflection points to be the nuclei of instability, the subsequent evolution yields two separate possibilities, one can see the decay of perturbations in fig-

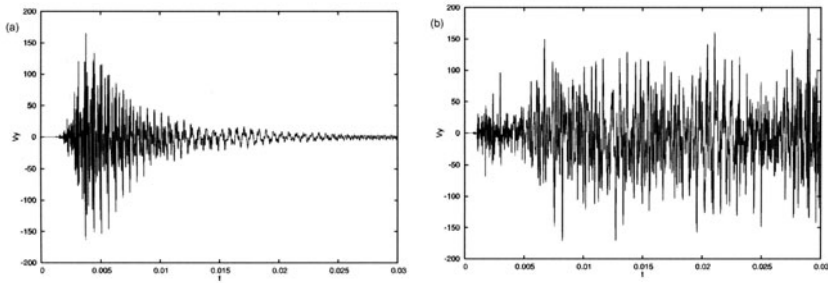


Figure 6. Temporal flow evolution at $R = 350$ ($Re = 3500$, $Ha = 10$), oscillogrames of the spanwise velocity component in the region of formation of the inflection points. (a) sub-critical 2D modulation $E(0) = 8 \cdot 10^{-3}$, the initial growth is eventually followed by the re-laminarization; (b) super-critical 2D modulation $E(0) = 10^{-2}$, 3D instability of the modulated flow results in the transition to turbulence.

ure 6a) and the stochastic process in figure 6b). Therefore for the flow with $Re = 3500$ and $Ha = 10$ ($R = 350$) the critical modulation was determined to lie between $8 \cdot 10^{-3}$ and 10^{-2} .

To verify the parameter R as of being a governing one for the critical flow regime, we also performed a series of simulations at $Re = 7000$ and $Ha = 20$ (R is again kept at 350). The results of these runs demonstrated similar behaviour of the 2D and 3D perturbations, and as in the case above, a slight variation of $E(0)$ around 10^{-2} produced either re-laminarization or flow instability.

4. Conclusions

The process of instability and transition to turbulence in the Hartmann flow was studied numerically using full non-linear formulation of the Navier-Stokes equations. We investigated a two-step mechanism which had been proposed as the transition scenario for non-magnetic shear flows. The scenario implies (i) the flow to be modulated by 2D streamwise perturbations, which experience a large transient growth and modify the basic flow so that (ii) the latter is getting perceptual to small 3D random noise.

One of the most important objectives we pursued was the search for the critical Reynolds number R_c . The two-step mechanism resulting in the streak breakdown scenario coupled with realistic amplitudes of perturbations was found to yield the range of critical parameters $350 \leq R_c < 400$, that perfectly matches the recent experimental results by Moresco & Alboussière (2003).

Summing up the results of this study, the transition scenario proposed for non-magnetic shear flows was successfully extended to the particular case of the

Hartmann flow and was shown to provide an explanation of the instability observed in the MHD experiments.

Acknowledgments

The authors express their gratitude to the Deutsche Forschungsgemeinschaft for financial support in the frame of the "Forschergruppe Magnetofluidynamik" at the Ilmenau University of Technology.

References

- G. Branover, A. Tsinober, Magnetohydrodynamics of incompressible fluids. Nauka, Fys. Mat. Lit., Moscow, 1970
- D. Gerard-Varet, Amplification of small perturbations in a Hartmann layer, *Phys. of Fluids* 14 (2002) 1458-1467
- D.S. Krasnov, E. Zienicke, O. Zikanov, T. Boeck, A. Thess, Numerical study of instability and transition to turbulence in the Hartmann flow, submitted to *J. Fluid Mech.*
- R.J. Lingwood, T. Alboussière, On the stability of the Hartmann layer, *Phys. of Fluids* 11 (1999) 2058-2068
- P. Moresco, T. Alboussière, Experimental study of the instability of the Hartmann layer, submitted to *J. Fluid Mech.*
- P.J. Schmid, D.S. Henningson, *Stability and transition in shear flows*, Springer, Berlin, 2001
- O. Zikanov, A. Thess, Direct numerical simulation of forced MHD turbulence at low magnetic Reynolds number. *J. Fluid Mech.* 358 (1998) 299-333

STUDIES OF TRANSITIONAL AND TURBULENT FLOWS IN ROTOR-STATOR CAVITY USING HIGH-PERFORMANCE COMPUTATIONS

Eric Serre, Patrick Bontoux and Brian Launder*

*Laboratoire de Modélisation et Simulation Numérique en Mécanique L3M
IMT - La Jetée ; Technopôle de Château-Gombert; 38 rue Joliot-Curie,
F-13451 Marseille Cedex 20*

**Department of Mechanical, Aerospace & Manufacturing Engineering
Manchester M60 1QD, UK*

serre1@L3m.univ-mrs.fr

Abstract In this paper, flows confined between a rotating and a stationary disc are investigated using direct numerical simulation based on a pseudo-spectral method. The structure of these flows is very complex involving laminar, transitional and turbulent flow regions and moreover the turbulence is strongly inhomogeneous and anisotropic. Consequently, these flows are very challenging for the turbulence modellers. The present contribution extends the direct numerical simulations (DNS) from the transitional into the turbulent flow regime. In this work, two cases of flow are studied in annular cavities of aspect ratios $L(=R/H)=2.35$ and $L=4.72$. Our work aims at using DNS as a tool for turbulence research. The instantaneous quantities have been analysed and the results have been averaged so as to provide target turbulence data for any subsequent modelling attempts at reproducing the flow.

1. Introduction

Besides its fundamental importance as a three-dimensional prototype flow, confined flow between rotating discs has been extensively examined because of its relevance to many industrial applications such as computer disc-drive or turbomachinery.

A characteristic of the rotor-stator flow is that the stator layer becomes turbulent at a lower Reynolds number than the boundary layer close to the rotating disc. Thus, the structure of these flows is highly complex involving laminar, transitional and turbulent flow regions. Moreover, as a consequence of confinement, flow curvature and rotation effects, the turbulence is strongly inhomogeneous and anisotropic.

Consequently, these flows are very challenging for turbulence modelling. Indeed, the turbulence model must be able to predict the low-Reynolds-number flow not only near the discs but also in the core of the flow. Moreover, the model has to predict precisely the location of the transition from the laminar to the turbulent regime, even though the transition process is bounded by instabilities, and so cannot be completely represented by a steady flow model. One of the most important failures of eddy viscosity models in predicting this type of flow is an overestimate of the extent of the relaminarized zone on the inner part of the rotating disc (Iacovides & Theofanopoulos, 1991), leading to erroneous Ekman layer predictions and rotation rates in the central core. Second moment closures provide a more appropriate level of modelling to predict such complex flows (Hanjalic & Launder, 1976; Launder & Tselepidakis, 1996), but even if they provide a correct distribution of laminar and turbulent regions, the Reynolds stress behaviour is not fully satisfactory, particularly near the rotating disc.

At present, computer performance only permits direct numerical simulation of transitionally turbulent cavity flows, using high-order numerical methods. Nevertheless, even though the Reynolds numbers are well below those arising in industrial practice, this approach can still make a significant contribution to the improvement of turbulence models for rotating disc flows. Indeed, a DNS provides accurate instantaneous quantities which help clarify the intrinsic flow structures associated with turbulent rotating flows. Also, the numerical data can be averaged so as to provide target turbulence data for any subsequent modelling attempts at reproducing the flow.

Computational approaches for turbulent flow in such configurations have to date assumed the mean flow to be axisymmetric and steady, a view point consistent with earlier experiments (Itoh et al., 1992). However, while the geometry may be strictly axisymmetric, visualization studies (Abrahamson et al., 1989; Humphrey et al., 1995) have revealed the presence of non-axisymmetric large scale vortical structures within co-rotating discs, for both laminar and turbulent regimes. In a recent paper, Owen (2000) has drawn attention to difficulties in predicting the flow in certain rotor-stator configurations and speculated that the cause might be related to the formation of large scale vortical instabilities. DNS were therefore started to highlight 3D structures in enclosed rotor-stator cavities.

2. Geometrical and mathematical models

The geometry considered is that of two discs enclosing an annular domain of radial extent $\Delta R = R1 - R0$, where $R0$ and $R1$ are the inner and the outer radii, respectively. Two cylinders of height H bound the solution domain; the origin of the z -axis is located at mid-height between the discs. The internal and

external cylinders are termed the shaft and the shroud, respectively. The upper disc of the cavity rotates at uniform angular velocity $\Omega = \Omega e_z$ while the other is at rest.

Two parameters define the geometry: these may be taken as the curvature parameter $Rm = (R1 + R0)/\Delta R$ and the aspect ratio $L = \Delta R/H$. In this work $Rm = 2.35$ and two values of L are considered: $L = 4.72$ and $L = 2.35$ in order to vary the space between the discs.

The governing equations are the 3D Navier-Stokes equations written in the velocity-pressure formulation, together with the continuity equation and appropriate boundary and initial conditions. It is convenient to write these using a cylindrical polar coordinate system (r, z, θ) , relative to a stationary observer with the origin at the centre of the cylinder. The velocity components are, u , v , w , and p is the pressure. The scales for the dimensionless variables of space, time and velocity are $[H/2, \Omega^{-1}, \Omega R1]$, respectively.

No-slip boundary conditions apply at all walls; there $u = w = 0$. For the tangential velocity, the boundary conditions are $v = 0$ on the stator ($z = -1$) and $v = (Rm + r)/(Rm + 1)$ on the rotating disc ($z = 1$). The external end-wall is fixed ($v = 0$) while the internal one is fixed ($L = 4.72$ cavity) or rotating ($L = 2.35$ cavity).

3. Numerical method

The numerical solution is based on a pseudo-spectral collocation, Chebyshev in both radial and axial directions (r, z) and, in view of the 2π - periodicity of the solution in this configuration a Fourier-Galerkin method is used in the tangential direction.

The problem of velocity-pressure coupling has been overcome by the use of an improved projection scheme for time discretization (see details in Serre & Pulicani, 2001), reducing the fictitious slip velocity at the boundary. The time scheme is semi-implicit, second-order accurate. It corresponds to a combination of the second-order Euler backward differentiation formula and the Adams-Bashforth scheme for the non-linear terms.

The grid size is $301 \times 97 \times 64$ ($L = 4.72$ cavity) and $129 \times 129 \times 96$ ($L = 2.35$ cavity) in r, z , directions, respectively. The time step adopted is $\delta t = 510^{-5}$ ($\simeq 120 \times 10^3$ iterations per rotation 2π). The numerical strategy consists of increasing step by step the rotation rate from the base steady state to the highest Reynolds number allowed by the computer's performance. The performance of the solver has been optimised with respect to a vector-parallel Nec SX5 supercomputer.

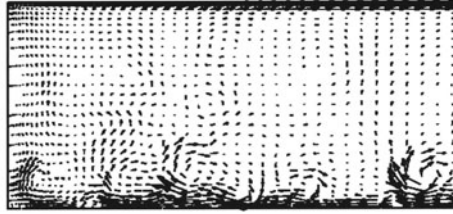


Figure 1. Instantaneous velocity field in a meridional plane $(r, z, \pi/4)$. $L=4.72$ cavity, $Re=300000$. $L=2.35$ cavity, $Re=110000$.

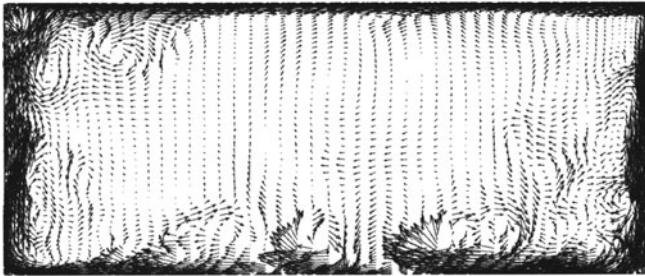


Figure 2. Instantaneous velocity field in a meridional plane $(r, z, \pi/4)$. $L=2.35$ cavity, $Re=110000$

4. Numerical results

4.1 Instantaneous data.

The instantaneous velocity field is represented for both cavities in a meridional plane $(r, z, \pi/4)$ in Fig. 1 and Fig. 2. As observed in experiments (Itoh et al., 1992; Cheah et al., 1994), there is a strong asymmetry between the Ekman and Bödewadt layers, laminar and turbulent flows coexisting within the cavity. Indeed, the turbulent motion is mainly confined to the vicinity of the lower fixed disc while a large part of the rotating disc layer remains laminar, except at the both ends, as expected from the experiments of Itoh et al. (1992) where the rotating layer became turbulent only for a local Reynolds number $Re_r (= \Omega r^2 / \nu) = 3.6 \times 10^5$.

In the $L = 2.35$ cavity, where the space between the discs is the largest, and where the inner end-wall rotates, the turbulent motion at small radii in the rotating disc layer and in the shaft layer as well, is very clear in contrary to the $L = 4.72$ cavity where the shaft is at rest. This turbulent motion is brought about by the strong jet from the rotating shaft impinging the disc. The inner stationary shaft in the $L = 4.72$ cavity has an evident relaminarizing effect and

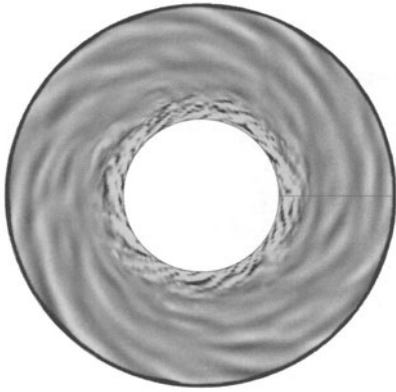


Figure 3. Iso-lines of the instantaneous axial component of the velocity in the rotorlayer showing. $L=2.35$ cavity, $Re=110\,000$

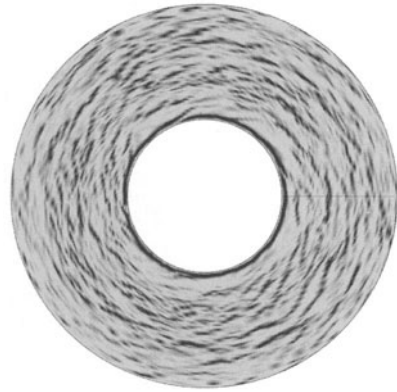


Figure 4. Iso-lines of the instantaneous axial component of the velocity in the stator layer. $L=2.35$ cavity, $Re=110\,000$

no vortices growing in the stator layer reach the Ekman layer of the rotating disc (Fig.1).

The stator flow now consists of rather tangled co-rotating vortices which originate near the shroud and move radially inward following the main flow direction. The growth of these vortices strongly affects the structure of the Bödewadt layer (Fig. 1). At large radii, quite large scale spiral arms can be observed in the instantaneous flow in Fig. 3a and certainly related to the Ekman layer instability which is expected to occur at these radii. The characteristic length scale of these spirals is much larger than in the transitional regime. In the stator flow, vortices develop in both cavities into quite axisymmetric structures of very small scale, showing a pretty strong turbulent level Fig. 3b. In contrary to DNS results carried out in the $L = 4.72$ cavity, in both transitional (Serre *et al.*, 2001) and turbulent regimes, a non-axisymmetric large vertical structure has been found in the core flow of the higher $L = 2.35$ cavity (Fig. 4). This structure resembles a 9-sided polygon and it is consistent with the observations in co-rotating cavities (Abrahamson *et al.*, 1989; Humphrey *et al.* 1995), and with the flow visualizations described in Serre *et al.* (2002). The structure extends from the mid-height cavity to the vicinity of the Ekman layer, in the non-viscous part of the flow.

4.2 Statistical data.

The statistical data presented in this section are averaged both in time and in the homogeneous tangential direction. The statistical steady state is supposed to be reached when the time fluctuations of the averaged values are less than 1 %. The averaged quantities are written using capital letters. As found in

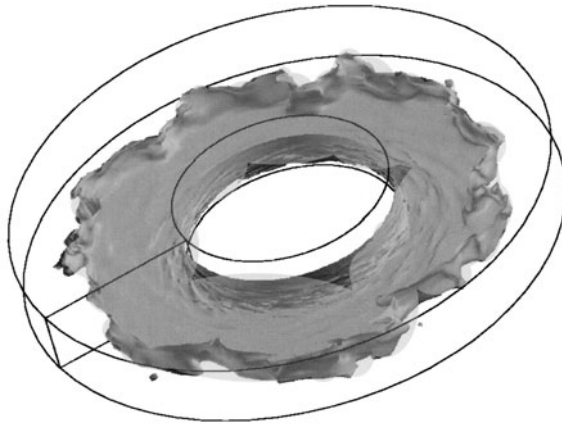


Figure 5. Iso-surface of vertical component of the velocity showing a non-axisymmetric large vertical structure in the core flow of the $L=2.35$ cavity, $Re=110000$.

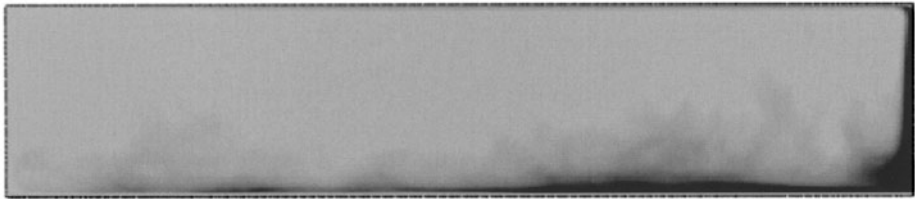


Figure 6. Iso-lines of turbulent kinetic energy k in the meridional plane $(r, z, \pi/4)$. $L=4.72$ cavity, $Re=300000$.

experimental studies and broadly inferred by the instantaneous views (Fig.1 and Fig.2), the two disc boundary layers are separated by a core in nearly solid body rotation. The distribution of the tangential and radial mean velocities across the gap between the discs at mid-radius in the $L = 4.72$ cavity shows the difference in thickness and shape of the radial velocity profile near the two discs. Such behavior suggests that the stator layer is turbulent at mid-radius while the rotor layer still remains laminar. That is the primary explanation that the core circumferential velocity is only about one third of that of the rotor at the same radius.

The spatial distribution of the turbulent kinetic energy k is shown in meridional planes of both cavities in Fig. 5 and Fig. 6. The kinetic energy has been normalised with the square of the wall friction velocity on the stator, u_τ . This reference velocity is well suited to describe the main characteristics of the stationary wall in rotating cavities (Cheah *et al.*, 1994; Iacovides & Toumanakis, 1993). The figures below provide quantitative evidence that

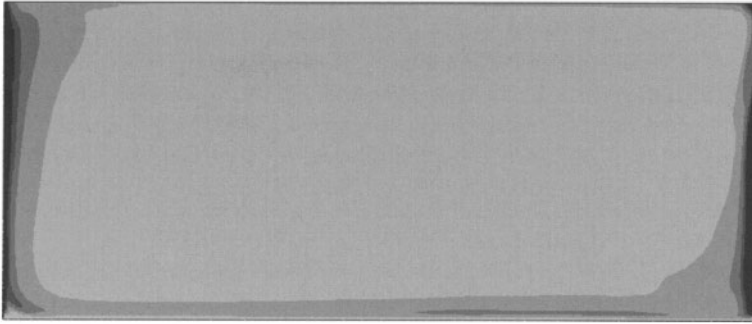


Figure 7. Iso-lines of turbulent kinetic energy k in the meridional plane $(r, z, \pi/4)$. $L=2.35$ cavity, $Re=110000$.

the turbulence is concentrated near the stationary disc. In the narrower cavity ($L = 4.72$), the maximum of k is located at the shroud-stator junction where the instantaneous velocity vector field exhibits the largest vortex (Fig. 1). In the higher cavity ($L = 2.35$), the maximum of turbulence energy is localized in both the shroud and the shaft layers. In these flow regions the flow is like a strong swirling jet. In the shroud layer, the Ekman layer outflow is strongly decelerated bringing the occurrence of large vortices (Fig. 2). In contrary, in the shaft layer the Bödewadt layer outflow is strongly accelerated carrying the vortices of the stator layer up to the rotor layer. Such observation shows the large effect of the endwall layers on the turbulent flow when the inter-disc space is large enough.

References

- Abrahamson, S.M., Eaton, J.K., Koga, D.J.: *The flow between shrouded co rotating disks*, Physics of Fluids A, pp. 241-251, (1991).
- Cheah, S. C., Iacovides, H. J., Jackson, D. C., Ji, H., Launder, B.E.: *Experimental investigation of enclosed rotor-stator disc flows*, Exp. Thermal Fluid Sci., vol. 9, pp. 445-455, (1994).
- Hanjalic, K., Launder, B. E.: *Contribution towards a Reynolds stress closure for low-Reynolds number turbulence*, J. Fluid Mechanics, vol. 74, part 4, pp. 593, (1976).
- Humphrey, J.A.C., Schuler, C.A., Webster, D.R.: *Unsteady laminar flow between a pair of disks co-rotating in a fixed cylindrical container*, Physics of Fluids A, vol. 7, pp. 1225-1240, (1995).
- Iacovides, H., Theofanopoulos, I. P.: *Turbulence modelling of axisymmetric flow inside rotating cavities*, Int. J. Heat Fluid Flow, vol. 12, (1991).
- Iacovides, H., Toumanakis, P.: *Turbulence modelling of flow in axisymmetric rotor-stator systems*, Vth Int. Symp. On Refined Flow Modelling and Turbulence Measurements, Paris France, Sept. 7-10 (1993).

- Itoh, M., Yamado, Y., Imao, S., Gouda, M.: *Experiments on turbulent flow due to an enclosed rotating disc*, Symp. on Eng'rg Turbulence Modelling and Measurements (Ed. W. Rodi and E.N. Ganic), Elsevier, pp. 659-668, (1992).
- Launder, B. E., Tselepidakis, D. P.: *Application of a new second moment closure to turbulent channel flow rotating in orthogonal mode*, Int. J. Heat Fluid Flow, vol. **15**, (1994).
- Owen, J.M.: *Flow and heat transfer in rotating disc systems*, CHT01, Turbulence Heat and Mass Transfer (Ed. Y. Nagano, K. Hanjalic and T. Tsuji), Aichi Shuppan Press, pp. 33-58, (2000).
- Serre, E., Crespo del Arco E., Bontoux P.: *Annular and spiral patterns in flows between rotating and stationary disc*, J. Fluid. Mech., vol. **434**, pp. 65-100, (2001).
- Serre, E., Pulicani, J. P.: *3D pseudo-spectral method for convection in rotating cylinder*, Intl. J. of Computers and Fluids, vol. **30/4**, pp.491-519, (2001).
- Serre, E., Czarny, O., Iacovides, H., Bontoux, P., Launder, B.E.: *Precessing vortex structures within rotor-stator disk: DNS and visualization studies*, Advances in Turbulence IX, CIMNE, Barcelona, pp. 421-424, (2002).

DNS OF A LAMINAR SEPARATION BUBBLE AFFECTED BY FREE-STREAM DISTURBANCES

Jan Wissink and Wolfgang Rodi

Institute for Hydromechanics, University of Karlsruhe

Kaiserstr. 12, D-76131 Karlsruhe, Germany

wissink@ifh.uni-karlsruhe.de, rodi@ifh.uni-karlsruhe.de

Abstract A series of direct numerical simulations of laminar, separating flow affected by various levels of free-stream disturbances has been performed. The free-stream disturbances were found to trigger a Kelvin-Helmholtz instability. The size of the separation bubble was found to be significantly reduced and the location of re-attachment was found to move upstream when the level of free-stream disturbances was increased. Downstream, the near-wall turbulent flow only very slowly assumes "normal" turbulent boundary layer statistics.

Keywords: DNS, laminar separation, Kelvin-Helmholtz instability, Free-stream disturbances

1. Introduction

Recently, a number of three-dimensional (3D) Direct Numerical Simulations (DNS) of Laminar Separation Bubble (LSB) flow have been performed (see e.g. Alam and Sandham 2000; Maucher *et al.* 2000; Spalart and Strelets 2000; Wissink and Rodi 2003a). In these simulations transition is triggered by explicitly introducing disturbances into the boundary layer (Alam and Sandham 2000; Maucher *et al.* 2000), by numerical round-off error (Spalart and Strelets 2000; Wissink and Rodi 2002a), or by oscillations in the outer flow (Wissink and Rodi 2003a). When the oncoming flow contains free-stream fluctuations, the separation will be inhibited such that the LSB becomes considerably smaller or completely disappears. This situation is for instance encountered in flow over turbine blades subject to periodically oncoming wakes, where the impinging fluctuations carried by the wakes periodically reduce separation to a large extent (see also Wissink 2003). A similar phenomenon was observed by Wissink and Rodi (2003b) in a simulation of boundary layer separation along a curved wall, where the disturbances introduced into the flow by a LSB were found to significantly affect a second flow separation observed farther downstream. Similarly, in turbine cascades free-stream disturbances

are known to inhibit the formation of separation bubbles. Since it is important to accurately predict this phenomenon, further DNS of boundary layer separation affected by free-stream disturbances are carried out as part of the German Research Foundation (DFG) project "Periodic Unsteady Flow in Turbo-Machinery".

1.1 Computational Aspects

The geometry is chosen in accordance with experiments performed in a companion DFG project by Prof. Hourmouziadis' group (see e.g. Lou and Hourmouziadis 2000) at the Technical University of Berlin and is given in Figure 1. As in LSB simulations performed earlier (Wissink and Rodi 2002a; Wissink and Rodi 2003a), the special shape of the upper boundary of the computational domain induces an adverse streamwise pressure gradient for $x/L > 0.3$ which causes the boundary layer flow to separate.

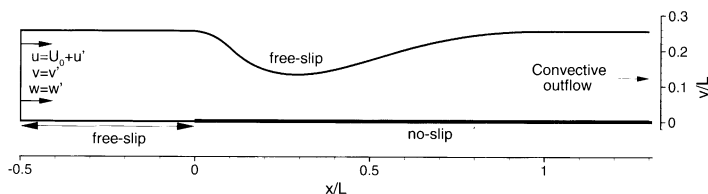


Figure 1. The computational domain.

For the DNS a relatively low Reynolds number (based on the mean inflow velocity U_0 and the length scale L - see Figure 1) of $Re = 60\,000$ is chosen. To save computational points, instead of a no-slip boundary condition, a free-slip boundary condition is applied along the curved upper wall, which allows the employment of a relatively coarse mesh in this region. Along the lower wall, for $x/L > 0$ a no-slip boundary condition is prescribed while upstream of $x/L = 0$ a free-slip boundary condition is applied. Along the latter part of the boundary, wiggles that originate from the stagnation point at $x/L = 0$ are explicitly removed. Any remaining numerical disturbances are found to be damped by the favourable pressure gradient downstream. In the spanwise direction, periodic boundary conditions are employed, while at the outlet a convective boundary condition is selected. Based on experience gained in earlier simulations of LSB flows (Wissink and Rodi 2002a; Wissink and Rodi 2002b; Wissink and Rodi 2003a), the size of the spanwise direction is selected to be $0.08L$, which is sufficient to accommodate all important modes. At the inlet boundary, free-stream disturbances $(\tilde{u}, \tilde{v}, \tilde{w})$ are added and

$$(u, v, w) = U_0(1, 0, 0) + \alpha(\tilde{u}, \tilde{v}, \tilde{w})$$

Table 1. Overview of the simulations; the grid column shows the number of points in the x , y and z -direction, respectively, l_x is the extent of the computational domain in the streamwise direction and Tu is the fluctuations level at the inlet, defined in (1).

<i>Simulation</i>	<i>Grid</i>	l_x	$Tu(\%)$
A	$1038 \times 226 \times 128$	$2.1L$	0
B	$1926 \times 230 \times 128$	$3.5L$	5
C	$1926 \times 230 \times 128$	$3.5L$	7

is prescribed. The parameter α can be varied such that the desired level of fluctuations at the inflow plane is obtained. In the numerical simulations, a second-order central, cell-centred finite-volume method is applied for the discretisation of space, while for the time-integration a three-stage Runge-Kutta method is used. To avoid the decoupling of the pressure field and the velocity field owing to the collocated variable arrangement, the momentum-interpolation procedure of Rhie and Chow (1983) is employed. In Breuer and Rodi (1996) a more detailed description of the employed numerical algorithm can be found. As listed in Table 1, various simulations in which the level

$$Tu = \sqrt{\frac{1}{3} \frac{(\overline{u'^2} + \overline{v'^2} + \overline{w'^2})}{U^2 + V^2}}, \quad (1)$$

of the oncoming disturbances is varied, have been performed. The fluctuations, introduced at the inlet, stem from a separate Large Eddy Simulation (LES) of "isotropic" turbulence in a cubic box and were kindly made available by Jochen Fröhlich of the University of Karlsruhe. The size of the cubic box is rescaled to $0.08L$ in order to match the spanwise size employed in the simulations. By stacking several copies of the box in the y -direction, its size is enlarged to allow a convenient interpolation of the turbulent fluctuations to the computational nodes of the inflow plane. By identifying the x -direction of the box with time and making use of its cyclic nature, a constant stream of fluctuations is obtained and superposed on the inlet uniform flow-field (see also Kalitzin *et al.* 2003). The size of the rescaled box determines the smallest frequency available in the free-stream disturbances to be $f = f_0 = 12.5$, where f is made non-dimensional using U_0 and L . The calculations are performed on massively parallel computers. The mesh is divided into a number of partially overlapping blocks of equal size. A near-optimal load-balancing is achieved by allotting one block for each processor. Communication is performed using the standard Message Passing Protocol (MPI). Simulation A has been performed on the SP-SMP at the Computing Centre in Karlsruhe using 60 processors, while

Simulations B and C have been performed on the Hitachi SR8000-F1 at the Computing Centre in Munich using 256 processors.

2. Results

In Figures 2 (a) and (b), the levels of free-stream fluctuations obtained in Simulations B and C, respectively, are shown. The fluctuation levels in the x -

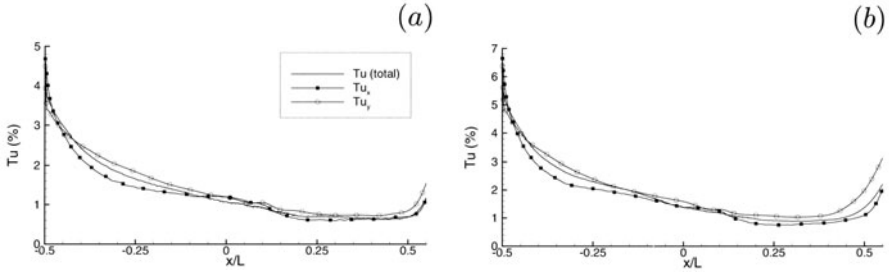


Figure 2. Level of free-stream fluctuations at $y/L = 0.065$, from the inlet up to and beyond the location of separation. (a): Simulation B, (b): Simulation C.

direction and the y -direction are defined by $Tu_x = (\overline{u'^2}/(U^2 + V^2))^{0.5}$ and $Tu_y = (\overline{v'^2}/(U^2 + V^2))^{0.5}$ respectively. In both simulations, the dissipative nature and other inaccuracies of the second-order interpolation of the free-stream fluctuations to the computational nodes results in a sharp decrease in the Tu -level immediately downstream of the inlet. For $-0.5 < x/L < 0.35$, the fluctuations remain approximately isotropic. Farther downstream, the Tu_y -level is found to grow significantly faster than the Tu and the Tu_x levels. The locations of flow separation, $x/L \approx 0.372$ in Simulation A and $x/L \approx 0.375$ in Simulation B, virtually coincide with the onset of the accelerated growth of the vertical fluctuations observed for $x/L > 0.375$. Hence, the Kelvin-Helmholtz (K-H) instability of the separated boundary layer witnessed in Figure 5, which leads to an up-down wavering of the separated boundary layer, which also influences the free-stream, is the most likely source of this phenomenon. As already noted in the introduction and illustrated by the comparable levels of Tu , Tu_x and Tu_y just downstream of the inflow plane observed in Figure 2, the fluctuations added to the inflow are isotropic as they stem from a separate LES of "isotropic" turbulence. In Figure 3 (a), the frequency distribution of the v -signal at $(x/L, y/L, z/L) = (-0.45, 0.065, 0.04)$, obtained in Simulation B, is shown. The results are extracted from 500 snapshots equally dividing a time-interval of 2.40 time-units. Most of the dominant frequencies stemming from the added inlet disturbances - $f_0 = 12.5$ and its higher harmonics - clearly stand out from the rest. Apart from the maxima at $f = 12.5, 25.0, 37.5, \dots$, a low-level ($\sim 10^{-4}$) numerical noise can be observed that slowly declines with increasing f . For $f \geq 37.5$, the decline of the

higher harmonics of f_0 is faster than the decline of the numerical noise, eventually making them indistinguishable from the numerical noise contained in the adjacent modes. In Figure 3 (b), the energy contents of the most important

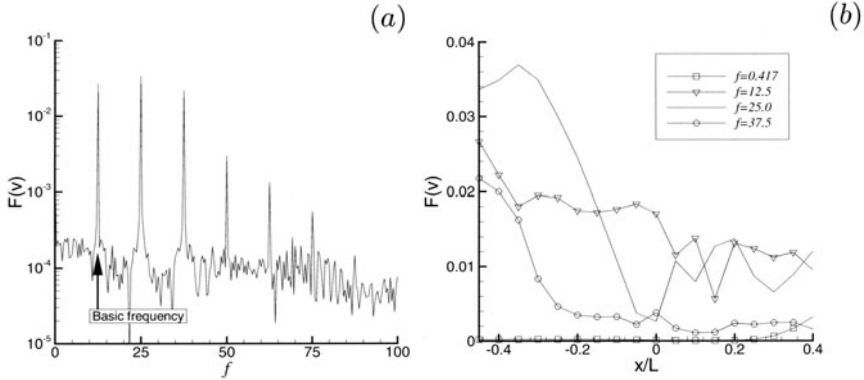


Figure 3. Simulation B: (a): Frequency spectrum of the v -velocity at midspan at $x/L = -0.45, y/L = 0.065$. (b): Evolution of the energy contents upstream of $x/L = 0.4$ of some of the most important modes.

frequencies present in Simulation B, upstream of $x/L = 0.4$, has been plotted along the line $(y/L, z/L) = (0.065, 0.04)$. Especially the higher dominant frequencies are found to be damped when moving in the downstream direction. For $x/L > 0.2$, the lowest resolved frequency, $f = 0.417$, suddenly starts to grow. This mode very likely corresponds to the low-frequency wavering mode observed by Spalart and Strelets (2000). After rescaling, to account for the different level of inflow disturbances, the results shown in Figure 3 (a) and (b) are virtually identical to the corresponding results obtained in Simulation C (not shown here). In Figure 4 (a,b), the frequency spectra of the spanwise averaged v -velocity at four locations, P_1, P_2, P_3, P_4 inside the separated shear layer have been plotted for Simulations A and B, respectively. The respective locations of $P_1 - P_4$ are identified in Figure 4 (c) and (d). In the absence of explicitly added free-stream disturbances, the Kelvin-Helmholtz (K-H) instability will be triggered by numerical inaccuracies. Though these inaccuracies are not explicitly analysed, one may assume that their frequency spectrum resembles white noise, as evidenced in Figure 3 (a). Hence, in the spectrum shown in Figure 4 (a) all unstable K-H modes will show up. The most unstable one is found to be the mode with frequency $f_1 = 14.0$, while the second-most unstable mode has a frequency of $f_2 = 12.4$. The latter frequency almost coincides with the basic frequency, $f_0 = 12.5$, present in the free-stream disturbances added in Simulations B and C. It is therefore to be expected that the unstable mode with frequency $f = f_0$ will be the fastest growing one in the K-H instability found in Simulations B and C. The latter is confirmed for Simulation B by the spec-

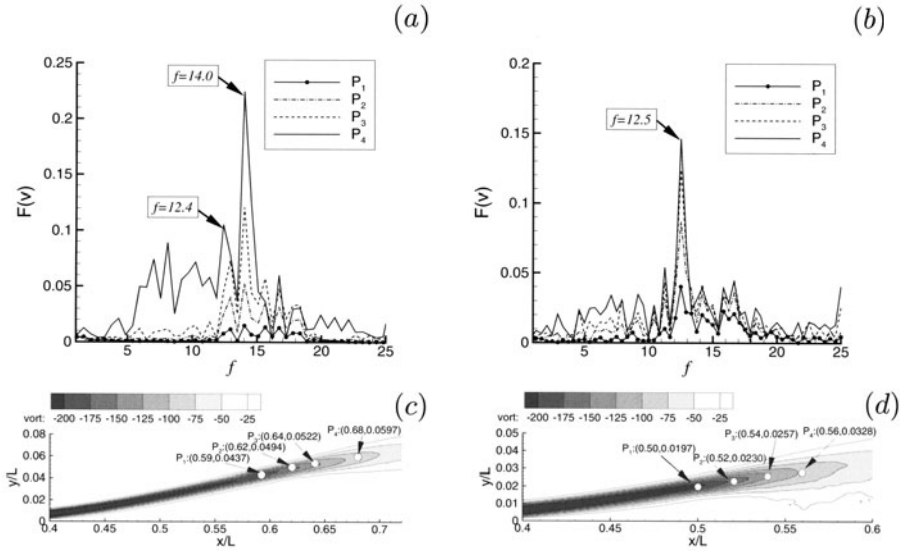


Figure 4. Simulation A: (a) Frequency spectrum of the spanwise averaged v -velocity at the points P_1, P_2, P_3, P_4 identified in (c). Simulation B: (b) Frequency spectrum of the spanwise averaged v -velocity at the points P_1, P_2, P_3, P_4 identified in (d). (c) and (d) show time-averaged spanwise vorticity contours of Simulations A and B, respectively.

tra plotted in Figure 4 (b). The maximum at $f = f_0$ becomes more and more pronounced when moving from P_1 downstream to P_4 . As a result, at P_4 the mode corresponding to $f = f_0$ reaches an amplitude that is almost three times as large as the amplitude of the second most important mode. By comparing Figure 4 (c) to Figure 4 (d), an impression is obtained of the difference in size of the separation bubbles generated in Simulation A and Simulation B, respectively. In Figure 5 (a) and (b), three-dimensional illustrations of the separated shear layer are displayed, using snapshots of the spanwise vorticity isosurface $\omega_z = -150$. The figure provides a clear illustration of the significant reduction in size of the laminar separation bubble owing to the free-stream disturbances such as added in Simulation C. The reduction in size is accompanied by an upstream shift in the location of transition. In both graphs, traces of vortex shedding can be observed which are characteristics for a K-H instability. The spanwise modes that are also observed to grow inside the separated boundary layer of Simulation C, are assumed to be of secondary importance compared to the primary K-H instability. Downstream of the separation bubbles, small scale vortical structures found near the flat plate correspond to the onset of the formation of a turbulent boundary layer from an initially wake-like flow. The near-wall turbulent flow is found to assume only very slowly the "standard" turbulent boundary layer characteristics. In Figure 6 the shape factor,

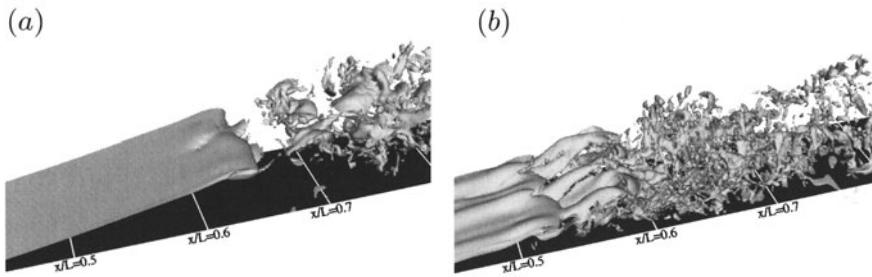


Figure 5. Snapshots of the iso-surface of the spanwise vorticity at $\omega_z = -150$; (a): Simulation A, (b): Simulation C.

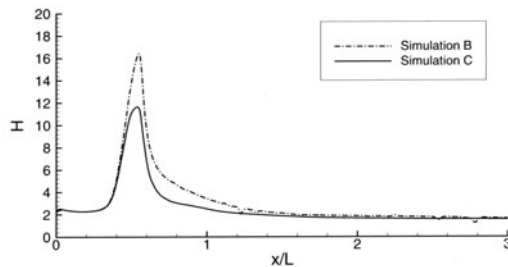


Figure 6. Shape factor of Simulations B and C

H , obtained in Simulations B and C is shown. Prior to separation, H reaches values of 2.3 – 2.5, which are typical for a laminar boundary layer flow. At separation, H grows to values in excess of $H = 10$, where the higher level of fluctuations present in Simulation C is found to reduce the maximum of H compared to Simulation B. Farther downstream H gradually assumes values between 1.6 – 1.8, typical for a turbulent boundary layer.

3. Discussion and Conclusions

Direct numerical simulations of a laminar separation bubble with and without explicitly added free-stream disturbances have been performed. The simulations serve to gain insight into the physical mechanisms and to provide data for the development of turbulence models to be applied, for instance, in turbo-machinery flow simulations. Free-stream fluctuations are introduced in the computational domain by interpolation of data stemming from a separate large-eddy simulation of "isotropic" turbulence in a cubic box, of which the x -direction is identified with time. Because of this, the spectrum of the free-stream disturbances is not continuous but discrete, consisting of a basic frequency, f_0 , and its higher harmonics. The most unstable mode in Simulation A is not part of the discrete frequency spectra in the Simulations B and C. Since the basic frequency in the Simulations B and C is virtually identical

to the frequency of the second most unstable mode in Simulation A, it is this mode which is identified as the most unstable mode in both Simulations B and C. Evidence of a Kelvin-Helmholtz instability is found in all simulations in the form of a characteristic, quasi-periodic vortex shedding from the separated shear layer. Downstream of the separation bubbles, a turbulent wake-like flow is obtained which only very slowly assumes the "standard" characteristics of a turbulent boundary layer.

Acknowledgments

The authors wish to thank the German Research Foundation (DFG) for funding this project and the steering committee of the supercomputing facilities in Bavaria for granting computing time on the Hitachi SR8000-F1 in Munich.

References

- Alam, M., Sandham, N.D. (2000). *Direct numerical simulation of 'short' laminar separation bubbles with turbulent reattachment*. J. Fluid Mech., **410**, 1–28.
- Breuer, M., Rodi, W. (1996). *Large eddy simulation of complex turbulent flows of practical interest*. In: Flow Simulation with High Performance Computers II, Notes on Num. Fluid Mechanics, Vieweg Verlag.
- Kalitzin, G., Wu, X., Durbin, P.A. (2003). *DNS of fully turbulent flow in a LPT passage*. Int. J. of Heat and Fluid Flow., **24**, 636–644.
- Lou, W., Hourmouziadis, J. (2000). *Separation under steady and periodic unsteady main flow conditions*. In: Proceedings of the 45th ASME International Gas Turbine & Aeroengine Technical Congress, Munich Germany.
- Maucher, U., Rist U., Kloker, M., Wagner, S. (2000). *DNS of laminar-turbulent transition in separation bubbles*. In: Krause, E., Jäger, W. (eds) High-Performance Computing in Science and Engineering. Springer Berlin Heidelberg.
- Rhie, C.M., Chow, W.L. (1983). *Numerical Study of the Turbulent Flow Past an Airfoil with Trailing Edge Separation*. AIAA J., **21**, 1525–1532.
- Spalart, P.R., Strelets, M.Kh. (2000). *Mechanisms of transition and heat transfer in a separation bubble*. J. Fluid Mech., **403**, 329–349.
- Wissink, J.G., Rodi, W. (2002a). *DNS of Transition in a Laminar Separation Bubble*. In: I.P. Castro and P.E. Hancock (eds.), Advances in Turbulence IX, Proceedings of the Ninth European Turbulence Conference, 727–730.
- Wissink, J.G., Rodi, W. (2002b). *DNS of transition in periodic, unsteady flow*. In: M. Savill (ed.), ERCOFTAC Bulletin, **54**.
- Wissink, J.G., Rodi, W. (2003a). *DNS of a laminar separation bubble in the presence of oscillating flow*. Accepted for publication in Flow, Turbulence and Combustion.
- Wissink, J.G. (2003). *DNS of separating, low Reynolds number flow in a turbine cascade with incoming wakes*. Int. J. of Heat and Fluid Flow., **24**, 626–635.
- Wissink, J.G., Rodi, W. (2003b). *Direct numerical simulation of boundary layer separation along a curved wall with oscillating oncoming flow*. In: S. Wagner, W. Hanke, A. Bode, F. Durst (eds.), High Performance Computing in Science and Engineering Munich 2002, 113–123.

2.2 COMPRESSIBLE FLOWS

DNS OF TRANSONIC FLOW ABOUT A SUPERCRITICAL AIRFOIL

Igor Klutchnikov and Josef Ballmann

*Mechanics Department, RWTH Aachen University,
Templergraben 64, D-52062 Aachen, Germany*

klutchnikov@lufmech.rwth-aachen.de

Abstract A high-order in space central difference scheme with flux-corrected transport has been employed for numerical simulation of unsteady three-dimensional compressible fluid flow about the supercritical airfoil NLR7301 in the transonic regime with shock-boundary layer interaction. The high order in space enables to reproduce well vortical structures and to predict transition to turbulent flow as well as to perform DNS. Numerical results of the method are compared with experimental mean flow data.

Keywords: Direct numerical simulation, high-order difference method, transonic flow, transition to turbulent flow, supercritical airfoil

1. Introduction

Shock-boundary layer interaction enhances transition to turbulence in transonic airfoil flow. Numerical methods solving the Reynolds averaged Navier-Stokes equations using turbulence models are not able to correctly predict experimentally observed shock-boundary layer interactions or flow separation in that regime. This motivates us to apply the high-order method developed in [1] for DNS and to compare the results with experimental mean flow data available in the AGARD test for the NLR7301 airfoil [3]. Flow conditions are laminar inflow at Mach number $M_\infty = 0.7$, Reynolds number based on chord-length $Re_c = 2.14 \cdot 10^6$ and fixed angle of attack $\alpha = 2.5^\circ$.

2. Numerical Method

The problem to be solved is three-dimensional with an infinite extension in the z -direction which is perpendicular to the main flow plane with the airfoil ((x,y) -plane). Oncoming flow is in x -direction. The Navier-Stokes equations for unsteady three-dimensional compressible fluid flow about the airfoil are transformed from Cartesian to curvilinear coordinates $\xi(x,y), \eta(x,y), \zeta = z$

and written in non strong conservation form:

$$\mathbf{U}_{,t} + \frac{1}{J} \mathbf{F}_{,\xi}^c + \frac{1}{J} \mathbf{G}_{,\eta}^c + \mathbf{H}_{,z}^c = \frac{1}{J} \mathbf{F}_{,\xi}^d + \frac{1}{J} \mathbf{G}_{,\eta}^d + \mathbf{H}_{,z}^d. \quad (1)$$

Here \mathbf{U} is the solution vector of conservative variables, \mathbf{F}^c , \mathbf{G}^c , \mathbf{H}^c and \mathbf{F}^d , \mathbf{G}^d , \mathbf{H}^d represent the convective and dissipative fluxes, J is the Jacobian of the transformation. With $\alpha = uy_{,\eta} - vx_{,\eta}$, $\beta = vx_{,\xi} - uy_{,\xi}$

$$\mathbf{U} = \begin{bmatrix} \rho \\ \rho u \\ \rho v \\ \rho w \\ \rho E \end{bmatrix}, \quad \mathbf{F}^c = \begin{bmatrix} \rho\alpha \\ \rho u\alpha + py_{,\eta} \\ \rho v\alpha - px_{,\eta} \\ \rho w\alpha \\ (\rho E + p)\alpha \end{bmatrix}, \quad \mathbf{G}^c = \begin{bmatrix} \rho\beta \\ \rho u\beta - py_{,\xi} \\ \rho v\beta + px_{,\xi} \\ \rho w\beta \\ (\rho E + p)\beta \end{bmatrix},$$

$$\mathbf{H}^c = \begin{bmatrix} \rho w \\ \rho uw \\ \rho vw \\ \rho w^2 + p \\ (\rho E + p)w \end{bmatrix}, \quad \mathbf{F}^d = \begin{bmatrix} 0 \\ \tau_{xx}y_{,\eta} - \tau_{xy}x_{,\eta} \\ \tau_{xy}y_{,\eta} - \tau_{yy}x_{,\eta} \\ \tau_{xz}y_{,\eta} - \tau_{yz}x_{,\eta} \\ (u_j\tau_{xj} - q_x)y_{,\eta} - \\ -(u_j\tau_{yj} - q_y)x_{,\eta} \end{bmatrix},$$

$$\mathbf{G}^d = \begin{bmatrix} 0 \\ \tau_{xy}x_{,\xi} - \tau_{xx}y_{,\xi} \\ \tau_{yy}x_{,\xi} - \tau_{xy}y_{,\xi} \\ \tau_{yz}x_{,\xi} - \tau_{xz}y_{,\xi} \\ (u_j\tau_{yj} - q_y)x_{,\xi} - \\ -(u_j\tau_{xj} - q_x)y_{,\xi} \end{bmatrix}, \quad \mathbf{H}^d = \begin{bmatrix} 0 \\ \tau_{xz} \\ \tau_{yz} \\ \tau_{zz} \\ u_j\tau_{zj} - q_z \end{bmatrix},$$

u , v and w are the Cartesian velocity components, ρ , p and E are density, pressure and total specific energy, τ and \mathbf{q} are the stress tensor and heat flux vector, respectively. As computational domain we take a C-H shaped grid space around the rectangular wing segment with finite width and periodic boundary conditions in z direction.

The numerical method developed in [1] is of arbitrary even order $N = 2, 4, 6, 8, 10, \dots$ in space and employs central differences for spatial discretization together with an explicit time integration using a two-step Richtmyer scheme of second order:

$$\mathbf{U}_{i_r+1/2}^{n+1/2} = L_r \mathbf{U}_{i_r+1/2}^n - 0.5\lambda_r \mathbf{A}_{ri_r+1/2}^n (R_r \mathbf{U}_{i_r+1/2}^n) \quad (2)$$

$$\begin{aligned} \mathbf{U}_{\bullet}^{n+1} &= \mathbf{U}_{\bullet}^n - \sum_{r=1}^3 \lambda_r \{ (\mathbf{F}_{ri_r+1/2}^{cn+1/2} - \mathbf{F}_{ri_r-1/2}^{cn+1/2}) \\ &\quad - (\mathbf{F}_{ri_r+1/2}^{dn} - \mathbf{F}_{ri_r-1/2}^{dn}) - (S_r \mathbf{U}_{i_r+1/2}^n - S_r \mathbf{U}_{i_r-1/2}^n) \}, \end{aligned}$$

$$(\mathbf{F}_1, \mathbf{F}_2, \mathbf{F}_3) = (\mathbf{F}, \mathbf{G}, \mathbf{H}), \quad (\lambda_1, \lambda_2, \lambda_3) = \left(\frac{\Delta t}{J_{\bullet} \Delta \xi}, \frac{\Delta t}{J_{\bullet} \Delta \eta}, \frac{\Delta t}{\Delta z} \right). \quad (3)$$

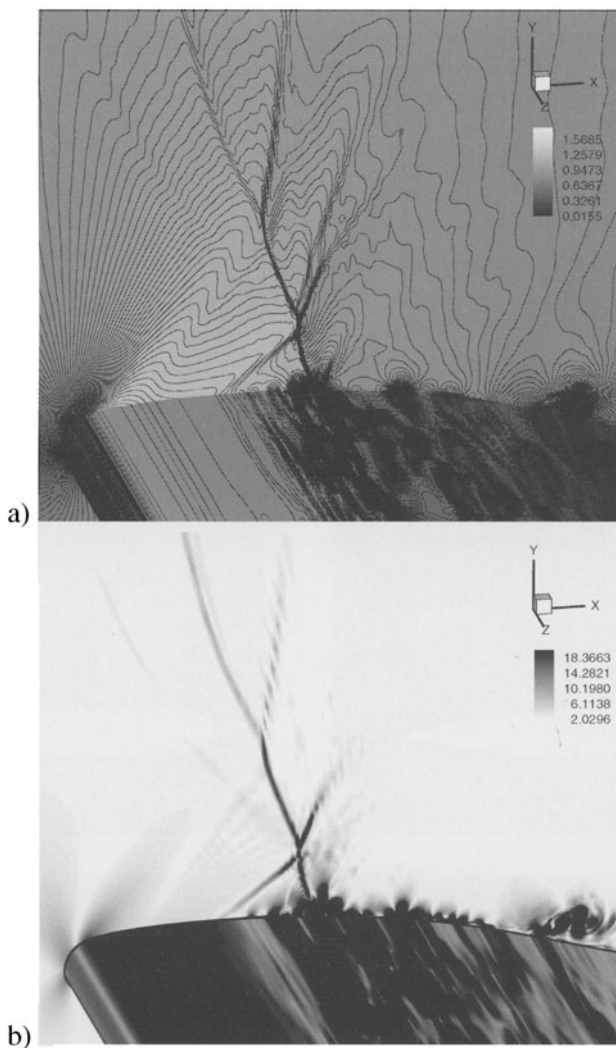


Figure 1. DNS of 3D flow about the airfoil NLR7301 for $M_\infty = 0.7$, $\alpha = 2.5^\circ$. Instantaneous contours of the distributions of a)Mach number and b)vorticity at one time level

Here \mathbf{A}_r is the flux Jacobian, and L_r , R_r and S_r are special discrete operators in space. Upper indices n and $n + 1/2$ correspond to time levels and lower indices i_r , $r = 1, 2, 3$ are running in the space directions $r = 1, 2, 3$ from $i_r = 1$ to $i_r = i_{rmax}$. A detailed description of the space operators in the method can be found in [1], [2]. For the steep gradients which may occur in the shock-boundary layer interaction the FCT algorithm (Flux Corrected Transport) is used.

Boundary conditions at solid walls are the contact and no-slip conditions.

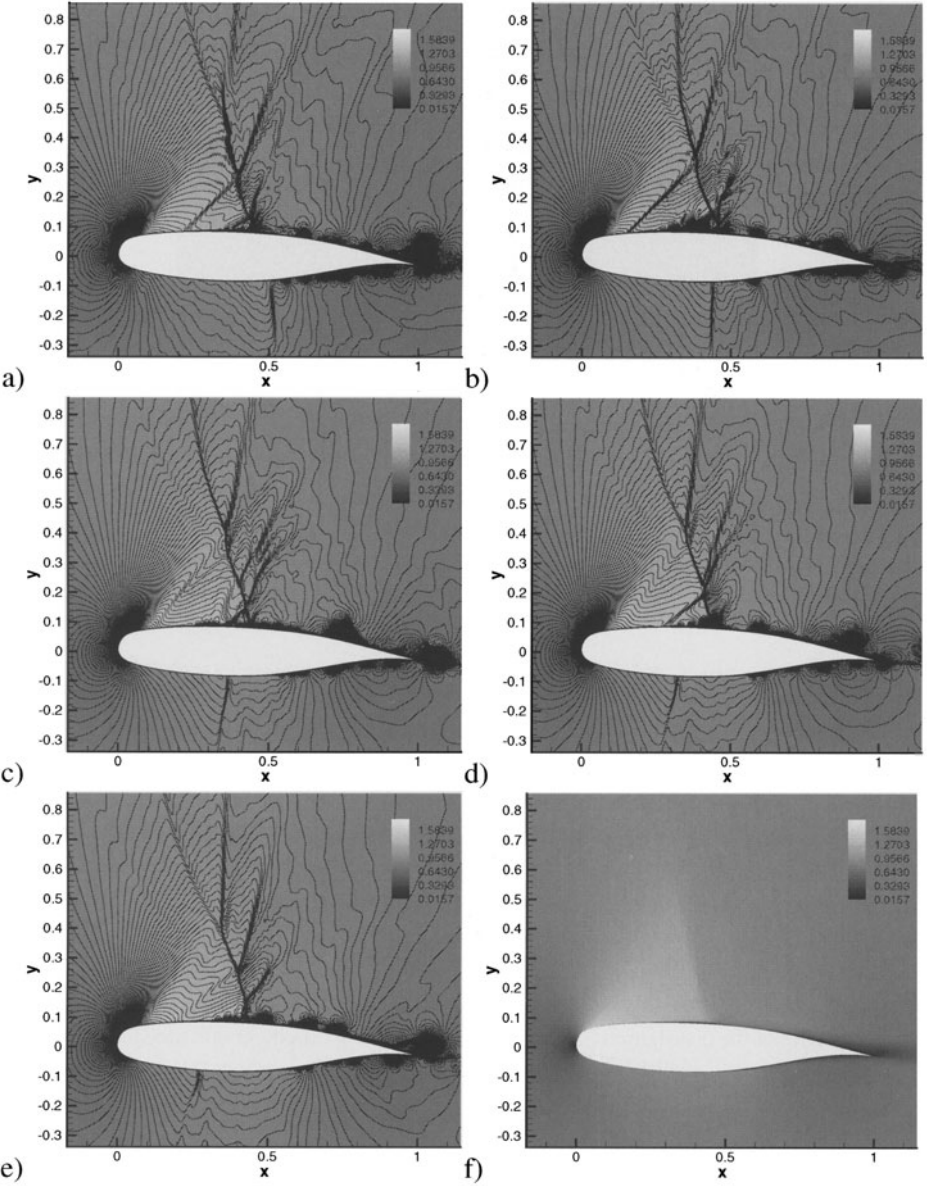


Figure 2. DNS of 3D flow about the airfoil NLR7301 for $M_\infty = 0.7$, $\alpha = 2.5^\circ$. From a) to e): Instantaneous distributions of Mach number in the plane $z = 0$ at different times with interval $3.43 \cdot 10^{-4} s$. f): Mean distribution over $2.7 \cdot 10^5$ time steps corresponding to $2.3 \cdot 10^{-3} s$

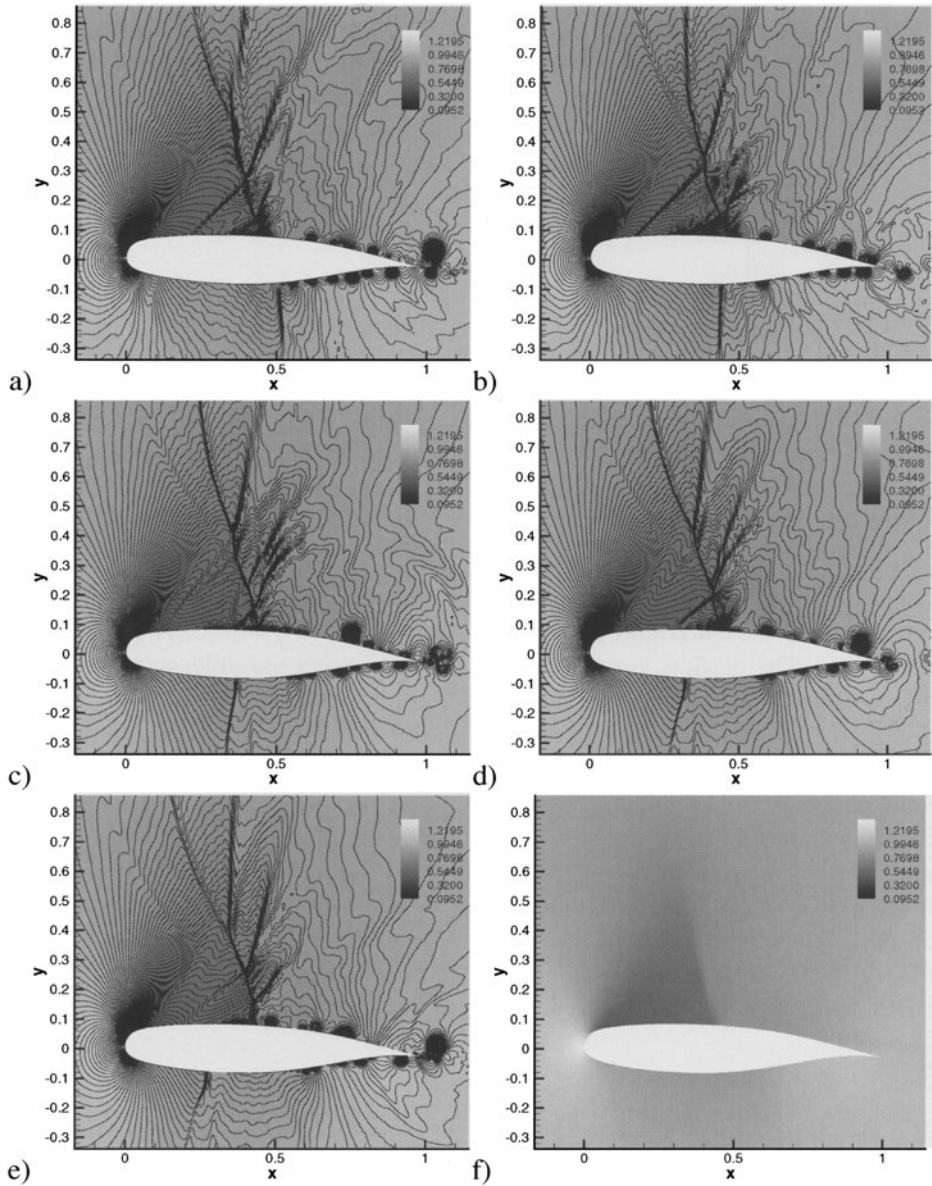


Figure 3. DNS of 3D flow about the airfoil NLR7301 for $M_\infty = 0.7$, $\alpha = 2.5^\circ$. From a) to e): Instantaneous distributions of pressure in the plane $z = 0$ at different times with interval $3.43 \cdot 10^{-4} s$. f): Mean distribution over $2.7 \cdot 10^5$ time steps corresponding to $2.3 \cdot 10^{-3} s$

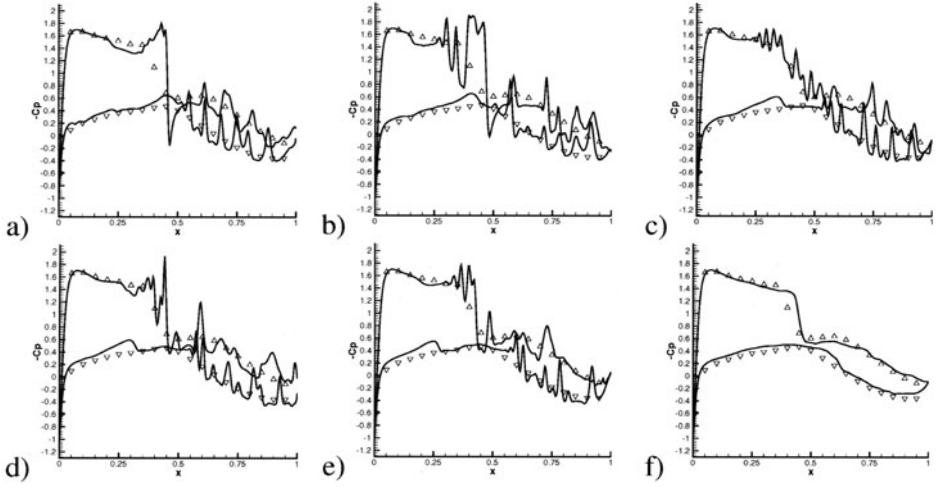


Figure 4. DNS of 3D flow about the airfoil NLR7301 for $M_\infty = 0.7$, $\alpha = 2.5^\circ$. From a) to e): Instantaneous distributions of pressure coefficient in the plane $z = 0$ at different times with interval $3.43 \cdot 10^{-4} s$. f): Mean distribution over $2.3 \cdot 10^{-3} s$. Symbols: Experiment [3].

On the artificial boundary restricting the computational domain, subsonic flow prevails. The inflow conditions are: $u = u_\infty$, $\rho = \rho_\infty$, $v = 0$, $w = 0$, p extrapolated. The outflow conditions are: $p = p_\infty$, other variables extrapolated. Extrapolation on each of the boundaries is performed in the outward normal direction. For the approximation of the order N of the boundary conditions values are assigned to $N/2$ fictitious points outside of the computational domain using symmetry and anti-symmetry principles.

Firstly, to get information about the numerical parameter settings with low numerical effort, two-dimensional simulations in the main flow plane were performed on grids of different resolution [4]. Then, 3D flow simulation was done on the C-H type grid with $1280 \times 130 \times 120$ grid points. The computational domain is $L_x = 40c$, $L_y = 40c$ and $L_z = 1c$. The grid stretching exponent in the η direction is 2.5. The spatial order of the method was chosen $N = 8$.

3. Results

The values found for boundary-layer related quantities along the first grid surface $\eta = const.$ are $y^+ < 1$, $x^+ < 20$ and $z^+ < 10$, the Reynolds number based on $U_\tau < 0.002$ was found $Re_\tau < 400$. Boundary-layer flow on the upper side is laminar from the leading edge downstream to the shock closing the supersonic region of the transonic flow field. Fig.1 shows instantaneous contour lines of Mach number (Fig.1a) and vorticity (Fig.1b) in surfaces $\eta = const.$ and $\xi = const.$ In the boundary-layer bordering on the supersonic region the flow is subsonic and the pressure gradient is smaller than in

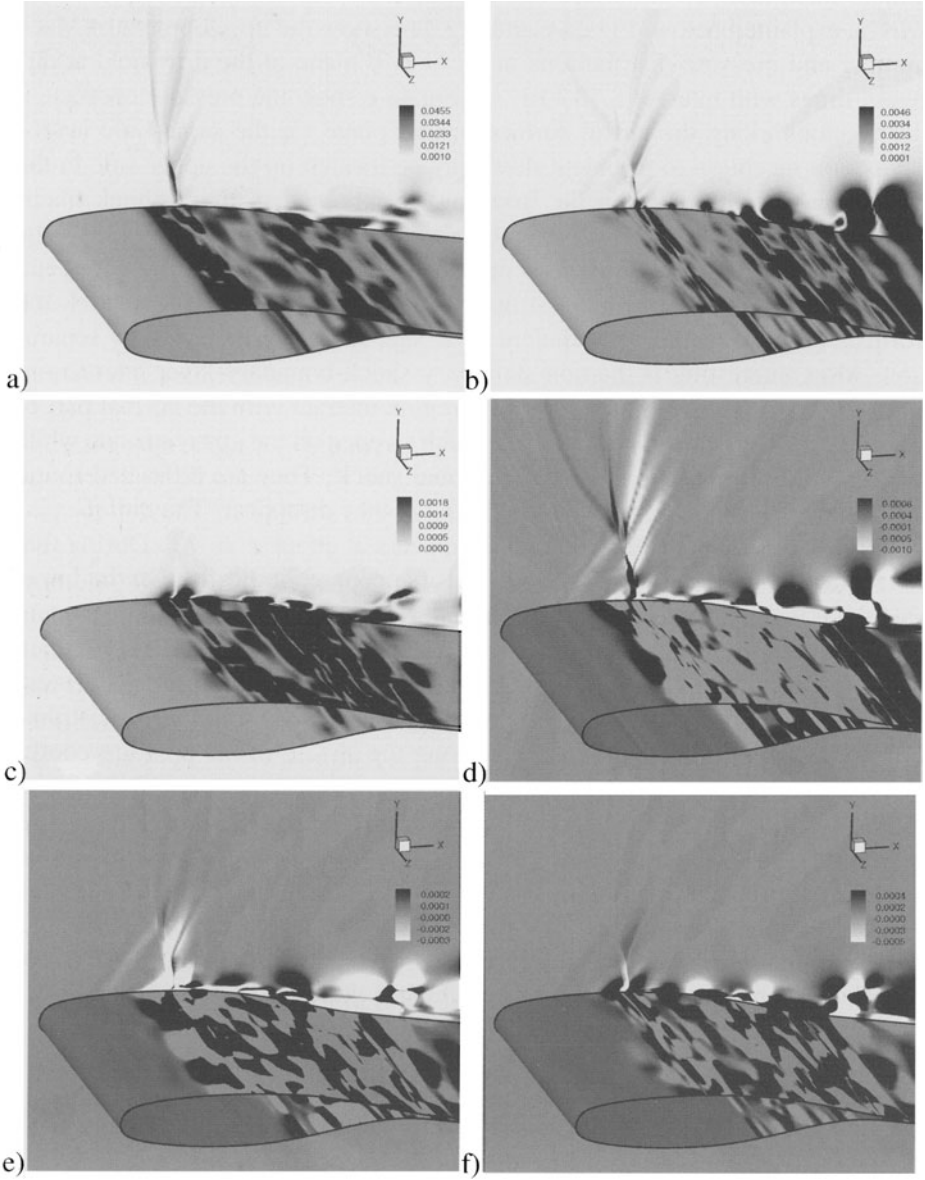


Figure 5. DNS of 3D flow about the airfoil NLR7301 for $M_\infty = 0.7$, $\alpha = 2.5^\circ$. Instantaneous contours of the Reynolds stress components : a) u'^2 , b) v'^2 , c) w'^2 , d) $u'v'$, e) $u'w'$, f) $v'w'$

the mainflow part. A λ -shock is formed consisting of an oblique shock followed downstream by a normal shock. The position of the normal shock is almost fixed at $x = 0.4$ while the oblique shock behaves differently which will be explained below. Fig.2a-e and Fig.3a-e show the development of Mach number and pressure distributions in the $z = 0$ plane of the flow field at different times with interval $3.43 \cdot 10^{-4} s$. Fig.4a-e show the pressure coefficient distributions along the airfoil surface in that plane for the same time levels. Transition inception to turbulent flow may be located on the upper side in the supersonic domain between the front and rear branch of the λ -shock manifesting itself in strong vortex separation and interaction with the shock. The boundary-layer thickness increases drastically while first two-dimensional and then three-dimensional vortical structures are formed. Behind the shock the vortices develop further to turbulent flow and, finally, turbulent flow separation. Most interesting is the non-stationary shock-boundary layer interaction. The vortices originated in the transition region interact with the normal part of the λ -shock. This causes sonic waves which steepen on the upstream side while propagating in y -direction along the normal shock. They are diffracted round the supersonic region being weakened, finally they disappear. The oblique part of the λ -shock moves upstream and disappears at about $x = 0.1$. During that time a new oblique shock is formed. This happens periodically. On the lower side the transition region begins to form at $x = 0.6$ with first two-dimensional and then three-dimensional vortical structures orientating themselves in main flow direction. The values of vorticity at the lower side are about 40 percent of those at the upper side. Fig.2f, Fig.3f and Fig.4f show the mean distributions of Mach number, pressure, and, along the airfoil, of the pressure coefficient. Means were taken over $2.7 \cdot 10^5$ time steps corresponding to $2.3 \cdot 10^{-3} s$. Results for the pressure coefficient agree well with experimental data of [3]. Fig.5 shows instantaneous contours of the Reynolds stress components for the three-dimensional flow. The fluctuations make the different positions of the transition regions on the upper and lower side of the airfoil clearly visible. The computations took 540 hours on CRAY T3E-1200 with 80 CPUs of Forschungszentrum Juelich, Germany, which is gratefully acknowledged.

References

- [1] I. Klutchnikov. Direct Numerical Simulation of Turbulent Compressible Fluid Flow. Habilitation Thesis, Russian Academy of Sciences, Moscow, 1998 (in Russian).
- [2] I. Klutchnikov, J. Ballmann. Direct Numerical Simulation of Supersonic Turbulent Ramp and Step Flow. DNS/LES-Progress and Challenges, Proceedings of the Third AFOSR International Conference on DNS/LES, USA, 479-486, 2001.
- [3] AGARD-R-702. Compendium of Unsteady Aerodynamic Measurements, 1982.
- [4] I. Klutchnikov, J. Ballmann. DNS of Transonic Flow about an Oscillating Airfoil. Proceedings of the 13. DGLR-Fach-Symposium der STAB, Munich, 2002, accepted.

DNS AND LES OF THE TRANSITION PROCESS IN A LAMINAR SEPARATION BUBBLE

Olaf Marxen and Ulrich Rist

Institut für Aerodynamik und Gasdynamik, Universität Stuttgart, D-70550 Stuttgart, Germany

olaf.marxen@iag.uni-stuttgart.de, rist@iag.uni-stuttgart.de

Abstract A region of strong local adverse pressure gradient acting on a laminar flat-plate boundary layer can produce a closed fully laminar separation bubble for sufficiently small pressure rise and Reynolds number. However, such a flow field is hydrodynamically highly unstable and transition will occur in the region of adverse pressure gradient. Due to an interaction with the potential flow, the transition process may even suppress laminar separation completely.

Direct numerical simulation (DNS) of oblique transition in a steady laminar separation bubble is carried out. The mean flow deformation is found to play an important role even upstream of the transition location. However, with proper treatment of the upper boundary it is possible to take the upstream influence into account and to obtain results that are height independent in accordance with the physical model of an unbounded domain. Hence, DNS results can serve as a reference for an analysis of the large-eddy simulation (LES) technique. Such an analysis of LES is carried out based on a (scale) separation step associated with an explicit filter and a (subfilter-scale) modeling step to obtain closure. It is shown that filtering of the Navier-Stokes equations is not a formality and that the subgrid-scale model has to be adopted to the filter accordingly. Numerical results for a discrete filter together with a relaxation-term model lead to guidelines for the choice of the explicit filter and the desired action of the turbulence model.

Keywords: transition, laminar separation bubble, DNS, LES

Introduction

A laminar boundary layer separates in a region of adverse pressure gradient on a flat plate and can reattach while being still laminar in case of a sufficiently small pressure rise and low Reynolds number, forming a laminar separation bubble (LSB). However, such a flow field is hydrodynamically unstable and will amplify incoming disturbances by several orders of magnitude. Therefore, the laminar separation bubble is likely to be the location of transition to turbulence. Through its upstream influence, in some cases the transition process

is able to completely suppress separation by an interaction of the mean flow deformation with the potential flow (so-called viscous-inviscid interaction). Numerical techniques applied to complex, separated and transitional flows rely mainly on direct numerical simulations (DNS, see e.g. Alam and Sandham, 2000, Wasistho, 1997) to keep uncertainties connected with a turbulence model to a minimum. In many technical applications laminar separation plays an important role, e.g. on low pressure turbine blades. Thus, there is need for numerical methods to accurately capture the behaviour of laminar separation bubbles that are less expensive than DNS. One of these methods is the so-called large-eddy simulation that aims at capturing the motion of large coherent structures while modeling the small-scale turbulence. Only a few large-eddy simulations (LES) of LSB's are reported in literature (Yang and Voke, 2001, Wilson and Pauley, 1998). A detailed comparison of results from both techniques for a flow field where DNS is still feasible to provide a reference can serve to shed light on modeling uncertainties. The first part of the paper addresses issues related to establishing a proper reference case by means of DNS.

The methodology of LES consists of two steps: separation of variables into resolved and unresolved scales (*separation step*) by application of a spatial filter, and replacing the resulting unclosed (subgrid- or subfilter-scale) stresses by a turbulence model (*modeling step*). For a long time, the separation step was considered a mere formality and its quantitative effect on the solution of the equations of motion has only recently drawn more attention (Pruett, 2001, Guerts and Holm, 2003). The present work aims at analysing the quantitative effect of isolated parts of the LES method on the numerical results. This is believed to provide deeper insights compared to a full LES run with its complex interaction of filter, model, and discretization strategy. Dependence of the results on turbulence model and (explicit) filtering operation will be discussed in the second part of the paper.

1. Numerical Method and Definition of the Base Flow

Numerical Method. Spatial direct numerical simulation of the full three-dimensional Navier-Stokes equations in vorticity-velocity formulation were carried out in a disturbance formulation for incompressible flow. All quantities are divided into a steady part $U_b(x, y)$ and a fluctuation $u(x, y, z)$. Finite differences ($4^{th}/6^{th}$ order) on a Cartesian grid are used in streamwise and wall-normal direction while a spectral ansatz is applied in spanwise direction. An explicit fourth-order Runge-Kutta scheme is used for time integration. Upstream of the outflow boundary a buffer domain smoothly ramps down all disturbances. These disturbances are introduced via blowing/suction through a narrow slot in the wall near the inflow boundary. Details of the numerical

method can be found in Kloker, 1998. In addition, grid stretching is applied in wall-normal direction (Meyer, 2003).

Definition of the Base Flow. A generic test case was chosen that has already been well-studied by means of DNS (Rist and Maucher, 1994). It models a physical situation as shown in Fig. 1. All quantities are non-dimensionalized resulting in a Reynolds number $Re=10^5$. The streamwise axis x is denoted as for a Blasius boundary layer. To illustrate this, c_f -values for the Blasius solution are added to Fig. 2. In contrast to Rist and Maucher, 1994, the integration domain starts slightly further downstream at $x_0=1.021576$ and ends at $x_e=3.36468$. The Reynolds number based on the displacement thickness δ_1 at the inflow boundary is $Re_{\delta_1}=570$. The domain height equals $y_{max}=\Delta_M \cdot \delta_1$ with $\Delta_M=23.2$ at the inflow boundary. Characteristic boundary-layer parameter distributions are given in Fig. 2. Boundary-layer thicknesses (e.g. δ_1) are computed based on the spanwise vorticity (see Spalart and Strelets, 2000). The flow field was obtained from a calculation where a distribution for the streamwise velocity was prescribed at the upper boundary to impose the pressure gradient. The calculation was advanced until a steady state was reached. Using this steady laminar solution as a base flow, the unsteady development with controlled disturbance input is computed as discussed in the next section.

2. Direct Numerical Simulation of Transition in a LSB

Disturbance Input and Resolution Requirement. The transition scenario studied here is similar to the oblique case O in Rist and Maucher, 1994. Below, the notation (h, k) will be used to denote modes with h -times the fundamental frequency $\beta = 18$ and k -times the fundamental spanwise wave number $\gamma = 40$. A single pair of oblique waves $(1, \pm 1)$ is introduced in a disturbance strip

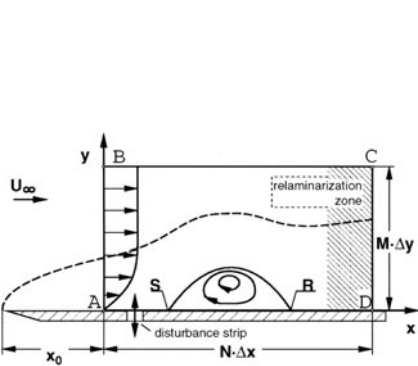


Figure 1. Physical configuration.

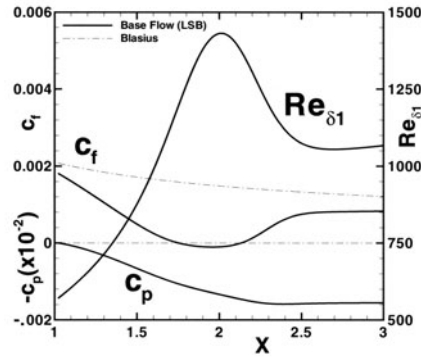


Figure 2. Base flow values for surface pressure c_p , skin friction coefficient c_f , and local Reynolds number Re_{δ_1} .

between $x = 1.152475$ and $x = 1.283375$ with a v -amplitude of $A_v = 2 \cdot 10^{-4}$ each. The buffer domain started at $x = 3.102881$.

The DNS was carried out with $N=1970$ grid points in streamwise direction, $M=225$ grid points in wall-normal direction and $K=63$ (complex, i.e. asymmetric) spanwise modes. In wall-normal direction grid points were clustered at the wall. Resolution in time was 1600 time steps per fundamental period.

Results were highly sensitive to underresolution in wall-normal direction (not shown). However, 15 (real, i.e. symmetric) spanwise modes proved to be sufficient to predict correct mean values shortly beyond the transition location (Fig. 3), while showing an overshoot in the skin friction in the turbulent part. The calculation was advanced for at least 20 periods before analysing the data to get rid of initial transients, visible e.g. as mode $(0.5, 0)$ in Fig. 4.

Mean Flow Deformation and Upper Boundary. The small disturbance input is sufficient to completely suppress separation (Fig. 3). In particular, it is remarkable that the mean flow deformation (MFD) (mode $(0, 0)$ in the present notation) is the largest observable disturbance even far upstream around the location of the disturbance strip (Fig. 4). Such an effect was not observed for subharmonic or fundamental breakdown that lead to saturated spanwise rollers but not to true turbulent flow (Rist, 1998), were a relatively small deviation of mean flow values was seen only downstream of disturbance saturation.

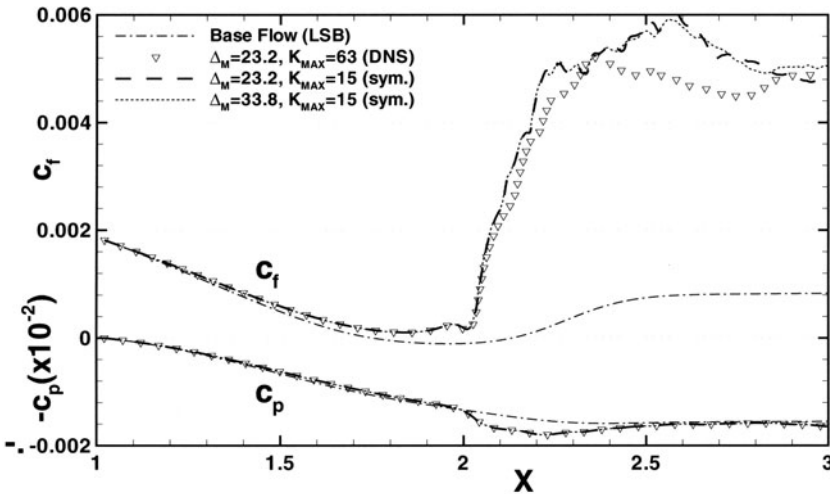


Figure 3. Comparison of c_p and c_f for two different spanwise resolutions $K=15$ and $K=63$ and two different domain heights $\Delta_M=23.2$ and $\Delta_M=33.8$.

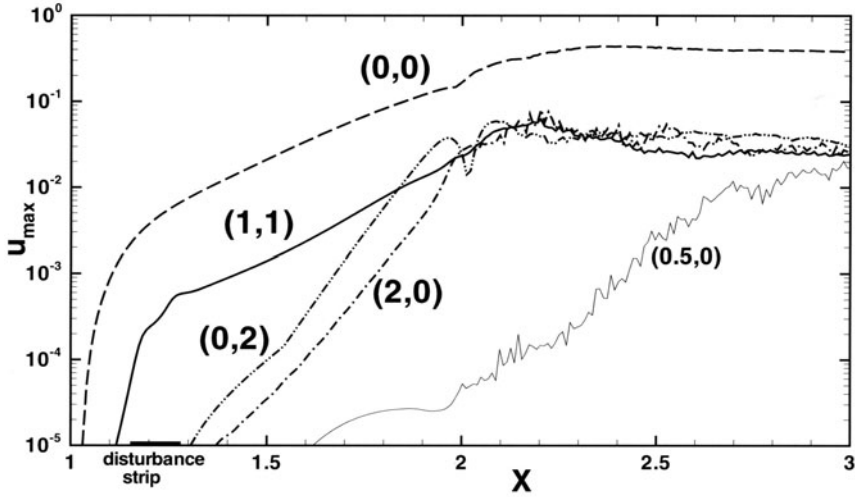


Figure 4. Amplification of the maximum streamwise velocity fluctuation u_{max} for the DNS ($K=63$, $\Delta_M=23.2$), Fourier analysed in time and spanwise direction.

Because of the importance of the MFD even at the upper boundary, the original formulation of the upper boundary condition $\frac{\partial v}{\partial y} = -\alpha v$ was replaced by a boundary-layer interaction model. It is based on a source/sink distribution at the wall, which strongly depends on the disturbances introduced. With such a boundary condition independence on the domain height could be obtained (Fig. 3). This independence is important since the underlying physical model is a boundary layer with an adverse pressure gradient, i.e. an unbounded domain, and not a channel flow.

3. Analysis of Large-Eddy Simulation

The DNS solution presented in the last section will serve as a reference for the following analysis of LES. This analysis is carried out according to the two steps introduced before. In the next paragraphs, a filter operation is defined as the convolution integral:

$$u_i^*(x) = G_2 * u_i = \int G_2\left(\frac{x-x'}{\Delta}, x\right) u_i(x') \frac{dx'}{\Delta}. \quad (1)$$

Derivation of the Filtered Equations. Even though the calculations discussed in this paper were obtained with the vorticity-velocity formulation of the Navier-Stokes equations, derivation of the equations for LES will be demonstrated for primitive variables since this is more familiar in the literature. For numerical simulations the curl of the equations is taken and only

commutative filters are applied. Starting point are the momentum equations:

$$\frac{\partial u_i}{\partial t} + \frac{\partial u_j u_i}{\partial x_j} + \frac{\partial p}{\partial x_i} - \frac{1}{Re} \frac{\partial^2 u_i}{\partial x_k \partial x_k} = 0. \quad (2)$$

First, the (*scale*) *separation step* is carried out by adding a term to both sides of the equations (bold in eq. (3)), which is similar to the non-linear term, however with the velocities replaced by their filtered counterpart $u_i^* = G_2 * u_i$ (Fig. 5). The resulting equation is filtered with a spectral filter with cut-off wave number k_c . Spectrally filtered variables will be denoted by a tilde: $\tilde{u}_i = G_S * u_i$ (analogous to eq. (1)). With the additional constraint that the transfer function of G_2 is (only) 0 for $k > k_c$, the following equality holds: $u_i^* = G_2 * u_i = G_2 * \tilde{u}_i = \tilde{u}_i^*$. Note that the resulting equations are still exact, assuming we prescribe periodic boundary conditions:

$$\underbrace{\frac{\partial \tilde{u}_i}{\partial t} + \frac{\partial \tilde{u}_j^* \tilde{u}_i^*}{\partial x_j} + \frac{\partial \tilde{p}}{\partial x_i} - \frac{1}{Re} \frac{\partial^2 \tilde{u}_i}{\partial x_k \partial x_k}}_{\text{dependent on scales } k < k_c \text{ only}} = \underbrace{\frac{\partial \tilde{u}_j^* \tilde{u}_i^*}{\partial x_j} - \frac{\partial u_j u_i}{\partial x_j}}_{\text{dependent on all scales } k}. \quad (3)$$

If eq. (3) would be solved on a grid that can resolve scales up to $k = k_c$, the right-hand side of that equation would be the so-called subgrid-scale term (SGS term). The second term on the left-hand side cannot generate scales $k \geq k_c$ and does not depend on them. Furthermore, formally eq. (3) does not depend on the choice of G_2 while the quantitative value of the right-hand side will. Thus, it could as well be called the subfilter-scale term.

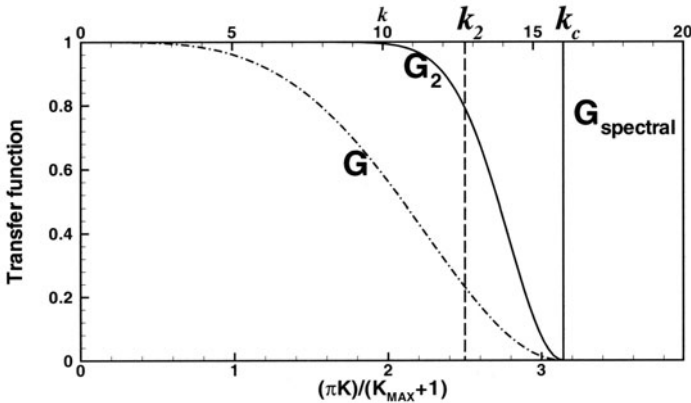


Figure 5. Filter transfer functions as a function of wave number.

The second step is the (*subfilter-scale*) *modeling step*. The right hand side will be replaced by a term that depends only on scales below the cut-off k_c to obtain closure. In the LES terminology, such a term is called a turbulence or SGS model. One simple model is a so-called relaxation term, e.g. $\chi (\tilde{u}_i^* - \tilde{u}_i)$:

$$\frac{\partial \tilde{u}_i}{\partial t} + \frac{\partial \widetilde{u_j^* u_i^*}}{\partial x_j} + \frac{\partial \tilde{p}}{\partial x_i} - \frac{1}{Re} \frac{\partial^2 \tilde{u}_i}{\partial x_k \partial x_k} = \chi (\tilde{u}_i^* - \tilde{u}_i). \quad (4)$$

Note that all necessary steps have been carried out now, solving eq. (4) will be called a LES. For constant χ only(!) the right-hand side acts purely dissipative. In that case, the present closure can be related to the approximate deconvolution model (ADM) (Stolz et al., 2001a; Stolz et al., 2001b). However, to arrive at the equations used in ADM, another filter G has to be applied to eq. (4): $\bar{u}_i = G * u_i$. With the constraint that $G_2 = Q_N * G$ and $Q_N = \sum_{\nu=0}^N (1-G)^\nu$, one obtains:

$$\frac{\partial \bar{u}_i}{\partial t} + \frac{\partial \overline{u_j^* u_i^*}}{\partial x_j} + \frac{\partial \bar{p}}{\partial x_i} - \frac{1}{Re} \frac{\partial^2 \bar{u}_i}{\partial x_k \partial x_k} = -\chi (I - Q_N * G) * \bar{u}_i, \quad (5)$$

$$\begin{aligned} \text{with } \bar{\tilde{u}_i} &= \bar{u}_i = I * \bar{u}_i, \\ \bar{\tilde{u}_i^*} &= G * (Q_N * G * \tilde{u}_i) = (G * Q_N) * \bar{u}_i = (Q_N * G) * \bar{u}_i. \end{aligned}$$

Numerical Results. From what has been shown in the last paragraph it is obvious that the last step (to arrive at the ADM equations) is not necessary, and with it the whole procedure of filtering and deconvolution, since closure was obtained already in the second step. This was earlier recognized by Winck-

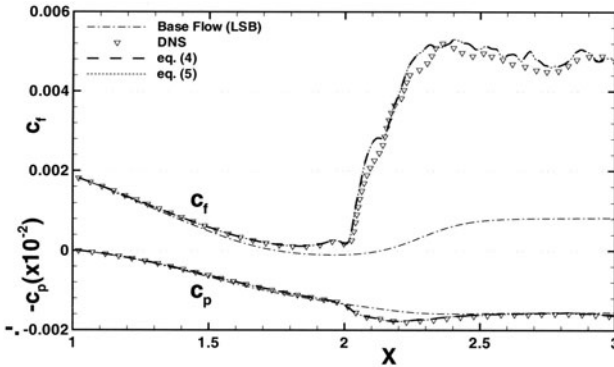


Figure 6. Results of eq. (4) and eq. (5) for $K=15$, filtering in z only.

elmans and Jeanmart, 2001. In particular, eq. (4) and eq. (5) will yield equal results, if the solution of eq. (4) is filtered in a postprocessing step.

This was checked by applying the filtering only in the spanwise direction using 15 Fourier harmonics ($K=15=k_c-1$), where the present numerical method is in accordance with the assumption of periodicity. The turbulence model is given by the relaxation term with constant $\chi = 572.96 = \frac{\Delta t}{4}$. The choice of χ was motivated from the consideration that it should be fairly large to have a visible effect on the results while allowing for time-step refinement studies without causing the simulation to become unstable. As a filter G , a symmetric 5 point stencil was used, applied in Fourier space via its transfer function (Fig. 5), so that the integral in eq. (1) reduces to a product for each Fourier harmonic. Results show that solution of eq. (4), G_2 obtained from $Q_N * G$ with $N=5$, and eq. (5) are in fact equal as expected (Figs. 6, 7).

The spectrum (Fig. 7) reveals that the present LES is under-dissipative in the medium wave-number range ($5 \dots 10$). Such a behaviour was also observed by Winckelmans and Jeanmart, 2001. In the following an explanation is suggested. If k_2 is the cut-off wave number of G_2 , the relaxation term in eq. (4) affects only scales $k > k_2$. However, filtering of the velocities $\tilde{u} \rightarrow \tilde{u}^*$ before plugging them into the non-linear term on the left-hand side will affect scales

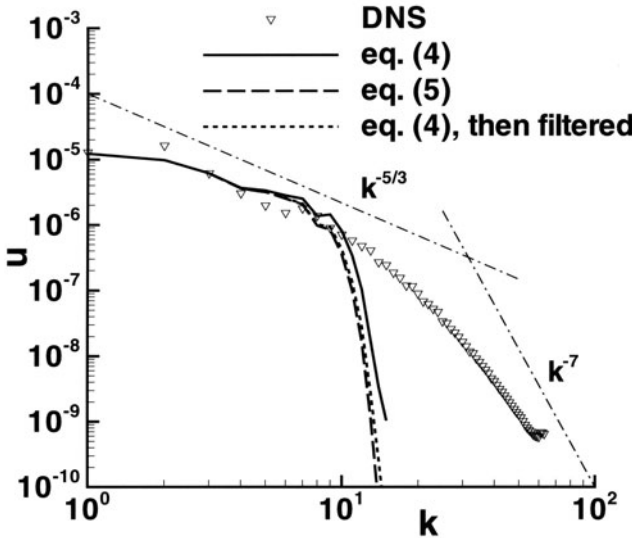


Figure 7. Spanwise spectra for the streamwise velocity integrated over the interval $[x = 2.5, 2.75; y = 0, y_{max}]$.

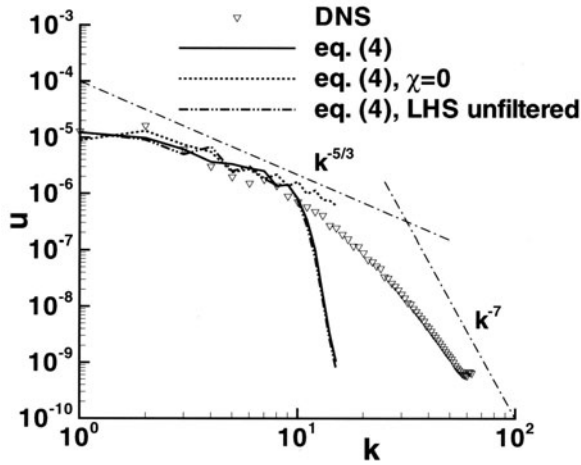


Figure 8. Same as Fig. 7. Results of eq. (4) for $K=15$, $\chi = 0$ and LHS unfiltered.

$k < k_2$ by suppressing an influence of scales in the range $k > k_2$ on them. Assuming that this effect would have been dissipative (i.e. scales in the range $k > k_2$ would act in a way as to draw energy from scales $k < k_2$), the complete model is not dissipative enough for scales $k < k_2$. Setting $\chi=0$ or leave the non-linear term on the left-hand side unfiltered does not change the situation significantly (Fig. 8), since both relaxation and explicit filtering act in a similar manner.

4. Conclusions

DNS of laminar-turbulent transition in a separation bubble was carried out. A large mean flow deformation reaching far upstream was observed and attributed to a viscous-inviscid interaction. This lead to a formulation of the upper boundary to yield height-independent results. The DNS-result was chosen as a reference case for a subsequent analysis of LES. This analysis consisted of two steps: a (scale) separation and a (subfilter-scale or SGS) modeling step. The first step is associated with an explicit filter applied to the non-linear term while the second step yields closure through a turbulence model. It was shown that the form of the filtered momentum equations does not depend on the choice of the filter while the quantitative value of the SGS model will.

From the observations made, the following guidelines for the choice of the filter G_2 and the SGS-model can be derived: G_2 should be designed such that $k_2 \leq \min(\frac{2}{3}k_c, k_{accurate}^{FD})$ and the turbulence model should not only act on wave numbers $k > k_2$ but also on smaller ones. The constraint on G_2 reduces

errors originating from aliasing and finite differencing (k^{FD} is the modified wave number), while the modeling aspect was discussed in the previous section.

Acknowledgments

Financial support of this research by the Deutsche Forschungsgemeinschaft DFG under grant Ri 680/10-2 is gratefully acknowledged.

References

- Alam, M. and Sandham, N. (2000). Direct Numerical Simulation of 'Short' Laminar Separation Bubbles with Turbulent Reattachment. *J. Fluid Mech.*, 410:1–28.
- Guerts, B. and Holm, D. (2003). Regularization modeling for large-eddy simulation. *Phys. Fluids*, 15(1):L13–L16.
- Kloker, M. (1998). A robust high-resolution split-type compact FD scheme for spatial direct numerical simulation of boundary-layer transition. *Appl. Sci. Res.*, 59:353–377.
- Meyer, D. (2003). *Direkte numerische Simulation nichtlinearer Transitionsmechanismen in der Strömungsgrenzschicht einer ebenen Platte*. Dissertation, Universität Stuttgart.
- Pruett, C. (2001). Toward the de-mystification of LES. In Liu, C., Sakell, L., and Beutner, T., editors, *DNS/LES Progress and Challenges*, page 231. Greyden, Columbus, OH.
- Rist, U. (1998). Zur Instabilität und Transition in laminaren Ablöseblasen. Habilitation, Universität Stuttgart, Shaker Verlag, Aachen.
- Rist, U. and Maucher, U. (1994). Direct numerical simulation of 2D and 3D instability waves in a laminar separation bubble. In *Application of Direct and Large Eddy Simulation to Transition and Turbulence*, number AGARD CP-551, pages 34.1–7. 74th Fluid Dynamics Symposium.
- Spalart, P. and Strelets, M. (2000). Mechanisms of Transition and Heat Transfer in a Separation Bubble. *J. Fluid Mech.*, 403:329–349.
- Stolz, S., Adams, N., and Kleiser, L. (2001a). An approximate deconvolution model for large-eddy simulation with application to incompressible wall-bounded flows. *Phys. Fluids*, 13(4): 997–1015.
- Stolz, S., Adams, N., and Kleiser, L. (2001b). The approximate deconvolution model for large-eddy simulation of compressible flow and its application to shock-boundary-layer interaction. *Phys. Fluids*, 13(10):2985–3001.
- Wasistho, B. (1997). *Spatial Direct Numerical Simulation of compressible boundary layer flow*. Phd. thesis, University of Twente.
- Wilson, P. and Pauley, L. (1998). Two- and three-dimensional large-eddy simulations of a transitional separation bubble. *Phys. Fluids*, 10(11):2932–2940.
- Winckelmans, G. and Jeanmart, H. (2001). Assessment of some models for LES without/with explicit filtering. In Geurts, B., Friedrich, R., and Metais, O., editors, *Direct and Large-Eddy Simulation - IV*, volume 8, pages 55–66. Ercoftac Series, Kluwer Academic Publishers, Dordrecht, Boston, London.
- Yang, Z. and Voke, P. (2001). Large-Eddy Simulation of Boundary-layer and Transition at a Change of Surface Curvature. *J. Fluid Mech.*, 439:305–333.

CROSSFLOW VORTICES NEAR THE ATTACHMENT LINE OF A SWEEP AIRFOIL AT $M = 8$

Jörn Sesterhenn and Rainer Friedrich

Abstract We consider the flow in the vicinity of the leading edge of a parabolic profile in swept supersonic flow. In terms of the attachment–line instability, which is expected at the leading edge, the sweep–Reynolds number is above $Re = 642$, the sweep–Mach number is $M = 1.25$, and the ratio of nose radius to viscous length scale is $R/\delta \approx 400$. The wall is adiabatic. The parameters are chosen such that we could expect exponential disturbance growth of the leading edge instability for *incompressible, flat-plate flow*. No precise information about the formation of the attachment–line instability in the *compressible, curved-surface case* is known.

The response of the boundary layer due to random perturbations in the stagnation region as well as entropy disturbances ahead of the shock is investigated numerically. In sequel, both the leading edge instability and a crossflow instability are excited. In the present configuration the crossflow instability clearly dominates.

Keywords: compressible leading edge flow, Görtler–Hämmerlin instability, crossflow vortices, stability, transition

1. Introduction

Empirically, the attachment–line instability was found to be important for laminar/turbulent transition on swept wings since the early fifties. A review of the early theoretical and experimental work may be found in Poll, 1979. The linear stability analysis by Hall et al., 1984 for the incompressible flat plate yields a critical Reynolds number $Re = 583$. This Reynolds number is based on the spanwise velocity and the viscous length scale $\delta = \sqrt{\nu / (\frac{\partial u_\infty}{\partial x})}$. This finding is consistent with DNS studies as for example performed by Spalart, 1988. Flat plate experiments do not exist and curved surface experiments supposedly confirm this results. But recently a finite nose radius was found to increase the critical Reynolds number. Based on linear stability analysis, Lin and Malik,

1997 predict an increase up to $Re = 637$ for $R/\delta = 143$. The flat plate case is recovered for $R/\delta > 1430$.

For the weak compressible regime on a flat plate, Le Duc et al., 2002 confirmed the existence of the instability for $Re = 642$. On a curved surface this instability was observed by Schwertfirm, 2002. Additionally, disturbances downstream from the leading edge were found. Since they were located at the end of the computational domain it was uncertain whether they were physical or not.

In the present study the supersonic case is investigated where the parameters at the stagnation line are similar to Le Duc et al., 2002 and Schwertfirm, 2002. The computational domain is significantly enlarged in the chordwise direction to investigate the effects observed in Schwertfirm, 2002.

2. Numerical Method

We use a characteristic-type numerical scheme which was developed for direct numerical simulations of compressible transitional and turbulent flows by Sesterhenn, 2001. In these flows low numerical dissipation and dispersion are important and a primitive variable formulation is employed in order to achieve high accuracy and performance. Shocks are treated explicitly with a shock-fitting procedure as demonstrated in Fabre et al., 2001. Thus, the shock location is an unknown of the computation and the grid has to be time-dependent. The main feature of the scheme is a multidimensional wave decomposition of the Euler equations which lend themselves easily to a high order (typically 5th) discretization. Boundary conditions can be treated in a physical manner.

In the present case we use a grid of $350 \times 128 \times 8$ points. The resolution of eight points in spanwise direction is able to resolve the principal mode. This is sufficient for the present purpose. The shock is treated with a shock-fitting method. At the outflow, non-reflecting boundaries are employed. The spanwise direction is treated periodically. The coordinate system is orientated as follows: The origin is at the nose of the body. The x -axis points into the chordwise direction and z denotes the spanwise direction. The velocity components in (x, y, z) are called, as usual, (u, v, w) . The spanwise extent of the computational domain $L_z \approx 25\delta$ is chosen to approximately match the wavelength of the expected instability. Clearly, this setup only allows a given wavelength instability and does not reveal the most unstable wave.

3. Results

3.1 Base flow

The base flow is computed first for each Reynolds number. It is independent of the spanwise coordinate and can be computed in two dimensions. The computational domain is then expanded into the third direction to the desired length L_z . This length is chosen according to the stability diagram of the incompressible flat plate flow depicted in Figure 1. The ordinate is expressed in spanwise wavelengths $\beta = \frac{2\pi\delta}{L_z}$. Please note that the depicted stability diagram is valid for the incompressible flat plate. In the present paper we show results

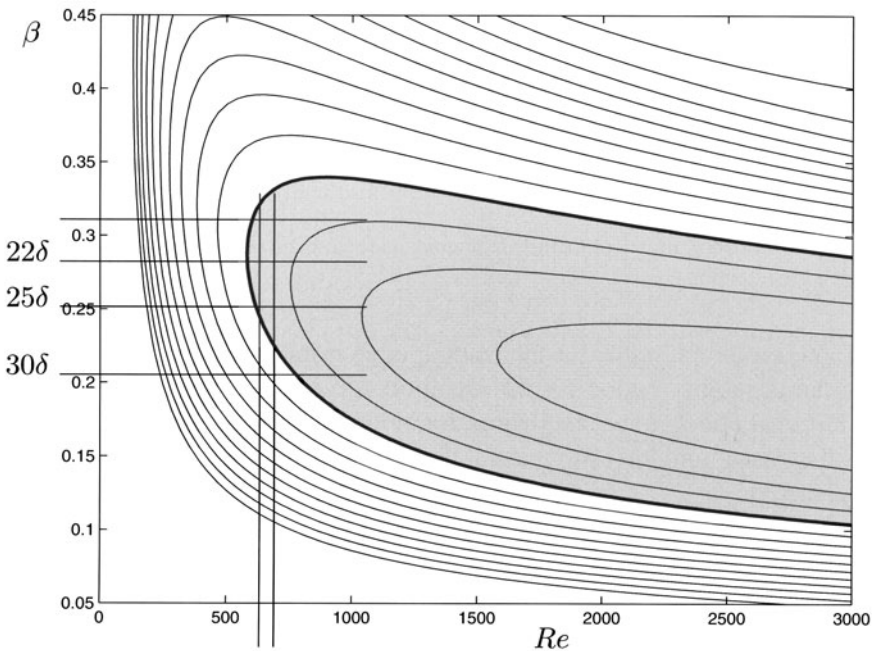


Figure 1. Stability diagram of the incompressible flat-plate Hiemenz-flow. (Courtesy Obrist and Schmid, 2003)

for $Re = 642$ and $Re = 700$ at lengths ranging from $L_z = 20$ to $L_z = 30$, corresponding to a range of β from 0.31 to 0.21.

3.2 Random Perturbation

This base flow was seeded with random perturbations in all flow quantities using a relative amplitude of 10^{-7} as compared to the free-stream values. Disturbance growth is observed for all flow cases, as depicted in Figure 2 for $Re = 700$ and $L_z = 20\delta, 22\delta, 30\delta$. Unfortunately $L_z = 30\delta$, corresponding to

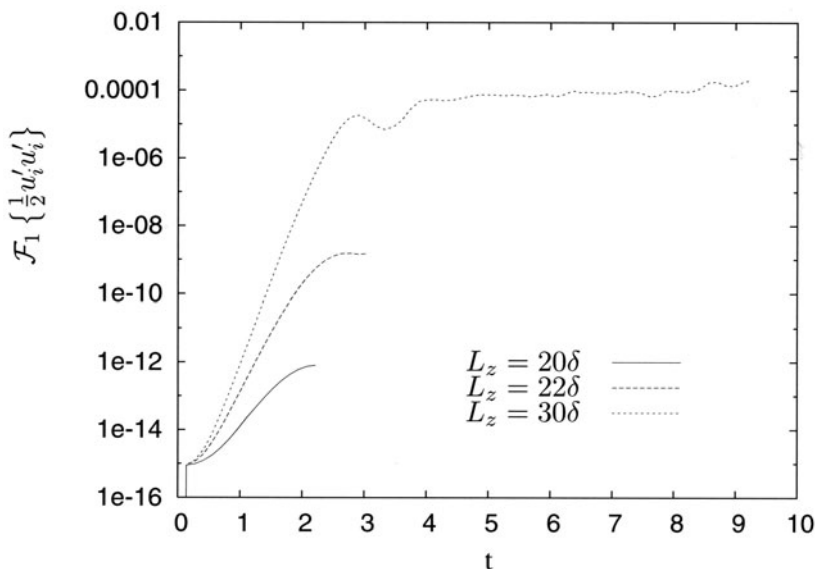


Figure 2. Disturbance growth of the first harmonic mode in spanwise direction for $Re = 700$ and random perturbation

$\beta = 0.209$, should be stable for the leading edge instability, since it is already outside the instability region for the incompressible, flat plate and we expect both additional effects to be stabilising. Examination of the growing structures reveals the growth of a crossflow instability. More details will be presented in the next section.

3.3 Entropy Perturbation

To enhance the growth of the leading edge flow we perturbed the flow in the freestream by a convected entropy disturbance of the form

$$s = s_\infty + \epsilon \left(1 + a \cos \frac{2\pi z}{L_z} \right) C_v e^{-\left(\frac{(x-x_o)^2 + (y-y_o)^2}{C^2} \right)}. \quad (1)$$

The interaction of this disturbance with a shock was investigated in Fabre et al., 2001. Entropy-, vorticity- and acoustic disturbances are generated. The vorticity disturbances resemble the shape of the leading edge instability; thus, we expect it to trigger the latter more successfully than random perturbations. Again, the crossflow vortices grow dominantly. Their shape is shown in Figure 3 by use of the Q -criterion. Positive values of $Q = -\frac{1}{2}u_{i,j}u_{j,i}$ indicate regions with dominance of rotation $r_{ij} := \frac{1}{2}(u_{i,j} - u_{j,i})$ over shear $s_{ij} := \frac{1}{2}(u_{i,j} + u_{j,i})$. Figure 4 represents a cut normal to the parabolic surface in the region of the

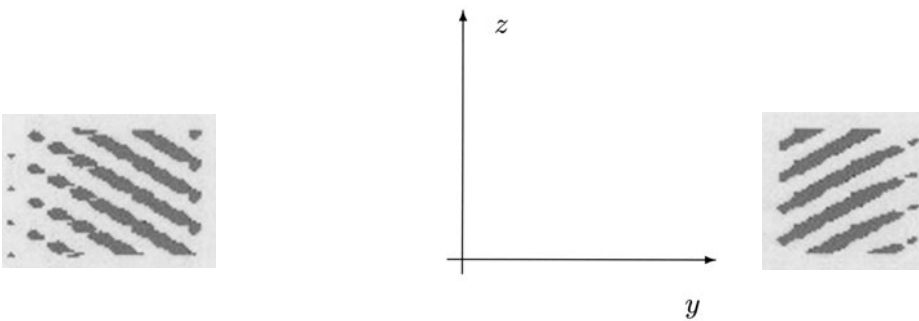


Figure 3. Shape of the crossflow vortices shown as a positive isosurface of $Q = -\frac{1}{2}u_{i,j}u_{j,i}$. The view is directed towards the stagnation line, extending vertically in between the two spots and the leading edge flow is directed from bottom to top.

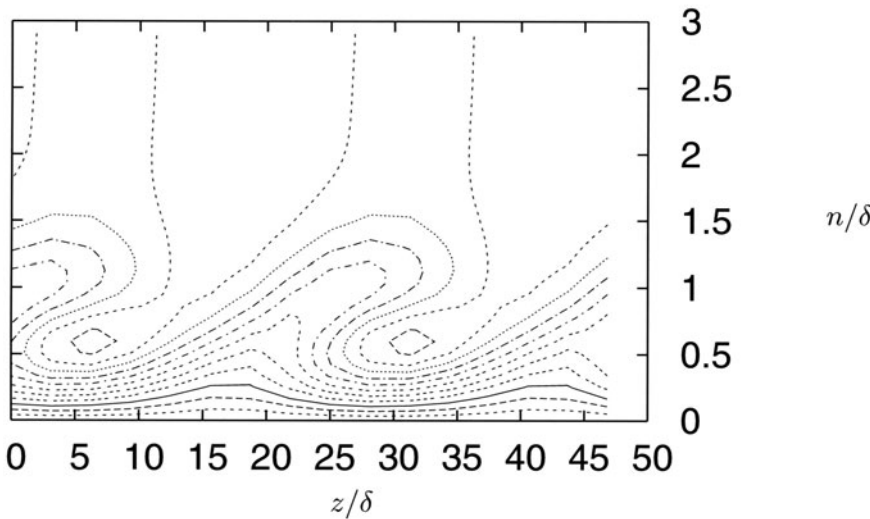


Figure 4. Contours of chordwise velocity in the crossflow vortices. $L_z = 25\delta$

crossflow vortices. Lines of constant chordwise velocity are depicted. The location of the first appearance of crossflow vortices was found to coincide with the location of maximal streamline curvature.

$$K^2 = \frac{\dot{r}^2 \ddot{r}^2 - (\dot{r} \ddot{r}^2)}{(\dot{r}^2)^3}. \quad (2)$$

The dot denotes a derivative with respect to time.

The following figures 5 and 6 show the Fourier coefficient in the spanwise direction of the disturbance velocity component v at three instances in time. The first diagram shows its value along the wall normal direction at $s = 171\delta$, the second figure depicts its maximum along the s coordinate, s being the arclength of the parabola. At $t = 4.3$, the external disturbance has reached approximately $s = 650\delta$ and at $(n/\delta, s/\delta) = (-1, 171)$ an instability appears.

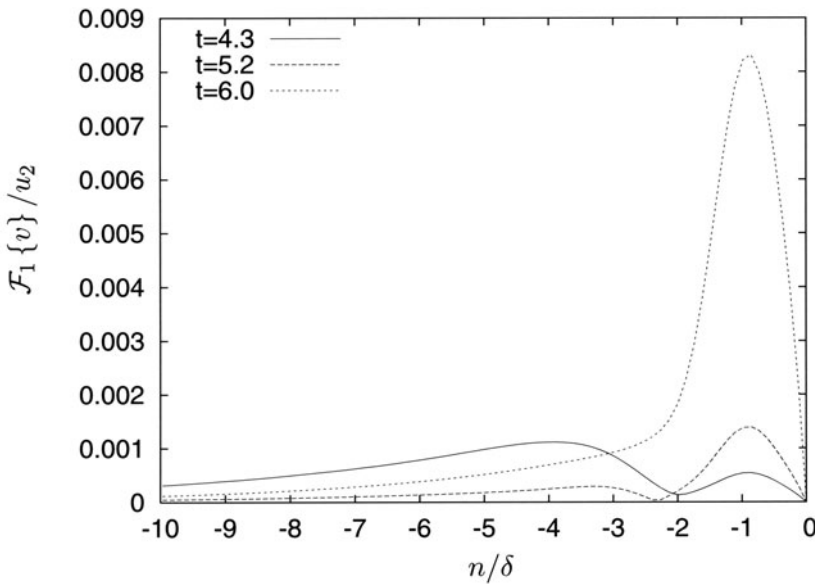


Figure 5. Principal Fourier mode of the v velocity in wall normal direction

Over the course of time, the external disturbance travels past the body and the localised instability increases. At $t = 6.0$ a second vortex forms which grows and finally merges with the first one. The maximum disturbance velocity gains values higher than 35% of the normal velocity behind the shock. Subsequently higher modes appear which would require substantially higher grid resolution in the z -direction.

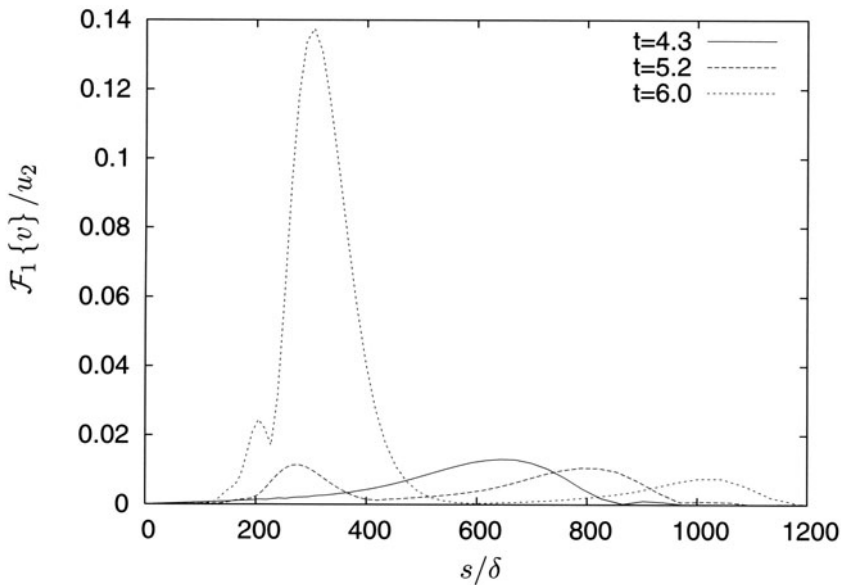


Figure 6. Maximum Value of the principal Fourier mode of the v velocity in s direction

4. Conclusion

In the present flow configuration we expected an attachment line instability, originating at the stagnation line and extending over a certain range of the profile. On the contrary, we found a crossflow instability off the attachment line.

This instability dominates clearly in the present configuration. From our present view, the attachment line instability is overemphasised in the literature and future studies have to reveal the relative importance of both instabilities for a wider range of parameters.

References

- Fabre, David, Jacquin, Laurent, and Sesterhenn, Jörn (2001). Linear interaction of a cylindrical entropy spot with a shock. *Physics of Fluids*.
- Hall, P., Malik, M., and Poll, D.I. (1984). On the stability of an infinite swept attachment-line boundary layer. *Proc. R. Soc. Lond.*, A(395):229–245.
- Le Duc, Anne, Sesterhenn, Jörn, and Friedrich, Rainer (2002). Direct numerical simulation of instabilities of the compressible swept Hiemenz flow. In Dussauge, J.P. and Chikhaoui, A., editors, *Aerodynamics and Thermochemistry of High Speed Flow*.
- Lin, Ray-Sing and Malik, Mujeeb R. (1997). On the stability of attachment-line boundary layers. part 2. the effect of leading edge curvature. *J. Fluid Mech.*, 333:125–137.

- Obrist, Dominik and Schmid, Peter (2003). On the linear stability of swept attachment-line boundary layer flow. Part 1. Spectrum and asymptotic behaviour. *Journal of Fluid Mechanics*.
- Poll, D.I.A. (1979). Transition in the infinite swept attachment-line boundary layer. *Aeronautical Quarterly*, 30:607–628.
- Schwertfirm, Florian (2002). DNS von Instabilitäten in der dreidimensionalen kompressiblen Strömung entlang der Vorderkante eines gepfeilten Tragflügels. Master's thesis, TU-München, Fachgebiet Strömungsmechanik.
- Sesterhenn, Jörn (2001). A characteristic-type formulation of the Navier–Stokes equations for high order upwind schemes. *Computers & Fluids*, 30(1):37–67.
- Spalart, P.R. (1988). Direct numerical study of leading edge contamination. Technical Report CP-438, Fluid Dyn. of 3D Turb. Shear Flows and Transition, AGARD.

TURBULENT FLOWS INVOLVING COMPLEX PHYSICAL PHENOMENA

3.1 MULTIPHASE AND NON-NEWTONIAN FLOWS

LARGE-EDDY SIMULATION OF SMALL-SCALE OCEAN TURBULENCE COUPLED WITH BUOYANT PLUMES

Baixin Chen, Yongchen Song, Masahiro Nishio and Makoto Akai

National Institute of Advanced Industrial Science and Technology

1-2-1 Namiki, Tsukuba 305-8564, Japan

b.chen@aist.go.jp

Lars Golmen

Norwegian Institute for Water Research, N-5005 Bergen, Norway

Abstract To examine the turbulent characteristics of a small-scale ocean (length scale at $L=O(10^3\text{ m})$) disturbed by buoyant plumes, a numerical experiment is performed by employing Large-eddy simulation technology and two-fluid theories. This includes a simulation of reconstruction of the statistically stationary state of a small-scale ocean and the simulation of two-fluid plumes. For numerical reconstruction of a small-scale ocean, the observation data of the instantaneous flow field on the West Coast of Hawaii Island is applied to the determination of the turbulent structure with the aid of the forced-dissipative mechanism. The dynamics of buoyant droplets is described by an Eulerian scheme with the assumption of treating the droplets as a quasi-fluid. The two-way coupling between turbulent ocean and droplets is performed through exchange sub-models for momentum and mass. The predictions of turbulence spectra indicate that the buoyant plumes improved indistinctly the horizontal turbulent characteristics, however, they significantly modified the temperature spectrum in the lower wavenumber range. For plumes, the dynamics in the regime near the injection exit are dominated by interactions between turbulent ocean and droplets/solution. Outside of this regime, water column of solution is governed by the ocean turbulent flow.

Keywords: Small-scale ocean, turbulence, two-phase plume, LES

1. Introduction

Turbulent two-phase plumes in the stratified environment are the kinds of phenomena in the ocean that occur naturally, such as the buoyant hydrothermal plume discharging dissolvable chemical species and suspend particles into seawater from the sea floor (Rona et al, 1991). Others are created artificially, such

as the buoyant liquid CO_2 plume and CO_2 enriched seawater peeling plume developed by directly releasing liquid CO_2 into the ocean at a middle depth to mitigate the CO_2 concentration from the atmosphere as proposed by Marchetti (1977). A fundamental understanding of the mechanism of plume formation and evolution is therefore essential for various applications in oceanic and environmental engineering. Experimentally, the plume structure and the three types of intrusions in a linearly stratified ambient were indicated depending on the bubble flow rate with respect to the stratification (Asaeda & Imberger, 1993). Theoretically, the analysis models of mass flux entraining in and peeling out the plume were developed to predict the plume efficiency and basic structure (Asaeda & Imberger, 1993). Numerically, LES had been applied to the examination of the homogeneous stably stratified shear turbulent flow (Kaltenbach, Gerz & Schumann, 1994). The effect of microbubbles on developed turbulence was also analyzed, from which it was demonstrated that two-way coupled microbubbles can reduce the turbulent energy in decaying turbulence and in turbulent mixing layers under certain conditions (Druzhinin & Elghobashi, 2001).

On the other hand, recent field observation data from the deep ocean provided new information of small-scale ocean turbulent flow (Maeda et al, 2000), from which the kinetic energy spectrum was obtained. These data can then be applied to the numerical modeling to reexamine the technologies currently used. The major objective of this study, from the point of view of practical application, is to make an attempt to numerically reconstruct a 'real' small-scale ocean with the aid of available observation data and LES. With this reconstructed 'real' ocean, the dynamics of the introduced buoyant droplets and solution plumes are further investigated by a two-way coupling method. The interactions between plumes and seawater column, including mass and momentum exchanges, are realized through the source terms of the governing equations for each phase.

2. Numerical Reconstruction of a Small-scale Ocean

As the basis for the numerical reconstruction of the small-scale ocean, field observation and data are briefly summarized here. The field observation was performed on the West Coast of Hawaii Island ($19^{\circ}43.3624'N$, $156^{\circ}04.605W$), where the depth is 874.9m and three sets of temperature and current sensors were employed vertically at 20m, 230m and 440m from the bottom, respectively. The time interval of the measurement was set to two minutes and the data was recorded as the mean value over 15 seconds. The vertical distributions of temperature and salinity, which are used to calculate the density, were

obtained separately. The details of the field observation can be found in the CRIEPI Report (Maeda et al, 2000).

Data analysis has shown that the mean horizontal velocity is in the order of $U_m \sim 2.0 \text{ cm/s}$ and appeared to be a shear flow from the bottom. The time period without being influenced from the tide is about 6 hours. According to these basic data, the small-scale ocean to be reconstructed numerically is set up with the following assumptions: 1) The special scale of the ocean is in the order of $L \sim O(500 \text{ m})$ and the resolution should be smaller than 2.5 m ($\Delta \leq 2.5 \text{ m}$); 2) The flow dynamics inside this 'ocean' can be reasonably regarded as a horizontal-quasi-homogeneous and stratified turbulent shear flow; and 3) The Taylor hypothesis of frozen convection is applicable. The turbulent dynamics of this ocean is then described by a set of Navier-Stokes based equations in a large-eddy simulation version, which are given, in dimensionless form using the reference length $L=500 \text{ m}$, velocity $U_0=1.0 \text{ m}$, time $t=L/U_0$, density $\rho_0=1000 \text{ kg/m}^3$, and scalars Φ_{max} , respectively, by:

$$\partial_t(\bar{\rho}\hat{u}_i) + \partial_j(\bar{\rho}\hat{u}_i\hat{u}_j) = -\partial_i\hat{p} + \partial_j(2\nu\hat{S}_{ij} - \hat{\tau}_{ij}) + (\bar{\rho} - 1)g_i + F_t\delta_{mi} \quad (1)$$

$$\partial_t(\bar{\rho}\hat{\varphi}) + \partial_i(\bar{\rho}\hat{u}_i\hat{\varphi}) = \partial_i(\bar{\rho}D_\varphi\partial_i\hat{\varphi}) - \partial_i(\bar{\rho}\hat{q}_i) \quad (2)$$

in which resolved variables, (\wedge) , include the velocity vector, \hat{u}_i , the piezometric pressure, \hat{p} , defined by the pressure and the hydrostatic pressure, and scalars, $\hat{\varphi}$, including temperature and salinity. The scalar variables are used to calculate the density of seawater, ρ_s , using the equation of state for seawater. \hat{S}_{ij} is the strain rate. The turbulent dissipation and transport terms, $\hat{\tau}_{ij}$ and \hat{q}_i , in sub-grid scale are estimated by means of a Structure Function model (Lesieur & Métais, 1996) with turbulent Prandtl number, $Pr_t = 0.7$.

In practice, the dimensionless computation domain is a cubic box with dimensions $x_1=1.0$, $x_3=0.2$ (horizontal), and $x_2=0.6$ (vertical), respectively. A uniform grid of $N_1=256$, $N_2=128$, and $N_3=64$ points is used. The initial fields are given by the mean horizontal velocity $u_1=u_m(x_2)$; $u_2=u_3=0$, temperature $T=T_m(x_2)$, and salinity $S=S_m(x_2)$, which are derived from the observation data (Maeda et al, 2000) for the vertical distributions only. The turbulent field is then created by perturbing these mean profiles at a narrow band of wavenumber k_f through the source term appearing on the right hand side of (1), $F_t\delta_{mi}$ when $m=i$. This turbulent force is generated and controlled (Grossmann & Lohse, 1992) by:

$$F_t = \bar{\rho}\epsilon u'_0(k, t) / \sum_{k \in k_f} u'_0(k, t) u'_0(k, t) \implies k \in k_f \quad (3)$$

where ϵ is the sub-grid scale turbulent dissipation rate and $u'_0(k, t)$, is a forcing intensity variable, which should be adjusted to match the kinetic energy spectrum of the observations associated with the sub-grid scale model. It is

not difficult to find out from (3) that the total energy input will be dissipated equally by sub-grid scale dissipation once the statistical state is approached. The forcing is performed in three directions in the same way and the forcing positions are determined randomly by a random number generator.

The equations, (1)–(2), associated with the equation of continuity, closed by the SGS structure function models and forced by (3), were numerically solved by a finite-volume method in a staggered grid system. Discretization of the momentum and scalar equations was accomplished by a second-order central-difference scheme. The flow variables were advanced in time by an implicit three-level second order scheme and the SIMPLEC algorithm was applied to solve the momentum equation. The top of the domain is a free surface that was treated as a rigid slip wall. This is a reasonable and simple approach when no mass transfer is assumed at the top. The bottom of the domain was considered to be a no-slip boundary for velocity vectors and a zero-flux boundary for scalars. The horizontal sides are all open boundaries.

The preliminary results from the numerically reconstructed small-scale ocean are presented in Fig. 1. As can be seen from the instantaneous flow field shown by the contours of horizontal velocities (Fig.1, left) in the central section ($x_3 = 0.1$) after the steady state being approached, the basic flow characteristics of the small-scale oceanic flow appear to be reproduced well. To examine the mean characteristics, the vertical profile of the mean velocity, $u_{1m}(x_2)$ (dimensionless), samples from the central section are plotted in Fig. 1 (right) together with the observation data, which is the initial distribution, for comparison. The statistical properties of the turbulent flow field are presented by the one-dimensional kinetic energy and temperature spectra, respectively, which are shown in Fig. 2. The data are sampled from the central section. For the horizontal turbulent kinetic energy spectrum, the prediction is well accepted in comparison with the observation data (Fig.2, left). This spectrum represents the homogenous characteristics of small-scale ocean turbulence. However, a large discrepancy is found (Fig.2, right) with respect to the temperature spectrum in comparison with observation data, especially in the region of the lower wavenumber range. Associated with this, the spectrum of the vertical velocity is also in disagreement with the observation data at lower wavenumber (Fig. 2, right). This is due to the effect of potential energy and the equipartition of forcing in the momentum equations. These differences seem to assume implicitly that there exists an additional thermo-source rather than the kinetic only, which is not accounted for in the model, but dominates over the thermal field even in this small scale. Because the physical mechanism of this lower wavenumber thermo-source (large scale thermobaric instability or some kinds of buoyancy forcing) is not clear currently, no artificial modification is made here and it is kept as an open problem for further investigation.

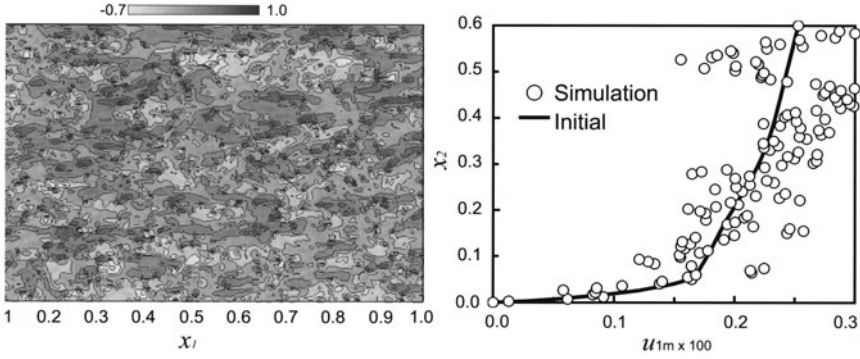


Figure 1. Contour of horizontal velocity of the reconstructed flow field (left) and the mean velocity (right).

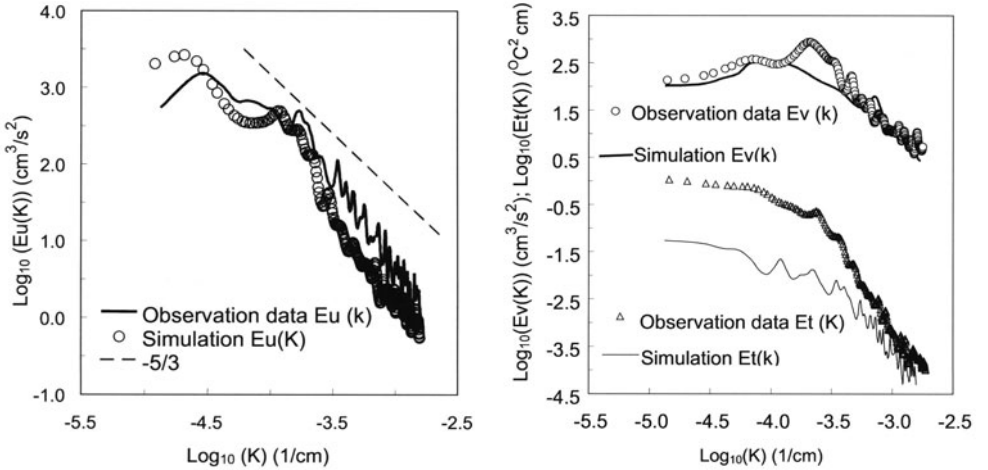


Figure 2. Predictions of one-dimensional kinetic energy spectra, for horizontal (left) and vertical (right-top) velocities, and temperature spectra (right-bottom) and data.

3. Modeling of Buoyant Plumes in Small-scale Turbulent Ocean

To simulate the generation and evolution of buoyant plumes in a 'real' ocean, dissolvable droplets of liquid CO_2 are injected into the reconstructed small-scale turbulent ocean discussed in section 2. Since the simulation must account for a large quantity of droplets being injected continuously, an Eulerian-Eulerian two-fluid frame is adopted to describe the dynamics of the droplet plume under the memory limitations of present-generation computers. As a quasi-fluid, the continuum equation for droplets is decomposed into two equations for droplet void fraction, α , and number density, f , in order to estimate

diameter shrinkage resulting from droplet dissolution. For simplicity, droplet coalescence, secondary break-up, and collisions are assumed to have negligible effect on the number density function. Details of the two-phase flow model can be found in Chen et al, (2002).

Numerical experiments were performed by setting the physical properties of the droplets as follows, with reference to the natural species (CO_2 and CH_4) in the ocean. The density ratio $\rho_0/\rho_d=1.08$; the ratio of initial diameter of droplets to the grid size is $D_0/\Delta=0.035$ ($D_0=7.0\text{mm}$) and the initial void fraction of droplets is $\alpha_0=1.0\%$. It is assumed that the solution of droplets is denser than the ambient seawater, the density ratio of solution to seawater is a linear function of the mass concentration of solute (Song et al, 2002). For momentum exchange, the source term can be expressed as:

$$\dot{F}_d = 0.75(\pi/6)^{1/3} \rho_d \nu_w \hat{\alpha}^{2/3} \hat{f}^{1/3} C_d |\hat{u}_j - \hat{u}_{dj}| (\hat{u}_j - \hat{u}_{dj}) \quad (4)$$

where the subscript 'd' indicates the droplet; ν_w is the kinematic viscosity of seawater and the drag coefficient being estimated by $C_d=24(1+0.125 Re^{0.72})$ while the dissolution coefficient is calculated through the Sherwood number to invoke the effect of the flow field.

The simulation is started by spinning-up the small-scale ocean to a full turbulence state and then being maintained by the forced-dissipative mechanism. By the ocean reconstruction mentioned in Section 2, droplet injection is then initiated on a grid of $n_1=45$, $n_2=8$, and $n_3=32$ points. The droplet equations are solved to obtain new source terms that couple with the ocean flow field. This computational cycle was terminated and began again at the next time step when the density difference between cycles fell below a selected threshold.

The fully-developed plumes (in the central section) of droplets and solution predicted from the model are given in Fig.3, where the droplet plume is visualized by its diameter and the solution by its concentration. In the region downstream of the injection exit, the solution column descends downward due to the high solution concentration. It significantly dispersed the original ocean turbulent structure locally. The statistical analysis of the data sampled from layers of this region predicts, as shown in Fig. 4, that the horizontal kinetic energy spectrum seems to be insensitive to this disturbance, which indicates that the droplet drag seems to be negligible in comparison with the ocean turbulence.

Contrarily, in comparison with the original ocean spectra, the temperature spectrum was significantly improved especially on the lowerwavenumber side and approached that for the observation data. This result identifies a suggestion that, apart from the equipartition forcing by equation (3), there exists a kind of lower frequency buoyancy forcing, which is the force balanced by the potential energy and makes the small-scale ocean to appear as a homogeneous turbulence like what was observed from the field observation

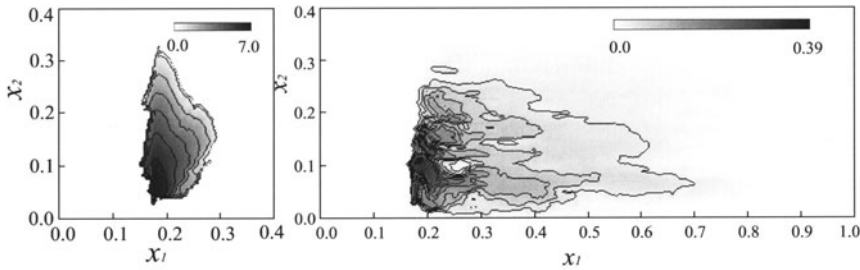


Figure 3. Modeling prediction of two-phase plumes; the droplet plume by droplet diameters; Solution plume (right) by concentration.

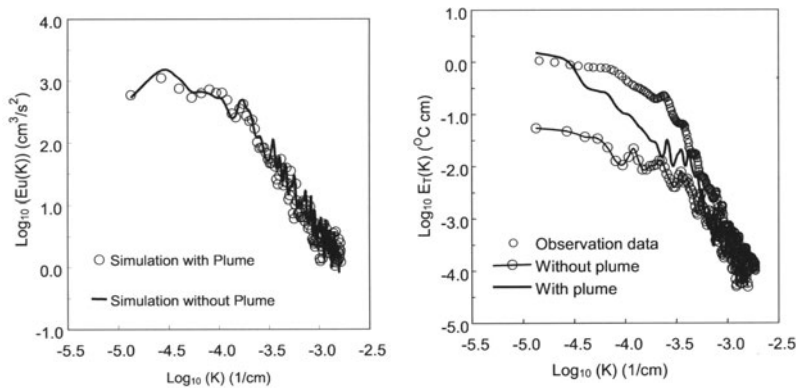


Figure 4. Comparison of results for the effects of a plume on the turbulent spectra. Horizontal kinetic energy spectrum (left) and temperature spectrum (right).

data. Thus, the dissipative term in (3) should be extended to include the potential energy.

4. Conclusions

A numerical model of simulating the small-scale ocean turbulence coupled with buoyant plumes is developed with the use of LES and two-phase flow theories. With the aid of field observation data, the predictions indicated that the buoyant plume could significantly disturb the vertical turbulent structure of the small scales, without disturbing distinctly the horizontal one.

Acknowledgments

This study is part of the investigations within Research Projects of ARCS and of CO_2 Ocean Sequestration funded by NEDO, Japan.

References

- Aseada, T. and Imberger, J.: *Structure of Bubble Plumes in Linearly Stratification Environments*, J. Fluid Mech. vol. 294, pp. 35-57, (1993).
- Chen, B. Nishio, M., Song, Y., Someya, S., and Akai, M.: *Numerical Visualization of Two-phase Plume Formation in a Stratification Flow Environment*, Ann. N.Y. Acad. Sci., vol. 972, pp. 285-291, (2002).
- Druzhinin, O. A., and Elghobashi, S.: *Direct Numerical Simulation of a three-dimensional spatially Developing bubble-laden Mixing Layer with Two-way Coupling*, J. Fluid Mech. vol. 429, pp. 23-35, (2001).
- Grossmann, S. and Lohse, D.: *Intermittency in the Navier-Stokes Dynamics*, Z. Phys. B: Condens. Matter. vol. 89, pp.11-16, (1992).
- Kaltenbach, H.-J. Gerz, T. and Schumann, U.: *Large-eddy Simulation of Homogeneous Turbulence and Diffusion in stably Stratified Shear Flow*, J. Fluid Mech. vol. 280, pp. 1-40, (1994).
- Lesieur, M. and Métais, O.: *New Trends in Large-eddy Simulations of Turbulence*, Annu. Rev. fluid. Mech. vol. 28, pp. 45-82, (1996).
- Maeda, Y., Shitashima, K., Nakashiki, N. and Ohsumi, T.: *Direct Measurements of Current in West Coast of Hawaii Island*, Technical Note, CRIEPI, Japan, (in Japanese) (2000).
- Marchetti, C.: *On Geoengineering and the CO₂ Problem*, Climatic Change, vol. 1, pp.59-68, (1977).
- Rona, P.A., Palmer, D. R., Jones, C., Chayes, D.A., Czarnecki, M., Carey, E. W., and Geurrero, J.C.: *Acoustic Imaging of Hydrothermal Plumes, East Pacific Rise, 21ON, 109OW*, Geophys Res. Lett., vol. 18(12), pp.2233-2236, (1991).
- Song, Y. Nishio, M., Chen, B., Someya, S., Uchida, T. and Akai, M.: *Measurement of the Density of CO₂ Solution by Mach-Zehnder Interferometry*, Ann. N.Y. Acad. Sci., vol. 972, pp. 206-212, (2002).

LES OF TURBULENT BUBBLE FORMATION AND BREAK-UP BASED ON INTERFACE TRACKING

Petar Liovic,¹ Djamel Lakehal¹ and Jong-Leng Liow²

¹*Institute of Energy Technology
ETH-Zurich, Switzerland*

liovic@iet.mavt.ethz.ch, lakehal@iet.mavt.ethz.ch

²*School of Engineering
James Cook University, Australia*

jongleng.liow@jcu.edu.au

Abstract A 3D finite-difference method featuring piecewise planar volume tracking and explicit sub-grid scale modeling is used to simulate the violent, turbulent bubbling resulting from air venting into a water pool through a downcomer pipe. A moderate-sized mesh and domain decomposition-based parallelism were used for a $O(10^5) - O(10^6)$ -timestep computation, in order to extract turbulence statistics representative of long-time simulation of fully-developed flow. Volume tracking is seen to be a robust basis for super-grid scale simulation of the bubble rise, fragmentation and coalescence phenomena; it captures the kinematics of interfaces that are adequately resolved on the grid, and preserves the existence of bubbles and liquid jets breaking up to grid-scale (1–2 cells) size. Interface deformations are seen to strongly correlate with the large-scale structures forming at the front in the gas phase. Enhanced energy decay according to the 8/3 power law seen in bubbly flow is generally attained, with also some tendency towards the Kolmogorov K41 slope. The bubbling is turbulent on the gas side, and the main sources of turbulence are bubble break-up and gas jetting from the downcomer tip.

Keywords: Bubbling, LES, turbulence, volume tracking, VOF

1. Introduction

In the context of the migration from space-averaged modeling of interfacial flow to direct simulation approaches, interface tracking is increasingly complementing interdispersed-phase modeling of practical flows. Analogously, Large-Eddy Simulation (LES) is increasingly making inroads into the equiv-

alent domain traditionally dominated by RANS (Reynolds-averaged Navier-Stokes) modeling in transient studies of turbulence. In both approaches, the physics is simulated down to the grid-resolved level: in the case of interface tracking, the grid scale represents the minimum resolvable interfacial radius of curvature, while in turbulence the grid scale represents the minimum resolvable eddy length scale. The incorporation of the sub-grid scale physics is to an extent analogous, in that they represent *modeling* approaches in multiphase flow and turbulence computational modeling, respectively. Direct simulation of interfacial kinematics and physics using interface tracking-based finite-difference/finite-volume (FD/FV) methods has already been demonstrated as a powerful framework for solving flows dominated by massive topological changes and interfacial physics [1],[2],[3]. Little has been done, however, to capture the turbulence in these simulations. This work represents a first attempt to couple explicit SGS modeling for LES into an interface tracking-based FD/FV code for the simulation of bubbling due to air venting through a downcomer. It also constitutes a first attempt to apply the standard statistical turbulence analysis to improve our understanding of turbulence in a particularly vigorous flow scenario (as compared to fundamental studies such as [4]).

2. Numerical Method

2.1 The filtered governing equations

The filtered equations of motion for incompressible two-phase flow in the one-fluid context can be written as

$$\frac{\partial \tilde{u}_j}{\partial x_j} = 0 \quad (1)$$

$$\frac{\partial}{\partial t} (\rho \tilde{u}_i) + \frac{\partial}{\partial x_j} (\rho \tilde{u}_i \tilde{u}_j) = \frac{\partial}{\partial x_j} \left[-\tilde{p} \delta_{ij} + 2\mu \tilde{S}_{ij} - \tau_{ij} \right] + \rho g_i + F_k \quad (2)$$

where use was made of the conventional decomposition of the stress tensor into resolved and subgrid-scale (SGS) components, i.e. $\tau_{ij} \equiv \rho (\tilde{u}_i \tilde{u}_j - \tilde{u}_i \tilde{u}_j)$. The hatted quantities ($\tilde{\phi}$) denote the filtered variables obtained by applying a convolution filter G over the entire domain D :

$$\tilde{\phi} = G \otimes \phi = \int_D G(\mathbf{x} - \mathbf{x}') \phi(\mathbf{x}') d\mathbf{x}' \quad (3)$$

The last term of Eq. 2 represents the surface tension force. Material properties including the density and viscosity ($\eta = \rho, \mu$) are defined as

$$\eta \equiv f_k \eta_G + (1 - f_k) \eta_L \quad (4)$$

where f_k is the volume fraction indicator function delineating pure gas phase ($f_k = 1$) from pure liquid ($f_k = 0$) phase; volume-averaging at interface regions yields mixed-phase regions upon discretisation, in which case

$0 < f_k < 1$. The color function f_k is advected by the flow according to the topological equation

$$\frac{\partial f_k}{\partial t} + \frac{\partial(\tilde{u}_j f_k)}{\partial x_j} = 0 \quad (5)$$

To promote robustness, we use the velocity formulation of the momentum equation used in [3], rather than Eq. 2 directly.

2.2 Numerical Schemes

For accurate simulation of transient high-density-ratio flows in complex 3D geometries, we have developed the MFVOF-3D code, and it has been used here. The code uses MPI-facilitated parallelism based on domain decomposition, a projection method to update the flow field solution, and subdomain-based computation and Additive Schwarz Krylov subspace solvers for scalable parallel performance.

Vigorous bubbling places special demands on interface tracking methods, in that any particular method must robustly and accurately capture all stretching, fragmentation and coalescence phenomena induced by the bubbling. The range of interface length scales and high-curvature interfaces generated in bubble break-up, liquid filamentation, bubble coalescence and other phenomena, are a major challenge to particle-based and level-set methods, in that rigorous volume conservation at the local level becomes necessary, and the breaking of few closed surface into multiple closed surfaces (and vice versa) must be captured. Ultimately, volume tracking based on piecewise planar interface reconstruction (commonly known as PLIC-VOF (Piecewise Linear Interface Calculation) [5]) is the only interface tracking scheme currently capable of robustly, and for the most part accurately, tracking the movements, creation and destruction of all resolvable interfaces in the 3D solution domain. With 3D PLIC-VOF in the code, bulk-property distributions such as density and viscosity are geometrically extracted from the interface reconstructions using Eq. 4. The location of the interface as described by the color function is also used to model surface tension, using the fully kernel-based variant of the Continuum Surface Force (CSF) method [6] implemented in [3].

In using explicit SGS modeling in this study within the framework of Large-Eddy Simulation, we rely on the effective viscosity and the use of the velocity formulation to maintain stability, and use second-order centered differencing for the advection terms. We use the Smagorinsky kernel for SGS modeling. In the study by [7] of turbulence in bubbly flow using the dynamic SGS modeling approach of [8], an average damping coefficient result of $C_S = 0.1$ was obtained, with relatively small scatter; this value was used in our model. Turbulence damping in near-wall mesh cells is achieved using the van Driest wall damping.

3. Simulation of large–bubble formation at a downcomer

3.1 Problem Setup

The computational domain of height and breadth 450mm , corresponding to the experiment [1, 2], was discretised using an orthogonal, non–uniform 64^3 mesh. The xy –plane (z vertical) is refined in a “core bubbling” region about the downcomer to an equivalent 96×96 mesh spacing. The downcomer (inner–diameter 50mm , outer–diameter 72mm), was centrally located, with its tip 180mm above the bottom of the domain, and its diameter was resolved by 10 cells. Except for the inflow area, the top boundary is represented as an out–flow boundary. The bottom of the domain is modelled using a no–slip boundary condition, while the vertical walls are modeled using free–slip boundary conditions.

The air venting flow–rate studied is 10 l/s – a specific case documented in [1], but not fully described in [2]. The Reynolds number of the pipe flow of air is 17000. The 10 l/s flow represents something of a transition between lop–sided (in 8 l/s case) and symmetric (in 16 l/s case) bubble rise. The bulk flow is initially quiescent, and a white noise perturbation was superimposed on the initial velocity field. The simulation was performed in parallel as a 16–CPU computation. Using a Courant number of 0.2 and signal sampling at 1000 Hz , simulation of 1.0 second took one month of computation.

3.2 Transient large–scale bubbling phenomena

Figures 1(a)–(c) show sample frames of the $f_k = 0.5$ iso–surface contour to identify interface locations. For qualitative comparison, Figure 1(d)–(f) displays sample frames of bubble surfaces captured on video at the same flow rate. Phenomena worth noting include essentially symmetric bubble growth and symmetric bubble rise, “fingering” of the upper bubble surface during rise (Figure 1(a)), and lop–sided bubble detachment and rise (Figure 1(b)). The simulation of the observed bubble fragmentation demonstrates the ability of VOF to robustly capture even the most challenging interface kinematics in a seemingly realistic manner, even down to generating and preserving the satellite bubbles. Along with the transition from symmetric bubble plume rise about the downcomer to lop–sided rise and chopped–up interfaces, there is also the transition from lop–sided to symmetric and smoother surfaces – a restoration of organised from non–organised events. Figure 1(f) shows a typical shape of a large symmetric bubble that forms quasi–periodically. In the current simulation, however, we have had difficulty in regaining such a smooth single–large–bubble surface at subsequent bubbles; Figure 1(c) represents an approach to the experimental result. Event–sensitivity to air flow rate is high in this transition region, but poor resolution of the interface, the turbulence about the interface,

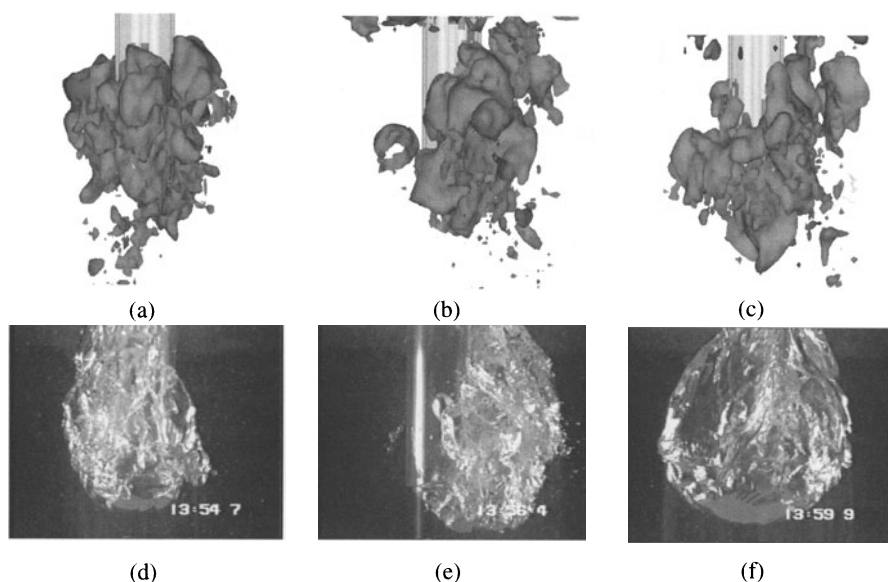


Figure 1. Frames of the bubbling resulting from air venting through a downcomer, for air flowing at 10 l/s into a water bath: (a)–(c) simulation, (d)–(f) experiment (from [1, 2]).

and the use of a non-high-resolution momentum advection scheme, are possible contributors to subsequent bubble growth not completely regaining spatial topological symmetry and “smoothness”. In the case of zero capacitance pipe gas flow (constant volumetric flow rate venting), Meier [1] found bubble growth to consist less of a distinguishable growth/detach pattern, and instead featured a near-continuous escaping of gas to the side – a pattern of bubble growth seen in full animation of our flow field results. In such a case, pressure signal analysis was considered useless in [1]; bubble counting exclusively was used to determine the bubble frequency in constant flowrate venting, although considered in [1] to be highly uncertain. To be consistent with Meier [1], bubble counting was used in the current study to determine bubble frequency. Based on clearly distinguishable downward penetrations of bubble growth, the present simulation yields a bubbling frequency of at least 7 Hz (1–2 Hz is a realistic level of the under-prediction uncertainty due to poorly distinguishable downward penetrations we may have failed to pick up). At the upper end of the flowrate spectrum used in the experiment schedule of [1], the bubbling frequency was also determined to be 7–9 Hz. Another event that is observed, but not shown here in either set of frames, is the violent break-up of bubbles at a distance $4D$ to $5D$ above the downcomer. This break-up takes the form of a “mushroom cloud” - an abrupt inversion and lateral expansion of the bubble plume high above the downcomer tip, and resembles bubble swarming i.e.

massive fragmentation into smaller bubbles. Although this bubble swarming is captured in simulation, the outflow boundaries are in very close proximity to the area of the computational domain the phenomenon occurs in, such that (potentially spurious) physics would be imposed. As an event essentially downstream of the bubbling at the downcomer, simulated bubble swarming will have little effect on the flow solution and turbulence characteristics in the region of interest; in any case, bubble swarming high above the downcomer tip is beyond the scope of the current investigation.

3.3 Interface/turbulence interaction

Figure 2 presents average and root-mean-square (rms) results in the yz -plane through the centre of the downcomer. The degree of symmetry in these time-averaged results indicates that the one second of simulation is an approach to a long-time average, but also demonstrates the need for even more computation to average out the asymmetries. The rms results show significant velocity fluctuation to coincide with the bubble plume. The most intense velocity fluctuation is in the bubbling-jet area under the downcomer tip, while a second area at $4D$ to $5D$ above the downcomer tip coincides with the mushroom-cloud region. More generally, gas-side velocity fluctuation is substantially greater than liquid-side fluctuation.

Figure 3 shows instantaneous results at $t = 0.24s$, with panel (a) showing the velocity vector map and interface location. The interplay between the interface and the large-scale structures formed in the gas phase is clearly seen. These coherent structures, of various length scales, are preferably localised at the interface regions forming distinct lobes – a contributor to the fingering seen in Figure 1. Some of the high-vorticity regions indeed coincide with the high-shear flow zones between the structures within the distinct lobes. High vorticity and strain-rates are shown to be concentrated in the downcomer-tip region of the gas-side flow, but there is also a clear damping of vorticity approaching the interface from the gas side – consistent with observation from DNS of counter-current stratified flow [4]. The contribution of the SGS eddy viscosity reveals that higher values coincide with high-velocity-fluctuation and high-vorticity gas-side flow regions. In [7], the two-fluid/dynamic SGS model provided ratios of $\mu_T/\mu < 20$ in the “bubbling-core” region. Locally higher values of μ_T/μ in Figure 3(d) means that a considerable portion of the spectra has been washed out. The Smagorinsky SGS model used in the present work is known to be overly dissipative and to not accommodate backscatter, and is one contribution to the possible overprediction of the ratio μ_T/μ . In addition, with eddy length scales correlating with interfacial length scales, and given Figure 1 shows an abundance of grid-scale (1–2 cell breadth) length scales, turbulence

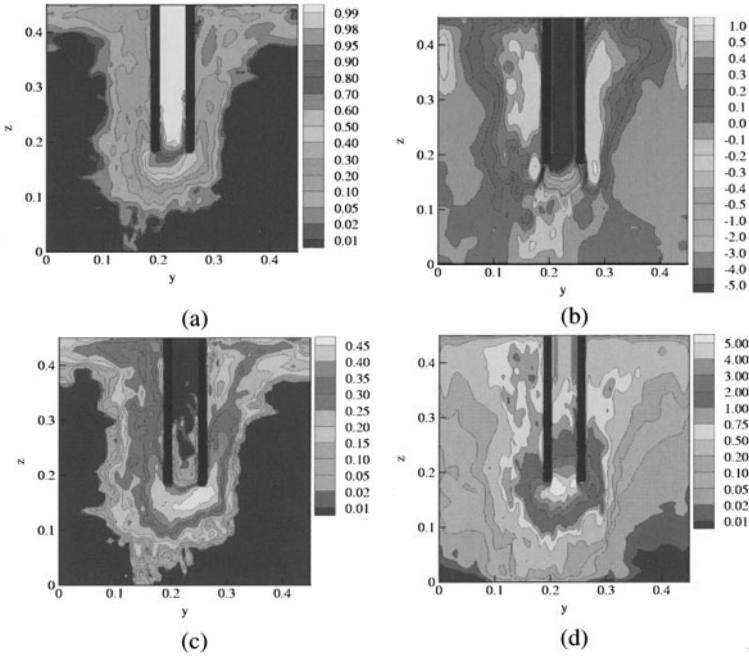


Figure 2. yz -plane distributions of time-averaged variables: (a) average void fraction, (b) average w -velocity, (c) root-mean-square void fraction, and (d) root-mean-square w -velocity.

is under-resolved at certain locations in the flow. Away from the bubble plume, both in the pipe flow and the liquid-side flow, turbulence is low.

3.4 Energy spectra

For the spectra shown in Figure 4(a), signal recording for the duration of the simulation is concentrated on azimuths: (a) 45mm below the downcomer tip, and 20mm off-axis, (b) 45mm below the downcomer tip, and 65mm off-axis, and (c) 45mm above the downcomer tip, and 45mm off-axis. In each azimuth, signals at 16 equally-spaced points were recorded, as well as the spatial average. The top row of Figure 4 shows the energy spectra obtained for each azimuth. Energy decay in the inertial sub-range based on the space-averaged signals follow the $-5/3$ and $-8/3$ power laws. The $-5/3$ power law behaviour in the spectra of all signals from azimuth (a) confirm that the turbulence underneath the tip of the downcomer is shear-dominated. The tendency towards the $-8/3$ power law in Figures 4 (b) and (c) is consistent with the experimental result for bubbly flows documented by Lance and Bataille [9], and which has been obtained in two-fluid modeling by Lakehal *et al.* [7]. The energy spectra for sample individual points in azimuths (b) and (c) more clearly exhibit

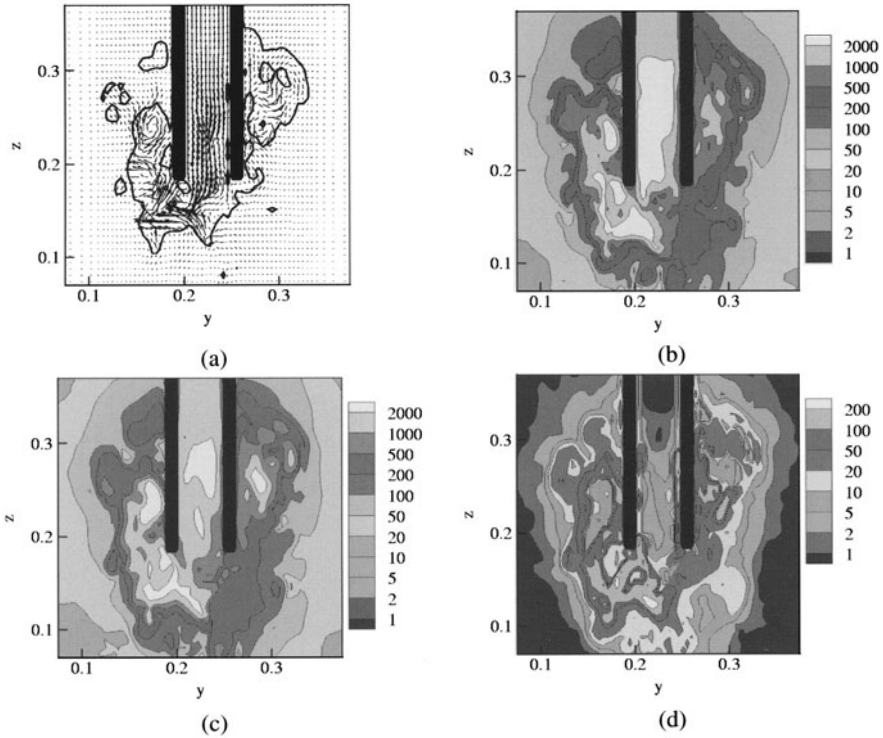


Figure 3. Profiles at $t=0.24s$, (a) $f_k = 0.5$ contour (interface location) and velocity vector map, (b) vorticity magnitude, (c) $\sqrt{S_{ij}S_{ij}}$, and (d) μ_T/μ , in the yz -plane through the axis of symmetry.

the $-8/3$ power law slope – the enhanced outscatter away resulting from the pseudo-turbulence described by [9]. In contrast to the shear-dominated turbulence in the inflow (bubble-)jet region, the results of azimuths (b) and (c) clearly show that the turbulence above and to the side of the downcomer tip region is buoyancy-dominated.

4. Conclusion

In this work, VOF-based interface tracking and explicit SGS modeling of unresolved eddy length scales were successfully combined to generate a realistic transient simulation-based solution to turbulent bubble formation and break-up resulting from air venting through a downcomer. The statistical analysis of the data shows the flow to be turbulent, and azimuthal-averaging yields energy spectra slopes in the inertial sub-range ranging from $-5/3$ to $-8/3$. Dissipative turbulence is found to be most pronounced in two distinct regions – in the vicinity of the downcomer tip where the flow is dominated by inertia,

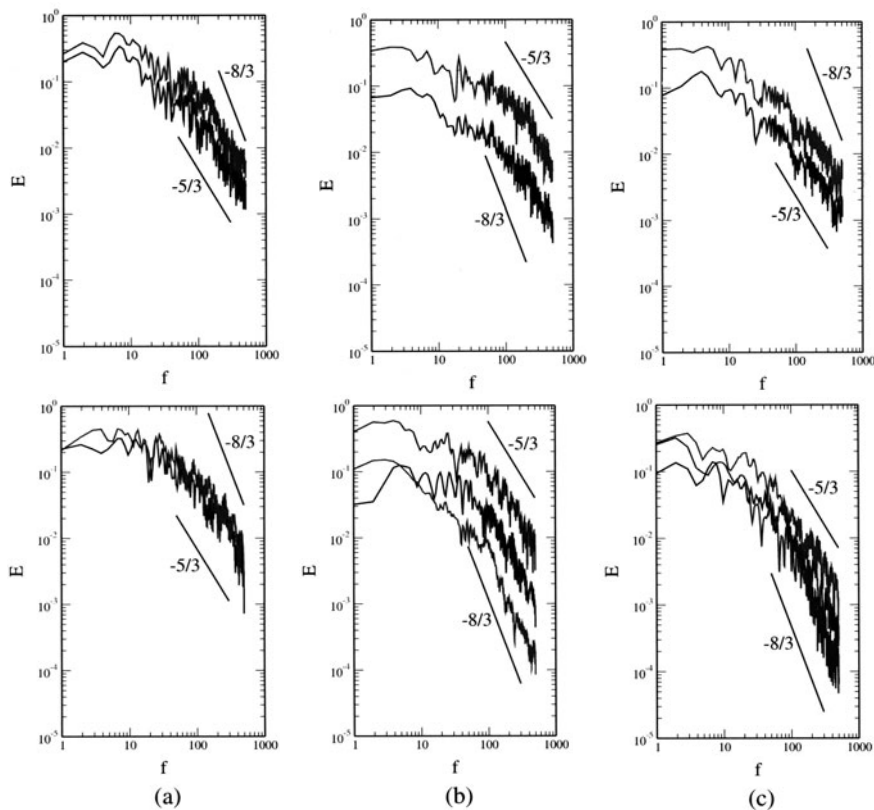


Figure 4. Energy spectra for averaged and point signals, for azimuths (a) 45mm below tip, 20mm off-axis, (b) 45mm below tip, 65mm off-axis, and (c) 45mm above tip, 45mm off-axis. The point signals shown are representative signals from a few of the 16 points that are equally spaced along each azimuth.

and in a buoyancy-driven flow region well above the downcomer tip. Numerical surface tension-induced bubble break-up and the difficulty in regaining smooth large-scale bubble surfaces over time highlight the need for finer meshes and refined numerical schemes to better resolve the medium and large interface length scales. Specifically, a migration away from the overly dissipative Smagorinsky kernel to more advanced SGS models, combined with damping of ν_T and high-resolution momentum advection approaching interfaces, would result in the required turbulence damping approaching interfaces that could help preserve the smoothness of large bubble surfaces.

Acknowledgements

The authors acknowledge the national supercomputing resources provided by the Swiss Center for Scientific Computing (CSCS) of Manno, the High Performance Computing Section at James Cook University, Townsville, Australia, and the Australian Partnership for Advanced Computing (APAC), Canberra.

References

- [1] Meier, M., “Numerical and experimental study of large steam-air bubbles injected in a water pool”, PhD dissertation, ETH–Zurich (1999).
- [2] Meier, M., Yadigaroglu, G., and Andreani, M., “Numerical and experimental study of large steam-air bubbles injected in a water pool”, *Nuclear Science and Engineering*, 136:363–375 (2000).
- [3] Liovic, P., Rudman, M., and Liow, J.-L., “Numerical modelling of free surface flows in metallurgical vessels”, *Applied Mathematical Modelling*, 26:113–140 (2002).
- [4] Fulgosi, M., Lakehal, D., Banerjee, S. and De Angelis, V., “Direct numerical simulation of turbulence in a sheared air-water flow with a deformable interface”, *Journal of Fluid Mechanics*, 482:319–345 (2003).
- [5] Rider, W.J., and Kothe, D.B., “Reconstructing volume tracking”, *Journal of Computational Physics*, 141:112–152 (1997).
- [6] Brackbill, J.U., Kothe, D.B., and Zemach, C., “A continuum method for modeling surface tension”, *Journal of Computational Physics*, 100:335–354 (1992).
- [7] Lakehal, D., Milelli, M., and Smith, B.L., “Large-eddy simulation of bubbly turbulent shear flows”, *Journal of Turbulence*, 3:1–21 (2002).
- [8] Germano, M., Piomelli, U., Moin, P., and Cabot, W.H., “A dynamic subgrid-scale eddy viscosity model”, *Physics of Fluids*, 3:1760–1765 (1991).
- [9] Lance, M., and Bataille, J., “Turbulence in the liquid phase of a uniform bubbly air–water flow”, *Journal of Fluid Mechanics*, 222:95–118 (1991).

LARGE-EDDY SIMULATION OF A PARTICLE-LADEN TURBULENT CHANNEL FLOW

A.W. Vreman¹, B.J. Geurts¹, N.G. Deen² and J.A.M. Kuipers²

¹ *Mathematical Sciences, J.M. Burgers Center*

² *Fundamentals of Chemical Reaction Engineering Group, Faculty TNW*

University of Twente, P.O. Box 217

7500 AE Enschede, The Netherlands

a.w.vreman@utwente.nl

Abstract Large-eddy simulations of a vertical turbulent channel flow with 420,000 solid particles are performed in order to get insight into fundamental aspects of a riser flow. The question is addressed whether collisions between particles are important for the flow statistics. The turbulent channel flow corresponds to a particle volume fraction of 0.013 and a mass load ratio of 18, values that are relatively high compared to recent literature on large-eddy simulation of two-phase flows. In order to simulate this flow, we present a formulation of the equations for compressible flow in a porous medium including particle forces. These equations are solved with LES using a Taylor approximation of the dynamic subgrid-model. The results show that due to particle-fluid interactions the boundary layer becomes thinner, leading to a higher skin-friction coefficient. Important effects of the particle collisions are also observed, on the mean fluid profile, but even more on particle properties. The collisions cause a less uniform particle concentration and considerably flatten the mean particle velocity profile.

Keywords: Large-eddy simulation, turbulence, two-phase flow

1. Introduction

A vertical turbulent channel flow with solid particles is simulated in order to model a section of a riser flow. The turbulent riser is often an industrial environment for important chemical processes, for example the catalytic cracking of oil. Detailed simulations may considerably increase our understanding of the physical dynamics of riser flows, which is required because the scale-up of these flows is very complicated. More knowledge about the formation of clusters of solid particles in these flows may eventually lead to more efficient industrial processes.

Vertical gas-solid flows have been studied experimentally (e.g. Kulick et al. 1994; Nieuwland 1995) and with simulations. Simulations can be performed using a two-fluid model in which the solid phase is modeled as a fluid using continuous variables (e.g., Nieuwland 1995). This approach is subject to relatively many modeling assumptions. A more accurate approach is to conduct simulations with a Lagrangian tracking of the motion of each individual particle (Hoomans et al. 1996), where the forces between the fluid and each particle are modeled with a drag law.

Recently the latter technique has been combined with DNS/LES of the fluid flow. Direct numerical simulation (DNS) solves all turbulent scales in the flow, whereas large-eddy simulation (LES) solves the large-scales and models the effect of the small scales with a subgrid-model. These techniques are able to give proper detailed descriptions of the turbulence in a channel flow. LES/DNS of channel flows with solid particles have been performed before (Yamamoto et al. 2001, Squires and Simonin 2002, Portela et al. 2002, Marchioli et al. 2003), but the total volume fraction of particles in these studies remains rather small (0.01 percent) and not all of these works include particle collisions and particle-fluid interactions.

The purpose of this paper is to present LES of a channel flow in which the particle volume concentration is much higher (1.3 percent), in order to study a case which is closer to industrial applications. The simulations are four-way coupled, which means that both particle-fluid and particle-particle interactions (collisions) are included. The discrete particle module developed by Hoomans et al. (1996) is used, in which the spherical particles have a finite size and all (inelastic) collisions are taken into account. The LES-equations of the gas-phase are closed with an approximation of the dynamic subgrid-model.

In order to study both the effect of the particle collisions and the effects of the particle-fluid interactions we compare the following three simulations: (1) a turbulent channel flow without particles, (2) a turbulent channel flow with particles, but without collisions (two-way coupled case) and (3) a turbulent channel flow with colliding particles (four-way coupled case). The differences between cases 1 and 2 quantify the effects of the particle-fluid interactions and the differences between cases 2 and 3 quantify the effects of the particle collisions.

2. The equations for gas-solid channel flow

Description of the gas phase

The Navier-Stokes equations that govern a compressible flow in a porous medium read:

$$\partial_t(\rho\epsilon) + \partial_j(\rho\epsilon u_j) = 0, \quad (1)$$

$$\partial_t(\rho\epsilon u_i) + \partial_j(\rho\epsilon u_i u_j) = -\partial_i(\epsilon p) + \partial_j(\epsilon\sigma_{ij}) + (\rho\epsilon g + \epsilon p_g)\delta_{i3} + f_i, \quad (2)$$

$$\partial_t(\epsilon e) + \partial_j((e + p)\epsilon u_j) = \partial_j(\epsilon\sigma_{ij}u_i) + (\rho\epsilon g + \epsilon p_g)u_3 + f_i u_i - \partial_j(\epsilon q_j) \quad (3)$$

where the symbols ∂_t and ∂_j denote the partial differential operators $\partial/\partial t$ and $\partial/\partial x_j$ respectively.

The coordinate x_3 denotes the streamwise direction of the channel flow, x_2 is the normal and x_1 is the spanwise direction. The domain is rectangular and the channel width, height and depth equal $L_2 = 0.05m$, $L_3 = 0.30m$ and $L_1 = 0.075m$ respectively. No-slip boundary conditions are imposed in the x_2 -direction and periodic boundary conditions are assumed for the stream- and spanwise directions. Furthermore, ρ is the density, ϵ is the porosity, \mathbf{u} the velocity, p the pressure and $e = p/(\gamma - 1) + \frac{1}{2}\rho u_k u_k$ the total energy per volume unit. The constant γ denotes the ratio of specific heats $C_P/C_V = 1.4$. The viscous stress σ_{ij} is defined as the product of viscosity $\mu = 3.47 \cdot 10^{-5} kg/(ms)$ and strain-rate

$$S_{ij}(u) = \partial_i u_j + \partial_j u_i - \frac{2}{3}\delta_{ij}\partial_k u_k. \quad (4)$$

The heat-flux q_j is defined as $-\kappa\partial_j T$ where T is the temperature and $\kappa = 0.035W/(mK)$ the heat-conductivity coefficient.

Pressure, density and temperature are related to each other by the equation of state for an ideal gas $\rho RT = M_{gas}p$, where $R = 8.314J/(molK)$ is the universal gas constant and $M_{gas} = 0.0288kg/mol$ is the mass of the gas per mol. The gravitation acceleration equals $g = -9.81m/s^2$, p_g is an external pressure gradient and the symbol f_i denotes the force of the particles on the flow per volume unit.

The equations formulated above are equivalent to the equations governing a compressible ideal gas with velocity \mathbf{u} , temperature T , density $\rho^c = \epsilon\rho$, pressure $p^c = \epsilon p$, viscosity $\mu^c = \epsilon\mu$ and heat-conductivity $\kappa^c = \epsilon\kappa$. Therefore to solve this flow it is convenient to use a standard compressible code with an addition of the forcing terms representing gravitation and the forces from the particles on the fluid.

We are interested in a section of a riser flow with a vertical velocity of about $4m/s$. The parameters of the fluid in the riser are close to those for air. The initial fluid density equals $\rho_1 = 1.0kg/m^3$. With a normal value of the initial pressure (around $10^5 N/m^2$) the flow has a very low Mach number around 0.01, which is extremely expensive to simulate with a compressible solver. Therefore we use a much lower pressure ($340N/m^2$) which results in a Mach number of approximately 0.2. At this Mach number the turbulent channel flow

can still be regarded as incompressible, i.e. a further reduction of the Mach number does not significantly change the turbulent statistics, including pressure fluctuations.

The flow is driven by the pressure gradient p_g , which is a function of time only and its level is such that the total fluid mass flow is constant. For a channel flow without particles the value of p_g corresponds to $\tau_w = 0.0625 N/m^2$, $u_\tau = 0.25 m/s$ and $Re_\tau = 180$.

Description of the solid phase

The discrete particle model is a hard sphere collision model. It calculates the motion of particles in the fluid and includes the particle collisions with a general restitution coefficient of 0.97, a tangential restitution coefficient of 0.33 and friction coefficient of 0.1. The forces on a particle that are taken into account are gravitation, pressure and the drag force resulting from the velocity difference with the surrounding fluid. The Ergun and Wen & Yu drag law is used, which is precisely described in Hoomans et al. (1996). The mean velocity of the riser is low enough to neglect the heat transfer during particle collisions and the heat transfer between particles and fluid. The particle diameter equals $0.4 mm$ and the particle density equals $\rho_2 = 1500 kg/m^3$. The number of particles is $N_p = 419904$. With the parameters above the average volume fraction of the particles becomes 0.013. The Stokes-response time equals $0.4 s$.

Description of the numerical method

The equations for the fluid phase are solved with a second-order finite volume method on a collocated grid. The equations are discretized in the divergence form as described by equations (1-3). The control volume of the convective and pressure terms equals eight grid-cells. Control volumes of one cell are used to discretize the derivatives that are required for the viscous/subgrid-fluxes and for the divergences of these fluxes. The integrations over cell-faces are all performed with the trapezoidal rule.

The grid contains $N_1 \times N_2 \times N_3$ cells and is only non-uniform in the normal direction. The simulations presented in the following are performed on a grid with $N_1 = 32$ and $N_2 = N_3 = 64$. The first grid point $x_{2,1} = 0.2 mm$ in the normal direction corresponds with $y^+ = 1.5$. The porosity parameter ϵ is determined by counting the particles within each cell of an auxiliary grid, which is uniform and contains $32 \times 25 \times 64$ cells, chosen such that in each direction the mesh-spacing of this grid is considerably larger than the particle diameter (Hoomans et al 1996). Linear interpolation routines communicate the information from grid-nodes to particle positions and vice-versa.

The discretization in time is explicit: a second-order Runge-Kutta method for the fluid phase and Euler for the particles. The time step equals $2 \cdot 10^{-5} s$ for the fluid phase and $10^{-4} s$ for the solid phase. The simulations run until at least $t = 5 s$, while statistics are accumulated between $t = 3 s$ and $t = 5 s$.

3. Subgrid-modeling

The equations governing the fluid phase are solved by means of LES, which implies that a 'bar'-filter is applied to the equations (1-3), with filter width Δ_i in the x_i -direction taken equal to the grid-spacing. The filtered equations are similar to equations (1-3), with the difference that in the left-hand side of the momentum equation a subgrid-stress is included, $\partial_j \tau_{ij}$ with

$$\tau_{ij} = \overline{\rho \epsilon u_i u_j} - \overline{\rho \epsilon} \overline{u_i} \overline{u_j} / \overline{\rho \epsilon}. \quad (5)$$

For a full presentation of the filtered equations for compressible flow we refer to Vreman et al. (1995). The dynamic model (Germano et al. 1991) for τ_{ij} is based on the Smagorinsky eddy-viscosity

$$m_{ij} = -c_S \overline{\rho \epsilon} \Delta^2 S(\tilde{u}) S_{ij}(\tilde{u}), \quad S = (\frac{1}{2} S_{ij} S_{ij})^{\frac{1}{2}}, \quad \Delta = (\Delta_1 \Delta_2 \Delta_3)^{\frac{1}{3}}, \quad (6)$$

where $\tilde{u}_i = \overline{\rho \epsilon u_i} / \overline{\rho \epsilon}$, a sort of Favre-filter for compressible flows with porosity. The dynamic procedure employs an extra filter with a larger filter width $\hat{\Delta} = 2\Delta$, and the dynamic coefficient c_S is computed by

$$c_S = \frac{\langle M_{ij} L_{ij} \rangle}{\langle M_{ij} M_{ij} \rangle}, \quad (7)$$

where $\langle \cdot \rangle$ denotes an average over the homogeneous directions in the channel and

$$L_{ij} = [\overline{\rho \epsilon} \tilde{u}_i \tilde{u}_j]^\wedge - \widehat{\overline{\rho \epsilon} \tilde{u}_i \tilde{u}_j} / \widehat{\overline{\rho \epsilon}}, \quad (8)$$

$$M_{ij} = -\widehat{\overline{\rho \epsilon}} (\sqrt{5} \Delta)^2 S(\widehat{\overline{\rho \epsilon} \tilde{u}} / \widehat{\overline{\rho \epsilon}}) S_{ij}(\widehat{\overline{\rho \epsilon} \tilde{u}} / \widehat{\overline{\rho \epsilon}}) + [\overline{\rho \epsilon} \Delta^2 S(\tilde{u}) S_{ij}(\tilde{u})]^\wedge. \quad (9)$$

The notation $[\cdot]^\wedge$ indicates that the hat-filter is applied to the expression between the brackets. The factor $\sqrt{5}$ is related to the choice of top-hat filters and a ratio of 2 between test-filter and basic filter (Vreman et al. 1997).

Next we simplify the dynamic model in line with the approaches described by Pope (2000, p. 623) and Chester et al. (2001). Thus, in the following Taylor expansions are used to approximate the tensors L_{ij} and M_{ij} . In this paper, only the $O(\Delta^2)$ terms are taken into account. For the tensor L_{ij} this results in an expression similar to the gradient model,

$$L_{ij} = \frac{1}{3} \overline{\rho \epsilon} \Delta_k^2 \partial_k \tilde{u}_i \partial_k \tilde{u}_j. \quad (10)$$

For the simplification of M_{ij} we use that $\hat{w} = \overline{w} + O(\Delta^2)$, which yields

$$M_{ij} = -4 \overline{\rho \epsilon} \Delta^2 S(\tilde{u}) S_{ij}(\tilde{u}). \quad (11)$$

The dynamic coefficient is again obtained with equation (8). Thus the simplified procedure for c_S , with simplified L_{ij} and M_{ij} , does not need explicit test-filtering. The resulting coefficient essentially equals the dissipation of the eddy-viscosity model to the dissipation of the gradient model.

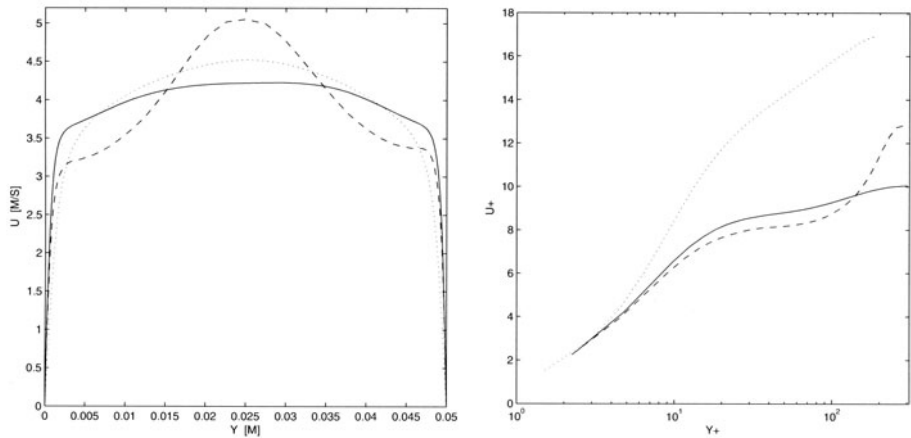


Figure 1. Dimensional (left) and non-dimensional (right) mean streamwise fluid velocity $\langle u_z \rangle$. Simulation with colliding particles (solid), with non-colliding particles (dashed) and without particles (dotted).

The computations presented in this paper have been performed with this approximated dynamic model (equations (6-7,10-11)), which is much cheaper to evaluate than the standard dynamic model. Simulations with other subgrid-models are currently performed, for example with the standard dynamic model (using equations (8-9)) and with a multi-scale subgrid-model (Vreman 2003).

4. Results

Results of the simulations are shown in figures 1-3. A comparison between the case without and the cases with particles in figure 1 shows that due to particle-fluid interactions the boundary layer becomes thinner (figure 1a) leading to a higher skin-friction coefficient (figure 1b). We also observe important effects of the collisions, on the mean fluid velocity profile (figure 1), but even more on particle properties (figures 2-3). The mean particle velocity with collisions is flatter than without collisions (figure 2a). We also observe that the near-wall particle velocity is positive and does not drop to zero. This is in agreement with the observation that the mean fluid velocity profile in the boundary layer is enhanced by the forces of the particles on the fluid.

Comparison of the cases with and without collisions shows that the collisions cause a less uniform particle concentration, as demonstrated by figures 2b-3. An increase of the particle concentration near the walls is only observed for the case that includes collisions (figure 2b). Although significant, the increase remains rather small, which is attributed to the fact that the particles are coarse. The near-wall effect was observed to be much stronger in a more diluted simulation using finer particles ($d_p = 0.04mm$) and a volume concentration of $1.3 \cdot 10^{-5}$. Figure 3a shows that the case with collisions contains regions with

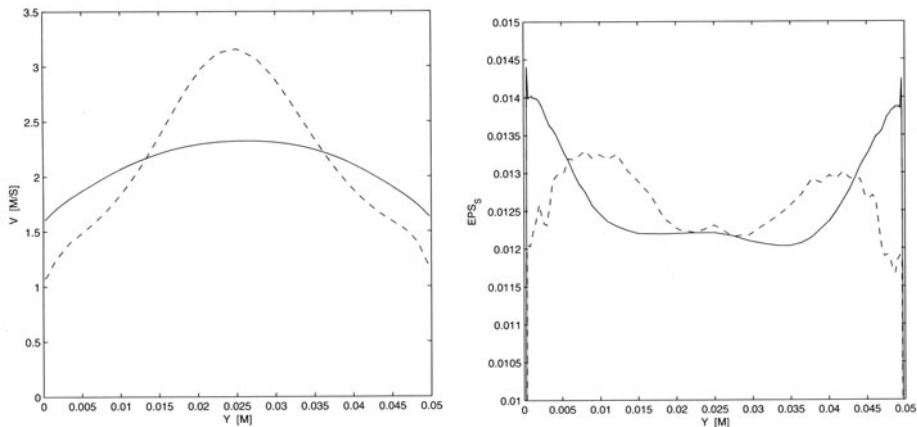


Figure 2. Mean streamwise particle velocity $\langle v_z \rangle$ (left) and mean volume fraction of the particles $\langle \epsilon_s \rangle$ (right). Simulation with colliding particles (solid) and with non-colliding particles (dashed).

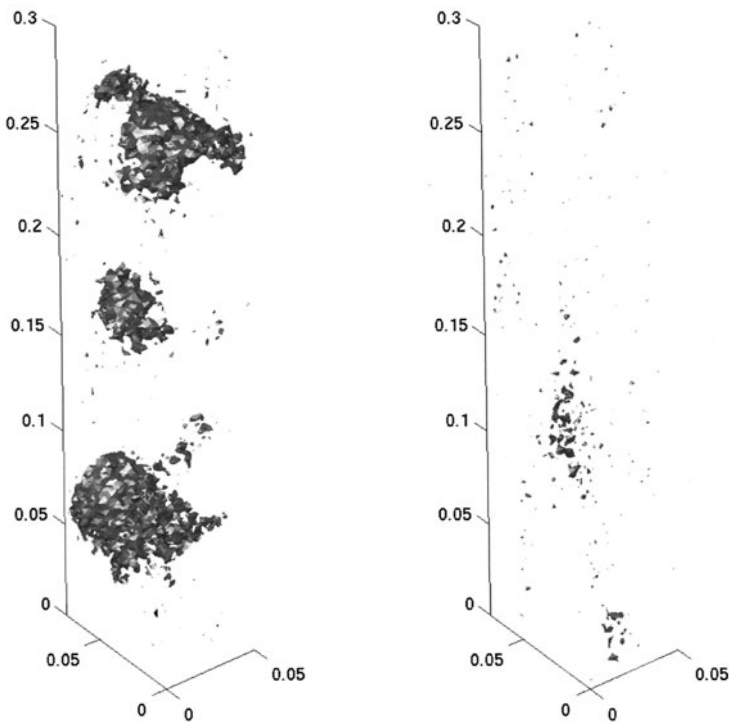


Figure 3. Isosurfaces $\epsilon_s = 0.03$ at $t = 3$ s with collisions (left) and without collisions (right).

relatively high particle density, which are transported upward by the mean velocity. Without collisions these regions are considerably smaller and less dense (figure 3b), and thus it may be concluded that the particle-particle interactions play a crucial role in the formation of regions with increased particle density. We conclude therefore that particle-fluid forces and collisions between particles strongly alter important properties of both phases. This indicates the necessity of a full four-way coupled model for detailed simulations of such flows.

Acknowledgments

A.W. Vreman is grateful to J.G.M. Kuerten for useful discussions on this topic and to J.M. Link for assistance with the discrete particle model. The initial conditions for turbulent channel flow were provided by N.D. Sandham. The computations were performed through grant NCF SC-144.

References

- Chester, S., Charlette, F., and Meneveau, C. (2001). "Dynamic model for LES without test filtering: Quantifying the accuracy of Taylor series approximations", *Theor. Comp. Fluid Dyn.* 15, 165-181.
- Germano, M., Piomelli, U., Moin, P., and Cabot, W.H. (1991). "A dynamic subgrid-scale model", *Phys. Fluids A* 3, 1760-1765.
- Hoomans, B.P.B., Kuipers, J.A.M., Briels, W.J., and van Swaaij, W.P.M. (1996). "Discrete particle simulation of bubble and slug formation in a two-dimensional gas-fluidized bed: A hard-sphere approach", *Chem. Eng. Science* 51, 99-118.
- Kulick, J.D., Fessler, J.R., and Eaton, J.K. (1994). "Particle response and turbulence modification in fully developed channel flow", *J. Fluid Mech.* 227, 109-134.
- Marchioli, C., Giusti, A., Salvetti, M.V., and Soldati, A. (2003). "Direct numerical simulation of particle wall transfer and deposition in upward turbulent pipe flow", *Int. J. of Multiphase Flow* 29, 1017-1038.
- Nieuwland, J.J. (1995). "Hydrodynamic modeling of gas-solid two-phase flows", PhD-Thesis, University of Twente.
- Pope, S.B. (2000), "Turbulent flows", Cambridge University Press.
- Portela, L.M., Ferrand, V., Bijlard, M.J., and Oliemans, R.V.A. (2002). "Effect of the turbulence-dynamics modification on turbulence models for particle-laden wall-bounded flows", *Proceedings of the 10th workshop on two-phase flow predictions, Merseburg*, 152-163.
- Squires, K.D., and Simonin, O. (2002). "Recent advances and perspective of DNS and LES for dispersed two-phase flow", *Proceedings of the 10th workshop on two-phase flow predictions, Merseburg*, 152-163.
- Vreman, A.W. (2003). "The filtering analog of the variational multi-scale method in large-eddy simulation", *Phys. Fluids*, to appear in the September issue.
- Vreman, B., Geurts, B.J., and Kuerten, J.G.M. (1995), "A priori tests of large-eddy simulation of the compressible plane mixing layer", *J. Eng. Math.* 29, 299-237.
- Vreman, B., Geurts, B.J., and Kuerten, J.G.M. (1997). "Large-eddy simulation of the turbulent mixing layer", *J. Fluid Mech.* 339, 357-390.
- Yamamoto, Y., Potthoff, M., Tanaka, T. Kajishima, T., and Tsuji, Y. (2001). "Large-eddy simulation of turbulent gas-particle flow in a vertical channel: effect of considering inter-particle collisions", *J. Fluid Mech.* 442, 303-334 (2001).

ANALOGY BETWEEN SUBGRID-SCALE NONLINEAR MODEL AND CONSTITUTIVE EQUATIONS FOR VISCOELASTIC FLUIDS

Kiyosi Horiuti

*Department of Mechano-Aerospace Engineering, Tokyo Institute of Technology,
2-12-1 O-okayama, Meguro-ku, Tokyo 152-8552, Japan.*

khoriuti@mes.titech.ac.jp

Abstract The nonlinear model, which is quadratic in the mean velocity gradients, has been extensively used as the subgrid-scale (SGS) model in large-eddy simulation (LES) [1, 2]. It is well known that the nonlinear model is analogous to the viscoelastic terms in the second-order Rivlin-Ericksen fluid which is used in the analysis of the polymer diluted solutions [3]. In the present study, the analogy between the nonlinear model and the viscoelastic model is investigated. It is shown that the terms contained in both models are similar, but the sign of certain components is reversed in the viscoelastic model. The impact of the difference in the signs for the formation of the turbulent structures is shown in the homogeneous isotropic turbulence.

Keywords: subgrid-scale model, nonlinear model, Newtonian fluid, viscoelastic fluid

1. Introduction

Since turbulence consists of eddies with a very wide size range, the small scales should be coarsely grained. One of the methods available for this reduction of degrees of freedom is large-eddy simulation (LES). In LES, a coarse graining of the small scales is performed by applying a filtering operation to the raw variables, and the entire field (f) is decomposed into the grid scale component (\bar{f}), and the subgrid-scale (SGS) component (f'). The filtered Navier–Stokes equations can be derived as

$$\frac{\partial \bar{u}_i}{\partial t} + \frac{\partial (\bar{u}_i \bar{u}_j)}{\partial x_j} = -\frac{\partial \tau_{ij}}{\partial x_i} - \frac{\partial \bar{p}}{\partial x_i} + \nu \frac{\partial^2 \bar{u}_i}{\partial x_k \partial x_k}, \quad (1)$$

where \bar{u}_i ($i = 1, 2, 3$) denotes the grid-scale velocity field, \bar{p} the grid-scale pressure, and ν the kinematic viscosity. The SGS stress tensor, $\tau_{ij} = (\bar{u}_i \bar{u}_j - \bar{u}_i \bar{u}_j)$, results from coarse graining of the SGS.

Approximation of the SGS stress tensor has been commonly carried out using the scale-similarity model. The representative one is the Bardina model [4]. The lowest-order approximation of the Bardina model using the Taylor expansion is the nonlinear model:

$$\tau_{ij} \simeq \frac{\bar{\Delta}^2}{12} \frac{\partial \bar{u}_i}{\partial x_k} \frac{\partial \bar{u}_j}{\partial x_k}, \quad (2)$$

where $\bar{\Delta}$ is the characteristic SGS length scale. This model exhibits a good performance for approximating the exact SGS stress [2]. The nonlinear model, Eq. (2), can be decomposed as,

$$\tau_{ij} \simeq \frac{\bar{\Delta}^2}{12} \frac{\partial \bar{u}_i}{\partial x_l} \frac{\partial \bar{u}_j}{\partial x_l} = \frac{\bar{\Delta}^2}{12} \{ (\bar{S}_{ik} \bar{S}_{kj} - \bar{\Omega}_{ik} \bar{\Omega}_{kj}) - (\bar{S}_{ik} \bar{\Omega}_{kj} + \bar{S}_{jk} \bar{\Omega}_{ki}) \}, \quad (3)$$

where $\bar{S}_{ij} = (\partial \bar{u}_i / \partial x_j + \partial \bar{u}_j / \partial x_i) / 2$ and $\bar{\Omega}_{ij} = (\partial \bar{u}_i / \partial x_j - \partial \bar{u}_j / \partial x_i) / 2$. The nonlinear model can be derived as the approximate solution for the algebraic stress model [5, 6].

It is well known that there are similarities between the mean turbulent flow of a Newtonian fluid and the laminar flow of viscoelastic fluids [3]. In fact, the nonlinear model has a structure similar to that of a Rivlin-Ericksen fluid which is used to describe the flows of dilute polymer solutions. The aim of this paper is to reveal similarities and differences between the nonlinear model and the constitutive models for the viscoelastic fluids.

2. The viscoelastic constitutive equations

In the present study, we consider the Oldroyd-A and -B constitutive equations which provide a fair representation of a viscoelastic fluid [7]. The Oldroyd-A constitutive equation can be given with the Navier-Stokes equations as

$$\frac{\partial u_i}{\partial t} + \frac{\partial (u_i u_j)}{\partial x_j} = -\frac{\partial p}{\partial x_i} + \beta \nu \frac{\partial^2 u_i}{\partial x_k \partial x_k} - (1 - \beta) \frac{\nu}{\lambda} \frac{\partial c_{ij}}{\partial x_j}, \quad (4)$$

$$\frac{\partial c_{ij}}{\partial t} + u_k \frac{\partial c_{ij}}{\partial x_k} = -(c_{ik} \frac{\partial u_k}{\partial x_j} + \frac{\partial u_k}{\partial x_i} c_{kj}) - \frac{1}{\lambda} c_{ij}, \quad (5)$$

where c_{ij} denotes the conformation stress tensor, λ the relaxation time, and β the ratio of solvent viscosity contribution to total viscosity of solution [7]. Equations (4) and (5) are described in a dimensional form.

An approximate solution for the Oldroyd-A model can be derived as follows with the initial condition at $t = 0$ as $c_{ij}(0) = \delta_{ij}$.

$$c_{ij}(t) \approx \delta_{ij} - \int_{-\infty}^t e^{-\frac{t-s}{\lambda}} 2S_{ij}(s) ds$$

$$+ \int_{-\infty}^t dr \int_{-\infty}^r ds e^{-\frac{t-s}{\lambda}} 2 \left(S_{ik}(s) \frac{\partial u_k}{\partial x_j}(r) + \frac{\partial u_k}{\partial x_i}(r) S_{kj}(s) \right), \quad (6)$$

in which the convective terms were not included. The approximate solution, Eq. (6), contains the time-memory effect, which is important to describe the behavior of the viscoelastic fluid since a material that has no memory cannot be elastic [7]. For simplicity, we assume the steady state in the present study. Then, Equation (6) can be approximated as

$$c_{ij}(t) \approx \delta_{ij} - 2\lambda S_{ij} + 2\lambda^2 \{2S_{ik}S_{kj} + (S_{ik}\Omega_{kj} + S_{jk}\Omega_{ki})\}. \quad (7)$$

We terminated the expansion at the order of λ^2 . The higher-order terms with respect to λ consist of the third and higher-order products of S_{ij} and Ω_{ij} [5, 6]. Inserting the c_{ij} term in Eq. (7) into Eq. (4), we derive the approximate momentum equation for the Oldroyd-A constitutive equation as

$$\frac{Du_i}{Dt} = -\frac{\partial p}{\partial x_i} + \nu \frac{\partial^2 u_i}{\partial x_k \partial x_k} - 2(1-\beta)\nu\lambda \frac{\partial}{\partial x_i} [2S_{ik}S_{kj} + (S_{ik}\Omega_{kj} + S_{jk}\Omega_{ki})], \quad (8)$$

As a result, the approximation for the conformation stress tensor, c_{ij} , derived using the Oldroyd-A constitutive equation is analogous to the approximation for the SGS stress tensor, τ_{ij} , obtained using the variant of the nonlinear model (nonlinear variant model) as

$$\tau_{ij} \simeq \frac{\bar{\Delta}^2}{12} \{(\bar{S}_{ik}\bar{S}_{kj} - \bar{\Omega}_{ik}\bar{\Omega}_{kj}) + (\bar{S}_{ik}\bar{\Omega}_{kj} + \bar{S}_{jk}\bar{\Omega}_{ki})\}. \quad (9)$$

This similarity arose because the underlying concept for the LES equation is that it describes the motion of a specific hypothetical non-Newtonian or viscoelastic fluid [8].

An alternative constitutive equation of the conformation stress tensor, c_{ij} , is the Oldroyd-B equation as

$$\frac{\partial c_{ij}}{\partial t} + u_k \frac{\partial c_{ij}}{\partial x_k} = (c_{ik} \frac{\partial u_j}{\partial x_k} + \frac{\partial u_i}{\partial x_k} c_{kj}) - \frac{1}{\lambda} c_{ij}. \quad (10)$$

The approximate solution for Eq. (10) can be derived as

$$c_{ij} \approx -\delta_{ij} - 2\lambda S_{ij} + 2\lambda^2 \{-2S_{ik}S_{kj} + (S_{ik}\Omega_{kj} + S_{jk}\Omega_{ki})\}. \quad (11)$$

The solution yielded by the Oldroyd-B constitutive equation is analogous to the solution obtained using the Oldroyd-A equation (7), and the $(S_{ik}\Omega_{kj} + S_{jk}\Omega_{ki})$ term is contained in both Oldroyd-A and Oldroyd-B equations. It should be noted that its coefficient is $+1$, whereas that for the nonlinear model (Eq. (3)) is -1 . We note that in the previous studies which dealt with the nonlinear model for the Newtonian fluids [5], the coefficient for the $(\bar{S}_{ik}\bar{\Omega}_{kj} + \bar{S}_{jk}\bar{\Omega}_{ki})$ term in Eq. (3) was set equal to the negative values.

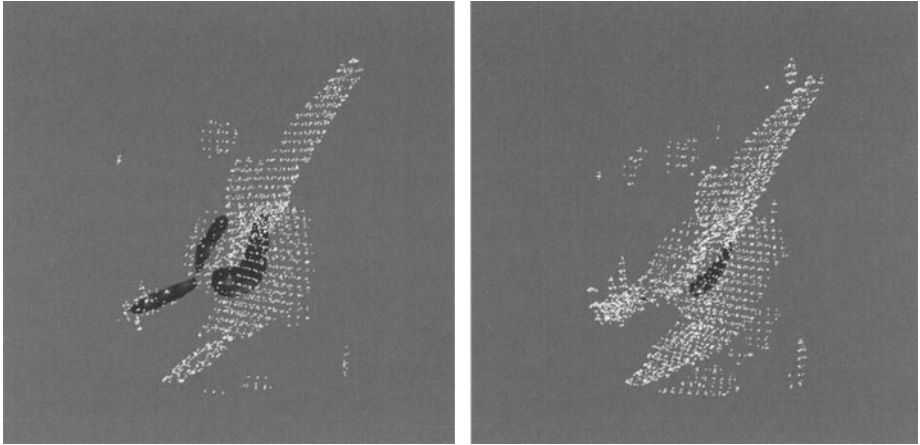


Figure 1. Isosurfaces of the flat sheet (drawn using the white mesh) and the tubes (drawn in the black color) at $t = 1.9$; left: Case I, right: Case II.

3. Numerical assessment

To reveal the effect of the difference in the sign of the $(S_{ik}\Omega_{kj} + S_{jk}\Omega_{ki})$ term on the evolution of turbulence fields, we carried out direct numerical simulation (DNS) and LES calculations of the decaying homogeneous isotropic turbulence by incorporating the nonlinear model and nonlinear variant model using 256, 256 and 256 grid points, respectively, in the x, y and z directions. To avoid the appearance of unphysical instabilities incurred by the nonlinear model, aliasing errors were removed using the 3/2 rule. For details of the DNS data, see Horiuti [9]. Assessment was done using the data at the instant when the Taylor microscale Reynolds number, $R_\lambda \approx 88$. Turbulent structures can be divided roughly into two groups: the vortex tube-like structure and the vortex sheet-like structure. We focus on the difference in the generation of these structures yielded by the nonlinear and variant models. Two cases of LES calculations were considered. In Case I, the nonlinear model, Eq. (3), was used, while in Case II, the nonlinear variant model, Eq. (9), was used. It was found that when the nonlinear model was used, the temporal evolution of the turbulence field was close to that of the data obtained by applying filter operation to the data of DNS, i.e., the solution for the Newtonian fluid, whereas when the nonlinear variant model was used, the result which is somewhat different from Case I was obtained.

Figure 1 shows the isosurfaces for the tube structures and the sheet structures obtained from Cases I and II at $t = 1.9$. The tubes were visualized using the second-order invariant of the grid-scale velocity gradient tensor, $Q(= -(\bar{S}_{ik}\bar{S}_{ki} + \bar{\Omega}_{ik}\bar{\Omega}_{ki})/2)$, which were drawn in the black color in the figure.

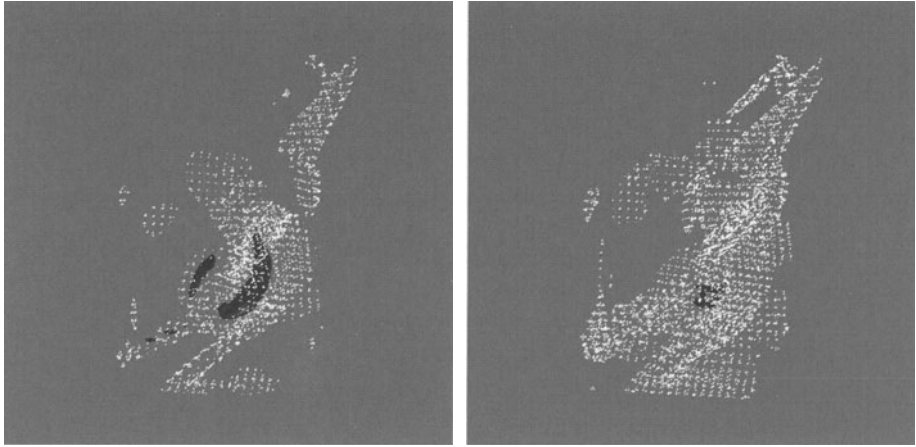


Figure 2. Isosurfaces of the flat sheet (white mesh) and the tubes (black) at $t = 1.95$; left: Case I, right: Case II.

To identify the sheets, we utilized the eigenvalue of the $-(S_{ik}\Omega_{kj} + S_{jk}\Omega_{ki})$ term, $[-(S_{ik}\Omega_{kj} + S_{jk}\Omega_{ki})]_+$, since it was shown that the magnitude of this eigenvalue is very large in the vicinity of the centre of the vortex sheet similar to the Burgers' vortex layer [10] (the flat sheet [9], drawn using the white meshes in the figure). In the present study, the eigenvalues and corresponding eigenvectors were reordered according to the degree of alignment of the eigenvectors with the vorticity vector, ω . The eigenvalue, the eigenvector of which is maximally aligned with ω is chosen as the z -component, the largest remaining eigenvalue as the $+$ component, and the smallest one as the $-$ component. It can be seen in Fig. 1 that, the sheet structures were formed in both Cases, but the tube structure obtained from Case II occupies a smaller fraction of volume than that from Case I. At a later stage ($t = 1.95$) shown in Fig. 2, this difference becomes more considerable, i.e., in Case II, the sheet structure prevails, and the tube structure is barely formed.

It was shown in Horiuti *et al.* [11] that the vortex tubes are generated along the vortex sheet as follows. At certain locations along the flat sheet, compression of the vorticity in the stretching (z -)direction takes place. The pressure Hessian term tends to relax this occurrence of compression, and in place of the compression and reduction of the vorticity in the z -direction, the azimuthal vorticity in the $+$ direction grows. This growth is concentrated along the sheet, and the azimuthal vorticity gradually accumulates to form the vortex tube through a focusing process. Then, the flat sheet folds around this concentrated vortex tube, forming the spiral vortex sheet emanating from the tube core. Consistency of the analytical estimate of the time evolution of the representative variables, e.g. the strain-rate and vorticity, with a scenario of the

transformation process shown above was presented in Horiuti *et al.* [11]. It appears that this process for the transformation of the vortex sheet into the vortex tube has been disrupted in Case II,

4. Viscoelastic effect on a sheet-tube transformation

To elucidate the implication of the difference in the weighing coefficient for the $(S_{ik}\Omega_{kj} + S_{jk}\Omega_{ki})$ term in the nonlinear and nonlinear variant models for the formation of turbulent structures, we analyzed the properties of the $(S_{ik}\Omega_{kj} + S_{jk}\Omega_{ki})$ term. The most relevant feature of the $(S_{ik}\Omega_{kj} + S_{jk}\Omega_{ki})$ term is that it vanishes in the total production term, $P(= -\tau_{ij}\bar{S}_{ij})$, thus the $(S_{ik}\Omega_{kj} + S_{jk}\Omega_{ki})$ term makes no contribution to the production of the total SGS energy. The contribution of this term, however, is not eliminated when the generation term for the vorticity is considered. The generation term for the SGS enstrophy, $(\bar{\omega}_i\bar{\omega}_i - \bar{\omega}_i\bar{\omega}_i)/2(= \bar{\Omega}_{ij}\bar{\Omega}_{ij} - \bar{\Omega}_{ij}\bar{\Omega}_{ij})$, due to the τ_{ij} term is

$$P_\omega = \varepsilon_{ilm}\bar{\omega}_i \frac{\partial^2 \tau_{mj}}{\partial x_l \partial x_j}, \quad (12)$$

where ε_{ilm} is the alternating tensor. The P_ω term can be written as the inner product of the vorticity vector, ω , with the SGS vortex-stretching vector, $\mathbf{W}_i^{\text{SGS}}$, the i -th component of which is $W_i^{\text{SGS}}(= \varepsilon_{ilm}(\partial^2 \tau_{mj}/\partial x_l \partial x_j))$. When ω and $\mathbf{W}_i^{\text{SGS}}$ are projected onto the basis of the strain-rate eigenvectors, P_ω can be decomposed as

$$P_\omega = \bar{\omega}_z W_z^{\text{SGS}} + \bar{\omega}_+ W_+^{\text{SGS}} + \bar{\omega}_- W_-^{\text{SGS}}. \quad (13)$$

Figure 3 shows the contours in the cross section of the $x-z$ plane at $y = 0.25$ and $t = 1.95$, for the z -component of this decomposed P_ω term, $\bar{\omega}_z W_z^{\text{SGS}}$, due to the $(S_{ik}\Omega_{kj} + S_{jk}\Omega_{ki})$ term, in which τ_{ij} was set equal to $\bar{p}\bar{\Delta}^2(\bar{S}_{ik}\bar{\Omega}_{kj} + \bar{S}_{jk}\bar{\Omega}_{ki})/12$. It can be seen in the contours of the eigenvalue, $[-(S_{ik}\Omega_{kj} + S_{jk}\Omega_{ki})]_+$, which are plotted in flood, that the sheet is wrapped around and emanating from the tube core. In Case I, the tube core is clearly formed, whereas in Case II, the concentrated core region is not clearly seen as was found in Figs. 1 and 2. The contours of the $\bar{\omega}_z W_z^{\text{SGS}}$ term are plotted using the lines. Positive values were plotted by solid lines, and negative ones by dashed lines. In Case I, the $\bar{\omega}_z W_z^{\text{SGS}}$ term is predominantly positive along the sheet, while it is negative in the core region of the tube. In Case II, the $\bar{\omega}_z W_z^{\text{SGS}}$ term is predominantly negative along the sheet.

Negative $\bar{\omega}_z W_z^{\text{SGS}}$ term implies that the SGS enstrophy is backwardly transferred into the grid scale, strengthening the vorticity in the z -direction. Thus, in Case I, the SGS enstrophy was backwardly transferred into the grid scale selectively in the tube core region, but it was forwardly transferred into the SGS in the other regions, indicating that the role of the $(S_{ik}\Omega_{kj} + S_{jk}\Omega_{ki})$

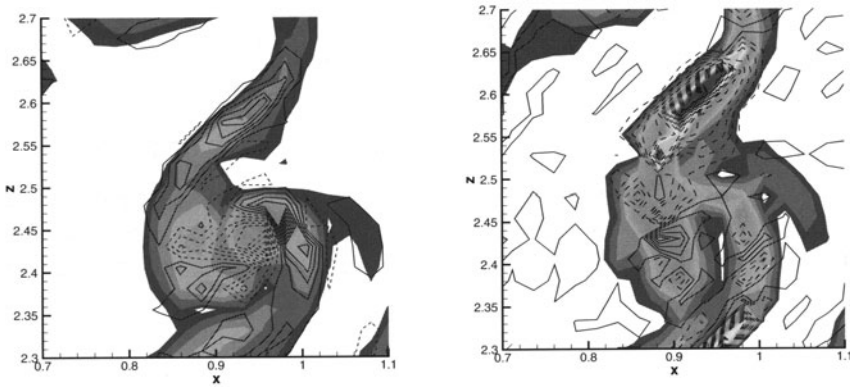


Figure 3. Contours of the eigenvalue, $[-(S_{ik}\Omega_{kj} + S_{jk}\Omega_{ki})]_+$, and the $\bar{\omega}_z W_z^{SGS}$ term in the $x - z$ plane at $y = 0.25$ and $t = 1.95$; left: obtained from Case I, right: from Case II.

term is to enhance the generation of the core region of the vortex tube. In Case II, the grid-scale vorticity in the stretching (z -)direction is strengthened in the flat sheet region. As a result, in Case II, the $(S_{ik}\Omega_{kj} + S_{jk}\Omega_{ki})$ term tends to disrupt the transformation of the flat sheet into the vortex tube by snapping the sheet back to the original flat shape. We note that the values for the z -component of the P_ω term due to the $\bar{\Delta}^2(\bar{S}_{ik}\bar{S}_{kj} - \bar{\Omega}_{ik}\bar{\Omega}_{kj})/12$ term were predominantly positive in both Cases I and II (figure not shown).

It should be noted that a marked difference between the Oldroyd constitutive equations and the nonlinear variant model is that the coefficient for the former, $2(1 - \beta)\nu\lambda$, consists of the quantities associated with molecular processes, whereas the coefficient for the latter consists of the characteristic quantity of the bulk flow (the grid interval), since the former describes the molecular motions and interactions within the fluid, while the latter deals with the interactions between the bulk (grid scale) and the unresolved SGS. To reveal the analogy between these two models more clearly, we evaluate the actual amplitude of the coefficients in terms of the Weissenberg number. By equating the coefficient of the model Eq. (9), $\bar{\Delta}^2/12$, to the coefficient of the viscoelastic term in Eq. (8), $2(1 - \beta)\nu\lambda$ with $\beta = 0.8$, $\nu = 0.00014$, we obtain an estimate of the value of the relaxation time $\lambda \approx 0.36$. Using the rms value of the $S_{ik}S_{ki}$ term to estimate a characteristic strain rate, κ , of the flow, the estimate for the Weissenberg number, We , was obtained as $We = \lambda\kappa \approx 7.8$ at $t = 1.9$ in Case II. In Sureshkumar *et al.* [12], the critical Weissenberg number based on the wall friction velocity, We_τ , for drag reduction in a channel flow was a value of order 10. This value is rather close to the value obtained in the present study, although the mechanism for drag reduction in a channel may be different from that found in the present study.

5. Summary

We have derived the approximate solutions for the Oldroyd constitutive equations for the polymer diluted fluids, and shown that the $(S_{ik}S_{kj} - \Omega_{ik}\Omega_{kj})$ and the $(S_{ik}\Omega_{kj} + S_{jk}\Omega_{ki})$ terms are yielded similarly as in the nonlinear model which is commonly used in the Reynolds averaged models and LES. Marked difference between this approximate solution and the nonlinear model was in the signs for the coefficients of the $(S_{ik}\Omega_{kj} + S_{jk}\Omega_{ki})$ term, i.e., -1 for the nonlinear model, and +1 for the Oldroyd solution. We have conducted the LES calculation of homogeneous isotropic turbulence to elucidate the roles of the $(S_{ik}\Omega_{kj} + S_{jk}\Omega_{ki})$ term for the generation of turbulence. It was shown that when the coefficient was set equal to -1, the solution was close to the filtered DNS data, while when +1, the process of transformation of the flat sheet into the vortex tube was disrupted because the viscoelastic effect similar to that in the Oldroyd fluid was incurred by the identified term on the flat sheet. It is feasible to set the coefficient equal to -1 to approximate the Newtonian fluids, and $+1$ to approximate the viscoelastic fluids. We note that in the Oldroyd-A fluid, the forward cascade of the kinetic energy of the fluid occurred on average, and the elastic energy was increased in turn, whereas in the Oldroyd-B fluid, the backward scatter of the kinetic energy of the fluid occurred on average [11].

This work was partially supported by Grants-in-Aid from the Ministry of Education, Culture, Sports, Science and Technology, Japan (Nos. 12650156 and 14550141).

References

- [1] C.G. Speziale, *J. Fluid Mech.* **178** (1987) 459.
- [2] R.A. Clark, J.H. Ferziger, and W.C. Reynolds, *J. Fluid Mech.* **91** (1979) 1.
- [3] R.S. Rivlin, *Q. Appl. Maths* **15** (1957) 212.
- [4] J. Bardina, Ph.D. dissertation, Stanford University, Stanford, California (1983).
- [5] T.B. Gatski and C.G. Speziale, *J. Fluid Mech.* **254** (1993) 59.
- [6] K. Horiuti, *Phys. Fluids A* **2** (1990) 1708.
- [7] J. G. Oldroyd: *Proc. Roy. Soc. Lond. A* **200** (1950) 523.
- [8] A. Muschinski, *J. Fluid Mech* **325** (1996) 239.
- [9] K. Horiuti, *Phys. Fluids* **13** (2001) 3756.
- [10] K. Horiuti, in press in *J. Fluid Mech.* (2003).
- [11] K. Horiuti, S. Abe, T. Itami, and Y. Takagi, in *Proc. of Int. Symp. on Turbulent Shear Flow Phenomena*, Ed. by N. Kasagi *et al.* (2003) 823.
- [12] R. Sureshkumar, A. N. Beris, and R. A. Handler, *Phys. Fluids* **9** (1997) 743.

TURBULENT CHANNEL FLOW OF A SUSPENSION OF SMALL FIBROUS PARTICLES IN A NEWTONIAN SOLVENT

Michael Manhart and Rainer Friedrich

Fachgebiet Strömungsmechanik, Technische Universität München

*Boltzmannstr. 15, 85748, München, Germany **

michael@flm.mw.tum.de

Abstract A Direct Numerical Simulation (DNS) of turbulent channel flow of dilute suspensions of small, Brownian fibres in a Newtonian solvent is presented. The DNS investigates the potential of drag reduction under situations, where no internal elasticity of the additives is present. The DNS is solving the microscopic equations for the suspended fibres and couples the resulting stresses into a (macroscopic) DNS of the solvent. The microscopic equations for the conformation of the fibres as well as the resulting stresses are derived by the rheological theory of dilute suspensions of Brownian particles in Newtonian solvents. These equations are solved by a Monte-Carlo method. First results show a dramatic reduction of the Reynolds shear stress. However, only a mild reduction of the drag is observed because the fibres generate considerable shear stress components at the wall at the configuration chosen.

Keywords: Drag reduction, fibre suspensions, rheology, direct numerical simulation

1. Introduction

The effect of drag reduction has not only been observed in the context of flexible polymers but also in dilute solutions of surfactants, stiff polymers (Xanthan gum), rigid or flexible fibres and rigid-rod like particles (for an overview, see Gyr and Bewersdorff, 1995). The conditions under which drag reduction due to small amounts of additives can occur in turbulent flows are not yet fully understood. The elastic theory of de Gennes (1990) assumes purely elastic effects to be responsible for drag reduction. But, as examples show (Radin et al., 1975; Kan, 1990; Moyls and Sabersky, 1978), it is possible that there exists another alternative mechanism based on viscous effects acting via the

*Funding provided by DFG, (SFB 438) and Leibniz Computing Centre, München

orientation of the suspended fibres or particles, respectively. This is supported by Virk and Wagger (1990) who postulate two mechanisms for drag reduction: a type-A and a type-B mechanism. Type B behaviour appears in suspensions in which the polymer molecules are already in a stretched state when the fluid is at rest, in type A drag reduction, the molecules become stretched only due to the action of the flow. Both differ significantly in their 'onset' behaviour. Virk and Wagger (1990) postulate that in both types of drag reduction only the stretched molecules are active. In order to understand drag reduction mechanisms in polymeric and fibre suspensions, it is therefore important to focus research not only on purely elastic models but also on rigid fibres or particles, respectively.

A considerable body of literature is devoted to the rheological properties of dilute suspensions of rigid, neutrally buoyant axisymmetric Brownian particles or fibres suspended in Newtonian liquids. Jeffery (1922) analytically derived an equation for the rotary motion and the generated stress field of a small, inertia-free ellipsoidal particle in the Stokes flow limit. From Jeffery's analysis, a rigorous theoretical framework can be derived for the stress field generated in dilute suspensions of sufficiently small particles in a Newtonian solvent. Such theory requires, that the particles are not interacting with each other. The presence of body forces, Brownian motion or particle interactions can be taken into account by the addition of more terms. Brenner (1974) summarized the dynamical rheological theory for axially symmetric particles including spherical dumbbells and long slender bodies with either blunt or bluff pointed ends. According to this framework, the rheological properties of dilute suspensions of such bodies, including Brownian diffusion, can be expressed in terms of volume fraction of the suspended particles, the viscosity of the homogeneous Newtonian carrier fluid and five nondimensional scalar material constants which depend only upon the shape of the suspended particles.

Applications of numerical methods for the description of suspended Brownian fibres in turbulent flows are rare. Den Toonder et al. (1997) have used a strongly simplified model to show the effect of rigid fibres onto turbulent pipe flow. This model, based on purely viscous arguments, was able to produce some drag reduction and to modify the turbulence structure in a way that is in line with experimental observations. These results could be confirmed in a direct numerical simulation (DNS) of turbulent channel flow (Manhart and Friedrich, 1999). So far, for a microstructure such as dilute suspensions of Brownian rigid fibres or particles, no macroscopic relations for the stress field generated by the microstructure have been derived, as it has been done for elastic dumbbell models by the FENE-P approximation (see Bird, 1987). The FENE-P model, resulting in transport equations for the non-Newtonian stress components, has already been successfully applied in DNS of turbulent channel flow (e.g. Sureshkumar et al., 1997 among others).

In the present paper, the modification of turbulence structure by a dilute suspension of small rigid fibres in a channel flow ($Re_\tau = 180$) is investigated by means of DNS of the flow field together with a Lagrangian Monte-Carlo method for solving the underlying Fokker-Planck equation of the conformation vector.

2. Theory

The dynamics of an incompressible fluid consisting of a Newtonian solvent with a minute amount of added polymers can be described by the conservation of mass and momentum:

$$\nabla \cdot \mathbf{u} = 0 \quad (1)$$

$$\rho \frac{D\mathbf{u}}{Dt} = -\nabla p + \nabla \cdot (\boldsymbol{\tau}^N + \boldsymbol{\tau}^{NN}) \quad (2)$$

Here, \mathbf{u} is the velocity vector, ρ the density and p the pressure. $\boldsymbol{\tau}^N$ is the part of the stress tensor attributed to the Newtonian solvent and $\boldsymbol{\tau}^{NN}$ is the non-Newtonian part of the stress tensor due to the suspended particles. For the Newtonian part of the stress tensor $\boldsymbol{\tau}^N$ the following constitutive equation is generally accepted:

$$\boldsymbol{\tau}^N = 2\mu\mathbf{D}, \quad (3)$$

where μ is the dynamic viscosity and \mathbf{D} is the rate-of-strain tensor

$$\mathbf{D} = (\nabla\mathbf{u} + \nabla\mathbf{u}^T)/2. \quad (4)$$

For the contribution of the polymeric molecules to the stress tensor $\boldsymbol{\tau}^{NN}$, a non-Newtonian constitutive relation has to be supplied. The stress caused by the presence of particles is a function of the moments of their orientation distribution function. The orientation distribution function is a probability density function of the orientation angle which is determined by the dynamics of the particles. If the particles are sufficiently small, their dynamics will be affected by Brownian motion, which results in a stochastic differential equation. The orientation of a single fibre follows Jeffery's equation (Jeffery, 1922) describing the rotational motion of small ellipsoidal particles due to the action of the velocity gradient tensor of the surrounding fluid (orientation vector \mathbf{n} and elongation coefficient κ , strain rate tensor \mathbf{D} , rotation rate tensor $\boldsymbol{\Omega}$). This equation has been derived by an analytical solution of the Stokes flow equations valid for small particles ($Re \ll 1$).

$$\frac{D\mathbf{n}}{Dt} = \boldsymbol{\Omega} \cdot \mathbf{n} + \kappa [\mathbf{D} \cdot \mathbf{n} - (\mathbf{n} \cdot \mathbf{D} \cdot \mathbf{n})\mathbf{n}] + \boldsymbol{\Gamma}(t). \quad (5)$$

A stochastic term $\boldsymbol{\Gamma}$ describes the effect of Brownian motion on the rotation and depends on the size of the particle. It can be formally represented as the

increment of a Wiener process \mathbf{W} .

$$\Gamma(t) = \sqrt{2D_r} \frac{\partial \mathbf{W}}{\partial t} \quad (6)$$

The rotary diffusivity D_r quantifies the effect of the Brownian motion by a Péclet number $Pe = \dot{\gamma}/D_r$ being the ratio of hydrodynamic forces vs. stochastic forces onto the particle ($\dot{\gamma}$ is a typical velocity gradient). D_r can be computed by the rheological theory of rigid fibres as outlined in (Brenner, 1974; see also Manhart, 2003). By integrating equation (5) for a sufficient number of independent particles, the moments of the distribution function, $\langle \mathbf{nn} \rangle$ and $\langle \mathbf{nnnn} \rangle$ can be computed. From these moments and five material constants μ_i , the additional non-Newtonian stress tensor is determined which is dependent of the mass or volume fraction V_p , the aspect ratio r and the size of the particles.

$$\begin{aligned} \boldsymbol{\tau}^{NN} = & 2\mu_0 \mathbf{D} + \mu_1 \mathbf{ID} : \langle \mathbf{nn} \rangle + \mu_2 \mathbf{D} : \langle \mathbf{nnnn} \rangle + \\ & 2\mu_3 (\langle \mathbf{nn} \rangle \cdot \mathbf{D} + \mathbf{D} \cdot \langle \mathbf{nn} \rangle) + 2\mu_4 D_r (3 \langle \mathbf{nn} \rangle - \mathbf{I}) \end{aligned} \quad (7)$$

3. Numerical scheme

For the simulation of the coupled fluid/particle system, two different simulation methods are used. The turbulent flow field on the macroscopic level is provided by a direct numerical simulation (DNS). The conformation of the fibres is computed by a Monte-Carlo simulation using information of the time dependent velocity derivative tensor seen by a fluid element traveling with the flow in a Lagrangian framework.

Our DNS method for the solution of Eqs. (1) and (2) uses an explicit version of the projection or fractional step method of Chorin (1968). We use a Leapfrog scheme for the explicit time advancement of the momentum equation. The flow variables are defined on a non-equidistant Cartesian mesh in a staggered arrangement. The specific discrete formulations are derived by integrating the equations over the corresponding control cells surrounding the definition points of the individual variables. We are using the mid-point rule for approximating the fluxes by the variables. The required interpolations and the approximation of the first derivatives are performed by fourth order compact interpolation and difference formulations, respectively (Meri et al., 1998). The Poisson equation is solved by a direct method using Fast-Fourier transformations in the homogeneous streamwise and spanwise directions of the channel flow and a tridiagonal matrix solver in wall-normal direction. The DNS of turbulent channel flow is documented in (Manhart and Friedrich, 1999). We performed grid resolution studies and evaluated the influence of the discretisation order on the results.

The distribution function $\Psi(\mathbf{n}, t)$ of the orientation angle of the suspended particles is computed by a stochastic simulation method (Monte-Carlo simula-

tion). For a sufficient number of particles, the Jeffery equation (5) is integrated using the derivative tensor obtained by the DNS of turbulent channel flow. An Euler time step is used for the time integration. Numerical tests show, that the conformation distribution function is relatively insensitive against the time stepping, which justifies the low order of the Euler time step. The Brownian term is modelled by a stochastic Wiener process with a Gaussian distribution, which itself is modeled by a random number generator. In combination with an Euler time step, it is sufficient to use random numbers with uniform distribution as increments of the Wiener process (Öttinger, 1996). A detailed verification of the stochastic simulation method for the microstructure can be found in (Manhart, 2003). The tests showed, that the stochastic simulation method is able to predict the orientation distribution function and the corresponding results from rheological theory of small Brownian particles suspended in a Newtonian solvent in uniform shear flow.

The coupling between the DNS of the flow field and the Monte-Carlo simulation of the microstructure goes two-way. First, the velocities and the velocity derivative tensor have to be interpolated from the Euler grid to the particle positions. Second, the non-Newtonian stress tensor has to be interpolated from the Lagrangian particle positions to the Euler grid. The velocity and the velocity derivative tensor are estimated at the instantaneous positions of the particles by fourth order interpolations and difference formulae which ensure a continuous velocity derivative tensor in time.

For the interpolation of the stress tensor computed on the Lagrangian positions, the quantities are distributed among the eight cell centers of the Euler grid surrounding the Lagrangian position of a particle. We assume a linear variance of the quantity between two Eulerian positions and build the average over N_P particles sharing the same neighbouring Eulerian cells.

For the runs presented here, we used a total number of $1.28 \cdot 10^9$ individual fibres clustered into a total number of $1.28 \cdot 10^7$ clusters. A cluster consists consequently of 100 fibres sharing their Lagrangian position and velocity derivative tensor. The statistical independence of the individual particles is guaranteed by the stochastic nature of equation (5). The advantage of the clustering is a presmoothing of the stress tensor along the Lagrangian paths. The algorithm has been implemented on a Hitachi SR8000 high-performance computer of the Leibniz Computing Centre in Munich. We are using MPI for parallelisation, which is done over particle clusters of the Lagrangian part. This parallelisation strategy is justified, because the computing time spent in the Lagrangian part is much more than the one spent in the DNS part. Overall, a time step of the whole coupled simulation takes 8.8 CPU-seconds on 128 PE's or 16 nodes, respectively, of the SR8000.

4. Results

The configuration chosen is a turbulent channel flow at $Re_\tau = 180$. In order to save computational resources, we performed our simulations on a relatively small domain, covering $6.2 \cdot 1.9 \cdot 2.0$ channel half-widths h in streamwise x -, spanwise y - and wall-normal z -direction. This allows for a resolution of 17.7 and 10.6 wall units in x - and y -directions. In wall-normal direction, the grid is refined to 2.7 wall units at the wall, which leads to a wall distance of 1.35 wall units of the first grid point. This resolution is achieved by a grid of $64 \cdot 32 \cdot 64$ grid points. The statistical results differ only marginally from the ones in a channel with larger domain size which lets us assume that the main effects of turbulence production and redistribution are covered in our simulation.

The influence of the fibres onto the turbulent channel flow is controlled by three parameters, the size, the aspect ratio and the volume concentration of the particles. The size enters equation (5) by the strength of the Brownian motion $\Gamma(t)$ which is characterized by the Péclet number Pe , here defined using global quantities as the bulk velocity u_b and the channel half width h by

$$Pe = \frac{u_b/h}{D_r}. \quad (8)$$

In the following, we present results of a series of runs in which the aspect ratio and Péclet number are kept constant to $r = 50.0$ and $Pe = 98.0$, respectively. Our channel flow is run at a Reynolds number based on wall friction of $Re_\tau = 180$ corresponding to a bulk Reynolds number of $Re_b = u_b \cdot h/\nu = 2816$. Table 1 gives an estimation of the particle size as a function of the channel half width, when an experimental device is run with water at a temperature of $T = 293K$. That table shows that when we are considering such Péclet numbers, the length scales of the additives are in the range of 10 to 100 micrometers. Larger additives, i.e. longer fibres with the same aspect ratio, have larger Péclet numbers.

Table 1. Fibre length scales, that result in a Péclet number of $Pe = 98$ in dilute suspensions of fibres in turbulent channel flow of water ($Re_b = 2816$, temperature $T = 293K$)

channel half width in m	0.05	0.1	0.2	0.5
fibre length in $m \cdot 10^{-6}$	9.7	15.4	24.5	45.0

We have run a reference simulation with Newtonian flow. From a realization of this flow field, we introduced the fibres, initialized with random orientation angles and with a random distribution in space. For a period of about $90h/u_b$, the fibres have been allowed to adjust to the flow without back-influence on the

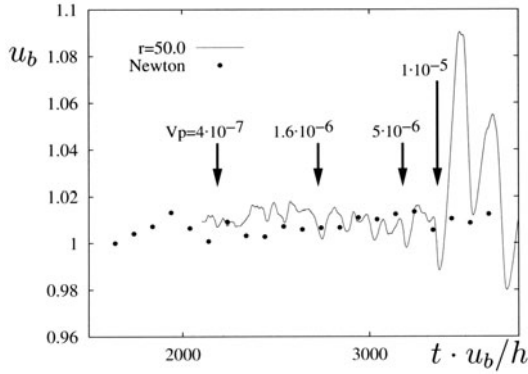


Figure 1. Variation of bulk velocity with varying the volume fraction of the fibres

flow. This is accomplished by setting the volume fraction to zero for that period. After that, we increased the volume fraction in small steps starting from $V_p = 4 \cdot 10^{-7}$ as indicated in Figure 1. This figure shows the development of the bulk velocity through the channel with varying volume fraction of the fibres and a constant pressure drop. We see that below $V_p = 1 \cdot 10^{-5}$, there is nearly no alteration of the bulk velocity indicating no drag reduction. Above that value strong oscillations of the bulk velocity appear, indicating a massive change of the turbulence structure. The bulk velocity averaged over the period between the introduction of the $V_p = 1 \cdot 10^{-5}$ ($T = 3359$) and ($T = 3897$) is $u_b = 1.025$ instead of $u_b = 1.0079$ for the long-term averaged Newtonian case. That means, we have achieved a marginal drag reduction for this period. More simulation studies with different parameter sets are on the way to investigate if higher drag reductions can be achieved.

In the following, we investigate the alteration of the turbulence structure and the internal stress balance that led to the strong oscillations of the bulk velocity. For that, we plot the shear stress balances in the flow.

$$T_{13} = \tau_w(1 - z/h) = \mu \frac{\partial \langle u \rangle}{\partial z} - \rho \langle u'w' \rangle + \langle \tau_{13}^{NN} \rangle \quad (9)$$

The total stress T_{13} which varies linearly across the channel, is the sum of a solvent contribution $\mu \frac{\partial \langle u \rangle}{\partial z}$, a turbulent $\rho \langle u'w' \rangle$ and a contribution coming from the fibres $\langle \tau_{13} \rangle$, which is given by (6). In Figure 2, the shear stresses are plotted for the period $3268 < t < 3359$, just before the volume fraction was switched from $5 \cdot 10^{-6}$ to $1 \cdot 10^{-5}$. In Figure 3, the stresses are averaged over the subsequent period $3359 < t < 3448$ ($V_p = 1 \cdot 10^{-5}$). The volume fraction of $V_p = 5 \cdot 10^{-6}$ is not able to change the shear stresses considerably. However, there is a noticeable stress contribution from the fibres at the wall of nearly 20%

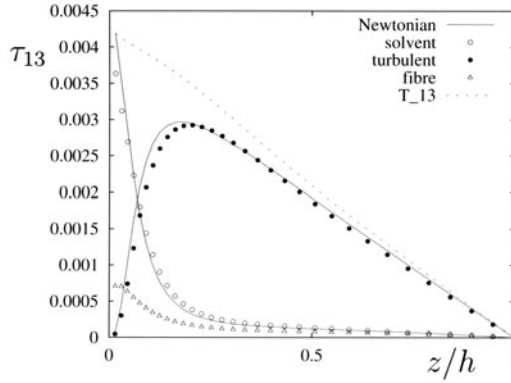


Figure 2. Shear stress contributions in comparison with Newtonian flow. Averaging done over the period $3268 < t < 3359$, ($V_p = 5 \cdot 10^{-6}$)

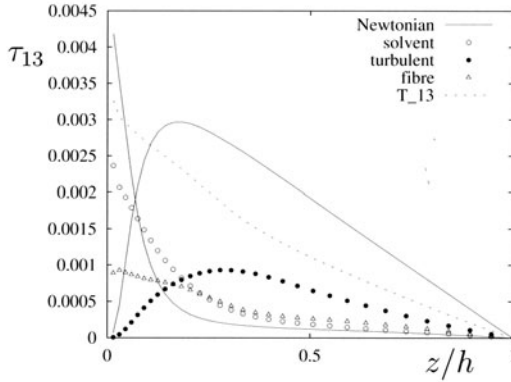


Figure 3. Shear stress contributions in comparison with Newtonian flow. Averaging done over the period $3359 < t < 3448$, ($V_p = 1 \cdot 10^{-5}$)

of the wall shear stress. This stress contribution has to be compensated by a modification of the turbulent shear stress, which is small but sufficiently high to keep the bulk velocity at its Newtonian value. When the volume fraction exceeds a certain limit (here $V_p = 1 \cdot 10^{-5}$), we observe a drastic damping of the turbulent stresses (Figure 3) which is larger than the contribution of the fibres and consequently leads to an overall stress reduction and an acceleration of the flow that manifests itself in an increase of the solvent contribution of the stress. The flow is not yet in equilibrium when averaged over the period displayed in this Figure which results in a deviation of the total stress from the long-term averaged value from equation (9).

5. Summary

We presented an algorithm for DNS of turbulent channel flow of dilute suspensions of fibres in a Newtonian solvent. The algorithm couples a Finite Volume solver for the flow field with a Monte-Carlo solver for the fibre microstructure. The equations for the microstructure are solved along Lagrangian paths following infinitesimal small fluid volumes. The stresses generated by the suspended fibres are computed from solving equations coming from the rheological theory of rigid elongated Brownian particles. The only assumptions made for the derivation of the rheological equations are that (i) the fibres are small enough to follow the Stokes flow assumptions, (ii) the fibres are inertia free, (iii) the fibres are axisymmetric and (iv) the suspension is sufficiently dilute that no interactions among the fibres take place. Their dynamics are affected by Brownian motion that is accounted for by a stochastic term in the evolution equation for the fibres' orientation and a relaxation term in the stress equation.

We solve the coupled equations for a turbulent channel flow in a reasonably large computational domain at a Reynolds number of $Re_\tau = 180$. The influence of the fibres on the flow field is governed by three parameters, the Péclet number, the aspect ratio and the volume fraction of the fibres. In the present paper, we present first results of runs holding the aspect ratio and the Péclet number constant at values of $r = 50.0$ and $Pe = 98$, respectively. Increasing the volume fraction in small steps reveals a noticeable modification of the turbulence structure taking place for volume fractions larger than $V_p = 1 \cdot 10^{-5}$. The non-Newtonian stresses damp the turbulent stresses considerably. The observed reduction is even more than the one observed in simulations undertaken in visco-elastic flows using the FENE-P (Sureshkumar et al., 1997). Unfortunately, this turbulent stress reduction is compensated in part by a considerable shear stress contribution of the fibres, which assumes wall values approximately 20% of the total wall shear stress thus leading to reduced solvent contributions to the wall shear stress. This goes in hand with smaller velocity gradients at the wall thus reducing the flow throughput in the channel. Consequently, the reduction of the fibre contribution to the shear stress seems to be the key to drag reduction in dilute fibre suspensions. An investigation of the rheological behaviour of fibres in turbulent channel flow undertaken without back-reaction on the flow (Manhart, 2003) gives some hints which parameter combinations could be appropriate to achieve this goal. The shear stress component of the non-Newtonian stress tensor becomes smaller with larger Péclet numbers and larger aspect ratios. The next numerical test will then be to increase the Péclet number and aspect ratio.

Acknowledgments

The authors wish to thank the Leibniz Computing Centre of the Bavarian Academy of Sciences and the HLRB for providing the computational facilities. The work has been supported by the DFG in the framework of the Sonderforschungsbereich 438.

References

- Bird, R., Curtiss, C., Armstrong, R., and Hassager, O. (1987). *Dynamics of Polymeric Liquids, Vol. 2, Kinetic Theory*. John Wiley and Sons, 2nd edition.
- Brenner, H. (1974). Rheology of a dilute suspension of axisymmetric Brownian particles. *Int. J. Multiphase Flow*, 1(2):195–341.
- Chorin, A. J. (1968). Numerical solution of the Navier-Stokes equations. *Math. Computat.*, 22:745–762.
- de Gennes, P. (1990). *Introduction to polymer dynamics*. Cambridge University Press.
- den Toonder, J., Hulsen, M., Kuiken, G., and Nieuwstadt, F. (1997). Drag reduction by polymer additives in a turbulent pipe flow: numerical and laboratory experiments. *J. Fluid Mech.*, 337:193–231.
- Gyr, A. and Bewersdorff, H.-W. (1995). *Drag Reduction of turbulent flows by additives*, volume 32 of *Fluid mechanics and its applications*. Kluwer Academic Publishers, Dordrecht.
- Jeffery, G. (1922). The motion of ellipsoidal particles immersed in a viscous fluid. *Proc. R. Soc. Lond. A*, 102:161–179.
- Kan, R. S. (1990). Drag reduction by particle addition. In Bushnell, D. M. and Hefner, J. N., editors, *Viscous drag reduction in boundary layers*, volume 123 of *Progress in Astron. & Aeron.*, pages 433–456.
- Manhart, M. (2003). Rheology of suspensions of rigid-rod like particles in turbulent channel flow. *Journal of Non-Newtonian Fluid Mechanics*, 112(2-3):269–293.
- Manhart, M. and Friedrich, R. (1999). Direct numerical simulation of turbulent channel flow of a viscous anisotropic fluid. In Bungartz, H.-J., Hoppe, R., and Zenger, C., editors, *Lectures on Applied Mathematics, Proceedings of the symposium organized by the SFB 438 "Mathematical Modelling, Simulation and Intelligent Systems" on the occasion of Karl-Heinz Hoffmann's 60th birthday, Munich June 30 - July 1, 1999*, pages 277–296, Heidelberg. Springer.
- Meri, A., Wengle, H. Dejoan, A. V. E., and Schiestel, R. (1998). Applications of a 4th-order hermitian scheme for non-equidistant grids to LES and DNS of incompressible fluid flow. In Hirschel, E., editor, *Vol. 66, Notes on numerical fluid mechanics*, pages 382–406. Vieweg-Verlag, Braunschweig.
- Moyls, A. L. and Sabersky, R. H. (1978). Heat transfer and friction coefficients for dilute suspensions of asbestos fibers. *Int. J. Heat Mass Transfer*, 21:7–14.
- Öttinger, H. (1996). *Stochastic processes in polymeric fluids*. Springer, Berlin.
- Radin, I., Zakin, J. L., and Patterson, G. (1975). Drag reduction in solid-fluid systems. *AIChE J.*, 21:358–371.
- Sureshkumar, R., Beris, A., and Handler, R. (1997). Direct numerical simulation of the turbulent channel flow of a polymer solution. *Phys. Fluids*, 9(3):743–755.
- Virk, P. and Wagger, D. (1990). Aspects of mechanisms in type B drag reduction. In Gyr, A., editor, *Structure of Turbulence and Drag Reduction*, pages 201–212. IUTAM Symp. Zürich/Switzerland 1989, Springer.

3.2 ACTIVE AND PASSIVE SCALARS

LARGE-EDDY SIMULATION OF A STABLY STRATIFIED FLOW OVER LONGITUDINALLY RIDGED WALLS

V. Armenio, L. Falcomer

Dipartimento di Ingegneria Civile, Università di Trieste, Piazzale Europa 1, 34127, Trieste, Italy

armenio@univ.trieste.it; falcomer@univ.trieste.it

G. F. Carnevale

Scripps Institute of Oceanography, University of California San Diego, La Jolla, CA 92093 USA

gfc@castor.ucsd.edu

Abstract

Large-eddy simulations are carried out to investigate turbulent flow in a stably-stratified open channel with longitudinal ridges along the bottom wall. The Boussinesq form of the governing equations is solved for different levels of stratification. The results of the simulations show that stratification creates two separate regions: a free-surface region, characterized by the presence of the thermocline, where vertical large-scale motion is strongly inhibited and a wall region, characterized by reduced vertical mixing at the turbulent scales and enhanced large-scale secondary flows that tend to mix mass and momentum in the cross-stream plane.

Keywords: Large-eddy simulation, stably stratified flows, complex geometry.

1. Introduction

Stably stratified turbulent flows are common in environmental and geophysical applications. These flows have been widely studied in the past using analytical, numerical, laboratory and field investigations. Most investigations have dealt with problems characterized by simple flow field and geometry, for example, homogeneous turbulence and wall bounded turbulence over flat walls (e.g., Rohr et al., 1988, Komori et al., 1983, Armenio and Sarkar, 2002). Comparatively few investigations have been devoted to the relevant cases of stratified turbulent flows over a topography (see for example Hunt and Snyder,

1980; Ding et al., 2003 for the stratified flow around 3D hills)

Canyon-like (or along-ridge) topography is worth investigating for its own relevance in atmospheric as well as in oceanographic applications. When a fluid is confined within a shallow straight channel, relevant secondary effects are known to rise. In particular, through the resulting imbalance of the normal Reynolds stresses in the cross-stream plane, this topography produces secondary large-scale recirculations that are able to supply additional vertical mixing of mass and momentum (Speziale, 1987). When the length-scale of the spanwise disturbance at the bottom is not small if compared to the vertical extension of the channel, the secondary recirculation spans throughout the vertical extension of the domain so that patches of fluid from the bottom are pushed up to the top and *vice-versa*. Although the neutrally stratified turbulent flow field over trapezoidal longitudinal ridges located over a bottom wall has been investigated in the past (see for example Nezu and Nakagawa, 1984; Kawamura and Sumori, 1999; Falcomer and Armenio, 2002), its stably stratified counterpart has not been studied as yet.

The question we should like to address in the present paper is the following: How does stable stratification affect the large-scale secondary motion that in a neutrally stratified flow supplies an effective mean for vertical transport of fluid from the bottom to the top?

We consider an idealized geometry, constituted by an infinite array of trapezoidal finite-amplitude ridges running longitudinally along the bottom wall. The study is performed numerically using Large-Eddy simulation. The response of the flow field for several levels of stratification is analyzed, going from the case of a neutrally stratified flow to the case of strong stratification.

2. Mathematical formulation

We assume that the total density field can be decomposed into a bulk density ρ_0 and a perturbation density $\rho(x, y, z, t)$ with $\rho_0 \gg \rho(x, y, z, t)$, and that the acceleration of the fluid particles is much smaller than the gravitational one. In this case the Boussinesq approximation to the Navier-Stokes (NS) equations holds and we can neglect the density change in the fluid except in the gravity term (for a detailed discussion refer to Kundu, 1990). The filtered NS equations read as:

$$\frac{\partial \overline{u_i}}{\partial x_i} = 0, \quad (1)$$

$$\frac{\partial \overline{u_i}}{\partial t} + \frac{\partial \overline{u_j} \overline{u_i}}{\partial x_j} = -\frac{\partial \overline{p}}{\partial x_i} + \frac{1}{Re} \frac{\partial}{\partial x_j} \frac{\partial \overline{u_i}}{\partial x_j} + F \delta_{i1} - Ri \rho \delta_{i3} - \frac{\partial \tau_{ij}}{\partial x_j}, \quad (2)$$

$$\frac{\partial \overline{p}}{\partial t} + \frac{\partial \overline{u_j} \overline{p}}{\partial x_j} = \frac{1}{Re Pr} \frac{\partial}{\partial x_j} \frac{\partial \overline{p}}{\partial x_j} - \frac{\partial \lambda_j}{\partial x_j}. \quad (3)$$

In Eq. 1- 3, \overline{u}_i denotes the i - component of the filtered velocity field made dimensionless with a reference velocity U_r , \overline{p} is the filtered pressure made non dimensional with $\rho_0 U_r^2$, F is the nondimensional, mean, driving, pressure gradient, $Ri = g\delta\Delta\rho/\rho_0 U_r^2$ is the reference Richardson number with g the gravitational acceleration, $\Delta\rho$ the density gap as defined in the following and δ the height of the channel, $Re = U_r\delta/\nu$ is the reference Reynolds number and Pr is the Prandtl number of the fluid. In the present work we consider $Pr = 5$ that stands for thermally stratified water. The density $\overline{\rho}$ in the above equations is the filtered, perturbation density field made dimensionless with $\Delta\rho$. The terms τ_{ij} and λ_j respectively represent the SGS contribution to the momentum flux and to mass transport. Equation 3 represents the transport equation of the temperature field $T(x, y, z, t)$, after considering that ρ changes with T according to $d\rho/\rho = -\alpha dT$ with α the thermal expansion coefficient. Finally, referring to Fig. 1, henceforth x, y and z respectively denote the streamwise, spanwise and vertical directions.

The height of the ridges is chosen $h_r = 0.125\delta$. At the top boundary the

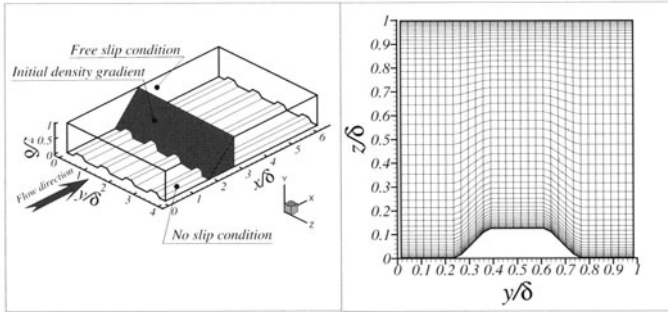


Figure 1. Schematic of the problem under investigation and grid cells in the cross-stream plane

channel has a free surface, that can be simulated by imposing a free-slip condition on the velocity field. A no-slip boundary condition is imposed at the bottom wall. The friction Reynolds number of the simulations ($Re_\tau = u_\tau\delta/\nu$ with u_τ the friction velocity evaluated using the wall stress of an equivalent plane-channel flow) is set equal to 400, thus, the ridge is 50 wall-units high. The dimensions of the computational domain are $L_x = 2\pi\delta$, $L_y = 1.25\pi\delta$ and $L_z = \delta$, and the simulations have been carried out using a $64 \times 128 \times 48$ grid. The present grid resolution has been proved to give accurate results for the plane-channel flow as well as for the case of ridged walls. Periodic boundary conditions are used in both the streamwise and spanwise directions. The density field is set constant at the free-surface $\rho(x, y, \delta, t) = \rho_{top}$ and at the bottom of the troughs $\rho(x, y, 0, t) = \rho_{bot}$. The density field is made non-dimensional with the density difference $\Delta\rho = \rho_{bot} - \rho_{top} > 0$. Since the bottom wall is

Case	Re_τ	Ri_τ	Pr	Re_b	u_b
<i>C0</i>	400	0	5	6369	0.68
<i>C1</i>	400	50	5	7107	0.77
<i>C2</i>	400	100	5	7487	0.81
<i>C3</i>	400	200	5	8224	0.89
<i>C4</i>	400	300	5	8677	0.94

Table 1. Summary of the cases investigated together with relevant bulk quantities. Note that $Re_b = u_b \delta / \nu$ with u_b the bulk velocity in the channel and that $Ri_\tau = Ri U_\tau^2 / u_\tau^2$

not constant in height, the density distribution at the bottom topography is held constant and equal to $\rho_{bot}[1 - z_b(y)/\delta]$ with $z_b(y)$ the vertical coordinate of the bottom topography. Different levels of stratification are considered spanning a wide range of Richardson numbers as illustrated in Table 1. Eq. 1- 3 are solved using a 2nd order accurate in time and in space finite difference method, whereas the SGS stresses and buoyancy fluxes are modeled using respectively a dynamic mixed model and a dynamic eddy diffusivity model. Details are provided in Armenio and Piomelli, 2000; Armenio and Sarkar, 2002.

3. Discussion

The presence of longitudinal ridges at the bottom wall induces a distortion of the mean streamwise velocity along the spanwise direction and the presence of a secondary recirculation in the cross-stream plane. The mean streamwise velocity is affected by stratification (Fig. 2a): specifically, the vertical shear $\partial U / \partial z$, and hence the bulk velocity (see Table 1), increase going from *C0* to *C4*. This is a well known effect (Armenio and Sarkar, 2002) related to the decrease of the Reynolds stress $\langle u'w' \rangle$ caused by the inhibited vertical transport of momentum; furthermore, the dome of the isolines over the ridge appears more pronounced as stratification increases. This effect is observable in the near-wall region and it is due to the rise of the secondary Reynolds stress $\langle u'v' \rangle$. This stress remains very small within the free-surface region independent of the level of stratification, whereas it increases in the wall region due to the effect of topography. Overall, the ratio $\langle u'v' \rangle / \langle u'w' \rangle$ increases with stratification in the near-wall region, and this causes the rise of the horizontal shear $\partial U / \partial y$ over the inclined walls of the ridge. Stable stratification also causes a strong variation of the mean spanwise and vertical components of velocity V and W . In particular, the increase of stratification tends to suppress V and W in the free-surface region (Fig. 2b,c); on the other hand it enhances the cross-stream velocity field (see Fig. 2b,c) in the *log*-region as well in the near-wall region. Indeed, since the maximum streamwise velocity U_{max} increases by a factor 1.4 going from *C0* to *C4*, Fig. 2b,c shows that a similar increase occurs

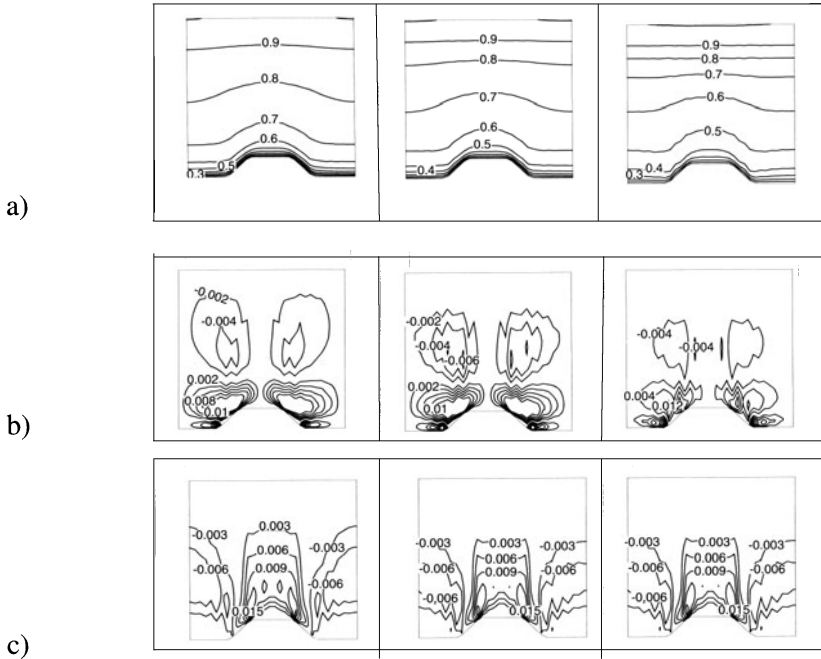


Figure 2. Cross-stream distribution of the mean velocity components for three levels of stratification, C1,C2,C4 from the left to the right: a) U/U_{max} ; b) V/U_{max} ; c) W/U_{max} .

to the cross-stream velocity field. The analysis of Fig. 2b,c shows that the main secondary circulation is progressively reduced in height by stratification and confined in a region far from the free surface. Figure 2b,c also shows that the small recirculation located at the bottom corner of the ridges appears progressively enhanced both in size and in intensity going from C0 to C4.

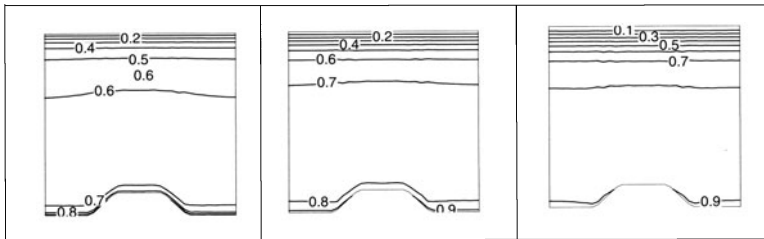


Figure 3. Cross-stream distribution of $\langle \rho \rangle / \Delta \rho$ for three levels of stratification, C1,C2,C4 from the left to the right.

The cross-stream recirculations are related to the rise of a mean streamwise component of the vorticity field Ω_x . It can be easily shown that the transport equation for Ω_x does not contain any explicit, destruction, buoyancy

term, rather, stratification indirectly affects Ω_x through modification of the cross-stream distribution of the normal Reynolds stresses $\langle v'v' \rangle$, $\langle w'w' \rangle$ and of the cross-stream Reynolds stress $\langle v'w' \rangle$. The mean streamwise vorticity, that quantifies the intensity of the secondary recirculations, increases with stratification. In particular, the production terms related to the anisotropy of the normal Reynolds stresses $\langle v'v' \rangle - \langle w'w' \rangle$ and to the cross-stream Reynolds stress $\langle v'w' \rangle$ change with stratification. Most of the production of mean vorticity is due to the anisotropy term in the core region as well as at the trough of the ridge. The behavior described above is basically due to the fact that stratification has two main effects on the flow field: first, it increases anisotropy, in that vertical fluctuations are more likely to be suppressed than horizontal ones; second, it suppresses sweep-ejection events, and hence, cross-correlation between the velocity components, namely the off-diagonal Reynolds stresses $\langle u'_i u'_j \rangle$. As already observed, the increased stratification destroys the secondary motion in the free-surface region. The analysis of the vorticity field and the related production terms shows that, at the free surface, the streamwise vorticity is very small in all cases because such is the cross-stream variation of the anisotropy term and of the cross-stream Reynolds stress.

The increase of stratification also produces the rise of a strong thermocline (density gradient due to a corresponding temperature gradient) in the free surface region, and, at the same time, its progressive intrusion toward the core region (Fig 3). As a result, stable stratification creates a potential barrier at the free surface where vertical motion is strongly inhibited. It follows that the secondary motion (in general weak compared to the mean flow) is suppressed in the thermocline. Since the turbulent vertical transport of mass, quantified by $\langle \rho'w' \rangle$ is also strongly suppressed in the free surface region, we can conclude that under stratification the free surface region is characterized by absence of vertical transfer of mass and/or momentum.

The wall stresses appear affected by stable stratification. Figure 4 shows the spanwise distribution of the primary (streamwise) wall stress as well as that of the secondary (spanwise) wall stress, made non-dimensional with the value obtained in the case of an equivalent plane-channel flow. The behavior of the primary wall stress strongly depends on stratification. In the trough τ_x decreases with stratification, whereas the opposite is true over the inclined wall and at the crest of the ridge. This is due to the way stratification affects the primary Reynolds stress $\langle u'w' \rangle$, that, in turn, affects the wall stress. The secondary Reynolds stress is basically related to the presence of the secondary, small recirculation located near the wall. As observed above, this recirculation appears enhanced going from C0 to C4, and consequently large values of the secondary wall stress are expected in the location where the small cellular

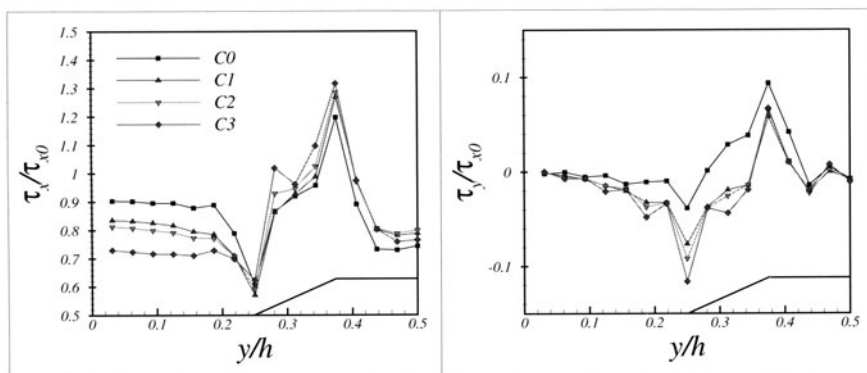


Figure 4. Spanwise distribution of a) primary wall stress; b) secondary wall stress for four levels of stratification (C0 to C3). The quantities are made dimensionless with the wall stress of an equivalent plane channel flow.

motion is more active, namely, the bottom corner.

4. Concluding remarks

The response of a free-surface channel flow with longitudinal ridges at the bottom wall under stable stratification has been investigated numerically. The mean secondary recirculation that tends to drive warm fluid from the free surface region toward the ridge in the trough region as well as cold fluid from the crest of the ridge up to the free surface, thus contributing to the overall, large-scale, vertical mixing of mass and momentum appears reduced in size by the increased stratification. Specifically, stable stratification tends to generate a strong thermocline in the free surface region that, creating a barrier of potential energy, is responsible for the suppression of vertical large-scale transport and small-scale mixing. On the other hand, the increased anisotropy in the cross-stream Reynolds stresses due to stratification causes the production terms of the mean streamwise vorticity to grow and, consequently, enhances large-scale transport in the near wall region. The flow results thus split into two separate regions, the above, free surface region characterized by completely suppressed vertical motion, both at the large-scale and at the small scales, and a near wall region where large-scale motion is enhanced.

The present research has been granted by Regione Friuli Venezia Giulia under contract “Approccio Multiscala alla Dinamica delle Dispersioni di Particolato nel Friuli Venezia Giulia”. The computations have been run on the SP4 of CINECA (Italy). GFC is funded in part by NSF grants OCE 01-28991 and OCE 01-29301.

References

- Armenio, V. and Piomelli, U. (2000). A lagrangian mixed subgrid-scale model in generalized coordinates. *Flow Turbulence Combust.*, 65:51.
- Armenio, V. and Sarkar, S. (2002). An investigation of stably stratified turbulent channel flow using large-eddy simulation. *J. Fluid Mech.*, 459:1.
- Ding, L., Calhoun, R., and Street, R. (2003). Numerical simulation of strongly stratified flow over three-dimensional hill. *Bound-Layer Meteor.*, 107:81.
- Falcomer, L. and Armenio, V. (2002). Large-eddy simulation of secondary flow over longitudinally ridged walls. *J. Turbulence*, 3:008.
- Hunt, J. and Snyder, W. (1980). Experiments on stably and neutrally stratified flow over a model three-dimensional hill. *J. Fluid Mech.*, 96:671.
- Kawamura, H. and Sumori, T. (1999). Dns of turbulent flow in a channel with longitudinally ridged walls. In *Direct and Large-Eddy simulation III*, page 405. P.R. Voke and N.L. Sandham and L. Kleiser Ed., Kluwer Academic Publishers.
- Komori, S., Ueda, H., Ogino, F., and Mizushima, T. (1983). Turbulent structure in a stably stratified open-channel flow. *J. Fluid Mech.*, 130:13.
- Kundu, P. K. (1990). *Fluid Mechanics*. Academic Press.
- Nezu, I. and Nakagawa, H. (1984). Cellular secondary currents in straight conduit. *J. Hydr. Eng.*, 110:173.
- Rohr, J., Itsweire, E., Helland, K., and Atta, C. V. (1988). Growth and decay of turbulence in a stably stratified shear flow. *J. Fluid Mech.*, 195:77.
- Speziale, C. (1987). On non linear $k-l$ and $k-\epsilon$ models of turbulence. *J. Fluid Mech.*, 178:459.

LARGE EDDY SIMULATION OF CONJUGATE HEAT-TRANSFER USING THERMAL WALL-FUNCTIONS

Alexandre Chatelain^{1,2}, Frédéric Ducros¹ and Olivier Métais²

¹CEA Grenoble, 17, rue des Martyrs - 38054 Grenoble Cedex 9, France
alexandre.chatelain@cea.fr , frederic.ducros@cea.fr

²LEGI, Institut de Mécanique de Grenoble, BP 53 - 38041 Grenoble Cedex 9, France

Abstract Large Eddy Simulations of a passive scalar were done using wall-functions for both wall-friction and wall heat flux on the plane channel flow configuration with solid walls. Conjugate heat-transfer simulations have been carried out at low ($Re_\tau = 150$) and high ($Re_\tau = 395$) Reynolds numbers using a wall-function strategy. Attention was not only paid on the temperature fluctuations in the fluid and inside the solid wall, but also on the temperature signal spectrum inside the solid as well as in the first off wall point in the fluid. The main purpose of this work is intended to stress on the misleading effects (especially when focusing on temperature fluctuations) of wall-function type meshes in the fluid-solid thermal interaction frame-work.

Keywords: Large Eddy Simulation, Turbulence, Wall function, Conjugate Heat-transfer, Temperature, Thermal fatigue, Channel flow,

1. Introduction

Conjugate heat transfer simulations are a key issue for a lot of applications especially when focusing on the thermal fatigue acting on industrial devices (nuclear field, turbomachinery, heat-exchangers, electronic cooling...). Most industrial configurations are subject to high Reynolds numbers and the turbulent character of the flow must be taken into account. However, due to prohibitive computational costs, research engineers can not solve all the scales of turbulence, nor the viscous sub-layer near the wall. Therefore, a good way to solve as accurately as possible these problems is to make use of wall-functions (to model the near-wall region) in conjunction with Large Eddy Simulation (LES) techniques so that the unsteady character of the flow can be considered and temperature fluctuations estimated.

Little research has been carried out on conjugate heat transfer problems, also because experimental devices are difficult to obtain in order to measure temperature fluctuations inside the solid structure. Kasagi *et al.* [1], who developed a deterministic near-wall turbulence model, studied the interaction between a solid wall and a near-wall turbulent fluctuating temperature field, with comparisons at various Prandtl, thermal activity ratios K and wall thicknesses. Tiselj *et al.* [2] carried out DNS simulations of a plane channel flow considering the heat conduction in the solid wall at low Reynolds number ($Re_\tau = 150$).

The main problem of using wall-functions for conjugate heat-transfer problems is that the level of the fluctuations at the wall can not be taken into account properly since the first off-wall point may be situated much farther in the log region, thus not catching the peak's maximum of fluctuations for instance. Secondly, the frequency spectrum of the temperature fluctuations at the interface with the solid will not contain a proper frequency range. Thus some frequencies can be "lost" (or over-estimated) in the wall function region which is not in accordance with good thermal fatigue predictions where attention must not only be paid to the amplitude of the fluctuations, but also on the frequency spectrum.

The purpose of this work is to emphasize the fact that the use of standard wall function approaches can lead to biased predictions of thermal fatigue problems and that more sophisticated strategies may need to be found in order to treat accurately high Reynolds conjugate heat transfer problems.

2. Conjugate heat transfer physical parameters

Conjugate heat transfer problems are subject to two major parameters which influence the thermodynamical fluid-structure interface behavior. The thermal activity ratio defined as: $K = \sqrt{\frac{(\rho C_p \lambda)_f}{(\rho C_p \lambda)_s}}$ (f for fluid and s for solid) influences the fluid-structure interaction in such a way that when $K \rightarrow \infty$ the wall temperature fluctuations tend to an iso-flux boundary-condition behavior (maximum temperature fluctuations), whereas when $K \rightarrow 0$ the interface behaves like an isothermal wall with no temperature fluctuations. The solid wall thickness, denoted by d , induces a similar behavior: when $d \rightarrow 0$ the interface will reduce to an isoflux boundary condition; whereas minimum wall temperature fluctuations are obtained when $d \rightarrow \infty$. Usually, solid wall thickness in its dimensionless form reads as: $d^{++} = d^+ \sqrt{\frac{\alpha_f}{\alpha_s}}$, where α denotes the thermal diffusivity ($d^+ = du_\tau/\nu$ as usually defined from wall units).

3. Governing equations, numerics and physical modeling

The governing set of equations for our incompressible Navier-Stokes equations with scalar transport in their filtered LES form is the following:

$$\frac{\partial \tilde{u}_i}{\partial t} + \frac{\partial \tilde{u}_i \tilde{u}_j}{\partial x_j} = -\frac{1}{\rho} \frac{\partial \tilde{p}}{\partial x_i} + \frac{\partial}{\partial x_j} \left[(\nu + \nu_t) \left(\frac{\partial \tilde{u}_i}{\partial x_j} + \frac{\partial \tilde{u}_j}{\partial x_i} \right) \right] \quad (1)$$

and:

$$\frac{\partial \tilde{T}}{\partial t} + \frac{\partial \tilde{u}_i \tilde{T}}{\partial x_i} = \frac{\partial}{\partial x_i} \left[(\alpha_f + \alpha_t) \frac{\partial \tilde{T}}{\partial x_i} \right] + Q_f. \quad (2)$$

where the $\tilde{(\)}$ stands for a standard filtering operator. The adopted SGS stress model is the selective structure function details of which can be found in Métais and Lesieur [3]. A constant sub-grid scale Prandtl number equal to 0.9 is taken for the eddy diffusivity term in the temperature equation. The temperature equation inside the solid reads as :

$$\frac{\partial T}{\partial t} = \alpha_s \frac{\partial^2 T}{\partial x_i^2} + Q_s \quad (3)$$

where the thermal diffusivity of the solid α_s is supposed to be constant. Q_f and Q_s are two internal heat sources in the fluid and solid respectively which counter-balance each other by a simple heat balance so that temperature is uniformly produced in the fluid and retrieved in the solid (in order to obtain an homogeneous temperature field in the main flow direction).

Computations in this work were done on an orthogonal cartesian mesh, where variables are located on a staggered grid (velocity components on the faces, temperature and pressure in the center of gravity of the elements).

A third order Runge-Kutta time integration scheme was used. A second order centered convection scheme was used for momentum equation, whereas a third order QUICK scheme [4] with FRAM limiter was used for the temperature transport [5].

4. Wall function strategy

The local instantaneous wall heat flux introduced in the diffusive terms of the energy equation is calculated following: $\varphi_w(\vec{x}_w, t) = \lambda_f \frac{T_f - T_w}{d_{eq}(\vec{x}_w, t)}$ (\vec{x}_w denotes a point on the wall surface) where λ_f is the thermal conductivity of the fluid, T_w is the wall temperature and T_f is the first off-wall temperature point. $d_{eq}(\vec{x}_w, t)$ is a local instantaneous equivalent distance that characterizes the thickness of the turbulent boundary layer. One can introduce the non-dimensional temperature T^+ in wall units which is defined as:

$T^+ = \frac{T_f - T_w}{T_\tau}$, where $T_\tau = \frac{\varphi_w}{\rho C_p u_\tau}$ is the friction temperature and u_τ is the usual friction velocity. The equivalent distance is calculated analytically by:

$$d_{eq} = \frac{\alpha_f}{u_\tau} T^+ (y^+ = d^+, Pr) \quad (4)$$

where the evaluation of T^+ is given by a general profile with a fitting function given by Kader [6] based on experimental results at various Prandtl and Reynolds numbers:

$$T^+ = Pr y^+ e^{-\Gamma} + [2.12 \ln(1 + y^+) + \beta(Pr)] e^{-1/\Gamma} \quad (5)$$

where: $\Gamma = \frac{10^{-2}(Pr y^+)^4}{1 + 5 Pr^3 y^+}$. In the fluid-structure interaction case, wall heat flux at the interface is equal to: $\varphi_w = \frac{T_f - T_s}{\mathcal{R}_{eq}}$ where \mathcal{R}_{eq} denotes the equivalent thermal resistance between the two grid points (fluid and solid) on each part of the interface which is calculated as: $\mathcal{R}_{eq} = \frac{d_{eq}}{\lambda_f} + \frac{\Delta_s}{\lambda_s}$ (Figure 1).

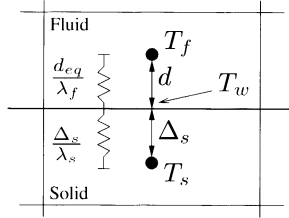


Figure 1 Fluid-Solid interaction and wall-function strategy.

5. Numerical results

The configuration of interest is the bi-periodic plane channel flow. The domain size for the channel is $(4\pi h, 2h, \pi h)$ (with $64 \times 55 \times 40$ mesh points) for the $Re_\tau = 150$ case and $(2\pi h, 2h, \pi h)$ for the $Re_\tau = 395$ case (with $50 \times 100 \times 60$ mesh points for the wall-resolved LES (*W.Res. LES*) and $(32)^3$ mesh points for the wall-modeled case, which is the mesh size introduced in all wall-function studies at high Reynolds numbers in plane channel flow and that gave good results in the estimation of mean and fluctuating velocity fields - see Cabot *et al.* [7] for a complete survey on the topic).

5.1 Reference cases

These simulations (*Case* T_0/Q) correspond to the case where wall temperature is set constant and equal to: $T_w = 0$ on both walls and an internal

heat source produces energy inside the fluid. Prandtl number is taken equal to $Pr = 0.025$ (eg. sodium) and 0.71 (eg. air).

Figure 2 shows mean temperature profiles and fluctuating profiles for both Prandtl number values for *Case* T_0/Q . Profiles are compared with DNS data of Kawamura *et al.* who performed similar DNS simulations [8]. Mean temperature profiles show good agreement with the available DNS data: in particular, the first point is placed correctly for both logarithmic and buffer regions.

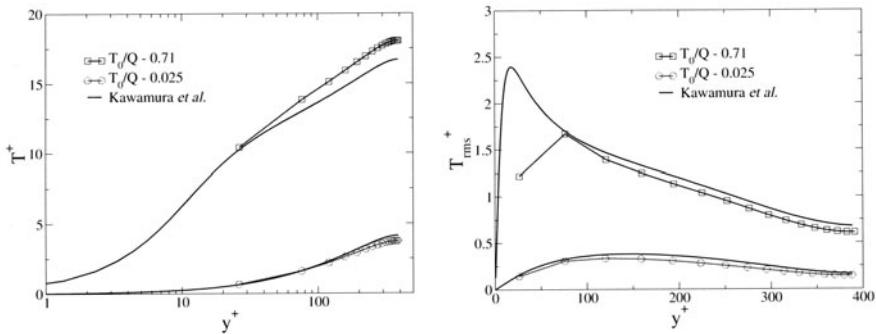


Figure 2. *Case* T_0/Q temperature profiles: Mean (left) and Fluctuations (right).

If we look at the temperature fluctuations (Figure 2, right), we see good agreement between wall-function calculations and DNS data over the resolved regions. However, the fluctuation of the first point does not match the required peak prediction at $y^+ \simeq 18$ for the case with $Pr = 0.71$, *Case* $T_0/Q = 0.71$ and under predicts the first point fluctuation by 50%. This bad behavior is explained by the fact that a zero fluctuation condition is imposed at the wall thus having an important impact on the fluctuation level of the first point in a numerical point of view.

The identified drawback on the first point of the fluctuations profile can eventually have no consequences on the results, as long as precise temperature fluctuations within the solid are not of interest.

5.2 Consequences for conjugate heat transfer cases

The conjugate heat transfer case considers the same fluid domain size as in the ideal case computations coupled with two solid walls of thickness d . All outer wall boundaries are assumed adiabatic except at the fluid-solid wall interface. First, a parametric study is carried out at low Reynolds number ($Re_\tau = 150$) for which the thermal activity ratio ($K = 0.1, 1$ and 5) varies at constant solid wall thickness ($d^{++} = 50$). Afterwards, a new series of simulations were done at constant $K = 1$ and varying wall thickness: $d^{++} = 10, 20$ and 50 . For sake of simplicity, all simulations were done with a ratio: $\alpha_f/\alpha_s = 1$ in order to

have: $y^+ = y^{++}$.

Prandtl number is equal to 0.71 (air) for all conjugate heat transfer simulations. Results show good qualitative and physical behaviors. Temperature fluctuation profiles inside the solid and fluid are given in Figure 3 for varying thermal activity ratios K , together with their corresponding ideal isothermal and isoflux cases. We observe that fluctuation profiles differ only depending on K for wall distances smaller than $y^+ \simeq 20$. Therefore, one already sees that if a good prediction must be done on the wall temperature fluctuation, mesh refinement should be in accordance with grid spacings lower than $\Delta y^+ \simeq 5 - 10$ at the wall.

Fluctuations are seen to have already very small levels inside the solid for values of $K \simeq 0.1$, which is actually the case for most industrial applications (eg. water/copper: $K = 0.0436$, water/steel: $K = 0.21$).

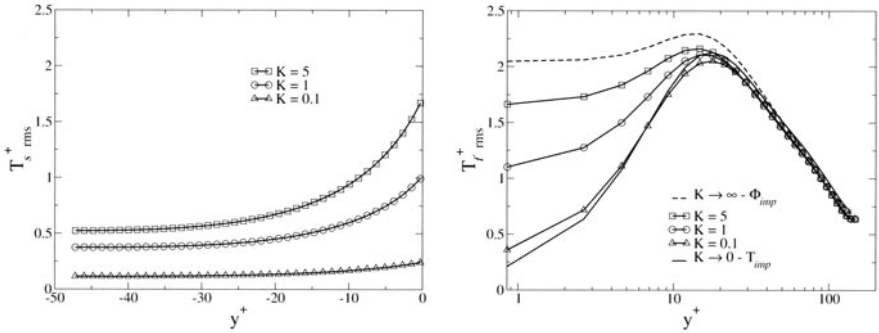


Figure 3. Conjugate heat transfer Case CHT 150 temperature fluctuations profiles: Solid (left) and Fluid (right).

On the contrary, it is noticed (Figure 4(a)) that for small values of the wall thickness ($d^{++} < 10$), the maximum limiting behavior of the isoflux condition is almost achieved for the wall fluctuations. Therefore, the higher the Reynolds number (as it is the case in industrial configurations), the higher the wall temperature fluctuations.

In the simple case of a one-dimensional semi-infinite wall with adiabatic condition at one end subject to an harmonic periodic signal at $y = 0$ on the wall, the thermal analysis gives the inner wall signal evolution S , for a given wall temperature signal amplitude S_0 , a frequency f , at a wall distance y and for a solid diffusivity α_s : $S \propto S_0 \cdot \exp\left(-y\sqrt{\pi\alpha_s f}\right)$ [9]. Purpose of Figure 4(b) is to show that a similar quasi one-dimensional behavior can be obtained for the signal amplitude of each Fourier mode in the turbulent framework. Indeed, it is seen on Figure 4(b) that very good accordance is achieved for the decreasing behavior of the temperature energy spectrum between the full initial LES turbulent spectrum and the one-dimensional analysis. (The presented signal

spectrums were obtained by Fast Fourier Transform (FFT) of the temperature signal inside the solid wall).

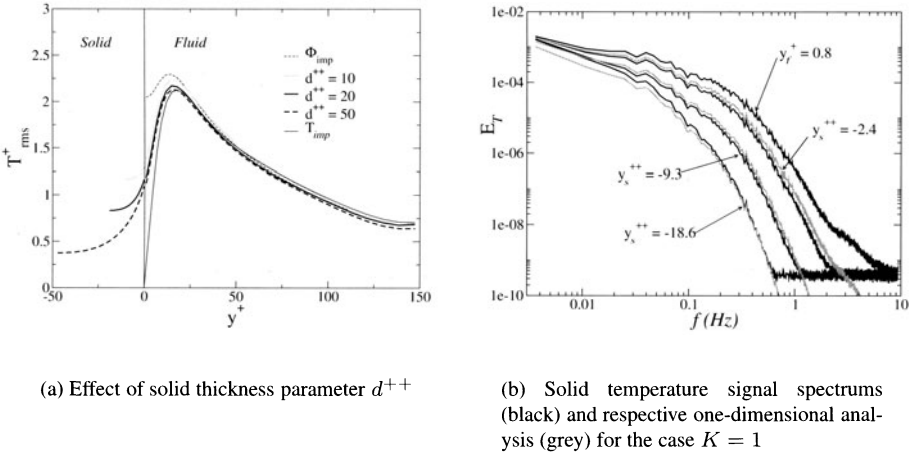


Figure 4. Conjugate heat transfer *Case CHT 150*.

Conjugate heat transfer simulations at high Reynolds number are then carried out at $Re_\tau = 395$ with $K = 1$ and $d^{++} = 50$ for both wall resolved (*Case CHT - Res. LES*) and wall function case strategy (*Case CHT - WF*). As expected, the temperature fluctuations level in the solid is underestimated (Figure 5 on the left): indeed, even if the total shape is recovered thanks to the same solid properties, the fact that fluctuations are about twice smaller than in the similar wall resolved case leads to an overall underestimation of about 40 to 50 % in that case. This behavior clearly comes from the bad prediction of the temperature fluctuation of the first fluid mesh point, and from the fact that the near-wall peak and turbulent character of the flow is completely modeled by the wall-function.

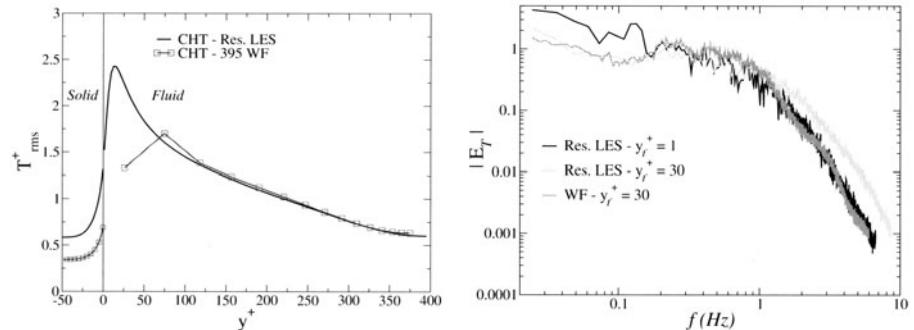


Figure 5. Conjugate heat transfer *Case CHT 395*: temperature fluctuations profiles in the solid and fluid (left) and (normalised) temperature spectrums in the fluid (right).

On Figure 5 (right side), we note that the temperature frequency spectrum at the first near wall cell of *Case CHT - WF* clearly shows the same spectrum behavior as the corresponding point in the resolved LES *Case CHT - Res. LES* at $y^+ = 30$, with a difference in the high frequency range, where the energy corresponds to the one obtained at the first point of *Case CHT - Res. LES* at a distance $y^+ = 1$ to the wall. This behavior can be explained by the fact that even situated in the logarithmic region, the temperature field of the first point in the wall-function simulation gets the feed-back of the solid damping effect, which leads to a decrease of the energy contained in the high frequency temperature fluctuations.

6. Conclusions

LES of conjugate heat-transfer of a plane channel flow with solid walls have been carried out at high Reynolds number using a wall function for the wall heat-flux. It was found that coarse mesh simulations using wall-functions can lead to a damping effect on the level that the temperature fluctuations can reach, in the present case, at least 50% underestimation inside the solid wall.

It is then clear that attention must be paid on the necessity to try to either solve accurately the near-wall fluctuation characteristics of the temperature (even in the industrial context), or to find a new strategy in order to rebuild the temperature fluctuations phenomenon based on a LES approach in accordance with good thermal fatigue predictions.

References

- [1] Kasagi N., Kuroda A., Hirata M. Numerical investigation of near-wall turbulent heat transfer taking into account the unsteady heat conduction in the solid wall. *Int. J. Heat Mass Transf.* 1989; 111:385–392
- [2] Tiselj I., Bergant R., Mavko B., Bajsic I., Hetsroni G. DNS of turbulent heat transfer in channel flow with heat conduction in the solid wall. *J. of Heat Transf.* 2001; 123:849–857
- [3] Métais O., Lesieur M. Spectral large-eddy simulations of isotropic and stably-stratified turbulence. *J. Fluid Mech.* 1992; 239:157–194
- [4] Leonard BP. Simple high-accuracy resolution program for convective modeling of discontinuities. *Int. J. for Num. Meth. in Fluids.* 1988; 8:1291–1318
- [5] Chatelain A, Ducros F, Métais O. LES of turbulent heat transfer: proper convection numerical schemes for temperature transport. *Submitted to the Int. J. for Num. Meth. in Fluids.*
- [6] Kader B. A. Temperature and concentration profiles in fully turbulent boundary-layers. *Int. J. Heat Mass Transf.* 1981; 24(9):1541–1544
- [7] Cabot W. and Moin P., Approximate wall boundary conditions in the LES of high Reynolds number flow. *Flow Turb. Comb.* 1999; 63
- [8] Kawamura H., Abe H., Matsuo Y. DNS of turbulent heat transfer in channel flow with respect to Reynolds and Prandtl number effects. *Int. J. Heat Fluid Flow.* 1999; 20:196–207
- [9] Sacadura, J-F. (1978). *Initiation aux Transferts Thermiques*. Technique et Documentation.

MODELING OF A PASSIVE SCALAR IN A TURBULENT PIPE FLOW USING A DIRECT NUMERICAL SIMULATION

J. de Hoogh, M.P.B. Veenman and J.G.M. Kuerten

Department of Mechanical Engineering

Technische Universiteit Eindhoven, The Netherlands

j.d.hoogh@tue.nl

Abstract One of the consequences of diffusion theory is that fluctuations in a turbulent flow can be expressed in terms of the mean component, for example the scalar gradient hypothesis. It is known that the diffusion theory is not correct for high Reynolds numbers. In this paper a numerical method is developed for the computation of particle concentration in a turbulent pipe flow. In this way the validity of diffusion theory can be accessed.

Keywords: Diffusion theory, DNS, Scalar Gradient hypothesis

1. Introduction

Diffusion theory is based on the assumption that the movement of particles in a turbulent flow can be described by a stochastic differential equation for particle positions. Within this theory, a Fokker - Planck probability equation can be derived which corresponds to a convection-diffusion equation for particle concentration. Moreover, the scalar gradient hypothesis can be derived. For the diffusion theory to be valid, two assumptions should be satisfied [5]. Firstly the Markov approximation for particle velocity should be valid and secondly, the random displacement of a fluid particle, measured over a time period which corresponds to the correlation time of the fluid, is required to be small compared to the external length scale of the flow. Recently, Brouwers [5] showed that for all relevant turbulent flows this latter assumption is not satisfied. To investigate this further the development of a passive scalar, that describes the Eulerian particle concentration, is calculated using a Direct Numerical Simulation. This makes it possible to assess the validity of the scalar gradient hypothesis.

2. Numerical Method

To be able to check the validity of the scalar gradient hypothesis a DNS is used to calculate the turbulent velocity field in a cylindrical pipe. The numerical method used [14] is based on a Fourier - Galerkin expansion in axial and tangential direction. In radial direction a Chebyshev polynomial expansion is used and time integration is performed by a second-order accurate time-splitting method that is a combination of the Crank-Nicolson and Adams-Bashforth methods. A Poisson equation for the pressure is solved to comply with the demand for a divergence-free velocity field. To this code a conservation equation for a passive scalar, with a molecular diffusion term, is added,

$$\frac{\partial c}{\partial t} + \mathbf{u} \cdot \nabla c = \frac{2}{ReSc} \Delta c, \quad (1)$$

with c the concentration and Re and Sc the Reynolds and Schmidt number resp. The Reynolds number is given by $Re = \frac{u^* D}{\nu}$, where D is the diameter of the pipe and u^* the friction velocity and ν the kinematic viscosity. In all results shown $Re = 370$. The Schmidt number equals $Sc = \frac{\nu}{D} = 1$ and represents the ratio between the kinematic viscosity and the diffusion coefficient (D). When the same spectral method is used for the scalar concentration as for the velocity field, good results are obtained for cases where the concentration is sufficiently smooth. However, the spectral method has two disadvantages. First, it can only be used if the concentration is periodic in axial direction, which makes a particle source impossible. Second, local grid refinement, which becomes important when the concentration field can exhibit local small-scale structure due to higher Schmidt numbers, is impossible. Therefore, a finite volume method is implemented that allows different grids for the velocity and concentration to be used together. To be able to solve the concentration on a different grid, the velocity is interpolated using a fourth-order accurate scheme [10]. Using Gauss's theorem equation (1) is rewritten into

$$\iiint_V \frac{\partial c}{\partial t} dV + \iint_A \mathbf{u} \cdot \mathbf{n} c dA = \frac{2}{ScRe} \iint_A \frac{\partial c}{\partial n} dA \quad (2)$$

with V an arbitrary volume with boundary A and \mathbf{n} the outward unit normal. The concentration can now be calculated using fluxes through the boundaries of the control volume. Using standard, second-order accurate methods the concentration gradient, needed for the diffusion part of equation (2), can be calculated. For the convective part the concentration at the boundaries of each control volume has to be calculated. To this purpose a general approach is introduced [9], where the flux on a boundary, $f_{j+\frac{1}{2}}$, between grid points j and $j+1$ is decomposed in a convective and a dissipative part:

$$f_{j+\frac{1}{2}} = C_{j+\frac{1}{2}} - D_{j+\frac{1}{2}}. \quad (3)$$

Here $C_{j+\frac{1}{2}}$ is the convective part, calculated as

$$C_{j+\frac{1}{2}} = \frac{1}{2} \{u_{j+1}c_{jr} + u_jc_{jl}\}, \quad (4)$$

with c_{jr} and c_{jl} denoting approximations for the concentration in points to the left and right of $j + \frac{1}{2}$. The second term, $D_{j+\frac{1}{2}}$, is a diffusive part and is different for every method used. In this research two methods are used, Roe's first order upwind method and the MUSCL method [12]. Roe's method is defined by,

$$D_{j+\frac{1}{2}} = \frac{1}{4} \{|u_{j+1} + u_j|(c_j - c_{j+1})\} \quad (5)$$

with $c_{jr} = c_{j+1}$ and $c_{jl} = c_j$ and is a first-order accurate upwind method. A more accurate method is found in the MUSCL approach [11], that makes use of limiter functions which add additional numerical diffusion at those points where the gradient exceeds predefined limits. In standard notation the method is written as

$$\begin{aligned} D_{j+\frac{1}{2}} &= \frac{1}{4} \{|u_{j+1} + u_j|(c_{jl} - c_{jr})\} \\ c_{jl} &= c_j + \frac{1}{4} \left((1 - \xi) \widetilde{\Delta_{j+\frac{1}{2}} c} + (1 + \xi) \widetilde{\Delta_{j-\frac{1}{2}} c} \right) \\ c_{jr} &= c_{j+1} - \frac{1}{4} \left((1 - \xi) \widetilde{\Delta_{j+\frac{3}{2}} c} + (1 + \xi) \widetilde{\Delta_{j+\frac{1}{2}} c} \right) \\ \widetilde{\Delta_{j+\frac{1}{2}} c} &= \text{minmod}(\Delta_{j+\frac{1}{2}} c, \omega \Delta_{j-\frac{1}{2}} c) \\ \widetilde{\Delta_{j+\frac{1}{2}} c} &= \text{minmod}(\Delta_{j+\frac{1}{2}} c, \omega \Delta_{j+\frac{3}{2}} c) \\ \Delta_{j+\frac{1}{2}} c &= c_{j+1} - c_j \\ \text{minmod}(a, b) &= \frac{1}{2} \left(\text{sign}(a) + \text{sign}(b) \right) \min(|a|, |b|) \end{aligned}$$

with parameters ξ and ω that can be chosen within the constraints $-1 < \xi < 1$ and $1 \leq \omega \leq \frac{3-\xi}{1-\xi}$. The MUSCL method is, within these boundaries, second order accurate and if $\xi = \frac{1}{3}$ the method has even a third order accuracy [9]. Here the values for ξ and ω are set to $\frac{1}{3}$ and $\frac{3}{2}$ resp. In order to conserve particles, as a boundary condition at the wall the Neumann condition, $\frac{\partial c}{\partial n} = 0$, is applied. At the center of the pipe a unique and continuously differentiable solution is created by combining all control volumes in tangential direction, as is shown in figure 1. In axial and tangential direction a periodic boundary condition is applied. The boundary condition in axial direction is problem dependent and can be altered to fit the problem at hand. For time integration the same method is used as for the velocity.

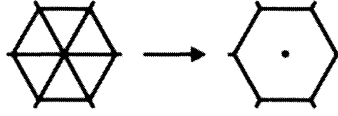


Figure 1. Schematic overview of the element treatment in tangential direction at the center of the pipe.

3. Results

3.1 Comparison of numerical methods

In order to compare the different numerical methods an initial concentration

$$c^0(r, \varphi, z) = \frac{1}{\sigma_r \sqrt{2\pi}} e^{\left(-\frac{1}{2} \frac{r^2}{\sigma_r^2} - \frac{1}{2} \frac{(z-2)^2}{\sigma_z^2}\right)} \quad (6)$$

with periodic boundaries in axial and tangential direction is used, with $\sigma_r = 0.05$ and $\sigma_z = 0.5$. Results are generated with an identical initial velocity field that is a fully developed turbulent pipe flow using 109 points on a non-uniform grid in radial direction and 128 Fourier modes in the periodic directions. The length L of the pipe equals 10 times the radius R . An identical grid was used for the spectral implementation of the concentration. Both finite volume methods use $100 \times 96 \times 192$ points uniformly distributed in radial, tangential and axial direction respectively. Because the Schmidt number is equal to one, the resolution of the concentration and the velocity grid can be similar. The difference in radial direction is explained by the difference in the point distribution. For the velocity grid a non-uniform grid is used with grid refinement near the element boundaries that is not needed in the concentration grid. The concentration is mainly distributed around the center of the pipe and that allows for half the points to be used in tangential direction, identical to the velocity field where at the innermost element mode reduction is applied. To compare the results the mean radius is culculated as a function of time

$$\bar{r} = \frac{1}{2} \frac{\int_0^R \int_0^{2\pi} cr^2 d\varphi dr}{\int_0^R \int_0^{2\pi} \int_0^L cr dz d\varphi dr}. \quad (7)$$

This mean radius is also easily computed for the Lagrangian particles. Figure 2 shows that the spectral and Lagrangian methods have less diffusion than the MUSCL method and Roe's first order upwind method. The higher diffusivity of both finite volume methods is due to the added numerical diffusion. However, the difference between the spectral and finite volume method is small.

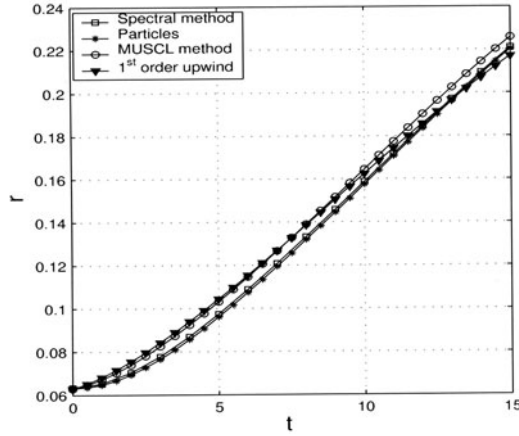


Figure 2. Comparison of the mean radius of the blob as a function of time for four different methods

3.2 Point source

A further test is conducted with a point source at $z = 0$ defined by,

$$c^0(r, \varphi, 0) = \frac{1}{\sigma_0 \sqrt{2\pi}} e^{(-\frac{1}{2} \frac{r^2}{\sigma_0^2})} \quad (8)$$

with a standard deviation of $\sigma_0 = 8.5 \cdot 10^{-3} D$ for $t \geq t_0$. The solution is non-periodic in axial direction so that a spectral method cannot be applied. Because of the higher accuracy the MUSCL method is preferred over Roe's method. At $z = L$ the boundary condition has to be altered and is changed into a discrete form of $\frac{\partial^2 c}{\partial z^2} = 0$. The development of the point source can be visualized using the mean concentration at the centerline and the normalized standard deviation (corrected for a finite source)

$$\sigma' = \frac{\sqrt{(\sigma^2 - \sigma_0^2)}}{D} \quad ; \quad \sigma(z)^2 = \frac{1}{2} \frac{\int_0^\infty r^3 \bar{c}(r, z) dr}{\int_0^\infty r \bar{c}(r, z) dr} \quad (9)$$

as a function of the axial coordinate. \bar{c} denotes the concentration, averaged over time and tangential direction. Over 200 independent concentration fields are computed, starting from the point when the concentration has first reached the end of the pipe and is assumed to be fully developed. In figure 3 the present results are compared with experimental results [1],[2]. They are almost undistinguishable from numerical results by Brethouwer [4].

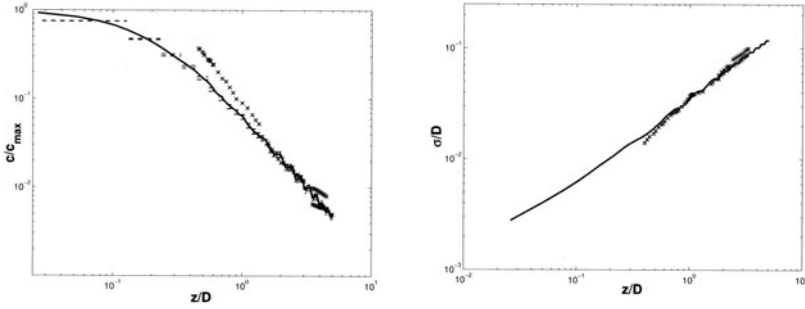


Figure 3. (left) The mean concentration at the center of the pipe against the axial position. (right) The dimensionless standard deviation in radial direction plotted as a function of the axial position. Experimental data is indicated by (\times)

3.3 Scalar gradient hypothesis

To check the validity of the scalar gradient hypothesis, it is written in simplified form as

$$\overline{u'_r c} = - \frac{C_{\mu t} k(r)^2}{\epsilon(r) Pr_t} \frac{\partial \bar{c}}{\partial r} \quad (10)$$

with u'_r the velocity fluctuation in radial direction, k the turbulent kinetic energy and ϵ the dissipation, which are known from previous DNS calculations [14]. $C_{\mu t}$ is a constant equal to 0.09 and Pr_t is the turbulent Prandtl number and is set to 1. The scalar gradient hypothesis can be checked by plotting both the right hand side and the left hand side of equation (10) for different values of the axial coordinate using numerical data. In figure 4 it can be seen that at both axial positions there is a substantial difference between the right hand side and the left hand side of equation (10). This is in agreement with results found in [6] on the eddy viscosity. Moreover, it can be seen that a different value for Pr_t does not give overall agreement. A position dependent Prandtl number might be a solution but that is not desirable. The differences between both sides of equation (10) are of $O(1)$, in agreement with the findings of [5].

4. Discussion and conclusion

The results obtained from the current research point out that it is possible to calculate the development of concentration in a turbulent flow using different

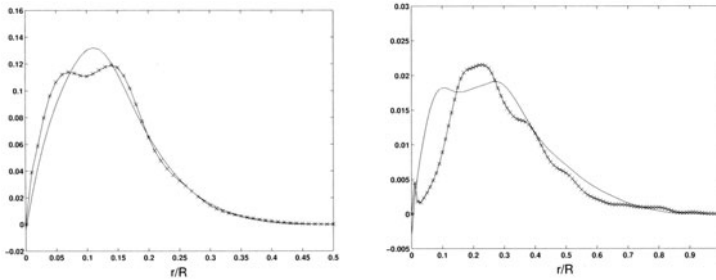


Figure 4. The left-hand (solid) side and right-hand (\times) side of equation (10) are plotted as a function of the axial coordinate at ($z = 2D$ (left) and $4.5D$ (right)).

numerical approaches. It is clear that each method has its own (dis)advantage and that the most suitable method depends on the problem. The numerical results confirm the theory that the scalar gradient hypothesis is only valid in order of magnitude [5].

In all simulations shown, the Schmidt number used is equal to unity. However, in reality Schmidt numbers of the order 10^4 are common, which for turbulent flows leads to concentration length scales much smaller than the smallest velocity length scales. On the grid used presently such small-scale phenomena cannot be captured. Future research will focus on increasing the Schmidt number and finding better numerical schemes to decrease the effect of numerical diffusion. One approach is to replace the MUSCL method with a third order accurate standard upwind scheme that already gives promising results. A presumably better method can be found in local refinement of the computational grid. For many problems the concentration is equal to zero in large parts of the domain and these parts can be computed on a coarse grid. The areas that do contain concentration can be computed with a much finer grid, that is able to capture the small-scale phenomena introduced by the higher Schmidt number. Using the results computed on the refined area, the coarse grid approximation can be updated using local defect correction techniques [3]. The goal is to create a method that can perform simulations with Schmidt numbers of order 10^4 with a minimum of computational costs. The results of these simulations can be used to develop a better subgrid model for a passive scalar in a turbulent flow.

Acknowledgement

The project is funded by the Netherlands Organization for Scientific Research (NWO) under Computational Science research grant 635.000.002.

References

- [1] Aanen, L., Teleska, A., Westerweel, J., Measurement of turbulent mixing using PIV and LIF, *Machine Vision and Graphics*, **8** (1999) 529-543.
- [2] Aanen, L., *Measurement of turbulent scalar mixing by means of a combination of PIV and LIF*, Ph.D. Thesis, Delft University of Technology, 2002.
- [3] Anthonissen, M.J.H., *Local defect correction techniques: analysis and application to combustion*, Ph.D. Thesis, Eindhoven University of Technology, 2001.
- [4] Brethouwer G., *Mixing of passive and reactive scalars in turbulent flows: A numerical study*, Ph.D. Thesis, Delft University of Technology, 2000.
- [5] Brouwers J.J.H., On diffusion theory in inhomogeneous turbulence, *J. Eng. Math.* **44** (2002) 277-295.
- [6] De Bruin I., *Direct and Large-Eddy Simulation of the Spatial Turbulent Mixing Layer*, Ph.D. Thesis, Twente University of Technology, 2001.
- [7] Eggels J.G.M., *Direct and Large Eddy Simulation of Turbulent Flow in a Cylindrical Pipe Geometry*, Ph.D. Thesis, Delft University of Technology, Department of Aero- and Hydrodynamics, 1994.
- [8] Van Kampen N.G., *Stochastic processes in Physics and Chemistry, revised and enlarged edition*. Elsevier, Amsterdam, 1992.
- [9] Kuerten J.G.M., *Computational Fluid Dynamics III*, Lecture notes, University of Twente, 1999.
- [10] Kuerten J.G.M., M.P.B. Veenman and J.J.H. Brouwers, Numerical simulation of the motion of particles in turbulent flow, in: Geurts B.J., Friedrich R., Metais O. (eds.), "Direct and Large-eddy Simulation IV", Enschede, (2001) 11-20.
- [11] Van Leer B., Towards the ultimate conservative difference scheme II. Monotonicity and onservation combined in a second-order scheme, *J.Comput. Phys.* **14** (1974) 361-370.
- [12] LeVeque R.J., *Numerical Methods for Conservation Laws*, Birkäuser Verlag, 1992.
- [13] Stratonovich R.L., *Topics in the Theory of Random Noise*, Gordon and Breach, New York, 1967.
- [14] Veenman M.P.B., J.G.M. Kuerten and J.J.H. Brouwers Particle dispersion in inhomogeneous turbulent flow, in: Liu C., Sakell L., Beutner T. (eds.), "DNS/LES progress and Challenges", Arlington, Texas, (2001) 549-556.

LES AND EXTREME VALUE THEORY

Modelling the Upper Tail of the PDF of Concentration in Turbulent Dispersion

Zhengtong Xie, Peter R. Voke, Paul Hayden and Alan G. Robins

Fluids Research Centre, University of Surrey, Guildford GU2 7XH, U.K.

z.xie@surrey.ac.uk, p.voke@surrey.ac.uk

Abstract Using large-eddy simulation (LES), we calculate the concentration fluctuations of passive plumes from an elevated (ES) and a ground-level source (GLS) in a turbulent boundary layer over a rough wall. The mean concentration, relative fluctuations and spectra are found in good agreement with the wind-tunnel measurements. The Generalised Pareto Distribution (GPD) is applied to model the upper tail of the probability density function of concentration time series, collected at many typical locations for GLS and ES from both LES and experiments. The relative maxima and return levels against downstream distance, which are estimated from numerical data, are in good agreement with those from experimental data.

Keywords: large-eddy simulation, atmospheric dispersion, rough wall, extreme value theory, generalized Pareto distribution, relative maxima.

1. Introduction

High concentrations of pollutants in the atmosphere, although usually of very low frequency, can be extremely dangerous to human health or can exceed flammability or explosion limits. Modelling their occurrence is a challenge. LES can provide instantaneous three dimensional flow and concentration data in the study of dispersion from a point source release. Unfortunately, we can normally only simulate ABL flows over a couple of hours (or wind tunnel flows over less than a minute) by LES, owing to current computer capabilities and the resulting high expense of simulation. Such a time duration cannot provide sufficient information to fix the upper tail of the probability density function (PDF), any more than normal experiments due to the high expense. Lack of detailed information of the upper tail of PDF can make the standard estimation of extreme events severely biased.

Extreme value theory (EVT) is the branch of statistics concerned with modelling the tails of probability distributions and hence performing probability extrapolations. Classically, EVT referred Fisher & Tippett, 1928 to the Three-Types Theorem for Maxima, with types I, II and III widely known as the Gumbel, Fréchet and Weibull types respectively. The work was extended by von Mises Mises, 1954 and Jenkinson Jenkinson, 1955, who independently derived the generalized extreme value distribution (GEV) of these three seemingly disparate families. A typical application of this model is to fit the distribution to a series of maximum data (for instance, annual maximum rainfall). However, the technique of characterizing a GEV distribution just by using maximum data during some fixed period is obviously of very low efficiency. Several techniques, such as point process characterization, threshold methods, the Generalized Pareto Distribution (GPD) Picands, 1975, the r -largest order statistics method and so on, which manage to take more extreme data to be processed, have been proposed to obtain higher data-using efficiency.

At present, EVT is used in a wide variety of scientific disciplines, but the most common application area may be in environmental design. It has also been applied to the study of atmospheric dispersion with some success Smith, 1989; Munro et al., 2001. However, there are many open problems worthy of further study. In the current paper, we couple LES and EVT to overcome the manifest limitations of existing approaches and to provide a capability that neither can provide alone. Wind tunnel measurements are also used for validation.

2. LES for turbulent flow over a rough surface

We consider incompressible air flow over a rough surface at very high Reynolds number. In the horizontal directions the flow is periodic. At the top of the domain, stress free conditions are imposed. At the bottom boundary a wall model relates the surface stress to the tangential velocity components at the first inner grid point. A new wall model is proposed which exhibits more satisfactory performance than previous models for the LES of the turbulent boundary layer over a rough surface Xie et al.. To quantify the subgrid viscosity, we use the mixed-scale model of Sagaut Sagaut, 1995. The momentum equations are discretized in space using a second-order central differencing finite-volume method. We use a staggered grid which is uniform in both horizontal directions and slightly stretched in the vertical direction. All quantities (including the passive scalar) are advanced in time through time splitting with two steps, giving a second-order explicit scheme.

The numerical results are judged by comparison with the wind tunnel measurements. We choose the boundary layer depth D and friction velocity u_* as reference length and reference velocity. The computational domain size is $4D \times 1.47D \times D$. The roughness element height z_h is $0.0125D$ and the

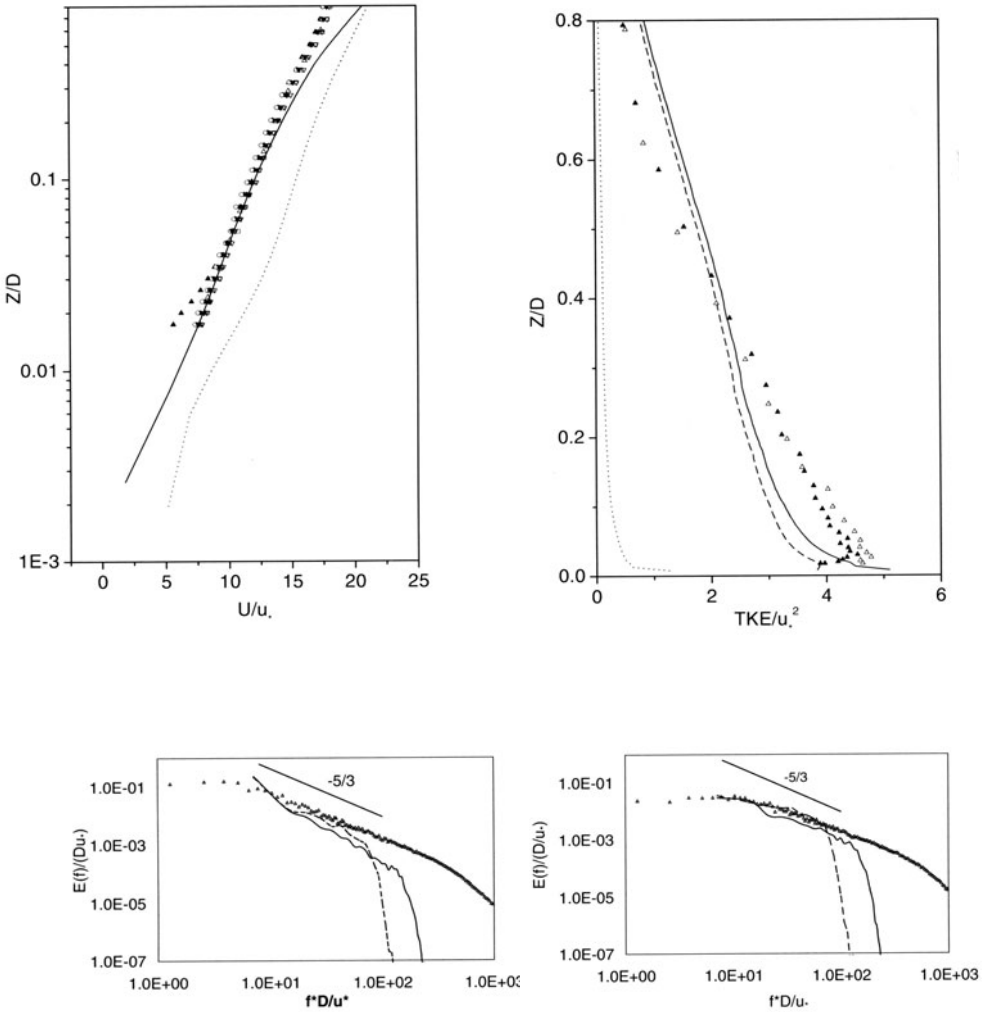


Figure 1. **Top left:** Streamwise mean velocity. Lines, LES: solid, with new wall model; dashed, with Schumann's wall model; symbols, measurements. **Top right:** Turbulent kinetic energy. Lines, LES: dashed, resolved; dotted, sub-grid; solid, total; symbols, measurements. **Bottom:** Spectra. Lines, LES; solid, fine mesh; dashed, medium mesh; symbols, measurements; bottom left, of streamwise velocity; bottom right, of vertical velocity.

roughness length z_0 is $0.00114D$. We discretise the computational domain on a fine mesh of $256 \times 128 \times 128$, which is the default mesh; a medium mesh of $128 \times 64 \times 64$ was also used for comparison. Some results are shown in Fig. 1.

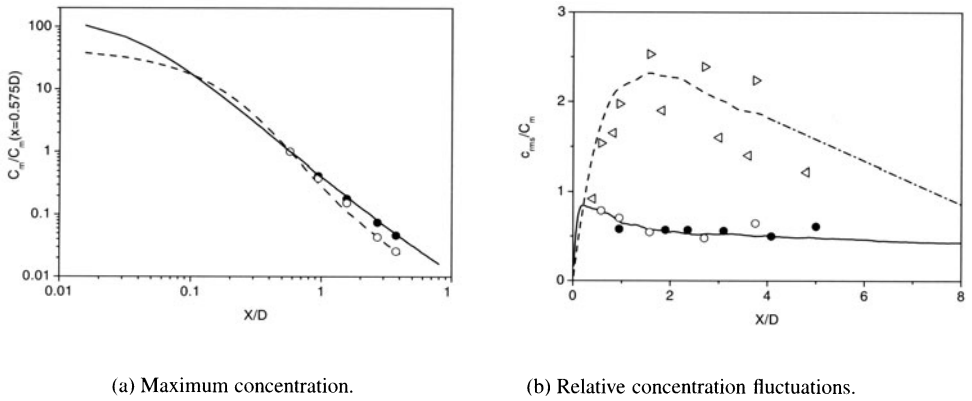


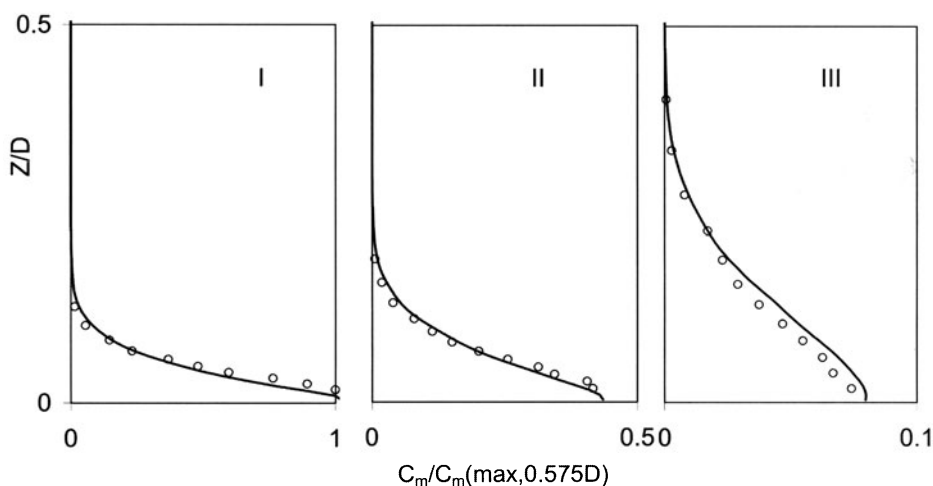
Figure 2. (a): —, LES, ES; \circ , measurements, ES; —, LES, GLS; \bullet measurements, GLS. (b): \triangleright , our measurements; \triangleleft , Thomson's stochastic model, —, LES, ES; —, extrapolated from LES, ES; —, LES, GLS; \circ , measurements, GLS; \bullet , Fackrell and Robins' measurements, GLS.

3. LES for dispersion of point source release

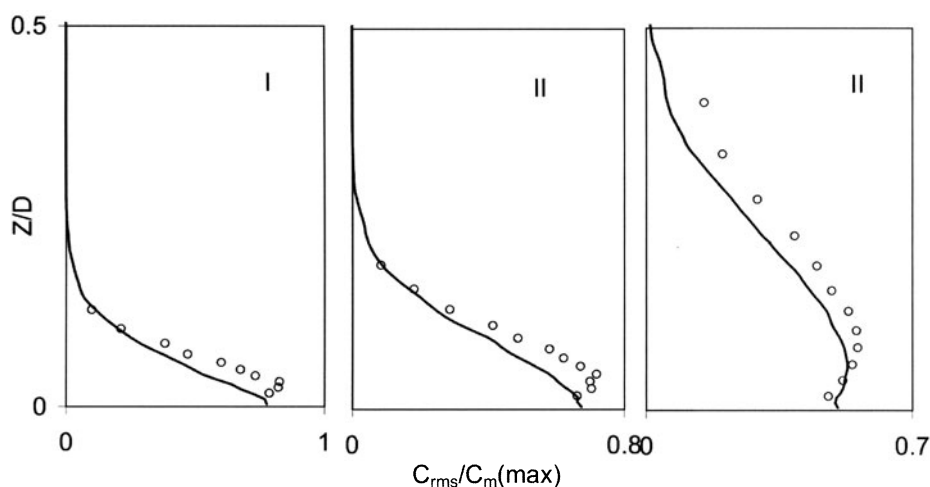
Up to now most studies realised in heat transfer or concentration dispersion problems Sykes & Henn, 1992 apply a subgrid eddy viscosity combined with a subgrid eddy Prandtl number or Schmidt number, which are set as constant or calculated dynamically. In the present study, we adopt the above concept using a constant Schmidt number with a value of 1.2, $K_s = \nu_s/Sc$, where ν_s is subgrid viscosity Xie et al., Sc is the Schmidt number.

The scalar transfer equation is discretized in space using the second-order finite-volume method. The diffusion term is discretized by central differencing. However, more attention needs to be paid to the convection term. Firstly, we must avoid negative concentration which can be generated by so-called overshoot from central differencing. Secondly, we must avoid numerical diffusion, as the gradient of concentration may be very high at the edge of plume cloud. We use the Bounded Quadratic Upwind Scheme (SMART) scheme to discretize the convection term, as it is a well verified scheme with low numerical diffusion and second-order accuracy, it successfully avoids generating negative concentration, and it does not cost much in terms of additional computation.

We study the turbulent dispersion of a steady source release in a neutral atmospheric boundary layer. The statistical data obtained using LES have been carefully compared with measurements. The elevated source (ES) is located at approximately $0.44D$ (depth of the boundary layer) while the ground-level source (GLS) is located close to the rough lower surface. Fig.2 (a) shows the maximum concentration at various streamwise positions, normalized by the maximum concentration at $x/D = 0.575$. The trend of the maximum con-



(a) Mean concentration, plume centre.

(b) $c_{rms}/C_m(max)$.Figure 3. I, $x=0.575D$; II, $x=0.95D$; III, $x=2.7D$. —, LES; \circ , measurements.

centration with downstream position for ES and GLS are slightly different. Fig.2 (b) shows the relative concentration fluctuations, where C_m is the maximum mean concentration and c_{rms} is the maximum r.m.s on the vertical central line ($y = 0$) at each x station. For the ES, both measurements and the LES predict larger relative intensities than Thomson's model, which was proposed

to suit homogeneous turbulence. Turning to the comparison between measurements and LES, the difference may be accounted for in several ways, such as the slight difference of resolution and source size. For the GLS, the results are in good agreement with the current measurements and the experimental data of Fackrell and Robins (1982). Since the mean maximum concentration decreases approximately with a power law, Fig.2 (a), the contribution of the background noise to c_{rms} in the experiments cannot be small; this is likely to be the main factor resulting in an overestimation of the relative concentration fluctuation at the point farthest downstream. Vertical profiles of mean concentration and $c_{rms}/C_m(max)$ are plotted in Fig.3 for GLS.

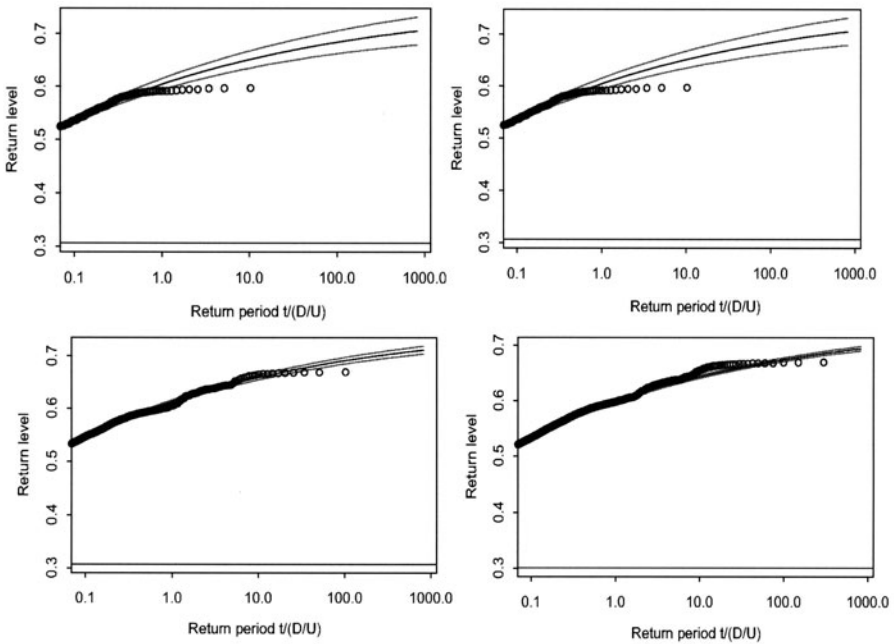


Figure 4. Return level extrapolation. LES, very coarse mesh; from left to right, then top to bottom, 10K, 100K, 1M, 3M time steps respectively. Circles, LES data; Lines, EVT predicted with 95% confidence intervals.

4. EVT prediction

The Generalized Pareto Distribution is applied to model extreme events in the time series: $G_{\xi\sigma}(\Gamma) = 1 - (1 + \frac{\xi}{\sigma}\Gamma)^{-1/\xi}$, where Γ , ξ and σ are argument, shape and scale parameters respectively, and $\sigma > 0$, $\Gamma > 0$, $1 + \xi\Gamma/\sigma > 0$. ξ, σ need to be fitted by likelihood method Davison & Smith, 1990. Taking $\xi < 0$ restricts Γ to a finite upper limit Munro et al., 2001. In environmental studies the quantity of most interest is the return level, which is defined as the

value which we expect to be exceeded on average once in a given period. For a threshold u , let τ denote the time period; the return level is then given by $r = u - [1 - (\nu\tau)^\xi]\sigma/\xi$, where ν is the crossing rate of the threshold. Theoretically the return level r is independent of the threshold u . Provided $\xi < 0$, the local maximum is easily deduced from the above equation: $\Gamma_0 = u - \sigma/\xi$. A simple numerical experiment was conducted just to verify the EVT. The dispersion of the ES release was calculated by LES up to several million time steps, while the instantaneous concentration was recorded. Time series with different durations (from 10 thousand to 3 million steps) were processed separately using EVT. The results are plotted in Fig.4, where the EVT-predicted solid lines are quite comparable and the 95% confidence intervals tend to decrease with increasing time steps. This indicates that EVT results obtained from short term data can predict the return period of the occurrence of extreme events.

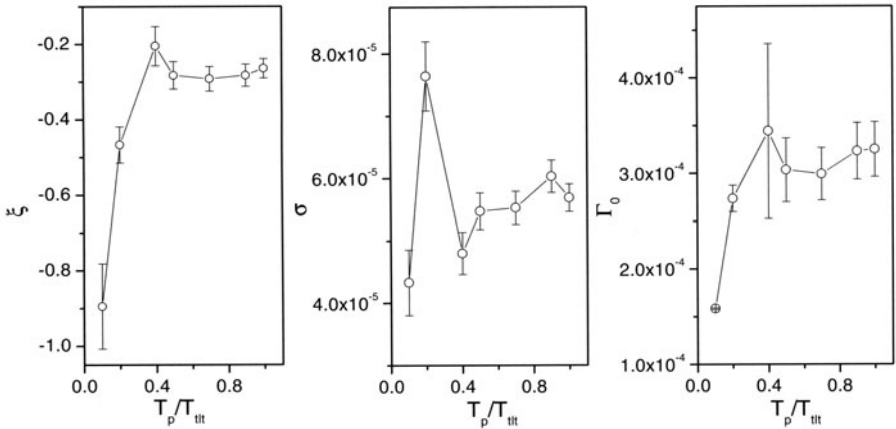


Figure 5. Parameters fitted from short-term and long-term series at the observing station of x=7.8D, GLS. Bars: ξ and σ , standard error; Γ_0 , 95% confidence interval.

The data of concentration processed using EVT are collected from both LES and experiments. Instantaneous concentrations are recorded at many typical locations. All of the time series have been carefully assessed by checking the sampling errors. A technique of “declustering” is applied to pre-process the data before GPD is fitted to them Davison & Smith, 1990; Munro et al., 2001; Smith, 1989, where the key is to specify a threshold u and a cluster time interval T_c . Specifically, two exceedances are considered to belong to the same cluster when the interval between them is shorter than the cluster interval. Only the maxima of the clusters are retained to form the new series, which is considered independent. The cluster interval is believed to be related to the scale of autocorrelation of the time series. Only two sets of time series are

processed here. One is located at the height of source for the ES and the other is located at ground level for the GLS.

In order to check the robustness of prediction, the GPD parameters from the short-term series are compared with those from the long-term series. These series with different durations are processed using the same threshold and cluster time interval. The parameters ξ and σ and the local maximum Γ_0 are compared. One typical example is shown in Fig.5. Note the parameters tend to constants, which demonstrates the process is robust.

Fig.6 shows the relative maxima and return levels at several downstream locations for GLS and ES, where the relative maxima and relative return levels are respectively defined as maximum concentration (upper limit) and return levels normalized by local mean concentration. Despite the large confidence interval for LES, the relative maxima and return levels for LES are all in good agreement with those for the measurements, except the comparison at $X/D=2.7$ for ES. Note the relative maxima are over 40 for ES at $X/D=2.7$. Compared with Fig.6 A for GLS, the magnitude and the trend against downstream distance of the relative maximum in Fig.6 C for ES are quite different, which suggests the turbulence background dominates the extreme concentrations. We note that Fig.6 C is a very similar shape to the plot of relative intensity of fluctuations for ES, where the peak is located around $X/D = 2.0$ as well. Sykes et al Sykes & Henn, 1992 pointed out that the relative intensity of the fluctuations for an ES decays towards zero downstream, which is also confirmed in our LES. In Fig.6 C, there is an evident decay towards zero downstream. However, the trend far downstream for both relative intensity and relative maximum for GLS still remains an issue. From the current LES data and measurements for the GLS (see Fig.2), the relative intensity has a very slight drop at $x/D = 1.0$. After $x/d = 2.0$ downstream, it clearly approaches a constant. The relative maximum still has a slight drop after $x/D = 4.0$, which makes the downstream trend not so obvious.

5. Conclusion and discussion

The relative maxima and return levels estimated from numerical data are in good agreement with those from experimental data. A remarkable difference of occurrence of extreme concentrations is found between elevated source release and ground-level source release, suggesting the turbulence background plays a very important role, dominating the occurrence of very large concentrations. It is noted that the plots of relative maxima are more or less similar in shape to the relative intensities. Is there any similarity or a simple relation between the relative maxima and relative intensities (or a higher order moment)? If so, a lot of work could be saved to obtain the relative maxima. Our conclusion is not only that EVT can be used with remarkable success on both LES and

experimental data to predict the occurrence of rare events and PDF tails, but that this method also gives rise to new insights into the physics and statistics of dispersion in the shear-driven atmospheric boundary layer.

References

- Davison A C and Smith R L 1990. Models for exceedances over high thresholds (with discussion) *J. R. Statist. Soc. B* **52** 393-442
- Fackrell J E and Robins A G 1982. Concentration fluctuations and fluxes in plumes from point sources in a turbulent boundary layer *J. Fluid Mech.* **117** 1-26
- Fisher R A and Tippett L H C 1928. Limiting forms of the frequency distribution of the largest or smallest member of a sample *Proc. Cambridge Phil. Soc.* **24** 180-190
- Jenkinson A F, 1955. The frequency distribution of the annual maximum (or minimum) values of meteorological elements *Q. J. Roy. Meteorol.* **87** 158-171
- Mises R von 1954. La distribution de la plus grande de n valeurs In selected papers II pp271-294 Providence RI: mer. Math. Soc.
- Munro R J, Chatwin P C and Mole N 2001. The high concentration tails of the probability density function of a dispersing scalar in the atmosphere *Bound.-Layer Meteorol.* **98** 315-339
- Picands J 1975. Statistical inference using extreme order statistics *Ann. Statist.* **3** 119-131
- Sagaut P 1995. '*Simulations numériques d'écoulements décollés avec des modèles de sous-maille*' PhD Thesis, University of Paris VI, France
- Smith R L 1989. Extreme value analysis of environmental time series: an application to trend detection in ground-level ozone *Statist. Sci.* **4** 367-393
- Sykes R L and Henn D S 1992. LES of concentration fluctuations in a dispersing plume *Atmos. Env.* **26A** 3127-3144
- Xie Z, Voke P R, Hayden P and Alan G R (to be published) Large-eddy simulation of turbulent flow over a rough surface, *Bound.-Layer Meteorol.*

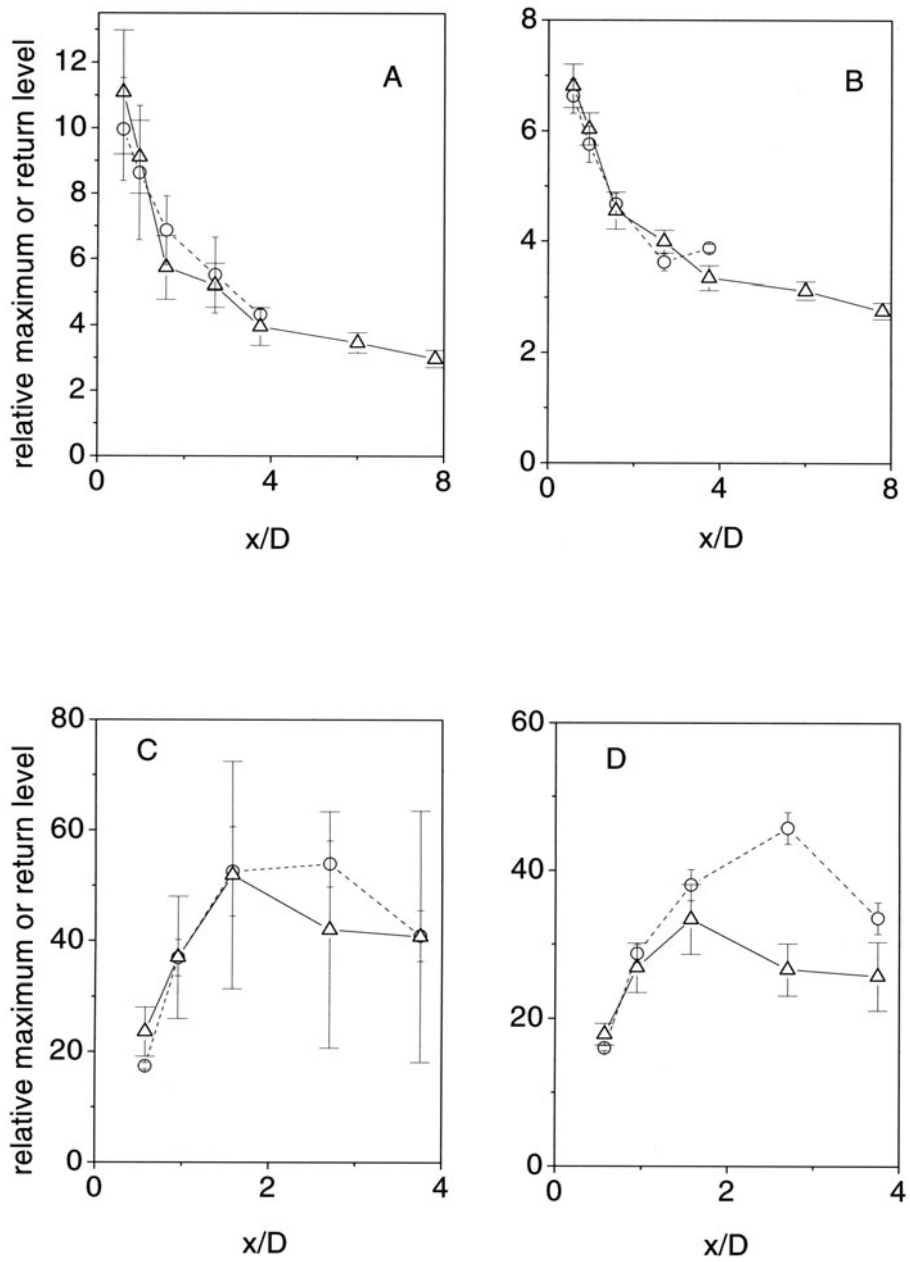


Figure 6. Relative maxima and return levels. Bars: 95% confidence intervals; —△—: LES; - - -○- -: measurements. A: GLS, relative maxima; B: GLS, return level for return period of 3.6 times of whole LES duration; C, D: ES, as A, B respectively.

3.3 NONPREMIXED AND PREMIXED TURBULENT COMBUSTION

SIMULATION OF THREE-DIMENSIONAL TURBULENT FLAMES

Dominique Thevenin

*Lab. of Fluid Dynamics and Technical Flows, Inst. of Fluid Dynamics and Thermodynamics
University of Magdeburg, Universitaetsplatz 2, 39106 Magdeburg (GERMANY)*

Dominique.Thevenin@vst.uni-magdeburg.de

Abstract

Systems relying on turbulent combustion are used in many practical applications and in broad areas of technological importance, in particular for energy generation, transportation and process engineering. It is also of central concern in many security issues (fires, explosions) and has considerable impact on the environment and on air quality. Because turbulent flames are so widespread it is important to improve our understanding of their properties. In order to do so, accurate numerical simulations of simple configurations are essential. Direct Numerical Simulations (DNS) are ideally suited for such studies since they do not rely on any hypothesis concerning the turbulence. For the prediction of pollutant emissions, reliable models must of course be added to describe the chemical and diffusion processes. For more complex geometries and higher Reynolds numbers, Large-Eddy Simulations (LES) represent the only alternative to date. Due to the huge cost of such simulations, we were generally forced to restrict ourselves to two-dimensional flames up to very recently. Even if such computations already lead to interesting conclusions, it is clear that they may miss many aspects that are important to describe the coupling between combustion and turbulence, since turbulence is intrinsically three-dimensional. Considering the growth in computer power and the latest progress in algorithms and programming languages, several groups have developed recently 3D codes for turbulent combustion. In this work we describe in particular our latest results for three-dimensional DNS, still relying on realistic models to describe chemical processes.

Keywords: direct numerical simulation, large-eddy simulation, combustion

1. Introduction

Due to the overwhelming practical importance of systems relying on turbulent combustion, it is essential to improve their performance and reliability and diminish their pollutant emissions. Developments in numerical combustion have had a great impact on our understanding of combustion by allowing studies of many problems that could not be tackled by more classical analytical or exper-

imental methods. It has thus become possible to consider the full complexity of combustion phenomena and for example calculate the detailed structure of flames including complex kinetics, multispecies thermodynamics and transport. These numerical studies have first considered laminar flames, since this constitutes a somewhat easier configuration. They have been later on extended to turbulent flames, in particular using Direct Numerical Simulations. In DNS all scales are calculated without resorting to a closure model. Direct simulations have thus been used to analyze many different problems which were otherwise intractable (Poinso et al., 1996; Vervisch & Poinso, 1998; Poinso & Veynante, 2001). Fundamental problems treated with DNS yield results which may then be used to improve physical submodels, as needed by Large-Eddy Simulations (LES) or Reynolds-Averaged Navier-Stokes (RANS) approaches.

2. Framework and State of the Art

Simulations of the compressible Navier-Stokes equations are carried out by solving five conservation equations (continuity, momentum $\times 3$, energy). Reacting flows usually require N_s supplementary equations, where N_s stands for the number of reacting species considered. In the case of detailed chemistry, the value of N_s varies typically between 8 for hydrogen-oxygen flames, around 30 for methane-air flames and 100 or more for higher hydrocarbons. This leads of course to huge computing time requirements, but is the most accurate manner - and often the only possibility - to investigate for example pollutant formation in a quantitative way.

Different routes have been used in the past to reduce the computational cost, depending on the most important physical phenomena in the configuration of interest: (a) reducing the physical complexity, for example by considering only chemical reactions without heat release (b) reducing the spatial dimensions by working only in two dimensions (c) diminishing the cost of the chemistry by using reduction methods. Several methods have been frequently combined to further reduce the CPU times.

Although turbulence is known to be a fundamentally three-dimensional phenomenon, direct simulations have been frequently carried out in two dimensions to reduce the computational cost (Poinso et al., 1996; Vervisch & Poinso, 1998; Hilbert & Thevenin, 2002). Physically, it is known that the influence of heat release can tend to reduce the growth of three-dimensional instabilities in some configurations. Turbulence with more or less organized 2D structures is also observed in some important cases (mixing layers, wakes, jets), which partly justifies this choice from a physical point of view. Results obtained through two-dimensional DNS have greatly helped in understanding basic features of turbulent combustion. Nevertheless, it is clear that the main reason for limiting computations to 2D is of course the induced tremen-

dous reduction in needed computing times and memory. Post-processing two-dimensional DNS results is also much more straightforward than for full 3D data, where the post-processing step can become dominant in terms of computing time and require unavailable disk and memory space.

When using detailed chemistry models to represent the chemical reactions, the supplementary cost incurred represents over 70% of the total computational cost. This includes the time spent to determine complex multispecies transport properties, thermodynamic coefficients and reaction rates. In other words, the cost of solving the fluid dynamics balance equations is almost negligible when compared with the cost of treating the chemistry and diffusion. It is almost impossible to incorporate directly such detailed models in three-dimensional solvers at reasonable computing costs and new solutions must be found if we wish to obtain single-processor CPU times below a few months. The problems appearing when using accurate physical models to simulate turbulent flames have been reviewed in great detail in a recent paper (Hilbert et al., 2003). . . along with the interest of doing it!

As a whole three-dimensional direct simulations of reacting flows using accurate physical models are fairly recent. One possibility is to improve computer algorithmics and parallelization, and carry out three-dimensional DNS including detailed reaction schemes on very powerful supercomputers using the same approach as in 2D (Tanahashi et al., 2000; Bell et al., 2002; Mizobuchi et al., 2002). This is of course an interesting solution but leads to very high computing costs, which become of the order of magnitude of one year on a single-processor machine, limiting the possible use of such simulations to investigate turbulent combustion in a systematic way. Reaching statistical convergence is also a difficult issue, since repeating the computations (a need explained for example in Hilbert & Thevenin, 2002) is even more costly in terms of CPU time. Using the most powerful existing parallel supercomputers (ASCI machines in the USA, Numerical Wind Tunnel or Earth Simulator in Japan) is then generally needed to achieve acceptable turn-over times for such computations. Recent publications demonstrate the interest of this approach but put simultaneously into evidence the huge computing cost induced. For example direct comparisons between DNS and experimental results will soon become possible (Bell et al., 2003).

The problems encountered in DNS also apply for LES. Up to recently, Large-Eddy Simulations of reacting flows have been limited to two dimensions (for example Angelberger et al., 2000; Colin et al., 2000), even if they use only a single-step reaction to describe the chemistry. The increase in computing cost resulting from more complex, larger geometries and considerably higher Reynolds numbers cannot be compensated by this cheap description of chemical processes. Moreover, specific difficulties are encountered in LES, since the reaction zones are generally smaller than the grid step, meaning that chemical

processes become subgrid-scale phenomena. This point has been discussed in more detail in other publications (Candel et al., 1999; Thevenin, 2002) and cannot be considered extensively here. Despite these huge computing costs, it is possible to find some recent publications relying on three-dimensional LES for turbulent flames (for example Forkel and Janicka, 2000; Menon, 2001; Mahesh et al., 2003). Even if the employed chemistry models are still generally limited in their complexity, interested configurations can now be computed by using parallel supercomputers and extensive comparisons with experimental results begin to appear.

In the rest of this paper, we present our recent work on three-dimensional DNS of reacting flows. For this purpose we choose to examine the development of a flame in a turbulent flow, since this represents a very important combustion process, found in many practical applications. Current understanding is still unsatisfactory and severely limits prediction capabilities.

3. Three-dimensional DNS of a turbulent premixed flame

A three-dimensional DNS code, called π^3 and written in Fortran 95 has been developed in our group. A strong reduction of computing times is obtained by combining a low-Mach number approach, well suited to most configurations, with an accurate reduction technique for the chemistry.

3.1 Low-Mach number approximation

For most applications of interest, like for example furnaces and boilers, but also inside the combustion chambers for automotive or aeronautical/aerospace applications, the maximum Mach number is generally quite small, at least in the region where combustion takes place. It is then unnecessary and inefficient to employ a fully compressible formulation to investigate numerically such configurations. The low-Mach number approximation allows an important speed-up, since the stability restrictions associated in particular with the Courant-Friedrichs-Lewy (CFL) condition are practically released. We use a pressure-projection method to implement the low-Mach number formulation in our DNS code. This procedure is described in detail along with the validation steps in other articles (de Charentenay et al., 2001; de Charentenay et al., 2002).

3.2 Description of chemical processes

Our previous DNS code *parcomb* employed full reaction schemes to describe chemical processes, which is of course the most accurate technique but rapidly leads to unacceptable computing costs in three dimensions, since tens or even hundreds of additional transport equations must be solved.

As an alternative we build on top of the *Intrinsic Low-Dimensional Manifold* (ILDM) technique (Maas & Pope, 1992). This technique relies on the identification of low-dimensional subspaces in composition space, on which chemical processes are restricted. After computing this manifold all the information (values of the mass fractions, mass production terms, thermodynamic coefficients, binary diffusion coefficients, ...) is stored in a database. This database is finally called during the direct simulation to get the information needed to integrate the system in time. Instead of requiring a transport equation for each chemical species present in the reaction system, we only need a transport equation for the coordinates of the manifold. The ILDM method has been widely validated and a very good agreement is achieved for a variety of fuels and conditions, compared to full reaction schemes.

The classical ILDM method requires a very high number of dimensions when low-temperature kinetics have to be included in the manifold. In order to avoid this problem we have developed a related method, called FPI for *Flame Prolongation of ILDM* (Gicquel et al., 2000; Fiorina et al., 2003). In this case we still obtain the same attracting subspace as the standard ILDM technique in the high-temperature region, near the equilibrium point. But instead of increasing the dimension of this manifold when considering lower temperatures, we simply prolongate the obtained manifold by using the laminar premixed flame structure corresponding to the same fresh gas composition. This means that, when a point of the CFD computation does not fall any more on the standard ILDM manifold, we use for this missing information the correlation between species coming from the corresponding laminar flame. At the difference of the ILDM method, there is no rigorous mathematical explanation to justify this approximation in the low-temperature region. On the other hand, this procedure takes into account exactly the correct boundary conditions both on the high- and low-temperature boundaries, and of course relies on a physically-exact flame structure to relate the species outside the ILDM manifold. Many tests have been carried out to check the accuracy of the FPI method. Flame speed, extinction limits and the radical profiles are predicted almost exactly when compared to the full reaction scheme, while obtaining a reduction factor in computing times varying between 5 and 30. Combining the low-Mach number approach and the chemistry reduction using FPI leads to a typical speed-up of two orders of magnitude compared to the fully compressible formulation employing full reaction schemes. Thanks to this considerable acceleration, three-dimensional DNS become feasible.

The FPI database used in the present computations for methane combustion has been obtained starting from a detailed reaction scheme of Lindstedt including 29 species and 141 reactions. It is parametrized by two coordinates. The employed database has been computed with a unity Lewis number hypothesis for simplicity purposes.

3.3 Numerics and results

Time integration is performed using a fourth-order Runge-Kutta procedure. Spatial derivatives are computed using a sixth-order centered approximation. The pressure perturbation is determined by solving a Poisson equation using a spectral method in the associated Fourier space.

The code π^3 has not been parallelized yet. All results presented here have been therefore obtained on a single Athlon PC with 1 GB of memory. Typical computing times are 2 to 3 hours for a two-dimensional simulation, and 300 to 400 hours for a three-dimensional computation. The grid spacing is constant and uniform, equal to 55 μm for all simulations. This relatively coarse grid-step is possible thanks to the FPI approximation. We only need to solve the two FPI-coordinates to determine all the chemical species. Minor, stiff radicals like HCO or CH_2O are not directly solved, but deduced from the FPI database. It is therefore possible to use coarser grids compared to simulations relying on full reaction schemes. The two- and three-dimensional computations are carried out in computational domains of 8 mm length in each direction. Fully premixed methane/air flames at an equivalence ratio $\phi = 1.59$, atmospheric pressure and fresh gas temperature of 298 K are considered. This high value of ϕ has been retained to facilitate the computations, and in particular to get a larger flame width and lower density jump through the flame, leading to a smoother time- and space-integration.

We initialize a perfectly spherical laminar flame kernel at zero velocity and superpose a field of synthetic turbulence using a homogeneous isotropic turbulence field corresponding to a von Karman spectrum with Pao correction for near-dissipation scales. The Reynolds number is $\text{Re}_{l_t} = l_t u' / \nu_u = 74$ based on the integral length of turbulence. The characteristic time-scale of the large turbulent structures is $\tau_{l_t} = l_t / u' = 0.72$ ms. All computations have been carried out up to a non-dimensional time $\tilde{t} = t / \tau_{l_t} = 1.67$. Some typical results are shown in Fig.1. Considerable quantitative differences between corresponding two- and three-dimensional simulations have already been identified (Thevenin et al., 2002).

4. Conclusions

In order to go to three-dimensional simulations with acceptable computing costs, new modeling approaches are requested. We have successfully developed a 3D direct simulation code relying on the low-Mach number approximation and on the FPI chemistry reduction technique. The needed computational times in 3D are similar to those of our previous, two-dimensional compressible code relying on full reaction schemes. This new code has been used here to investigate the development of a premixed methane/air flame in a turbulent flow,

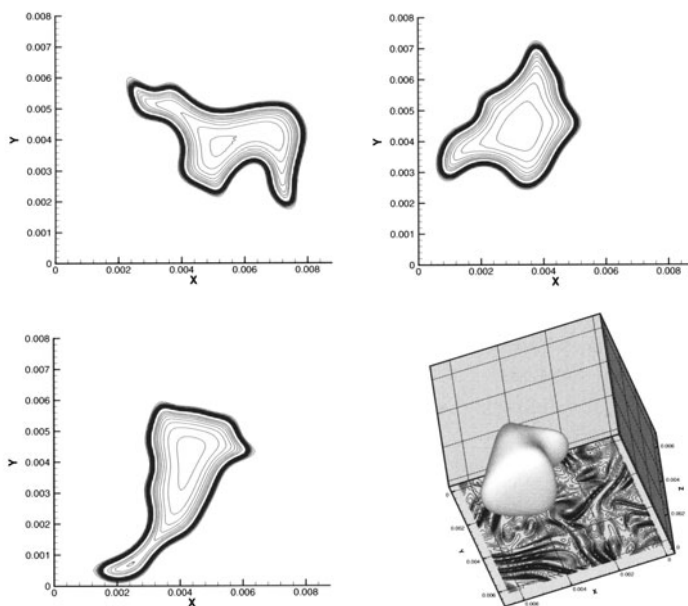


Figure 1. Instantaneous field of the CH_2O mass fraction, an important intermediate radical for methane oxidation. The bottom right figure correspond to a full three-dimensional computation (isosurface of CH_2O plus vorticity isosurfaces in the bottom plane), the three other figures are associated with two-dimensional computations using exactly the same physical parameters. Differences only result from the specific initial conditions employed to start the computation, even if the global properties of turbulence are the same in all cases.

as observed after spark ignition. Further configurations will be investigated in the near future.

Acknowledgments

The support of O. Gicquel, J. de Charentenay and R. Hilbert in developing π^3 is gratefully acknowledged.

References

- Angelberger, C., Veynante, D. and Egolfopoulos, F.: LES of chemical and acoustic forcing of a premixed dump combustor. *Flow. Turb. Combust.* **65**:205-222 (2000).
- Bell, J.B., Day, M.S., Almgren, A.S., Cheng, R.K. and Shepherd, I.G.: Numerical simulation of premixed turbulent methane combustion. In Bathe, K.J., Ed., *Computational Fluid and Solid Mechanics*. Elsevier, pp.1247-1250 (2003).
- Bell, J.B., Day, M.S. and Grcar, J.F.: Numerical simulation of premixed turbulent methane combustion. *Proc. Combust. Inst.* **29**, in press (2002).

- Candel, S., Thevenin, D., Darabiha, N. and Veynante, D.: Progress in numerical combustion. *Combust. Sci. Tech.* **149**:297-337 (1999).
- Colin, O., Ducros, F., Veynante, D. and Poinso, T.: A thickened flame model for large eddy simulations of turbulent premixed combustion. *Phys. Fluids* **12**(7):1843-1863 (2000).
- de Charentenay, J., Thevenin, D. and Zamuner, B.: Direct numerical simulation of turbulent H_2/O_2 premixed flames using compressible and low-Mach formulations. In Geurts, B.J., Friedrich, R. and Metais, O., Eds., *Direct and Large-Eddy Simulation IV*. Kluwer Academic Publishers, pp.129-136 (2001).
- de Charentenay, J., Thevenin, D. and Zamuner, B.: Comparison of direct simulations of turbulent flames using compressible or low-Mach number simulations. *Int. J. Numer. Meth. Fluids* **39**(6):497-516 (2002).
- Fiorina, B., Baron, R., Gicquel, O., Thevenin, D., Carpentier, S. and Darabiha, N.: Modelling non-adiabatic partially premixed flames using flame-prolongation of ILDM. *Combust. Theory Modelling* **7**:449-470 (2003).
- Forkel, H. and Janicka, J.: Large-eddy simulation of a turbulent hydrogen diffusion flame. *Flow. Turb. Combust.* **65**:163-175 (2000).
- Gicquel, O., Darabiha, N. and Thevenin, D.: Laminar premixed hydrogen/air counterflow flame simulations using Flame Prolongation of ILDM with differential diffusion. *Proc. Combust. Inst.* **28**:1901-1908 (2000).
- Hilbert, R., Tap, F., El-Rabii, H. and Thevenin, D.: Impact of detailed chemistry and transport models on turbulent flame simulations. *Prog. Energy Combust. Sci.*, accepted for publication (2003).
- Hilbert, R. and Thevenin, D.: Autoignition of turbulent non-premixed flames investigated using direct numerical simulations. *Combust. Flame* **128**:22-37 (2002).
- Mahesh, K., Constantinescu, G. and Moin, P.: A numerical method for large-eddy simulation in complex geometries. In Bathe, K.J., Ed., *Computational Fluid and Solid Mechanics*. Elsevier, pp.23-30 (2003).
- Maas, U. and Pope, S.B.: Implementation of simplified chemical kinetics based on intrinsic low-dimensional manifolds. *Proc. Combust. Inst.* **24**:103-112 (1992).
- Menon, S.: The use and relevance of reacting LES in engineering design cycle. In Geurts, B.J., Friedrich, R. and Metais, O., Eds., *Direct and Large-Eddy Simulation IV*. Kluwer Academic Publishers, pp.509-516 (2001).
- Mizobuchi, Y., Tachibana, S., Shinjo, J. and Ogawa, S.: A numerical analysis on structure of turbulent hydrogen jet lifted flame. *Proc. Combust. Inst.* **29**, in press (2002).
- Poinso, T., Candel, S. and Trounev, A.: Applications of direct numerical simulation to premixed turbulent combustion. *Prog. Energy Combust. Sci.* **21**:531-576 (1996).
- Poinso, T. and Veynante, D.: *Theoretical and numerical combustion*. Edwards Publishing, PA, 2001.
- Tanahashi, M., Fujimura, M. and Miyauchi, T.: Coherent fine-scale eddies in turbulent premixed flames. *Proc. Combust. Inst.* **28**:529-535 (2000).
- Thevenin, D.: Direct- and Large-Eddy Simulations of turbulent flames. In *5th World Congress on Computational Mechanics (WCCM V)*, Vienna, Austria, CD-ROM ISBN 3-9501554-0-6 (2002).
- Thevenin, D., Gicquel, O., de Charentenay, J., Hilbert, R. and Veynante, D.: Two- versus three-dimensional direct simulations of turbulent methane flame kernels using realistic chemistry. *Proc. Combust. Inst.* **29**, in press (2002).
- Vervisch, L. and Poinso, T.: Direct numerical simulation of non-premixed turbulent combustion. *Ann. Rev. Fluid Mech.* **30**:655-692 (1998).

LARGE-EDDY SIMULATION OF A GAS TURBINE COMBUSTION CHAMBER

Effect of the subgrid scale flame thickness on the flame dynamics

Christophe Duwig

*Division of Fluid Mechanics - Department of Heat and Power Engineering
Lund Institute of Technology - Box 118 - SE 22100 Lund*

Christophe.Duwig@vok.lth.se

Laszlo Fuchs

*Division of Fluid Mechanics - Department of Heat and Power Engineering
Lund Institute of Technology - Box 118 - SE 22100 Lund*

Laszlo.Fuchs@vok.lth.se

Abstract A analysis of the subgrid scale flame thickness in the LES framework is presented. The influence of the subgrid flame thickness has been tested numerically on a swirl stabilized flame using a flamelet formulation. The analysis introduces a non-dimensional number a , characteristic for flame and the filter. The values of this number are computed for different LES combustion models and lie in a wide range. The variations of the number a lead to completely different flame dynamics showing the importance of subgrid flame thickness modelling in the LES framework.

Keywords: Large Eddy Simulation, Premixed combustion, Flamelet model, Flame dynamics

1. Introduction

Due to new emission regulations, environmental issues of power generation play an important role in the economic viability of modern power plants. In order to reduce harmful emissions, the current trend of design of industrial combustion devices is to operate under fuel lean and premixed conditions. Under such conditions, the peak temperature is reduced with a risk for increase in the level of CO emission, occurrence of flashback and flame blow-out. There-

fore, a more accurate prediction of the combustion device behavior is required in order to design efficient, safe and clean burners.

Recently the increase in computer power brought the hope of being able to resolve and understand the combustion instabilities using Large Eddy Simulation (LES). If LES has been shown to be a suitable numerical technique able to resolve large structure dynamics in Gas Turbine combustors, no ultimate solution has been yet proposed to model the Sub-Grid Scale (SGS) combustion. However, in order to understand the flame instabilities, one has to capture the flame dynamics and the subgrid scale flame speed and thickness through a SGS model. In most of the LES combustion models, the subgrid scale flame thickness is controlled by the SGS diffusion term. The SGS diffusion coefficient is often chosen in order to stabilize the numerics and its choice is seldom supported by physical arguments. Surprisingly, no studies of the influence of the subgrid scale diffusion modelling on the flame dynamics has been published so far.

In this paper, a flamelet formulation for premixed combustion, with an emphasis on the subgrid flame thickness modelling, is presented (Duwig, 2002). The formulation is used to simulate a swirling reacting flow in a typical gas turbine combustion chamber. The results are used to assess the influence of the filtered flame thickness on the flame dynamics. We have reduced the SGS term to be dependent on a single parameter, depending on the diffusivity of the fuel and filter thickness. The simulations show that the flame dynamics are strongly dependent on this parameter.

2. Flamelet formulation for LES

A major difficulty in LES of reacting flows is that chemical reactions occur at scales much smaller than the resolved ones. This implies that the dynamics of the flame at small scales (i.e. flame propagation, stretching and its instantaneous thickness, including local quenching and ignition) are filtered out. In contrast to turbulence no universal behaviour of the small scales of the flame have been defined in terms of measurable (mean) values and the local scale sizes. The lack of a theory analogous to Kolmogorov's theory, makes SGS modelling much more problematic. Therefore, a general theory can be developed under simplifying assumptions, as done here. In the present paper, a premixed flamelet formulation developed by Duwig (2002) and (2003) is being used. Within the flamelet regime, we assume a scale separation between turbulence and chemistry. The chemical length scales are by several orders of magnitudes smaller than the turbulent scales. Consequently, the reaction rate is modelled by a Dirac function, δ . However, in the LES framework the filtered reaction rate has to be computed. To derive such an expression, we consider a 1-D turbulent flame. The progress variable c (typically, we use the dimen-

sionless temperature) being 0 when unburned and 1 when burnt. The progress variable in 1-D, satisfies the following filtered equation (using a Gaussian kernel):

$$\begin{aligned} \rho_u S_L \Xi \frac{d\tilde{c}}{dx} &= \rho_u D_c \frac{d^2\tilde{c}}{dx^2} + \int_{-\infty}^{+\infty} \frac{\rho_u S_L}{\Delta} \Xi \sqrt{\frac{6}{\pi}} \cdot \delta(x') \cdot e^{-\frac{6 \cdot |x-x'|^2}{\Delta^2}} \cdot dx' \\ &= \rho_u D_c \frac{d^2\tilde{c}}{dx^2} + \frac{\rho_u S_L}{\Delta} \Xi \sqrt{\frac{6}{\pi}} \cdot e^{-\frac{6x^2}{\Delta^2}} \end{aligned} \quad (1)$$

where, $\rho_u, \Delta, S_L, D_c, \delta$ and Ξ denote the unburned gas density, the filter length, the laminar flame speed, the effective diffusion, the Dirac function and the wrinkling factor (i.e. the increase of flame surface generated by turbulence), respectively. A non-dimensional number $a = \frac{S_L \Delta \Xi}{D_c}$ and a normalized coordinate $X = \frac{x}{\Delta}$ are introduced. All this leads to a simple ODE:

$$\frac{d\tilde{c}}{dX} = \frac{1}{a} \frac{d^2\tilde{c}}{dX^2} + \sqrt{\frac{6}{\pi}} \cdot e^{-6X^2} \quad (2)$$

The boundary conditions for this equation are:

$$\tilde{c} \rightarrow 0; \quad \left. \frac{d\tilde{c}}{dX} \right|_{X \rightarrow -\infty} \rightarrow 0 \quad (3)$$

The non-dimensional number a expresses in dimensionless form the relative importance of the turbulent filtered flame speed and its thickness as compared to the effective diffusivity. The production term, on the right hand side of equation (2), $\Pi_c = \sqrt{\frac{6}{\pi}} e^{-6X^2}$ is plotted against the (density weighted) filtered c in Figure 1 for four values of $a = (1, 3, 6, 10)$. This data is used to close the filtered transport equation system.

The closed (density weighted) filtered progress variable equation can be written as:

$$\frac{\partial \tilde{\rho} \tilde{c}}{\partial t} + \nabla \cdot (\tilde{\rho} \tilde{u} \tilde{c}) = \frac{\rho_u S_L \Xi}{a} \nabla^2 \tilde{c} + \frac{\rho_u S_L \Xi}{\Delta} \Pi_c(\tilde{c}, a) \quad (4)$$

3. Subgrid scale flame thickness: analysis using the non-dimensional number a

The non-dimensional parameter a enters naturally the reactive-diffusive balance and is used to characterize the subgrid flame thickness. A general expression of the parameter is:

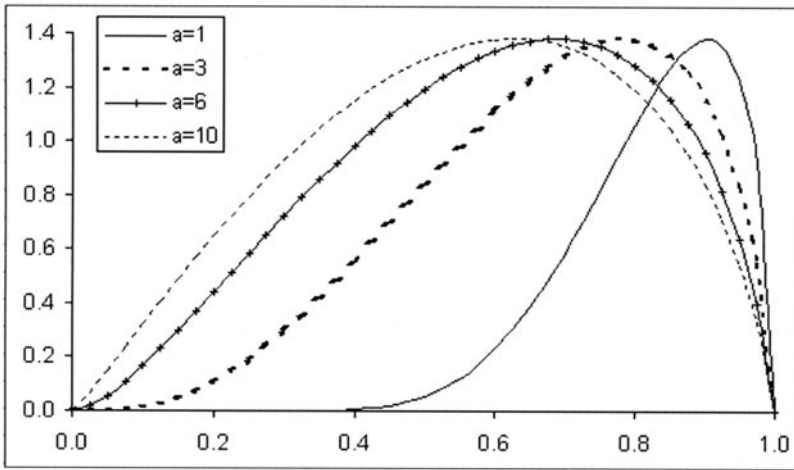


Figure 1. Normalized filtered reaction rate vs density weighted progress variable, for some parameter values

$$a = \frac{\int_0^1 \overline{w_c}(\tilde{c}) d\tilde{c} \cdot \Delta^2}{\rho D} \quad (5)$$

This parameter compares the integral filtered reaction rate (i.e. the turbulent flame speed for a quasi-planar flame) and the diffusion term. Thus, the parameter a has a physical component related to the diffusivity of mass, scales of the flow chemistry (flame speed), flame-flow interaction (wrinkling factor) and finally the filter size as compared to flow length scale. The problem can be reduced to a single parameter that is highly dependent on the underlying assumptions.

In the limit of laminar flames, we find that $a \sim \Delta/(D/S_L) \sim \Delta/l_F$ where l_F denotes the laminar flame thickness. It is the ratio of the broadening due to filtering and the one due to diffusion. For gas turbine applications, a is of the order of 2-6. Here, we use the value of $a=4$. Values of $a \ll 1$ correspond to an infinitely thick flame whereas $a \gg 1$ is equivalent to a filtered infinitely thin flame (in this case the filtered flame thickness would be Δ) recovering the results of Boger (2000) as reported by Duwig (2002).

The parameter a enters naturally the reactive-diffusive balance equation and is used here to characterize the subgrid flame thickness. Table 1 shows the numbers a that correspond to several LES combustion models. If one is assuming a bi-modal pdf we have an infinitely thin flame corresponding to the Bray-Moss-Libby model (Bray et al. 1989). In this case a is infinitely large. However, to ensure a proper flame propagation speed, Boger (2000) used the KPP theorem to modify the BML-LES approach introducing an additional diffusion term. It

is worth noticing that this term has no physical meaning but is rather small. A more popular approach is to use the analogy with the momentum transport and model the diffusion with a Smagorinsky like expression. Here that non-dimensional number a is not related at all to the flame structure but rather to the momentum transport constant C_S (so-called Smagorinsky constant) and the turbulent Schmidt number Sc_t . Colin et al. (2000) used a thickening technique to be able to resolve the flame on the LES grid keeping the propagation velocity constant. Thickening increases the diffusion and results in a decrease of the parameter a .

Table 1 shows that these combustion models cover a broad range of values of the parameter a . On one hand it is not surprising as the turbulent diffusion term is often modelled with less efforts than the filtered reaction rate and used to stabilize the numerical methods. On the other hand, the effect of the subgrid flame thickness on the flame dynamics is still not fully understood but preliminary results presented in this paper are assessing the importance of the subgrid flame thickness modelling in the context of LES. These results will be introduced and presented in the following.

Table 1. Values of the non-dimensional number a for different combustion models.

Model	a	typical value
BML	infinity	
BML-KPP (Boger, 2000)	$16 \sqrt{\frac{6}{\pi}}$	22
Smagorinski-type	Sc_t/C_S	1-3
Thickened Flame (Colin et al., 2000)	$\Delta/(F\delta_L)$	0.05-0.2
Present formulation	$\Delta/(\delta_L)$	2-3

4. Numerical methods and presentation of the test case

The present flamelet formulation has been implemented into a Cartesian finite difference LES code solving the incompressible Navier-Stokes equations with variable density. The code is third-order accurate for the convective terms Kawamura et al. (1984) and fourth-order accurate for the diffusion term. Within a time step, the defect correction technique is used to solve the flow field. A third order finite difference scheme is used for time integration. More details can be found in Gullbrand et al. (2001). The Cartesian finite differences techniques are fast, easily coded and accurate. These advantages make them suitable for LES of reacting flows. For the Navier-Stokes equations, the implicit model (so-called IMM, in Gullbrand et al. (2001)) is used as subgrid scale model. No explicit modelling of the subgrid scale turbulent transport is done but the truncation error of the scheme acts as a subgrid scale model.

Reacting flows in an Alstom AEV gas turbine burner have been studied. The geometry, corresponding to an experimental rig, contains a premixing pipe, of diameter D_p and length $1.2D_p$, discharging into a rectangular box. The dimensions in x,y and z direction are: $4D_p \times 3.8D_p \times 3.8D_p$, respectively. Experimental mean velocity profiles are used for inlet boundary conditions. The Reynolds number at the inlet is 150000 and the swirl number 0.52. The grid used for this study has about 1.8 M cells (Duwig, 2003). Three computations have been carried out using different values of the a parameter; namely 1, 4 and a variable value; i.e. $\frac{\Xi}{a} = \frac{1}{a_L} + \frac{1-\Xi}{a_T}$ with $a_L = \frac{\Delta}{l_F}$ and $a_T = \frac{\Delta}{1.5 \cdot l_F}$. The last relation aims at accounting for the thickening of the flamelet in the extended flamelet regime (Duwig, 2003) and leads in our case to $a \sim 2.3$. It is worth noticing that no turbulence is imposed explicitly at the inlet; both turbulence and the large scale structures related to unsteady vortex-breakdown are developing naturally in the flame region. Flame stabilization by swirl is highly sensitive to very small perturbations. This effect is observable by introducing small variations in the inlet velocity profile, or by any other geometrical disturbances.

5. Results and interpretation

Figure 2 shows the mean temperature profile in the three cases. The flame is anchored by the vortex-breakdown and anchored at the stagnation point. In all three cases, the stagnation point is located at the premixing pipe exit. The effect of the number a on the flame brush is significant, low values of a lead to a thicker flame brush. Moreover, the flame opening angle also decreases with decreasing a .

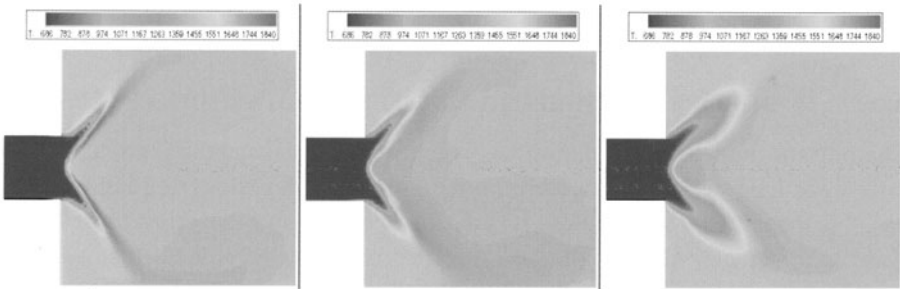


Figure 2. Axial cut of the mean temperature (K), left: $a=4$, center: variable a , right: $a=1$.

Figure 3 shows the pdf of the velocities and temperature at a point in the flame brush. The case $a=4$ leads to high thin peaks showing low fluctuations. The two other cases have wider Probability Density Function (PDF) showing more turbulent fluctuations. An explanation for the result is that the flame front

affects the large eddies. The steeper the flame front, the less it will be sensitive to the large eddies and it will tend to damp them out. On the other hand, decreasing a makes the flame thicker and more sensitive to the large eddies. The fluctuations are affecting the flame front motion which implies increasing the flame brush thickness.

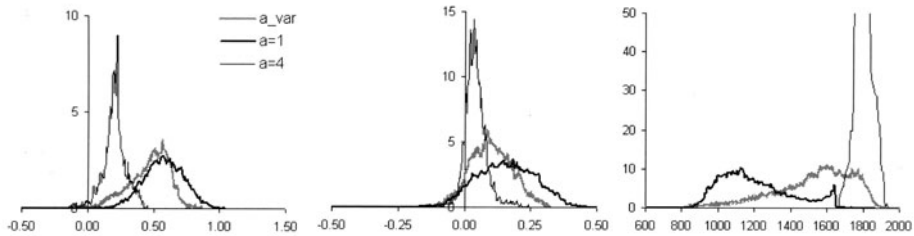


Figure 3. Probability density function 1D downstream the premixing pipe exit, 1D from the axis, left: axial velocity, center: tangential velocity, right: temperature (K).

The previous interpretation is supported by the frequency analysis presented in figure 4. It is clearly seen that the large values of a are damping turbulence in the flame brush ($y=D$) but the characteristic high frequency at Strouhal number $St \sim 1.8$ is captured in all cases. This frequency corresponds to the spiral mode of the vortex core (Duwig, 2003). The case $a=1$ does not show a single characteristic frequency but a wide range of characteristic frequencies around $St \sim 1$. These high frequencies correspond to rather small eddies which are more likely to be damped by a thin flame front. The cases of variable a and $a=1$ are more similar in the medium frequency range ($St<0.1$).

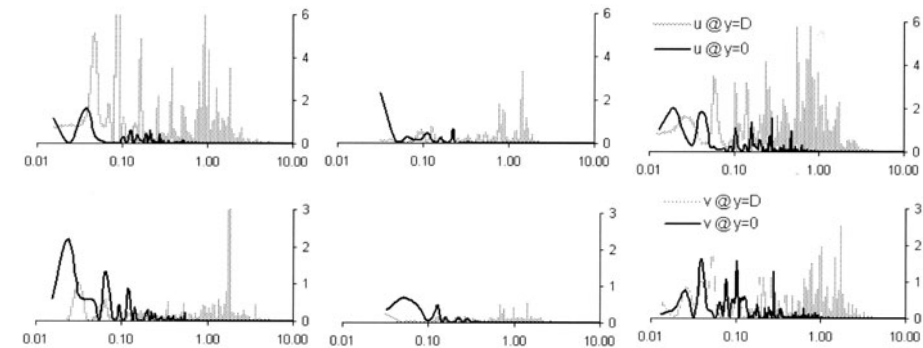


Figure 4. Fourier transform of the axial (up) and tangential (down) component of the velocity, 1D downstream the premixing pipe exit, on the axis ($y=0$) and 1D from the axis ($y=D$) vs the Strouhal number St , left: a var, center: $a=4$, right: $a=1$.

The present results suggest that Thickened Flame technique or Smagorinsky type closure (low number a techniques) would overpredict the turbulence in the $St \sim 1$ range as well as the flame brush thickness. On the other hand, BML type models would simulate a flame less sensitive to turbulence and underpredict the flame motion.

6. Summary

The effect of the subgrid flame thickness on the flame dynamics in the LES framework has been analyzed. The analysis introduced a non-dimensional number a comparing the integral reaction rate and the diffusion. The values of this number was computed for different LES combustion models and differed significantly depending on the model. Using a flamelet formulation, the influence of the subgrid flame thickness has been tested numerically on a swirl stabilized flame for three values of the parameter a . Results were presented with mean temperature fields, one point PDF and frequency analysis. The variations of the model single parameter lead to completely different flame dynamics showing the importance of subgrid flame thickness modelling in the LES framework.

Acknowledgments

The work was supported by the Swedish Energy Authority within the TPE program. This support is greatly acknowledged. The computations were run on HPC2N facilities with the SNAC project.

References

- Boger, M. (2000). *Modélisation de sous-maille pour la simulation aux grandes échelles de la combustion turbulente prémélangée*. PhD Thesis, Ecole Centrale Paris, France.
- Bray, K.N.C., Champion, M., Libby, P.A. (1989). *The interaction of turbulence and chemistry in premixed turbulent flames*, In *Turbulent Reactive Flows*, pp. 541-563, Lecture notes in engineering, Springer Verlag.
- Colin, O., Ducros, F., Veynante, D., Poinso, T. (2000). *A thickened flame model for Large Eddy Simulation of Turbulent premixed combustion*, *Physics of Fluids*, 12(7), pp 1843-1863
- Duwig, C. (2002). *A flamelet formulation for Large Eddy Simulation* in *Advances in Turbulence IX*, Proceedings of the ninth European turbulence Conference, Eds IP Casro & PE Hancock.
- Duwig, C. (2003) *Studies of gas turbines combustion chambers: use of new fuels and development of new tools*, PhD Thesis, Lund Institute of Technology, Lund, Sweden.
- Gullbrand, J., Bai, X.S., Fuchs, L. (2001) *High-order cartesian grid method for calculation of incompressible turbulent flows*, *Int. J. Num. Meth. Fluids*, 36, pp. 687-709
- Kawamura, T., Kuwahara, K. (1984) *Computation of high Reynolds number flow around a circular cylinder with surface roughness*, AIAA paper, 84-0340

MODELING OF POLLUTANT FORMATION NEAR LEAN BLOW-OUT IN GAS TURBINE ENGINES

G. Eggenpieler and S. Menon

School of Aerospace Engineering

Georgia Institute of Technology

Atlanta, GA, 30332, USA

suresh.menon@ae.gatech.edu

Keywords: Large-Eddy Simulations, Broken-Reaction-Zone, Lean Blow Out

Abstract Large Eddy Simulation (LES) of turbulent premixed combustion close to Lean Blow Out (LBO) in a gas turbine engine has been performed. Combustion near LBO is shown to occur in the broken reaction zone regime where classical flamelet assumption breaks down. A subgrid combustion model based on the linear-eddy mixing (LEM) model is implemented to simulate premixed combustion over a wide range of operational conditions, including combustion near LBO. Pollutant (*CO* and *NO*) formation is predicted using transport models and compared with data over a range of operating conditions. It is shown that inclusion of unburned hydrocarbons (UHC) due to local quenching is very important in the prediction of CO emission.

Keywords: Linear-Eddy-Mixing, combustion regimes, pollutants

1. Introduction

Current design studies of next generation gas turbine engines are focusing on the prediction of combustion dynamics and emissions (*CO*, *NO*, *UHC*) as a function of the operating conditions. Of particular interest is flame stabilization and emission near Lean Blow Out (LBO). LBO is a catastrophic phenomenon that occurs when the fuel-air mixture is very lean and the operating conditions are close to the lean flammability limit. Exponential increase in *CO* occurs near LBO and is followed by global extinction. Predicting the performance of gas turbine engine near LBO is now a major research effort. Although LBO occurs in both liquid-fueled and premixed systems, this paper focuses primarily on premixed combustion.

LES modeling based on the thin flame approach (e.g., G -equation) has been proved successful in the flamelet and thin-reaction-zone (TRZ) regimes for prediction of flame structure and heat release (Kim and Menon, 2000; Pitsch and Duchamp De Lageneste, 2002). However, as the operating condition approaches the LBO limit, the flame loses its flamelet-type structure and falls into the broken-reaction-zone (BRZ) regime where local quenching and re-ignition occurs (Meneveau and Poinso, 1991). Figure 1 is a diagram for turbulent premixed combustion (Pitsch and Duchamp De Lageneste, 2002) in which the typical operating regimes for both laboratory and industrial devices are shown. As shown, typical lean combustion in full-scale gas turbine engines occurs at the extreme limit of TRZ (in contrast, all laboratory flames are well within the flamelet applicable regime), and, as the condition becomes leaner, the combustion mode moves into the BRZ regime. Thus, in order to address combustion in a typical gas turbine, a simulation model that can handle combustion over the entire operational regime (TRZ-BRZ) is needed. The present effort focuses on a subgrid combustion model that can handle this wide range without requiring any ad hoc adjustable parameters.

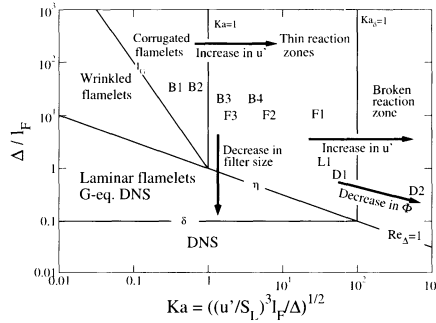


Figure 1. Premixed combustion regimes and locations of typical flames: B-type (Bédard and Cheng, 1995), F-type (Mansour et al., 1998), General Electric LM-6000 (Kim and Menon, 2000) (L1) and the current DOE-HAT combustor (D1 for $\Phi > 0.6$ and D2 for $\Phi < 0.5$). Here, l_F is the flame thickness, u' the sub-grid velocity fluctuations, S_L the laminar flame speed and Δ is the grid size.

In this paper, the implementation of the linear-eddy mixing (LEM) model (Kerstein, 1991a; Menon and Kerstein, 1992) as a subgrid model in LES is demonstrated with a particular focus on its application to combustion near the LBO limit. Past stand-alone studies have shown that the LEM model can handle combustion under a wide range of conditions (Smith and Menon, 1996; Sankaran and Menon, 2000) and thus, is considered a natural candidate for the present application. LES of premixed combustion in a DOE-HAT com-

bustor simulated earlier using a thin-flame model (Eggenspieler and Menon, 2003b) is revisited here using the LEM subgrid methodology.

2. LES-LEM Methodology and Resolution of Scales

In LES using the LEM subgrid model (called LES-LEM hereafter) both large scale and sub-grid processes are simulated concurrently, but separately. Thus, the compressible LES equations for mass, momentum and energy are solved using a finite-volume scheme that is fourth-order accurate in space and second-order in time. A localized dynamic subgrid kinetic energy model (Kim et al., 1999) is employed for the subgrid closure of the subgrid stresses and the heat flux. Earlier (Kim et al., 1999; Kim and Menon, 2000; Stone and Menon, 2002; Eggenspieler and Menon, 2003b), this LES solver was used to study premixed combustion in gas turbines using the thin-flame LES model (called GLES hereafter). In the present effort, the thin-flame model is replaced by a subgrid multi-scalar LEM model in LES-LEM. LES-LEM has also been applied to various applications (Chakravarthy and Menon, 2000; Sankaran et al., 2003) and validated against high-Re data.

The details are avoided here, for brevity. However, some features of the LES-LEM approach are worth highlighting. In LES-LEM, all small-scale processes, such as subgrid turbulent mixing, multi-scalar diffusion, finite-rate kinetics and heat release are simulated locally in each LES cell in a high-resolution 1D domain, while the large-scale advection of scalar by the LES velocity fields is implemented via a 3D Lagrangian technique that advects the subgrid scalar fields. Full conservation of mass is maintained at every time step. Reaction kinetics and molecular diffusion can be simulated exactly (i.e., without any LES closure) within the subgrid in this LES-LEM approach.

The concurrent subgrid and supergrid processes in LES-LEM evolve at their respective time scale and the resolution is chosen such that all the important length scales are resolved. Using the DOE-HAT combustor operating close to LBO as an example, Fig. 2 (a) shows that the flame thickness is resolved at the LES level (Δ_{LES}) and that the reaction zone (δ_{RR}) is resolved at the LEM level. The effect of a typical subgrid eddy (Δ_{Eddy}) (which is of the order of δ_{RR}) is explicitly included in the subgrid stirring model in LEM (Kerstein, 1991a).

The time-scales are also reasonably well resolved. The reaction-diffusion equations evolve at the characteristic time step which is a minimum of the diffusion time step, Δt_{diff} and the chemical time step Δt_{chem} . In the current study, $\Delta t_{diff} = \Delta t_{chem}$, and a direct integration (using SVODE) is used to evolve the finite-rate kinetics. The different time scales involved in this simulation are in Fig. 2 (b). The ratio of LES time (Δt_{LES}) to the stirring time (Δt_{stir}) step is shown in Figs. 3 (a) and (b). Here, Δt_{stir} is the time interval

between two successive small-scale stirring events. The stirring time decreases with increase in u' and as a result, a large number of stirring events occur in regions of high u' (e.g., shear layer). If combustion also occurs in these high u' regions, the flame structure can be significantly perturbed by subgrid turbulent fluctuations, even leading to local quenching.

The stirring events model the effect of turbulent eddies on the scalar field using a mapping procedure (Kerstein, 1991b). The eddy size is randomly chosen using a known PDF $f(l)$ (Sankaran and Menon, 2000) of eddy sizes l . The expected eddy size ($E(l) = \int_{\eta}^{\bar{\Delta}} f(l)l dl$) is an important parameter in LES-LEM. The variation of $(l_F/E(l))^2$, where l_F is the flame thickness, for an equivalence ratio (Φ) of 0.41 shows that, close to the dump plane where the flame is located (Fig. 3a), $(l_F/E(l))^2$ reaches 100, the stirring frequency is high and flame quenching is expected. At 12 mm from the dump plane (Fig. 3b), $(l_F/E(l))^2$ slightly decreases but Δt_{stir} increases much more and thus, the probability of flame quenching via aerodynamic stretch is reduced.

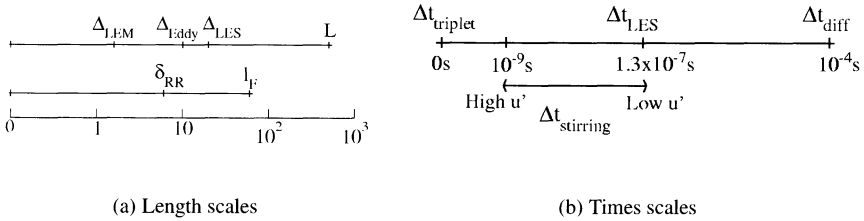


Figure 2. Length and time scale resolution for $\Phi=0.41$ in the DOE-HAT.

Finally, the Karlovitz number at the flame front (Ka_F) variation for different equivalence ratio is shown in Figs. 4(a-c) at various axial locations. Ka is large in regions of high turbulence (i.e., shear layers) and when Φ is decreased. Thus, as LBO is approached, combustion is in the BRZ regime in a significant region of the combustor. The current LES-LEM approach can simulate combustion in both the flamelet and the BRZ regime without requiring an ad hoc adjustments, and therefore, offers an approach to study LBO.

3. Flame Propagation and Emission Prediction

In the GLES approach, the G -equation model is used to locate the flame front and thus, to obtain the proper heat release without simulating a multi-species flow. Although very cost effective, GLES requires a model for the turbulent flame speed, $S_T = S_T(u', S_L)$, to close the GLES equation. A flame speed

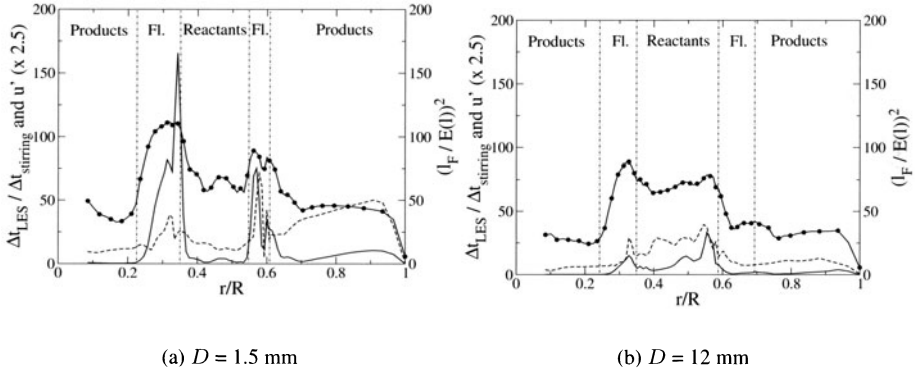


Figure 3. Radial variation of the local instantaneous $\Delta t_{LES} / \Delta t_{stirring}$, sub-grid velocity fluctuations u' and $(l_F/E(l))^2$ for $\Phi = 0.41$. Here, R is the combustion chamber radius and D is the axial distance from the dump plane. The region delimited by vertical lines and denoted *Fl.* represents the location of the flame. Legend: — : $\Delta t_{LES} / \Delta t_{stirring}$, - - : u' , -●- : $(l_F/E(l))^2$

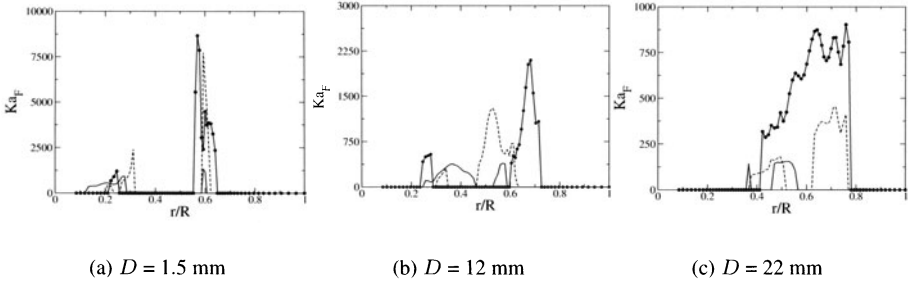


Figure 4. Radial profiles of the flame front Karlovitz number Ka_F for different equivalence ratio. $Ka_F = KaH$ where $H=1$ in the flame region and $H=0$ otherwise. Legend: - - : $\Phi=0.53$, -●- : $\Phi=0.44$, -●- : $\Phi=0.41$.

model $S_T = S_L(1 + \beta(u'/S_L)^2)^{1/2}$ (which has been calibrated in high Φ flamelet combustion for a fixed range of u'/S_L) was used earlier (Kim and Menon, 2000). As the mixture becomes lean, S_L decreases and so u'/S_L can become very large making this type of flame speed model invalid. As a result, the typical flame length predicted by this type of model is likely to be nonphysical. Furthermore, as combustion moves from TRZ to the BRZ regime, the flamelet assumption also breaks down. In contrast, in the LES-LEM approach, when a finite-rate mechanism is employed inside the LEM, the turbulent flame speed and the flame length (if they exist) can be *predicted* rather than modeled (as

in GLES). In the BRZ regime, LES-LEM allows the prediction of the heat release effect within the subgrid without requiring any flame speed model or thin-flame assumption.

Table I shows typical turbulent flame lengths predicted by LES-LEM and GLES under varying conditions. Here, for $S_{T,1} : \beta = 20.0, (u'/S_L)_{max} = 16.56$ and for $S_{T,2} : \beta = 10.0, (u'/S_L)_{max} = 10.0$. It is seen that the flame length can be adjusted significantly in the GLES approach, whereas the LES-LEM prediction is without any adjustment in the model. Since the operating conditions vary over a wide range of u'/S_L in a real gas turbine combustor, ad hoc adjustment of the S_T model is inappropriate.

Φ	LES-LEM	GLES $S_{T,1}$	GLES $S_{T,2}$
0.53	3.5	1.5	-
0.45	6.5	3.0	-
0.41	7.5	3.5	> 10.0

Table 1. Flame length (in cm) for different equivalence ratio and different combustion model.

The accuracy and computational cost of LES-LEM, however, does depend on the chemistry model employed. However, parallel optimization and improved kinetics modeling can address these issues. For example, the LES-LEM with five species but with no finite-rate kinetics is only 10 percent more expensive than GLES while LES-LEM with direct integration is 7 times more expensive. Techniques that have been shown to speed up chemistry evaluation, such as ISAT (Sankaran and Menon, 2000) and Artificial Neural Network (Menon, 2001) are currently being implemented.

In the present study, we compare the ability of GLES and LES-LEM to capture flame dynamics and heat release for a range of Φ , then evaluate their ability to predict CO and NO emission. Modeled transport equations for CO and NO are solved in the LES grid for both GLES and LES-LEM in exactly the same manner (Held et al., 2001; Eggenspieler and Menon, 2003a). CO prediction requires additional modeling for local quenching and the effect of UHC . Here, the steady-state Intermittent Turbulence Net Flame Stretch (ITNFS) model (Meneveau and Poinso, 1991) is employed without any change.

Figures 5a and b show respectively, CO and NO emission predictions in the DOE-HAT combustor. For $\Phi > 0.45$, CO emission is close to its equilibrium value while for $\Phi < 0.45$, UHC production due to flame quenching must be taken into account. The NO emission prediction is reasonable considering the models employed here. Although, the current predictions are limited by the global mechanism and the models employed, it can be seen that LES-LEM does a reasonable job at all the simulated conditions. The GLES also appears to do an adequate job as well, but the aforementioned issues regarding the

limitation of the flame speed model in the BRZ regime are still valid in these calculations. In fact past studies (Eggenspieler and Menon, 2003a) show that the S_T model parameters can be adjusted at low Φ to get a better agreement (even without inclusion of UHC effect). However, such ad hoc changes cannot be employed in LES of real systems.

For $\Phi < 0.5$, the ITNFS model indicates that 2 to 4 percent of the flame quenches. The LES-LEM approach is able to capture the effect of turbulent structures smaller than the flame thickness, and thus, aerodynamic quenching can be simulated provided that a proper chemical mechanism capable of extinction and re-ignition is employed. Future simulations will address this particular issue using ISAT/ANN approach.

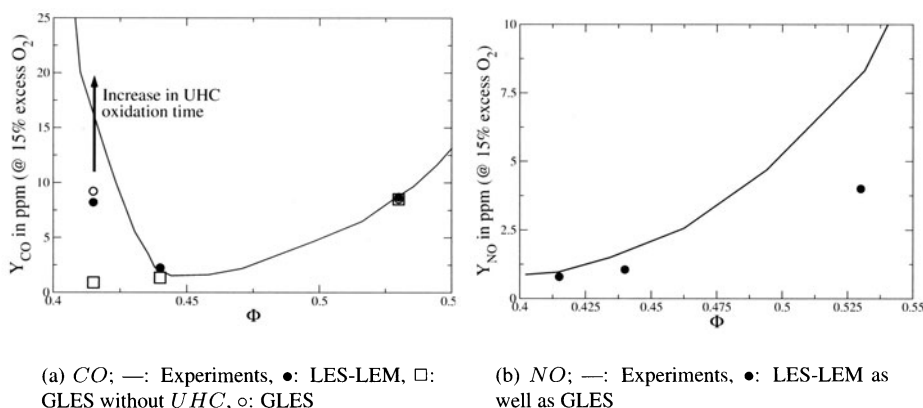


Figure 5. Prediction of CO and NO emission near LBO. Data for DOE-HAT at 38.1 cm downstream of the dump plane (Bhargava et al., 2000).

4. Conclusion

It is demonstrated in this study that combustion near LBO occurs in a regime where the classical flamelet assumption breaks down and this necessitates the need for an alternate method. The LES-LEM is developed and it is shown that it can be used over a wide range of operating conditions without requiring any model adjustments. Pollutant (CO and NO) emission is predicted using modeled equations and compared with data over a range of operating conditions. It is shown that inclusion of unburned hydrocarbons (UHC) due to local quenching is very important in the prediction of CO emission. Future studies will address pollutant emission near LBO by using a more realistic reaction mechanism within the LEM.

References

- Bédât, B. and Cheng, R. K. (1995). Experimental study of premixed flames in intense isotropic turbulence. *Combustion and Flame*, 100:486–494.
- Bhargava, A., Kendrick, D. W., Colket, M. B., Sowa, W. A., Casleton, K. H., and Maloney, D. J. (2000). Pressure effects on NO_x and CO emission in industrial gas turbines. *Trans. of the ASME*, 2000-GT-8.
- Chakravarthy, V.K. and Menon, S. (2000). Large-eddy simulations of turbulent premixed flames in the flamelet regime. *Combustion Science and Technology*, 162:1–48.
- Eggenspieler, G. and Menon, S. (2003a). Finite rate chemistry modeling for pollutant emission prediction near lean blow out. *AIAA-2003-4941*.
- Eggenspieler, G. and Menon, S. (2003b). LES of premixed combustion and pollutant emission in a doe-hat combustor. *AIAA-2003-0309*.
- Held, T. J., Mueller, M. A., and Mongia, H. C. (2001). A data-driven model for NO_x , CO and UHC emissions for a dry low emissions gas turbine combustor. *AIAA-2001-3425*.
- Kerstein, A. R. (1991a). Linear-eddy modeling of turbulent transport. part 6. microstructure of diffusive scalar mixing fields. *Journal of Fluid Mechanics*, 231:361–394.
- Kerstein, A. R. (1991b). Linear-eddy modeling of turbulent transport. part 5: Geometry of scalar interfaces. *Physics of Fluids A*, 3(5):1110–1114.
- Kim, W.-W. and Menon, S. (2000). Numerical simulations of turbulent premixed flames in the thin-reaction-zones regime. *Combustion Science and Technology*, 160:119–150.
- Kim, W.-W., Menon, S., and Mongia, H. C. (1999). Large-eddy simulation of a gas turbine combustor flow. *Combustion Science and Technology*, 143:25–62.
- Mansour, M.S., Peters, N., and Chen, Y.C. (1998). Investigation of scalar mixing in the thin reaction zones regime using a simultaneous ch-lif/rayleigh laser technique. *Proceedings of the Combustion Institute*, 27:767–773.
- Meneveau, C. and Poinso, T. (1991). Stretching and quenching of flamelets in premixed turbulent combustion. *Combustion and Flame*, 86:311–332.
- Menon, S. (2001). The use and relevance of reacting les on engineering design cycle. *Direct and Large Eddy Simulation IV*, pages 509–516.
- Menon, S. and Kerstein, A. R. (1992). Stochastic simulation of the structure and propagation rate of turbulent premixed flames. *Proceedings of the Combustion Institute*, 24:443–450.
- Pitsch, H. and Duchamp De Lageneste, L. (2002). Large-eddy simulation of premixed turbulent combustion using a level-set approach. *Twenty-Ninth Symposium (International) on Combustion*, pages 2001–2008.
- Sankaran, V. and Menon, S. (2000). The structure of premixed flame in the thin-reaction-zones regime. *Proceedings of the Combustion Institute*, 28 (to appear).
- Sankaran, V., Porumbel, I., and Menon, S. (2003). Large-eddy simulation of a single-cup gas turbine combustor. *AIAA-2003-5083*.
- Smith, T.M. and Menon, S. (1996). One-dimensional simulations of freely propagating turbulent premixed flames. *Combustion Science and Technology*, 128:99–130.
- Stone, C. and Menon, S. (2002). Adaptive swirl control of combustion instability in gas turbine combustors. *Proceedings of the Combustion Institute*, 29:155–160.

DIRECT NUMERICAL SIMULATION OF TURBULENT NON-PREMIXED FLAMES

Influence of transport model

Renan Hilbert and Dominique Thévenin

LSS (Lehrstuhl für Strömungsmechanik und Strömungstechnik)

Otto-von-Guericke-Universität Magdeburg

Postfach 4120

D-39016 Magdeburg, Germany

renan.hilbert@vst.uni-magdeburg.de, dominique.thevenin@vst.uni-magdeburg.de

Abstract The influence of the transport model used for the simulation of a turbulent non-premixed flame is investigated using Direct Numerical Simulations (DNS) of hydrogen/air flames, with a complete kinetic-chemical scheme and three different models for the evaluation of diffusion velocities. The results are post-processed in order to extract local flame structures in terms of profiles in the space of the mixture fraction. The differences induced by the use of the different transport models are discussed.

Keywords: Direct Simulation, Non-premixed Flames, Turbulent Combustion

1. Introduction

Turbulent non-premixed flames are encountered in many practical configurations such as direct injection Diesel engines, or gas turbine combustion chambers. They correspond to situations where the reactants, fuel and oxidizer, are not initially mixed and originate from two separate streams and thus rely on complex physical phenomena that are strongly coupled: turbulence, mixing of the reactants and chemical kinetics involving a large number of species and reactions. The Direct Numerical Simulation of turbulent non-premixed combustion is an ideally suited tool for the investigation of such flames (Vervisch and Poinso, 1998; Vervisch, 2000), that is a good help for the assessment of the importance of various physical mechanisms and for the development and improvement of RANS- or LES- turbulent combustion models (Veynante and Vervisch, 2002). In the first DNS studies of non-premixed turbulent flames, the combustion chemistry was approximated by a single-step model (Vervisch and Poinso, 1998). But, the growing need for accurate predictions of pollutant

species now leads to the necessity of a correct description of multi-component chemical systems and noticeable progress can only be achieved by taking into account to some extent detailed reaction schemes (Hilbert et al., 2003). Compared to non-reactive simulations, the simulation of reactive flows requires additional balance equations to be solved (one for energy and one for each chemical species considered) and physical models for the chemistry source terms and for transport properties (Thévenin et al., 1997; Poinso and Veynante, 2001). Detailed chemical kinetics of any practical fuel are thus nowadays still difficult to use in DNS.

In the present study, Direct Numerical Simulations of H_2/N_2 /Air turbulent non-premixed flames have been performed incorporating detailed models for chemistry and transport; the choice of hydrogen is motivated by the fact that this kinetic is well known and easily described by a small enough reaction scheme, thus allowing "reasonable" CPU times for the simulations. The effort is then intended towards the investigation of the effect of the transport model on flame structures while keeping the same chemistry.

In this paper, the numerical code and physical models are first described, and the configuration is presented. Typical results are shown, that put into evidence the necessity of an adequate post-processing methodology to extract physically meaningful information. Results are then presented and discussed in terms of local flame structures in the mixing space.

2. Numerics

The DNS code employed in this work, called *parcomb*, has been described in detail in previous publications (Thévenin et al., 1996) and already used for flame structure analysis and model development (Hilbert et al., 2002). It solves the full compressible Navier-Stokes equations. The flow solver is coupled with libraries for chemistry and transport, that allow to take into account detailed multi-step reaction schemes, an accurate description of thermodynamic coefficients (determined using 5th-order polynomial fits of experimental measurements), and different levels of modelling for the description of diffusion velocities. The initiation of a pseudo-turbulent velocity field is performed in the associated Fourier space, via a von Kármán spectrum with Pao correction, in the form given by Hinze (Hinze, 1975). The phases of the turbulent velocity components are considered to be uncorrelated and are therefore given by a random-number generator. In this study, a chemical scheme involving 8 species (H_2 , O_2 , H_2O , H , O , OH , HO_2 , H_2O_2) plus nitrogen and 37 irreversible elementary reactions (Maas and Warnatz, 1988) is used to describe combustion of H_2 in Air and three models are considered for the expression of the diffusion velocities of the species and briefly described now. The differences mainly lie

in the way the diffusion coefficients are calculated. Precise formulations and more details can be found elsewhere (Hilbert et al., 2003).

The Lewis number is non-dimensional and compares the species diffusivity to the heat conductivity. It is defined as:

$$\text{Le}_i = \frac{\lambda}{\rho C_p D_i} \quad (1)$$

with λ the thermal conductivity of the mixture, ρ the density, C_p the specific heat capacity at constant pressure and D_i the diffusion coefficient of the species i into the mixture. Based on this definition, the unity Lewis number approach assumes that all the species Lewis numbers are constant and equal to one, i.e. that all species have the same diffusion coefficient as heat. In this case, differential diffusion between species is obviously not accounted for, but this assumption is very useful in simple cases, especially when only two reacting species are considered, because it allows to derive theoretical solutions for simplified flame structures (Burke and Schumann, 1928; Williams, 1985).

For the second case, a constant value of the Lewis number is given for each individual species in the flow. In this case, differential diffusion, i.e. the fact that lighter species can diffuse faster than heavier ones in the mixture, is accounted for. The diffusion coefficient is deduced from the thermal conductivity. The values retained here for the Lewis numbers are : $\text{Le}_{H_2} = 0.30$, $\text{Le}_{O_2} = 1.10$, $\text{Le}_{H_2O} = 0.83$, $\text{Le}_H = 0.18$, $\text{Le}_O = 0.70$, $\text{Le}_{OH} = 0.73$, $\text{Le}_{HO_2} = 1.10$, $\text{Le}_{H_2O_2} = 1.12$, $\text{Le}_{N_2} = 0.92$.

The third case corresponds to the use of a mixture-averaged diffusion coefficient, in the form given by Hirschfelder (Hirschfelder et al., 1954). This model is sometimes denoted as "zero-th order approximation" as it corresponds to keep only the diagonal terms of the complete diffusion matrix (Ern and Giovangigli, 1994) and is the one also used in the package TRANSPORT (Kee et al., 1983) from Sandia. The main difference with the preceding model is that, in this case, the species diffusion coefficient is directly dependent on the local composition, pressure and temperature. Note that for the two last approaches, mass conservation is not automatically ensured and that a correction velocity has to be used to overcome this problem (Poinso and Veynante, 2001; Hilbert et al., 2003).

Three similar simulations have been run with *parcomb*, where the only difference was the transport model, with the three different levels described above. For each calculation, a laminar non-premixed flame of hydrogen diluted in nitrogen and air is first ignited in a one dimensional configuration with *parcomb*. The initial conditions correspond to $Y_{H_2} = Y_{H_2}^\infty = 0.0291$ and $T = 300$ K on the fuel side, $Y_{O_2} = Y_{O_2}^\infty = 0.233$ and $T = 300$ K on the oxidizer side. An appropriate nitrogen complement is added everywhere. With these values, the global mixture ratio ϕ equals 1.0. A uniform grid spacing of $25 \mu\text{m}$ is used in

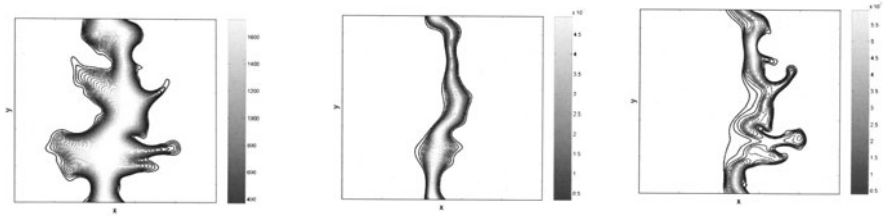


Figure 1. Typical turbulent 2D DNS results: instantaneous fields of temperature, mass fractions of intermediate species OH and of minor species H_2O_2 obtained with the detailed transport model.

both directions, resulting in a 401×401 grid mesh for a $1 \text{ cm} \times 1 \text{ cm}$ two-dimensional domain. After the initialisation of the 1D laminar flame, resulting profiles are uniformly extended in the y -direction and a pseudo-turbulent velocity field is imposed on top of it. In the x -direction, both boundaries are considered as non-reflecting outflow boundaries with pressure relaxation, while periodicity is assumed along the y -direction. The same random numbers have been used three times, so that the initial synthetic turbulent velocity field is exactly the same in each case. It corresponds to a RMS velocity $u' = 2.19 \text{ m/s}$ and an integral turbulent length-scale $\Lambda = 1.0 \text{ mm}$, resulting in a turbulent Reynolds number $Re_t = 139$, associated with an eddy turn-over time $t_c = \Lambda/u' = 0.45 \text{ ms}$.

3. Typical results

As time evolves during the simulation, turbulence is slowly decaying and interacts with the initially-flat profiles. Turbulence wrinkles the flame front and either thickens or enlarges it, depending on the local conditions. On the other hand, the heat released by the chemical activity in the vicinity of the flame front modifies the local properties of the turbulence through viscous damping. Turbulent results are analysed after two characteristic eddy-turn over times, i.e. 0.90 ms after the 2D restart of the simulation. A Linux PC with a 2Ghz processor and 1Gb RAM was used for the simulations. The resulting computing time was about 70 hours for each of the three turbulent simulations. Typical results are displayed in Fig. 1. These simulations deliver a huge amount of data to post-process (Thévenin and Baron, 1999).

4. Post-processing and discussion

The physical description of turbulent non-premixed combustion often relies on the introduction of a conserved scalar, denoted as the mixture fraction that takes value 0 on the oxidizer side and 1 on the fuel side, and allows a formal decoupling between turbulent mixing on one hand and a description of the local flame structure in the mixing space (or Z -space) on the other hand. Local turbulent flame structures can then be considered to be dependent on the action of the turbulent field on the flame front, expressed via the scalar dissipation rate χ (Veynante and Vervisch, 2002). In simplified cases, analytical relations may be obtained, but the use of detailed chemistry and transport modify the classical assumptions. A better understanding of the local turbulent flame structures (in terms of profiles in the mixture fraction space) when multi-step chemistry and differential diffusion are accounted for is thus a key element for the development of turbulent combustion models.

When taking into account multiple species and differential diffusion, it is not possible to give a unique definition for the mixture fraction Z (Hilbert and Thévenin, 2001). The following definition is used here (Bilger, 1988):

$$Z = \frac{1/2Z_H/W_H + (Z_O^\infty - Z_O)/W_O}{1/2Z_H^\infty/W_H + Z_O^\infty/W_O} \quad (2)$$

where W denotes molar weight, Z_j the mass fraction of element j in the mixture, and ∞ initial compositions on respectively oxidizer and fuel sides. With this definition, the stoichiometric conditions correspond here to $Z = Z_{st} = 0.5$. The definition of the scalar dissipation rate χ , is also not straightforward because of the non-unicity of the value of the diffusion coefficient when considering differential diffusion (Hilbert et al., 2002). The expression retained here is based on the heat diffusion coefficient λ , to allow comparisons between the different simulations:

$$\chi = 2 \frac{\lambda}{\rho C_p} |\nabla Z|^2 \quad (3)$$

where ρ is the density and C_p the mean specific heat. Physically, χ is the inverse of a diffusion time and characterises the speed at which the reactants move towards each other on a molecular level, and is therefore often retained as a characteristic parameter to quantify the effects of finite rate chemistry and the departure from equilibrium.

The post-processing of turbulent results is performed as follows: the flame front is first identified to the isoline of mixture fraction corresponding to the stoichiometric conditions $Z = Z_{st}$. On each of the points along this curve one can define a cut line: the starting point is the considered point and every following point is determined by following the local gradients of mixture fraction. The advancement step is chosen to be constant. The value of the scalar dissipation rate at the stoichiometry, and profiles of species mass fractions, heat

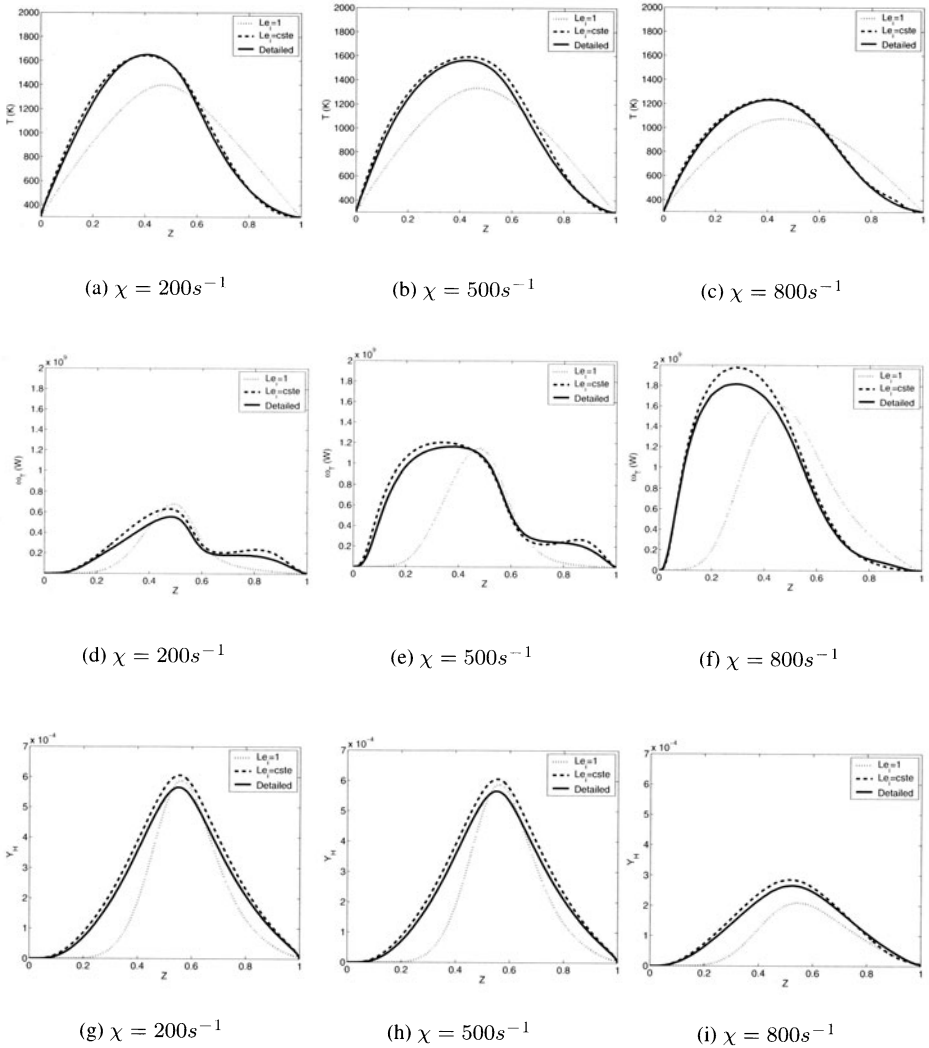


Figure 2. Typical local flame structures: temperature (top), heat release (middle) and H mass fraction (bottom)

release, mixture fraction and temperature along the cuts across the Z -isolevels are extracted from the 2D DNS results, using specific routines developed with the commercial software Matlab, to allow automatic post-processing. Typical results are presented on Fig. 2 in the form of local flame structures obtained through the post-processing methodology described above, correspond-

ing to different values of the scalar dissipation rate. The flame structures obtained with the constant non-unity Lewis numbers and the mixture-averaged diffusion velocities are very similar. In this case, the Lewis number approach yields a good approximation of detailed transport, contrarily to what could be observed previously in other configurations (Hilbert and Thévenin, 2002). As expected, the maximum flame temperature decreases (Fig. 2(a) to 2(c)) and the heat released (Fig. 2(d) to 2(f)) increases with increasing values of the dissipation rate. It also appears clearly that differential diffusion plays a significant role on local flame structure. The obtained profiles are symmetric relatively to the stoichiometric conditions $Z = Z_{st} = 0.5$ when unity Lewis numbers are considered (which is consistent with theoretical approaches), but no more when differential diffusion is accounted for. In this case, the fact that the lightest species are carried faster towards the reaction zone completely changes the burning rate repartition (Fig. 2(d) to 2(f)). The reaction is enhanced in the $Z < Z_{st}$ domain because of the highest presence of H (Fig. 2(g) to 2(i)) and H_2 (not shown).

5. Conclusions

A turbulent non-premixed H_2 /Air flame has been simulated using direct numerical simulations with a complete chemical scheme and three different levels of modelling of the diffusion velocities: unity Lewis numbers for all species, constant non-unity Lewis numbers and multicomponent diffusion velocities with Hirschfelder's formulation. The comparison of the flame structures obtained with the different models was performed and discussed. More work is needed to increase our understanding of non-premixed flame structures, in particular these results will be checked in the future in 3D simulations (Thévenin et al., 2002).

References

- Bilger, R. W. (1988). The structure of turbulent nonpremixed flames. *Proc. Combust. Inst.*, 22:475–488.
- Burke, S. P. and Schumann, T. E. W. (1928). Diffusion flames. *Industrial and Engineering Chemistry*, 20:998–1005.
- Ern, A. and Giovangigli, V. (1994). *Multicomponent Transport Algorithms*. Lecture Notes in Physics, New Series M: Monographs. Springer-Verlag, New York, NY.
- Hilbert, R., Tap, F., El-Rabii, H., and Thévenin, D. (2003). Impact of detailed chemistry and transport on turbulent flames simulations. *Prog. Energy Combust. Sci.* Accepted for publication.
- Hilbert, R., Tap, F., Veynante, D., and Thévenin, D. (2002). A new modeling approach for the autoignition of a nonpremixed turbulent flame using DNS. *Proc. Combust. Inst.*, 29. In press.
- Hilbert, R. and Thévenin, D. (2001). Turbulent non-premixed flames investigated using direct simulations with detailed chemistry. In Pollard, A. and Candel, S., editors, *Proc. IUTAM*

- Symposium on Turbulent Mixing and Combustion*, pages 251–258. Kluwer Academic Publishers.
- Hilbert, R. and Thévenin, D. (2002). Autoignition of turbulent non-premixed flames investigated using direct numerical simulations. *Combust. Flame*, 128(1–2):22–37.
- Hinze, J. O. (1975). *Turbulence in Fluids*. McGraw Hill Book Company.
- Hirschfelder, J. O., Curtiss, C. F., and Bird, R. B. (1954). *Molecular Theory of Gases and Liquids*. John Wiley & Sons.
- Kee, R. J., Warnatz, J., and Miller, J. A. (1983). A FORTRAN computer code package for the evaluation of gas-phase viscosities, conductivities, and diffusion coefficients. Technical Report SAND89-8009, Sandia National Laboratories.
- Maas, U. and Warnatz, J. (1988). Ignition processes in carbon-monoxide-hydrogen-oxygen mixtures. *Proc. Combust. Inst.*, 22:1695–1704.
- Poinsot, T. and Veynante, D. (2001). *Theoretical and numerical combustion*. R. T. Edwards.
- Thévenin, D. and Baron, R. (1999). Investigation of turbulent non-premixed flames using direct numerical simulations with detailed chemistry. In Chollet, J. P., Voke, P. R., and Kleiser, L., editors, *Direct and Large Eddy Simulation III*, pages 323–334. Kluwer Academic Publishers.
- Thévenin, D., Behrendt, F., Maas, U., Przywara, B., and Warnatz, J. (1996). Development of a parallel direct simulation code to investigate reactive flows. *Comp. Fluids*, 5(25):485–496.
- Thévenin, D., Gicquel, O., de Charentenay, J., Hilbert, R., and Veynante, D. (2002). Two- versus three-dimensional direct simulations of turbulent methane flame kernels using realistic chemistry. *Proc. Combust. Inst.*, 29.
- Thévenin, D., van Kalmthout, E., and Candel, S. (1997). Two-dimensional direct numerical simulations of turbulent diffusion flames using detailed chemistry. In Chollet, J. P., Voke, P. R., and Kleiser, L., editors, *Direct and Large Eddy Simulation II*, pages 343–354. Kluwer Academic Publishers.
- Vervisch, L. (2000). Using numerics to help understand nonpremixed turbulent flames. *Proc. Combust. Inst.*, 28:11–24.
- Vervisch, L. and Poinsot, T. J. (1998). Direct numerical simulation of non premixed turbulent flames. *Ann. Rev. Fluid Mech.*, 30:655–692.
- Veynante, D. and Vervisch, L. (2002). Turbulent combustion modeling. *Prog. Energy Combust. Sci.*, 28(3):193–266.
- Williams, F. A. (1985). *Combustion theory*. Addison-Wesley, 2nd edition.

TRANSIENT INFLOW-DATA FOR LES

The importance for real flames

A. Kempf, M. Klein, J. Janicka

Fachgebiet Energie- und Kraftwerkstechnik

Technische Universität Darmstadt, Germany

akempf@gmx.net, kleinm@hrzpub.tu-darmstadt.de

Abstract Transient inflow-conditions have a great effect on the LES/DNS of isothermal jets. Non-premixed jet-flames are even more sensitive to the inflow-conditions, since they influence mixing, stabilization and combustion at the nozzle. In this work, an LES and a steady flamelet model are used to compute the flow- and species fields. The turbulence-properties on the inflow are varied and their influence is investigated. The main-focus of this paper is to point out the importance of realistic transient inflow-conditions – in particular for reactive flows.

Keywords: LES, Inflow-Data, Artificial Turbulence, Non-Premixed Combustion, Flamelets

1. Introduction

It is well accepted that instable flows strongly depend on small perturbations. For example, the break-up point of turbulent jets is strongly influenced by the fluctuations found at the nozzle. In most simulations, the nozzle plane will be located on the inflow-boundary of the computational domain, so that the turbulence in the nozzle must be described by proper boundary conditions. For Reynolds Averaged Navier Stokes Simulations (RANS) this is obvious and can easily be accomplished. (For example, with the $k-\epsilon$ -model, the turbulent kinetic energy and the lengthscale must be set.) With Large Eddy Simulation (LES) or Direct Numerical Simulation (DNS), this is more complicated since the turbulent flow from the nozzle must be represented by transient boundary conditions on the inflow-plane. The strong effects of these transient boundary-conditions on LES/DNS have already been pointed out for plane jets [6, 11], two-phase-flow jets [6] and a flow with mixing behind an obstacle [5]. However, non-premixed flames may be even more sensitive to the inflow-conditions which determine mixing and combustion at the nozzle – and thus flame stabilization. To investigate their effect, a new inflow-generator for arbitrary geometries is applied to a well investigated jet-flame and the integral lengthscale

L is varied. This allows to discuss the influence of this inflow-parameter and will underline the importance of realistic inflow-conditions for LES and DNS. In the first section of this paper, the theory of large eddy simulation and flamelet modeling are revisited, the numerical procedure is sketched and the new inflow-data generator is presented. Next, the experimental and numerical setups are shown before the results are discussed in section three.

2. Simulation

The accurate transport equation for a given quantity Φ comprises the whole spectrum of lengthscales. To only describe the large-scale features of Φ , a spatial low-pass filter is applied. The resulting filtered equations describe the transport of the filtered fields. The difference between the filtered field $\bar{\Phi}(x_j, t)$ and the original field $\Phi(x_j, t)$ is the fine-structure $\Phi'(x_j, t)$. This work applies a top-hat filter that is based on the computational cell. With the finite volume approach, this Schumann-filter [12] simplifies the numerical procedure: Schumann-filtering is performed implicitly by approximating the values at the center of a cell with the mean value for the whole cell. Filtering the governing equations yields unknown correlations $\overline{\varrho\Phi}$ with the density ϱ . Defining $\tilde{\Phi} = \overline{\varrho\Phi}/\bar{\varrho}$, these equations are solved for Favre-filtered quantities $\tilde{\Phi} \neq \bar{\Phi}$.

2.0.1 Modeling of transport. The temporal development of the flame's large-scale features is computed by solving the modeled transport equations (1, 2, 3) for the (Favre-) filtered density $\bar{\varrho}$, velocity \tilde{u}_i and mixture fraction \tilde{f} , where incompressibility ($\partial\bar{\varrho}/\partial\bar{p} = 0$ but $\partial\bar{\varrho}/\partial\tilde{f} \neq 0$) is assumed.

$$\frac{\partial\bar{\varrho}}{\partial t} + \frac{\partial}{\partial x_j} (\bar{\varrho}\tilde{u}_j) = 0 \quad (1)$$

$$\begin{aligned} \frac{\partial}{\partial t} (\bar{\varrho}\tilde{u}_i) + \frac{\partial}{\partial x_j} (\bar{\varrho}\tilde{u}_i\tilde{u}_j) = \frac{\partial}{\partial x_j} \left[\bar{\varrho}(\nu_t + \nu) \left(\frac{\partial\tilde{u}_j}{\partial x_i} + \frac{\partial\tilde{u}_i}{\partial x_j} \right) \right] \\ - \frac{2}{3} \frac{\partial}{\partial x_j} \left[\bar{\varrho}(\nu_t + \nu) \frac{\partial\tilde{u}_k}{\partial x_k} \delta_{ij} \right] - \frac{1}{3} \frac{\partial}{\partial x_i} \bar{\varrho}\tau_{kk}^{\text{sgs}} + \frac{\partial\bar{p}}{\partial x_i} + \bar{\varrho}g_i \end{aligned} \quad (2)$$

$$\frac{\partial}{\partial t} (\bar{\varrho}\tilde{f}) + \frac{\partial}{\partial x_j} (\bar{\varrho}\tilde{f}\tilde{u}_j) = \frac{\partial}{\partial x_j} \left(\bar{\varrho} \left(\frac{\nu_t}{\sigma_t} + \frac{\tilde{\nu}}{\sigma} \right) \frac{\partial\tilde{f}}{\partial x_j} \right) \quad (3)$$

The filtered continuity equation (1) is similar to the original equation. The momentum equation (2) includes the filtered pressure \bar{p} and the gravitation $\bar{\varrho}g_i$. The subgrid-contribution to the momentum flux is modeled by the eddy viscosity ν_t and the trace of the subgrid-stress tensor τ_{kk}^{sgs} . This term can be discarded when a pressure parameter $\bar{P} = \bar{p} - 1/3\bar{\varrho}\tau_{kk}^{\text{sgs}}$ is introduced, which is determined by the pressure correction scheme. In the equation (3) for the filtered

mixture fraction \tilde{f} , the subgrid-fluxes are modeled from the eddy-diffusivity (ν_t/σ_t), which is determined from a turbulent Schmidt-number of $\sigma_t = 0.45$ [10]. The Smagorinsky model (4) [13] yields the turbulent viscosity that is required in eqs. (2) and (3). Its parameter C_s is provided by the dynamic Germano procedure [4] and the lengthscale Δ is equated with the filter width.

$$\nu_t = (C_s \Delta)^2 \sqrt{\frac{1}{2} \left(\frac{\partial \tilde{u}_j}{\partial x_i} + \frac{\partial \tilde{u}_i}{\partial x_j} \right)^2} \quad (4)$$

2.0.2 Modeling of combustion. This work uses the mixture fraction approach to determine the chemical state. The mixture fraction f is the local ratio of mass from the fuel-stream to the overall mass. Thus, $f = 0$ describes pure oxidizer, $f = 1$ pure fuel. For $0 < f < 1$, a mixture of oxidizer, fuel, products and intermediate species exists. Here, Bilger's definition of f is applied [1]. From the mixture-fraction f , the species mass-fractions x_α , are computed with the steady flamelet equation (5). Here, S_{x_α} denotes the chemical source-terms provided by a reaction mechanism. The scalar rate of dissipation χ is a function of the coefficient of diffusion (ν/σ) and the mixture fraction field f .

$$-\varrho \frac{\chi}{2} \frac{\partial^2 x_\alpha}{\partial f^2} = S_{x_\alpha} \quad (5)$$

$$\chi = 2 \frac{\nu}{\sigma} \left(\frac{\partial f}{\partial x_j} \frac{\partial f}{\partial x_j} \right) \quad (6)$$

With the mixture-fraction approach and equations (5) and (6), the species concentrations x_α , the temperature, the density and the viscosity are a function of the mixture-fraction f and the scalar rate of dissipation χ only.

In LES, only the filtered mixture fraction \tilde{f} and scalar rate of dissipation $\tilde{\chi}$ are known. However, any dependent quantity Φ (e. g. x_α , ϱ) is a non-linear function of f and χ , so that the subgrid-distribution of f and χ must be considered. The subgrid-distribution of the mixture fraction is assumed to be described by a β -PDF, which is a function of the subgrid-variance $\widetilde{f''^2}$. The subgrid-distribution of the scalar rate of dissipation, is assumed to follow a Dirac-function δ here. Thus, all dependent scalars can be computed from $(\tilde{f}, \tilde{\chi}, \widetilde{f''^2})$. This dependency is pre-integrated and tabulated, so that $\tilde{\Phi}$ can be determined by linear interpolation from the table. For the density, this table must be resolved very well to allow a stable and accurate LES.

The subgrid-variance $\widetilde{f''^2}$ is modeled as the resolved variance in a test-filter cell of twice the volume of the normal cell. This model has been suggested and applied by Forkel [3] and shows very good numerical properties. The filtered scalar rate of dissipation $\tilde{\chi}$ is estimated using the model by de Bruyn Kops et al. [2], who rely on the eddy-viscosity approach (eq. (7)).

$$\tilde{\chi} = 2 \left(\frac{\nu}{\sigma} + \frac{\nu_t}{\sigma_t} \right) \left(\frac{\partial \tilde{f}}{\partial x_j} \frac{\partial \tilde{f}}{\partial x_j} \right) \quad (7)$$

2.1 Numerical procedure

Following Forkel et al. [3], the conservation equations for mass $\bar{\varrho}$ (1), momentum $\bar{\varrho} u_i$ (2) and mixture $\bar{\varrho} f$ (3) were transformed to cylindrical coordinates (x, r, ϕ) and discretized by finite volumes. An explicit three-step low-storage Runge-Kutta scheme advances the solution from time-step n to $n+1$. For the scalars, each Runge-Kutta sub-step m features a prediction- and a correction-step to match the density computed from the chemical state and the density resulting from transport. Since only conserved scalars ($\bar{\varrho}$ and $\bar{\varrho} f$) are transported, the scheme was implemented in a fully conservative way and called “Echt Konservativer Transport” (EKT, fully conservative transport).

Diffusive fluxes of scalars and momentum were discretized by second order central schemes. For the convective fluxes of momentum, second order central schemes minimize numerical dissipation. However, the convection of $\bar{\varrho}$ and $\bar{\varrho} f$ was discretized by a TVD scheme, which ensures boundedness and inhibits numerical oscillations without introducing too much numerical diffusion.

2.2 Generating Inflow-Data

To describe the turbulence entering the solution domain, an inexpensive procedure is sought that reproduces the statistical properties of the flow. Such a procedure was suggested and tested by Klein [6] and has already been used by Kempf et al. [5]. This procedure creates a fluctuating signal \mathcal{U}_i in 3D, which corresponds to a prescribed spectrum or an integral lengthscale L . This signal is then scaled to result in a velocity field representing the appropriate Reynolds-Stress-Tensor.

The signal-generation is based on a random-field, which does not have a turbulent spectrum or lengthscale yet. However, by convolution with an appropriate filter, all modes can be filtered to result in a field \mathcal{U}_i with a turbulence-like spectrum and the proper lengthscales. Assuming that the two-point correlation function is a Gaussian, Klein [6] deduced a relation between the filter-coefficients and the integral lengthscale L .

Subsequently, the turbulent velocity fields u_i must be computed from the scalar fields \mathcal{U}_i . Therefor, the scalar fields \mathcal{U}_i are conditioned to a mean value of $\langle \mathcal{U}_i \rangle = 0$ and to correlations of $\langle \mathcal{U}_i \mathcal{U}_j \rangle = \delta_{ij}$. Then, the velocity field is constructed from the given Reynolds-Stress-Tensor R_{ij} according to the relation $u_i = \langle u_i \rangle + a_{ij} \mathcal{U}_j$. The tensor a_{ij} (eq. 8) is given by Lund et al. [8].

Following this procedure, a pseudo turbulent velocity field u_i is created. Slices of this are extracted and applied as inflow-data to the LES. It must be stressed

that the pseudo-turbulent velocity field does not satisfy the continuity equation, since it is based on statistical properties only. However, this procedure generates turbulence-like structures at a negligible computational cost.

$$a_{ij} = \begin{bmatrix} R_{11}^{0.5} & 0 & 0 \\ R_{21}/a_{11} & (R_{22} - a_{21}^2)^{0.5} & 0 \\ R_{31}/a_{11} & (R_{32} - a_{21}a_{31})/a_{22} & (R_{33} - a_{31}^2 - a_{32}^2)^{0.5} \end{bmatrix} \quad (8)$$

The former procedure relies on digital filters. Since these filters are defined in logical coordinates, the method will only provide the proper lengthscales on an equidistant Cartesian grid. However, instead of low-pass filtering the random field, a diffusion-process can be applied as well. Since diffusion is a process in physical space, this method works on any grid. It will be described in the following section.

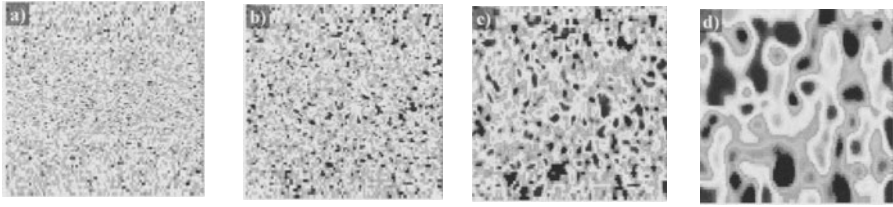


Figure 1. Plot of signal fields \mathcal{U}_j of different integral lengthscale L . The plots show a $50 \text{ mm} \times 50 \text{ mm}$ domain in the $x - r$ plane. The signals are scaled to $\sigma = 1$. The original random field is shown in (a). The integral lengthscales L of the following plots (b), (c) and (d) are 0.5 mm, 1 mm and 3 mm.

To start with, a random signal-field \mathcal{U}_j is created and normalized by the variance σ . Such a random field (in 2D) is shown in fig. 1.a. In the next step, diffusion according to

$$\frac{\partial \mathcal{U}_i}{\partial t} = \frac{\partial}{\partial x_j} \left[\mathcal{D} \frac{\partial \mathcal{U}_i}{\partial x_j} \right] \quad (9)$$

is applied to the random fields. This diffusion process removes the smallest structures and leaves the large structures unchanged, similar to a low-pass filter (so called “diffusion-filters” behave like diffusion on grids of cuboid cells). Hence, the typical lengthscale L in the field is increased by diffusion. Little diffusion leads to small lengthscales (fig. 1.b), while strong diffusion results in large lengthscales (fig. 1.d). Since diffusion reduces the amplitude of the random-fields \mathcal{U}_j , they must be normalized again.

Finally, the signal fields \mathcal{U}_j must be transformed to velocity fields, following the Lund-procedure as described in the previous section.

The inherent elegance of this approach is that every (Navier-Stokes) CFD code features modules for momentum diffusion. Hence, the correlated fluctuation fields can easily be generated from such codes. This just requires to add noise to the mean velocities and run the CFD-code with no convection or pressure correction, which will yield the proper fluctuating signals U_i . As well, this approach can be used to generate turbulent initial conditions, which can be very useful to speed up the convergence towards statistically constant fields.

3. Experimental and Numerical Setup

The "EKT Standardbrenner" [9] consists of a long fuel-pipe feeding the flame. Its diameter D is 8 mm and its length ensures fully developed turbulence. It ejects fuel at a bulk-velocity of 36.3 m/s, corresponding to a Reynolds number of $Re = 16,000$. Coaxial to the pipe, a wind-tunnel generates a laminar coflow (0.2 m/s), which feeds LDV particles and reduces environmental influence on the flame. In Tacke's hydrogen diluted Flame (HD) [14], the fuel consists of 23 % vol. of hydrogen and 77 % vol. of nitrogen. The jet velocity is close to the experimentally determined blow-off limit of 38.5 m/s, so that a significant amount of non-equilibrium chemistry occurs.

To model this flame, a cylindrical grid discretizes a computational domain of $30.5 D$ in diameter and $22.5 D$ in length. This is resolved by $257 \times 40 \times 32$ cells in axial, radial and circumferential direction, which is well sufficient for pointing out the influence of the inflow-boundary condition. On the inflow plane, the laminar coflow velocities and the transient velocities for the fully developed pipe-flow were enforced. The lengthscale L of the jet-turbulence was varied. The mixture fraction was set to 1 within the nozzle and 0 outside. For pressure, a zero gradient condition was applied. On the outflow plane, von Neumann conditions describe all quantities and on the annular surface, pressure and mixture fraction were set at zero. To allow for entrainment, the velocities are determined by solving a simplified momentum equation there. This leads to a typical CPU time of 100 hours on a PC (SPECfp2000 ≈ 1000).

4. Results

Four simulations of flame HD were performed for different inflow lengthscales L . All other parameters remained fixed to values obtained by Lawn [7]. The lengthscale L was determined from a simplified mixing-length approach $L = C \Delta_{wall}$, based on the wall-distance $\Delta_{wall} = D/2 - r$. The leading constant C is varied and its influence is discussed for $C \in \{0.2, 0.33, 0.66, 1.0\}$. For reference, another simulation was performed where only noise was applied to the inflow-cells, leading to fluctuations on the smallest resolved lengthscale. Figure 2.a shows the decay of the mean axial velocity along the centerline. For $C = 0.33$, the best prediction of the experimental data-points is obtained,

whereas with the bigger lengthscales, the spreading of the jet is over-estimated. For the means of mixture-fraction (fig. 2.c) and temperature (fig. 2.e), the same trend is observed. Furthermore, figs. 2.c and 2.e portend that the main difference between the results is a shift of the break-up point – as expected for non-reactive jets. This is consistent with the theory that perturbations just trigger the break-up, but further downstream, the jet develops independently from the inflow-conditions. For none-reactive jets, a self-similar flow would be observed, which can not be the case with combustion.

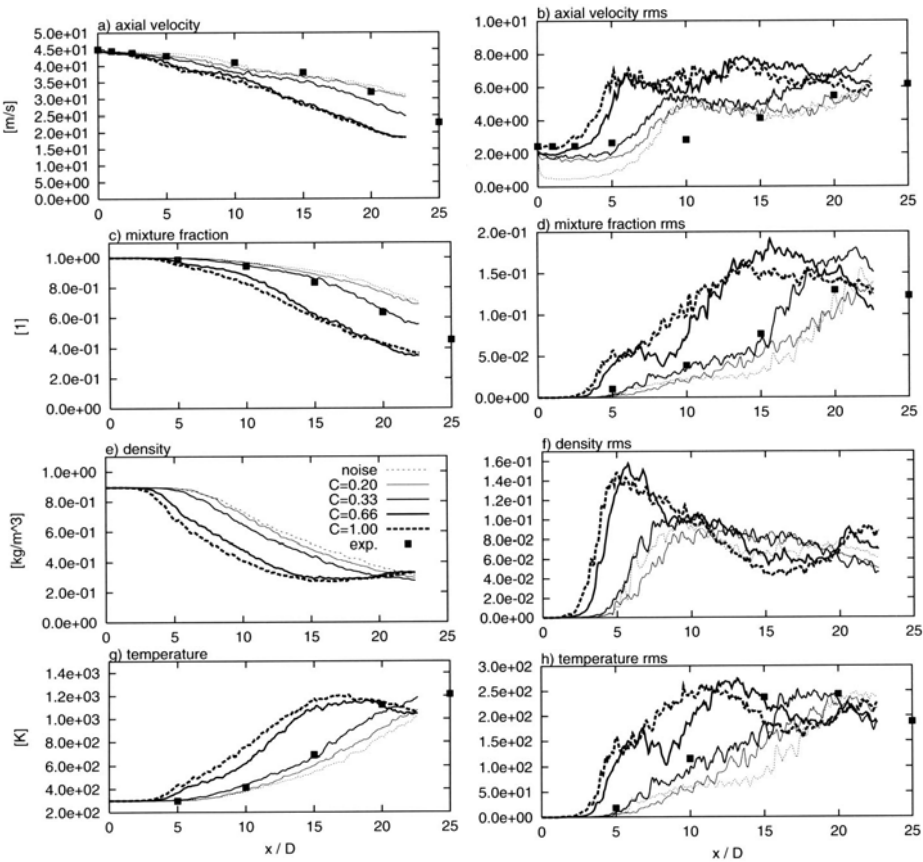


Figure 2. Development of means and fluctuations along the centerline. Large lengthscale fluctuation triggers jet-break up. For the caption, please refer to fig. 2.e.

Apart from the means, figure 2 shows the fluctuations of velocity, mixture-fraction, density and temperature as well. Here again, inspection reveals that the profiles are shifted upstream with increasing lengthscale. However, the maximum fluctuation-level of velocity and density is affected by the inflow-lengthscale as well: When the jet-breaks up closer to the nozzle, stronger fluctuation occurs. Especially the density (fig. 2.f), shows the sudden break-up.

A very interesting behavior is observed for the velocity fluctuation with “noise” inflow-condition (fig. 2.b): Almost all fluctuations are dissipated at the nozzle and only little turbulent kinetic energy enters the computational domain. This is due to the too short lengthscales imposed with noise.

Overall, a very reasonable prediction was obtained for the setting $C = 0.33$. For smaller values, the jet breaks up too late, for higher values, it will break up too close to the nozzle. Only a reasonable setting of the inflow-lengthscale allows for the proper prediction of the flow.

5. Conclusions

A grid-independent approach for generating transient, pseudo-turbulent inflow data for LES has been applied to jet-flames. A study, where the lengthscales were varied, shows the great effect the inflow-perturbations take on the break up of reactive jets. Without setting these proper lengthscales, reasonable results can hardly be expected – especially for reactive flows.

Acknowledgments

The authors gratefully acknowledge the financial support by the DFG (German Research Council) Sonderforschungsbereich 568 “Flow and Combustion in Future Gas Turbine Combustion Chambers”.

References

- [1] Bilger, R., Starnner, S., Kee, R., *Combust. Flame*, 80: pp. 135 - 149, 1990
- [2] S.M. de Bruyn Kops, J.J. Riley, G. Kosaly, Western States Section of the Combustion Institute, Spring Meeting: Paper No. 97S-051, 1997
- [3] H. Forkel, J. Janicka, *Large-Eddy Simulation of a turbulent Hydrogen Diffusion Flame*, 1st Symposium on Turbulent Shear Flow Phenomena, 1999
- [4] M. Germano, U. Piomelli, P. Moin, W. Cabot, *Phys. Fluids A* 3: pp. 1760 - 1765, 1991
- [5] A. Kempf, M. Klein, R. Bauer, A. Sadiki, J. Janicka, 9th Intl. Conference on Combustions, Paper No. 76: p. 27, Sorrento, Italy, 2002
- [6] M. Klein, A. Sadiki, J. Janicka, *J. Comp. Physics*, 186: pp. 652 - 665, 2002
- [7] C. J. Lawn, *J. Fluid Mech.* 48: pp. 477 - 505, 1971
- [8] T. Lund, X. Wu, D. Squires, *J. Comp. Phys.* 140: pp. 233 - 258, 1998
- [9] D.G. Pfuderer, A.A. Neubert, G. Früchtel, E.P. Hassel, J. Janicka, *Combust. Flame* 106 (3): pp. 301 - 317, 1996
- [10] H. Pitsch, H. Steiner, *Proc. Combust. Inst.* 28: pp. 35 - 40, 2000
- [11] S.A. Sarkar, S. Stanley, *AIAA Journal* 38, No. 9, September 2000
- [12] Schumann, U., Sweet, R., *J. Comp. Phys.* 20: pp. 171 - 182, 1976
- [13] J.S. Smagorinsky, *Monthly Weather Rev.* 91: pp. 99 - 164, 1963
- [14] M. Tacke, S. Linow, S. Geis, E. Hassel, J. Janicka, J.Y. Chen, *Proc. Combust. Inst.* 27: pp. 1139 - 1148, 1998

ENHANCEMENT OF MIXING AND COMBUSTION IN BUOYANT NON-CIRCULAR PLUMES

K. H. LUO

*Department of Engineering, Queen Mary,
University of London, London E1 4NS, UK*

K.H.Luo@qmul.ac.uk

Abstract Mixing and combustion of buoyant reacting flows from rectangular, square and round sources are investigated using Direct Numerical Simulation (DNS). The full Navier-Stokes equations and the finite-rate Arrhenius-type chemical reactions are simulated by high-order methods. Axis switching is observed in the rectangular plume of aspect ratio 3 but not in the case of aspect ratio 2. A new explanation of the aspect ratio effect is proposed, which is confirmed by the higher level of vorticity and entrainment rate along the major axis as compared with those along the minor axis. Finally, the DNS data are used to validate two newly constructed subgrid-scale (SGS) models for the highly non-linear radiative heat transfer source.

Keywords: Direct Numerical Simulation, Buoyancy, Mixing, Combustion, Radiation, Subgrid-Scale Modelling

1. Introduction

Non-circular jets are known to enhance entrainment and mixing as compared with circular jets (Gutmark & Grinstein, 1999). A potential application is in the control of turbulent diffusion flames, in which enhanced mixing could lead to higher combustion efficiency and lower level of pollutant emission. Past studies have been mostly concerned with momentum-driven, non-buoyant flames targeted at industrial applications. However, many important natural and man-made phenomena such as fires and aircraft engine exhaust involve low-speed, buoyancy-driven reacting plumes. The presence of buoyancy effects leads to extremely complicated couplings among flow instabilities, vortex dynamics, entrainment, mixing, turbulence, chemical reactions and even radiation. These phenomena are inherently unsteady, transient, and have a wide range of time

and length scales. Such multi-scale interactions present difficulties for experiment and the Reynolds Averaged Navier-Stokes (RANS) numerical approach. Large Eddy Simulation (LES) is a promising predictive tool for such applications (e.g. Zhou et al., 2002), but subgrid-scale (SGS) models for mixing, chemical reactions and especially radiation have not been well developed. In the meantime, Direct Numerical Simulation (DNS) has played an increasingly important role in providing fundamental insight and in forming active and passive control strategies for turbulence (Moin & Mahesh, 1998) and combustion (Docquier & Candel, 2002).

Recently, a series of fully three-dimensional (3D) DNS of transitional and turbulent reacting plumes have been performed to investigate (Jiang & Luo, 2001, 2003; Luo & Jiang, 2002): (a) mechanisms of combustion-induced buoyancy; (b) Froude number effects; (c) large-scale vortex dynamics and entrainment; (d) small-scale mixing and combustion; (e) effects of wall confinement; (f) effects of plume source configurations; (g) initial and boundary conditions, etc. The present work extends the simulation to a rectangular reacting plume of aspect ratio 3 and investigates the phenomenon of axis switching. Combined with the earlier results, effects of plume source configurations on mixing and combustion are scrutinized. The DNS data are then used to assess two SGS models that are newly constructed for radiative heat loss.

Cases	Heat value	Grid points	Computational box	Aspect ratio
Rect-AS2	1650	$108 \times 216 \times 288$	$3 \times 6 \times 8$	2
Rect-AS3	1250	$256 \times 256 \times 384$	$8 \times 8 \times 12$	3
Square	1250	$192 \times 192 \times 288$	$5 \times 5 \times 7.5$	1
Round	1250	$192 \times 192 \times 288$	$5 \times 5 \times 7.5$	

Table 1. Main simulation parameters. Other conditions are provided in the text.

2. Numerical Details

A general formulation was used in an in-house DNS code, DSTAR, which solved the 3D time-dependent compressible Navier-Stokes equations for flow and the species transport equations for combustion. As a result, the full coupling between turbulence and combustion through the fluctuating density and pressure was preserved, without invoking the Boussinesq simplification. A one-step global reaction was simulated, which was controlled by finite-rate Arrhenius chemistry. These governing equations were solved using high-order numerical schemes and high fidelity numerical boundary conditions. A series of simulations were performed of buoyant diffusion flames from round, square and rectangular sources. Table 1 shows the different cases and the main simulation parameters. The Froude number is 1.5. Other common parameters were

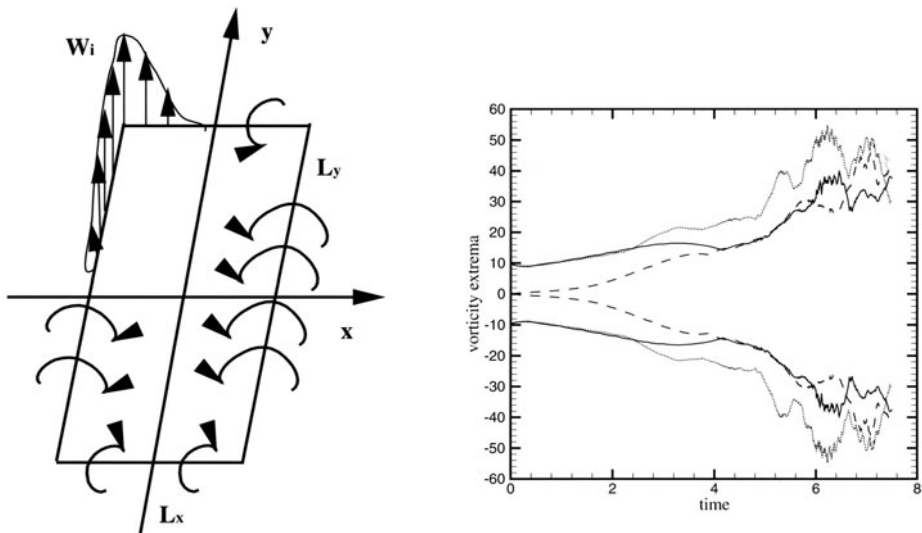


Figure 1. Left: A mechanism for aspect ratio effects: the self-induced vorticity along the major axis (ω_y) is larger than that along the minor axis (ω_x). Right: Vorticity extrema history of the buoyant reacting plume from a rectangular source of aspect ratio 3 (Rect-AS3). (— ω_x ; $\cdots \cdots \omega_y$; - - ω_z).

described in Jiang & Luo (2003). The grids used were able to resolve all scales involved. To facilitate comparison, the different cases used a common length scale for non-dimensionalization. The diameter of the round source was chosen, which had a non-dimensional value 1. The side lengths of the square and rectangular sources were chosen, so that their areas were equal to that of the round source.

3. Aspect Ratio Effects and Axis Switching

The Biot-Savart instability (Saffman, 1992) was identified as a mechanism for the enhanced vorticity level and entrainment rate of non-circular plumes compared with the circular ones (Gutmark & Grinstein, 1999; Luo & Jiang, 2002). According to the theory, the vortex-ring deformation rate, measured by the self-induced velocity w_d , is proportional to $C \log(1/\sigma) \vec{b}$, where C is the local azimuthal curvature of a thin inviscid vortex tube, σ its local cross-section, and \vec{b} the binormal to the plane containing the tube. The Biot-Savart theory predicts that a round, uniform ring would convect with a uniform speed without any change in shape whereas a vortex tube with corners will convect faster at corners than at other locations leading to vortex deformation and enhanced

vorticity level. However, it has been observed that entrainment and mixing are better in rectangular plumes than in square plumes.

Such aspect ratio effects were treated as a mechanism rather than a phenomenon in the existing literature (e.g. Gutmark & Grinstein, 1999). In Fig. 1, the aspect ratio effects are explained as follows: Consider a rectangular plume at the base as a vortex tube “ring”. Biot-Savart instability will induce vertical velocity W_i around the perimeter, whose local magnitude is directly proportional to the local azimuthal curvature. From a local point of view, the azimuthal curvature at any 90° corners must be the same, so that W_i of rectangular and square jets at the corners must be the same under identical conditions. At the midpoints along the sides between the corners, $W_i = 0$, since the local curvature is zero. Hence $\omega_x \sim \partial w / \partial y \sim W_{i,\max} / L_y$ and $\omega_y \sim \partial w / \partial x \sim W_{i,\max} / L_x$. Since $L_y > L_x$, we have $\omega_x < \omega_y$, i.e. vorticity along the major axis (y) should be larger than that along the minor axis (x). This is indeed seen in case Rect-AS3 in Fig. 1 as well as in case Rect-AS2. In the case Square, however, vorticity components along both axes are the same and slightly smaller than ω_x of the rectangular cases. Therefore, the overall entrainment and mixing in rectangular plumes are better than in square ones. Furthermore, as L_y increases relative to L_x (i.e. increasing the aspect ratio), the above trends will become stronger, leading to better overall entrainment in high-aspect-ratio jets/plumes. That is proved by comparing the vorticity extrema of cases Rect-AS3 (Fig. 1) and Rect-AS2 (not shown).

As entrainment along the major axis is stronger due to larger ω_y , it tends to make a rectangular jet more square or round. As the trend continues, it may “overshoot” to render the originally minor axis the major axis and vice versa. That is when axis switching occurs. The vortex structures represented by the pressure iso-surfaces in case Rect-AS3 are shown in Fig. 2. Close to the base, the vortical structures are mainly aligned along the major axis, due to the initial configuration and the dominance of ω_y . But at about $z = 6$, there is an axis switching as far as the vortex alignment is concerned. Further in the far field, λ -type vortices appear, which are more aligned with the vertical axis z rather than x and y , and are likely to be dominated by ω_z . The axis switching is demonstrated in Fig. 3 through the vertical vorticity ω_z fields at two heights. Such axis switching was not observed in case Rect-AS2.

4. SGS Models for Radiation Source

One of the key applications of DNS is for model assessment and validation. In LES, modelling of subgrid-scale phenomena has almost no reliable guidance except DNS data. In reacting flows, the chemical reaction rate, radiation and soot formation are all highly non-linear processes, whose modelling is a great challenge. While some previous efforts have been devoted to SGS modelling

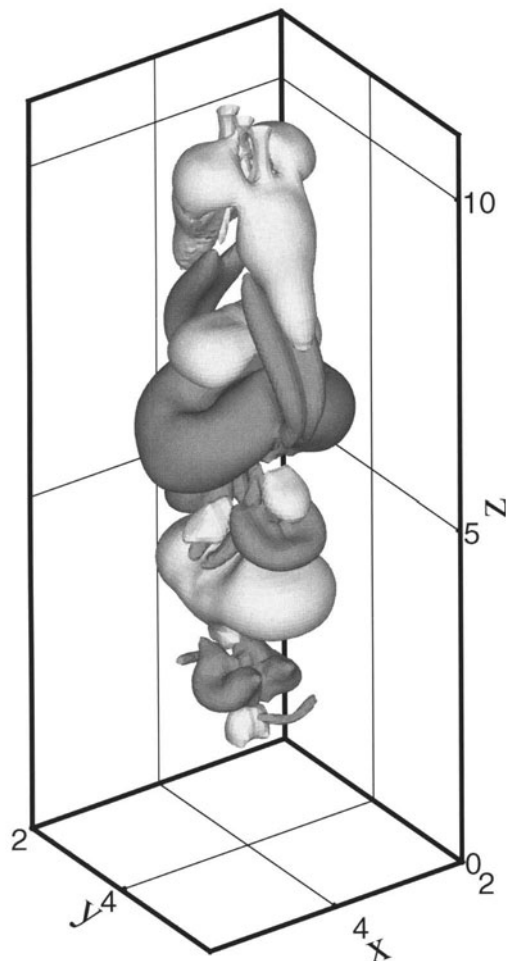


Figure 2. Representative pressure iso-surfaces at $t = 7.5$ of the buoyant rectangular reacting plume case Rect-AS3. Dark shade - $p = 17.7$; light shade - $p = 18.1$.

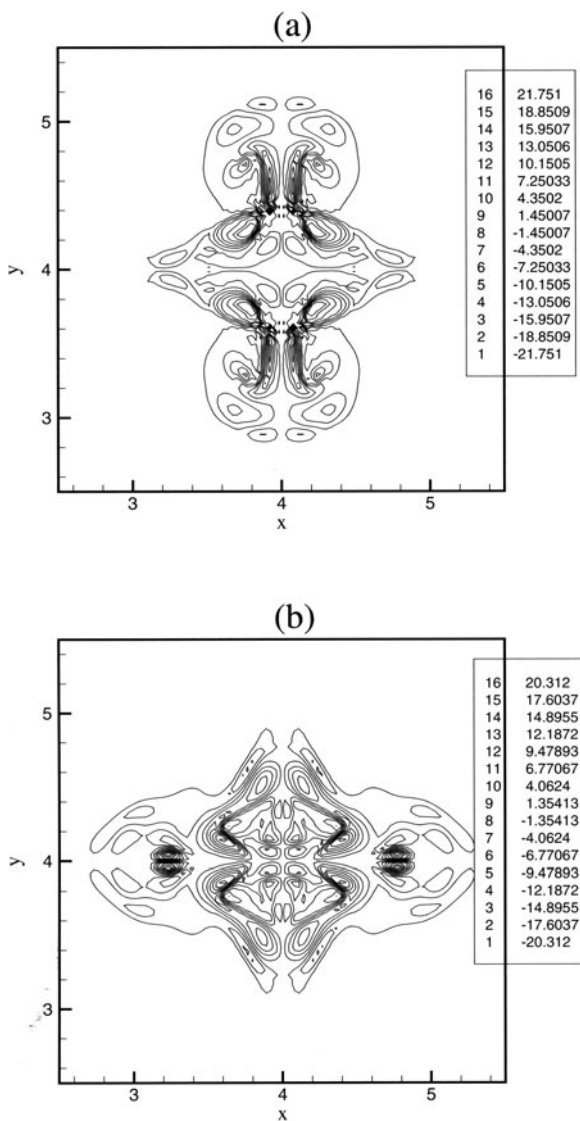


Figure 3. Contours of the vertical vorticity component ω_z at heights (a) $z = 5$ and (b) $z = 6$ at time $t = 7.5$ of case Rect-AS3, showing axis switching.

of the chemical reaction rate, there have been relatively few studies involving radiation and soot, which play key roles in many important applications such as fire dynamics.

The radiative transfer equation (RTE) describes the energy conservation of a ray of radiation traveling through a medium, attenuated by absorption and out-scattering but enhanced by emission and in-scattering. Both gases (such as H_2O and CO_2) and soot contribute to radiative heat transfer, and their relative dominance depends on the fuel and the spatial location. In most simulations, gray, optically thin gases and small-size particles are assumed, which reduces the RTE to:

$$\frac{dI}{ds} = [\alpha_g(T) + \alpha_s(T)] \left(\frac{\sigma_{SB} T^4}{\pi} - I \right) \quad (1)$$

where I is the radiative intensity in the s -direction, σ_{SB} the Stefan-Boltzmann constant. The Planck mean absorption coefficients of gases, α_g and soot, α_s are, in general, complex functions, but can be reasonably approximated by : $\alpha_g = A_p \exp(-T/E_p)$ and $\alpha_s = k_p f_v T$, where A_p , E_p and k_p are assumed to be constants, and f_v is the soot volume fraction. In LES, Eq. (1) can be solved by various approximation models such as the flux methods, discrete ordinate methods or discrete transfer methods in analogy to their treatment in RANS. In each case, it involves filtering and modelling the highly non-linear radiation source. There have been no attempts to model the RTE source, although DesJardin and Frankel (1999) approximated it by directly substituting the filtered variables into the term, effectively ignoring any turbulence-radiation interactions. However, following the scale similarity argument (Bardina et al., 1984; DesJardin and Frankel, 1999) and denoting the radiation source term in Eq. (1) as S_R , a scale similarity filtered radiation model (SSFRM) and a scale similarity resolved radiation model (SSRRM) can be constructed as follows:

$$\begin{aligned} (\tilde{I}_{n+1})_{SSFRM} &= \overline{S_R(\tilde{I}_n, \tilde{T}, \tilde{f}_v)} \\ &+ C_{FR} \left[\overline{S_R(\tilde{I}_n, \tilde{T}, \tilde{f}_v)} - S_R(\tilde{I}_n, \tilde{T}, \tilde{f}_v) \right] \end{aligned} \quad (2)$$

$$\begin{aligned} (\tilde{I}_{n+1})_{SSRRM} &= S_R(\tilde{I}_n, \tilde{T}, \tilde{f}_v) \\ &+ C_{RR} \left[\overline{S_R(\tilde{I}_n, \tilde{T}, \tilde{f}_v)} - S_R(\tilde{I}_n, \tilde{T}, \tilde{f}_v) \right] \end{aligned} \quad (3)$$

where \tilde{I}_n and \tilde{I}_{n+1} are the SGS radiative energy intensity entering and leaving a radiation control volume. The overline and tilde indicate spatial and Favre filtering, respectively. The model constants C_{FR} and C_{RR} are to be determined. Figure 4 shows the performance of the two models against the DNS data. By ignoring the effects of gas radiation and soot volume fraction, S_R is directly

proportional to T^5 . Both models show qualitative correlation with the filtered DNS data, with $C_{FR} = 1$ and $C_{RR} = 1$. Model SSRRM also shows quantitative agreement with the filtered DNS, but model SSFRM under-predicts the peak values. However, when the filter width Δ is reduced to 4 times the grid spacing, both models show almost perfect agreement with the filtered DNS data, qualitatively and quantitatively.

5. Conclusions

Dynamics of buoyant reacting plumes from rectangular, square and round sources were well reproduced by a high-order DNS methodology. Mixing and combustion were enhanced by the presence of corners in the non-circular plumes as compared with the circular one. Increasing the aspect ratio would augment such effects, and lead to axis switching. A mechanism for the aspect ratio effect was provided based on an extension of the Biot-Savart instability, and backed by the present DNS data.

Two new SGS models for radiative heat transfer were constructed on the basis of scale similarity. The scale similarity filtered radiation model (SSFRM) and the scale similarity resolved radiation model (SSRRM) showed excellent qualitative and quantitative agreement with filtered DNS data when a small filter width was used. When a large filter width was used, model SSFRM out-performed model SSRRM, quantitatively. These models require further assessment in *a posteriori* tests to establish their validity and generality.

References

- J. Bardina, J. H. Ferziger and W. C. Reynolds (1984), Improved turbulence models based on LES of homogeneous incompressible turbulent flows, Report No. TF-19, Department of Mechanical Engineering, Stanford University.
- P. E. DesJardin and S. H. Frankel (1998), Large-eddy simulation of a nonpremixed reacting jet: application and assessment of subgrid-scale combustion models, *Phys. Fluids A* 10 (9): 2298-2314.
- P. E. DesJardin and S. H. Frankel (1999), Two-dimensional large eddy simulation of soot formation in the near-field of a strongly radiating nonpremixed acetylene-air turbulent jet flame, *Combust. Flame* 119: 121-132.
- N. Docquier, S. Candel (2002), Combustion control and sensors: a review, *Progress in Energy and Combustion Sciences* 28 (2): 107-150.
- E. J. Gutmark and F. F. Grinstein (1999), Flow control with non-circular jets, *Annu. Rev. Fluid Mech.* 31: 239-272.
- X. Jiang and K. H. Luo (2001), Direct numerical simulation of transitional non-circular buoyant reactive jets, *Theoret. Comput. Fluid Dynamics* 15: 183-198.
- X. Jiang and K. H. Luo (2003), Dynamics and structure of transitional buoyant jet diffusion flames with side-wall effects, *Combustion and Flame* 133 (1-2): 29-45.

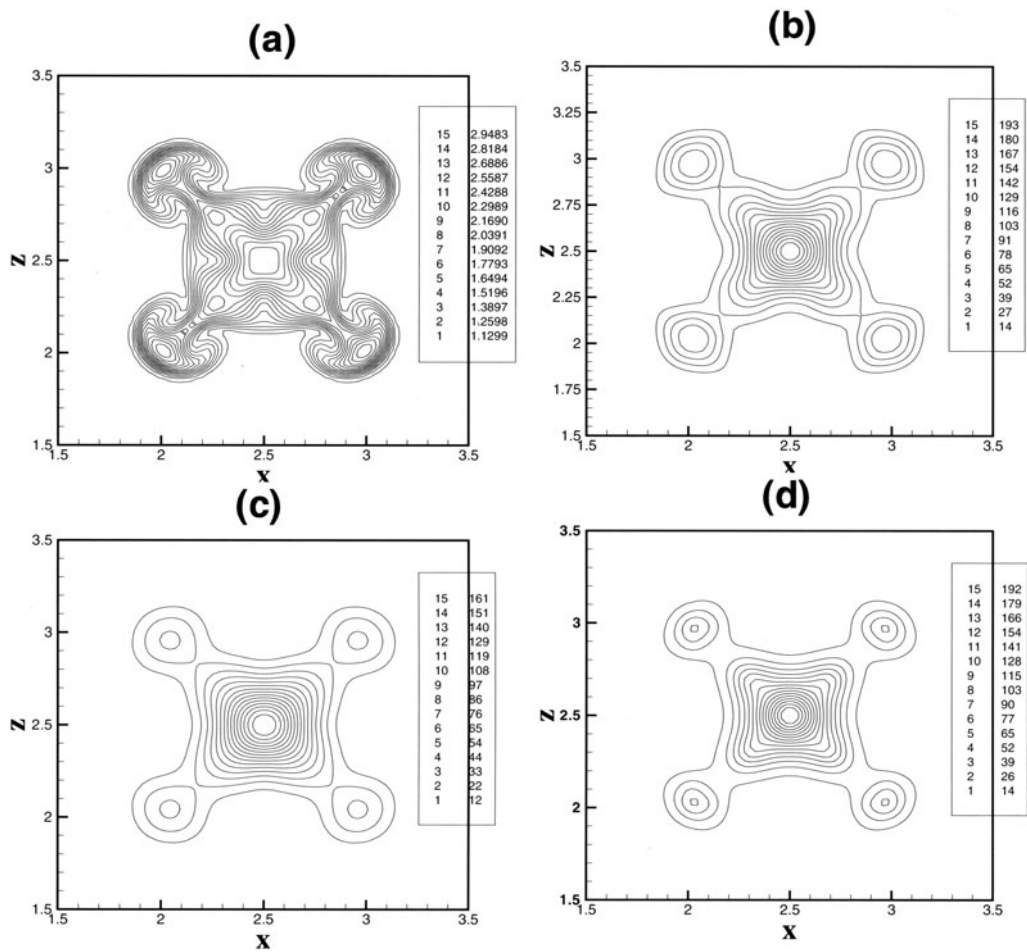


Figure 4. Scale similarity models for the SGS radiation source term. (a) The temperature field in a horizontal plane $z = 3$ of case Square; (b) The filtered DNS data of \tilde{T}^5 ; (c) SSFRM for \tilde{T}^5 ; (d) SSRRM for \tilde{T}^5 . A top-hat filter with a width 8 times the grid spacing in the DNS is used.

- K. H. Luo and X. Jiang (2002), Passive control of flow entrainment in buoyant reacting jets, in: I.P. Castro, P. E. Hancock, T. G. Thomas (Eds.), *Advances in Turbulence IX*, Proc. Ninth European Turbulence Conference, Southampton, U.K., 2-5 July, pp. 569-572.
- P. Moin and K. Mahesh (1998), Direct numerical simulation: A tool in turbulence research, *Annu. Rev. Fluid Mech.* 30: 539-578.
- P. G. Saffman (1992), *Vortex dynamics*, Cambridge University Press, Cambridge.
- X. Zhou, K. H. Luo and J. J. R. Williams (2002), Vortex dynamics in spatio-temporal development of reacting plumes, *Combust. Flame* 129: 11-29.

3.4 COMPRESSIBLE TURBULENCE

DNS OF AN OBLIQUE SHOCK WAVE IMPINGING UPON A TURBULENT BOUNDARY LAYER

Qinling Li and Gary N. Coleman

*School of Engineering Sciences, University of Southampton
Southampton, Hampshire, SO17 1BJ, UK*

q.li@soton.ac.uk, g.n.coleman@soton.ac.uk

Abstract A supersonic boundary layer at $M_\infty = 2$, with inflow displacement-thickness Reynolds number $Re_{\delta^*} = 3775$, is subjected to an impinging oblique shock. The spatially developing boundary layer is generated using an idealized unsteady analytic inflow profile that emulates the dynamical features of wall-bounded turbulence; this approach has the advantage of creating a self-contained simulation with deterministic inflow conditions that prompt the realistic transfer of energy from the mean flow to the turbulence, and thereby a realistic fully developed turbulent boundary layer in a fairly short downstream distance. The impinging shock induces a small separation bubble and significant intrinsic compressibility effects unrelated to mean property variations.

Keywords: DNS, turbulent compressible flows, shock/boundary-layer interaction

1. Introduction

In view of its technical importance, the challenge it poses for turbulence models, and its link in the chain of canonical flows amenable to DNS, we consider the interaction of an oblique-shock reflection and a turbulent boundary layer. In contrast to other shock/boundary-layer flows, such as the compression ramp and the bump, here the shock is created not by a change in curvature of the surface below the boundary layer, but by a change of direction (typically due to an external body) in the freestream flow. Provided the upstream Mach number is large enough, the impinging shock both causes the boundary layer to separate, and raises the possibility that intrinsic compressibility effects (those associated with dilatational fluctuations rather than spatial variations of mean properties) must be taken into account. These features point to the relevance and richness of this flow, and motivate the present study.

Other recent shock/boundary-layer DNS include the turbulent Mach 3 compression ramp by Adams (2000), and Lawal & Sandham's (2001) transitional

transonic flow over a Delery bump. DNS of a turbulent transonic boundary layer over a circular-arc bump was performed by Yao & Sandham (2002), who developed a method of prescribing analytic turbulent inflow perturbations, a version of which we employ below. An LES of the turbulent impinging-shock flow considered here has been done by Garnier, Sagaut & Deville (2002). A two-dimensional DNS of separation induced by an oblique shock impinging upon a supersonic laminar boundary layer was carried out by Wasistho (1997).

2. Approach

The fully compressible unsteady Navier-Stokes equations are solved using an entropy splitting technique to partition the inviscid flux derivatives into conservative and nonconservative parts. This produces solutions that possess non-linear stability properties, such that certain energy bounds are satisfied (Harten 1983, Gerritsen & Olsson 1998). Details are given in Li (2003). A Laplacian formulation of the viscous and heat conduction terms is employed to avoid odd-even decoupling associated with central-difference schemes. Fourth-order central differencing is used in the spanwise direction and the interior points in the streamwise and wall-normal directions. For the boundary points, a Carpenter *et al.* (1999) scheme is employed. An explicit low-storage third-order Runge-Kutta method is used to time advance the conservative variables. The resulting code has proved to be stable and robust in terms of grid resolution and domain size (Sandham, Li & Yee 2002).

2.1 Inflow conditions

An inverse van Driest transform is used as the basis for the mean streamwise velocity, incorporating both density effects and a Reynolds-number correction. Utilizing the Crocco-Busemann temperature-velocity relation, with wall temperature equal to the adiabatic wall value, we calculate the mean temperature and (invoking the $\partial P/\partial y = 0$ boundary-layer assumption) set the mean density to its inverse via the ideal-gas law. We assume the initial mean velocities in the wall-normal and spanwise directions are zero. These mean inflow quantities are imposed as initial conditions throughout the domain.

It has become increasingly evident that turbulent flows contain deterministic features: near-wall streaks are spaced in the spanwise direction in a surprisingly regular way. Moreover, the streaks interact with other parts of the flow through a sequence of events – lift up, oscillation, and break-up – in a quasi-periodic manner (Luchik & Tiederman 1987; McComb 1990). In light of these findings, we follow the approach developed by Yao & Sandham (2002) for their turbulent-bump simulation, by prescribing inflow disturbances according to ‘synthetic’ forms of both the inner- and outer-layer turbulence structures observed in canonical boundary layers. The major difference between their and

our approach is our use of the van Driest profile to define the mean velocity and the local density scaling for the fluctuations (see below). Distinct inner- and outer-layer perturbations with appropriate spanwise phase information are employed. The inner-layer perturbations ($j = 1$) emulate lifted streaks that peak at $y_{\max}^+ = 12$. The outer-layer peak perturbation locations ($j = 2, 3, 4$) are chosen at $y_{\max}/\delta_{\text{VD}}^* = 2.0, 3.0$ and 4.0 , where δ_{VD}^* is the kinematic displacement thickness of the van Driest profile (which due to density variations differs from the kinematic displacement thickness δ^* of the actual mean inflow velocity U). In addition, in order to make the outer region more realistic, a fourth outer-motion mode ($j = 5$) is added at $y/\delta_{\text{VD}}^* = 3$. The coefficients c_{ij} set the magnitude of the perturbations that peak at y_{\max}^+ ($j = 1$) or y_{\max} ($j = 2, \dots, 5$); ω_j is the forcing frequency, β_j and ϕ_j are respectively the spanwise wave-number and phase shift. The inner-layer forcing frequency $\omega_{j=1}$ is based on the assumption that the average time between bursts in wall units is about 153, the time required for the disturbance to pass through the $L_x^+ \approx 1530$ domain once at a convective velocity of $u_c^+ \approx 10$. Parameter values are listed in table 1. We consider density effects and Mach number dependence by employing a semi-local scaling of the velocity fluctuations, which has been demonstrated by Huang *et al.* (1995) and Guarini *et al.* (2000) to collapse results for Mach numbers up to 2.5. The streamwise ($i = 1$) and wall-normal ($i = 2$) disturbances, u'_i , are thus

$$u'_i = \sum_{j=1}^5 c_{ij} u_e A_j^{(i)}(y) e^{-A_j^{(i)}(y)} \sin(\omega_j t_j) \cos(\beta_j z_j + \phi_j), \quad (1)$$

where the bracket superscript (i) on $A_j(y)$ indicates an exponent, and

$$A_j(y) = \begin{cases} y^{**}/(y_{\max}^+)_j & j = 1 \\ y/(y_{\max})_j & j = 2, \dots, 5. \end{cases}$$

The temporal and spanwise dependence is respectively given by

$$t_j = \begin{cases} t \text{Re}_{\delta_{\text{VD}}^*}^2 / u_e^+ & j = 1 \\ t & j = 2, 3, 4, 5, \end{cases}$$

$$z_j = \begin{cases} z \text{Re}_{\delta_{\text{VD}}^*} / u_e^+ & j = 1 \\ z & j = 2, 3, 4, 5, \end{cases}$$

where j is the disturbance index in the wall-normal direction (1 for the inner-region and the others for the outer region), u_e^+ is the edge velocity in wall units, and $\text{Re}_{\delta_{\text{VD}}^*} = 1000$. The semi-local variable $y^{**}(y)$ is defined in terms of the wall shear stress τ_w and the y -local mean density $\langle \rho \rangle$ and mean dynamic viscosity $\langle \mu \rangle$, such that $y^{**} = \langle \rho \rangle y u_\tau^* / \langle \mu \rangle$, where $u_\tau^* = \sqrt{\tau_w / \langle \rho \rangle}$. This inflow condition defines eight streaks across the domain in the spanwise direction

Table 1. Inflow parameters.

j	c_{1j}	c_{2j}	$\frac{\omega_j \delta_{VD}^*}{u_e}$	$\beta_j \delta_{VD}^*$	ϕ_j	$(y_{\max}^+)_j$	$\frac{(y_{\max}^+)_j}{\delta_{VD}^*}$
1	$2(y_{\max}^+)_j$	$-0.032(y_{\max}^+)_j^2$	1/25	$\frac{2}{3}\pi u_e^+ / \text{Re}_{\delta_{VD}^*}$	0.0	12	-
2	6.0	-0.12	1/8	$\pi/6$	0.1	-	2.0
3	6.0	-0.12	1/16	$\pi/3$	0.2	-	3.0
4	6.0	-0.12	1/32	$\pi/2$	0.3	-	4.0
5	6.0	-0.12	1/20	$\pi/12$	0.4	-	3.0

with the distance between each of about 150 wall units. When density effects are taken into account, the streamwise u' and wall-normal v' perturbations are

$$u' = \frac{u'_1}{u_e^+} \left(\frac{T}{T_w} \right)^{\frac{1}{2}}, \quad v' = \frac{u'_2}{u_e^+} \left(\frac{T}{T_w} \right)^{\frac{1}{2}}, \quad (2)$$

where T_w is the wall temperature. The disturbance in the spanwise direction, w' , is derived from the two-dimensional divergence-free condition $\partial w' / \partial z = -\partial v' / \partial y$. A random perturbation, f' , with a maximum amplitude of 4% of the free-stream velocity, is used to break any remaining symmetries in the inflow condition, with $f' = c(r - 0.5)F(y)$, where r is a random number, $0 \leq r \leq 1$, $c = 0.08u_e$ and

$$F(y) = \begin{cases} (y^{**}/(y_{\max}^+)_1)^2 & y^{**} < (y_{\max}^+)_1 \\ e^{-((y-\delta_0)/\delta_{VD}^*)^2} & y > \delta_0 \\ 1 & \text{otherwise,} \end{cases}$$

and δ_0 is the inflow boundary-layer thickness of the inflow profile $U(y)$. The dependent variables at the inflow plane are thus defined as

$$\rho u = \rho(y) \left(U(y) + u' + f' \right), \quad (3)$$

$$\rho v = \rho(y) \left(v' + f' \right), \quad (4)$$

$$\rho w = \rho(y) \left(w' + f' \right), \quad (5)$$

$$E_t = \rho(y) C_v T(y) + \frac{1}{2} \left((\rho u)^2 + (\rho v)^2 + (\rho w)^2 \right) / \rho(y), \quad (6)$$

where $C_v T$ is the internal energy.

2.2 Parameters

DNS of a turbulent compressible zero-pressure-gradient (ZPG) isothermal-wall boundary layer both without and with an impinging shock are performed at freestream Mach number $M_\infty = 2$ and inflow Reynolds number based on the kinematic displacement thickness of the van Driest profile of $\text{Re}_{\delta_{\text{VD}}^*} = 1000$; the Reynolds number based on actual displacement thickness at the inlet is $\text{Re}_{\delta^*} = 3775$. A Prandtl number of $\text{Pr} = 0.70$ and temperature-dependent viscosity $\mu \sim T^\Omega$ with $\Omega = 0.67$ are assumed.

The rectangular domain size in the streamwise and spanwise directions are respectively $L_x = 200\delta_{\text{VD}}^* = 16\delta_0$ and $L_z = 24\delta_{\text{VD}}^* = 1.9\delta_0$ (the inflow boundary-layer thickness for $M_\infty = 2$ is $\delta_0 = 12.7\delta_{\text{VD}}^*$). We choose $L_y/\delta_{\text{VD}}^* = 30$, such that $L_y/\delta_0 = 2.4$. The spanwise domain L_z/δ_0 is bigger here than the 0.84 used in Maeder, Adams & Kleiser (2001), which they confirmed as acceptable by examining two-point correlations. The grid numbers in the streamwise N_x , wall-normal N_y , and spanwise N_z directions are $N_x \times N_y \times N_z = 512 \times 130 \times 96$. This choice, which was based on earlier experience with DNS of fully developed compressible wall-bounded turbulence (cf. Li 2003), is supported by the agreement of the resulting second-order statistics with those from incompressible DNS (figure 2), and the ability to capture steep gradients across the shock (figure 3). The grid is uniform in the streamwise x and spanwise z directions but stretched in the wall-normal y direction with a mapping function $y/\delta_{\text{VD}}^* = \sinh(b_y\eta_j)/\sinh(b_y)$, where $\eta_j = L_y(j-1)/(N_y-1)$ with $b_y = 4.0$. The streamwise and spanwise grid spacing are $\Delta x^+ = \langle \rho \rangle u_\tau \Delta x / \langle \mu \rangle = 19$ and $\Delta z^+ = \langle \rho \rangle u_\tau \Delta z / \langle \mu \rangle = 12$. In terms of the van Driest profile, there are six points in the sub-layer region ($y^+ < 10$), compared to ten points below $y^+ = 9$ for Spalart (1988).

Characteristic and a combined Dirichlet-characteristic conditions are applied to the outflow and upper boundary respectively, to minimize reflected waves (Li 2003). The flow is periodic in the spanwise direction.

The simulation was performed on a Cray T3E-1200E parallel computer. It started with a small domain of $L_x/\delta_{\text{VD}}^* \times L_y/\delta_{\text{VD}}^* \times L_z/\delta_{\text{VD}}^* = 50 \times 30 \times 24$, with a $N_x \times N_y \times N_z$ grid of $128 \times 130 \times 96$ run on 16 processor elements (PEs) for 100 non-dimensional time units (δ_{VD}^*/u_e) to allow the flow to reach steady state. Time (and spanwise) averages, denoted here by angle brackets $\langle \rangle$, were gathered over another 100 time units to allow validation of the code. The domain was then doubled in the x direction by filling the $50 < x/\delta_{\text{VD}}^* \leq 100$ region with instantaneous values of the dependent variables in the y - z plane at $x = 50\delta_{\text{VD}}^*$, and continuing on a $256 \times 130 \times 96$ grid with 32PEs for another 100 time units – enough for the freestream flow to pass through the entire domain once. Finally, the instantaneous $x = 100\delta_{\text{VD}}^*$ field was extrapolated throughout the full $L_x = 200\delta_{\text{VD}}^*$ domain with $N_x \times N_y \times N_z = 512 \times 130 \times 96$.

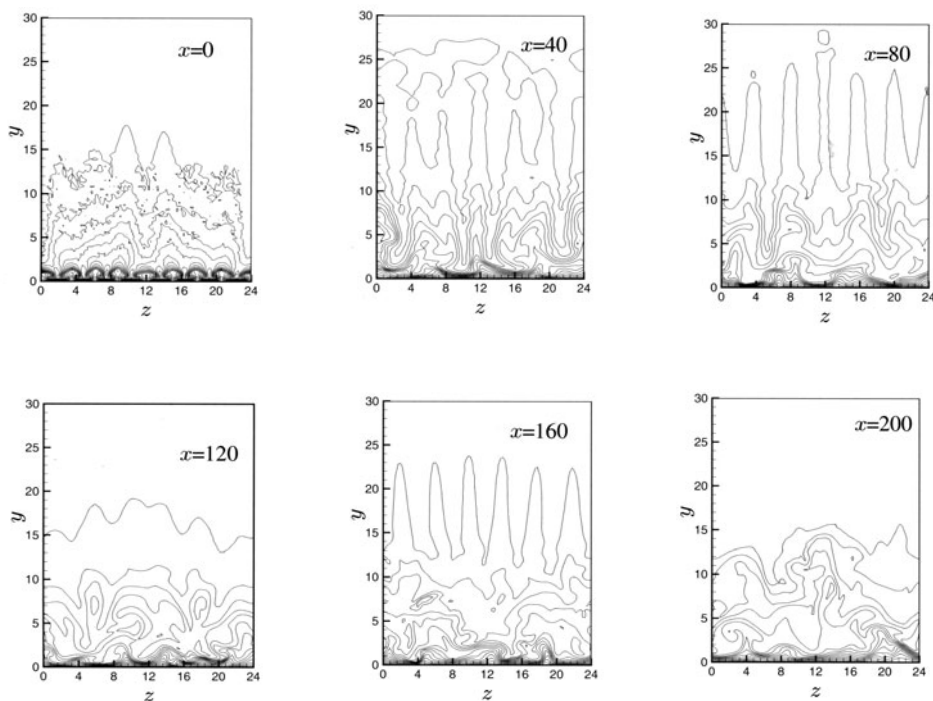


Figure 1. Instantaneous streamwise velocity contours at various streamwise locations. Coordinates y and z normalized by δ_{VD}^* .

The simulation was continued to allow the time- and spanwise-averaged final results to be gathered over a period of 200 and 230 δ_{VD}^*/u_e respectively, for the shock-free and impinging-shock cases.

3. Results

3.1 Shock-free flow

The synthetic inflow conditions are applied to the zero-pressure gradient shock-free boundary layer at $M_\infty = 2$, with inflow $Re_{\delta^*} = 3775$. The instantaneous streamwise velocity contours in figures 1 show how the flow develops in the streamwise direction. We note that the superimposed random fluctuations lead to breaking of the spanwise symmetry in the analytic streak/bursting motions at the inflow, such that the flow quickly approaches a realistic fully developed turbulent flow (see also figure 4a). The spatial development is also illustrated in figure 2, where normal-stress profiles at $x/\delta_{VD}^* = 80, 120, 160$ and 200 are compared with each other and the incompressible ZPG boundary layer of Spalart (solid symbols). They agree increasingly well with x with

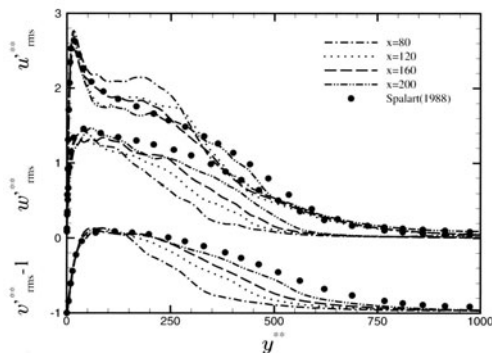


Figure 2 Root-mean-squared velocity fluctuations, normalized by semi-local scaling with $u_{\tau}^{**}(y) = \sqrt{\tau_w/\langle\rho\rangle}$ and $y^{**}(y) = y\langle\rho\rangle u_{\tau}^{**}/\langle\mu\rangle$.

the Spalart data, when the semi-local scaling is used. This implies that for $x \geq 100\delta_{VD}^*$ the turbulence has to a large extent recovered from any unphysical characteristics of the inflow, which in turn demonstrates that the modified Yao & Sandham van Driest/synthetic streak approach provides a reasonable compromise for spatial DNS between the convenience of purely artificial (non-deterministic) inflow conditions and the heavy cost and complexity of a separate precursor simulation. We chose $x/\delta_{VD}^* = 110$ as the location at which the oblique shock is triggered at the upper boundary of the domain. As we shall see below, this produces a shock/boundary-layer interaction near $x/\delta_{VD}^* = 140$, where for the shock-free flow the momentum-thickness Reynolds number is $Re_{\theta} = 922$, the shape factor is $H = 1.54$ and the local skin friction is $C_f = 0.00258$.

3.2 Oblique-shock/boundary-layer interaction

A 34° oblique shock is created at the upper boundary by imposing for $x \geq 110$ a negative vertical velocity V_e of $-0.082u_e$ (which deflects the outer flow downwards by 4.7°) and increasing the density and pressure by appropriate factors (1.201 and 1.293 respectively). The inviscid theoretical (dotted curve) and actual (dashed) freestream pressure distributions are shown in figure 3; note the step increase in C_p at $x/\delta_{VD}^* = 110$. Inviscid theory predicts that a regular reflection will occur at $x/\delta_{VD}^* = 154.5$ (indicated by the vertical line in figure 3a), with reflection angle of 32.7° , such that the reflection shock exits the domain at $x/\delta_{VD}^* = 200$ just below the upper boundary at $y/\delta_{VD}^* = 30$; the theoretical pressure downstream of the reflection shock is 1.653 times the value upstream of the incident shock (corresponding to $C_p = 0.23$; cf. figure 3a). The small jump in the actual freestream C_p near $x/\delta_{VD}^* = 40$ is due to a Mach wave created at the inflow, where the purely horizontal mean flow (with $V = 0$) first enters the domain. The much larger deviation from the inviscid C_p occurring near $x/\delta_{VD}^* = 160$ is the signature of the reflection shock

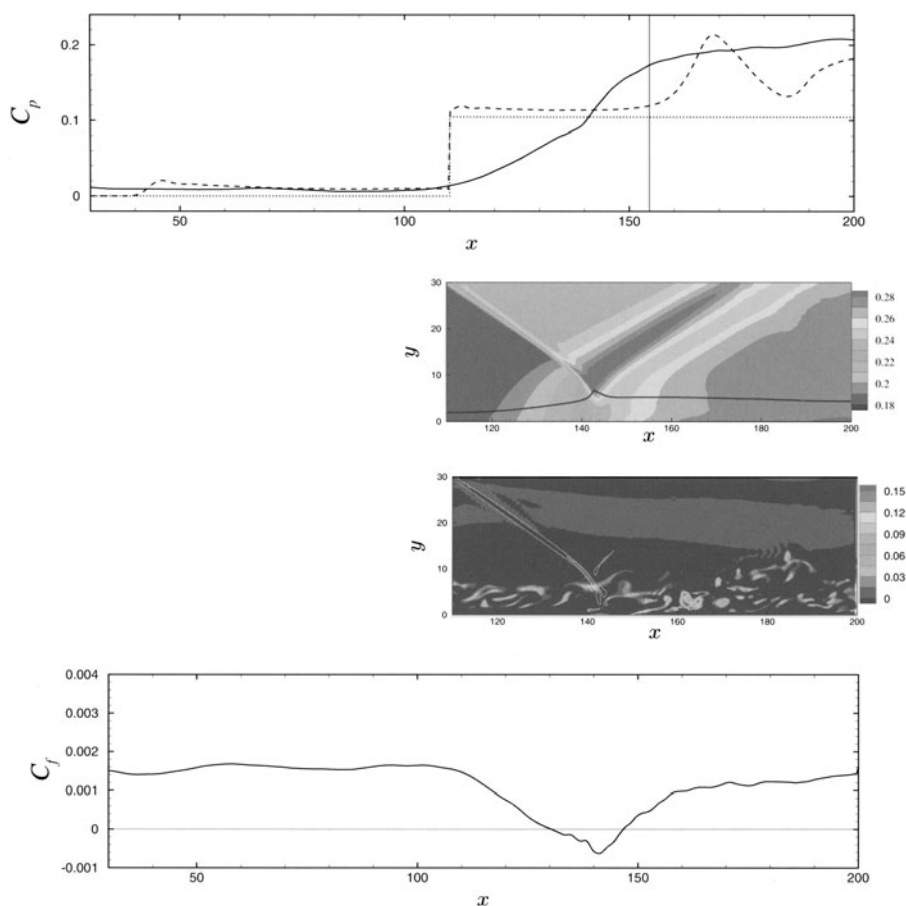


Figure 3. Top to bottom: a) Mean pressure coefficient C_p : , inviscid idealization at $y = 30$; , actual profile at $y = 30$; —, actual profile at $y = 0$. Vertical line denotes location of shock/surface reflection for inviscid flow. b) Mean pressure contours. c) Instantaneous spanwise vorticity (shaded) and dilatation (white curves) contours. d) Mean skin friction C_f . Coordinates x and y normalized by δ_{VD}^* .

leaving the domain: the boundary layer causes a steeper reflection shock (at approximately 40° to the surface, rather than the 32.7° inviscid prediction) and shifts it upstream (cf. the mean pressure contours in figure 3b). The utility of the integral upper-boundary condition, which filters outgoing characteristic waves (and thus modifies the Dirichlet condition on pressure), is apparent from the absence of any spurious reflections where the upper boundary intersects the reflection shock. The solid curve in figure 3a reveals how the mean pressure along the surface is affected by the boundary layer. The change in character from the supersonic outer flow to the subsonic region adjacent to

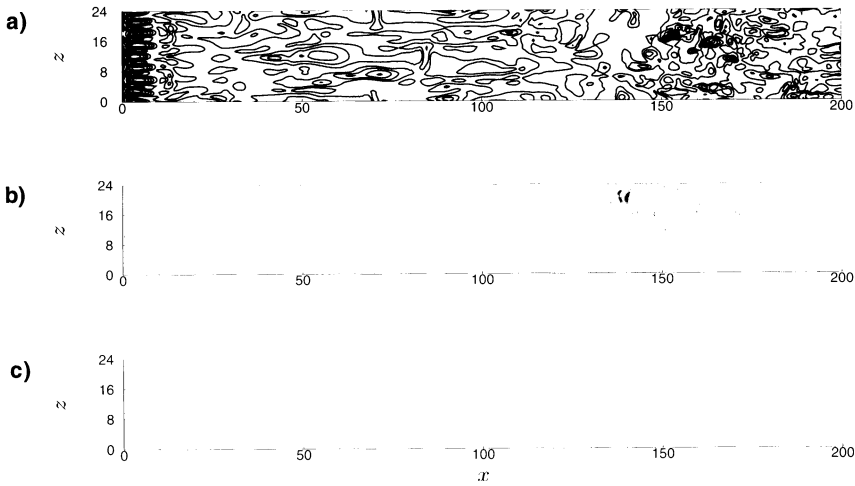


Figure 4. Instantaneous contours of $\partial u/\partial y$ at $y = 0$: a) $\partial u/\partial y > 0$. b) $\partial u/\partial y < 0$. c) $\partial u/\partial y = 0$. Coordinates x and z normalized by δ_{VD}^* .

the surface (the boundary of which is indicated by the sonic line (solid curve) in figure 3b), is illustrated by the smearing of the infinite (step-function) outer-layer pressure gradient, such that near the surface the adverse pressure gradient begins well upstream of the inviscid reflection point at $x/\delta_{VD}^* = 154.5$. The impinging shock considered here is strong enough to induce a small region of mean recirculation (figure 3d). The structure of the instantaneous separation is shown in figure 4. The lack of strong spanwise coherence of the $\tau_w = 0$ contours (figure 4c) implies the spanwise domain is sufficiently large. It also displays the qualitative difference between the mean and instantaneous structure of the separation bubble. The interaction of the impinging shock and the boundary-layer vorticity, and its role in any low-frequency unsteadiness of the bubble and ensuing development of the downstream flow (cf. figure 3c), will be addressed in future work.

The explicit compressibility terms in the turbulent kinetic energy budget associated with the incident and reflection shocks are quite large. For example, at $x/\delta_{VD}^* = 140$ the peak dilatational dissipation (not shown) is at least an order of magnitude larger than any of the incompressible terms at this location.

4. Closing remarks

The synthetic-streak/van Driest inflow conditions allow us to efficiently capture the interaction of an impinging oblique shock and a spatially developing $M_\infty = 2$ turbulent boundary layer with a self-contained DNS. In future studies we plan to use these results as a benchmark for testing common turbu-

lence models and modelling concepts, and developing a deeper understanding of high-speed turbulent boundary layers.

Acknowledgements

We are indebted to Professor Neil Sandham for his contribution to this work. Computer time was supplied through EPSRC Grant GR/M08424/02, under the auspices of the UK Turbulence Consortium.

References

- Adams N. A. Direct simulation of the turbulent boundary layer along a compression ramp at $M = 3$ and $Re_\theta = 1685$. *J. Fluid Mech.*, 420:47-83, 2000.
- Carpenter, M. H., Nordstrom, J. & Gottlieb, D. A stable and conservative interface treatment of arbitrary spatial accuracy. *J. Comput. Phys.*, 148(2):341-365, 1999.
- Garnier, E., Sagaut, P. & Deville, M. Large Eddy Simulation of Shock/Boundary-layer Interaction. *AIAA J.*, 40:1935-1944, 2002.
- Gerritsen, M. & Olsson, P. Designing an efficient solution strategy for fluid flow: II. Stable high-order central finite difference schemes on composite adaptive grids with sharp shock resolution. *J. Comput. Phys.*, 147:293-317, 1998.
- Guarani, S. E., Moser, R. D., Shariff, K. & Wray, A. Direct numerical simulation of a supersonic turbulent boundary at Mach 2.5. *J. Fluid Mech.*, 414:1-33, 2000.
- Harten, A. On the symmetric form of systems for conservation laws with entropy. , 151-164, 1983.
- Huang, P. G, Coleman, G. N. & Bradshaw, P. Compressible turbulent channel flow: DNS results and modelling. *J. Fluid Mech.*, 305:185-218, 1995.
- Lawal, A. A. & Sandham, N. D. Direct Simulation of transonic flow over a bump. *Proc. of Direct and Large-eddy Simulation, Twente*, 2001.
- Li, Q. Numerical study of Mach number effects in wall-bounded turbulence. *PhD Thesis*, University of Southampton, 2003.
- Luchik, T. S. & Tiederman, W. G. Timescale and structure of ejections and bursts in turbulent channel flows. *J. Fluid Mech.*, 174:529-552, 1987.
- Maeder, T., Adams, N. A. & Kleiser, L. Direct simulation of turbulent supersonic boundary layers by an extended temporal approach. *J. Fluid Mech.*, 429:187-216, 2001.
- McComb, W. D. The Physics of Fluid Turbulence. *Oxford Science Publication*, 1990.
- Sandham, N. D., Li, Q. & Yee, H. C. Entropy splitting for high-order numerical simulation of compressible turbulence. *J. Comp. Physics*, Vol. 178, 307-322, 2002.
- Spalart, P. R., Direct simulation of a turbulent boundary-layer up to $Re_\theta = 1410$. *J. Fluid Mech.*, 187:61-98, 1988.
- Wasistho, B., Spatial direct numerical simulation of compressible boundary layer flow. *PhD Thesis*, University of Twente, 1997.
- Yao, Y. F. & Sandham, N. D. DNS of turbulent flow over a bump with shock/boundary-layer interactions. *5th Int. Symp. on Eng. Tur. Modelling and Measurements*, Spain, 2002.

LARGE-EDDY SIMULATIONS OF COMPRESSIBLE MIXING LAYERS

C. Le Ribault

LMFA, UMR CNRS 5509, ECL, 36 avenue Guy de Collongue, 69134 Ecully, France

Leribault@mecaflu.ec-lyon.fr

Abstract Large eddy simulations (LES) are performed to study spatially evolving compressible mixing layers at different convective Mach numbers. Two subgrid models are investigated: the dynamic Smagorinsky model and the dynamic mixed model. Simulations at the low convective Mach number of 0.16 are first performed. The predictions of the mean field and of the Reynolds stresses are in good agreement with experimental results. Then, the convective Mach number is increased and simulations are performed at the higher convective Mach numbers of 0.5 and 0.84. The decrease of the growth rate and of the turbulence intensities with the convective Mach number is predicted. Results on the decrease of the production and of the transport terms are then presented.

1. Introduction

Compressible turbulent mixing layers play a critical role in many industrial domains such as in aeronautics and in combustion and propulsion research. The more important compressibility effect is the reduction of the spreading rate of a compressible mixing layer compared to the same low Mach number mixing layer [1],[2],[3]. The convective Mach number M_c , introduced by Bogdanoff, measures the intrinsic compressibility of a mixing layer. Lot of experiments also predict an influence of the compressibility on the turbulence statistics and on the Reynolds stresses [2],[4],[5].

Numerically, most of the simulations have been performed for temporal evolving mixing layers. DNS of temporal evolving mixing layers at different convective Mach numbers have been performed by Pantano *et al.* [6]. The compressible effects such as the reduction of the spreading rate and the turbulence intensities are predicted by this study. Direct numerical simulations of time evolving annular mixing layer have been done by Freund [7]. Different subgrid models have been compared by Vreman [9],[10] in the case of temporal evolving mixing layers.

Few simulations exist for spatially evolving mixing layers. This kind of simulations requires refined meshes and the construction of inflow boundary conditions. DNS of supersonic mixing layers have been performed by Kourta [8] to study the flow structures. A LES of a spatially evolving mixing layer has been performed by Doris at the convective Mach number of 0.64 [11]. But this convective Mach number is not high enough to obtain a significant reduction of the spreading rate.

Several attempts have been performed to try to understand the mechanisms responsible for the decrease of the spreading rate. However Vreman [10] and Pantano *et al.* [6] showed that the reduction of the turbulence kinetic energy and of the spreading rate were directly linked to the reduction of the turbulence production and of the fluctuating pressure.

My goal is to perform LES of spatially evolving mixing layers and to see if the LES is able to predict compressibility effects, such as the reduced growth rate, the reduction of the Reynolds stress and of the production. Two subgrid models (the dynamic Smagorinsky model and the dynamic mixed model) have been implemented in a DNS code. This code has already been successfully used to simulate the plane jet [12] and I now propose to use it for the mixing layers computations. A low convective Mach number mixing layer is first simulated ($Mc = 0.16$). Then, mixing layers at higher convective Mach numbers ($Mc = 0.5$ and $Mc = 0.85$) are presented. Results are compared to experimental results and to the DNS results of Pantano *et al.* [6].

2. Computational models

The flow is governed by the Navier-Stokes equations in their compressible form, representing mass conservation, momentum conservation and energy conservation. The Navier-Stokes equations in the LES approach are filtered. In this paper, the top-hat filter with a filter width Δ is used.

The filtered equations were described previously in Le Ribault [12]. The subgrid stress tensor $q_{ij} = \widetilde{u_i u_j} - \widetilde{u_i} \widetilde{u_j}$ is modeled, either by the dynamic Smagorinsky model, either by the mixed model. Those two models were described previously in [12] and for brevity, are not detailed in this paper. The filtered compressible flows equations and there modeling with the two subgrid models were also detailed in Vrenam [9]. The subgrid terms providing for the non-linearity of the viscous terms are neglected.

In the pressure equation, additional subgrid terms also appear:

$$\overline{\tau_{ij} \partial u_j} - \widetilde{\tau_{ij}} \partial \widetilde{u_j} \quad (1)$$

and

$$\overline{u_k \frac{\partial p}{\partial x_k}} + \gamma \overline{p \frac{\partial u_k}{\partial x_k}} - \widetilde{u_k} \frac{\partial \overline{p}}{\partial x_k} - \gamma \overline{p} \frac{\partial \widetilde{u_k}}{\partial x_k} \quad (2)$$

The first term is neglected. The pressure terms can be rewritten as:

$$\frac{\partial}{\partial x_k} \overline{u_k p} - \frac{\partial}{\partial x_k} \widetilde{u_k p} + (\gamma - 1) \left[\overline{p \frac{\partial u_k}{\partial x_k}} - \widetilde{p \frac{\partial u_k}{\partial x_k}} \right] \quad (3)$$

We introduce the notations: $a_k = \overline{p u_k} - \widetilde{p u_k}$ and $b = \overline{p \frac{\partial u_k}{\partial x_k}} - \widetilde{p \frac{\partial u_k}{\partial x_k}}$. These terms are modeled together through a dynamic Smagorinsky type model:

$$\frac{\partial}{\partial x_k} a_k + (\gamma - 1)b = -\frac{\partial}{\partial x_k} \left[\bar{\rho} \frac{\nu_T}{Pr_t} \frac{\partial}{\partial x_k} \left(\frac{\bar{p}}{\bar{\rho}} \right) \right] \quad (4)$$

with

$$\nu_T = 2C_d \Delta^2 |S^d| \quad (5)$$

Pr_t is a turbulent Prandlt number which is dynamically computed.

3. Numerical method

Since the numerical method has already been largely described by Le Ribault [12], only its principal characteristics are recalled here. For the velocity, spatial derivatives are computed using a non uniform fourth-order compact scheme based on the uniform scheme of Lele [13]. In order to ensure long-time nonlinear stability, a fourth-order non uniform compact filter is applied to the field at each iteration. A fourth-order Runge Kutta scheme is used for the time integration of the convective terms.

On the out-flow, the upper and lower side-wall boundaries, non-reflecting conditions, based on the characteristic equations are used. At the inflow boundary, the time variation of the incoming characteristic variables are specified while the equation for the outgoing characteristic variable is solved using internal biased derivatives. Moreover, to isolate the interior of the domain from the effects of the boundary conditions, a buffer zone is used on the non-reflecting boundaries.

At the inflow, an hyperbolic tangent profile is used for the longitudinal mean velocity. A broad-band forcing representative of isotropic turbulence is added and a lateral shape is applied such that the fluctuation intensity peaks in the middle of the shear layer.

4. The mixing layers parameters

Mixing layers at the convective Mach numbers of 0.16, 0.5 and 0.85 are simulated. For the three mixing layers, the velocity ratio U_2/U_1 is equal to 0.47. The momentum thickness δ_{θ_0} at the inflow is equal to 0.05. The Reynolds number, based on the momentum thickness δ_{θ_0} and the velocity difference, is equal to $Re = \rho \delta_{\theta_0} \Delta U / \mu = 300$. The sizes of the grids are also non-dimensionalized by the inflow momentum thickness. Table 1 summarizes the

dimensions of the computational domains and the number of grid points for the three cases.

Table 1 Simulation parameters

M_c	$L_x \times L_y \times L_z$	$N_x \times N_y \times N_z$
0.16	$800 \times 144 \times 160$	$185 \times 119 \times 50$
0.5	$1000 \times 144 \times 80$	$227 \times 119 \times 50$
0.85	$1200 \times 144 \times 80$	$294 \times 119 \times 50$

The grids have been kept as uniform as possible. Preliminary computations have been performed on different grids to check the accuracy of the results. These computations particularly show the importance to take an important number of nodes in the transversal direction z . In the y direction, the grid is very fine in the center of the mixing layer, then a slight stretching is used until the buffer zone. Only one filter size $\Delta = 2h$, where h is the local grid spacing, is used.

5. Low convective Mach number mixing layer

The purpose of this section is to validate the LES results for the low convective Mach number mixing layer by comparing the results with experimental data. The convective Mach number is equal to $M_c = 0.16$. At such convective Mach number, the physical characteristics of the mixing layer are similar to those of an incompressible mixing layer. After an initial transient, the mixing layer thickness grows linearly.

The spreading rate and the parameter S :

$$S = \frac{U_1 - U_2}{0.5(U_1 + U_2)} \frac{d\delta}{dx} \quad (6)$$

are then constant [14]. In this formula the mixing layer thickness is evaluated as:

$$\delta(x) = y_{0.9}(x) - y_{0.1}(x) \quad (7)$$

where $y_{0.9}$ is the coordinate where $U = U_2 + 0.9\Delta U$ and $y_{0.1}$ is the coordinate where $U = U_2 + 0.1\Delta U$. The range of experimental reported values for the parameter S is from $S \approx 0.06$ to $S \approx 0.11$ [14].

The parameter S predicted by the dynamic Smagorinsky model is equal to 0.091 and the value predicted by the dynamic mixed model is equal to 0.1. The spreading rate predicted by our computations is then in good agreement with the experimental values. Based on the momentum thickness, the dynamic Smagorinsky model predicts a growth rate equal to 0.014, while the dynamic model predicts a growth rate equal to 0.0142.

After an initial transient, the profiles of the mean flow and of the turbulent intensities reach self-similar profiles. The LES results are compared with the

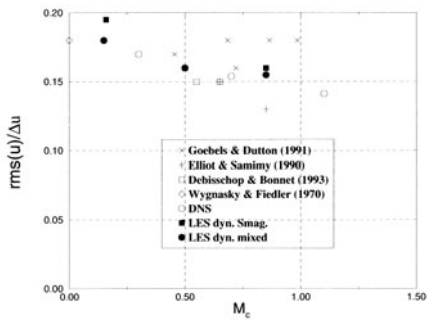


Figure 1a: Comparison of the mean streamwise velocity obtained with the two subgrid models - $Mc = 0.16$

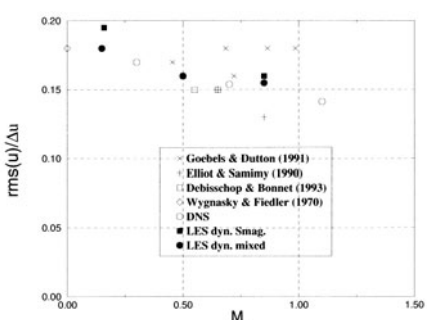


Figure 1b: Comparison of rms streamwise velocity obtained with the two subgrid models - $Mc = 0.16$

experimental results of Bell & Mehta [15] and Spencer & Jones [16]. All the LES profiles have been plotted at the same section $x/\delta_{\theta_0} = 700$. Fig.1a compares the similarity profiles of the mean streamwise velocity obtained by the two subgrid models. The coordinate is non-dimensionalized by the vorticity thickness δ_ω . Good agreement is obtained.

Fig.1b compares the similarity profiles of streamwise turbulence intensity. The peak intensities and the self-similar shape agree well with experiments. Table 2 summarizes more precisely the peak turbulence intensities for the two subgrid models, the DNS of Pantano & Sarkar [6] and the experimental results. The peak turbulence intensities were determined at the section $x/\delta_{\theta_0} = 700$.

Table 2 Comparison of peak turbulent intensities in experiments, in DNS and in LES

	<i>Bell & Mehta</i>	<i>Spencer & Jones</i>	<i>DNS[6]</i>	<i>dyn. Smag.</i>	<i>dyn. mixed</i>
rms(u)	0.18	0.19	0.17	0.195	0.18
rms(v)	0.14	0.125	0.134	0.15	0.135
rms(w)	0.145	0.13	0.145	0.16	0.16
\sqrt{uv}	0.10	0.12	0.103	0.13	0.115

The dynamic mixed model predicts slightly lower values than the dynamic Smagorinsky model as already observed in the case of the jet. The dynamic mixed model predictions are slightly closer to experimental results. The fluctuations are strongly three-dimensional with streamwise > spanwise > transverse intensity. This tendencies also appear in experiments and in DNS results.

6. Compressible mixing layers

Shear layer thickness growth rates from different experiments are plotted along with the DNS results and our LES results in Fig.2.

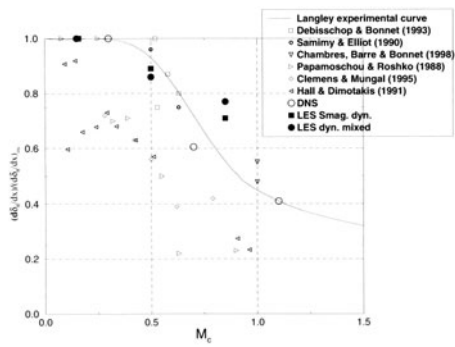


Figure 2 :Dependence of shear layer growth rate on M_c

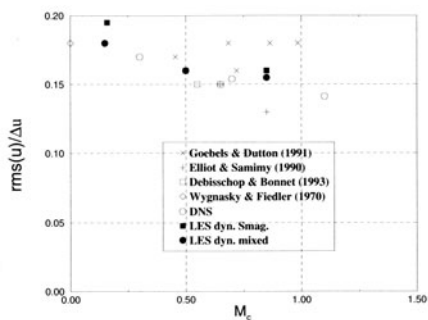


Figure 3a: Dependence of peak streamwise velocity on M_c

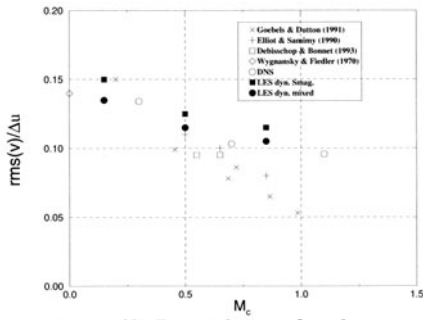


Figure 3b: Dependence of peak transverse velocity on M_c

The spreading rates are non-dimensionalized by the low Mach number mixing layer spreading rates. The spreading rate of the mixing layers decreases with the convective Mach number in agreement with experimental results. This reduction is however weaker than the reduction predicted by experimental results.

The figure 3 presents the dependence of the peak streamwise and transverse velocities on M_c . The results of the two turbulence models are compared to DNS and experimental results.

All the Reynolds stress components slightly decrease with the convective Mach number. But this decrease is more important on the components $rms(v)$ and $rms(w)$. The dynamic mixed model predicts values slightly closer to experimental results than the dynamic Smagorinsky model but the difference between the two models predictions is weak.

Sarkar [6] and Vreman [10] established the link between the diminution of the production and the spreading rate of mixing layers. Figure 4 shows the

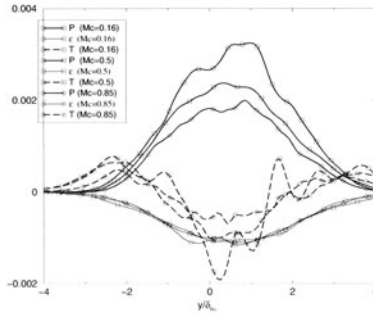


Figure 4 :Turbulent production, total dissipation and transport term for different M_c -
Dynamic Smagorinsky model

comparison of the turbulent production, total dissipation and transport term in the turbulent kinetic energy equation for the three different convective Mach numbers.

Results are presented for the dynamic Smagorinsky model. They are plotted at the sections $x/\delta_{\theta_0} = 700$ for $M_c = 0.16$, $x/\delta_{\theta_0} = 900$ for $M_c = 0.5$ and $x/\delta_{\theta_0} = 1100$ for $M_c = 0.86$. We can see an important decrease of the production and of the transport terms in function of the convective Mach number. The total dissipation (molecular dissipation plus subgrid dissipation) remains relatively unchanged. This agrees with the DNS results that show decreased turbulent production and transport terms with convective Mach number.

7. Conclusions

In this paper *a posteriori* tests of LES in the cases of spatially developing compressible mixing layers have been presented. Two different subgrid stress models are compared: the dynamic Smagorinsky model and the dynamic mixed model. Simulations at the low convective Mach number of 0.16 are first performed. Then, the convective Mach number is increased and simulations are performed at the higher convective Mach numbers of 0.5 and 0.84 more typical of compressible mixing layers. The quality of the LES models is determined by comparison with experiments.

Predictions of the two models are first compared in the case of the low Mach number mixing layer. Concerning the overall prediction of the mean field and the Reynolds stress, the two models are both in good agreement with experimental and DNS results. Self-similarity profiles are obtained for the mean velocity and the rms intensities. The peak values predicted by the dynamic mixed model are slightly closer to experimental results.

Then simulations of compressible mixing layers are performed. The decrease of the growth rate and of the turbulence intensities with the convective Mach

number is predicted. The decrease of the growth rate is however slightly weaker than the experimental one. The prediction of the dynamic mixed model for the turbulence intensities are also slightly closer to experimental results. The decrease of the production and the transport terms is also predicted.

Acknowledgements

I thank Professor Sarkar for fruitful discussions about this work during my stay at San Diego. The support of NEC SX-5 of Idris is acknowledged.

References

- [1] Papamoschou D., Roshko A.: "The compressible turbulent shear layer: an experimental study", *J. Fluid. Mech.*, Vol. 197, 1988, pp. 453-477.
- [2] Elliot G.S., Samimy M. "Compressibility effects in free shear layers", *Physics of Fluids A*, Vol. 2, No.7, 1990, pp. 1231-1240.
- [3] Barre S., Quine C., Dussauge J. : "Compressibility effects on the structure of supersonic mixing layers: experimental results", *J. Fluid Mechanics*, Vol. 259, 1994, pp. 47-78.
- [4] Clemens N.T., Mungal M.G.: "Large-scale structure and entrainment in the supersonic turbulent mixing layer", *J. Fluid Mech.*, Vol. 284, 1995, pp. 171-216.
- [5] Goebel S.G., Dutton J.C.: "Velocity measurements of compressible, turbulent mixing layers", *AIAA Journal*, Vol. 29, No.4, 1991, pp. 538-546.
- [6] Pantano C., Sarkar S. : "A study of compressibility effects in the high-speed turbulent shear layer using direct simulation", *J. Fluid Mech.*, Vol. 451, 2002, pp.329-71.
- [7] Freund J.B., Lele S.K., Moin P. : "Compressibility effects in a turbulent annular mixing layer 1. turbulence and growth rate" *J. Fluid Mech*, Vol. 421, 2000, pp. 229-267.
- [8] Kourta A., Sauvage R, "Computation of supersonic mixing layers", *Physics of Fluids*, Vol. 14, No.11, 2002, pp. 3790-3797.
- [9] Vreman B., "Direct and large eddy simulation of the compressible turbulent mixing layer", PhD dissertation, University of Twente, 1995
- [10] Vreman A.W., Sandham N.D., Luo K.H.: "Compressible mixing layer growth rate and turbulence characteristics", *J. Fluid Mech.*, Vol. 320, 1996, pp. 235-258.
- [11] Doris L., Tenaud C., Ta Phuoc L.: "LES of spatially developing 3D compressible mixing layer", *C. R. Acad. Sci.*, t. 328, Série II b, 2000, pp. 567-573.
- [12] Le Ribault C., Sarkar S., and Stanley S., "Large eddy simulation of a plane jet", *Phys. of Fluids*, Vol. 11, No.10, 1999, pp. 3069-3083.
- [13] Lele, S.K., "Compact finite difference schemes with spectral like resolution," *J. Comp. Phys.*, Vol. 103, No..1, 1992, pp. 16-42.
- [14] Pope B., "Turbulent flows", Cambridge University Press, 2000
- [15] Bell J.H., Mehta R.D.: "Development of a two-stream mixing layer from tripped and un-tripped boundary layers", *AIAA J.*, Vol. 28, No.12, 1990, pp.2034-2042.
- [16] Spencer B.W., Jones B.G.: "Statistical investigation of pressure and velocity fields in the turbulent two-stream mixing layer", *AIAA Paper*, Vol. 71, 613, 1971
- [17] Samimy M., Elliot G.S. : "Effects of compressibility on the characteristics of free shear layers", *AIAA Journal*, Vol.28, No.3, 1990, pp. 903-923.

ON THE TURBULENCE STRUCTURE IN COMPRESSIBLE TURBULENT ISOTHERMAL CHANNEL FLOW

S. Sarkar ¹, H. Foysi ² and R. Friedrich ²

¹*Department of Mechanical and Aerospace Engineering, University of California San Diego
9500 Gilman Drive, La Jolla CA 92093-0411
USA*

sarkar@ucsd.edu

²*Fachgebiet Strömungsmechanik, TU München
Boltzmannstr. 15, 85748 Garching
Germany*

holger@flm.mw.tu-muenchen.de

r.friedrich@lrz.tum.de

Abstract Direct numerical simulations of isothermal channel flow, with Mach numbers ranging from $M = 0.3$ to $M = 3$ and Reynolds numbers ranging from $Re_\tau = 180$ to $Re_\tau = 560$ have been performed. Their statistical analysis shows that changes in the turbulent stress peak values are linked to the changes in the corresponding pressure strain components. The strong attenuation of the pressure strain correlations relative to their incompressible values, is shown to be due to decreasing velocity derivative fluctuations for $x_2^* < 35$, as well as to the decreased mean density with respect to its wall value.

Keywords: compressible channel flow, variable property variation, Reynolds stress anisotropy, pressure-strain

1. Introduction

The investigation of compressible turbulent channel flow provides the possibility of studying compressibility effects in wall-bounded flows, without the occurrence of other complicating phenomena like flow separation or shocks. (Coleman et al., 1995), performed the first DNS of compressible channel flow between cooled isothermal walls at Mach numbers of $M = 1.5$ and $M = 3$. They found the dominant compressibility effects to be caused by strong mean property variations and reported the validity of the Van-Driest transformation. (Huang et al., 1995), investigating the same database, showed that the di-

lational dissipation, as well as the pressure-dilatation provided only negligible contributions. They introduced a semi-local scaling for the turbulence intensities, which accounted for some aspects of the mean property variation. (Lechner et al., 2001), simulated compressible channel flow at a Mach number of 1.5 and reported an increase in the normal Reynolds stress anisotropies whereas the shear stress anisotropy was reduced compared to the incompressible channel flow simulation of (Moser et al., 1999). (Foyi et al., 2003b), investigated compressible isothermal channel flow for Mach numbers of $M = 0.3$ up to $M = 3$, and discussed outer and inner scalings for the turbulent stresses and pressure-strain-tensor. Their simulations showed clearly a reduction of the pressure-strain components in the compressible case with respect to incompressible channel flow simulations. However, so far no satisfactory explanation has been given, for the observed changes in the Reynolds stress anisotropies and the reduction in the pressure-strain correlations.

The objective of this work is to study in more detail the changes of the turbulent stresses due to compressibility and to give an explanation for their behaviour.

Table 1. Flow and computational parameters

Case	M	Re	Re_τ	$\frac{L_{x1}}{h}$	$\frac{L_{x2}}{h}$	$\frac{L_{x3}}{h}$	$T_w(K)$
M0.3	0.3	2820	181	9.6	2	6	298
M1.5	1.5	3000	221	4π	2	$4\pi/3$	500
M2.5	2.5	5000	455	2π	2	$2\pi/3$	500
M3.0	3.0	6000	560	2π	2	$2\pi/3$	500

Table 2. Flow and computational parameters (cont.)

Case	N_{x1}	N_{x2}	N_{x3}	Δx_1^+	Δx_{2min}^+	Δx_{2max}^+	Δx_3^+
M0.3	192	129	160	9.12	1.02	4.21	6.84
M1.5	192	151	128	14.46	0.84	5.02	7.23
M2.5	256	201	128	11.16	1.17	7.46	7.44
M3.0	256	221	128	13.37	0.89	9.38	8.91

2. DNS parameters and description of the numerical method

The Navier-Stokes equations are solved in a nonconservative pressure-velocity-entropy formulation, casting the hyperbolic part of the equations in characteristic form ((Sesterhenn, 2001)). The hyperbolic part is then discretized via 5th-order compact upwind schemes ((Adams and Shariff, 1996)) and the viscous and heat conduction terms using 6th-order compact schemes developed

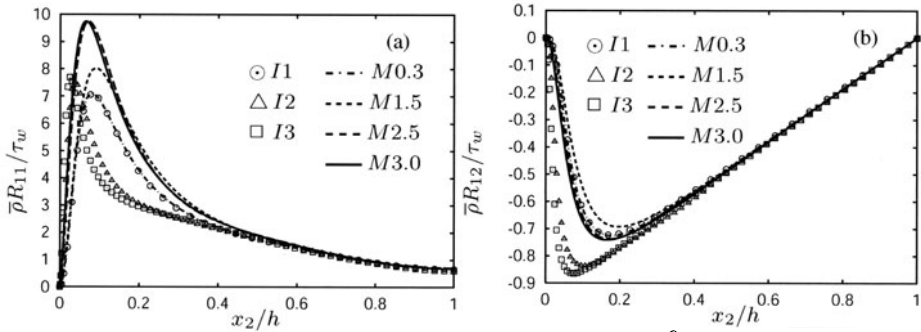


Figure 1. Outer scaling of the turbulent stresses: a) $\bar{\rho}R_{11} = \overline{\rho u_1''^2}$ b) $\bar{\rho}R_{12} = \overline{\rho u_1'' u_2''}$

by (Lele, 1992). Time integration is performed based on a third-order ‘low-storage’ Runge-Kutta method, proposed by (Williamson, 1980). A uniform body force is added to the momentum equation, replacing the mean streamwise pressure gradient and allowing for periodic boundary conditions in this direction. Periodicity in spanwise direction is assumed as well. The Prandtl number is 0.7 and the viscosity is chosen to be proportional to the 0.7th power of the temperature. Tables 1 and 2 show the parameters used in the simulations, where the global Mach and Reynolds numbers are defined as $M = u_{av}/c_w$ and $Re = \rho_w u_{av} h / \mu_w$, respectively. Here, h denotes the channel half width, ρ_m the bulk density $\rho_m = \int_0^h \bar{\rho} dx_2 / h$, u_{av} is defined as $u_{av} = \int_0^h \bar{u} dx_2 / h$ and the viscosity and speed of sound are calculated for constant wall temperature T_w . The friction Reynolds number is defined as $Re_\tau = \rho_w u_\tau h / \mu_w$, with the friction velocity $u_\tau = \sqrt{\tau_w / \rho_w}$ being a result of the simulation. The grid resolution for the different flow cases has been verified by looking at the energy spectra of the flow variables. The resolution is therefore sufficient to resolve the near wall region. The influence of the domain size has been investigated by looking at the two-point correlations. An additional simulation of case M3.0 using twice the domain size in the homogeneous directions has been performed to check the validity of the results. Furthermore cases M1.5 and M3.0 have been compared with the data of (Coleman et al., 1995).

3. Outer scaling

(Coleman et al., 1995), showed that τ_w is the proper outer scaling for the turbulent shear stress (see figure 1a). In (Foyi et al., 2003b), it was observed that this scaling holds for all other turbulent stress components, too (see as an example figure 1b). In addition to that they derived an outer scaling for the terms in the Reynolds stress budget, $\tau_w u_{av} / h$, which was used before by (Huang et al., 1995) for scaling the turbulent kinetic energy budget. As can be seen from figure 2, this scaling collapses the profiles of the pressure strain correlation in

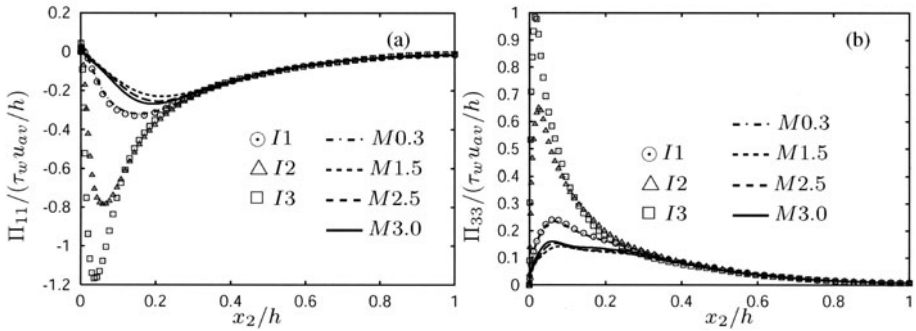


Figure 2. Outer scaling of Π_{ij} , normalized by $\tau_w u_{av}/h$: a) Π_{11} b) Π_{33}

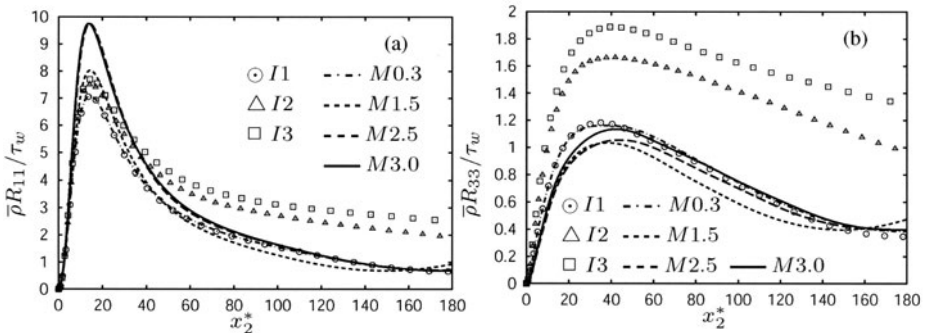


Figure 3. Inner scaling of the turbulent stresses: a) $\bar{\rho}R_{11} = \overline{\rho u_1'^2}$ b) $\bar{\rho}R_{33} = \overline{\rho u_3'^2}$

the outer layer for all Reynolds and Mach numbers. In the near wall region, on the other hand, large deviations in the peak values are observed, necessitating an inner scaling, which reduces the differences between the compressible and incompressible cases.

4. Inner scaling

(Huang et al., 1995) had suggested a semi-local scaling, using local values of density and viscosity to get:

$$u_\tau^* = \sqrt{\tau_w/\bar{\rho}}, \quad x_2^* = x_2 \bar{\rho} u_\tau^* / \bar{\mu}. \quad (1)$$

Although Figures 3a and 3b, showing the streamwise and spanwise turbulent stresses, indicate that the peak position is nearly the same for all cases, there is still a considerable difference between the amplitudes of these quantities for the compressible and incompressible cases near the wall. The streamwise turbulent stress peaks concerning the compressible cases are increased, whereas the spanwise turbulent stress peaks are decreased compared to the corresponding incompressible ones. In order to better understand the mechanism underlying

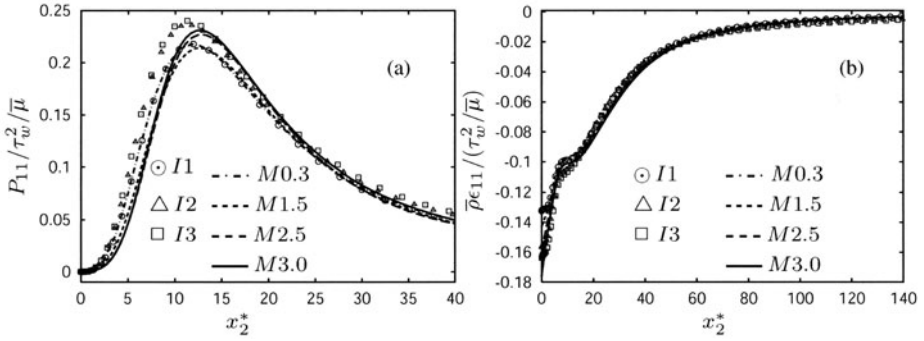


Figure 4. Inner scaling of the production (a) and dissipation (b) in the $\bar{\rho}R_{11}$ -budget

these observations, the streamwise turbulent stress budget is considered:

$$\begin{aligned}
 0 = & -\overline{\rho u_1'' u_2''} \frac{\partial \tilde{u}_1}{\partial x_2} - \frac{\partial}{\partial x_2} \left(\overline{\rho u_1''^2 u_2''} / 2 - \overline{u_1' \tau_{12}} \right) + \\
 & \overline{u_1''} \left(\frac{\partial \overline{\tau_{12}}}{\partial x_2} - \frac{\partial \bar{p}}{\partial x_1} \right) + \overline{p' \frac{\partial u_1'}{\partial x_1}} - \overline{\tau_{1j} \frac{\partial u_1'}{\partial x_j}}, \quad (2)
 \end{aligned}$$

where the individual terms describe production P_{11} , turbulent and viscous diffusion TD_{11} , VD_{11} , mass flux variation M_{11} , pressure-rate-of-strain correlation Π_{11} and turbulent dissipation DS_{11} . The two dominant terms in this equation, the production and dissipation terms, are plotted in Figures 4a and 4b, respectively. The profiles are normalized by $\tau_w^2/\bar{\mu}$, a scaling that emerges naturally from the combination of the integrated mean momentum equation and the logarithmic law for the Van-Driest transformed velocity, to obtain $P_{11} \propto \tau_w^2/\bar{\mu}(1/x_2^* - 1/h^*)$ away from the viscous sublayer. This inner scaling seems to work well for all Reynolds and Mach numbers, in collapsing the profiles of the turbulent production and dissipation terms for the compressible and incompressible cases, with only small deviations in the region $x_2^* < 10$, originating from the viscosity variation. But a look at the pressure strain correlation Π_{11} ($\Pi_{ij} = \overline{p' s'_{ij}} = \overline{p' (\partial u_i''/\partial x_j + \partial u_j''/\partial x_i)}/2$) in Figure 5a, which is a sink term in the streamwise turbulent stress budget, reveals a large attenuation of the compressible curves compared to the incompressible ones, thus forming a major contribution to the change in the turbulent stress mentioned above. The reduction of Π_{33} , shown in figure 5b (a source term in the spanwise turbulent stress budget) explains in a similar fashion the observed reduction of $\bar{\rho}R_{33}$.

4.1 Pressure strain correlation

4.1.1 Correlation coefficient. The reason for the observed reduction in amplitude of the pressure strain correlation, is first examined by looking at the correlation coefficient $\xi_{ij} = \Pi_{ij}/(\{\partial u_i''/\partial x_j\}_{rms} p_{rms})$ of Π_{11} and Π_{22} ,

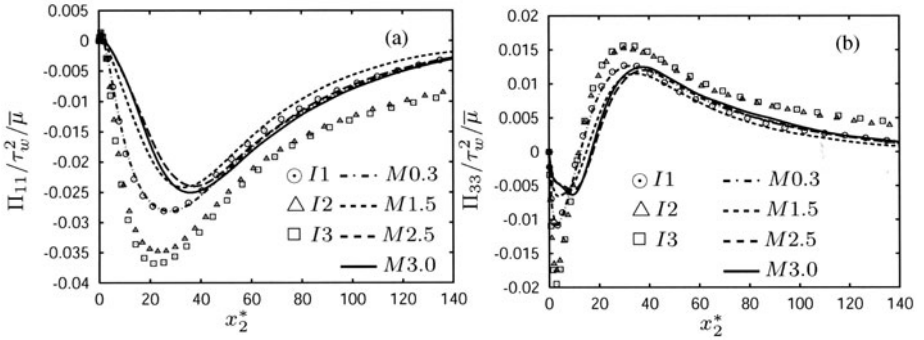


Figure 5. Inner scaling of the pressure strain correlation Π_{ij} : a) Π_{11} b) Π_{33} .

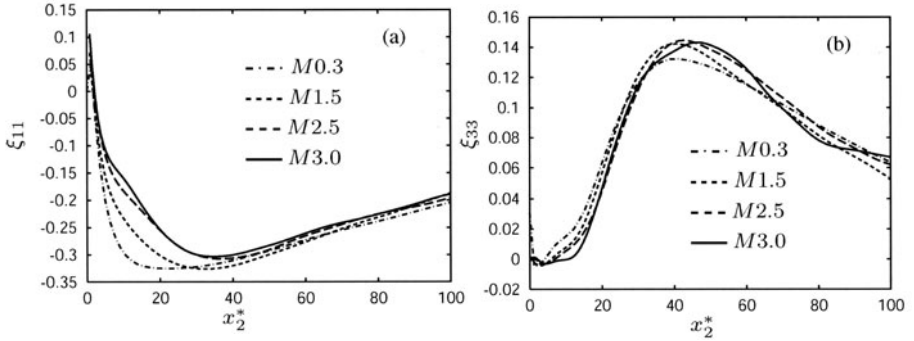


Figure 6. Correlation coefficient ξ_{ij} of Π_{ij} : a) ξ_{11} b) ξ_{33}

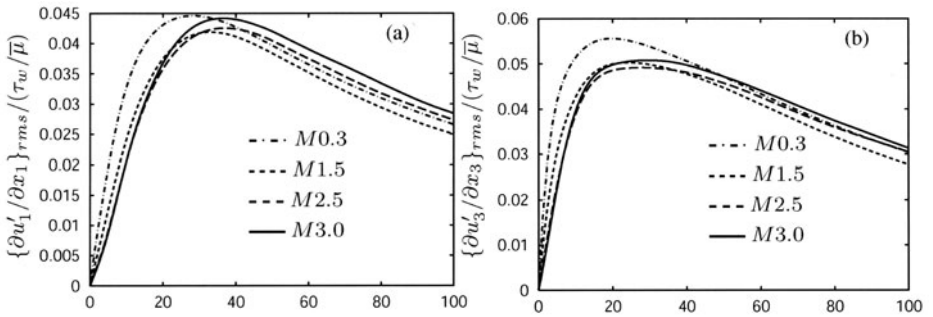


Figure 7. Rms of the streamwise velocity derivatives, normalized by $\tau_w^2/\bar{\mu}$: a) $\partial u'_1/\partial x_1$ b) $\partial u'_3/\partial x_3$.

shown in figure 6. By comparing cases M0.3 and M1.5 one sees a reduction of ξ_{11} in the compressible case compared to the incompressible case, for $x_2^* < 35$, indicating an *increasing decorrelation* with increasing Mach number. Figure 8 indicates furthermore a strong attenuation of the pressure fluctuations in the compressible cases, compared to the corresponding incompressible ones. We will show later that the attenuation of p_{rms} is associated with a reduc-

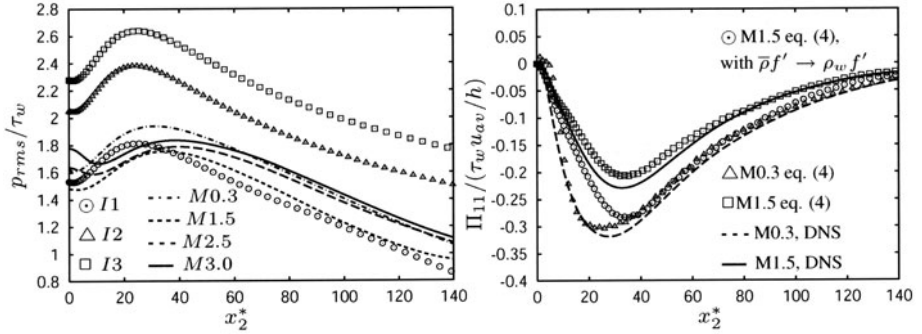


Figure 8. (a) Rms of the pressure, normalized by τ_w (b) Comparison of Π_{11} computed by (4) with the DNS.

tion of $\bar{\rho}$ with respect to its wall value. Accordingly, there is a reduction of Π_{33} . ξ_{33} , unlike ξ_{11} , exhibits only minor changes whereas the velocity derivative fluctuations $\{\partial u'_3/\partial x_3\}_{rms}$ show the same decrease in the compressible cases as $\{\partial u'_1/\partial x_1\}_{rms}$. Thus, all components of Π_{ij} decrease, indicating *decreased redistribution of energy*.

4.1.2 Greens function analysis. The behaviour of the pressure fluctuations and their influence on the pressure strain correlation can be examined by looking at the Green's function solution $G(x_1, x_2, x'_2, x_3)$ of the Poisson equation for the pressure fluctuations (for details see (Foyi et al., 2003a))

$$\begin{aligned} \nabla^2 p' = & -\bar{\rho}(u_i''u_j'' - \overline{u_i''u_j''})_{,ij} - 2\bar{\rho}\tilde{u}_{1,2}u_{2,1}'' + s'_{ij,ij} - 2\bar{\rho}_{,2}(u_2''u_j'' \\ & - \overline{u_2''u_j''})_{,j} - \bar{\rho}_{,22}(u_2''^2 - \overline{u_2''^2}) - 2\tilde{u}_{1,2}(\rho'u_2'')_{,1} - (\rho'u_i''u_j'' \\ & - \overline{\rho'u_i''u_j''})_{,ij} - D_{tt}\rho' =: \bar{\rho}f'. \end{aligned} \quad (3)$$

The operator $D_{tt} = \partial_{tt} + 2\tilde{u}_j\partial_{jt} + \tilde{u}_i\tilde{u}_j\partial_{ij}$ usually leads to a convected wave equation; here we neglect ρ' and justify this *a posteriori*. The pressure strain term can then be written as ($y = (x_2/h - 1)$)

$$\Pi_{ij}(y) = \int_{-1}^1 \bar{\rho}(y') \overline{G * f'(x_1, y, x_3; y') s'_{ij}} dy' + \overline{B' s'_{ij}} \quad (4)$$

with G the homogeneous Green's function for $\partial p'/\partial y = 0$ at the wall, and B' denoting an additional contribution from the boundary. Figure 8b shows a good agreement of this calculation with the DNS data. To elucidate the variable density effect, the density variation is replaced by its corresponding wall value, shown as circles in Figure 8b. One clearly sees that the magnitude of the pressure strain term now increases showing good agreement for $x_2^* > 35$ with the quasi-incompressible case. The deviation near the wall is probably

associated with the decrease of the correlation coefficient, ξ_{ij} , and the velocity derivative fluctuations as discussed earlier.

5. Summary and conclusions

DNS of supersonic channel flow has been used to investigate and explain the behaviour of the turbulent stresses in compressible wall-bounded flows. By looking at the streamwise turbulent stress balance scaled with the semi-local quantity $\tau_w^2/\bar{\mu}$, the compressible counterpart to $\rho u_\tau^4/\nu$, the pressure strain components are identified to be the main reason, for increasing the streamwise turbulent stress peaks and decreasing the wall-normal and spanwise turbulent stress peak values compared to incompressible flow. This can be explained, for the most part, by the decrease of the density $\bar{\rho}$ relative to ρ_w . Very near the wall, there is an additional decrease due to a reduction in the strain rate and its correlation with the pressure.

Acknowledgments

The work was supported by the Deutsche Forschungsgemeinschaft. The computations were performed on the Hitachi SR8000-F1 at the Leibniz Rechenzentrum. S. Sarkar thanks the Alexander von Humboldt Foundation for support of his stay in Munich.

References

- Adams, N. A. and Shariff, K. (1996). A high-resolution hybrid compact-ENO scheme for shock-turbulence interaction problems. *J. Comput. Phys.*, 127:27.
- Coleman, G., Kim, J., and Moser, R. (1995). Turbulent supersonic isothermal-wall channel flow. *J. Fluid Mech.*, 305:159–183.
- Foysi, H., Sarkar, S., and Friedrich, R. (2003a). Compressibility Effects and Turbulence Scalings in Supersonic Channel Flow. *submitted to J. Fluid Mech.*
- Foysi, H., Sarkar, S., and Friedrich, R. (2003b). On Reynolds Stress Anisotropy in Compressible Channel Flow. *Proceedings, Third International Symposium on Turbulence and Shear Flow Phenomena, Sendai, Japan, 2003.*
- Huang, P., Coleman, G., and Bradshaw, P. (1995). Compressible turbulent channel flows: DNS results and modelling. *J. Fluid Mech.*, 305:185–218.
- Lechner, R., Sesterhenn, J., and Friedrich, R. (2001). Turbulent supersonic channel flow. *J. Turbulence*, 2:1–25.
- Lele, S. K. (1992). Compact Finite Differences Schemes with Spectral-like Resolution. *J. Comput. Phys.*, 103:16–42.
- Moser, R., Kim, J., and Mansour, N. N. (1999). Direct numerical simulation of turbulent channel flow up to $Re_\tau = 590$. *Phys. Fluids*, 9:943–945.
- Sesterhenn, J. (2001). A characteristic-type formulation of the Navier–Stokes equations for high order upwind schemes. *Comput. Fluids*, 30:37.
- Williamson, J. K. (1980). Low-Storage Runge-Kutta Schemes. *J. Comput. Phys.*, 35:48–56.

3.5 NOISE GENERATION AND RADIATION

NOISE RADIATION FROM HIGH-SPEED JETS: SOME INSIGHTS FROM NUMERICAL SIMULATIONS

Sanjiva K. Lele

*Department of Aeronautics & Astronautics
and Department of Mechanical Engineering
Stanford University
Stanford, California 94305-4035*

Abstract The noise emanating from high-speed jets consists of jet mixing noise and shock-associated noise with its tonal and broadband components. This paper summarizes well-known features of high-speed jet flows and their relationship to the noise radiated by the jet. Open issues on which different opinions exist are also noted. In this context key findings from numerical simulations of jet flows, and model problems related to jet flows are highlighted. The mechanism responsible for the generation of strong screech noise is discussed, and the role of large-scale structures in jet mixing noise and broadband shock-associated noise are stressed. Implications of a new analytical model of shock-cell noise generation are discussed, and in particular the scaling of shock-associated noise from heated jets.

1. Introduction

The prediction and reduction of jet noise has been a major theme of aeroacoustics research for over 50 years. More stringent community noise regulations require further reductions in jet noise along with other engine-noise components. Technical reviews of jet noise are available [1], [2], [3], [4]. The proceedings of Jet Noise Workshop [5] provides a recent perspective. Key features of jet noise are noted in this paper along with the current understanding of the underlying noise source mechanisms. Examples from recent work on high-fidelity numerical simulations are given and the progress towards physics-based prediction methods is summarized.

2. Representation of jet turbulence

Jet flows contain both quasi-organized large-scale motions reminiscent of instability wave disturbances or wave-packets, and more irregular turbulent mo-

tions. Yet such a decomposition is not formally used in current jet noise theory. Methods such as the wavelet decomposition [6] and proper orthogonal decomposition[7] are being applied to jet flows and their noise, but at present the available information is limited [8], [9], [10], [11]. This type of decomposition is yet to be used in a comprehensive method for noise prediction. One of the following two *extreme* views¹ is commonly adopted for the jet flow:

- A) *all fluctuations represent turbulence*; no explicit representation of the organized wave-packets [13],[14], [15],[16],[17] is used,
- B) *all large-scale motions or ‘large-scale turbulence structures’ correspond to instability waves* [18], [19], [20], [22], [21]; turbulence is assumed to only contain ‘fine-scale’ components [23].

Viewpoint-A is purely statistical and leads to a representation of turbulence-associated noise sources in terms of space-time correlations. Lighthill [24], [25], [26] adopted this view. Statistical representations of acoustic sources have been sought in many studies [27], [28], [29] including recent work [30], [31]. Many studies take into account the effect the jet mean-flow has on the radiated noise, a feature shared by Tam’s fine-scale noise model [23], also see [32]. Although a statistical representation does not rule out the presence of orderly structure in jet turbulence, this information is not explicitly reflected in current models.

Viewpoint-B treats the dynamics of *large-scales* as instability wave-packets². This requires the mean-flow to be specified, or predicted. RANS equations, sometimes with adjusted model coefficients, are often used. Integral methods are used to represent the non-linear interactions between the wave-packet and other ‘background’ disturbances, including finer-scale turbulence [39], [21], [40]. It is arguable if an accurate prediction of instability wave-packets can be managed efficiently within the framework of a small set of interacting modes, such as the non-linear disturbance equations NLDE [41] or nonlinear parabolized stability equations NPSE [42]. Recently using PSE [93] identified the potential importance of supersonically-convected entropic non-uniformities in the core of a heated jet (called ‘core-modes’) to the noise radiation. NPSE has also shown remarkable accuracy in strongly nonlinear two-dimensional shear layers[43]. DNS data from a supersonic turbulent jet [44] also reveals the importance of nonlinearity for modal amplitude prediction. Noise radiation predictions using NPSE are under development.

¹With notable exceptions of Liu[35] and Michalke [12] and references therein.

²The large-scale eddy-structure in jets has been linked to the linearized instability characteristics of the mean-flow [21], [33]. A flow disturbance at a fixed frequency initially grows in amplitude and subsequently decays due to mean flow spreading and nonlinear interactions, giving rise to a *wave-packet* with a carrier wavenumber and modulation amplitude which change slowly along the jet [34]. This modulation results in noise radiation from subsonically convected ‘instability wave’ disturbances [35], [36], [37], [38].

Tam et. al. [45] show that far-field jet noise spectra are well described by two empirical spectra, one attributed to large-scales and the other to fine-scales. There is, however, no experimental evidence of a scale-gap between large and fine-scales in turbulent jets. Jet turbulence is intrinsically a multi-scale phenomena. Hence the predictions of the noise radiated by the large-scales need to be combined with the noise radiated by turbulence at other scales, intermediate and fine-scales.

Lighthill's theory provides an estimate for the jet mixing noise. At 90° from the jet axis this theory gives

$$\frac{p'}{p_\infty} \sim \left\{ \frac{\rho_j}{\rho_\infty} \left(\frac{u'}{U_j} \right)^2 \left(\frac{f D_j}{U_j} \right)^2 \left(\frac{L}{D_j} \right)^3 \right\} M_a^4 \frac{D_j}{r}, \quad (1)$$

where $M_a = U_j/C_\infty$ is the 'acoustic Mach number' of the jet, f , L and u' are *representative* scales for the peak frequency, correlation length, and turbulent velocity scale. Traditionally the prefactor in $\{\}$ is taken to be a constant, yielding the famous U_j^8 law for OASPL. Unfortunately, independent estimates of all factors in (1) as a function of jet operating conditions are not available. Reasons for departure from the U_j^8 scaling thus remain ambiguous. Consider the noise of heated jets [57]: at low jet speed heating increases OASPL but the opposite is observed at higher speeds, and the shape of the noise spectra are also affected. However, Tam et. al. [45] show that the noise spectra at 90° fit the empirical fine-scale spectrum in heated supersonic jets. Does this imply that a correlation such as (1) may still hold? An empirical fit to OASPL, is also given in [45] and the trend of data falling on different straight lines on a log-log plot for different T_r/T_∞ (T_r is the reservoir stagnation temperature) is stressed. This trend in the data can also imply a change in the prefactor in (1) as T_r/T_∞ is varied, but there is insufficient data to draw a conclusion.

Even though (1) does not account for many physical effects which are important in the jet flow, such as refraction of high-frequency sound by the flow and the coherent nature of low-frequency disturbances, it has served as a useful guide towards less noisy propulsive jets. Besides lowering the mixed-flow jet velocity which gives dramatic noise reduction, other methods which alter jet eddy-structures by geometrical changes to the nozzle (such as with chevron, tabs, mixer lobes), or micro-jets and other actuators to reduce turbulence intensity near the end of the potential core have shown noise reduction benefits. But it is oversimplistic to characterize the entire jet flow field with a single length scale l , and time scale $1/f$, as implied in (1). Empirical models have been derived which use two or three separate scales for different regions of the jet, but these may not have the sensitivity needed for significant design changes. Manipulation/control of jet mixing to achieve less noisy flow at full-scale (in EPNL) is an art.

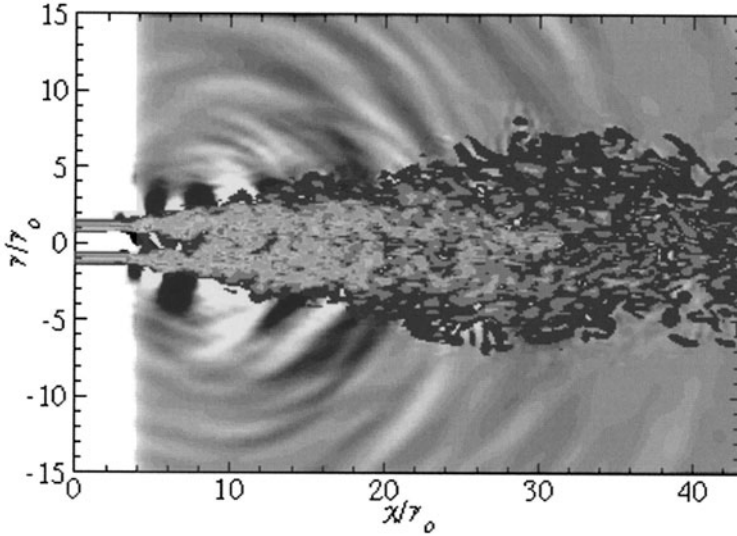


Figure 1. Contours of dilatation (outside the jet) overlaid on contours of $\|\omega\|$ (in the jet) from LES of a $M_j = 0.9$ jet by Bodony & Lele [49]

It is well known that scaling such as (1), along with the attendant ‘Doppler factors’, is inadequate for the overall noise level in the jet-noise peak direction, say at 30 to 50° from the jet axis. The spectral shape is significantly different [45], and OASPL varies more rapidly than Lighthill’s V_j^8 scaling [45]. The frequency of the peak noise is *curiously* independent of the jet speed V_j and $fD_j/C_\infty \sim \text{const}$ is observed [58], [57], [45]. At present there is no comprehensive theory³ to predict the most *dominant* noise radiation from a jet. A predictive decomposition of jet turbulence which enables improved noise predictions over all observer angles remains an open topic for new research.

A computational alternative to the methods based on specific decompositions is to lump all large-scale disturbances together and model only the unresolved-scales. This sidesteps the issue of wave-packet/irregular turbulence decomposition and is the general approach of large-eddy simulation (LES). Significant progress in the use of LES for jet noise predictions has been made recently [46], [47], [48], [49] (see figure 1 as an illustration) and new insights on

³For supersonically convecting eddy-structures, *Mach wave* radiation is dominant along a preferential direction. This mechanism permits a linearized theory which is quite successful [37], see [59], [60], [61], [62] and has stimulated low noise configurations for dual-stream jets [63].

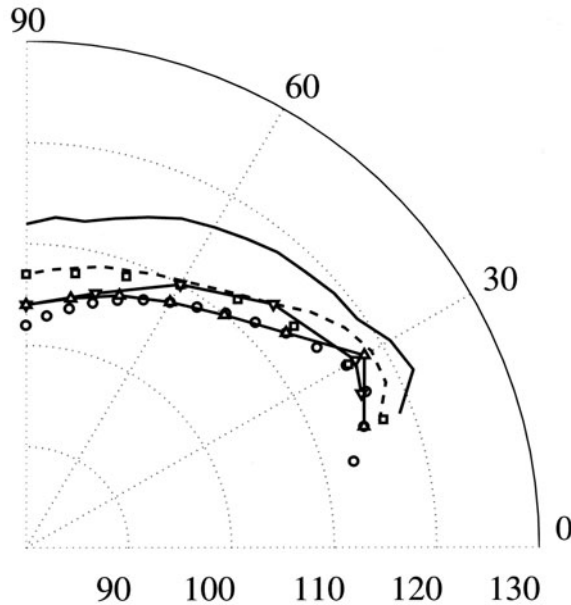


Figure 2. OASPL directivity at a distance of $60r_o$ from the jet exit. Original calculation, — and New calculation, - - from Bodony & Lele [49]; [51], \circ ; [52], \square ; [53], \triangle - -;

noise generation in turbulent jets are expected from such studies in the next few years. Due to computer resource limitations (see [50]) current jet LES studies use inlet conditions of an artificially thickened shear-layer. This can adversely impact the natural development of azimuthal variations in the jet and the radiated noise levels, as shown in figure 2, 3, unless special care is taken [49]. Efforts to include the nozzle geometry in the calculations are also being pursued and require careful development and validation. Theoretical/modeling guidance towards less noisy designs remains an aim of on-going studies.

3. Jet screech and shock-associated noise

Imperfectly-expanded jets produce additional noise due to the interaction of the jet turbulence, particularly its large-scales, with the shock-cell structure existing within the jet. Its tonal components called jet screech, requires a feedback loop [64]. Tam's review [4] discusses the present physical understanding of these noise components. At the nozzle lip *embryonic* shear-layer disturbances are generated, which convect and amplify in the developing shear-layers. Their interaction with the second/third shock-cell generates acoustic waves which travel upstream to the nozzle lip and close the loop. The phase criterion for

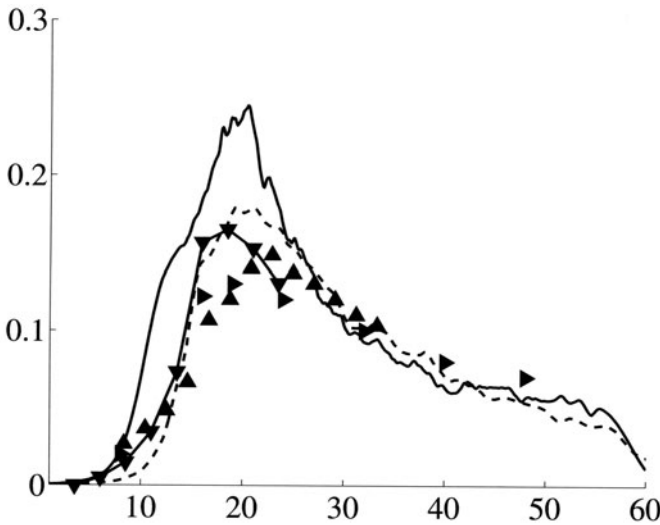


Figure 3. Centerline root-mean-square streamwise fluctuations along the jet axis; Original calculation, — and new calculation, — — from Bodony & Lele [49]; [46], — ∇ —; [55], \triangle ; [56], \triangleright .

constructive reinforcement over the feedback loop provides a formula for the frequency of screech tones with good agreement with data (see [65]). However, predictions of screech amplitude, its directivity and the nonlinear staging phenomena are not available [4]. Developing methods for noise predictions in flows involving a resonance, including jet screech and cavity flows, is an area of active research.

Shock-associated noise is typically most intense in the direction upstream to the jet and exhibits spectral bumps with peak frequency increasing with the inlet angle χ . Harper Bourne & Fisher's pioneering study [74] explained these features using a phased-array of simple noise sources located at the end of each shock-cell each phased according to the convective time delay for a turbulent eddy to pass over each shock-cell. The Lagrangian correlation time limits the spatial coherence of the noise sources. Tam and Tanna [75] noted that a phased-array of simple sources predicts noise radiation at harmonically related tones which are not observed, and proposed a distributed-source model for the shock-cell noise generation. In their model the turbulent motions are regarded as stochastic instability waves (viewpoint B). Its non-linear interaction with the wave-guide modes (representing the shock-cell structure) radiates sound. This interaction implies flow disturbances with upstream-directed supersonic phase speed and results in upstream-directed Mach waves. Specific frequencies radiate preferentially at particular angles from the inlet axis. This basic model was given a firm mathematical foundation in later work by Tam [22], who

also gave a semi-empirical formula for predicting the shock-cell noise, and showed its effectiveness with detailed comparisons to the narrow band shock-cell noise measurements by Norum and Seiner [78] and others. This semi-empirical model has been refined further [76], [77] and represents the present state-of-the-art in shock-cell noise prediction.

Despite its success some significant limitations exist in using this model. The noise prediction is based on an *assumed* spatio-temporal distribution of near-field pressure disturbances which are supposed to result from a nonlinear interaction between the large-scale instability waves of the jet and its shock-cell structure. The former is modeled with a Gaussian wavepacket shape and the latter is an empirical modification of the Prandtl-Pack solution. In this sense Tam's prediction is based on a *model* of the near-field pressure fluctuation; it does not model the sound sources. As a result, further extensions of this semi-empirical formula⁴, to account for co-annular or other nozzle configurations are difficult, and the semi-empirical near-field pressure model leaves unsettled questions about the scaling of shock-cell noise.

In principle LES can be used to study the noise-generation mechanisms in an imperfectly-expanded jet, but this is computationally demanding. Besides representing the multi-scale jet turbulence, the shock-cell structure which involves steep gradients in the early jet, would also need to be accurately captured. Such a calculation is yet to be attempted, but detailed study of related model problems [79], [80] has provided insights into improving shock-cell noise prediction methods.

4. Sound generation in jet screech

Shen & Tam [66] used a hybrid method to study jet-screech. They solve the jet 'mean' flow using the unsteady RANS approach. The k - ϵ equations, with coefficients for jet flows, were solved in the turbulent flow region and the (axisymmetric) Euler equations are solved in the exterior region. The nozzle geometry is retained with a multiple block mesh with the highest resolution in the near-nozzle region. The calculations which use DRP scheme aim to predict the amplitude and directivity of screech tones. This type of URANS approach can be justified when the spatial and temporal scales L_a , τ_a , of the dominant acoustic waves *and* their 'source processes' satisfy $L_a \gg L$, and $\tau_a \gg \tau$, where L and τ are representative spatial and temporal scales of the turbulence. The former condition is easily satisfied but the latter holds only marginally for the observed screech tones. URANS has also been used in other resonant acoustics phenomena such as supersonic cavity tones [67]. In recent work Tam et. al.

⁴As noted already by Tam (1987, 1990), the spectral peaks predicted by the formula for small inlet angles are too narrow.

have extended this approach to non-axisymmetric modes and shown that the mode-switching phenonema observed in screech from circular jets is reproduced. This raises expectations that a simple dynamical systems model could predict jet screech behavior, also see [68].

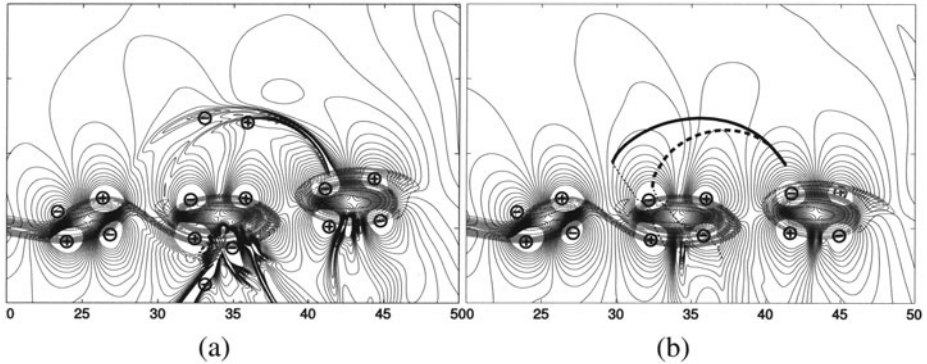


Figure 4. A snapshot of results from screech model problem. a) DNS result; b) Geometrical acoustics result. Solid lines show contours of dilatation whose sign is marked. Also overlaid are contours of vorticity at the same instant. From Suzuki & Lele (2003)

A similar suggestion that the sound generation process in jet screech can be modeled with simpler models has emerged from DNS studies. Manning & Lele [70] studied an isolated screech-noise source region in a shear layer. Inflow boundary conditions are used to specify instability-wave eigenmodes which grow downstream and form large-scale vortices. Boundary conditions are also used to independently specify a compression wave which is stationary in the supersonic stream. The interaction of the vortices with the compression-expansion wave generates sound. Upstream boundary conditions are designed to ‘absorb’ the upstream travelling sound and thus suppress the re-excitation of the shear-layer. Other critical boundary conditions are a ‘quiet’ treatment of the outflow zone so that large-scale vortices and sound travel out of the domain without a significant reflection. The numerical boundary conditions are quite challenging and require a careful validation [69]. The snapshots from DNS [70] illustrate the sound generation process. As the large-scale shear-layer vortices convect past the interaction location, the tip of the compression wave oscillates significantly. During the time when the so-called braid region passes over the compression wave tip, a part of this wave is observed to leak across the shear-layer towards the ambient region initiating a sharp cylindrical compression wave. Refraction of this wave back into the supersonic flow can also be observed. This is an upstream travelling Mach wave within the supersonic flow.

The DNS data [70] show that the radiated sound pressure level is proportional to the ‘local’ pressure rise in the shock-cell structure at the noise-source location. This is consistent with the experimental data on broadband shock-associated noise [74], [75] which show a proportional scaling. This proportional scaling draws attention to a ‘linear’ mechanism of sound-generation. The linear scaling is further verified by a separate calculation using the linearized Euler equations (LEE) about the non-linear unsteady flow of the shear layer. Primary features of the radiated signal observed in DNS agree very well with the LEE calculation. The radiated sound level is, however, *not* necessarily proportional to the amplitude of the unsteady disturbances in the shear layer. An amplitude threshold is observed below which the radiated sound is proportionally weak, but above it strong radiation occurs. As the shear-layer disturbances grow, they form distinct vortices (clumps of vorticity) and braid regions between them. Using Stuart’s solution [71] (which contains an amplitude parameter A which controls vorticity clumping) of the (incompressible) Euler equation as a baseflow, it was found that a vortex-laden mixing layer also shows the same thresholding behavior as the full DNS.

The model of geometrical acoustics to track ray trajectories and wavefronts through the unsteady baseflows of the vortex-laden mixing layer offers an explanation [70] of the DNS results. The initial ray direction corresponds to the stationary Mach waves in the supersonic stream. For small A all rays are reflected back towards the supersonic flow, but as A increases a small window of rays penetrate across the mixing layer; the onset of transmission occurring around $A \approx 0.54$. The size of the ray bundle which is transmitted above this threshold grows initially but saturates at high A ; this limits the maximum transmission across the mixing layer as observed in full DNS. In more recent studies Suzuki & Lele [72] have provided a mathematical justification of the ray-acoustics limit for the jet-screech problem. They show that the problem of propagation of a weak shock, with a steep gradient, in a vortex-laden mixing layer is analogous to the ray-tracing approach of high-frequency geometrical acoustics. Taking this approach to the next order, they also show that the amplitude of the radiated sound can be satisfactorily predicted. An example of this is shown in figure 4. The prediction of the radiated shock front agrees closely with the DNS observation. Recent measurements [73] in a screeching jet have provided an unprecedented detail of the unsteady jet flow during the screech cycle. These data support the notion that vorticity clumping in the jet shear layer plays a major role in determining the screech amplitude.

5. Broadband shock-cell noise generation

Recent numerical simulations have also given new insights into the broadband shock-cell noise generation. Consider the schematic of an underexpanded jet in

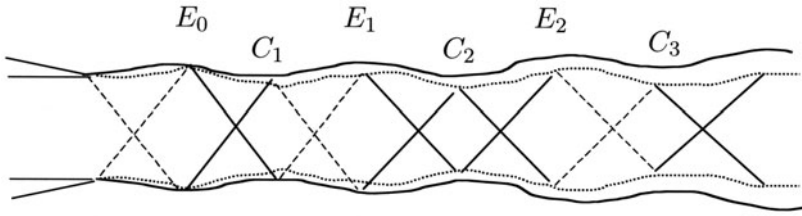


Figure 5. A schematic representation of the shock cell structure in a moderately under-expanded jet. Solid lines drawn within the jet represent compression waves, similar dashed lines are expansion waves. Shock-cell shear-layer interaction locations are labeled.

figure 5. The shock-cell structure in early parts of a jet comprises of relatively steep compression waves or shocks. The turbulent eddies in the early jet have a short life time, thus each interaction with the shock-cell structure behaves as an isolated source region. Lui & Lele [79] have conducted DNS studies of noise generation from such an ‘isolated noise source’. Figure 6 shows a visualization of the noise radiation from the interaction of a turbulent shear layer with an isolated shock-cell. The cylindrical waves originating from the interaction region are attributed to this interaction. This radiation is approximately omni-directional with an apparent origin somewhat downstream of the interaction site. A detailed study of the noise-generation [80] shows that the observed sound is generated closer to the supersonic edge of the shear-layer and travels downstream before radiating into the ambient. This explains the downstream shift in the apparent source. The magnitude of the radiated pressure was found to scale with the imposed pressure change in the incident compression wave, a scaling observed in experiments. Interestingly, the spectral peak of the radiated noise corresponds closely with the spectral peak of the turbulence in the shear-layer at the interaction location. This can be observed in figure 7 (a)-(b) which shows the frequency spectrum of TKE near the interaction location and the (noise) pressure spectrum at an upstream observer point, respectively. This coincidence is significant since the elevated spectral level of shock-cell noise typically extends to frequencies much higher than the mixing-noise peak at $\chi = 90^\circ$. First few shock-cell shear-layer interactions, see figure 5, can potentially generate noise at these high frequencies. A theoretical model which captures many features of the DNS results has also been developed recently [81]. This model provides analytical predictions for the noise radiation from the interaction of shear-layer disturbances with an isolated shock-cell. Its formulation draws from previous theoretical work by Kerschen & Cain [82] and Tam [22]. The noise source terms associated with the shock shear-layer interaction are reformulated using generalized functions and the result is simplified

by appeal to observations from DNS. The radiated noise depends on the local shock and turbulence properties; the model shows the streamwise (turbulent) velocity fluctuation, $\frac{u_1'}{U_j}$, and the local (shockcell) pressure amplitude Δp to be controlling variables. Such a model can provide useful extensions of the existing shock-cell noise prediction methods, and efforts along these lines are underway.

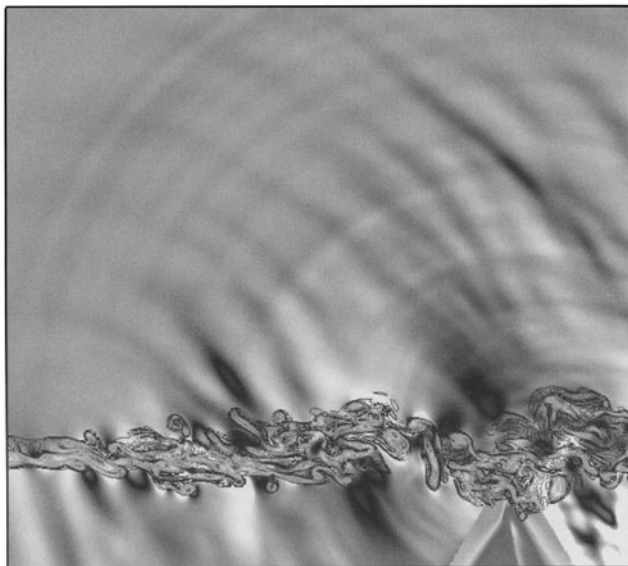


Figure 6. Visualization from DNS of the interaction of a compression wave with a turbulent shear layer. Contours of vorticity magnitude show the shear layer and the compression wave and its reflection are observed in the pressure contours (triangle shape). Contours of dilatation in gray-scale show the sound field. The noise generated by the interaction of turbulence with the compression wave appears as weak cylindrical waves. $M_1 = 1.2$, $M_2 = 0.0$, $\Delta p/p_1 = 0.2$ Figure 3 from Lui & Lele, 2002.

Lui & Lele's DNS provides data on space-time correlations relevant to shock-cell noise prediction. Such data have guided the development of a statistical shock-cell noise model. It is common in shock-cell noise literature to associate the radiated noise amplitude with the shock-cell pressure amplitude Δp . The new model [81] provides a mathematical basis/explanation of this scaling. It also explains why shock-cell noise is independent of the jet velocity (for a given pressure ratio). This remarkable property of heated jets appears to be without a rational explanation in the published literature! The explanation found is very simple [81]. The shock-cell noise sources, for example the unsteady stress-fields due to the interaction, are proportional to the local

(mean) jet density and are bilinear in the turbulence velocity $u_i^{(t)}$ and shock-cell-associated velocity disturbance $u_i^{(s)}$. For small amplitude disturbances the latter (Mach waves) is proportional to Δp but is also inversely proportional to the local (mean) jet density. If the local turbulence intensity $u_i^{(t)}/U_j$ is insensitive to the jet temperature, the radiated shock-cell noise is proportional to Δp and independent of U_j and T_j , etc. This simple scaling property is shared by a more complete shock-cell noise model which accounts for the spatially extensive noise-sources. This simple scaling can be contrasted with the empirically determined amplitude factor in Tam's formula [76] which shows good agreement with data but with no explanation offered for the specific empirical function used.

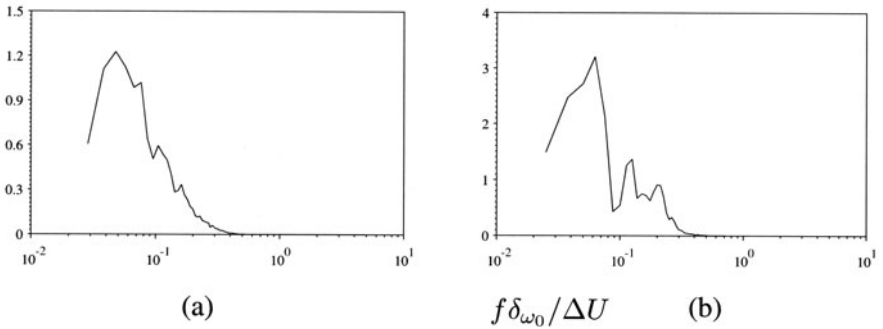


Figure 7. (a) Frequency spectrum of u_1' near the interaction location and (b) spectrum of the radiated noise (pressure) measured at approximately 45° from the upstream direction. Both spectra are pre-multiplied by the frequency f . From Lui & Lele (2003)

Using the insights from the DNS, new physics-based noise prediction approaches for shock-cell noise are being developed. These include extensions of the semi-empirical approach of Tam, and predictions based on (numerically) solving the instability wave shock-cell interaction problem. These approaches capture the noise radiated by the complete jet and preliminary results are very encouraging.

5.1 Sound generation in a near-sonic jet

DNS and LES studies of a turbulent jet and its noise radiation have recently been reported. Freund [53], [54], [83] have reported results from DNS of near-sonic and supersonic low Reynolds number jets. The overall features of the flow, such as the mean flow profiles, the rate of spreading of the jet, turbulence profiles, and overall SPL and its directivity are in remarkable agreement with the available experimental data [51] (at low Reynolds numbers). Also reported was an analysis of the noise-sources based on Lighthill's formulation, such as the spatial distribution of sound-source-strength and its frequency-

wavenumber dependence. It is intriguing that the source-distribution responsible for the dominant noise radiation from this turbulent jet has a very simple wave-packet structure. At present it is not known whether this simple source structure would persist if the early shear-layers of the jet were also turbulent, but this is a distinct possibility. There is experimental evidence for wave-packet-like source distributions. Laufer and Yen [86] and Crow [87] interpreted their jet noise measurements in terms of a line-antenna model of the jet. Crighton [85] analyzed the noise radiation from the jet's orderly structure in terms of a wave-packet model, and this idea has been exploited by Fuchs and Michalke [88]. Crighton and Huerre [38] developed the model problem of radiation from a wave-packet further and characterized its radiation as 'superdirective'. Colonius et al. [84] also found that the noise radiation from organized vortex-pairings could be represented as a 'superdirective' radiation from a wave-packet. Further analysis of the data gathered from such DNS/LES studies of jets would be forthcoming in future and this will provide a fertile ground for developing new source approximations, and for developing hybrid methods for computations and noise predictions. An interesting use of jet DNS data is reported by Freund et. al [89]. The time dependent data was filtered to remove the scales containing most of the turbulent kinetic energy via spatial filtering and the dynamics of the very-large-scales were studied. This severe filtering did not affect the dominant low-frequency noise radiation from the jet confirming the importance of very-large scales to noise radiation. Further processing of the data is continuing.

Development of LES for aeroacoustic predictions is a very active area of ongoing work. Appropriate treatment of turbulent inflow, SGS models, and noise models for the scales not captured in LES are being pursued. Comments on the current status of LES for jet noise were made earlier. Control of numerical errors is very critical in such calculations. Constantinescu & Lele [48] conducted the LES of a near-sonic jet using high-order compact finite difference schemes. They devised a special treatment of the governing equations near the cylindrical co-ordinate singularity [90]. They also note that, as the Reynolds number of the jet is increased a problem associated with energy-pile up near the grid-scales is encountered. This is attributed to aliasing errors from non-linear terms; the sub-grid model alone is not sufficient to prevent energy pile up. A spatial filtering of the solution, with an eighth-order compact filter [91], is applied every 200 time steps. This procedure is adopted in further work [49]. A recent study of jet LES by Bogey & Bailly [92] relies entirely on high wave number filtering as a surrogate SGS model with striking results on jet turbulence and noise.

Acknowledgments

The author is grateful to the organizers of the DLES5 Conference for their invitation to present this talk. A talk similar in content was presented at the ASME/JSME Fluids Engineering Conference at Honolulu in July 2003. Partial support for this work from Boeing and the Aeroacoustics Research Consortium via the Ohio Aerospace Institute is gratefully acknowledged. The author is deeply thankful to Prof. J. Freund, Dr. T. Manning, Dr. T. Suzuki, Dr. C. Lui and Mr. D. Bodony for their permission to reproduce results from collaborative work.

References

- [1] Lilley, G. M. in Vol 1, NASA R. P. 1258, 1991.
- [2] Tam, C. K. W. in Vol 1, NASA R. P. 1258, 1991.
- [3] Goldstein, M. E. in Vol 1, NASA R. P. 1258, 1991.
- [4] Tam, C. K. W., *Ann. Rev. Fluid Mech.*, 1995, **27**, p. 17-43.
- [5] Proceedings of the Jet Noise Workshop, NASA/CP 2001-211152, Nov. 2001.
- [6] Farge, M. *Ann. Rev. Fluid Mech.*, 1992, **24**, p. 395-457.
- [7] Berkooz, G., Holmes, P. and Lumley, J. L. *Ann. Rev. Fluid Mech.*, 1993, **25**, p. 539-575.
- [8] Freund, J. B. and Colonius, T. 2002, AIAA-2002-0072.
- [9] Citriniti, J. H. and George, W. K., *J. Fluid Mech.*, **418**, 2000, p. 137-166.
- [10] Arndt, R. E. A., Long, D. F. and Glauser, M. N., *J. Fluid Mech.*, **340**, 1997, p. 1-33.
- [11] Gordeyev, S. V. and Thomas, F. O., *J. Fluid Mech.*, **414**, 2000, p. 145-194.
- [12] Michalke, A. and Fuchs, H. V., *J. Fluid Mech.*, **70**, 1975, p. 179-205.
- [13] Davies, P. O. A. L., Fisher, M. J. and Barratt, M. J., *J. Fluid Mech.*, **15**, 1963, p. 337-367, and Corrigendum *J. Fluid Mech.*, **15**, 1963, p. 559.
- [14] Bradshaw, P., Ferriss, D. H. and Johnson, R. F., *J. Fluid Mech.*, **19**, 1964, p. 591-624.
- [15] Zaman, K. B. M. Q., *J. Sound Vib.*, **106**, 1986, p. 1-6.
- [16] Hussein, H. J., Capp, S. P. and George, W. K., *J. Fluid Mech.*, **258**, 1994, p. 31-75.
- [17] Panchapakesan, N. R. and Lumley, J. L., *J. Fluid Mech.*, **246**, 1993, p. 197-223.
- [18] Plaschko, P., *Phys. Fluids*, **24**, 1981, p. 187-193.
- [19] Plaschko, P., *Phys. Fluids*, **26**, 1983, p. 2368-2372.
- [20] Tam, C. K. W. and Chen, K. C., *J. Fluid Mech.*, **92**, 1979, p. 303-326.
- [21] Morris, P. J., Giridharan, M.G. and Lilley, G. M., *Proc. Royal Soc. London, Ser. A*, **431**, 1990, p.213-243., also Vishwanathan, K. and Morris, P. J., *AIAA J.*, **30**, 1992, p.1529-1536.
- [22] Tam, C. K. W., *J. Sound Vib.*, **116**, 1987, p. 265-302.
- [23] Tam, C. K. W. and Auriault, L. *AIAA J.* 1999, **37**, p. 145-153.
- [24] Lighthill, J., *Proc. Roy. Soc. A.*, 1952, **211**, p. 564-587.
- [25] Lighthill, M. J., *Proc. Roy. Soc. A.*, 1962, **267**, p. 147-182.
- [26] Lighthill, M. J., *AIAA J.*, 1963, **1**, p. 1507-1517.

- [27] Ffowcs Williams, J. E., *Phil. Trans. Roy. Soc. A.*, 1963, **255**, 469-503.
- [28] Lilley, G. M. AGARD CP 131, Noise Mechanisms, 1974.
- [29] Goldstein, M. E., *Aeroacoustics*, 1976, McGraw Hill.
- [30] Bailly, C., Lafon, P., Candel, S., *AIAA J.*, **35**, 1997, p. 1688-1696.
- [31] Khavran, A. , *AIAA J.*, 1999, **37**, p. 832-841.
- [32] Morris, P. J. and Farrasat, F., 2002, *AIAA J.*, **40**, p. 671-680.
- [33] Gaster, M., Kit, E. and Wygnanski, I., *J. Fluid Mech.*, **150**, 1985, p. 23-39.
- [34] Crighton, D. G. and Gaster, M., *J. Fluid Mech.*, **77**, 1976, p. 397-413.
- [35] Liu, J. T. C., *J. Fluid Mech.*, **62**, 1974, p. 437-464.
- [36] Tam, C. K. W. and Morris, P. J., *J. Fluid Mech.*, **98**, 1980, p. 349-381.
- [37] Tam, C. K. W. and Burton, D. E., *J. Fluid Mech.*, **138**, 1984, p. 273-295.
- [38] Crighton, D. G. and Huerre, P., *J. Fluid Mech.*, **220**, 1990, p. 255-268.
- [39] Mankbadi, R. and Liu, J. T. C., *Phil. Trans. Royal Soc. A*, **298**, 541-602.
- [40] Tam, C. K. W. and Morris, P. J., *J. Sound Vib.*, **102**, 1985, p. 119-151.
- [41] Morris, P. J., Long, L. N., Scheidegger, T. E., Wang, Q. and Pilon, A. R., AIAA-98-2290.
- [42] Yen, C. and Messersmith, N. 1999. AIAA 99-1859.
- [43] Day, M., Mansour, N. and Reynolds, W. C., *J. Fluid Mech.*, **446**, 2001, p. 375-408.
- [44] Mohseni, K., Colonius, T. and Freund, J. B., *Phys. Fluids*, **14**, 2002, p. 3593-3600.
- [45] Tam, C. K. W., Golebiowski, M. and Seiner, J. M. AIAA 96-1716.
- [46] Bogey, C., Bailly, C. and D. Juve. AIAA/CEAS-2000-2009.
- [47] Zhao, W., Frankel, S. and Mongeau, L. AIAA 2000-2078.
- [48] Constantinescu, G. S. and S. K. Lele, AIAA Paper, 2001-0376, Reno.
- [49] Bodony, D. J. and Lele S. K., 2002, submitted to *Theor. Comput. Fluid Dyn.*
- [50] Freund, J. B. and S. K. Lele. 2003. in *High Speed Jet Flows* Editors: G. Raman, D. McLaughlin, P. Morris, Taylor & Francis.
- [51] Stromberg, J. L., Mc Laughlin, D. K. and Troutt, T. R. 1980. *J. Sound Vib.*, **72**, 159-176.
- [52] Mollo-Christensen, E., Kolpin, M. A. and Martuccelli, J. R. 1964. *J. Fluid Mech.*, **18**, 285-301.
- [53] Freund, J. B., *J. Fluid Mech.*, **438**, 2001, p. 277-305.
- [54] Freund, J. B. AIAA 2002-2423.
- [55] Lau, J. C., Morris, P. J. and Fisher, M. J. 1979. *J. Fluid Mech.*, **93**, 1-27.
- [56] Zaman, K. B. M. Q. 1986. *J. Sound Vib.*, **106**, p. 1-16.
- [57] Tanna, H. K. 1977. *J. Sound Vib.*, **50**, p. 405-428.
- [58] Ahuja, K. K. 1974 *J. Sound Vib.*, **29**, p. 155-168.
- [59] Troutt, T. R. and McLaughlin, D. K., *J. Fluid Mech.*, **116**, 1982, p.123-156.
- [60] Tam, C. K. W., Chen, P. and Seiner, J. M., *AIAA J.*, **30**, 1992, p.1747-1752.
- [61] Seiner, J. M., Bhat, T. R. S. and Ponton, M. K., *AIAA J.*, **32**, 1994, p.2345-2350.
- [62] Mankbadi, R. , Hixon, R., Shih, S. H., Povinelli, L. A., *AIAA J.*, **36**, 1998, p. 140-147.
- [63] Papamoschou, D. and Debiassi, M. *AIAA J.*, **39**, p. 380-387.
- [64] Powell, A. *Proc. Phys. Soc. London* **66**, 1953, p. 1039-1056.

- [65] Raman, G., *Prog. Aerospace Sci.*, **34**, 1998, p. 45-106.
- [66] Shen, H. and Tam, C. K. W., *AIAA J.*, **36**, 1998, p. 1801-1809.
- [67] Zhang X., Rona A. and Lilley, G. M. CEAS/AIAA Aeroacoustics Conference, Vol 1, 1995, p. 285-292.
- [68] Walker, S. and Thomas, F. O., *Phys. Fluids*, **9**, 1997, p. 2562-2579.
- [69] Manning, T. and S. K. Lele. *AIAA paper*, 98-0282, Reno.
- [70] Manning, T. A. and S. K. Lele. *AIAA Paper*, 2000-2081.
- [71] Stuart, J. T., *J. Fluid Mech.*, **29**, 1967, p. 417-440.
- [72] Suzuki, T. and Lele, S. K. *J. Fluid Mech.*, **490**, 2003, p. 139-167.
- [73] Alkisslar, M. B., Krothapalli, A. and Lourenco, L. M. 2003. to appear in *J. Fluid Mech.*
- [74] Harper-Bourne, M. and Fisher, M. J. AGARD CP 131, Noise Mechanisms, 1974.
- [75] Tam, C. K. W. and Tanna, H. K., *J. Sound Vib.*, **81**, 1982, p. 337-358.
- [76] Tam, C. K. W., *J. Sound Vib.*, **140**, 1990, p. 55-71.
- [77] Tam, C. K. W. *AIAA J.*, **30**, 1992, p. 2395-2401.
- [78] Norum, T. D. and Seiner, J. M., NASA TM 84521, 1982.
- [79] Lui, C. and Lele, S. K., AIAA-2002-0074, Reno, 2002.
- [80] Lui, C. and Lele, S. K. AIAA-2003-3315, Hilton Head.
- [81] Lele, S. K. 2003. submitted to *Phys. Fluids*.
- [82] Kerschen, E. J. and Cain, A. 1995. AIAA Paper 95-0507.
- [83] Freund, J. B., Lele, S. K. and Moin, P., *AIAA J.*, **38**, 2000, p. 2023-2031.
- [84] Colonius, T., S. K. Lele, and P. Moin, *J. Fluid Mech.*, **330**, 1997, pp. 375-409.
- [85] Crighton, D. G. *Progr. Aerospace Sci.*, **16**, 1975, p. 129-146.
- [86] Laufer J. and Yen T. C., *J. Fluid Mech.*, **134**, 1983, p. 1-31.
- [87] Crow, S. C., *Bull. Am. Phys. Soc.*, 1972.
- [88] Fuchs, H. V. and Michalke, A. *Progr. Aerospace Sci.*, **14**, 1973, p. 229
- [89] Freund, J. B., Bodony, D. J. and Lele, S. K. 2002. in Proc. CTR Summer Program 2002.
- [90] Constantinescu, G. and Lele, S. K., *J. Comput. Phys.*, **183**, 2002, p. 165-186.
- [91] Visbal, M. R., and Gaitonde, D. V. 1998. AIAA 98-0131, Reno.
- [92] Bogey, C. and Bailly, C. 2002. in Proceedings of CEAS Workshop 'From CFD to CAA'.
- [93] Bertolotti, F. P. and Colonius, T., AIAA 2003-1062, Reno.

FLOW PATTERNS AND SOUND GENERATION IN LOW SPEED CAVITIES

E. J. Avital¹ and R.E. Musafir²

¹*Engineering, Queen Mary, University of London, Mile End Rd, London E1 4NS, UK*

²*Universidade Federal do Rio de Janeiro, COPPE, CP68503, 21945-970, Brazil*

e.avital@qmul.ac.uk, rem@serv.com.ufrj.br

Abstract Incompressible LES was coupled with the Lighthill-Curle acoustic analogy expressed in two forms in order to investigate flow patterns and sound generation in open cavities of basic configurations. Previously experimentally observed flow patterns were reproduced. High RMS levels of the transverse velocity were found at the corners of the rear wall with the side walls. Eliminating these corners by using an elliptic cylindrical cavity configuration reduced considerably the RMS levels. Inflow disturbance was found necessary to kick a cavity tone within the time scale of the simulations. The two acoustic predictions showed good agreement and that the dipole noise emitted by the elliptical cavity was lower than in the corresponding box configuration.

Keywords: low speed open cavity, cavity tone, dipole noise

1. Introduction

Open cavities can be found in a wide spectrum of engineering problems ranging from aircraft to cars and sea vessels. Once the cavity is opened to the outside flow it can exhibit strong flow oscillations due to a feedback mechanism between the rear and the front walls. These oscillations can cause an increase in the drag, structural fatigue and generate undesired noise. Much attention has been given to the high speed cavity due to its application to the aircraft industry and particularly to the bomb bay configuration, e.g. Avital (2001). Less attention has been given to the low speed case and its sound generation mechanism, although it has implications to the automobile industry and underwater vessels. This study will concentrate on the very low Mach number case, which is appropriate for underwater applications.

Flow patterns in 2D rectangular water cavities were studied experimentally by Rockweel and Knisley (1979). They observed the generation of vortical structures in the shear layer and described three possible scenarios of the shear layer impinging over the rear wall. Complete clipping occurred when the vor-

tical structure swept back into the cavity, partial clipping took place when part of the structure managed to escape the cavity and 'escape' occurred when the entire structure was swept away from the cavity. All these events were observed to occur alternately. Water cavity tones were studied experimentally by Burroughs and Stinebring (1994). They defined a cavity tone as the shear flow tone amplified by the feedback mechanism inside the cavity at frequencies that enhanced the shear layer instability at the front wall. It was found that the frequencies of the tones varied almost linearly with the flow speed and at low speed only one tone existed. Increasing the flow velocity caused the appearance of a second tone with a lower frequency. The appearance of the lower frequency tone was also associated with a jump in the frequency of the higher frequency tone.

Howe (1997) analyzed analytically the occurrence of cavity tones at the zero Mach number limit. The shear layer over the cavity was modelled as a vortex sheet and its fluctuations were taken as the sound source. A linear analysis led to an elaborate eigenvalue problem for the tones' frequencies. Numerical solutions of that problem led to good agreements with experimental data of a subsonic case extrapolated to the zero Mach number.

In terms of computational studies, most were done for compressible flows. This approach is not appropriate for very low Mach numbers since there is a very large difference between the length scales of the flow field and the sound field. Furthermore, the radiated acoustic energy is a small fraction of the hydrodynamic energy. Thus, an indirect approach was chosen where the flow field was simulated using the LES method and the emitted sound was calculated using acoustic models. The formulation of this approach is given in the next section, followed by hydrodynamic and acoustic results for various 3D cavity configurations.

2. Mathematical and Numerical Formulation

The cavity acts as a compact source in the very low Mach number case and thus as explained above a hybrid method was chosen where the flow and sound fields were calculated by different techniques. The flow field was assumed to be incompressible and was simulated using our 3D structured finite volume *Lithium* code that had already been used to simulate flows around slender and bluff bodies, e.g. Motallebi et al. (2002) and Avital & Musafir (2003). The flow was simulated using the LES technique, where the subgrid stress (SGS) was modelled using the eddy viscosity model. To ease the computational burden of simulating the various cavity configurations the Smagorinsky model was used with damping functions near walls. Avital (2001) found that when compared with the dynamic model for subsonic cavity flow, there was no noticeable effect on the modes' frequencies and only a moderate effect on the amplitudes

of secondary modes. A test simulation for a basic box cavity configuration showed that the effect of the dynamic model was not significant either for the current cavity tone behaviour.

Further ease in the computational effort was sought by using the moderately upwind third order *Quick* scheme for the convection terms. Mittel and Moin (1997) found that this could affect the high frequency spectrum for vortex shedding from a cylinder. However, the cavity tones were expected to be of low frequency (Burroughs and Stinebring, 1994). The LES simulations of Kawamura et al. (2002) that also used a non dynamic eddy viscosity model and the *Quick* scheme, confirmed this observation by achieving good agreement with experimental data of low frequency fluctuations. The diffusion terms were calculated using a second order central scheme while the time marching was achieved using a third-order Runge-Kutta (RK) scheme and the projection method.

The 3D cavity was taken as embedded inside a flat plate, see for example Figures 1. As in Avital (2001) a single spatial grid was used where the shape of the cavity was captured using the ghost points method. The values of the velocity and pressure on these points were determined using no-slip wall conditions and the projection method boundary condition for the pressure. A gentle grid mapping was applied to cluster grid points in the cavity region. This introduces commutation errors but when applied where required, grid mapping increases the overall numerical accuracy (Avital and Luo, 1999). No gradient boundary conditions were imposed at the upper side of the computational domain and free slip wall conditions were used at the spanwise sides. A simple convection outflow condition was used at the outflow and the inflow streamwise velocity was specified using the power law profile $(y/\delta)^{1/7}$ as in Avital (2001). A passive scalar was also simulated for flow illustration and checking numerical resolution.

In the zero Mach number limit the compact cavity acts as a dipole and quadrupole contribution is neglected. Using Curle's theory one gets that the sound pressure fluctuations p' are

$$p'(\bar{x}, t) = -\frac{1}{4\pi} \frac{\partial}{\partial x_j} \int_S \frac{p(\bar{y}, t - r/c_0)}{r} dS_j(\bar{y}), \quad (1)$$

where \bar{x} is the location of the listener, \bar{y} is the location of the source, $r = |\bar{x} - \bar{y}|$, p is the hydrodynamic pressure given by the LES solver, S is the surface area of the cavity's contour and exterior, and the index j denotes the direction normal to the integration surface. The compact cavity acts as a dipole in the streamwise and spanwise direction and does not have a component in the stream-normal direction (Howe, 1997). It can be shown that due to the exterior flat plate, the far field pressure in the compact limit is given by

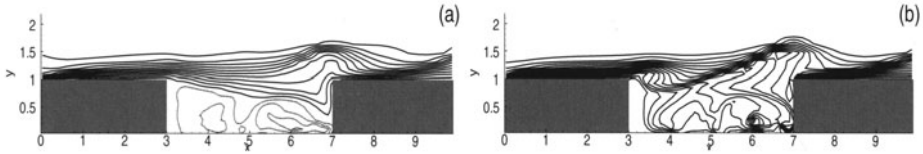


Figure 1. Contours of instantaneous (a) axial velocity with 15 levels from -0.3 to 0.95 and (b) passive scalar with 15 levels from 0.05 to 0.95 in the mid plane of the box cavity of $w/d = 1$

$$p'(\bar{x}, t) = \frac{x_j}{2\pi c_0 |\bar{x}|^2} \int_{S_{walls}} \frac{\partial p}{\partial t}(\bar{y}, t - \bar{x}/c_0) dS_j(\bar{y}). \quad (2)$$

S_{walls} stands for the surface area of the cavity's walls, j is 1 or 3 and the components of the integral in (2) will be referred as the streamwise and spanwise dipoles according to j .

Howe (1997) expressed the far field sound using the hydrodynamic velocity measured at the cavity's top plane,

$$p'(\bar{x}, t) = \frac{\rho_0 x_j}{2\pi c_0 |\bar{x}|^2} \int_S y_j \frac{\partial v}{\partial t}(\bar{y}, t - \bar{x}/c_0) dy_1 dy_3, \quad (3)$$

where j is 1 or 3, y_1 is the streamwise direction, y_3 is the spanwise direction and S is now the surface area of the cavity's top plane. The origin of the \bar{y} co-ordinates is located at the centre of that plane. The calculation of (2) and (3) can be carried out by recording the appropriate hydrodynamic values from the LES, followed by second order time differentiation and surface integration.

3. Results

Simulations were carried out for 3D cavity configurations, a box with width to depth ratio $w/d = 1$, a wider box of $w/d = 2$ and a cylindrical cavity with an ellipse shape in the streamwise-spanwise plane and maximum width to depth ratio of 1. The last configuration will be called an elliptical cavity for short. All cavities had length to depth ratio of $l/d = 4$. The computational box was $10d$ long in the streamwise direction, $2d$ in the spanwise direction and $7d$ in the transverse direction. Symmetry assumption was used at the cavity's mid plane, which will be noted as $z = 0$. Avital (2001) found that the symmetry assumption could have a suppressing effect on secondary modes in the compressible case, but this effect diminished as Re_d was increased from a few thousands. Re_d in the current simulation was 5000. The symmetry assumption also makes the spanwise dipole zero as also taken by Howe (1997). This can be justified by arguing that the streamwise drag is dominant, however further study should be carried out over this point as outlined in the summary section.

The ratio of the cavity's depth to the inflow boundary layer's momentum thickness was taken as $d/\Theta = 35$. A random inflow disturbance of 10% was applied

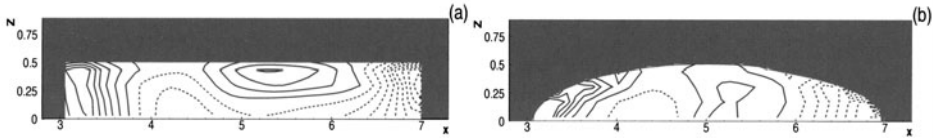


Figure 2. Instantaneous transverse velocity contours in the cavity's top plane, showing 15 contour levels between -0.25 to 0.15, where negative values are noted by dotted lines. Figure 2(a) is for the narrow box cavity, and 2(b) is for the elliptical cavity, both with $w/d = 1$ and $z = 0$ is a plane of symmetry

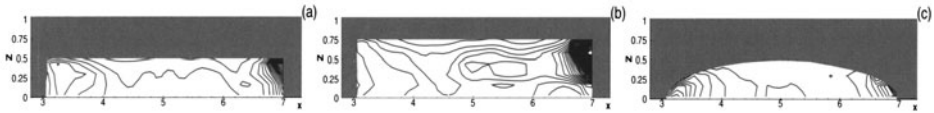


Figure 3. RMS transverse velocity contours in the cavity's top plane, for (a) the box cavity of $w/d = 1$ with 20 levels between 1.e-3 to 0.03, (b) the box cavity of $w/d = 2$ with 40 levels between 1.e-3 to 0.06, and (c) the elliptical cavity of $w/d = 1$ with 10 levels between 1.e-3 to 0.015. $z = 0$ is a plane of symmetry

in the streamwise velocity, where for comparison purposes one simulation was carried out without the inflow disturbance for the narrow box cavity configuration. Thus if not mentioned, the following results are for the cases with the inflow disturbance. These results were produced using a grid of (151,101,31) points and a clustering ratio of 2 to 1 near the walls in the xy plane. This was found to be sufficient to capture the large scale structures.

Typical contour plots of the instantaneous streamwise velocity and passive scalar for the box cavity of $w/d = 1$ are given in Figure 1. The shear layer is seen to widen considerably over the cavity, which is typical for open cavity flow. Secondary flow is observed inside the cavity, where vector plots showed a small vortex at the aft bottom of the cavity. The passive scalar contours show the generation of a vortex near the forward wall, a behaviour observed by Rockwell & Knisley (1979) for a similar level of Re_d . Together the two figures point to a partial clipping occurring near the rear wall at that instant. Contours of the instantaneous transverse velocity v are given in Figures 2 for the upper planes of the box cavity of $w/d=1$ and the elliptical cavity. Both cavities show a similar pattern in the streamwise direction of alternating sign in v , pointing to spanwise vortices in the shear layer. However, there is also a variation in the spanwise distribution of v , showing the cavity has a significant 3D behaviour as found in Avital (2001) for the compressible case.

The Root Mean Square (RMS) of the transverse velocity are shown in Figures 3. It is seen that in the narrow box cavity of Figure 3(a), the highest level of RMS is near the rear wall. This agrees with the observation of Rockwell & Knisley (1979), who reported that the highest level of the transverse velocity fluctuations was near the rear wall. The wider box cavity shows twice the maximum RMS level. In both cavities the high RMS levels are located near the

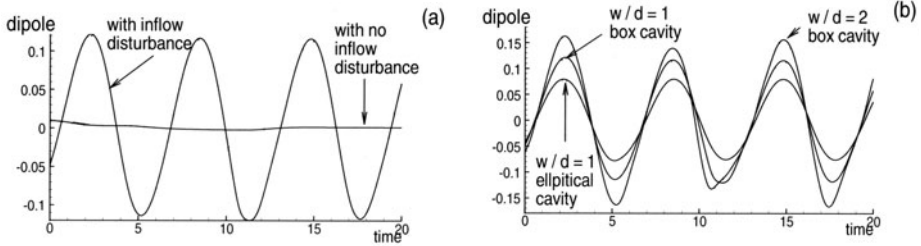


Figure 4. Time evolution of the streamwise dipole as expressed in (2). Figure 4(a) is for the narrow box cavity of $w/d = 1$ with 10% random disturbance in the streamwise velocity and without inflow disturbance. Figure 4(b) is for the various cavity configurations as noted, all with 10% inflow disturbance.

corner of the rear wall with the side wall. Therefore if this corner is eliminated we can expect a considerable reduction in the RMS levels and this is indeed what we see in the elliptical cavity of Figure 3(c). The maximum of the RMS levels are now half of those of the narrow box cavity and the levels near the front edge are even a bit higher than those near the rear edge. This has a strong implication for the sound generation because the sound source is proportional to the transverse velocity's time derivative by (3).

The time evolutions of the streamwise dipole as expressed in (2) are shown in Figures 4 for various simulation conditions. From Figure 4(a) it is seen that adding an inflow disturbance increases considerably the dipole amplitudes and without it there is no periodic behaviour in the dipole, meaning no cavity tones at least in the frequencies captured within the length scale shown in Figure 4(a). This behaviour is similar to the finding of Avital (2001), who found that an inflow disturbance was necessary to kick the full range of the compressible cavity flow modes. Switching off the inflow disturbance caused the present cavity tone to damp. Whether this is due Reynolds number or numerical modelling effects remains a question for future work.

As postulated from the analysis of Figure 3, the wide box cavity has the dipole with the highest amplitude in Figure 4(b), while the elliptical cavity produces the lowest amplitude. All shown dipoles show a strong periodic component at $St_L \equiv fL/U = 0.63$ and the wide box cavity also shows some low frequency components that are not fully captured within the time scale of Figure 4(b). This value of St_L demonstrates the low frequency of the simulated cavity tone, e.g. for $U = 10\text{m/s}$ and $L = 1\text{m}$ f is only about 6 Hz. Substituting $M = 0$ in Rossister's formula that is for compressible cavity flow modes (Heller & Bliss, 1975), leads to $St_L = 0.43$ for the first mode. However, Rossister's formula was derived for $M > 0.4$ and Tam & Block (1978) also got that it under-predicted the frequencies when used for low Mach numbers. Extrapolating from Figure 5 in that reference, which gives a wide range of experimental data of cavities for $M > 0.1$, one gets $St_L = 0.52 \pm 0.12$. On the other hand Howe (1997) gives $St_L \simeq 0.7$ for the first mode.

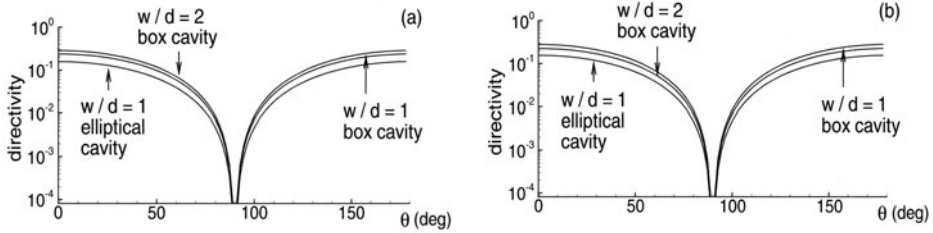


Figure 5. Narrow band directivity of the cavity's tone by (a) equation (2) and (b) equation (3). Both directivities are normalized by $1/(2\pi c_0^3)$ and ρ_0 was normalized to one in the LES and thus as well in (3)

Narrow band directivities of the cavity tone at $St_L = 0.63$ are shown in Figures 5 using equations (2) and (3). Both agree that the wide box cavity is the noisiest and the elliptical cavity is the quietest, and there is also excellent agreement in terms of absolute noise levels.

4. Summary

Incompressible LES was coupled with acoustic predictions based on two expressions derived from Curle's theory in order to investigate flow patterns and sound generation in open cavity. The simulations were carried out for a moderately low Reynolds number of $Re_d = 5000$ and three basic 3D cavity configurations. The simulations showed flow patterns of shear layer widening over the cavities, vortex generation in the shear layer, partial clipping and high fluctuations near the rear edge. These patterns agreed well qualitatively with experimental observations reported in the literature.

The wider box cavity showed the highest RMS levels of transverse velocity, where the peak was located near the rear wall corners with the side walls. The elliptical cavity configuration that did not have such corners showed the lowest RMS levels of v . Inflow disturbance was found necessary to kick a cavity tone within the time scale of the simulations, causing a strong periodic component in the streamwise component. The elliptical cavity emitted the lowest noise level. Excellent agreement was found between the two expressions.

Further study is planned to simulate the spanwise dipole by abandoning the symmetry assumption in the cavity's midplane and to look at higher Reynolds numbers. The artificial roughness in the elliptical cavity's side walls, caused by the use of a single rectangular grid, will be eliminated using curvilinear coordinates. Further interest will be into incorporating sub-grid effects into the acoustic prediction and thus capturing broadband noise.

Acknowledgement

Itanium and Origin 3400 time was provided by EPSRC. Many thanks to Prof. T. Miloh of Tel Aviv University for drawing the attention to the subject.

References

- Avital E.J. and Luo K.H. (1999) Large eddy simulations of cold and hot mixing layers, *DLES III*, ed. Voke P.R., Sandham N.D. and Kleiser L., Dordrecht, Kluwer Academic, pp. 175-188
- Avital E.J. (2001) Direct and large eddy simulations of compressible open cavity flows, *DLES IV*, ed. Geurts BJ, Friedrich R. and Metais O., Kluwer Academic, pp. 213-220
- Avital E.J. and Musafir R.E. (2003). Simulations of flow and sound fields for acoustic barrier in the presence of wind, *Proc. of 10th ICSV conference*, pp. 1461-1468
- Burroughs, C.B. and Stinebring D.R. (1994) Cavity flow tones in water. *J. Acoust. Soc. Am.*, **95**(3), 1256-1263
- Heller H.H. and Bliss D.B. (1975), The physical mechanism of flow-induced pressure fluctuations in cavities and concepts for their suppression, AIAA 75-0491
- Howe, M.S. (1997) Edge, cavity and aperture tones at very low Mach numbers. *J. Fluid Mech.*, **330**, 61-84
- Kawamura T., Mayer S., Garapon A. and Sorensen L. (2002), Large eddy simulation of a flow past a free surface piercing cylinder, *J. Fluids Eng.*, **124**, 91-101
- Motallebi, F., Avital, E. and Dabnichki, P. (2002). On the aerodynamics of two man bobsleigh, *Proc. of 4th Sport Eng. conference*, Blackwell Science, pp. 346-352
- Rockwell, D. and Knisley C. (1979) The organized nature of flow impingement upon a corner, *J. Fluid Mech.*, **93**(3), 413-432
- Tam, C.K.W. and Block P.J.W. (1978) On the tones and pressure oscillations induced by flow over rectangular cavities *J. Fluid Mech.*, **89**(2), 373-399

DIRECT NUMERICAL SIMULATION OF THE ACOUSTIC FIELD OF A TURBULENT OFFSET JET

Bendiks Jan Boersma

J.M. Burgerscentre,

Delft University of Technology

Mekelweg 2, 2628 CD, The Netherlands

email: b.j.boersma@wbmt.tudelft.nl

Abstract In this paper we use Direct Numerical Simulation (DNS) to study the acoustic field generated by a round turbulent jet flowing parallel to a solid wall. The Reynolds and Mach number based on jet nozzle velocity and diameter are 2,500 and 0.5 respectively. It is shown that the wall alters the direction of the emitted sound considerably and that the amplitude of the sound increases when compared to the sound emitted by a free jet.

Keywords: Direct Numerical Simulation (DNS), Aeroacoustics

1. Introduction

The acoustic field of a free round turbulent jet at moderate Mach numbers and low Reynolds numbers is nowadays fairly well understood, see for instance, Freund (2001). However, in engineering practice, most jets have very large Reynolds numbers and flow into a confined space. Examples of confined jets are numerous: a jet flame in a combustion chamber, a fuel jet in a cylinder but also the jet engine of an airplane during take-off. In this case the runway acts as a confinement.

In this paper we will study the flow and acoustic field of a round turbulent jet flowing parallel to a flat wall. This type of flow is in the literature known as an offset jet. Most of the literature about this subject is for two-dimensional jets, see for instance Lai & Lu (2000). It is a well known fact that a jet flowing parallel to a solid surface tends to move closer to the surface. This phenomena is known as the so-called Coanda effect.

The acoustic sources in this flow, which with some simplifications can be expressed as the Weiss function $(S \cdot S - \Omega \cdot \Omega)/4$, in which S is the strain rate tensor and Ω the vorticity tensor. The value of the Weiss function will depend

on the distance to the wall. For small distances between jet centerline and the solid wall we expect a considerable increase in S and Ω and thus a larger acoustic emission.

In this paper we will present some results obtained from three direct numerical simulations, one without a solid wall and two with a solid wall parallel to the jet centerline.

2. Governing equations

In this section we will give the governing equations for the flow and the acoustic field. We have chosen for a fully compressible approach, i.e. the sound is calculated directly without the use of an acoustic analogy (Goldstein 1974).

The flow is governed by the compressible continuity and momentum equations. With help of index notation and Einstein's summation convention these equations can be written as:

$$\frac{\partial \rho}{\partial t} + \frac{\partial \rho u_i}{\partial x_i} = 0, \quad (1)$$

$$\frac{\partial \rho u_i}{\partial t} + \frac{\partial}{\partial x_j} \rho u_i u_j + \frac{\partial p}{\partial x_i} = \frac{\partial}{\partial x_i} \tau_{ij}, \quad (2)$$

where u_i is the velocity of the fluid, ρ the density, p the pressure, and τ_{ij} the Newtonian stress tensor which is defined as

$$\tau_{ij} = \mu \left(\frac{\partial u_i}{\partial x_j} + \frac{\partial u_j}{\partial x_i} - \frac{2}{3} \frac{\partial u_k}{\partial x_k} \right).$$

In this definition of the stress tensor μ is the dynamic viscosity of the fluid. In a compressible approach an equation for the internal energy has to be used. Here we will use a formulation which uses the total energy, i.e. the sum of the internal energy $\rho C_v T$, plus the kinetic energy $\rho u_i u_i / 2$. This equation reads:

$$\frac{\partial E}{\partial t} + \frac{\partial}{\partial x_i} u(E + p) = \frac{\partial}{\partial x_i} \kappa \frac{\partial T}{\partial x_i} + \frac{\partial}{\partial x_i} u_i \tau_{ij} \quad (3)$$

In which E is the total energy T the temperature and κ the thermal diffusivity of the gas. The equation of state for an ideal gas

$$p = \rho R_g T,$$

with R_g as the gas constant, is used to relate the thermodynamic properties. The equation given above are non-dimensionalised with the radius R of the jet, the speed of sound c_∞ the ambient density ρ_∞ and the ambient temperature c_∞^2 / C_p (C_p is the specific heat at constant pressure) as reference values, the

specific heat ratio $\gamma = C_p/C_v$ is taken equal to 1.4 (air). The important non-dimensional numbers which result from the scaling are the Reynolds and Mach number which are given by:

$$Re_{ac} = \frac{\rho_{\infty} c_{\infty} R}{\mu} \quad Ma = \frac{u}{c_{\infty}}$$

where u is a characteristic velocity scale. Here we use for u the jet exit velocity. The Reynolds number given above is not very significant for the present flow because no information about the flow is incorporated in the Reynolds number. Therefore, we redefine the Reynolds number as the product of the Reynolds and Mach number:

$$Re = Re_{ac} \cdot Ma = \frac{\rho u R}{\mu}$$

The Prandtl number κ/μ was taken equal to unity.

2.1 Numerical method

In this section we will shortly describe the numerical method. The computational grid is non-uniform in all coordinate directions. The non-uniform computational grid is mapped on a uniform mesh in the computational space. On this uniform mesh all the spatial derivatives in the governing equation (1), (2) and (3) are approximated with help of a 8th order compact finite difference scheme, Lele (1992). The time integration of equations (1), (2) and (3) is carried out with a fourth order explicit Runge-Kutta scheme.

2.2 Boundary conditions

At the inflow and outflow boundary of the domain small artificial layers are added to the computational domain. In these layers a local supersonic advection velocity is added to the equations. In this way we can specify the three velocity components density and energy at the in and outflow. At the inflow the following velocity profile has been used (see for instance Michalke 1984):

$$U(r) = Ma \left[\frac{1}{2} - \frac{1}{2} \tanh \left(\frac{(r-1)}{\delta} \right) \right]$$

where δ is a measure for the thickness of the shear layer.

At the lateral boundaries we specify characteristic boundary conditions. To avoid reflections at these boundaries a small sponge layer is added to the computational domain to damp spurious incoming acoustic waves. Such a sponge layer is also placed at the inflow and outflow boundary. At the solid wall no-slip conditions for the three velocity components are specified. Furthermore the total energy E is kept at its reference value at the wall, which corresponds to a wall with a fixed temperature (isothermal wall), in this case $T = c_{\infty}^2/C_p$.

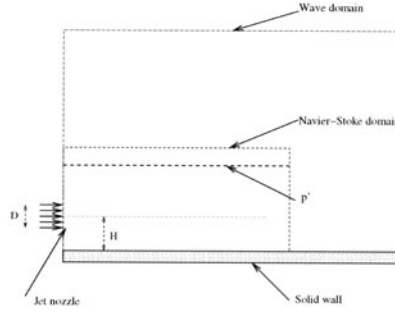


Figure 1. A sketch of the computational geometry and the surface where the information between the Navier-Stokes domain and the wave domain is exchanged, D is the diameter of the jet and H is the distance between the jet centerline and the solid wall.

The density of the flow at the solid wall is extrapolated from the flow field with a 3rd order accurate extrapolation. Of course no sponge layer is used at the solid wall.

2.3 Acoustic far field

The acoustic far field could in principle be calculated with help of the Navier-Stokes equations. However, this would be very costly and is not necessary because in the far field the flow is at rest. Therefore, we calculate the acoustic far field by solving the wave equation for the pressure perturbation p' with boundary conditions obtained from the Navier-Stokes solution. The wave equation for p' simply reads:

$$\frac{\partial^2 p'}{\partial t^2} - c^2 \frac{\partial^2 p'}{\partial x_i^2} = 0 \quad (4)$$

The boundary conditions for the pressure perturbation at large distances from the noise source are (radiation conditions):

$$\frac{\partial p'}{\partial t} = \pm c \frac{\partial p'}{\partial x_i}$$

where the sign is chosen in such a way that waves are traveling only out of the computational domain. Close to the acoustic source the boundary condition for the wave equation is taken from the Navier-Stokes solution, i.e. $p'_{wave} = p'_{NS}$. The wave equation is discretized with 6th order compact-finite difference for the spatial derivatives and with a fourth order Runge Kutta method in time (the same method as was used for the Navier-Stokes equations). A sketch of the computational domain is shown in Figure 1.

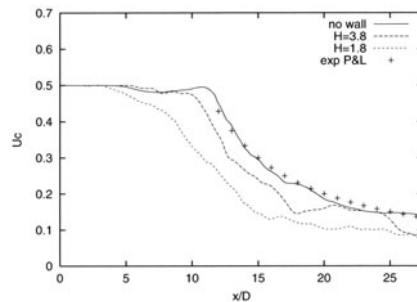


Figure 2. The mean velocity along the centerline of the jet. Due to a lack of data fields there is some scatter in the mean velocity profiles.

2.4 Results

In this section we will present some results obtained from three different simulations. In all the three simulations the Reynolds and Mach number are 5,000 (based on jet radius R) and 0.5 respectively. The thickness of the shear layer δ was in all cases $R/7.5$. The only difference between the simulations is the distance H between the jet centerline and the wall. We took $H = \infty$ which corresponds to a free jet, $H = 3.8R$ and $H = 1.8R$. The computational grid for the Navier-Stokes equations consisted of $190 \times 140 \times 140$ points in the flow, spanwise and wall normal direction respectively. The grid size used in the present calculations are finer than were used by us before, Boersma *et al.* (1998), and should be sufficient to capture all important flow scales. The grid for the wave equation is larger and consisted of $300 \times 240 \times 240$ points in the flow, spanwise and wall normal direction respectively. The computations have been performed on 10 CPU's of an SGI-Origin 3800. Typical run times are 200 hours for a full simulation. Unfortunately, not all statistics are fully converged at present.

In Figure 2 we show the decay of the jet centerline velocity obtained from the three simulations. The symbols in Figure 2 denote the experimental data for a free jet reported by Panchapekesan & Lumley (1993). If a function $b/(x - x_0)$ is fitted through the data for $x > 10D$, b is called the decay rate of the jet and x_0 the virtual origin of the jet, see for instance Boersma (1998). Surprisingly not only the decay rate b but also the virtual origin x_0 of the free jet are in very good agreement. Clearly the decay rate of the jet becomes larger when the distance between the jet centerline and the solid wall becomes smaller.

In Figure 3 we show a 3D plot of the divergence of the velocity $\nabla \cdot u$ overlaid with the vorticity magnitude. The divergence of the velocity, or dilatation, is a good measure for the radiated sound because in absence of mean fluid motion

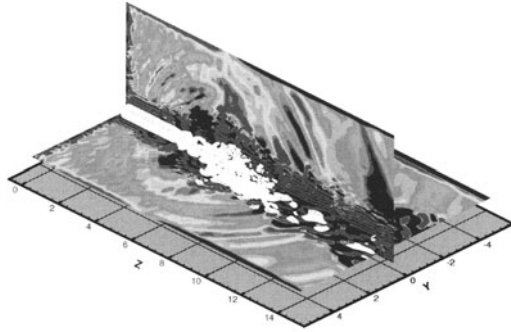


Figure 3. The divergence of the velocity ($\nabla \cdot u_i$) overlaid with the vorticity obtained from the simulation with $H = 3.8R$.

and using $p' = c^2 \rho'$ we can rewrite the continuity equation as

$$\frac{\partial p'}{\partial t} = -\rho c^2 \nabla \cdot u_i \quad (5)$$

where p' is the acoustic pressure perturbation. The solid wall in the results presented in Figure 3, is located at $z = -3.8R$. The figure illustrates that roughly 5 jet diameters downstream of the jet nozzle the jet breaks up and becomes three dimensional, which is made visible with help of the vorticity magnitude. At the point where the jet becomes three dimensional also sound waves are generated, which are made visible with the divergence of the velocity. The large values of the divergence of the velocity at the sides of the computational domain is caused by the small sponge layer which is placed around the domain to damp incoming acoustic waves (see previous section). As can be seen from Figure 1 this region is not used for the acoustic far field calculation. From Figure 3 it can also be observed that the amplitude of the sound emitted in the direction parallel to the wall is less than the sound emitted in the direction perpendicular to the solid wall.

In Figure 4 we show the dilatation obtained from the three simulations. The free jet radiates sound under an angle of approximately 30° with the jet center-line, which is in agreement with literature angles. When the wall approaches the jet this angle becomes larger. This is also clear from Figure 5 in which we show the near and far field sound obtained for the case with $H = 3.8R$. The result for the far field shows that the sound emission is large for angles of

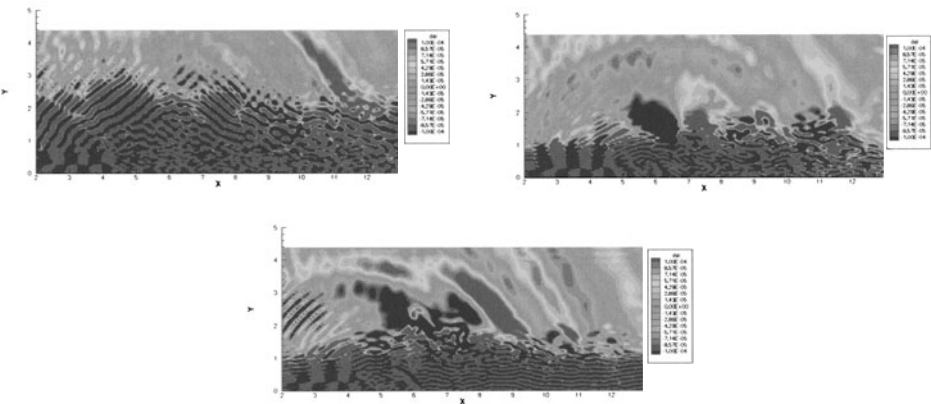


Figure 4. The dilatation of the velocity $\nabla \cdot u_i$. Top left figure for $H = \infty$, top right figure for $H = 3.8R$, lower figure for $H = 1.8R$. (Contour levels are the same for all figures.)

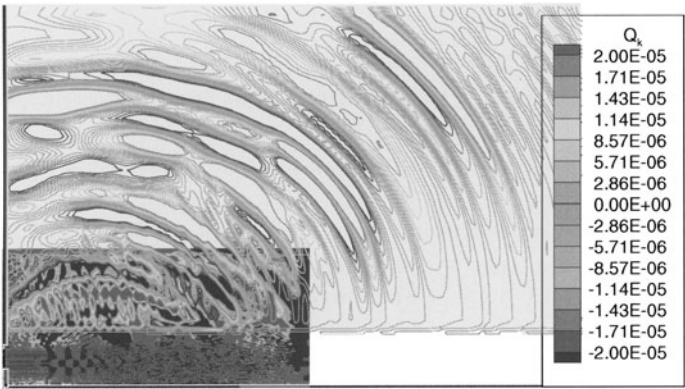


Figure 5. The near and far field sound visualized with the divergence of the velocity (near field) and with $\partial p'/\partial t$ (far field) for the case $H = 3.8R$.

approximately $50^\circ - 70^\circ$ with the jet centerline. The amplitude of the sound increases also when the wall is closer to the jet centerline.

3. Conclusion

In this paper we have used direct numerical simulation to calculate the sound field generated by a round turbulent jet which is flowing parallel to a solid wall. It has been found that the solid wall enhances the acoustic emission of the jet and also the angle under which the sound is emitted. This behavior of the acoustic field of the jet is also observed in real life.

The results presented here are preliminary of nature and a better validation of the numerical results is required. At present we are investigating the possibility to build an experimental setup to perform this validation.

Acknowledgments

This work was sponsored by the National Computing Facilities Foundation (NCF) for the use of supercomputer facilities, with financial support from the Dutch Organization for Scientific Research (NWO).

References

- [1] Boersma, B.J., G. Brethouwer, & F.T.M. Nieuwstadt, 1998, A numerical investigation on the effect of the inflow conditions on the self-similar region of a round jet, *Phys of Fluids*, **10**, 899-909.
- [2] Freund, J., 2001, Noise sources in a low-Reynolds-number turbulent jet at Mach 0.9, *J. Fluid Mech.*, **438**, 277-305.
- [3] Goldstein, M., 1974, Aeroacoustics, *MacGraw Hill*
- [4] Lai, J.C.S., & Lu, D., 2000, An inclined wall jet: Mean flow characteristics and effects of acoustics excitation, *Exp. in Fluids*, 45-55.
- [5] Lele, S.K., 1992, Compact finite difference schemes with spectral like resolution, *J. Comp. Phys.*, **103**, 16-42.
- [6] Michalke, A., Survey on jet instability theory, *Prog. Aerospace Sci.* 21, 159-199, 1984.
- [7] Panchapakesan, N., & Lumley, J., 1993, Turbulence measurements in an axisymmetric jets of air and helium, Part 1. Air jet, *J. Fluid Mech.*, **246**, 197-223.

TURBULENT FLOWS IN COMPLEX GEOMETRIES AND IN TECHNICAL APPLICATIONS

4.1 LES-RANS COUPLING AND DETACHED EDDY SIMULATION

MERGING LES AND RANS STRATEGIES: ZONAL OR SEAMLESS COUPLING?

K. Hanjalić and M. Hadžiabdić

*Department of Multi-scale Physics, Delft University of Technology
Lorentzweg 1, 2628 CJ Delft, The Netherlands*

hanjalic@ws.tn.tudelft.nl

L. Temmerman and M. Leschziner

*Department of Aeronautics, Imperial College London
Prince Consort Road, London SW71AZ, United Kingdom*

Abstract We discuss some issues concerned with zonal and seamless combinations of LES and URANS methods that are aimed at the simulation of flows at high Reynolds numbers with affordable, RANS-type grid density. The zonal method combines one- and two-equation RANS models in the near-wall layer with the conventional LES in the outer region, with the interface specified in terms of wall distance. In the seamless approach, a single two-equation eddy-viscosity model is used both as a URANS model in the near-wall region and for the subscale motion in the outer LES region. Because the true challenge to hybrid simulation is in correct representation of wall-attached layers with relatively coarse grids, we focus on testing the methods in fully-developed channel flow at high Reynolds number ($Re_\tau = 2000$) with only $64^2 \times 32$ grid points for the minimal channel domain.

Keywords: Hybrid LES/RANS, zonal and seamless coupling

1. Introduction

Formidable grid-resolution challenges posed by LES of wall-bounded turbulent flows for high Reynolds numbers and complex geometries have triggered significant efforts in exploring alternative computational approaches, focused primarily on combining elements of LES and RANS rationales. A common strategy is to use a RANS-type method in the near-wall region, which is held to require clustering in the wall-normal direction only, as opposed to clustering in all three directions, as demanded in LES. This results in a relatively mild (logarithmic) increase in the number of grid points with the Reynolds number, as compared to an almost quadratic dependence in LES of wall-bounded flows.

The well-known grid sensitivity of LES is illustrated in Fig. 1 by a dramatic failure to reproduce the log-law in fully developed plane channel flow with LES on a typical wall-normal-clustered RANS grid of $64 \times 64 \times 32$ for a domain of size $2\pi h \times 2h \times \pi h$ (denoted as LES coarse). Acceptable solution quality requires more than an order of magnitude finer grid, as illustrated in the same figure by the well-resolved ("reference") LES with $512 \times 128 \times 128$ cells for a domain of size $2\pi h \times 2h \times \pi h/2$, satisfying the standard LES criteria for grid spacing.

The primary target of hybrid approaches is to reduce the enormous discrepancy in predictive realism demonstrated in Fig. 1, whilst retaining the grid density typical of that used in RANS computations and whilst returning the principal spectral dynamics of turbulence. The research pursued by various

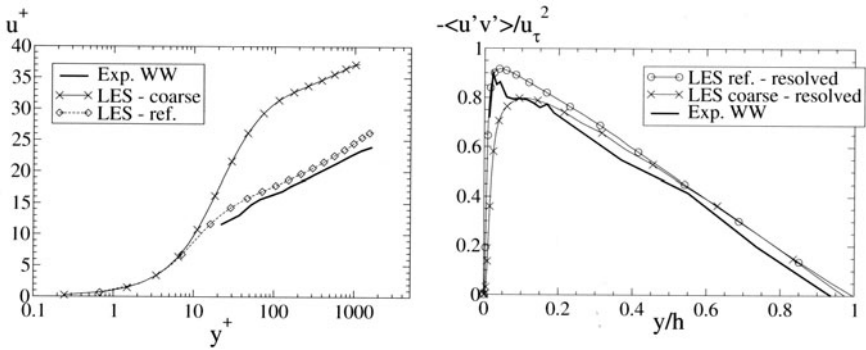


Figure 1. Reference ($512 \times 128 \times 128$) and coarse-mesh ($64 \times 64 \times 32$) LES of fully-developed channel flow for $Re_\tau = 2000$, compared with experiments of Wei and Willmarth (1998).

groups over the past few years has revealed, however, that the problem is more complex than originally envisaged: the two approaches differ in essence, and their simple merging poses serious problems in reconciling different physics. This is especially acute in wall-attached flows without strong forcing introduced, for example, by vortex shedding. Similar problems arise whether a zonal approach is adopted, in which a conventional RANS method in the near-wall region is coupled to a conventional LES scheme with a grid-size-based sub-grid-scale model in the outer flow, or whether a "seamless" methodology is constructed, in which the same model is applied throughout the flow with a continuous sub(-grid)-scale model modification. Although common RANS models, when applied to the near-wall layer and subjected to LES-derived perturbations at the RANS-LES interface, return a velocity response quite close to that a wall-resolving LES would give in the layer, some dynamically important small-scale structures in the buffer layer are missing, leading to a failure to reproduce correctly even the standard log-law in equilibrium wall flows. This physical inconsistency seems intractable to approaches based on simple merging, because the same form of equations are solved irrespective of their nature

(filtered or time-averaged), and the modifications to sub(-grid)-scale models reported in the literature generally fail to cure the problem. In an effort to compensate for the loss of small-scale motion caused by RANS-type near-wall modelling, Piomelli *et al.* (2003) have recently proposed the addition of extra spectral forcing to the RANS region. While this has been found to be beneficial, the nature of the forcing and the generality of the technique remain subjects for debate and continuing study. In this paper, we investigate the characteristics of certain options for zonal modelling without spectral forcing.

2. Alternative Strategies Reviewed

The plausibility of combining RANS and LES in an effort to exploit their best respective attributes has long been recognized. Two approaches can be distinguished. One entails hybrid two- (or three-) layer "zonal" methods, wherein conventional or modified RANS and LES schemes are applied selectively to particular flow sub-domains in which the schemes chosen offer decisive advantages. The other comprises smooth "seamless" methods with a single sub-scale model for the whole flow, which tends to a RANS model as the wall is approached and to a LES sub-grid-scale model away from the wall.

Balaras *et al.* (1996) proposed a zonal model with a parabolic "thin-shear-layer" (TSL) treatment of the wall layer imbedded into the overall LES field and using a van Driest mixing-length RANS model. The TSL solution then provided the wall-shear stress as a boundary condition for the LES equations outside the wall layer. Cabot and Moin (2000) extended this TSL approach by solving, simultaneously with the LES, the parabolic momentum equations for the streamwise and spanwise velocity components in which the turbulent stress was defined in terms of eddy viscosity from a RANS-type mixing-length model. Davidson (2001) experimented with several versions of hybrid zonal approaches, using a two-equation $k - \omega$ model for the RANS wall layer and a one-equation sub-grid-scale model for the outer LES region. Hamba (2001) adopted an opposite route by applying LES in the near-wall layer and solving one-dimensional $k - \varepsilon$ model in the outer region, but concluded that such an approach is less efficient than the more common strategies with RANS application near the wall. Other hybrid models have also been reported in the literature. A general observation emerging from these studies is that most hybrid models suffer from the difficulty of reconciling the conditions on either side of the interface, and the related numerical solutions show visible discontinuities and irregularities at and around the interface.

A different route was followed by Spalart *et al.* (1997) in their "Detached Eddy Simulation" (DES). Here, the same one-equation Spalart-Allmaras (SA) model for eddy viscosity is used both as RANS model in the near-wall region and as a sub-grid-scale model in the outer-flow region. The model contains a

single length scale for which the wall distance is used in the RANS region and a characteristic grid size in the LES region. This ensures a continuous transition from one region to the other (albeit with a grid-dependent scale-switching location), giving a continuous eddy-viscosity variation. This is the main reason for the relatively good representation achieved by this method in attached flows, although recent scrutiny (Piomelli *et al.*, 2003) has revealed some fundamental deficiencies of the method. Spalart *et al.* (1997) have claimed that DES reproduces massively separating flows much better than URANS, but it is arguable that this conclusion applies only to URANS with the SA model. It is well known that the success of URANS depends on the type of model used, and more advanced models can provide successful predictions of separated flows of comparative quality to those achieved with LES on coarse grids, as demonstrated by Benhamadouche and Laurence (2003) and Laurence (2003). Indeed, the use of a single transport equation (SA) for the eddy viscosity is questionable, especially in complex configurations. Hence, in the view of the writers, massively separated flows dominated by vigorous large-scale structures of a deterministic character and fairly well defined separation lines, induced by high-curvature geometric features, are not the best subjects for testing the merits of hybrid approaches, especially not at low-to-moderate Reynolds numbers. Much more challenging are incipiently or 'weakly' separated flows which are strongly affected by wall-proximity processes, where no conventional RANS model is able to resolve, without a drastic and arbitrary reduction in the eddy viscosity the model would normally provide, the flow's spectral dynamics. In such circumstances, introducing a LES in the outer region on a grid that would be too coarse for a pure LES, can be beneficial as a means of maintaining a credible spectral representation in the outer region.

While zonal approaches require, self-evidently, less empiricism than RANS, the crucial issues and problem areas to address are the location and definition of the interface, the nature of the matching conditions, especially for flows in complex geometries, and the receptivity of the RANS region to unsteadiness provided at the interface from the LES solution. These are issues discussed in what follows below.

3. Some Deductions from *a-priori* Testing

In order to gain insight into some of the above questions, especially that of the receptivity of the near-wall RANS layer to LES perturbations, we performed *a-priori* tests by solving the time-dependent RANS equations with the one-equation model of Wolfshtein (1968) in the wall region of a plane channel extending to $y^+ = 65$. Full wall-resolved LES, performed in parallel over the complete channel, served to provide the instantaneous boundary conditions for the velocity and turbulence energy at the wall-remote boundary of the RANS

layer. Despite the simplicity of the RANS model (only the equation for the turbulence kinetic energy was solved, whereas the length scale was provided from algebraic formula in terms of the wall distance), the RANS solution revealed a very high level of receptivity to the unsteady LES forcing at the edge, as illustrated in Fig. 2. Thus, the two sets of instantaneous velocity profiles, one from the wall-resolved LES, show hardly any qualitative differences. The time records of velocity at $y^+ = 60$ also show close similarities, with broadly equal spans of amplitude, although the RANS record appears to lack some higher frequencies. A similar behaviour is observed in respect of the friction velocity, as well as for the correlation between the wall-shear stress and velocity at various distances from the wall, both in terms of magnitudes and directions. While this can be regarded as a favourable indication that RANS is able to

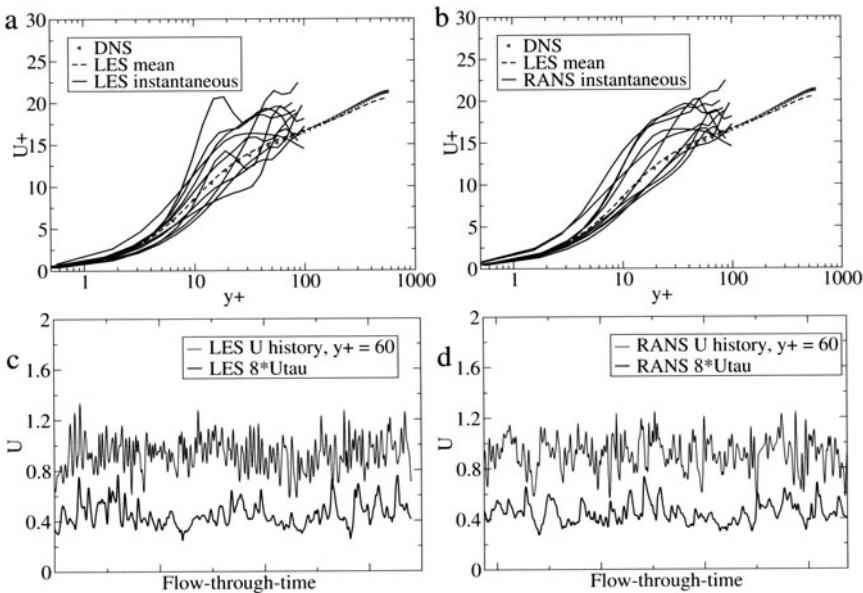


Figure 2. Above: Instantaneous velocity plots for LES (a) and *a priori* RANS (b) compared to time-mean of reference DNS. Below: Histograms of streamwise velocity at $y^+ = 60$ and of Wall-friction velocity for LES (c) and *a priori* RANS (d).

reproduce turbulence features realistically, at least for larger scales (and does not return "pseudo turbulence", as claimed by some authors), this finding has some undesirable consequences and implications: because the RANS model provides a much larger modelled contribution to the turbulence statistics than LES, while the resolved RANS and LES contributions are comparable, the total (resolved plus modelled) second moments (as well as modelled viscosities) in the RANS region exceed by far the corresponding total LES (or DNS) values. This results in a discontinuity in the turbulence energy and total eddy viscosity, suggesting the need to impose constraints and appropriate modifica-

tions to the eddy viscosity, so as to ensure compatibility of two solutions on either side of the interface. This is the subject of the following section.

4. Testing Hybrid Models for High-Re Channel Flows

4.1 Scope of Study

We present here a series of computations for fully developed channel flow at $Re_\tau = 2000$, performed with two-equation RANS models applied within zonal and seamless strategies. The computational domain has the dimensions $2\pi h \times 2h \times \pi h$, where h is the half-channel width. In all cases, the same mesh is used - namely, $64 \times 64 \times 32$ - resulting in typical grid spacing of $\Delta x^+ = \Delta y^+ = 200$ and Δz^+ ranging from 0.5 at the wall to 200 at the centre. Statistics have been assembled by averaging over a period of 12 channel convective lengths. The error in the predicted skin-friction coefficient is evaluated relative to the well known friction law of Dean $C_{f,Dean} = 0.073 * Re_b^{-0.25}$

4.2 Zonal Modelling

In an effort to address the issue of *double-counting* of turbulence effects in the RANS layer, a dynamic approach has been chosen here to adjust the turbulence viscosity in the RANS layer based on implications deduced from the LES solution. The interface is simply chosen to lie anywhere within the turbulent region.

In an early zonal-modelling option, presented by Temmerman *et al.* (2003), a one-equation turbulence-energy model is solved in both the RANS and LES sub-domains. The RANS and SGS models differ only in the manner in which the dissipation rate and eddy viscosity are defined. The two methods are bridged at the interface by interchanging velocities, modelled turbulence energy and turbulent viscosity, the last subject to the continuity constraint across the interface:

$$\nu_{LES}^{mod} + \nu_{LES}^{res} = \nu_{RANS}^{mod} + \nu_{RANS}^{res} \quad (1)$$

where the resolved LES viscosity may be extracted from:

$$\nu_{LES}^{res} = \frac{\langle \overline{u_i u_j}^{res} \overline{S_{ij}} \rangle}{\langle \overline{S_{ij} S_{ij}} \rangle} \quad (2)$$

with the overbar identifying filtered quantities and $\langle \rangle$ denoting averaging over the two homogeneous directions (in fully-developed channel flow) on both sides of the interface. Because the resolved stresses are constrained to be continuous across the interface, by virtue of the velocity-exchange process, equations (1) and (2) imply at the interface:

$$\nu_{LES}^{res} = \nu_{RANS}^{res} \quad (3)$$

This constraint was met by forcing the coefficient C_μ in the RANS eddy-viscosity model to take an interface value consistent with the condition (note averaging $\langle \rangle$ in homogeneous planes):

$$\langle \nu_{RANS}^{mod} \rangle = C_{\mu,int}^{av} \langle (k_{RANS}^{mod})^{1/2} l \rangle \quad (4)$$

The smooth transition from the RANS value $C_\mu = 0.09$ to the interface value $C_{\mu,int}$ is effected by the empirical exponential function:

$$C_\mu = 0.09 + (C_{\mu,int} - 0.09) \frac{1 - \exp(-y/\Delta)}{1 - \exp(-y_{int}/\Delta_{int})} \quad (5)$$

one of several options, where int denotes the interface location.

The above strategy was found by Temmerman *et al.* (2003) to give channel-flow results much closer to the reference LES than the coarse-grid LES, but still not fully satisfactory. Whereas the RANS model returned a favourable representation close to the wall, and the LES provided the correct log-law slope in the outer region, the region around the interface showed signs of insufficient level of total viscosity. Choosing different locations for the interface simply shifted this region along with the interface location.

Attention was then shifted to a two-equation model for the RANS region. The particular model selected was that of Abe *et al.* (1994). The turbulent viscosity is now given by:

$$\nu_{RANS}^{mod} = C_\mu f_\mu k^2 / \varepsilon \quad (6)$$

where f_μ is a damping function which is part of the model. Hence, $C_{\mu,int}$ now arises from equations (6) and (3) as:

$$C_{\mu,int}^{av} = \frac{\langle \nu_{LES}^{mod} \rangle}{\langle f_\mu k^2 / \varepsilon \rangle} \quad (7)$$

The solution of the RANS model requires the specification of boundary conditions for k and ε at the RANS/LES interface. When a k -equation-based sub-grid-scale model is used, this provides the sub-grid-scale energy, hence yielding the required boundary value for k , while ε may be evaluated from $k^{3/2}/C_l y$. For more complex flows, where the characteristic wall distance is not clearly defined, this may pose a problem, however.

The results presented below were obtained with a *dynamic* sub-grid-scale model for LES which does not provide explicitly the sub-grid-scale energy. Rather, this is estimated, based on similarity arguments, from:

$$k_{SGS} = \frac{1}{2} [(\widehat{U} - \overline{U})^2 + (\widehat{V} - \overline{V})^2 + (\widehat{W} - \overline{W})^2] \quad (8)$$

where \widehat{U} is the test-filtered velocity (over 2Δ), and \overline{U} the filtered velocity.

Preliminary testing with the above RANS model revealed the original proposal for C_μ by Temmerman *et al.* (2003) to produce excessive modelled turbulent viscosity in the near-wall region, up to $y^+ = 25$, and this was therefore modified to the following form:

$$C_\mu = \begin{cases} \frac{15.0}{40.0 - y^+} (0.09 + (C_{\mu,int} - 0.09) \frac{1 - \exp(-y/\Delta)}{1 - \exp(-y_{int}/\Delta_{int})}), & \text{if } y^+ < 25 \\ 0.09 + (C_{\mu,int} - 0.09) \frac{1 - \exp(-y/\Delta)}{1 - \exp(-y_{int}/\Delta_{int})}, & \text{if } y^+ > 25 \end{cases} \quad (9)$$

The variation of C_μ (eq. 9) for three different interface locations is shown in Fig. 3a. They illustrate that, depending on the location of the interface, the implied interface C_μ can be as low as 0.01. Fig. 3b demonstrates that the instantaneous value varies greatly in time, reflecting the presence of high-frequency perturbations on the LES side. Thus, the use of an averaged value clearly filters out, to some degree, the transmission of perturbations to the RANS layer. Fig. 4 shows variations of time-averaged velocity, turbulent viscosity and turbulent shear stress (the modelled component as well as the total). The solutions which relate to the present considerations are those identified by " $C_{\mu,int}^{av}$ ". The others will be considered below. The two-equation model has been found to lead to some predictive improvements in respect of the velocity relative to the one-equation model, partly because of the modifications to C_μ , but also because two turbulence variables (here k and ε) are obtained from their respective transport equations, and this is expected to yield a better response of the RANS model to external perturbations relative to the use of a single variable. However, the interface-zone anomaly, implying insufficient effective viscosity in this region, is still visible in Fig. 4a. In an attempt to

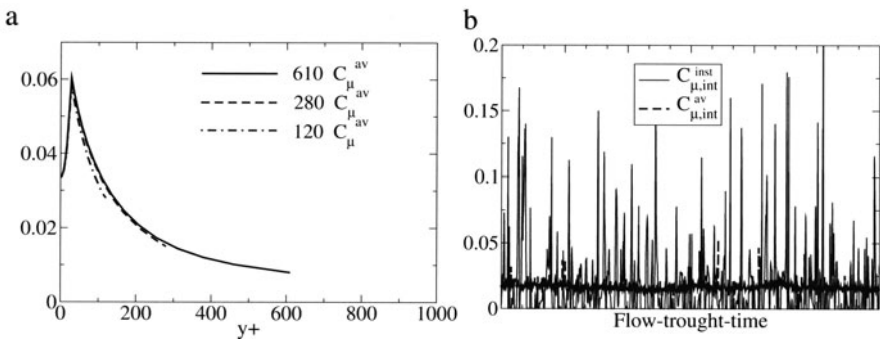


Figure 3. Variation of (time-invariant) C_μ across the flow (a), and histograms of the instantaneous and homogeneously-averaged C_μ at the RANS/LES interface.

compensate for this deficiency and to introduce a more faithful spectral representation into the RANS layer, tests were conducted with *instantaneous* values of $C_{\mu,int}^{inst} = \nu_{LES}^{mod}/(f_\mu k^2/\varepsilon)$ imposed at the interface. As shown in Fig. 3b, the instantaneous interfacial $C_{\mu,int}^{inst}$ is much 'noisier' (negative values are clipped)

than its averaged counterpart, $C_{\mu,int}^{av}$. As is demonstrated in Fig. 4a, use of $C_{\mu,int}^{inst}$ instead of $C_{\mu,int}^{av}$, diminishes the unphysical bump in the velocity profile around the interface. Although this option cannot generate realistic streaks and other missing small-scale structures that are inaccessible to URANS, it seems that $C_{\mu,int}^{inst}$ provides some extra unsteady forcing, thus generating some missing high frequencies and improving the effective eddy viscosity. The beneficial effect of artificial forcing in the interface zone has also been reported by Piomelli *et al.* (2003) with their "stochastic backscatter" generated by random numbers, uncorrelated in two directions, with an envelope dependent on the wall-distance. The present use of $C_{\mu,int}^{inst}$ is similar in spirit, but much simpler. Returning to Fig. 4, it is observed that placing the interface closer to the wall results, as anticipated, in an increase of the resolved stresses and decrease in the eddy viscosity. However, the eddy viscosity shows a nearly discontinuous behaviour, with the low value at the interface resulting in an excessive velocity gradient in this region. This anomaly becomes more and more pronounced with the interface moved closer to the wall. Moving the interface away from the wall improves the results: the variation of eddy viscosity is more gradual and the velocity profile is smoother. The predicted friction factor also improves, with an error of 9% for $y_{int}^+ = 120$, using $C_{\mu,int}^{av}$, diminishing to 3.3% for $y_{int}^+ = 610$ with $C_{\mu,int}^{inst}$. In essence, by increasing the near-wall layer, a heavier burden is placed on URANS, and the role of LES in the outer region is progressively reduced to capturing only the very large structures in the channel-core region and thus providing unsteady forcing to the RANS region, rather than returning the true and complete large-scale turbulence spectrum. This is illustrated in Fig. 5 which shows contours of instantaneous streamwise vorticity in a cross-flow plane. Fig. 5a, corresponding to $y_{int}^+ = 120$ and $C_{\mu,int}^{av}$, contains elements of typical streaky near-wall structures, with streak centres around $y^+ = 70$. However, because of the coarse spanwise mesh spacing ($\Delta z^+ \approx 200$), the streaks are much wider ("superstreaks"), and their distance is much larger ($z^+ = 500$) than in reality, represented by the highly-resolved LES result shown in Fig. 5d. The interface at $y^+ = 120$ cuts through the middle of the streaks-populated region, which also partly explains the source of the interface anomaly in the mean velocity. Moving the interface closer to the wall would lead to a greater proportion of the small-scale structures being captured, but reproducing faithfully the streak topology would require the grid to be refined substantially, especially in the spanwise direction, thus departing from the main motivation for the hybrid approach.

Moving the interface further away from the wall leads to the streaky pattern becoming progressively indistinct, although for $y^+ = 280$, this pattern is still visible, partly because here $C_{\mu,int}^{inst}$ has been used, as opposed to $C_{\mu,int}^{av}$ in Fig. 5a. The streak centres are moved further from the wall to about $y^+ = 100$, but their distance remains roughly the same, determined by the mesh spacing

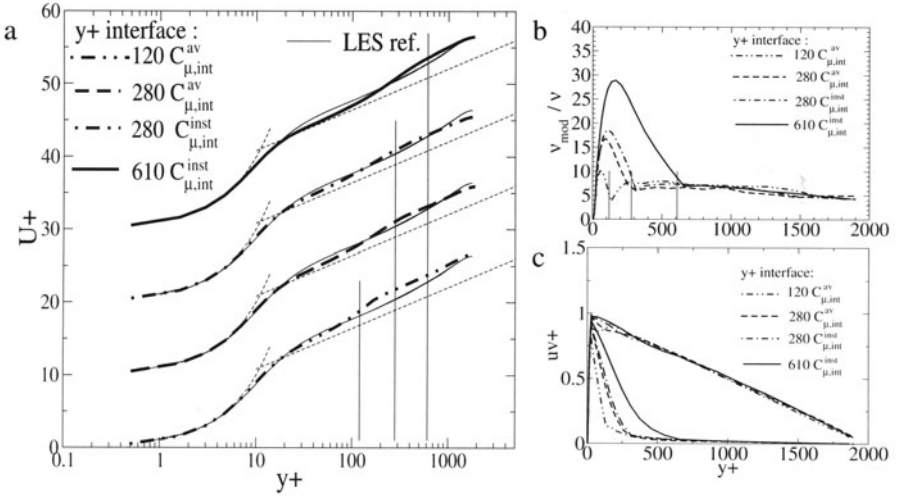


Figure 4. Zonal RANS/LES results for different interface locations. a) Mean velocity; b) modelled eddy viscosity (normalized with ν); c) Total and modelled turbulent shear stress.

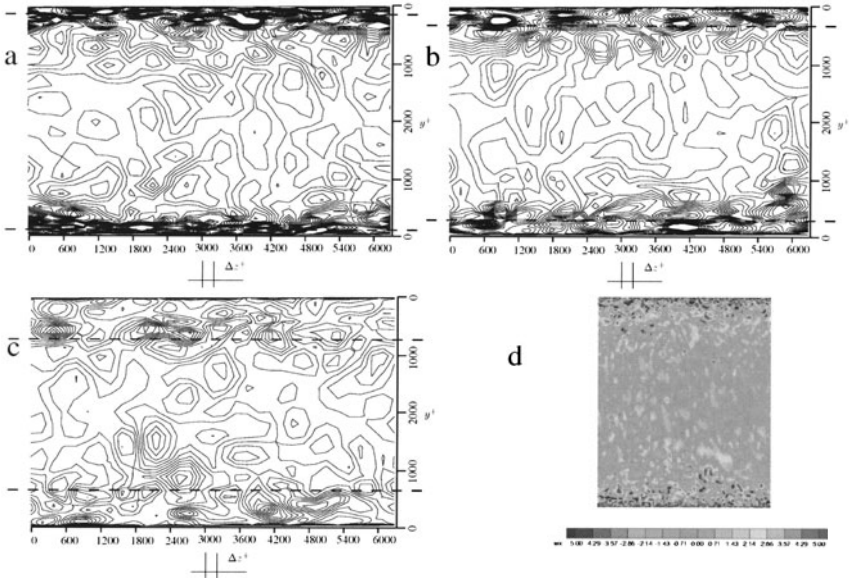


Figure 5. Contours of streamwise vorticity in planes normal to the flow: a) $y_{int}^+ = 120$, with $C_{\mu, int}^{av}$; b) $y_{int}^+ = 280$, with $C_{\mu, int}^{inst}$; c) $y_{int}^+ = 610$, with $C_{\mu, int}^{inst}$. d) Fine-grid (reference) LES.

in the spanwise direction. However, in Fig. 5b, the interface is already at the edge of the streak-populated region and in Fig. 5c, much beyond it.

This, seemingly paradoxical finding that better predictions of velocity and second-moment turbulence statistics are obtained when the RANS/LES interface is placed further away from the wall, thus leading to a loss of the near-wall turbulence structure, is disconcerting on fundamental grounds, but has

favourable implications in respect of simulating complex flows at very high Re numbers. In such cases, the very thin wall boundary layers cannot be resolved in any event, and the interface must inevitably be placed at high y^+ values.

4.3 Seamless Coupling with a Single RANS/LES Model

This approach employs a single $k - \varepsilon$ model to provide the modelled eddy-viscosity for the unresolved motion in the complete flow. The characteristic length scale used for defining eddy viscosity is not directly linked to the mesh size, but is defined via the standard form used in two-equation modelling, here in terms of k and ε . For practical reasons, the model of Abe *et al.* (1994) has been adopted to serve as the RANS limit. This model is claimed to be robust and to return high-quality RANS predictions for a number of flows. The sub-scale model differs from its RANS parent only in respect of the coefficient C_{e2} . The form adopted here originates from the sub-grid-scale model of Dejoan and Schiestel (2001):

$$C_{e2} = C_{e1} + \frac{0.4}{1.0 + \beta \left(\frac{0.41y}{l_f} \right)^{2/3}} \quad (10)$$

where y is the near-wall distance, which in more complex flows can be replaced by a suitable turbulence scale, $l_f = (\Delta x \Delta y \Delta z)^{1/3}$ and β is an empirical constant, here assigned the value 4.0. Additional damping of f_μ in the viscous region ($y^+ < 30$) was also introduced to compensate for resolved stress from unsteady RANS.

Fig. 6 shows results obtained with the seamless model for the same conditions as in the previous section. The mean-velocity variation in Fig. 6a is compared with the reference LES solution, as well as with our DES result with the original SA model Nikitin *et al.* (2000). The remaining plots show the variation of resolved, modelled and total turbulence energy (b), the turbulent or sub-scale viscosity (c) and the resolved and modelled turbulent shear stress (d). In contrast to the zonal approach, the modelled eddy viscosity is here seen to vary smoothly from the RANS to the LES regions. The magnitude of the modelled turbulent viscosity is similar to that resulting from the zonal model with the interface at $y^+ = 610$. Consequently, the respective mean-velocity profiles are similar as well. The C_f error is 5.5%. The peak of the total kinetic energy is well predicted, but the total turbulence energy is excessive in the region $80 < y^+ < 600$, which reflects a degree of *double-counting* of turbulence effects.

Contours of instantaneous streamwise vorticity in a plane normal to the flow and of streamwise velocity in a plane parallel to the wall at $y^+ = 280$ are shown in Fig. 7. The general impression of the structural features is similar to that gained from the zonal model when the interface is placed relatively far from the wall. In both cases, "super-streaks" can be observed. The formation

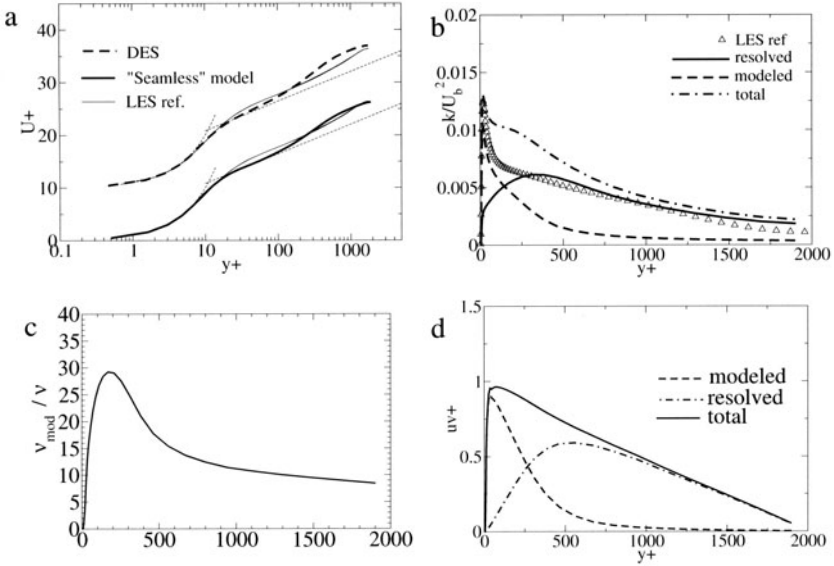


Figure 6. Seamless-model results with modified $k - \varepsilon$ sub-scale model: a) velocity profiles, compared with DES and reference LES; b) total, resolved and modelled kinetic energy; c) modelled eddy viscosity; d) total, resolved and modelled shear stress.

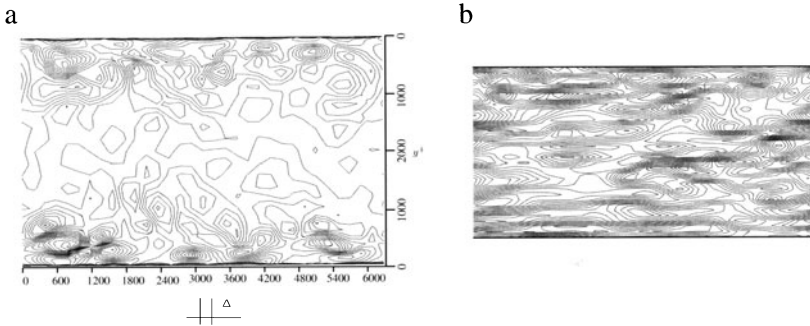


Figure 7. Seamless-model results: (a) contours of streamwise vorticity in a plane normal to the flow; (b) contours of velocity in a plane parallel to the wall.

and size of these structures are largely determined by the mesh, and increasing the level of the modelled turbulent viscosity in the RANS region tends to enlarge them.

5. Conclusions

Based on our exploration and related work reported in the literature, it is justified to conclude that hybrid RANS/LES models, either in zonal or seamless versions, are feasible and promising. Most hybrid models give substantially better solutions than the equivalent coarse-grid LES. It is likely, therefore, that

they will be increasingly used for the simulation of complex flows at high Reynolds numbers. Extensive testing over the past few years of a substantial number of alternative formulations has demonstrated that, notwithstanding the significant advantages derived from hybrid modelling, no model form yields an entirely satisfactory representation of near-wall turbulence with a RANS-type grid, especially for attached flows. The main source of defects is that, irrespective of the model used, insufficient near-wall grid resolution simply cannot capture the details of the small-scale streaky structure near the wall. The imperfection of hybrid models needs to be viewed, however, against the fact that these use a small fraction of the number of grid cells required for trustworthy, well-resolved LES (for the channel flow discussed in this paper, the hybrid grid had less than 1% of cells of the fine LES grid).

The zonal approach seems especially appealing, because outside the wall boundary layers, the conventional LES method is used without any intervention in respect of sub-grid modelling. However, even if the RANS model is adjusted to meet the constraints of continuity of eddy viscosity as well as other quantities at the interface, an insufficient level in small-scale activity that RANS feeds into LES across the interface produces, in most circumstances, non-physical features in the velocity profile around the interface. Another problem in zonal modelling is the need to prescribe the interface location, although this can be automated, in principle, in terms of grid spacing. As regards the sensitivity of the solution to the interface location, the present study has shown that placing the RANS/LES interface close to the wall ($y^+ \leq 120$) produces too low levels of eddy viscosity. Beyond a distance $y^+ = 280$, the position of the interface becomes less influential. The mean-velocity profile is influenced predominantly by the modelled viscosity up to $y^+ = 120$. The anomalous kink observed in the velocity profile in the interface region appears to be caused by the rapid change in viscosity across the interface, rather than by inappropriate local interface properties.

It has been observed that most of the hybrid models, including DES, reproduce better the log-law when the interface is moved away from the wall. This appears paradoxical in view of the fact that the use of RANS over a larger region diminishes the realism with which structural features are captured. The interface anomaly diminishes also when the interface is moved *very* close to the wall, say around or below $y^+ = 30$, but this requires an increasingly high grid density, contradicting the main goal of the hybrid approach.

Seamless coupling returns generally better, smoother results with no discontinuities, as experienced also with DES. However, this approach requires an adjustment of the LES subgrid-scale model. For simple flows this is readily done in terms of wall-distance and grid-size ratio, but for complex flows this may be more difficult.

References

- Abe, K., Kondoh, T. and Nagano, Y. (1994) A new turbulence model for predicting fluid flow and heat transfer in separating and reattaching flows - I. flow field calculations, *Int. Journal of Heat and Mass Transfer*, **37** pp. 139-151.
- Balaras, E., Benocci, C. and Piomelli, U. (1996) Two-layer approximate boundary conditions for large-eddy simulations, *AIAA J.*, **34** (6) pp. 1111-1119.
- Benhamadouche, S. and Laurence, D. (2003) LES, coarse LES, and transient RANS comparisons on the flow across a tube bundle, *Int. J. Heat and Fluid Flow*, **24** pp. 470-479.
- Cabot, W. and Moin, P. (2000) Approximate wall boundary conditions in the large-eddy simulation of high Reynolds number flows, *Flow, Turbulence and Comb.*, **63** pp. 269-291.
- Davidson, L. and Peng, S.-H. (2001) A hybrid LES-RANS model based on one-equation SGS model and two-equation $k-\omega$ model, in E. Lindborg *et al.* (eds.) *Turbulence and Shear Flow Phenomena 2 (Proc. Int. Symp., Stockholm, Sweden, 27-29 June 2001)*, **2** pp. 175-180.
- Dejoan, A. and Schiestel, R. (2001) Large eddy simulations of non-equilibrium pulsed turbulent flow using transport equations subgrid scale model, in E. Lindborg *et al.* (eds.) *Turbulence and Shear Flow Phenomena 2 (Proc. Int. Symposium, Stockholm, Sweden, 27-29 June 2001)*, KTH Stockholm, Sweden pp. 341-346.
- Hamba, F. (2001) An attempt to combine large eddy simulation with the $k-\varepsilon$ model in a channel-flow calculation, *Theor. Comp. Fluid Dyn.*, **14** pp. 323-336.
- Laurence, D. (2002) Large eddy simulation of industrial flows?, in B. E. Launder and N. Sandham (eds.) *Closure Strategies for Turbulent and Transitional Flows* Cambridge University Press, Cambridge, UK.
- Nikitin, N. V., Nocoud, F., Wasistho, B., Squires, K. D. and Spalart, P. R. (2000), An approach to wall modeling in large-eddy simulations, *Phys. Fluids*, **12**(7) pp. 1629-1632.
- Piomelli, U., Balaras, E., Pasinato, H., Squires, K. D. and Spalart, P. R. (2003) The inner-outer layer interface in large-eddy simulations with wall-layer models, *Int. J. Heat and Fluid Flow*, **24** pp. 538-550.
- Spalart, P. R. (2000) Strategies for turbulence modelling and simulations, *Int. J. Heat and Fluid Flow*, **21** pp. 252-263.
- Spalart, P. R., Jou, W. H., Strelets M. and Allmaras, S. R. (1997) Comments on the feasibility of LES for wings, and on a hybrid RANS/LES approach, in C. Liu and Z. Liu (eds.) *Advances in LES/DNS* Greyden Press, Columbus, OH, USA.
- Temmerman, L., Leschziner, M. A. and Hanjalić K. (2002) A-priori studies of a near-wall RANS model within a hybrid LES/RANS scheme, in W. Rodi and N. Fueyo (eds.) *Engineering Turbulence Modelling and Experiments 5, (Proc. 5th Int. Symp., Mallorca, Spain, 16-18 September 2002.)*, pp. 317-326.
- Temmerman, L., Leschziner, M. A. and Hanjalić K. (2003) A combined RANS-LES strategy with arbitrary interface location for near-wall flows, in N. Kasagi *et al.* (eds.) *Turbulence and Shear Flow Phenomena 3 (Proc. Int. Symp., Sendai, Japan, 25-27 June 2003)*, pp. 929-934.
- Wei, T. and Willmarth, W. W. (1989) Reynolds-number effects on the structure of a turbulent channel flow, *J. Fluid Mech.*, **204**, pp. 57-95. (also AGARD-AR-345, AGARD, 1998, pp. 122-).

DETACHED-EDDY SIMULATION: CURRENT STATUS AND PERSPECTIVES

Kyle D. Squires

MAE Department, Arizona State University, Tempe, AZ 85287-6106, U.S.A.

squires@asu.edu

Abstract Detached-Eddy Simulation (DES) is a hybrid technique proposed in 1997 as a numerically feasible and plausibly accurate approach for predicting massively separated flows. Since its inception the method has been applied to a range of configurations including simple shapes such as cylinders, spheres and aircraft forebodies, in addition to complex geometries including fighter aircraft. The accuracy of DES predictions has typically been far superior to that of steady or unsteady Reynolds-averaged Navier-Stokes methods while at the same time avoiding the Reynolds-number limitations that plague Large-Eddy Simulation. Based on research performed to date, the method appears sound and responds well to the type of boundary layer separation (i.e., laminar or turbulent), and to grid refinement. However, it is possible to degrade predictions using a grid density that is both too fine for RANS and too coarse for LES. Examples of applications of the technique are presented, along with a summary of some of the important findings and directions for future research.

Keywords: Turbulence simulation and modeling, hybrid methods, high Reynolds numbers

1. Introduction

Detached-Eddy Simulation (DES) is a hybrid technique first proposed by Spalart *et al.* (1997) for prediction of turbulent flows at high Reynolds numbers (see also Spalart 2000). Development of the technique was motivated by estimates which indicate that the computational costs of applying Large-Eddy Simulation (LES) to complete configurations such as an airplane, submarine, or road vehicle are prohibitive. The high cost of LES when applied to complete configurations at high Reynolds numbers arises because of the resolution required in the boundary layers, an issue that remains even with fully successful wall-layer modeling.

Traditionally, high Reynolds number separated flows have been predicted using solutions of the steady or unsteady Reynolds-averaged Navier-Stokes equations (RANS or URANS). One disadvantage of RANS methods applied to

massive separations is that the statistical models are designed and calibrated on the basis of the mean parameters of thin turbulent shear flows containing numerous, and relatively “standard”, eddies. Such eddies are not representative of the comparatively fewer and geometry-specific structures that typically characterize massively separated flows. The advantages then offered by LES provide strong motivation for its application, i.e., direct resolution of the dominant unsteady structures. In addition, while RANS or URANS does not appear to constitute a viable long-term approach for predicting massively separated flows at high Reynolds numbers, the calibration range of most models is sufficient to yield acceptable accuracy of a relatively broad range of attached flows. In Detached-Eddy Simulation (DES), the aim is to combine the most favorable aspects of the two techniques, i.e., application of RANS models for predicting the attached boundary layers and LES for resolution of time-dependent, three-dimensional large eddies. The cost scaling of the method is then favorable since LES is not applied to resolution of the relatively smaller-structures that populate the boundary layer.

In natural applications of the method, the entire boundary layer is treated by RANS and with an LES treatment of the separated regions. One of the issues confronting hybrid RANS-LES methods is the “grey area” in which a shear layer, after separation, must generate “LES content” (random eddies) which it did not possess in the boundary layer upstream. The process of generating LES content is more easily accommodated by a thin shear layer that is rapidly departing from the wall and for configurations with fixed separations (e.g., as occurs over geometries with sharp corners). In the examples summarized below, the challenge of separation prediction varies with the geometry and as will be shown, flow field predictions obtained using DES are encouraging. In the next section, an overview of the technique is presented, followed by a summary of some recent examples. A brief discussion then follows of some of the current issues requiring research in order to extend the range of applications amenable to accurate prediction using DES.

2. Detached-Eddy Simulation

The base model employed in the majority of DES applications to date is the Spalart-Allmaras one-equation model (Spalart and Allmaras 1994, referred to as “S-A” throughout). The reader is referred to Strelets (2001) for an analogous formulation based on the SST model. The S-A model contains a destruction term for its eddy viscosity $\tilde{\nu}$ which is proportional to $(\tilde{\nu}/d)^2$, where d is the distance to the wall. When balanced with the production term, this term adjusts the eddy viscosity to scale with the local deformation rate S and d : $\tilde{\nu} \propto Sd^2$. Subgrid-scale (SGS) eddy viscosities scale with S and the grid spacing Δ , i.e., $\nu_{SGS} \propto S\Delta^2$. A subgrid-scale model within the S-A formulation can then be

obtained by replacing d with a length scale Δ directly proportional to the grid spacing.

To obtain the model used in the DES formulation, the length scale of the S-A destruction term is modified to be the minimum of the distance to the closest wall and a lengthscale proportional to the local grid spacing, i.e., $\tilde{d} \equiv \min(d, C_{DES}\Delta)$. In RANS predictions of high Reynolds number flows the wall-parallel (streamwise and spanwise) spacings are usually on the order of the boundary layer thickness and larger than the wall-normal spacing. Choosing the lengthscale Δ for DES based on the largest local grid spacing (i.e., one of the wall-parallel directions) then ensures that RANS treatment is retained within the boundary layer, i.e., near solid walls, $d \ll \Delta$ and the model acts as S-A, while away from walls where $\Delta \ll d$ a subgrid model is obtained.

There are several advantages to the DES formulation described above. The technique is non-zonal and simple in formulation, the transition between RANS and LES is seamless in that there is a single equation with no explicit declaration of RANS versus LES zones. The formulation using a single model only leads to a discontinuity in the gradient of the length scale that enters the destruction term of the turbulence model (this discontinuity would be easily removed by rounding the min function that determines the lengthscale). The change in the lengthscale leads to a model that becomes region-dependent in nature – in most cases a RANS model in the boundary layers and a subgrid model in separated regions. Incorporation of the grid spacing into the model is compatible with the existence of a filter width in LES that controls the end of the energy cascade. Grid refinement then provides a means to increase the range of scales and improve the fidelity of the calculation. This feature is quite unlike the role of grid refinement in RANS in which the role of the turbulence model remains important even in the fine-grid limit. While a natural choice, and an aspect of nearly all hybrid methods, incorporating the grid spacing into the model highlights the importance of grid design for any turbulence-resolving simulation technique. In boundary layers, as the grid spacing in the wall-parallel directions becomes smaller than about half of the boundary-layer thickness, the DES limiter reduces the eddy viscosity below its RANS level, though without allowing LES behavior. The resulting solution creates insufficient total Reynolds stresses, an issue that was raised in the original paper presenting the method by Spalart *et al.* (1997).

3. Applications

The DES applications summarized in this section are “natural” in the sense that boundary layers upstream of separation are handled by the RANS model, with the “LES region” comprising the detached regions away from the wall.

The configurations include the flow over a sphere, around an aircraft forebody, and over fighter aircraft. With the exception of the sphere, all of the computations summarized in this manuscript were performed using the commercial flow solver *Cobalt*. The examples presented are representative of the variation in geometric complexity in research efforts undertaken to date and highlight the advantages of hybrid methods in general, and DES in particular, for prediction of high Reynolds number turbulent flows.

3.1 Turbulent Flow over a Sphere

The sphere belongs to the class of separated flows for which the location of flow detachment is not fixed by the geometry nor subject to external effects which might otherwise determine the location of boundary layer separation and/or force unsteadiness. These features in turn supply strong motivation for application of DES in order to assess both the strengths and limitations of the method.

As also the case for the circular cylinder, the sphere is known for its drag crisis, which reflects the substantial differences in separation between laminar and turbulent boundary layers. An illustration is provided in Figure 1, which shows contours of the instantaneous vorticity obtained from DES predictions of the sub-critical flow at $Re = 10^4$ (Constantinescu *et al.* 2003) and super-critical flow at $Re = 1.14 \times 10^6$ (Constantinescu *et al.* 2002). At $Re = 10^4$, the DES prediction is of a laminar boundary layer separation at an azimuthal angle measured from the forward stagnation point of around 82° , in good agreement with experimental measurements (Achenbach 1972). The super-critical solution at $Re = 1.14 \times 10^6$ shown in the right frame of the figure experiences turbulent boundary layer separation at an azimuthal angle around 120° , the DES prediction of the separation location also in good agreement with the experimental measurements reported by Achenbach (1972). Both frames in Figure 1 show a range of eddies that are resolved to the grid scale, the chaotic structure a result of the LES treatment in the wake.

The DES prediction of the laminar boundary layer separation in the sub-critical solution of the sphere is essentially a Large-Eddy Simulation, with the subgrid eddy viscosity predicted from a one-equation model (the S-A model modified in its destruction term). The non-trivial requirement that the turbulence model remains dormant in the laminar regions of the flow is achieved using the Spalart-Allmaras model. For the sub-critical flow over the sphere in Figure 1, the simulation is performed using the “tripless” approach proposed by Travin *et al.* (2000), which has the effect of disabling the model up to separation.

The solution for the high Reynolds number sphere shown in Figure 1 is of the fully turbulent flow modeled by seeding a small level of eddy viscosity into the domain upstream of the sphere, sufficient to ignite the turbulence model

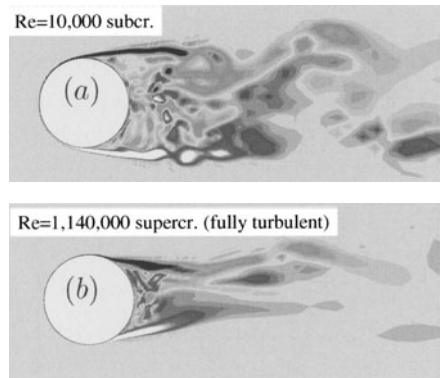


Figure 1. Contours of the instantaneous out-of-plane vorticity from DES predictions of the flow over a sphere. (a) sub-critical solution at $Re = 10^4$ with laminar boundary layer separation; (b) super-critical flow experiencing turbulent boundary layer separation at $Re = 1.14 \times 10^6$.

as the fluid enters the boundary layers. Compared to the prediction at the lower Reynolds number, the fully turbulent treatment of the solution yields marked changes in the flow structure, with flow detachment substantially further aft compared to the laminar separation case. As also shown by Constantinescu *et al.* (2003), there are substantial differences between DES and URANS predictions of the time-dependent features of the solutions, with the URANS suppressing the development of turbulent eddies, reducing the three-dimensionality of the flow, and yielding essentially steady and axisymmetric solutions.

Prediction of flows experiencing turbulent boundary layer separation increase the burden on the model in predicting boundary layer growth and separation, now under control of a RANS model in DES. This increase in the empirical content of the approach is not inconsequential – essentially the entire boundary layer must be treated by RANS in applications and therefore the “RANS region” can substantially influence the overall accuracy of the prediction. The larger empirical input seems unavoidable at present since LES of the boundary layer, even with wall-layer modeling, is cost-prohibitive for full configurations. A comparison of the pressure distributions to experimental measurements is shown in Figure 2. The DES prediction of the sub-critical flow at a Reynolds number of $Re = 10^5$ is in good agreement with the measurements of Achenbach (1972), the figure shows that the value and angular position of the minimum in C_p is recovered. For both the sub- and super-critical solutions the back pressure (at $\theta = 180^\circ$) is also reasonably accurate, in turn yielding relatively accurate predictions of the drag. The figure is further useful for reinforcing the

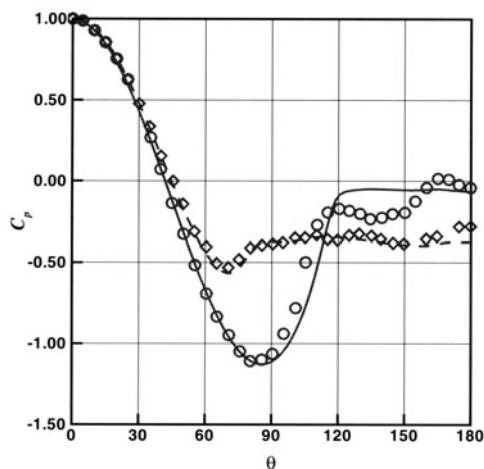


Figure 2. Pressure coefficient (averaged over the azimuthal coordinate). DES: ---- $Re = 10^5$; — $Re = 1.14 \times 10^6$. Achenbach (1972): \diamond $Re = 1.62 \times 10^5$; \circ $Re = 1.14 \times 10^6$.

importance of the boundary layer treatment. In the super-critical regime, the delay in flow detachment substantially deepens C_p compared to the laminar separation solution. The fully turbulent DES predictions are, overall, in good agreement with the measurements. A difference compared to the sub-critical flow ($Re = 1.62 \times 10^5$) in the experiments is the greater variation in the pressure downstream of separation, an effect not produced in the simulations.

As also the case for the circular cylinder, even in the super-critical regime there are possibly substantial regions of the sphere in which the attached boundary layer is laminar. The details of flow separation and transition in the flow over the sphere are complex and the fully turbulent treatment summarized above is simplistic. A consequence of the simple, but well-defined, treatment of the boundary layers in the super-critical regime leads to relatively large discrepancies between the predicted and measured skin friction as shown in Constantinescu *et al.* (2002).

3.2 Flow around an Aircraft Forebody

The second example that represents an increase in geometric complexity compared to the sphere is the model of an aircraft forebody (Figure 3). Part of the motivation for the interest in the aerodynamics of such configurations is supplied by considerations of stability and control of aircraft at high angle of attack. The unsteady separated flow around the forebody exerts considerable

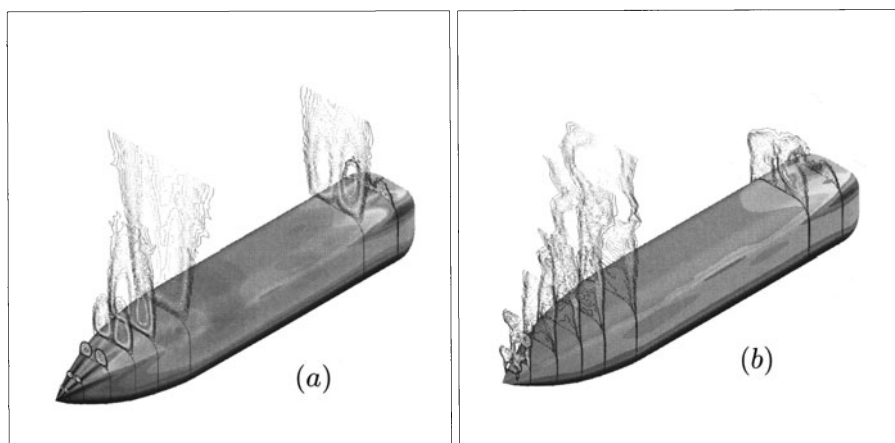


Figure 3. Ratio of the instantaneous eddy viscosity to the molecular value at eight axial locations for which pressure distributions are measured. Angle of attack of the freestream $\alpha = 90^\circ$, $Re = 2.1 \times 10^6$. (a) URANS; (b) DES. Surface colored by pressure.

leverage, especially on modern fighter aircraft for which the forebody represents a relatively long moment arm.

The particular configuration described here was reported by Viswanathan *et al.* (2003) – a rectangular ogive forebody for which the length of the aft section is four times the width (“diameter”, D), the cross-section being a rounded square in which the corner radius is $1/4$ of the width and with a hemispherical end cap. Computations were performed at the highest Reynolds number for which measurements are available, $Re = 2.1 \times 10^6$ (based on freestream speed and diameter). Such a choice not only simplifies the simulation design in that predictions of the fully turbulent flow are a useful approximation to the experimental conditions, a more significant advantage is that the Reynolds number is representative of realistic flight configurations.

Shown in Figure 3 are contours of the eddy viscosity ratio along the ogive at the eight axial stations for which pressure measurements are available for assessing simulation results. DES predictions and URANS results obtained using the S-A model are shown for the freestream flow at angle of attack $\alpha = 90^\circ$. On the lee side, the URANS prediction shows that the wake is comprised of a pair of counter-rotating coherent vortical motions, as evidenced by the contours of the eddy viscosity in the planes and the signature of these structures on the surface pressure, especially along the forebody. The DES prediction, on the other hand, exhibits a more chaotic structure in the corresponding planes. Also apparent is the more uniform pressure on the leeward surface of the forebody, the figure showing a marked difference compared to the URANS result.

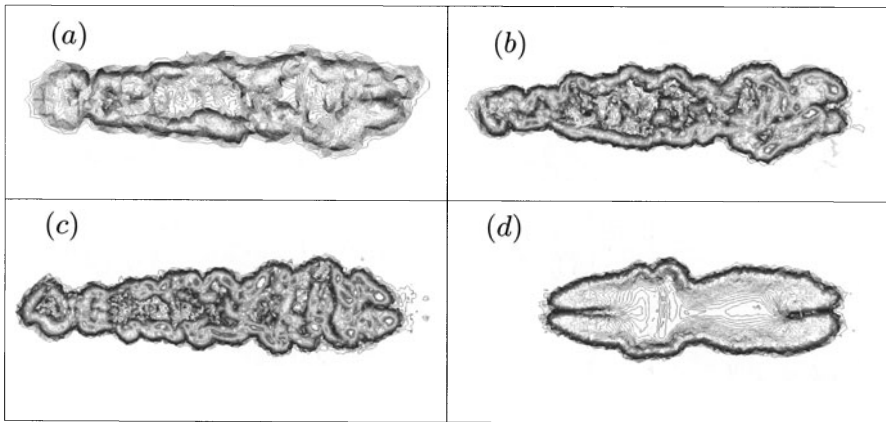


Figure 4. Contours of the instantaneous vorticity magnitude in the plane $y = D$, view is towards the freestream velocity. (a) coarse grid of 2.1×10^6 cells; (b) baseline grid of 6.5×10^6 cells; (c) fine grid of 8.75×10^6 cells; (d) URANS prediction on baseline grid.

A view of the influence of mesh refinement within DES is provided in Figure 4 in which contours of the instantaneous vorticity magnitude are shown in a plane normal to the freestream flow, in the wake of the ogive one-half diameter downstream of the rear surface. Calculations of the flow around the ogive were performed using unstructured grids, enabling a uniform refinement that was applied along each coordinate direction and with the corresponding grid sizes ranging from 2.1×10^6 to 8.75×10^6 cells. The DES predictions in the figure show a tapering of the wake towards the forebody. Figure 4 also shows that with increases in mesh resolution a wider range of scales is resolved, with substantial variation along the axial (“spanwise”) coordinate.

A comparison of the pressure distribution predicted at the fourth axial station from the forebody nose (c.f., Figure 3) using DES and S-A URANS to the experimental measurements of Pauley *et al.* (1995) are shown in Figures 5. The angle θ is measured positive in the clockwise direction with $\theta = 0$ corresponding to the windward symmetry plane. As shown in the figure, the strong coherent vortices predicted in the RANS solution correspond to a large variation in pressure on the leeward side that differs markedly from the experimental measurements. The DES prediction of the pressure coefficient, on the other hand, is in excellent agreement with the measurements, a result of the more accurate resolution of the unsteady shedding that yields a uniform pressure profile on the leeward side.

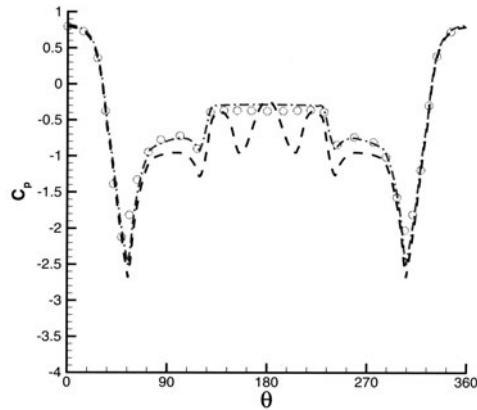


Figure 5. Pressure coefficient at $x/L = 0.166$ (fourth axial station from the nose), $Re = 2.1 \times 10^6$. DES: —○—; URANS: ----; Pauley *et al.* (1995): ○.

3.3 Flow around fighter aircraft

3.3.1 F-15E at 65 degrees angle of attack. Forsythe *et al.* (2003) have recently reported DES predictions of the flow over an F-15E at $\alpha = 65^\circ$. An extensive flight-test database has been compiled on the F-15E that comprised the primary means of assessing DES predictions. The simulations were performed at standard day conditions corresponding to a chord-based Reynolds number of 13.6×10^6 and Mach number of 0.1. The investigation reported by Forsythe *et al.* (2003) was relatively comprehensive, examining sensitivity of DES predictions to mesh and timestep refinement, in addition to a comparison against RANS results obtained using the Spalart-Allmaras model.

Shown in Figure 6 is an isosurface of the instantaneous vorticity magnitude. The shear layer development off the leading edge of the wings is apparent in Figure 6, the LES treatment in the wake allows the development of an array of eddies. The computations reported by Forsythe *et al.* (2003) were performed on unstructured grids and with uniform mesh refinement along each coordinate direction. Contours of the instantaneous vorticity magnitude are shown in Figure 7 in a plane 680 inches aft of the aircraft reference point. As also observed for the geometrically-simpler forebody described above, a wider range of scales is captured with mesh refinement. The figure also shows that even the coarse grid comprised of 2.85×10^6 elements resolves at least some eddy content – with a few small structures visible above the wing.

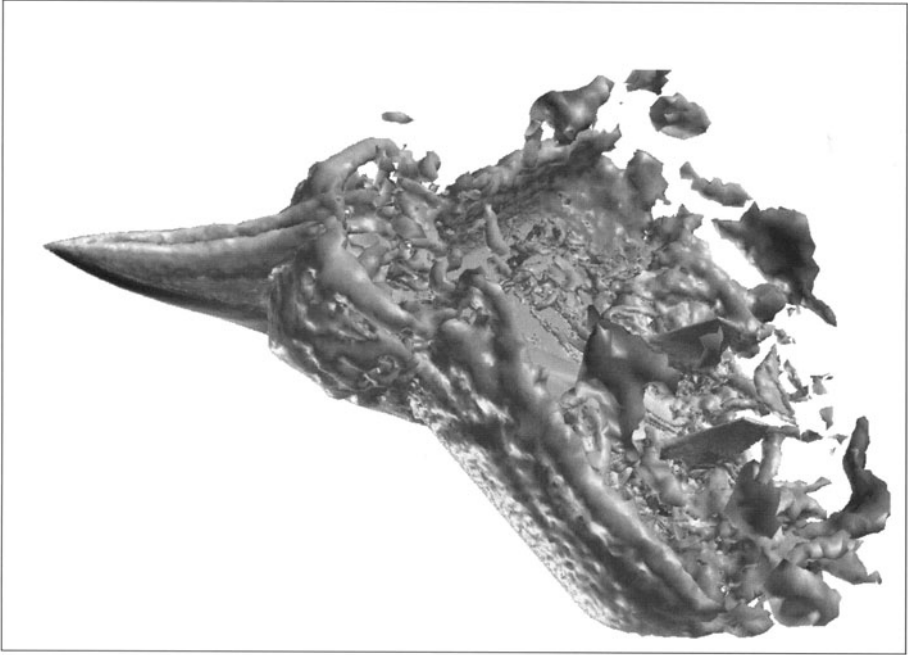


Figure 6. Isosurface of the instantaneous vorticity over the F-15E at 65° angle of attack.

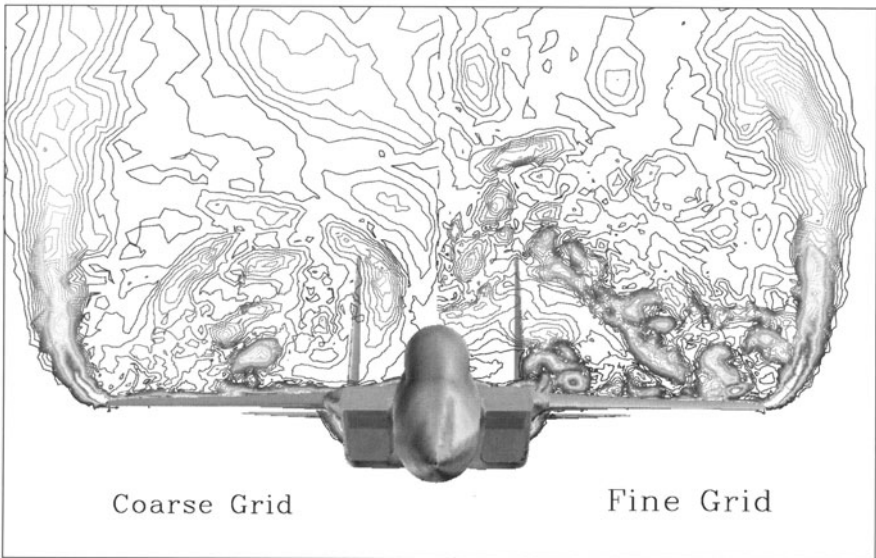


Figure 7. Contours of the instantaneous vorticity magnitude at 680 inches behind the aircraft reference point. Left frame: coarse grid comprised of 2.85×10^6 cells. Right frame: fine grid comprised of 10.0×10^6 cells. Aircraft surface colored by pressure.

Forsythe *et al.* (2003) found that DES predictions of the lift and drag were within 5% of flight-test data. Such predictions should be considered excellent, even once it is recognized that at $\alpha = 65^\circ$, separation prediction is less challenging than at lower angles of attack and the success of DES can be attributed to its LES treatment of the separated regions. In the F-15E, regions of the flow over the aircraft such as the forebody were not resolved as well as in the component study reported by Viswanathan *et al.* (2003) and summarized above. Accommodating a resolution of the forebody comparable to that employed by Viswanathan *et al.* (2003) while also including the entire aircraft remains very challenging.

3.3.2 Abrupt wing stall over the F-18E. Forsythe and Woodson (2003) have recently reported DES and RANS predictions of the shock-separated flow over the F/A-18E. The work was motivated by the fact that during the envelope expansion flights of the F/A-18E/F, the aircraft encountered “wing drop”, an event traced to an abrupt wing stall on either the left or right wing panel, causing a sudden and severe roll-off in the direction of the stalled wing. The phenomena is complex, measurements on a model of a pre-production F/A-18E reported by Schuster and Byrd (2003) showed that the surface pressure variations were highly unsteady and indicative of shock oscillation.

Shown in Figure 8a are time-averaged lift coefficients as a function of angle of attack. The predictions are obtained from a model of a pre-production F/A-18E with $10^\circ/10^\circ/5^\circ$ flaps (leading-edge flaps/trailing-edge flaps/aileron flaps) at Mach 0.9 and without tails. DES predictions from a baseline and adaptively refined grid are shown, along with experimental measurements and RANS predictions. Figure 8a shows that the DES prediction on the baseline grid follows the lift curve to 9° angle of attack and with a subsequent decrease in the lift relative to the measured values. Using the adaptively refined grid, the DES predictions in the figure exhibit an improved agreement between simulation and experiment. Neither of the RANS results shown in Figure 8a follows the measured lift as closely as the DES predictions.

Shown in Figure 8b is a visualization of the instantaneous vorticity for the aircraft at 9° angle of attack. Unsteady pressure measurements show that the average pressure distribution is a result of an unsteady shock traveling forward and backward over the wing (Schuster and Byrd 2003). Forsythe and Woodson (2003) show that DES predictions exhibit a similar unsteady shock motion, the asymmetry in the flow structure in Figure 8b is a result of the unsteady shock motion, an effect that leads to large-magnitude low-frequency oscillations in the rolling moment. This inherently unsteady effect is captured in the DES, the work also showed that unsteady shock oscillations are a potential trigger event for abrupt wing stall.

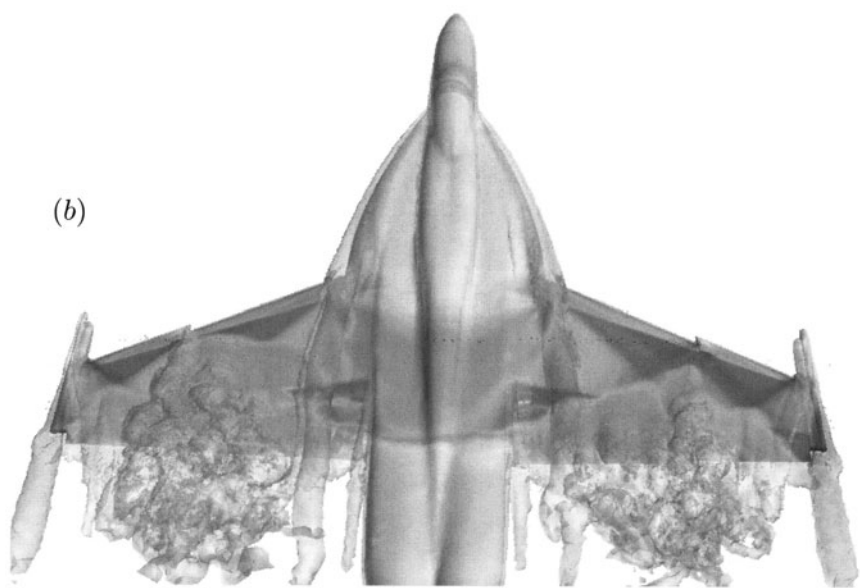
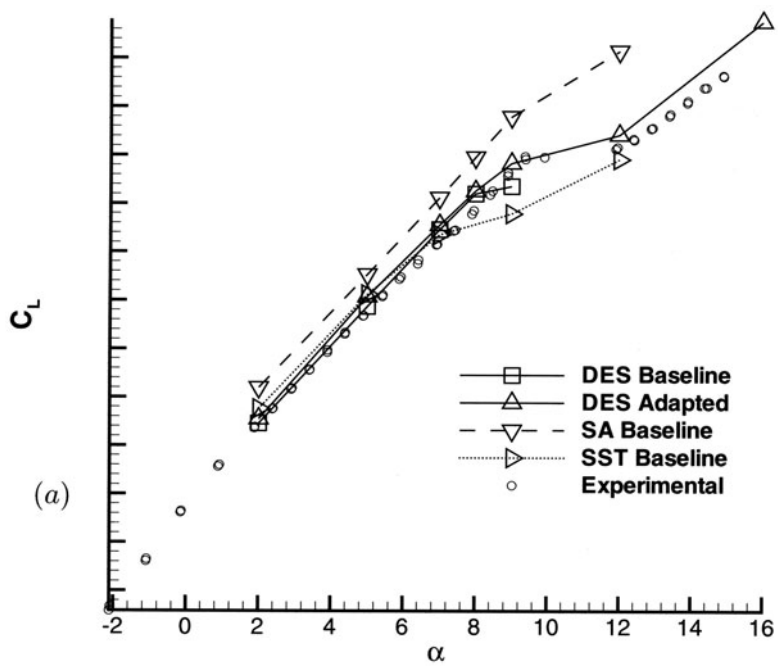


Figure 8. (a) Lift coefficient vs. alpha for the no tails F/A-18E. (b) Instantaneous isosurface of vorticity colored by pressure on the F/A-18E at 9° angle of attack.

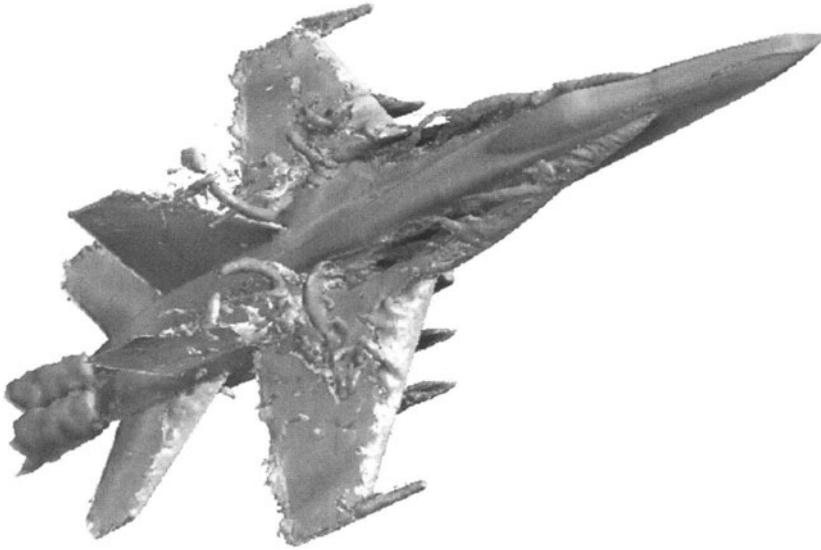


Figure 9. Isosurface of the instantaneous vorticity over the F-18C at 30° angle of attack.

3.3.3 Vortex burst over the F-18C. Morton *et al.* (2003) applied DES to prediction of the flow over an F-18C at $\alpha = 30^\circ$. Part of the motivation for the work is the fact that the F-18 utilizes wing leading edge extensions to generate vortices which enhance the wing lift and with the twin vertical tails canted in order to intercept the strong vortex field and increase maneuverability. At large angle of attack, these vortices break down upstream of the vertical tails, resulting in a loss of yaw control and severe aeroelastic effects. The flow field is inherently unsteady and requires an accurate prediction of vortex breakdown. These and other aspects challenge prediction and the flow appears to be well outside the boundaries of accurate prediction by RANS or URANS techniques.

The simulations reported in Morton *et al.* (2003) were performed at a chord-based Reynolds number of 13.9×10^6 and Mach number of 0.28. The work also provided an opportunity to apply and assess an important technology for eddy-resolving simulation of full aircraft – Adaptive Mesh Refinement. Shown in Figure 9 is an isosurface of the instantaneous vorticity magnitude. The development of the leading-edge extension vortex is apparent, also captured are smaller-scale structures that develop around the vortex. Figure 9 also shows that vortex breakdown occurs over the wing, as observed in flight and tunnel tests at $\alpha = 30^\circ$. Morton *et al.* (2003) found that the DES prediction of the location of vortex breakdown was slightly aft of that observed in flight and tun-

nel tests at $\alpha = 30^\circ$, though the differences compared to measurements were due to changes in the configuration considered in the calculations.

4. Summary

The examples summarized above highlight the strengths of the method, including a rational treatment of the attached boundary layers and the LES capability of the technique in separated regions. In massively separated flows, the demarcation between the RANS and LES regions is clear – a RANS model is applied to prediction of the attached boundary layer, new instabilities result in a rapid development of eddy structure in the wake that comprises the LES region. The eddy content evolves rapidly in the wake, the direct resolution of the energy-containing structures improves the visual description of the solutions and, more importantly, the quantitative prediction of, for example, the pressure distribution and forces and moments.

As true for any simulation technique that directly resolves turbulent eddies, and especially for applications aimed at complex geometries, grid design and construction is crucial to the overall success of the simulation. The reader is referred to Spalart (2001) for a guide on construction of DES grids. Grid adaption continues to evolve as a useful tool, the use of mesh adaption currently relies strongly on user guidance and therefore the need for expert users remains. Nevertheless, the developing experience base from DES applications considered to date make much more probable the success of multi-disciplinary efforts in areas such as aero-acoustics and fluid-structure interaction where accurate prediction of unsteady and three-dimensional turbulent eddies are required. Application of DES to these and other areas will further stress numerical treatments, requiring high fidelity from the underlying numerical schemes, among other factors.

For application of DES beyond regimes for which it was originally intended, e.g., to attached flows or flows exhibiting shallow separations, the influence of the “grey area” between the RANS and LES regions is more significant. An investigation relevant in this regard is that reported by Nikitin *et al.* (2000), in which DES was applied “as is”, i.e., without any adjustment to the model, to turbulent channel flow. One of the goals of the investigation was to assess the method outside the original design range of massively separated flows. The channel flows in Nikitin *et al.* (2000) possessed sufficient wall-parallel grid spacings to resolve turbulent fluctuations in the core of the channel, not near the walls. Logarithmic velocity profiles were established in the RANS and LES regions, but with a “buffer layer” between the two regions in the vicinity of the RANS-LES interface and under-predictions in the skin friction of $\mathcal{O}(15)$ percent. Recently, it has been shown that stochastic forcing added to the momentum equations, accounting for backscatter of energy from the mod-

eled to the resolved scales, can eliminate this mismatch (Piomelli *et al.* 2003). While the method outlined in Piomelli *et al.* (2003) is heuristic and introduced new parameters that are not preferable in routine applications, the findings are encouraging and motivate attempts at generalizing the approach.

Extension of DES to a wider range of flows will continue to motivate improvements in physical modeling and numerical aspects related to solution of the Navier-Stokes equations. Candidate flows include those exhibiting shallow separations and reattaching boundary layers, one motivating factor being the uneven performance of RANS models in predicting these flows. In these regimes, LES treatment within the boundary layer is attractive since it is possible to exploit the accuracy of the technique and grid-refinement possibilities inherent to the method – a proposition that is expensive, but will be useful and necessary for some applications.

Acknowledgments

This manuscript reflects substantial input and thoughtful comments over a range of DES research projects undertaken with Dr. Philippe Spalart, Dr. Jim Forsythe, and Dr. Scott Morton. The financial support of the Air Force Office of Scientific Research (Program Managers: Dr. Thomas Beutner and Dr. John Schmisser), Office of Naval Research (Program Managers: Dr. Patrick Purtell and Dr. Ronald Joslin) and NAVAIR (Program Manager: Dr. Shawn Woodson) is gratefully acknowledged.

References

- [1] Achenbach E.: *Experiments on the flow past spheres at very high Reynolds numbers*, J. Fluids Mech., **54**, pp. 565-575, (1972).
- [2] Constantinescu G., Pacheco R., Squires K.D.: *Detached-Eddy Simulation of flow over a sphere*, AIAA Paper 2002-0425, (2002).
- [3] Constantinescu G., Chapelet M., Squires K.D.: *On turbulence modeling applied to flow over a sphere*, AIAA Journal, **41**, pp. 1733-1742, (2003).
- [4] Forsythe, J.R., Woodson, S.H.: *Unsteady CFD calculations of abrupt wing stall using Detached-Eddy Simulation*, AIAA Paper 2003-0594 (accepted for publication in AIAA Journal of Aircraft), (2003).
- [5] Forsythe J.R., Squires K.D., Wurtzler K.E., Spalart P.R.: *Detached-eddy simulation of the F-15E at high alpha*, AIAA Journal of Aircraft, **40**, (2003).
- [6] Morton S.A., Steenman M.B., Cummings R.M., Forsythe J.R.: *DES grid resolution issues for vortical flows on a delta wing and an F-18C*, AIAA Paper 2003-1103, (2003).
- [7] Nikitin N.V., Nicoud F., Wasistho B., Squires K.D., Spalart P.R.: *An approach to wall modeling in Large-Eddy Simulations*, Phys. Fluids **12**, pp. 7-10, (2000).
- [8] Pauley, H., Ralston, J., Dickes, E.: *Experimental study of the effects of Reynolds number on high angle of attack aerodynamic characteristics of forebodies during rotary motion*, NASA CR 195033, (1995).

- [9] Piomelli, U., Balaras, E., Pasinato, H., Squires, K.D., Spalart, P.R.: *The inner-outer layer interface in Large-Eddy Simulations with wall-layer models*, Int. J. Heat and Fluid Flow, **24**, pp. 538-550, (2003).
- [10] Schuster, D., Byrd, J.: *Transonic unsteady aerodynamics of the F/A-18E at conditions promoting abrupt wing stall*, AIAA Paper 2003-0593, (2003).
- [11] Spalart P.R.: *Strategies for turbulence modelling and simulations*, Int. J. Heat Fluid Flow, **21**, pp. 252-263, (2000).
- [12] Spalart P.R.: *Young person's guide to Detached-Eddy Simulation grids*, NASA CR-2001-211032, (2001).
- [13] Spalart, P.R., Allmaras, S.R.: *A one-equation turbulence model for aerodynamic flows*, La Recherche Aerospatiale, **1** pp. 5-21, (1994).
- [14] Spalart P.R., Jou W.H., Strelets M., Allmaras S.R.: *Comments on the feasibility of LES for wings, and on a hybrid RANS/LES approach*, 1st AFOSR Int. Conf. on DNS/LES, Aug. 4-8, 1997, Ruston, LA. In: Advances in DNS/LES, C. Liu and Z. Liu Eds., Greyden Press, Columbus, OH, USA (1997).
- [15] Strelets M.: *Detached eddy simulation of massively separated flows*, AIAA-2001-0879, (2001).
- [16] Travin A., Shur M., Strelets M., Spalart P.R.: *Detached-Eddy Simulations past a Circular Cylinder*, Flow, Turb. Comb., **63**, pp. 293-313, (2000).
- [17] Viswanathan, A., Squires, K.D., Forsythe, J.R.: *Detached-Eddy Simulation around a fore-body at high angle of attack*, AIAA Paper 2003-0263, (2003).

DETACHED-EDDY SIMULATION OVER A REFERENCE AHMED CAR MODEL

S. Kapadia, S. Roy

*Computational Plasma Dynamics Laboratory, Department of Mechanical Engineering
Kettering University, Flint, Michigan 48504, USA*

kapa9202@kettering.edu, sroy@kettering.edu

M. Vallero

*United States Air Force Academy, Department of Aeronautical Engineering
Colorado Springs, CO 80840, USA*

K. Wurtzler and J. Forsythe

*Cobalt Solutions, LLC
Springfield, OH 45504, USA*

wurtzler@cobaltcfd.com, forsythe@cobaltcfd.com

Abstract This paper presents a Spalart-Allmaras based Detached-Eddy Simulation (DES) of the Ahmed reference car model with 25° and 35° slant angles using unstructured grids and the solver *Cobalt*. Comparisons are made to experimental laser doppler velocity measurements as well as total and surface pressure integrated drag. The Reynolds number based on body length was 2.78×10^6 , making the boundary layers approaching the slant fully turbulent. The flow over the base slant in the experiments is attached at 25° and separated at 35° . This causes a large drop in the drag with the increased slant angle as the vortices on the side of the slant are weakened due to the separation. These cases stress turbulence models due to the need to accurately predict the boundary layer separation over the slant as well as predict the pressures in the massively separated base region accurately. The DES results are compared to the experiments as well as the Spalart-Allmaras RANS model. DES is seen to predict separation at 25° slant angle, in contrast to the experiments. Drag is relatively close to the experiments, but the distribution of drag is more on the rear than on the slant due to the separation. At the 35° slant angle, DES is in good agreement to the experimental drag, with the correct distribution, while RANS over-predicts the drag.

Keywords: Turbulence simulation and modeling, hybrid methods, high Reynolds numbers, Automotive Aerodynamics

1. Introduction

Numerical simulation of the flow around complex configurations offers a powerful tool for analysis, e.g., a means to screen configurations prior to costly and time-consuming ground based tests. One example is automobile design in which Computational Fluid Dynamics (CFD) could be used to provide detailed information on performance (drag and downforce) as well as acoustics. Prediction of car aerodynamics has greatly challenged CFD because of the highly turbulent massively separated flow behind automobiles.

Most current engineering approaches, even to the prediction of unsteady flows, are based on solution of the Reynolds-averaged Navier-Stokes (RANS) equations. The turbulence models employed in RANS methods, at first sight, parameterize the entire spectrum of turbulent motions. While often adequate in steady flows with no regions of flow reversal, or possibly exhibiting shallow separations, it appears inevitable that RANS turbulence models will be unable to accurately predict the phenomena dominating flows characterized by massive separations.

To overcome the deficiencies of RANS models for predicting massively separated flows, Spalart *et al.* (1997) proposed Detached-Eddy Simulation (DES) with the objective of developing a numerically feasible and accurate approach combining the most favorable elements of RANS models and Large Eddy Simulation (LES). The primary advantage of DES is that it can be applied at high Reynolds numbers (as can Reynolds-averaged techniques) but also resolves geometry-dependent, unsteady three-dimensional turbulent motions as in LES. This paper presents a Spalart-Allmaras based DES calculation of the Ahmed reference car model with 25° and 35° base slant angle using unstructured grids and the commercial unstructured solver *Cobalt*. Comparisons are made to the experiments of Lienhart *et al.* (2003) who made detailed off body measurements using LDA. Also total drag, as well as integrated pressure drag by component (slant, rear, front) are compared against the experiments of Ahmed *et al.* (1984). The Reynolds number based on body length was 2.78×10^6 , making the boundary layers approaching the slant fully turbulent. The flow over the base slant in the experiments is attached at 25° and separated at 35°. This causes a large drop in the drag with the increased slant angle as the vortices on the side of the slant are weakened due to the separation.

2. Detached-Eddy Simulation

The base model employed in the majority of DES applications to date is the Spalart-Allmaras one-equation model (Spalart and Allmaras 1994, referred to as “S-A” throughout). The S-A model contains a destruction term for its eddy viscosity $\tilde{\nu}$ which is proportional to $(\tilde{\nu}/d)^2$, where d is the distance to the wall. When balanced with the production term, this term adjusts the eddy viscosity

to scale with the local deformation rate S and d : $\tilde{\nu} \propto Sd^2$. A subgrid-scale model within the S-A formulation can then be obtained by replacing d with a length scale Δ directly proportional to the grid spacing.

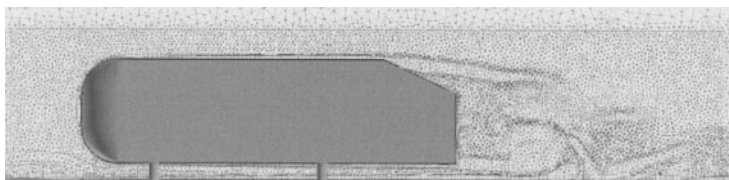
To obtain the model used in the DES formulation, the length scale of the S-A destruction term is modified to be the minimum of the distance to the closest wall and a lengthscale proportional to the local grid spacing, i.e., $\tilde{d} \equiv \min(d, C_{DES}\Delta)$. In RANS predictions of high Reynolds number flows the wall-parallel (streamwise and spanwise) spacings are typically the order of the boundary layer thickness and larger than the wall-normal spacing. Choosing the lengthscale Δ for DES based on the largest local grid spacing (i.e., one of the wall-parallel directions) then ensures that RANS treatment is retained within the boundary layer. Numerous applications have been performed using the current code [6] as well as a higher-order structured chimera code [7].

While a natural choice, and an aspect of nearly all hybrid methods, incorporating the grid spacing into the model can lead to inaccuracies as a DES grid is refined [5]. In boundary layers, as the grid spacing in the wall-parallel directions becomes smaller than about half of the boundary-layer thickness, the DES limiter reduces the eddy viscosity below its RANS level, though without allowing LES behavior. The resulting solution creates insufficient total Reynolds stresses, and can result in under-prediction of skin friction or early separation. Making the model more robust for these situations is currently being researched.

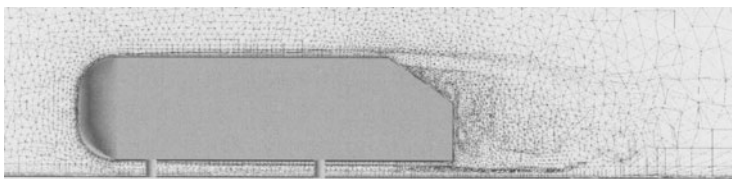
3. Calculation Details

The geometry used is depicted in [2] and shown in Figure 1. The body length (L) was 1044 mm. The grids for both slant angles were comprised of stretched prisms near the body, and tetrahedra elsewhere. The posts were included in both grids, although they were not included in the drag coefficient, just as in the experiments. The origin of the coordinate system was taken on the intersection of the symmetry and ground planes and level with the rear of the vehicle. The x-axis ran down the body, while the z-axis ran up. The posts were 50 mm tall, putting the bottom of the vehicle at $z=50\text{mm}$.

The 25° slant angle grid is pictured in Figure 1(a), and was created using the commercial program *Gridgen*. The grid contained 4.6×10^6 cells for the full geometry (both left and right sides), with clustering in a block surrounding the body. For the RANS calculation, a half body grid was used (2.3×10^6 cells), and symmetry assumed. The average y^+ for the first cell off the wall was < 0.3 , with a geometric stretching factor of 1.3. The 35° slant angle grid is pictured in Figure 1(b), and was created using *VGRIDns* [3]. The grid contained 3.1×10^6 cells for the full geometry (both left and right sides), with clustering in a block surrounding the body. The RANS calculations were also done on the full



(a) 25° slant angle



(b) 35° slant angle

Figure 1. Images of the grid in the symmetry plane, with countours of vorticity for an instantaneous DES solution.

geometry (i.e. symmetry was not assumed). The average y^+ for the first cell off the wall was < 0.3 , with a geometric stretching factor of 1.3. Also shown in Figure 1 are contours of vorticity for the DES calculations showing evidence of LES content.

Boundary conditions were chosen to mimic the 3/4 open wind tunnel [2]. That is, the ground plane and the vehicle were set to no-slip, while the remaining boundaries were set to a far-field boundary condition. The extent of the ground plane upstream was chosen to give the correct boundary layer thickness assuming an empirical boundary layer growth. The resulting boundary layer was slightly thicker than the experiments at $x = -1444\text{mm}$; at $y = 30\text{mm}$, the CFD velocity was 92% of freestream rather than 99%. The boundaries were about $\pm 6L$ upstream and downstream, $4L$ high, and $\pm 6L$ from the symmetry plane. The freestream velocity was set to 40 m/s, with $Re_L = 2.78 \times 10^6$.

RANS calculations were performed using a specified minimum global CFL of 1×10^6 , and marched to a steady solution. DES calculations used a timestep of $7.2 \times 10^{-5}\text{sec}$, resulting in a non-dimensional timestep of 0.01 when non-dimensionalised by body height and freestream velocity. Initial transient from the DES were removed (first 2700 iterations), and time averages taken over an additional 6500 iterations, based on examining the convergence of a running time average of drag.

4. Results

For the 25° slant angle, Figure 2 depicts velocity vectors and contours of streamwise velocity for the simulations compared to the experiments at $x=0\text{mm}$, at the back of the vehicles. The strong side vortices in the experiments are clearly seen. Figure 2(a) compares S-A RANS to the experiments. The computed vortices are weaker, potentially because of the turbulence model and/or grid resolution. Although not shown, the S-A RANS separated at the beginning of the slant, but reattached prior to the back of the vehicle, just as in the experiments. The boundary layer thickens more along the centerline for the experiments than the computations, however. This could be due to a weaker adverse pressure gradient in the computations due to lower pressures on the rear (see drag results in Table 1).

S-A DES results are next shown in Figure 2(b). The flow is seen to separate with a large region of reverse velocity and weak vortices at the rear of the vehicle. Since DES would be expected to give lower eddy viscosity it is unlikely that the vortex is weaker due to the model. Instead it is presumed that the model has weakened the boundary layer, allowing it to separate, in turn weakening the vortices. The experimental boundary layer profile is almost 100mm thick at the rear because it is on the verge of separating. This places the RANS/LES interface deep into the boundary layer for this case, which weakens the turbulence model, as previously discussed.

To examine this effect, a calculation was performed where RANS was maintained prior to the back of the vehicle (i.e. $\tilde{d} = d$ for $x < 0$), and DES after the back of the vehicle (S-A DES-MOD – see Figure 2(c)). Although the situation improved, with a more shallow separation, the problem was not completely fixed. The presence of separation is probably due to different pressure gradients between the RANS calculations and this calculation due to differences in pressure on the back end.

The resulting drag coefficients are shown in Table 1. The drag on the slant, rear, and front is pressure drag only, for both the experiments and computations. Although DES agrees most closely to the experiments for the total drag, it is likely due to compensating errors. The drag on the slant is under-predicted due to the separation. RANS gives a reasonable prediction for the slant drag, due to predicting attached flow, but over-predicts the drag on the rear. Overall, none of the simulations are very satisfying.

The 35° slant angle case is examined next in Figure 3 by looking at velocity vectors and contours on the symmetry plane, since the flow at this angle is fairly two-dimensional with respect to the span in the experiments and computations. Since there were no measurement close to the body, the contours should be ignored close to the body for the experimental plot (Figure 3(a)). For the RANS results (Figure 3(b)), the velocity profile on the slant just prior

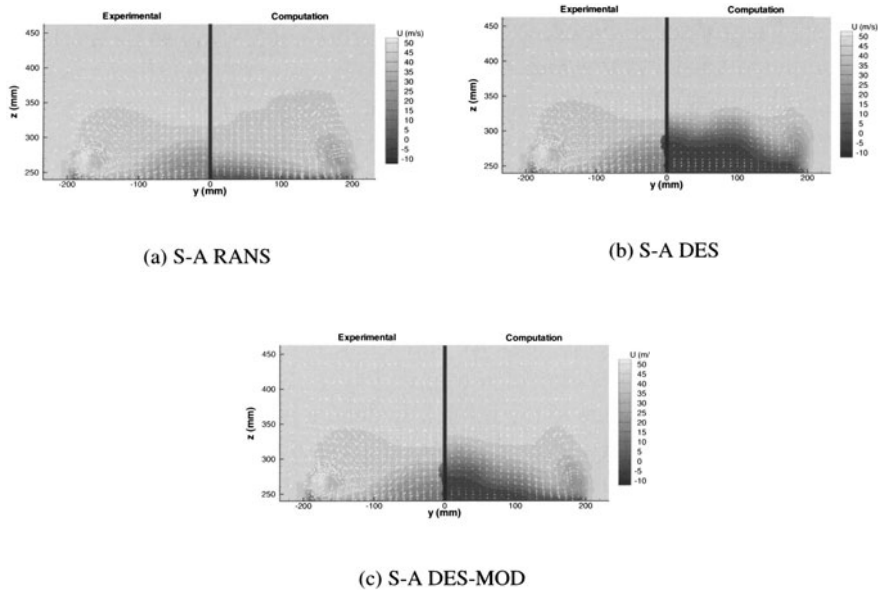


Figure 2. Time-averaged velocity vectors and streamwise velocity contours at $x=0\text{mm}$, experimental [2] vs. computed.

Model	Slant	Rear	Front	Viscous	Total
S-A DES	0.084	0.127	0.027	0.042	0.281
S-A DES-MOD	0.106	0.104	0.028	0.044	0.283
S-A RANS	0.137	0.127	0.029	0.045	0.338
Exp[1]	0.145	0.077	0.019	0.057	0.298

Table 1. Drag Coefficients on the Ahmed body with 25° slant angle

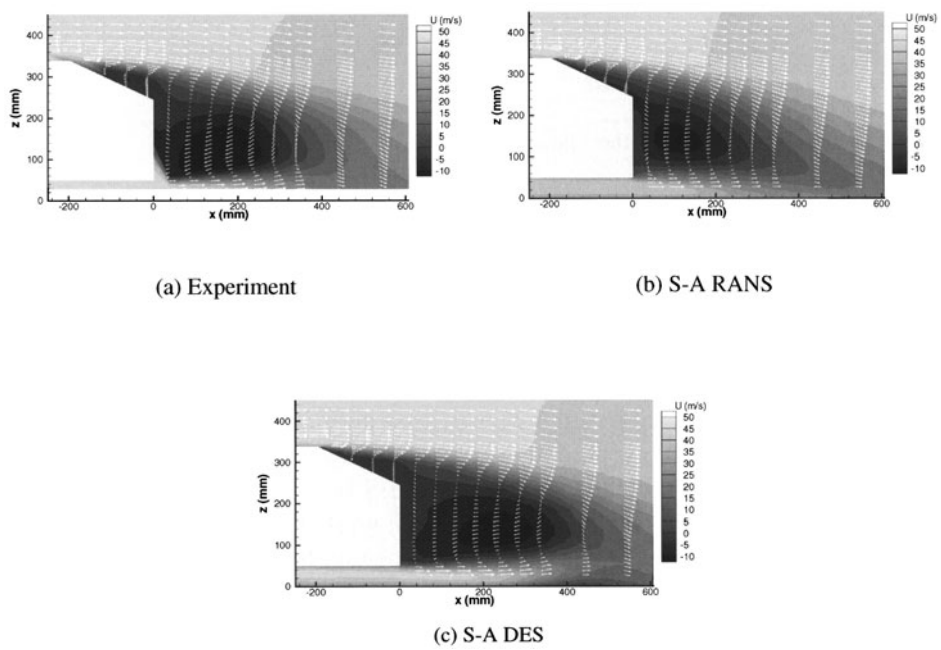


Figure 3. Time-averaged velocity vectors and streamwise velocity contours at $y=0\text{mm}$ (symmetry plane), experimental [2] vs. computed.

to the rear contains a peak velocity that is too high, and the zero velocity point is too close to the body. The shear layer is more straight from the slant to far downstream than in the experiments, where the shear layer curves down once behind the rear of the vehicle. Also, the separation bubble terminates too close to the body (at about $x=280\text{mm}$). The DES results agree more closely to the experiments, with a shear layer that curves down after the rear, a better matched velocity profile near the back end of the slant, and a more correct separation bubble size (although a little longer than the experiments).

The resulting drag coefficients are shown in Table 2. S-A RANS over-predicts the drag on both the slant and the rear. S-A DES provides an accurate prediction of the total drag, as well as its distribution. The good agreement to experiments in the wake suggests these accuracy is likely due to the ability to predict the wake accurately.

5. Summary

This paper presented a Spalart-Allmaras based Detached-Eddy Simulation of the Ahmed reference car model with 25° and 35° slant angles. These cases

Model	Slant	Rear	Front	Viscous	Total
S-A DES	0.087	0.095	0.029	0.041	0.252
S-A RANS	0.130	0.115	0.031	0.044	0.319
Exp[1]	0.097	0.090	0.015	0.055	0.257

Table 2. Drag Coefficients on the Ahmed body with 35° slant angle

stress turbulence models due to the need to accurately predict the boundary layer separation over the slant as well as predict the pressures in the massively separated base region accurately. Cases on the verge of separating (or mildly separated and reattached like the 25° case) continue to pose strong challenges to predictive methods. Small differences in separation prediction (and possibly reattachment) may lead to apparently substantial differences as observed in the present case at 25°. At the 35° slant angle, DES is in good agreement to the experimental drag, with the correct distribution, while RANS over-predicts the drag. DES also accurately predicted the wake behind the 35° slant angle.

Acknowledgments

The authors would like to gratefully acknowledge the help of Dr. Michael Strelets who shared his group's unpublished Ahmed DES results and Prof. Kyle Squires for reviewing this manuscript.

References

- [1] Ahmed, S.R., Ramm, G., and Faltin, G., "Some Salient Features of the Time-Averaged Ground Vehicle Wake," SAE 840300, 1984.
- [2] Lienhart, H. and Becker, S., "Flow and Turbulence in the wake of a simplified car model," SAE Technical Paper Series, 2003-01-0656. Reprinted from: Vehicle Aerodynamics 2003 (SP-1786), 2003 SAE World Congress, Detroit, Michigan, March 3-6, 2003.
- [3] Pirzadeh, S., 1996, "Three-dimensional Unstructured Viscous Grids by the Advancing Layers Method," *AIAA Journal*, **34**, pp. 43-49.
- [4] Spalart, P.R. and Allmaras, S.R., 1994, "A One-Equation Turbulence Model for Aerodynamic Flows," *La Recherche Aerospatiale* **1**, pp. 5-21.
- [5] Spalart P.R., Jou W.H., Strelets M., Allmaras S.R.: *Comments on the feasibility of LES for wings, and on a hybrid RANS/LES approach*, 1st AFOSR Int. Conf. on DNS/LES, Aug. 4-8, 1997, Ruston, LA. In: Advances in DNS/LES, C. Liu and Z. Liu Eds., Greyden Press, Columbus, OH, USA (1997).
- [6] Squires, K.D., Forsythe, J.R., Morton, S.A., Strang, W.Z., Wurtzler, K.E., Tomaro, R.F., Grismer, M.J. and Spalart, P.R., "Progress on Detached-Eddy Simulation of massively separated flows", *AIAA 02-1021*, January 2002.
- [7] Strelets M., *Detached eddy simulation of massively separated flows*, AIAA-2001-0879, 2001.

LARGE EDDY AND DETACHED EDDY SIMULATIONS FOR BROADBAND NOISE PREDICTION IN COMPLEX GEOMETRIES

Massimiliano Ciardi and William N. Dawes

University of Cambridge, Engineering Department, Cambridge, UK

Abstract This paper deals with the specific issues of implementing a Large Eddy Simulation (LES) module in an unstructured solver, tailored to broadband noise analysis in turbomachinery. Four Sub-Grid-Scale (SGS) models have been introduced, focusing attention on complex geometries and the peculiarities of the unstructured implementation. For these reasons a two-dimensional extension of the LES solver has been developed and implemented. It should allow an easier approach to a proper LES solution, especially when dealing with geometries of high complexity. The problem of limiting the commutative error when using an implicit filter and unstructured grids has also been addressed. An appropriate filter size function has been introduced and a specific test has been performed in order to tune the parameters of this function. Investigation of the interaction between numerical diffusion and subgrid scale terms has also been carried out.

Keywords: LES, DES, Hybrid RANS/LES, Explicit filtering

1. Introduction

Correlations based on theoretical and on experimental methods are the traditional approaches to predict broadband noise in turbomachinery. Because of the large number of factors that interact to produce broadband noise, so far, they have not given a clear explanation of the physical mechanisms of the sources. Computational Fluid Dynamics (CFD) seems to offer an advantage over classical methods, since it can provide an extensive description of the flow field without imposing restrictive assumptions. Unsteady Reynolds Averaged Navier-Stokes solvers (URANS) give a rough description of the unsteadiness of the flow, but are limited to the dominant low frequency modes. Therefore, they can be used quite successfully for tone noise analysis, but not for broadband noise analysis. On the other hand, Large Eddy and Detached Eddy Simulations (LES/DES) resolve a wider range of turbulent scales, but are still affordable in many realistic applications.

The two main aspects that characterize our LES/DES implementation are the

fact that we want to deal with complex geometries and the need to exploit the solutions to extract acoustic information.

The solver used is the Rolls-Royce code HYDRA (Moinier and Giles [1]). It is an unstructured hybrid code with an edge-based data structure. All the computational grids have been generated by the Newt mesh generation system (Dawes et al. [2]).

2. SGS Models

Four different SGS models have been implemented. Three of them are based on the original Smagorinsky model (Smagorinsky [3]). The three Smagorinsky-based models implemented (Hybrid1, Hybrid2 and Dynamic) try in different ways to compensate for the shortcomings of the original approach.

Hybrid1 This approach is based on a blend of the standard Smagorinsky SGS model with the Spalart-Allmaras one equation turbulence model (Spalart et al. [4]). The near wall treatment implemented is inspired by the hybrid LES-RANS approach. The two domains are connected through a region where eddy viscosity is determined by linear interpolation (Ciardi and Dawes [5]).

Detached Eddy Simulation (DES) The standard DES approach (Spalart et al. [6]) has been implemented. It uses a modified version of the Spalart-Allmaras one equation turbulence model.

Hybrid2 This model is based on a different way to blend RANS and LES. At each position in space, the eddy viscosity is evaluated twice, using LES (Smagorinsky) and RANS (Spalart-Allmaras turbulence model). The eddy viscosity used is then selected as the minimum of the two:

$$\nu_r = \min(\nu_r^{RANS(S.A.)}, \nu_r^{LES(Smagorinsky)}) \quad (1)$$

This choice should give the best compromise in all the different regions of the flow (Ciardi and Dawes [5]). This approach has been used previously for acoustic applications (Batten et al. [7]).

Dynamic Smagorinsky Model The original Dynamic Smagorinsky Model proposed by Germano [8] has been introduced. The explicit filter implemented follows the approach of the discrete interpolation filters proposed by Marsden et al. [9]. This approach can be tuned to achieve a specific order of accuracy for the commutative error, while retaining the possibility to use a variable filter size and unstructured grids. In this implementation, second order has been imposed to match the order of accuracy of the discretisation scheme in use.

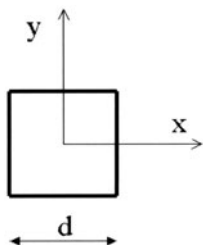


Figure 1 The square cylinder testcase.

3. ERCOFTAC Square Cylinder Testcase

Preliminary two-dimensional tests have been performed using the square cylinder (Figure 1) selected by Rodi and Ferziger as an international testcase and later included in the 1996 ERCOFTAC workshop as testcase LES2 (Voke [10]). The solutions have been performed with a Reynolds number of 21400, in agreement with the experiments of Lyn et al. [11]. The two-dimensional treatment presented in section 4 has been used for all the models involving the Smagorinsky expression of the SGS stress tensor (Hybrid1, Hybrid2 and Dynamic).

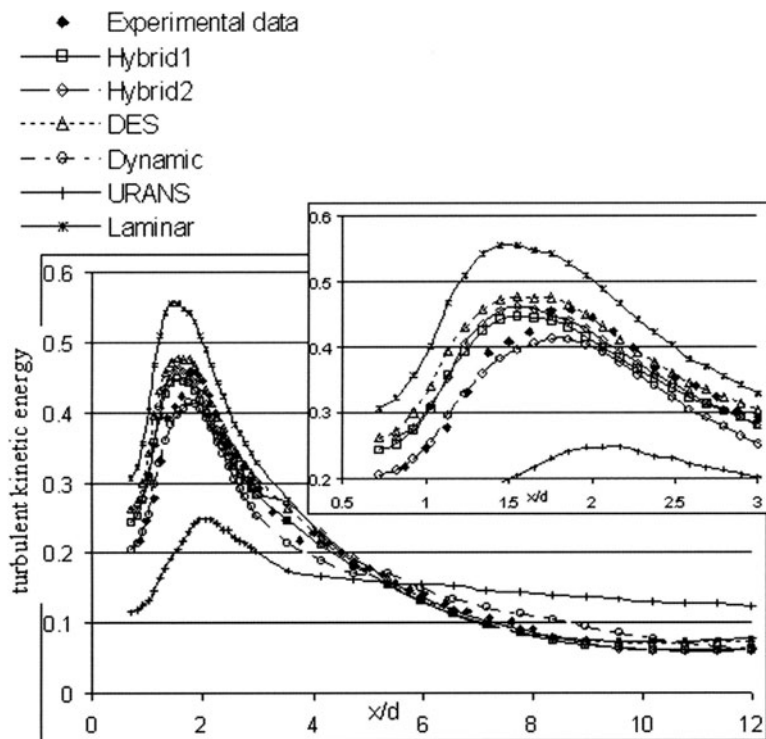


Figure 2. Square Cylinder Testcase. Turbulent kinetic energy profiles along the centreline.

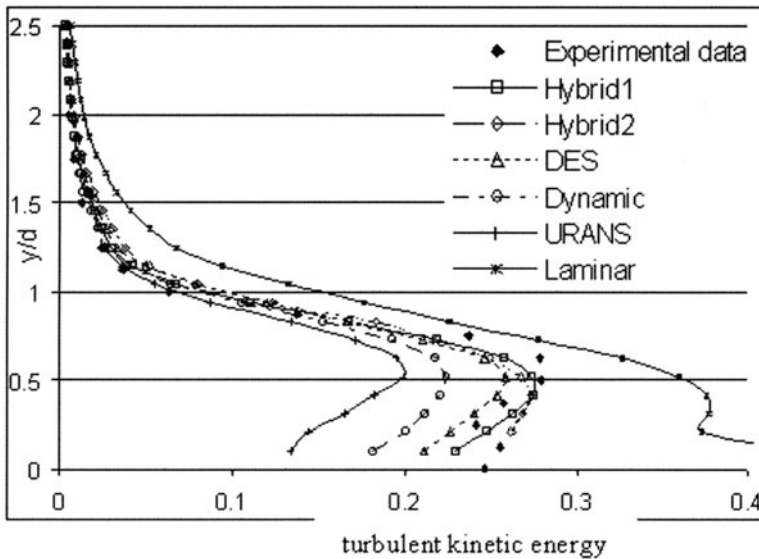


Figure 3. Square Cylinder Testcase. Turbulent kinetic energy profiles at $x/d = 1$.

Figure 2 shows turbulent kinetic energy profiles along the centreline. Figure 3 shows turbulent kinetic energy profiles at $x/d = 1$. Solutions have also been performed with Unsteady RANS (URANS) and without the SGS model (Laminar). URANS is obviously not capable of reproducing the turbulent fluctuations. In general Hybrid1, Hybrid2 and DES perform quite well with Hybrid2 being slightly better. Overall the agreement of the statistics with the experiments is satisfactory, in particular considering the limitations of the preliminary 2D approach. The Dynamic model offers the poorest results but this is probably a consequence of the 2D approach. In two dimensions, vorticity dynamics are such that backscatter becomes an extensive phenomenon. The Dynamic approach is trying to model backscatter locally whenever it occurs, but if it occurs extensively (as it does in 2D), for stability reasons, the value of the Smagorinsky coefficient is clipped. The model is consequently over-dissipative in 2D.

4. 2D Extension of the Smagorinsky Model

When dealing with complex geometries, it is convenient to be able to perform quick preliminary 2D solutions. On the other hand, vorticity dynamics are inherently 3D and cannot be captured by 2D solutions, therefore LES is inherently a 3D approach. From a numerical point of view, we can try to mimic the

3D terms that cannot be evaluated in 2D, using similarity with existing terms. In particular, whenever the Smagorinsky model is used, there are terms in the rate of strain tensor that are zero only because we are not representing the spanwise direction. If x_1 is taken along the freestream direction, and x_3 is the spanwise direction, not modelled in the 2D solution, we impose the following conditions for the rate of strain tensor, used by the Smagorinsky model:

$$\begin{aligned} \frac{\partial u_1}{\partial x_3} &\simeq \frac{\partial u_1}{\partial x_2} & \frac{\partial u_3}{\partial x_3} &\simeq \frac{\partial u_2}{\partial x_2} & \frac{\partial u_3}{\partial x_1} &\simeq \frac{\partial u_2}{\partial x_1} \\ \frac{\partial u_3}{\partial x_2} &\simeq \frac{1}{2} \left(\frac{\partial u_2}{\partial x_2} + \frac{\partial u_2}{\partial x_1} \right) & \frac{\partial u_2}{\partial x_3} &\simeq \frac{1}{2} \left(\frac{\partial u_2}{\partial x_2} + \frac{\partial u_2}{\partial x_1} \right) \end{aligned} \quad (2)$$

This approach should compensate for the order of magnitude of eddy viscosity. However it is imposing a non-physical correlation to terms that should be physically correlated, therefore it should only be used for preliminary solutions. Figure 4 shows how the correction is having the expected effect for the square cylinder testcase. The Hybrid1 SGS approach is used with and without the 2D treatment, comparing turbulent kinetic energy profiles along the centreline.

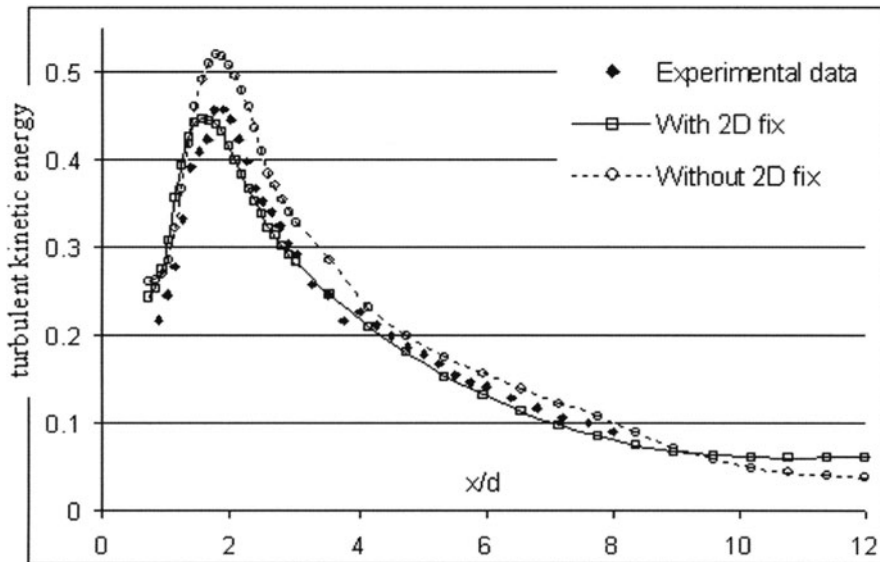


Figure 4. Test for the 2D treatment of the Smagorinsky approach, ERCOFTAC square cylinder testcase, Hybrid1 model. Turbulent kinetic energy profiles along the centreline.

5. The Filter-Size Function

The size of the filter is usually related to the size of the cells in the mesh. If the filter is too big, the quality of the mesh will not be fully exploited. If it is too small, some of the non-filtered components will not be resolved by the mesh and will corrupt the solution because of aliasing. The choice of the filter size is critical because it directly affects the accuracy of the solved equations. Since the equations are not averaged, but filtered, the filtering operation must commute with space and time differentiation for the equations to be correct. In general, to have a constant width for a filter is a sufficient condition to be commutative. However, if we keep the filter width constant throughout the domain we are forced to base it on the longest edge of all the elements, and we do not exploit the flexibility of the unstructured mesh.

In this implementation, the filter size is evaluated as a blend of a local dimension (proportional to the longest edge length connected to the node) and a global dimension (proportional to the longest edge length in the domain).

$$\Delta = C_{filt1} ((1 - C_{filt2}) \Delta_M + C_{filt2} \Delta_{MEL}) \quad (3)$$

Where Δ_M is the local edge length, Δ_{MEL} is the maximum edge length in the mesh, C_{filt1} and C_{filt2} are user defined coefficients.

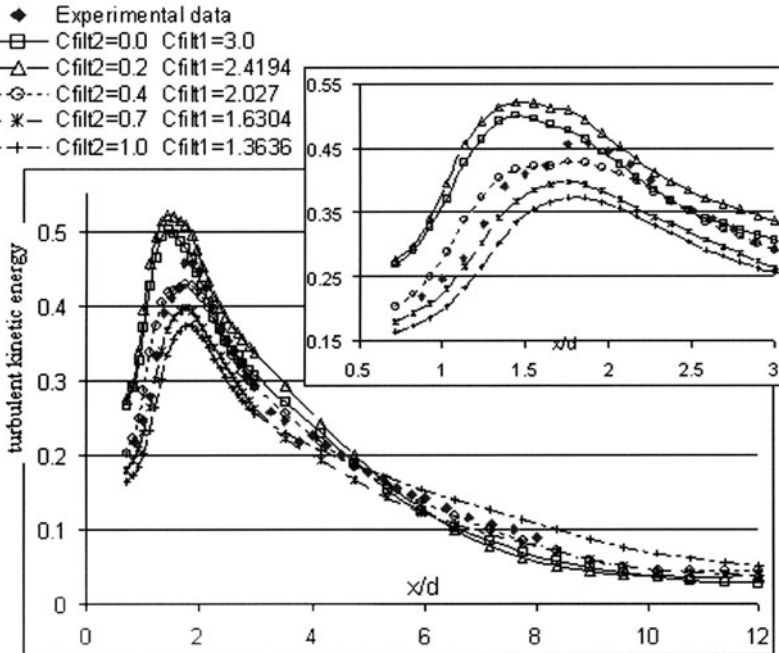


Figure 5. Test for the Filter-size function, ERCOFTAC square cylinder testcase, Hybrid2 model. Turbulent kinetic energy profiles along the centreline.

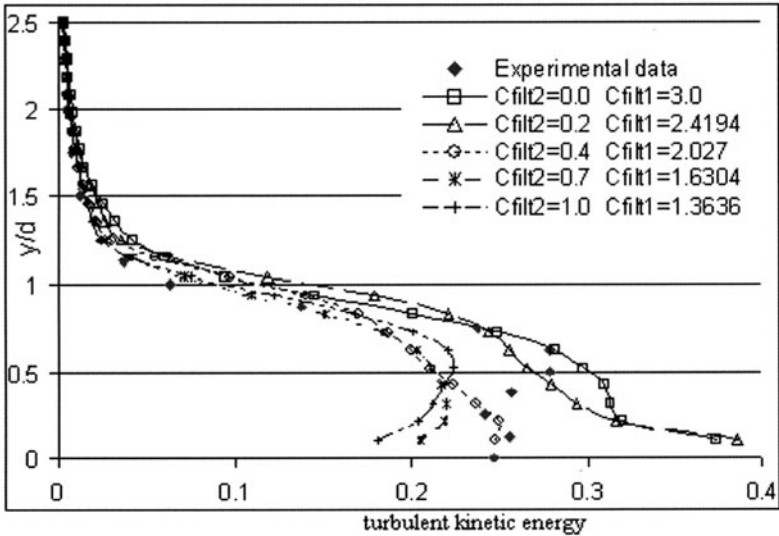


Figure 6. Test for the Filter-size function, ERCOFTAC square cylinder testcase, Hybrid2 model. Turbulent kinetic energy profiles at $x/d = 1$.

A test has been performed using the square cylinder testcase and the Hybrid2 version of the solver. Different values of C_{filt2} are used, while keeping the same value of the filter size in the main domain (three times the local edge length). This is achieved by changing accordingly the value of C_{filt1} . Figure 5 shows turbulent kinetic energy profiles along the centreline, Figure 6 at $x/d = 1$. The effect of the filter-size function is quite strong and cannot be uniquely attributed to commutative errors. The optimal value of C_{filt2} seems to be between 0.2 and 0.4. Lower values correspond to a highly variable filter size in the domain. This has two main consequences. First of all it implies an increased amount of commutative error. Secondly, in the near wall region, it forces the filter to have a smaller size. As a consequence, smaller structures are resolved by the solver. Downstream these structures are corrupted by aliasing, when they are convected into regions where the mesh is coarser. This is particularly evident in Figure 6, where, close to the cylinder, fluctuations are obviously overpredicted, when a small value of C_{filt2} is used. Higher values of C_{filt2} show the limitation of a coarse filter size in the near-wall region. Important energetic structures in the flow are not resolved. As a consequence turbulent kinetic energy is in these cases generally underpredicted.

6. SGS Models and Numerical Viscosity

The square cylinder test case is used to assess the effect of the interaction between numerical diffusion and SGS terms. The aim of the analysis is to plot energy spectra and to detect if they include an inertial range. Indeed, numerical viscosity can have a significant value, as long as it does not push the cut-off wavenumber outside the inertial range. 2D solutions with the Hybrid1 model are considered, with two levels of mesh refinement and two ratios of average filter-size/mesh-size for the finer grid. Energy spectra are then evaluated along the centreline, two edge lengths downstream of the cylinder centre. The coarse mesh is an unstructured triangular mesh with 14900 nodes and has the same average spacing of the structured grids used by the participants of the ERCOFTAC Workshop (Voke [10]). The fine mesh is an unstructured triangular mesh with 68700 nodes and has an average edge length that is half of the average edge length in the coarse mesh.

The different solutions are identified as: Hybrid1-A, Hybrid1-B, Hybrid1-C.

Hybrid1-A Coarse mesh, average ratio filter-size/mesh-size of 2.

Hybrid1-B Fine mesh, average ratio filter-size/mesh-size of 4.

Hybrid1-C Fine mesh, average ratio filter-size/mesh-size of 2.

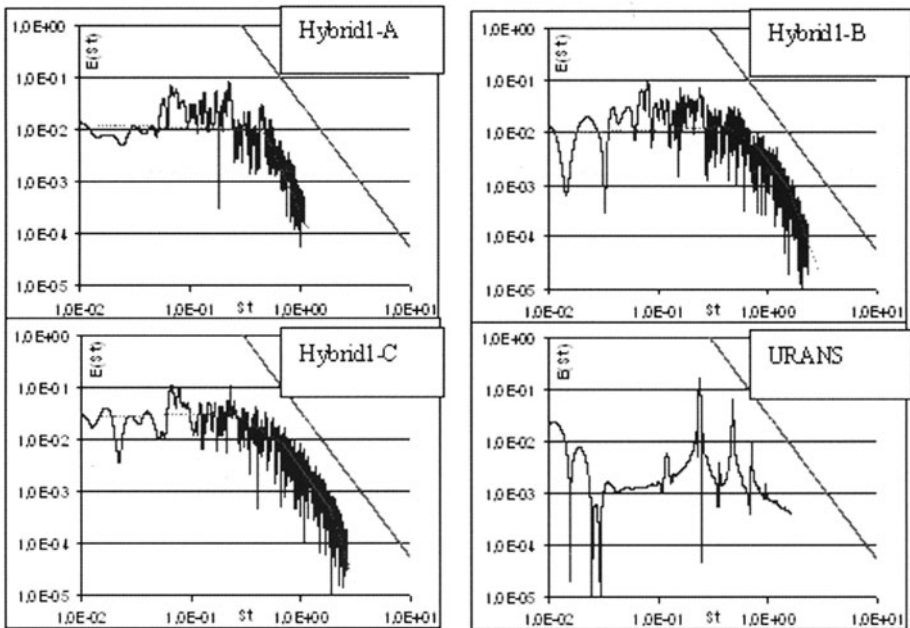


Figure 7. ERCOFTAC square cylinder testcase. Energy spectra two edge lengths downstream of the cylinder centre. Solid lines show the trend in the inertial range.

Hybrid1-A and Hybrid1-B have the same filter size throughout the domain. The energy spectra are presented in Figure 7. With the coarse mesh, the energy cascade does not include an inertial range, showing the increased numerical dissipation of the specific unstructured implementation. When a finer mesh is used, an inertial range appears in the energy spectrum and it becomes wider if the filter size is reduced. The energy spectrum of the URANS solution is completely different, since URANS do not give a complete description on any continuous range of wavenumbers in the spectra.

Comparing Hybrid1-A and Hybrid1-B (which have the same filter size) we find that, with the coarser mesh, the numerical dissipation is larger than the SGS eddy viscosity, and stops the energy cascade before the inertial range. Considering Hybrid1-B and Hybrid1-C (which have the same fine mesh but different filter sizes), we find that a smaller filter size improves the quality of the solution, because it better exploits the potential of the mesh in terms of resolution. Consequently, we can conclude that even within the framework of our unstructured implementation, it is still possible to apply correctly an LES technique, as long as we are able to sufficiently refine the mesh.

7. Conclusions

Four different SGS modelling approaches have been examined, including different approaches to blend LES and RANS, and a dynamic model together with a second order commutative filter. They have been tailored to complex geometries and, consequently, to unstructured grids. Preliminary tests have been performed on a 2D test case, giving promising results in terms of turbulent statistics. A 2D extension of the LES solver has also been produced, giving a significant improvement over the original approach, when preliminary 2D solutions are carried out. An analysis on the effect of the filter-size function has been performed, showing the extreme importance of this aspect for the unstructured implementation. An analysis on the interaction between numerical dissipation and SGS terms has also been carried out. It shows that within the framework of our unstructured implementation, it is still possible to apply an LES technique, as long as we are able to sufficiently refine the mesh.

Acknowledgments

This project is funded by Rolls-Royce plc and the DTI via the DTI/CARAD programme (technical monitor Leigh Lapworth). The authors are grateful for cooperation and discussions with John Coupland (Rolls-Royce plc).

References

- [1] Moinier, P. and Giles, M. B. (1998). *Preconditioned Euler and Navier-Stokes calculations on unstructured grids*. 6th ICFD Conference on numerical methods for fluid dynamics,

Oxford, UK.

- [2] Dawes, W.N. and Dhanasekaran, P.C. and Demargne, A.A.J. and Kellar, W.P. and Savill, A.M. (2001). *Reducing bottlenecks in the CAD-to-mesh-to-solution cycle time to allow CFD to participate in design*. ASME Journal of Turbomachinery.
- [3] Smagorinsky, J. (1963). *General circulation experiments with the primitive equations: I. The basic equations*. Mon. Weather Rev. 91, 99-164.
- [4] Spalart, P.R. and Allmaras, S.R. (1994). *A one-equation turbulence model for aerodynamic flows*. Rech. Aerosp. 1:5-21.
- [5] Ciardi, M. and Dawes, W.N. (2003). *Development of a Large Eddy and Detached Eddy Simulation capability for broadband noise prediction on unstructured meshes*. AIAA Paper 2003-3734, 33rd AIAA Fluid Dynamics Conference.
- [6] Spalart, P.R. and Jou, W.H. and Strelets, M. and Allmaras, S.R. (1997). *Comments on the feasibility of LES for wings and on a hybrid RANS/LES approach*. Advances in DNS/LES, ed. C Liu, Z Liu, pp 137-48. Columbus, OH: Greyden.
- [7] Batten, P. and Goldberg, U.C. and Chakravarthy S.R. (2000). *Sub-grid turbulence modeling for unsteady flow with acoustic resonance*. AIAA Paper 2000-0473, 38th Aerospace Sciences Meeting, Reno, NV.
- [8] Germano, M. (1992). *Turbulence: the filtering approach*. J. Fluid Mech. 238:325-36.
- [9] Marsden, A.L. and Vasilyev, O.V. and Moin, P. (2000). *Construction of commutative filters for LES on unstructured meshes*. Annu. Res. Briefs-2000, pp. 179-192. Center Turbul. Res., Stanford Univ., Calif.
- [10] Voke, P.R. (1997). *Flow past a square cylinder: Test Case LES2. Direct and Large-Eddy Simulation II*. Ed Chollet et al. 355-373. Kluwer Academic, Dordrecht.
- [11] Lyn, D.A. and Einav, S. and Rodi, W. and Park, J.H. (1995). *A laser doppler velocimetry study of ensemble-averaged characteristics of turbulent near wake of a square cylinder*. J. Fluid Mech. 304, 285.

4.2 EFFECTS OF WALL PERMEABILITY, ROUGHNESS AND PRESSURE-GRADIENT

TURBULENT CHANNEL FLOW OVER A PERMEABLE WALL

Wim-Paul Breugem & Bendiks-Jan Boersma

Laboratory for Aero and Hydrodynamics

Delft University of Technology

Mekelweg 2, 2628 CD, The Netherlands

email: w.p.breugem@wbmt.tudelft.nl

Abstract The influence of wall permeability upon a turbulent channel flow is studied numerically. Similar to a Large Eddy Simulation we pursue an approach in which we describe the large-scale flow behavior in the porous medium. A closure is adopted for the drag, whereas dispersion is currently neglected. The results show that wall permeability increases the friction factor and enhances turbulent mixing.

Keywords: Wall permeability, Turbulence, Volume-Averaging Method

1. Introduction

The study of flow over porous media covers a wide range of research areas, especially in geophysics. Examples of this are the study of the atmospheric boundary layer over plant canopies like forests (Finnigan, 2000), or over porous river beds. Within a wider context this problem falls in the class of turbulence modification due to wall effects. The aim of our research is to study the change in the structure and dynamics of turbulent flow over a permeable wall with respect to an impermeable wall.

There are a few recent publications in which wall permeability is modeled via special boundary conditions. Jiménez et al. (2001) take the wall-normal velocity proportional to the wall-pressure fluctuation, and a no-slip condition is imposed for the horizontal velocities. Opposite to this, Hahn et al. (2002) impose a zero wall-normal velocity, but allow for a slip velocity in the horizontal directions. In the present study we pursue a different approach in which we directly solve the governing equations for the volume-averaged flow in the porous medium.

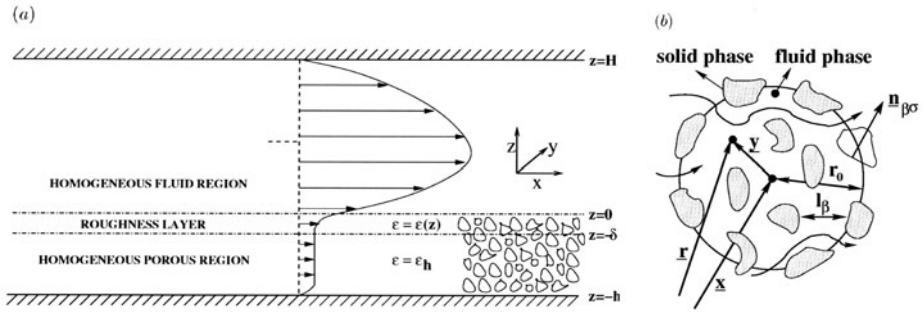


Figure 1. (a) Sketch of the flow geometry (not on scale). (b) Illustration of the method of volume averaging for a disordered porous medium.

2. Flow geometry, governing equations and numerical procedure

The flow geometry is sketched in figure 1.a. Following Ochoa-Tapia & Whitaker (1995), we distinguish between three regions. The channel or the homogeneous fluid region is located between $z = 0$ and $z = H$. The roughness layer between $z = -\delta$ and $z = 0$ is characterized by rapid changes in the porosity. The third region is the homogeneous porous region between $z = -h$ and $z = -\delta$ with a constant porosity ($\epsilon = \epsilon_h$). The walls at $z = H$ and $z = -h$ are impermeable.

We follow an approach in which only the large-scale flow behavior in the porous medium is described. This is defined mathematically as a weighted average over a small volume (Quintard & Whitaker, 1994):

$$\langle \underline{u} \rangle |_{\underline{x}} = \frac{1}{\epsilon} \int_V \gamma(\underline{r}) m(\underline{r} - \underline{x}) \underline{u}(\underline{r}) dV \quad (1)$$

where the brackets denote the intrinsic volume average, V is the total averaging volume, and $\epsilon = V_f/V$ the porosity with V_f the volume of the fluid phase inside the averaging volume V . The indicator function γ equals 1 when \underline{r} points in the fluid phase (β -phase) and 0 when \underline{r} points in the solid phase (σ -phase). It is important to realize that the spatially filtered flow is defined both in the β - and the σ -phase, and that it is an infinitely differentiable function in space provided that $m \in C^\infty$. Quintard & Whitaker (1994) analyzed which weight functions are appropriate for flow in a porous medium. For flow in a disordered porous medium a popular one is the top hat distribution: $m = 3/(4\pi r_0^3)$ for $r \leq r_0$ and $m = 0$ for $r > r_0$, where r_0 is the radius of the spherical volume over which the averaging takes place and which is sketched in figure 1.b. The choice of r_0 is constrained by the requirements that $l_\beta \ll r_0 \ll L$ and $r_0^2 \ll L_\epsilon L$. l_β , L and L_ϵ are typical length scales of respectively the pores, the volume-averaged flow field, and of variations in the porosity.

Quintard & Whitaker (1994) applied the spatial filtering (1) to the Stokes equations. It is straightforward to include also the inertial terms. The Volume-Averaged Navier-Stokes (VANS) equations for incompressible, Newtonian flow read

$$\begin{aligned}
 \frac{\partial \langle \underline{u} \rangle}{\partial t} &+ \langle \underline{u} \rangle \cdot \nabla \langle \underline{u} \rangle + \frac{1}{\epsilon} \nabla \epsilon \langle \widetilde{\underline{u} \underline{u}} \rangle = -\frac{1}{\rho} \nabla \langle p \rangle \\
 &+ \nu \nabla^2 \langle \underline{u} \rangle + \nu \frac{\nabla \epsilon}{\epsilon} \nabla \langle \underline{u} \rangle + \nu \frac{\nabla^2 \epsilon}{\epsilon} \langle \underline{u} \rangle \\
 &+ \frac{1}{\epsilon} \int_{A_{\beta\sigma}} m \left[\underline{n}_{\beta\sigma} \left(-\underline{\underline{I}} \frac{\tilde{p}}{\rho} + \nu \nabla \tilde{\underline{u}} \right) \right] dA \\
 \nabla \cdot \epsilon \langle \underline{u} \rangle &= 0
 \end{aligned} \tag{2}$$

In the above equations $A_{\beta\sigma}$ is the interface area between the β - and the σ -phase, $\underline{n}_{\beta\sigma}$ the normal vector at $A_{\beta\sigma}$ pointing from the β - into the σ -phase, and $\underline{\underline{I}}$ the unity tensor. The velocity $\tilde{\underline{u}}(\underline{x})$ is the spatial deviation of the velocity \underline{u} from the volume-averaged velocity $\langle \underline{u} \rangle$, i.e.: $\tilde{\underline{u}}(\underline{x}) = \underline{u}(\underline{x}) - \gamma \langle \underline{u} \rangle|_{\underline{x}}$. The basic assumption in the derivation of the VANS equations is that the volume-averaged flow field contains negligible small-scale variations: $\int_V m(\underline{r} - \underline{x}) \langle \underline{u} \rangle|_{\underline{r}} dV \approx \langle \underline{u} \rangle|_{\underline{x}}$. This assumption imposes the earlier mentioned constraints on the filter width.

The VANS equations are similar to the filtered Navier-Stokes equations used in a Large Eddy Simulation (LES). The third term at the left-hand-side of equation (2) is the dispersion term and represents the effect of stresses on pore scale on the large-scale flow field. The last term at the right-hand-side of equation (2) represents the drag force per unit mass that the flow field encounters as at the interface area $A_{\beta\sigma}$ the flow must obey the no-slip condition. The dispersion and drag terms are responsible for a transfer of kinetic energy from the large-scale to the small-scale flow field. In order to solve the VANS equations we need closures of these terms expressed in the volume-averaged flow field. The thickness δ of the roughness layer depends on the structure of the porous medium and, related to this, the choice of the filter. As we consider flow over a homogeneous porous medium, δ is of the order of the filter width. For the porosity we adopt a fifth-order polynomial in the wall-normal coordinate z . The coefficients are determined from the requirements that the porosity and its first and second order derivatives must be continuous at $z = -h$ and $z = 0$:

$$\begin{aligned}
 -\delta \leq z \leq 0 : \quad \epsilon(z) &= -6(\epsilon_h - 1) \left(\frac{z}{\delta} \right)^5 - 15(\epsilon_h - 1) \left(\frac{z}{\delta} \right)^4 \\
 &\quad - 10(\epsilon_h - 1) \left(\frac{z}{\delta} \right)^3 + 1
 \end{aligned} \tag{4}$$

In the literature it is customary to replace the surface integral in (2) by:

$$\frac{1}{\epsilon} \int_{A_{\beta\sigma}} m \left[\underline{n}_{\beta\sigma} \left(-\underline{I} \frac{\tilde{p}}{\rho} + \nu \nabla \tilde{\underline{u}} \right) \right] dA = -\nu \underline{K}^{-1} (\underline{I} + \underline{F}) \cdot \epsilon \langle \underline{u} \rangle \quad (5)$$

where \underline{K} and \underline{F} are referred to as respectively the permeability and the Forchheimer tensor. A popular semi-empirical relation for the two tensors is the Ergun–equation (MacDonald et al., 1979) for flow through packed beds. It assumes that the two tensors are isotropic and it relates them to the porosity and the mean particle diameter:

$$F = \frac{1}{100(1 - \epsilon)} \frac{d_p \|\epsilon \langle \underline{u} \rangle\|}{\nu} \quad (6)$$

$$K = \frac{d_p^2 \epsilon^3}{180(1 - \epsilon)^2} \quad (7)$$

The mean particle diameter d_p is defined as six times the ratio of the total volume V_p to the total surface area A_p of the σ -phase: $d_p = 6V_p/A_p$.

In the literature for flow in porous media the dispersion term is normally neglected. Based on an order-of-magnitude analysis we consider this term of minor importance as compared to the drag term, and therefore we also neglect this term in the present study. For clarity, from now on we will omit the brackets that denote the volume average.

The VANS equations are discretized in space with a pseudo-spectral method for the horizontal direction and with a second-order finite-volume method for the wall-normal direction. The grid is non-uniform in the wall-normal direction with grid points clustered around $z = 0$ and $z = H$. The equations are advanced in time with a semi-implicit pressure-correction method. The VANS equations are integrated in time with the explicit, second-order Adams-Bashfort scheme, except the terms $\nu \nabla^2 \epsilon \langle \underline{u} \rangle / \epsilon$ and $-\nu K^{-1} \epsilon \langle \underline{u} \rangle$. For numerical stability reasons, they are integrated with the implicit, second-order Crank-Nicholson scheme.

3. Turbulence statistics

We show results from four simulations, in which we only varied the porosity ϵ_h in the homogeneous porous region. We will refer to them as E95, E80, E60, and I with ϵ_h equal to respectively 0.95, 0.8, 0.6 and 0 (impermeable wall case). The mean particle diameter is $d_p/H = 0.01$. The thickness of the roughness layer equals $\delta/H = 0.02$, which is actually an appropriate value for an ordered rather than for a disordered porous medium. The dimensions of the domain are $L_x/H = 5$ and $L_y/H = 3$ in respectively the streamwise and the spanwise direction. The height of the porous medium is always $h/H = 1$, except in case I, where no-slip conditions were used at $z = 0$. The grid resolution in the channel equals 256x192x192 for respectively the streamwise, spanwise

case	Da	Re_τ^t	dx^{t+}	dy^{t+}	dz_c^{t+}	dz_p^{t+}	$\lambda(\cdot 10^{-3})$	Re_K
E95	$1.9 \cdot 10^{-4}$	407	7.9	6.4	0.5 – 5.3	0.5 – 8.5	20.6	36.9
E80	$7.1 \cdot 10^{-6}$	354	6.9	5.5	0.4 – 4.6	0.4 – 7.4	9.4	3.4
E60	$7.5 \cdot 10^{-7}$	350	6.8	5.5	0.4 – 4.6	0.4 – 7.3	8.1	0.8
I	∞	350	6.8	5.5	0.4 – 4.6	–	8.1	0

Table 1. Characteristics of the simulations. dx^{t+} and dy^{t+} are the grid spacings in respectively the streamwise and the spanwise direction, made dimensionless with ν/u_τ^t . dz_c^{t+} and dz_p^{t+} are the dimensionless grid spacings in the wall-normal direction in respectively the channel and the porous medium.

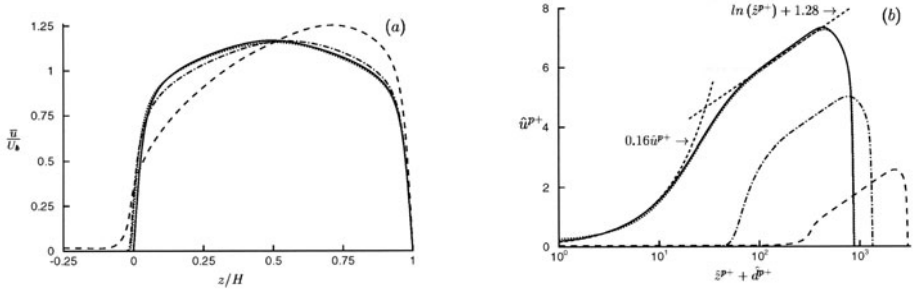


Figure 2. Mean-velocity profiles; (a) Dimensionalized by the bulk velocity U_b , as function of the non-dimensional wall-normal position z/H . For clarity, the region $z/H < -0.25$ is omitted. (b) Normalized with \hat{u}^p , as function of the non-dimensional shifted wall-normal position $z^{p+} + d^{p+}$. The two dashed line pieces are the standard fits for the impermeable wall case, with $\kappa = 0.4$ and $d = 0$. —, case I; ···, case E60; - · -, case E80; ---, case E95.

and wall-normal direction. The grid resolution in the porous region amounts $256 \times 192 \times 128$. In all cases the bulk Reynolds number is fixed at $Re_b = 5500$. Table 1 gives for each simulation the Reynolds number based on the friction velocity u_τ^t at the top wall, $Re_\tau^t = u_\tau^t H / \nu$, with $u_\tau^t = \sqrt{\nu \partial u / \partial z|_H}$. Also listed in the table are the Darcy number $Da = K/H^2$, the grid spacings, the computational time step, and the friction factor $\lambda = -H (\partial \bar{p} / \partial x) / (\rho U_b^2)$. The turbulence statistics of case I are in good agreement with the results obtained by Kim et al. (1987).

In figure 2.a mean velocity profiles are shown for different values of the wall porosity. The higher the wall porosity, the more skewed the profiles are with their maximum moving towards the top wall. This is already an indication that increasing wall porosity increases the flow resistance, and this is also clear from the higher value of the friction factor λ in table 1. The profiles become flatter in the porous wall region, and the velocity at the interface ($z = 0$) increases for higher wall porosity. The mean velocity profiles are utilized to obtain a characteristic velocity scale u_τ for the porous wall region. It is customary to adopt the following velocity profile for the logarithmic layer:

$$\bar{u} = \frac{u_\tau}{\kappa} \ln \left(\frac{z + d}{z_0} \right) \quad (8)$$

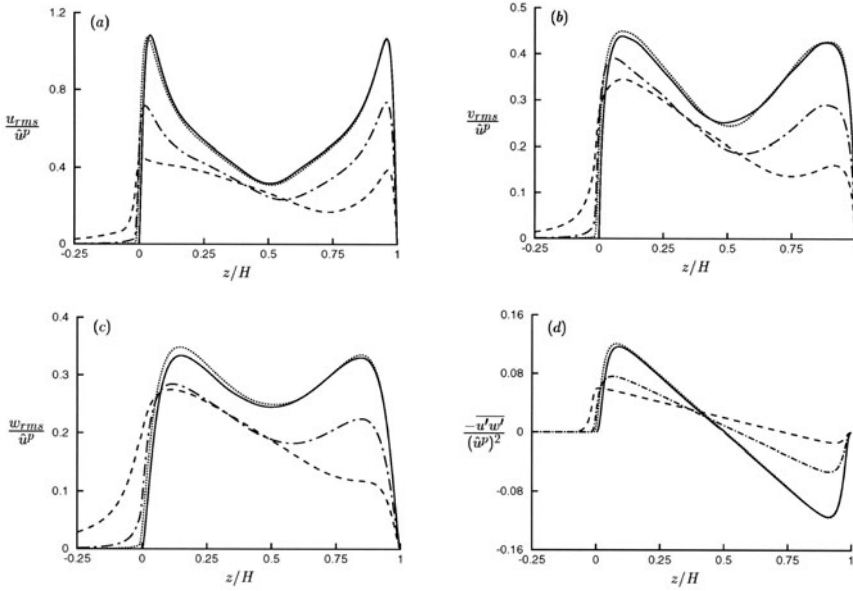


Figure 3. Reynolds-stress profiles. For clarity, the region $z/H < -0.25$ is omitted. (a) $\sqrt{u'^2}/\hat{u}^p$; (b) $\sqrt{v'^2}/\hat{u}^p$; (c) $\sqrt{w'^2}/\hat{u}^p$; (d) $-\overline{u'w'}/(\hat{u}^p)^2$. —, case I; ···, case E60; - - -, case E80; ---, case E95.

in which κ is the Von Kármán constant, d the displacement height and z_0 the equivalent roughness height. In general, both d/H and z_0 will depend on the Reynolds number $u_\tau H/\nu$ and on the geometry of the wall. For both smooth and rough walls, the Von Kármán constant is often taken equal to 0.4. For porous walls however, it can not be excluded that κ depends on the geometrical properties of the wall such as the porosity and mean particle diameter. To circumvent the problem of choosing a value for κ , we define a new velocity scale $\hat{u} = u_\tau/\kappa$. We refer to this velocity as the modified friction velocity. The least-square method is used to calculate the modified friction velocity from the fit of the logarithmic law (8) to the mean velocity profile, see figure 2.b. The modified friction velocity is used to define the permeability Reynolds number $Re_K = \hat{u}^p \sqrt{K}/\nu$ and the roughness Reynolds number $Re_d = \hat{u}^p d_p/\nu$, where the superscript p refers to the porous wall region. The first Reynolds number basically shows that the ratio between the typical length scale \sqrt{K} of the pores and of the near-wall turbulence ν/\hat{u}^p . When this ratio is small, the wall-blocking effect prevails and eddies can not travel freely into the wall. Note that for large enough $\hat{u}^p H/\nu$ the smallest eddies will always be able to permeate the wall. This implies a fundamental Reynolds number dependency for flow over a permeable wall and this hampers the scaling of the turbulence quantities. In case E60 and E95 the permeability Reynolds number is respectively 0.8 and 36.9, see table 1, and this explains why in case E60 the wall

behaves as almost hydraulically impermeable, whereas in case E95 the flow is strongly affected. The roughness Reynolds number indicates the effect of surface roughness, with the roughness height l_r of the order of d_p . Hinze (1975) defines the condition of a fully rough wall, when no viscous sublayer can be distinguished, as: $u_\tau l_r / \nu > 55$. Taking $\kappa = 0.4$ for a rough wall, this is equivalent with $\hat{u} l_r / \nu > 138$. Although this criterion is based on experiments with rough but impermeable walls, it gives some clues about the importance of roughness in our simulations. In case E60 and E95 the roughness Reynolds number is equal to respectively 8.9 and 26.7. Thus, we consider roughness effects to be of minor importance as compared to the effect of permeability. In figure 3 profiles of the Reynolds stresses are presented. The profiles of case E60 and case I almost collapse with each other. The Reynolds-stress profiles in cases E80 and E95 have a smaller magnitude in the porous wall region with respect to case I, except close to the porous wall. However, when the profiles are normalized with the bulk velocity U_b , the Reynolds stresses in cases E80 and E95 have a larger magnitude as compared to case I, except the profile of u_{rms} in case E80. This is also clear from our observation that in cases E80 and E95 the Reynolds-stress profiles have a larger peak in the porous wall region than in the top wall region, except again the profile of u_{rms} in case E80, which has a similar peak value in the top wall region. Figure 3.d shows that wall porosity enhances turbulent mixing as in case E95 the Reynolds-shear stress is much larger in the region near the porous wall than in the region near the top wall. Down in the porous wall the Reynolds-shear stress decreases more rapidly than the normal Reynolds stresses. It can be shown that the velocity fluctuations far down in the porous wall are induced by large-scale pressure fluctuations in the porous wall region, and that the streamwise and wall-normal velocity component are $\pi/2$ out of phase and consequently do not contribute to the Reynolds-shear stress.

4. Summary and discussion

In this paper we presented a flavor of our numerical results for turbulent channel flow with a permeable lower wall. The results show that wall permeability has a pronounced effect on the turbulent channel flow when the permeability Reynolds number Re_K is significantly larger than 1. There exists a fundamental Reynolds number dependency for flow over a porous wall, which hampers the scaling of turbulence quantities. A new velocity scale is proposed for the turbulence in the porous wall region. The so-called modified friction velocity incorporates also the Von Kármán constant. The mean velocity profiles suggest that in our simulations wall roughness is of minor importance. Wall permeability increases the friction factor, and enhances turbulence mixing. The Reynolds stresses, normalized with the modified

friction velocity, have a lower peak in the high porosity cases as compared to the impermeable wall case. On the other hand, compared to the top wall region they have, at least for $\epsilon = 0.95$, a larger peak in the porous wall region. In a future paper (Breugem et al., 2003) more detailed results can be found. The next step in our research is the evaluation of the closures for the VANS equations, especially the model for the drag in the roughness layer and the ignorance of dispersion. The development of closure models is hampered by the lack of detailed experimental and numerical data. We are currently performing a DNS of a turbulent channel flow over a three-dimensional array of cubes that can meet this deficiency.

Acknowledgments

This work was sponsored by the National Computing Facilities Foundation (NCF), with financial support from the Dutch Organization for Scientific Research (NWO).

References

- Finnigan, J. 2000 Turbulence in plant canopies. *Annual Review of Fluid Mechanics* **32**, 519-571.
- Jiménez, J., Uhlmann, M., Pinelli, A. & Kawahara, G. 2001 Turbulent shear flow over active and passive porous surfaces. *Journal of Fluid Mechanics* **442**, 89-117.
- Hahn, S., Je, J., & Choi, H. 2002 Turbulent channel flow with permeable walls. *Journal of Fluid Mechanics* **450**, 259-285.
- Ochoa-Tapia, J.A. & Whitaker, S. 1995 Momentum transfer at the boundary between a porous medium and a homogeneous fluid – I. Theoretical development. *Int. J. Heat Mass Transfer* **38**, 2635-2646.
- Quintard, M., & Whitaker, S. 1994 Transport in ordered and disordered porous media II: Generalized volume averaging. *Transport in Porous Media* **14**, 179-206.
- MacDonald, I.F., El-Sayed, M.S., Mow, K., & Dullien, F.A.L. 1979 Flow through porous media: the Ergun equation revisited. *Industrial and Engineering Chemistry* **18**, 199-208.
- Hinze, J.O. Turbulence. McGraw-Hill, New York, 1975.
- Breugem, W.P., Boersma, B.J., Uittenbogaard, R.E. & Nieuwstadt, F.T.M. 2003 The turbulent flow over a porous bed — *in preparation*.
- Kim, J., Moin, P., & Moser, R. 1987 Turbulence statistics in fully developed channel flow at low Reynolds number. *Journal of Fluid Mechanics* **177**, 133-166.

BUDGETS OF REYNOLDS STRESS IN A ROUGH WALL CHANNEL FLOW

S. Leonardi, E. Mostarda, P. Orlandi

Dipartimento di Meccanica ed Aeronautica Università di Roma "La Sapienza"

leonardi@kolmogorov.ing.uniroma1.it

R.A. Antonia

Disc. of Mech. Eng., University of Newcastle, NSW Australia

Abstract Direct numerical simulations have been carried out for a fully developed turbulent channel flow with a smooth upper wall and a lower rough wall. Two different roughness elements are considered, circular cylinders and square bars for $\lambda/k = 4, 8$, where λ is the distance between the elements and k the height. For $\lambda/k = 4$, circular rods yield a larger roughness function and turbulent intensities than square bars. As λ/k increases, the dependence on the shape of the elements becomes less important. For $\lambda/k = 8$, the two different surfaces have approximately the same roughness functions, and turbulent intensities. However, circular rods are more effective than square bars in terms of an increased momentum transfer since the corresponding total drag is about 10% smaller for the rods than for the square bars. The increase of turbulent intensities observed between $\lambda/k = 4$ and 8 reflects differences in the budgets of the normal turbulent intensity.

1. Introduction

Turbulent flows over rough surfaces occur in many situations. In general, rough walls tend to be three-dimensional, with length scales that may vary significantly, for example, between those encountered in pipe flows and those associated with environmental flows, especially those developing over urban areas. A systematic study of 3-D roughness is nearly impossible; to date, the majority of experimental investigations have been concerned with 2-D models of roughness, typically with either square or circular elements, infinite in the spanwise direction (z) and equispaced in the streamwise direction (x). In spite of this simplification, those models have proven to be useful for understanding

the physics. Near the surface (up to 3 roughness heights), the velocity profiles are very strongly influenced by the shape and distribution of roughness. Far from the wall, the effect of the roughness is to shift the mean velocity profile, with respect to that on a smooth wall, by an increment ΔU^+ , referred to as the roughness function (where "+" denotes wall units). Raupach *et al.* (1992) showed that ΔU^+ is proportional to $\log k^+$ (k is the height of roughness elements) both for 3-D and 2-D rough walls. However, it is apparent that although very different surface geometries may produce the same effect on the mean velocity profile, the turbulence generating mechanism may differ substantially. Hence, the budgets of the Reynolds stress and turbulent kinetic energy have to be examined in detail to understand the effect of the roughness on the overlying flow. In this paper, we use Direct Numerical Simulations (DNSs) of a turbulent channel flow with either circular rods or square bars on the bottom wall. In both cases, two values of the pitch between the elements, λ , were considered, $\lambda/k = 4$ and $\lambda/k = 8$. As the distance between the circular rods is not constant within the cavity, λ was chosen as the geometrical reference parameter in preference to the width w used by Leonardi *et al.* (2003a). Periodic boundary conditions apply in x and z , and there is a no slip condition at the wall in the wall-normal direction (y). The computational box is $8h \times 2h \times \pi h$ in x, y and z respectively. Three different grids have been used, $200 \times 140 \times 97$, $400 \times 140 \times 97$ and $300 \times 140 \times 97$. The first two are non uniform in y while the third is non uniform in x, y . Since results obtained with the $300 \times 140 \times 97$ and $400 \times 140 \times 97$ grids are virtually identical, only results for the latter grid are shown here. The Reynolds number is $Re = 4200$ and corresponds to $Re_\tau = 180$ when both walls are smooth. The flow rate has been kept constant in all simulations. The Navier-Stokes equations have been discretized in an orthogonal coordinate system using the staggered central second-order finite-difference approximation. Details of the numerical method can be found in Orlandi (2000). The roughness is treated by the immersed boundary technique described in detail by Fadlun *et al.* (2000). For this particular surface (with an infinite aspect ratio), with k^+ ranging between 60 and 80, the flow can be assumed to be "fully rough" (Bandyopadhyay 1987), so that the roughness function ΔU^+ depends only on k^+ .

2. Mean Flow

Mean streamlines over square bars have been discussed in detail in Leonardi *et al.* (2003a). Similar results have been obtained for circular rods. Velocity profiles in wall units are compared to the smooth wall in fig.1. The origin in the normal direction, d_o , was found by fitting the present velocity profiles to $\bar{U}^+ = 1/0.41 \ln y^+ + C'$, where $U_\tau \equiv (\tau/\rho)^{1/2}$, τ is the wall shear equal to the sum of the viscous (or skin frictional) drag and the form drag. For $\lambda/k = 4$,

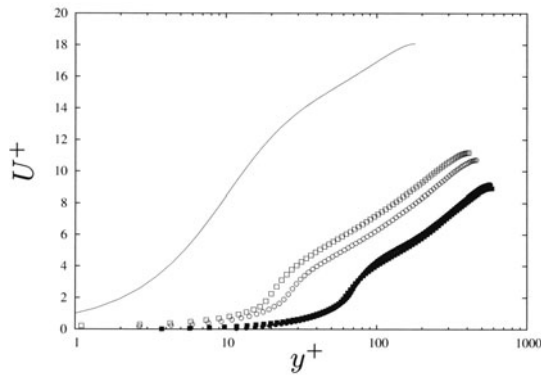


Figure 1. Mean velocity in wall units. \square and \blacksquare square elements; \circ and \bullet circular elements. Empty symbols $\lambda/k = 4$, full symbols $\lambda/k = 8$, —, smooth channel.

the two surfaces have approximately the same U_τ but $\Delta U^+ = C - C'$ ($C = 5.5$) is larger for the circular rods. For $\lambda/k = 8$, the velocity profiles almost collapse on the same curve, despite the smaller U_τ for the circular elements. The roughness function at $\lambda/k = 8$ is larger than that at $\lambda/k = 4$. Furuya *et al.* (1976) and Leonardi *et al.* (2003a) showed, for circular rods and square bars respectively, that $\lambda/k = 8$ is the distance between the elements which maximizes ΔU^+ . The value of the roughness function, about 10 for $\lambda/k = 4$ and 12 for $\lambda/k = 12$, is in good agreement with the values found in the experiments on turbulent boundary layers by Krogstad & Antonia (1999) and Furuya (1976).

3. Turbulent intensities and budgets

Distributions of the normal stresses across the channel are shown in fig.2. The coordinate x_2 (non-dimensionalized with h) has its origin in the plane of the crests, with the upper wall at $x_2 = 2$ and roughness elements lie in the range $-0.2 \leq x_2 \leq 0$. Above the plane of the crests, all three normal stresses are larger than those above the flat wall. However, $\langle u^2 \rangle$ is only about twice as large as that over the smooth wall, while $\langle v^2 \rangle$ and $\langle w^2 \rangle$ are about 8 times larger ($\langle \rangle$ denotes averaging with respect to time x and z). Leonardi *et al.* (2003b), in agreement with Kim (personal communication), showed that when $\langle u^2 \rangle$ is scaled in wall units, (not shown here), it is lower than that over a flat wall. On the other hand, $\langle v^{+2} \rangle$ and $\langle w^{+2} \rangle$ are larger over the rough surface. Therefore, the main effect of roughness is to increase the normal and spanwise velocity fluctuations leading to an overall increase of isotropy (Smalley 2002). The dependence of the maximum of the normal stresses on λ/k and type of roughness closely resembles, that of the roughness function. The largest values

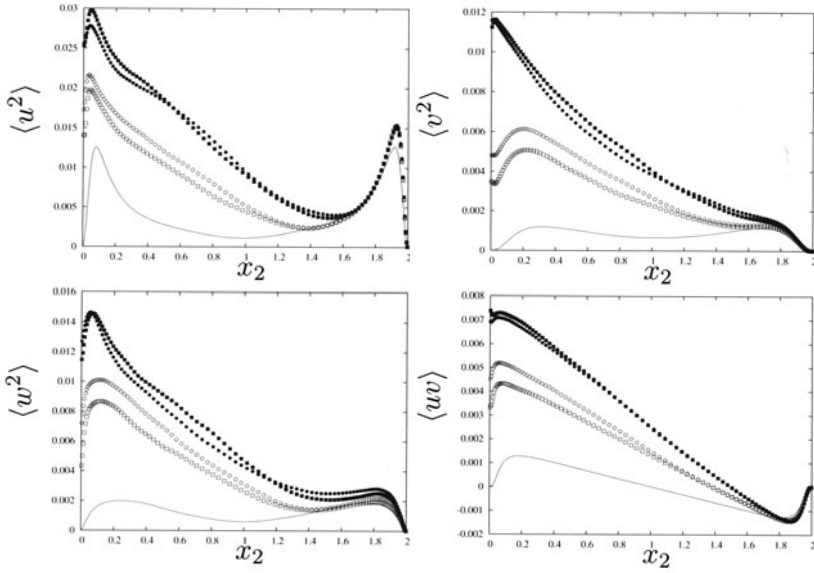


Figure 2. Normal turbulent intensities and Reynolds shear stress, Symbols as in figure 1.

of the *rms* are observed for $\lambda/k = 8$ and the smallest (square bars) are for $\lambda/k = 4$. On the upper wall (smooth) the distributions of the normal stresses coincide, implying that the perturbations due to the roughness on the lower wall do not seem to affect the mechanisms for producing and sustaining turbulence near the upper wall. The minimum of the stresses is at the centreline for a smooth channel, is shifted upwards by the roughness. The minimum value of $\langle u^2 \rangle$ is at $x_2 = 1.55$, (about 3 roughness heights beyond the centreline), in close agreement with the LES results of Cui *et al.* (2003) ($x_2 = 1.52$). The increase of $\langle v^2 \rangle$ near the rough wall is so large that it decreases gradually to the local peak on the upper wall, without going through a minimum.

For $\lambda/k = 4$, the drag of the circular elements is about the same as for the square bars, but $\langle uv \rangle$ and $\langle v^2 \rangle$ are larger. For $\lambda/k = 8$, $\langle uv \rangle$ and $\langle v^2 \rangle$ are approximately the same, but the total drag is about 10% smaller with the rods. For $\lambda/k = 8$, both surfaces have the same ΔU^+ and stresses, so that the shape of the elements is not important. On the other hand, when the elements are very close each other the flow is affected by λ/k and the type of roughness. To understand the mechanism behind the increase of turbulent intensities, the budgets of the Reynolds stress were computed from the equations

$$\frac{D\langle u_i^2 \rangle}{Dt} = -2\langle u_i u_k \rangle \frac{\partial U_i}{\partial x_k} - 2\langle u_i \frac{\partial P}{\partial x_i} \rangle - 2\nu \langle (\frac{\partial u_i}{\partial x_k})^2 \rangle + \nu \langle \frac{\partial^2 u_i^2}{\partial x_k^2} \rangle - \langle \frac{\partial u_i^2 u_k}{\partial x_k} \rangle, \quad (1)$$

where x_1, x_2, x_3 are equivalent to x, y, z and u_1, u_2, u_3 to u, v, w , and repeated indices imply summation. Figure 3 shows a comparison of the $\langle u^2 \rangle$

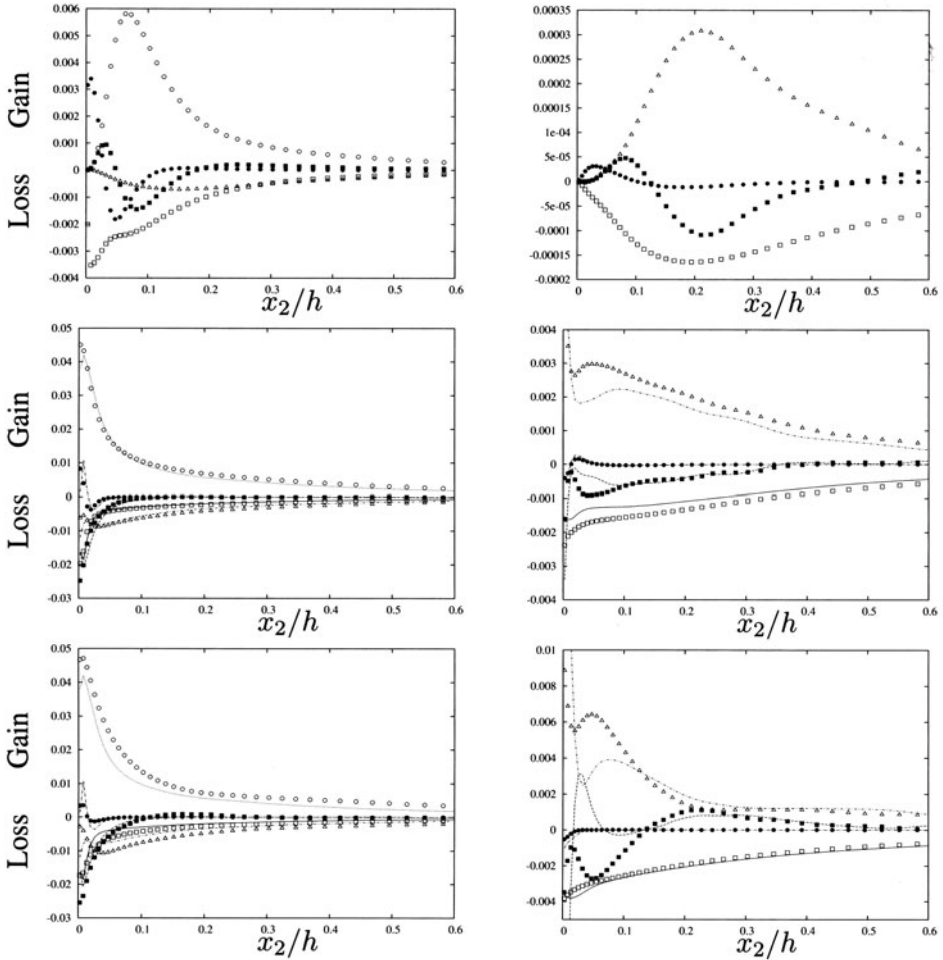


Figure 3. Budgets of $\langle u^2 \rangle$, left, and $\langle v^2 \rangle$ right. From top to bottom, smooth channel, $\lambda/k = 4$, $\lambda/k = 8$. Symbols rods, lines square elements. \triangle , $---$ $-2\langle u_i \frac{\partial P}{\partial x_i} \rangle$; \blacksquare , $----$ $-\frac{\partial u_i^2 u_k}{\partial x_k}$; \square , $—$ $-2\nu \langle \frac{\partial \langle u_i \rangle^2}{\partial x_k} \rangle$; \bullet , $---$ $\nu \langle \frac{\partial^2 u_i^2}{\partial x_k^2} \rangle$; \circ , \cdots $-2\langle u_i u_k \rangle \frac{\partial U_i}{\partial x_k}$.

and $\langle v^2 \rangle$ budgets between smooth and rough walls. For the flat channel $\mathcal{P}_{11} = -2\langle uv \rangle \partial U / \partial y$ is the dominant production term. For $x_2/h > 0.3$, the velocity-pressure gradient term, $\Pi_{11} = -2\langle u \partial P / \partial x \rangle$, and the dissipation, $\epsilon_{11} = -2\nu \langle (\partial u / \partial y)^2 \rangle$, are of similar magnitude and balance the production. For a rough surface, Π_{11} is larger than ϵ_{11} up to $x_2 = 0.05$ and the production due to the mean shear is mostly redistributed to the other stress. Near a smooth

wall, \mathcal{P}_{11} and Π_{11} tend to zero, the dissipation is maximum. The turbulent transport term, $T_{11} = -\langle \partial u^2 v / \partial y \rangle$, and viscous diffusion, $\nu \langle \partial^2 u / \partial y^2 \rangle$ become positive, acting as production terms. On a rough surface, instead, the production is maximum in the plane of the crest and it is balanced by the velocity-pressure gradient term, by the dissipation and by the turbulent transport term. The latter is largest, and is of opposite sign relative to the flat wall. In fact, in a flat channel the excess of the production in the buffer layer is convected towards the wall where it is dissipated. On the other hand, in the plane of the crests, the production is larger than the dissipation, and the excess is convected within the cavity where it is dissipated.

The velocity pressure–gradient term, $(\Pi_{22} = -2\langle v \partial P / \partial y \rangle)$, is the production term for $\langle v^2 \rangle$, and the dissipation, $\epsilon_{22} = -2\nu \langle (\partial v / \partial y)^2 \rangle$, is the dominant sink across most of the channel (fig.3). The viscous diffusion term is small compared to the other terms except very near the wall. To a good approximation, the transport term balances the difference between the contributions from the velocity-pressure gradient and dissipation terms. For a smooth channel, at $x_2 \simeq 0.2$ Π_{22} is larger than ϵ_{22} and the energy excess is transported towards the wall where the dissipation exceeds the production.

For $\lambda/k = 4$, $\Pi_{22} > \epsilon_{22}$ up to $x_2 \simeq 0.35$, the energy excess is transported within the cavity where it is dissipated. For $x_2 > 0.35$, the dissipation and velocity pressure–gradient terms are of similar magnitude.

A different behaviour is observed for $\lambda/k = 8$; near the wall, Π_{22} is about twice as large for the rods than the square bars, while the dissipation is essentially the same. The transport term, which has to balance the other two terms, is positive in the case of the square elements and negative for the circular rods. For the circular rods, there is a flux of energy towards the cavity, while for the square bars, the flux of energy is in the opposite direction, away from the wall. In spite of the two surfaces having approximately the same roughness function and turbulent intensities, the mechanism for producing and sustaining turbulence is quite different. Whereas, over a flat surface, $\Pi_{22} > \epsilon_{22}$, so that the transport term is negative, over the roughness with $\lambda/k = 8$, the transport term is positive.

The budgets for $\langle u^2 \rangle$ and $\langle w^2 \rangle$ (not shown here) depend weakly on λ/k and on the type of surface (fig. 3) even though the corresponding turbulence intensities increase significantly as λ/k increases. On the other hand, the budget of $\langle v^2 \rangle$ and, in particular, the velocity pressure–gradient term depend strongly on the shape of the elements and on the ratio λ/k . Orlandi *et al.* (2003) considered the velocity distribution in the plane of the square bar roughness crests and carried out three direct numerical simulations with flat walls and only one non-zero velocity component. When a non-zero normal velocity was imposed at the wall, the effect on the flow closely resembled that due to the real roughness. Also, Leonardi *et al.* (2003a) observed a similar behaviour between

ΔU^+ and the form drag for a wide range of λ/k . The present results thus further corroborate the previous findings by underlying the importance of the distribution of pressure and normal velocity above a rough wall.

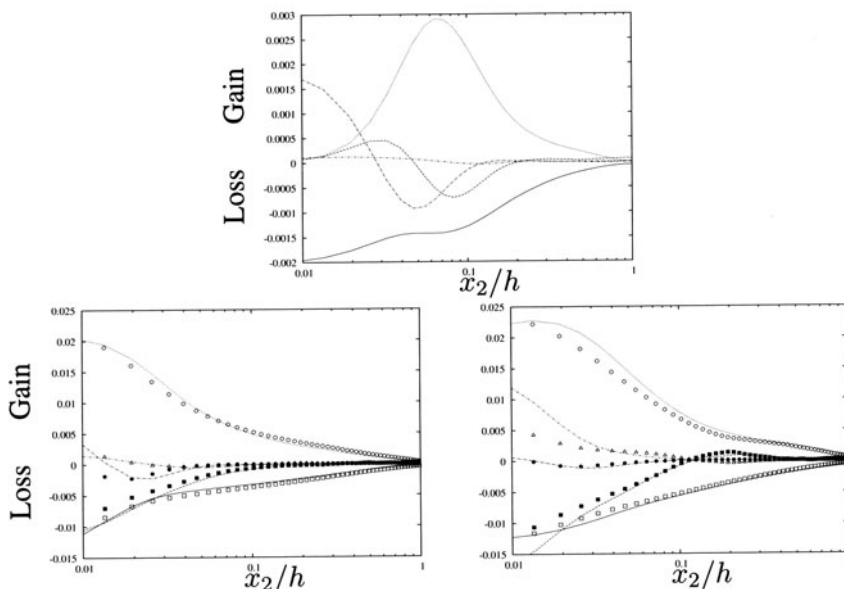


Figure 4. Budgets of the turbulent kinetic energy. Top, smooth channel, left $\lambda/k = 4$, right $\lambda/k = 8$. Rods symbols, square bars lines. \square , — : dissipation; \blacksquare , ---- : turbulent convection; \circ , : production; \bullet , —·— : turbulent diffusion; \triangle , --- : pressure.

From equation (1) the equation for the conservation of the turbulent kinetic energy can be obtained

$$0 = -\langle uv \rangle \frac{\partial U}{\partial y} - \frac{\partial \langle Pv \rangle}{\partial y} - \nu \left\langle \left(\frac{\partial u_i}{\partial y} \right)^2 \right\rangle + \nu \frac{\partial^2 \langle k \rangle}{\partial y^2} - \frac{\partial \langle kv \rangle}{\partial y}, \quad (2)$$

where $k = 0.5 u_i^2$. Over a rough wall, the production and dissipation terms are about 6 times larger than those over a flat wall. The viscous diffusion term is reduced; in fact, the second derivative in y is smaller than over a flat wall since the non-slip condition is confined to the extent of the elements only. On the other hand, the turbulent convection ($d\langle vk \rangle/dy$) is largely increased. In particular near the wall, the turbulent convection is approximately the same as the dissipation and represents the transfer of energy from the outer flow to the cavities.

4. Conclusions

Direct numerical simulations have been carried out with either rod or square bar roughness on one wall. The budgets of the Reynolds stress have high-

lighted the changes in the mechanism for producing and sustaining turbulence. Roughness increases the redistribution of energy through the velocity pressure-gradient term, leading to an overall increase of isotropy. The turbulent convection becomes significant since there is a transfer of energy from the overlying flow to the cavity where it is dissipated. Although the present results concern 2D roughness only, we speculate that the mechanism for real 3D surfaces has to be similar. Therefore, the present budgets should guide the development of rough-wall flow models. Since the important terms to be modeled involve the pressure and wall-normal velocity, which are very difficult to measure, the DNS should become a valuable tool for modeling rough wall flows.

Acknowledgments

We acknowledge the support of the Australian Research Council, and the Ministero dell' Istruzione, dell' Università e della Ricerca and Centro di Eccellenza di Meccanica Computazionale, Politecnico di Bari.

References

- Bandyopadhyay, P.R. (1987). Rough-wall turbulent boundary layers in the transition regime. *J. Fluid Mech.* **180**, pp.231–266.
- Cui J., Virendra C. Patel & Ching-Long Lin 2003. Large-eddy simulation of turbulent flow in a channel with rib roughness. *Int. J. of Heat and Fluid Flow* **24** 372–388.
- Fadlun, E. A., Verzicco, R., Orlandi, P. & Mohd-Yusof, J. 2000. Combined immersed boundary finite-difference methods for three-dimensional complex flow simulations. *J. Comput. Phys.* **161**, 35–60.
- Furuya, Y., Miyata, M. & Fujita, H. 1976. Turbulent boundary layer and flow resistance on plates roughened by wires. *J. Fluids Eng.* **98**, 635–644.
- Krogstad, P.-Å. & Antonia, R. A. 1999. Surface roughness effects in turbulent boundary layers. *Expts. Fluids* **27**, 450–460.
- Leonardi, S., Orlandi, P., Smalley, R.J., Djenidi, L. & Antonia, R.A. (2003a). Direct numerical simulations of turbulent channel flow with transverse square bars on one wall. *J. Fluid Mech.* **491**, 229–238.
- Leonardi, S., Orlandi, R.J., Djenidi, L. & Antonia, R.A. (2003b). Structure of turbulent channel flow with square bars on one wall. *Proceeding of Turbulent Shear Flow Phenomena 3*. Sendai Japan 25–27/06/03.
- Orlandi, P. 2000. *Fluid Flow Phenomena : A Numerical Toolkit*, Dordrecht, Kluwer.
- Orlandi P., Leonardi S., Tuzi R. & Antonia A.R. 2003 DNS of turbulent channel flow with wall velocity disturbances *To appear in Physics of Fluids*,
- Raupach, M. R., Antonia R.A. & Rajagopalan S. 1991. Rough-wall turbulent boundary layers. *Appl. Mech. Rev.* **44**, 1–25.
- Smalley R.J., Leonardi S., Antonia R.A., Djenidi L. & Orlandi P. (2002). Reynolds stress anisotropy of turbulent rough wall layers. *Exps. Fluids* **33** 31–37.

EFFECT OF APPLICATION AND REMOVAL OF ADVERSE PRESSURE GRADIENT TO TURBULENT WALL LAYERS

Christopher P. Yorke and Gary N. Coleman

*School of Engineering Sciences, University of Southampton,
Southampton, Hampshire, SO17 1BJ, UK*

c.p.yorke@soton.ac.uk, g.n.coleman@soton.ac.uk

Keywords: Turbulence, DNS, Channel Flow, Pressure Gradient, Recovery, Turbulence Models

Abstract DNS was performed of a turbulent channel flow with a geometry which simulates the effect of the application and removal of an Adverse Pressure Gradient (APG). Statistics are presented for the periods before and after the cessation of the APG, with the aim of better understanding the dominant mechanisms. Four popular turbulence models were tested under the same conditions and their performance compared to the DNS.

1. Introduction

This study investigates the mechanisms at work in a turbulent boundary layer, when an Adverse Pressure Gradient (APG) is applied and subsequently removed. Flows of this type are common in engineering applications. Previous DNS studies of APG boundary layers (eg. Spalart & Watmuff [10], Spalart & Coleman [9]) have focused primarily upon the application of the APG, with less attention to the recovery region. These computations have also tended to be very expensive, since they must account for the spatial development of the boundary layer, and the complications associated with the inflow boundary conditions (requiring for example fringe zones or precursor simulations). As explained below, we circumvent many of these difficulties by using a time-developing strained-channel analogue of the spatial case, which leads to significant advantages both for the DNS and the ensuing model testing for which the DNS results act as benchmark data.

Capturing the recovery of a perturbed boundary layer is a notoriously difficult task for Reynolds-Averaged Navier Stokes (RANS) models. Castro & Epik [2], among others, have shown that the recovery process is typically a very

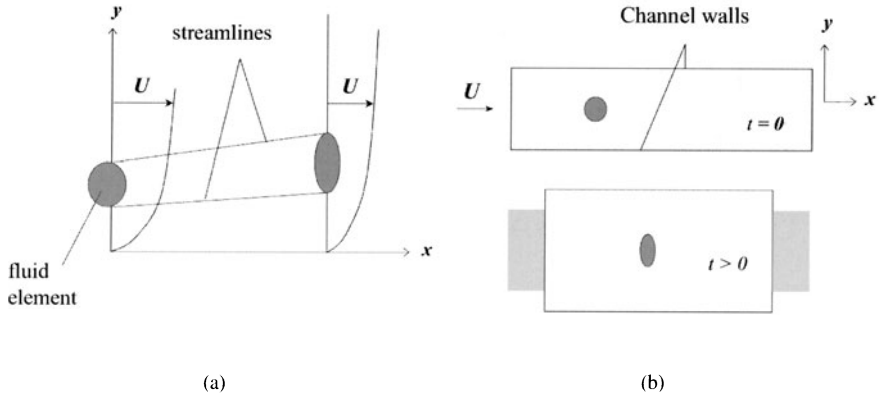


Figure 1. Side view of 2D APG boundary layer. a) Spatially developing flow. b) Initial and deformed domain of time-developing strained-channel idealization.

long one, involving delicate balances between various terms in the transport equations. The implied challenge to both turbulent simulation and RANS predictions, coupled with its technical importance, motivates the present study.

In this work, we use DNS to consider the behaviour of an idealized turbulent boundary layer as it responds to the sudden application and removal of an APG. In parallel with the DNS study, RANS models are used to calculate the same flow and their performance in reproducing the flow statistics is assessed. Our ultimate goal is to isolate features in common turbulence models which are responsible for the model's ability/inability to accurately predict perturbed boundary layers.

2. Approach

2.1 DNS

The DNS emulates a spatially developing low-Mach-number APG boundary layer using an uncomplicated plane-flow geometry with no uncertainty on boundary conditions. This is achieved by simultaneously applying in-plane wall motion and straining the domain of an incompressible turbulent channel flow.

The in-plane wall motion duplicates the bulk deceleration of an APG, reducing the wall shear stress by causing the difference between the mean centreline velocity \bar{u}_c and wall velocity u_w to decrease. The applied strain reproduces the irrotational plane-strain (streamwise compression with wall normal divergence) found in an APG. Spatial changes are thus replaced with temporal ones, as the channel turbulence is subjected to the deformation history from the spatial

case. The strain field imposed is spatially uniform such that $U_i = A_{ij}x_j$ with $\partial A_{ij}/\partial x_j = 0$ where $A_{ij} \equiv \partial U_i/\partial x_j$, which steps from zero to a constant value at $t = 0$. The streamwise and wall-normal strains are equal and opposite with the streamwise compression $A_{11} \equiv \partial U/\partial x < 0$ while the wall-normal divergence, $A_{22} \equiv \partial V/\partial y > 0$. To maintain volume continuity $A_{11} = -A_{22}$. The corresponding wall motion $u_w(t)$ is specified such that when viewed in the reference frame attached to the moving walls, the centre-line velocity satisfies $\bar{u}_c(t) = \bar{u}_c(0) \exp(A_{11}t)$ and thus decreases with time at a rate set by the uniform deceleration $A_{11} < 0$.

This approach has the advantage of producing the desired perturbation while maintaining a simple parallel-flow geometry. Additionally since the Reynolds-averaged statistics from the DNS satisfy a one-dimensional unsteady problem, model testing can be carried out quickly and efficiently. Two principal features captured by the DNS are the divergence of the outer-layer streamlines and the weakening (and possible reversal) of the mean wall-shear stress τ_w . Absent features are streamline curvature and, on flow separation, the detached/curved shear layers that result from the eruption of the near-wall vorticity. The reversed-flow layer remains very thin with this approach.

The DNS is generated by the fully spectral method described in [3] and applied to the case of a relatively weak APG, with $A_{22} = -A_{11}$, chosen to be 31% of $u_\tau(0)/\delta(0)$, the ratio of the initial friction velocity to the initial channel half-width. Simulations have been carried out using initial Reynolds numbers $\text{Re}_\tau = u_\tau \delta / \nu$ of 360 and 600. Additionally for the $\text{Re}_\tau = 600$ case the APG has been removed after a finite time and the flow has been allowed to recover towards the unstrained steady state. The strain is removed instantaneously at time $t = t_R$ while simultaneously the acceleration of the walls is halted such that the wall velocity is maintained at $U_c(t)/U_c(0) = \exp(A_{11}t_R)$.

Results for the $\text{Re}_\tau = 390$ case are taken from [4]. Because the flow is unsteady they are one ensemble with 21 samples. Additionally symmetry is invoked thereby doubling the number of samples. The $\text{Re}_\tau = 600$ results are new and are derived from a single run, again doubled by symmetry. For both cases there is periodicity in the streamwise and spanwise directions allowing plane averages to be produced for the cross-channel profiles at each time.

The new code used for the $\text{Re}_\tau = 600$ case is a development of that used for the $\text{Re}_\tau = 390$ case. The original code was written for a serial machine and had to be converted for use on the new UK based HPCX IBM Power4 machine and a Cray T3E. This involved conversion from the NASA language Vectoral [11] to Fortran 90, and addition of the MPI message passing calls necessary for the parallel architecture. Initial steady state conditions were calculated using 8000 HPCX CPU hours, while the strained run was carried out on the Cray T3E using 40,000 CPU hours.

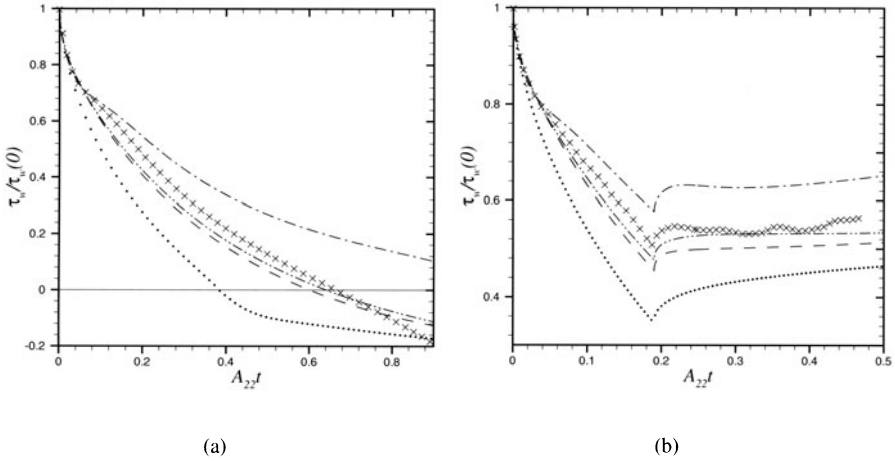


Figure 2. DNS and model histories of wall shear stress. a) $Re_\tau(0) = 390$ taken from [4] b) $Re_\tau(0) = 600$, BL; ----, SA; —, LS; — · —, SST; ×, DNS.

2.2 Models

Four models have been tested for the same conditions under which the DNS was carried out. When applied to RANS models these conditions reduce to a one dimensional time-developing problem. The models are, in order of complexity, the Baldwin-Lomax (BL) algebraic model [1], the Spalart-Allmaras (SA) one-equation eddy-viscosity transport model [8], the Launder-Sharma (LS) low-Reynolds-number k - ϵ model [5] and the Menter Shear-Stress Transport (SST) model [6]. These were chosen as they have current or historical relevance to aerospace CFD applications.

Numerical solutions were produced with each model using the unsteady finite-difference code described in [12]. 400 grid points between the channel wall and centre were used, which were monotonically clustered near the wall, with the first grid point 0.12 initial wall units above the wall in all four models. For the $Re_\tau = 390$ case a fixed time step of 1.25×10^{-2} was used for all but the SST model which required a time step of 3.125×10^{-3} . For the $Re_\tau = 600$ case all the models used a fixed time step of 4.0×10^{-3} . These values generate grid independent results. Well defined initial conditions were developed by a steady-state version of the code and it was verified that the unsteady version would hold these values when $A_{ij} = 0$.

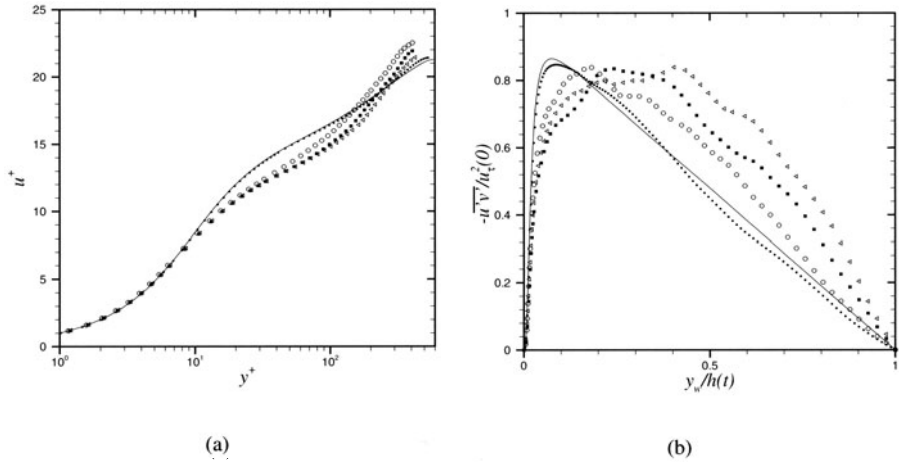


Figure 3. a) Velocity profiles b) DNS profiles of Reynolds stress normalized by initial u_τ^2 . \cdots , Initial unstrained Profile; — , Moser et. al. $Re_\tau = 590$ DNS data [7]; \circ , $A_{22}t = 0.19$; \blacksquare , $A_{22}t = 0.33$; \triangle , $A_{22}t = 0.44$

3. Results

3.1 APG Region

Fig.2 shows the history of the wall shear stress for the two Reynolds numbers, normalized by the initial wall shear stress. The $Re_\tau = 390$ case, (a), shows the behaviour from the initiation of the strain until flow reversal has been achieved. This can be considered to be analogous to separation in boundary layers; the behaviour of the models when compared to the DNS qualitatively agrees with that found for spatial cases. The BL model shows its usual (for sub-sonic cases) underestimation of the wall shear stress while the LS model remains completely unreversed during the time period under investigation. The performance of both the one-equation SA and two-equation SST models is encouraging and demonstrates how model accuracy does not always correlate directly with model complexity. A more complete study of the models for the applied strain period can be found in [12]

3.2 Relaxation Region

The initial results produced for the relaxing flow case reconfirm the notion that relaxation is indeed a slow process. The results here show a single realization where the flow has been strained for a period of 0.19 time units (such that the channel walls are 21% further apart than before the strain was first applied) and then has been allowed to relax. At present the DNS has been continued

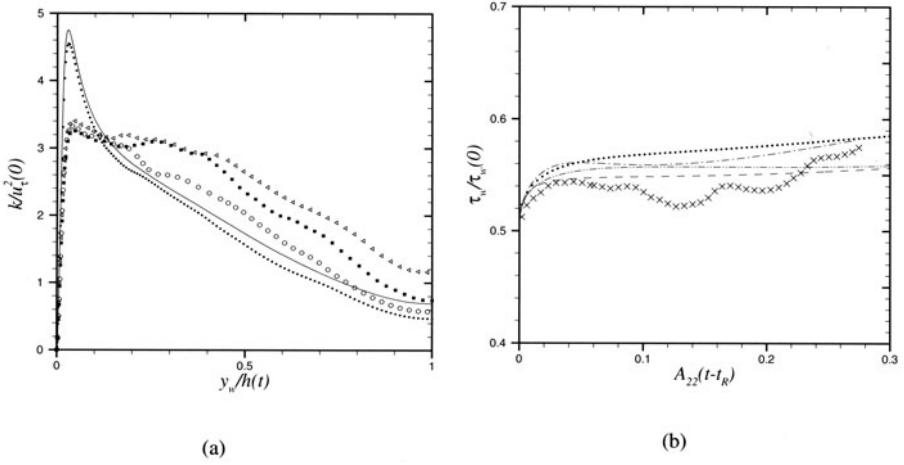


Figure 4. a) DNS profiles of Turbulence Kinetic Energy normalized by initial u_τ^2 , Initial un-strained Profile; ———, Moser et. al. [7] $Re_\tau = 590$ DNS data; \circ , $A_{22}t = 0.19$; \blacksquare , $A_{22}t = 0.33$; \triangle , $A_{22}t = 0.44$ b) Profiles of wall shear stress during relaxation when RANS models are relaxed from the same wall shear value; , BL; ----, SA; — · —, LS; — — —, SST; \times , DNS.

for approximately 1.5 times the strained time period and as can be seen, the flow is far from that of a steady state flow. This is consistent with the findings of Castro & Epic [2] who showed that it took 71 boundary layer thicknesses for the velocity profile of an equilibrium boundary layer to form following a separation bubble. Our mean centreline flow at present has been convected 16 channel half-widths. It should be noted however that the wall shear in our case is only reduced to 0.5 of its original value rather than full separation.

If we look at the mean velocity profiles (Fig.3a) we can see that the major deviation from the pre-strain profiles is in the outer region. From the point of relaxation we see a slow drop in the outer-layer velocity which corresponds with the expected behavior. Past works have shown the velocity reduces to lower than the log-law levels and then rebounds. On continuation of the simulation it is likely that this effect will be seen. The Reynolds shear-stress profile (Fig.3b) shows the maximum of the profile becomes less well defined and continues to move towards the centre of the channel even after the removal of the strain. Correspondingly the Turbulent Kinetic Energy's (TKE) peak (Fig.4a) broadens, however there is an increase in the total TKE of the flow. For this to occur there must be an imbalance between the production and dissipation. When further work is carried out and more ensembles obtained, examination of the budgets can be carried out to further study this.

When considering the performance of the turbulence models under these conditions there is a difficulty in isolating the performance of the models solely under the relaxing conditions. It can be seen from Fig.2b that if the performance is judged on a combination of both the strained and the relaxed sections of the flow, the models which perform well under strain tend to continue that good performance in the relaxed region. When the strain was halted at a the wall shear value corresponding to the DNS results rather than a specified time the performance of the models can be judged more on their performance during the relaxation process. Here again we see in Fig.4b that those models which perform well under strained conditions behave in the most realistic manner, although at this point in the relaxation process it is difficult to see an overall trend.

4. Conclusions

Initial findings of a study on the behaviour of turbulent wall layers under and recovering from an APG have been presented. For the case where the strain is applied, simulations have been carried out at a higher Reynolds number than previously considered. The performance of the models tested here at the new Reynolds number was found to be comparable to the lower Reynolds number for the time period investigated. The initial simulation results produced for the relaxation case confirm again the fact that recovery is a comparably slow process and that the simulation method has the possibility of giving insight into the relevant dynamical mechanisms.

Acknowledgements

Our thanks goes to EPSRC for providing the computer time used in this project, through grant GR/M08424/02 and managed through the UK Turbulence Consortium.

References

- [1] Baldwin, B. S. and Lomax, H., Thin-layer approximation and algebraic model for separated turbulent flows, *AIAA Paper* 78–257.
- [2] Castro, I. P. and Epik, E., Boundry Layer Development After a Separated Region, *Journal of Fluid Mechanics* Vol. 374 (1998) 91–116
- [3] Coleman, G. N., Kim, J., Spalart, P. R., A Numerical Study of Strained Tree-Dimensional Wall-Bounded Turbulence, *Journal of Fluid Mechanics* Vol. 416 (2000) 75–116
- [4] Coleman, G. N., Kim, J., Spalart, P. R., Direct Numerical Simulation of a Decelerated Wall-Bounded Turbulent Shear Flow, *To Appear in Journal of Fluid Mechanics* (2003)
- [5] Launder, B. E. and Sharma, B. I., Application of the Energy Dissipation Model of Turbulence to the Calculation of Flow Near a Spinning Disc, *Letters in Heat and Mass Transfer*, Vol. 15 (1972) 301–314

- [6] Menter, F. R. Two-Equation Eddy-Viscosity Turbulence Models for Engineering Applications, *AIAA Journal* Vol. 32 (1994) 1598–1605
- [7] Moser, R. D., Kim, J., Mansour, N. N., Direct numerical simulation of turbulent channel flow up to $Re_\tau = 590$, *Physics of Fluids*, Vol. 11 (1999) 943–945
- [8] Spalart, P. R. and Allmaras, S. A., One-equation Turbulence Model for Aerodynamic Flows, *La Recherche Aérospatiale*, Vol. 1 (1994) 5–21
- [9] Spalart, P. R. and Coleman, G. N., Numerical Study of a Separation Bubble With Heat Transfer, *European Journal of Mechanics B/Fluids* Vol. 16 (1997) 169–189
- [10] Spalart, P. R. and Watmuff, J. H., Experimental and Numerical Study of a Turbulent Boundary Layer with Pressure Gradients, *Journal of Fluid Mechanics* Vol. 249 (1993) 337–371
- [11] Wray, A., Personal Communication
- [12] Yorke, C. P. and Coleman, G. N., Assessment of Common Turbulence Models for an Idealized Adverse Pressure Gradient, *To Appear in European Journal of Mechanics B/Fluids*

4.3 FLOWS INVOLVING STREAMLINE CURVATURE AND SWIRL

LARGE EDDY SIMULATIONS OF TURBULENT FLOW IN CURVED AND S-SHAPE DUCTS

Cécile Münch, Jérôme Hébrard and Olivier Métais

L.E.G.I

BP. 53, 38041 Grenoble Cedex 09, France

cecile.munch@hmg.inpg.fr

Abstract We present Large-Eddy Simulations (LES) of the turbulent compressible flow in a curved and an S-shape duct of square cross section. The aim is to predict the three-dimensional structures which develop inside the cooling channels of heat exchangers and which dominate the heat transfer with the heated wall. We first consider a curved duct with one curvature only and then an S-shape duct with two opposite curvatures. We observe the formation of Görtler vortices which are moved close to the convex wall by the radial pressure gradient between the two curved faces. These are associated with a secondary flow of over 20% of the streamwise velocity. We determine the influence of wall heating and consecutively consider the case of concave wall heating and of convex wall heating. Due to the secondary flow associated with the Görtler vortices, we observe an enhancement of the heat flux in the first case and an inhibition in the second case.

Keywords: Turbulence, heat transfer, large eddy simulation

1. Introduction

The prediction of heat and mass transport processes in curved ducts is of interest for engineering applications like compressors, turbines, cooling ducts of rocket engines. Several experimental and theoretical investigations have been performed to study the turbulent flow within a curved duct without any heating: Hunt (1979), Hoffmann (1985), Humphrey (1981), Kim (1994) and Saric (1994). These works have brought to light the destabilizing effect of the concave wall when the convex wall has conversely a stabilizing action. Resulting from this centrifugal instability, vortices, called Görtler vortices, appear on the concave wall and an intense cross-stream flow develops. Numerical studies have been performed by Humphrey (1981), Silva (2003): the difficulty lies in the correct prediction of this cross-stream flow (called secondary flow) and

of the related turbulence characteristics. As far as the relationship between Görtler vortices and heat transfer is concerned, Toe *et al.* (Toe (2002)) have experimentally investigated the boundary layer over a concave heated wall of a duct. Yee *et al.* (Yee (1980)) have numerically looked at the influence of the Görtler vortices on the heat exchanges over a curved heated wall for a laminar flow. No numerical work has yet been devoted to the study of the combined effect of curvature and heating in a closed duct for turbulent flow. We here perform Large Eddy Simulation (LES) to investigate the turbulent flow and the associated turbulent structures in a curved duct and an S-shape duct of square cross-section. After the presentation of the numerical procedure (section 2), we first study the turbulent flow within curved ducts without any heating (called isothermal duct). We then consecutively consider two distinct configurations of heating: heating applied on the concave wall and applied on the convex wall. The heating of the concave-convex wall of the S-shape duct combines the two different heating types. Our main goal is here to investigate the mutual influence of the Görtler vortices and the heat transfer.

2. Numerical Methods

We solved the LES modified three-dimensional compressible Navier-Stokes equations. The subgrid-scale model is the selective structure function model proposed by Lesieur and Métais (1996). To complete the Navier-Stokes filtered equations, we use three supplementary relations and equations: (i) the Sutherland empirical law to describe the molecular viscosity variation with temperature. (ii) The gas is considered as an ideal gas with the corresponding equation of state. (iii) The turbulent Prandtl number is equal to 0.6.

Curvilinear coordinates are used and the equations are discretized with a fully-explicit McCormack scheme (Kennedy (1997)), second order in time and fourth order in space.

Two configurations of ducts, having a square cross section, are represented on Figure 1. The first duct presents only one curvature, whereas the second one exhibits a double curvature with a concave-convex wall on one side and a convex-concave wall on the other side (S-shape duct). The curved computational domain has a length of $12.6 D_h$ in the streamwise direction (s) where D_h is the hydraulic diameter. The curved section starts at a distance $2.4 D_h$ upstream from the inlet and extends $5.3 D_h$ downstream from the exit of the duct. The curved part is defined by a curvature radius measured at the centerline chosen to be $9.5 D_h$, and an angle of 30° .

For the S-shape duct, $15 D_h$ long, an oblique straight section separates both curved regions and a long straight outlet of length $6 D_h$ is added as a recovery region. Both angles for the curved parts are equal to 20° and the radius of curvature measured at the centerline is equal to $6.5 D_h$.

The parameters of the simulations are the following: Reynolds number, $Re = 6000$ based on the mean bulk velocity U_b (see Salinas (2002) for definition); Mach number $Ma = 0.5$; molecular Prandtl number $Pr = 0.7$. A nonuniform numerical mesh is used with $160 * 50 * 50$ nodes, in the streamwise direction (called s), in the direction normal to the curved walls (called n) and in the spanwise direction (called z) respectively. In the n and z directions, an hyperbolic-tangent stretching is utilized : the first node closed to the wall is situated at 1.8 wall units. We here use the same grid resolution than Salinas and Métais (2002) for the straight duct with the same Reynolds number: these authors indeed showed that such a resolution is sufficient to obtain good comparisons with DNS and laboratory experiments.

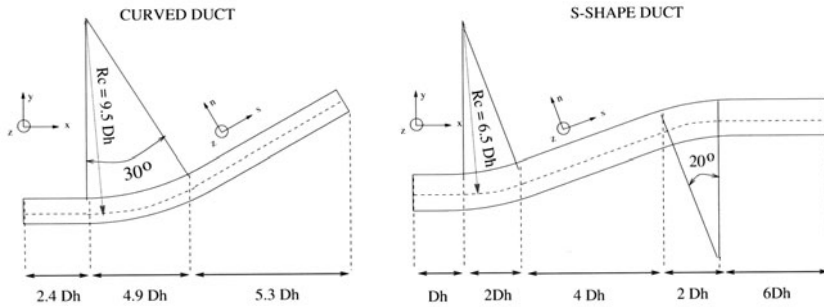


Figure 1. Geometry of computational domains

The boundary conditions consist of a no-slip condition for the velocity, and a uniform temperature imposed on the four walls. One original feature of the present computation is that a fully developed turbulent state is achieved at the duct inlet thanks to the simultaneous computation of a periodic duct which provides a turbulent field at each instant. The inflow and outflow boundary conditions are obtained through the use of the characteristics conditions proposed by Poinso and Lele (Poinso (1992)). The reader can refer to Salinas and Métais (2001) for further details.

3. Isothermal ducts

We first consider ducts with all walls at the same imposed temperature T_w . Figure 2 clearly shows the formation of two intense Görtler vortices in both ducts (curved and S-shape). These are clearly visible through positive Q isosurfaces where Q is the second invariant of the velocity gradient tensor, which constitutes a good way to identify intense vortices (Hunt (1988), Dubief (2000)). The destabilization of the flow occurs on the concave wall but the pressure gradient between the inner and outer curved walls implies a displacement of the longitudinal vortices towards the convex face. On figures 3 and 4, we represent the mean velocity projected in sections perpendicular to the mean flow

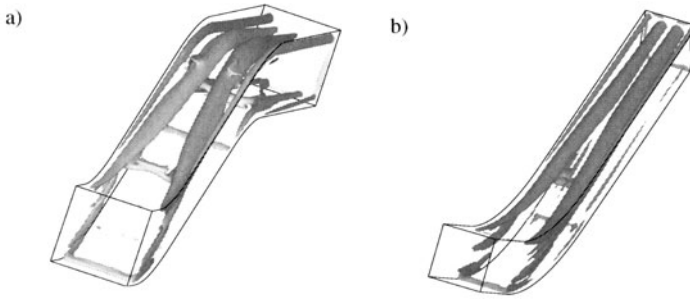


Figure 2. Visualization of Görtler vortices by Q-isosurfaces : a) S-shape duct, b) Curved Duct

showing the secondary flows : this allows to follow the flow development as we move downstream. We defined mean quantities as the averaging in time. A similar behavior can be observed at the beginning of the curved duct and of the S-shape duct. Due to the curvature, the centrifugal forces as well as the radial pressure gradient increase. Insofar as the balance between these two terms is not reached, a secondary flow directed from the concave to the convex wall appears mainly localized near the side wall of the duct. Eventually, this transverse flow generates two cells near the convex wall (see figure 3b and figure 4b). As we move downstream these two cells come closer together generating an important ejection in the middle plane of the convex wall. They are also at the origin of two recirculating vortices, counter-rotating with respect to the main two vortices, and localized in the far corners of the convex wall and the side walls. In the S-shape duct, the effects of the second curvature can be observed on figure 4c and d, we observe as before the formation of a secondary flow directed from the concave to the convex wall, which is now located at the bottom of the duct. This eventually yields the appearance of recirculating vortices localized near the bottom wall.

In figure 5a and b, we represent the maximum value of secondary flow intensity defined as $I_{max}(s) = \max_{n,z} \left(\sqrt{\left(\frac{V}{U_b}\right)^2 + \left(\frac{W}{U_b}\right)^2} \right)$ as a function of the downstream distance in the duct. In the inlet part, the maximum intensity represents about 2% of the bulk velocity, as found by Salinas (2002) in the straight duct. Right from the beginning of the curved part (first dotted line) the cross flow intensifies reaching around 24% of the bulk velocity for the curved duct and 21% for the S-shape duct. Note that the maxima are reached near the end of the curved parts. For both ducts, the oblique part induces a net decrease but the intensity is still much stronger than at the inlet. For the S-duct, the second curve causes another rise but of lower intensity than the first one, it corresponds to the new vortices created near the concave-convex wall of the duct. An ex-

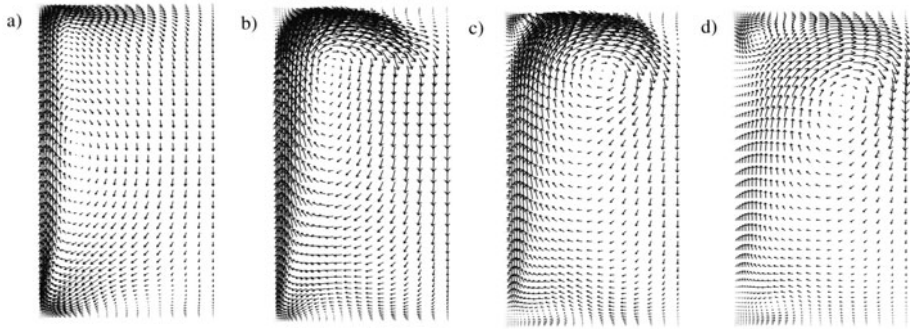


Figure 3. Mean velocity vectors projected on cross-sections of the curved isothermal duct showing the secondary flows for : a) $s/D_h = 3.6$ at the beginning of the curved part, b) $s/D_h = 6.7$ at the end of the curved part, c) $s/D_h = 8.32$ at the beginning of the oblique part, d) $s/D_h = 12.4$ at the outlet. The concave wall is at the bottom and the convex wall is at the top of each section.

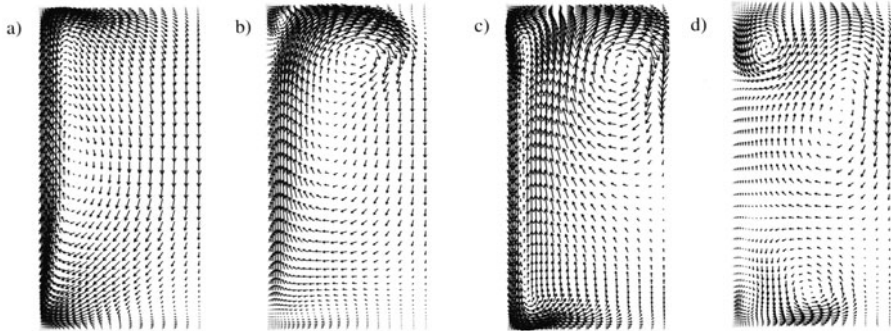


Figure 4. Mean velocity vectors projected on cross-sections of the S-shape isothermal duct showing the secondary flows for : a) $s/D_h = 2$ at the middle of the first curved part, b) $s/D_h = 5$ at the middle of the oblique part, c) $s/D_h = 7.5$ at the beginning of the second curved part, d) $s/D_h = 13$ at the middle of the outlet part. The concave-convex wall is located at the bottom of each section.

amination of the turbulent energy, defined as $k = \frac{1}{2} \langle u'_i u'_i \rangle$, near each curved wall at different streamwise positions confirms these effects. As shown in figure 6, the turbulence intensity rises near the concave wall: the peak intensity is enhanced by 25% as compared to the straight duct. Conversely, it declines strongly close to the opposite convex wall by about 75%. After the curvature,

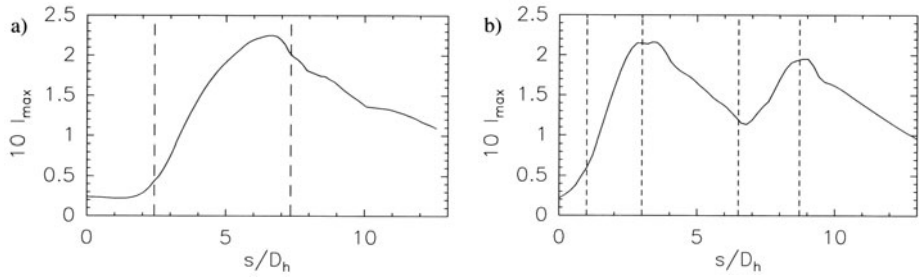


Figure 5. Maximum of mean secondary flow intensity in the non-heated a) curved duct, b) S-shape duct, the vertical lines delimit the beginning and the end of curvatures.

the maximal value near the concave wall tends to recover its value at the inflow. In the S-shape duct, the same trend can be observed with a systematic increase of the turbulent kinetic energy close to the concave wall and a decrease close to the convex wall. This confirms the destabilizing effect of concave curvature and stabilizing for convex one, also found by Humphrey (1981), Kim (1994), Silva (2003).

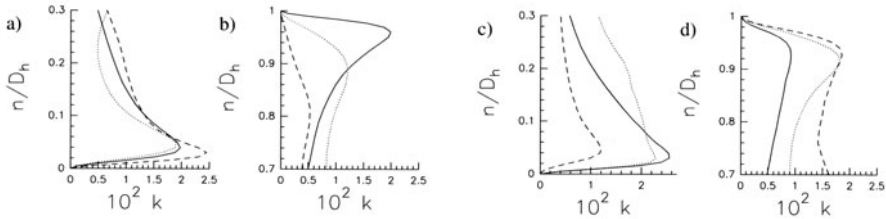


Figure 6. Turbulent kinetic energy at $z/D_h = 0.5$. On the left, in the curved non-heated duct for $-s/D_h = 1$, $-s/D_h = 3.6$, ... $s/D_h = 12.4$ a) near the concave wall, b) near the convex wall. On the right, in the non-heated S-shape duct for $-s/D_h = 2$, $-s/D_h = 7.5$, ... $s/D_h = 13$ c) near the concave-convex wall, d) near the convex-concave wall

4. Heated curved ducts

We now discuss the heat transfer effects in curved and S-shape ducts. We here neglect gravitational effects and all the changes are due to compressibility. In the curved duct, we simulate two distinct cases to study the influence of the two different types of curvature on heat transfer. Firstly, the temperature of the concave wall is taken equal to three times the temperature on the three other walls. Secondly, heating is applied on the same way but on the convex wall. For the heated S-shape duct, the temperature of the concave-convex wall is similarly taken equal to three times the temperature on the three other walls. In figure 7,

we represent the secondary flows in the curved duct for both cases of heating. The intensity of the secondary flow attains values up to 5% of the bulk velocity at the inlet $s/D_h = 1$ in each case. This increase arises not only close to the heated wall but also on the sidewalls. After the curvature, at $s/D_h = 8.32$, curvature effects are still dominant. We may however observe some significant modifications of the flow structures induce by the heating. When the convex wall is heated, the two Görtler vortices are further apart and have an enhanced intensity with a vorticity of $1.2 U_b/D_h$ versus $1.05 U_b/D_h$ in the non-heated case. When the concave wall is heated, the normal flow away from the concave wall is stronger than in the non-heated case but this ejection can not develop since it opposes the transverse flow coming from the convex wall associated with the two Görtler vortices. On figure 8, we represent the cross stream flow in the heated S-duct. As mentioned earlier, the secondary vortices near the heated wall are intensified: here, we see that two vortices appearing near the concave-convex wall at $s/D_h = 13$ are much larger than in the non-heated case. Figure 9 shows the mean heat flux, $Q_w(s, z) = \kappa \frac{\partial T}{\partial n}|_{wall}$,

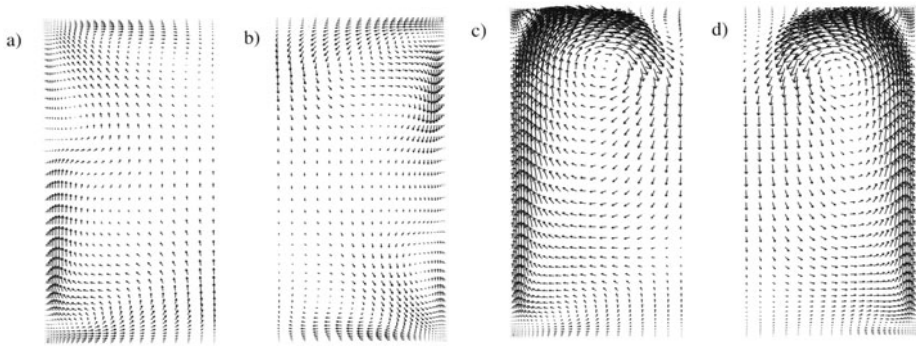


Figure 7. Mean velocity vectors projected on two cross-sections of each curved heated ducts : a) concave heated wall at $s/D_h = 1$, b) convex heated wall at $s/D_h = 1$, c) concave heated wall at $s/D_h = 8.32$, d) convex heated wall at $s/D_h = 8.32$. The concave wall is at the bottom and the convex wall is at the top of each section n.

(κ being the thermal conductivity) in the central plane of the ducts non-dimensionalized by its averaged value on the whole heated wall,

$$Q_{wm} = \frac{1}{12.4 D_h^2} \int_0^{D_h} \int_0^{12.4 D_h} Q_w(s, z) ds dz,$$

for both cases of heating in the curved ducts (see Fig. 9a) and in the S-shape duct (see 9b). As shown by Salinas and Métais (2002), strong ejections in the middle plane of the heated wall induce a strong reduction of the heat flux in that

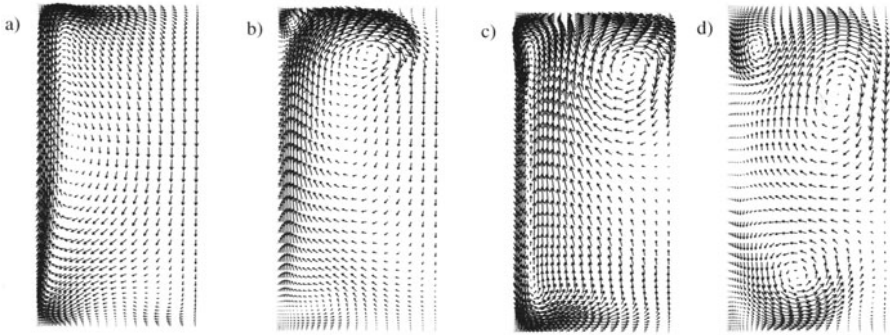


Figure 8. Mean velocity vectors projected on four cross-sections of the heated s-duct for a) $s/D_h = 2$, b) $s/D_h = 5$, c) $s/D_h = 7.5$, d) $s/D_h = 13$. The concave-convex heated wall is at the bottom of each section.

plane : indeed, the transport of the hot fluid away from the heated wall gives rise to a region where the temperature is quasi-homogeneous. It is associated with weak temperature gradients and therefore weak heat fluxes. When the convex wall of the curved duct is heated, the heated wall sees first the formation of ejections in its straight part before the curvature and second the formation of a strong normal flow associated with the Görtler vortices. Both ejections imply a continual decrease of the heat flux in the duct central plane. Conversely, when the concave wall is heated, the early decrease in the straight part is followed by a strong increase. This second stage is attributable to the formation of the Görtler vortices which induce an intense transport of cold fluid away from the convex towards the concave hot wall: this amplifies the temperature gradients near the concave wall and consequently the heat flux. At the end of the curved part, the difference between the two fluxes is maximal: concave wall heating yields a heat flux five times higher than convex wall heating. Downstream from the curved part, the intensity of the Görtler vortices decreases. The ejection of hot fluid near the heated convex wall is weaker, therefore the heat flux increase slightly. It implies also a reduction of the secondary flow intensity driving cold fluid from the core toward the heated concave wall, this means a weaker heat flux. For the S-shape duct, we observe similar effects. The first curved wall is associated with an increase of the heat flux since the heated wall is concave. A diminution due to the oblique straight part follows. When the heated wall becomes convex, the formation of two new counter-rotating structures near this wall enhance the ejection of hot fluid implying a sharp decrease of the heat flux.

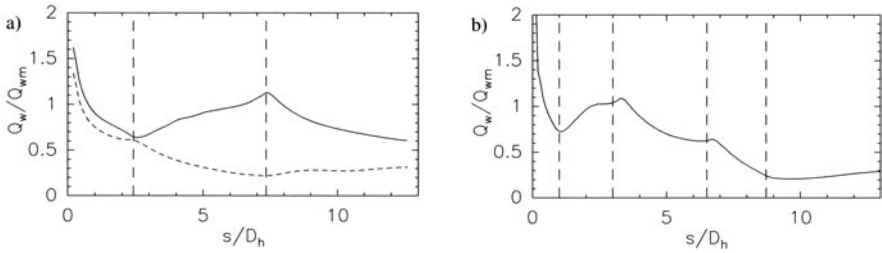


Figure 9. Mean heat flux in the duct central plane non-dimensionalized by its averaged value on the heated wall a) in the curved duct with heating applied on the concave wall —, on the convex wall - - b) in the S-shape duct on the heated concave-convex wall

5. Conclusion

LES of the turbulent flow in curved and S-shape ducts of square cross-section have been carried out to investigate curvature effects. We have observed that an intense secondary motion develops perpendicular to the mean flow, due to the imbalance between the centrifugal force and the radial pressure gradient. In the curved duct two quasi-steady counter rotating vortices of Görtler type appear near the convex wall. In the S-shape duct, the two successive curvatures generate four longitudinal structures. We have next investigated the combined effects of curvature and heating and separately considered the case of heating applied on a concave wall and heating applied on a convex wall. In agreement with previous findings, we observe that the application of heating on a duct wall yield the formation of an ejection in the central plane of the heated wall. In this study, we found that when the concave wall is heated, the ejection from the heated wall has difficulties to develop since it is in competition with the normal flow away from the convex wall associated with the Görtler vortices. In that case, the heated flux are important ought to the enhanced temperature gradients near the heated wall. When the convex wall is heated, the heating enhances the ejection of hot fluid away from the heated wall associated with the Görtler vortices. This strong ejection of hot fluid corresponds with a very weak heat flux near the heated wall.

Acknowledgments:

Some of the computations were carried out at the IDRIS (Institut du Développement et des Ressources en Informatique Scientifique, Paris). This work was sponsored by the CNES and the CNRS.

References

- Dubief, Y., Delcayre, F.: *On coherent-vortex identification in turbulence*, Journal of Turbulence, vol. **1**, 11, (2000).
- Hoffmann, P.H., Muck, K.C., Bradshaw, P.: *The effect of concave surface curvatures on turbulent boundary layers*, J. Fluid Mech., vol. **161**, pp. 371-403, (1985).
- Humphrey, J.A.C., Whitelaw, J.H., Yee, G.: *Turbulent flow in a square duct with strong curvature*, J. Fluid Mech., vol. **103**, pp. 443-463, (1981).
- Hunt, I.A., Joubert, P.N.: *Effects of small streamline curvature on turbulent duct flow*, J. Fluid Mech., vol. **91**, pp. 633-659, (1979).
- Hunt, J., Wray, A., Moin, P.: *Eddies, stream, and convergence zones in turbulent flows* Center of Turbulence research, J. Fluid Mech., CTR -**S88**, (1988).
- Kennedy, C.A., Carpenter, M.H.: *Comparison of several numerical Methods for simulation of compressible shear layers*, NASA technical paper, **Paper 3484**, (1997).
- Kim, W.J., Patel, V.C.: *Origin and decay of longitudinal vortices in developing flow in a curved rectangular duct*, J. Fluids Engineering, vol. **116**, pp. 45-52, (1994).
- Lesieur, M., Métais, O.: *New trends in large eddy simulations of turbulence*, Ann.Rev.Fluid Mech., vol. **28**, pp. 45-82, (1996).
- Poinsot, T., Lele, S.: *Boundary conditions for direct simulations of compressible viscous flows*, J. Comput Phys., vol. **101**, pp. 104-129, (1992).
- Salinas Vazquez, M., Metais, O.: *Large-eddy simulation of spatially growing thermal boundary layer in a turbulent square duct*, Direct and Large-Eddy Simulation, **IV**, pp. 277-284, Kluwer Academic Publishers, (2001).
- Salinas Vazquez, M., Metais, O.: *Large-eddy simulation of the turbulent flow through a heated square duct*, J. Fluid Mech., vol. **453**, pp. 201-238, (2002).
- Saric, W.S.: *Görtler vortices*, Ann. Rev. Fluid Mech., vol. **26**, pp. 379-409, (1994).
- Silva Lopes, A., Piomelli, U., Palma, J.M.L.M.: *Large eddy simulation of the flow in an S-duct*, AIAA, **2003-0964**, (2003).
- Toe, R., Ajakh, A., Peerhossaini, H.: *Heat transfer enhancement by Görtler instability*, Int. Journal of Heat and Fluid Flow, vol. **23**, pp. 194-204, (2002).
- Yee, G., Chilukuri, R., Humphrey, J.A.C.: *Developing flow and heat transfer in strongly curved ducts of rectangular cross section*, Journal of Heat Transfer, vol. **102**, pp. 285-291, (1980).

LARGE EDDY SIMULATION OF A FLOW WITH MULTIPLE STREAMWISE CURVATURES

A. Silva Lopes¹, U. Piomelli² and J.M.L.M. Palma¹

¹*Faculdade de Engenharia da Universidade do Porto, Porto, Portugal*
asl@fe.up.pt, jpalma@fe.up.pt

²*Department of Mechanical Engineering*
University of Maryland, College Park, MD 20742, USA
ugo@eng.umd.edu

Abstract The flow in an S-duct at $Re_b = 2U_b h_{in} / \nu = 13,800$ was modeled by large-eddy simulation, using a Lagrangian-dynamic eddy-viscosity subgrid-scale model and a non-orthogonal grid system. The stabilizing and destabilizing effects due to convex and concave curvature were predicted by the numerical method. The major changes in the turbulence occurred in the regions of curvature change, where the boundary layers were subjected to pressure gradients. The instantaneous streamwise velocity fluctuations showed a regular, well-organized pattern of low- and high-speed streaks, probably due to the Taylor-Görtler vortices commonly seen in boundary layers near concave surfaces. An unsteady separation region, with multiple recirculation bubbles, was observed in the transition region between the convex and concave regions.

Keywords: Large-eddy simulation, curved ducts, turbulence.

1. Introduction

The effects of streamline curvature on turbulence have been the subject of various studies and it is well-known that concave and convex curvature respectively increase and decrease radial mixing relatively to a flat surface (Kármán, 1934; Bradshaw, 1973; Patel and Sotiropoulos, 1997). The destabilizing effect of the concave surfaces is enhanced by the presence of Taylor-Görtler vortices, which transport streamwise momentum in the wall normal direction and increase turbulence production by a secondary-strain field. The importance of these vortices in the instability of laminar curved boundary layer is well-established (Saric, 1994), but in turbulent flows their presence is more difficult to visualize. Works like Petitjeans and Wesfreid, 1994, suggest that they are only promoted by non uniformities in upstream flow.

A review of experimental and numerical studies of curved flows can be found in Patel and Sotiropoulos, 1997. We only point out that most of the experimental or numerical works (Barlow and Johnston, 1988; Moser and Moin, 1987; Lund and Moin, 1996) study the effect of a single curvature. The study of curvature changes received less attention, despite the practical importance given by the occurrence in many engineering devices.

Our objective is to present the results of large-eddy simulations of the flow in an S-duct. This flow has all the possible curvature changes involving flat surfaces, concave and convex curvatures and was previously studied by Bandyopadhyay and Ahmed, 1993, who used an S-shaped wind tunnel. Our goal is to provide both statistical data and instantaneous flow visualizations. In this article we report the results of an initial simulation at a lower Reynolds number than the experimental work. In the next section, the numerical model and technique used will be described. The numerical results will be presented and some conclusions will be drawn.

2. Model

The continuity and the Navier-Stokes equations for the filtered velocity and pressure fields are:

$$\frac{\partial \bar{u}_i}{\partial x_i} = 0, \quad (1)$$

$$\frac{\partial \bar{u}_i}{\partial t} + \frac{\partial (\bar{u}_j \bar{u}_i)}{\partial x_j} = \frac{2}{Re_b} \frac{\partial^2 \bar{u}_i}{\partial x_j \partial x_j} - \frac{\partial \tau_{ij}}{\partial x_j} - \frac{\partial \bar{p}}{\partial x_i}, \quad (2)$$

The equations were made dimensionless by the bulk velocity at the inlet U_b and the duct half-height at the inlet h_{in} ; the bulk Reynolds number is thus defined as $Re_b = 2U_b h_{in} / \nu$, where ν is the kinematic viscosity of the fluid. $\tau_{ij} = \overline{u_i u_j} - \bar{u}_i \bar{u}_j$ are the subgrid stresses, modeled in this study using the Lagrangian dynamic approach proposed by Meneveau et al., 1996.

2.1 Physical domain and boundary conditions

The physical domain was an S-shaped duct, composed of an initial flat section, two curved sections and another flat section, each one (flat or curved) 504 mm long; the radius of the curves was also 504 mm. The walls were slightly divergent (with an angle of 0.2°), to keep a near-zero pressure gradient along the centerline. At the inlet section the distance between the two walls was $2h_{in} = 102$ mm and $2h_{out} = 116$ mm at the outlet. The spanwise width of the computational domain was πh_{in} . This is the same geometry as used in the experimental work, with the exception that in the experiment side-walls were present, whereas in our simulation periodic boundary conditions are used, and

the simulations were conducted at $Re_b = 13,800$, while the experiments were at $Re_b = 50,400$. Calculations at a higher Reynolds number are underway. To mimic the experimental setup, which at the inlet section had two boundary layers separated by an inviscid core, we used the rescaling technique proposed by Lund et al., 1998, with a boundary-layer thickness $\delta/h_{in} = 0.08$. Since the Reynolds-number of the LES was lower than that of the experiment by a factor of four, the local Reynolds number (based on free stream velocity and momentum thickness) is $Re_\theta = 60$. Under these conditions, the applicability of the rescaling method (which was based on high Reynolds-number considerations) is dubious. Therefore, we also performed calculations in which isotropic turbulence was added to the mean velocity profile obtained with the rescaling and others in which the instantaneous velocity profile from a fully developed turbulent channel-flow calculation was imposed at the inlet.

At the walls, no-slip conditions were used, while the convective condition $\partial \bar{u}_i / \partial t + U_b \partial \bar{u}_i / \partial x = 0$ was used at the outlet. To avoid any perturbation from the outlet condition in the region of interest, a buffer layer of length $10h_{in}$ was appended to the physical domain.

2.2 Numerical technique

The differential equations were discretized on a non-staggered grid using the finite volume approach and a coordinate transformation to calculate the derivatives with respect to the Cartesian directions. Both convective and diffusive fluxes were approximated by second-order central differences. The temporal discretization was performed using a fractional-step procedure and a Runge-Kutta scheme with four sub-steps and third-order accuracy. The Poisson equation was solved by an iterative SIP method, and the code was parallelized by a domain-decomposition technique with MPI message-passing routines.

3. Results and Discussion

A grid refinement study was performed, to assess the accuracy of the simulations. Four different grids were used: a coarse grid with $320 \times 80 \times 48$ nodes (streamwise, wall-normal and spanwise directions), an intermediate one with $484 \times 96 \times 64$ nodes, a fine one with $724 \times 112 \times 96$ nodes and a very fine grid with $932 \times 112 \times 128$ nodes. The grids were uniform in the spanwise direction and stretched in the wall-normal direction using a hyperbolic tangent function. In the streamwise direction they were stretched near the inlet and expanded near the outlet; the very fine grid was also refined in the region of curvature change (where the streamwise spacing was half of that in the fine one).

The skin-friction coefficient ($C_f = 2\tau_w / \rho U_b^2$) obtained with the different grids is compared in Fig. 1a. Differences exist mainly in the top wall, where the

boundary layer separates intermittently; elsewhere, the three finest meshes seem to have reached convergence.

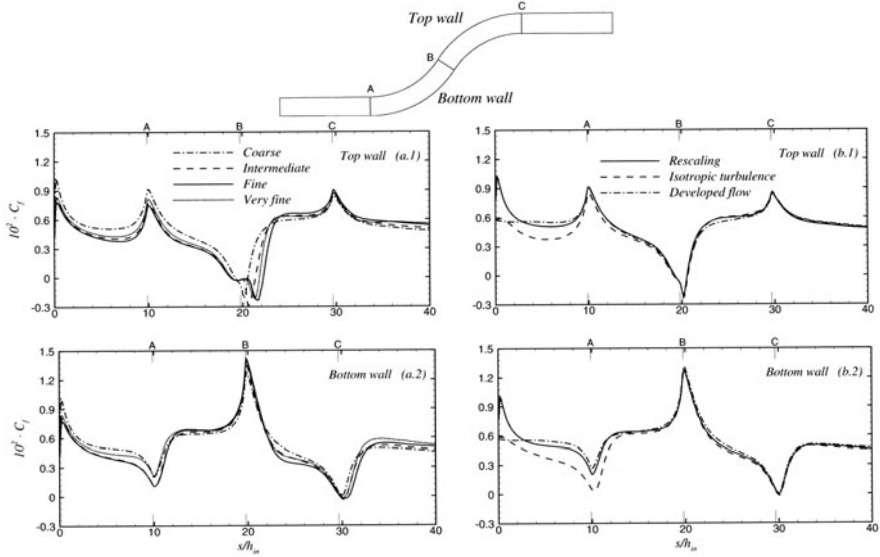


Figure 1. Skin friction coefficient distribution obtained from simulations using different grids (a) and different inlet conditions (b).

A comparison performed between the different inlet conditions (rescaling, isotropic turbulence and fully-developed channel-flow), using the coarse grid, showed differences in the skin-friction essentially limited to the first flat section (Fig. 1b). An increase in C_f near the inlet in the simulation performed with the rescaling was due to the low Reynolds-number effects, that caused the thin boundary layer to revert to a laminar profile. After the end of the first flat section (location A), however, the differences between the various simulations are small. Other comparisons also indicated that the inlet conditions do not affect significantly the flow after the first curvature change.

3.1 Mean statistics

The results presented in this section are from a simulation performed with the very fine grid and the developed channel-flow inlet condition, which was preferred to the rescaling technique. The near-wall flow experiences a favorable pressure-gradient (FPG) when the convex curvature begins, and an adverse one (APG) when the concave curvature begins. The acceleration or deceleration of the near-wall flow has significant implications both on the dynamics of the mean flow and on the turbulent eddies: the FPG has a stabilizing effect on tur-

bulence, the APG a de-stabilizing one; unsteady separation could be observed (at this Reynolds number) whenever there was an APG.

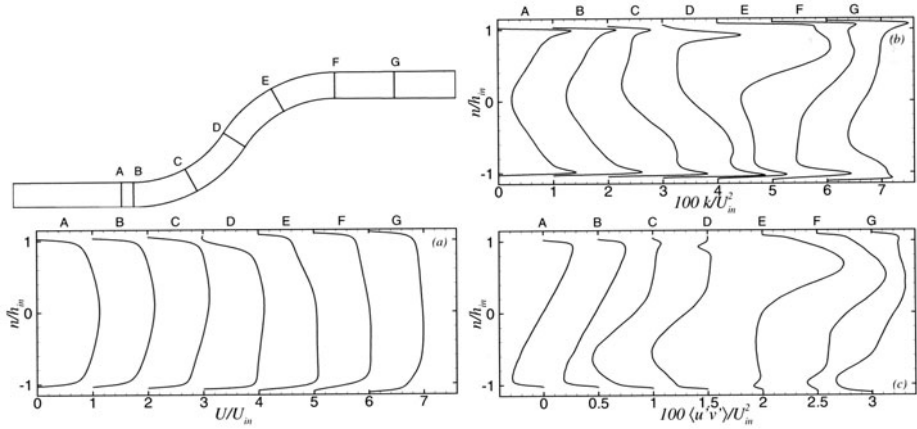


Figure 2. Mean velocity (a), turbulent kinetic energy (b) and shear stress (c) profiles at $s/h_{in} = 8.9$ (A), 9.9 (B), 14.8 (C), 19.8 (D), 24.7 (E), 29.6 (F) and 34.6 (G).

The mean velocity, turbulent kinetic energy ($k = \langle u_i'^2 \rangle / 2$) and Reynolds shear-stress ($\langle u'v' \rangle$) profiles at several locations are shown in Fig. 2. The mean velocity profile is symmetric in the first flat section (section A), but becomes asymmetric at the beginning of the first curve (section B). In the first curve, it becomes fuller close to the concave wall (section C), due to the enhanced mixing caused by the curvature (Lund and Moin, 1996) and amplified by the pressure gradients in the transition to the curve (APG on the bottom wall, FPG at the top). Also, the mean velocity normalized by the local friction velocity ($u_\tau = (\tau_w/\rho)^{1/2}$) remains below the logarithmic law on the concave side, above it on the convex one, as in Moser and Moin, 1987. The pressure gradients and the curvature cause the turbulent kinetic energy and Reynolds shear stress to increase on the concave wall, decrease on the convex one. Moser and Moin, 1987, observed the same behavior, but found that the differences between the two sides are decreased if the local wall-stress is used to normalize the data. In our case they remain significant even under this rescaling, which can be due to the smaller radius of curvature in our calculation (lower by a factor of 8), and also to the intermittent separation that was observed in the transition between the flat and the concave regions, due to the APG, which decreases the mean wall-stress and increases the asymmetry of the normalized profile. The growth of the turbulent kinetic energy on the concave wall is due to $\langle v'^2 \rangle$ and $\langle w'^2 \rangle$, while $\langle u'^2 \rangle$ varies little; on the convex side, all the normal stresses decrease.

The separation in the transition between the two curves (near section D) increases turbulence production and interacts with the curvature and pressure-gradient effects to create larger modifications of the turbulence in the second curved section (since the entering flow is already significantly out of equilibrium) and to increase the Reynolds stresses. In the second curve, as in the first, stronger changes occur on the concave side: the turbulent kinetic energy and the shear stress display a two-layer structure, with one peak near the concave wall, and another closer to the duct center (sections E and F), a behavior also observed in the boundary layer over a bump Wu and Squires, 1998. The near-wall peak in the turbulent kinetic energy is displayed only by the $\langle u'^2 \rangle$ stress and results from the recovery of the inner shear production corresponding to the sudden friction increase and the formation of a new internal layer; the internal layer with the decaying peak further away from the wall is a remnant of the one formed by the adverse pressure gradient and most of its turbulent kinetic energy comes from the $\langle v'^2 \rangle$ and $\langle w'^2 \rangle$ stresses.

The transition from the second curve to the final recovery region follows a behavior similar to the previous one. The flow separates near the bottom wall, enhancing the turbulence production and, therefore, increasing the turbulent kinetic energy and the shear stresses (sections F and G). In the final recovery region the flow relaxes to the flat-plate laws (section G).

3.2 Instantaneous fields

Contours of the streamwise velocity fluctuations in two planes close to the lower and upper walls display a very regular array of low- and high-speed streaks on the lower wall in the curved regions (Fig. 3). Their spacing is approximately h_{in} or 200 wall units (using the value of u_τ at the beginning of the curved section). The streaks are more coherent and well-organized than typical in flat-plate boundary layers — compare with the first flat section or the recovery region. This could be due to the FPG in the transition between the two curves (which tends to make the streaks longer, see Piomelli et al., 2000); however, since the streaks appear well before that transition, it is more likely that the cause are well-organized roll cells or Taylor-Görtler vortices that form near concave surfaces. The streamlines in the cross-plane ($n - s$) confirm this conjecture.

In the transition between the two curves the flow was found to separate intermittently. The long-time averaged streamlines show a single bubble along the wall. Instantaneous visualizations, however, highlight a complex topology with two bubbles, whose size and positions are time-dependent (Fig. 4). Furthermore, near the wall, a very small bubble rotating in the opposite direction of the large ones can be observed at some instants, and a reattachment of the main flow (as in Fig. 4b) at others.

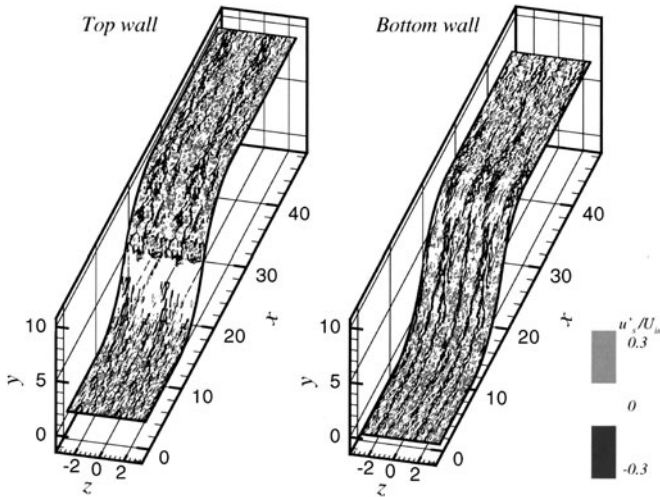


Figure 3. Contours of the streamwise velocity fluctuations in planes parallel to the walls.

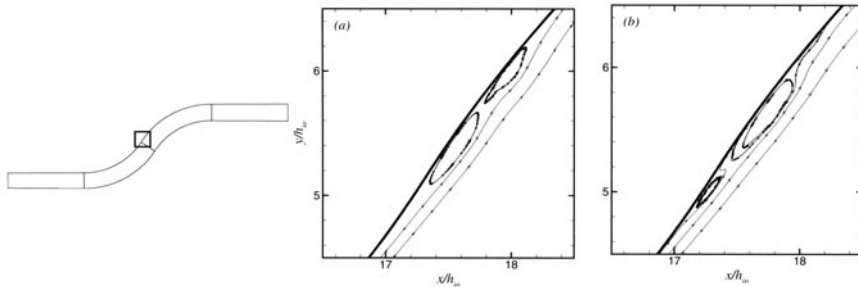


Figure 4. Instantaneous streamlines near separation at different times.

4. Conclusions

The large-eddy simulation of the flow in an S-shaped duct was performed. This flow can be considered composed of elementary blocks: the first flat region, the first curve, the second curve, the final recovery region and the transitions between any two consecutive regions. The boundary-layer features in the transition regions were essentially dictated by the pressure gradient (favorable if it was going to a convex or leaving a concave region and adverse if it was going to a concave or leaving a convex region) and not by the curvature. In the curved regions we observed an increase of turbulent activity on the concave side, a corresponding decrease in the convex one. The convex-to-concave curvature transition region exhibited an instantaneous separation with

two bubbles, whose size and position were time dependent, and periods of reattachment between the bubbles. This separation caused also the flow in the second curved region to be significantly different from that in the first one. The boundary layer exhibited intermittent separation every time it was subjected to an adverse pressure gradient, which increased the turbulence production. Visualization of the streamwise turbulent fluctuations showed coherent structures along the concave walls; these well-ordered structures are an indication of the presence of Taylor-Görtler vortices.

Acknowledgments

A. Silva Lopes acknowledges partial support by the Portuguese Foundation for Science and Technology (FCT) through grant SFRH/BPD/5674/2001. The work was partly sponsored by contract Bullet N. 33980/99. A. Silva Lopes and U. Piomelli acknowledge the partial support of the Office of Naval Research through Grant N000140110993, monitored by Dr. R.D. Joslin. Part of the computational time used was provided by the National Center for Supercomputing Applications (U.S.A.).

References

- Bandyopadhyay, P.R. and Ahmed, A. (1993). Turbulent boundary layers subjected to multiple curvatures and pressure gradients. *J. Fluid Mech.*, 246:503–527.
- Barlow, R.S. and Johnston, J.P. (1988). Structure of a turbulent boundary layer on a concave surface. *J. Fluid Mech.*, 191:137–176.
- Bradshaw, P. (1973). *Effects of Streamline Curvature on Turbulent Flow*. AGARD — Advisory Group for Aerospace Research & Development, AGARDograph N. 169.
- Kármán, T. (1934). Some aspects of the turbulence problem. In *Proc. Fourth Int. Congress of Applied Mechanics*, page 54. Cambridge University.
- Lund, T.S. and Moin, P. (1996). Large-eddy simulation of a concave wall boundary layer. *Int. J. Heat Fluid Flow*, 17:290–295.
- Lund, T.S., Wu, X., and Squires, K.D. (1998). Generation of turbulent inflow data for spatially-developing boundary layer simulations. *J. Comput. Phys.*, 140(2):233–258.
- Meneveau, C., Lund, T.S., and Cabot, W.H. (1996). A Lagrangian dynamic subgrid-scale model of turbulence. *J. Fluid Mech.*, 319:353–385.
- Moser, R.D. and Moin, P. (1987). The effects of curvature in wall-bounded turbulent flows. *J. Fluid Mech.*, 175:479–510.
- Patel, V.C. and Sotiropoulos, F. (1997). Longitudinal curvature effects in turbulent boundary layers. *Prog. Aero. Sci.*, 33:1–70.
- Petitjeans, P. and Wesfreid, J.E. (1994). Spatial evolution of Görtler instability in a curved duct of high curvature. *AIAA J.*, 34:1793–1800.
- Piomelli, U., Balaras, E., and Pascarelli, A. (2000). Turbulent structures in accelerating boundary layers. *J. of Turbulence*, 1:001.
- Saric, W.S. (1994). Görtler vortices. *Annu. Rev. Fluid Mech.*, 26:379–409.
- Wu, X. and Squires, K.D. (1998). Numerical investigation of the turbulent boundary layer over a bump. *J. Fluid Mech.*, 362:229–271.

COMPARISON OF SOME SGS MODELS FOR TURBULENT FLUXES OF MOMENTUM AND A PASSIVE SCALAR IN SWIRLING CO-ANNULAR JETS

Robert Zoltan Szasz, Johan Revstedt and Laszlo Fuchs

Lund Institute of Technology

Dept. of Heat and Power Engineering

robert-zoltan.szasz@vok.lth.se

Abstract LES computations have been carried out in a geometry involving three co-annular swirling jets. Three explicit models are compared to the case without any explicit model. The influence on the mean values have found to be small, while the fluctuations are influenced in the developing region of the jets. The magnitude of the dissipation effect is dominating over other effects of the sub-grid scales (such as backscatter and non-local effects). Using implicit dissipation (based upon the numerical scheme) is not a problem if the spatial resolution is adequate and when the inertial sub-range is well resolved. Three SGS models for the scalar transport equations have also been evaluated. The passive scalar is affected both by the momentum SGS terms as well as the SGS term of the scalar equation.

Keywords: LES, SGS, IMP, DDM, SSM, EDM, Swirl

1. Introduction

The increasing environmental restrictions, in particular with respect to levels of NO_x , require the development of new combustion technologies. Lean premixed or partially premixed combustion is a method for reducing the formation of so-called thermal NO_x . However, lean combustion is inherently less stable. In addition, the flame has to be anchored within the chamber. In most gas turbines this flame-holding is achieved by the inflow swirl. At sufficiently high levels of swirl an internal recirculation zone is formed. This increases the residence time of the fuel and helps to re-ignite eventually unburned mixtures.

A crucial problem for such burners is related to the instability of the flame. A common source of such instability is believed to be related to thermo-acoustical mechanisms. In addition, one finds fluid-dynamical instabilities due to swirl and the shear-layers of the co-annular jets. These instabilities lead to vortex-breakdown, precession of the separation bubble and the possible formation of multiple modes of spiral type, occurring also in the turbulent regime. Axi- and asymmetric instabilities in low Reynolds number flows have been studied experimentally, recently by Loiseleux and Chomaz [6].

Another essential factor for combustion is the turbulent mass transfer of the injected fuel. Inhomogeneities of the fuel-air mixture, besides contributing to flame instability, often leads to "hot spots" and as a result to the increase of emission levels. Naughton et al. [7] observed enhanced mixing in the case of swirling jets, as compared to the non-swirling counterparts. The better mixing was explained by the authors with the increased turbulence levels and longer residence time.

Here, LES computations of the isothermal flow field in a gas turbine combustion chamber are presented. Previous studies on the same geometry [11] revealed high sensitivity of the flow field to the combustion chamber size and swirl level, while the Reynolds number was found to be less important. The present paper focuses on the influence of the SGS models on the flow field and mixing. Three explicit SGS models are considered (Scale Similarity Model, Dynamic Divergence Model and Exact Differential Model) both for the momentum and scalar transport equations. The results are compared with the base case involving no explicit SGS model. In a different co-annular swirling flow field Gullbrand et al. [3] obtained small differences in the mean values corresponding to different SGS models. However, they observed significant influence on the turbulent fluctuations.

2. Problem description

We consider the flow field in a geometry corresponding to a single burner of a gas turbine combustion chamber. Three co-annular swirling jets are injected into the combustion chamber, providing 8%, 17% and 75% of the total mass flux, respectively. The swirler vanes have angles of 45° , 38° and 52° . In the computations all lengths are normalized with the outer diameter of the outer swirler. The combustion chamber has a rectangular cross section of 3×3 diameters and a length of 8 diameters.

3. Numerical methods

The flow is considered to be incompressible and isothermal. Mixing has been studied by injecting a uniformly distributed, passive scalar through the middle swirler. The Schmidt number is taken to be equal to unity.

$$u_{i,i} = 0 \quad (1)$$

$$u_{i,t} + u_j u_{i,j} = -p_{,i} + \frac{1}{Re} (u_{i,j})_{,j} \quad (2)$$

$$c_{,t} + u_j c_{,j} = \frac{1}{ReSc} (c_{,j})_{,j} \quad (3)$$

The computational domain is discretized using a Cartesian staggered grid with the possibility of having local refinements in regions with high gradients. Each refinement level implies halving the grid size in all three-directions. The finest local grid has 64 intervals, in each direction, across the inlet. A retrospective study shows that the spatial resolution is by an order of magnitude smaller than the computed longitudinal Taylor micro-scale in the proximal part of the burner. Thus, the spatial resolution is more than adequate for LES. The solver is based on the finite differences method with third order discretization of the convective terms and fourth order discretization of the diffusive terms, respectively. Implicit iterations are used for the Navier-Stokes equations and an explicit four-step Runge-Kutta method for the scalar transport.

At the inlet constant values of the velocity components are imposed complying with the given mass flow and swirl angle through each of the co-annular inlets. The resulting Reynolds number, based on the outer swirler diameter, is 20000. No-slip velocity is imposed on the side-walls, while at the outlet flux-conserving zero gradient boundary conditions are applied.

3.1 Turbulence modeling

Eddy viscosity based models rely highly on turbulence isotropy. This is not the situation in most practical applications. Nejad et al. [8] demonstrated that $k - \epsilon$ based models cannot handle swirling flow fields in their standard form. Repp et al. [10] concluded that Reynolds-stress closure models predict better the main features of the flow field, however, the spreading rate of the jets were underestimated. In contrast to these turbulence models, Large Eddy Simulations (LES) have the potential of handling not only non-isotropic turbulence, but also transitional flows and flows that contain, in addition to turbulence, also coherent structures. These characteristics are features of the swirling flows under consideration here.

Three different explicit SGS models are compared with the base case, which is a computation without an explicit SGS model (denoted as IMP in what follows). The three models are based on different ideas and they are described shortly in the following subsections.

3.1.1 No explicit SGS model (IMP). One of the purposes of the SGS models is to account for the dissipation of energy at the scales smaller than

the grid size. The truncation error of the numerical discretization has also a dissipative effect, which should be taken into account even when explicit SGS models are used. As it was pointed out by Olsson and Fuchs [9], this numerical dissipation is of the same order of magnitude as the SGS stress itself, when the resolution of the grid is high enough. In the IMP approach, the only physical effect that is accounted for is dissipation of turbulent kinetic energy on the small scales. This is achieved by the discretization scheme itself. The magnitude of the numerical dissipation can be estimated by:

$$\tau_{ij,j} = -\frac{1}{4} |\bar{u}_j| h^3 \frac{\partial^4 \bar{u}_i}{\partial x_j^4} \quad (4)$$

3.1.2 Scale Similarity Model (SSM). The SSM is based on the assumption that the resolved and unresolved stresses have similar behavior for different filters. In the computations, the model proposed by Liu et al. [5] is used:

$$\tau_{ij} - \frac{1}{3} \delta_{ij} \tau_{kk} = C_L (\widehat{\bar{u}_i \bar{u}_j} - \widehat{\bar{u}_i} \widehat{\bar{u}_j}) \quad (5)$$

The first filter (denoted by bar) was considered to be the implicit filtering by the discretization, while the second filter was a Gaussian filter with a filter size equal to the double grid size. The model constant, C_L , was imposed to be unity.

3.1.3 Dynamic Divergence Model (DDM). The dynamic SGS model proposed by Germano et al. [2] has a drawback due to the fact that the single model parameter is not uniquely determined. To avoid this difficulty, and to account for possible anisotropy of the SGS mode parameter, Held and Fuchs [4] proposed to apply the dynamic procedure to the divergence of the SGS stress tensors. In this way one parameter will be obtained for each direction. The model parameter is computed for each direction by:

$$C_d = \frac{L_{ij,j}}{\beta_{ik,k} - \hat{\alpha}_{il,l}} \quad (6)$$

where $L_{ij,j} = T_{ij,j} - \hat{\tau}_{ij,j} = (\widehat{\bar{u}_i \bar{u}_j} - \widehat{\bar{u}_i} \widehat{\bar{u}_j})_{,j}$ is the divergence of the resolved stress, $T_{ij,j} = C_d \beta_{ij,j}$ the divergence of the Subtest Stress Tensor, and $\tau_{ij,j} = C_d \alpha_{ij,j}$ the SGS stress tensor. For further details refer to [4].

3.1.4 Exact Differential Model (EDM). One may show that by requiring specific forms for the averaging kernel, an (almost uniformly) exact de-filtering can be computed from the filtered data [1]. By applying directly the

explicit relation between the filtered and unfiltered data, Fuchs [1] obtained explicit expressions for the SGS stress tensor:

$$\tau_{ij,j} = -\Delta^2 \left(\frac{\partial \tilde{u}_i}{\partial t} + \frac{\partial \tilde{u}_i \tilde{u}_j}{\partial x_j} + \frac{\partial \tilde{u}_j \tilde{u}_i}{\partial x_j} - \Delta^2 \frac{\partial \tilde{u}_i \tilde{u}_j}{\partial x_j} + \frac{\partial \tilde{p}}{\partial x_i} - \mu \frac{\partial^2 \tilde{u}_i}{\partial x_j \partial x_j} \right) \quad (7)$$

where tilde denotes the Laplacian of the variable. The expression includes both space- and time-derivatives which shows that the SGS model can be only approximately expressed in terms of local variables and spatial-gradients.

4. Results and discussions

4.1 Flow turbulence

The swirling flow forms a large central recirculating region. Smaller recirculating regions are formed near the corners of the combustion chamber. The different SGS models yield very similar results in terms of the extent of the recirculation regions (both the primary and near the corners). However, downstream of the primary recirculation zone one can observe the effects of the SGS terms. These effects are seen in the mean velocity distribution at downstream stations.

The radial profile of the mean axial velocity component at 0.5 diameters downstream is shown in Figure 1. One can observe that the jets are merged already at this distance. Furthermore, the velocity profiles are almost identical, indicating no influence of the SGS models in this region. Further downstream the influence is more evident. Figure 2 presents the axial velocity profile along a radial line at four diameters. A stronger recirculation can be observed for DDM and IMP. For the tangential velocity profile (See figure 3) a near solid-body rotation is observed. The different SGS models behave similarly, except the SSM, which resulted in higher angular speed.

Table 1 compares the Max and L2 norms of the divergence of the SGS stresses computed by the different models. Additionally, the magnitude of the numerical dissipation (estimated by (4)) is given. The SGS stresses are evaluated on a grid with a spacing of $H = 0.0625$. As one can observe, the numerical dissipation is significantly larger than any of the explicit SGS models. This may explain the low influence of the SGS models on the mean velocity values. The magnitude of the SGS stresses is similar in streamwise and spanwise directions. DDM predicts larger SGS stresses than SSM or EDM. It should be noted that the estimate of the truncation errors is applicable only for the smooth components of the solution and the values given here are overestimated, since they are based on the instantaneous data. Hence, the primary comparison should be in terms of the size of the explicit SGS models. For example, here as for

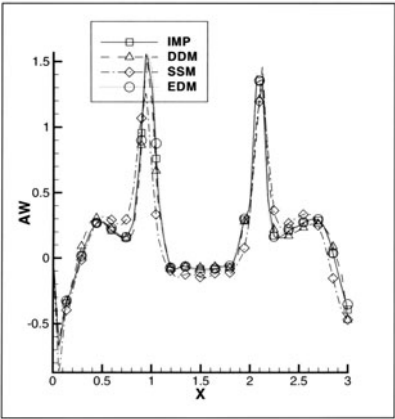


Figure 1. Average axial velocity at Z=0.5

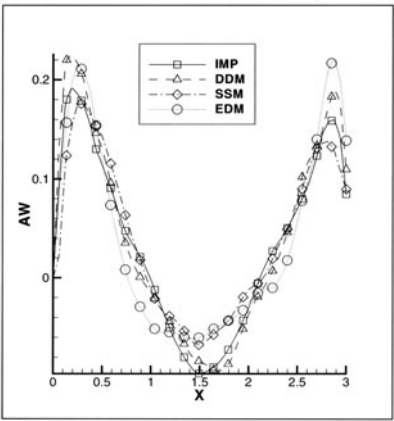


Figure 2. Average axial velocity at Z=4.0

other developing jets, [3], the strong backscatter of the SSM leads to faster development of the jet as compared to DDM or EDM.

Table 1. Comparison of the SGS stresses on level 5 with grid spacing $H=0.0625$

Direction	Max Norm			L2 Norm		
	x	y	z	x	y	z
IMP	779086.3	760826.4	955673.9	13967.2	12853.8	16209.7
DDM	239126.8	431006.7	302219.4	3082.4	3320.1	4052.3
SSM	108811.7	120260.2	82077.0	2952.1	3096.2	3120.2
EDM	77498.6	100287.6	76826.0	1379.5	1393.9	1409.2

The sensitivity to SGS is larger for the fluctuating components. The SGS effects are mostly pronounced for the SSM, as compared to the other cases (Figure 4). Further downstream, however, all four models give similar levels of the velocity fluctuations. Along the centerline (not shown here) the highest rms values are obtained at around two diameters, corresponding to the central part of the internal recirculation zone.

The turbulent kinetic energy spectra at a point situated on the symmetry axis at one diameter downstream are presented in Figures 5 and 6 for the implicit and DDM models, respectively. In the case of the DDM model the spectrum follows the $-5/3$ line, on a wider range. One can observe that the ratio of the cut-off frequencies is two for the considered cases, due to the presence of explicit filtering in DDM.

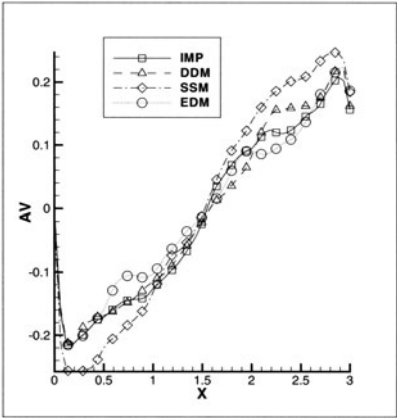


Figure 3. Average tangential velocity at $Z=4.0$

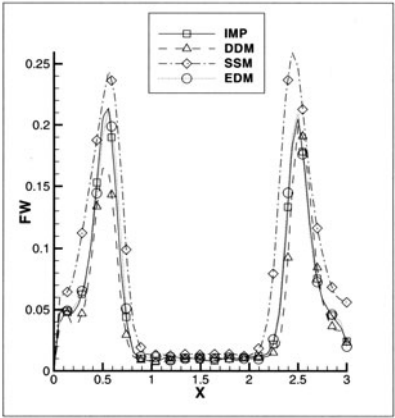


Figure 4. RMS of the axial velocity at $Z=1.0$

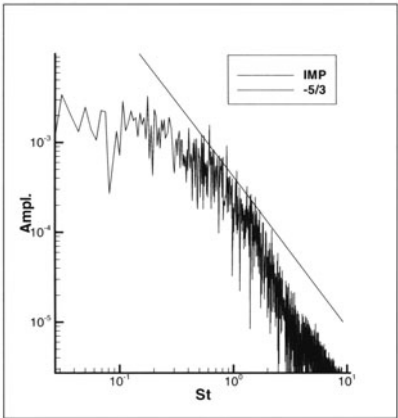


Figure 5. Turbulent kinetic energy spectra at $Z=1$, IMP

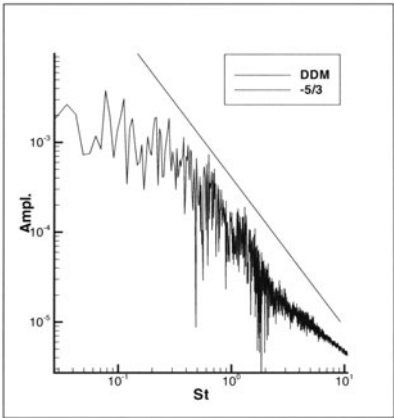


Figure 6. Turbulent kinetic energy spectra at $Z=1$, DDM

4.2 Mixing of passive scalar

Mixing was studied by evaluating a passive scalar injected at the second swirler. For the scalar transport equation three explicit SGS models were considered corresponding to the three explicit momentum SGS models: Concentration Dynamic Divergence Model (CDDM), Concentration Stress Similarity Model (CSSM) and Concentration Exact Differential Model (CEDM). These models are evaluated in comparison with a case without any explicit SGS model for the scalar transport.

Figure 7 shows the mean and rms values of the passive scalar along a radial line situated at one diameter downstream of the nozzle. The four lines correspond to results obtained with the different concentration SGS models. For the momentum equations no explicit model was used so that the effects of the SGS for the scalar can be isolated. The CIMP and CSSM models give similar results. The results obtained with the CDDM and CEDM models are also close to each other, however they predict higher concentration values with approximately 10%. The rms values present even larger differences. The lowest levels of fluctuations are predicted by the CSSM model. The largest scalar fluctuations were obtained using the CDDM model, the values are between 50-100% higher than in the CSSM case.

When using only the momentum SGS models, their effect on the scalar can be assessed. The results of the average concentration values reveals significant influence of the SGS models. The largest difference between the mean scalar concentrations are as much as 40% in the central part. EDM gives the lowest scalar concentrations, while the maximum values are obtained with the SSM model. The influence on the rms values is less pronounced (except the results corresponding to EDM). The results show that the momentum SGS model has a weaker effect on the scalar concentration fluctuations, than the SGS models of the scalar transport equation.

5. Concluding remarks

Three explicit SGS models for the momentum equations have been compared with a case without any explicit model. It was found that the influence on the mean velocity components is small. This is due to the fact that the magnitude of the explicit SGS models is small as compared to the order of magnitude of the dissipation due to the numerical discretization. This dissipation, however, is not unphysical since the inertial sub-range is well resolved by the computational grid. The SSM model produced larger velocity fluctuations than the other models close to the inlet region, while far from the inlet all models predicted similar values of turbulent intensity.

Three SGS models for the scalar transport equations were evaluated as well. Both the mean and rms concentration values were largely influenced by the

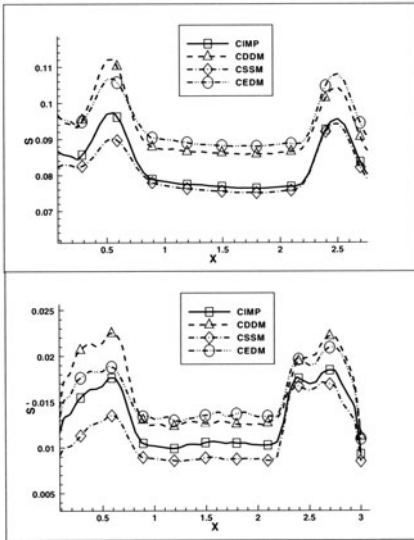


Figure 7. Mean (top) and rms scalar concentrations along a radial line at $Z=1$, computed with different concentration SGS models

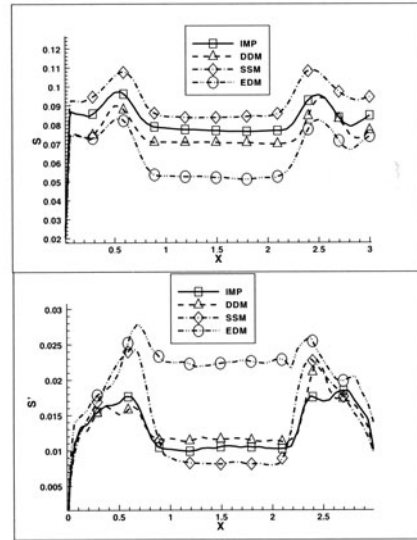


Figure 8. Mean (top) and rms scalar concentrations along a radial line at $Z=1$, computed with different momentum SGS models

concentration SGS model. The momentum SGS models were found to influence more the mean values than the concentration SGS models, whereas the rms profiles were affected in the opposite manner.

6. Acknowledgements

The financial support from the Swedish Research Council (VR) is greatly acknowledged. The authors would like to thank as well the computational facilities provided by the super-computing center at Lund University (LUNARC) and the Swedish National Supercomputer Center (NSC).

References

- [1] Fuchs, L. (1996). "An Exact SGS-Model for LES," In *Advances in Turbulence*, Kluwer Academic Publishers, Gavrilakis, L., Machiels, L., and Monkewitz, P.A. (editors), pp.23-26.
- [2] Germano, M., Piomelli, U., Moin, P., and Cabot, W.H. (1991). "A Dynamic Subgrid-scale Eddy Viscosity Model," *Phys.Fluids A*, Vol. 3, pp. 1760-1765.
- [3] Gullbrand, J., Revstedt, J., and Fuchs, L. (1999). "A Comparison of Subgrid Scale Models for Large Eddy Simulation of a Co-Annular Swirling Flow Field," *First Int. Symposium on Turbulence and Shear Flow Phenomena*, Banerjee, S. and Eaton, J.K. (editors), pp.747-752.

- [4] Held, J., and Fuchs, L. (1997). "Large Eddy Simulation of Compressible Separated Flow Around a NACA 0012 Wing Section", AIAA paper 97-1931.
- [5] Liu, S., Meneveau, C., and Katz, J. (1994). "On the Properties of Similarity Subgrid-Scale Models as deduced from Measurements in a Turbulent Jet," *J. Fluid Mech.*, Vol. 275, pp. 83-119.
- [6] Loiseleux, T., and Chomaz, J.M. (2003). "Breaking of rotational symmetry in a swirling jet experiment," *Phys. Fluids*, Vol. 15(2), pp. 511-523.
- [7] Naughton, J.W., Cattafesta, L.N., and Settles, G.S. (1997). "An experimental study of compressible turbulent mixing enhancement in swirling jets," *J. Fluid Mech.*, Vol. 330, pp. 271-305.
- [8] Nejad, A.S., Vanka, S.P., Favaloro, S.C., Samimy, M., Langenfeld, C. (1989). "Application of Laser Velocimetry for Characterization of Confined Swirling Flow", *J. of Engineering for Gas Turbines and Power*, Vol. 111, pp. 36-45.
- [9] Olsson, M., and Fuchs, L. (1996). "Large Eddy Simulation of the Proximal Region of a Spatially Developing Circular Jet", *Phys. Fluids*, Vol. 8, pp. 2125-2137.
- [10] Repp, S., Sadiki, A., Schneider, C., Hinz, A., Landenfeld, T., Janicka, J. (2002). "Prediction of swirling confined diffusion flame with a Monte Carlo and a presumed-PDF model", *Intl. J. of Heat and Mass Transfer*, Vol. 45, pp. 1271-128.
- [11] Szasz, R.Z., Caraeni, D.A., Fuchs, L. (2001). "Study of mixing in swirling turbulent jets," A. Pollard and S. Candel (editors.), *IUTAM Symposium on Turbulent Mixing and Combustion*, pp. 221-233.

4.4 FLOW CONTROL AND FLUID-STRUCTURE INTERACTION

LES OF CONTROLLED TURBULENT FLOW OVER A ROUNDED STEP

Jens Neumann and Hans Wengle

Institut für Strömungsmechanik und Aerodynamik, LRT WE 7

Universität der Bundeswehr München, 85577 Neubiberg, Germany

hans.wengle@unibw-muenchen.de

Abstract The influence of a passive (no external energy input) and an active (via energy input) control method on the flow characteristics of a turbulent separated and reattaching flow is investigated. A surface-mounted fence and an oscillating blowing/suction jet are utilized as passive and active control method, respectively. The impact of these methods is analyzed here for a flow with (a freely evolving) separation along a smoothly contoured convex surface. The results of large-eddy simulations (LES) of the turbulent flow over a rounded step at $Re_h = 9100$ reveal the importance of properly chosen control parameters which can lead to significant reductions of the size of the recirculating flow region.

Keywords: separation, reattachment, passive and active control, LES

1. Introduction

In many technological applications, flow control is applied to overcome the negative consequences (e.g. performance degradation) arising from the separation of a wall-bounded flow. One criterion (among others) for the classification of separated flows is to distinguish between separation fixed by sharp edges of the surface geometry and separation from smooth surfaces caused by adverse pressure gradients (Alving and Fernholz, 1996). For the development of control approaches in the past, studies of the physical and technological background were performed mainly based on the former category (denoted as geometry-induced separation) with the control applied to reduce the size of the separated flow region as much as possible. Especially for the extensively studied configuration of the flow over a backward-facing step with a fixed separation at the step edge, significant size reductions are reported for a number of different control approaches (see e.g. in Neumann, 2003). The goal of the present work is to adapt these methods to a flow with separation caused by an adverse pressure gradient which is generated by a mild convex curvature of the surface geometry. In this context, large-eddy simulations (LES) are performed

in order to assess the effects of the control, to detect dependencies on certain control parameters and to elucidate the underlying flow physics.

The scope of this study is restricted to a flow with an oncoming turbulent boundary layer and a two-dimensional geometry. For this purpose, the flow over a smoothly contoured (rounded) step at a Reynolds number of $Re_h = 9100$ (based on the step height, h , and the free-stream velocity, U_∞) was selected. A detailed experimental database (Song, 2002) is available for this flow. In a first step, the results of uncontrolled LES with different grids are validated in comparison to this experiment. Then, two particular open-loop control methods are applied: a *passive* method (no external energy input) using a small surface-mounted fence placed upstream of separation and an *active* method (via energy input) realized by a thin spanwise jet with time-periodic blowing/suction. The setup for the passive method can be compared with the non-oscillating version of the backward-facing step experiments of Miao et al., 1991. Similar methods of control by increasing the turbulence level upstream of separation are described in Isomoto and Honami, 1989. The active method is adapted from the experiments of Chun and Sung, 1996 for the backward-facing step. This method was also applied for diffuser flows by Obi et al., 1993 and Brunn and Nitsche, 2003. Viswanath et al., 2000 report on separation control of a rounded step flow using tangential blowing.

2. Numerical approach

The code MGLET, used here, is a finite-volume solver for the incompressible Navier-Stokes equations on staggered cartesian non-equidistant grids. A second-order central scheme is used for the spatial discretization. For the time advancement, an explicit second-order time step (leapfrog) is utilized. The dynamic Smagorinsky subgrid scale model is used. In order to represent arbitrarily shaped bodies (e.g. the rounded step) within the cartesian grid, an immersed boundary condition (Tremblay et al., 2002) is applied.

A fine grid with $N_x \cdot N_y \cdot N_z = 1008 \cdot 160 \cdot 303$ grid cells in streamwise (x), spanwise (y) and vertical (z) direction is employed for a highly resolved LES of the uncontrolled flow (keeping in mind the available computing resources). In order to assess the effects of control parameter variations (with less computational requirements), all LES with passive or active control are performed on a coarse(r) grid with $544 \cdot 80 \cdot 125$ grid cells. Both grids extend over the same domain $(L_x, L_y, L_z) = (42.0, 5.0, 7.2)$, measured in units of h . The inflow boundary is placed $18.0h$ upstream of the origin of the coordinate system which is located at the beginning of the circular curvature (with radius $6.05h$) of the rounded step (see *figure 1*).

For the passively controlled cases, the control fence with a moderate height, H_f , is positioned at X_f . The proper choice (of the combination) of these two

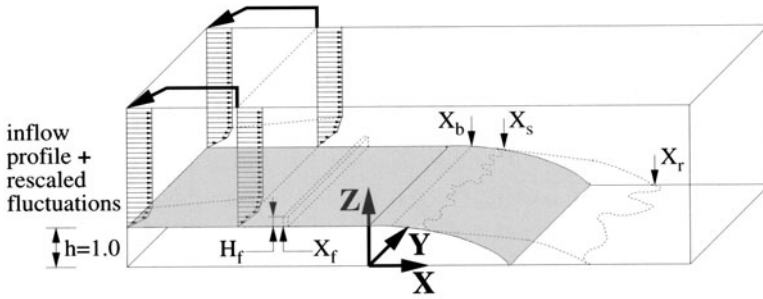


Figure 1. Schematic view of the flow

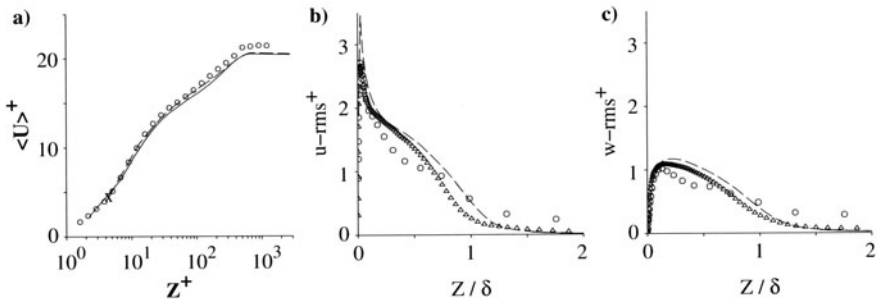


Figure 2. a) Mean streamwise velocity, $\langle U \rangle$, b) streamwise (u_{rms}) and c) vertical (w_{rms}) velocity fluctuations at $X = -6.67$: fine grid LES (full line, wall-nearest cell center at +), coarse grid LES (dashed line, wall-nearest cell center at x), experiments of Song, 2002 (circles), direct numerical simulation (DNS) of Spalart, 1988 at $Re_\theta = 1400$ (triangles)

parameters mainly determines the control success in the backward-facing step case (Neumann and Wengle, 2003). The active control jet is realized by imposing a time-periodically varying velocity for the wall-nearest grid cells at a position X_b . Then, the corresponding forcing amplitude, A_b , and frequency, $St_b = f_b h / U_\infty$, are the two other important control parameters. The oscillating jet is prescribed in wall-normal direction for all active control cases.

For the generation of the oncoming turbulent boundary layer, rescaled fluctuations from a downstream position $X = x/h = -6.7$ are superimposed to a mean boundary layer profile at the inflow plane $X = -18.0$ (Manhart, 1998). Periodicity is assumed in the spanwise direction. Slip and zero-gradient boundary conditions are utilized at the top and back (outflow) end of the computational domain, respectively.

3. Results

LES validation. For the oncoming turbulent boundary layer at a reference location $X = -6.7$, only moderate deviations between the experiments and the LES on both grids can be observed from figure 2. From the profiles of the

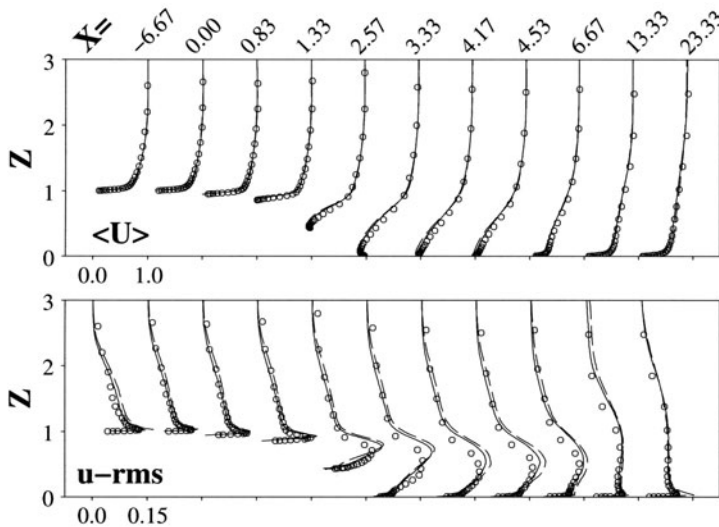


Figure 3. Mean streamwise velocity component, $\langle U \rangle$, and fluctuations, u_{rms} : fine grid LES (full line), coarse grid LES (dashed line), experiments of Song, 2002 (circles)

streamwise (u_{rms}) and vertical (w_{rms}) velocity fluctuations, some freestream turbulence becomes visible which is apparent only in the experiments. Furthermore, the reduced experimental rms -values in the region $Z/\delta \approx [0.2; 0.6]$ are explained by Song, 2002 as a (downstream) remnant of an upstream convex curvature (Gillis and Johnston, 1983) of the experimental apparatus.

The displacement and momentum thickness of the oncoming turbulent boundary layer at $X = -6.7$ are slightly underpredicted (within a 10% range) showing a trend to less deviations from the experimental reference at a finer LES grid. Based on the momentum thickness, θ , the Reynolds number is $Re_\theta \approx 1100$. In figure 2, the rms -profiles of a DNS of Spalart, 1988 at $Re_\theta = 1400$ are included. The grid resolution in viscous units (based on the friction velocity, U_τ , at the reference location $X = -6.7$) is ($\Delta X^+ = 5 \dots 52$, $\Delta Y^+ = 14$, $\Delta Z^+ = 5 \dots 41$) for the fine grid and ($\Delta X^+ = 18 \dots 114$, $\Delta Y^+ = 28$, $\Delta Z^+ = 9 \dots 120$) for the coarse grid.

From the profiles of the mean streamwise velocity, $\langle U \rangle$, and its fluctuations, u_{rms} , in figure 3, it can be seen that throughout the entire domain the agreement between the LES and the experiment (Song, 2002) is quite satisfactory. In the region of the separated and reattaching shear layer (within $X = [1.33; 6.67]$), the u_{rms} -profiles of the LES exhibit higher maximum values at slightly too large distances from the (bottom) wall. Despite increasing the total number of grid points (from coarse to fine resolution) by a factor of more than 8, these deviations from the experiment decrease only slightly.

case	forcing type and parameters	$\langle X_s \rangle$	$\langle X_r \rangle$	$\Delta \langle X_{r-s} \rangle$
<i>r_02_c</i>		1.4	4.9	
<i>rf_02_c0</i>	passive: $H_f = 0.33$, $X_f = -4.0$	2.9	3.9	-71%
<i>rf_02_c1</i>	passive: $H_f = 0.20$, $X_f = -4.0$	2.7	4.2	-57%
<i>rf_02_c2</i>	passive: $H_f = 0.20$, $X_f = -2.0$	2.8	4.0	-66%
<i>rb_02_c0</i>	active: $St_b = 0.20$, $A_b = 0.5U_\infty$, $X_b = 0.0$	2.3	4.5	-37%
<i>rb_02_c1</i>	active: $St_b = 0.05$, $A_b = 0.5U_\infty$, $X_b = 0.0$	2.1	4.6	-29%
<i>rb_02_c2</i>	active: $St_b = 0.20$, $A_b = 0.5U_\infty$, $X_b = 1.3$	—	—	-100%
<i>rb_02_c3</i>	active: $St_b = 0.20$, $A_b = 0.2U_\infty$, $X_b = 1.3$	2.4	4.3	-46%
<i>rb_02_c4</i>	active: $St_b = 0.05$, $A_b = 0.2U_\infty$, $X_b = 1.3$	1.5	4.9	-3%
<i>rb_02_c5</i>	active: $St_b = 0.10$, $A_b = 0.2U_\infty$, $X_b = 1.3$	1.5	4.8	-6%

Table 1. Mean separation, $\langle X_s \rangle$, and reattachment, $\langle X_r \rangle$, location and deviation of the mean longitudinal backflow length, $\Delta \langle X_{r-s} \rangle = \Delta(\langle X_r \rangle - \langle X_s \rangle)$, from the uncontrolled case (*r_02_c*)

The time-averaged streamwise positions of separation, $\langle X_s \rangle$, and reattachment, $\langle X_r \rangle$, are 1.3 and 4.5 in the experiment versus 1.2 (1.4) and 4.7 (4.9) for the fine (coarse) grid LES, respectively. Compared with the experimental data, the resulting deviations of +9% (+9%) of the mean backflow length, $\langle X_r \rangle - \langle X_s \rangle$, for the fine (coarse) grid LES are somewhat higher than for the LES of Wasistho and Squires, 2001.

Controlled flow. In table 1, the control parameters and results of the controlled LES cases (with the coarse grid) are listed. Parameter variations discussed below are displayed in boxes. The change of the mean backflow length, $\Delta \langle X_{r-s} \rangle = \Delta(\langle X_r \rangle - \langle X_s \rangle)$ (compared with the uncontrolled coarse grid LES named *r_02_c*), was selected to measure the control success.

For the *passively controlled cases*, the fence height, H_f , and its streamwise position, X_f , was varied. Significant reductions of the mean backflow length of more than 50% can be observed for all three cases (table 1). For the higher fence, and for the position closer to the rounded step (at a constant height $H_f = 0.2$), the control success is improved. However, the optimum position, X_f for a maximum reduction of the mean backflow length, depends on the fence height, H_f , and is therefore very likely different for both investigated fence heights. In this context, a generally higher *potential* for decreasing the backflow length can be presumed for an increasing fence height. These assumptions are supported by (sharp-edged) backward-facing step results (Neumann and Wengle, 2003). Three parameters are varied for the *actively controlled cases*, the frequency (St_b), the amplitude (A_b) and the position (represented by the streamwise position, X_b) of the oscillating jet. The frequency $St_b = 0.2$ is found to cause the strongest reductions of the mean backflow length when A_b and X_b are kept

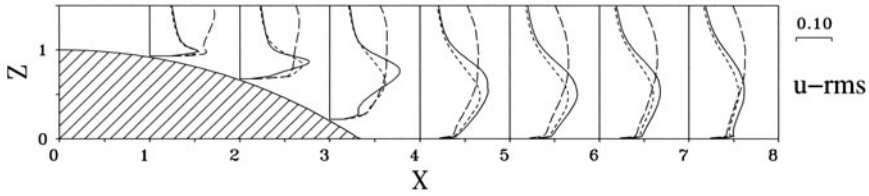


Figure 4. Streamwise velocity fluctuations, u_{rms} : unforced (r_{02_c} , full line), passively forced (rf_{02_c0} , long dashed line) and actively forced (rb_{02_c3} , short dashed line) case

constant (table 1). An increasing energy input, i.e. increasing A_b from $0.2U_\infty$ to $0.5U_\infty$, leads to an increased control success (at constant St_b and X_b). At constant values of St_b and A_b , the downstream position $X_b = 1.3$ (located near the mean separation point, $\langle X_s \rangle$, of the uncontrolled flow) yields a shorter backflow length than the position $X_b = 0.0$. For sufficiently optimized control parameters, the backflow region can not only be reduced significantly in size, it can even disappear entirely (as in case rb_{02_c2}). The forcing frequency $St_b = 0.1$ of case rb_{02_c5} corresponds to a Strouhal number $St_\theta = 0.011$ based on the momentum thickness, θ , at the separation point, $\langle X_s \rangle = 1.3$, of the uncontrolled flow. The weak control success (-6%) at this forcing frequency (compared with the much stronger backflow reduction of -46% for case rb_{02_c3} at $St_b = 0.2$) shows that the optimum frequency of the actively controlled flow over the rounded step does *not* correspond to the optimum frequency $St_\theta \approx 0.01$ found for the (sharp-edged) backward-facing step (Chun and Sung, 1996).

Comparing the passive and active control approach with regard to its impact on the flow, profiles of the streamwise velocity fluctuations, u_{rms} , and snapshots of the instantaneous structure of the backflow region are displayed in figure 4 and figure 5, respectively. Beside the uncontrolled case (r_{02_c}), two representative controlled cases (rf_{02_c0} , rb_{02_c3}) are selected to simplify the comparison. The u_{rms} -profiles at $X = 1.0$, i.e. downstream of the passive control fence (at $X_f = -4.0$) but upstream of the active blowing/suction jet (at $X_b = 1.3$), reveal an increased turbulent activity of the oncoming passively controlled flow and virtually no (upstream) influence of the active control (figure 4). For the passive control, the enhanced turbulence levels in the region far away from the bottom wall ($Z \geq 1.0$) decrease only slightly with increasing streamwise distance from the rounded step. Furthermore, the u_{rms} -peaks of the separated and reattaching shear layer for the passive control are much less distinct than for the uncontrolled flow. At $X = 3.0$ close to the wall, i.e. inside the recirculation zone relatively close to separation (for all cases), both control methods provoke increased fluctuations which are damped below the uncontrolled level further downstream (close to reattachment and in the redeveloping boundary layer region). For the actively controlled flow downstream

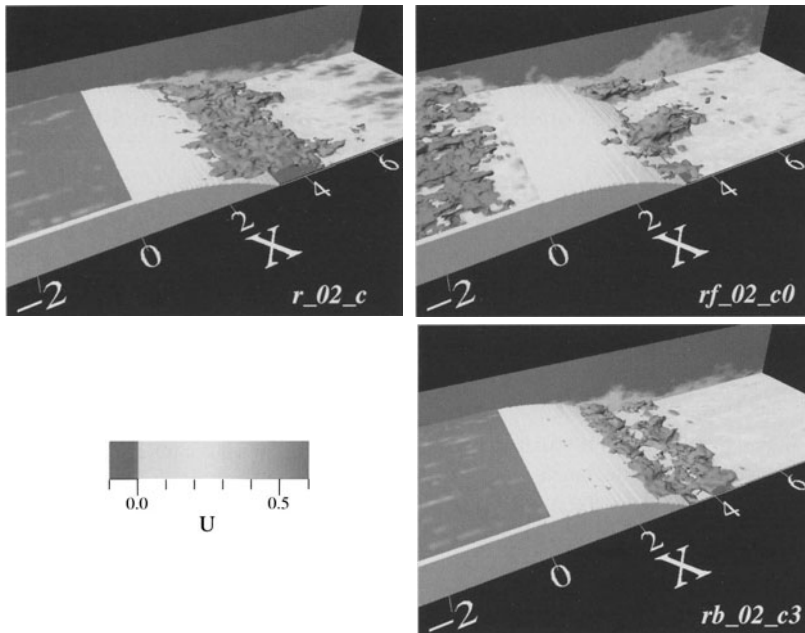


Figure 5. Isosurfaces of the instantaneous streamwise velocity component $U = 0.0$ (gray) for the unforced (r_{02_c}), passively forced (rf_{02_c0}) and actively forced (rb_{02_c3}) case

of reattachment, the damped u_{rms} -peaks (at $Z \approx 0.5$) indicate an accelerated relaxation of the redeveloping boundary layer in comparison with the uncontrolled flow (Neumann, 2003).

In contrast to the uncontrolled flow, the instantaneous spanwise structure of the passively controlled backflow region is disrupted in single backflow packets which can reach a considerable height above the bottom wall (figure 5). Downstream of the oscillating jet, the actively controlled flow is dominated by two-dimensional roller structures which interact with the oncoming boundary layer flow.

4. Conclusion

Large-eddy simulations (LES) of (open-loop) controlled turbulent flow over a rounded step are performed to analyze the impact of two particular control approaches on a flow with its separation induced by an adverse pressure gradient. A coarse grid solution (5.4 million grid cells) was successfully validated by comparison with a highly resolved LES (48.9 million grid cells) and experimental reference data (Song, 2002). A significant reduction of the backflow length between the mean separation, $\langle X_s \rangle$, and reattachment, $\langle X_r \rangle$, location can be achieved by optimizing the streamwise position, X_f , of the passive control fence with respect to its height, H_f . For the actively controlled case,

the amount of energy input (i.e. the amplitude, A_b) needed to reduce (or even to erase) the mean backflow depends sensitively on a proper choice of the forcing frequency, St_b , and forcing position, X_b . It is found that the impact of the different control methods on the flow structure differs substantially.

Acknowledgments

The support by the Deutsche Forschungsgemeinschaft (DFG, grant number We 705/7), by the Leibniz Computing Center (LRZ) of the Bavarian Academy of Sciences, and by the Computing Center of the Universität der Bundeswehr München is gratefully acknowledged.

References

- Alving, A. and Fernholz, H. (1996). Turbulence measurements around a mild separation bubble and downstream of reattachment. *J. Fluid Mech.*, 322:297–328.
- Brunn, A. and Nitsche, W. (2003). Separation control by periodic excitation in a turbulent axisymmetric diffuser flow. *Journal of Turbulence*, 4(009).
- Chun, K. and Sung, H. (1996). Control of turbulent separated flow over a backward-facing step by local forcing. *Exp. Fluids*, 21:417–426.
- Gillis, J. and Johnston, J. (1983). Turbulent boundary-layer flow and structure on a convex wall and its redevelopment on a flat wall. *J. Fluid Mech.*, 135:123–153.
- Isomoto, K. and Honami, S. (1989). The effect of inlet turbulence intensity on the reattachment process over a backward-facing step. *J. Fluids Engineering*, 111:87–92.
- Manhart, M. (1998). Direct numerical simulation of turbulent boundary layers on high performance computers. In Krause, E. and Jaeger, W., editors, *High performance Computing in Science and Engineering 1998*. Springer Verlag.
- Miau, J., Lee, K., Chen, M., and Chou, J. (1991). Control of separated flow by a two-dimensional oscillating fence. *AIAA Journal*, 29:1140–1148.
- Neumann, J. (2003). *Passive und aktive Beeinflussung turbulenter Stufenüberströmungen*. PhD thesis, Universität der Bundeswehr München, München, Germany.
- Neumann, J. and Wengle, H. (2003). DNS and LES of passively controlled turbulent flow backward-facing step flow. *Flow Turbulence and Combustion*, 71:1–14.
- Obi, S., Ohizumi, H., Aoki, K., and Masuda, S. (1993). Turbulent separation control in a plane asymmetric diffuser by periodic perturbation. In Rodi, W. and Martelli, F., editors, *Engineering Turbulence Modelling and Experiments 2*, pages 633–642. Elsevier Science Publishers.
- Song, S. (2002). *Reynolds number effects on a turbulent boundary layer with separation, reattachment and recovery*. PhD thesis, Stanford University, USA.
- Spalart, P. (1988). Direct simulation of a turbulent boundary layer up to $Re_\theta = 1410$. *J. Fluid Mech.*, 187:61–98.
- Tremblay, F., Manhart, M., and Friedrich, R. (2002). LES of flow around a circular cylinder at a subcritical Reynolds number with cartesian grids. In Friedrich, R. and Rodi, W., editors, *Advances in LES of Complex Flows*, pages 133–150. Kluwer Academic Publishers.
- Viswanath, P., Ramesh, G., and Madhavan, K. (2000). Separation control by tangential blowing inside the bubble. *Exp. Fluids*, 29:96–102.
- Wasistho, B. and Squires, K. (2001). Numerical investigation of the separated flow over a smoothly contoured ramp. In *Proc. 2nd Symp. Turbulence and Shear Flow Phenomena*, pages 405–410 (Vol. III), Stockholm, Sweden.

APPLICATION OF DNS AND LES TO PREDICTION OF TUBE FLOW-INDUCED VIBRATIONS

Elisabeth Longatte, Zaky Bendjeddou
*EDF Research & Development Division,
Fluid Mechanics and Heat Transfer Department, Chatou, France*
elisabeth.longatte@edf.fr, zaky.bendjeddou@edf.fr

Mhamed Souli
*Lille University, Mechanical Engineering Department,
Villeneuve d'Ascq, France*
mhamed.souli@univ-lille1.fr

Abstract In many industrial applications, mechanical structures like rod cluster control assembly, fuel assembly and heat exchanger tube bundles are subjected to complex flows causing possible vibrations and damage. Fluid forces can be split into two parts : turbulent forces not affected much by structure motion and fluid-elastic forces coupled with tube motion and responsible for possible dynamic instability development leading to possible short term failures through high amplitude vibrations. Most classical fluid force identification methods rely on structure response experimental measurements associated with extensive data processing. Owing to recent improvements in Computational Fluid Dynamics, hydraulics force identification is now practicable in the presence of industrial configurations. The present paper is devoted to the numerical simulation of flow-induced vibrations of tubes and tube bundles submitted to single-phase turbulent flows. Large Eddy Simulation or Direct Numerical Simulation with or without code coupling are applied to the prediction of turbulent or fluid-elastic forces responsible for tube vibrations in the presence or not of strong coupling effects.

Keywords: LES, turbulence, code coupling, ALE, fluid structure interactions, flow-induced vibrations, tube bundles

1. Introduction

Numerical simulation of fluid structure interactions and particularly of tube flow-induced vibrations is investigated in the present paper. The purpose is to predict numerically tube bundle vibrations generated by single-phase cross

flows by using Computational Fluid Dynamics (CFD) codes involving specific numerical methods for multi-physic problems. As far as flow-induced vibrations are concerned, the purpose is to estimate thermo-hydraulics force effects on structure motion and in the same time to account for possible coupling between tube motion and part of fluid forces, so-called fluid-elastic forces, in order to predict possible dynamic instabilities enabling short term failures through high magnitude vibrations. These simulations are now reachable in configurations involving basic geometry thanks to recent improvements in CFD.

Fluid forces acting on mechanical structures can usually be split into two parts: structure motion independent forces generated by flow turbulence patterns, fluid-elastic forces responsible for possible dynamic instability development and induced by a real coupling between flow and structure motion. Tube motion independent forces generated by near-wall pressure fluctuations can be computed numerically by using CFD because they are not affected by structure pattern and dynamic motion effects. It is possible to assume that tube walls are rigid and turbulent force calculation only requires a near-wall unsteady field computation performed on a fixed non-moving mesh. Numerical simulation of fluid-elastic effects requires a real coupling between mechanical models and CFD calculations accounting for wall motion effects on flow patterns and conversely. Such a calculation is still impracticable for industrial purposes through lack of sufficient numerical resources but simplified configurations can be tested.

The present paper provides an overview of three physical problems involving flow-induced vibrations in tube bundles that can be solved by using CFD codes. Specific turbulence models like Large Eddy Simulation (LES) are used, methods for moving boundaries are required like Arbitrary Lagrange Euler formulation (ALE) and numerical scheme adapted to multi-physics problems and code coupling are presented. The first part is related to the study of tube vibrations generated by turbulence in the presence of weak fluid-elastic coupling effects. In the second part LES is applied to identification of flow fields in tube bundles in the presence of cross flows. Finally numerical simulations of flow-induced vibrations in tube bundles in cross flows using ALE and code coupling are presented in the last section and results are discussed in terms of tube vibration frequency according to available experimental data.

2. Identification of turbulent force spectra using LES

2.1 Physical problem

When fluid-elastic effects are reduced to added mass and damping effects, there is no strong flow structure coupling and structure motion effects acting on turbulent flow patterns can be neglected. It is then possible to perform thermo-

hydraulics and mechanics calculations separately to study flow-induced vibrations (Longatte et al. 2001, Moreno et al. 2000). Turbulent force spectrum and time record can be simulated on a non-moving computational domain with a fixed structure by using Large Eddy Simulation (LES) and they are introduced as inlet data into the mechanical calculation providing the structure vibratory response. This computational process was applied to the prediction of a single tube dynamic response generated by a turbulent mainly axial flow in a non-confined area. The test case corresponds to a configuration previously studied experimentally at EDF by Granger and Perotin (1997). A tube is submitted to a turbulent three-dimensional flow crossing a perforated plate located just above the rod and generating mainly axially high turbulent fluctuations near the tube. Eddies are generated along the rod and finally the fluid is evacuated by a lateral outlet. The square test section size (260 mm) is large in front of the tube diameter (15 mm) and confinement effects may be neglected. Hence fluid-elastic effects are restricted to added mass and damping effects due to the fluid that can be deduced from experimental prediction. The computational process is described below.

2.2 Numerical methods

As structure motion does not affect turbulent fluid forces, fluid and structure calculations are performed separately. First fluid computation involving LES is performed with a rigid solid non-moving tube and provides unsteady flow fields. Near-wall fluid forces on the tube are estimated in terms of power spectral density and a modal spectral mechanical calculation is carried out to compute the tube dynamic response. Fluid force magnitude and spectrum calculation requires near-wall refined turbulence modelling in order to capture unsteady pressure fluctuations. LES are becoming more and more important in research industrial applications, especially when accurate near-wall unsteady field estimates are required. In the present paper a Large Eddy Simulation is performed in order to compute turbulent force spectra and mean values distributed along the rod. The Smagorinsky model was applied to the simulation of turbulence in plane duct for instance and good results were obtained. However this modelling features disadvantages. For example it does not account for wall effects on the subgrid scale turbulent stresses unless a specific damping function is applied to reduce the Smagorinsky constant near the wall. A suitable Van Driest function was used by Moin (1982) in order to improve the numerical scheme behaviour. Other models tending to be more efficient in the presence of near-wall turbulence were developed (Bardina 1989, Germano 1992).

In the present article the Smagorinsky modelling is used to predict turbulent forces acting on a rod submitted to an axial flow with $C_s = 0.065$. Possible

errors induced by the Smagorinsky modelling can be compensated by sufficient mesh refinement near the wall. Further studies will be carried out in order to compare the results obtained by using other techniques. A dynamic model will be considered by adjusting the constant of the subgrid scale model as a function of space and time.

2.3 Numerical results

Main numerical results deduced from LES and from mechanics calculation are presented below. Turbulent forces are expressed in terms of spectra and numerical solutions are validated by using comparisons with available experimental data. Then tube dynamic response deduced from numerical force estimates are compared to experimental measurements in terms of physical stress. Numerical fluid forces are compared to experimental data in Figure 1 in terms of power spectral density. They feature the expected patterns in terms of broadband, slope and magnitude. Finally the tube mechanical response resulting from previously identified forces is in good agreement with experimental measures. These results tend to show that LES provides reasonable estimates of fluid force spectra in the presence of complex geometry configurations embedded in turbulent flows. Accurate information is reachable about flow patterns responsible for structure flow-induced vibrations. Practical application to tube bundle vibration study is considered below.

3. Identification of flow fields in tube bundles using LES

3.1 Physical problem

In the presence of high fluid-elastic effects, when tubes are subjected to cross flows for example, LES performed on a fixed non moving mesh may also provide interesting information about spectra, lift and drag coefficients in tube bundles. Fluid forces acting on a staggered tube array in cross flows were identified by using a 3D LES. Numerical results were compared to solutions provided by DNS, 2D, 3D Rij- ε modelling and experimental data in terms of mean velocity and Reynolds tensor (Benhamadouche and Laurence 2002). Results tended to show that 3D LES provides realistic flow patterns around the tube for further study of vibrations.

3.2 Numerical methods

In what follows LES are carried out in the presence of fixed in-line tube bundles in cross flow without structure motion in order to validate thermo-hydraulics fields. Calculations are carried out in reduced tube bundle cells including periodic conditions in order to reduce CPU time. The purpose is to estimate fluid forces acting on a fixed tube located in the middle tube of an array of fixed

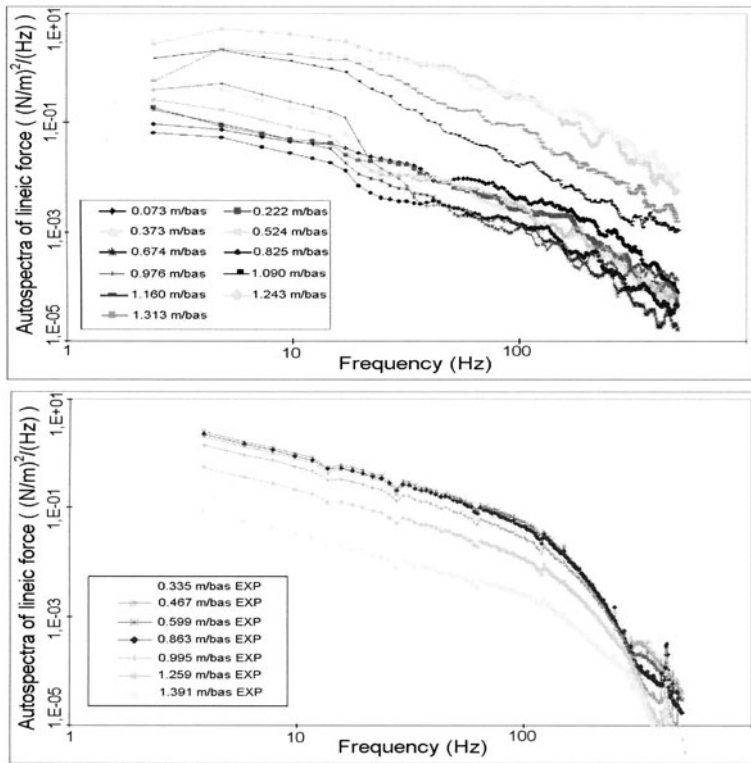


Figure 1. Near-wall fluid force power spectral density along a tube in turbulent flow estimated numerically with LES (upper) and experimentally with an inverse method (lower).

tubes. Solutions are estimated in terms of drag and lift mean and root mean square values.

3.3 Numerical results

A part of numerical results are presented below and compared for several Reynolds numbers to experimental measurements of Chen (1987) for a pitch ratio $P/D=1.75$ where P designates the pitch diameter and D the tube diameter. A comparison between numerical and experimental values of RMS of drag and lift coefficients is given by Figure 3. The expected tendency is retrieved by numerical solution particularly for small Re number (Chen 1987). For $Re=70000$ the numerical solution obtained with LES is in good agreement with the experimental solution plotted for tube number 4 located in the middle of tube bundle like in the simulation.

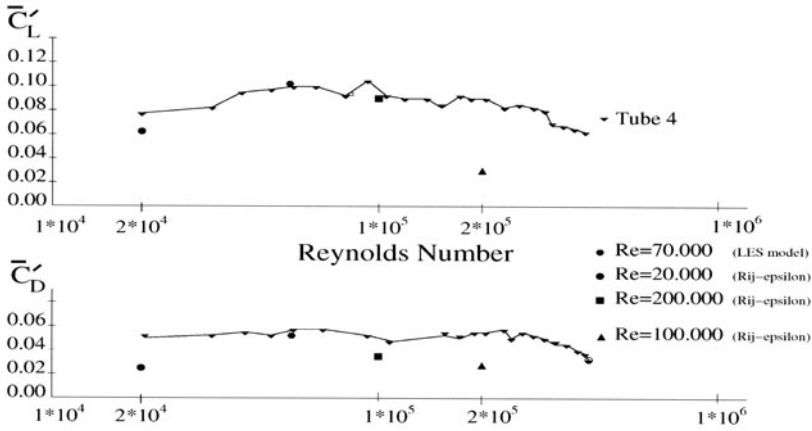


Figure 2. Comparison between numerical simulation (RANS and LES model) and experimental measurement of lift (upper) and drag (lower) root mean square values for a middle tube (tube 4) in an array of fixed tubes submitted to cross flow for different Reynolds number (Chen 1987).

4. Identification of fluid-elastic forces in tube bundles using ALE and code coupling

4.1 Physical problem

To predict flow structure coupling, a fully computational process for simulation of tube bundle flow-induced vibrations was developed relying on a flow structure code coupling. The methodology consists in solving in the same time thermohydraulics and mechanics problems by using an Arbitrary Euler Lagrange (ALE) formulation for the fluid computation (Souli et al. 2001). The purpose is to take into account the coupling between flow and structure motions in order to be able to capture fluid-elastic effects. The ALE formulation is particularly appropriate in the presence of moving wall boundaries as boundary motion is taken into account in the fluid calculation while element shape properties are preserved (Bendjeddou et al. 2002).

4.2 Numerical methods

From a numerical point of view there are three steps in the computation : the fluid problem is solved on the computational domain; fluid lift and drag forces acting on the flexible tube are estimated ; then these forces are introduced in the structure problem whose computation provides the tube displacement and velocity used to deform the fluid computational domain. Implicit and explicit code coupling processes were tested.

4.3 Numerical results

In the present work this process was applied to the identification of fluid-elastic parameters of a single flexible tube moving in a fixed tube bundle. The fluid calculation is performed on a finite tube bundle cell featuring periodicity. The coupling process previously mentioned was applied to the prediction of tube vibration frequency in still water and in flow. Tube motion is generated by an initial displacement. Numerical results are compared to experimental data of Granger et al. (1993) in terms of tube frequency in fluid at rest and in flow. Results are reported in Figure 3 and a good agreement is observed. Other configurations have been tested and the same tendency was retrieved. Convergences in mesh and time were tested in order to ensure the validity of our results. Further validations are required to build numerical tools for study of tube bundle stability in presence of cross flows (Chen 1987, Price and Paidoussis 1996).

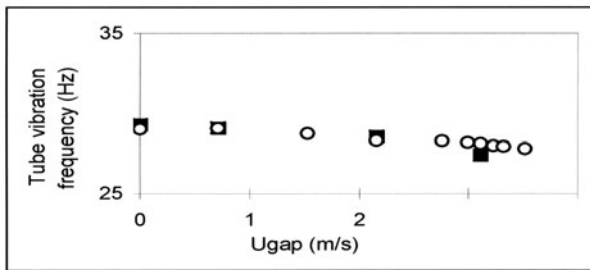


Figure 3. Tube vibration frequency in flow f_f (Hz) in terms of gap velocity U_{gap} (m/s) estimated numerically (black points) and experimentally by Granger et al. (1993) (white points).

Conclusion

Numerical results presented in this article illustrate possible applications of CFD to the study of flow-induced vibration problems in tube and tube bundles. Classical approaches are involved in the presence of weak fluid structure coupling. Specific methods using moving meshes are required for the identification of strong flow structure interactions. Further developments are carried out to improve numerical tools and enable the prediction of tube bundle vibration frequency, damping and stiffness in complex configurations.

Acknowledgments

Authors would like to express their sincere thanks to MM. Caruso, Archambeau, Benhamadouche and Adobes for their helpful contribution in the present work.

References

- Bardina J., Ferziger J.H., Reynolds W.C., (1989), *Improved subgrid-scale models for Large Eddy Simulation*, Rept TF-19Dept Mech. Eng. Stanford CA.
- Benhamadouche S., Laurence D., (2002), *LES, coarse LES and transient RANS comparisons on the flow across a tube bundle*, Engineering Turbulence Modeling and Measurements conference 5, Elsevier.
- Bendjeddou Z., Longatte E., Souli M., (2002), *Numerical simulation of tube bundle vibrations in cross flows*, FSI, AE&FIV+N conference, proceedings, New Orleans.
- Chen S.S., (1987), *Flow-induced vibration of circular cylindrical structures*, Hemisphere Publishing Corporation.
- Germano M., (1992), *Turbulence, the filtering approach*, J. Fluid Mech., 238, 325-336.
- Granger S., Perotin L. (1997), *An inverse method for the identification of a distributed random excitation acting on a vibrating structure: Part 2: Flow-induced vibration application*, ASME Fluid-Structure Interactions, Dallas.
- Granger S., Campistron R., Lebre J., (1993), *Motion-dependent excitation mechanisms in square in-line tube bundle subject to water cross-flow : an experimental modal analysis*, J. Fluid. Struc., 7, 521-550.
- Longatte E., Laurence D., Barré F., Leduc P., (2001), *Application of Large Eddy Simulation to a flow-induced vibration problem*, ASME PVP, Conference on Flow-Induced Vibrations, Atlanta.
- Moin P., KIM J., (1982), *Numerical investigation of turbulent channel flow*, J. Fluid Mech., 118, 341-377.
- Moreno M.M., De Langre E., Le Quere P., (2000), *A large eddy simulation of the turbulent forcing spectrum induced by axial flow on a rod*, Conference on flow-induced vibrations 7, Lucerne.
- Price S.J., Paidoussis N., (1986), *A single-flexible-cylinder analysis for the fluidelastic instability of an array of flexible cylinders in cross-flow*, J. Sound Vib., 108, 193-199.
- Souli M., Zolesio J.P. (2001), *Arbitrary Lagrangian-Eulerian and free surface methods in fluid mechanics*, Comput. Methods Appl. Mech. Engrg., 2758.

DNS OF THE FLOW AROUND A CIRCULAR CYLINDER USING AN IMMERSED BOUNDARY METHOD

E.R.A. Coyajee & B.J. Boersma

J.M. Burgerscentre, Delft University of Technology,

Mekelweg 2, 2628 CD, The Netherlands

email: e.r.a.coyajee@wbmt.tudelft.nl

Abstract In this study, the immersed boundary method of Kim, Kim and Choi (2001) is used to simulate the flow around a circular cylinder. The concept of the immersed boundary method is to represent complex geometries on a regular Cartesian grid, enabling highly efficient calculation of a flow. First results of a simulation at $Re_D = 1600$ are presented. Realistic values of drag and lift coefficient, Strouhal number and mean velocities are obtained.

Keywords: Direct Numerical Simulation (DNS), immersed boundary, Cartesian grid, circular cylinder.

1. Introduction

Several methods have been developed to simulate the presence of complex geometries in a turbulent flow. Different methods may be preferred to solve particular problems, depending on accuracy and efficiency. An ideal method in terms of efficiency would be one for which the addition of a complex (moving) geometry does not cause a significant increase in computational effort. Immersed boundary methods offer the opportunity to solve a flow on a regular Cartesian grid, using a fast direct Poisson solver. Therefore, presence, shape and location of the immersed boundary are indifferent to the grid, making this class of methods highly efficient in terms of the previous definition.

For a rigid boundary, such as has been simulated here, some of the existing immersed boundary methods are not very attractive. In the scheme proposed by Lai and Peskin (1977), rigidity must be approximated by a very stiff elastic interface, causing restrictions on the timestep which are too severe in relation to time-scales occurring in the flow. Recently, this problem has been addressed by Lima E Silva et al. (2003), who have adjusted the method to deal with a

rigid boundary. This method, however, still uses spreading of point forces which smears out the solution near the boundary and which is known to be first order accurate.

Another immersed boundary concept, using feedback forcing, was proposed by Goldstein et al. (1993) and further developed by Saiki and Biringen (1997). For this virtual boundary method, Lee (2003) has provided a stability analysis and a scheme with a reasonable timestep criterion. In spite of the progress made, Lee suggests that there are still several issues to be resolved, concerning accuracy near the immersed boundary.

Compared to the previous methods, an even more efficient forcing method was introduced by Fadlun et al. (2000). Following Mohd-Yusof (1997), Fadlun et al. (2000) enforce the no-slip condition at the boundary by simply adjusting velocity components next to the boundary on the fluid side of the domain. In spite of its efficiency and stability, the method requires a fine resolution near the boundary to justify the linear velocity profile that is imposed by the interpolation procedure. Therefore, Kim et al. (2001) propose to force the flow by adjusting velocity components directly within the boundary of the object. To our knowledge, this method has only been demonstrated in 3D for stationary or rotating spheres producing laminar wakes.

In this work, the validity of the method of Kim et al. (2001) is studied in case of a turbulent wake evolving behind a stationary cylinder. In the near future we aim to extend this method to deal with moving objects.

2. Immersed boundary concept

The following Navier-Stokes equations for incompressible flow are considered:

$$\frac{\partial u_i}{\partial t} + \frac{\partial u_i u_j}{\partial x_j} = -\frac{\partial p}{\partial x_i} + \frac{1}{Re} \frac{\partial^2 u_i}{\partial x_j \partial x_j} + f_i, \quad (1)$$

and the continuity equation:

$$\frac{\partial u_i}{\partial x_i} - q = 0. \quad (2)$$

Here, Re is the Reynolds number, x_i are Cartesian coordinates, u_i corresponding velocities and p the pressure. Furthermore, f_i and q respectively represent momentum and mass sources.

The concept of immersed boundary methods in general is to prescribe f_i such that no-slip boundary conditions are simulated over an arbitrarily curved boundary on a regular grid. In the current method, discrete momentum sources f_i are prescribed to fulfill the no-slip condition, but only on cell faces located directly within the immersed boundary (figure 1). Due to the introduction of the momentum sources, discrete mass conservation may be violated. Therefore, mass sources are introduced for cells that are intersected by the boundary.



Figure 1. Schematic diagram of the arrangement of velocity vector components, momentum and mass sources in the vicinity of an immersed boundary.

3. Numerical method

Figure 2 shows the computational domain, its dimensions and coordinate system. From here on, the x -direction will be referred to as the streamwise, the y -direction as the transverse and the z -direction as the spanwise direction. In the streamwise direction, flow is forced by uniform laminar inflow ($u/u_\infty = 1$ and $v = w = 0$) at $x = -4.25D$. At $x = 10.5D$, a convective boundary condition ($\partial u_i / \partial t + u_\infty \partial u_i / \partial x = 0$) is used for outflow. Free-slip boundary conditions are prescribed at $y = \pm 5.0D$ ($\partial u / \partial y = \partial w / \partial y = 0$ and $v = 0$). For the spanwise direction, periodic boundary conditions are prescribed at $z = 0$ and $z = \pi D$.

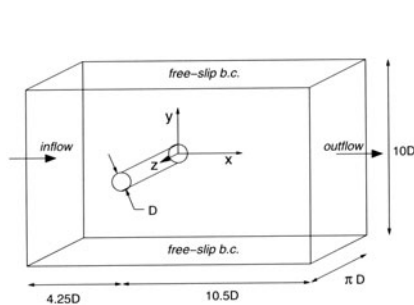


Figure 2. Sketch of the geometry used

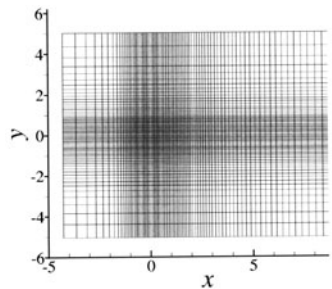


Figure 3. View of computational grid in the xy -plane. Only one out of four grid lines is shown.

Equations (1) and (2) are spatially discretized on a Cartesian mesh. A staggered arrangement is used for the streamwise and transverse velocity, u and v . The spanwise velocity, w , is collocated with the pressure at the center of the volumes. The difference in arrangement of the velocity components is a result of using second order central finite-differences for the discretization of the

non-uniform streamwise and transverse directions whereas a Fourier spectral method is used for discretizing the spanwise direction.

For time integration of equations (1) and (2), the third order Adams-Bashforth method is used in the framework of a fractional step method with pressure-correction. Both the convective and the diffusive terms are treated explicitly, giving the following time advancement scheme:

$$\frac{u_i^* - u_i^n}{\Delta t} = \frac{23}{12}(A(u_i^n) + D(u_i^n)) - \frac{16}{12}(A(u_i^{n-1}) + D(u_i^{n-1})) + \frac{5}{12}(A(u_i^{n-2}) + D(u_i^{n-2})) - G(P^{n-1/2}) + f_i^{n+1}, \quad (3)$$

$$L(P^*) = \frac{1}{\Delta t}(DIV(u_i^*) - q^{n+1}), \quad (4)$$

$$u_i^{n+1} = u_i^* - \Delta t G(P^*), \quad (5)$$

$$G(P^{n+1/2}) = G(P^{n-1/2}) + G(P^*), \quad (6)$$

where A , D , G , L and DIV respectively represent discrete advective, diffusive, gradient, Laplace and divergence operators.

Obviously, the momentum source in eq. (3), f_i^{n+1} , must be determined ahead of the evaluation of eq. (3)-(6). This is done as follows: the intermediate velocities u_i^* can be pre-determined at locations just outside the immersed boundary, since no momentum sources are required in their evaluation. Subsequently, the velocity at a location just inside the boundary, denoted by U_i^* , can be determined by second order interpolation such that the i -component of the velocity is equal to zero on the immersed boundary itself. Finally, the momentum source is determined from eq. (3) by substituting U_i^* for u_i^* and solving for f_i^{n+1} .

The mass source, q , is defined by Kim et al. as follows:

$$q^{n+1} = \sum_i \alpha \frac{\mathbf{u}^* \cdot \mathbf{n}}{\Delta x_i} \quad (7)$$

where α equals 1 or 0 if a cell face respectively does or does not contain a momentum source and \mathbf{n} is the unit normal vector outward each cell face. In this study, we have omitted the spanwise velocity components from the mass source. This would be permitted since continuity sources are required only for velocity components in a direction normal to the interface and the spanwise velocity component is never forced as a normal velocity, but only as a pure tangential velocity. Our motivation for deviating from the method of Kim et al. is a consequence of instabilities found when using the original definition, which in 3D has only shown to be effective for spheres. To explain the nature of the instability, using Kim et al.'s original definition, further study is required.

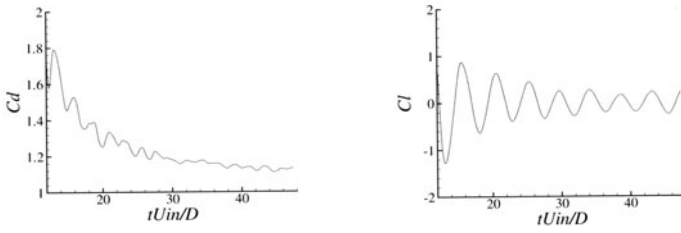


Figure 4. Time traces of the drag coefficient (left) and lift coefficient (right).

4. Results

In this section first results will be presented of a simulation performed at $Re_D = 1600$. The grid is shown in figure 3. In a square area surrounding the cylinder, ($|x| \leq 0.6D, |y| \leq 0.6D$), an equidistant mesh is used, where $\Delta x = \Delta y = \frac{1}{64}D$. Downstream, the grid is stretched by 1% from cell to cell in the x -direction. In the y -direction, the grid is stretched by 2% up to $|y| = 2.5$, subsequently increasing to 5% at $|y| = 5$. The total number of grid points used equals $352 \times 256 \times 64$, for the x , y and z -direction. Based on the DNS of Tremblay, Manhart and Friedrich (2002), for which we assume the boundary layer to be sufficiently resolved, it can be derived that the current resolution is roughly one half of what is required in the cylinder area. However, the current resolution was considered appropriate for a first test of the method. Drag and lift coefficients are easily computed for the current method by integrating each momentum source over its discrete volume and summing all sources over the computational domain. Consequently, these coefficients can be used to monitor the development of the turbulent wake in the calculation.

In figure 4, dimensionless drag and lift coefficients are plotted over the last 36 time units, tU_∞/D , of our simulation. From the time traces, it is clear that the drag and lift coefficients are just starting to fluctuate around a long-time average. From this we concluded the wake is just reaching a fully developed state. Therefore, we only used data acquired over the last three shedding cycles, 64 realizations of the flow field in total, to produce the following results.

We determined a mean drag coefficient $\overline{C_d} = 1.14$ and a Strouhal number $St = 0.220$. Let us compare these values to those reported in studies for $Re = 3900$, where $\overline{C_d} = 1.04, 1.03$ and $St = 0.210, 0.220$ (Kravchenko and Moin (2001), Tremblay et al. (2002)). The mean drag coefficient, which depends weakly on Re for $Re = 1600$ to 3900, is a bit high. However, it may be expected to decrease as the simulation advances and also if we increase the domain in the transverse direction. The Strouhal frequency seems reliable, since it only weakly depends on the Reynolds number in the subcritical regime.

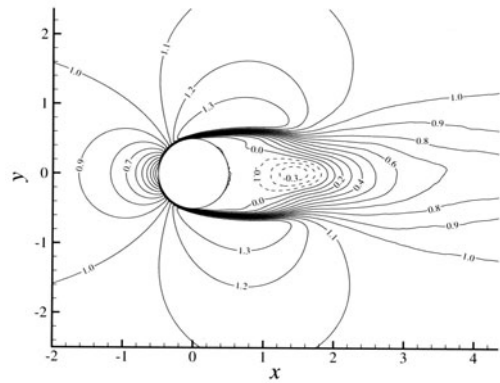


Figure 5. Contours of mean streamwise velocity. Negative values are dashed.

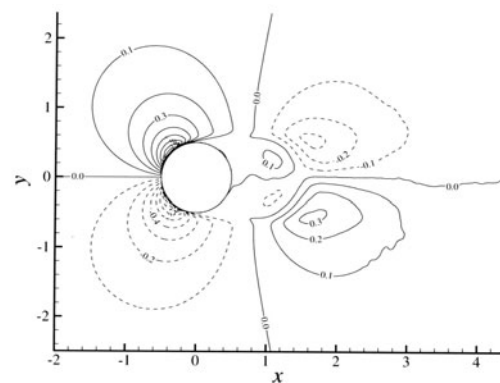


Figure 6. Contours of mean transverse velocity. Negative values are dashed.

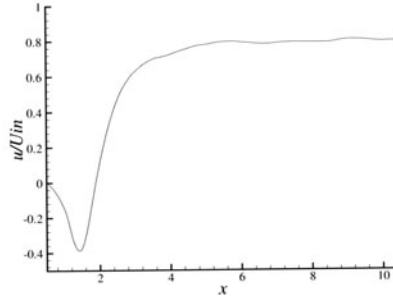


Figure 7. Mean streamwise velocity along the centerline of the cylinder wake.

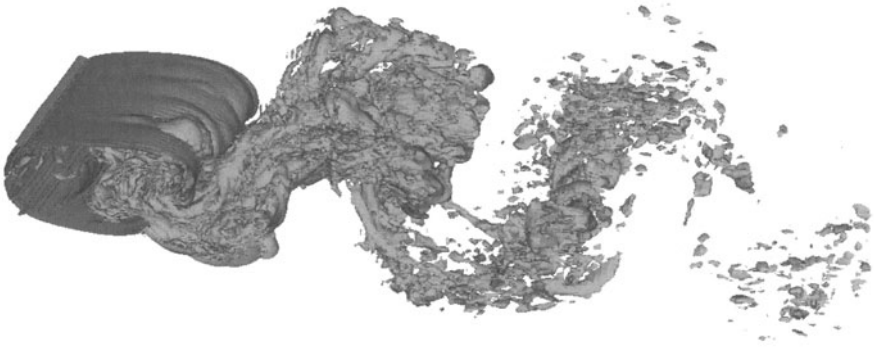


Figure 8. Magnitude of vorticity. Iso-surface for $\omega D/U_\infty = 4$.

In figure 5 and 6, we present contour plots of the mean velocity component in the x and y -direction. In spite of the limited amount of shedding cycles over which data has been acquired and the limited calculation time, the profiles are fairly smooth, clearly displaying the features of the wake. The wiggles, appearing between 60° and 90° from the front stagnation point (especially for the v -component), indicate lack of resolution. Preliminary results of a simulation with $\Delta x = \Delta y = \frac{1}{128}D$ in the area of the cylinder show smooth profiles of mean u and v .

In figure 7, we show the mean profile of the streamwise velocity along the centerline of the wake. In figure 8, instantaneous vorticity magnitude is visualized. The isosurface shows the instabilities in the shear layers on the cylinder. Also, the development of the Von Karman street can be observed.

5. Discussion

For the current method, routines which calculate the momentum and mass sources required only 1% of the total calculation time. Placing additional geometries in the flow will therefore increase computation time only marginally. This clearly demonstrates the efficiency of the method used. Although the present results are preliminary of nature, they promote continuation of the work. Obviously, simulating at $Re = 3900$ would be desirable, allowing direct quantitative comparison with detailed results of other researchers. At an improved resolution, higher order statistics of the turbulent flow field need to be evaluated.

Acknowledgments

This work was sponsored by the National Computing Facilities Foundation (NCF) for the use of supercomputer facilities, with financial support from the Dutch Organisation for Scientific Research (NWO).

References

- [1] Fadlun, E.A., Verzicco, R., Orlandi, P. and Mohd-Yusof, J., Combined immersed-boundary finite-difference methods for three-dimensional complex flow simulations, *J. Comp. Phys.*, **161**, 35 (2000).
- [2] Goldstein, D., Handler, R. and Sirovich, L., Modelling a no-slip flow boundary with an external force field, *J. Comp. Phys.*, **105**, 354 (1993).
- [3] Kim, J., Kim, D. and Choi, H., An immersed-boundary finite-volume method for simulations of flow in complex geometries, *J. Comp. Phys.*, **171**, 132 (2001).
- [4] Kravchenko, A., and Moin, P., Numerical studies of flow around a circular cylinder at $Re_D = 3900$, *Phys. Fluids*, **12**, 403, 2000.
- [5] Lai, M.-C. and Peskin, C., An immersed boundary method with formal second order accuracy and reduced numerical viscosity, *J. Comp. Phys.* **160**, 705 (2000).
- [6] Lee, C., Stability characteristics of the virtual boundary method in three-dimensional applications, *J. Comp. Phys.* **184**, 559 (2003).
- [7] Lima E Silva, A.L.F., Silveira-Neto, A. and Damasceno, J.J.R., Numerical simulation of two-dimensional flows over a circular cylinder using the immersed boundary method, *J. Comp. Phys.*, **189**, 351 (2003).
- [8] Mohd-Yusof, J., Combined immersed boundaries/B-spline methods for simulations of flows in complex geometries, CTR annual research briefs, NASA Ames/Stanford University, 1997.
- [9] Saiki, E.M. and Biringen, S., Numerical simulation of a cylinder in uniform flow: application of a virtual boundary method, *J. Comp. Phys.*, **123**, 450 (1997).
- [10] Tremblay, F., Manhart, M. and Friedrich, R., LES of flow around a circular cylinder at a subcritical Reynolds number with cartesian grids, *Advances in LES of complex flows*, 133-150, 2002.

COMBINATION OF THE IMMERSED BOUNDARY METHOD WITH COMPACT SCHEMES FOR DNS OF FLOWS IN COMPLEX GEOMETRY

Philippe Parnaudeau^{1,2}, Eric Lamballais¹, Dominique Heitz²,
Jorge H. Silvestrini³

¹*Laboratoire d'Etudes Aérodynamiques UMR 6609,
Université de Poitiers, CNRS
Téléport 2 - Bd. Marie et Pierre Curie B.P. 30179
86962 Futuroscope Chasseneuil Cedex, France*

²*Cemagref, UR TERE,
17, avenue de Cucille, CS 64427
Rennes F-35044 France*

³*Departamento de Engenharia Mecânica e Mecatrônica,
Faculdade de Engenharia,
Pontifícia Universidade Católica do Rio Grande do Sul
Av. Ipiranga 6681, 90619-900 Porto Alegre - RS, Brasil*

Abstract We present a direct forcing method better suited for the use of compact finite difference schemes in Direct Numerical Simulation. The new forcing creates inside the body an artificial flow preserving the no-slip condition at the surface but reducing the step-like change of the velocity derivatives across the immersed boundary. This modification is shown to improve results both qualitatively and quantitatively for conventional and complex flow geometries.

1. CONTEXT OF THE STUDY

Despite the continual progress of computers, direct and large eddy simulation of turbulent flows in complex geometries remains a difficult task. For each flow configuration, a compromise must be specifically determined in order to correctly describe the physics of the flow for a reasonable computational cost (speed, memory requirement, code complexity). The choice of the computational grid is well known to be crucial for the determination of this compromise. In order to take accurately small details of the geometry into account, the most popular method is to generate sophisticated grids following the body geometry. However, such grids are frequently very distorted, resulting in a degradation of the numerical accuracy associated with a significant increase of the global computational cost.

An alternative method to avoid the drawbacks of the body fitted approach consists in extending capabilities of codes based on simplified grids *via* the use of the ‘immersed boundary method’. The basic idea of this technique is to mimic the effect of a solid surface on the fluid through a forcing applied in the body region. This operation is performed by additional terms introduced in Navier-Stokes equations. Various formulations are proposed in the literature with various names like ‘virtual boundary method’, ‘fictitious domain method’ or ‘penalization method’.

1.1 Short review of immersed boundary methods

Here, we use the generic term ‘immersed boundary method’ introduced by [9] where this idea was employed to consider the full interaction between elastic solids and the fluid. For more simplified situations where the motion of solid surfaces is a known of the problem, three types of forcing can be distinguished: (i) feedback forcing [4], (ii) algebraic forcing [2], (iii) direct forcing [13, 3]. The feedback forcing is based on an artificial term that can ‘freeze’ efficiently the fluid in the body region through a damping oscillation process. The algebraic forcing is a simplified form of the feedback one where the time integral term is suppressed. With this simplification, it is possible to establish a physical analogy where the forcing can model realistically a porous medium, the limit case of a zero porosity corresponding to the modelling of a solid obstacle¹. Unfortunately, feedback and algebraic forcings have a common drawback related to their numerical stability properties. Schematically, both methods lead to a severe additional restriction on the time step to maintain very low residual velocities in locations where no-slip conditions are expected. In order to avoid this limitation (often very expensive in terms of computational cost), the use of the direct forcing technique is very attractive. In this third method, which introduces no additional numerical stability restriction, the boundary condition is ensured in a quite straightforward way by prescribing directly the velocity in forcing region at each step of the time integration. Finally, note that it can be easily shown [7] that feedback and algebraic methods can behave asymptotically (for a ‘vanishing porosity’) like a direct forcing method when their common modelling term is time integrated with a forward (implicit) Euler scheme.

¹This physical analogy can be exploited advantageously in order to interpret the meaning of the residual flow inside the modelled body (establishment of a d’Arcy law where velocity and pressure gradient are proportional) and to make easier the computation of the associated drag and lift [11]. Another advantage of this second forcing is related to its algebraic nature that offers the possibility to study theoretically its asymptotic convergence towards the case of a purely solid wall [1, 5].

1.2 Goals of the present study

In this paper, we are interested in the strategy where the direct forcing is combined with centred finite difference schemes of high accuracy. Such a combination is *a priori* problematic due to the discontinuities of the velocity derivatives created by the forcing. More precisely, the sudden application of the forcing inside the virtual boundary guarantees only the C^0 continuity of the solution whatever the spatial resolution is. The numerical code used for this study solves the incompressible Navier-Stokes equations discretized on a cartesian collocated grid with the aid of 6th order compact schemes. Despite their very favourable accuracy properties, these finite difference schemes are *a priori* not well suited for the numerical treatment of a discontinuity, even if the jump condition concerns only the first derivative. This problem is related to the quasi-spectral behaviour of compact schemes that leads to spurious oscillations in a similar way as spectral methods in presence of discontinuities (Gibbs phenomenon). In preliminary calculations based on the same numerical code as here, [7] reported that the creation of spurious oscillations in the neighbourhood of the obstacle was increased when a direct forcing was used instead of a feedback method. Since this problem was not mentioned in previous studies based on second order accurate codes [13],[3],[10], it was concluded by [7] that the spurious oscillations were a consequence of the spectral-like nature of the spatial discretization.

In this work, we propose a direct forcing method better suited for compact schemes. Basically, the idea is to create inside the body a flow preserving the no-slip condition at the surface but reducing the step-like change of the first derivative of velocities across the immersed boundary. This modification is shown to improve results both qualitatively and quantitatively.

2. FORMALISM

Schematically, the direct method consists in the application of the velocity condition $\mathbf{u}(\mathbf{x}, t) = \mathbf{u}_0(\mathbf{x}, t)$ in the forcing region. The target velocity field $\mathbf{u}_0(\mathbf{x}, t)$ is *a priori* a known of the problem, at least at the locations where boundary conditions are expected. The discrete integration of the incompressible Navier-Stokes equations with a Δt^2 Adams-Bashforth scheme gives

$$\frac{\mathbf{u}^{n+1} - \mathbf{u}^n}{\Delta t} = \frac{3}{2}\mathbf{F}^n - \frac{1}{2}\mathbf{F}^{n-1} - \nabla \tilde{\pi}^{n+1} + \tilde{\mathbf{f}}^{n+1} \quad (1)$$

with

$$\mathbf{F} = -\boldsymbol{\omega} \times \mathbf{u} + \nu \Delta \mathbf{u}, \quad \tilde{\pi}^{n+1} = \frac{1}{\Delta t} \int_{t_n}^{t_{n+1}} \pi \, dt \quad (2)$$

where $\pi = p/\rho + \mathbf{u} \cdot \mathbf{u}/2$ is the modified pressure (p and ρ are the pressure and the constant density respectively) while $\boldsymbol{\omega}$ is the vorticity field. The direct

forcing term takes simply the expression

$$\tilde{\mathbf{f}}^{n+1} = \varepsilon \left(-\frac{3}{2}\mathbf{F}^n + \frac{1}{2}\mathbf{F}^{n-1} + \nabla \tilde{\pi}^{n+1} + \frac{\mathbf{u}_0^{n+1} - \mathbf{u}^n}{\Delta t} \right) \quad (3)$$

with $\varepsilon = 1$ in the body region and $\varepsilon = 0$ everywhere else. Note that for simplicity, we consider only a motionless body surface (no time dependence of the mask function ε). In this case, the simplest method to ensure no-slip conditions is to use a zero target velocity field, namely $\mathbf{u}_0 = \mathbf{0}$. As already discussed in the preceding section, this simplified forcing generates discontinuities on the first derivative of velocities that are problematic when spectral or spectral-like schemes are used. In order to avoid this difficulty, the approach proposed in this study consists in estimating a target velocity field \mathbf{u}_0 that allows the no-slip condition at the boundary while reducing the presence of discontinuities.

In order to do this, a first possibility is to estimate \mathbf{u}_0 as the reverse to the flow immediately outside the body. For instance, for a circular cylinder of diameter D , a quite natural choice for the target velocity is $\mathbf{u}_0(r, \theta, z, t) = -\mathbf{u}(D - r, \theta, z, t)$ where (r, θ, z) are cylindrical coordinates associated to the circular body geometry. This type of forcing has already been tested by previous authors [13, 3] but only for the prescription of the inner velocities at the closest grid points to the body surface. In the present context of compact schemes, such a selective action would not be efficient enough due to the non-local character of the derivative estimation. Then, we define a target velocity in the full body domain as

$$\mathbf{u}_0(r, \theta, z, t) = -f(r)\mathbf{u}(D - r, \theta, z, t) \quad (4)$$

where the modulation function

$$f(r) = \sin(2\pi r^2/D^2) \quad (5)$$

is adjusted to ensure the regularity of inner velocities and to avoid the singularity at $r = 0$. Naturally, other choices of $f(r)$ are possible provided that the three following conditions are verified (i) $f(D/2) = 1$: accurate reverse condition near the body surface, (ii) $f(0) = 0$: singularity cancellation and (iii) $0 \leq f(r) \leq 1$ with moderate first and second derivatives for $0 \leq r \leq D/2$. For instance, $f(r) = \frac{1}{2}[1 - \cos(2\pi r/D)]$ is another suitable modulation function. Here, we choose the expression (5) because it cancels slightly more rapidly the target velocity when $r \rightarrow 0$, but it should be recognized that this choice is partly arbitrary.

In addition, it is possible to apply the reverse condition only to the tangential component of the velocity, the normal component being simply cancelled. Such a forcing leads to concentric streamlines inside the cylinder. Note this cancellation of the normal velocity inside the body does not create additional

discontinuities due to the incompressibility condition at the boundary that guarantees a zero normal derivative for this velocity component. In preliminary calculations (not presented here), we observed that both treatments of the internal normal velocity (reverse condition or cancellation) lead to equivalent results. In the data presented below, the normal inner velocity was maintained to zero except for the case of the tapered cylinder where the reverse condition was directly applied at the vectorial level. In complex geometry, the reverse condition is easier to implement because no projection of the velocity vectors is necessary in order to distinguish normal and tangential components. Naturally, the estimation of the target velocity using (4) on a cartesian grid needs to perform interpolations. Here, we only use a multilinear interpolation to prescribe the internal flow from the knowledge of the external one. Despite the second order accuracy of this procedure (which is significantly lower than the formal accuracy of the numerical code itself), it will be shown in the following that important benefits can be obtained from the use of 6th order compact schemes. An important point is that the target velocity field is not *a priori* divergence free. For this reason, the verification of the incompressible condition $\nabla \cdot \mathbf{u}^{n+1} = 0$ must be discarded inside the body by allowing a mass source/sink in region where $\varepsilon = 1$. Following the approaches proposed by [13, 6], a first possibility is to impose $\nabla \cdot \mathbf{u}^{n+1} = \varepsilon \nabla \cdot \mathbf{u}_0^{n+1}$. Here, we use a slightly modified condition $\nabla \cdot \mathbf{u}^{n+1} = \nabla \cdot (\varepsilon \mathbf{u}_0^{n+1})$ that was found to reduce more efficiently oscillations in the vicinity of the obstacle.

In the framework of the fractional step method, several adjustments are necessary in order to eliminate the various couplings introduced by the forcing method. In this context, a three step advancement yields

$$\frac{\mathbf{u}^* - \mathbf{u}^n}{\Delta t} = \frac{3}{2}\mathbf{F}^n - \frac{1}{2}\mathbf{F}^{n-1} - \nabla \tilde{\pi}^n + \tilde{\mathbf{f}}^* \quad (6)$$

$$\frac{\mathbf{u}^{**} - \mathbf{u}^*}{\Delta t} = \nabla \tilde{\pi}^n \quad (7)$$

$$\frac{\mathbf{u}^{n+1} - \mathbf{u}^{**}}{\Delta t} = -\nabla \tilde{\pi}^{n+1} \quad (8)$$

with the associated forcing term

$$\tilde{\mathbf{f}}^* = \varepsilon \left(-\frac{3}{2}\mathbf{F}^n + \frac{1}{2}\mathbf{F}^{n-1} + \nabla \tilde{\pi}^n + \frac{\mathbf{u}_0^{n+1} - \mathbf{u}^n}{\Delta t} \right) \quad (9)$$

where the target velocity \mathbf{u}_0^{n+1} is estimated by

$$\mathbf{u}_0^{n+1}(r, \theta, z, t) = -f(r)\mathbf{u}^*(D - r, \theta, z, t) \quad (10)$$

In first analysis, it can be expected that the splitting error introduced by the use of $\tilde{\mathbf{f}}^*$ in (6) and \mathbf{u}^* in (10) instead of $\tilde{\mathbf{f}}^{n+1}$ and \mathbf{u}^{n+1} respectively is only Δt^2 without any consequence on the final order of the time advancement.

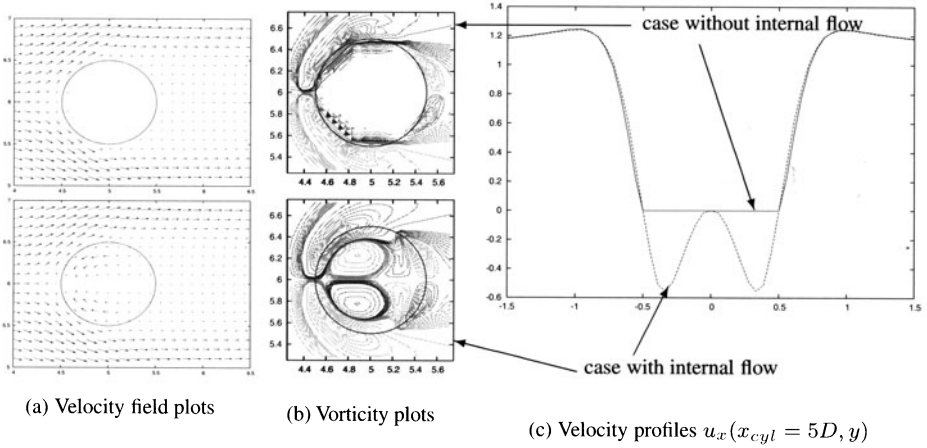


Figure 1. Comparison between two direct forcing methods with and without internal flow at $Re = 40$. The computational domain $(L_x, L_z) = (20D, 12D)$ is discretized on $n_x \times n_z = 361 \times 217$ grid points and the numerical code is based on Δx^6 compact schemes.

The last step is to derive a Poisson equation compatible with the condition $\nabla \cdot \mathbf{u}^{n+1} = \nabla \cdot (\varepsilon \mathbf{u}_0^{n+1})$. Here, we propose to use the approximation $\nabla \cdot (\varepsilon \mathbf{u}_0^{n+1}) = \nabla \cdot (\varepsilon \mathbf{u}^{**})$ that leads to the pressure equation

$$\nabla \cdot \nabla \tilde{\pi}^{n+1} = \frac{\nabla \cdot [(1 - \varepsilon) \mathbf{u}^{**}]}{\Delta t} \quad (11)$$

where the conventional Poisson equation is recovered for $\varepsilon = 0$ whereas inside the body, the condition $\varepsilon = 1$ yields the Laplace equation. Note that other variations on the method are possible, especially concerning the correction step (8) that can be conditioned by ε as in [13] where the pressure cells are explicitly masked (in this case, a two step splitting is only necessary). In this work, the correction by pressure gradients is performed everywhere in the computational domain *via* a fractional method in three steps.

3. RESULTS

3.1 Steady 2D wake at $Re = 40$

The benefit of the use of a non-zero target velocity is shown in figure 1 where a constant flow around a 2D cylinder is considered (see the caption of figure 1 for details about the simulation parameters). Two cases are compared depending on the target velocity treatment that can be zero (no internal flow) or given by (4) for the tangential component. The comparison between both forcing methods shows clearly the improvement offered by the use of a reverse flow inside the body. First, the examination of the longitudinal velocity profiles (1c view) obtained in each case shows clearly the more realistic near-body

Table 1. Comparison of statistical results obtained from various combinations between the forcing method and the numerical code accuracy. All DNS are performed using a computational domain $(L_x, L_y, L_z) = (20D, 2\pi D, 12D)$ discretized on $n_x \times n_y \times n_z = 361 \times 48 \times 216$ grid points. Data of DNS II' are from [7]. The streamwise location of the cylinder is $x_{cyl} = 5D$.

<i>DNS</i>	<i>I</i>	<i>II</i>	<i>III</i>	<i>IV</i>	<i>II'</i>
Forcing method	direct	direct	direct	direct	feedback
Internal flow	yes	no	yes	no	no
Scheme accuracy	Δx^6	Δx^6	Δx^2	Δx^2	Δx^6
Strouhal number	0.206	0.196	0.211	0.213	0.20
$L_{R_{xx}}/D$	1.38	1.55	1.22	1.27	1.64
$\text{Max}[R_{xx}]/U^2$	0.26	0.20	0.32	0.31	0.19

behaviour of the velocity when the first derivative discontinuity is avoided. The improvement of the near-body data is confirmed by the examination of vorticity isocontours (1b view). Note in particular the reduction of spurious vorticity when a reverse flow is imposed inside the cylinder. Quantitatively, by comparison to previous [14] or highly resolved results, we observe that the characteristic length scales of the flow are predicted more accurately when using the new forcing with the present spatial resolution. For instance, we verified that this new method allows a satisfactory prediction of the length of the wake bubble that is $L_w = 2.30D (\pm 0.03D)$, in good agreement with [14] who found $L_w = 2.27D$. In contrast, the use of a zero target velocity field leads to an overestimation of 10%, i.e., $L_w = 2.50D (\pm 0.03D)$. Finally, note that we verified that when the spatial resolution is increased, both forcing methods allow the convergence towards the correct length of the wake bubble while reducing considerably the spurious vorticity in the neighbourhood of the cylinder.

3.2 Unsteady 3D wake at $Re = 300$

In this section, we compare four DNS combining three different forcing methods with two numerical codes based on Δx^2 or Δx^6 (compact) centred finite difference schemes (see table 1 and its caption for more details about the simulation parameters). Concerning the length scale selection, similar trends as for $Re = 40$ are recovered for this unsteady case at higher Reynolds number. The formation length $L_{R_{xx}}$ (deduced from the streamwise location where the Reynolds stress R_{xx} reaches its maximum) is better predicted using the forcing (4) whereas the use of $\mathbf{u}_0 = \mathbf{0}$ leads to a typical 10% overestimation, in agreement with previous observations of [7] based on DNS using the feedback forcing method. Compared to reference values, an improvement of the Strouhal number prediction is also obtained. However, the comparison be-

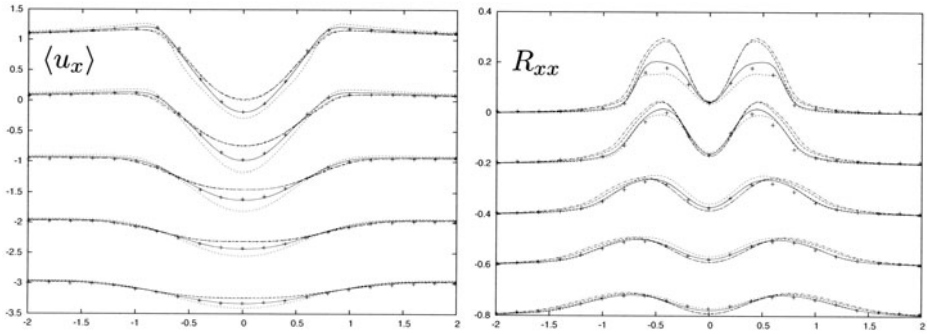


Figure 2. Profiles of longitudinal velocity statistics at different streamwise locations $(x - x_{cyl})/D = 1.2, 1.5, 2.0, 2.5, 3.0$. — : DNS I; ····· : DNS II; ---- : DNS III; - · - · : DNS IV; + : reference data obtained by spectral DNS based on a cylindrical grid [8].



Figure 3. Isosurfaces of vorticity modulus $\omega = 1.5U_c/D$. Left: DNS I, right: DNS III.

tween DNS III and IV shows that these improvements are not obtained when Δx^2 schemes are used, this insensitivity to the forcing method (with or without internal flow) being consistent with the previous observations of [3]. Present conclusions can be confirmed by the examination of $\langle u_x \rangle$ and R_{xx} profiles presented in figure 2 for each case. The improvement offered by the use of Δx^6 compact schemes is clearly shown, especially when the forcing with internal flow is applied (DNS I). Conversely, the overestimation of the longitudinal velocity fluctuations obtained for both DNS III and IV emphasizes the interest of the use of highly accurate schemes, even if the formal accuracy is significantly lower due to the forcing method itself. Note that this present overestimation is consistent with the results of [10] who used also a numerical code based on Δx^2 schemes. Physically, at marginal resolution, the combination of Δx^2 schemes with a direct forcing method seems to inhibit the 3D motions near the cylinder. This phenomenon can be shown not only by statistical results but also through instantaneous visualizations. For instance, figure 3 presents a comparison between isosurfaces of vorticity modulus obtained from DNS I and III. The artificial inhibition of 3D motions in DNS III is clearly confirmed, especially through the lack of longitudinal vortices (stretched between the Karman structures) compared to results from DNS I.

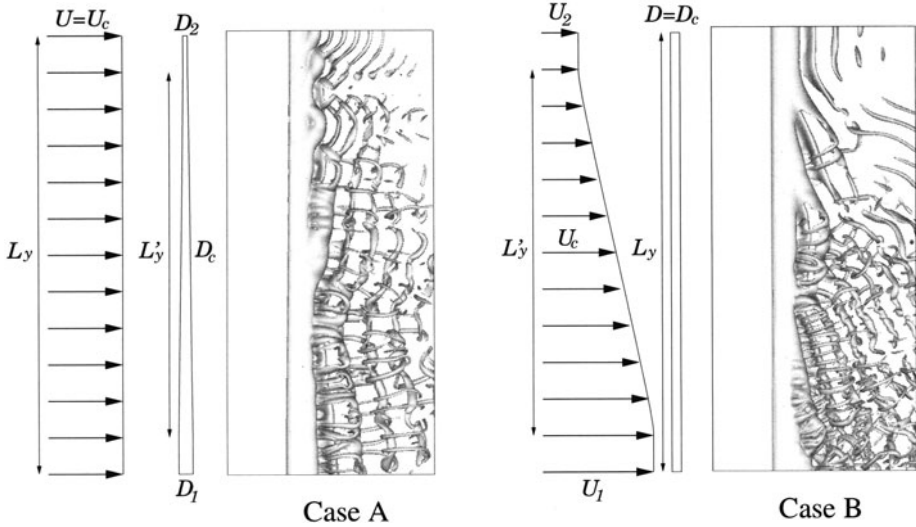


Figure 4. Comparison of instantaneous vorticity visualizations. The computational domain $(L_x, L_y, L_z) = (22D_c, 48D_c, 12D_c)$ is discretized on $n_x \times n_y \times n_z = 397 \times 385 \times 216$ grid points with $L'_y = 40D_c$ and $x_{cyl} = 7D$. Data of Case B are from [12] who used a feedback forcing method.

3.3 Unsteady 3D wakes in complex geometry

In this section, two specific wake configurations are compared (see the caption of figure 4 for details about the simulation parameters). The case A corresponds to a flow of constant velocity $U = U_c$ over a tapered cylinder with a diameter $D(y)$ ranging from $D_2 = D_c/2$ to $D_1 = 3D_c/2$. The case B consists in a shear flow ($U_2 < U(y) < U_1$ with $U_2 = U_c/2$ and $U_1 = 3U_c/2$) over a cylinder of constant diameter $D = D_c$. For each case, $D(y)$ or $U(y)$ vary linearly from $y = -L'_y/2$ to $y = L'_y/2$ (see figure 4) and the common Reynolds number $Re_c = U_c D_c / \nu$ is 200. Hence, both flow configurations cover an equivalent range of local Reynolds number $Re = UD/\nu$ with $100 < Re < 300$. Moreover, in both cases, a local adjustment of the vortex shedding frequency f on the local diameter $D(y)$ or velocity $U(y)$ can be expected by limiting (in first analysis) the deviation of the local Strouhal number $St = fD/U$ from its value for a conventional wake. Note that such a local selection leads to high frequencies in the low Re region for case A and the opposite situation for case B. Naturally, this selection cannot be purely local due to the preservation of the coherence of the flow motion in y -direction. The vortical organization obtained for each case is presented in figure 4. Despite the similarities between these two flow configurations, the local mechanisms of vortex shedding lead to the formation of well marked cells in case A whereas in case B, the main effects are linked to the selection of oblique structures (note however that a cellular pattern of vortex shedding can also be identified for case B by means of a fre-

quency analysis [12]). The occurrence of dislocations (phase breaking, tearing of vortices) can be observed in both cases, but these phenomena are found to be more frequent for case A. A quantitative comparison between these two flows (frequency analysis, mean and fluctuating motions) is currently in progress.

Acknowledgments

Calculations were carried out at the IDRIS. This study was partially supported by the Région Poitou-Charentes and the CNRS.

References

- [1] P. Angot, C.-H. Bruneau, and P. Fabrie. A penalization method to take into account obstacles in incompressible viscous flows. *Numer. Math.*, **81**:497–520, 1999.
- [2] E. Arquis and J. P. Caltagirone. Sur les conditions hydrodynamiques au voisinage d'une interface milieu fluide-milieu poreux : application à la convection naturelle. *C. R. Acad. Sci.*, **299**(1):1–4, 1984. Série II.
- [3] E. A. Fadlun, R. Verzico, P. Orlandi, and J. Mohd-Yusof. Combined immersed-boundary finite-difference methods for three-dimensional complex flow simulations. *J. Comp. Phys.*, **161**:35–60, 2000.
- [4] D. Goldstein, R. Handler, and L. Sirovich. Modeling a no-slip boundary condition with an external force field. *J. Comp. Phys.*, **105**:354–366, 1993.
- [5] N. K.-R. Kevlahan and J.-M. Ghidaglia. Computation of turbulent flow past an array of cylinders using a spectral method with Brinkman penalization. *Eur. J. Mech. B/Fluids*, **20**:333–350, 2001.
- [6] J. Kim, D. Kim, and H. Choi. An immersed-boundary finite-volume method for simulations of flow in complex geometries. *J. Comp. Phys.*, **171**:132–150, 2001.
- [7] E. Lamballais and J. Silvestrini. Direct numerical simulation of interactions between a mixing layer and a wake around a cylinder. *J. Turbulence*, 3:028, 2002.
- [8] R. Mittal and S. Balachandar. On the inclusion of three-dimensional effects in simulations of two-dimensional bluff-body wake flows. In *Proc. of ASME Fluids engineering division summer meeting*, Vancouver, British Columbia, Canada, 1997.
- [9] C. S. Peskin. Flow patterns around heart valves: a numerical method. *J. Comp. Phys.*, **10**:252–271, 1972.
- [10] U. Piomelli and E. Balaras. Numerical simulations using the immersed boundary technique. In *Proc. third AFSOR International Conference on Direct and Large-Eddy Simulations*, Arlington, Texas, USA, 2002.
- [11] K. Schneider and M. Farge. Adaptive wavelet simulation of a flow around an impulsively started cylinder using penalisation. *Appl. Comput. Harmon. Anal.*, **12**:374–380, 2002.
- [12] J. Silvestrini and E. Lamballais. Direct numerical simulation of oblique vortex shedding from a cylinder in shear flow. In *Proc. 3rd International Symposium on Turbulence and Shear Flow Phenomena*, Sendai, Japan, 2003.
- [13] F. Tremblay, M. Manhart, and R. Friedrich. DNS of flow around a circular cylinder at a subcritical Reynolds number with cartesian grid. In *Proc. of the 8th European Turbulence Conference, EUROMECH*, Barcelona, Spain, 2000.
- [14] T. Ye, R. Mittal, H. S. Udaykumar, and W. Shyy. An accurate cartesian grid method for viscous incompressible flow with complex immersed boundaries. *J. Comp. Phys.*, **156**:209–240, 1999.

4.5 AERODYNAMIC AND TURBOMACHINERY FLOWS

PERSPECTIVES OF LES IN TURBOMACHINERY DESIGN

Peter Flohr and Carlos Härtel

Alstom (Switzerland) Ltd.

CH-5401 Baden

peter.flohr@power.alstom.com, carlos.haertel@power.alstom.com

Abstract Three-dimensional simulations have become widespread in the analysis of turbomachinery flows over the past decade. Air-intake configurations, blade passages, internal cooling systems, or combustor flows are all investigated using advanced CFD techniques today. However, while the value of CFD for basic research is out of question, its use in the design process of turbomachinery components has remained very limited. Steady 3D computations are often done for final design assessment only, and unsteady methods like uRANS and LES are hardly employed at all. Given the broad design experience already available in the industry today, uRANS and LES are likely to be employed in future design efforts only where flow unsteadiness plays a critical role and where its effects cannot readily be predicted with sufficient accuracy using simplified correlations or steady-state computations. As an example, the present paper discusses a complex swirl-combustor application where LES or uRANS are needed in order to capture large-scale instabilities, which have a substantial impact on the mixing properties of the flow.

Keywords: Turbomachinery flows, unsteady aerodynamics

1. Introduction

Turbomachinery offers some of the most complex applications of fluid dynamics, with intense turbulence, complicated-shaped domains, chemical reactions and heat transfer being just a few of the challenges that development engineers have to cope with. For better understanding of the physics of turbomachinery flows, advanced CFD techniques are widely used in academic and industrial research. On the other hand, the *design* of turbomachinery components is still largely based on one- or two-dimensional approaches today. Many of the computational tools used, like e.g. throughflow codes, treat the flow in a semi-empirical manner, employing tabulated datasets for characterizing stage

efficiencies and aerodynamic performance. CFD is normally applied for final design cross-checking only, and is restricted then to steady-state calculations. Among the main reasons why simplified tools are often preferred over more complete simulations in the design process, is the computational expense associated with the latter. This is already true for steady simulations and even more so for unsteady RANS (uRANS) and Large-Eddy Simulation (LES). If more detailed resolution of flow phenomena in space and time were to produce much better predictions of the performance of a turbomachinery component (say, of its efficiency, stall margin, or emission levels), the additional computational effort could be justified; however, this is often not warranted. Given the broad design experience in the industry, CFD results have to compete with established design rules and correlations that were validated extensively in the past. Moreover, design robustness and operational safety require to stay clear of critical unsteady flow regimes – like rotating stall, surge, or stage clocking, to name but a few – where uRANS and LES could be most advantageous for flow analysis.

To what extent LES may enter the design process in the future will depend on the competitive advantage that LES (or for that matter uRANS) has over more “traditional”, simpler approaches. Advantage must be measured here in terms of both accuracy and effort. It is conceivable, for example, that unsteady simulations partly displace series testing of blades in wind tunnels, provided that accuracy isn’t compromised. The correlations and blade characteristics obtained would be used in subsequent steps of the design procedure just like experimental data are employed today. On the other hand, it is unlikely that LES can become economical for studying design variants of complete multi-stage engines in the foreseeable future; even if optimistic improvements in overall accuracy are assumed, the effort required would be prohibitive.

A field where the strength of LES may pay off first is the aerodynamic design of advanced gas-turbine combustors. Here the reliable prediction of the mixing properties of the flow is of crucial importance for achieving low NO_x emissions. Since these mixing properties may be strongly affected by large-scale flow unsteadiness – which steady-state approaches inevitably miss out – the potential for uRANS and LES is appreciable. In the following sections we will illustrate this point, using the Alstom EV burner as a case study where the advantages of unsteady CFD can be already recognized.

2. The Alstom EV burner

As a typical example of a lean-premix burner, the Alstom EV burner is depicted in a perspective sketch in figure 1. Like most modern gas turbine burners, it incorporates swirl. Towards the exit, vortex break-down occurs, which forms a recirculation zone that stabilizes the premix flame. The gaseous fuel is injected

via holes distributed along the swirler slots. The strong swirl inside the burner cone leads to rapid mixing such that the fuel-air mixture is very homogeneous at the burner exit.

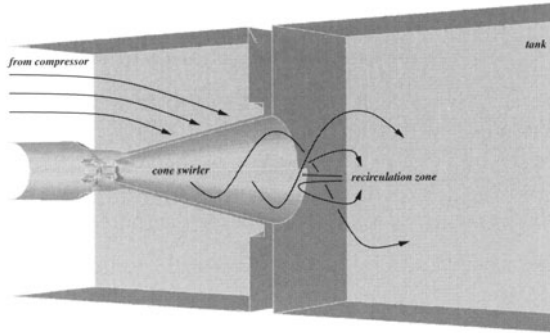


Figure 1. The Alstom EV burner: The flow enters the swirler through the two inlet slots on the cone shell in circumferential direction. Between the shells, a swirling conical flow develops which breaks down near the exit. Gaseous fuel is injected into the passing air stream along the burner slots.

3. Numerical setup

The geometry used in the CFD simulations corresponds to the setup sketched in figure 1. The body-fitted mesh with 500,000 cells is fully unstructured and based on hexahedral cells in the burner cone and in the combustor, while tetrahedral cells are used to resolve the geometrically complex parts of the burner, as well as the plenum upstream of the swirler.

The turbulence was parameterised using models of different complexity. At the simplest level, the standard $k - \epsilon$ model was used. At an intermediate level, a full Reynolds-stress transport model was used. At the most involved level, the large-eddy simulation approach was used, and the subgrid turbulent stress was obtained from the Smagorinski-Lilly eddy viscosity. Scalar transport was always modeled through a gradient-diffusion model with constant turbulent Prandtl number $Pr_t = 0.7$.

To keep numerical costs at a reasonable level, the fuel injectors were not resolved explicitly. Rather, a simplified setup was chosen, where the fuel is injected into the flow shortly downstream of the injector location, through a numerical source in a single grid cell. The position of the injection point was determined from experimental observation.

Table 1 shows a summary of the numerical schemes used for the simulations. Where possible, the most accurate schemes were employed. However, the RSM simulations did not lead to converged solutions for 2nd order discretiza-

Turbulence model	<i>steady</i>		<i>unsteady</i>	
	$k - \epsilon$	<i>RSM</i>	<i>RSM</i>	<i>LES</i>
Pressure	2nd order	1st order	2nd order	2nd order
Momentum	QUICK	1st order	QUICK	2nd order central
Pressure-Vel. coupl.	SIMPLE	SIMPLE	SIMPLE	SIMPLE
Reynolds stresses	-	1st order	QUICK	-
Turb. kin. energy	QUICK	1st order	QUICK	-
Turb. diss. rate	QUICK	1st order	QUICK	-
Species transp.	QUICK	1st order	QUICK	QUICK
temporal discr.	-	-	2nd order	2nd order

Table 1. Summary of the numerical setup employed for the simulations presented here.

tion due to the strong helical flow instability which was picked up by this model. To avoid the transient flow, either 1st order discretization had to be used or the flow needed to be modeled on a half grid (taking into account the polar symmetry in the geometry, thereby suppressing the appearance of a helical flow instability).

All simulations were carried out on the same grid setup to make the simulations comparable. The grid resolution was based on a posteriori tests where the turbulent integral length scale was estimated from a $k - \epsilon$ simulation, and the final cell size was chosen to be significantly below this scale.

4. Analysis of the mean burner flow

The prediction of the position of the vortex breakdown is plotted in figure 2. All steady simulation approaches fail to predict both, the position of the vortex breakdown as well as the magnitude of the axial jet ahead of the breakdown when compared against LDA measurements in the watertunnel at the same operating conditions. The results are normalized with the nominal burner flow U_N , and a characteristic burner size D_N . Only the unsteady RSM and LES simulations capture the flow pattern appropriately.

The axial and tangential flow components in a line cut perpendicular to the burner axis are displayed in figure 3. Here, the discrepancies between the models is not so evident. Only the axial velocity component of the $k - \epsilon$ model is significantly off which is due to the discrepancy in the breakdown position. Also included in this figure is a result from the simulation where the burner symmetry has been used to suppress the instability in order to achieve 2nd order accurate RMS solutions. While the prediction of the breakdown position appeared to be significantly improved when compared against the $k - \epsilon$ and 1st order RSM solutions (figure 2), the analysis of the velocity profiles in figure 3 reveals significant discrepancies for this modeling approach. Thus, this modeling approach was not followed further.

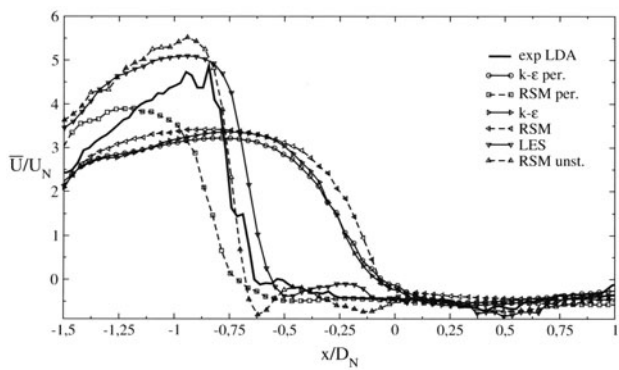


Figure 2. Normalized axial velocity along the burner axis. 0 corresponds to the burner exit position.

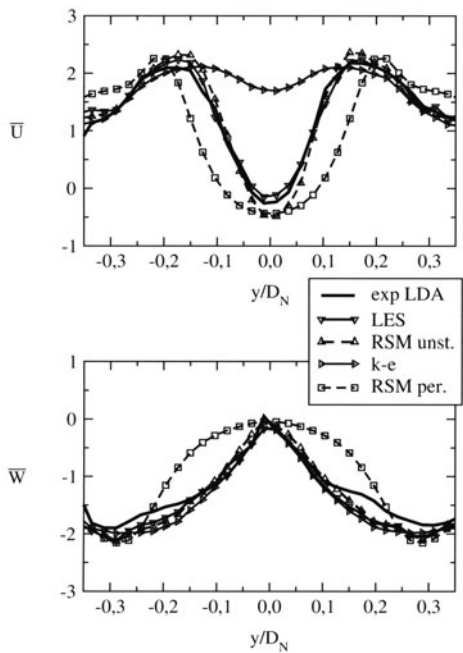


Figure 3. Normalized axial velocity (top) and tangential velocity (bottom) in a line cut perpendicular to the burner axis. Cut is taken shortly before the expansion into the combustion chamber.

The correct prediction of mixing will not only depend on the correct prediction of the mean burner flow but also on the turbulent fluctuation field. In figure 4 we plot the axial and transversal turbulent fluctuations at the same line cut from figure 3. The turbulence levels from the $k - \epsilon$ simulation are underpredicted

by a factor of two in the centre of the flow, and completely miss out the peaks in turbulence intensity which are associated with regions of high shear in the flow. As the complexity of the model is increased, the turbulent fluctuations are captured better and for the LES, excellent agreement with the watertunnel data is reached.

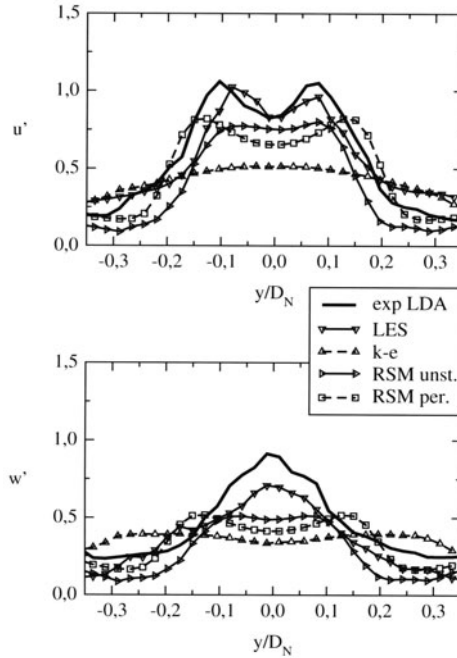


Figure 4. Normalized axial (top) and transversal (bottom) turbulent fluctuations in a line cut perpendicular to the burner axis. Cut is taken shortly before the expansion into the combustion chamber.

5. Analysis of mixing and the unsteady flow

The burner mixing fields have been analysed at various axial locations in planes perpendicular to the burner axis. In these simulations fuel was injected only at a single fuel injector in the slot. Watertunnel measurements allowed to compare both the absolute location of the single fuel streak as well as the mixing quality in terms of its unmixedness. We present here only the main results in terms of the unmixedness U . The spatial unmixedness is summarized for all simulations in figure 5. The $k - \epsilon$ simulation smears out the fuel too much almost immediately after the injection point and leads to underpredicting unmixedness at the burner exit by more than 100%. Whilst the unsteady simulations appear to give good (and in the case of LES excellent) agreement at the burner exit,

the unmixedness is overpredicted by almost a factor of 3 in the vicinity of the injector. This finding was surprising at first but became clearer after analysing also the temporal unmixedness. By definition, the temporal unmixedness in the flow can only be obtained from transient simulations and in figure 6 we show the results of this analysis for the large-eddy simulation in terms of both spatial and temporal unmixedness. In the experiment, the temporal unmixedness is much larger than the spatial, indicating that near the fuel injector large variations in time with respect to the local fuel position exist. This is caused by strong fluctuations of the fuel jet around its mean position. In the large-eddy simulation, this trend near the injector is completely reversed and temporal unmixedness is below the spatial. It turned out that this is a direct consequence of the modeling approach for the fuel injector. The assumption of a steady fuel flow inside the burner slot is not representative of the strongly fluctuating fuel jet which emanates from the nozzle in reality. However, this effect is strongly damped out as the fuel travels downstream through the burner and excellent agreement with the experiment is reached at the burner exit plane.

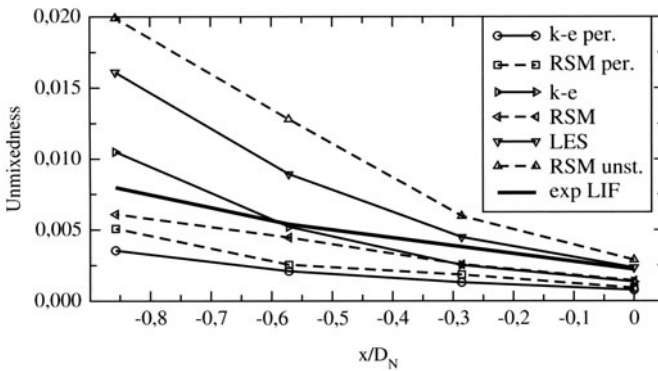


Figure 5. Spatial unmixedness versus axial position. 0 corresponds to the burner exit position.

The effect of the flow instability which is picked up by both the unsteady RSM and by the LES simulations is now analysed in more detail. It has been noted before (Paschereit *et al.* 2000) that the burner flow exhibits a helical flow instability at a Strouhal number $St = 1.3$.

To quantify the contribution of this flow instability to the turbulent mixing process, we apply now a triple decomposition technique (Matsumura & Antonia 1993) where the turbulent fluctuations a are split into a random part a' and a coherent part \tilde{a} :

$$A = \bar{A} + \underbrace{\tilde{a} + a'}_a \quad (1)$$

Using this decomposition technique, the coherent structure \tilde{a} can be determined by analysing the Fourier-transformed spectra of all the locations and

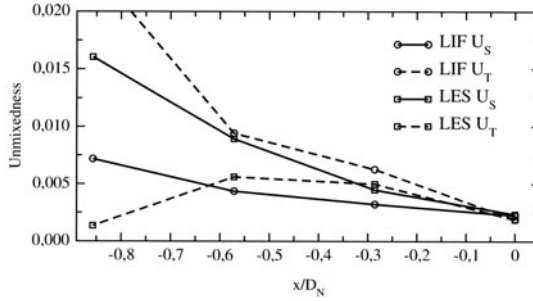


Figure 6. Temporal (U_T) and spatial (U_S) unmixedness versus axial position. 0 corresponds to the burner exit position.

extracting phase ϕ and amplitude \hat{a} for the frequency ω of the desired coherent structure. This implies for the coherent structure \tilde{a} ,

$$\tilde{a} = \hat{a} \sin(\omega t + \phi). \quad (2)$$

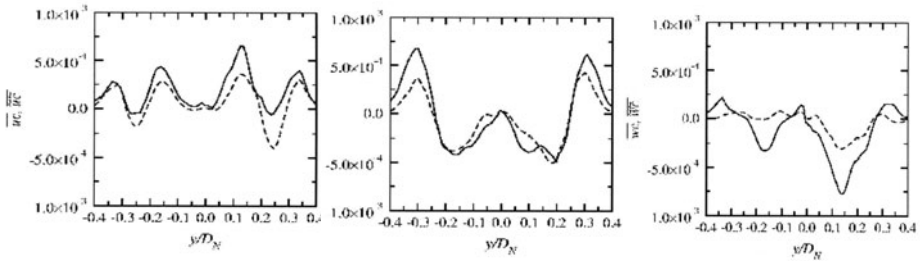


Figure 7. Total turbulent scalar transport and coherent part only, plotted at the selected line cut from figure 3. u, v, w are axial, radial, and tangential velocity components. (—) global turbulent transport; (---) coherent turbulent transport.

The Fourier decomposition allows to formulate analytical expressions for the stresses associated with the coherent motion. For example, for the coherent normal Reynolds stress \tilde{u}^2

$$\tilde{u}^2 = (\hat{u} \sin(\omega t + \phi))^2 \quad (3)$$

Integrating over one period T of the instability

$$\overline{\tilde{u}^2} = \frac{1}{T} \int_0^T \hat{u}^2 \sin^2(\omega t + \phi) dt = \frac{\hat{u}^2}{T} \left[\frac{t}{2} - \frac{1}{4\omega} \sin(2(\omega t + \phi)) \right]_0^T \quad (4)$$

leads to

$$\overline{\widehat{u}^2} = \frac{1}{2} \widehat{u}^2. \quad (5)$$

Similarly, for the coherent Reynolds shear stresses and coherent turbulent species transport,

$$\overline{\widehat{uv}} = \frac{1}{2} \widehat{uv} \cos(\Delta\phi) \quad (6)$$

and

$$\overline{\widehat{uc}} = \frac{1}{2} \widehat{uc} \cos(\Delta\phi). \quad (7)$$

The phase difference $\Delta\phi$ is $\Delta\phi = \phi_u - \phi_v$.

The contribution of the coherent flow structure to the turbulent Reynolds stresses is not displayed here but is in the order of 25-50% of the overall turbulent stresses. Even more dramatically is the contribution of the coherent structure to the turbulent scalar transport and this is displayed in figure 7. Both axial (left) and radial (middle) turbulent transport, and to a slightly lesser extend the circumferential (right) transport, are dominated by the coherent structure. In fact, the middle graph shows how the coherent structure transports fuel into the centre of the flow (i.e., the recirculation zone) and how it also transports fuel outwards to the walls of the swirler. This finding has an important implication for the modeling of such flows: any steady-state simulation technique will necessarily fail to consider the effects of the coherent vortex motion. It is concluded that the mixing process simulated in steady-state computations is not appropriate if a dominant coherent flow instability is present, and this finding should be taken into consideration if steady-state computations are used to analyse the mixing field in swirl-stabilized burners.

6. Concluding remarks

In a case study for LES in turbomachinery flows, the flow and mixing pattern in a swirl-stabilized gas turbine burner has been analysed. All steady-state simulations of this configuration essentially failed to either predict the recirculation zone or the turbulence level correctly. However, for the unsteady RSM and full LES-turbulence models very good agreement with experiments for velocity, turbulence, and mixing fields could be observed. Indeed, a detailed analysis of the LES via a triple decomposition technique showed how the large-scale coherent structure completely dominates the mixing process. This suggests that such flows can only be properly modeled by unsteady simulations (or perhaps by steady-state approaches with flow-specific model tuning).

While the potential of LES in gas turbine combustors has been outlined in this study, a final word of caution is in order. For gas turbine combustor flows, appropriate LES combustion models are still being developed and validated

(Flohr & Pitsch 2000), and simulations including combustion for design purposes appear out of reach until today. Also, as the fundamental understanding of the processes in gas turbine combustion is far from complete, the application of unsteady CFD tools (and, in fact, all numerical and analytical tools) needs to be embedded always in a systematic development procedure where careful validation of CFD tools, the exploration of the range of applicability of a particular model, as well as detailed experimental analysis throughout the development all remain crucial and complementary steps for successful gas turbine combustor design.

References

- P. Flohr, and H. Pitsch. (2000). "A turbulent flame speed closure for LES of industrial burner flows." Center for Turbulence Research, Annual research briefs.
- T. F. Fric. (1993). "Effects of Fuel-Air Unmixedness on Nox Emissions", *Journal of Propulsion and Power*, Vol. 9, No. 5, pp. 708-713.
- M. Matsumura and R. A. Antonia. (1993). "Momentum and heat transport in the turbulent intermediate wake of a circular cylinder", *Journal of Fluid Mechanics*, vol. 250, pp. 651-668
- C. O. Paschereit, P. Flohr, E. Gutmark and M. Bockholts. (2000). "Numerical and experimental analysis of acoustically excited combustion instabilities in gas turbines", AIAA 2000-2076, 6th AIAA/CEAS Aeroacoustic Conference 12-14 June 2000.

LARGE-EDDY SIMULATION OF A JET IN A CROSSFLOW

Xuyao GUO, Matthias MEINKE and Wolfgang SCHRÖDER

Aerodynamisches Institut, RWTH Aachen

Willnerstr. zw. 5 und 7, 52062 Aachen, Germany

Tel.: +49-241-8095410, E-mail: office@aia.rwth-aachen.de

Abstract The flow field induced by the interaction between a single jet flow exhausting from a pipe and a turbulent flat plate boundary layer at a local Reynolds number of $Re_\infty = 400,000$ is numerically studied using large-eddy simulation (LES). The ratio R of the jet velocity to the cross stream velocity is 0.1. The flow regime investigated corresponds to that of gas turbine blade film cooling. In order to provide the realistic time-dependent turbulent inflow information for the crossflow an LES of a spatially developing turbulent boundary layer is simultaneously performed using a rescaling method for compressible flow. The main flow features such as the separation area inside the pipe and the recirculation downstream of the jet exit are analyzed.

Keywords: LES, jet in crossflow (JICF)

1. Introduction

The highly complex flow phenomenon of a jet in a crossflow (JICF) is encountered in a variety of engineering problems. Depending on the ratio R of the jet velocity to the cross stream velocity, several examples of this flow can be found, for instance, in turbomachinery when film cooling of turbine blades or jets into combustors are considered, in V/STOL aircraft in transition flight, and in the case of waste disposal from smoke stacks into the atmosphere. The numerical simulation of such problems requires a correct prediction of the interaction between the jet and the surrounding laminar or turbulent boundary layer. The interaction itself is characterized by the development of a horseshoe-like vortex wrapped around the exit jet and a counter-rotating vortex pair (CVP), which is formed as the jet transitions into the crossflow direction and dominates the far field.

Due to the practical significance numerous investigations have been carried out over the last fifty years to gain more knowledge about the vortex structures and dynamics in the flow field. Most studies, however, do not consider the turbu-

lent boundary layer and the relatively small velocity ratio R , which is typically encountered when the cooling of gas turbine blades is inquired. Furthermore, an accurate prediction of the flow using the presently available Reynolds averaged turbulence models is impaired by the strong curvature of the streamline as well as the reverse flow (Hahn and Choi, 1997). Therefore, it is essential to apply a more precise numerical tool such as large-eddy simulations (LES) to investigate in detail the flow field and the vortex dynamics in the vicinity and further downstream of the jet exit.

2. Flow Configuration

The flow model for the simulation is shown in figure 1. The same configuration is experimentally analyzed using the particle image velocimetry (PIV) technique. The origin of the frame of reference coincides with the plate surface and the center of the hole. The coordinates x, y, z represent the streamwise, normal, and spanwise direction.

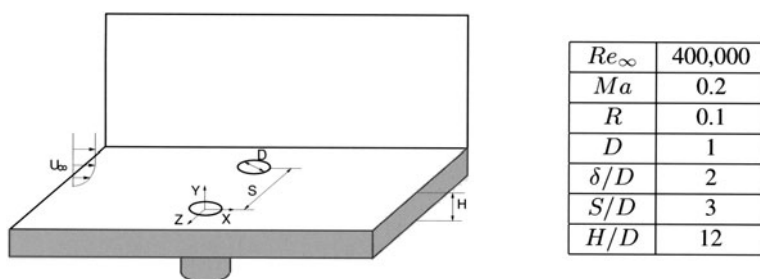


Figure 1. Flow Parameters and Schematic of the Flow Configuration

To mimic the flow parameters in a gas turbine a turbulent flat plate boundary layer at a local Reynolds number of $Re_\infty = 400,000$ and a Mach number $Ma = 0.2$ interacts with a jet, which is part of a complete row of jets that are located perpendicular to the streamwise direction of the boundary layer flow. The ratio of the local boundary layer thickness to the hole diameter is $\frac{\delta}{D} = 2$. Although the velocity ratio $R = 0.1$ is rather small, it is, nonetheless, a typical value when film cooling for gas turbine blades is considered. The whole integration domain comprises a plenum under the jet hole, a pipe connecting the plate and the plenum, and the region where the boundary layer interacts with the jet. Since the plenum is part of the computational domain no empirical information such as the discharge coefficient has to be prescribed. The flow rate and the velocity distribution at the jet exit are sought in the overall computation. The flow parameters and the geometrical parameters are summarized in figure 1.

3. Numerical Method

The governing equations for an LES are obtained by a convolution of the Navier-Stokes equations for an ideal gas with a low-pass filter of width Δ , which corresponds in this study to a local average in each grid cell (Rogallo and Moin, 1984). Since the turbulent flow is characterized by strong interactions between various scales of motion, schemes with a large amount of artificial viscosity significantly impair the level of energy distribution governed by the small-scale structures and therefore distort the physical representation of the dynamics of small as well as large eddies. To remedy this problem the advective fluxes are approximated in this study by a mixed central-upwind AUSM (advective upstream splitting method) scheme with low numerical dissipation, which has been shown in (Meinke et al., 2002). Similar to the MILES approach (Fureby and Grinstein, 1999), the inherent dissipation of the numerical scheme serves as a minimal implicit SGS model. The viscous terms are approximated by a central scheme and an explicit five-step Runge-Kutta time stepping scheme is used for the temporal integration. These discretization schemes result in an overall approximation of the method of second-order accuracy in space and time.

In the simulation of turbulent boundary layers the problem of how to prescribe time-dependent turbulent inflow conditions at the upstream boundary is encountered. The formulation of the inflow boundary condition for the JICF calculation is based on a slicing technique. That is, the flow variables at the entrance of the domain are obtained from a simultaneously conducted LES of a spatially developing turbulent boundary layer flow, as shown in figure 2, such that the level of turbulence intensity is physically correct. To implement the auxiliary flat plate turbulent boundary layer simulation where an inflow boundary condition is also needed a rescaling technique for compressible flow is applied (El-Askary et al., 2001).

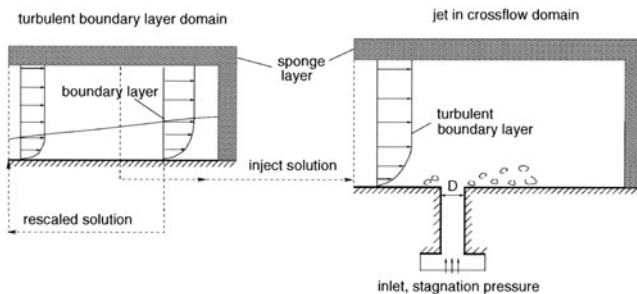


Figure 2. Sketch of the Boundary Conditions

On the wall the non-slip condition holds and an adiabatic surface is assumed. In the spanwise direction full periodic boundary conditions are imposed. The stagnation pressure value is specified at the inlet of the plenum (Fig. 2) such that the jet flow is driven by the pressure difference between the plenum and the crossflow. At the outer circumferential surface of the plenum the mass flux is assumed to vanish asymptotically. A characteristic approach is applied at the outflow boundaries of the JICF domain. To damp possible numerical reflections introduced by the outflow boundary conditions a sponge layer zone is used, as shown in figure 2, in which source terms S are added to the governing equations. The source terms are computed as a function of the deviation of the instantaneous solution \bar{Q} from an appropriate analytical distribution Q_a based on the logarithmic law, $S = \sigma(\bar{Q}(t, \vec{x}) - Q_a(\vec{x}))$, which is valid far downstream from the interaction region. The parameter σ is a function of the distance from the boundaries and decreases from σ_{max} to 0 within the sponge layer zone. The value for σ_{max} is chosen to be 0.5, which was determined in test simulations under the condition to efficiently minimize numerical reflections.

4. Results and Discussion

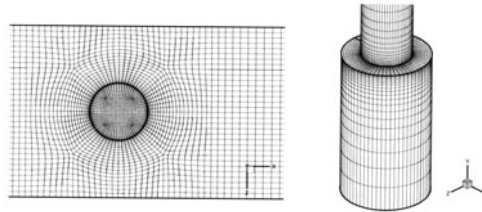


Figure 3. Grids of JICF, Top View of the Jet Exit Region (Left) and Plenum (Right), Every 2nd Grid Point Is Shown

From the simultaneously performed turbulent boundary layer simulation the time-dependent flow properties at a certain plane are extracted and prescribed as inflow condition for the JICF calculation. The inflow boundary of the JICF domain is located $8D$ upstream of the jet hole center such that the influence of the jet flow on the upstream flow field can be neglected. The grid lines at the inlet area coincide with those of the boundary layer simulation, i.e., no interpolation of the solution is required. Various parts of the computational grid of the jet in a crossflow problem are shown in figure 3. The total mesh consists of 4.6 millions grid points distributed in 32 blocks, 5 of which are used for the turbulent boundary layer over the flat plate simulation. The grid points are clustered near the solid surfaces. The first control volume next to the flat

plate has the dimension of $\Delta y = 0.004D$, which corresponds to $\Delta y^+ = 1.0$ scaled by the friction velocity of the incoming turbulent boundary layer. With this resolution the near-wall coherent structures, which contain most of the turbulent energy and distribute the turbulent energy from the streamwise into the other directions, are captured.

In the left picture of figure 4 the mean streamwise velocity profile in inner-law scaling from the turbulent boundary layer simulation is compared with the logarithmic law, which consists of the viscous sublayer $y^+ \leq 5.0, u/u_\tau = y^+$, the buffer layer $5.0 < y^+ \leq 30.0, u/u_\tau = 5.0 \ln y^+ - 3.05$, and the logarithmic layer $y^+ > 30.0, u/u_\tau = 2.5 \ln y^+ + 5.5$. The numerical solution matches the sublayer profile and slightly deviates from the analytical distribution in the outer part of the boundary layer, which is due to the clustered mesh in the wall normal direction. In the right picture the turbulence intensities are compared with data from (Lund et al., 1998). The distributions evidence the good agreement with the findings from the literature right near the wall such that it can be stated that reliable inflow data are provided by the flat plate LES.

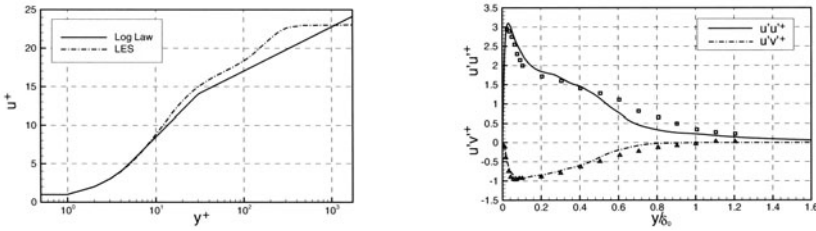


Figure 4. Turbulent Boundary Layer Simulation Compared with Analytical Solution (Left) and Data from Lund et al (Symbols) (Right).

The temporal evolution of the streamlines in the central plane near the jet exit is shown in figure 5. Compared with the experimental investigations for $R \geq 0.5$ in (Andreopoulos and Rodi, 1984) and (Kelso et al., 1996), several significant flow features in the present low R case can be identified. A rather large separation area exists along the leading edge of the pipe. It consists of two counter-clockwise eddies with a clockwise eddy lying between them, which is analogous to the horseshoe vortex structure depicted in (Kelso et al., 1996). Due to the small velocity ratio hardly any separation upstream of the jet exit can be observed. The boundary layer separates just at the edge of the exit. Due to the increased pressure in the interaction region of the boundary layer and the jet a reverse flow region forms inside the pipe with several small vortices. There is no classical horseshoe vortex structure, since the main circulation is determined by the jet not by the boundary layer. The vortical structure is highly

unsteady, i.e., the vortices are shed from the edge of the exit resulting in an oscillating flow field in the interaction region.

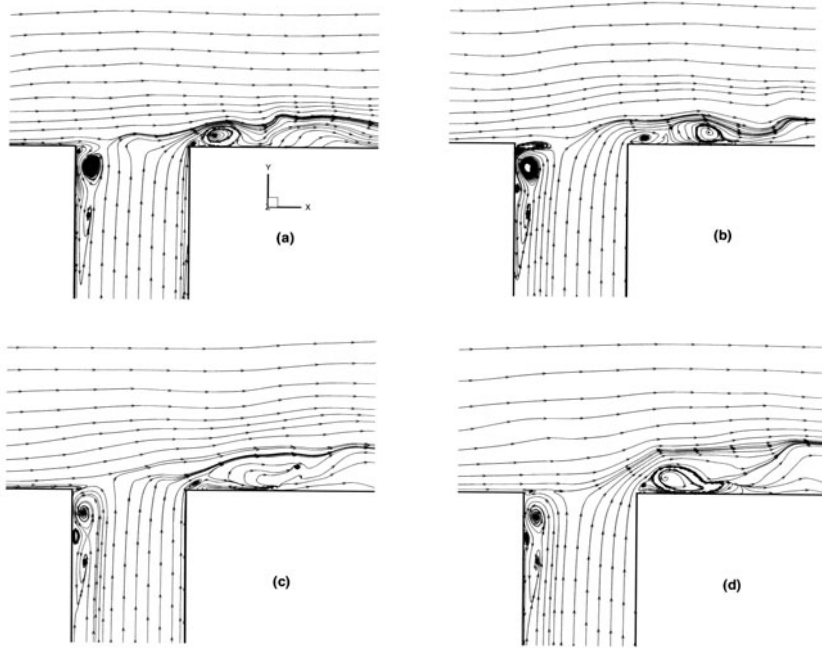


Figure 5. Streamlines in the Central Plane Near the Jet Exit at $R = 0.1$

Depending on the R value the interaction is different for each flow. If the velocity ratio is large, e.g., $R = 2$, the jet flow penetrates right into the freestream and behaves as a rigid obstacle mounted on the plate. A vortex structure is formed upstream of the jet exit. In contrast to the small velocity ratio case the blocking effect of the jet on the crossflow is significant. The crossflow behaves as if it encounters a pipe-like barrier. Although the flow undergoes a strong pressure rise on the windward side of the artificial pipe only tiny little vortices below the jet exit might occur since the inertia forces of the jet are large enough to overcome the pressure forces.

More information about the development of the vortex structures at $R = 0.1$ is given by visualizing the vortices using the λ_2 -criterion (Jeong and Hussain, 1995) in figure 6. On the leeside of the jet exit the wake region with a complex unsteady three-dimensional flow pattern develops. First, the negative boundary layer vorticity caused by the trailing edge of the pipe forms vortices, whose axes point in the spanwise direction. Second, the vorticity generated by the crossflow-jet interaction at the upstream edge of the jet hole is wrapped around

the jet and rolls up into streamwise vortical structures, which interact with the spanwise vortices. These are convected downstream and experience a shedding, bursting and regenerating process. Downstream of the jet exit a recirculation region occurs (Fig. 7) and in the wake patches of positive and negative vorticity can be observed. On the windward side of the jet flow the shear layer vortices, which are formed by the Kelvin-Helmholtz instabilities in the case of the strong jet flow, are not found in this study due to the small velocity ratio. In figure 6 the shade indicates the local Ma number mapped onto the λ_2 -contours. In the left picture the turbulence characteristics within the boundary layer over the flat plate are clearly visible. Due to the ratio $R = 0.1$ the jet flow possesses in the outer region of the boundary layer only a slight impact on the vortical pattern, which is indicated by the somewhat bulkier vortex structure just downstream of the jet exit. The flow pattern of the separation inside the pipe is shown in the right picture. The vortices flow around the jet and extend into the crossflow. That is, the vortices that determine the heat transfer downstream of the jet evolve at $R = 0.1$ from the interior of the pipe.

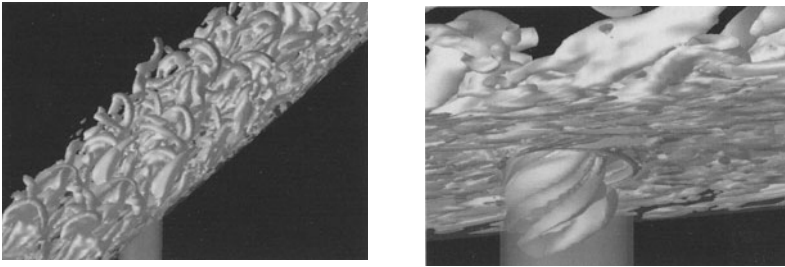


Figure 6. λ_2 -Contours Near the Jet Exit at $R = 0.1$; Top View (Left), Bottom View (Right)

Some pronounced features in the flow can be clarified by time averaging the instantaneous solutions. In figure 7 the 3D streamlines in the vicinity of the wall are depicted using an averaged flow field. In the region where the wake is formed the streamwise velocity of the crossflow accelerates and the conservation of mass requires fluid to move towards the plane of the symmetry. Very close to the wall a reverse flow region occurs. Fluid from the cross stream is entrained into this region, travels upstream, and is lifted upwards by

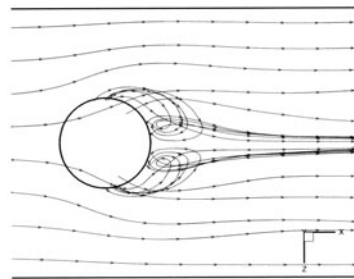


Figure 7. Streamlines of the Mean Flow Field in the Wake Region of the Jet

the jet flow and washed downstream in the shear layer formed by the jet and the crossflow. The symmetry of the mean flow field in figure 7 indicates the averaging time, which contains 125 time units that are defined by the ratio of the diameter of the hole to the freestream velocity of the outer flow D/u_∞ , to be sufficient for the analysis.

5. Conclusion

Large-eddy simulations (LES) of a jet in a crossflow (JICF) problem have been carried out to investigate in detail the intricate vortex structures in the low velocity ratio case $R = 0.1$. The parameters used in the calculation correspond to those encountered in film cooling of turbine blades. A rather large separation region is found on the windward side of the jet. It occurs within the pipe and the vortices wrap around the edge of the pipe and extend into the crossflow. A complicated unsteady wake region is formed on the leeside of the jet exit. The entrainment of the cross stream in this area prevents the cooling jet to effectively cover the wall surface just downstream of the jet exit and decreases the cooling efficiency.

Acknowledgments

The support of this research by the Deutsche Forschungsgemeinschaft (DFG) in the frame of SFB 561 is gratefully acknowledged.

References

- Andreopoulos, J., and Rodi, W., 1984, "Experimental Investigation of Jets in a Crossflow," *Journal of Fluid Mechanics*, Vol. 138, pp.93-127.
- El-Askary, W. A., Meinke, M., and Schröder, W., 2001, "Towards the Numerical Analysis of Trailing-Edge Noise," *Deutscher Luft- und Raumfahrtkongress 2001*, Hamburg.
- Fureby, C., and Grinstein, F. F., 1999, "Monotonically Integrated Large Eddy Simulation of Free Shear Flows," *AIAA Journal*, Vol. 37, pp.544-556.
- Hahn, S., and Choi, H., 1997, "Unsteady Simulation of Jets in a Cross Flow," *Journal of Computational Physics*, Vol. 134, pp.342-356.
- Jeong, J., and Hussain, F., 1995, "On the Identification of a Vortex," *Journal of Fluid Mechanics*, Vol. 285, pp.69-94.
- Kelso, R. M., Lim, T. T., and Perry, A. E., 1996, "An Experimental Study of Round Jets in Crossflow," *Journal of Fluid Mechanics*, Vol.306, pp.111-144.
- Lund, T. S., Wu, X., and Squires, K. D., 1998, "Generation of Turbulent Inflow Data for Spatially-Developing Boundary Layer Simulations," *Journal of Computational Physics*, Vol. 140, pp.233-258.
- Meinke, M., Schröder, W., Krause, E., and Rister, T., 2002, "A Comparison of Second- and Sixth-Order Methods for Large-Eddy Simulations," *Computers & Fluids*, Vol. 31, pp.695-718.
- Rogallo, R. S., and Moin, P., 1984, "Numerical Simulation of Turbulent Flows," *Annual Review of Fluid Mechanics*, Vol. 16, pp.99-137.

SEPARATED FLOW PAST AN AIRFOIL AT HIGH ANGLE OF ATTACK: LES PREDICTIONS AND ANALYSIS

Nikola Jovičić and Michael Breuer

Institute of Fluid Mechanics, Univ. of Erlangen-Nürnberg, D-91058 Erlangen, Germany

njovicic/breuer@Istm.uni-erlangen.de

Abstract The objective of this study is the prediction and analysis of the turbulent flow past an unswept wing at high angle of attack. The LES predictions were based on two different subgrid-scale models (Smagorinsky and Dynamic). The Reynolds number ($Re_c = 10^5$) and the angle of attack ($\alpha = 18^\circ$) were chosen such that the flow exhibits a trailing-edge separation at the lowest Re_c realizable within the corresponding experiment COSTWING. At these operating conditions, many interesting flow phenomena appear, e.g., a thin separation bubble, transition, separation, and large-scale vortical structures. Qualitatively the predictions based on both SGS models show the same aforementioned flow features, although some noteworthy differences become evident, e.g., the shape and size of the separation bubble. This has a strong impact on the transition process and thus the succeeding development of the entire flow yielding quantitative deviations regarding C_p , C_f or k . The differences can be attributed to a well-known shortcoming of the Smagorinsky model. In addition, the paper aims at a deeper insight into the nature of turbulent separated flows. For that purpose the LES data were analyzed according to the anisotropy-invariant theory which provides an improved illustration of what happens in a turbulent flow. Therefore, the anisotropy invariants at various locations in the flow were displayed in the invariant map in order to analyze the state of turbulence in distinct regions.

Keywords: LES, separated turbulent flow, SGS models, anisotropy-invariant theory

1. Introduction

In order to study the physics of pressure-induced separation at high Reynolds numbers, LES is accepted to be a valuable tool. It allows to investigate highly unsteady turbulent flows which are dominated by large separation and recirculation regions, vortex formation and shedding, or shear layer instabilities and transition. A typical aerodynamic application is the flow past wings at extreme operating conditions, where stall is observed. A flow of this kind is experimentally investigated within the COSTWING experiment (Lerche &

Dallmann, 1999). A nominally 2D airfoil based on a NACA-4415 profile is mounted inside a wind tunnel. In contrast to the LESFOIL project (Mellen et al., 2002) which was mainly a feasibility study of LES for the Aerospatiale A-airfoil at a high Reynolds number $Re_c = 2.1 \times 10^6$, the objective of the present investigation is to study the physics of the turbulent flow past highly inclined airfoils. Because the main outcome of LESFOIL was the realization that a proper resolution plays a dominant role for successful LES predictions, a much lower $Re_c = 10^5$ still yielding a practically relevant trailing-edge stall was considered. This case allows to fulfill the basic requirement of an appropriate resolution assuring that all important flow features can be captured reasonably. Hence it makes sense to analyze the results in order to improve the understanding of the physics of pressure-induced separation. At first the paper provides some informations about the influence of different SGS models. More precisely, the effect of dynamically computing the value of C_S within the Germano/Lilly SGS model (**D**ynamic model, denoted **D**) is compared to a fixed value of C_S (**S**magorinsky model, denoted **S**). In comparison to a first study (Breuer & Jovičić, 2001; Jovičić et al., 2003) at $Re_c = 20,000$, the SGS model is expected to play a major role at $Re_c = 10^5$. Based on the outcome of this comparison, only the results of case **D** were analyzed in more detail with respect to the anisotropy-invariant theory.

2. Numerical Methodology

The LES code *LES OCC* is based on a 3-D finite-volume method for arbitrary non-orthogonal and non-staggered grids (Breuer & Rodi, 1996; Breuer, 1998, 2002). The spatial discretization of all fluxes is based on central differences of second-order accuracy. A low-storage multi-stage Runge-Kutta method (second-order accurate) was applied for time-marching. For modeling the non-resolvable SGS the well-known Smagorinsky model (1963) with Van Driest damping ($C_S = 0.1$) and the dynamic approach by Germano (1991) and Lilly (1992) were taken into account. In order to stabilize the dynamic model, averaging was carried out in the spanwise homogeneous direction as well as in time using a recursive digital low-pass filter (Breuer, 2002). *LES OCC* is highly vectorized and additionally parallelized. The simulations were carried out on the SMP-system Hitachi SR8000-F1 with a sustained performance of about 40.9 GFlops on 16 SMP nodes.

3. Flow Configuration & Numerical Parameters

In the experimental setup by Lerche & Dallmann (1999) a NACA-4415 profile is mounted inside a plane channel of height $3c$ (c = chord length). Upstream and downstream of the profile the channel has a length of $2c$ and $3c$, respectively. In order to exclude the unknown effect of any wall function in

the simulations, the no-slip and impermeability conditions are employed at the surface of the airfoil. To save grid points, the channel walls are approximated by slip conditions. In the experiment either statistically two-dimensional or spanwise periodical flow structures are expected. Therefore, periodicity in the spanwise direction is assumed and a spanwise computational domain of depth $z_{max} = 1.0 \times c$ is chosen based on a detailed investigation (Breuer & Jovičić, 2001b). At the inlet a constant velocity u_∞ is prescribed, whereas at the outlet a convective boundary condition is applied (Breuer, 1998, 2002).

The simulations were performed using a block-structured C-type grid consisting of 16 blocks with about 16.23 million control volumes (CVs) in total. The grid points are clustered in the vicinity of the airfoil and at the leading and trailing edges. The height of the first layer of CVs along the airfoil surface is about $\Delta y/c = 0.005$, corresponding to $y^+ \approx 2$ in the separation bubble and $y^+ \approx 1$ in the recirculation region. Motivated by the stability limit of the explicit scheme a dimensionless time step $\Delta t = 8 \cdot 10^{-5}$ was chosen ($CFL < 1$). The time-averaged results are based on averaging intervals of at least 80 dimensionless time units and additional averaging in the spanwise direction. This time interval was found to be sufficiently large verified by the convergence of the statistics.

4. Comparison of Results for Two SGS Models

Compared to $Re_c = 20,000$ where a leading-edge stall was observed, at $Re_c = 10^5$ a completely different flow situation occurs. As can be seen from the time-averaged flow field in Fig. 1, the oncoming flow hits the profile and initially a very thin laminar boundary layer evolves. At the profile nose the flow is strongly accelerated. Shortly after, the boundary layer separates due to the strong adverse pressure gradient followed by an immediate transition to turbulence in the shear layer close to the wall. Thus, the turbulent flow reattaches and a closed separation bubble is formed. Despite the still existing adverse pressure gradient, the turbulent boundary layer remains attached up to approximately $0.6\text{--}0.7c$ where it separates at last. Finally, at the trailing edge a recirculation region emerges rotating in clockwise direction. However, in contrast to $Re_c = 20,000$ no dominating trailing-edge vortices and no asymmetric shedding motion including a corresponding Strouhal number could be observed. The boundary layer at the leeward side remains attached along a large portion of the chord and consequently the flow field does not show typical flow features observed in bluff-body configurations.

At first glance, the predictions with both SGS models seem to resemble each other yielding eddy viscosities $\nu_t/\nu = \mathcal{O}(10)$. However, looked at closely, some noteworthy differences become evident, e.g., concerning the shape and influence of the separation bubble. In case *S* the maximum thickness of the

bubble is $\Delta y/c = 0.00752$ (covered by 12 CVs in height) which is more than twice as high as predicted in case **D** ($\Delta y/c = 0.00323$). At the same time, the bubble is also shifted slightly upstream in case **S** compared to **D**, whereas its length is approximately the same.

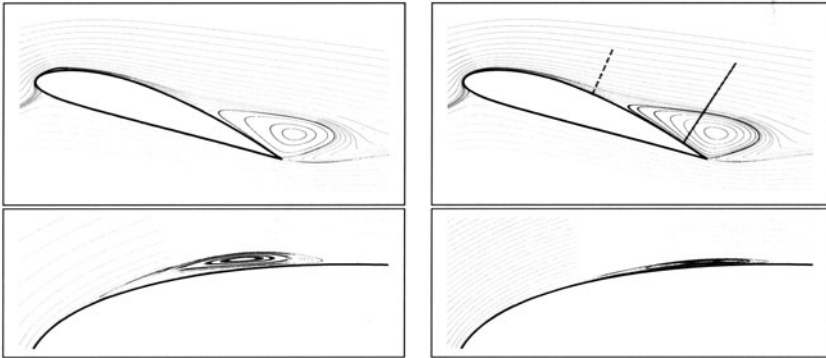


Figure 1. Streamlines of the time-averaged flow field (top) and a zoomed profile nose region (bottom), $Re_c = 10^5$, $\alpha = 18^\circ$, case **S** (left) and case **D** (right).

Another discrepancy is found with respect to the separation of the turbulent boundary layer. In case **S** a slightly delayed separation ($x/c \approx 0.687$) is predicted in comparison with case **D** ($x/c \approx 0.625$). Obviously, these differences also influence quantitative values such as the distributions of the pressure coefficient C_p , the local skin friction coefficient C_f , or the turbulent kinetic energy k . From Fig. 2 it is apparent that, due to its greater thickness, in case **S** the bubble has a distinct impact on the C_p distribution. Thus, in the region of the separation bubble an almost constant pressure is observed. Thereafter, the pressure increases up to the point where the turbulent boundary layer separates at the rear part of the airfoil and again a nearly constant pressure is found. Contrarily, the presence of the bubble predicted in case **D** is hardly noticeable in the corresponding C_p distribution. Besides the bubble region the pressure distribution is equal in both simulations.

In the C_f distribution (Fig. 2, right) huge discrepancies exist between both simulations, especially in the region of the separation bubble where case **S** yields much higher absolute values than **D**. Furthermore, this also applies to almost the entire windward side of the airfoil where **S** overpredicts the wall shear stress in comparison to **D**. Because here the flow is attached and laminar, one would not expect any deviations in the C_f distributions between the results of both SGS models. A detailed investigation proved that case **S** yields non-zero values of the eddy viscosity in the boundary layer ($\nu_t/\nu \approx 1.2$) although the flow is laminar. This shows a well-known shortcoming of the Smagorinsky model with fixed C_S which is unable to distinguish laminar and turbulent flow regions and hence produces non-zero eddy-viscosity values in laminar flows.

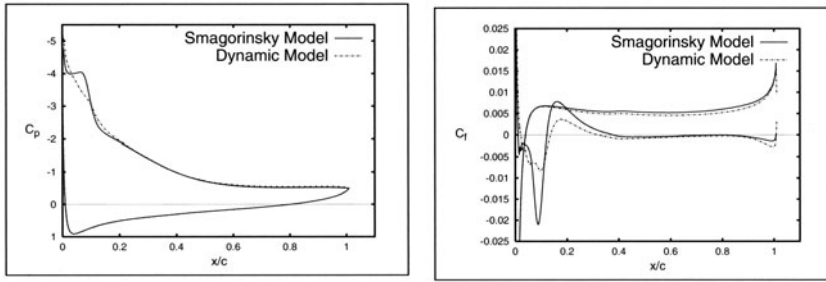


Figure 2. Surface pressure (C_p) and skin friction (C_f) distribution of the spanwise and time-averaged flow, $Re_c = 10^5$, $\alpha = 18^\circ$.

In contrast, the dynamic model determines the distribution of C_S from the resolved flow and thus is able to predict the amount of turbulent viscosity properly ($\nu_t/\nu \approx 0$).

It is obvious that this observation is also the main reason for the differences with respect to the size and position of the separation bubble. Due to increased eddy-viscosity values in the accelerated boundary layer in front of the bubble predicted in case *S* which causes a damping of the instabilities at least to some extent, the transition process is delayed compared to *D*. This influences the entire development of the flow in the nose region and leads to a thicker separation bubble in case *S* compared to *D*. Furthermore, large deviations in the distributions of k (not shown here) are found.

Integral quantities such as time-averaged lift and drag coefficients are only weakly affected by the choice of the SGS model. Both, lift and drag coefficients are almost equal for both SGS models applied: $\overline{C}_l = 1.532$ vs. 1.545 for *S* and *D*; $\overline{C}_d = 0.128$ vs. 0.126 for *S* and *D*, respectively. Corresponding experimental data are under way (Kreplin, personal communication, 2003) but not available yet. Compared to the lower- Re_c case, noticeably smaller amplitudes in the fluctuations of the lift and drag signals are found for $Re_c = 10^5$.

5. Anisotropy-Invariant Theory

In order to gain a deeper insight into the nature of turbulence for separated flows, the simulations were also analyzed according to the anisotropy-invariant theory. According to Lumley and Newman (1977) the state of turbulence can be characterized by the amount of anisotropy defined as $a_{ij} = \overline{u_i u_j} / (2k) - 1/3 \delta_{ij}$ that prevails in the flow. By cross-plotting the scalar invariants $II_a = a_{ij} a_{ji}$ and $III_a = a_{ij} a_{jk} a_{ki}$ of the anisotropy tensor a_{ij} , the state of turbulence can be displayed with respect to its anisotropy. It can be shown that all physically realizable turbulence has to lie within a small region called *invariant map* which is bounded by the limiting cases of two-component and axisymmetric turbulence (see Fig. 3). However, different states of turbu-

lence are represented by different parts of the invariant map. Thus, by transferring the anisotropy into the invariant map, more detailed informations about the intrinsic turbulence can be obtained. In the present study, this was done for various portions of the flow in order to analyze the state of turbulence in distinct regions. First, a complete cross-section of the domain was transferred to the invariant map taking the resolved Reynolds stresses of case **D** into account. In doing so, almost the entire map was covered demonstrating the complexity of the investigated flow and also indicating that all imaginable states of turbulence occur.

In order to examine the turbulence behavior at specific locations in the flow, the anisotropy along two straight lines normal to the profile (see Fig. 1, case **D**) is extracted and displayed in the invariant map shown in Fig. 3(a). The first line is located at $x/c = 0.5$ in the region of the attached turbulent boundary layer. The second line is placed close to the trailing edge ($x/c = 0.9$) in the recirculation region. The anisotropy determined along these lines leaves a trace in different parts of the invariant map indicating the different states of turbulence that occur. Starting from the airfoil surface, the turbulence states at both lines are close to the two-component limit (upper boundary of the map). This finding is as expected since close to solid walls the fluctuations normal to the wall are strongly damped and therefore only two components remain. In addition, the starting state of turbulence of the first normal line at $x/c = 0.5$ is also very close to the two-component isotropic state which is represented by the left corner point **A** of the map. Such a turbulence is characterized by the existence of only two fluctuating components of equal strength. From experiments and also from numerical databases it has been found that wall-bounded turbulence reaches the two-component isotropic state in the proximity of the wall if the Reynolds number is sufficiently large, e.g., in channel flows this state is approached close to the walls with increasing Re . Hence in the present airfoil flow at $x/c = 0.5$, the velocity fluctuations in both the spanwise and streamwise directions are equal in size in the direct vicinity of the wall. Away from the wall, the curves representing the anisotropy cross the map and come close to the right branch of the map for both lines, indicating that some kind of axisymmetric turbulence is present in that parts.

Finally, the region where the separation bubble is observed is analyzed in the same way. As can be seen from Fig. 3(b), the complete upper part of the invariant map is covered, reaching from the isotropic two-component limit (point **A**) up to the one-component limit at the upper right corner point **B** of the triangle. This indicates how the nature of turbulence can differ even within a very small portion of the flow. Furthermore, it becomes apparent why it is so difficult to predict such complex features by the use of any kind of near-wall modeling. Most near-wall models are based on rather simple assumptions and

hence, can not adjust themselves to such strongly different states of turbulence as observed in the invariant map for the separation bubble.

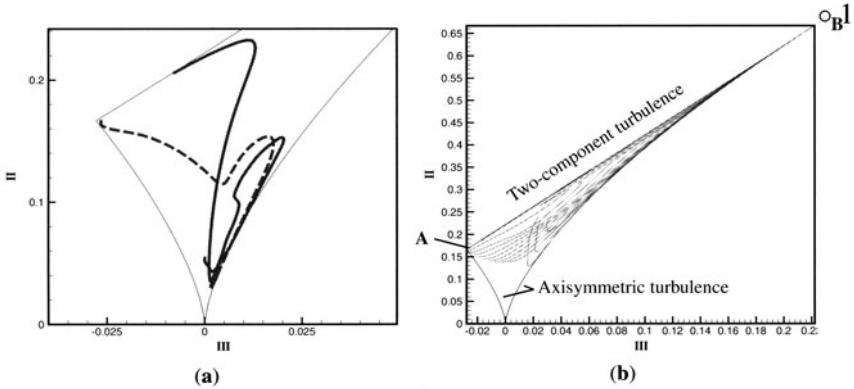


Figure 3. Anisotropy-invariant map showing (a) the anisotropy of the flow at two lines normal to the profile, $x/c = 0.5$ (dashed) and $x/c = 0.9$ (solid) and (b) the anisotropy of the flow in the region of the separation bubble close to the profile nose.

Thus, analyzing the flow using the anisotropy-invariant theory reveals new details of turbulence which is not easy to observe in the physical space. However, further effort has to be put on these investigations in the ongoing work.

6. Conclusions

Based on LES even complex turbulent flows such as the separated flow past an unswept wing can be tackled. At $Re_c = 10^5$ a trailing-edge stall is observed. Consequently, the flow in the nose region is laminar only along a short distance. Thereafter, a tiny laminar separation bubble is found triggering the transition process to turbulence. The turbulent boundary layer is able to resist to the adverse pressure gradient over a long distance but finally separates at $x/c \approx 65\%$ leading to a recirculation region in the vicinity of the trailing edge. The deviations observed between the results of both SGS models can be attributed to well-known deficiencies of the Smagorinsky model for transitional flows. A further refinement of the near-wall grid actually on the way will strengthen the confidence in the predictions based on the dynamic approach. Nevertheless, the enormous amount of valuable data generated allow to study the physics of separated flows in detail and to analyze the state of turbulence in different flow regions as demonstrated by the anisotropy-invariant theory.

Acknowledgments

This work is supported by the *Deutsche Forschungsgemeinschaft* under contract number BR 1847/2 and CPU time by HLRB Munich.

References

- Breuer, M., Rodi, W.: *Large-Eddy Simulation of Complex Turbulent Flows of Practical Interest*, In: Flow Simulation with High-Performance Computers II, Notes on Numer. Fluid Mech., vol. **52**, pp. 258–274, Vieweg, (1996).
- Breuer, M.: *Large-Eddy Simulation of the Sub-Critical Flow Past a Circular Cylinder: Numerical and Modeling Aspects*, Int. J. for Numer. Methods in Fluids, vol. **28**, pp. 1281–1302, (1998).
- Breuer, M., Jovičić, N.: *An LES Investigation of the Separated Flow Past An Airfoil at High Angle of Attack*, 4th Workshop on DNS and LES, Enschede, The Netherlands, July 18–20, 2001, ERCOFTAC Series, vol. **8**, pp. 165–172, (2001).
- Breuer, M., Jovičić, N.: *Separated Flow Around a Flat Plate at High Incidence: An LES Investigation*, J. of Turbulence, vol. **2**, pp. 1–15, (2001b).
- Breuer, M.: *Direkte Numerische Simulation und Large-Eddy Simulation turbulenter Strömungen auf Hochleistungsrechnern*, Habilitationsschrift, Univ. Erlangen-Nürnberg, Berichte a. d. Strömungstechnik, ISBN 3-8265-9958-6, Shaker, (2002).
- Germano, M., Piomelli, U., Moin, P., Cabot, W.H.: *A Dynamic Subgrid Scale Eddy Viscosity Model*, Phys. of Fluids A, vol. **3**(7), pp. 1760–1765, (1991).
- Jovičić, N., Evans, G., Breuer, M., Friedrich, R.: *Comparison of Two Large-Eddy Simulations for a Stalled Airfoil Flow Using Different Finite-Volume Formulations*, Notes on Numer. Fluid Mech. & Multidisc. Design, vol. **86**, pp. 293–306, (2003).
- Lerche, Th., Dallmann, U.Ch.: *Das Prinzipexperiment COSTWING I: Dokument. der Aufbauphase*, Inst. f. Strömungsmech., DLR Göttingen, IB 223–99 A04, (1999).
- Lilly, D.K.: *A Proposed Modification of the Germano Subgrid Scale Closure Method*, Phys. of Fluids A, vol. **4**(3), pp. 633–635, (1992).
- Lumley, J.L., Newman, G.: *The Return to Isotropy of Homogeneous Turbulence*, J. of Fluid Mechanics, vol. **82**, pp. 161–178, (1977).
- Mellen, C., Fröhlich, J., Rodi, W.: *Lessons From the European LESFOIL Project on LES of Flows Around an Airfoil*, AIAA Paper, AIAA–2002–0111, (2002).

LES OF CYLINDER WAKE T106 TURBINE BLADE INTERACTION

M. Opiela, M. Meinke and W. Schröder

Aerodynamisches Institut, RWTH Aachen

Wüllnerstr. zw. 5 und 7, 52062 Aachen, Germany

Tel.: +49-241-8095410, E-mail: office@aia.rwth-aachen.de

Abstract Large-eddy simulations (LES) are performed on moving block-structured grids for a simple model of a turbine stage at different Reynolds numbers and exit Mach numbers without any freestream turbulence. The wake of a moving cylinder interacts with a T106 turbine blade. To ensure flux conservation between the rotor and stator within the numerical algorithm a sliding interface is applied. In order to determine the effect of the upstream wake the flow field around the turbine blade was simulated numerically with and without a moving cylinder. Results of the LES with different resolutions of the computational grid are presented in comparison with experimental data and other simulations. Good agreement between simulations and measurements concerning time averaged and fluctuating quantities for the moving cylinder and the turbine blade was achieved.

Keywords: LES, moving grid, wake, blade, turbine

1. Introduction

Concerning the low pressure turbine (LPT) of an aero-engine the Reynolds number based on the blade-chord length changes by a factor of 3 to 4 between sea-level take-off and cruising altitude. Depending on this condition the extension of the laminar, transitional, and turbulent boundary layer zones differ. In addition, the stator blade loading and heat transfer as well as the boundary layer characteristics are influenced periodically by the wake flow generated by the upstream rotor. For loss predictions and further improvements of the efficiency it is essential to use turbulence models which are able to predict the location of the onset of boundary-layer separation and transition on low-pressure turbine blades that are periodically influenced by the passing wakes of the upstream blades.

Algebraic and one- or two-equation turbulence models suffer from the drawback that they must be adapted to different flow conditions and fail in regions

of curved streamlines or swirling flow. Whereas direct numerical simulations (DNS) of compressible flow problems in moving grid coordinates at technically relevant Reynolds numbers are currently out of reach due to the high computational costs, large-eddy simulations can be performed since the overall computational effort is considerably less than that of a DNS. There are large coherent structures that dominate the wake-blade interaction and the wake flow behind the blade itself makes LES a promising numerical method for such flow problems.

2. Numerical method

The governing equations for the LES are the filtered Navier-Stokes equations for compressible flows in moving coordinates. For the integration in time an explicit 5-step Runge-Kutta scheme of second-order accuracy is used. The convective terms are conservatively formulated for moving and deforming grids with appropriate metric terms. They are discretized using a modified mixed central-upwind AUSM scheme (Liou & Steffen, 1993). The pressure term is treated separately from the Euler-fluxes and discretized using central differences. This decomposition leads to a scheme, which exhibits a very little numerical dissipation and as such was found to be well suited for the LES of different flow problems. Using central differences the viscous stresses were approximated to second-order accuracy.

In general various subgrid scale models that are supposed to simulate the impact of the unresolved fine-scale eddies on the turbulent flow are used. There are some drawbacks of the dynamic model of Germano et al. (1991) and models containing the eddy-viscosity ansatz which are discussed in detail in (Opiela, 2003). Moin and Kim performed a large-eddy simulation of a turbulent channel flow using a somewhat finer grid resolution in the wall-normal direction without incorporating any subgrid scale model (Moin & Kim, 1982) and compared the results with the direct numerical simulation of exactly the same flow problem. Since they found such an excellent agreement, the LES findings, computed without any subgrid modeling, are used as reference data in the literature. Further investigations of internal and external flows based on discretization schemes up to sixth order confirmed this result (Meinke & Schröder, 2002). Therefore, no subgrid scale model is used in this analysis.

2.1 Problem definition

The geometry of the model used for the wake-blade interaction as well as the main geometric and flow parameters are shown in figure 1 and listed in table 1.

These parameters defined in detail in (Sieverding, 2000) are chosen according to an experiment performed at the University of Cambridge within the framework of the BRITE-Euram project TURMUNSFLAT. The Profile T106

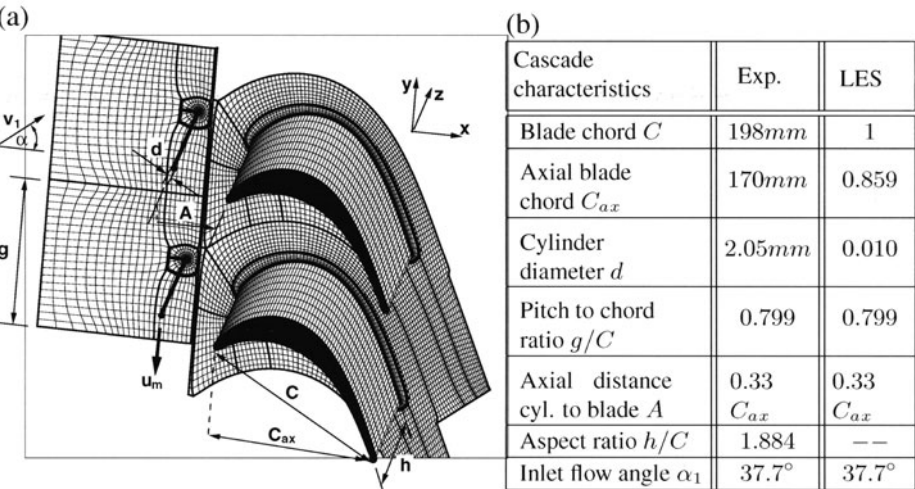


Figure 1. (a) Cascade geometry; (b) main geometrical parameters of the cascade.

Flow parameters for the LES		$Re_2 = 160000$		$Re_2 = 260000$		$Re_2 = 500000$	
		with cylinder	none	with cylinder	none	with cylinder	none
Inlet	ρ_1/ρ_0	0.997	0.998	0.990	0.999	0.923	0.923
	Ma_1	0.091	0.091	0.139	0.144	0.405	0.404
Outlet	ρ_2/ρ_0	0.986	0.986	0.964	0.966	0.853	0.856
	Ma_2	0.158	0.158	0.263	0.263	0.590	0.590
Re_2 (adjusted)		160200	160200	263817	263817	500000	500000
moving cylinder	u_m/a_0	0.098	—	0.154	—	0.354	—
	v_{1ax}/u_m	0.714	—	0.715	—	0.889	—
	Re_{cyl}	1688	—	2681	—	5911	—

Table 1. Main flow parameters for the LES.

is typical of current low pressure turbine profiles and has a design exit Mach number of $Ma_2 = 0.59$. The flow angle of the cylinder is equal in magnitude and opposite in sign to the design exit flow angle ($\alpha_2 = -63.2^\circ$) to mimic a 50 percent reaction turbine. A high aspect ratio h/C was chosen in the experimental investigations to guarantee a satisfactory two-dimensional flow at mid span, such that in the numerical simulations periodic boundary conditions in the spanwise direction could be used. The experiments regarding the influence of a moving cylinder wake were conducted for Reynolds numbers Re_2 based on the chord length of the blade C and the velocity downstream the blade v_2 of $Re_2 = 160000$ and $Re_2 = 260000$. These were essentially incompressible flow conditions, such that for the compressible solver the Mach numbers based on the exit velocity were approximated to $Ma_2 = 0.158$ and $Ma_2 = 0.263$. For the design exit Mach number of $Ma_2 = 0.59$ with $Re_2 = 500000$ only experimental data of Hoheisel et al. (1987) for the case without the impact

of a cylinder wake are available. The corresponding Reynolds numbers in the frame of reference for the moving cylinder are $Re_{cyl} = 1688, 2681, \text{ and } 5911$.

2.2 Computational grid

For the LES of the wake-blade interaction a coarse grid with 2 million grid points arranged in 13 structured blocks is used. The size of the domain of integration in the spanwise direction is twice the cylinder diameter with 33 grid points where the distance between the grid planes in the spanwise direction is equal to $\Delta z^+ = 0.44$ and the distance of the first grid line normal to the blade surface on the suction side near the trailing edge is equal to $\Delta n^+ = 0.11$. The cylinder surface is resolved in the circumferential direction with 33 and the blade with 433 grid points. A sliding interface is used for the connection of the moving and non-moving part of the grid to avoid any kind of interpolation and to ensure flux conservation across the interface. A critical point in the simulation of the flow problem is the resolution of the wake generated by the cylinder. Due to its movement the wake passes nearly through the whole flow field. Additionally, a nearly equidistant distribution of the grid points is required across the sliding interface, which is located between the grid blocks around the cylinder and those around the blade. Therefore, small spatial steps are required in the major part of the domain of integration which leads to a large number of grid points for the simulation of this flow problem. In order to examine the influence of the grid resolution on the solution of the LES a finer grid with about 16 million grid points distributed in 42 blocks was generated. In this case the size of the domain of integration in the spanwise direction is three times the cylinder diameter with 53 grid points where the distance between the grid planes in the spanwise direction is equal to $\Delta z^+ = 0.41$ and the distance of the first grid line normal to the blade surface is equal to $\Delta n^+ = 0.03$. The cylinder surface is resolved in the circumferential direction with 321 and the blade surface with 969 grid points.

2.3 Boundary conditions

At the inflow boundary only the inflow angle $\alpha_1 = 37.7^\circ$ is prescribed, whilst at the outflow boundary a non-reflecting boundary condition with pressure level relaxation is imposed. In addition a sponge layer is used to minimize the reflection of spurious waves back into the domain of integration. In the spanwise and lateral direction periodic boundary conditions are used for the 2d- and 3d-case. At the blade surface a no-slip condition and a constant wall temperature is prescribed. Also for the moving cylinder an isothermal surface is assumed whilst the velocity at the wall is equal to the velocity of the moving system.

3. Results

In figure 2 distributions of the time and spanwise averaged velocity on the centerline of the near wake of the moving cylinder and across the wake in a distance of 2.02 cylinder diameters downstream of the center of the cylinder, obtained with the LES for $Re_{cyl} = 1688$ and $Re_{cyl} = 2681$, are plotted in comparison with experimental data and LES results of (Beaudan & Moin, 1994) for $Re_{cyl} = 3900$. Good agreement can be observed up to ten cylinder diameters downstream of the cylinder and for about two cylinder diameters perpendicular to the wake centerline. The physics of the cylinder wake for the Reynolds-numbers $Re_{cyl} = 1688$ and $Re_{cyl} = 3900$ is almost alike which is why the velocity distributions differ only slightly. The time averaged two-point correlations of the velocity fluctuations u' and w' in figure 3 as a function of the spanwise direction (z/D) in the cylinder wake at a distance of 0.59 diameter downstream to the cylinder center obtained with the LES on the coarse grid shows that the domain size is large enough. The visualization of the turbulent cylinder wake using the λ_2 criterion (Jeong & Hussain, 1995) for the LES on the fine resolved grid for $Re_{cyl} = 1688$ indicates in the spanwise direction three coherent structures downstream the cylinder. Each structure consists of counter-rotating vortices with an axis in the streamwise direction marked by dark and light surfaces. The finer resolved grid for the LES gives only a small improvement of the results. This shows that the coarse grid has already a sufficient resolution in the near wake region of the cylinder for the wake-blade interaction. In figure 4 the time and spanwise averaged blade surface pressure distributions $C_{p2} = (P_{01} - p)/(P_{01} - p_2)$ and $c_p = (p - p_\infty)/((\rho_\infty/2)u_\infty^2)$ computed on the coarse grid at $Re_2 = 260000$ are plotted in comparison with experimental data and DNS results. A good agreement on the pressure side and on the suction side of the blade up to $S/S_{max} \approx 0.6$ and $x/C_{ax} \approx 0.7$, respectively, can be observed. Furthermore, it is shown in figure 5 that even the time and spanwise averaged velocity profile and the corresponding RMS-profile at $S/S_{max} = 0.95$ obtained with the coarse grid for $Re_2 = 160000$ match the experimental data quite well. The displacement thickness δ_1 , momentum thickness Θ and the shape factor H_{12} on the suction side of the blade of the coarse grid LES at $Re_2 = 260000$ confirm the satisfactory quality of the findings in the region of $0.8 < S/S_{max} < 1.0$. On the left hand side of figure 7 the turbulent flow field of the wake blade interaction at $Re_2 = 260000$ is visualized by the λ_2 -criterion. After the vortical structures of the cylinder wake have passed the leading edge of the blade they are stretched above the suction side due to the acceleration caused by the pressure gradient in the streamwise direction. Since the convection speed on the pressure side near the leading edge of the blade is lower than that on the suction side the wake gets deformed when passing over the blade. Near the trailing edge the wake structures are also

stretched due to the acceleration and they are aligned to the blade wake flow direction. The right hand side of figure 7 compares the blade surface pressure distribution and the shape factor H_{12} on the suction side of the blade for the coarse grid LES at $Re_2 = 500000$ with and without the influence of a passing cylinder wake with the experimental data of Hoheisel et al. (1987). A compressible LES has to be performed since in this case the density varies by more than 20 percent. For both quantities a good agreement can be observed. The plot for the shape factor H_{12} shows that the passing cylinder wake prevents the formation of a 'bubble-type' transition.

4. Conclusions

Large-eddy simulation for a simple model of a wake-blade interaction in low pressure turbines has been presented on a moving grid using a sliding interface technique. Good agreement with experimental data has been achieved concerning time-averaged and fluctuating quantities for the moving cylinder and the T106 turbine blade at different Reynolds and Mach numbers. Even the results obtained on a relatively coarse mesh showed a convincing agreement between measurements and simulations.

Acknowledgments

This work was supported by the European Union within the BRITE-EURAM project TURMUNSFLAT under contract number CT96-0143.

References

- Beaudan, P., and Moin, P., "Numerical experiments on the flow past a circular cylinder at sub-critical Reynolds numbers", *Technical Report TF-62, Center Turb. Res.*, 1994.
- Thomas, P. D., and Lombard, C. K., "Geometric Conservation Law and its Application to Flow Computations on Moving Grids", *AIAA Journal*, Vol. 17(10), pp. 1030-1037, 1979.
- Jeong, J., and Hussain, F., "On the identification of a vortex", *Journal of Fluid Mechanics*, Vol. 285, pp.69-94, 1995.
- Liou, M. S. and Steffen Jr., C. J., "A new flux splitting scheme", *J. Comput. Phys.*, Vol. 107, pp. 23-39, 1993.
- Germano, M., Piomelli, U., Moin, P., and Cabot, W., "A dynamic subgrid-scale eddy viscosity model", *Phys. Fluids*, Vol. A 3(7), pp. 1760-1765, July, 1991.
- Moin, P., and Kim, J., "Numerical investigation of turbulent channel flow", *Journal of Fluid Mechanics*, Vol. 118, pp. 341-377, 1982.
- Meinke, M., Schröder, W., Krause, E., and Rister, T., "A comparison of second- and sixth-order methods for large-eddy simulations", *Comp. & Fluids*, Vol. 31, pp. 695-718, 2002.
- Sieverding, C., *Brite EURAM project TURMUNSFLAT, CT96-0143, Final Report*, 2000.
- Hoheisel, H., Kiock, R., Lichtfuss, H. J., and Fottner, L., "Influence of Free-Stream Turbulence and Blade Pressure Gradient on Boundary Layer and Loss behavior of Turbine Cascades", *Transactions of the ASME*, Vol. 109, pp. 210-219, Apr. 1987.
- Opiela, M., "Grobstruktur-Simulation der Interaktion des Nachlaufs eines bewegten Kreiszylinders mit einer Turbinenschaufel", *PhD thesis*, Aerodyn. Inst. RWTH Aachen, July 2003.

Figures

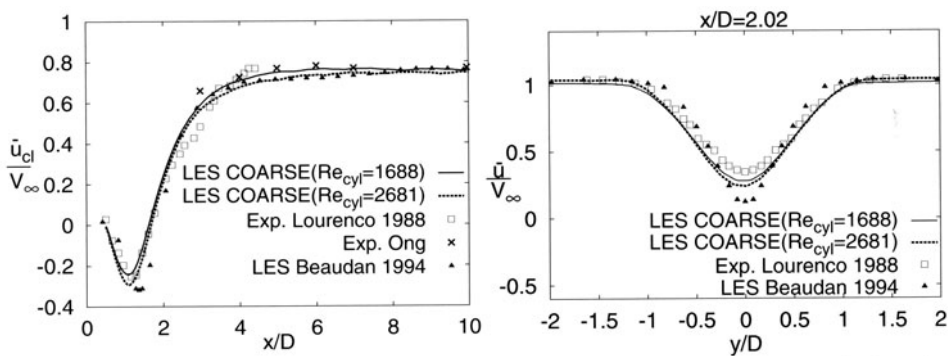


Figure 2. Time and spanwise averaged velocity on the centerline (left) of the cylinder wake and across the wake in a distance of 2.02 cylinder diameters downstream of the moving cylinder.

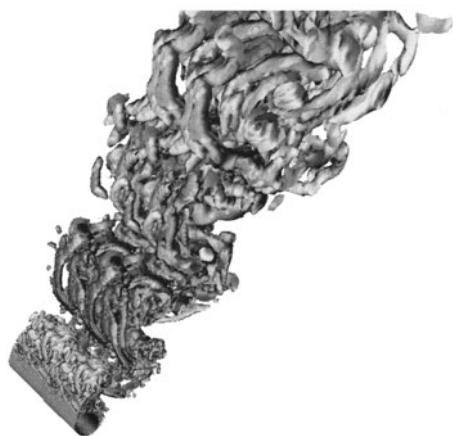
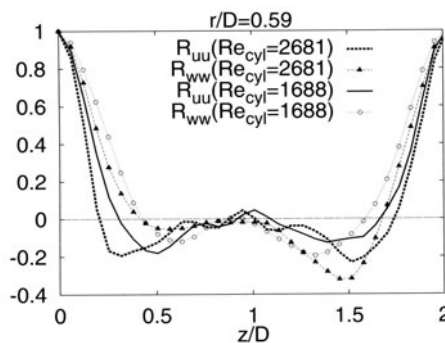


Figure 3. Time averaged two-point correlations across the cylinder wake (left) and visualization of the instantaneous turbulent cylinder wake by the λ_2 -criterion.

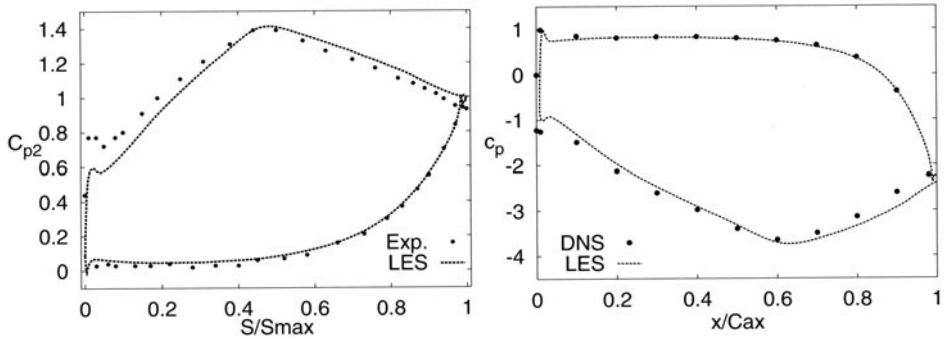


Figure 4. Time and spanwise averaged blade surface pressure distribution C_{p2} (left) and c_p (right) at $Re_2 = 260000$.

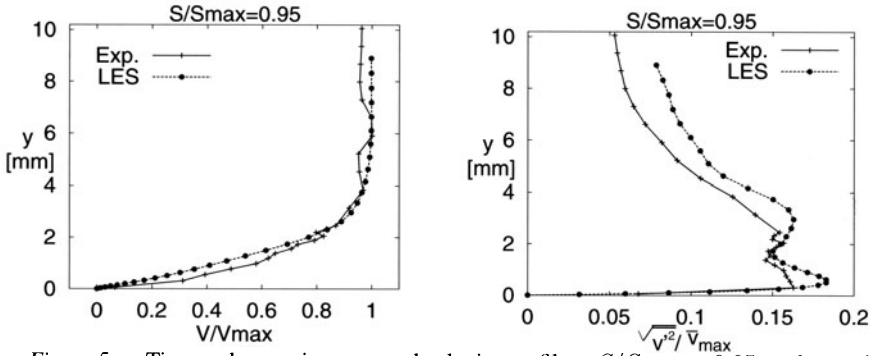


Figure 5. Time and spanwise averaged velocity profile at $S/S_{max} = 0.95$ on the suction side of the blade (left) and corresponding RMS-profile (right) at $Re_2 = 160000$.

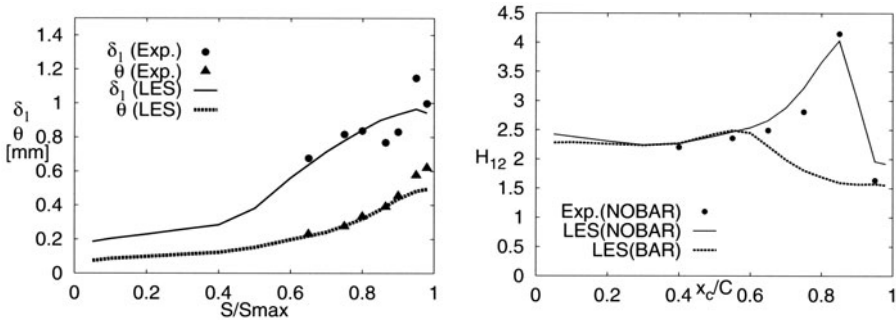


Figure 6. Time and spanwise averaged displacement thickness δ_1 , momentum thickness Θ (left), and shape factor H_{12} (right) on the blade suction side at $Re_2 = 260000$.

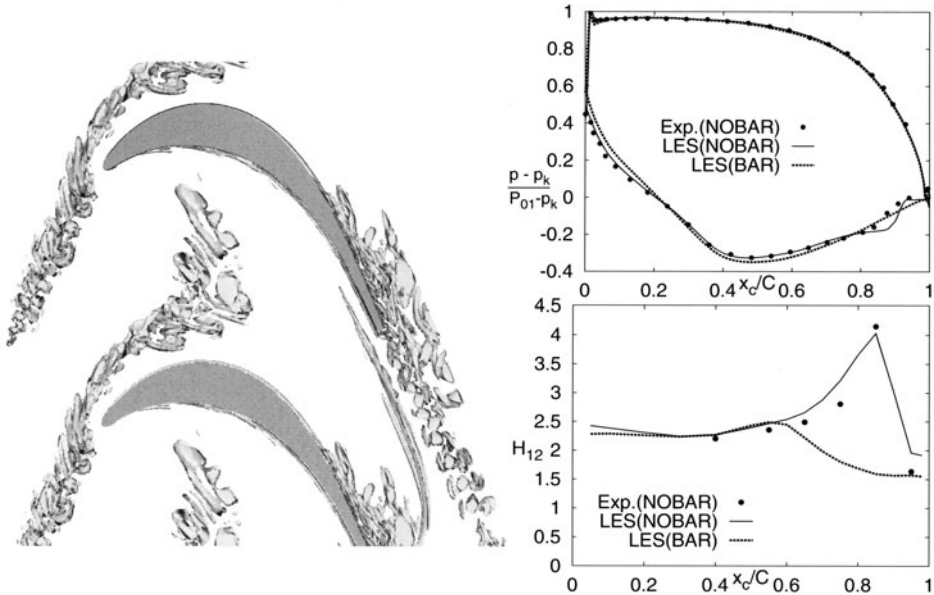


Figure 7. Visualization of the wake-blade interaction with the λ_2 -criterion at $Re_2 = 260000$ (left); time and spanwise averaged blade surface pressure distribution and shape factor H_{12} at $Re_2 = 500000$ (right).

LES OF WAKE-BLADE INTERFERENCE IN A LOW-PRESSURE TURBINE

B. Raverdy, I. Mary

ONERA, 29 av. de la Division Leclerc, 92322 CHATILLON cedex, FRANCE

Bruno.Raverdy@onera.fr

Ivan.Mary@onera.fr

P. Sagaut

LMM, 4 place Jussieu, case 162, 75252 Paris, FRANCE

sagaut@lmm.jussieu.fr

J.M. Roux

Snecma Moteurs, Turbine Aero and Cooling Department, Centre de Villaroche, 77550 Moissy-Cramayel, FRANCE

jean-michel.roux@snecma.fr

Abstract The aim of the present work is to predict and describe the boundary layer transition process influenced by an incoming upstream turbulent wake generated by a moving cylinder for a subsonic blade turbine configuration. High-resolution Large-Eddy Simulation type computations have been carried out for the T106 low-pressure blade turbine at Mach number of 0.1 and chord based Reynolds number of $1.6 \cdot 10^5$ and have been compared with experiments.

Keywords: LES, transition, wake-blade interference

1. Introduction

In the turbomachinery field, the flow around the turbine blades is often characterized by a high level of incoming turbulence and the presence of both separation and intermittency phenomena. Indeed in a complete stage the flow around the blade of a stator blade (static) is strongly influenced by the flow generated upstream by a rotor blade (moving), which periodically creates a high level of incoming turbulence for the stator. Therefore the prediction of the performances of some specific blade profiles with RANS models is often unsatisfying, because the capabilities of such turbulence models are still limited when intermittent and transitional phenomena occur in the flow. Several experimental studies have been carried out recently (see [1],[2] for instances) in order to build some data bases for RANS model validation and to get a better knowledge of such complex flow. As the Reynolds number based on the blade chord is quite moderate ($\approx 10^5$) in Low Pressure Turbine (LPT), DNS and LES of wake-blade interference could be achieved recently in order to

evaluate their feasibility on current supercomputers and to get a better understanding of the flow dynamics. DNS [3],[4] have been performed on very fine mesh (up to 57×10^6 cells), and the physical analysis was focused on stream-wise vortices, which occur periodically in the boundary layer located in the pressure side of the stator blade. However the flow configuration of these DNS is a simplification of the experimental setup. Indeed the wake is not generated by a rotor stage, but modeled by an unsteady inflow condition, which has a strong influence on the stator boundary layers development [3]. Moreover these DNS results require additional validation, since there is no comparison with experimental measurements. In order to study a real experimental configuration Meinke [5] performed LES on a moving grid around the rotor and a static grid around the rotor blade with the help of a sliding boundary condition. However only one passage of the moving bar was calculated with a grid composed of 1.8×10^6 cells due to the computational cost (300 CPU hours on a Fujitsu VPP300). Moreover its mesh resolution in the wake of the rotor was undoubtedly too coarse to allow an accurate representation of the wake vortices. Recent studies [6],[7] have shown for isolated profiles that accurate LES can be performed even at Reynolds number higher than 10^6 thanks to the use of a local mesh refinement. Therefore the objective of this work is to assess the feasibility of a well resolved LES for a wake/blade interaction configuration with this technique. The influence of the subgrid scale model is investigated and results are compared to the experimental data [2].

2. Numerical method

2.1 General description

The three-dimensional unsteady filtered Navier-Stokes equations are discretized using a cell-centered finite volume technique and a structured mesh. Concerning the subgrid-scale modeling, two models have been evaluated: the Selective Mixed Scale Model [8] and the MILES approach proposed in [9], which has been successfully employed in [7] to simulate the flow around a stator blade without incoming wake. The numerical method is identical to those developed to perform LES of the flow around a two-dimensional wing profile [6]. The convective fluxes, which are fully described in [6], are discretized by a second-order accurate hybrid centered/upwind scheme based on a wiggle detector in order to minimize the numerical dissipation. An implicit second-order accurate backward differentiation formula is used to approximate the temporal derivative. A Newton-like sub-iteration technique is employed to solve the non linear problem, whereas the inversion of the linear system relies on lower upper Symmetric Gauss Seidel (LU-SGS) implicit method (see [10] for more details). As well-resolved LES of complex flows at a realistic Reynolds number requires a huge amount of grid cells, it becomes essential to optimize the

cell distribution. In a structured solver, this can be achieved by the means of multi-domain/multi-resolution methods. The technique retained in this study is described in [11] and is an adaptation for a complex geometry context of the method proposed in [12].

2.2 Sliding interface

To perform simulation of the interaction between the cylinder wake and the blade boundary layer, a sliding interface is employed for the connection of the moving and non-moving parts of the grid. This method, which is very fast compared to the Chimera technique, avoids interpolation and guarantees the flux conservation across the interface. However there are several constraints concerning the mesh resolution in the directions normal and parallel to the interface. In the parallel direction, a uniform distribution must be used to allow a correct connection between moving and non-moving parts of the grid. In the direction normal to the interface the mesh size must be identical to those employed in the parallel direction in order to get a square cell in the plane of the blade. Otherwise there is a strong discontinuity in the slope of the grid when the center of a moving cell is coincident with a vertex of the non-moving grid. This sliding interface condition has been coupled with a local mesh refinement technique [[12]] in order to optimize the number of cells in the computation (see Fig.1).

3. Numerical results

3.1 Flow configuration

The T106 low-pressure blade turbine has been retained to evaluate the feasibility of the LES of wake-blade interference. Measurements of velocity and Reynolds stress profiles have been carried out by Hodson [2] for different levels of incoming turbulence. A first attempt to model the fluid on this configuration have been realized (Raverdy [7]) without passing wake. In the present case, an upstream wake is generated by the vertical motion of a cylinder (see Fig.2). This cylinder has a diameter equal to $d/C = 0.01$ and a translation velocity equal to the inlet uniform velocity. The cylinder is positioned at $0.28C$ in front of the blade. The inlet uniform flow angle and the exit angle are equal to 37.7 and -63.2 degrees, respectively. The pitch to chord (g/C) is equal to $g/C = 0.799$. The Reynolds number, based on the blade chord and exit velocity, is equal to 1.6×10^5 , whereas the inlet Mach number is set to 0.1 .

3.2 Computational setup

The topology retained to build the mesh is the same for both static blade and moving cylinder located in the cylinder grid. The mesh is composed of a combination of O grid (around the cylinder and the blade) and H grid in the oth-

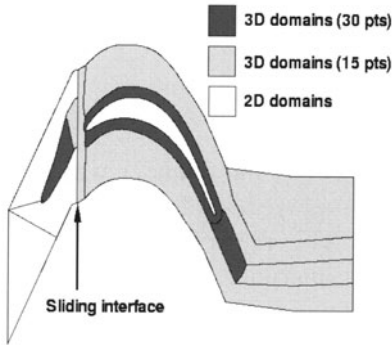


Figure 1. Grids topology

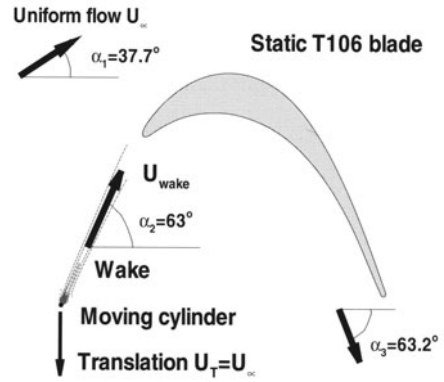


Figure 2. Flow configuration

ers parts of the computational domain (cylinder wake, inter-blade channel and far field). The computational domain is spread between $x/C=-0.5$ and $x/C=2$, in x -direction, and represents 3.2% of the blade chord in the spanwise direction. The mesh resolution in the near-wall blade region is chosen such that $\Delta x^+ < 30$, $\Delta y^+ < 2$ and $\Delta z^+ < 10$. The mesh characteristics are summarized in the Table 1 and compared with those of [3],[5],[4]. The grid is nearly identical to those of [3],[4], excepted the spanwise extent which is at least four times smaller in the present simulation, However, this choice does not prevent the development of three-dimensional solution. Indeed it is shown in [7] that the present spanwise extent is sufficient to simulate the flow without the wake, whereas it is larger than three times the cylinder diameter. As the turbulent structures generated by the cylinder have a size in the spanwise direction approximately equals to one cylinder diameter [13], the spanwise extent, which is approximately three times larger than the cylinder diameter, may be sufficient to capture the dynamics of both the wake and boundary layer zones. Coarser resolution have been used at the exit of the moving domain and in the center part of the inter-blade channel (see Fig.1) in order to adapt the resolution to the size of the wake vortices in the spanwise direction. Moreover nearly rectangular cells are used in the zone of the cylinder wake in order to prevent a spatial filtering of the turbulent vortices. Thanks to the coarse/fine coupling technique, only 1.4×10^6 cells are located in the rotor grid and 4×10^6 in the stator grid. All simulations are obtained by using periodic conditions in the far field and in the spanwise direction. Non reflecting characteristic boundary conditions are applied for the upstream and downstream limits of the computational domain. The time step is equal to $4.5 \times 10^{-7} s$ in order to have a maximal value of the CFL number inferior to 16 with the use of only 4 sub-iterations in the approximate Newton method. For average quantities, the averaging procedure is

performed in the homogeneous spanwise direction and in time over four wake passing periods. Around 40 CPU hours are required on a NEC SX5 to compute one wake passing period.

	Present grid	Ref. [3]	Ref. [5]	Ref. [4]
Cells around the blade	980	1152	433	771
Cells in the inter blade passage	290	384	130	256
Cells in the spanwise direction	15/30	128	32	128
Spanwise extent L_z/C	3.2%	15%	2%	25%
Wake	simulated	modeled	simulated	modeled
Total cells number ($\times 10^6$)	5.4	57	1.9	25

Table 1. Stator grid description

3.3 Results

Two simulations have been performed with the Selective Mixed Scale Model (LES MSM) and with the MILES approach (LES MILES). In order to evaluate the accuracy of the present simulations mean flow quantities are compared with experimental data. The pressure coefficient, which is presented in the Fig.3a), is in very good agreement with the experimental data of Engber and Fottner [1] despite the fact that those measurements were realized at higher Mach number. As the flow experiment of Hodson [2] was carried out with the same physical parameters as those used in the simulations, the comparison of the simulated and experimental velocity field is more relevant for the validation. Both the mean streamwise and RMS velocity profiles in the wall normal coordinate system are shown in the Fig.3b) and 4, respectively. For the mean streamwise velocity profiles the results are in good agreement with the experimental data from $x/C = 0.83$ to $x/C = 1$, excepted at $x/C = 0.95$ where the simulations predict a too strong deceleration of the flow. Concerning the RMS velocity profiles, the agreement with the experiment is satisfying up to $x/C = 0.95$. From this position the computations slightly over-predict the turbulence level especially in the lower part of the boundary layer. Concerning the influence of the SGS models, it can be noticed that this parameter does not have a large effect in the present computations, despite the fluid and subgrid viscosity ratio is about one. As the overall agreement between the LES and the experimental data are satisfying, one can suppose that the influence of the incoming wake on the boundary layer is well represented by the simulations. The Fig.5, which shows four different snapshots of a Q-criterion [14] iso-surface during one wake passing period, illustrates the influence of the cylinder wake on the turbulent structures located in the stator boundary layers. On the suction side, the boundary layer becomes turbulent because of the incoming turbulence due to the wake passage. But the flow rapidly relaminarizes when the wake goes downstream, which is in agreement with [3]. Near the trailing edge the same phenomenon occurs, but two-dimensional vortices are present in the boundary layer when the flow is laminar. The same structures were observed in the sim-

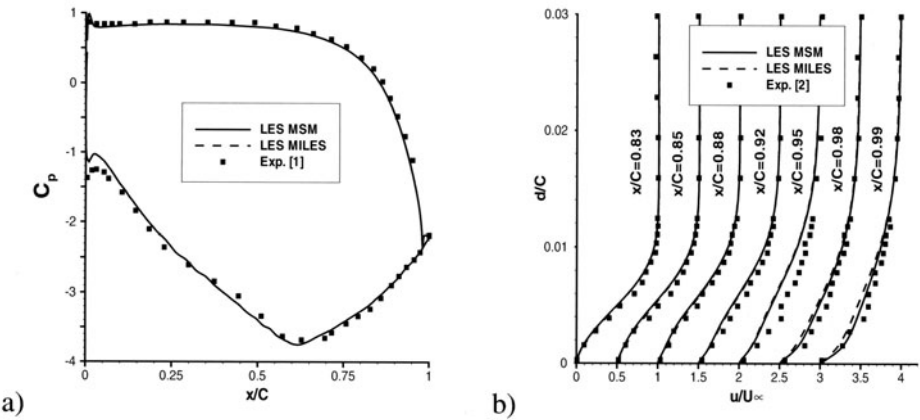


Figure 3. a) Mean pressure coefficient; b) Mean velocity profiles

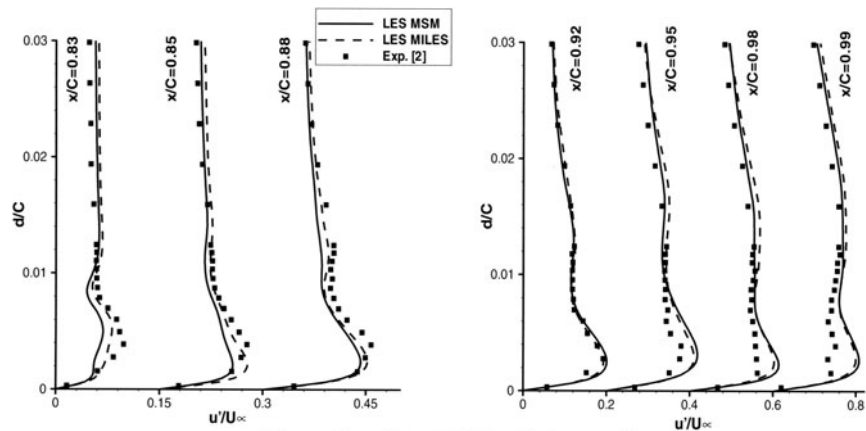


Figure 4. Mean RMS velocity profiles

ulation of Meinke [5], whereas the flow always remains fully turbulent in this zone in the DNS of Wu and Durbin [3] and Wissink [4]. But this difference is certainly due to the wake parameters retained in [5],[4], which are not identical to those of the present simulations concerning the cylinder velocity translation and the axial distance between the cylinder and the leading edge of the stator. Concerning the pressure side, longitudinal vortices due to the straining of the wake are present in the boundary layer, which is in agreement with the flow analysis done in [3],[4].

4. Conclusions

Well-resolved LES of the wake-blade interference in a Low Pressure Turbine have been carried out at a realistic Reynolds number and compared to available

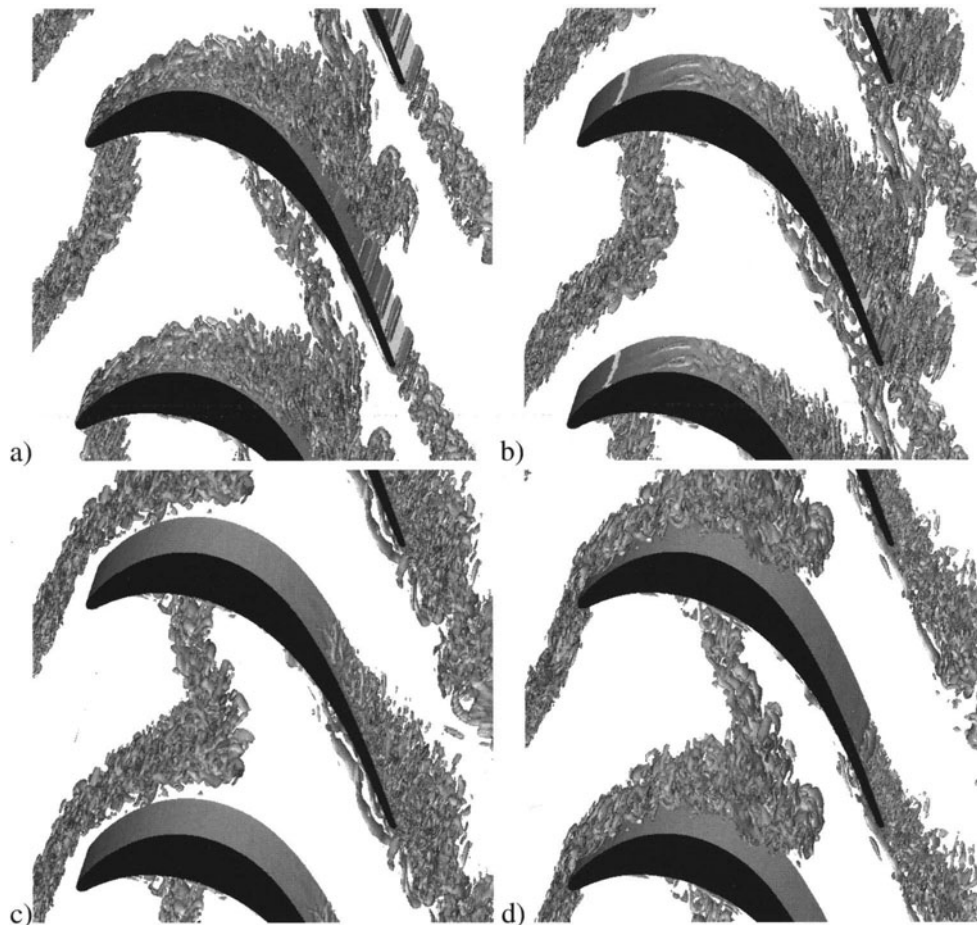


Figure 5. Instantaneous Q-criterion iso-surface at $t/T=$: a) 0.25 b) 0.5 c) 0.75 d) 1.

experimental data. From an industrial point of view, the mean and the RMS velocity profiles are in satisfying agreement with the experimental data. Moreover the use of a local mesh refinement technology allows the computational cost to be significantly reduced, since only 40 CPU hours are needed on a NEC SX5 to compute one wake passing period. Therefore LES should appear in a near future as a potential tool to predict some complex flow configuration in the turbomachinery domain, for which RANS model are still not enough accurate.

Acknowledgments

This work was supported by the Consortium Industry Research Turbomachinery. H. Hodson and L. Fottner very kindly provided the authors with experimental results.

References

- [1] Engber M. and Fottner L., "The effect of incoming wakes on boundary layer transition of a highly loaded turbine cascade", *AGARD-CP-571*, 1996.
- [2] Hodson H., "Turbulence Modeling for Unsteady Flows in Axial Turbine: TUR-MUNSFLAT", *Brite-EURAM III, Von Karman Institute, Brite-Euram Project, Final Technical Rept.*, CT96-1043, pp. 85-114, 2000.
- [3] Wu X. and Durbin P., "Evidence of longitudinal vortices evolved from distorted wakes in a turbine passage", *J. Fluid Mech.*, Vol. 446, pp. 199-228, 2001.
- [4] Wissink L. G., "DNS of separating low Reynolds number flow in a turbine cascade with incoming wakes", *Proceedings of Engineering Turbulence Modelling and Experiments - 5*, W. Rodi and N. Fueyo Eds, Mallorca, Spain, 16-18 september 2002.
- [5] Meinke M., "Turbulence Modeling for Unsteady Flows in Axial Turbine: TUR-MUNSFLAT", *Brite-EURAM III, Von Karman Institute, Brite-Euram Project, Final Technical Rept.*, CT96-1043, pp. 187-203, 2000.
- [6] Mary I. and Sagaut P., "Large-Eddy simulation of flow around an airfoil near stall", *AIAA J.*, Vol. 40, No. 6, pp. 1139-1145, 2002.
- [7] Raverdy B., Mary I., Sagaut P. and Liams N., "High-Resolution Large-Eddy Simulation of the flow around a low pressure turbine blade", *AIAA J.*, Vol. 41, No.3, pp. 390-397, 2003.
- [8] Lenormand E., Sagaut P. and Ta Phuoc L., "Moderate Reynolds number large-eddy simulation of compressible channel flow", *Int. J. Numer. Meth. Fluids*, vol. 32, pp. 369-406, 2000.
- [9] Boris J.P., Grinstein FF., Oran E.S. and Kolbe R.L., "New Insights into Large Eddy Simulation", *Fluid Dynam. Res.*, Vol. 10, pp. 199-228, 1992.
- [10] Péchier M., "Prévision numériques de l'effet Magnus pour des configurations de munitions", *PhD. Thesis*, université de Poitiers, France, 1999.
- [11] Mary I., "LES of the vortex breakdown behind a delta wing", *Int. J. Heat and Fluid Flow*, Vol. 24, pp. 596-605, 2003.
- [12] Quéméré P., Sagaut P. and Couailler V., "A new multi-domain/multi-resolution method for LES", *Int. J. Numer. Methods Fluids*, Vol. 36, pp. 391-416, 2001.
- [13] Williamson C., "Vortex dynamics in the cylinder wake", *Ann. Rev. Fluid Mech.*, Vol. 28, pp. 477-526, 1996.
- [14] Hunt J.C.R., Wray A.A. and Moin P., "Eddies, stream, and convergence zones in turbulent flows", *Center for Turbulence Research, Stanford, CA, Proceedings summer program*, pp. 193-208, 1988.

LES OF PASSING WAKES INFLUENCING TRANSITION ON TURBINE BLADES

S. Sarkar

Department of Mechanical Engineering, Indian Institute of Technology, Kanpur, India
subra@iitk.ac.in

Peter R Voke

Fluids Research Centre, School of Engineering, The University of Surrey, Guildford, UK
p.voke@surrey.ac.uk

Abstract Large-eddy simulations of wakes passing over highly cambered LP turbineblades (the T106 profile) for a Reynolds number of 1.6×10^5 are performed using wake data extracted from precursor simulations. The wake data are interpolated at the inlet plane of the cascade taking into account the kinematics of flow. We describe the effects of the wake kinematics and wake turbulence on the boundary layer developing over the suction surface of the blades. An insight into the underlying physical mechanism including the formation of rollup vortices during the wake-induced transition over an inflexional boundary layer is presented and the results are compared with experiment and DNS.

Keywords: Simulation, turbomachinery, wakes, transition.

1. Introduction

The study on the boundary layer developing over low-pressure (LP) turbine blades under the influence of passing wakes has received a great deal of attention owing to the importance of high lift blades. Periodic passing wakes from the upstream blade row have a strong influence on the flow field and heat transfer characteristics of the downstream blades. The resulting flow field is highly unsteady and the boundary-layer transition is greatly affected through phenomena known as wake-induced transition and calming. LP turbines operate at Reynolds numbers in the range of 0.9 to 2×10^5 , leading to the formation of a separation bubble on the suction side under steady flow condition. The interaction of oncoming wakes with this separation bubble further complicates the transition process, posing a challenge to researchers. Although significant progress has been made in understanding bypass transition based on attached

boundary layers (Myles 1991, Liu and Rodi 1992, Walker 1993, Schulte and Hodson 1998, Wu et al. 1999), the behaviour of a separated boundary layer under the influence of unsteady wakes has not been adequately addressed. Recent experiments conducted by Stieger and Hodson (2003) have provided an insight into the transition process resulting from the interaction of convective wakes and separation bubbles.

The present study describes the application of LES as a high-resolution time-dependent calculation to elucidate the flow dynamics and mechanism including the formation of rollup vortices during the wake-induced transition over a turbine blade. Realistic simulation of these processes is of great importance to the design of turbomachinery blades. Successful prediction of transition start and length, along with the structure of boundary layer transition would help in efficient design of turbine and compressor stages. Moreover, the problem of wake-induced transition over a turbine blade is not only of engineering interest but also of fundamental importance from the viewpoint of flow stability.

2. Numerical methods

The computational techniques employed have previously been applied to flat-plate bypass transition (Voke and Yang, 1995) and also to transition with reattachment following a geometry-induced separation (Yang and Voke, 2001). The methods are based on the fully covariant Navier-Stokes equations discretised using symmetry-preserving (and hence conservative) finite differences. The pressure problem is Fourier transformed in one dimension (in which periodicity of the flow and so uniformity of the geometry is imposed) and solved iteratively using multi-grid acceleration in the other two dimensions. The extension to highly skewed meshes around high-lift (and hence strongly cambered) modern LP turbine blades is non-trivial: the iterative solutions on such meshes do not always converge well or parallelise efficiently. These technical problems have been solved over the past three years, resulting in highly efficient LES code for simulation of turbulence even in strongly distorted 2D geometries.

DNS/LES poses a more stringent mesh requirement than Reynolds-averaged Navier Stokes computation. For the present study, a H-grid of good quality within the blade passage is developed by applying a power-law to the control functions appearing in the elliptic grid generation scheme of Hsu and Lee (1991). The grid lines generated are nearly orthogonal to boundaries. The simulations are performed on a grid with 384 points in the streamwise, 192 in the blade-to-blade plane and 32 in the spanwise directions with average y^+ less than 2.0 at the first grid point. The domain is 10 percent of chord in the spanwise direction. For modeling the non-resolvable subgrid scales (SGS), the classical Smagorinsky model with model constant of 0.125 and the wall

damping function modified to prevent extreme values near separation regions are used. To simulate the transitional flow, the low Reynolds number model of Voke (1996), which was derived following the dissipation spectrum, has been used.

Most experimental studies on the unsteady wake-induced transition have been performed by sweeping a row of wake-generating cylinders upstream of a flat plate or a cascade. However, the characteristics of these generated wakes have not been clearly specified. The large-scale simulations of wake passage over highly cambered blades (T106 profile) for a Reynolds number of 1.6×10^5 are performed using wake data extracted from precursor simulations. The wake-data are generated on a refined grid of $248 \times 384 \times 32$ for the flow passing a thin cylinder (2 percent of chord) and are interpolated at the inlet plane of cascade considering the kinematics of flow by matching the velocity triangles. The effects of wakes on the transition and calming process over the turbine blades in terms of the wake deficit and turbulent intensity are quantified. The computation required $13.5\mu\text{s}/\text{iteration}/\text{grid}$ based on 32 processors of an Origin 3000. Each wake passing cycle corresponds to 12000 time-steps. After 5 wake passing cycles, data are collected for the phase averaging over 8 cycles. In practice the simulation took about two months to perform.

3. Results and discussion

The principal objectives of the study are to gain insight into the underlying physical mechanisms of wake effects on transition over a separated boundary layer and also to explore key factors such as wake turbulence scale and intensity on transition and calming. All data gathered are analysed by phase averaging as well as through the study of instantaneous dynamics and spectral analyses. The LES results are compared with both experiments and DNS.

The unsteady wakes produce an incident flow that has two distinctive characteristics: a free-stream velocity defect described by kinematics and associated high turbulence during the wake passing. b Although the kinematics of the wake is partly responsible for the character of the boundary layer developing over the downstream blade rows, the effect of wake turbulence and its convection through the blade passage are also very important. The realistic representation of wake data is vital for the successor simulation of wake convection through a turbine cascade passage. The wake is generated by a small cylindrical wire, the dimension of which is about 2 percent of the blade chord. The mean turbulent kinetic energy and vorticity are symmetric along the line of symmetry of the cylinder. Spectral analysis of streamwise component of velocity indicates a value of Strouhal number of 0.2 with a wide spectrum in the spanwise direction.

The distortion of the migrating wake segments within the blade passage is characterized by bowing, orientation, elongation and stretching. After being segmented at the leading edge, the suction side and the pressure-side wakes behave differently. The suction-side portion wraps around the leading edge and is pulled towards the surface by the high flow velocity. This high acceleration over the suction surface creates stretching and thickens the wake width over the suction surface. The pressure side leg of the wake segment is under the action of a velocity field with nearly uniform direction but increasing strength away from the wall. The direction of the convective velocity is nearly perpendicular to the wake axis. This makes the wake rotate slowly in a counter-clockwise direction as it is convected downstream. Elongation of the wake is also gradual and is nearly traverse to the base flow. The difference in convective velocities near the suction and pressure side also causes bowing of the wake segment. As the downstream half of the pressure side is approached, the flow velocity undergoes a change in direction and increase in magnitude. The velocity is turned such that it becomes nearly parallel to the wake axis. This causes severe stretching and thinning of the wake segment.

The effect of a negative jet is also observed. A wake segment within the blade passage may be identified as a perturbation jet pointing towards the source of the wake. This negative jet has a velocity across the blade passage that causes the wake fluid to convect towards and impinge upon the suction surface. As the wake fluid impinges on the surface, it splits into two streams, one pointing downstream which accelerates the flow downstream of the approaching wake and one pointing upstream which retards the flow after the wake has passed. The negative jet effect within the blade passage also produces a pair of counter-rotating vortices. This can also be explained as a local concentration of vorticity produced by convection.

Further results on the transport and development of vorticity and turbulence kinetic energy, drawn from three-dimensional visualisations, will be presented elsewhere. How the boundary layer development, transition and calming are affected by the kinematics and turbulence of wake passing will be explained briefly in the following sections.

The time-averaged wall-static pressure coefficients with wake passing over the T106 blade from the present LES are compared with the undisturbed surface pressure distributions from experiment by Professor L. Fottner's group at the Univ. der Bundeswehr, München, Germany and the corresponding distributions with wake passing from the DNS of Wu and Durbin (2001), Fig 1a. The agreement between the present LES and DNS of Wu and Durbin is seen to be excellent. Small discrepancies between the simulations and the experiment may be attributed to different inflow conditions, endwall effects and compressibility. The phase-averaged wall static pressure coefficients over the rear part of the blade (magnified view) are presented in Fig 1b. As the wake is crossing

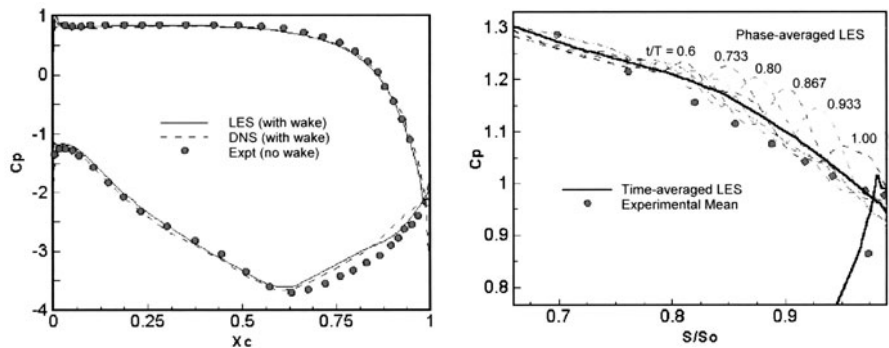


Figure 1. (a) Left: Time-averaged wall static-pressure coefficient C_p : present LES; DNS by Wu and Durbin 2001; and experiment (München). (b) Right: Phase-averaged C_p distributions on the T106 blade: present LES and experiment (Cambridge).

over the steady flow separation location, a series of large amplitude pressure oscillations are observed, particularly for $t/T > 0.73$ and the wake position $S/S_o > 0.70$. Figure 1b reveals that the peak-to-valley amplitude of these pressure fluctuations is $\Delta C_p = 0.15$. The corresponding experimental value is 0.3 [Stieger, 2002]. During the time $0.4 < t/T < 0.7$, as the wake is approaching the separation region, no pressure fluctuations over the rear part of the blade are observed. This is attributed to the calmed region of the boundary layer. It is worthwhile to mention that these pressure fluctuations are dependent on the wake turbulence intensity and length scale.

The process of phase averaging eliminates random fluctuations and shows large amplitude fluctuations, so the pressure oscillations reflected in the phase-averaged results indicate that they are formed by deterministic coherent structures in the flow. Recent work of Stieger *et al.* (2003) has shown that the formation of rollup vortices as the wake passes over the separating boundary layer is the cause of these pressure oscillations.

Velocity vectors plotted at $t/T = 0.85$ (not shown) indicate that velocity profile becomes inflexional at about $S/S_o = 0.8$ and a small separation bubble has formed. This is followed by two large regions of flow separation. Stream-line patterns illustrate that these separated regions are the manifestation of vortices formed as the wake passes over the region of inflexional velocity profiles. Iso-contours of spanwise vorticity depict the development of cats-eye patterns in the computed flow field, typical of the Kelvin-Helmholtz instability; thus these vortices embedded in the boundary layer are formed by rollup of the separated shear layers through an inviscid instability as the shear layers are perturbed by the wake fluid. Once the vortices are formed, the region of separation changes remarkably by convection of these coherent structures. The

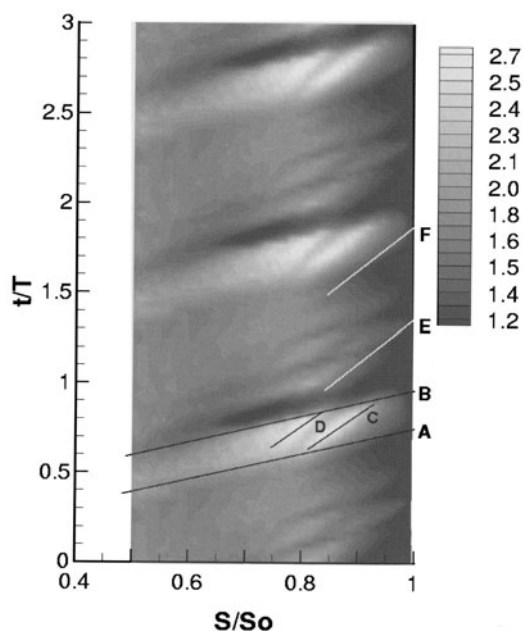


Figure 2. Space-time diagram of shape factor H .

3D views (figures not presented because of space) also illustrate longitudinal streaky structures, characteristics of transitional boundary layers [Alfredsson and Matsubara (1996), Westin et al (1994), Henningson et al (1993) and Wu et al (1999)]. The breakdown of these streaks into small and irregular structures that enhance turbulence is observed downstream. The visualization of the computed flow along with the experimental evidence lead to the firm conclusion that the pressure fluctuations on the rear part of the blade occur owing to the formation of vortices caused by the rollup of shear layers via the Kelvin-Helmholtz mechanism as the wake passes over the inflexional boundary layer. The transition process occurring on LP turbine blades is multi-modal and unsteady. A number of authors [Mayle (1991), Welker (1993), Addison and Hodson (1992), Schulte (1995) and Halstead et al (1997)] have described the development of the boundary layer through space-time (S-T) diagrams during wake passing. We highlight the state of boundary layer and the wake interaction by presenting the shape factor, H , in an S-T diagram, Fig 2. Two trajectory lines A and B denote the maximum and minimum velocity that occur owing to the kinematics of the passing wakes (the negative jet effect already explained). The centreline of the wake lies in between the trajectories A and B. When compared with the corresponding diagram presented by Stieger and Hodson

(2003), some discrepancies in the state of the boundary layer are observed, although the time-dependent nature is predicted well.

The outer part of the boundary layer is accelerated along A by the approaching wake. A delay in response to this increase of velocity occurs in the inner boundary layer due to viscous effects. As a result, the outer part of the boundary layer accelerates more than the inner part and the level of H is increased in between lines A and B and downstream of $S/S_o = 0.6$. The coherent structures marked by C and D originating along the wake centreline are distinctly revealed by an increased level of shape factor. This is attributed to the thickening of the shear layer due to vortices formed by rollup of laminar shear layer over the inflexional velocity profile. These structures travel downstream at a speed lower than the local free-stream, following the trajectories C and D, and finally break down to a turbulent boundary layer creating a wedge-shaped perturbation. A typical wake-induced transition, forming a turbulent strip, occurs at $S/S_o = 0.7$ along the trajectory B. This process, which lags behind the wake passing, may be attributed to the diffusion of wake turbulence into the boundary layer, causing bypass transition. Orth (1993) mentioned that the disturbance caused by periodic passing wake enters the boundary layer early and convects with it before triggering transition. The line E, drawn at 35 percent of the free-stream speed, is parallel to the trailing edge of the wake-induced turbulent strip. The turbulence created by the breakdown of the coherent structures C and D also merges with the turbulent strip. Some difference of the state of the boundary layer between the computation and experiment (Stieger and Hodson, 2003) is found between the trajectories E and F. A few wedge-shaped turbulent perturbations are evident between lines E and F. We suggest that even behind the line E, up to F, transition takes the form of bypass transition through disturbances either from the free-stream or from the breakdown of coherent structures generated by inviscid instability of the shear layer. The calming of the boundary layer is evident just beyond the trajectory line F, characterized by a slow increase of shape factor.

4. Conclusions

An innovative method has been presented using coupled simulations of flow past a small cylinder for generating a wake, providing space- and time-dependent inflow conditions for the successor large-eddy simulation of wake interaction with an LP turbine blade. The kinematics of wake convection illustrates a dramatic difference in wake deformation between the pressure and suction sides. The suction-side wake is highly irregular with a good deal of small-scale turbulence. The pressure-side wake suffers from severe stretching and thinning with the decay of turbulence. The large amplitude of pressure fluctuations over the rear half of the suction surface represent a novel type of

wake-boundary-layer interaction. As the wake passes over inflexional boundary layer, coherent vortices are generated owing to inviscid instability over the last 30 percent of the surface length. The vortices play an important role in the generation of turbulence and thus decide the transitional length, which becomes time-dependent. The source of the pressure fluctuations on the rear part of the suction surface is also identified as the formation of these coherent structures. The calmed region is nothing but attached flow with fewer perturbations as the boundary layer tends to relax after wake passing, but the level of turbulent intensity suggest the boundary layer is still transitional.

Acknowledgments

The support of the UK Engineering and Physical Sciences Research Council and of Rolls-Royce plc for this work is gratefully acknowledged.

References

- Alfredsson P H, and Matsubara M, 1996. Streak structure in transition, *Transitional Boundary Layers in Aeronautics*, (ed. R.A.W.M. Henkes and L.J. Ingen), pp. 374-386. Elsevier.
- Bisset D K, Antonia R A and Browne L.W.B, 1990. Spatial organization of large structures in the turbulent far wake of a cylinder, *Journal of Fluid Mech.*, **218**, 439-461.
- Halstead D E, Wisler D C, Okiishi T H, Walker, G J, Hodson H P and Shin H W, 1997. Boundary layer development - part 1: composite picture; part 2: compressors; part 3: LP turbines; part 4: computational analysis, *ASME J. Turbomachinery*, **119**, 114-127, 128-138, 225-237, 426-443.
- Henningsson D S, Lundbladh A and Johansson A V, 1993. A mechanism for bypass transition from localized disturbances in wall-bounded shear flows, *Journal of Fluid Mech.*, **250**, 169-207.
- Hue K and Lee S L, 1991. A numerical technique for two-dimensional grid generation with grid control at all of the boundaries, *J. Comput. Phys.*, **96**, 451-469.
- Hussain A K M F and Hayakawa M, 1987. Eduction of large-scale organized structure in a turbulent plane wake, *Journal of Fluid Mech.*, **180**, 193-229.
- Liu X and Rodi W, 1992. Measurement of unsteady flow and heat transfer in a linear turbine cascade, ASME Paper No. 92-GT-323.
- Mayle R E, 1991. The role of laminar turbulent transition in gas turbine engines, *ASME J Turbomachinery*, **113**, 509-537.
- Rogers M M, 2000, "The evolution of strained turbulent plane wakes". *Journal of Fluid Mech.*, (submitted).
- Schulte V and Hodson H P, 1998. Unsteady wake-induced boundary layer transition in high lift LP turbine, *ASME J Turbomachinery*, **120**, 28-35.
- Stadt Müller P and Fottner L, 2002. A test case and experimental measurements on T106, private communication with Lothar Hilgenfeld.
- Voke P R and Yang Z, 1995. Numerical Study of Bypass Transition, *Phys. Fluids*, **7**, 2256-2264.
- Voke P R, 1996. Subgrid-Scale Modelling at Low Mesh Reynolds Number, *Theoret. Comput. Fluid Dynamics*, **8**, 131-143.
- Yang Z Y and Voke P R, 2001. Large-Eddy Simulation of Boundary Layer Separation and Transition at a Change of Surface Curvature, *J. Fluid Mech.*, **439**, 305-333.

LES OF FLOW IN A LOW PRESSURE TURBINE CASCADE WITH ONCOMING WAKES

The effect of Wake Strength and Frequency

Jan Wissink, Wolfgang Rodi

*Institute for Hydromechanics, University of Karlsruhe,
Kaiserstr. 12, D-76131 Karlsruhe, Germany*

wissink@ifh.uni-karlsruhe.de, rodi@ifh.uni-karlsruhe.de

Vittorio Michelassi

*Dipartimento di Ingegneria Meccanica e Industriale, Università Roma Tre,
Via della Vasca Navale 79, 00146 Rome, Italy*

michelas@uniroma3.it

Abstract Three-dimensional large eddy simulations of flow in a low-pressure turbine cascade consisting of modern highly loaded turbine blades have been performed. The effects of the variation of frequency and strength of the impinging wakes on the suction side boundary layer transition are studied. Weak impinging wakes with a low frequency only manage to mildly trigger unstable modes, leading to a natural transition scenario. With increasing strength and/or frequency, the triggering becomes more intense and a by-pass transition scenario is obtained. In none of the simulations the boundary layer is found to become fully turbulent.

Keywords: LES, Transition, Free-stream disturbances

1. Introduction

Because of advances in computational power, recently DNS and LES of flow in a Low-Pressure Turbine (LPT) cascade have become feasible (Fujiwara *et al.* (2002); Kalitzin *et al.* (2002); Michelassi *et al.* (2003a); Wissink (2003); Wu and Durbin (2001)). As part of the German Research Foundation (DFG) project "Periodic Unsteady Flow in Turbo-machinery" three-dimensional Large Eddy Simulations (LES) of flow in such a LPT cascade, consisting of modern highly loaded low-pressure turbine blades, are carried out and some of the more qualitative results are reported here. Earlier LES

of flow in a similar cascade were performed by Fujiwara *et al.* (2002), while experiments in such a cascade were performed by Schulte and Hodson (1998). For boundary layer flow around a turbine blade, three types of transition can be distinguished (Mayle (1991)). When the impinging disturbances are very weak, the boundary layer is only mildly triggered and a natural transition scenario driven by Tollmien-Schlichting waves will appear (Schlichting (1979)). Owing to the large free-stream turbulence levels in a real multi-stage environment this scenario is very unlikely to occur. Provided the Reynolds number is large enough, stronger impinging disturbances will usually give rise to by-pass transition (Wu *et al.* (1999)). Here, some of the stages of natural transition are skipped. By-pass transition is usually characterised by the appearance of longitudinal streaks that become unstable to spanwise disturbances, resulting in the formation of turbulent spots which grow as they are convected in the downstream direction and subsequently merge to form a fully turbulent boundary layer. In regions with a strong adverse pressure gradient, the boundary layer is likely to separate. Since such a separated boundary layer is very unstable, it will usually undergo rapid transition to turbulence. The near wall turbulent flow will relax downstream and, provided the length of the blade is large enough, eventually form a turbulent boundary layer (Wissink (2003)).

1.1 Computational Aspects

The computational domain is chosen to resemble the experiments performed by Schulte and Hodson (1998) and is given in Figure 1. The experiments

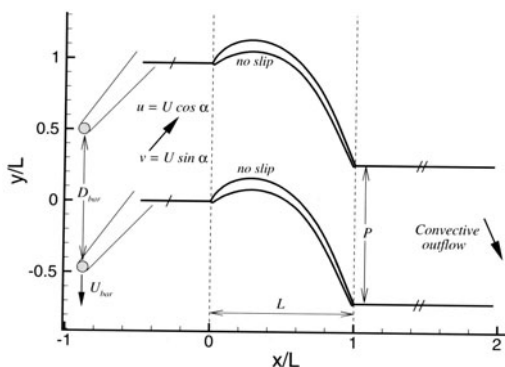


Figure 1. The computational domain.

were performed employing a Reynolds number of $Re = 130\,000$ (based on chord length and exit conditions). For the LES a Reynolds number (based on the mean inflow velocity U_0 and the axial chord length L - see Figure 1) of $Re = 100\,000$ is chosen. The latter Reynolds number is large enough for the boundary layer to become unstable, while still allowing a good resolu-

Table 1. Overview of the large eddy simulations.

Simulation	Incoming wakes	D_{bar}	d
A	No	—	—
B	Yes	P	$0.0157L$
C	Yes	$\frac{1}{2}P$	$0.0157L$
D	Yes	$\frac{1}{2}P$	$0.0315L$
E	Yes	P	$0.0315L$

tion of the flow using a relatively moderate number of 11.5×10^6 grid points. The mesh was optimised using experience gained in earlier Direct Numerical Simulations (DNS) and LES of periodic unsteady flow in a T106 cascade (Michelassi *et al.* (2003a); Wissink (2003)). In the y -direction, 20–25 grid points are placed inside the boundary layer, and the grid sizes, in wall-units, in the streamwise and spanwise direction are less than 60 and 12–18, respectively. As illustrated in Figure 1, periodic boundary conditions are employed in the y -direction for $x/L < 0$ and $x/L > 1$, while on the surface of the blade no-slip boundary conditions are prescribed. The size of the spanwise direction, where periodic boundary conditions are applied, is $l_z = 0.15L$. At the outflow plane a convective boundary condition is prescribed, while at the inflow plane artificial turbulent wakes are introduced, superposed on the mean flow field $(u, v, w) = U(\cos \alpha, \sin \alpha, 0)$, where $\alpha = 30.46^\circ$. The wake data has been kindly made available by Xiaohua Wu and Paul Durbin of Stanford University. Its statistical properties are described in Wu *et al.* (1999). The artificial wake data corresponds to plane wakes generated by a row of bars, located in the plane $x/L = -0.60L$, moving in the negative y -direction with speed $U_{bar} = 1.23U$. The pitch between blades is $P = 0.9694L$. The distance between bars, D_{bar} , and the diameters of the bars, d , is varied to be able to study both wake-wake interaction and the effect of the strength of the wake on the boundary layer transition (see Table 1). The simulations are performed using a second-order accurate central finite-volume discretisation of the three-dimensional, incompressible Navier-Stokes equations in space, combined with a three-stage Runge-Kutta method for the time-integration. To avoid a decoupling of the pressure field and the velocity field due to the collocated variable approach used, the momentum interpolation procedure of Rhie and Chow (1983) is employed. For a more detailed description of the code we refer to Breuer and Rodi (1996). The SubGrid-Scale (SGS) model employed in the LES is the dynamic model by Germano *et al.* (1991). The calculations have been performed on the Hitachi SR8000-F1 of HLRS (University of Stuttgart) using 64 processors and the standard Message Passing Interface (MPI) protocol for communication between blocks.

2. Results

In Figures 2 (a) and (b), the respective time-averaged wall static-pressure coefficients of the simulations listed in Table 1 are displayed along with the experiments of Schulte and Hodson (1998), which were performed using the same blade geometry with slightly different operating conditions. The wall static-pressure coefficient, C_p , defined by $C_p = (P_{01} - P)/(P_{01} - P_2)$, where P is the local static pressure, P_{01} is the inlet total pressure, and P_2 is the outlet static pressure, is plotted as a function of the normalised wall-coordinate, S/S_{max} . The wall coordinate is normalised such that $S/S_{max} = 0$ corresponds to the leading edge, while $S/S_{max} = 1$ corresponds to the trailing edge. The time averaged data are obtained by averaging the well developed flow field during 3.15 time-units in Simulation *A* and, alternatively, during 10 periods of simulation in Simulations *B*–*E*, where one period corresponds to a tangential sweep over the bar distance D_{bar} . Figure 2 (a), shows that a reasonably good agreement

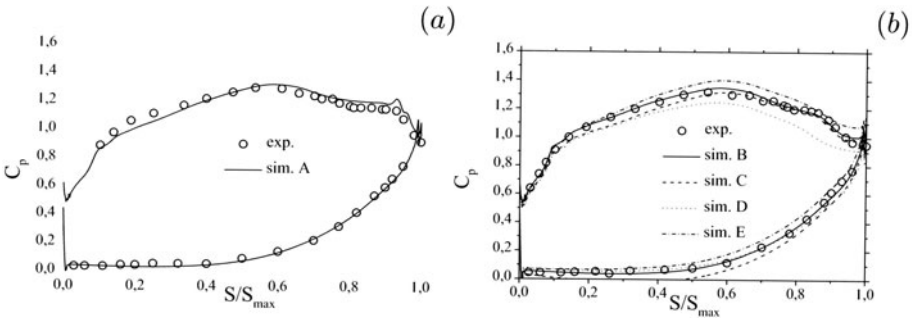


Figure 2. Time-averaged wall static-pressure coefficient. (a): Without wakes (Simulation A), (b): with wakes (Simulations B-E).

is obtained between the measurements and Simulation *A*, performed in the absence of wakes. While the static pressure distribution along the pressure side is captured very well in the simulation, along the suction side small deviations can be observed. Here, the small peak near $S/S_{max} \approx 0.9$ indicates that the flow is likely to separate near the trailing edge. This is confirmed by the LES-results, which show that the flow separates at $S/S_{max} \approx 0.72$ and re-attaches just upstream of the trailing edge. In Figure 2 (b), the simulations with variable incoming wake strength and frequency are compared with typical experimental results obtained using $0.0157L$ diameter bars and with only one wake per blade-pitch. As expected, the best agreement between the measurements and the computations is found for Simulation *B*, where similar operating conditions are employed as in the experiments. All the computed results exhibit a "knee" in the static pressure distribution at approximately $S/S_{max} = 0.85$. This position on the suction side of the blade corresponds to the transition to

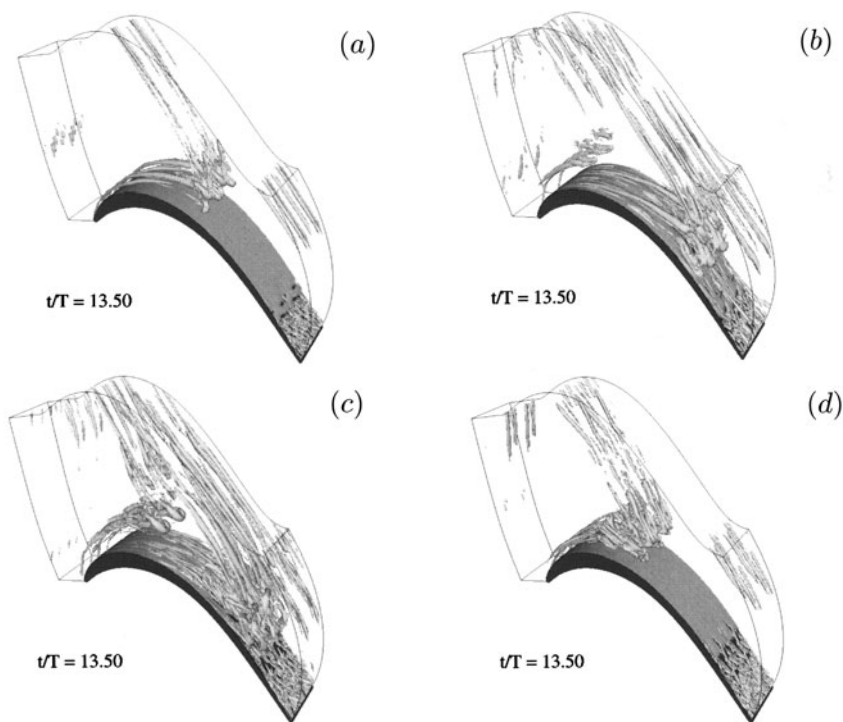


Figure 3. Snapshots of vortical structures found inside the passage between two turbine blades. The vortical structures have been made visible using the λ_2 criterion of Jeong and Hussain (1995). (a): Simulation B; (b): Simulation C; (c): Simulation D; (d): Simulation E.

turbulence of the boundary layer. Observe that the decrease of the suction side static pressure for $S/S_{max} > 0.8 - 0.85$ becomes smoother with increasing wake strength. Note that some of the observed differences between the four static pressure distributions can be attributed to the different inlet total pressure. These differences stem from the variable losses induced by the different wakes starting at the inlet section and continuing downstream.

In Figure 3 snapshots of the vorticity field inside the passage between blades are shown. The figure clearly illustrates the more intense triggering of the suction side boundary layer in the simulations with increased wake-strength (Simulations D and E) and increased wake-frequency (Simulations C and D). In the latter simulations, the boundary layer has only little time to relaminarise in between two subsequent impinging wakes, such that during the entire period a large part of the suction side boundary layer is found to carry disturbances. Comparing the effects of the increase of wake-strength and wake-frequency to one another, the increase of wake frequency is found to have the largest effect on the suction side boundary layer. A series of snapshots showing close-ups

of vortical structures present inside the downstream half of the suction side boundary layer is displayed in Figure 4 (Simulation *B*) and Figure 5 (Simulation *D*). The figures illustrate the dynamics of these vortical structures during

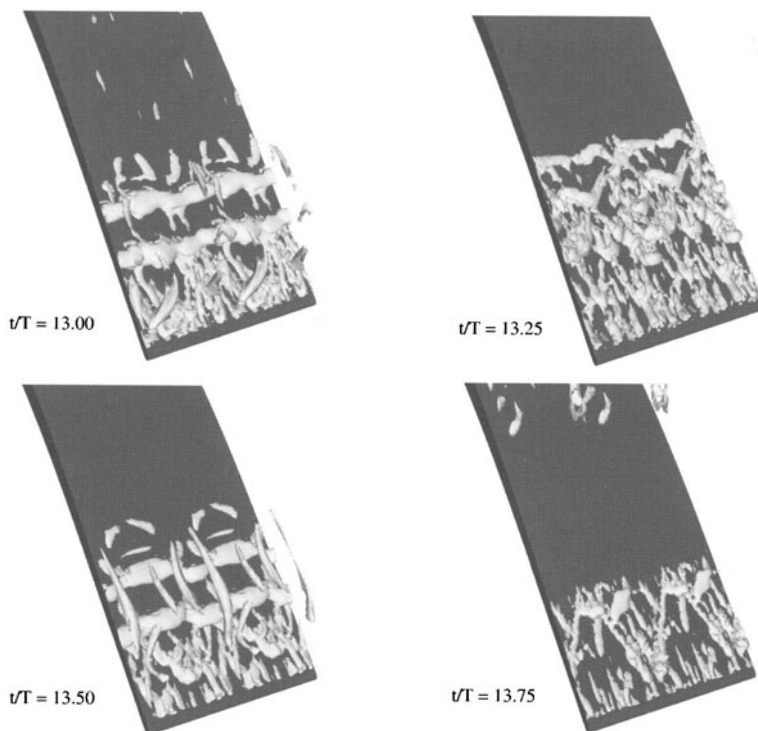


Figure 4. Simulation *B*: snapshots showing the evolution of vortical structures along the suction side near the trailing edge during one period. The λ_2 criterion has been used to identify vortical structures.

one period. The relatively weak wakes with a low frequency in Simulation *B* (see Figure 4) only mildly trigger the suction side boundary layer and leave it ample time to relaminarise. Only very close to the trailing edge, some disturbances remain present in the boundary layer at all times. In the snapshots at $t/T = 13.25$ and $t/T = 13.50$, various Λ -vortices can be observed. The spanwise rollers, visible at $t/T = 13.00$, correspond to Tollmien-Schlichting waves, which are triggered by the impinging wakes and form the first stage of natural transition. The laminar-turbulent transition is found to end approximately when the Λ -vortices start to become unstable. Here, one has to keep in mind that the boundary layer is only reasonably resolved and the resolution of the wakes in the passage between blades is hardly sufficient. In an earlier LES of flow in a T106 cascade at $Re = 148\,000$, similar resolution problems were found to delay boundary layer transition (Michelassi *et al.* (2003b)).

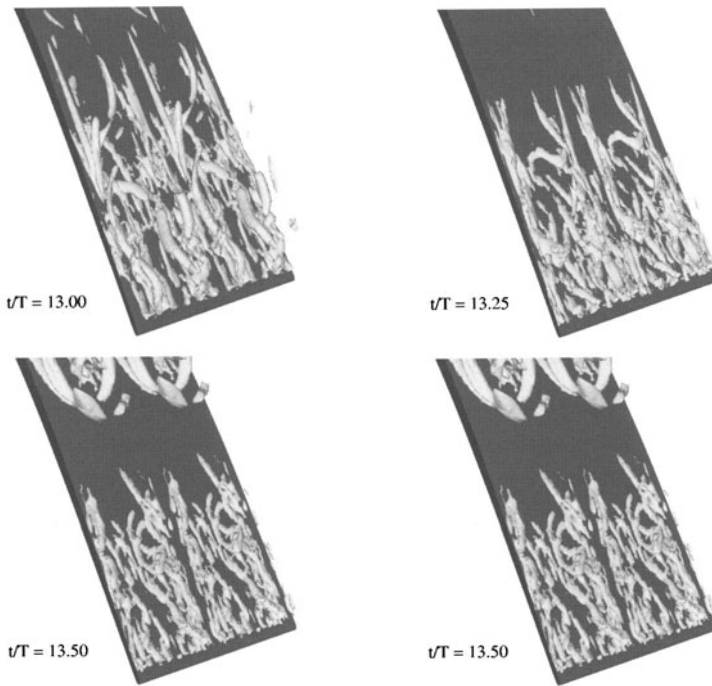


Figure 5. Simulation D: snapshots showing the evolution of vortical structures along the suction side near the trailing edge during one period. The λ_2 criterion has been used to identify vortical structures.

The vortical structures found in Simulation *D* (see Figure 5), which is the simulation with the highest wake-frequency and the strongest wakes, are found to be much more pronounced than in Simulation *B*. Along the downstream half of the suction side many longitudinal, streamwise vortical structures are observed of which the scale becomes smaller when approaching the trailing edge. Though no turbulent spots were found, the streak-like structures do indicate the presence of a by-pass transition scenario. As in Simulation *B*, even near the trailing edge the suction side boundary layer does not turn fully turbulent at any time.

3. Conclusions

Large eddy simulations of flow in a modern highly loaded turbine cascade have been performed. The comparison of the wall static-pressure with experiments performed by Schulte and Hodson (1998) shows a fair agreement. By varying the frequency and the strength of the wakes, a qualitative study of the laminar-turbulent transition of the suction side boundary layer flow has been made. In the simulation with weak impinging wakes and a low wake-frequency, a nat-

ural transition scenario is obtained, while the streaky structures found in the simulation with the strongest wakes and the highest wake-frequency give evidence of a by-pass transition scenario. In none of the simulations the boundary layer flow managed to become turbulent.

A fuller account of the results will be given in a future publication.

Acknowledgments

The authors wish to thank the German Research Foundation (DFG) for funding this project and the steering committee of the supercomputing facilities of HLRS in Stuttgart for granting computing time on the Hitachi SR8000-F1.

References

- Breuer, M., Rodi, W. (1996). *Large eddy simulation of complex turbulent flows of practical interest*. In: Flow Simulation with High Performance Computers II, Notes on Num. Fluid Mechanics, Vieweg Verlag.
- Fujiwara, H., Voke, P.R., Arakawa, C. (2002). *Large Eddy Simulation of TL10 LP Turbine blade row*. In: Rodi, W., Fueyo, N. (eds) Engineering Turbulence Modelling and Experiments 5, Elsevier 751–758.
- Kalitzin, G., Wu, X., Durbin, P.A. (2002). *DNS of fully turbulent flow in a LPT passage*. In: Rodi, W., Fueyo, N. (eds) Engineering Turbulence Modelling and Experiments 5, Elsevier 741–750.
- Germano, M., Piomelli, U., Moin, P., Cabot, W.H. (1991). *A dynamic subgrid-scale eddy viscosity model*. Phys. Fluids A, **3** (7) 1760–1765.
- Jeong, J., Hussain, F. (1995). *On the identification of a vortex*. J. Fluid Mech., **285**, 69–94.
- Mayle, R.E. (1991). *The role of laminar-turbulent transition in gas turbine engines*. ASME J. of Turbomachinery., **113**, 509–537.
- Michelassi, V., Wissink, J.G., Rodi, W. (2003a). *Analysis of DNS and LES of flow in a low-pressure turbine cascade with incoming wakes and comparison with experiments*. Accepted for publication in Flow, Turbulence and Combustion.
- Michelassi, V., Wissink, J.G., Fröhlich, J., Rodi, W. (2003b). *Large-eddy simulation of flow around a low pressure turbine blade with incoming wakes*. To appear in AIAA J.
- Schlichting, H. (1979). *Boundary layer theory*. McGraw-Hill New York.
- Schulte, V., Hodson, H.P. (1998). *Unsteady, wake-induced boundary layer transition in high lift LP turbines*. ASME J. of Turbomachinery, **120**, 28–34.
- Rhie, C.M., Chow, W.L. (1983). *Numerical Study of the Turbulent Flow Past an Airfoil with Trailing Edge Separation*. AIAA J., **21**, 1525–1532.
- Wissink, J.G. (2003). *DNS of separating, low Reynolds number flow in a turbine cascade with incoming wakes*. Accepted for publication in Int. J. of Heat and Fluid Flow.
- Wu, X., Durbin, P.A. (2001). *Evidence of longitudinal vortices evolved from distorted wakes in a turbine passage*. J. Fluid Mech., **446**, 199–228.
- Wu, X., Jacobs, R.G., Hunt, J.C.R., Durbin, P.A. (1999). *Simulation of boundary layer transition induced by periodically passing wakes*. J. Fluid Mech., **398**, 109–153.

ERCOFTAC SERIES

1. A. Gyr and F.-S. Rys (eds.): *Diffusion and Transport of Pollutants in Atmospheric Mesoscale Flow Fields*. 1995 ISBN 0-7923-3260-1
2. M. Hallbäck, D.S. Henningson, A.V. Johansson and P.H. Alfredsson (eds.): *Turbulence and Transition Modelling*. Lecture Notes from the ERCOFTAC/IUTAM Summerschool held in Stockholm. 1996 ISBN 0-7923-4060-4
3. P. Wesseling (ed.): *High Performance Computing in Fluid Dynamics*. Proceedings of the Summerschool held in Delft, The Netherlands. 1996 ISBN 0-7923-4063-9
4. Th. Dracos (ed.): *Three-Dimensional Velocity and Vorticity Measuring and Image Analysis Techniques*. Lecture Notes from the Short Course held in Zürich, Switzerland. 1996 ISBN 0-7923-4256-9
5. J.-P. Chollet, P.R. Voke and L. Kleiser (eds.): *Direct and Large-Eddy Simulation II*. Proceedings of the ERCOFTAC Workshop held in Grenoble, France. 1997 ISBN 0-7923-4687-4
6. A. Hanifi, P.H. Alfredson, A.V. Johansson and D.S. Henningson (eds.): *Transition, Turbulence and Combustion Modelling*. 1999 ISBN 0-7923-5989-5
7. P.R. Voke, N.D. Sandham and L. Kleiser (eds.): *Direct and Large-Eddy Simulation III*. 1999 ISBN 0-7923-5990-9
8. B.J. Geurts, R. Friedrich and O. Métais (eds.): *Direct and Large-Eddy Simulation IV*. 2001 ISBN 1-4020-0177-0
9. R. Friedrich, B.J. Geurts and O. Métais (eds.): *Direct and Large-Eddy Simulation V*. Proceedings of the fifth international ERCOFTAC workshop on direct and large-eddy simulation, held at the Munich University of Technology, August 27-29, 2003. 2004 ISBN 1-4020-2032-5